

Advances in Cognitive Neurodynamics

Takashi Omori · Yoko Yamaguchi
Yutaka Sakaguchi · Naoyuki Sato
Ichiro Tsuda *Editors*

Advances in Cognitive Neurodynamics (III)

Proceedings of the
Third International Conference
on Cognitive Neurodynamics – 2011

 Springer

Advances in Cognitive Neurodynamics (III)

Yoko Yamaguchi
Editor

Advances in Cognitive Neurodynamics (III)

Proceedings of the Third International
Conference on Cognitive
Neurodynamics – 2011

 Springer

Editor
Yoko Yamaguchi
Laboratory for Dynamics of Emergent
Intelligence
RIKEN Brain Science Institute
Wako City
Japan

ISBN 978-94-007-4791-3 ISBN 978-94-007-4792-0 (eBook)

DOI 10.1007/978-94-007-4792-0

Springer Dordrecht Heidelberg New York London

Library of Congress Control Number: 2008928127

© Springer Science+Business Media Dordrecht 2013

This work is subject to copyright. All rights are reserved by the Publisher, whether the whole or part of the material is concerned, specifically the rights of translation, reprinting, reuse of illustrations, recitation, broadcasting, reproduction on microfilms or in any other physical way, and transmission or information storage and retrieval, electronic adaptation, computer software, or by similar or dissimilar methodology now known or hereafter developed. Exempted from this legal reservation are brief excerpts in connection with reviews or scholarly analysis or material supplied specifically for the purpose of being entered and executed on a computer system, for exclusive use by the purchaser of the work. Duplication of this publication or parts thereof is permitted only under the provisions of the Copyright Law of the Publisher's location, in its current version, and permission for use must always be obtained from Springer. Permissions for use may be obtained through RightsLink at the Copyright Clearance Center. Violations are liable to prosecution under the respective Copyright Law.

The use of general descriptive names, registered names, trademarks, service marks, etc. in this publication does not imply, even in the absence of a specific statement, that such names are exempt from the relevant protective laws and regulations and therefore free for general use.

While the advice and information in this book are believed to be true and accurate at the date of publication, neither the authors nor the editors nor the publisher can accept any legal responsibility for any errors or omissions that may be made. The publisher makes no warranty, express or implied, with respect to the material contained herein.

Printed on acid-free paper

Springer is part of Springer Science+Business Media (www.springer.com)

Preface

Five decades of brain research have led to the emergence of a new field, spanning the entire spectrum of cognition from synaptic dynamics to social interactions, and which integrates nonlinear neurodynamics operating simultaneously at and across various scales. A new kind of scientist is emerging, schooled in multiple academic disciplines, comfortable in working with data from different levels, and conversant with the mathematical and computational tools that are essential to cross the boundaries of these disciplines.

Cognition, in its essence, is dynamic and multilayered, and the pursuit of new clues inevitably leads us from one layer to the next, both reductionist and holistic. A new trend in the study of cognition from the point of view of neurodynamics has emerged as a result of the rapidly evolving developments of the activity within the field of Nonlinear Dynamics and Cognitive Science.

In order to promote the integration of Cognitive Science and Neurodynamics as a whole, the International Conference on Cognitive Neurodynamics has been held biannually since 2007 under the support of the editorial board meeting of Cognitive Neurodynamics (Springer). The first conference, ICCN2007, was held in Shanghai, and the second, ICCN2009, in Hangzhou, also in China.

And this was the third ICCN, at The Hilton Niseko Village, Hokkaido, Japan, from June 9–13, 2011. Due to the tragedies of the Great East Earthquake and ensuing tsunami in Japan, many people had difficulty in attending, so we are very grateful for the efforts of those who nonetheless helped to make ICCN2011 a success. There were 161 participants from 17 countries, 6 plenary talks by Prof. Leslie Kay, Prof. Robert Kozma, Prof. Soo-Young Lee, Prof. Hajime Mushiake, Prof. Noriko Osumi, and Prof. Peter Robinson, 130 papers, and invited lectures by 3 renowned researchers, Prof. Shun-ichi Amari, Prof. Minoru Tsukada, and Prof. Walter Freeman.

The conference ranged from a microscopic model of the neural impulse to a macroscopic model of the sleeping rhythm. Key sessions were: Neuronal Impulse, Patterns and Bifurcation, Integrative and Multi-level Approaches for Cognitive Neurodynamics, Model Complexity in Neural Network Phenomena, Toward Understanding of Intelligence: Collaboration between Neuroscience and Robotics, Spatiotemporal Network Dynamics, Shaping Embodied Neurodynamics through

Interaction, Mathematical and Statistical Aspects of Neurodynamics, Dynamic Patterns of Neural Activity in Human Information Processing, and Neural Basis of Biological Timing. We express our sincere appreciation to all the session organizers. We also appreciate the session presenters who maintained discussions throughout the sessions and at the poster presentations.

Another highlight was the young researcher session in which we asked young researchers to discuss and create a tentative collaboration plan which was then evaluated by the senior researchers. The young researchers learned much from the suggestions of the senior people. We also wish to acknowledge the Dynamic Brain Forum (DBF), co-organized with ICCN2011, and in particular, Prof. Jan Lauwerence for his organization of DBF sessions.

Historically, DBF was the “Origin of Brain Dynamics Study”, the core research field of ICCN. DBF was initiated by the Japanese “Gang of Five” who were focused on nonlinear dynamics and their activity led to related work in Cognitive Neurodynamics in China which finally resulted in ICCN2007. So, ICCN owes much to DBF for their research field concept establishment, and ICCN2011 was happy to have coordinated with DBF2011. The next ICCN2013 will be held in Sigtuna, Sweden, by Prof. Hans Lijenstrom (Swedish Univ. of Agricultural Science). We look forward to sharing fresh topics and ideas both among the people who originally gathered at Niseko and with all other attendees.

We would also like to express our gratitude to the supporting organizations, Grant-in-Aid for Scientific Research on Innovative Areas “The study on the neural dynamics for understanding communication in terms of complex hetero systems (No.4103)” of MEXT Japan, RIKEN BSI, and Tamagawa University Global COE Program “Origins of the Mind”; for financial support from SCAT, sponsorship by Springer, FIRST project and Budapest Seminar, and co-sponsorship by JNNS, INNS and CNS. We hope all the supporting activity will continue to foment the development of this fast-moving and exciting scientific field.

Yoko Yamaguchi
Takashi Omori
Ichiro Tsuda

Contents

Part I Global Scope of Cognitive Neurodynamic Systems

Artificial Cognitive Systems with Active Learning and Situation Awareness Capabilities	3
Soo-Young Lee	
Dynamic Neuronal Representation in the Prefrontal Cortex	9
Hajime Mushiake, Keisetsu Shima, Kazuhiro Sakamoto, Yuichi Katori, and Kazuyuki Aihara	
Timing at Multiple Scales in Olfactory Perception	17
Leslie M. Kay	
Structure, Stability, Dynamics, and Geometry in Brain Networks	23
Peter A. Robinson	
Mathematical Theory of Neural Networks: A Personal and Historical Survey	31
Shun-ichi Amari	
Memory Information Representation in the Hippocampus	37
Minoru Tsukada	

Part II Neuronal Impulse Patterns, Bifurcations and Model Complexity

Functional Significance of Rall's Power of Three Halves Law in Cortical Nonpyramidal Cells	45
Yoshiyuki Kubota, Masaki Nomura, Fuyuki Karube, and Yasuo Kawaguchi	

A Computational Study of the Role of the Sub-thalamic Nucleus in Behavioral Switching During Saccadic Movements	53
Rengaswamy Maithreye and V. Srinivasa Chakravarthy	
Spiking Neural Network Ink Drop Spread, Spike-IDS	59
Mohsen Firouzi, Saeed Bagheri Shouraki, and Mohammad Ghomi Rostami	
A Biophysical Model of Neuro-Glial-Vascular Interactions	69
Bankim S. Chander and V. Srinivasa Chakravarthy	
Model Complexity in the Study of Neural Network Phenomena	77
Claus C. Hilgetag, Marc-Thorsten Hütt, and Changsong Zhou	
From Spiking Neurons to Neural Fields: Bridging the Gap to Achieve Faster Simulations of Neural Systems	83
Peter A. Robinson and Jong Won Kim	
Multi-population Network Models of the Cortical Microcircuit	91
Tobias C. Potjans and Markus Diesmann	
Attentional Cholinergic Projections May Induce Transitions of Attractor Landscape via Presynaptic Modulations of Connectivity	97
Hiroshi Fujii, Takashi Kanamaru, Kazuyuki Aihara, and Ichiro Tsuda	
Forced Wakefulness for Entrainment to Permanent Shift Work: A Computational Study	105
Svetlana Postnova and Peter A. Robinson	
Towards a Modeling and Simulation Platform for Multi-level Neuronal Networks	113
Yoshiyuki Asai, Hideki Oka, Taishin Nomura, and Hiroaki Kitano	
Part III Mathematical and Statistical Aspects of Neurodynamics	
Robust Computation in Two Dimensional Neural Field	123
Yuzuru Sato and Shun-ichi Amari	
Dynamical Synapses Enhance Mobility, Memory and Decoding	131
C.C. Alan Fung, K.Y. Michael Wong, and Si Wu	
Input Dependent Variability in a Model of the Striatal Medium Spiny Neuron Network	139
Adam Ponzi and Jeff Wickens	
Selection Criteria for Neuromanifolds of Stochastic Dynamics	147
Nihat Ay, Guido Montúfar, and Johannes Rauh	

A Manipulative Approach to Neural Dynamics by Combined TMS-EEG 155
 Keiichi Kitajo, Yumi Nakagawa, Yutaka Uno, Ryohei Miyota, Masanori Shimono, Kentaro Yamanaka, and Yoko Yamaguchi

Long-Tailed Statistics of Corticocortical EPSPs: Origin and Computational Role of Noise in Cortical Circuits 161
 Jun-nosuke Teramae, Yasuhiro Tsubo, and Tomoki Fukai

On a Theory of Precise Neural Control in a Noisy System 169
 Wenlian Lu, Shun-ichi Amari, Jianfeng Feng, and David Waxman

Real-Time Wireless Sonification of Brain Signals 175
 Mohamed Elgendi, Brice Rebsamen, Andrzej Cichocki, Francois Vialatte, and Justin Dauwels

Part IV Spatiotemporal Network Dynamics and Biological Timing

Oscillator Cell Networks in the Hypothalamic Suprachiasmatic Nucleus, the Mammalian Circadian Clock 185
 Sato Honma, Daisuke Ono, and Ken-ichi Honma

Oscillator Network Modeling of Circadian Rhythm in the Suprachiasmatic Nucleus 191
 Isao Tokuda, Hirokazu Fukuda, and Naoto Hayasaka

In Vivo Monitoring of Circadian Output in *Clock* Mutant Mice 199
 Wataru Nakamura

Modular Organization Enables Both Self-Organized Criticality and Oscillations in Neural Systems 207
 Shengjun Wang, Claus C. Hilgetag, and Changsong Zhou

Traveling Waves in Locally Connected Chaotic Neural Networks and Their Phenomenological Modeling 213
 Makito Oku and Kazuyuki Aihara

Spatial Filtering by a Two-Dimensional Interconnected Network with Spike Timing Dependent Synaptic Plasticity Depending on Its Temporal Properties 221
 Kazuhisa Fujita

Neural Model for Hierarchical Processing of Auditory Information in Mammal’s Cortex 227
 Yusuke Hara and Yoshiki Kashimori

Modeling Dynamics of the Human Limbic System 233
 Mark H. Myers and Robert Kozma

Part V Dynamic Patterns of Neural Activity in Human Information Processing

Infant's Primitive Walking Reflex from the Perspective of Learning in the Uterus	243
Hiroki Mori and Yasuo Kuniyoshi	
Socially Developmental Robot based on Self-Induced Contingency with Multi Latencies	251
Hidenobu Sumioka, Yuichiro Yoshikawa, Masanori Morizono, and Minoru Asada	
On the Brain's Dynamical Complexity: Coupling and Causal Influences Across Spatiotemporal Scales	259
Emmanuelle Tognoli and J.A. Scott Kelso	
Formulating a Cognitive Branching Task by MTRNN: A Robotic Neuroscience Experiments to Simulate the PFC and Its Neighboring Regions	267
Fady Alnajjar, Yuichi Yamashita, and Jun Tani	
Neurodynamical Account for Altered Awareness of Action in Schizophrenia: A Synthetic Neuro-Robotic Study	275
Yuichi Yamashita and Jun Tani	
Self-Organizing Dynamic Neural Fields	281
Nicolas P. Rougier and Georgios Is. Detorakis	
Spontaneous EEG Activity and Biases in Perception of Supra-Threshold Stimuli	289
Andrey R. Nikolaev, Sergei Gepshtein, and Cees van Leeuwen	
Functional Roles of Corticofugal Plasticity in Detecting a Moving Target in Bat's Auditory System	297
Yoshitaka Muto, Yoshihiro Nagase, and Yoshiki Kashimori	
The Origin of the Spatial Pattern of Amplitudes in Trial-Averaged MEG	303
David M. Alexander, Peter Jurica, Andrey R. Nikolaev, Mikhail Zvyagintsev, Klaus Mathiak, and Cees van Leeuwen	
Rhythm Matters: A Case in Attentional Blink	311
Chie Nakatani and Cees van Leeuwen	
Complex Network Topology and Dynamics in Networks Supporting Precisely-Timed Activity Patterns	317
Chris Trengove, Cees van Leeuwen, and Markus Diesmann	

Part VI Toward Understanding of Intelligence: Collaboration Between Neuroscience and Robotics

Neural Synchrony for Expert Memory in Shogi (Japanese Chess) Players 325
 Hironori Nakatani and Yoko Yamaguchi

Neuronal Synchrony During the Planning and Execution Period in the Prefrontal Cortex..... 331
 Kazuhiro Sakamoto, Katsutoshi Yamamoto, Naohiro Saito, Kazuyuki Aihara, Jun Tanji, and Hajime Mushiake

A Constructive Approach for Investigating the Emergence of Role Division in Social Interactions 339
 Kenichi Minoya, Takaya Arita, and Takashi Omori

Estimating Similarity Judgment Processes Based on Neural Activities Measured by Near-Infrared Spectroscopy (NIRS) 347
 Yoshihiko Suzuki and Shohei Hidaka

Autonomous Robot with Internal Topological Representation 355
 Pitoyo Hartono and Thomas Trappenberg

SUDOKU Puzzle: The Neurodynamics of Intelligence to Choose the Right Solution from Many Possible Options in a Hypothetical Reasoning 363
 Hiroaki Wagatsuma

Part VII Dynamic Brain Forum

Heterogeneity-Induced Pulse Generators 371
 Yasumasa Nishiura, Takashi Teramoto, and Masaaki Yadome

Balancing Robustness with Plasticity Through Evolution and Learning .. 379
 Kunihiko Kaneko

Influence of the Endogenous Acetylcholine on STDP Induction..... 387
 Takeshi Aihara, Eriko Sugisaki, Yasuhiro Fukushima, and Minoru Tsukada

Transition Dynamics in Spatial Choice 393
 Hiroshi Nishida, Muneyoshi Takahashi, Jin Kinoshita, and Johan Lauwereyns

Perseveration of Response Sequences as a Mechanism Underlying 3,4-Methylenedioxymethamphetamine (MDMA or ‘Ecstasy’) Induced Memory Impairments 401
 David N. Harper

Multiple Neural Circuits in Value-Based Decision-Making	409
Masamichi Sakagami	
Towards Understanding of Neural Dynamics in Communicating Brains	415
Ichiro Tsuda	
The Organization of Neuronal Discharge on Timescales of Milliseconds and Seconds Is Related to the Spatial Response Properties of Hippocampal Neurons	421
Eduard Kelemen and André A. Fenton	
An Animal Model of Decision Making: Vicarious Trial-and-Error in Tasks Requiring Memory for Visual Associations or Spatial Locations	429
Paul A. Dudchenko, David Bett, Elizabeth Allison, Karola Kaefer, and Emma R. Wood	
Correlated Brain Activations During Formation of Memory for Future Plans	437
Jiro Okuda, Maki Suzuki, and Toshikatsu Fujii	
Cognitive Modeling of Human-Robot Interaction Estimating Other's Internal State	443
Takashi Omori, Ayami Yokoyama, Kasumi Abe, and Takayuki Nagai	
Symbol Communication Systems Integrate Implicit Information in Coordination Tasks	453
Takeshi Konno, Junya Morita, and Takashi Hashimoto	
Intermittent Brain Motor Control Observed in Continuous Tracking Task	461
Yutaka Sakaguchi	
Molecular and Neural Mechanisms for Behavioral Choice Between Two Conflicting Alternatives in <i>C. elegans</i>	469
Takeshi Ishihara	
Modulating the Phase Coherence of Neuronal Population Oscillations in the Gamma Band	475
B. Sancristóbal, R. Vicente, A.J. Pons, G. Pipa, and J. Garcia-Ojalvo	
The Phase Space of Lateral Thought	483
Eleonora Russo and Alessandro Treves	
Learning and Decisions as Functional States of Cortical Circuits	491
José M. Delgado-García, Raudel Sánchez-Campusano, and Agnès Gruart	

Causal Effects for Prediction and Deliberative Decision Making of Embodied Systems 499
 Nihat Ay and Keyan Zahedi

Part VIII Widespread of Cognitive Neurodynamics Modeling

Ongoing Global Phase Pattern and Visual Signal Detection 509
 Daisuke Shimaoka, Keiichi Kitajo, Kunihiko Kaneko, and Yoko Yamaguchi

Model on Visualization and Analysis for Peripheral Drift Illusion 515
 Keiichiro Inagaki and Shiro Usui

Differentiation Through Symbolic Communication 523
 Takuma Torii and Takashi Hashimoto

Theoretical Analysis of Phase Resetting on Matsuoka Oscillators 531
 Kazuki Nakada, Yasuomi D. Sato, and Kiyotoshi Matsuoka

“Memories as Bifurcations”: A Simple Model 537
 Tomoki Kurikawa and Kunihiko Kaneko

Biologically Inspired Closed-Loop Model of Precision Grip Lifting Task 543
 Ankur Gupta, Manikanta Avinash, Deepa Kandaswamy, Muthu Kumar, Suresh Devasahayam, K. Srinivasa Babu, and V. Srinivasa Chakravarthy

A Communicative Model: Can We Interpret Neural Dynamics of Understanding? 551
 Yongtao Li and Ichiro Tsuda

Mechanisms for Generating Intermittency During Manual Tracking Task 559
 Tetsumasa Asano, Jun Izawa, and Yutaka Sakaguchi

Multi-dynamics Learning Algorithm Based on SOM² 567
 Satoshi Matsushita, Takashi Ohkubo, and Tetsuo Furukawa

Saccade Dynamics in Error Trials During Visual Search 575
 Atsushi Fujimoto, Satoshi Nishida, and Tadashi Ogawa

Design and Dynamics of Active-Touch Sensory Model 583
 Tatsuo Yanagita

Human Object Recognition Based on Internal Models of the Human Hand 591
 Masazumi Katayama and Tatsuya Kurisu

Estimation of Children’s Interest Dynamics While Communicating with Robots	599
Takayuki Shimotomai, Kasumi Abe, Ayami Yokoyama, Takayuki Nagai, and Takashi Omori	
Robotic Motion Coach: Effect of Motion Emphasis and Verbal Expression for Imitation Learning	607
Tetsunari Inamura and Keisuke Okuno	
Synthetic Approach to Understanding Meta-level Cognition of Predictability in Generating Cooperative Behavior	615
Jun Namikawa, Ryunosuke Nishimoto, Hiroaki Arie, and Jun Tani	
Neural Correlates of Cognitive Dissonance and Decision Conflict	623
Keise Izuma, Madoka Matsumoto, Kou Murayama, Kazuyuki Samejima, Sadato Norihiro, and Kenji Matsumoto	
Cantor Coding of Song Sequence in the Bengalese Finch HVC	629
Jun Nishikawa and Kazuo Okanoya	
Inhibitory Network Dependency in Cantor Coding	635
Yasuhiro Fukushima, Yoshikazu Isomura, Yutaka Yamaguti, Shigeru Kuroda, Ichiro Tsuda, and Minoru Tsukada	
Sequential Memory Retention by Stabilization of Cell Assemblies	641
Timothee Leleu and Kazuyuki Aihara	
Statistical Estimation of Non-uniform Distribution of Dendritic Membrane Properties	649
Toshiaki Omori, Toru Aonishi, and Masato Okada	
Context-Dependent Call Variation in the Male Bengalese Finch	657
Midori Osada and Tetsu Okumura	
Capturing the Global Behavior of Dynamical Systems with Conley-Morse Graphs	665
Zin Arai, Hiroshi Kokubu, and Ippei Obayashi	
A Heuristic Model of Intra-brain Communications Using Chaos in Artificial Neuron Systems	673
Yu Arai, Ryota Mori, Fuyuki Aoto, and Shigetoshi Nara	
Transitory Memory Retrieval in the Neural Networks Composed of Pinsky-Rinzel Model Neurons	683
Hiromichi Tsukada, Yutaka Yamaguti, Hiroshi Fujii, and Ichiro Tsuda	

Dynamic Information Processing in the Frontal Association Areas of Monkeys During Hypothesis Testing Behavior 691
 Norihiko Kawaguchi, Kazuhiro Sakamoto, Yoshito Furusawa, Naohiro Saito, Jun Tanji, and Hajime Mushiake

Simple Dynamical Models to Understand the Mechanisms of Drug Addiction 699
 Takashi Tateno

Toward an Animal Model of Spatial Hemineglect: Preliminary Investigation 711
 Masatoshi Yoshida

Prestimulus Neural Oscillations Contribute to Recollection and Familiarity 717
 Florence Kleberg, Keiichi Kitajo, Masahiro Kawasaki, and Yoko Yamaguchi

Contribution of the Cholinergic Innervation to Early Memory Development in the Neonate Para-Hippocampal System 727
 Alexandre Pitti and Yasuo Kuniyoshi

Unintentional Synchronization of Behavior in Japanese Monkeys 745
 Yasuo Nagasaka, Zenas C. Chao, Naomi Hasegawa, Tomonori Notoya, and Naotaka Fujii

Effects of Medial Amygdala Lesions upon Social Behaviour in Mice 753
 Yu Wang, Yuki Takayanagi, and Tatsushi Onaka

Theta-Burst Stimulation Induces Long-Term Potentiation During Beta Oscillation, but Not During Epileptic Discharges, in Rat Hippocampal Slices 759
 Motoshi Nishimura and Kiyohisa Natsume

Integration of Hetero Inputs to Guinea Pig Auditory Cortex Established by Fear Conditioning 765
 Yoshinori Ide, Muneyoshi Takahashi, Johan Lauwereyns, Minoru Tsukada, and Takeshi Aihara

The Theta Cycle and Spike Timing During Fixation in Rat Hippocampal CA1 773
 Muneyoshi Takahashi, Yoshio Sakurai, Yoshikazu Isomura, Minoru Tsukada, and Johan Lauwereyns

Reactivation Hypothesis in Episodic Memory: From the Findings of Neuroimaging Studies 781
 Aya Ueno, Jiro Okuda, and Toshikatsu Fujii

Model-Based Analysis of Functional Connectivity During Associative Learning in Schizophrenia 787
Mihály Bányai, Vaibhav Diwadkar, and Péter Érdi

Neuronal Activity in the Prefrontal Cortex During Performance of a Dual Task Consisting of a Main- and An Interrupting-Task 795
Atsushi Miyazaki, Toshi Nakajima, Keisetsu Shima, and Hajime Mushiake

Functional Analysis of the Hippocampus Using Opto-fMRI 803
Yoshihumi Abe, Masaki Sekino, Yugo Fukazawa, Hiromu Yawo, Hiroyuki Ohsaki, and Tatsuhiro Hisatsune

Modulation of Cortico–Hippocampal EEG Synchronization with Visual Flicker: A Theoretical Study 809
Naoyuki Sato

Transition of Firing Patterns in a CA1 Pyramidal Neuron Model 817
Dan Ma, Shenquan Liu, and Lei Wang

The Effects of Leakage Conductance on Firing Properties in a Compartment Neuron Model 825
Lei Wang and Shenquan Liu

Numerical Analysis of Parkinson’s Disease in a Basal Ganglia Network Model 833
Xiaofeng Xie, Shenquan Liu, Xuemiao Pan, and Lei Wang

Erratum E1

Index 843

Part I
Global Scope of Cognitive Neurodynamic
Systems

Artificial Cognitive Systems with Active Learning and Situation Awareness Capabilities

Soo-Young Lee

1 Introduction

From 1998 to 2008 we had developed Artificial Brain inspired by brain information processing mechanism, which had successfully demonstrated lower-level secretarial functions [1]. From 2009 we are now extending this approach toward higher cognitive functions for intelligent agents, i.e., Artificial Cognitive System (ACS).

The essential functions of ACS for intelligent agents are proper *decision making* and following *action (behavior)*. The decision making is based on *situation awareness*, which is also based on *knowledge representation and accumulation*. These five modules will be developed based on computational models of *proactive knowledge development* and *self identity*. Eventually both hardware and software will be developed.

The research will utilize relevant previous researches for audio-visual perception as well as cognitive science, and extend into computational models and HW/SW systems.

However, the cognitive scientific knowledge is not good enough due to poor temporal and spatial resolutions. Among available non-invasive techniques, fMRI provides about 1 mm^3 spatial resolution with 1 s temporal resolution, while EEG and MEG provide 1 ms temporal resolution with 1 cm resolution. Although there exist many attempts to combine fMRI and EEG/MEG for cognitive modeling, it is beyond current status-of-art technologies to measure brain signals with enough spatial and temporal resolutions.

In this position paper we propose to combine fMRI and EEG experiments, and the missing links will be filled-in from engineering knowledge, especially

S.-Y. Lee (✉)

Department of Electrical Engineering and Brain Science Research Center,
Korea Advanced Institute of Science and Technology, Daejeon, South Korea
e-mail: sylee@kaist.ac.kr

the information theory. In Sect. 2 we present the higher cognitive functions to be implemented for our intelligent agents, i.e., Artificial Cognitive System (ACS), and the multidisciplinary multimodal approach will be presented in Sect. 3.

2 Artificial Cognitive Systems

The ACS will be based on our previous works on *Artificial Brain* and its secretarial developments, called *OfficeMate*, and then further extended with additional functions.

The *Artificial Brain* was developed through Korean Brain Neuroinformatics Research Program from 1998 to 2008. It was a joint effort of researchers from many different disciplines including neuroscience, cognitive science, electrical engineering, and computer science, and about 35 professors and 70 professors from many Korean universities were involved in the program.

The Korean Brain Neuroinformatics Research Program had two goals, i.e., to understand information processing mechanisms in biological brains and to develop intelligent machines with human-like functions based on the mechanism. In 2008 we had developed an integrated hardware and software platform, i.e., *Artificial Brain*. With two microphones, two cameras (or retina chips), and one speaker, the *Artificial Brain* looks like a human head, and has the functions of vision, auditory, cognition, and behaviour. Also, with this platform, we had developed a testbed application, i.e., “artificial secretary” alias *OfficeMate*, which might reduce the working time of human secretary by a half.

As shown in Fig. 1, the information processing functions in the *Artificial Brain* consist of four modules. Among five human sensory processes the *vision* and

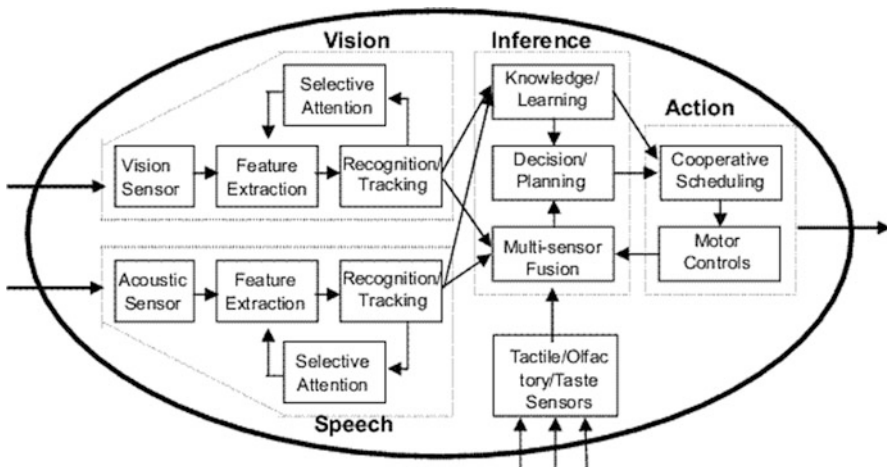


Fig. 1 Functional modules of Artificial Brain



Fig. 2 Basic concept of Artificial Cognitive Systems

the *auditory* modules provide the richest information, and complex information processing is performed. All the sensory information is integrated in the *inference* module, which provides learning, memory, and decision-making functions. The last module, *action* module, generates signals for required sensory motor controls. Although there may be many feedback pathways in biological brains, feed-forward signal pathways are mainly depicted here for simplicity.

The *Artificial Brain* may be trained to work for specific applications, and the *OfficeMate* was our choice of the application test-bed. Similar to office secretaries the *OfficeMate* would help users for office jobs such as scheduling, telephone calls, data search, and document preparation. The *OfficeMate* should be able to localize sound in normal office environment, rotate the head and cameras for visual attention and speech enhancement. Then it would segment and recognize the face. The lip reading would provide additional information for robust speech recognition in noisy environment, and both visual and audio features would be used for the recognition and representation of “machine emotion.” The *OfficeMate* would use natural speech for communications with the human users, while electronic data communication may be used between *OfficeMates*. Some role of secretarial jobs had been demonstrated.

We are now further extending the approach toward higher cognitive functions for intelligent agents, i.e., Artificial Cognitive Systems (ACSs). As shown in Fig. 2, based on the computational models of proactive knowledge development (PKD) and self-identity (SI), we would like to build functional modules for Knowledge Representation & Accumulation, Situation Awareness, Decision Making, and Human Behavior. The developed ACS will be tested against the new Turing Test for the situation awareness.

Models of Proactive Knowledge Development: The model of self-developing knowledge development will include active learning by asking proper questions based on the estimation of itself and environment.

Models of Self-Identity and Emotion: The model of self-identity and emotion will be developed based on recurrent neural network, of which internal hidden state represents one self-identity or emotion.

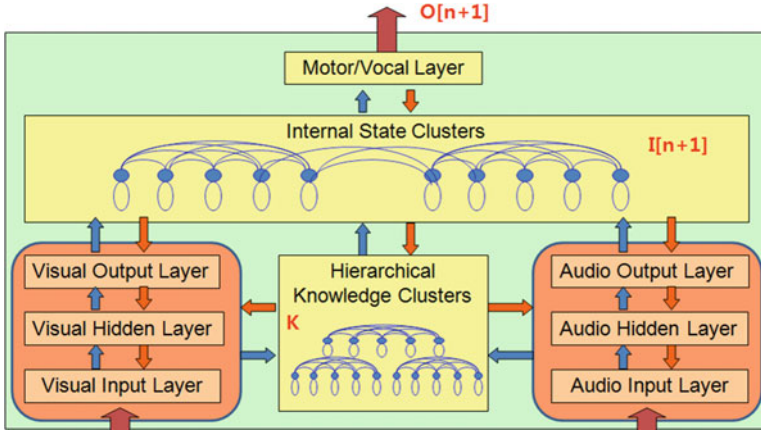


Fig. 3 Neural network model of Artificial Cognitive Systems

Knowledge Representation and Accumulation: Basic units of knowledge, i.e., features, and hierarchical network architecture based on the features will be developed for knowledge accumulation from bilateral interaction with environment (people, other robots, internet).

Situation Awareness: Recognition algorithm of unknown environment and situation will be developed based on (common) knowledge, previous experience, and self-identity.

Decision Making: The model of decision making based on situation, user models, and its own internal states will be developed.

Human Behavior: Action models will be developed for facial expression, hand motion, and speeches.

Artificial Systems Development: Hardware and software development. Figure 3 shows the neural network model of ACS.

New Turing tests: The Test problems will consist of several video clips, and the performance of the ACSs will be compared against those of human with several levels of cognitive ability.

As a simple demonstration, the developed personality-based agent model was applied to the Prisoners' Dilemma problems, and demonstrated the personality may be evolved by the interaction with other agents, i.e., the opponent of the Prisoners' Dilemma game. Actually to make its own decision the Agent tries to estimate the opponent's behavior, and different personality evolves for different opponent. In a society of many adaptive Agents they interact each other throughout many generations, and may co-evolve to different societies. In our experiments the society usually evolves cooperative or competing society of homogeneous Agents. In the cooperative society each Agent converges to a personality with mutual benefits, while it converges to egoist personality in the competing society.

The network architecture of ACS in Fig. 3 has internal state clusters to model the self-identity. The output (action) is a function of the internal states as well as audio-visual inputs. Also, the output makes change of the internal states.

Although audio and visual pathways are separated in brain anatomy, as demonstrated by McGurk effect [2] audio-visual interaction occurs in human perception. The hierarchical knowledge clusters perform this audio-visual interaction as well as their interaction with action and internal states. It is also important to have hierarchy for easy knowledge addition and deletion.

3 Multi-modal Multi-disciplinary Approach

For the development of ACS we need mathematical models of higher cognitive functions, which may not be available at this moment. Therefore, in addition to utilizing existing knowledge, we are conducting our own cognitive experiments.

Figure 4 shows how we would like to come up with mathematical models of higher cognitive functions in metaphor. When ten blind men are trying to figure out an elephant, each man just knows one small part of the elephant. As shown in the upper-left corner, the collection of knowledge does not do much good. Provided the relative locations of ten blind men were known in the upper-right corner, one may obtain some vague idea on an element. Then, one tried to utilize domain knowledge to extract something useful from the vague idea. In this case one may utilize the fact

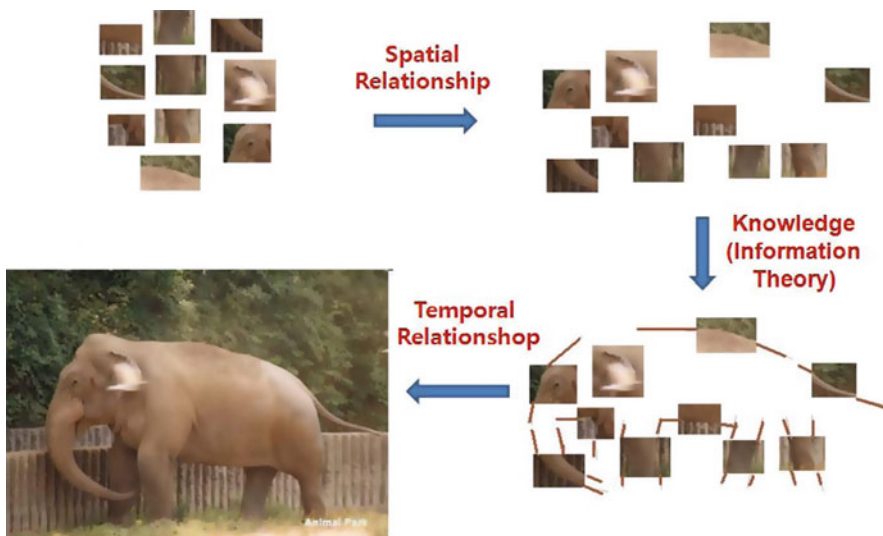


Fig. 4 Combining multimodal data from cognitive neuroscience and engineering knowledge from information technology for mathematical models of higher cognitive functions

that any edge is likely to be extended, and the result in the lower-right shows clear picture of an elephant. If one adds temporal dynamics, it will become much clearer and even distinguishes legs and noise. The figure shows usefulness of combining multimodal data for both high temporal and spatial resolutions while the missing links are filled in by domain information theory.

4 Conclusion

For the intelligent agents we propose to learn from brain information processing mechanism. Although the cognitive neuroscience dose not yet provide enough knowledge to build mathematical models of higher cognitive functions such as situation awareness and self-identity, we can utilize multimodal measurements such as fMRI with higher spatial resolution and EEG for higher temporal resolution. The still-existing missing links will be filled-in from engineering knowledge such as information theory.

Acknowledgments This research was supported by Basic Science Research Program through the National Research Foundation of Korea (NRF) funded by the Ministry of Education, Science and Technology (2009-0092812 and 2010-0028722).

References

1. Lee, S.Y., 2005, Artificial Brain and OfficeMate based on Brain Information Processing Mechanism, In *Studies in Computational Intelligence: Challenges for Computational Intelligence*, Vol. 63, pp. 123–143, 2007. 05., Springer.
2. McGurk, H & MacDonald, J, 1976, Hearing lips and seeing voices, *Nature*, Vol 264(5588), pp. 746–748

Dynamic Neuronal Representation in the Prefrontal Cortex

Hajime Mushiake, Keisetsu Shima, Kazuhiro Sakamoto, Yuichi Katori,
and Kazuyuki Aihara

Abstract The present paper investigated the neural mechanisms underlying dynamic neural representation in the prefrontal cortex (PFC), which is thought to play a crucial role in flexible cognitive behavior. Neural representation is discrete or continuous according to the information to be encoded. The multistable attractor model is a plausible theory of flexible control of representation. Attractor states are dependent on functional connectivity in which neuronal subpopulations actively communicate with one another at any particular moment in time. We discussed new optogenetics tools to manipulate the state of local circuits to investigate dynamical neural function.

Keywords Prefrontal cortex • Attractor • Dynamics

H. Mushiake (✉)

Department of Physiology, Tohoku University School of Medicine, 2-1 Seiryō-machi,
Aoba-ku, Sendai 980-8575, Japan

CREST, JST, Tokyo, Japan

e-mail: hmushiak@med.tohoku.ac.jp

K. Shima

Department of Physiology, Tohoku University School of Medicine, 2-1 Seiryō-machi,
Aoba-ku, Sendai 980-8575, Japan

K. Sakamoto

Research Institute of Electrical Communication, Tohoku University, 2-1-1 Katahira,
Aoba-ku, Sendai 980-8577, Japan

Y. Katori

Collaborative Research Center for Innovative Mathematical Modelling, Institute of Industrial
Science, The University of Tokyo, 4-6-1 Komaba, Meguro-ku, Tokyo 153-8505, Japan

FIRST, Aihara Innovative Mathematical Modelling Project, JST, Tokyo, Japan

K. Aihara

Collaborative Research Center for Innovative Mathematical Modelling, Institute of Industrial
Science, The University of Tokyo, 4-6-1 Komaba, Meguro-ku, Tokyo 153-8505, Japan

Y. Yamaguchi (ed.), *Advances in Cognitive Neurodynamics (III)*,

DOI 10.1007/978-94-007-4792-0_2,

© Springer Science+Business Media Dordrecht 2013

1 Introduction

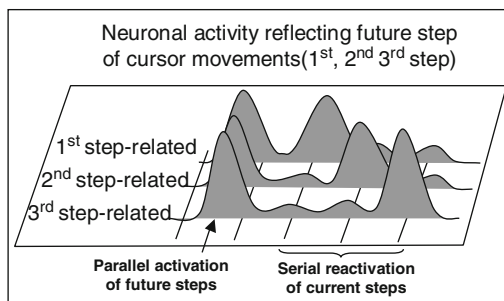
The brain interacts with the world through the body and creates representations of the internal state of the body and external state of the environment to cope with the ever-changing world in a flexible manner. Recent studies have revealed that the prefrontal cortex (PFC) plays a crucial role in flexible cognitive behavior by adaptively encoding various aspects of goal-directed behavior through cross-modal and cross-temporal integration according to a given behavioral context [1–4]. Adaptive representation depends on functional connectivity in which neuronal subpopulations constantly communicate with one another. Thus, it is important to understand the mechanisms underlying the dynamic processing of neural activity in local PFC circuits.

We investigated the neural mechanisms underlying flexible performance during cognitive tasks in non-human primates by analyzing the neuronal dataset using a representation-level approach to determine the information encoded by each neuron and a dynamic-system approach to describe the neural system as a state defined by a set of variables mapped in the state space over time [5–7]. The physiological variables measured included field potential, spiking activity, membrane potentials, and other quantitative physiological parameters. The representation-level and dynamic-system approaches are not mutually exclusive and represent two sides of the coin. We examined the neural mechanisms underlying flexible cognitive control by reviewing recent findings on representational and dynamic approaches. Moreover, we discuss the need for innovative research tools to study dynamic neural states *in vivo*. Optogenetics, a promising new tool, allowed us to manipulate the state of local circuits with high space–time resolution.

2 Dynamic Representation of Information

Neurons in the PFC are thought to be involved in an executive function by dynamically processing neural representations to cope with future demands in a prospective manner. Accumulating evidence indicates that prefrontal neurons not only hold external and internal information in a working memory but also transform online information from one type of behaviorally relevant information to another in a flexible manner [8–14]. These studies have suggested the existence of two types of representation: discrete and continuous. Our previous studies investigating PFC involvement in flexible mapping between goals and actions provide an example of dynamic representational changes in discrete information. Monkeys were trained to perform a path-planning task that required the use of two manipulanda to move the cursor from an initial position in a maze displayed on the computer screen to reach a given goal [10, 11, 14]. The goal was one of four peripheral positions in the maze that could be reached by various combinations of cursor movements. Several PFC neurons exhibited initial selectivity for the final goal and subsequent

Fig. 1 Examples of discrete representation



selectivity for the immediate goal of the first action during the preparatory period [10, 11]. We also observed neuronal activity representing the first, second, and third steps of future actions during the late preparation period [14]. Three examples of PFC neuronal activity associated with the first, second, and third steps of the path-planning task are shown in Fig. 1. Each neuron exhibited a distinct response only for the preferred future action. Furthermore, many of these neurons were reactivated during the execution period of each step. Therefore planned future actions were represented in a parallel manner in advance and serially executed with stepwise reactivation of the PFC neurons.

Behavioral tasks requiring an association between different types of discrete representations often involve a transition between different classes of representation. For example, stimulus–response association task involves the transition between representations of sensory domain and motor domain.

In a recent paper [15], we described continuous representation with a graded magnitude of neural activity. Interval timing of an action is a continuous variable, but a particular interval is often specified in a discrete manner. The pre-supplementary motor area (pre-SMA) is located in the medial frontal cortex and is closely connected with the prefrontal areas. To investigate pre-SMA-encoded interval timing, we trained animals to perform a time-production task that required them to determine a hold time of three different intervals before initiating a key-release movement in response to three color cues on the computer screen. We found two types of responses in the pre-SMA: a ‘time-specific’ response that reflected the retrieval of a specific interval of time in response to a visual cue and a ‘time-graded’ response that exhibited decay or build-up changes in activity depending on the length of the interval (Fig. 2).

The time-specific discrete responses and time-graded continuous parametric responses contributed equally to the generation of interval timing. Continuous and discrete representations also appear to play a crucial role in decision-making. Gold and Shadlen [16] claimed that the neural process underlying decision making requires a continuous process of evidence accumulation and a binary decision by filtering continuous magnitude data with adjustable thresholds in their work using perceptual decision-making tasks. Furthermore, a study that compared two vibration frequencies in the frontal cortex during a decision-making task reported integration of discrete and parametric neural presentations [9].

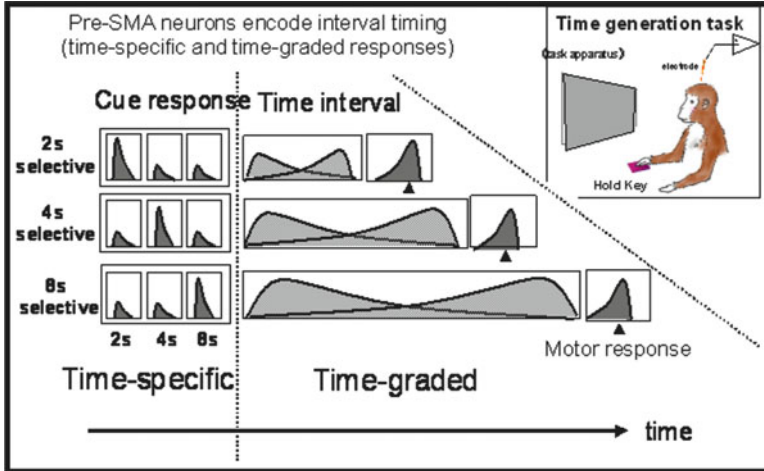


Fig. 2 Examples of parametric representation

3 Representations as Attractor States

Theoretically, the working memory-related persistent neuronal activity commonly observed in the PFC is thought to be an attractor state in that relatively small amounts of variation in this state lead it back to the same state [6, 17, 18]. Multiple attractors consist of ensembles of neurons with resting and active states such that a memory state can be represented by one state of attractors. This formulation is plausible insofar as a state of local circuits is dynamically stable in time. However, in real-time situations in the face of various behavioral demands, neural representations in one dimension at one epoch must be dynamically linked with different-dimensional representations at the next epoch to cope with various internal and external changes. Representations can be switched by reorganizing attractor states according to short-term changes in synaptic efficacy such as synaptic facilitation or depression. In this way, attractor states allow a neural system to work within different characteristic frames of reference corresponding to different types of representations. In our preliminary studies, we observed neural model-based dynamic multiple-attractor states that reproduce representational changes from goals to actions in the PFC. In this model, information in one modality is encoded by multiple attractor states of a neural population. When the attractor state is transformed into another state by short-term changes in synaptic efficacy, an overlapping but different cluster of neurons encodes information in that modality. Thus, the multi-dimensional information is represented as a different configuration of neurons, and short-term synaptic changes in local circuits contribute to maintain or shift attractor states in local circuits (i.e., synapse ensembles [19]). We believe dynamically reorganizable multi-attractor model can be applicable to flexible representational changes across multi-dimensional information observed in the PFC.

4 Local Circuits Underlying Dynamic Representation

Attractor states are maintained and modulated at different hierarchical levels in local neural circuits [17, 20]. (1) The intrinsic regenerative dynamics of single neurons involves positive feedback between membrane depolarization/spike discharges and active inward currents that can produce persistent activity outlasting a transient input current pulse. (2) Excitatory and inhibitory balance within inputs to dendrites of a single neuron and/or within a local circuit play an important role in the maintenance or switching of attractor states working within excitatory recurrent collaterals. (3) Cortico–cortical interactions contribute to the coordination of attractors by biasing weights of information flows within interconnected target areas. (4) Neurons in the various cortical areas are interlinked through multiple semi-open loops such as the thalamo–cortical loop, cortico–basal ganglia, and cortico–cerebellar loop. These loops may contribute to the selection, maintenance, and suppression of attractor states. Furthermore, changes in one hierarchical level may influence neural states in other levels. Contingent phenomena caused by an ensemble of neurons, such as oscillation of local field potentials, synchronous activities, and fluctuations in neuronal activities within local circuits, may influence the maintenance or reorganization of neural states. Until recently, the study of dynamic attractor states within cortical circuits has been difficult because an appropriate method to manipulate the state of local circuits with high resolution of space and time was not available.

5 Optogenetics as a New Tool to Manipulate Local Circuits

Optogenetics, a promising new tool for the assessment of neural states, uses a combination of genetic and optical methods to control targeted neurons by inducing inward or outward currents across stimulated membranes [21]. Recently, channelrhodopsin-2 (ChR2)-mediated photo stimulation of neurons has been used to investigate the state of neural networks in vivo. Preliminary results using transgenic rats expressing ChR2 in neurons demonstrated that optogenetic injection of the patterned oscillatory currents (opto-current clamp) caused state changes in local circuits [22]. Optically induced perturbation of local circuits are a useful method to study the mechanisms underlying attractor-state reorganization at the mesoscopic level.

6 Discussion and Conclusions

Transiently active ensembles of neurons dynamically represent relevant information in the cortical association areas including the prefrontal cortex. We classified representations into two types according to whether the information to be encoded

was a discrete (binary) or continuous (parametric) representation. Dynamic changes in representation are thought to reflect a multiple-attractor state, which is dependent on rapidly changing functional connectivity in the cell assembly. According to this idea, it is very important to intervene and evaluate the state of local circuits in vivo experiments of animals with high time and space resolution. Recent progress in bio-opto engineering including optogenetics has allowed us to optically manipulate the state of local circuits in the cortex while simultaneously electrically monitoring their activity. Innovative bio-optical methods for neuroscience will open new avenues for understanding neural dynamics.

References

1. Fuster, J. M. "The Prefrontal Cortex, Fourth Edition" Academic Press. (2008).
2. Miller EK, Cohen JD. An integrative theory of prefrontal cortex function. *Annu Rev Neurosci.* 24(2001):167–202.
3. Duncan, J. An adaptive coding model of neural function in prefrontal cortex. *Nat. Rev. Neurosci.* 2(2001): 820–829.
4. Tanji, J., and Hoshi, E. Role of the lateral prefrontal cortex in executive behavioral control. *Physiol. Rev.* 88(2008), 37–57.
5. Haken, H. Principles of brain functioning: Berlin, Heidelberg, New York, Springer. (1996).
6. Amit DJ. Modeling Brain Function: The World of Attractor Neural Networks. Cambridge University Press. (1992)
7. Izhikevich EM. Dynamical Systems in Neuroscience The MIT Press (2010)
8. Rainer G, Rao SC, Miller EK. Prospective coding for objects in primate prefrontal cortex. *J Neurosci.* 19(13)(1999):5493–505.
9. Romo R, Brody CD, Hernández A, Lemus L. Neuronal correlates of parametric working memory in the prefrontal cortex. *Nature.* 399(1999):470–3.
10. Saito N, Mushiake H, Sakamoto K, Itoyama Y, Tanji J. Representation of immediate and final behavioral goals in the monkey prefrontal cortex during an instructed delay period. *Cereb Cortex.* 15(2005):1535–46.
11. Sakamoto K, Mushiake H, Saito N, Aihara K, Yano M, Tanji J. Discharge synchrony during the transition of behavioral goal representations encoded by discharge rates of prefrontal neurons. *Cereb Cortex.* 18(2008):2036–45.
12. Genovesio A, Tsujimoto S, Wise SP Feature- and order-based timing representations in the frontal cortex. *Neuron.* 63 (2009):254–66.
13. Tanji J, Mushiake H. Which object appeared longer? *Neuron.* 63 (2009):148–9.
14. Mushiake H, Saito N, Sakamoto K, Itoyama Y, Tanji J. Activity in the lateral prefrontal cortex reflects multiple steps of future events in action plans. *Neuron.* 50(2006):631–41.
15. Mita A, Mushiake H, Shima K, Matsuzaka Y, Tanji J. Interval time coding by neurons in the presupplementary and supplementary motor areas. *Nat Neurosci.* 12(2009):502–7.
16. Gold JJ, Shadlen MN. The neural basis of decision making. *Annu Rev Neurosci.* (2007) 30:535–74.
17. Wang XJ. Synaptic reverberation underlying mnemonic persistent activity. *Trends Neurosci.* 24(2001):455–63.
18. Rolls, E. T., Loh, M., Deco, G., and Winterer, G. (2008). Computational models of schizophrenia and dopamine modulation in the prefrontal cortex. *Nat. Rev. Neurosci.* 9, 696–709.
19. Buzsaki G, Neural syntax: cell assemblies, synapsembles, and readers. *Neuron.* 68 (2010):362–85.

20. Haider B, McCormick DA Rapid neocortical dynamics: cellular and network mechanisms. *Neuron*. 62(2009):171–89.
21. Zhang F, Aravanis AM, Adamantidis A, de Lecea L, Deisseroth K. Circuit-breakers: optical technologies for probing neural signals and systems. *Nat Rev Neurosci*. 8(2007):577–81.
22. Wen L, Wang H, Tanimoto S, Egawa R, Matsuzaka Y, Mushiake H, Ishizuka T, Yawo H. Opto-current-clamp actuation of cortical neurons using a strategically designed channelrhodopsin. *PLoS One*.5(9) (2010) :e12893.

Timing at Multiple Scales in Olfactory Perception

Leslie M. Kay

Abstract Olfactory perception spans multiple time scales, from sub-millisecond and millisecond generation and timing of action potentials to developmental time. In this paper I review recent research addressing the mesoscopic scale and interactions with events that occur on longer time scales. Oscillatory local field potential frequency and coherence patterns can be modulated by behavioral state, sniffing patterns, intentional processes, learning, and circadian changes in gene expression. The olfactory system also shows species-selective interactions with development and expression of seasonality related to reproductive status, immune response and affective state. Causal interactions at different temporal scales represent the rule rather than the exception in this system.

Keywords Temporal scale • Olfactory bulb • Oscillation • Local field potential

1 Introduction

The olfactory system uses timing information at several different scales, from milliseconds to weeks, and we now see that these scales have the potential to interact in ways that set up the possibility for complex dynamical effects. The interactions occur across processes and mechanisms, from gene expression to sensory perception to affective state. We track these effects primarily through electrophysiology and surgical and behavioral manipulations. Mesoscopic neural processing of odor information is represented by temporal information at the millisecond to hundreds of

L.M. Kay (✉)

Department of Psychology, Institute for Mind and Biology, The University of Chicago,
Chicago, IL 60637, USA

e-mail: lkay@uchicago.edu

milliseconds scale, from gamma oscillations of the local field potential (40–100 Hz) to inhalations and sniffs (2–12 Hz). However, if we expand our scope to include several longer time scales, the picture is more complex and more interesting.

When we view the many scales which can interact in this system, we begin to identify a set of control and order parameters that may influence and be influenced by mesoscopic activity [1, 2]. The processes encompassed by these parameters range from attentional changes in neuromodulator levels to gene expression patterns associated with sexual development and seasonal responsiveness. These parameters occupy temporal scales from milliseconds to months or even years, and time becomes a source of complexity.

2 Temporal Processing Scales

Mesoscopic activity is best represented by the local field potential (LFP). This signal shows the cooperative activity of hundreds to thousands of neurons. Because the LFP is the local population coherence, this signal represents what downstream neurons are likely to receive. The coherent signal is what best survives any pathway that disperses activity, referred to by Freeman as the ‘brain laundry’ [2]. Three oscillatory bands dominate the LFP spectrum in the olfactory system, the gamma, beta (~20 Hz) and theta (2–12 Hz) bands. Each of these bands represents different aspects of olfactory behavior and relies on different circuits [3].

Gamma oscillations represent local firing precision of neurons in the olfactory bulb (OB) and the insect antennal lobe, the analog of the vertebrate OB [2, 4]. When downstream neurons in the piriform cortex (PC) or the insect mushroom body are viewed as feature detectors, we see that mesoscale activity translates downward to affect the probability of a single spike in downstream neurons. Neurons in the PC are sensitive to a few spikes arriving in a brief (~5–10 ms) time window. Mushroom body neurons fire when specific antennal lobe neurons are activated in tight temporal precision. Gamma oscillations and mitral cell precision are local events and are enhanced when central input to the OB is removed.

We and others have proposed that olfactory system beta oscillations serve to couple areas for distributed processing and may also facilitate the transfer of information from the OB to the PC and hippocampus [5–8]. In contrast to gamma oscillations, beta oscillations rely on central input to the OB; when this input is removed, beta oscillations disappear [9]. We presume that these oscillations represent coordinated firing of neurons within and across multiple areas, since they appear in multiple areas as the result of associative learning or sensitization.

Theta oscillations and the sensorimotor act of sniffing overlap in the OB. In this structure, and to a lesser extent in the PC, theta oscillations represent rodents’ respiratory behavior. Interactions between scales are apparent when rats and rabbits change their sniff frequencies. During high frequency sniffing gamma oscillations often decrease in periodicity, indicating less global precision in the underlying mitral cell population [10, 11]. Glomerular activation patterns in the input layer of the

olfactory bulb are also affected by the type of sniff [12]. These data suggest that mesoscopic changes effected by the type of sniff an animal takes can influence lower level activity on the scale of a few milliseconds.

There is more detail in the form of temporal structure of odorant mixtures as they diffuse through the mucosal layer and bind to olfactory receptors. Human subjects are sensitive to this timing information [13], and rats also appear to be (J Dink and LM Kay, unpublished observations).

While we are accustomed to think of mesoscopic phenomena as representing collective activity at lower levels, processes at much longer timescales affect mesoscopic activity in often complex ways. I divide these into several categories based on their temporal scales: (1) seconds to minutes, (2) minutes to hours, (3) hours to days, and (4) seasonal and developmental timeframes.

On the scale of seconds to minutes, there are a growing number of studies that address the relationships between behavioral state and LFP signal characteristics. Most obvious are the changes that occur within a single behavioral trial, as a subject moves from one behavioral epoch to the next [10]. Rats are trained to a sequence of behavioral state changes that over time adopt relatively high precision. For instance, trained rats produce a stereotyped sampling duration, in our hands ~ 550 ms, to accomplish a binary odor discrimination at $>90\%$ performance levels in either a go/no-go or 2-alternative choice paradigm. Operant responses are also on the order of 500 ms [14]. LFP statistics change along with these behavioral epochs with some features apparently dependent on the task [3].

Arousal states can affect coupling and information flow within the olfactory system. Urethane anesthesia produces sleep-like slow- and fast-wave states. Slow-wave states are accompanied by increased low frequency (<15 Hz) coherence between the PC and limbic structures, such as the hippocampus and amygdala. Information flow in this state proceeds from the hippocampus toward the periphery. During fast-wave states the PC has greater coherence with the OB, and information flow is from the periphery towards the hippocampus, as it is in waking states [5, 6, 15]. Coupling strength thus oscillates on the scale of seconds to many minutes, and this slow coupling and decoupling interacts with the direction and fidelity of information transfer.

Slow monotonic changes in neuromodulator levels or other processes associated with attention or affective state can gradually change mesoscopic features, such as the power of gamma oscillations during discrimination of high-overlap odors [16]. However, because neuromodulator release can be regulated on the order of hundreds of milliseconds [17], this parameter change could provide more complexity than can be predicted from a simple monotonic rise or slow periodicity.

On the scale of minutes to hours, spanning into days, we begin to see long term changes in connection strength and gene expression that can affect the circuit that produces mesoscopic activity. It is not until rats have reached criterion performance on a task (often over many days) that beta oscillations in the OB exceed baseline levels [7]. However, once a rat has learned one discrimination and transfers that knowledge to a second odor set, beta oscillation coherence between the OB and both

the dorsal and ventral hippocampus remains elevated, even when beta oscillations in the OB are at baseline levels [8]. Beta coherence between the two hippocampal subfields remains at baseline levels until the rat reaches criterion performance on the new odor set. At this point coherence between the dorsal and ventral hippocampus is again elevated.

Studies which address the ways in which rodents learn the rules of olfactory behavior and transfer them to new stimulus sets show that once rule learning is established, the properties of LTP and LTD in both the PC and the hippocampus are altered, as are patterns of gene expression that support these changes in connectivity [18, 19].

Circadian time influences processes that may present at the mesoscopic scale. PER gene expression modifies OB neuron excitability and shows entrainable circadian rhythms that persist independent of the suprachiasmatic nucleus [20, 21]. These rhythmic forces are likely to affect mesoscopic activity, perception and behavior.

Seasonal and developmental time. Olfactory bulbectomy (complete removal of both olfactory bulbs) clearly affects odor perception, but bulbectomy also influences affective state independent from loss of the sense of smell. Bulbectomy is a robust model for unipolar depression. It produces behavior in rats that is reminiscent of depression-linked anxiety, and the animals respond to chronic, but not acute, treatment with anti-depressants, as do humans [22]. Olfactory bulbectomy also has species-specific effects on reproductive responses to changes in day length. Seasonal reproductive responsiveness, normally absent in rats, is released when rats are bulbectomized prepubertally [23]. Syrian hamsters, which do show seasonal changes in reproductive status, lose this seasonality after bulbectomy [24]. Bulbectomy has no gonadal effects on seasonally reproductive Siberian hamsters, but they do present changes in immune response to seasonal cues [25, 26]. We have recently shown that day length modulates the depressive effects of bulbectomy in laboratory rats and that postpubertal bulbectomy does not release the seasonal reproductive response [27]. These results together show that second order neural pathways from the olfactory system to the suprachiasmatic nucleus can modulate developmental, immunological and affective processes, and that the timing of this manipulation is crucial to the constellation of effects and varies across species.

3 Conclusion

Interactions between temporal scales are ubiquitous in the olfactory system, from millisecond to seasonal and even developmental time. Each of these processes might be viewed as control parameters that can be manipulated by various physical methods, such as neurotransmitter levels, day length, time of day, sniffing rate, etc. Each can eventually be understood at a mechanistic level. How might we then use this information to understand perceptual awareness in intact brains?

We are used to thinking of processes that occur on longer timescales as having approximately monotonic effects on mesoscopic and perceptual processing. However, actual effects can be much more complex and produce emergent order parameters that drive perception, hierarchical processing, flexible learning of new goals, and even higher order processes such as self-autonomy [28, 29]. By examining interactions among temporal scales we will enable a description that relies on complex dynamics related to perception, and it is here that we may make the leap from coding-based sensory information to describing an individual's awareness and understanding.

Acknowledgments LMK received funding for this work from the NIDCD (R01-007995) and an Institute for Mind and Biology Seed Grant.

References

1. Haken, H., *The Science and Structure of Synergetics*. 1984, New York: Van Nostrand Reinhold Company. 255.
2. Freeman, W.J., Characteristics of the synchronization of brain activity imposed by finite conduction velocities of axons. *International Journal of Bifurcation and Chaos*, 2000. **10**(10): 2307–2322.
3. Kay, L.M., J. Beshel, J. Brea, C. Martin, D. Rojas-Líbano, and N. Kopell, Olfactory oscillations: the what, how and what for. *Trends in Neurosciences*, 2009. **32**(4): 207–214.
4. Kay, L.M. and M. Stopfer, Information processing in the olfactory systems of insects and vertebrates. *Seminars in Cell & Developmental Biology*, 2006. **17**(4): 433–442.
5. Gourévitch, B., L.M. Kay, and C. Martin, Directional coupling from the olfactory bulb to the hippocampus during a go/no-go odor discrimination task. *Journal of Neurophysiology*, 2010. **103**(5): 2633–2641.
6. Kay, L.M. and J. Beshel, A beta oscillation network in the rat olfactory system during a 2-alternative choice odor discrimination task. *Journal of Neurophysiology*, 2010. **104**(2): 829–839.
7. Martin, C., R. Gervais, E. Hugues, B. Messaoudi, and N. Ravel, Learning modulation of odor-induced oscillatory responses in the rat olfactory bulb: A correlate of odor recognition? *Journal of Neuroscience*, 2004. **24**(2): 389–397.
8. Martin, C., J. Beshel, and L.M. Kay, An olfacto-hippocampal network is dynamically involved in odor-discrimination learning. *Journal of Neurophysiology*, 2007. **98**(4): 2196–2205.
9. Martin, C., R. Gervais, B. Messaoudi, and N. Ravel, Learning-induced oscillatory activities correlated to odour recognition: a network activity. *European Journal of Neuroscience*, 2006. **23**: 1801–1810.
10. Kay, L.M., Two species of gamma oscillations in the olfactory bulb: dependence on behavioral state and synaptic interactions. *Journal of Integrative Neuroscience*, 2003. **2**(1): 31–44.
11. Kay, L.M., A challenge to chaotic itinerancy from brain dynamics. *Chaos*, 2003. **13**(3): 1057–1066.
12. Verhagen, J.V., D.W. Wesson, T.I. Netoff, J.A. White, and M. Wachowiak, Sniffing controls an adaptive filter of sensory input to the olfactory bulb. *Nature Neuroscience*, 2007. **10**(5): 631–639.
13. Laing, D.G., A. Eddy, G.W. Francis, and L. Stephens, Evidence for the temporal processing of odor mixtures in humans. *Brain Research*, 1994. **651**(1–2): 317–28.

14. Frederick, D.E., D. Rojas-Líbano, M. Scott, and L.M. Kay, Rat behavior in go/no-go and two-alternative choice odor discrimination: differences and similarities. *Behavioral Neuroscience*, 2011. **125**(4): 588–603.
15. Wilson, D.A. and X. Yan, Sleep-like states modulate functional connectivity in the rat olfactory system. *Journal of Neurophysiology*, 2010. **104**(6): 3231–3239.
16. Beshel, J., N. Kopell, and L.M. Kay, Olfactory bulb gamma oscillations are enhanced with task demands. *Journal of Neuroscience*, 2007. **27**(31): 8358–8365.
17. Sarter, M., V. Parikh, and W.M. Howe, Phasic acetylcholine release and the volume transmission hypothesis: time to move on. *Nature Reviews Neuroscience*, 2009. **10**(5): 383–U86.
18. Cohen, Y., I. Reuveni, E. Barkai, and M. Maroun, Olfactory learning-induced long-lasting enhancement of descending and ascending synaptic transmission to the piriform cortex. *Journal of Neuroscience*, 2008. **28**(26): 6664–6669.
19. Quinlan, E.M., D. Lebel, I. Brosh, and E. Barkai, A molecular mechanism for stabilization of learning-induced synaptic modifications. *Neuron*, 2004. **41**(2): 185–192.
20. Granados-Fuentes, D., A. Tseng, and E.D. Herzog, A circadian clock in the olfactory bulb controls olfactory responsivity. *Journal of Neuroscience*, 2006. **26**(47): 12219–12225.
21. Abraham, U., J.L. Prior, D. Granados-Fuentes, D.R. Piwnica-Worms, and E.D. Herzog, Independent circadian oscillations of period1 in specific brain areas in vivo and in vitro. *Journal of Neuroscience*, 2005. **25**(38): 8620–8626.
22. Kelly, J.P., A.S. Wrynn, and B.E. Leonard, The olfactory bulbectomized rat as a model of depression: An update. *Pharmacology & Therapeutics*, 1997. **74**(3): 299–316.
23. Nelson, R.J. and I. Zucker, Photoperiodic control of reproduction in olfactory-bulbectomized rats. *Neuroendocrinology*, 1981. **32**(5): 266–71.
24. Clancy, A.N., B.D. Goldman, A. Bartke, and F. Macrides, Reproductive effects of olfactory bulbectomy in the Syrian hamster. *Biol Reprod*, 1986. **35**(5): 1202–9.
25. Prendergast, B.J., J. Galang, L.M. Kay, and L.M. Pyter, Influence of the olfactory bulbs on blood leukocytes and behavioral responses to infection in Siberian hamsters. *Brain Research*, 2009. **1268**: 48–57.
26. Prendergast, B.J., L.M. Pyter, J. Galang, and L.M. Kay, Reproductive responses to photoperiod persist in olfactory bulbectomized Siberian hamsters (*Phodopus sungorus*). *Behavioural Brain Research*, 2009. **198**(1): 159–164.
27. Tacopina, S., H. Lee, L. Pyter, B.J. Prendergast, and L.M. Kay, Interaction between day length and anxiety measures in olfactory-bulbectomized Wistar rats. *Society for Neuroscience Annual Meeting*, 2011. Washington DC.
28. Yamashita, Y. and J. Tani, Emergence of functional hierarchy in a multiple timescale neural network model: a humanoid robot experiment. *PLoS Computational Biology*, 2008. **4**(11): e1000220.
29. Tani, J., Autonomy of self at criticality: the perspective from synthetic neuro-robotics. *Adaptive Behavior*, 2009. **17**(5): 421–443.

Structure, Stability, Dynamics, and Geometry in Brain Networks

Peter A. Robinson

Abstract The role of physical and geometrical constraints in determining structure of brain networks is outlined. It is shown that requirements imposed by dynamics, stability, and network geometry strongly constrain possible networks to structures that strongly resemble those found in real brains.

1 Introduction

Observed brain networks exhibit complex patterns of anatomical interconnections and functional dynamics. Brain networks are subject to a range of competing constraints that limit the range of possible network architectures. These constraints include long-recognized limitations on physical volume, speed of processing, path length, and metabolic load [1]. More recently recognized constraints include requirements that networks must be dynamically stable with respect to epilepsy-like disruptions of activity [2], but must remain in an “edge of chaos” state of near-marginal stability to enable complex behavior and rapid functional adaptability [3]. Moreover, this level of dynamical stability must be maintained as functional and/or anatomical connections are made and broken on time scales spanning task performance, information processing, development, and evolution [3], a criterion that echoes Simon’s observations on the advantages of modularity in complex systems [4].

The above considerations imply that only certain types of theoretically possible networks can actually be relevant to the real brain. More abstract

P.A. Robinson (✉)

School of Physics, University of Sydney, Sydney, NSW 2006, Australia

Brain Dynamics Center, Sydney Medical School—Western, University of Sydney,
Westmead, NSW 2145, Australia

e-mail: robinson@physics.usyd.edu.au

information-theoretic criteria such as maximizing complexity or mutual information may be relevant in quantifying complex behavior [1], but must ultimately arise from physical principles.

This paper briefly reviews how principles such as a requirement of stability against seizures, and geometric constraints imposed by the two-dimensional (2D) cortical geometry, strongly limit the types of brain architectures that are possible. Neural field theory (NFT) [5] provides a useful means of testing network stability properties [3, 6–8] and this paper concentrates on this approach.

2 Models

Connectivities between different brain regions (or *nodes*) are typically expressed in terms of brain connection matrices (CMs) that usually have 50–1,000 nodes, each representing 10^8 – 10^9 neurons. The structure of such CMs and their corresponding networks is most often studied by examining quantities such as clustering, degree distribution, and other graph-theoretic measures, without direct reference to the physical properties of the actual brain from which the CM has been abstracted. Alternatively, network architectures—e.g., regular, random, small-world, modular, hierarchical, as illustrated in Fig. 1—are hypothesized and their network properties are compared with those of observed brain structures to find the best match.

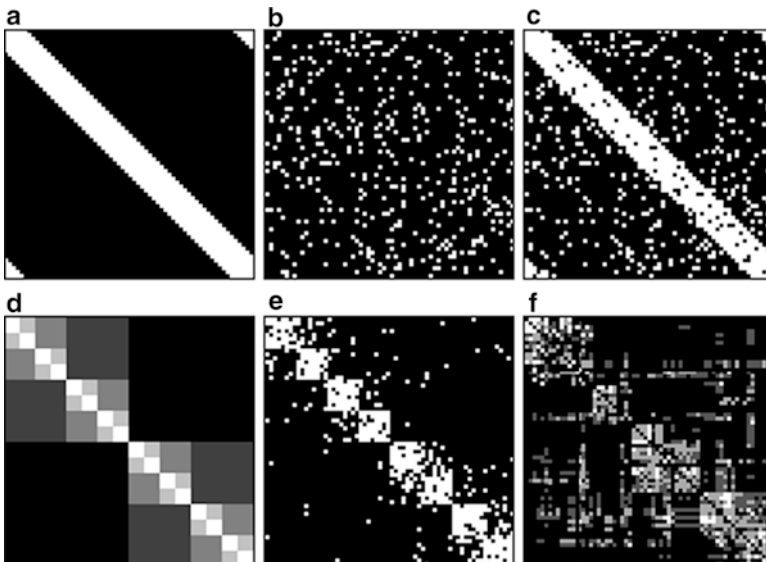


Fig. 1 Schematic connection matrices (CMs) of networks with neural populations labeling rows and columns, and *white* entries for a connection between a given row and column [2]. (a) Regular network. (b) Random network. (c) Small world network. (d) Hierarchical network *shaded* to show density of connections. (e) Exemplar hierarchical network. (f) Cat cortical CM (Adapted from [9])

A number of studies have examined the dynamics of activity in brain networks. Early investigations mostly assumed or enforced stability of dynamics, but recent work has examined the roles of network structure in stability [2,3,6–8]. For example, the ability of hierarchical networks (HNs) to restrict spread of seizure-like activity has been examined by using a simplified spreading model [2]. Here, we focus on the problem of what network architectures can exist under requirements that their dynamics be stable under the changing circumstances found in real brains.

Many approaches exist to studying brain network dynamics, most directly by simply connecting large numbers of model (e.g., integrate-and-fire) neurons according to a specific CM. However, to represent the extremely large numbers of neurons represented by each node of an observed CM it is more practical to endow each node with physiology based neural population dynamics, embodying their average behavior. These nodes are then linked according to the CM of interest to study network dynamics and stability. Here we focus on recent approaches based on NFT [3,6–8].

The model focused on here incorporates the synaptodendritic dynamics that result in the soma potential, the resulting average firing rate, and the consequent field of outgoing pulses $\phi(t)$ that propagates between nodes with a damping rate γ that reflects the finite average time taken to reach axonal terminals. In the limit nodes are close enough to treat as a continuum this model has been extensively used to investigate the corticothalamic system, producing excellent agreement with a wide range of other neural activity phenomena [5].

To analyze brain networks we assume there are no spatial dependences within a given population (i.e., node), which is assumed to comprise identical neurons, with a soma voltage response time $1/\alpha$ to incoming spikes. Linear perturbations of the neural field ϕ_a , for each population a about its steady state are then described in Fourier space by Gray and Robinson [6]

$$D(\omega)\phi_a(\omega) = \sum_b G_{ab}\phi_b(\omega), \quad (1)$$

$$D(\omega) = (1 - i\omega/\alpha)^2(1 - i\omega/\gamma)^2, \quad (2)$$

where ω is the angular frequency, G_{ab} is the connection gain (the number of action potentials produced in a per action potential from b); if $G_{ab} > 0$, the connection is excitatory and if $G_{ab} < 0$ it is inhibitory. Only cases with $G_{ab} = g = \text{constant}$ are considered here.

Letting $\mathbf{G} = [G_{ab}] = g\mathbf{C}$ be the matrix of gains, where \mathbf{C} is the CM, (1) can be written

$$\mathbf{A}(\omega)\Phi(\omega) = 0, \quad (3)$$

where $\mathbf{A} = \mathbf{G} - \mathbf{D}$, Φ is a column vector of the ϕ_a , $\mathbf{D} = D(\omega)\mathbf{I}$, and \mathbf{I} is the identity matrix. Equation (3) describes the linear dynamics of a network of neural populations with no external input and thus determines its stability via the solutions ω of the dispersion relation

$$\det \mathbf{A}(\omega) = 0. \quad (4)$$

The set of solutions of (4) is termed the *dispersion spectrum*. In the complex ω plane the boundary between stable and unstable regions is the real axis, and networks with dispersion solutions at this boundary are marginally stable. The solution ω_1 with the largest imaginary part $\text{Im}\omega$ is least stable and determines the network's overall stability. We term this the *dominant solution*. Setting $\lambda = D(\omega)$, the dispersion relation is

$$\det(\mathbf{G} - \lambda\mathbf{I}) = 0, \quad (5)$$

whose solutions ω are obtained by solving

$$\lambda - D(\omega) = 0, \quad (6)$$

for each eigenvalue λ of \mathbf{G} . The set of eigenvalues is the *spectrum* of the network, denoted $\text{Sp}(\mathbf{G})$. If all λ in $\text{Sp}(\mathbf{G})$ have corresponding ω with $\text{Im}(\omega) < 0$, the network is stable. However, if there is any λ corresponding to $\text{Im}(\omega) \geq 0$, it is unstable. The eigenvalue λ_1 corresponding to ω_1 is the least stable and is termed the *dominant eigenvalue*. For $\omega_1 \ll \alpha$, one can make the approximation

$$\omega_1 = i(\sqrt{g\lambda_1} - 1). \quad (7)$$

3 Results

In this section we show how physical conditions constrain network architectures. We first test various proposed cortical network architectures for the dynamical stability of their activity and find constraints on network parameters. For example, the regular network in Fig. 1a has $g\lambda_1 = kg$ and hence is stable only for $kg < 1$, where k is the number of neighbors to which each node is connected—i.e., the *degree*. For the random network in Fig. 1b, we find $g\lambda_1 \approx npg$ and hence that the criterion for a high probability of stability P_s is $npg < 1$ where n is the number of nodes and p is the probability of a connection between a randomly chosen pair of nodes. Figure 2a illustrates this criterion for various n , p , and g , with the transition from high to low P_s sharpening as n increases [6]. Random networks always become unstable as n increases if local properties remain the same [10]. Figure 2b shows the spectrum of a marginally stable random network, with $\omega_1 = 0$.

Real brain networks are highly clustered (i.e., there are disproportionately many short-range connections), but have short mean path length L between nodes. Regular brain networks have high clustering C and large L , with the reverse for random networks. Small world (SW) networks have been proposed to circumvent these problems. The CM of such networks, shown in Fig. 1c, can be constructed by severing a small fraction p of the connections of a regular network and randomly rewiring them between other pairs of nodes. This introduces a few long-range connections that dramatically reduce L but leave C high. Figure 3 shows L and C vs. p , demonstrating an intermediate SW regime with large C and small L .

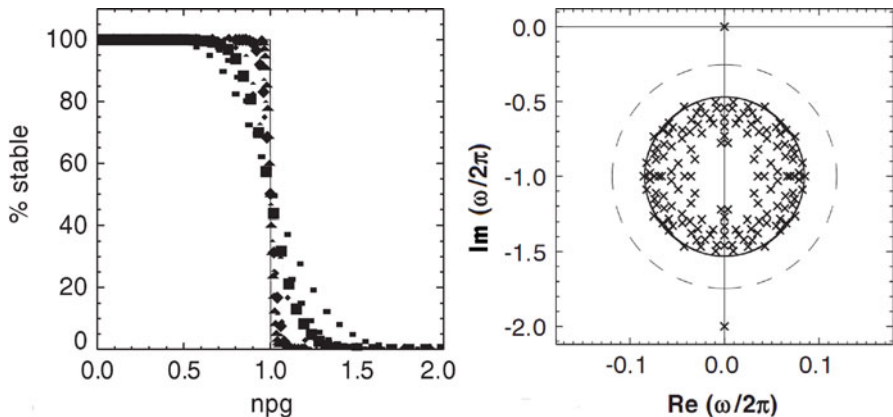
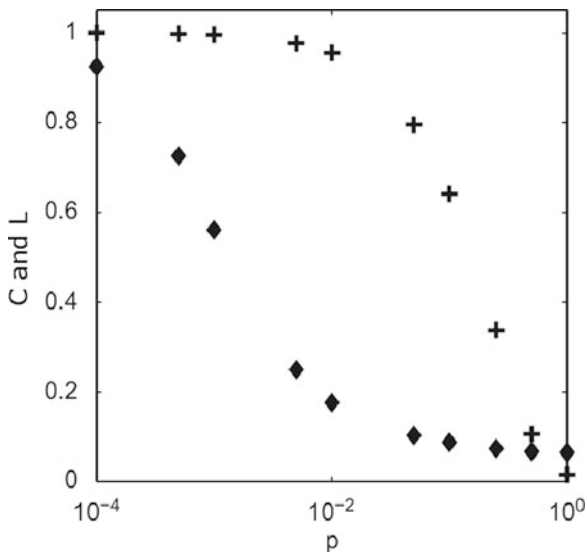


Fig. 2 Stability of random excitatory networks (Adapted from [6]). (a) Probability of stability P_s of vs. npg . (b) Dispersion spectrum for $npg = 1$

Fig. 3 SW clustering (*pluses*) and path length (*diamonds*) vs. rewiring probability p (Adapted from [7])



For $p \ll 1$, the stability of SW networks is chiefly determined by the regular backbone. The network becomes approximately random if $np \sim 1$, in which case λ_1 increases with n .

We have examined constraints on C and L in networks of specified structure, but real brains undergo evolution (increase of size, complexity), development (growth, neural pruning), learning (formation of connections), and information processing (transient connections). The *dynamical reconnectability* requirement that the network remain stable under all these processes imposes additional constraints

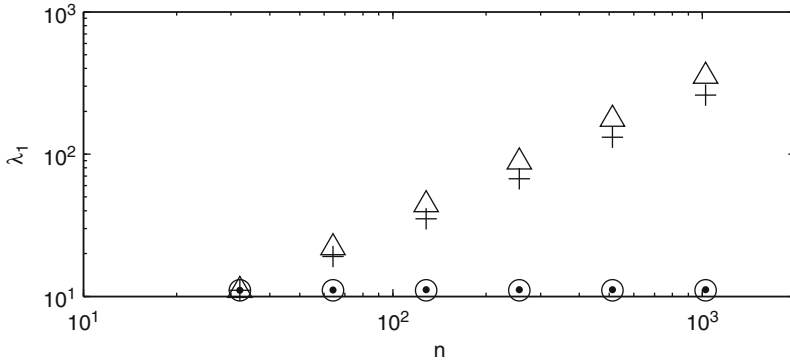


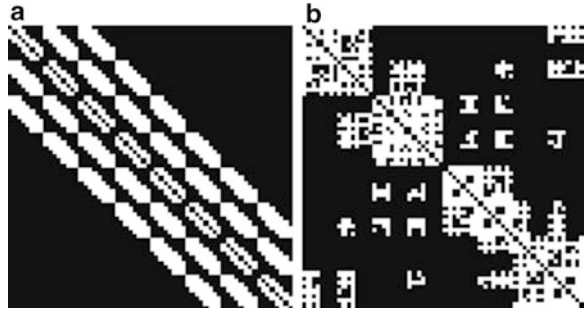
Fig. 4 Principal CM eigenvalue λ_1 vs. n for random (triangles), SW (pluses), regular (circles), and hierarchical (dots) networks [3]

on structure [3]. Moreover, networks must have a number of connections n_c that increases only in proportion to n to keep wiring to a constant fraction of brain volume [3]. To enable dynamic reconnection, networks must also be able to be combined or divided without appreciably changing their architecture, stability, or the strength of more than a small fraction f of connections, ideally with $f \rightarrow 0$ as $n \rightarrow \infty$ [3]. These conditions enable the evolutionary, developmental, and functional reorganizations required and reflect the principle that complex structures are most efficiently assembled from working substructures [4].

It was recently found [3] that a modular hierarchical network (HN) can satisfy dynamical reconnectability constraints while still maintaining high C and low L . Such a network's connectivity probability is shown in Fig. 1d, which exhibits a hierarchical fall-off in blocks successively further from the diagonal; a specific realization drawn from this distribution is shown in Fig. 1e [3, 11]. Figure 4 shows that the resulting λ_1 remains near-constant as n increases, so stability is unchanged [3], and networks can remain in a marginally stable “edge of chaos” state of complex dynamics.

The cortex is approximately a 2D sheet and is highly uniform in its anatomical structure. This might appear to contradict findings of structure in CMs; however, most cortical connections are short-range, thereby inducing *geometric modularity* that can be disguised by the CM representation if nodes are not indexed appropriately. For example, indexing a 2D regular network in a spatial raster pattern yields the CM in Fig. 5a, whereas if close nodes maintain close indexes, the CM in Fig. 5b results [8]. Remarkably, this shows a structure very similar to the HN and cat CMs in Fig. 1e, f, even though no explicit network modularity or hierarchy is present [8]. This network satisfies the dynamical reconnectability criteria, has high C and (because it is 2D) low L . Moreover, with suitable choice of parameters, quantitative measures of these quantities and modularity closely match those of the cat cortex [8].

Fig. 5 2D regular network CMs [8]. (a) With raster labeling. (b) With geometrically close nodes having closer labels than in (a)



4 Discussion

Structural, dynamic, and geometric constraints together imply that only certain types of networks can be relevant to the real brain, without invoking abstract criteria such as maximization of complexity or mutual information in network activity. CMs of suitably constrained networks closely resemble observed ones, suggesting that physical constraints strongly limit the allowable types of brain networks. One possible architecture is that of a modular hierarchical network, which has small-world properties and can robustly maintain dynamics near marginal stability. Regular 2D networks with a preponderance of short range connections can also satisfy the physical constraints discussed—a result that may resolve the apparent contradiction between the appearance of modularity in CMs and the high degree of uniformity in cortical architecture.

Acknowledgments I thank J. Henderson and D. Gummersal for modifying some figures. The Australian Research Council supported this work.

References

1. Bullmore, E., and Sporns, O. (2009). *Nat. Rev. Neurosci.* **10**, 186–198.
2. Kaiser, M. (2007). *Phil. Trans. Roy. Soc. A*, **365**, 3033–3045.
3. Robinson, P. A., Henderson, J. A., Matar, E., Riley, P., and Gray, R. T. (2009). *Phys. Rev. Lett.* **103**, 108104.
4. Simon, H. A. (1962). *Proc. Am. Phil. Soc.* **106**, 467–482.
5. Deco, G., Jirsa, V. K., Robinson, P. A., Breakspear, M., and Friston, K. F. (2008). *PLoS – Comp. Biol.* **4**, e1000092.
6. Gray, R. T., and Robinson, P. A. (2007). *Neurocomput.* **70**, 1000–1012.
7. Gray, R. T., Fung, C. K. C., and Robinson, P. A. (2009). *Neurocomput.* **72**, 1565–1574.
8. Henderson, J. A., and Robinson, P.A. (2011). *Phys. Rev. Lett.* submitted.
9. Scannell, J. W., Blakemore, C., and Young, M. P. (1995). *J. Neurosci.* **15**, 1463–1483.
10. May, R. M. (1972). *Nature* **238**, 413–414.
11. Sporns, O. (2006). *BioSystems*, **85**, 55–64.

Mathematical Theory of Neural Networks: A Personal and Historical Survey

Shun-ichi Amari

Abstract Mathematical neuroscience has become an important discipline of neuroscience, although it has not yet been fully established. We state historical remarks on the progress of mathematical neuroscience from the personal viewpoint. We also show some formulations of mathematical neuroscience with historical comments. We conclude with long-standing unsolved problems.

Keywords Mathematical neuroscience • Statistical neurodynamics • Neural field • Learning and memory

1 Introduction

Since theoretical approaches to dynamics of neural networks has a long history, it is difficult to give a full survey. Instead, I show here a personal perspective, summarizing my own researches for nearly a half century. There have been the rise and fall of theoretical approaches, but I am glad to say that computational and mathematical neuroscience has gradually been established itself as an important discipline of brain science.

One may ask why mathematical neuroscience is necessary and what it is. The brain has been created through the long history of evolution, so that it looks indeed a very complex system having no definite design principles. However, there must be fundamental principles that guarantee the capability of information processing by using a large number of neural elements through parallel dynamical interactions and learning. The nature has found these principles through random searches of evolution, so that the brain uses them in a very complicated style,

S. Amari (✉)

Laboratory for Mathematical Neuroscience, RIKEN Brain Science Institute,
Saitama 351-0198, Japan
e-mail: amari@brain.riken.jp

not well designed. This means that it is difficult to find the principles only by accumulating experimental findings. We need pierce theoretical eyes, especially mathematical theories to discover the principles, where simplified abstract models of neural networks would be used. We can then construct more realistic models based on these principles, where computational neuroscience plays an important role.

Historical Remarks on Mathematical Neuroscience

Prehistory: There were a number of important researches before the 1950s. One may mention such big names as Rashevsky, Wiener, Rosenbluth, and Ashby among many others.

Old period: The perceptron introduced by Rosenblatt was epoch-making, by initiating study on brain-inspired learning machines and lots of works followed. Caianiello also contributed dynamical aspects of learning by proposing the adiabatic method. Zeeman proposed the topology of the brain, where homology theory was used. Based on these intriguing works, there emerged lots of mathematical researches in America (W. Freeman, M. Arbib, S. Grossberg), in Europe (J. Cowan, Ch. Von der Malsburg, T. Kohonen) and in Japan (K. Fukushima, K. Nakano, S. Amari). We should not forget Russian activities (L.I. Rozonoer, Y.Z. Tsympkin and others), which were isolated from the western world.

It was this period that a number of mathematical theories and models were established. They include statistical neurodynamics, neural field theory, learning theory, associative memory and neural self-organization.

Strum-und-drang: It was a big surprise to me that a new trend called the connectionism emerged in the early 1980s. The connectionism appealed researchers with the slogan ‘parallel distributed processing (PDP)’, and welcomed from a wide range of science and engineering community. Not only brain scientists but cognitive scientists, physicists, engineering scientists, etc. joined enthusiastically to the new trend, and it was said that this would generate industries of scale of billions of dollars. Although this dream did not realize, its scientific impact was extraordinarily strong.

The old theories were rediscovered again together with lots of newly developed theories and models. This trend successfully connected different methods and fields of research, searching for miracle of the brain, in particular how distributed and parallel computation works together with learning.

Contemporary research: After the boom, lots of deeper researches are going on today both in the direction of understanding the mechanism of the brain and in the direction of engineering applications. In particular, it is widely recognized that computational neuroscience is a very important part of brain science. Integration of robotics and neuroscience is another important aspect. I am glad to see that the term ‘mathematical neuroscience’ has become popular now.

Topics of Mathematical Neuroscience

1. Dynamics of neuron pools, neural oscillators and statistical neurodynamics

Given a pool of neurons, its dynamics may be written as

$$\tau \frac{du_i}{dt} = -u_i + \sum w_{ij} \varphi \{u_j(t)\} + s_i - h, \quad (1)$$

where u_i is the (average) membrane potential of neuron i , w_{ij} is the connection weight from neuron j to neuron i , φ is a sigmoidal function, s_i the external input and h is threshold. This is called the Hopfield network, but it was used in Amari [7], (discrete-time version in [3]), Wilson and Cowan, 1972, etc. There are rich dynamic aspects covered by this simple model, such as multi-stability, oscillation and chaos.

When the connection weights are randomly assigned subject to a probability law, we may investigate dynamical behaviors common to all such networks. This approach is called statistical neurodynamics. When a network consists of a number different neuron pools, for example, pools of excitatory and inhibitory neurons, by introducing macroscopic variables $U_\alpha(t)$ of average membrane potential for pool α , statistical neurodynamics derives the macroscopic equation

$$\begin{aligned} \tau \frac{dU_\alpha(t)}{dt} = & -U_\alpha(t) + \sum W_{\alpha\beta} \Psi \{U_\beta(t)\} \\ & + S_\alpha - H, \end{aligned} \quad (2)$$

where

$$X_\alpha = \Psi(U_\alpha) \quad (3)$$

is the activity level (firing rate) of pool α , and studies the dynamical properties.

When the network consists of excitatory neurons and inhibitory neurons, we may consider two types of macro-variables U_e and U_i . The dynamical behavior is multi-stable or oscillatory, depending of the parameters. The neural oscillation of this type was first demonstrated by Amari (discrete-time dynamics, [3] and continuous time, Amari [7]). Wilson and Cowan, 1972 proposed a similar equation, so that it is now call the Wilson-Cowan neural oscillator.

Chaotic behaviors and oscillations are very important. Sompolinski is the first who demonstrated the chaotic behaviors in a random network of asymmetric connection. Aihara demonstrated the role of chaotic behavior in decision systems and associative recall dynamics. Tsuda postulated that such chaotic dynamics constitutes a fundamental principle of the brain.

Yamaguchi is one of the first who remarked the importance of neural oscillations in information processing. She analyzed the role of the phase in the hippocampus. Now it is a hottest topic in brain science to integrate information in various areas of the brain.

2. Dynamics of neural fields

Neurons are arranged in the cerebrum as a multilayer 2-dimensional neural field. Its dynamics was proposed by Wilson and Cowan, 1973. Amari [4] followed their idea to give a rigorous mathematical analysis of the dynamics and its stability. Ermentrout applied the field theory to explain hallucination. Now dynamics of neural field is one of hot topics, applied to explain working memory, psychological phenomena and robotics navigation.

The equation is written as

$$\begin{aligned} \tau \frac{\partial U_\alpha(\xi, t)}{\partial t} = & -U_\alpha(\xi, t) \\ & + \sum_\beta \int W_{\alpha\beta} (|\xi - \xi'|) \Psi \\ & \{U_\beta(\xi', t)\} d\xi' + S_\alpha(\xi, t) - h. \end{aligned} \quad (4)$$

Here ξ is a (two-dimensional) coordinates of the field.

3. Associative memory

A prototype model of dynamics of associative memory was proposed in 1972 by a number of researchers. The model rediscovered by Hopfield, the so called the Hopfield model, is exactly the same as that proposed and analyzed by Amari [8]. He also proposed the association mechanism of a sequence of patterns by using an asymmetric connection matrix.

It is a great achievement of Hopfield who proposed the concept of capacity, which was analyzed by physicists, using the replica method. The dynamics of recall was analyzed by Amari and Maginu [13], showing a very complex basins of attraction. This was generalized by Okada to a higher-order theory. J. Hawkins considers this type of association mechanism a fundamental principle of the brain and proposed to construct a brain-inspired machine.

The prototype associative memory model is too simple to explain the memory mechanism of the real brain. However, it inspired the physiological and molecular-biological study of the hippocampus.

4. Learning and self-organization, reinforcement learning

A general theory of classic synaptic learning was proposed by Amari [6]. This includes associative, supervised and unsupervised learning. It includes the PCA mechanism, which later rediscovered by Oja. The self-organization of feature extraction was shown possible through the balance of inhibitory and excitatory synapses. This was the same as the BCM mechanism proposed later except for the interpretation (sliding threshold or enhancement of inhibition).

The self-organization of neuron pools and neural fields was proposed by von der Malsburg and Willshaw and Malsburg. Their models and theories were epoch-making. Amari and Takeuchi [10] applied it to show the dynamics of self-organizing neural fields. Based on these prior research, Kohonen proposed the SOM model.

The classic theory does not cover the following new research topics. Reinforcement learning is an old topic of research, but its neural version was proposed by Barto and Sutton. Since then, it is a hot topic of research both in brain science, where basal ganglia and dopamine neurons play a role, and robotics learning.

Beyond the rate firing resume, information processing by neuronal spikes has been remarked, since this gives more detailed description of neural activities, and synchronization of spikes are hot topic. See Diesmann et al for the classic dynamical analysis of propagation and formation of neural synchrony. A learning mechanism called STDP is also a hot topic of research, where it generates automatically inhibitory effect of synapses, giving richer phenomena.

5. Statistical analysis of neuronal spikes

Neurons are believed to generate spikes not deterministically but rather stochastically due to various fluctuations. Spikes of neurons are correlated spatially and temporally. There are extensive studies of statistical analysis of neuronal spikes. Consider a joint probability distributions of spikes of n neurons $p(x_1, \dots, x_n)$, where each x_i takes 0 or 1 depending on the non-existence or existence of a spike.

Neuronal spikes are correlated. Usually only pairwise correlations are taken into account, but higher-order correlations such as intrinsic triplewise correlations exist. In order to elucidate their roles, it is useful to consider the set S of all such probability distributions. This forms an $(2^n - 1)$ -dimensional manifold. Since S is an exponential family, we can introduce a dually flat coordinate systems together with a Riemannian metric. The firing rate coordinate system is dually flat, and its dual represents higher-order interactions. Since these two coordinate systems are blockwise dually orthogonal, we can decompose (joint) firing rates and (higher-order) correlations orthogonally.

6. Machine learning

The perceptron is a learning machine proposed by Rosenblatt. The learning algorithm of its multilayer version, called the multilayer perceptron, was proposed by Amari [2], and then rediscovered many researchers, in particular by connectionists, and has become popular under the name of the error backpropagation learning algorithm. Although it is used in many applications, there are difficulties: slow convergence and local minima.

In order to overcome the local minima problem, the support vector machine is used and become popular with the kernel method. Another approach is the boosting method where weak learners are integrated to give a good performance. Information geometry is used in its theoretical analysis.

The dynamics of learning in multilayer perceptron was studied in [2] (the results are later rediscovered by Heskes and Kappen). It was shown by statistical physical method that the retardation of learning (called the plateau phenomena) is given rise to by the symmetrical structure of the machine, where the symmetry breaking is required. This is the cause of the retardation.

It was shown that symmetry causes singularities in the manifold of perceptrons where learning trajectories are embedded. The Fisher information

degenerates at the singularities. Amari [18] proposed a new learning method called the natural gradient, which avoids the difficulty of slow convergence. The dynamical behavior learning near singularities are studied in detail.

Unsolved Problems

We mentioned some long-standing mathematical problems which have not yet been solved in the oral presentation.

List of Selected Papers by Amari

1. Amari, S.: *Mathematical Theory of Neural Networks* (in Japanese). Sangyou-tosyo (1978).
2. Amari, S.: *Theory of Adaptive Pattern Classifiers*. *IEEE Trans.* **EC-16(3)** (1967) 299–307.
3. Amari, S.: *Characteristics of Randomly Connected Threshold-Element Networks and Network Systems*. *Proc. IEEE.* **59(1)** (1971) 35–47.
4. Amari, S.: *Neural Theory of Association and Concept -Formation*. *Biological Cybernetics* **26** (1977) 175–185.
5. Amari, S., Yoshida, K., Kanatani, K.: *A Mathematical Foundation for Statistical Neurodynamics*. *SIAM J. Appl. Math.* **33** (1977) 95–126.
6. Amari, S.: *Dynamics of Pattern Formation in Lateral-Inhibition Type Neural Fields*. *Biological Cybernetics* **27** (1977) 77–87.
7. Amari, S.: *Characteristics of Random Nets of Analog Neuron-Like Elements*. *IEEE Trans. Systems, Man and Cybernetics* **SMC-2(5)** (1972a) 643–657. (also *Artificial Neural Networks Theoretical Concepts*. ed. Vemri, V.. *IEEE Comp. Soc.* (1988))
8. Amari, S.: *Learning Patterns and Pattern Sequences by Self-Organizing Nets of Threshold Elements*. *IEEE Trans. Computers* **C-21(11)** (1972b) 1197–1206.
9. Amari, S.: *A Method of Statistical Neurodynamics*. *Kybernetik* **14** (1974) 201–215.
10. Amari, S., Takeuchi, A.: *Mathematical Theory on Formation of Category Detecting Nerve Cells*. *Biol. Cybernetics* **29** (1978) 127–136.
11. Takeuchi, A., Amari, S.: *Formation of Topographic Maps and Columnar Microstructures*. *Biol. Cybernetics* **35** (1979) 63–72.
12. Amari, S.: *Field theory of self-organizing neural nets*. *IEEE Trans. Systems, Man and Cybernetics* **SMC-13(9&10)** (1983) 741–748.
13. Amari, S., Maginu, K.: *Statistical neurodynamics of associative memory*. *Neural Networks* **1(1)** (1988) 63–73.
14. Amari, S.: *Mathematical Foundations of Neurocomputing*. *Proceedings of the IEEE* **78(9)** (1990) 1443–1463.
15. Amari, S.: *A Universal Theorem on Learning Curves*. *Neural Networks* **6(2)** (1993) 161–166.
16. Amari, S., Kurata, K., Nagaoka, H.: *Information Geometry of Boltzmann Machines*. *IEEE Trans. on Neural Networks* **3(2)** (1992) 260–271.
17. Amari, S.: *The EM Algorithm and Information Geometry in Neural Network Learning*. *Neural Computation* **7(1)** (1995) 13–18.
18. Amari, S.: *Natural Gradient Works Efficiently in Learning*. *Neural Computation* **10(2)** (1998) 251–276.
19. Amari, S., Ozeki, T., Park, H.: *Learning and Inference in Hierarchical Models with Singularities*. *Systems and Computers in Japan* **34(7)** (2003) 34–42.
20. Amari, S.: *Conditional Mixture Model for Correlated Neuronal Spikes*. *Neural Computation* **22(7)** (2010) 1718–1736.

Memory Information Representation in the Hippocampus

Minoru Tsukada

Abstract The hippocampal network consists of three types of synapses that form a circuit. A spatiotemporal signal serves as the input to the hippocampus and is transmitted through a synapse in the dentate gyrus (DG) to the CA3, then through another synapse to the CA1. There also exists a simultaneous input which directly connects to the CA1.

Keywords Hebb learning rule • Spatio-temporal learning rule (non-Hebb) • Dendritic-soma system

1 Long Term Potentiation (LTP), Depression (LTD) and Hebbian Type Learning Rule

Hebb [15] formulated the idea that modification is strengthened only if the pre- and post-synaptic elements are activated simultaneously. Experimentally, long term potentiation (LTP) and long term depression (LTD) are generally considered to be the cellular basis of learning and memory. Recently, a series of experiments provided direct empirical evidence of Hebb's proposal [5, 8–11, 20, 21, 25, 36]. These reports indicated that synaptic modification can be induced by repetitive pairing of EPSP and back-propagating action potentials (BAPs). The influence of location dependency of synaptic modification along dendritic trees was examined in the CA1 area of rat hippocampal slices. A pair of electrical pulses was used to stimulate the Schaffer-commissural collaterals (SC) and stratum oriens (SO). Then we estimated the profile of LTP and LTD at a layer specific location from the proximal to distal region of the SR.

M. Tsukada (✉)

Brain Science Institute, Tamagawa University, 6-1-1 Tamagawagakuen, Machida, Tokyo, Japan
e-mail: tsukada@eng.tamagawa.ac.jp

These instances of LTP and LTD showed a globally symmetric window of spike timing similar to a “Mexican hat function.” We tested the location dependence of synaptic modification along dendritic trees. A symmetric window was obtained at the proximal region of the SR where GABAergic interneurons are projected, while an asymmetric window was obtained at the distal region of the SR where there is no projection of GABAergic interneurons.

2 Spatio-Temporal Learning Rule (Non Hebbian)

The spatiotemporal learning rule (STLR), proposed as a non-Hebbian type by Tsukada et al. [32], Tsukada and Pan [33] consisted of two defining factors: (a) cooperative plasticity without a postsynaptic spike and (b) temporal summation.

Neurophysiological evidence of “temporal summation” was obtained by applying temporal stimuli to Schaffer collaterals of CA3 [1–3, 31, 32]. Cooperative plasticity by using two stimulus electrodes to stimulate the Schaffer-commissural collaterals (SC) [34]. The functional connection/disconnection depends on the input-input timing dependent LTP (cooperative plasticity) [12]. This is different from the Hebbian learning rule, which requires coactivity of pre- and post-cell. However, the magnitude LTP is also influenced by BAPs. From these experimental results, it can be concluded that the two learning rules, STLR and HEBB, coexist in single pyramidal neurons of the hippocampal CA1 area.

3 The Functional Differences Between STLR and HEBB

The two rules are applied to a single-layered feed-forward network with random connections and their abilities to separate spatiotemporal patterns are compared with those of other rules, including the Hebbian learning rule and its extended rules [33]. The differentiation of output-patterns represented in learned networks was analyzed by their Hamming distances.

HEBB produced the same output pattern, with a Hamming distance of zero, for all of the different spatiotemporal input patterns. This proves that the Hebbian learning rule cannot discriminate among different spatiotemporal input patterns. The spatiotemporal learning rule had the highest efficiency in discriminating among spatiotemporal pattern sequences. The novel features of this learning rule were induction of cooperative plasticity without a postsynaptic spike and the time history of its input sequences. According to the Hebbian rule, connections strengthen only if the pre- and post-synaptic elements are activated simultaneously, and thus, the Hebbian rule tends to map all of the spatio-temporal input patterns with identical firing rates into one output pattern. HEBB has a natural tendency to attract analogous firing patterns into a representative one, put simply, “pattern completion.” In contrast, the spatio-temporal rule produces different output patterns depending on

each individual input pattern. From this, the spatiotemporal learning rule has a high ability in pattern separation, while the Hebbian rule has a high ability in pattern completion.

4 Interaction of Both Rules in a Dendrites-Soma System

The neuron can learn both the input context and its value function by top-down information, i.e. input contexts can be characterized by the top-down information.

Acetylcholine dependent plasticity. The role of soma spiking in relation to top-down information raises a number of interesting computational predictions. Hippocampal theta is one of the candidates of top-down information which is driven by the brain area, “the medial septum/the horizontal limbs of the diagonal band (MS/DB)” [6]. During active waking, acetylcholine from MS/DB input makes theta rhythms in CA3 and CA1 through interneurons. Synaptic modification by theta rhythms constricts the input window of neural information to theta band frequency [13, 14]. During quiet waking or slow-wave sleep, theta band constraints emerged owing to the low concentration of acetylcholine. The theta stimulation of adult rat hippocampal synapses induces LTP [29]. On the other hand, pyramidal neurons in CA1 area directly receive acetylcholine input from MS/DB . Acetylcholine input carries top-down modulation (motivational and/or attention) to the CA1 neuron. Direct acetylcholine application increased the amplitude of the BAP [26, 30], and increased the efficacy of LTP [24]. In conclusion, the regulation of the state of CA1 neurons by acetylcholine input reflects top-down modulation related to the value function of episodic memory by direct and indirect ways.

Noradrenergic dependent plasticity. Another candidate of extrinsic modulation is noradrenaline. Noradrenergic input carries emotional and/or arousal information [27]. The hippocampus receives a major noradrenergic input from the locus ceruleus (LC). Concurrent with acetylcholine input, noradrenergic input contributes to a synergistic effect at the same synapses [35], and enhances the synaptic process of learning [23]. Including noradrenaline, such neuromodulator molecules as serotonin and histamine may alter neuronal throughput and BAPs (so-called “meta-plasticity”) in such a way that these transmitters diffuse broadly.

Multi-functional synapse [17]. CA1 pyramidal neurons receive three inputs from different sources of information. The first one is sensory events as bottom-up through a gamma window [7], and the information is consolidated in synaptic weight space by using STLR. The second is the contexts as top-down signals through theta window [4, 22, 28], and modify the sensory information by using Hebbian learning rule. The third is neuromodulator (i.e. dopamine [16], acetylcholine, noradrenarine, etc.) inputs which relates to reward, attention, emotion, and controls the bias of its synaptic plasticity.

5 Conclusion

We have shown, experimentally, that both STLR and HEBB coexist in single pyramidal cells of the hippocampal CA1 area [18, 19]. Based on these facts, a theoretical neuron model was proposed that consolidates both local (bottom-up) and global (top-down) information into its synaptic weight space. The proposed model presented a computational framework for understanding the sophisticated context-sensitive mechanisms in the hippocampal CA1 neurons, depending on the value of novelty (dopamine dependent plasticity), motivational or attentional values through the theta rhythm (acetylcholine dependent plasticity), and emotional or arousal information (noradrenergic dependent plasticity).

References

1. T. Aihara, M. Tsukada, M.C. Crair, S. Sinomoto, (1997). Stimulus-Dependent Induction of Long-Term Potentiation in CA1 Area of the Hippocampus: Experiment and Model. *Hippocampus* 7, 416–426.
2. T. Aihara, Y., Kobayashi., H. Matsuda, H. Sasaki, M. Tsukada, (1998). Optical imaging of LTP and LTD induced simultaneously by temporal stimulus in hippocampal CA1 area. *Soc. Neurosci. Abs.* 24, 1070.
3. T., Aihara, M. Tsukada, H. Matsuda, (2000). Two dynamic processes for the induction of long-term in hippocampal CA1 neurons. *Biol. Cybern.* 82, 189–195.
4. B.H. Bland, J. Jackson, D. Derrie-Gillespie, T. Azad, A. Rickhi, J. Abriam, (2006). Amplitude, frequency, and phase analysis of hippocampal theta during sensorimotor processing in a jump avoidance task. *Hippocampus* 16, 673–681.
5. C.A. Boettiger, A.J. Doupe. (2001). Developmentally restricted synaptic plasticity in a songbird nucleus required for song learning. *Neuron* 31, 809–818.
6. G. Buzsaki, L. Leung, C.H. Vanderwolf, (1983). Cellular bases of hippocampal EEG in the behaving rat. *Brain Res. Rev.* 6, 169–171.
7. J. Csicsvari, B. Jamieson, K.D. Wise, G. Buzsaki. (2003). Mechanisms of gamma oscillations in the hippocampus of the behaving rat. *Neuron* 37, 311–322
8. D. Debanne, S.M. Thompson, (1998). Associative long-term depression in the hippocampus in vitro. *Hippocampus* 6, 9–16.
9. D.E. Feldman, (2000). Timing based LTP and LTD at vertical inputs to layer II/III pyramidal cells in rat barrel cortex. *Neuron* 27, 45–56.
10. Y. Fregnac, D. Shulz, (1994). Models of synaptic plasticity and cellular analogs of learning in the developing and adult vertebrate visual cortex. In: Casagrande V P. Shinkman, editors. *Advances in neural and behavioral development*. Norwood, NJ: Ablex., 149–235
11. R.C. Froemke, Y. Dan, (2002). Spike-timing-dependent synaptic modification induced by natural spike trains. *Nature* 416, 433–438.
12. N.L. Golding, N.P. Staff, N. Spruston, (2002). Dendritic spikes as a mechanism for cooperative long-term potentiation. *Nature* 418, 326–331.
13. M. Hasselmo, (1999). Neuromodulation: acetylcholine and memory consolidation. *Trends Cogn. Sci.* 3, 351–359
14. M. Hasselmo, (2006). The role of acetylcholine in learning and memory. *Curr. Opin. Neurobiol.* 16, 710–715.
15. D.O. Hebb, (1949). *The organization of behavior*. New York, John Wiley.

16. J.A. Ihalainen, P.J. Riekkinen, M.G. Feenstra, (1999). Comparison of dopamine and norepinephrine release in mouse prefrontal cortex, striatum and hippocampus using microdialysis. *Neurosci Lett.* 277, 71–74.
17. J. Kay, W.A. Phillips, (1997) Activation functions, computational goals and learning rules for local processors with contextual guidance. *Neural Computation* 9, 895–910
18. J.E. Lisman, (1989). A mechanism for Hebb and the anti-Hebb processes underlying learning and memory. *Proc. Natl. Acad. Sci. USA* 86, 9574–9578.
19. J.E. Lisman, A.A. Grace, (2005). The hippocampal-VTA loop: controlling the entry of information into long-term memory. *Neuron* 46, 703–713.
20. J.C. Magee, D. Johnston, (1997). A synaptically controlled, associative signal for Hebbian plasticity in hippocampal neurons. *Science* 275, 209–213.
21. H. Markram, J. Lubke, M. Frotscher, B. Sakmann, (1997). Regulation of synaptic efficacy by coincidence of postsynaptic Aps and EPSPs. *Science* 275, 213–215.
22. R.S. Sainsbury, A. Heynen, C.P. Montoya, (1987). Behavioral correlates of hippocampal type 2 theta in the rat. *Physiol. Behav.* 39, 513–519.
23. C.L. Scheiderer, C.C. Smith, E. McCutchen, P.A. McCoy, E.E. Thacker, K. Kolasa, L.E. Dobrunz, L.L. McMahon, (2008). Coactivation of M(1) muscarinic and alpha1 adrenergic receptors stimulates extracellular signal-regulated protein kinase and induces long-term depression at CA3-CA1 synapses in rat hippocampus. *J. Neurosci.* 28, 5350–5358.
24. T. Shinoe, M. Matsui, M. Taketo, T. Manabe, (2005). Modulation of synaptic plasticity by physiological activation of M1 muscarinic acetylcholine receptors in the mouse hippocampus. *J. Neurosci.* 25, 11194–11200
25. P.J. Sjöström, G.G. Turrigiano, S.B. Nelson, (2001). Rate timing and cooperativity jointly determine cortical synaptic plasticity. *Neuron* 32, 1149–1164.
26. V. Sourdet and D. Debanne (1999) The Role of Dendritic. Filtering in Associative Long-Term Synaptic. Plasticity. *Learn. Mem.* 6, 422–447
27. A.H. Stegeren, (2008). The role of the noradrenergic system in emotional memory. *Acta Psychol (Amst)* 127, 532–41.
28. M. Takahashi, J. Lauwereyns, Y. Sakurai, M. Tsukada, (2009). A code for spatial alternation during fixation in rat hippocampal CA1 neurons. *J. Neurophysiol.* 102, 556–567.
29. M.J. Thomas, A.M. Watabe, T.D. Moody, M. Makhinson, T.J. O’Dell, (1998). Postsynaptic complex spike bursting enables the induction of LTP by theta frequency synaptic stimulation. *J. Neurosci.* 18, 7118–26.
30. H. Tsubokawa, W.M. Ross, (1997). Muscarinic modulation of spike back-propagation in the apical dendrites of hippocampal CA1 pyramidal neurons. *J. Neurosci.* 17, 5782–5791.
31. M. Tsukada, T. Aihara, M. Mizuno, H. Kato, K. Ito, (1994). Temporal pattern sensitivity of long-term potentiation in hippocampal CA1 neurons. *Biol. Cybern.* 70, 495–503.
32. M. Tsukada, T. Aihara, H. Saito, H. Kato, (1996). Hippocampal LTP depends on spatial and temporal correlation of inputs. *Neural Networks* 9, 1357–1365.
33. M. Tsukada, X. Pan, (2005). The spatiotemporal learning rule and its efficiency in separating spatiotemporal patterns. *Biol. Cybern.* 92, 139–146.
34. M. Tsukada, Y. Yamazaki, H. Kojima, (2007). Interaction between the Spatio-Temporal Learning Rule (STLR) and Hebb type (HEBB) in single pyramidal cells in the hippocampal CA1 Area. *Cogn. Neurodyn.* 1, 1157–1167.
35. A.M. Watabe, P.A. Zaki, T.J. O’Dell, (2000). Coactivation of beta-adrenergic and cholinergic receptors enhances the induction of long-term potentiation and synergistically activates mitogen-activated protein kinase in the hippocampal CA1 region. *J. Neurosci.* 20, 5924–31.
36. L.I. Zhang, H.W. Tao, C.E. Holt, W.A. Harris, M. Poo, (1998). A critical window for cooperation and competition among developing retinotectal synapses. *Nature* 395, 37–44.

Part II
Neuronal Impulse Patterns, Bifurcations
and Model Complexity

Functional Significance of Rall's Power of Three Halves Law in Cortical Nonpyramidal Cells

Yoshiyuki Kubota, Masaki Nomura, Fuyuki Karube, and Yasuo Kawaguchi

Abstract Neurons receive thousands of synaptic inputs onto their dendrites and soma, and spatially and temporally integrate these inputs to produce appropriate output in the form of action potentials generated in axons. The morphology of dendrites can influence the integration of synaptic input, as well as affect the pattern of action potentials. Using computer simulations of three different model neuron subtypes with different dendritic dimension of the same branching pattern identical to the authentic cortical interneuron in the rat frontal cortex: Martinotti cell, fast spiking basket cell, double bouquet cell, and large-basket cell, we found the functional significance of Rall's power of three halves law at the dendritic bifurcation point. It may facilitate even distribution of somatic depolarization into all compartments of the dendritic tree, and it may contribute equal signal conduction from soma to all dendritic branches.

Keywords Rall • Dendrite • Non-pyramidal cell • Back propagation

Y. Kubota (✉) • Y. Kawaguchi

Division of Cerebral Circuitry, National Institute for Physiological Sciences,
Okazaki 444-8787, Japan

Department of Physiological Sciences, The Graduate University for Advanced Studies
(SOKENDAI), Okazaki 444-8585, Japan

CREST, JST, Tokyo 102-0075, Japan
e-mail: yoshiy@nips.ac.jp

M. Nomura

Laboratory for Cellular Systems Modeling, RIKEN Research Center for Allergy
and Immunology (RCAI), Yokohama 230-0045, Japan

CREST, JST, Tokyo 102-0075, Japan

F. Karube

Division of Cerebral Circuitry, National Institute for Physiological Sciences,
Okazaki 444-8787, Japan

CREST, JST, Tokyo 102-0075, Japan

1 Introduction

Dendrite of neuron is a complex structure with many bifurcations and receives thousands of synaptic inputs. It spatially and temporally integrates these inputs to produce appropriate output in the form of action potentials generated in axons [1–4]. The morphology of dendrites can influence the integration of synaptic input, as well as affect the pattern of action potentials [5–7].

We analyzed dendritic trees in four morphologically distinct interneuron subtypes present in the rat frontal cortex: Martinotti (MA) cell, fast spiking (FS) basket cell, double bouquet (DB) cell, and large-basket (LB) cell, using three-dimensional reconstructions from light and electron microscopic observations, and found three conserved principles [8]. The first: cross-sectional area at any given point within a dendrite is proportional to the summed length of distally located dendrites beyond it. The second: total cross-sectional area is conserved at dendritic bifurcation points and also the Rall’s so called “three-halves power law” is right in dendrite bifurcations of these cortical cells. The third: dendritic cross-sections become more ellipsoidal at proximal locations, resulting in a conservation of the surface to volume ratio throughout the dendritic tree. Computer simulations using passive model cells found how these topological features compensate for distance dependent filtering of somatic EPSPs, while facilitating the even distribution of somatic depolarization into all compartments of the dendritic tree.

We hypothesize the Rall’s power of three-halves law [9] is a functional key structure for the equilibrated signal flow mechanism of the dendritic arborization. We made two kinds of computational passive model cells, which faithfully represent morphology of the real nonpyramidal cells, with active channels in soma and axon initial segment to activate spike to investigate the functional role of the law using NEURON simulator [10]. We also found that spike depolarization in soma distribute more evenly in the model cells which faithfully represent Rall’s power of three halves law.

2 Methods

Using an *in vitro* slice preparation containing the neocortex of juvenile rats p19–p23, we made whole-cell recordings to fill nonpyramidal cells with biocytin. After fixation, the morphologies of these neurons were recovered by DAB staining and reconstructed with Neurolucida. We selected four interneurons representing each of four nonpyramidal cell subtypes: a regular spiking nonpyramidal (RSNP) MA cell, a fast spiking FS cell, an RSNP DB cell, and a burst spiking nonpyramidal BSNP LB cell (Fig. 1). Neurons selected had at least a few complete dendritic trees not severed during slice preparation. Slices containing these neurons were re-sectioned into ultra-thin (90 nm) sections for 3-dimensional reconstruction of their dendritic structures [11]. Each subtype had stereotypical morphological properties of axonal and dendritic arborization that were previously described [12, 13].

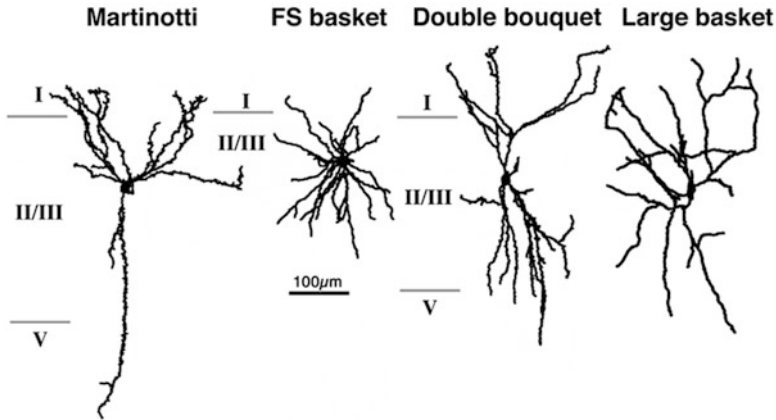


Fig. 1 Dendrite structures of neocortical cells representing four nonpyramidal neuron subtypes. Dendrites and soma of the Martinotti, FS basket, double bouquet and large basket cell. The property of their dendritic dimension was morphologically analyzed by the light and electron microscopic observations

All the simulation studies were done in NEURON platform [10]. The real morphology model neurons faithfully represented the present morphological results of the nonpyramidal cells, which follow the Rall's power of $3/2$ laws. Each model incorporates no active ion channels but passive leak channel. (Membrane resistance: $25,000 \Omega\text{cm}^2$, intracellular resistance: $200 \Omega\text{cm}$, membrane capacity: 100 F/cm^2 , equilibrium potential: 158 mV (MA cell), -72 mV (FS cell), -62 mV (DB cell) and -63 mV (LB cell)) [9]. To explore transmission of back-propagation of action potential, Nav1.2, Nav1.6 and Kv channels are introduced in the axon initial segment and the soma. Channel densities are distributed in the same way as described [14].

We also made the other type of model neurons in each nonpyramidal cell subtypes: "Conductance mismatch model cell A and B", which has branching points do not follow the Rall's power of three halves law. We modified diameters of thicker daughter dendrites at the branching point being half of their originals i.e. cross sectional area became quarter size in type A model. We made the diameter of smaller daughter dendrite 1.5 times larger than the original size i.e. cross sectional area become 2.25 times larger than the original, and the diameter of larger daughter dendrite half of the original size in type B model. The conductance mismatch model cells broke the Rall's power of three halves law at the bifurcation points to some extent.

3 Results

The functional significance of the Rall's power of three halves law was studied by computational passive models of reconstructed neuron morphologies (real-morphology model) and morphologies modified to eliminate branch point

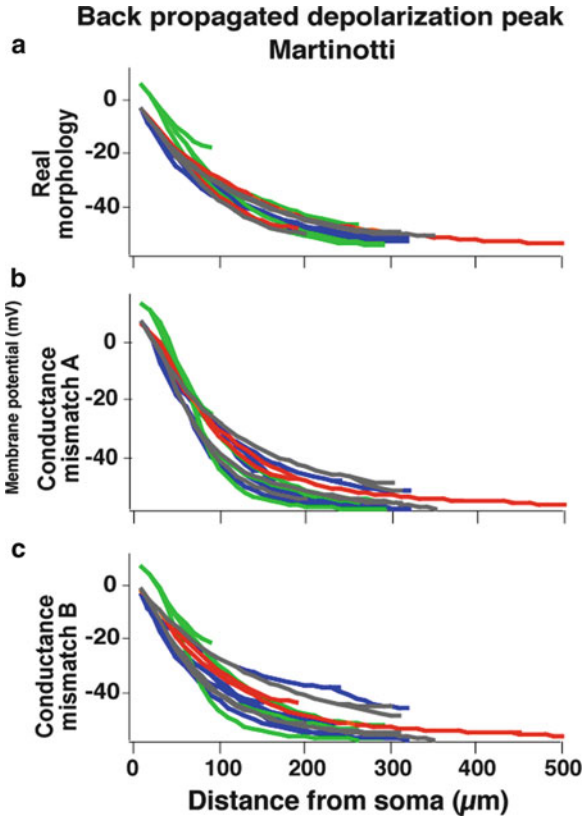


Fig. 2 Back propagated depolarization peak of three type of Martinotti cell model. **(a)** Plot of peak depolarization of dendritic compartments in response to a generated spike at soma in the real morphology model cells. The back-propagated current is evenly distributed in primary dendrites, and their associated trees. **(b)** Plot of peak depolarization of dendritic compartments in response to a generated spike at soma in the conductance mismatch model cell type A. The back-propagated current is rather variously distributed in different branches. **(c)** Plot of peak depolarization of dendritic compartments in response to a generated spike at soma in the conductance mismatch model cell type B. The back-propagated current is more variously distributed in different branches than the type A model cell

conductance matching (conductance-mismatch model) of four nonpyramidal cell subtypes (Fig. 2, see Sect. 2). We examined passive attenuation of somatically generated spike depolarization in computational models.

Firstly we compared the variability of back-propagated depolarization to different dendritic branches among the three Martinotti model cell subtypes. The somatic spike generated more even depolarization of dendritic branches in neurons with morphologically authentic branch points and consistently limited variation in peak depolarization irrespective of distance from the soma (Fig. 2a), while models with conductance mismatched branch points exhibited highly variable depolarization

Table 1 Conductance matching index of Martinotti cell

	Model			
	n	Real Morpho	Con Mis A	Con Mis B
Average	18	1.22	0.77	1.14
SD		0.15	0.18	0.22
Range		0.80–1.45	0.47–1.29	0.71–1.56

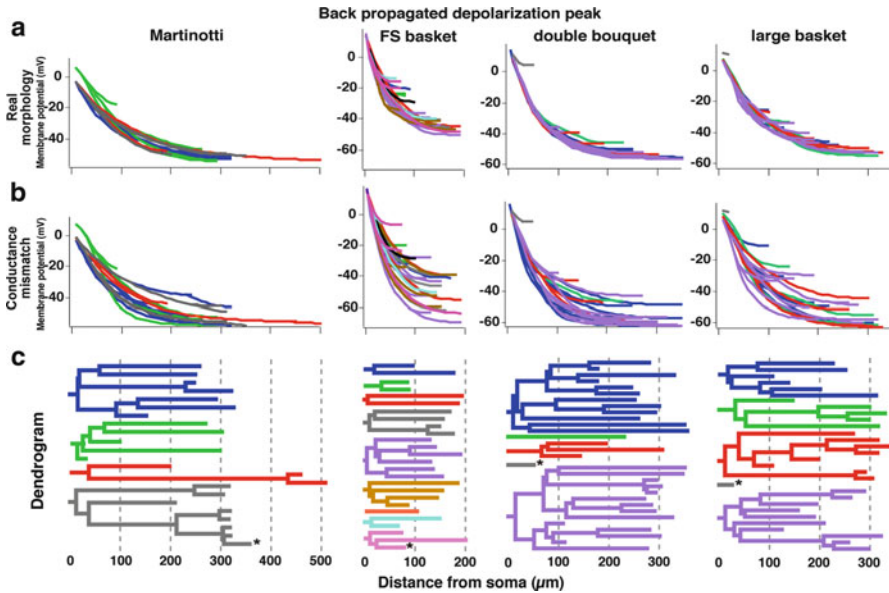


Fig. 3 Dendritic branch points are optimized for the uniform distribution of somatic voltage into the dendritic tree. (a) Plot of peak depolarization of dendritic compartments in response to a generated spike at soma in the real morphology model cells. The back-propagated current is evenly distributed in different branches. Primary dendrites, and their associated trees, are color coded as the dendrogram in c. (b) Plot of peak depolarization of dendritic compartments in response to a generated spike at soma in the conductance mismatch model cells. The back-propagated current is rather variously distributed in different branches. (c) Dendrogram of the model cells

of dendritic branches, with the magnitude of variability increasing with distance from the soma (Fig. 2b, c). Conductance mismatch model type B showed higher variability at the middle and distal range in the distance from soma than the type A (Fig. 2b, c). To quantify this relationship, we calculated the conductance matching index by dividing the summed dendritic $\sqrt{c \times a}$ of the two daughter branches by the $\sqrt{c \times a}$ of the parent dendrite [8], where ‘c’ is circumference and ‘a’ is cross sectional area of the dendrite (Table 1). The matching index of the type B model cell is similar to the real morphology model cell and the standard deviation is higher than the type A and real morphology model, therefore we chose type B for the further comparison of back propagated depolarization peak analysis with the real morphology model of the four subtypes. The similar results were observed in the

other neuron model subtypes, as well (Fig. 3). It indicated that the Rall's power of three halves law is an important structure for the even distribution of the back-propagated depolarization of somatic spike.

4 Discussions

We made three different type of model cell of four nonpyramidal cell subtypes to investigate the role of Rall's power of $3/2$ law and found that the law is a key structure to establish even distribution of somatic spike depolarization into different dendritic branches. The conductance mismatch models showed less even distribution of the depolarization than the real morphology model cell. It implicated that somatic depolarizing potential back propagation differently affect the different branches and it might change the firing pattern from the real morphology model cell, although further investigation is necessary.

We also believe that some model neurons may not respect the dendritic dimension of the real neuron [15]. We can make realistic membrane property and firing pattern of the model cell that resemble with the real neuron with adjustment of the active channel distribution and density appropriately. If the dendritic dimension of the models cell would be authentic, then the adjustment of the channel distribution should be easier and they could be similar to the real neuron. We can estimate the channel distribution of the real cell with referring them of the authentic model neuron.

Acknowledgements This work was supported by Grant-in-Aid for Scientific Research on Innovative Areas "Neural creativity for communication (No. 4103)" (22120518) from the MEXT of Japan.

References

1. Gullledge, A.T., B.M. Kampa, and G.J. Stuart, *Synaptic integration in dendritic trees*. J Neurobiol, 2005. **64**(1): p. 75–90.
2. Polsky, A., B.W. Mel, and J. Schiller, *Computational subunits in thin dendrites of pyramidal cells*. Nat Neurosci, 2004. **7**(6): p. 621–7.
3. Spruston, N., *Pyramidal neurons: dendritic structure and synaptic integration*. Nat Rev Neurosci, 2008. **9**(3): p. 206–21.
4. Williams, S.R. and G.J. Stuart, *Dependence of EPSP efficacy on synapse location in neocortical pyramidal neurons*. Science, 2002. **295**(5561): p. 1907–10.
5. Luebke, J.I., et al., *Dendritic vulnerability in neurodegenerative disease: insights from analyses of cortical pyramidal neurons in transgenic mouse models*. Brain Struct Funct, 2010. **214**(2–3): p. 181–99.
6. van Ooyen, A., et al., *The effect of dendritic topology on firing patterns in model neurons*. Network, 2002. **13**(3): p. 311–25.
7. Vetter, P., A. Roth, and M. Häusser, *Propagation of action potentials in dendrites depends on dendritic morphology*. J Neurophysiol, 2001. **85**(2): p. 926–37.

8. Kubota, Y., F. Karube, M. Nomura, A.T. Gullledge, A. Mochizuki, A. Schertel, and Y. Kawaguchi, *Conserved properties of dendritic trees in four cortical interneuron subtypes*. Scientific Reports, 2011. **1**: p. 89.
9. Rall, W., *Electrophysiology of a dendritic neuron model*. Biophys J, 1962. **2**(2 Pt 2): p. 145–67.
10. Hines, M.L. and N.T. Carnevale, *The NEURON simulation environment*. Neural Comput, 1997. **9**(6): p. 1179–209.
11. Kubota, Y., S.N. Hatada, and Y. Kawaguchi, *Important factors for the three-dimensional reconstruction of neuronal structures from serial ultrathin sections*. Front Neural Circuits, 2009. **3**: p. 4.
12. Karube, F., Y. Kubota, and Y. Kawaguchi, *Axon branching and synaptic bouton phenotypes in GABAergic nonpyramidal cell subtypes*. J Neurosci, 2004. **24**(12): p. 2853–65.
13. Kawaguchi, Y., F. Karube, and Y. Kubota, *Dendritic branch typing and spine expression patterns in cortical nonpyramidal cells*. Cereb Cortex, 2006. **16**(5): p. 696–711.
14. Hu, W., et al., *Distinct contributions of Na(v)1.6 and Na(v)1.2 in action potential initiation and backpropagation*. Nat Neurosci, 2009. **12**(8): p. 996–1002.
15. Behabadi, B.F. and B.W. Mel, *J4 at sweet 16: a new wrinkle?* Neural Comput, 2007. **19**(11): p. 2865–70.

A Computational Study of the Role of the Sub-thalamic Nucleus in Behavioral Switching During Saccadic Movements

Rengaswamy Maithreye and V. Srinivasa Chakravarthy

Abstract In this work, we have modeled the role of the STN-GPe during the switch from automatic to voluntary movement using the control of saccadic eye movement as an example. We show that our network model of the basal ganglia is able to reproduce some experimental results and suggests a novel role for the STN-GPe network as a source of exploration in the function of the basal ganglia. This is particularly relevant to the Reinforcement Learning driven view of the BG, where the explorer is a necessary component of the Reinforcement Learning (RL) apparatus.

1 Introduction

The basal ganglia (BG) are a set of seven deep brain nuclei which are thought to play an important role in decision making and action selection [1, 2]. There are two important and alternate pathways through which information can flow in the BG—the direct pathway (DP) and the indirect pathway (IP). These pathways are gated by the neuromodulator dopamine (DA), which is a key player in the function of the BG. The DP is selected in conditions of high DA and leads to a ‘Go’ response whereas the IP is selected in conditions of low DA and leads to a ‘No-Go’ response [3].

The RL framework has been extensively used to model the function of the BG, with the discovery that DA corresponds to the difference between the expected and actual reward [4]. The difference, called temporal difference or TD error is the basis for learning in the RL framework [5]. The RL framework involves an actor, which performs actions, a critic, which computes the value of performing an action and an explorer which enables the exploration of alternate actions. Subsequently, the dorsal

R. Maithreye • V.S. Chakravarthy (✉)
Department of Biotechnology, Indian Institute of Science, Madras 600036, India
e-mail: srinivasa.chakravarthy@gmail.com

striatum has been associated with the computation of the value of each state, thus functioning as a critic while both ventral striatum and motor cortex is thought to be analogous to the actor [6, 7]. However, no sub-cortical substrate for the explorer has been proposed. The explorer is an essential component of the RL machinery since it generates the alternatives that are required for learning to take place. We hypothesized that the Sub-Thalamic Nucleus (STN) is a good candidate for the role of the explorer in the BG since it possesses the complex activity required for this role [8]. Also, lesions of the STN are shown to lead to an increase in perseverative behavior where the animal repeats previously rewarding actions even after they cease to be rewarding [9].

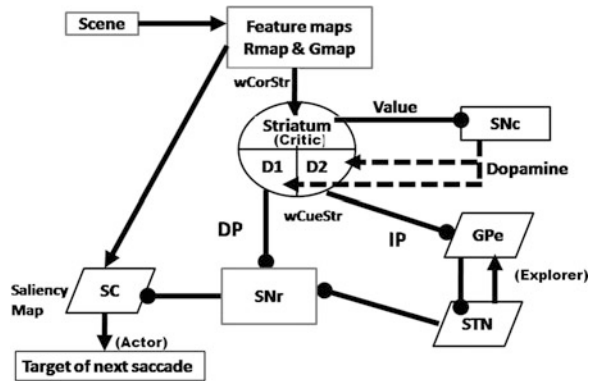
Recent work [10] has shown that the STN is a crucial link in the BG, especially during the switch from automatic to voluntary movements. During such a switch, a control signal to stop ongoing movement is thought to be sent via the hyperdirect link from cortex to STN, subsequent to which a new movement may be initiated. Interestingly, this work shows the presence of different types of STN neurons, (active only during switching to voluntary movement), some of which stop movement while others initiate new movement, lending support to our hypothesis that the STN can function as a source of exploration.

We have created a model of the BG with explicit representations of the striatum, the STN, the GPe and the SNr. We used this model to study the switch from automatic to voluntary movement using the same experimental set up as in [10], but without considering the hyperdirect pathway. We show that using only the direct and indirect pathways of response, we can match some of the reported experimental results, including the presence of ‘switch’ neurons which are active only during the switch from automatic to voluntary response.

2 Methods

A schematic version of the model is shown in Fig. 1. The task is to saccade to one of two targets whose color matches the cue color, which can change randomly [10]. While the cue color remains unchanged (non-switch trials), an automatic response would be sufficient whereas when the cue color changes (switch trials), voluntary control is required. The number of non-switch trials before a switch occurs can be varied. In our model, the input (i.e. the scene) consists of one red and one green dot whose position can alternate randomly. The cue can be either red or green and is supplied to the striatum, along with the red and green components of the input (called red and green feature maps- Rmap and Gmap respectively) via cortico-striatal and cue-striatal weights, both of which are trainable. The striatum, functions as the ‘critic’ and computes the value of the scene as a function of the previous reward. It is represented as comprising of DP and IP neurons, represented by separate CANNs of 1×20 neurons each [11]. The motor cortex (not represented explicitly) is considered to be the ‘actor’ which executes the saccade. The temporal difference (TD) error which is the average difference in the value between the

Fig. 1 Schematic representation of the model



current and previous scenes represents the dopamine (DA) signal, produced in response to a signal from the striatum by the *Substantia Nigra pars compacta* (SNc, not modeled). The magnitude of the DA signal is thought to select between the direct (DP) and indirect (IP) pathways by controlling the response from these neurons [3]. The response of the DP striatal neurons is directly passed on to the *Substantia Nigra pars reticulata* (SNr) whereas the response of the IP striatum is passed on to the *Globus pallidus externa* (GPe), which interacts with the Sub-Thalamic nucleus (STN) to produce an output. The STN-GPe network is modeled as an activator–inhibitor network of 20×20 neurons each, which possess lateral connections and reciprocal connections between STN and GPe. The firing rates of the STN and GPe neurons is assumed to be a function of DA such that these neurons are maximally active at low DA levels and their activity decreases with increasing DA [12]. The output of the STN-GPe network is summed and then passed on the SNr, again modeled as 1×20 layer of neurons. The signals from DP and IP are integrated in the SNr and sent to the Superior Colliculus (SC) where competition between signals directing movement to different locations is resolved, the saliency map is computed and the co-ordinates of the next saccade are determined as the location where the signal crosses a saliency threshold. When the cue color is unchanged, the DP is chosen and STN activity is low, whereas when cue color changes, DA levels decrease leading to activation of the IP and an increase in the firing rate of the STN and GPe neurons. STN neurons send a noisy signal to the SC, which functions to direct the saccade to a different location, thereby leading to exploration.

3 Results

We start out by examining the success rates in the switch and non-switch trials.

Success rates: Non-switch trials were 100% successful whereas the error rates in switch trials was 30% (Fig. 3a, blue curve). As the number of non-switch trials before a switch trial increased (3–10), the error rates also increased (from 16% to 40%).

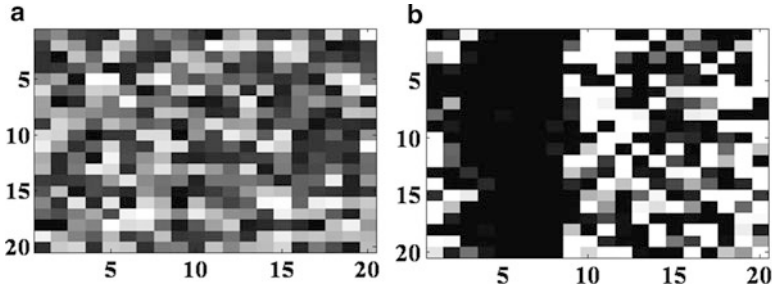


Fig. 2 Dynamics of the STN during (a) non-switch (high DA) and (b) switch trials (low DA). Here the X and Y axes represent the neuron positions while the color coding represents activity level with *white* representing maximum and *black* representing minimum activity

Time taken for switch and non-switch saccades: Switch trials (106 steps) took longer than non-switch trials (68 steps) (Fig. 3a, red curve). The wrong switch trials (112 steps) took slightly longer on average than the correct switch trials (104 steps). Here, the number of steps corresponds to the number of iterations required to cross saliency threshold.

Influence of DA on behavior of STN-GPe network: Since we were interested in the role of the STN in the functioning of the basal ganglia, we studied at the effect of DA levels on STN activity. Specifically, we looked at the STN response to high and low levels of DA. As can be seen from Fig. 2, at high levels of DA i.e. in non-switch trials, the STN network shows a nearly uniform low level of activity, as expected because of the low firing rate of STN neurons. At low levels of DA i.e. during the switch trials, much more complex activity is seen in the STN with a small region of intense activity as can be seen from Fig. 2b. Thus, we can see that different STN neurons behave differently.

We analyzed the activity of STN neurons in switch and non-switch trials and found that (i) the activity of the STN becomes more desynchronized in switch trials (average correlation between the neurons is 0.97 in case of non-switch trials as compared to an average correlation of 0.87 in the switch trials.) (Fig. 3b, c) and (ii) There is a small sub-population (20% of the 400 STN neurons) that shows distinctive activity as compared to the other neurons during the switch trials alone (Fig. 3c, red traces). These neurons are analogous to the ‘switch’ neurons reported in [10]. The activities of all the STN neurons during switch and non-switch trials are shown in Fig. 3b and c from which the distinct activity of the switch neurons (red curves, Fig. 3c) can be seen clearly.

4 Discussion

The role of the STN in the basal ganglia has been debated much in the past. It has been proposed variously that the STN functions to delay decisions till correct information is available[12] or alternately that it functions to carry a specific stop

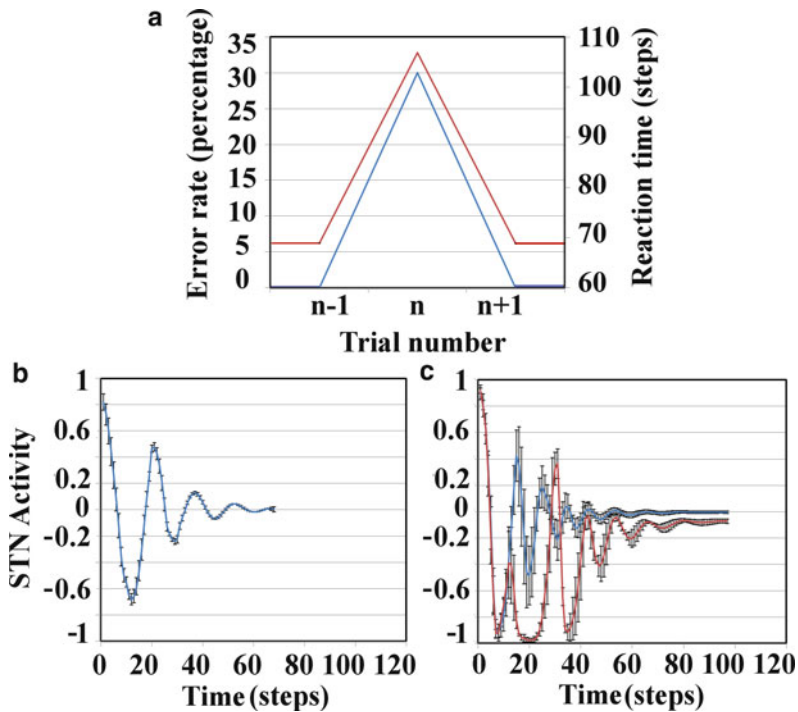


Fig. 3 (a) Error rates (*blue*) and reaction time (*red*) in switch and non-switch trials. STN activity during (b) non-switch and (c) switch trials. Activity of all the neurons is shown

signal during switching from automatic to voluntary responses [10]. Here, we propose an alternative view of STN function, where it acts as a source of exploration or noise in the BG. We show through our model that such a view is also compatible with experimental evidence. Using our model, we are able to match the success rates in and also show the presence of specialized switch neurons in the STN. The time of occurrence of correct and incorrect switch trials is the main factor that does not match with experimental results. It is likely that the hyperdirect pathway, which is not included in the current version of the model, is necessary to achieve this effect. Future studies would include this pathway as well.

Acknowledgments R.M. wishes to acknowledge the IIT-Madras postdoctoral fellowship for funding.

References

1. Redgrave P, Prescott TJ, Gurney K (1999b) The basal ganglia: a vertebrate solution to the selection problem? *Neuroscience* 89:1009–1023.
2. Chakravarthy VS, Joseph D, Bapi RS. What do the basal ganglia do? A modeling perspective. *Biol Cybern.* 2010 Sep;103(3):237-53.

3. Albin, R. L., Young, A. B. and Penney, J. B. The functional anatomy of basal ganglia disorders. *Trends Neurosci.* **12**, 366–375 (1989).
4. Schultz W, Dayan P, Montague PR (1997) A neural substrate of prediction and reward. *Science* 275:1593–1599.
5. Sutton RS, Barto AG (1998) Reinforcement learning: an introduction. MIT Press, Cambridge
6. O’Doherty J, Dayan P, Schultz J, Deichmann R, Friston K, Dolan RJ. (2004) Dissociable roles of ventral and dorsal striatum in instrumental conditioning. *Science.* 304:452–454.
7. Houk JC, Davis JL, Beiser DG (1995) Models of information processing in the basal ganglia. MIT Press, Cambridge
8. Sridharan, D., Prashanth, P.S., and Chakravarthy, V.S. (2006). The role of the basal ganglia in exploration in a neural model based on reinforcement learning. *International Journal of Neural Systems*, 16, 111–124.
9. Baunez C, Humby T, Eagle DM, Ryan LJ, Dunnett SB, Robbins TW.(2001) Effects of STN lesions on simple vs choice reaction time tasks in the rat: preserved motor readiness, but impaired response selection. *Eur J Neurosci.* 13:1609–1616.
10. M. Isoda and O. Hikosaka, “Role for subthalamic nucleus neurons in switching from automatic to controlled eye movement”, *J Neurosci.* 9,7209–7218.
11. D. I. Standage, T.P. Trappenberg and R.M. Klein, “Modelling divided visual attention with a winner-take-all network”, *Neural Networks*, vol. 18, pp. 620–627, 2005.
12. M.J. Frank, “Hold your horses: A dynamic computational role for the subthalamic nucleus in decision making,” *Neural Networks*, vol. 19, 2006, pp. 1120–1136

Spiking Neural Network Ink Drop Spread, Spike-IDS

Mohsen Firouzi, Saeed Bagheri Shouraki, and Mohammad Ghomi Rostami

Abstract ALM is an adaptive recursive fuzzy learning algorithm which is inspired by some behavioral features of human brain functionality. This algorithm is fairly compatible with reductionism concept in philosophy of mind in which a complex system is representing as combination of partial simpler knowledge or superposition of sub-causes effects. This algorithm utilizes a fuzzy knowledge extraction engine which is called Ink Drop Spread in brief IDS. IDS is inspired by non-exact operation paradigm in brain, whether in hardware level or inference layer. It enables fine grained tunable knowledge extraction mechanism from information which is captured by sensory level of ALM. In this article we propose a spiking neural model for ALM where the partial knowledge that is extracted by IDS, can be captured and stored in the form of Hebbian type Spike-Time Dependent Synaptic Plasticity as is the case in the brain.

1 Introduction

Today according to some biological evidences, we know that information processing in biological neural networks is being performed in the form of spike time dependent temporal coding that is called spike coding. This computation paradigm enables fast temporal and spatial processing simultaneously and prepares powerful networks with considerably less neurons and interconnects in comparison with conventional rate coding ANNs [1].

Besides micro-level neurophysiological findings of brain machine, some clinical researches have been done to study the black box of human mind through another

M. Firouzi (✉) • S.B. Shouraki • M.G. Rostami

Research Group for Brain Simulation and Cognitive Science, Artificial Creatures Lab,
Electrical Engineering School, Sharif University of Technology, Azadi Avenue, Tehran,
P.O.Box: 11365-9517, Iran

e-mail: mfirouzi@ee.sharif.edu; bagheri-s@sharif.edu; ghomirostami@ee.sharif.edu

point of view. Due to some evidences, human intelligence deals with real world phenomena with qualitative non-exact concepts which is generated by non-exact distributed hardware structure, that is mentioned as brain [2]. Moreover it appears that human brain confronts with real world complex problems by breaking down them into simpler and more comprehensible concepts the way that consumes less energy to acquire information and obtain knowledge. Then these fine grained partial knowledge could be refined and they are integrated by an inference process to make decision and recognition [3].

ALM was developed based on this set of hypotheses with the purpose of human brain learning simulation [3]. ALM is an adaptive recursive fuzzy algorithm which tries to express a Multi-Input Multi-Output (MIMO) system as a fuzzy combination of some simpler Single-Input Single-Output (SISO) sub-systems. This viewpoint of ALM to human learning process is compatible with some reductionism concepts in philosophy of mind in which a complex system is supposed as sum of its parts. In other words this fact can be represented more specifically in causal reductionism, which implies that the causes acting on the whole are simply the sum of the effects of the individual causalities of the parts [4]. This integrative approach has been used in some related works such as CAM Brain Machine which has been proposed by De Garis [5].

In this work we propose a spiking neural model for ALM. This Hybrid Model comprises single layer feed-forward multi-synaptic spiking neural structures in which partial knowledge can be extracted and stored through synaptic plasticity of SRM neurons. These partial knowledge are unified by fuzzy inference layer eventually to make decision surface. This work is a good reminder to need for unification of brain studies in different attitudes.

In next section IDS is explained in more detail, in Sect. 3 proposed model is presented and finally in Sect. 4 some evaluation results are reported.

2 Ink Drop Spread, IDS

As we discussed before in ALM a MIMO system is broken down into simpler SISO systems. Each SISO system is interpreted as x_i-y_j grid plane which is called IDS unit and consists of projected data points corresponding to specific interval domains of another input variables. Figure 1 shows a simple 2-input single-output ALM with two partitions for each variable domain. As we can see in Fig. 1 ALM can be represented in three layer: input layer, where input pattern variable is distributed in IDS units in correspondence with membership of another variables to fuzzy intervals. Modeling layer as most important layer of ALM in which IDS operator operates on IDS units to extract partial knowledge. IDS is like a Gaussian Ink Drop with radius R which spreads around each projected data points in order to extract two important features in partial knowledge space: Narrow trajectory (Ψ in Fig. 1) which describes input-output characteristic of IDS units and Spread value (σ in Fig. 1) which shows importance degree and effectiveness of partial knowledge in

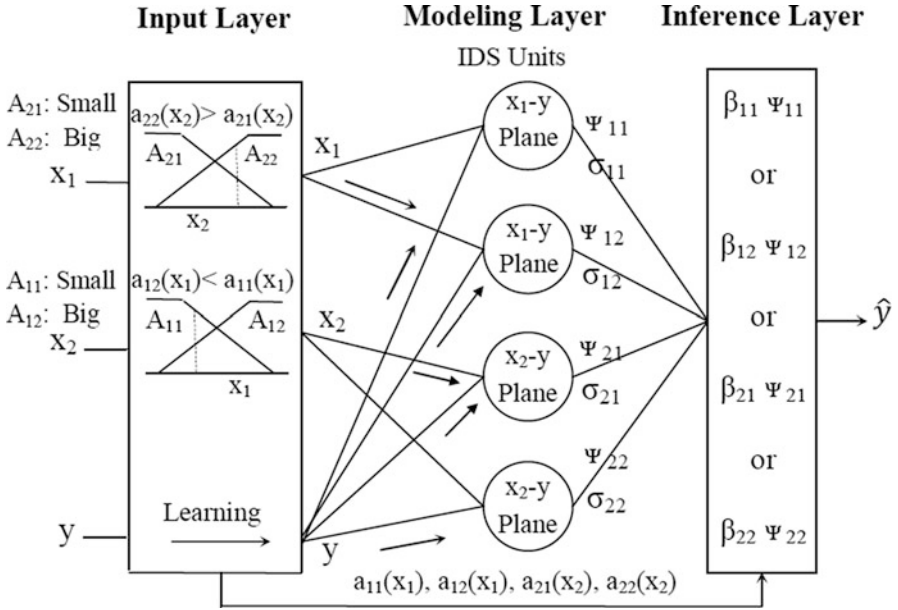


Fig. 1 Structure of 2-input 1-output ALM

overall system. This effectiveness is related reversely with Spread value. Finally these features are consolidated by fuzzy inference layer of algorithm to make overall input-output modeling surface. Mathematical implementation of Narrow and Spread is described as follow:

$$\Delta d(x, y) = e^{-\frac{(x-p_1)^2}{0.22 \cdot R^2}} \times e^{-\frac{(y-p_2)^2}{0.22 \cdot R^2}}, \sqrt{(x-p_1)^2 + (y-p_2)^2} \leq R \quad (1)$$

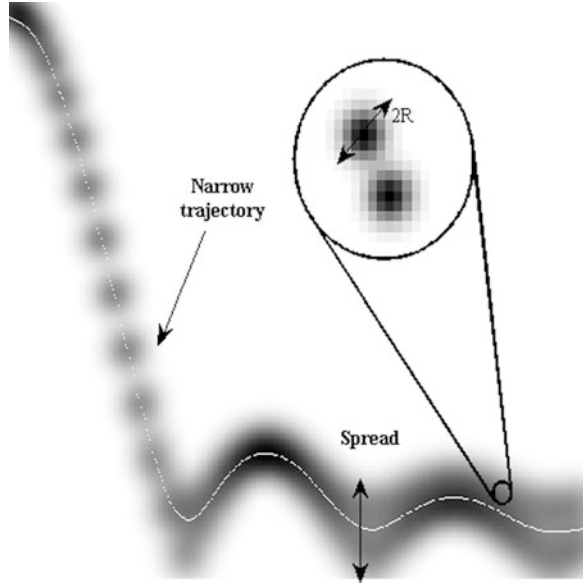
Where $\Delta d(x,y)$ is ink intensity in point (x,y) of IDS plane, (p_1, p_2) is the point of ink drop and R is Ink radius. Narrow path and Spread are described as (2), (3) respectively:

$$\psi(x_i) = \frac{\sum_{j=1}^n I_{ij} \times y_{ij}}{\sum_{j=1}^n I_j} \quad (2)$$

Where n is IDS grid plane resolution, I_{ij} denotes as Ink intensity for each y_j values corresponding to x_i .

$$\sigma(x) = \max \{y | d(x, y) > 0\} - \min \{y | d(x, y) > 0\} \quad (3)$$

Fig. 2 A simple IDS plane, after applying IDS



In Fig. 2 a simple IDS unit after IDS operation is presented. Also extracted narrow trajectory and spread value is shown. In inference layer of ALM, a Fuzzy inference unit applies narrow and spread values to generate a rule base in order to integrating partial knowledge and extract knowledge expertness existing in data samples. In the case of N -input with m_i partitions for i th input variable, the number of combination rules and IDS units corresponding to i th input which is denoted by l_i and total number of rules, L is as follows:

$$l_i = \prod_{k=1, \neq i}^N m_k \quad (4)$$

$$L = \sum_{i=1}^N l_i = \sum_{i=1}^N \prod_{k=1, \neq i}^N m_k \quad (5)$$

Also the k th rule of i th input variable, R_{ik} ($k = 1, 2, \dots, l_i$) can be described as:

$$\begin{aligned} R_{ik} : & \text{if } x_1 \in A_{1j_1} \wedge x_2 \in A_{2j_2} \wedge \dots \wedge x_{i-1} \in A_{i-1j_{i-1}} \wedge \\ & x_{i+1} \in A_{i+1j_{i+1}} \wedge \dots \wedge x_N \in A_{Nj_N} \text{ then } Y = \psi_{ik} \end{aligned} \quad (6)$$

Where $1 \leq j_s \leq m_s$, the overall output of model is obtained by (7):

$$Y \text{ is } \beta_{11}\Psi_{11} \text{ or } \dots \beta_{ik}\Psi_{ik} \text{ or } \dots \text{ or } \beta_{N \ 1N}\Psi_{N \ 1N} \quad (7)$$

$$\beta_{ik} = \frac{\alpha_{ik} \gamma_{ik}}{\sum_{p=1}^N \sum_{q=1}^{l_p} \alpha_{pq} \gamma_{pq}}, \alpha_{ik} = \log\left(\frac{1}{\sigma_{ik}}\right) \quad (8)$$

3 Spiking Neural Network IDS, Spike-IDS

3.1 Network Architecture

Network architecture of this work which is shown in Fig. 3 comprises multiple delayed synaptic terminals which is imitated by multiple synaptic gap in biological neurons. Each sub-synapse has specific arranged delay and synaptic weight. Membrane potential that is called internal state variable for a post-synaptic neuron j with m sub-synapse for each connection can be expressed as:

$$x_j(t) = \sum_{i \in \Gamma_j} \sum_{k=1}^m w_{ij}^k \varepsilon(t - t_i - d^k) \quad (9)$$

$$\varepsilon(t) = \frac{t}{\tau} e^{(1-\frac{t}{\tau})} \quad (10)$$

Where $\varepsilon(t)$ is simplified model of biological Excitatory Post-Synaptic Potential, t_i is firing time of pre-synaptic neuron i , d^k is fixed delay for k th sub-synapse which is arranged from zero ($d^k = \{0, 1, \dots, m-1\}$) and w_{ij}^k stands for synaptic weight of k th sub-synapse of i, j connection. Besides Γ_j is set of pre-synaptic neurons which are connected to post-synaptic neuron j . When internal state variable, x_j , exceeds from threshold voltage, ϑ , neuron j fired in t_j . this model of neuron is called as Spike Response Model in brief SRM [6].

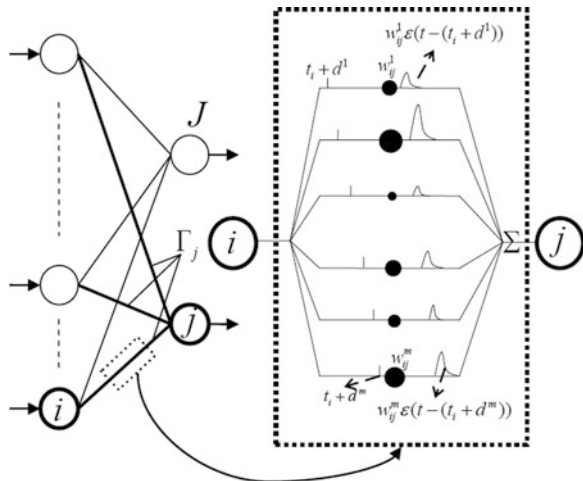


Fig. 3 General architecture of Spike ANN which is used in this work

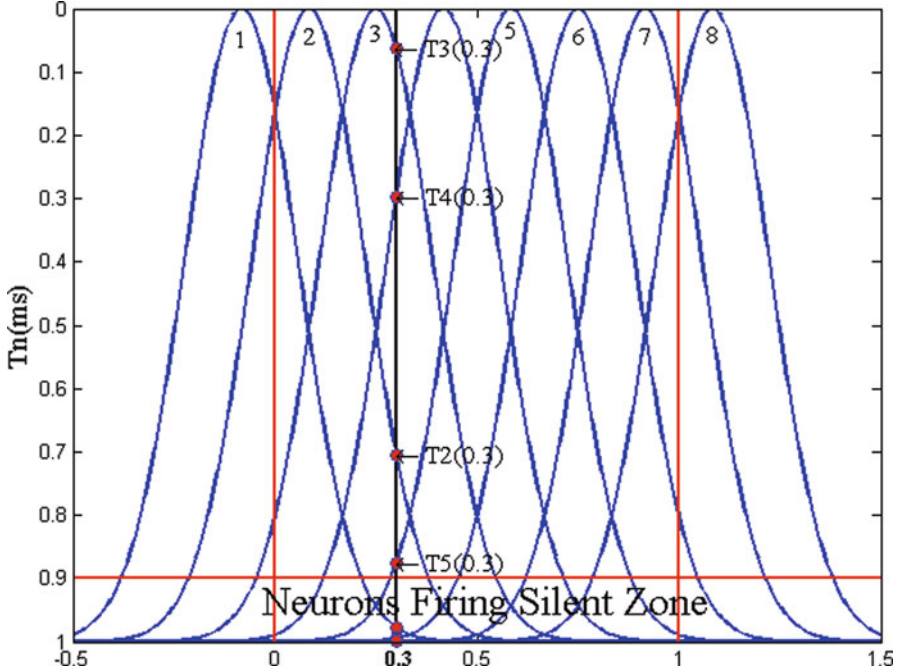


Fig. 4 Gaussian receptive fields for eight neurons encoding and delays for 0.3 as input

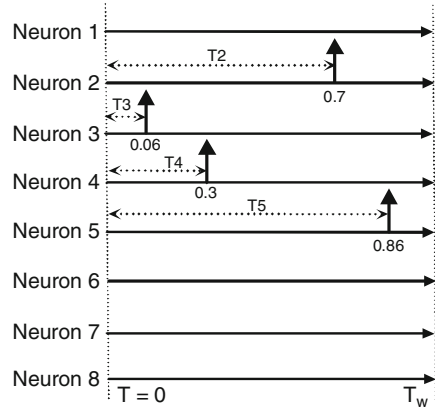
3.2 Information Coding

Proposed coding is a kind of population delay coding [7] which is inspired by non-exact spatial coding of IDS operator. In this coding scheme analog input or output variables are encoded with graded overlapping Gaussian receptive field profiles. Receptive fields capture spatial content of input variable in spike time delay format and store output features in RBF-like output neurons with same coding. Each input and output neuron stands for each receptive field with specific center and width.

In Fig. 4 overlapping Gaussian receptive fields for eight neurons are shown. Normalized firing times of related neurons for analog value of 0.3 is shown in Fig. 5. Neurons related to receptive fields which fire in more than 0.9 ms are supposed to be silent neurons and never to be fired. Center and Width of Gaussian receptive fields for n profiles are set as follows:

$$C_i = \frac{2(i-3)}{2(n-2)}, \quad \omega_i = \frac{1}{\gamma_i(n-2)} \quad (11)$$

Fig. 5 General scheme of spike delays for spike neurons related to 0.3 as input



3.3 Learning Algorithm

The learning algorithm is based on reinforcement Hebbian learning algorithm. It is demonstrated that there is a temporal reinforcement learning process in biological neuronal systems [1, 7]. When a neuron is stimulated artificially by extracellular electrode pulse train in way that enforced to be fired, EPSP which is made by a single spike stimulus from same connection gap has been strengthened in comparison with before pulse train stimulus and spike generation. This Hebbian type reinforcement plasticity mechanism is known as STDP in precise temporal coding [8]. These biological findings demonstrate that pre-synaptic neurons which contribute in firing of a post-synaptic neuron should be rewarded. Therefore to implement STDP like mechanism, a learning window which is defined as a function of time difference between firing times of t_i and t_j is proposed. This time window controls updating the weights based on this time difference as bellow ($\Delta t_{ij}^k = t_i - t_j + d^k$):

$$\Delta w_{ij}^k = \eta L(\Delta t_{ij}^k), w_{init} = 0, \quad 0 < w < 3 \quad (12)$$

$$L(\Delta t) = (1 + b)e^{\frac{(\Delta t - \delta)^2}{2(\kappa - 1)}} - b, \quad \kappa = 1 - \frac{v^2}{2 \ln(b/b + 1)} \quad (13)$$

This function reinforces synapses between neurons i, j with rate η if $\Delta t_{ij}^k < v$ and depress synaptic weight if $\Delta t_{ij}^k > v$. Figure 6 presents learning window. It is noticeable that because of time constant τ in EPSP (10), the firing of neuron i contributes in firing of neuron j not exactly after distribution of spike. Therefore learning window should be shifted slightly to achieve this consideration. In Fig. 6 δ denotes this shifting and usually sets to $-\tau$ value. Parameter v indicates reward

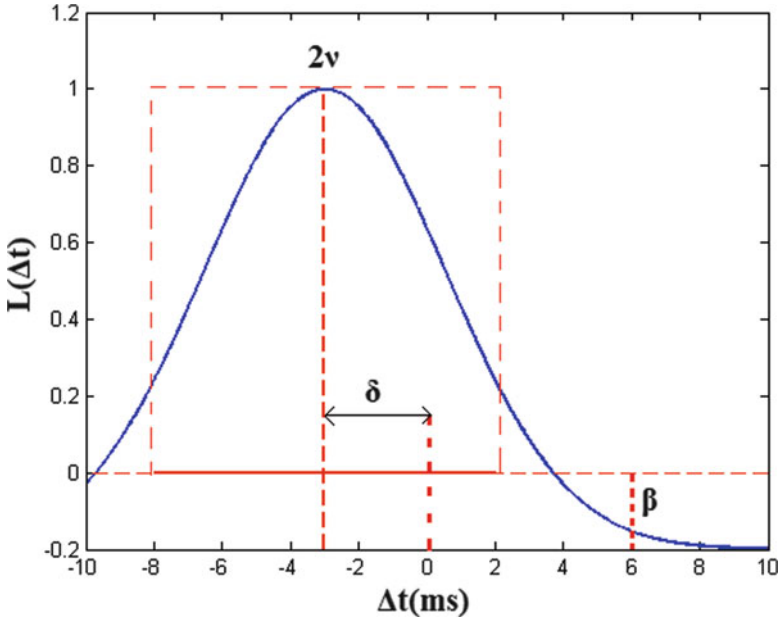


Fig. 6 Learning window of proposed SNN

neighborhood and b determines penalty depth. Also silent neurons should be penalized. So Δw_{ij} for weights between silent input neurons and fired output neuron is set to $-\eta$.

3.4 Narrow and Spread Extraction

General overview of learning steps is as follow: Initial value for W_{ij}^k sets to zero; regarding to single-input single-output structure of IDS units, input and output domain is encoded by receptive profiles; according to learning window the synaptic weights are updated in accordance with input-output firing times. In another viewpoint, proposed learning algorithm is a coding from Ink intensity in IDS plane into spike firing time in SNNs which enables tunable non-exact view to crisp data such as IDS. This learning algorithm implements overlapping Ink Drops which strengthens each other by successive weight updating for neighboring data points. Also in this learning method firing time of output neurons means to activation degree of related sensing profile. So by consolidating output firing times like COG Defuzzification, Narrow can be implemented in modeling phase. Also by thanks

of spatial arrangement of neurons, difference of receptive field centers for last and first fired output neurons stands for Spread value similar to IDS spread and narrow extraction method. Mathematical form of aforementioned mechanism is as:

$$\tilde{\psi}(x_{in}) = \frac{\sum_{i=1}^{m_o} T_i C_i}{\sum_{i=1}^{m_o} T_i}, \quad \tilde{\sigma}(x_{in}) = C_{last} - C_{first} \quad (14)$$

Where m_o is number of output receptive fields, T_i is firing time of stimulated output neuron i and C_i is related receptive field center, C_{last} and C_{first} are centers of receptive fields related to last and first fired output neurons and ψ and σ stand for Spike-IDS extracted narrow and spread values in modeling phase.

4 Evaluation Results

To evaluate proposed structure with IDS we choose a non-linear function approximation problem (two-input single-output system modeling) which is used as a benchmark in related works [9].

$$y(x_1, x_2) = \sqrt{2\left(\frac{\sin(x_1)}{x_1}\right)^2 + 3\left(\frac{\sin(x_2)}{x_2}\right)^2} \quad (15)$$

Where $1 \leq x_1, x_2 \leq 10$, also in order to verify the model accuracy, the error was measured using the fraction of variance unexplained (FVU) [9]:

$$FVU = \frac{\sum_{i=1}^L (\bar{y}(x_i) - y(x_i))^2}{\sum_{i=1}^L (y(x_i) - \bar{y})^2}, \quad \bar{y} = (1/L) \sum_{k=1}^L y(x_k) \quad (16)$$

Where x_l is l th input vector ($l=1,2,\dots,L$), y^{\setminus} denotes the output of a constructed model. The FVU value is calculated from 2,500 points at regular intervals over the input domains. Table 1 shows mean value of FVU error over ten random learning data sets with different set-size and partition numbers for proposed approach and IDS. Spike-IDS consists 15 input and 25 output neurons with 12 sub-synapse and learning parameters are experimentally set as: $\tau = 3$, $b = 0.2$, $\delta = -3$, $\nu = 5$, $\gamma = 1.4$, $\eta = 0.3$, $\vartheta = 10 \text{ mV}$ with epoch number 15. Resolution of IDS units is set to 256 and IDS radius is set to medium size, equal to 9 [9]. It is illustrated from Table 1 that Spike-IDS has good ability to model subjected system as well as IDS. Also it seems in the case of deficiency of knowledge, when learning set size is small, smaller partitioning that means less granularity, causes better performance and vice versa.

Table 1 FVU error of system modeling for Spike-IDS approach in comparison with IDS with medium Ink Drop size (9) over different training set number and different partition number

Number of partitions	IDS vs. spike-IDS	Training set size			
		100	250	400	550
5	IDS	0.171	0.068	0.043	0.039
	Spike-IDS	0.095	0.089	0.061	0.055
8	IDS	0.256	0.059	0.034	0.022
	Spike-IDS	0.153	0.057	0.051	0.025
12	IDS	0.35	0.083	0.036	0.021
	Spike-IDS	0.221	0.046	0.042	0.023

5 Conclusion

A novel Spike type artificial neural model of ALM learning algorithm is proposed in which IDS knowledge extraction mechanism is implemented by temporal synaptic plasticity of SRM neurons. This Hybrid algorithm is inspired by some integrative approach of behavioral and some structural features of human brain activity. The results show that Spike-IDS can extract human knowledge expertness as well as IDS.

References

1. Thorpe, S., Delorme, A., Van Rullen, R., “*Spike based strategies for rapid processing*”, Neural Networks, vol. 14 (6–7), (2001) 715–726.
2. Fields H.L., Martin, J.B., “*Pain: Pathophysiology and management*”, Harrison’s principles of internal medicine, 13th edition, McGraw-Hill, (1994)
3. Shouraki, S.B., Honda, N., “*Recursive fuzzy modeling based on fuzzy interpolation*”, Journal of Advanced Computational Intelligence, Vol.3, No.2, (1999), 114–125.
4. Polkinghorne, J.C., “*Belief in God in an Age of Science*”, Yale Univ Press, New Haven, (1998), Chapter 3.
5. de Garis, H., Korkin, M., Fehr, G., “*The CAM-brain machine (CBM): an FPGA based tool for evolving a 75 million neuron artificial brain to control a lifesized kitten robot*”, Autonomous Robots, Vol. 10, Issue 3, (2001), 235–249.
6. Gerstner, W., Kistler, W.M., “*Spiking Neuron Models*” The Cambridge University Press, Cambridge, 1st edition, (2002) chapter 10.
7. Bohte, S.M, La Poutre, H., and Kok, J.N., “*Unsupervised clustering with spiking neurons by sparse temporal coding and multilayer rbf networks*”. Neural Networks, IEEE Transactions on, Vol 13 No 2, (2002), 426–435.
8. Bi, G.Q., Poo, M.M, “*Synaptic modification in cultured hippocampal neurons: dependence on spike timing, synaptic strength, and postsynaptic cell type*”, Journal of Neuroscience, No.18, (1998), 10464–10472.
9. Firouzi, M., Shouraki, S.B., Tabandeh, M., Mousavi, S.H.R, “*A novel pipeline architecture of Replacing Ink Drop Spread*”, Second World Congress on Nature and Biologically Inspired Computing, Kitakyushu, Japan, (2010), 127–133.

A Biophysical Model of Neuro-Glial-Vascular Interactions

Bankim S. Chander and V. Srinivasa Chakravarthy

Abstract Functional neuroimaging techniques measure hemodynamic response as an indirect indicator of neuronal activity. These imaging techniques consider only forward pathway (neuron \rightarrow astrocyte \rightarrow vessel) and often the effect of metabolic feedback on neural activity is ignored. To understand brain's computation, we propose a biophysical model of neuro-glial-vascular interaction forming a functional loop. This model describes key biochemical signaling pathways involved in astrocyte mediated neuro vascular coupling using a series of first order nonlinear differential equations.

Keywords Neuron • Astrocyte • Vessels • Cerebral circulation • Neurovascular interactions

1 Introduction

Unlike other cells, neurons convey “hunger” signals to the vascular network via an intervening layer of glial cells (astrocytes); vessels dilate and release glucose which fuels neuronal firing. Modeling neurovascular interaction has particular application in quantitative interpretation of Functional Magnetic Resonance Imaging (*fMRI*) which measures blood oxygenation level dependent (BOLD) signal as an indicator of neuronal activity. However, such models focus on the forward branch of this loop (neuron \rightarrow astrocyte \rightarrow vessels), whereas for a reliable, quantitative understanding of neurovascular interactions, it is necessary to study the entire loop consisting of neurons-astrocytes-vessels. Neuronal firing causes release of neurotransmitter which triggers release of vasodilator by astrocytes. Vasodilators released from

B.S. Chander • V.S. Chakravarthy (✉)
Laboratory for Computational Neuroscience, Department of Biotechnology, Indian Institute of Technology Madras, Chennai 600036, Tamil Nadu, India
e-mail: schakra@ee.iitm.ac.in

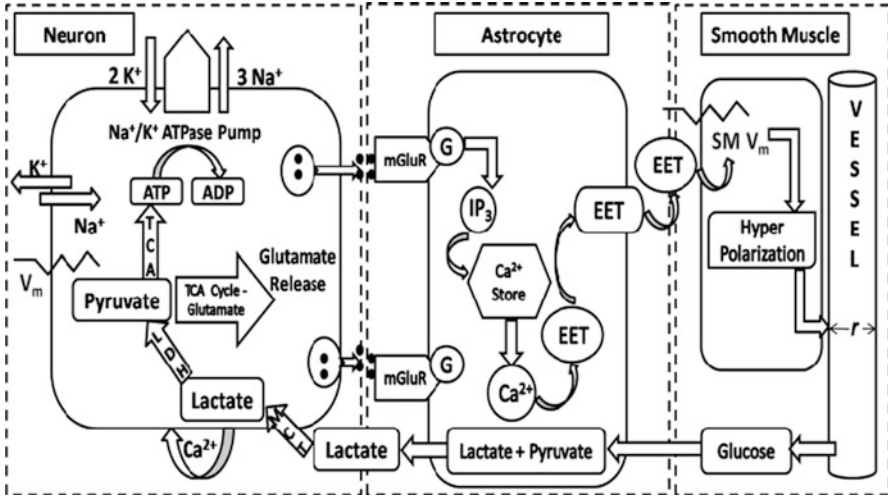


Fig. 1 Schematic of biophysical signaling pathways

astrocytic endfeet cause blood vessels to dilate and release glucose into the interstitium, part of which is taken up by the astrocytic endfeet. Glucose is converted into lactate in the astrocyte and transported into the neuron. Glucose from the interstitium and lactate (produced from glucose) from astrocyte are converted into ATP in the neuron. Neuronal ATP is used to drive the Na-K pumps, which maintain ionic gradients necessary for neuronal firing (Fig. 1). Using the model described below we have attempted to study the effect of metabolic feedback on neuronal activity.

2 Model

The modeling components are designed as follows: Hodgkin-Huxley (HH) model is used as neuron model; astrocyte model is from [1]; the model for metabolic feedback is from [2]. Glial K^+ buffering and Na-K ATPase pump activity is incorporated to compensate for changes in ion concentration across the membrane due to neural firing [3]; the model for synaptic glutamate release is taken from [4]. The model describes the events in the neurovascular loop as follows. On application of an external current, the neuron generates action potentials (APs), which cause quantal release of glutamate. The glutamate flux is given by the number of glutamate molecules (n) times the reaction flux of exocytosis. The latter is equal to the number of releasable vesicles (N_{rel}) multiplied by exocytosis rate constant ($P_{rel} * I_{Ca}$), where P_{rel} is release probability of the vesicles and I_{Ca} is calcium current associated with each action potential. N_{rel} is the product of two factors: the dimensionless ratio of releasable vesicles (R_{rel}) and the sum of empty and releasable vesicles (N_{tot}). Synaptic clearance of glutamate occurs with time constant τ_G .

$$\frac{d[Glu(t)]}{dt} = \frac{nN_{tot}R_{rel}P_{rel}I_{Ca}}{N_A V_s} - \frac{[Glu]}{\tau_G} \quad (1)$$

Synaptic glutamate triggers Inositol trisphosphate (IP_3)-mediated Ca^{2+} transient in astrocyte which generates Epoxyeicosatrienoic Acid (EET). This leads to hyperpolarization of smooth muscle which causes relaxation and consequent vasodilation. Dynamics of $[IP_3]$, $[Ca^{2+}]$ and $[EET]$ in astrocyte is described by a set of three simultaneous non-linear differential equations [1].

$$\frac{\partial[IP_3]}{\partial t} = r_h^* G^* - k_{deg}[IP_3] \quad (2)$$

$$\frac{d[Ca^{2+}]}{dt} = \beta_{cyt} (J_{IP_3} - J_{pump} + J_{leak}) \quad (3)$$

$$\frac{d[EET]}{dt} = V_{EET} * ramp([Ca^{2+}] - [Ca^{2+}]_{min}) - .2 \frac{[EET]}{[EET] + 18} \quad (4)$$

where rh^* and k_{deg} are constants, G^* is the ratio of activated G-protein due to synaptic glutamate to total G-protein. J_{IP_3} , J_{pump} and J_{leak} are the rates of Ca^{2+} concentration change due to release through IP_3 receptor channels, pump uptake into the ER, and leak from the ER respectively; β_{cyt} is a constant factor describing Ca^{2+} buffering. V_{EET} is a constant production rate of EET and $[Ca^{2+}]_{min}$ is the minimum $[Ca^{2+}]$ for EET required for production. The clearance of EET is given by the subtraction term in the Eq. (4). Smooth muscle membrane potential (V_m) is described as a nonlinear function of $[EET]$ and change in vessel radius (r) is assumed to be linearly related to smooth membrane potential.

$$V_m = 5 - 80 \frac{1}{1 + e^{-2[EET]}} \quad (5)$$

$$r = r_{min} + (r_{max} - r_{min}) \left[\frac{V_{max} - V_m}{V_{max} - V_{min}} \right] \quad (6)$$

where r_{min} and r_{max} refers to minimum and maximum vessel radius corresponding to constricted and dilated state respectively. V_{min} and V_{max} refer to minimum and maximum smooth muscle membrane potential corresponding to relaxed and contracted state respectively. Vessel dilation facilitates glucose release into interstitium. The model of metabolic flux [2, 5] is based on experimentally determined glucose and lactate transporter concentration values, glucose and lactate kinetics in endothelium, neuron and astrocyte. Glucose is metabolized in astrocyte to produce pyruvate and lactate. Lactate is transported to neuron via interstitium and is metabolized to ATP , which fuels Na-K pump required for maintaining ionic gradients. The pump dynamics are described as

$$A_{pump} = \left(1 + \frac{Km_K}{[K^+]_o}\right)^{-2} \left(1 + \frac{Km_{Na}}{[Na^+]_i}\right)^{-3} \left(1 + \frac{K_{ATP}}{[ATP]}\right)^{-1} \quad (7)$$

where pump activity (A_{pump}) is a function of potassium ion concentration outside the neuron ($[K^+]_o$); sodium ion concentration inside the neuron ($[Na^+]_i$) and cytosolic ATP concentration. K_{ATP} , Km_K and Km_{Na} are constants [3]. Sodium (I_{Na}) and potassium (I_K) currents as functions of pump activity are

$$I_K = -2 * I_{max} * A_{pump} \quad (8)$$

$$I_{Na} = 3 * I_{max} * A_{pump} \quad (9)$$

where I_{max} is the maximum pump current. The rate of ion accumulation [3] across membrane due to net current of a particular ion is expressed as

$$\frac{d[ion]_i}{dt} = \frac{I_{\Sigma(ion)} * S}{F * V_i} \quad (10)$$

$$\frac{d[ion]_o}{dt} = -\frac{I_{\Sigma(ion)} * S}{F * V_e} \quad (11)$$

where, subscripts 'i' and 'o' refer to internal and external respectively. S is the surface area of the neuron and V_i and V_e is the intracellular and extracellular volume respectively. The delicate balance between the pump current and ion channel current determines the net ion transfer across the neuronal membrane. To sustain neuronal firing the pump current must nullify the channel current and thereby maintain the ionic gradient across the membrane.

3 Results

On application of stimulus current beyond a threshold, the neuron exhibits firing. Only when there is a sufficient glial K^+ buffer capacity firing is continuous.

Variation in neuronal membrane potential and synaptic glutamate concentration follow the same pattern as shown in Figs. 2 and 3 respectively. Glutamate pulses cause release of *EET* by astrocyte.

A delay of 1 s is observed in release of *EET* (Fig. 4) after activation of mGluR by synaptic glutamate. Vessel dilation (Fig. 5) occurs instantly on *EET* release by astrocyte.

Vessel dilation (Fig. 5) improves glucose and lactate flux into the interstitium. Glucose and lactate reserve of neuron and astrocyte is exhausted within 1 s after onset of neuronal firing. On vessel dilation, glucose and lactate is instantly available for astrocyte (Fig. 6) and neuron (Fig. 7).

Fig. 2 Variation in membrane potential, E_{Na} and E_K when stimulated with 0.1 mA/cm^2

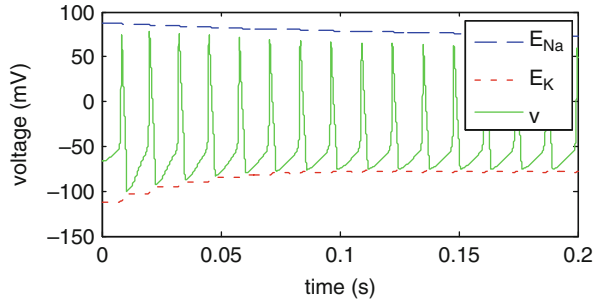


Fig. 3 Variation in synaptic glutamate concentration in response to action potentials

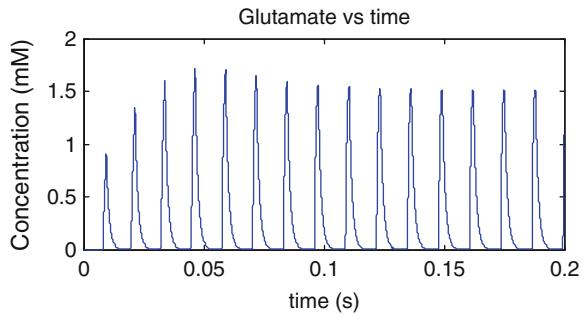


Fig. 4 Variation in extracellular $[EET]$ between astrocyte and smooth muscle cell

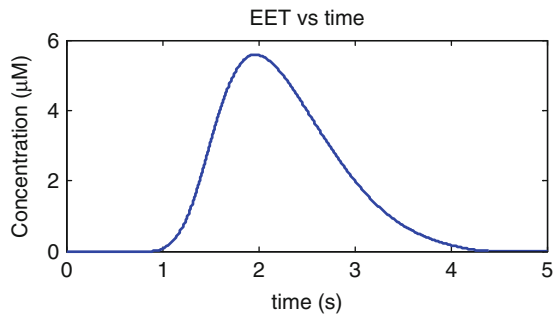


Fig. 5 Vessel dilation upon action of EET

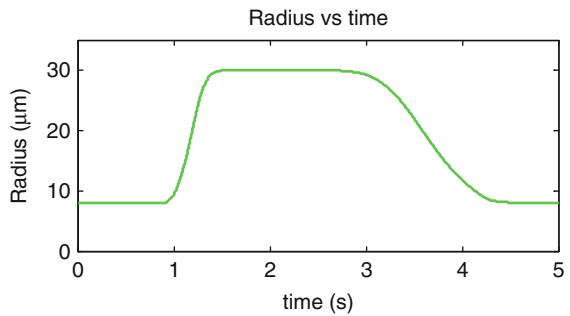


Fig. 6 Variation of glucose (*Glc*) and lactate (*Lac*) concentration in astrocyte

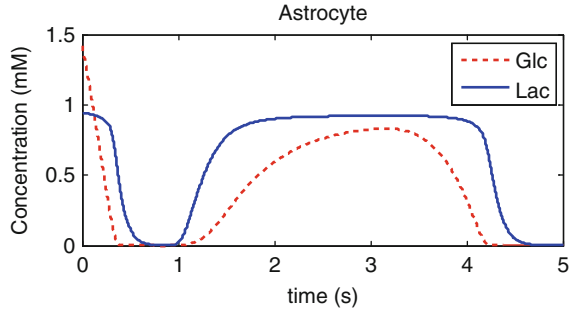


Fig. 7 Variation of glucose (*Glc*) and lactate (*Lac*) concentration in neuron

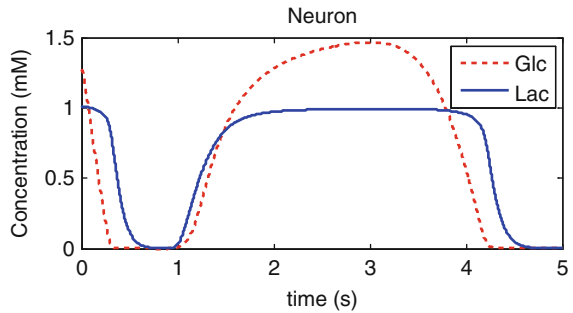
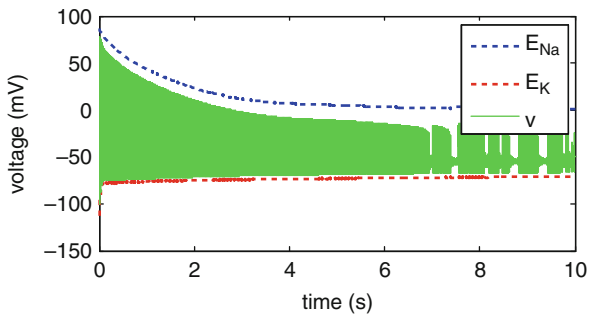


Fig. 8 Variation in membrane potential, E_{Na} and E_K when vessel is constricted to $10 \mu\text{m}$



Lactate is oxidized via Tricarboxylic Acid (*TCA*) cycle to generate *ATP* which is used for maintaining ionic gradient across neuronal membrane. For subthreshold stimulation and low initial [*ATP*], bursting or firing with initial pause is observed.

Neurovascular interactions under pathological conditions like blocked glutamate transmission or constricted vessels are also studied, which show reduction in duration of neuronal firing and amplitude of APs when compared with normal operation (Fig. 8).

4 Discussions

The proposed model can be scaled up to network level to explore role of “metabolic plasticity” (activity dependent variation in astrocyte-vessel interaction) in neurovascular interactions. The model suggests that brain’s computations may be more comprehensively understood in terms of neuro-glial-vascular dynamics and not in terms of neural firing alone.

References

1. M.R. Bennett, L. Farnell, and W.G. Gibson, “Origins of blood volume change due to glutamatergic synaptic activity at astrocytes abutting on arteriolar smooth muscle cells.,” *Journal of theoretical biology*, vol. 250, Jan. 2008, pp. 172–85
2. S. Mangia, I. a Simpson, S.J. Vannucci, and A. Carruthers, “The in vivo neuron-to-astrocyte lactate shuttle in human brain: evidence from modeling of measured lactate levels during visual stimulation.,” *Journal of neurochemistry*, vol. 109 Suppl , May. 2009, pp. 55–62.
3. H. Kager, W.J. Wadman, and G.G. Somjen, “Simulated Seizures and Spreading Depression in a Neuron Model Incorporating Interstitial Space and Ion Concentrations,” *Cell*, vol. 27710, 2000, pp. 495–512.
4. C.-C.J. Lee, M. Anton, C.-S. Poon, and G.J. McRae, “A kinetic model unifying presynaptic short-term facilitation and depression.” *Journal of computational neuroscience*, vol. 26, Jun. 2009, pp. 459–73.
5. Suzuki, Akinobu, Sarah A Stern, Ozlem Bozdagi, George W Huntley, Ruth H Walker, Pierre J Magistretti, and Cristina M Alberini. “Astrocyte-neuron lactate transport is required for long-term memory formation.” *Cell* 144, no. 5 (March 4, 2011): 810–23.

Model Complexity in the Study of Neural Network Phenomena

Claus C. Hilgetag, Marc-Thorsten Hütt, and Changsong Zhou

Abstract In this paper, we explore features of neural network dynamics that were identified in simulation approaches with highly complex models (representing large populations of coupled oscillators) on the one hand, or basic discrete excitable models, on the other. Both types of modeling approaches could produce features such as irregular sustained network activity or modular functional connectivity. This observation poses the question, what are the essential model features that lead to characteristic phenomena of neural network dynamics?

1 Introduction

The increasing affordability of computer power has produced a recent trend in neural network modeling towards large-scale and supercomputational approaches, taking into account detailed biophysical properties of the individual network elements (neurons or neuronal populations). However, there are a number of network phenomena that can also be replicated with much simpler models. For example,

C.C. Hilgetag (✉)

Department of Computational Neuroscience, University Medical Center Hamburg-Eppendorf,
20246 Hamburg, Germany

Department of Health Sciences, Boston University, 02215 Boston, MA, USA

School of Engineering and Science, Jacobs University, Bremen, 28759, Bremen, Germany
e-mail: c.hilgetag@gmail.com

M.-T. Hütt

School of Engineering and Science, Jacobs University, Bremen, 28759, Bremen, Germany
e-mail: m.huett@jacobs-university.de

C. Zhou

Department of Physics, Hong Kong Baptist University, Kowloon Tong, Hong Kong
e-mail: cszhou@hkbu.edu.hk

modularity of functional connectivity has been observed in models ranging in complexity from large populations of coupled oscillators [1] to networks formed by discrete excitable nodes [2].

These observations pose the question: How intricate does a neural model have to be in order to produce a particular network phenomenon, such as irregular sustained activity, bursting, neural avalanches or slow-frequency coupling of high-frequency oscillators? What are the minimal models for these phenomena, what features (e.g., noise, delays, heterogeneity of connections) do they need to include? While analytical answers for most of these questions may be still out of reach, we seek an improved practical understanding of essential parameters and constraints for neural network modeling.

2 Methods

We explored two kinds of neural node models of different complexity: a detailed, continuous model of coupled populations of FitzHugh-Nagumo oscillators (CO), as in [1], or alternatively, discrete excitable (DE) nodes with few categorical states (susceptible, active, refractory) operating in discretized time [2]. The choice of these models was motivated by the desire to explore the global network dynamics produced by a popular continuous model on the one hand and a basic, minimal dynamic model on the other. We used these models to investigate the relation between network topology and global dynamics for different benchmark networks (random, scale-free, modular networks) as well as biological neural networks, such as the large-scale connections among more than 50 cat cortical areas [3]. In the case of the DE model, the correlations were expressed through the dynamic modularity Q_{dyn} , which computes the alignment between the topological and functional groupings of network nodes according to different features, such as topological modularity (TM) or centrality (CN). Q_{dyn} was determined as a function of the rate of spontaneous node excitations f , which may be interpreted in terms of high or low levels of background activity or noise in the system.

3 Results

Despite greatly disparate model complexity, both kinds of models were capable of producing intricate, sustained dynamics at the network level, see Fig. 1. Both models also produced modular dynamics that corresponded to the modular network connectivity, see Fig. 2. The dominance of the modular topology of the cat cortical network was reflected in a distinct increase of Q_{dyn} for the TM-dependent correlation for high levels of spontaneous node activity f , while distance from central hub nodes appeared to play only a marginal role. Other networks, however, such as the cellular network of *C. elegans* displayed a strong dependency on the distance

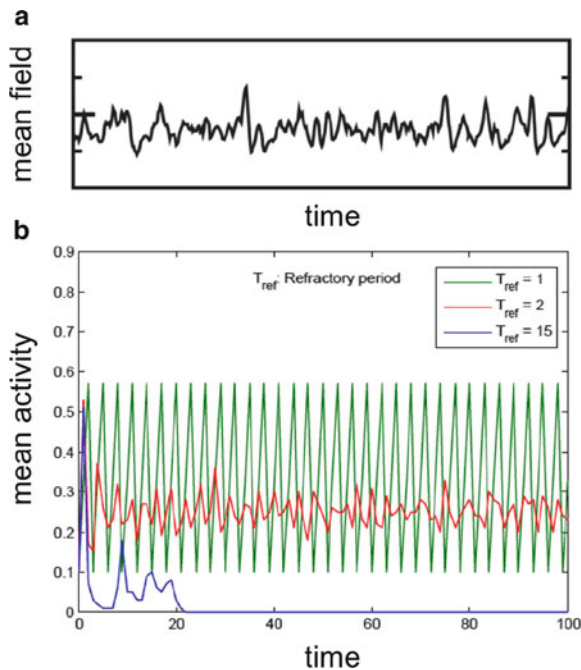


Fig. 1 CO and DE models for exploring neural network topology. (a) Mean field activity produced by the large-scale coupled oscillator (CO) model, based on coupled populations of Fitzhugh-Nagumo oscillators [1]. Weak global coupling results in patterns of irregular multi-frequency activity. (b) Mean activity produced by a basic discrete excitable (DE) model [2]. Intermediate ranges of stochastic refractory periods result in sustained irregular activity (*red trace*). Thus, both modeling approaches, despite great differences in their complexity, may produce intricate network dynamics that can be used to probe network topology

to central nodes for a wide range of f [2]. Similarly to the exploration of cat cortical connectivity by the DE model, the CO model showed a close alignment of the modular functional connectivity with the underlying structural modularity. This alignment is demonstrated in Fig. 2 through the correspondence between anatomical connections (small black dots) and functional connections (blue circles) of cat cortical areas.

4 Discussion and Conclusions

It is currently unclear how much detail and model complexity at the node level are required in order to explore essential phenomena of global network dynamics, such as irregular multi-frequency activity and modular functional connectivity. While it has been suggested that the appropriate tuning of features such as coupling,

References

1. Zhou C, Zemanova L, Zamora G, Hilgetag CC, Kurths J (2006) Hierarchical organization unveiled by functional connectivity in complex brain networks. *Phys Rev Lett* 97: 238103
2. Müller-Linow M, Hilgetag CC, Hütt MT (2008) Organization of excitable dynamics in hierarchical biological networks. *PLoS Comput Biol* 4: e1000190
3. Scannell JW, Burns GA, Hilgetag CC, O'Neil MA, Young MP (1999) The connectional organization of the cortico-thalamic system of the cat. *Cereb Cortex* 9: 277–299
4. Kötter R, Sommer FT (2000) Global relationship between anatomical connectivity and activity propagation in the cerebral cortex. *Philos Trans R Soc Lond, B, Biol Sci* 355: 127–134
5. Hilgetag CC, Burns GAPC, O'Neill MA, Scannell JW, Young MP (2000) Anatomical connectivity defines the organisation of clusters of cortical areas in macaque monkey and cat. *Phil Trans R Soc Lond B* 355: 91–110
6. Hilgetag CC, Kaiser M (2004) Clustered organization of cortical connectivity. *Neuroinformatics* 2: 353–360
7. Deco G, Jirsa V, McIntosh AR, Sporns O, Kötter R (2009) Key role of coupling, delay, and noise in resting brain fluctuations. *Proc Natl Acad Sci USA* 106: 12207–8

From Spiking Neurons to Neural Fields: Bridging the Gap to Achieve Faster Simulations of Neural Systems

Peter A. Robinson and Jong Won Kim

Abstract Representing the neural activity in terms of spikes or rates are complementary approaches to computing neuronal dynamics. Likewise, communication between neurons via individual pairwise links or via smoothed fields are complementary approaches to modeling information transfer. Here it is shown that many intermediate and hybrid approaches exist, which enable different aspects of the dynamics to be probed and permit faster computation in many circumstances.

1 Introduction

There are two well-known limiting perspectives on how to model large neural systems. One is to simulate large numbers of individual spiking neurons in neural networks, where each model neuron has dynamics with some degree of physiological realism, and multiple neurons interact with one another via spikes [1]. In the opposite limit, neural firing rates are followed and neural properties and states are locally averaged over many neurons to obtain neural field equations for activity that propagates through neural tissue approximated as a continuum [2]. These limits are analogous to molecular and continuum approaches to materials, where neither limit gives the whole story and each uncovers some of the dynamics—i.e., they are complementary, not mutually exclusive [3, 4].

Spiking neural networks are most directly linked to the basic biophysics, but are extremely computationally intensive to simulate [5] and produce amounts of output so large as to make interpretation problematic [6]. On the other hand, neural

P.A. Robinson (✉) • J.W. Kim

School of Physics, University of Sydney, Sydney, NSW 2006, Australia

Brain Dynamics Center, Sydney Medical School—Western, University of Sydney, Westmead, NSW 2145, Australia

e-mail: robinson@physics.usyd.edu.au

field theory omits more biophysical details, but is advantageous for uncovering multiscale and emergent phenomena, such as brain oscillations and criticality [2]. These points highlight the importance of understanding the relationships between these limiting cases, including areas of overlap, which phenomena are accounted for most naturally and tractably by which level(s) of description, and how to simulate realistic systems most efficiently.

By re-examining the assumptions and approximations of rate-based vs. spiking-neuron theories, and pairwise vs. field-based interactions, it is shown that intermediate and hybrid possibilities exist. These include faster means of computing with spikes, ways to infer spiking properties from field theories, and improved ways to treat spike propagation using fields.

2 Models

2.1 Neuronal Dynamics

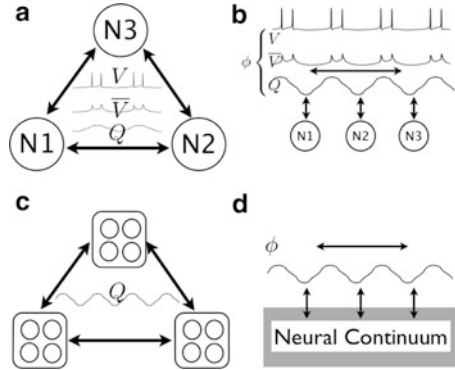
Spiking neuron models represent the most commonly considered way of approaching neural dynamics. These models range from biophysical conductance-based models, to idealized ones, such as integrate-and-fire models [5]. These types of models incorporate an input current, which can come from other neurons (see below), or from an artificial external source. If this current charges the soma sufficiently to exceed the firing threshold potential, the neuron will produce an action potential, or spike. Thus, many such models incorporate conductance equations that track various ion currents in and out of each cell, and the resulting changes of soma potential V . Such equations must be integrated with a sub-millisecond timestep δt throughout when dealing with networks of coupled neurons; typically $\delta t \approx 0.1$ ms.

One type of approximate spiking neuron model treats each neuron as a phase oscillator that produces one spike per cycle. Such models track the smoothly varying phase, rather than V , and one spike is produced each time the phase advances by 2π [1]. In many phase oscillator models, all spikes are assumed to be identical and the dynamical equations can be integrated with much larger time steps Δt (typically over 1 ms) than if every spike had to be temporally resolved [7].

In some cases, what is of interest is the spike rate Q , rather than spike timings. It has recently been shown that many types of *spiking* dynamics can be approximated using Q , rather than fast variables such as V [3]. Together with the phase interpretation above, this has enabled physiologically based spiking and bursting dynamics to be closely approximated while integrating using time steps Δt , or longer if Q only changes slowly [3].

Another way the dynamics can be simplified, and time steps extended, is by noting that spikes received by downstream neurons are subject to low-pass filtering by synaptic and dendritic dynamics, and by the effects of soma charging, giving a frequency cutoff of around ~ 20 Hz for typical parameters [8,9]. This means that fine

Fig. 1 Schematic of different models of neuronal dynamics and communication. **(a)** Spiking neurons of various types with pairwise connections. **(b)** Spiking neurons with communication via a field that carries V , smoothed spikes \bar{V} , or Q (NIC). **(c)** Populations pairwise connected. **(d)** NFT



structure in individual spikes has little effect on spike dynamics downstream. Hence, because the low-pass filtering is approximately linear [9], it is mathematically possible to move it to a point *before* axonal propagation [10, 11]. One can then adopt neuronal dynamics that generate *prebroadened* spikes, using longer time steps ($\sim \Delta t$). These spikes then interact with subsequent neurons without further synaptic or dendritic broadening, yielding dynamics identical to the original system. A key advantage of using prebroadened spikes is that axonal signals also need only be resolved on the scale Δt .

The types of neuronal dynamics discussed above are shown schematically in Fig. 1, some parts of which are discussed in Sect. 2.2. Overall, the ability to use simplified systems of equations with coarser time resolution in numerical integration can lead to speedups of up to 2–3 orders of magnitude relative to tracking individual spikes using conductance-based models: 10- to 100-fold from larger timesteps, and up to 10-fold, or even more, from simplification of the dynamical equations [5]. The maximum timestep may be further limited by the resolution required for specific applications.

2.2 Neuronal Communication

The simplest way to couple multiple neurons to study large-scale system dynamics is to track spikes via links between all relevant pairs of neurons. However, for N neurons this involves up to N^2 axonal links, in which signals must be resolved at the same timescale as individual neurons.

An alternative method of communicating between individual neurons is suggested by the particle-in-cell (PIC) method of plasma physics [12]. Instead of using N^2 pairwise interactions, we make the approximation that the interaction between two neurons depends only upon their spatial locations and spike timings. In this case, all neurons can be viewed as contributing to a field ϕ that carries spike profiles. These spikes can be sharp, broadened, of the phase oscillator type, or can be replaced by a spike rate in the case the neurons’ dynamics are rate-based. The field ϕ is then

propagated by solving its field equation (e.g., a damped wave equation). It then serves as the input to other neurons. Normally, ϕ conveys dynamical quantities in the form used in the internal dynamics of the model neurons. The advantage of this “neuron in cell” (NIC) method is that specification of the field can involve far fewer points than neurons. Hence, neural communication can be simulated much faster than via pairwise interactions. For example, N neurons interacting via field defined on $P \ll N$ points can be simulated in a time of order N rather than order N^2 , with fields carrying spikes or rates.

A further approximation is to take the multiple neurons represented by a given grid point and examine not their individual dynamics, but the mean rate-based dynamics of this whole group. This yields a population network model, in which populations at different locations interact [13]. Communication between these populations can then be calculated in a pairwise fashion in a time of order P^2 , at a time resolution of order Δt .

If the P neural populations are viewed as representing neurons in a single spatially continuous structure, such as the cortex, one can index them by position rather than via discrete labels. One then obtains a continuous neural field theory (NFT) of their averaged dynamics [2, 8]. This enables the dynamics of the entire system to be tracked in a time of order P , where P is large enough to resolve the linear scales of activity phenomena of interest. In the limit that the spatial structure of activity is not required, one can set $P = 1$ to obtain a neural mass theory (NMT) [2, 14], where the entire population of neurons is treated as a single point mass. For NMT to hold, time lags for signals to cross the system must be much less than the shortest phenomena of interest. Neural mass theories can be simulated in a time independent of N and P .

The above approaches to neural communications are shown schematically in Fig. 1.

3 Results

Relative runtimes of the above approaches to dynamics and communication constitute some of the key results, as described in Sect. 2. These are summarized in Table 1, which shows the runtime scalings to simulate networks consisting of a single type of neuron using the various methods. Scalings obtained from numerical implementations of several of these methods are illustrated in Fig. 2, which confirms the relative dependences on N and P .

Figure 3 shows some examples of computations carried out with the methods discussed here. It compares individual bursting neuron dynamics calculated via rate-based variables with those calculated via conductance-based equations. It is seen that there is a close parallel between both types of simulations. Indeed, if one integrates the total phase advance over each burst and divides by 2π , we predict 3 spikes per burst, exactly the number seen in the spike-based approach [3]. This demonstrates that phase- or rate-based approaches can yield accurate results for spike timings, even though they do not represent spikes explicitly.

Table 1 Scalings of runtimes for simulations of N neurons

Method	Runtime
C	$N^2/\delta t$
PO	$N^2/\Delta t$
PB	$N^2/\Delta t$
Rate	$N^2/\Delta t$
C NIC	$N/\delta t$
PO NIC	$N/\Delta t$
PB NIC	$N/\Delta t$
Rate	$N/\Delta t$
Population network	$P^2/\Delta t$
NFT	$P/\Delta t$
NMT	$1/\Delta t$

First four lines are for pairwise-coupled spiking models with C conductance, PO phase oscillator, PB prebroadened spikes, $\delta t \approx 0.1$ ms, $\Delta t \approx$ few ms. Next three lines are for communication via fields on $P \ll N$ grid points. Last three lines are for populations. Finer steps may be needed to resolve phenomena or satisfy the Courant condition

Fig. 2 Runtimes of pairwise-coupled neurons (*circles*), NIC (*squares* $P = 10$, *diamonds* $P = 100$), and NFT (*dashed* $P = 10$, *dash-dotted* $P = 100$) simulations vs. number of neurons N

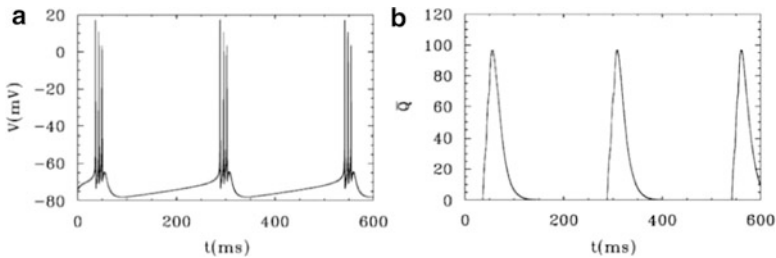
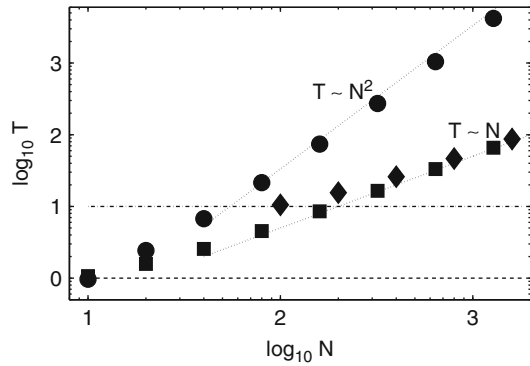


Fig. 3 Bursting neuron dynamics (Adapted from [3]). (a) From conductance-based equations. (b) From rate-based equations

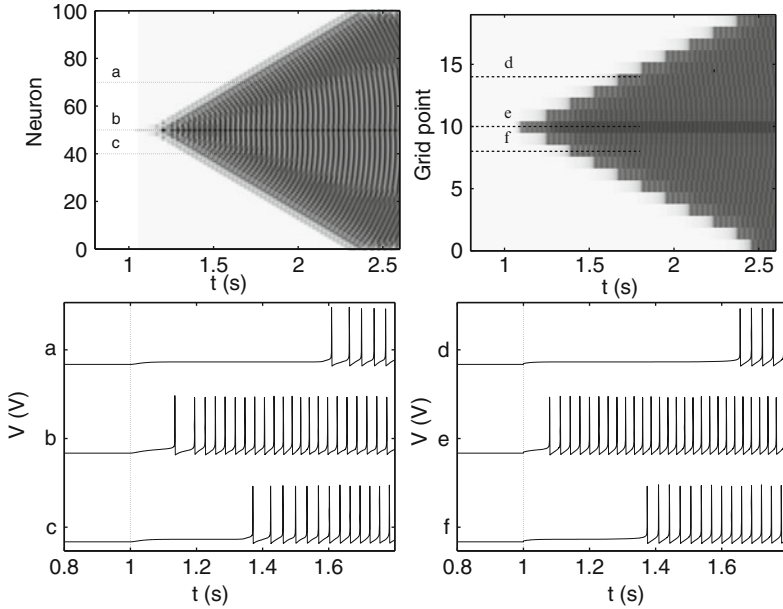


Fig. 4 Examples of system dynamics for $N = 100$, pairwise connected spiking neurons vs. NIC ($N = 100$ and $P = 20$). Resting neurons are triggered via a strong input current at the center at $t = 1.0$ s and firing propagates outward. Input current of (a) pairwise connected spiking neurons, (b) NIC. Firing patterns at the points denoted by *dotted horizontal lines* in (a) and (b) for (c) pairwise connected neurons, and (d) NIC

Figure 4 shows some preliminary results the networks of interacting neurons simulated with spiking-neuron and NIC methods, parameters otherwise being the same. We see that systems-level spreading of activity is very similar, as are the single-neuron firing patterns.

4 Discussion

A sequence of hybrid and intermediate approaches to brain modeling is introduced that combine features of spiking-neuron and neural-field approaches in various ways that balance the degree of physiological detail against speed of computation. It is shown that these can dramatically speed computations involving large ensembles of interacting neurons (see Fig. 1). These new methods provide alternatives that can be used to explore the boundary between the discrete and continuum limits to determine which systems-dynamic effects depend on which aspects of the neural dynamics and/or communication are retained. Mathematical details will be provided in a forthcoming work [7].

Acknowledgements The Australian Research Council and the Westmead Millennium Institute supported this work.

References

1. Gerstner, W., and Kistler, W. (2002). *Spiking Neuron Models* (Cambridge, Cambridge).
2. Deco, G., Jirsa, V. K., Robinson, P. A., Breakspear, M., and Friston, K. (2008). PLoS – Comp. Biol. **4**, e1000092, 1–35.
3. Robinson, P. A., Wu, H., and Kim, J. W. (2008). J. Theor. Biol. **250**, 663–672.
4. Wu, H., Robinson, P. A., and Kim, J. W. (2011). J. Comp. Neurosci. **31**, 61–71.
5. Izhikevich, E. M. (2004). IEEE Trans. Neural Networks, **15**, 1063–1070.
6. Markram, H. (2006). Nat. Rev. Neurosci. **7**, 153–160.
7. Robinson, P. A., and Kim, J. W. (2011). J. Neurosci. Meth., to be submitted.
8. Robinson, P. A., Rennie, C. J., and Wright, J. J. (1997). Phys. Rev. E, **56**, 826–840.
9. Koch, C. (1999). *Biophysics of Computation* (Oxford, Oxford).
10. Henke, H., Robinson, P. A., Drysdale, P. M., and Loxley, P. N. (2009). Biol. Cybern. **101**, 3–18.
11. Wilson, H. R., and Cowan, J. D. (1973). Kybernetik, **15**, 55–80.
12. Dawson, J. M. (1983). Rev. Mod. Phys. **55**, 403–447.
13. Gray, R. T., and Robinson, P. A. (2007). Neurocomput. **70**, 1000–1012.
14. Freeman, W. J. (1975). *Mass Action in the Nervous System* (Academic, New York).

Multi-population Network Models of the Cortical Microcircuit

Tobias C. Potjans and Markus Diesmann

Abstract In this paper, we investigate a data-based multi-population extension of the balanced random network model (BRN) (Amit DJ and Brunel N, *Cereb Cortex* 7:237–252, 1997; van Vreeswijk C and Sompolinsky H, *Science* 274:1724–1726, 1996). We observe that the findings based on the mono-layered network model, especially regarding the asynchronous irregular activity state, largely generalize to the multi-population model (MPM). In addition, the increased complexity of the network structure yields cell-type specific activity features which we relate to other data-based microcircuit models as well as to experimental data. We argue that the specificity of the connectivity between cell types is crucial to achieve consistency of simulated and in vivo activity.

T.C. Potjans (✉)

Institute of Neuroscience and Medicine (INM-6), Computational and Systems Neuroscience, Research Center Juelich, 52425 Juelich, Germany

Brain and Neural Systems Team, RIKEN Computational Science Research Program, 2–1 Hirosawa, Wako-shi, Saitama 351–0198, Japan
e-mail: t.c.potjans@fz-juelich.de

M. Diesmann

Institute of Neuroscience and Medicine (INM-6), Computational and Systems Neuroscience, Research Center Juelich, 52425 Juelich, Germany

Brain and Neural Systems Team, RIKEN Computational Science Research Program, 2–1 Hirosawa, Wako-shi, Saitama 351–0198, Japan

RIKEN Brain Science Institute, 2–1 Hirosawa, Wako-shi, Saitama 351–0198, Japan

Medical Faculty, RWTH Aachen University, Pauwelsstraße 30, 52074 Aachen, Germany

1 Introduction

Fifteen years ago, Amit and Brunel [1] and van Vreeswijk and Sompolinsky [2] simultaneously developed the BRN, employing the balance of excitation and inhibition to understand the dynamics of membrane potentials and asynchronous irregular spiking activity. However, it has been recently demonstrated that the spiking activity obtained by juxta-cellular recordings in awake animals is cell-type specific, see e.g. [3]. Although the mono-layered BRN continues to make important contributions to the understanding of experimentally observed cortical network dynamics it is indispensable to extend this model (see Fig. 1) to incorporate the multi-layered nature of the cortical microcircuit and to provide a link between the experimentally observed network structure and activity.

Here, we investigate, firstly, in how far the mono-layered models generalize to a data-based MPM [4]. Secondly, we analyze the relationship of the simulated cell-type specific activity and experimental data as well as other existing MPMs covering a broad range of neuronal description levels. We focus on the activity of layer 2/3 (L2/3) excitatory neurons that have been reported to exhibit spontaneous firing rates of less than 1 Hz.

2 Methods

We employ full-scale simulations of a spiking MPM of the cortical microcircuit comprising around 80,000 integrate-and-fire neurons and 0.3 billion synapses (Fig. 1b). We distinguish eight populations, corresponding to four excitatory and four inhibitory cell types in the cortical layers 2/3, 4, 5 and 6. The cell-type specific connectivity of the model is captured in an integrated connectivity map [4] which is predominantly based on existing anatomical [5] and physiological [6] connectivity maps. Furthermore, the integrated map introduces inter-layer connections specifically targeting interneurons which have been reported in studies based on multiple recordings and photostimulation in brain slices as well as electron microscope anatomy but which are elusive in light-microscope anatomy. All other parameters are determined in analogy to the BRN [1].

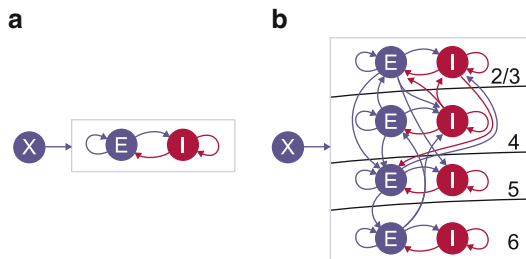
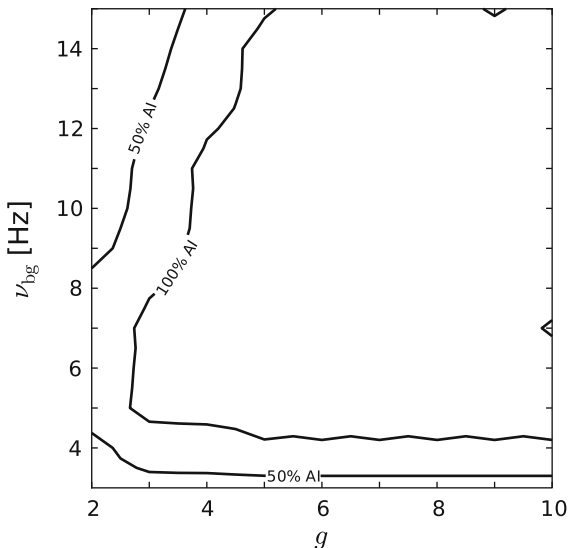


Fig. 1 (a) BRN [1,2] consisting of excitatory, E , and inhibitory, I , populations with external input, X , and (b) its multi-population extension [5]

Fig. 2 Regime of asynchronous irregular activity of the MPM. The isolines mark the regime where all populations (“100% AI”) or half of the populations (“50% AI”) fire asynchronously irregularly. It largely corresponds to the one from mono-layered models [7]



The presented simulation results consider changes in the relative inhibitory synaptic strength $g = -J_i/J_e$ and in the external inputs. The rate of Poissonian background spikes a single neuron receives is the product of the background rate ν_{bg} , modified for Fig. 2, and the number of background synapses N_{bg} , modified for the gray shaded bars shown in Fig. 3 [4].

Simulations are carried out using the NEST simulation tool (www.nest-initiative.org). We investigate the dependence of the activity state of the network on the balance of excitation and inhibition and the external input. We quantify the network state as irregular if the mean coefficient of variation of the interspike intervals of individual neurons in a population is between 0.7 and 1.2 and as asynchronous if the Fano Factor of the population firing rate (binned in 3 ms windows) is below 8. Firing rates represent the mean population firing rates.

3 Results

Figure 2 shows the regime of the asynchronous irregular activity of the MPM. We observe that the dependence of the activity state on ν_{bg} and g from mono-layered models [7] is largely conserved for the data-based MPM.

BRN activity is typically in the range of a few Hz and identical for excitatory and inhibitory populations [1]. In the MPM, see Fig. 3, the imposed cell-type specific connectivity structure yields cell-type specific firing rates. The distribution of firing rates is robust when the network is confronted with varying external inputs.

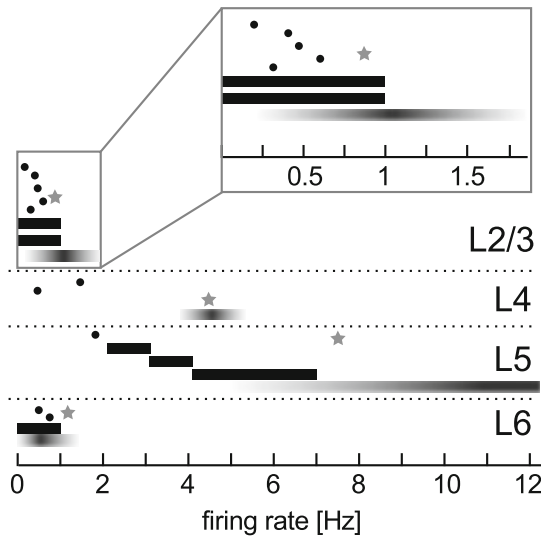


Fig. 3 Comparison of simulated and experimentally observed spontaneous firing rates of excitatory neurons in L2/3, L4, L5 and L6. *Black* colors denote experimental data from in vivo recordings in awake animals (e.g. [3], see [4] for an overview), *circles* indicating numerically given mean values and *bars* indicating given ranges (e.g. 4–7 Hz). Shades of *gray* indicate simulated data of the MPM based on the integrated connectivity map [4], *stars* indicating mean firing rates of the reference parametrization and *bars* indicating the mean \pm std when changing external inputs (see Methods)

Excitatory cells in L2/3 and L6 exhibit lowest firing rates with a mean value below 1 Hz and excitatory cells in L5 fire at highest rates and also show the largest variability.

Comparison to in vivo data Experimentally, cell-type specific spontaneous activity in awake animals has been measured by juxtacellular and multi-unit recordings as well as by two-photon imaging. The mean firing rates are shown in Fig. 3 in comparison to the simulated activity. Overall, we observe a good agreement of experiments and simulations, without any particular tuning of the simulated network. In particular, in L2/3, where most evidence is currently available, see [3], and L6, the low level of activation is preserved.

Relation to other MPMs Table 1 summarizes a number of recent spiking MPMs of the cortical microcircuit. The studies apply a wide range of neuron models, regarding morphologies (from point to multi-compartmental neuron models) and underlying dynamics (integrate-and-fire models (IAF), phenomenological models [11, 14] or Hodgkin-Huxley models [15]). Similarly, these studies span a range of research foci, e.g. the function of the frontal eye fields (FEF) or the computational performance of generic microcircuits. Regarding the connectivity, the majority of models build on one of the two previously introduced connectivity maps;

Table 1 MPMs of the local cortical network

	Neuron model	Connectivity	Focus
Izhikevich and Edelman	Multi-comp. Izhikevich	Anatomical map	Large-scale model
Heinzle et al.	Single-comp. cond.-based IAF	Anatomical map	FEF function
Traub et al.	Multi-comp. Hodgkin-Huxley	Own data-based	Fast oscillations
Hill and Tononi	Single-comp. Hill-Tononi	Own data-based	Slow oscillations
Haeusler and Maass	Single-comp. Hodgkin-Huxley	Physiological map	Comput. performance
Rasch et al.	Single-comp. Izhikevich	Physiological map	Stimulus-driven activity
Potjans and Diesmann	Single-comp. curr.-based IAF	Integrated map	Cell-type specific activity

The table lists, from top to bottom, a number of recent spiking, data-based MPMs [4, 8–13], with the applied neuron model, the chosen connectivity map and the main research focus

only the two works published in 2005 compile their own data-based maps. Our generalization of the BRN is the only MPM based on the inclusion of specific target type selection [4].

Due to the diverse research foci of these works, not all provide detailed information on the cell-type specificity of the simulated activity. Nevertheless, it is remarkable that none of these works reports firing rates in L2/3 or L6 as low as recent experiments. Hill and Tononi [11] provide a detailed comparison of simulated and experimentally observed spontaneous activity and observe that especially the simulated excitatory cells in L2/3 exhibit a higher activation than reported experimentally.

4 Discussion

We present evidence that the extension of cortical network models from BRNs to data-based MPMs conserves the main feature of the mono-layered models, the asynchronous irregular activity state. We furthermore compare our simulated spontaneous activity to experimental data from awake animals and also to a number of other MPMs.

In order to account for the cell-type specific features of *in vivo* activity, it is essential to consider MPMs. However, the parametrization of the connectivity of MPMs poses a major problem and previous models were not able to reproduce the strikingly low spontaneous activity especially in cortical layer 2/3, in spite of applying a wide range of modeling approaches to the description of the constituents of the network, the neurons and synapses. We argue that our integrated connectivity data set [4] captures essential information on connectivity, such as the specific target

type selection of a subset of inter-layer projections, which is not included in other available data sets but necessary for reproducing cell-type specific in vivo activity features.

We propose the comparison of cell-type specific spontaneous activity in simulations and experiments as a critical benchmark for MPMs.

Acknowledgments Partially supported by the Next-Generation Supercomputer Project of the Ministry of education, culture, sports, science and technology (MEXT) (Japan), the Helmholtz Alliance on Systems Biology, JUGENE grant JINB33 and EU Grant 269921 (BrainScaleS).

References

1. Amit, D.J., Brunel, N.: Model of global spontaneous activity and local structured activity during delay periods in the cerebral cortex. *Cereb. Cortex* **7** (1997) 237–252.
2. van Vreeswijk, C., Sompolinsky, H.: Chaos in neuronal networks with balanced excitatory and inhibitory activity. *Science* **274** (1996) 1724–1726.
3. de Kock, C.P.J., Sakmann, B.: Spiking in primary somatosensory cortex during natural whisking in awake head-restrained rats is cell-type specific. *Proc. Natl. Acad. Sci. USA* **106**(38) (2009) 16446–16450.
4. Potjans, T.C., Diesmann, M.: The cell-type specific cortical microcircuit: Relating Structure and Activity in a Full-Scale Spiking Network Model. *Cereb. Cortex* (2012). doi:[10.1093/cercor/bhs358](https://doi.org/10.1093/cercor/bhs358).
5. Binzegger, T., Douglas, R.J., Martin, K.A.C.: A quantitative map of the circuit of cat primary visual cortex. *J. Neurosci.* **39**(24) (2004) 8441–8453.
6. Thomson, A.M., West, D.C., Wang, Y., Bannister, A.: Synaptic connections and small circuits involving excitatory and inhibitory neurons in layer 2–5 of adult rat and cat neocortex: Triple intracellular recordings and biocytin labelling in vitro. *Cereb. Cortex* **12** (2002) 936–953.
7. Brunel, N.: Dynamics of sparsely connected networks of excitatory and inhibitory spiking neurons. *J. Comput. Neurosci.* **8**(3) (2000) 183–208.
8. Izhikevich, E.M., Edelman, G.M.: Large-scale model of mammalian thalamocortical systems. *Proc. Natl. Acad. Sci. USA* **105**(9) (2008) 3593–3598.
9. Heinzle, J., Hepp, K., Martin, K. A. C.: A microcircuit model of the frontal eye fields. *J. Neurosci.* **27**(35) (2007) 9341–9353.
10. Traub, R. D., Contreras, D., Cunningham, M. O., Murray, H., et al.: Single-column thalamo-cortical network model exhibiting gamma oscillations, sleep spindles, and epileptogenic bursts. *J. Neurophysiol.* **93**(4) (2005) 2194–2232.
11. Hill, S., TONI, G.: Modeling sleep and wakefulness in the thalamocortical system. *J. Neurophysiol.* **93**(3) (2005) 1671–1698.
12. Haeusler, S., Maass, W.: A statistical analysis of information-processing properties of lamina-specific cortical microcircuit models. *Cereb. Cortex* **17**(1) (2007) 149–162.
13. Rasch, M.J., Schuch, K., Logothetis, N.K., Maass, W.: Statistical comparison of spike responses to natural stimuli in monkey area V1 with simulated responses of a detailed laminar network model for a patch of V1. *J. Neurophysiol.* **105** (2011) 757–778.
14. Izhikevich, E.: Simple model of spiking neurons. *IEEE Transactions on neural networks.* **14**(6) (2003) 1569–1572.
15. Hodgkin, A.L., Huxley, A.F.: A quantitative description of membrane current and its application to conduction and excitation in nerve. *J. Physiol. (Lond)* **117** (1952) 500–544.

Attentional Cholinergic Projections May Induce Transitions of Attractor Landscape via Presynaptic Modulations of Connectivity

Hiroshi Fujii, Takashi Kanamaru, Kazuyuki Aihara, and Ichiro Tsuda

Abstract There is evidence of presynaptic modulation of inhibitions on pyramidal neurons in cortical layers 2/3, mediated by muscarinic M_2 -receptors activated by transient releases of the corticopetal acetylcholine associated with top-down attention. Little is known, however, regarding its system-level consequences and possible implications for cognitive functions. It is possible that, through a temporal modulation of connectivity between neurons, memory traces or the attractor landscape in the cortex might be significantly affected. We present a hypothetical argument on attractor ruins and temporal reconstructions of attractors by top-down attention. In this paper, we discuss the mathematical validity of this scenario with a computer study using a phase neuron model.

Keywords Transitions of attractor landscape • Presynaptic modulations of connectivity • Muscarinic M_2 -receptors • Corticopetal acetylcholine • Top-down attention • Temporal modulation of connectivity between neurons • Temporal reconstruction of attractors • Phase neuron model

H. Fujii (✉)

Department of Intelligent Systems, Kyoto Sangyo University, Kyoto 603-8555, Japan
e-mail: fujii@cse.kyoto-su.ac.jp

T. Kanamaru

Department of Innovative Mechanical Engineering, Faculty of Global Engineering, Kogakuin University, Tokyo 193-0802, Japan

K. Aihara

Institute of Industrial Science, The University of Tokyo, Tokyo 153-8505, Japan

I. Tsuda

Research Institute for Electronic Science, Hokkaido University, Kyoto 603-8555, Japan

Research Center for Integrative Mathematics (RCIM), Hokkaido University,
Kyoto 603-8555, Japan

1 Introduction

Purely *internal* cognitive process is an important and essential human activity. One example of such activity is “mental imagery.” When a person is asked: “which is longer – a donkey’s ears or an ear of corn?,” most people report that they visualize the objects, and “see” the pertinent properties [1]. As Kosslyn pointed out [1], this sort of introspection suggests that visual mental images reconstruct the spatial geometry of objects. Here, no external stimuli are involved. How are top-down signals implemented to help reconstruct internal representations of images in the absence of external stimuli?

The crucial significance of corticopetal acetylcholine (ACh) in cognitive functions is well recognized. Its deficiency, either due to diseases such as Alzheimer’s disease or dementia with Lewy bodies (DLB), or due to pharmacological treatments with an ACh antagonist (such as scopolamine or atropine) causes aberrant cognitive disorders such as *deficits of attention(s)* and *recurrent complex visual hallucinations* (RCVH) [2]. We have, however, only a vague concept regarding the representation of such images and the neural mechanisms involved.

In relation to these questions, the core of the arguments presented here will focus on the *intrinsic* cortical dynamics in *ongoing* states,¹ and their transitions to, and back from, more attractor(-like) states due to *transient* and *local* projections of corticopetal ACh. Kenet and coworkers investigated the brain’s “internal views” of the world through experiments in the cat visual cortex, with both eyes closed, that is, in the absence of external stimuli, and with no or at least minimal conscious attention(s) due to anesthetization [3]. They found that the ongoing brain state was *not* random, but continually fluctuating among a number of local *internal states*, which are inherent within hierarchical structures in the cortical circuits (Fig. 1).

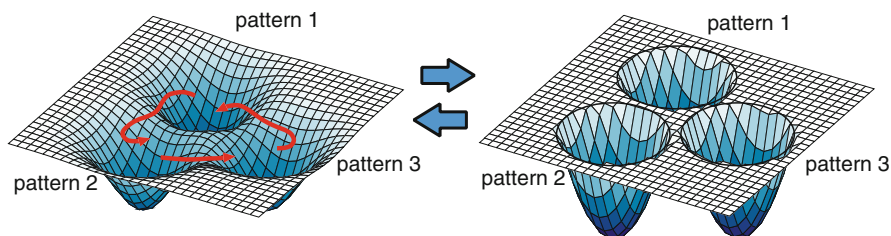


Fig. 1 Baseline level of ACh keeps the landscape with attractor ruins (*left*), while high level of ACh transiently released from the NBM makes a transition to a more attractor-like landscape temporarily (*right*). Note that by a landscape we mean the spatial structure of attractor basins. The “landscape” shown here is only for illustrative purpose

¹An “ongoing state” is used here to mean primarily layer 2/3 dynamical state of a local cortex with a circumstance where the cortex does not receive external input via layer 4, and also essentially no spike volleys to layer 1 (and probably also layer 6) as related to conscious attention.

From a dynamical systems standpoint, the transitory intrinsic states could be viewed as an expression of “attractor ruins” [4]² or “quasi-attractors”, observed in a *mesoscopic* dynamical system – the brain.

The authors presented a scenario of possible role for corticopetal ACh [5] in such transitions of attractor landscape, focused on the dynamics of the superficial layers (the layers 1 and 2/3).

We hypothesized that

1. In the absence of bottom-up external stimuli the layer 2/3 state exhibits transitory dynamics itinerant among attractor ruins until top-down attention occurs. This situation is maintained by the non-local baseline concentration of cortical ACh.

The attractor ruin² here is a dynamical systems-theoretical expression of *pre-built-in* “internal states” [3], “features” [6], “proto-objects” [7] or “templates” [8] appearing in various contexts. (See, also the Treisman theory: “pre-attentively, features are *free floating*” [6].)

2. The commencement of top-down attention reverses the process, and temporarily recovers the local landscape with attractors. This is a result of *transient* and *local* ACh release due to top-down attention via the NBM (nucleus basalis of Meinert) [9] which is bi-directionally activated by the mPFC (medial prefrontal cortex).
3. The selection of the orbit (state), i.e., the dynamical assignment of a specific attractor is achieved by *instantaneous* glutamatergic (Glu) top-down spike volleys projected onto layer 1.

Computer studies were conducted to clarify whether the scenario described above can be justified from a dynamical systems standpoint, based on realistic cortical network configurations. The model network used was the *phase neuron model* developed by one of the authors (T.K.). For full details, see Kanamaru et al. [10].

Our simulations reconstructed dynamics such as:

1. Ongoing state dynamics – transitive dynamics between attractor ruins at a *baseline level* of ACh.
2. Transition of the attractor landscape: from a landscape with attractor ruins at a baseline ACh level, to one with attractor-like states associated with transient ACh release onto layer 2/3.
3. Dynamic assignment of a specific attractor through instantaneous Glu spike volleys onto layer 1.

²An attractor ruin (or, quasi-attractor) must have a mechanism for allowing both transition and return to and from a state. A typical example of an attractor ruin is a perturbed structure of the non-classical Milnor attractor [13], which possesses the positive measure of attracting orbits, but may simultaneously possess the property of repelling orbits from itself.

2 Cholinergic Functions in the Cortex

With conscious attention, two kinds of top-down signals arrive at the cortex, i.e., Glu spike volleys from “higher” cortical levels (and from the matrix element of the thalamus), and corticopetal ACh ascended from the NBM. We hypothesize that, as with overt or covert attention to *external* stimuli, ACh is transiently projected also in *internal* attentions, in view of the *attention to memory*, or *the internal representation* hypotheses (see, for example, [11]).

The existing data on cellular effects of ACh mediated by either muscarinic or nicotinic receptors are, at present inconclusive, and sometimes controversial [12]. We are, however, primarily concerned with *transient* and *local* ACh released in concert with top-down attention [12, 14].

According to [12], both pyramidal neurons (PYRs) and GABAergic FS (fast spiking) interneurons (IN) in layer 2/3 are non-responsive to transient ACh release *post-synaptically*. However, recent studies suggest that such a transient release of ACh would induce a marked decrease of inhibition on layer 2/3 PYRs by IN [15, 16] as a result of cholinergic muscarinic (probably, M_2 receptor-mediated) presynaptic effects, which may bring about an extensive modulation of network connectivity. The system-level consequences of such cholinergic effects leading to transitions of attractor landscape are our main concern here. (see also the discussion in Sect. 4.)

The top-down Glu spike volleys projected onto layer 1 also play an essential role in the dynamic assignment of attractors to be stabilized, kicking the orbit into the basin of an assigned attractor. See, simulation 2, below (Fig. 3).

3 Computer Study Using the Phase Neuron Model

Here we provide a brief report of our simulation study on ACh-dependent transient modulation of presynaptic inhibition of pyramidal neurons (PYRs) in layer 2/3. See, [10] for the phase neuron model and full details of the results.

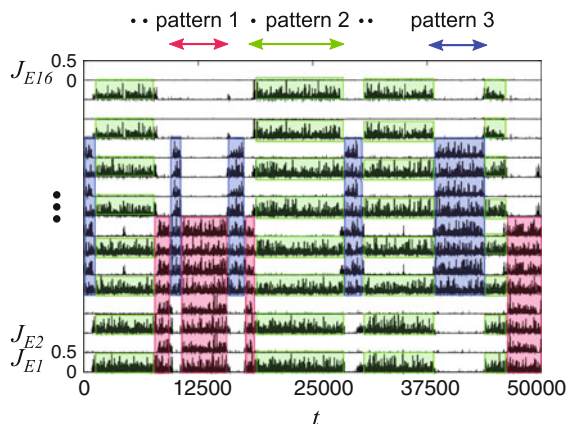


Fig. 2 Transitory dynamics among attractor ruins which appears corresponding with a baseline level of ACh. Firing rates of 16 “units” are shown here

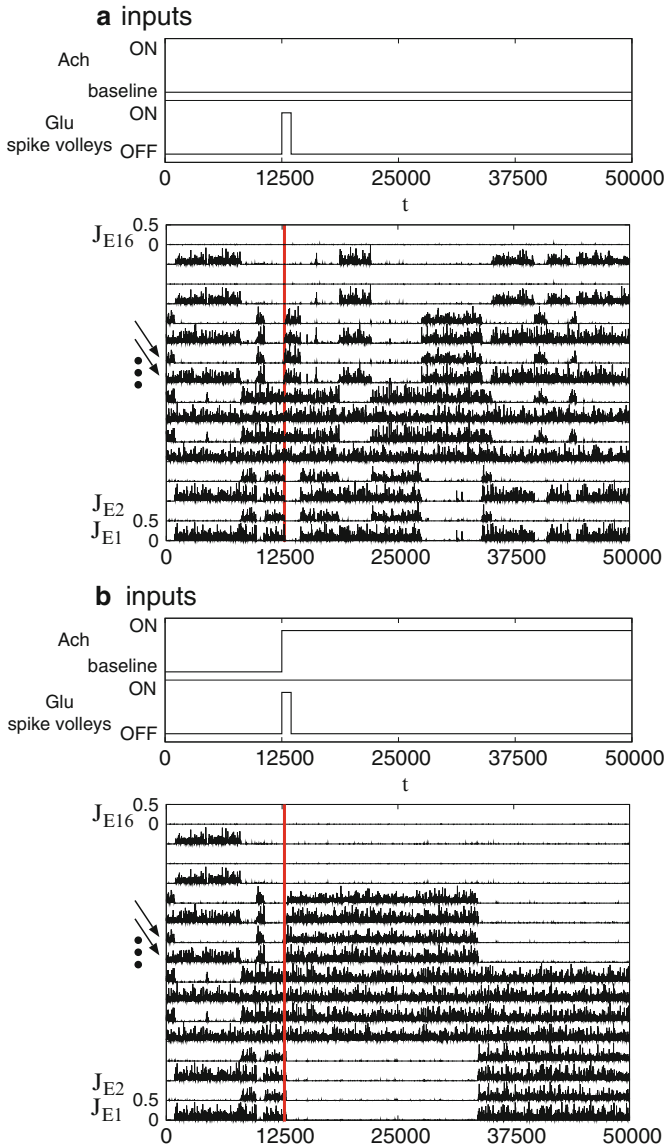


Fig. 3 Top-down spikes are projected during a brief period ($12,500 < t < 13,500$) onto units 9 and 10 (a) with a baseline level of ACh (top), and (b) with an increased level (bottom) of ACh, respectively. In the case of (b), the state transits, but does so temporarily to pattern 3, in which the units 9 and 10 are “active” members. The level of ACh determines how long the state is maintained. When ACh is phasically released in concert with the top-down spikes, the activated attractor is more transient (Data not shown here. See [10])

Simulation 1: *Transitory dynamics among attractor ruins at a baseline level of ACh.*

When ACh levels are low, at a *baseline level*, i.e., under a strong inhibition of PYRs (here the ACh level is “mimicked” by the strength of inhibitions of FS neurons on PYRs), the originally built-in attractors (designated as “pattern” 1, 2 and 3 in Fig. 2) are no longer stable, and the dynamics are chaotically transitive among the three attractor ruins.

Simulation 2: *Recovery of a specific attractor by an injection of brief top-down spikes onto the distal apical dendrites of PYR neurons in layer 2/3.*

When spikes are projected briefly onto a fragment (say units 9 and 10) of an attractor ruin (i.e., pattern 3) at a baseline ACh level, the dynamics maintain their transitive nature even under “top-down” inputs (Fig. 3a top). On the other hand, the whole pattern 3 is activated transiently when the ACh level is increased (Fig. 3b bottom). This is a *dynamic pattern completion* controlled by the ACh level.

4 Discussion

Attentional ACh decreases $IN \rightarrow PYR$ inhibitions in layer 2/3, while intra-cortical $PYR \iff PYR$ excitatory connections may be simultaneously depressed [17, 18], although there are studies suggesting that this may *depend on its concentration* [19]. Our simulations suggest that as long as the levels of excitatory and inhibitory inputs remain *balanced* during attention, our central proposition that ACh release transiently recovers the relevant attractor in the landscape still holds. (see [10].)

Acknowledgments The authors (H.F. and I.T.) were supported by a Grant-in-Aid for Scientific Research on Innovative Areas “The study on the neural dynamics for understanding communication in terms of complex hetero systems (No.4103)” (21120002) from The Ministry of Education, Culture, Sports, Science, and Technology, Japan. The second author (T.K.) was supported by a Grant-in-Aid for Encouragement of Young Scientists (B) (No. 20700215) from The Ministry of Education, Culture, Sports, Science and Technology of Japan. This research was also partially supported by the Aihara Project, the Funding Program for World-Leading Innovative Research and Development on Science and Technology (FIRST) from the Japan Society for the Promotion of Science (JSPS), initiated by the Council for Science and Technology Policy (CSTP).

References

1. Kosslyn, S. M.: Mental images and the brain. **Cogn. Neuropsychology** **22** (2005), 333–347.
2. Collerton, D. *et al.*, Why people see things that are not there: A novel Perception and Attention Deficit model for recurrent complex visual hallucinations. **Behavioural and Brain Science** **28** (2005) 737–794.
3. Kenet, T. *et al.*: Nerve cell activity when eyes are shut reveals internal views of the world. **Nature** **425** (2003) 954–956.

4. Tsuda, I.: Chaotic itinerancy as a dynamical basis of Hermeneutics in brain and mind. **World Futures** **32** (1991) 167–184.
5. Fujii, H. *et al.*: Top-down Mechanism of Perception: A Scenario on the Role for Layer 1 and 2/3 Projections Viewed from Dynamical Systems Theory, R. Wang and F. Gu (eds.), **Advances in Cognitive Neurodynamics II**, Springer-Verlag, (2010), 79–84.
6. Treisman, A. M., & Gelade, G.: A feature- integration theory of attention. **Cognit. Psychol.** **12** (1980) 97–136.
7. Rensink, R.A.: Visual sensing without seeing. **Psychological Science** **15** (2004):27–32.
8. Desimone, R. and Duncan, J.: Neural mechanism of selective visual attention. **Annu. Rev. Neurosci.** **18** (1995) 193–222.
9. Sarter, M. *et al.*: Phasic acetylcholine release and the volume transmission hypothesis: time to move on. **Nature Rev. Neurosci.** **10** (2009) 383–390.
10. Kanamaru, T, Fujii, H. and Aihara, K.: Transformation of Attractor Landscape via Cholinergic Presynaptic Modulations: A Computer Study with Phase Neuron Model. *In preparation.*
11. Ciaramelli, E. *et al.*, Top-down and bottom-up attention to memory: A hypothesis (AtoM) on the role of the posterior parietal cortex in memory retrieval. **Neuropsychologia** **46** (2008), 1828–1851.
12. Gullledge, A.T. *et al.*: Heterogeneity of phasic signaling in neocortical neurons. **J. Neurophysiol.** **97** (2007) 2215–2229.
13. Milnor, J.: On the Concept of Attractor, **Comm. Math. Phys.** **99** (1985), 177–195.
14. Parikh, V. *et al.*: Prefrontal Acetylcholine Release Controls Cue Detection on Multiple Timescales. **Neuron** **56** (2007) 141–154.
15. Salgado, H. *et al.*: Muscarinic M2 and M1 Receptors Reduce GABA Release by Ca2 Channel Modulation Through Activation of PI3K/Ca2-Independent and PLC/Ca2-Dependent PKC. **J. Neurophysiol.** **9** (2007) 952–965.
16. Kruglikov, I. and Rudy, B.: Perisomatic GABA Release and Thalamocortical Integration onto Neocortical Excitatory Cells Are Regulated by Neuromodulators. **Neuron** **58** (2008) 911–924.
17. Gil, Z. *et al.*, Differential Regulation of Neocortical Neocortical Synapses by Neuromodulators and Activity. **Neuron** **19** (1997), 679–686.
18. Hasselmo M. E. and McGaughy, J.: High acetyl- choline levels set circuit dynamics for attention and encoding and low acetylcholine levels set dynamics for consolidation. **Progress in Brain Research** **145**, 207–231.
19. Kuczewski, N. *et al.*: Acetylcholine modulates cortical synaptic transmission via different muscarinic receptors, as studied with receptor knockout mice. **J. Physiol.** **566** (2005), 907–919.

Forced Wakefulness for Entrainment to Permanent Shift Work: A Computational Study

Svetlana Postnova and Peter A. Robinson

Abstract A physiologically based model of sleep-wake cycles is used to examine the role of forced wakefulness during shifts on circadian entrainment of permanent shift workers. We demonstrate that forced wakefulness is crucial for entrainment to night and early morning shifts, while on afternoon and late evening shifts entrainment can be achieved simply due to changes in light. We explain this phenomenon by the properties of the human circadian pacemaker which requires non-photic entrainment for its phase advance in the early hours of the night. This finding is important for a better design of shift workers routine in order to decrease sleepiness.

Keywords Sleepiness • Fatigue • Circadian • Homeostatic • Sleep-wake cycles • Mathematical modeling

1 Introduction

Shift work and atypical sleep schedules are associated with an increased number of accidents due to sleepiness and fatigue [1–3], and lead to long-term health problems, including diabetes, obesity, and cancer [4]. These are hypothesized to be related to prolonged desynchronization among different circadian rhythms in the body.

S. Postnova (✉) • P.A. Robinson
School of Physics, The University of Sydney, NSW 2006, Australia

Center for Integrated Research and Understanding of Sleep, Woolcock Institute,
The University of Sydney, NSW 2037, Australia
e-mail: postnova@physics.usyd.edu.au

P.A. Robinson
Brain Dynamics Center, Sydney Medical School – Western, University of Sydney,
Westmead, NSW 2145, Australia
e-mail: robinson@physics.usyd.edu.au

Understanding of the mechanisms underlying circadian entrainment of workers to shift schedules will help to design conditions to reduce sleepiness and improve overall well-being of shift workers.

Sleep-wake cycles are controlled by a complex system of multiple interacting neurobiological structures. Understanding of their dynamics has been significantly advanced by computational approaches, and a number of mathematical models simulating performance of shift workers exist in the current literature [e.g., 5, 6]. Most of these models are built up using a high level approach of interacting functions formally simulating interaction between the circadian and homeostatic processes, which modulate sleep pressure and control sleep-wake transitions [7]. These models are very successful in predicting short-term effects of shift work on sleepiness and performance, but do not address long term changes and underlying physiological mechanisms. Recent advances in neurobiology of sleep [8] enabled development of physiologically based models of sleep-wake cycles [9–11] and allowed examination of long-term effects of shift work on sleep and entrainment, along with probing mechanisms underlying sleepiness on the level of the interacting brain nuclei [12].

In this work we use such a physiologically based model of sleep-wake cycles to understand the role of forced wakefulness during shifts on entrainment and sleepiness of permanent shift workers. It is well known that often, especially during night shifts, workers fall asleep either accidentally due to high sleep pressure or purposefully if given a chance when work load is low. Such naps improve performance of shift workers in short term, because they reduce an immediate sleep pressure [13]. In this paper we examine long term effects of free versus enforced wakefulness conditions during the shifts. We demonstrate that it is important to enforce wakefulness on the night shift to entrain to permanent shifts and reduce sleepiness in the long term.

2 Methods

The model used here is combined from two earlier models: a physiologically based model of the ascending arousal system (AAS) [9], and a model of the human circadian pacemaker entrained by light and non-photoc inputs [14]. The schematic of the model is shown in Fig. 1a. A similar combined model has already been used to study sleep of different circadian chronotypes and general mechanisms underlying sleepiness and entrainment of shift workers on different schedules [12, 15]. Therefore, here we briefly describe the key concepts involved in the model.

The AAS model is built up using neural mass modeling methods [9]. It simulates average voltages and firing rates of the wake-active group of monoaminergic neurons (MA) in the brainstem and the sleep-active ventrolateral preoptic nucleus (VLPO) in the hypothalamus. These inhibit one another, thereby contributing to the flip-flop like switch between sleep and wakefulness. The dynamics of the MA and the VLPO are under influence of the homeostatic (H) and circadian (C) processes [16].

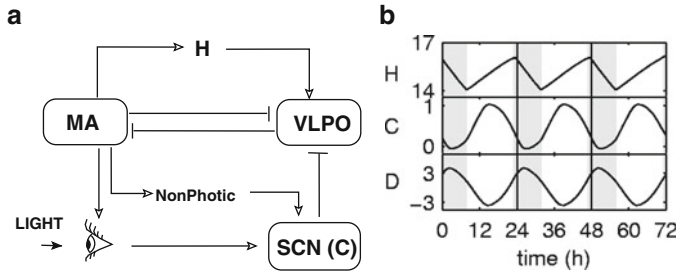


Fig. 1 (a) Schematic of the model. The *bar-headed lines* correspond to inhibitory connections, while *arrow-headed* – to excitatory. (b) Time course of the homeostatic H , circadian C , and total sleep drive D . *Shaded areas* indicate sleep intervals

The precise mechanisms of the H process are not yet known but are postulated to increase sleep pressure during wakefulness and dissipate it during sleep, as shown in top panel of Fig. 1b. Some of the proposed mechanisms include accumulation of somnogens during wakefulness, and synaptic plasticity of specific neurons [8, 10].

The circadian process modulates sleep drive depending on the time of the day and external “time givers” (the so-called zeitgebers), including light, feeding times, and locomotion. Change in zeitgebers leads to change of the phase of the circadian oscillator. The master circadian clock in the brain is the suprachiasmatic nucleus of the hypothalamus (SCN in Fig. 1a), which neurons change their firing rate depending on the time of the day. Maximum activity of the SCN is observed during the day and minimum during the night, as shown in Fig. 1b [16].

In the model presented here the circadian process C is incorporated as an input to the VLPO from the model of the human circadian pacemaker [14] as shown in Fig. 1a. This model uses Van der Pol oscillator to simulate circadian oscillations and accounts for the effects of light and of non-photic stimuli on the phase of the oscillator.

The combined effects of the circadian and homeostatic processes on sleep pressure give a total sleep drive $D = \nu_{vh}H + \nu_{vc}C$, where $\nu_{vh} > 0$ and $\nu_{vc} < 0$ are coupling constants. The coupling constant for the homeostatic process is positive because H promotes sleep, while the constant for the circadian process is negative, because C promotes wakefulness. Thus, D is minimal when C is maximal. The sleep drive D controls the transitions between sleep and wakefulness. During normal sleep-wake cycles, sleep is initiated when D is above a certain threshold value, and transition to wake happens when D is below it, as shown by the shaded areas in Fig. 1b.

In this study we examine the simplest case of permanent 8 h shifts without weekends and simplest light conditions in order to understand the general mechanisms. Therefore, in the absence of shift work the light input to the model is constant 200 lx between 08:00 and 22:00. During the shifts additional light input of the same intensity is introduced. During sleep light input is set to zero assuming that workers

sleep in total darkness. Forced wakefulness during shifts is implemented by keeping the MA and VLPO in wake state, while allowing dynamic changes of H and C (for detail see [12]).

The total sleep drive D is used here as the simplest measure of sleepiness. Average values of D during the shifts are used to compare sleepiness on different schedules and days.

3 Results

When shift work with forced wakefulness during the shifts is introduced, it results in increased total sleep drive D in the first days on the new schedule [12]. This happens due to reduced sleep time resulting from sleeping during a day; i.e., during high circadian input. The new external zeitgebers introduced due to shift, particularly the additional light input, lead to re-entrainment of the circadian oscillator and, finally, to re-establishment of normal sleep amount after a certain number of adaptation days. It has been shown that in the absence of days off on the night shifts mean daily sleep drive increases during the first 2–5 days on the new schedule, then starts to decrease, and stabilizes when circadian re-entrainment is achieved. For description of mechanisms, see [12].

Re-entrainment leads to change of the circadian phase and, accordingly, to a different location of the circadian maximum. With the considered light profile in the absence of shifts the circadian maximum, which corresponds to the minimum of D , is located at 15:00. Shift work moves the circadian maximum towards either later or earlier time depending on the time of the shift, as shown in Fig. 2.

As shown in Fig. 2a shift work leads to advance of D_{\min} to earlier time on the night shifts starting between 23:00 and 08:00, in the presence of forced wakefulness.

Fig. 2 Effects of forced wakefulness on circadian entrainment and sleep drive. **(a)** Timing of the minimal sleep drive ($t_{D_{\min}}$) depending on the shift onset. The *gray lines* indicate the borders of the shift interval relative to $t_{D_{\min}}$; **(b)** average sleep drive during shifts ($\langle D_{\text{shift}} \rangle$) depending on the time of the shift onset. The *solid line* refers to the shifts with forced waking, the *dashed line* to those with free sleep-wake activity

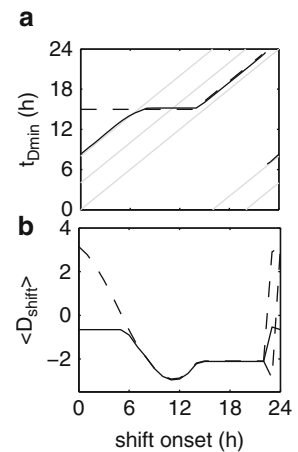
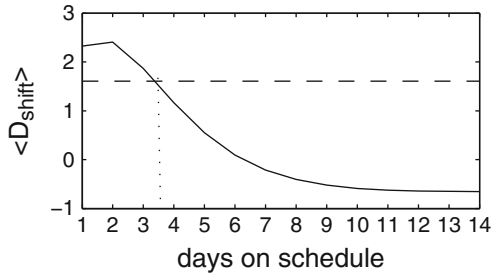


Fig. 3 Evolution of the average sleep drive $\langle D_{\text{shift}} \rangle$ for the shift starting at 3:00 on the schedules with (solid line) and without (dashed line) forced waking



On the afternoon and evening shifts, starting between 15:00 and 23:00 it leads to delay of D_{min} . Shifts starting between 8:00 and 15:00, which are normal work times, do not change circadian phase, and thus have the same timing of D_{min} .

The time course of D can be approximated by a sine wave (see Fig. 1b), thus minimal average sleep drive during the shifts is obtained when D_{min} is in the middle of the shift; i.e., for the shift onset at 11:00. Night shifts lead to a significantly higher $\langle D_{\text{shift}} \rangle$, because when entrainment is achieved D_{min} is at the border of the shift (see Fig. 2a).

With free sleep-wake activity during the shifts; i.e., sleep as allowed at any time of the shift, the model does not allow relocation of D_{min} to an earlier time during the night shifts, while on the other shifts the dynamics are the same (compare the solid and dashed lines in Fig. 2a). Therefore, $\langle D_{\text{shift}} \rangle$ for the night shifts is significantly higher in the case without forced wakefulness, as shown in Fig. 2b. This means that proper entrainment to night shifts can only be achieved when wakefulness is forced.

This finding is counterintuitive considering that napping on night shifts reduces sleepiness [13]. However, the reduction of sleepiness is observed only in the short term, while in the long term re-entrainment to the new external cues introduced by the shift is much more beneficial, as shown in Fig. 3.

This figure demonstrates an example of the change of the mean sleep drive during the night shift over the time span of 2 weeks. According to this plot the shifts with forced wakefulness lead to a higher D during the first 3 days on the new schedule, while afterward it starts decreasing until it stabilizes at much lower values of $\langle D_{\text{shift}} \rangle$ than those achieved without forced waking. Thus, the schedules with forced wakefulness are beneficial in the long term.

4 Discussion

In this study we have used a physiologically based mathematical model of sleep-wake cycles to study sleepiness of shift workers. We have showed that forced wakefulness during the shifts is essential to enable entrainment to night shifts, and that such re-entrainment is beneficial on long-term permanent schedules. We explain these dynamics by the fact that the human circadian pacemaker cannot be advanced

in the early hours simply by light inputs [16]. Non-photoc stimulation is required for re-entrainment, and this is achieved when wakefulness is enforced along with changed lighting.

In the presence of forced wakefulness the model shows good re-entrainment to the new zeitgebers. However, in practice, entrainment is not easily achieved, due to diverse social commitments and other factors affecting the timing of sleep and wakefulness. Thus, in future studies effects of random influences on entrainment should be implemented and examined. Future work will also include more complicated shift schedules, like rotating shifts, and account for effects of weekends.

In practice, when sleep is allowed during the shifts, the workers do not usually sleep until their sleep pressure is sufficiently decreased. Instead, they may just have short naps at different times of the shift until a next task has to be performed. Therefore, the model reproduces an idealized situation when the workers can sleep just following their sleep drive. It is expected that the average sleep drive on such shifts will be even higher than the one shown with the dashed line in Fig. 3. However, during the first day(s), $\langle D_{\text{shift}} \rangle$ on completely free sleep-wake schedules will still be lower than $\langle D_{\text{shift}} \rangle$ with forced waking. Also scheduled naps appearing at the same time every day may lead to different dynamics, since they may promote entrainment. This case should be examined in the future studies.

In summary, this study provides new insights into the conditions that allow to improve sleepiness of shift workers and demonstrates how physiologically based models of sleep expand applicability of modelling to understand sleepiness.

Acknowledgments This work is supported by the Australian Research Council and National Health and Medical Research Council.

References

1. Åkerstedt, T.: Work hours and sleepiness. *Neurophysiol Clin* 25 (1995) 367–375.
2. Dinges, D.F.: An overview of sleepiness and accidents. *J Sleep Res* 4 (1995) 4–11.
3. Boivin, D.B., Tremblay, G.M., James, F.O.: Working on atypical schedules. *Sleep med* 8 (2007) 578–589.
4. Knutsson, A.: Health disorders of shift workers. *Occup Med (Lond)* 53 (2003) 103–108.
5. Mallis, M.M., et al.: Summary of the key features of seven biomathematical models of human fatigue and performance. *Aviat Space and Env Med* 75 (2004) A4–A14.
6. Hursh, S.R., et al.: Fatigue models for applied research in warfighting. *Aviat Space and Env Med* 75 (2004) A44–A53.
7. Borbély, A.A.: A two process model of sleep regulation. *Hum Neurobiol* 1 (1982) 195–204.
8. Saper, C.B., et al.: Sleep state switching. *Neuron* 68 (2010) 1023–1042.
9. Phillips, A.J.K. and Robinson, P.A.: A quantitative model of sleep-wake dynamics based on the physiology of the brainstem ascending arousal system. *J Biol Rhythms* 22 (2007) 167–179.
10. Postnova, S., Voigt, K., Braun, H.A.: A mathematical model of homeostatic regulation of sleep-wake cycles by hypocretin/orexin. *J Biol Rhythms* 24 (2009) 523–535.

11. Kronauer, R.E., Forger, D.B., Jewett, M.E.: Quantifying human circadian pacemaker response to brief, extended, and repeated light stimuli over the photopic range. *J Biol Rhythms* 14 (1999) 500–515.
12. Postnova, S., et al.: Exploring sleepiness and entrainment on permanent shift schedules in a physiologically based model. *J Biol Rhythms* 27 (2012) 91–102.
13. Lumley, M., et al.: The alerting effects of naps in sleep deprived subjects. *Psychophysiol* 23 (1986) 403–408.
14. St. Hilaire, M.A., Klerman, E.B., Khalsa, S.B.S., et al.: Addition of non-photoc component to a light-based mathematical model of the human circadian pacemaker. *J Theor Biol* 247 (2007) 583–599.
15. Phillips, A.J.K., Chen, P.Y., Robinson, P.A.: Probing the mechanisms of chronotype using quantitative modeling. *J Biol Rhythms* 25 (2010) 217–227.
16. Moore, R.Y.: Suprachiasmatic nucleus in sleep-wake regulation. *Sleep Med* 8 (2007) 27–33.

Towards a Modeling and Simulation Platform for Multi-level Neuronal Networks

Yoshiyuki Asai, Hideki Oka, Taishin Nomura, and Hiroaki Kitano

Abstract We have been developing an open platform for enhancing the integrative life science called Physiome and systems biology, on which users can build mathematical models of biological and physiological functions with hierarchical structure, and perform simulations with parallel computing. We also have been proposing a XML-based language for describing a wide variety of models, and developing a model database in order to facilitate model sharing. Neuroscience is one of the research fields in which mathematical models played effectively important roles to reveal physiological principles. We will discuss on a possibility to apply our platform for neuroscience.

Y. Asai (✉)

Open Biology Unit, Okinawa Institute of Science and Technology, Okinawa, 904-0412, Japan
e-mail: yoshiyuki.asai@oist.jp

H. Oka

The Center for Advanced Medical Engineering and Informatics, Osaka University,
Osaka, 565-0871, Japan

T. Nomura

The Center for Advanced Medical Engineering and Informatics, Osaka University,
Osaka, 565-0871, Japan

Department of Mechanical Science and Bioengineering, Graduate School of Engineering Science,
Osaka University, Osaka, 560-8531, Japan

H. Kitano

Open Biology Unit, Okinawa Institute of Science and Technology, Okinawa, 904-0412, Japan

The Systems Biology Institute, Tokyo, 108-0071, Japan

Sony Computer Science Laboratories, Tokyo, 141-0022, Japan

1 Introduction

Accumulation of knowledge of physiology has opened a new scientific field, i.e. integrated life-science with the keywords such as Physiome [1] and systems biology [2], in which inter-level principles as well as intra-level disciplines are explored. Roles played by multi-scale and multi-level mathematical modeling of physiological functions are becoming more and more important, since mathematical models are capable of describing dynamics, i.e., time evolution of states of biological systems, quantitatively based upon physical and chemical principles or phenomenological logic governing system behaviors [3].

The framework for supporting to build such mathematical models of physiological functions and for archiving and sharing models is inevitable for further development. We have been developing an open platform called “*insilico* platform” [3], and now we are going to develop PhysioDesigner as a successor of the *insilico* platform, besides other pioneering efforts to promote physiome and systems biology, such as SBML and CellML [4]. On the platform, physiological functions are considered as an aggregate of modules which are easily viewed and edited on *insilico*IDE (ISIDE) [5], a main application to provide a integrated development environment in *insilico* platform. Based on this modularity, physiological functions are structuralized and modeled. The model is described in *insilico*ML (ISML), an XML based language, which we defined to well describe the modular and hierarchical structure of the models [6]. Using our platform users can integrate not only mathematical expressions but also experimentally obtained timeseries data and morphological data. We also developed databases (*insilico*DB: ISDB) to enhance sharing of models and those data.

Neuroscience is one of the scientific areas in which mathematical models have been playing active roles successfully through past decades. Now by combining computational and theoretical neuroscience, systems biology and neurophysiology, a new approach so called neurophysiome is arising. Several pioneering technologies such as NEURON, GENESIS, NeuroML [7] and so on in this field are supporting the basis of the theoretical and computational neuroscience. We will discuss on a possibility to apply our platform for neuroscience.

2 *insilico* Platform Outline

The *insilico* platform is composed of three blocks, i.e. ISML, ISIDE and ISDB.

ISML is a language specification based on XML to describe mathematical models of physiological functions. In a model in ISML, each of physiological entities is represented as a *module*. Each module is quantitatively characterized by several *physical-quantities*, which are used to represent constant/variable parameters as well as dynamical variables used in the definition of time evolution of the system

state, such as only ordinary differential equations, partial differential equations, rules for multi agent systems. ISML is also capable of describing the integration of morphological and time-series data to mathematical models.

The structural and functional relationships between two modules are defined by *edges* spanned between them. For example, if one module physically includes another module (e.g. cell membrane includes mitochondria) they are connected by a *structural edge*. If a module quantitatively affects to another module (e.g. an ionic current flowing a channel on a cell membrane changes the membrane potential), the two modules are linked by a *functional edge*. When a module wants to refer a value of a physical-quantity defined in the other module, the value can be transferred to the module along a functional edge spanned between the two modules.

A concept to make a kind of package of a physiological function has been introduced to ISML, which is called *capsulation*, in order to enhance the model sharing. Several modules acting together as a certain physiological function are encapsulated by a capsule module. All connections to (from) the encapsulated modules from (to) outside of the capsule must go through the capsule module to secure the independence of the encapsulated modules. By this isolation of modules, it becomes easy to reuse the encapsulated modules in other parts of the model or in other models.

We also have been developing a simulator *insilicoSim* (ISSim) [8]. In the framework of the *insilico* platform, the model construction and the simulation are clearly separated. Users can focus on the structure and logic of a model, and do not need to take care about algorithms for numerical calculations because ISSim takes care such issues instead of users. ISSim also can perform parallel computing for simulations of ISML models using multiple cores on a PC. This is one of advantages to use this platform since if users want to adopt a parallel computing technology on a multi-core environment, usually users are required to learn specific techniques additionally, which is a time consuming task. ISSim can parse SBML as well.

3 Examples of ISML Model

Figure 1 shows an example of ISML model displayed on ISIDE. This is a coupled two Hodgkin-Huxley (HH) model [9]. A HH model is a well-known conductance based model of an excitation of neuron membrane. The membrane potential can be calculated by an integration of three major ionic currents, i.e. voltage-dependent persistent Potassium ion (K^+) current, voltage-dependent transient Sodium ion (Na^+), and a leak current which is considered to be mainly carried by Chloride ion (Cl^-), and at the same time to represent other channels which are not described explicitly. The Na^+ and K^+ currents are regulated by three gating variables. In total the model is described by four ordinary differential equations corresponding to the membrane potential and three gating variables, and a couple of functions to calculate currents and so on. In Fig. 1 two HH neuron modules, one external

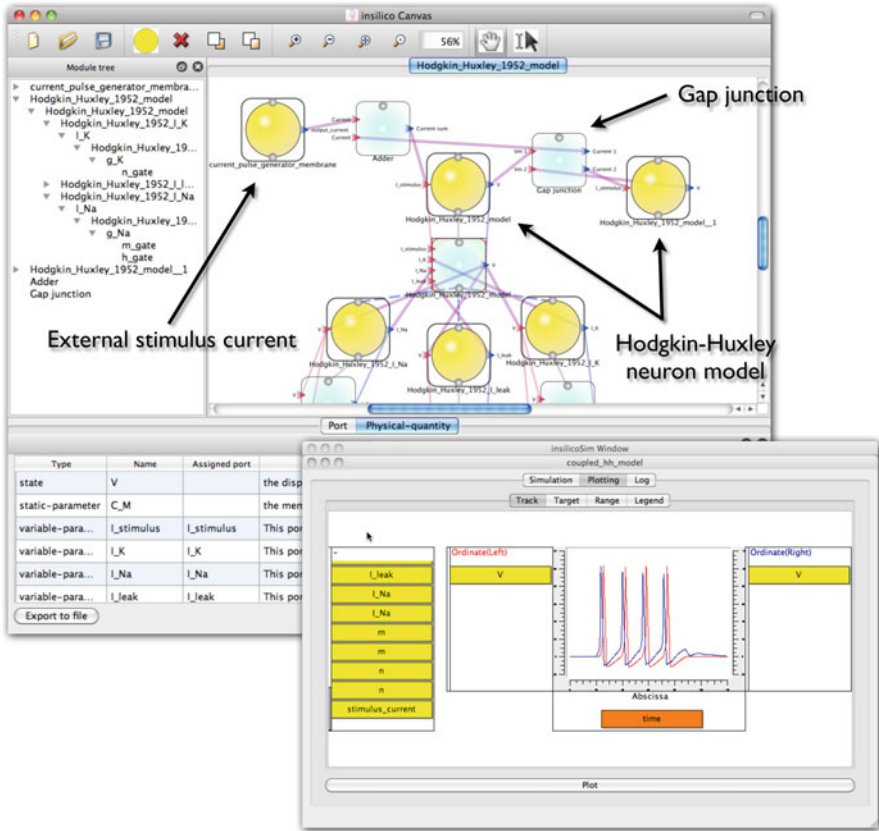


Fig. 1 An example of a hierarchical and modular expression of a coupled Hodgkin-Huxley neuron model on *insilicoIDE* and a simulation result computed by *insilicoSim*

stimulus current generator module, and a gap junction module are shown. Modules form tree structures on ISIDE. Double tapping on a module toggles showing and hiding modules in its sublayers. A HH neuron at the left side in Fig. 1 shows its substructure (three ionic current modules). The membrane of the HH neuron, each ionic currents, channel conductances, and channel gating variables are represented as modules. Equations and parameters are defined in each module.

4 Modeling with Morphology

To integrate morphological information into a model is inevitable for considering physiological functions. For now, the morphometric data can be utilized on ISIDE to define a domain on which partial differential equations are solved. For example,

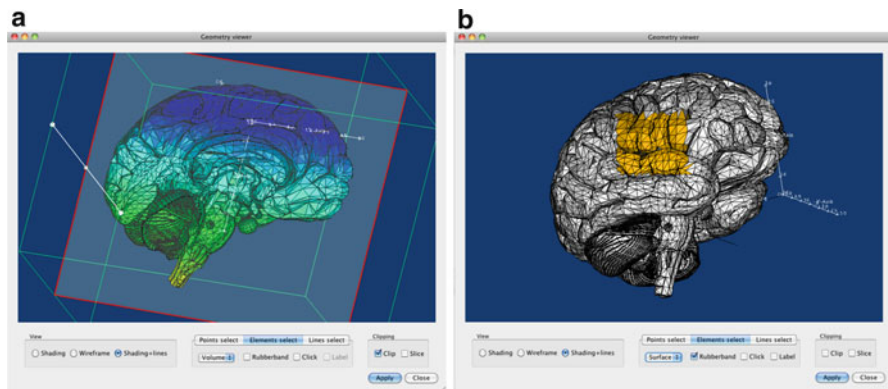


Fig. 2 Morphology viewer dialog. (a) A 3D morphology model with a slicing function to view the inside. (b) Selecting a region with a rubber band function to define a segment which is used to set, for example, an initial condition or boundary conditions

as shown in Fig. 2a, if one has morphometric data of a brain as an organ level model, the data can be integrated to the model. Segments can be defined on the morphology model to which an initial condition and boundary conditions can be defined (Fig. 2b). By combining the morphology with partial differential equations representing conduction of electric field and ordinary differential equations representing an excitable neuron membrane, users can construct a model, for example, reproducing the EEG evoked by a neuronal activity. A model including morphological data with partial differential equations can be numerically solved by FreeFEM++ which is a third-party free software developed at <http://www.freefem.org>.

5 Modeling with SBML

We proposed a method to create a multi-level model including cell and subcellular phenomena in cooperation with SBML [10]. We will directly utilize models described by SBML on *insilico* platform. SBML is a pioneering model description language for systems biology, such as subcellular signaling pathways, metabolic pathways, gene regulation, among others. The scheme of the hybridization of SBML and ISML is illustrated in Fig. 3.

ISML is designed to represent a functional network and hierarchical structure using its modular representation. The *insilico* platform provides a function to import a whole SBML model in a module of ISML. The model in SBML is not converted into ISML, but be wrapped by ISML and be kept in a module in the model. Then the module can represent the subcellular phenomena which is modeled by the SBML model. In this sense, the model is consequently written in a kind of hybrid language of SBML and ISML.

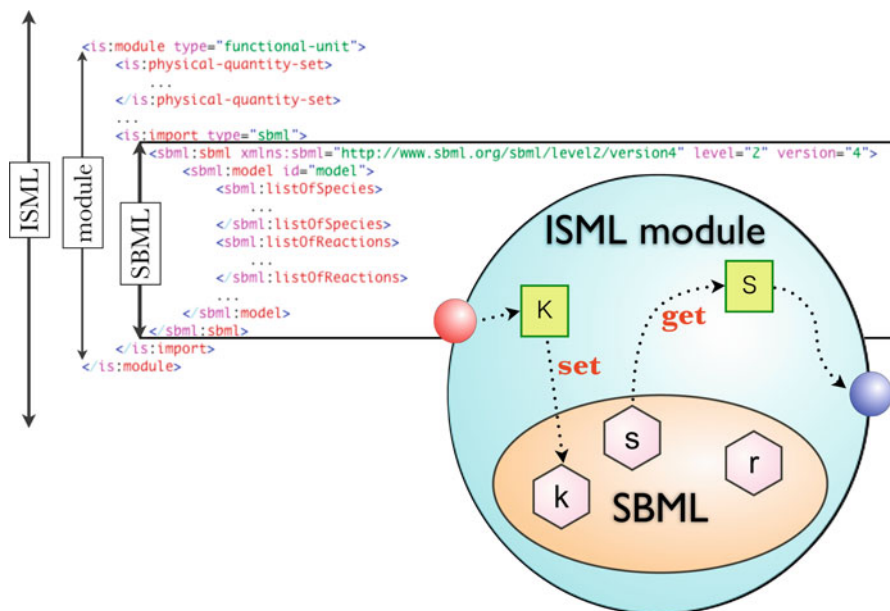


Fig. 3 Schematic diagram of a model written in SBML and ISML. XML shows an example of ISML description including a whole SBML model. In a schematic figure of a module, *squares* surrounded letters (K and S) represent physical-quantities of ISML. An *oval* in the module represents a SBML model in which three hexagons corresponding to species of SBML are described. The *dotted arrows* shows associations between physical-quantities and species. By these associations, numerical interactions between ISML and SBML are defined

There are “species” and “parameters” in SBML to represent quantitative attributes of biochemical entities. At a module including a SBML model, it is possible to define associations between physical-quantities and species/parameters. By this association, a physical-quantity can get a value from a species/parameters or can give a value to them, and the SBML model is effectively involved in the model. By linking the module including the SBML model to other modules by structural and functional edges, the SBML model eventually is integrated in the ISML module network in the senses of both structural and functional relationships.

6 Discussion

The platform we have been developing can be also applied to neuroscience among other fields. Let us take modeling of the basal ganglia as an example scenario. To consider the overall functioning of the basal ganglia-thalamocortical motor system, we can find neural network models [11] including projections among neuronal nuclei in the basal ganglia which may be affected by LTP and LTD at

striatum. A striatal synaptic plasticity has been modeled by Nakano et al. (2010) [12] incorporating all major signaling molecules such as dopamine- and cyclic AMP-regulated phosphoproteins. The model is written in SBML and shared at BioModels [13]. One of inputs to the model is dopamine concentration which is tightly related to the particular burst firing of the dopaminergic neurons in substantia nigra pars compacta. There is a dynamical system model [14] stored in ISDB, which reproduces the membrane potential dynamics of dopaminergic neurons. Though these models are just examples, we can find several models developed in each level such as molecular, single cell and network level. However, we can scarcely find models bridging multiple levels, and we expect that ISIDE and coming PhysioDesigner can be complementary technology to contribute to development of multilevel modeling based on SBML and ISML.

Acknowledgements This work is supported in part by MEXT Global COE program at Osaka University, and Grant-in-Aid for Scientific Research on Innovative Areas at Osaka university and at OIST.

References

1. Bassingthwaighe, J.B.: Strategies for the physiome project. *Ann Biomed Eng* **28**(8) (8 2000) 1043–58
2. Kitano, H.: Computational systems biology. *Nature* **420**(6912) (11 2002) 206–10
3. Nomura, T.: Toward integration of biological and physiological functions at multiple levels. *Frontiers in Systems Physiology* **1**(164) (2010)
4. <http://www.sbml.org/>, <http://www.cellml.org/>
5. Suzuki, Y., Asai, Y., Oka, H., Heien, E., Urai, T., Okamoto, T., Yumikura, Y., Tominaga, K., Kido, Y., Nakanishi, M., Hagihara, K., Kurachi, Y., Nomura, T.: A platform for *in silico* modeling of physiological systems III. *Conf Proc IEEE Eng Med Biol Soc* **2009** (2009) 2803–6
6. Asai, Y., Suzuki, Y., Kido, Y., Oka, H., Heien, E., Nakanishi, M., Urai, T., Hagihara, K., Kurachi, Y., Nomura, T.: Specifications of *insilico*ML 1.0: a multilevel biophysical model description language. *J Physiol Sci* **58**(7) (2008) 447–58
7. <http://www.neuron.yale.edu/neuron/>, <http://www.genesis-sim.org/GENESIS/>, <http://www.neuroml.org/>
8. Heien, E.M., Asai, Y., Nomura, T., Hagihara, K.: Optimization techniques for parallel biophysical simulations generated by *insilico*IDE. *IPSI Online Transactions* **2** (2009) 149–161
9. Hodgkin, A.L., Huxley, A.F.: A quantitative description of membrane current and its application to conduction and excitation in nerve. *The Journal of physiology* **117**(4) (1952) 500–544
10. Hucka, M., et al.: The systems biology markup language (SBML): a medium for representation and exchange of biochemical network models. *Bioinformatics* **19**(4) (2003) 524–31
11. Contreras-Vidal, J.L., Stelmach, G.E.: A neural model of basal ganglia-thalamocortical relations in normal and parkinsonian movement. *Biol Cybern* **73**(5) (10 1995) 467–76
12. Nakano, T., Doi, T., Yoshimoto, J., Doya, K.: A kinetic model of dopamine- and calcium-dependent striatal synaptic plasticity. *PLoS Comput Biol* **6**(2) (2 2010) e1000670
13. <http://www.ebi.ac.uk/biomodels/>
14. Li, Y.X., Bertram, R., Rinzel, J.: Modeling N-methyl-D-aspartate-induced bursting in dopamine neurons. *Neuroscience* **71**(2) (3 1996) 397–410

Part III
Mathematical and Statistical Aspects
of Neurodynamics

Robust Computation in Two Dimensional Neural Field

Yuzuru Sato and Shun-ichi Amari

Abstract In this paper, we discuss robust computation represented by collective motion of large neural dynamics. There exist stable traveling bumps and their collisions in a two dimensional neural field. By using the stable traveling bumps and their collisions, arbitrary logical operations can be constructed. The resulting computation processes in the neural field is structurally and orbitally stable and the basin measure of the dynamics of the computations is finitely positive. Thus, the computations are robust and constructive in the framework of dynamical systems theory.

1 Introduction

In which way, can information processing be embedded in spatio-temporal pattern dynamics? This problem has been broadly investigated in theoretical neuroscience based on contemporary notions of information processing.

Computational ability of network of neurons was first studied by McCulloch and Pitts [1] to show computational universality [2] directly constructing Boolean circuits by using binary neurons. Other developments of computation in network of neurons are found in studies on particle computation in cellular automata [3, 4], representing computational process as collective motion. With two-dimensional cellular automata (as a special case of binary neuron networks), universal computation

Y. Sato (✉)

RIES/Department of Mathematics, Hokkaido University, Kita 12 Nishi 6, Kita-ku, Sapporo, Hokkaido 060-0812, Japan

Laboratory for Mathematical Neuroscience, RIKEN Brain Science Institute, 2-1, Hirosawa, Saitama 351-0198, Japan

e-mail: ysato@math.sci.hokudai.ac.jp

S. Amari

Laboratory for Mathematical Neuroscience, RIKEN Brain Science Institute, 2-1, Hirosawa, Saitama 351-0198, Japan

is achieved as a new level of behavior that is different from the lower level of explicit spatial configurations. Universal computation is also achieved with carefully constructed finite dimensional dynamical systems. For example, three-dimensional flow which is topologically equivalent to universal Turing machine, can be implemented in a billiard system with finitely complex boundary [5]. Real number computation has been also studied in terms of computation in dynamical systems [6, 7] and the limit of analog computation has been discussed. However, these computations based on intrinsic symbolic dynamics are not robust but highly fragile.

Here we study robust computation represented by collective motion in large neural dynamics. There exist stable traveling bumps and their collisions in a two-dimensional two-component neural field [8, 9]. By using the stable traveling bumps and their collisions, arbitrary logical operations can be constructed. Unlike logical circuits in McCulloch-Pitts binary neurons, particle computation in cellular automata, and symbolic dynamics in flow, the computational process in the neural field is structurally and orbitally stable, and the basin measure of orbits of arbitrary computation is positive. Thus, the computations in the neural field are robust attracting sets. The initial conditions and boundary conditions are fully constructive in the framework of dynamical systems theory. In the following, we explain a two dimensional neural field model, show properties of stable traveling bumps and their collisions, and discuss robust computation in the neural field.

2 Two Dimensional Neural Field

A neural field model is a continuous version of neural network describing the spatio-temporal patterns of populational neuronal firing activities [8]. Let $\mathbf{x} = (x, y)$ be the coordinates of a two dimensional field, and $u(\mathbf{x}, t)$ and $v(\mathbf{x}, t)$ be excitatory and inhibitory variables at position \mathbf{x} . The activation-inhibition mechanism is described as,

$$\frac{\partial u(\mathbf{x}, t)}{\partial t} = L_{uu} [u(\mathbf{x}, t)] + L_{uv} [v(\mathbf{x}, t)] \quad (1)$$

$$\frac{\partial v(\mathbf{x}, t)}{\partial t} = L_{vu} [u(\mathbf{x}, t)] + L_{vv} [v(\mathbf{x}, t)] \quad (2)$$

where L_{uu} , L_{uv} , L_{vu} and L_{vv} are operators representing interactions of the field variables. The reaction-diffusion equation uses the linear Laplacian diffusion for L_{uu} together with pointwise interactions for L_{uv} [10], whereas the equation of a neural field uses non-local interactions for L_{uu} due to the synaptic connections of neurons, represented by a spatial convolution of the type

$$L_{uu} [u(\mathbf{x}, t)] = \int w(\mathbf{x} - \mathbf{x}') f [u(\mathbf{x}', t)] d\mathbf{x}', \quad (3)$$

where f is a nonlinear function. The typical equations for a 2D neural field are as follows:

$$\begin{aligned} \frac{\partial u(\mathbf{x}, t)}{\partial t} &= \int w_1(\mathbf{x} - \mathbf{x}') f_1[u(\mathbf{x}', t) - h_1] d\mathbf{x}' \\ &\quad - \int w_2(\mathbf{x} - \mathbf{x}') f_2[v(\mathbf{x}', t) - h_2] d\mathbf{x}' \\ &\quad - u(\mathbf{x}, t), \end{aligned} \quad (4)$$

$$\begin{aligned} \frac{\partial v(\mathbf{x}, t)}{\partial t} &= \int w_3(\mathbf{x} - \mathbf{x}') f_3[u(\mathbf{x}', t) - h_3] d\mathbf{x}' \\ &\quad - \int w_4(\mathbf{x} - \mathbf{x}') f_4[v(\mathbf{x}', t) - h_4] d\mathbf{x}' \\ &\quad - v(\mathbf{x}, t). \end{aligned} \quad (5)$$

Here, $u(\mathbf{x}, t)$ and $v(\mathbf{x}, t)$ are the mean potentials of excitatory and inhibitory neurons, respectively, at position \mathbf{x} and time t . The convolutive functions $w_1(\mathbf{x} - \mathbf{x}')$, \dots , $w_4(\mathbf{x} - \mathbf{x}')$ represent the synaptic efficacies from position \mathbf{x}' to \mathbf{x} . The functions f_1, \dots, f_4 denote the activation functions of neurons. They are activated by $u(\mathbf{x}, t)$ and in turn inhibited by $v(\mathbf{x}, t)$. The activation functions are sigmoidal functions or Heaviside functions satisfying $0 \leq f_i(u) \leq 1$, ($i = 1, 2, 3, 4$), and the synaptic efficacy functions $w_i(\mathbf{x}) \geq 0$ are radial symmetric, that is, $w_i(\mathbf{x})$ are functions of $\|\mathbf{x}\|$, for $i = 1, 2, 3, 4$. Hence, the two dimensional neural field is homogeneous and rotationally invariant.

The neural field model can be regarded as a special case of the field equation with excitation and inhibition mechanisms, similar to the standard reaction-diffusion equation. While the reaction-diffusion equation is restricted within local interactions due to diffusion term, the neural field model has a spatially wide range of interactions, i.e., non-local interactions, that exhibit richer dynamical phenomena. In the two dimensional two-component reaction-diffusion equation, the existence of spatially localized traveling objects has not been reported with local operators [11]. It is known that global operators added to two-component systems may induce a single stable traveling bump, but may not induce multiple solutions [12]. On the other hand, many three component systems with local operators show multiple travelling bumps.

An example of multiple stable traveling bumps in a two dimensional neural field model, which is a two-component system with non-local operators, is recently presented [9]. In this case, the spatial convolution term plays the role of the third component to stabilize the bump, which supports existence of multiple bumps.

3 Stable Traveling Bumps and Their Collisions

We use the following simple equations comprising a two-dimensional extension of the model given by Pinto and Ermentrout [13]

$$\frac{\partial u(\mathbf{x}, t)}{\partial t} = -u(\mathbf{x}, t) - v(\mathbf{x}, t) + \int w(\mathbf{x} - \mathbf{x}') f[u(\mathbf{x}', t) - h] d\mathbf{x}' \tag{6}$$

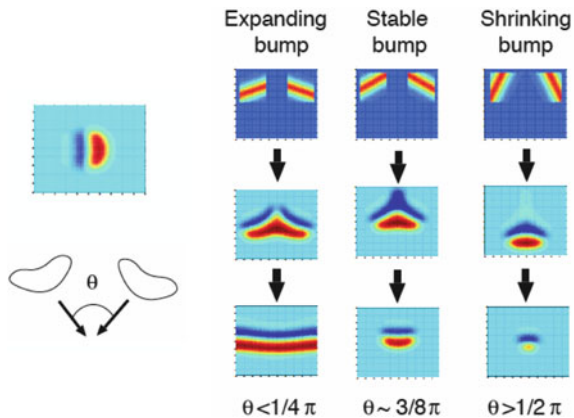
$$\frac{\partial v(\mathbf{x}, t)}{\partial t} = \alpha u(\mathbf{x}, t) - \beta v(\mathbf{x}, t), \tag{7}$$

where $\alpha = 0.6$, $\beta = 0.8/3$, $h = 3.0$, and

$$w(x, y) = 7.32e^{-\frac{x^2+y^2}{2}}, f[u] = \frac{1}{1 + e^{-2(u-4)}}. \tag{8}$$

Numerical experiments suggest that the field can be tristable, admitting the quiescent state, a stable traveling bump with a characteristic length (Fig. 1), and a traveling band solution growing to infinite length [9]. A number of traveling bumps may coexist in a field, and they strongly interact when they are close. When two bumps collide, they fuse into a single bump. The resulting bump converges to one of the tristable states depending on the collision angle (Fig. 1). The threshold angle is around $\frac{3}{8}\pi$. We use external inputs to control directions of motion of traveling bumps to adjust the collision angle. There are no standing objects other than the traveling bumps in the parameter settings because of the lack of diffusion terms, so that even with complex collisions, the resulting output is thought to be only one of the following: (1) quiescent state, (2) stable traveling bump, or (3) growing band solution, implying that the field is very “clean” without complex after effects. As

Fig. 1 Stable traveling bumps and their collisions in two dimensional neural field. The resulting bump converges to one of the tristable states (1) quiescent state, (2) stable traveling bump, or (3) growing band solution, depending on the collision angle. The threshold angle is around $\frac{3}{8}\pi$



for complex transitory collision phenomena, see [14] for the various collision and scattering phenomena of traveling spots in the reaction-diffusion equation with three components.

4 Robust Computation in Neural Field

The stability of localized traveling bumps does not require any geometric restriction or boundary to prevent them from propagating away. As an application of these findings to theoretical studies of neural information processing, we construct logical operations by using stable traveling bumps, their collisions, bump generators, and bump eliminators with local boundary conditions (Fig. 2).

Computational ability of networks of binary neurons was first studied by McCulloch and Pitts [1]. They constructed logical operations taking **dynamics of a single binary neuron** as an elementary mechanism and an **individual spike** as information carrier. Based on automata theory, computational universality of binary neuron networks was shown. Studies on reliable computation in probabilistic automata [15] were one of the extensions.

The theory was developed to “stochastic neural networks” to treat macroscopic statistics and dynamics, known as theory of neural networks. In Amari-Hopfield networks [17, 18], **stochastic functions formed by stochastic neurons** represent elementary mechanics and **distribution of spikes** does information carrier. Statistical inference plays a key role in this theory represented by the fact that a multilayer perceptron consists of sigmoidal neurons is a universal function approximator [16].

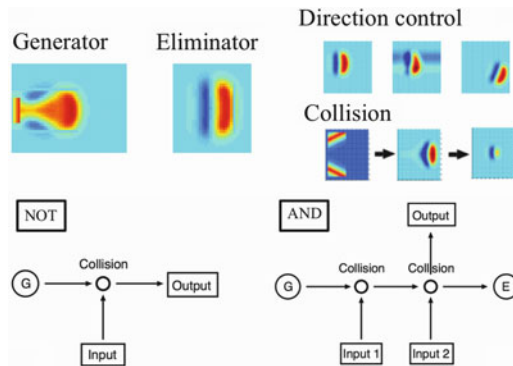


Fig. 2 Logical operation in two dimensional neural field: In the diagram below, (G) denotes the bump generator and (E) does the bump eliminator. The circle represents collisions of traveling bumps. The bump generator is constructed with periodically activated region and two fixed quiescent region adjusting the characteristic length of bumps. The bump eliminator is simply a fixed quiescent region whose size is about the characteristic length. Direction control is done by external pulse inputs. Controlled multiple bump collisions can work as logical NOT and AND operation with local boundary conditions

Statistical and information theoretic problems were unified into this theory to solve thousands of important problems in theoretical neuroscience such as memory capacity, classification, optimization, and statistical learning. Amari investigated statistical learning in neural networks introducing information geometry [19].

There are other developments of studies on logic and computation in spatiotemporal dynamics. Early studies are found in Conway's game of life [3] and particle computation in cellular automata [4]. In these systems, computational process is represented by collective motion. We can construct logical operations taking **dynamics of a large number of binary neurons** as elementary mechanism and **pattern dynamics of spikes** as information carrier. In life game computer, by taking two-dimensional cellular automata, universal computation is achieved as a new level of behavior that is different from the lower level of spatial configurations.

Based on stable traveling bumps and their collisions, we can construct logical operations taking **dynamics of a large number of stochastic neurons** as elementary mechanism and **pattern dynamics of distribution of spikes** as information carrier. Combining elementary logical operations, arbitrary logical operation can be executed in two dimensional neural field at the collective level (See also computation by waves in reaction diffusion dynamics with boundary conditions [20]). Unlike McCulloch-Pitts binary neurons, cellular automata, and symbolic dynamics in flow, the computational process in the neural field is structurally and orbitally stable, and the basin measure of orbits of arbitrary computation is positive. Thus, the computations in the neural field are robust attracting sets. The initial conditions and boundary conditions are fully constructive in the framework of dynamical systems theory. Spatial continuity, non-local interaction, and logical operation construction at the collective level support this result.

5 Discussion

We discussed robust computation with stable traveling bumps and their collisions in a two dimensional neural field. Logical operations can be constructed by using collisions of multiple traveling bumps with local boundary conditions. The presented results would be the simplest starting point to study neural information processing as spatial pattern dynamics in neural field.

Multiple bumps in neural field can be a model for working memory [21]. In this point of view, we may consider problems of memory formation, such as collisions of working memory, resulting propagation phenomena, and creation of new working memory as after effects. These spatial memory formation would imply short-term learning in neural field. Pattern dynamics in heterogeneous media [14] may be related to the multiple structured model for real neural systems corresponding to the boundary conditions for the robust computation. Rigorous mathematical analysis of traveling bumps, their collisions, and their controls will have to be conducted to explore these problems.

Acknowledgements Authors thank to Dr. H. Ando (Brain Science Institute, RIKEN), Dr. T. Teramoto (Chitose Institute of Science and Technology) and Prof. Y. Nishiura (Hokkaido University) for fruitful discussions. This work is supported by the visiting researchership at Laboratory for Mathematical Neuroscience at RIKEN Brain Science Institute.

References

1. McCulloch, W. S., Pitts, W.: *Bulletin of Mathematical Biophysics* **5** (1943) 115–133.
2. Turing, A.M.: *Proceedings of the London Mathematical Society* **2:42** (1936) 230–265.
3. Gardner, M.: *Mathematical games. Scientific American* **223** (1970) 120–123; Gardner, M.: *Mathematical games. Scientific American* **224** (1971) 112–117.
4. Crutchfield, J. P, Mitchell, M.: *PNAS*, **92** (1995) 10742–10746.
5. Moore, C.: *Phys. Rev. Lett.* **64** (1990) 2354–2357.
6. Siegelmann, H. T., Sontag, E.D.: *Theoretical Computer Science* **131: 2** (1994) 331–360.
7. Sato, Y., *Limit of analog computation.* (2011) in preparation.
8. Wilson, H. R., Cowan, J. D.: *Kybernetik* **13** (1973) 55–80; Amari, S.: *Biol. Cybern.* **27** (1977) 77–87.
9. Lu, Y., Sato, Y., Amari, S.: *Neural Computation*, **23:5** (2011) 1248–1260.
10. Turing, A. M.: *Philosophical Transactions of the Royal Society of London* **B 237** (1952) 37–72.
11. Vanag, V. K., Epstein, I. R.: *Chaos* **17** (2007) 037110.
12. Schenk, C. P., Or-Guil, M., Bode, M., Purwins, H. G.: *Phys. Rev. Lett.* **78** (1997) 3781–3784.
13. Pinto, D. J., Ermentrout, G. B.: *SIAM J. Appl. Math.* **62** (2001) 206–225.
14. Nishiura, Y., Teramoto, T., Ueda, K.: *Chaos* **15** (2005) 047509; Nishiura, Y., Teramoto, T., Ueda, K.: *Chaos*, **15** (2007) 037104; Teramoto, T. Suzuki, K., Nishiura, Y.: *Phys. Rev. E* **80** (2009) 046208.
15. von Neumann, J.: *Automata Studies*, Princeton University Press, (1956) 43–98.
16. Cybenko, G., *Mathematics of Control, Signals, and Systems*, **2:4** (1989) 303–314.
17. Amari, S.: (1971). *IEEE Proc.*, **59:1** (1971) 35–47; Amari, S.: *IEEE Trans. Computers* **C-21** (1972) 1197–1206.
18. Hopfield, J.J.: *PNAS* **79:8** (1982) 2554–2558.
19. Amari, S.: *Differential-geometrical methods in statistics. Lecture notes in statistics*, Springer-Verlag, Berlin, (1985).
20. Motoike, I. N., Yoshikawa, K.: *Chaos, Solitons & Fractals* **17** (2003) 455–461.
21. Laing, C. R., Troy, W. C., Gutkin, B., Ermentrout G. B.: *SIAM J. Appl. Math.* **63** (2002) 62–97.

Dynamical Synapses Enhance Mobility, Memory and Decoding

C.C. Alan Fung, K.Y. Michael Wong, and Si Wu

Abstract Depending on their activities, synapses in neural systems are dynamical in relatively short time scales. This effect is known as short-term plasticity (STP), which appears as short-term facilitation (STF) or short-term depression (STD). In this paper, we describe the effects of STD and STF on the intrinsic phases and plateau states. Consequently, we find that STD enhances the tracking performance in continuous attractor neural networks, and provides a mechanism for an iconic memory to shut off naturally. On the other hand, STF improves the precision in population decoding.

1 Introduction

The short-term plasticity (STP) of dynamical synapses appears in two forms: short-term facilitation (STF) and short-term depression (STD). STF is due to the accumulation of calcium ions caused by the pre-synaptic spikes. This effect enhances the release probability of neurotransmitters, and hence the connection efficacy. STD is due to the fact that the recovery time of neurotransmitters is much slower than the synaptic time scale [1].

In this paper, we will briefly describe the effects of STD and STF on the intrinsic dynamics and plateau states of neural systems, and consequently their

C.C. Alan Fung • K.Y.M. Wong (✉)
Hong Kong University of Science and Technology, Hong Kong, China
e-mail: alanfung@ust.hk; phkywong@ust.hk

S. Wu (✉)
Institute of Neuroscience, Chinese Academy of Sciences, Shanghai, China
State Key Laboratory of Cognitive Neuroscience and Learning, Beijing Normal University, Beijing, China
e-mail: wusi@bnu.edu.cn

impact on the performance of neural computation. We will use continuous attractor neural networks (CANNs) as our working model, but the results are applicable to general cases. CANNs are recurrent networks that can hold a continuous family of localized states. These states are localized in position, with neuronal activities decreasing from a maximum at the center to a background level with increasing distance from the center, and is hence usually known as *bumps* [3]. When an external stimulus changes position, the bump shifts its position accordingly among the continuous attractors. This process is called tracking, and hence can model how the brain processes continuous stimuli, such as orientations, head directions and spatial locations. As we shall see, dynamical synapses can enhance the tracking performance of CANNs, provide a mechanism for an iconic memory to shut off naturally, and improve the precision in population decoding.

2 Model

The state of a neuron is specified by the population-averaged neuronal current, $u(x, t)$, as well as the neuronal firing rate $r(x, t)$, where x is the *preferred stimulus* ranging from $(-\infty, \infty)$. $r(x, t)$ and $u(x, t)$ are related by $r(x, t) = u(x, t)^2 / [1 + k\rho \int dx'' u(x'', t)^2]$, in which k is the parameter controlling the global inhibition, and ρ is the density of neurons in the space of the preferred stimulus [2]. In simulations, there are N neurons with preferred stimulus ranging within $(-L/2, L/2)$. So, $\rho = N/L$ in simulations. The excitatory connection weight between different neurons are given by $J(x, x') \equiv (J_0 / \sqrt{2\pi a^2}) \exp[-(x - x')^2 / (2a^2)]$, where J_0 controls the strength of excitatory connection, and a represents the width of the tuning curves. For $a \ll L$, the results of simulations should be effectively the same as those with $L = \infty$.

The neuronal current is governed by Tsodyks et al. [3] and Fung [4]

$$\begin{aligned} \tau_s \frac{\partial u}{\partial t} = & I^{\text{ext}}(x, t) - u(x, t) \\ & + \rho \int dx' J(x, x') [1 + f(x', t)] p(x', t) r(x', t), \end{aligned} \quad (1)$$

where I^{ext} is the external stimulus, and τ_s is the synaptic time constant of the order 1 ms. The effects of dynamical synapses are introduced by including $f(x, t)$ for STF and $p(x, t)$ for STD in the last term of Eq. (1). They are governed by

$$\frac{\partial f}{\partial t} = -\frac{f(x, t)}{\tau_f} + \alpha (f_{\text{max}} - f(x, t)) r(x, t), \quad (2)$$

$$\frac{\partial p}{\partial t} = \frac{1 - p(x, t)}{\tau_d} - \beta [1 + f(x, t)] p(x, t) r(x, t), \quad (3)$$

where α and β are the parameters controlling STF and STD respectively. τ_f and τ_d are time scales for STF and STD, respectively. They are of the order 100 ms. In this paper, we study STD and STF separately, focusing on their individual effects.

3 CANNs with STD

3.1 Intrinsic Dynamics

In this section, three key intrinsic phases are introduced in the (k, β) space when there are no external stimuli. They are the *static* phase, *metastatic* phase and *moving* phase.

For the case without STD and STF, if k is below a critical value k_c , the steady state solution for Eq. (1) is a bump with a Gaussian profile, whose width is $\sqrt{2}a$ and whose center of mass is \hat{z} [2]. The value of \hat{z} can take a continuous range, characteristic of continuous attractor neural networks. One may expect that, when β is small enough, the shape of the steady state of $u(x, t)$ is *effectively Gaussian*. Also, the steady state of $p(x, t)$ has a background level of 1 depressed by a bump-shaped profile. Their profiles are shown in Fig. 1a. Based on this observation, we propose search for Gaussian-shaped solutions of Eqs. (1) and (3). We can then figure out the regions including *metastatic* and *static* phases (dashed line in Fig. 2) over the parameter space of (k, β) .

In the static phase, the height of the bump is stable and the velocity of the bump is zero. In the metastatic phase, the height of the bump remains stable, but the position of the center of mass is metastable, and is hence described as metastatic. This means that when the static bump is given a small displacement, the bump will continue to

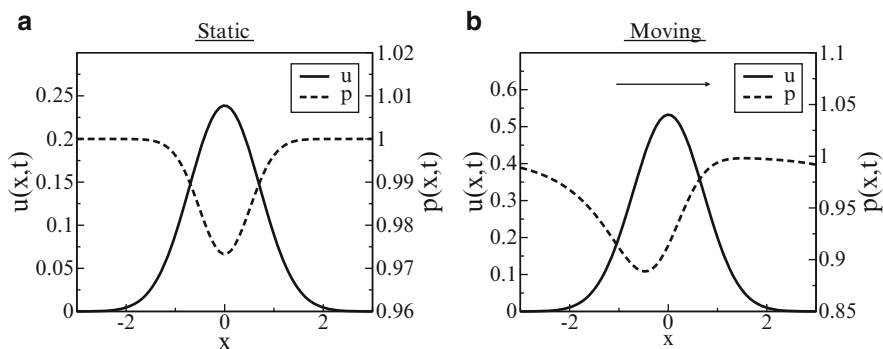
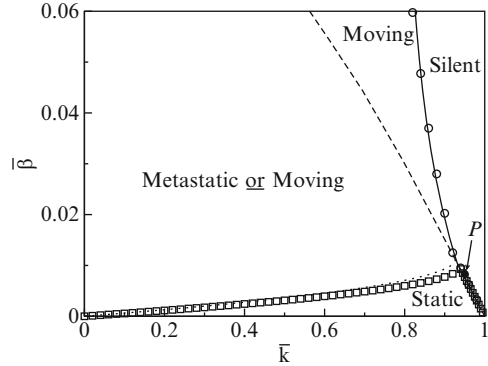


Fig. 1 Profiles of synaptic input current, $u(x, t)$, and synaptic depression, $p(x, t)$ for (a) static bumps and (b) moving bumps

Fig. 2 Phase diagram for STD. *Symbols*: simulations. *Curves*: theory. $\bar{\beta} \equiv \tau_d \beta / (\rho^2 J_0^2)$ and $\bar{k} \equiv k / k_c$ are rescaled β and k respectively



move spontaneously. The condition for this happen can be studied by introducing a small asymmetric distortion to the solution of Eqs. (1) and (3). By considering whether the variations diverge or converge, we can obtain the boundary between metastatic and static phases respectively, separated by the phase boundary indicated by the dotted line in Fig. 2.

The existence of spontaneously moving bumps in the network can be attributed to the presence of STD. This is because neurons tend to be less active in the locations of low values of $p(x, t)$, causing the bump to move away from locations of strong synaptic depression. For the moving bumps, the profile of $p(x, t)$ is no longer symmetric about the center of mass of $u(x, t)$, as shown in Fig. 1b. Therefore, the assumption of a Gaussian-shaped depression is not appropriate for the case of moving bumps. To solve this problem, higher order distortions are included in the term $1 - p(x, t)$. We note that a Gaussian distortion is the lowest order member of a family of distortions, commonly used to describe wave functions of the quantum harmonic oscillator. Successively higher order functions of this family can describe distortions in the position, width, and skewness etc. of the bump. Mathematically, this family of functions is complete, meaning that any arbitrary distortion can be expressed as a combination of these functions. This enables us to predict the boundary of the moving phase (solid line in Fig. 2). Beyond the boundary, only the silent phase with $u(x, t) = 0$ exists.

In the moving phase, the static bump cannot exist, and there are only moving bumps.

The metastatic nature of the bumps enhances the tracking performance of CANNs. When the network is tracking an external stimulus that changes position rapidly, metastability speeds up the movement of the bump, as shown in Fig. 3. Interestingly, when the synaptic depression is very strong, the network state can even overtake the moving stimulus, reminiscent of the phase precessing behavior of place cells in the hippocampus [5].

Fig. 3 The bump position when the stimulus position abruptly changes from $z_0/a = 0$ to $z_0/a = 3.0$ at $t = 0$. Symbols: numerical solutions. Lines: theory

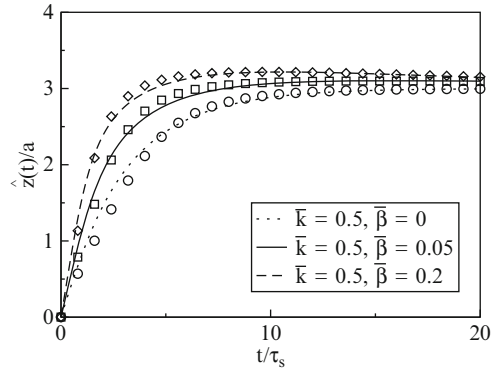
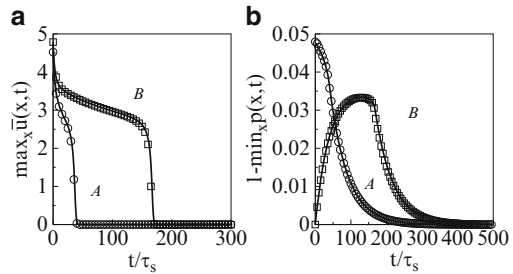


Fig. 4 Examples of plateau states. Symbols: simulations. Lines: theory. Parameters: $(\bar{k}, \bar{\beta}) = (0.95, 0.0085)$, i.e. point P in Fig. 2. $\bar{u} = \rho J_0 u(x, t)$ is the rescaled variable of $u(x, t)$



3.2 Plateau State

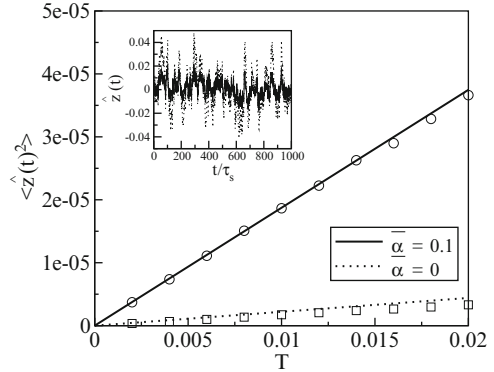
The plateau state provides a possible mechanism for the iconic memory. The presence of STD provides an extra parameter region in which the bump states are marginally unstable in amplitude, such as point P in Fig. 2.

Figure 4 shows two examples of plateau states, A and B , corresponding to different kinds of initial conditions. A corresponds to the initial condition that the network is under the influence of a stimulus for a long enough time, while B is for the case the presence of stimulus is just long enough to excite function $u(x, t)$.

Consider the initial state B . In the marginally unstable regime, the static bump solution just loses its stability. The bump is stable if the synaptic depression is fixed at a low level, but unstable at high level. Since the synaptic time scale is much shorter than that of STD, a bump can build up before the synaptic depression becomes effective. This maintains the bump in the plateau state with a slowly decaying amplitude as shown in Fig. 4a. After a time duration of the order τ_d , the STD reaches a threshold, as shown in Fig. 4b, and the bump state eventually decays to the silent state.

The plateau state for initial condition A does not last as long as that of B . However, since the system is marginally unstable, there are states at which the dynamics is very slow. When the system dynamics passes through these states, the relaxation of the bump is slowed down.

Fig. 5 Comparison of influences by the noisy stimuli of systems with and without STF. Parameters: $N = 80$, $a = 0.5$, $x \in [-\pi, \pi)$, $k/k_c = 0.25$, $\rho J_0 A = 1.596$ and $T = 0.02$



4 CANNs with STF

Compared with STD, STF has a qualitatively opposite effect on CANNs with dynamical synapses. STF provides an extra translational stability to a bump. To check this, we consider a noisy stimulus, $I^{\text{ext}}(x, t)$, which is a Gaussian function of width $\sqrt{2}a$, height A and centered at position $\eta(t)$, $\eta(t)$ being a white noise satisfying $\langle \eta(t)\eta(t') \rangle = 2Ta^2\tau_s\delta(t - t')$. In the inset of Fig. 5, the decoding results of CANNs with and without STF are shown. With STF, the CANNs can filter out the fluctuational effects due to the noises considerably. We calculate the influence of the noise on the decoding result is shown in Fig. 5. This figure shows that the presence of STF can improve the decoding efficiency when noises are present.

5 Discussion

In the absence of the stimulus, the CANN with STD favors different phases with different system parameters, (k, β) . For $k < k_c$ and small β , the static bump is stable. If one increases the strength of STD, β , the system will become translationally unstable. York et al. found similar behaviors in a system with uniform input current [6], while we found that this instability can improve the network reaction to changes of stimuli.

The plateau state is due to the marginal instability of the bump state. It can make the bump state last for a longer period such that the signal may have more time to propagate to neurons of subsequent layers. Hence we predict that STD should be important in early information pathways of the brain. For systems without dynamical synapses, this behavior is not easily seen. However, the presence of STD provides an extra parameter region so that the plateau state can be seen more easily. Indeed, how to shut off the activity of a CANN has been a challenging issue that received wide attention in theoretical neuroscience. Here, we show that STD may

provide an important mechanism that supports the signal for a relatively long time and allows the neuronal activity to turn off naturally.

STF has an effect qualitatively opposite to STD. Unlike STD, STF provides translational stability such that it can improve the decoding performance. With this property, CANNs with STF can be used as a noise filter processing noisy stimuli. Based on the different advantages of STD and STF, we predict that each of them should be dominant in different areas of the brain. STD should be dominant in areas where time-varying stimuli are processed, whereas STF should prevail in areas where accurate decoding of stimuli is required.

Acknowledgments This work is partially supported by the Research Grant Council of Hong Kong (grant numbers 604008 and 605010).

References

1. H. Markram, Y. Wang and M. Tsodyks, Differential signaling via the same axon from neocortical layer 5 pyramidal neurons. *Proc. Natl. Acad. Sci. U.S.A.*, **95** (1999) 5323–5328.
2. C. C. A. Fung, K. Y. M. Wong and S. Wu, A Moving Bump in a Continuous Manifold: A Comprehensive Study of the Tracking Dynamics of Continuous Attractor Neural Networks. *Neural Comput.* **22** (2010) 752–792.
3. M. V. Tsodyks, K. Pawelzik and H. Markram, Neural networks with dynamic synapses. *Neural Comput.* **10** (1998) 821–835.
4. C. C. A. Fung, K. Y. M. Wong, H. Wang and S. Wu, Attractor Dynamics with Synaptic Depression. *Advances in Neural Information Processing Systems*. **23** (2010) 640–648.
5. J. O’Keefe J and M. L. Recce, Phase relationship between hippocampal place units and the EEG theta rhythm. *Hippocampus* **3** (1993) 317–330.
6. L. C. York and M. C. W. van Rossum, Recurrent networks with short term synaptic depression. *J. Comput. Neurosci.* **27** (2009) 607–620.

Input Dependent Variability in a Model of the Striatal Medium Spiny Neuron Network

Adam Ponzi and Jeff Wickens

Abstract In previous work we have shown how a biologically faithful medium spiny neuron (MSN) network model of the striatum generates highly irregular firing and coherent population dynamics on slow timescales. Here we investigate how the firing irregularity depends on cortical activity. We find that irregularity is suppressed for many hundreds of msec after cortical stimulus onset in good agreement with several neural observations. We also find that most cells spike count time series display non-normal diffusion and fractal characteristics.

1 Introduction

In recent modeling work on the striatal MSN network [1, 2] we have shown that coherent cell assembly population dynamics on slow behaviourally relevant timescales can be generated by the MSN network providing the network has the sparse random striatally relevant connectivity of around 10% and cortical excitation is weak so that the cells are just above firing threshold. We demonstrated that at these connectivities even when simulations were completely deterministic individual cells displayed highly irregular firing, broadly distributed firing rates consistent with a power-law and that the network generated complex identity-temporal dynamics. Here we investigate how this MSN network generated variability interacts with cortical stimulation. We show that switches in cortical stimulation lead to a temporary suppression of noise in the network. It has been observed that, in many brain areas, stimuli cause significant suppression of neuronal variability [3–7]. Our results are in agreement with this.

A. Ponzi (✉) • J. Wickens
Okinawa Institute of Science and Technology (OIST), Onna-son, Okinawa, Japan
e-mail: adamp@oist.jp

2 Methods

The network is composed of model MSNs with parameters set so they are in the vicinity of a bifurcation from a stable fixed point to spiking limit cycle dynamical behaviour [1]. This models the dynamics in the UP state when the cells are all receiving excitatory drive to firing threshold levels of depolarization. To describe the cells we use the $I_{Na,p} + I_k$ model described in [8] which is two-dimensional and given by,

$$\begin{aligned} C \frac{dV_i}{dt} &= I_i(t) - g_L(V_i - E_L) \\ &\quad - g_{Na} m_\infty(V_i)(V_i - E_{Na}) \\ &\quad - g_k n_i(V_i - E_k) \\ \frac{dn_i}{dt} &= (n_\infty - n_i)/\tau_n \end{aligned} \quad (1)$$

having leak current I_L , persistent Na^+ current $I_{Na,p}$ with instantaneous activation kinetic and a relatively slower persistent K^+ current I_K . $V_i(t)$ is the membrane potential of the i -th cell, C the membrane capacitance, $E_{L,Na,k}$ are the channel reversal potentials and $g_{L,Na,k}$ are the maximal conductances. $n_i(t)$ is K^+ channel activation variable of the i -th cell. The steady state activation curves m_∞ and n_∞ are both described by, $x_\infty(V) = 1/(1 + \exp\{(V_\infty^x - V)/k_\infty^x\})$ where x denotes m or n and V_∞^x and k_∞^x are fixed parameters. τ_n is the fixed timescale of the K^+ activation variable. The term $I_i(t)$ is the input current to the i -th cell.

The parameters are chosen so that the cell is in the vicinity of a *saddle-node on invariant circle* (SNIC) bifurcation which is appropriate bifurcation to use for a model of an MSN in the UP state, because its dynamics are in good qualitative agreement with studies of MSN firing [1, 9–11].

The input current $I_i(t) = I_i^C(t) + I_i^M(t)$ in Eq. 1 is composed of two parts. One component $I_i^M(t)$ comes from the MSN inhibitory network and the other component $I_i^C(t)$ represents the current from excitatory sources, the cortex and the thalamus. We describe the excitatory component first.

We model the excitatory part as a stochastic process. In general the excitatory component will be given by Rall type synapses [12] $I_i^C(t) = (V_C - V_i(t))X_i(t)$ where $X_i(t) = \sum_l k_{il}^C a_{il}(t)$. V_C is the excitatory reversal potential, set here to the realistic value 0.0 mV. The MSN cells are considered to be contacted by many excitatory inputs l which are non-overlapping between the MSN cells i . k_{il}^C are fixed channel parameters from the l -th excitatory cortical or thalamic input to the i -th MSN cell, described below. The $a_{il}(t)$ are the quantities of postsynaptically bound neurotransmitter from the l -th excitatory input to the i -th MSN cell. They are given by $\tau_a \frac{da_{il}}{dt} = \sum_m \delta(t - t_{ilm}) - a_{il}$ where the dirac delta function $\delta()$ part represents a series of spikes from the l -th input to the i -th cell at times t_{ilm} and τ_a is a time scale which we set to the realistic value of 10 msec.

If we assume the spikes follow independent Poisson process with rates $r_{il}(t)$ then the contribution provided by many such processes is approximately Gaussian and we can replace the spike series by a term given by the mean rate plus a fluctuation proportional to the standard deviation, $r_{il}(t)dt + \epsilon_{il}(t)\sqrt{r_{il}(t)}d\tau$ where $\epsilon_{il}(t)$ is a standard normally distributed random variable (mean zero, std unity) [13]. Assuming that spikes are independent across i and l , the term $\sum_l \epsilon_{il}(t)k_{il}^C\sqrt{r_{il}(t)}d\tau$ which arises can also be replaced by its expectation and fluctuation $0 + \epsilon_i(t)\sqrt{dt\sum_l(k_{il}^C)^2r_{il}(t)}$ where $\epsilon_i(t)$ is standard normal noise term independent in i and t and we have used $\langle\epsilon_{il}(t)\rangle = 0$ and $\langle\epsilon_{il}(t)\epsilon_{ik}(t)\rangle = 0$, ($l \neq k$) and $\langle\epsilon_{il}(t)\epsilon_{ik}(t)\rangle = 1$, ($l = k$). Therefore we calculate $X_i(t)$ using,

$$\begin{aligned}\tau_a dX_i &= \left(\sum_l^{N_C} k_{il}^C r_{il}(t) - X_i \right) dt \\ &+ \epsilon_i(t) [dt \sum_l^{N_C} (k_{il}^C)^2 r_{il}(t)]^{1/2}.\end{aligned}$$

MSN cells are each contacted by around 10,000 cortical and thalamic cells and we therefore set $N_C = 10,000$. Average cortical firing rates are around 10 Hz and we therefore draw the 10,000 rates $r_{il}(t)$ for each MSN i independently randomly.

The k_{il}^C are also fixed in our simulations reported here, although in reality they may vary with short term facilitation and suppression as well as by *LTP* and *LTD*. We choose the k_{il}^C so that the MSN cells' input current $I_i^C(t)$ is just above the SNIC bifurcation point $I_{bif} = 4.51 \mu\text{A}/\text{cm}^2$ and accordingly draw the k_{il}^C independently uniformly from the interval $[0, 0.002]$. These values of excitatory input current mean that all cells would be firing if the network inhibition were not present. In fact the inhibitory network causes some cells to become quiescent by reducing the total input current to below the bifurcation point.

The inhibitory current part is provided by the GABAergic collaterals of the striatal network and given by $I_i^M(t) = (V_i(t) - V_M) \sum_j -k_{ij}^M g_j(t)$. These synapses are also described by Rall-type synapses [12] contributing to $I_i(t)$ where the current into postsynaptic neuron i is summed over all inhibitory presynaptic neurons j and V_M and k_{ij}^M are channel parameters. $g_j(t)$ is the quantity of postsynaptically bound neurotransmitter given by, $\tau_g \frac{dg_j}{dt} = \Theta(V_j(t) - V_{th}) - g_j$ for the j -th presynaptic cell. Here $V_{th} = -40 \text{ mV}$ is a threshold, and $\Theta(x)$ is the Heaviside function. g_j is a low-pass filter of presynaptic firing. The timescale τ_g should be set relatively large so that the postsynaptic conductance follows the exponentially decaying time average of many preceding presynaptic high frequency spikes. In all simulations here it is set so that postsynaptically bound transmitter exponentially decays to half its value in time $\tau_g \ln(2) \approx 34 \text{ msec}$.

The network structure is described by the parameters $k_{ij}^M = (k^M/p)\epsilon_{ij}Z_{ij}$ where ϵ_{ij} is another uniform quenched random variable on $[0.8, 1.2]$ independent in i and j . $Z_{ij} = 1$ if cells i and j are connected and zero otherwise. In the simulations

reported here we use random networks where cells i and j are connected with probability p , producing binomial degree distributions, and there are no self-connections, $Z_{ii} = 0$. k^M is a parameter which is rescaled by the connection probability p so that when the network connectivity is varied the average total inhibition on each cell is constant independent of p . k^M is set so that IPSPs are around $200 \mu\text{V}$, very similar to real striatal IPSPs, at connectivities of around $p = 0.1$ when the postsynaptic cell is just above firing threshold.

Striatal MSNs are likely to contact (and be contacted by) about 500 other MSNs[14–16]. Furthermore the probability of a connection is estimated to be fairly low, $p = 0.05\text{--}0.3$. To simulate a striatal network which respects these two figures would require, say, a network of around $500/0.2 = 2,500$ cells. However this neglects the fact that not all cells are cortically excited into the UP state and such never firing cells can be left out of network simulations. We suppose that only about 10–30% of MSNs are cortically excited at any time, and perform simulations of 500 UP state MSNs with sparse connectivities. All simulations were carried out with the stochastic weak second order Runge–Kutta integrator described in [17] with integration time step 0.1 msec.

3 Results

Here we investigate how the network responds to a switching input protocol. To this end we construct two fixed cortical input firing rate matrices, $r_{il}^{A,B}$ for two cortical inputs A and B , which do not vary in time. The input rate matrices are alternated every 2,000 msec. The synaptic weights k_{il}^C are fixed for the duration of the simulation the same for both inputs A and B . The fano factor is a standard tool used to understand how neural systems respond to varying stimulation. To make stimulus locked fano factors we first construct the spike count observations N_{mn}^{iT} which are the number of spikes fired by cell i in T msec window centered on $(T/2)n$ msec from the onset of the m th presentation of stimulus A . Stimulus locked fano factors are defined as $F_n^{iT} = \text{Var}\{N_{mn}^{iT}\}/\langle N_{mn}^{iT} \rangle$ where the expectations $\langle \dots \rangle$ are taken over all presentations m . The F_n^{iT} are then averaged over all cells i (which have at least one non-zero spike count among the averaged observations) and denoted F_n^T . The fano factor F_n^T time series versus time $(T/2)n$ msec for a range of T values for a single network simulation are shown in Fig. 1. Two things are evident, firstly the fano factors increase with time window size T and secondly the fano factors decrease suddenly after stimulus onset and then revert slowly.

In fact for a normally diffusive process the mean $\langle N_{mn}^{iT} \rangle$ and variance $\text{Var}\{N_{mn}^{iT}\}$ of the spike counts both increase linearly with time T and therefore the fano factor is independent of time T . However the process generated by the network diffuses faster than normal on average across cells so that while the mean spike count grows linearly with T the variance grows faster than this. The fano factor therefore grows with T . Indeed in Fig. 2 we plot $\log \text{Var}\{N_{mn}^{iT}\}$ where the variance is calculated over all stimulus presentations m and over all time epochs n versus $\log(T)$ for

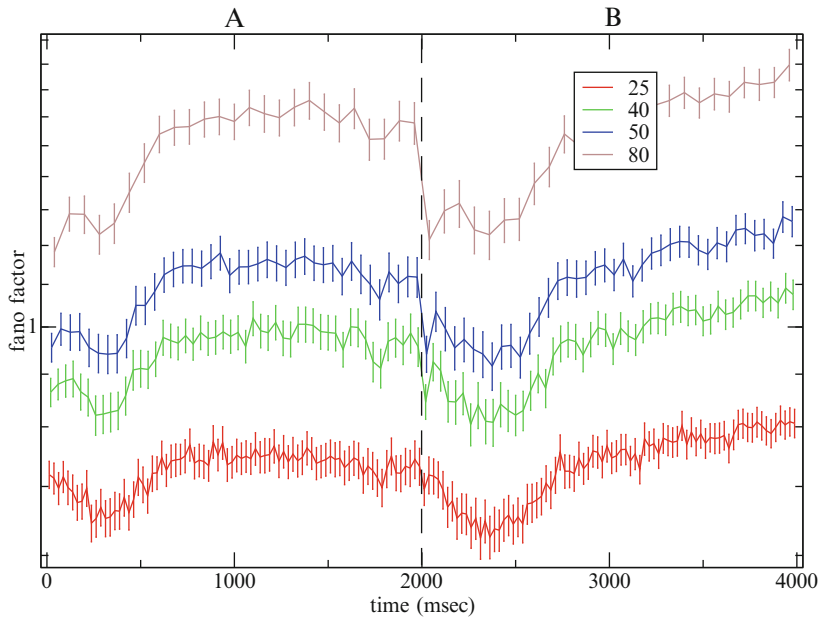


Fig. 1 Mean fano factor across all cells for a single network simulation versus time since stimulus A onset calculated for several different window sizes T , shown in the key. The smaller time windows have lower fano factors. The dashed vertical line shows stimulus B onset

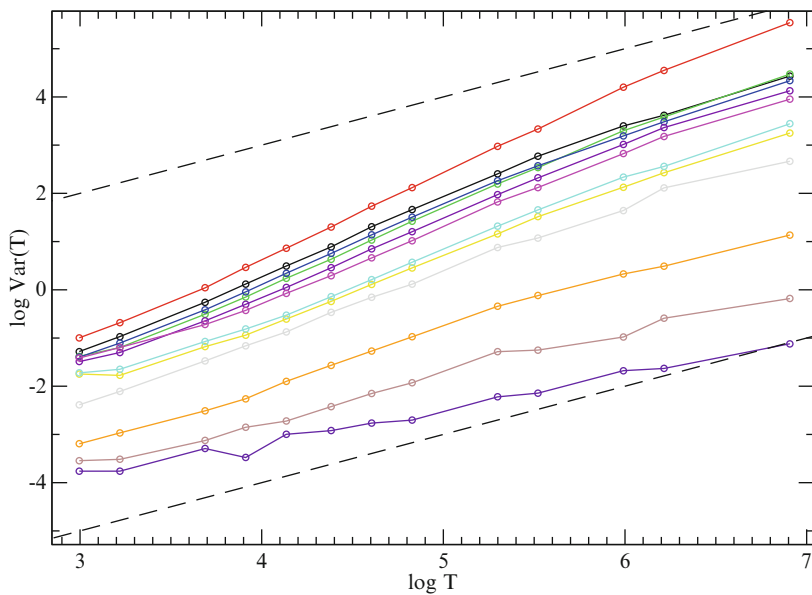


Fig. 2 Diffusion plots in log-log scale of spike count variance versus window size T for several randomly chosen cells from the simulation whose fano factor time series is shown in Fig. 1. Each cell is a different solid line. The dashed lines indicate linear behaviour

several different cells i , for the same simulation as shown in Fig. 1. The dashed lines describe linear behaviour $\text{Var}\{N(T)\} \propto T$. As can be seen for most cells the variance increases faster than linearly $\text{Var}\{N(T)\} \propto \alpha T^\beta$ where $\beta > 1$, for low T before becoming more linear at high T . This indicates that at low $T < 2,000$ msec the behaviour is superdiffusive with positive autocorrelation and a fractal dimension $D = 2 - \beta/2$ before reverting to normal diffusion for sufficiently long T . As can be seen there are also cells which display subdiffusion with $\beta < 1$ for low T . A cell's behaviour is probably dependent on the structure of its network connections, and not analysed here.

The time series of mean fano factors shown in Fig. 1 is also not constant throughout the whole 4,000 msec period. As can be seen the fano factor decreases after stimulus onset before increasing slowly. A similar behaviour has been observed in several experimental studies showing stimuli can cause a suppression of neural variability. Here it is caused by a transient effect after stimulus switching whereby the slow network dynamics do not quickly accommodate the new input rate distribution.

4 Discussion

Here we have shown that irregular firing generated by a biologically faithful network model of the striatum is suppressed for many hundreds of seconds after cortical stimulus onset. The slow network dynamics are much slower than any timescale represented in the model parameters. Although there are no striatal studies, many cortical and cerebellum experimental investigations report similar suppression of variability [3–7]. In the future we will investigate how this behaviour depends on network properties such as connectivity.

References

1. Ponzi A and Wickens J. (2010) Sequentially switching cell assemblies in random inhibitory networks of spiking neurons in the striatum *J. Neurosci* 30(17):5894–5911.
2. Ponzi A and Wickens J (2008) Cell Assemblies in Large Sparse Inhibitory Networks of Biologically Realistic Spiking Neurons *Advances in NIPS* 21:1273–1281.
3. Abbott, L.F., Rajan, K. and Sompolinsky, H. (2011) Interactions Between Intrinsic and Stimulus-Dependent Activity in Recurrent Neural Networks. In M. Ding and D. Glanzman, eds. *The Dynamic Brain: An Exploration of Neuronal Variability and Its Functional Significance*. (Oxford University Press, New York, NY).
4. Churchland, M.M., Yu, B.M., Cunningham, J.P., Sugrue, L.P., Cohen, M.R., Corrado, G.S., Newsome, W.T., Clark, A.M., Hosseini, P. Scott, B.B. Bradley, D.C., Smith, M.A., Kohn, A., Movshon, J.A., Armstrong, K.M., Moore, T., Chang, S.W., Snyder, L.H., Ryu, S.I., Santhanam, G., Sahani, M. and Shenoy, K.V. Stimulus onset quenches neural variability: a widespread cortical phenomenon. (2010). *Nature Neuroscience* 13, 369–378.

5. Churchland, M.M., Yu, B.M., Ryu, S.I., Santhanam, G. and Shenoy, K.V. Neural variability in premotor cortex provides a signature of motor preparation. *J. Neurosci* 26, 36973712 (2006).
6. Finn, I.M., Priebe, N.J. and Ferster, D. The emergence of contrastinvariant orientation tuning in simple cells of cat visual cortex. *Neuron* 54, 137152 (2007).
7. Mitchell, J.F., Sundberg, K.A. and Reynolds, J.J. Differential attentiondependent response modulation across cell classes in macaque visual area V4. *Neuron* 55, 13141 (2007).
8. Izhikevich EM (2005) *Dynamical Systems in Neuroscience: The Geometry of Excitability and Bursting*, MIT press.
9. Wickens JR and Wilson CJ (1998) Regulation of action-potential firing in spiny neurons of the rat neostriatum in vivo. *J. Neurophysiol.* 79: 2358–2364
10. Wilson CJ (1993) The generation of natural firing patterns in neostriatal neurons. In *Progress in Brain Research*, 99, 277, Arbuthnott GW, Emson PC (Eds).
11. Wilson CJ and Kawaguchi Y (1996) The Origins of Two-State Spontaneous Membrane Potential Fluctuations of Neostriatal Spiny Neurons *The Journal of Neuroscience*, 16(7):2397–2410
12. Rall W (1967) Distinguishing theoretical synaptic potentials computed for different somadendritic distributions of synaptic input. *J Neurophysiol.* 30(5):1138–68
13. Brunel N, Hakim V (1999) Fast global oscillations in networks of integrate-and-fire neurons with low firing rates. *Neural Comp.* 11, 1621–1671.
14. Wickens JR, Arbuthnott G, Shindou T (2007) Simulation of GABA function in the basal ganglia: computational models of GABAergic mechanisms in basal ganglia function. *Prog. Brain Research* 160, 316.
15. Pleniz D (2003) When inhibition goes incognito: feedback interaction between spiny projection neurons in striatal function. *Trends in Neurosciences* 26(8)
16. Tepper JM, Koos T, Wilson CJ (2004) GABAergic microcircuits in the neostriatum. *Trends in Neurosciences* 27(11)
17. Runge-Kutta methods for stochastic differential equations. Burrage K, Platen E.

Selection Criteria for Neuromanifolds of Stochastic Dynamics

Nihat Ay, Guido Montúfar, and Johannes Rauh

Abstract We present ways of defining neuromanifolds – models of stochastic matrices – that are compatible with the maximization of an objective function such as the expected reward in reinforcement learning theory. Our approach is based on information geometry and aims to reduce the number of model parameters with the hope to improve gradient learning processes.

1 Introduction

Within many formal models of neural networks the dynamics of the whole system can be described as a stochastic transition in each time step, mathematically formalized in terms of a stochastic matrix. Well-known models of this kind are Boltzmann machines [2], their generalizations [5], and policy matrices within reinforcement learning [7]. It is helpful to consider not only one stochastic matrix but a parametrized family of matrices, which forms a geometric object, referred to as a neuromanifold within information geometry [1,2]. This information geometric view point suggests to select appropriate neuromanifolds and to define corresponding learning processes as gradient flows on these manifolds. The natural

N. Ay (✉)

Max Planck Institute for Mathematics in the Sciences, Inselstrasse 22,
D-04103, Leipzig, Germany

Santa Fe Institute, 1399 Hyde Park Road, Santa Fe, NM, 87501, USA
e-mail: nay@mis.mpg.de

G. Montúfar • J. Rauh

Max Planck Institute for Mathematics in the Sciences, Inselstrasse 22,
D-04103, Leipzig, Germany
e-mail: montufar@mis.mpg.de; rauh@mis.mpg.de

gradient method, developed by Amari and co-workers (see for example [1]), proved the efficiency of the geometric approach to learning. The study of learning systems should further address the interplay between geometric properties and the quality of learning. In this paper we study criteria for the selection of neuromanifolds. We do not only focus on manifolds that are directly induced by neuronal models, but also study more general geometric objects that satisfy natural optimality conditions. Therefore, in the following we will talk about *models* instead of neuromanifolds.

We assume that learning maximizes an objective function $f : \mathcal{C} \rightarrow \mathbf{R}$ defined on the set \mathcal{C} of stochastic matrices. A model $\mathcal{N} \subseteq \mathcal{C}$ is consistent with f , if the set of maximizers of f can be reached through the learning. This implies that the maximizers should be contained in the closure of \mathcal{N} . If f is convex on \mathcal{C} , then each locally maximal value is attained at an extreme point (vertex) of \mathcal{C} , and therefore corresponds to a deterministic function. We refer to the following three examples in which optimal systems also turn out to be close to deterministic functions:

1. Optimal policies in reinforcement learning [6],
2. Dynamics with maximal predictive information as considered in robotics [8], and
3. Dynamics of neural networks with maximal network information flow [3].

This suggests to consider parametrizations that can approximate all extreme points of \mathcal{C} , the deterministic functions. In this paper we concentrate on the first example to illustrate the main idea.

2 The Main Geometric Idea

We first consider general convex sets and return to stochastic matrices in Sect. 3. The convex hull of a finite set $\xi^{(1)}, \dots, \xi^{(n)}$ in \mathbf{R}^d is defined as

$$\mathcal{C} := \left\{ \sum_{i=1}^n p(i) \xi^{(i)} : p(i) \geq 0 \forall i \text{ and } \sum_{i=1}^n p(i) = 1 \right\}.$$

The set of extreme points of this polytope \mathcal{C} is a subset of $\{\xi^{(1)}, \dots, \xi^{(n)}\}$. In general, there are many ways to represent a point $x \in \mathcal{C}$ as a convex combination in terms of a probability distribution p . Here, we are interested in convex combinations obtained from an exponential family. To be more precise, denote \mathcal{P}_n the set of probability measures $p = (p(1), \dots, p(n)) \in \mathbf{R}^n$ and consider the map

$$m : \mathcal{P}_n \rightarrow \mathcal{C}, \quad p \mapsto \sum_{i=1}^n p(i) \xi^{(i)}.$$

For a family of functions $\phi = (\phi_1, \dots, \phi_l)$ on $\{1, \dots, n\}$, we consider the exponential family \mathcal{E}_ϕ consisting of all $p \in \mathcal{P}_n$ of the form

$$p(i) = \frac{e^{\sum_{k=1}^l \lambda_k \phi_k(i)}}{\sum_{j=1}^n e^{\sum_{k=1}^l \lambda_k \phi_k(j)}}, \quad i = 1, \dots, n.$$

We denote the image of \mathcal{E}_ϕ under \mathfrak{m} by \mathcal{C}_ϕ . With the choice

$$\phi_k^*(i) := \xi_k^{(i)}, \quad i = 1, \dots, n, \quad k = 1, \dots, d,$$

the closure of the exponential family \mathcal{E}_ϕ can be identified with the polytope \mathcal{C} . This allows to define natural geometric structures on \mathcal{C} , such as a Fisher metric, by using the natural structures on the simplex \mathcal{P}_n . In the context of stochastic matrices this leads to a Fisher metric that has been studied by Lebanon [4] based on an approach by Čencov. The above construction also motivates the following definition: We call a family \mathcal{C}_ϕ an *exponential family* in \mathcal{C} if the vectors $\phi_k, k = 1, \dots, l$, are contained in the linear span of the vectors $\phi_k^*, k = 1, \dots, d$.

In general, the families \mathcal{C}_ϕ are not exponential families but projections of exponential families. In this paper the models \mathcal{C}_ϕ will play the role of neuromanifolds. We are mainly interested in models that are compatible with the maximization of a given function $f : \mathcal{C} \rightarrow \mathbf{R}$ in the sense that the closure of \mathcal{C}_ϕ should contain the maximizers of f . This is clearly not the only consistency condition, but here we focus on this assumption only.

As stated above, in many cases the local maximizers of f are elements of the set $\{\xi^{(1)}, \dots, \xi^{(n)}\}$, and hence the problem stated above reduces to finding a family $\phi = (\phi_1, \dots, \phi_l)$ of functions such that \mathcal{C}_ϕ contains that set in its closure. This is always possible with only two functions ϕ_1, ϕ_2 . One such family can be constructed as follows: Consider a one-to-one map φ of the n points $\xi^{(1)}, \dots, \xi^{(n)}$ into \mathbf{R} , for instance $\xi^{(i)} \mapsto i, i = 1, \dots, n$, and the following family of distributions:

$$\begin{aligned} p_{\alpha, \beta}(i) &= \frac{e^{-\beta(\varphi(\xi^{(i)})-\alpha)^2}}{\sum_{j=1}^n e^{-\beta(\varphi(\xi^{(j)})-\alpha)^2}} \\ &= \frac{e^{\lambda_1 \phi_1(i) + \lambda_2 \phi_2(i)}}{\sum_{j=1}^n e^{\lambda_1 \phi_1(j) + \lambda_2 \phi_2(j)}}, \end{aligned} \tag{1}$$

where $\phi_1(i) := \varphi(\xi^{(i)})$, $\phi_2(i) := \varphi^2(\xi^{(i)})$, and $\lambda_1 := 2\alpha\beta$, $\lambda_2 := -\beta$. It is easy to see that for $\alpha = \varphi(\xi^{(i)})$ and $\beta \rightarrow \infty$, the distribution $p_{\alpha, \beta}$ converges to the point measure concentrated in i . The convex combination $\sum_{j=1}^n p_{\alpha, \beta}(i) \xi^{(i)}$ therefore converges to the point $\xi^{(i)}$. This proves that the closure of this two-dimensional family in \mathcal{C} contains all the points $\xi^{(i)}, i = 1, \dots, n$. In general, the geometric properties of this family strongly depend on φ , as we discuss in the following section.

3 Application to Reward Maximization

Given non-empty finite sets \mathcal{X} and \mathcal{Y} , the stochastic matrices from \mathcal{X} to \mathcal{Y} are maps $(x, y) \mapsto \pi(x; y)$ satisfying

$$\pi(x; y) \geq 0 \text{ for all } x \in \mathcal{X}, y \in \mathcal{Y}, \text{ and}$$

$$\sum_{y \in \mathcal{Y}} \pi(x; y) = 1 \text{ for all } x \in \mathcal{X}.$$

The set of stochastic matrices is denoted by $\mathcal{C} := \mathcal{C}(\mathcal{X}; \mathcal{Y})$. Stochastic matrices are very general objects and can serve as models for individual neurons, neural networks, and policies. Each extreme point of this convex set corresponds to a deterministic function $f : \mathcal{X} \rightarrow \mathcal{Y}$ and is given as

$$\pi^{(f)}(x; y) = \begin{cases} 1, & \text{if } y = f(x), \\ 0, & \text{else.} \end{cases}$$

Although the number of these extreme points is $|\mathcal{Y}|^{|\mathcal{X}|}$, according to Sect. 2 there always exists a two-dimensional manifold that reaches all of them. Note that in the particular case of N binary neurons we have $\mathcal{X} = \mathcal{Y} = \{0, 1\}^N$ and therefore $(2^N)^{(2^N)}$ extreme points.

To illustrate the geometric idea we consider the example $\mathcal{X} = \{1, 2, 3\}$ and $\mathcal{Y} = \{1, 2\}$. This can, for instance, serve as a model for policies with three states and two actions. In this case \mathcal{C} is a subset of $\mathbf{R}^{\mathcal{X} \times \mathcal{Y}} \cong \mathbf{R}^6$ which can be identified with the hypercube $[0, 1]^3$ through the following parametrization (see Fig. 1a):

$$[0, 1]^3 \ni (r, s, t) \mapsto \begin{pmatrix} r & 1-r \\ s & 1-s \\ t & 1-t \end{pmatrix}.$$

To test the properties of that family with respect to the optimization of a function, we consider a map $(s, a) \mapsto \mathcal{R}_s^a$, which we interpret as *reward* that an agent receives if it performs action a after having seen state s . The policy of the agent is described by a stochastic matrix $\pi(s; a)$. The expected reward can be written as

$$f(\pi) = \sum_s p^\pi(s) \sum_a \pi(s; a) \mathcal{R}_s^a.$$

In reinforcement learning, there are several choices of p^π (see [7]). Here we simplify our study by assuming p^π to be the uniform measure.

We investigate the influence of the map φ and compare the natural gradient flow (gradient with respect to the Fisher metric, see [1]) with the ordinary gradient. For the experiments we drew a random reward matrix \mathcal{R} and applied gradient ascent

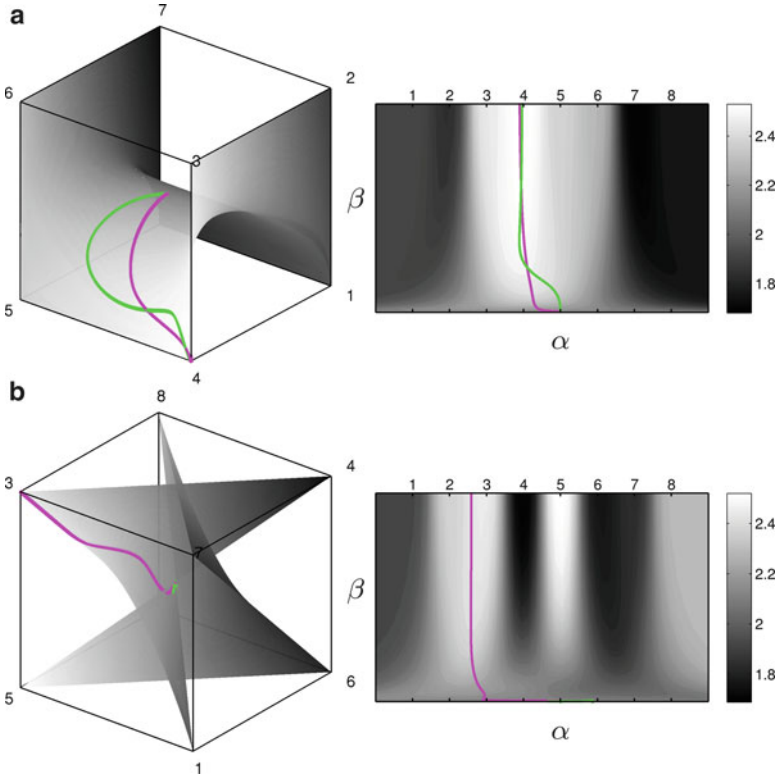


Fig. 1 Optimization with ordinary (*light*) and natural (*dark*) gradient on the model \mathcal{C}_ϕ for two different choices of φ . **(a)**: A Hamilton path $\varphi = (1, 2, 3, 4, 5, 6, 7, 8)$. **(b)**: An arbitrary map $\varphi = (1, 7, 3, 5, 2, 8, 4, 6)$

(with fixed step size) on $f(\pi)$ restricted to our model and several choices of φ (see Fig. 1a/b for typical outcomes). The optimization results strongly depend on φ . We restricted ourselves to the case that φ maps the vertices of \mathcal{C} onto the numbers $\{1, \dots, n\}$. Such a map is equivalent to an ordering of the vertices. We recorded the best results when φ corresponds to a Hamilton path on the graph of the polytope \mathcal{C} , i.e. a closed path along the edges of the polytope that visits each vertex exactly once. This way φ preserves the locality in \mathcal{C} , and the resulting model \mathcal{C}_ϕ is a smooth manifold. In Fig. 1a, both methods reach the global optimum $\begin{pmatrix} 0 & 1 \\ 1 & 0 \\ 0 & 1 \end{pmatrix}$. In Fig. 1b, φ is ‘unordered’. We see that the landscape $f(\pi_{\alpha,\beta})$ is more intricate and contains several local maxima. The natural gradient method only converged to a local but not global optimum, and the ordinary gradient method failed. In Fig. 1a/b every vertex ξ of the cube is labeled by $\varphi(\xi)$ for the corresponding φ .

4 Towards a Construction of Neuromanifolds

Here we approach implementations of policies π in the context of neural networks. We start with the case of two input neurons and one output neuron (Fig. 2, left). All neurons are considered to be binary with values 0 and 1. The input-output mapping is modelled in terms of a stochastic matrix π . The set of such 4×2 -matrices forms a four-dimensional cube. A prominent neuronal model assumes synaptic weights w_1 and w_2 assigned to the directed edges and a bias b . The probability for the output 1, which corresponds to the spiking of the neuron, is then given as

$$\pi(x_1, x_2; 1) = \frac{1}{1 + e^{-(w_1x_1 + w_2x_2 - b)}}. \tag{2}$$

This defines a three-dimensional model in the four-dimensional cube, see Fig. 3. Some extreme points are not contained in this model, e.g. the matrix $\pi(0, 0; 1) = \pi(1, 1; 1) = 0$, $\pi(0, 1; 1) = \pi(1, 0; 1) = 1$. This corresponds to the well-known fact that the standard model cannot represent the XOR-function. On the other hand, it is possible to reach all extreme points, including the XOR-function, with the two-dimensional models introduced above. However, there are various drawbacks of our models in comparison with the standard model. They are not exponential families but only projections. Moreover, we do not have a neurophysiological interpretation of the parameters.

Fig. 2 Two simple neural networks

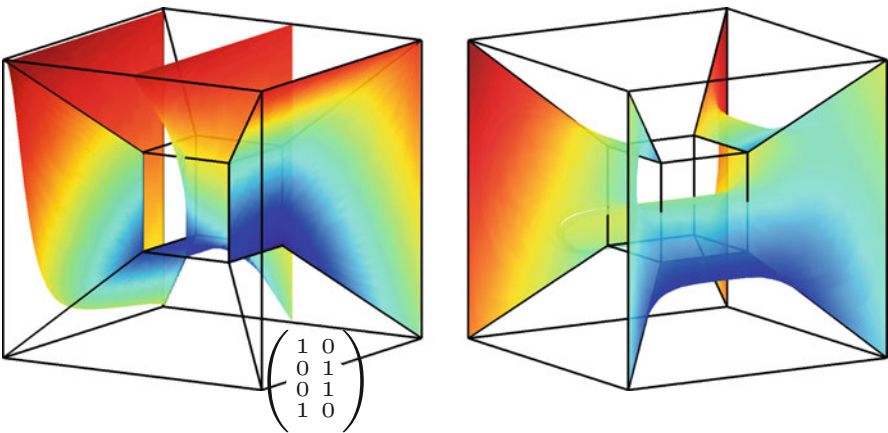
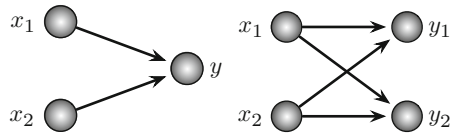
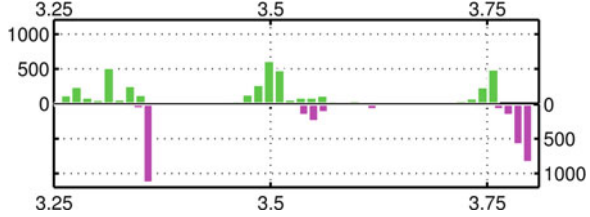


Fig. 3 The standard model given in Eq. (2) for three values of the bias parameter b (left) and the new model (right) introduced in Sect. 2

Fig. 4 Histogram of the objective value $f(\pi)$ after 500 steps of gradient ascent in \mathcal{N}_{new} . *Lower part:* natural gradient. *Upper part:* ordinary gradient



We now discuss models for the case of one additional output neuron. The system is modelled by stochastic 4×4 matrices, which form the 12-dimensional polytope $\mathcal{C} := \mathcal{C}(\{0, 1\}^2; \{0, 1\}^2)$. A natural assumption is the independence of the outputs Y_1 and Y_2 given the input pair X_1, X_2 . This is the case if and only if the input-output map of each neuron i is modelled by a separate stochastic matrix $\pi_i, i = 1, 2$. The stochastic matrix of the whole system is given by

$$\pi(x_1, x_2; y_1, y_2) = \pi_1(x_1, x_2; y_1) \cdot \pi_2(x_1, x_2; y_2).$$

This defines an 8-dimensional model $\mathcal{N}_{\text{product}}$ that contains all extreme points of \mathcal{C} . Furthermore, it contains the submodel $\mathcal{N}_{\text{standard}}$ given by the additional requirement that π_1 and π_2 are of the form (2). The model $\mathcal{N}_{\text{standard}}$ is an exponential family of dimension 6. However, as in the one-neuron case, $\mathcal{N}_{\text{standard}}$ does not reach all extreme points. Another submodel \mathcal{N}_{new} of $\mathcal{N}_{\text{product}}$ is defined by modelling each of the stochastic matrices π_i in terms of two parameters as described above. The following table gives a synopsis:

Model	Dim.	Exp. fam.	Reaches ext. points
\mathcal{C}	12	Yes	Yes
$\mathcal{N}_{\text{product}}$	8	Yes	Yes
$\mathcal{N}_{\text{standard}}$	6	Yes	No
\mathcal{N}_{new}	4	No	Yes

We conclude this section with the maximization of a reward function in the family \mathcal{N}_{new} , as in the previous section. Figure 4 shows a histogram of the results for a fixed randomly chosen reward \mathcal{R} after 500 steps for ordinary gradient and natural gradient methods. We chose a constant learning rate and 5,000 different initial values. Both methods find three local maxima. The natural gradient process tends to converge faster. Furthermore, it finds the global maximum for a majority of the initial values, which is not the case for the ordinary gradient.

5 Conclusions

We proposed and studied models which contain all extreme points in the set of stochastic matrices (the global maximizers for a variety of optimization problems).

These models have very few parameters and a rich geometric structure, and they allow a simple implementation of natural gradient methods. At this stage we do not suggest them for describing neural systems but as basis for extensions to more plausible models.

References

1. S. Amari. *Natural Gradient Works Efficiently in Learning*. Neural Comput., 10(2) (1998) 251–276.
2. S. Amari, K. Kurata, H. Nagaoka. *Information Geometry of Boltzmann machines*. IEEE T. Neural Networks, 3(2) (1992) 260–271.
3. N. Ay, T. Wennekers. *Dynamical Properties of Strongly Interacting Markov Chains*. Neural Networks 16 (2003) 1483–1497.
4. G. Lebanon. *Axiomatic geometry of conditional models*. IEEE Transactions on Information Theory, 51(4) (2005) 1283–1294.
5. G. Montúfar, N. Ay. *Refinements of Universal Approximation Results for DBNs and RBMs*. Neural Comput. 23(5) (2011) 1306–1319.
6. R. Sutton, A. Barto. *Reinforcement Learning*. MIT Press (1998).
7. R. Sutton, D. McAllester, S. Singh, Y. Mansour. *Policy Gradient Methods for Reinforcement Learning with Function Approximation*. Adv. in NIPS 12 (2000) 1057–1063.
8. K.G. Zahedi, N. Ay, R. Der. *Higher Coordination With Less Control – A Result of Information Maximization in the Sensorimotor Loop*. Adaptive Behavior 18 (3–4) (2010), 338–355.

A Manipulative Approach to Neural Dynamics by Combined TMS-EEG

Keiichi Kitajo, Yumi Nakagawa, Yutaka Uno, Ryohei Miyota,
Masanori Shimono, Kentaro Yamanaka, and Yoko Yamaguchi

Abstract We propose a new approach for manipulating neural dynamics by using combined TMS (Transcranial magnetic stimulation) – EEG (Electroencephalography) recordings. We demonstrate that we can perturb the phase dynamics of ongoing neural oscillations by TMS. Using the manipulative approach we can investigate (1) state-dependency in frequency-specific network connectivity by analyzing how

K. Kitajo (✉)

Laboratory for Cognitive Brain Mapping, RIKEN Brain Science Institute (BSI), Wako, Saitama 351-0198, Japan

Rhythm-Based Brain Computation Unit, RIKEN BSI – Toyota Collaboration Center,
RIKEN BSI, Wako, Saitama 351-0198, Japan

PRESTO, Japan Science and Technology Agency, Kawaguchi, Saitama 332-0012, Japan
e-mail: kkitajo@brain.riken.jp

Y. Nakagawa

Rhythm-Based Brain Computation Unit, RIKEN BSI – Toyota Collaboration Center,
RIKEN BSI, Wako, Saitama 351-0198, Japan

Y. Uno

Graduate School of Frontier Sciences, University of Tokyo, Kashiwa, Chiba 277-8564, Japan

R. Miyota

Laboratory for Dynamics of Emergent Intelligence, RIKEN BSI, Wako, Saitama 351-0198, Japan

M. Shimono

Department of Physics, Indiana University, Bloomington 47405, USA

Graduate School of Education, University of Tokyo, Tokyo 113-0033, Japan

K. Yamanaka

Department of Health Design, Showa Women's University, Tokyo 154-8533, Japan

Y. Yamaguchi

Rhythm-Based Brain Computation Unit, RIKEN BSI – Toyota Collaboration Center,
RIKEN BSI, Wako, Saitama 351-0198, Japan

Laboratory for Dynamics of Emergent Intelligence, RIKEN BSI, Wako, Saitama 351-0198, Japan

TMS-evoked phase reset of ongoing activity propagates from one cortical area to the rest of the brain in humans and (2) causal links between the neural dynamics and brain functions. We can causally confirm dynamical and computational models in manipulative manners using this approach.

1 Introduction

Growing evidence indicates that synchronous neural oscillations are important in mediating perceptual and cognitive processes [1, 2]. A lot of “neural correlates” studies demonstrated the correlation between synchronous neural activity and brain functions. It is important, however, to show causal links between the neural dynamics and brain functions, which are beyond the correlation between them. Stochastic resonance is one of the ways to manipulate neural oscillations and look at functional changes in the human brain [3]. To address this issue more directly we propose another new manipulative approach using TMS-EEG. New findings on the human brain start to emerge from combined TMS-EEG studies [4, 5]. Massimini et al. for example, demonstrated evidence for a breakdown of long-range effective connectivity during NREM sleep by combined TMS-EEG recordings analyzing propagation of TMS evoked response across the brain [5]. This study suggests that TMS can transiently perturb and modulate cortical ongoing activity in the human brain. No study, however, has shown frequency-specific, state-dependent changes in large-scale cortical synchronous network connectivity. We therefore investigated frequency-specific and state-dependent cortical network connectivity by analyzing how TMS-evoked phase perturbation of ongoing activity at one cortical area measured by EEG is propagated to the rest of the brain at different frequencies.

We propose that using the new manipulative approach we can investigate (1) state-dependency in frequency-specific network connectivity by analyzing how TMS-evoked phase reset of ongoing activity propagates from one cortical area to the rest of the brain and (2) causal links between the neural dynamics and brain functions in humans confirming dynamical and computational models.

2 Methods

In total 40 right-handed adult participants with normal or corrected-to-normal vision gave informed consent. The study was approved by the ethical committee of RIKEN. Using a 19-channel (Neuroprax, neuroConn, Germany) or a 64-channel (BrainAmp MR plus, Brain Products, Germany) TMS-compatible EEG amplifiers, we recorded TMS (Magstim rapid, The Magstim company, UK) – modulated ongoing brain activity while normal participants sit on a chair with their eyes closed or eyes open fixating a gray cross in the dark on a black background in the center

of a 19" CRT monitor (100 Hz refresh rate) at a distance of 95 cm. A chin rest maintained participants' head position throughout the experiment. Participants were instructed to avoid making eye movements or blinks.

EEG data were sampled at 4,096 Hz and off-line resampled at 1,024 Hz (Neuroprax) or sampled at 1,000 Hz (BrainAmp MR plus). EEG records were digitally re-referenced to averaged earlobe electrodes. Electrode impedances were kept below 10 k Ω .

We targeted TMS to the left primary motor cortex with intensity at the 95% motor threshold or the visual cortex with intensity at the 95% phosphene threshold. Participants were given 50–60 pulses in eyes-open and eyes-close conditions. In 19ch EEG experiments, 17 subjects participated in the motor area targeted experiments. 14 different subjects were identified as those who were able to see TMS-induced phosphenes and participated in the visual area targeted experiments. The electrooculogram (EOG) was recorded with electrodes positioned 1 cm from the outer canthi of both eyes and above and below the left eye. Epochs with artifacts caused by blinks or eye movements or amplifier saturation were detected using an amplitude criterion ($\pm 150\mu\text{V}$) and excluded from further analysis. Three subjects in the motor area targeted and four subjects in the visual area targeted experiments were excluded because too few epochs survived after the artifact rejection. The signal was segmented into a series of 3,000 ms-long epochs. Each epoch consists of 1,500 ms pre TMS and post TMS periods. The EEGLAB, Matlab toolbox was used for artifact rejection, visualization and topographic plots [6]. We band-pass filtered the EEG or EEG SCD (scalp current density) signals and computed instantaneous phase and amplitude of the filtered signal by constructing the analytic signal using the Hilbert transform or wavelet methods or a two-cycle complex exponential sequence [7]. By using these methods, we can dissociate instantaneous phase from amplitude of signals. Next, to quantify the TMS evoked phase reset of ongoing activity, we computed phase locking value (PLV), which is a measure of phase consistency across trials for each time/frequency point, according to the following [8]:

$$PLV(t, f) = \frac{1}{N} \left| \sum_{n=1}^N e^{i\varphi(t, f, n)} \right|$$

where $\varphi(t, f, n)$ is the instantaneous phase at time t and frequency f from an electrode of the n th trial. N is the number of trials.

3 Results

In all participants, we observed strong modulation of phase of ongoing activity by TMS. Figure 1 shows representative PLV headmaps from a single subject using a 64ch EEG SCD data at 10 Hz. In this case we stimulated the occipital pole at the

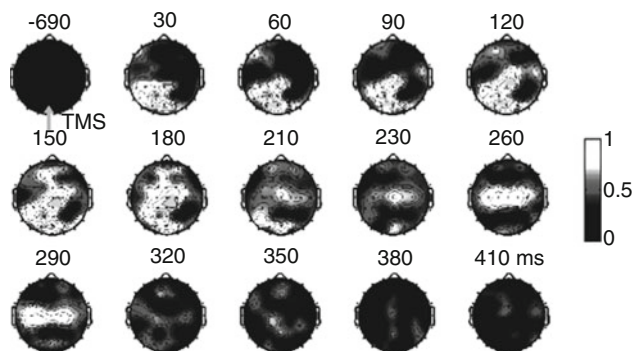


Fig. 1 Representative PLV head maps of EEG-SCD at 10 Hz at various times after single-shot TMS for a single subject. The visual area (*occipital pole*) was stimulated at the 95% phosphene threshold in the eyes-open condition

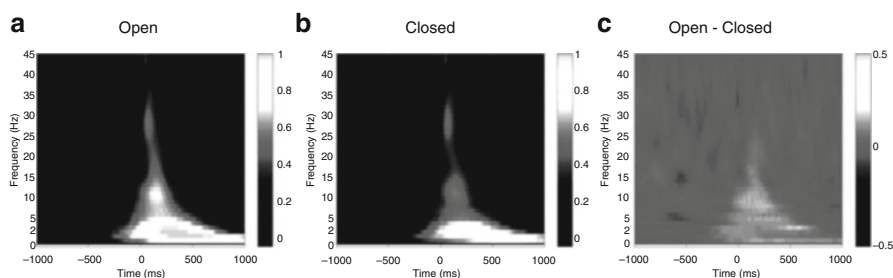


Fig. 2 PLV averaged across all channels and participants ($N = 14$) in eyes-open, eyes-closed conditions and difference between eyes-open – eyes-closed conditions for the motor area targeted TMS experiment

95% phosphene threshold. Strong phase reset was observed right after TMS around the target site. Then, the phase reset propagated from the visual area to the rest of the brain very globally and disappeared at around the motor cortex.

In our group experiments using 19ch EEG recordings, (Motor area targeted TMS: $N = 14$, Visual area targeted TMS: $N = 10$), we found significant increase in PLV by single shot TMS ($p < 0.05$, FDR corrected permutation test). Figures 2 and 3 show PLV time frequency diagrams averaged across all channels for the eyes-open and eyes-closed conditions in the motor area targeted and visual area targeted experiments, respectively. We found that global propagation of phase reset was most prominent at 3–6 Hz delta to theta ranges and 8–13 Hz alpha range in both eyes-open and eye-closed conditions. We observed more widespread and prolonged propagation of phase reset of ongoing activity in the eyes-open condition than in the eyes-closed condition most prominently around 10 Hz ($p < 0.05$, FDR corrected, permutation test) both in motor area targeted (Fig. 2) and visual area targeted experiments (Fig. 3).

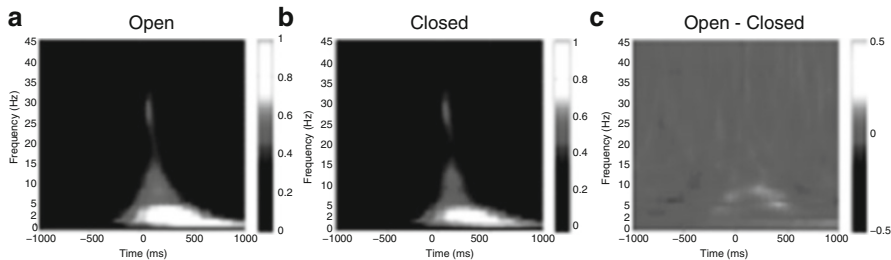


Fig. 3 PLV averaged across all channels and participants ($N = 10$) in eyes-open, eyes-closed conditions and difference between eyes-open – eyes-closed conditions for the visual area targeted TMS experiment

4 Discussions

We observed prominent phase reset of ongoing EEG by single-shot TMS. The phase reset propagated from the stimulated area to the rest of the brain in a frequency specific way. We speculate that phase reset propagated globally across coupled neural oscillators in the human brain. Large-scale cortico-cortical and/or thalamocortical synchrony networks [5] should be associated with global propagation of phase reset by a single-shot TMS.

We found more prominent propagation of phase reset in the eyes-open condition than in eyes-closed condition at around 10 Hz. It has been shown that the phase of pre-stimulus alpha oscillations modulates visual detection [9, 10]. It has been also demonstrated that detection of TMS-evoked phosphenes is modulated by alpha power [4, 11]. These studies and our results suggest the alpha-band synchrony networks might be mediating gain regulation of incoming flow of visual information.

Our study provides evidence that TMS-EEG can reveal frequency-specific, state-dependent changes in large-scale cortical synchronous network connectivity. Our results also indicate that TMS can reset and control the phase of ongoing oscillations locally and globally. We therefore speculate that we can manipulate global phase dynamics and look at functional consequences. This idea will lead to a new system neuroscience method for real-time control of neural dynamics for showing causal links between neural dynamics and brain functions.

In our preliminary experiments, we also used double-shot TMS and found frequency specific entrainment of ongoing oscillations. More specifically, we observed stronger phase reset at 6 Hz when giving double-shot TMS at 6 Hz than 10 Hz. The results suggest that repetitive TMS might be better in perturbing frequency specific synchronization networks.

In conclusion, TMS-EEG is an excellent manipulative tool for investigating (1) state-dependency in frequency-specific network connectivity by analyzing how TMS-evoked phase reset of ongoing activity propagates from one cortical area to the

rest of the brain in humans and (2) causal links between the neural dynamics such as the phase of ongoing activity and brain functions. By using this manipulative approach we can causally confirm dynamical and computational models.

Acknowledgments This work was supported by MEXT Grant-in-Aid for Scientific Research (B)(193200207), Grant-in-Aid for Scientific Research on Innovative Areas “The study on the neural dynamics for understanding communication in terms of complex hetero systems (No.4103)” (21120005), and JST PRESTO program. We thank Kumiko Uchiyama and Ayumi Honda for help in collecting data.

References

1. Varela, F. J., Lachaux, J. P., Rodriguez, E., Martinerie, J.: The brainweb: phase synchronization and large-scale integration. *Nature Rev. Neurosci.* 2 (2001) 229–239
2. Ward, L. M.: Synchronous neural oscillations and cognitive processes. *Trends Cogn. Sci.* 7 (2003) 553–559
3. Kitajo, K., Doesburg, S., Yamanaka, K., Nozaki, D., Ward, L., Yamamoto, Y.: Noise-induced large-scale phase synchronization of human-brain activity associated with behavioural stochastic resonance. *Europhys. Lett.* 80 (2007) 40009-1-6
4. Thut, G., Miniussi, C.: New insights into rhythmic brain activity from TMS-EEG studies. *Trends Cogn. Sci.* 13 (2009), 182–189
5. Massimini, M., Ferrarelli, F., Huber, R., Esser, S. K., Singh, H., Tononi, G.: Breakdown of cortical effective connectivity during sleep. *Science*, 309 (2005) 2228–2232
6. Delorme, A., Makeig, S.: EEGLAB: an open source toolbox for analysis of single-trial EEG dynamics including independent component analysis. *J. Neurosci. Methods* 134, (2004) 9–21
7. Naruse, Y., Matani, A., Hayakawa, T., Fujimaki, N.: Influence of seamlessness between pre- and poststimulus alpha rhythms on visual evoked potential. *NeuroImage*, 32 (2006), 1221–1225
8. Kitajo, K., Miyota, R., Shimono, M., Yamanaka, K., Yamaguchi, Y.: State-Dependent Cortical Synchronization Networks Revealed by TMS-EEG Recordings. *Advances in Cognitive Neurodynamics II* (2010) 145–148
9. Mathewson, K. E., Gratton, G., Fabiani, M., Beck, D. M., Ro, T.: To see or not to see: prestimulus alpha phase predicts visual awareness. *J. Neurosci.* 29 (2009), 2725–2732
10. Busch, N. A., Dubois, J., VanRullen, R.: The phase of ongoing EEG oscillations predicts visual perception. *J. Neurosci.* 29(2009), 7869–7876
11. Romei, V., Brodbeck, V., Michel, C., Amedi, A, Pascual-Leone, A, Thut, G.: Spontaneous fluctuations in posterior alpha-band EEG activity reflect variability in excitability of human visual areas. *Cereb. Cortex* 18(2007), 2010–2018

Long-Tailed Statistics of Corticocortical EPSPs: Origin and Computational Role of Noise in Cortical Circuits

Jun-nosuke Teramae, Yasuhiro Tsubo, and Tomoki Fukai

Abstract Neurons in the brain exhibit highly irregular asynchronous firing even without sensory stimulation. Here, we study the recently proposed hypothesis that a highly non-homogeneous distribution, typically lognormal distribution, of cortico-cortical EPSP (excitatory postsynaptic potential) accounts for the low-rate spontaneous irregular activity observed in vivo. When amplitude distribution of EPSPs among excitatory neuron pairs obeys the lognormal distribution, networks of leaky integrate-and-fire model neurons robustly show ongoing firing state with low firing rate. Moreover, consistent with cortical neurobiology, the obtained activity had high irregularity, low synchronicity, and dynamically balanced excitation-inhibition population activity. We derive effective evolution equations for excitatory and inhibitory population activities from a recurrent network of the leaky integrate-and-fire neurons coupled with highly non-homogeneous connections. Based on the evolution equation, we perform stability analysis of nontrivial solutions of the equation and reveal underlying mechanisms and computational functions of the noise in cortical circuits.

J. Teramae (✉)

Brain Science Institute, RIKEN, 2-1, Hirosawa, Wako, Saitama 351-0198, Japan

PRESTO, Japan Science and Technology Agency (JST), 4-1-8 Honcho, Kawaguchi, Saitama 332-0012, Japan

e-mail: teramae@riken.jp

Y. Tsubo

Brain Science Institute, RIKEN, 2-1, Hirosawa, Wako, Saitama 351-0198, Japan

T. Fukai

Brain Science Institute, RIKEN, 2-1, Hirosawa, Wako, Saitama 351-0198, Japan

CREST, Japan Science and Technology Agency (JST), 4-1-8 Honcho, Kawaguchi, Saitama 332-0012, Japan

1 Introduction

Even in the absence of sensory stimulation, cortical neurons exhibit highly irregular asynchronous firings in low spiking rate [1]. The spontaneous cortical activity, or noise in cortical circuits, is influential to our perception and also modifiable by sensory experiences [2–6], and have been discussed in relation with cortical activities during sleep [7]. However, the underlying mechanisms and computational roles of the intrinsic cortical noise have remained unclear until very recently. Recent electrophysiological recordings revealed that some corticocortical excitatory postsynaptic potentials (EPSPs) can be as large as several millivolts, while the majority is weak (<1 mv) [8, 9]. The highly non-homogeneous EPSP distribution is well described by long-tailed distributions, typically by the lognormal distribution.

Asynchronous irregular (AI) firing of cortical neurons has been studied in various model studies. Sparsely connected networks of binary neurons receiving external noise can generate ongoing states similar to the AI state [10]. Under the assumption that excitatory and inhibitory inputs to neurons is averagely balanced, inputs mediated by relatively strong synapses enable the model to generate large temporal fluctuations crucial for irregular firing. The network states realized with excitatory-inhibitory balance and external input have been extensively studied in sparsely connected networks of spiking neurons [11]. Such networks can generate AI states even without external noise [12, 13]. However, the generation of very low-rate asynchronous firing (<10 Hz) was difficult in the previous models [14]. The typical frequency of spontaneous cortical activity is as low as $1 \sim 3$ Hz in pyramidal neurons [1].

Previous models with weak and modest EPSPs require either highly synchronized input or asynchronous input at relatively high rates to evoke postsynaptic spikes. Therefore, these models are considered to show relatively high spontaneous firing rate to maintain spontaneously ongoing firing. However, if some EPSP is extremely large, as observed in *in vitro* experiments, we may solve the above difficulties of the previous models in generating low-rate spontaneous activity. Here, we consider the recently proposed hypothesis based on this possibility that the low-rate spontaneous irregular activity of neurons is due to the highly non-homogeneous EPSP distribution [15].

We study a recurrent network of excitatory and inhibitory leaky integrate-and-fire model neurons. While connections among neurons are randomly generated, we assume that amplitude of EPSPs on each excitatory neuron distribute according to a lognormal distribution which well reproduces experimental literatures. We develop a theory to describe activities of the lognormally connected network. This theory reveals that low-rate irregular firing emerges spontaneously in the lognormally connected network even without external input or background noise. Modeled activity is consistent with various experimentally known properties of intrinsic cortical activity, including high irregularity [16], low synchrony [17, 18], excitatory-inhibitory balance [19], for which several computational advantages are known, depolarized membrane UP state, and existence of precisely firing structures.

Moreover, depolarize membrane potential about 10 mV above the resting potential, which sustained by many synaptic inputs on small synapses maximizes spike transmission received at extremely strong synapses. This maximal spike transmission is confirmed experimentally by dynamic-clamp recordings of cortical neurons.

2 Methods

We consider the network consists of conductance-based leaky integrate-and fire model neurons,

$$\frac{dv}{dt} = -\frac{1}{\tau_m} (v - V_L) - g_E (v - V_E) - g_I (v - V_I),$$

where g_E and g_I are excitatory and inhibitory synaptic conductances which evolve as

$$\frac{dg}{dt} = -\frac{1}{\tau_s} g + \sum_j G_{ij} \sum_k \delta(t - t_{j,k} - d_{ij})$$

with synaptic decay time constant τ_s . $t_{j,k}$ is the k -th spike time of the j -th neuron, d_{ij} is the synaptic delay from neuron j to neuron I , G_{ij} characterize coupling strength of the connection. While we use random topology for the network structure, on each excitatory neuron, we fixed synaptic coupling strength between excitatory neuron pairs such that EPSPs measured at the resting membrane potential of the postsynaptic neuron distribute according to the lognormal distribution,

$$P(x) = \frac{1}{\sqrt{2\pi}\sigma x} \exp\left[-\frac{(\log x - \mu)^2}{2\sigma^2}\right]$$

whose average is

$$\exp\left(\mu + \frac{1}{2}\sigma^2\right)$$

and variance is

$$\exp(2\mu + \sigma^2) [\exp(\sigma^2) - 1].$$

Since the lognormal distribution has a right long-tail, a few EPSPs on each neuron can be extremely strong while majority of EPSPs are still sufficiently weak. We use uniform values of G for other types of connections. The network we have used consists of $N = 10,000$ and $N = 2,000$ inhibitory neurons with few mill second synaptic delays.

3 Results

In the lognormally connected network, we can divide the contribution of synaptic inputs to the firing rate into two components. The first component arises from weak and modestly strong synapses, which is estimated from the membrane potential fluctuations. The second component comes from a few extremely strong synapses which characterize long-tailed nature of the lognormal connectivity. Since output spikes are highly irregular and asynchronous, we can safely assume that input spike trains to each neuron are well described by independent identical Poisson processes. Denoting the rates of the Poisson processes as r_E and r_I for excitatory and inhibitory presynaptic neurons, respectively, we can adopt the diffusion approximation for dynamics of v , g_E and g_I to obtain a set of Langevin equations. Because of the nonlinearity of the Langevin equations, we need further approximation to solve these equations. Here we employ the assumption in which we remove the nonlinearity by replacing $v - V_E$ and $v - V_I$ with $V_0 - V_E$ and $V_0 - V_I$ in the equation. Here

$$V_0 = \tau_e \left(\frac{V_L}{\tau_m} + \langle g_E \rangle V_E + \langle g_I \rangle V_I \right)$$

and

$$\tau_e = \left(\frac{1}{\tau_m} + \langle g_E \rangle + \langle g_I \rangle \right)^{-1}$$

are the effective equilibrium membrane potential and the effective membrane time constant respectively.

With this approximation, we can obtain the stationary distribution function for normalized membrane potential u as

$$P(u, z) = \frac{1}{2\pi \sqrt{\sigma_{uu}\sigma_{zz}}} \exp\left(-\frac{u^2}{2\sigma_{uu}} - \frac{z^2}{2\sigma_{zz}}\right)$$

where z is du/dt . Since the probability current along the direction of u is given as zP , the first component of output firing rate of neurons are given as

$$r_{out,1} = \frac{e^{-\frac{\theta^2}{2\sigma_{uu}}}}{2\pi} \sqrt{\frac{\sigma_{zz}}{\sigma_{uu}}},$$

where θ is the gap to the firing threshold from V_0 .

The second component of output firing rate is given as the sum of products of presynaptic firing rate at an extremely strong synapse and the probability of postsynaptic firing in response to the evoked strong EPSP as

$$r_{out,2} = \sum_{strong\ EPSPs} \frac{r_E}{2} \left(\operatorname{erf} \left(\frac{\theta}{\sqrt{2\sigma_{uu}}} \right) - \operatorname{erf} \left(\frac{\theta - EPSP}{\sqrt{2\sigma_{uu}}} \right) \right),$$

where the erf(x) is an error function.

By utilizing self-consistency between input firing rates and output firing rates in recurrent networks, we finally obtain the evolution equations for the excitatory and inhibitory population of neurons. The obtained equation has a nontrivial fixed-point solution might correspond to the irregular spontaneous activity. To study the stability of the nontrivial solution, we apply the linear stability analysis around the fixed point and we obtain a closed-form equation for the stability index λ as,

$$(\lambda \tau_{e,E} + 1 - a_{EE} e^{-\lambda d_{EE}}) (\lambda \tau_{e,I} + 1 - a_{II} e^{-\lambda d_{II}}) = a_{IE} e^{-\lambda d_{IE}} a_{EI} e^{-\lambda d_{EI}}.$$

By solving the equation numerically, we can examine the stability of the spontaneous activity.

The result of the analysis shows that the fixed point is unstable if the second component of output firing rate which comes from the long tail of the lognormal EPSP distribution. However, an introduction of the second component easily stabilizes the fixed point. The fixed point is robust against modification of model parameters. Moreover, We also find that even though the second component significantly contributes to the sustaining spontaneous activity, the second term only is not sufficient to realize the sustained activity. Actually, removing the first component reduces the equilibrium membrane potential of neurons and drastically decreases firing probability of postsynaptic neuron to the strong EPSP. The fixed point disappears due to the reduction.

To confirm above analytical results from a different viewpoint, we compared AI states between the lognormally connected network and one in which the weights of recurrent synapses are distributed as a Gaussian that has the same mean and variance as the lognormal distribution. The resultant Gaussian-connected network only has relatively weak synapses. We numerically simulated the two models to obtain the regions of the parameter space spanned by inhibitory conductances in which AI states are stable with sufficiently low firing rates. The lognormally-connected network offers a wide region of the parameter space to AI states with low frequencies (<10 Hz), low synchronicity and highly irregular spiking (the average coefficient of variation ~ 1). In contrast, the stable region for low-frequency firing is narrow and irregular firing turns less asynchronous in the Gaussian-connected network. These results indicate that AI states are much more robust in the lognormally-connected network than in the Gaussian-connected network against changes in the network parameters.

To clarify the crucial role of strong synapses in generating low-frequency AI states, we added a small number of the strongest synapses from the lognormal EPSP distribution to each excitatory neuron in the Gaussian-connected network, and calculated diagrams similar to those for the lognormally-connected network. The diagrams obtained when the top five strongest synapses were added to each

excitatory neuron, which are surprisingly similar to those for original lognormal network. We further conducted a similar analysis when only the strongest synapse was added. Except that the region of parameter space for a stable asynchronous firing was slightly narrowed, the results were essentially unchanged. Thus, although we cannot rigorously separate ‘weak’ and ‘strong’ synapses for the lognormal EPSP distribution, the coexistence of both weak and strong synapses is essential for the generation of the AI state.

4 Discussions

The results of our analysis reveals that the long-tailed statistics of cortico-cortical EPSPs are responsible for stable maintenance of the intrinsic noise in networks of spiking neurons. The activity is maintained by coexistence of both input from a few strong synapses and that from many weak synapses which lifts membrane potential up to the high-conductance depolarized state. Due to the depolarized state, inputs on strong synapses are transmitted into output spikes of the neurons with high probability. Thus intrinsic noise in cortex is not just noise but significantly contribute to achieve reliable information transmission via spike trains in cortical circuit.

References

1. Hromádka T, Deweese MR, Zador AM (2008) Sparse representation of sounds in the unanesthetized auditory cortex. *PLoS Biol* 6:e16.
2. Katz LC, Shatz CJ (1996) Synaptic Activity and the Construction of Cortical Circuits. *Science* 274:1133–1138.
3. Arieli A, Sterkin A, Grinvald A, Aertsen A (1996) Dynamics of ongoing activity: Explanation of the large variability in evoked cortical responses. *Science* 273:1868–1871.
4. Kenet T, Bibitchkov D, Tsodyks M, Grinvald A, Arieli A (2003) Spontaneously emerging cortical representations of visual attributes. *Nature* 425:954–956.
5. Petersen CC, Hahn TT, Metha M, Grinvald A, Sakmann B (2003) Interaction of sensory responses with spontaneous depolarization in layer 2/3 barrel cortex. *Proc Natl Acad Sci USA* 100:13638–13643.
6. Berkes P, Orbán G, Lengyel M, Fiser J (2011) Spontaneous cortical activity reveals hallmarks of an optimal internal model of the environment. *Science* 331:83–87.
7. Steriade M (2003) *Neuronal Substrates of Sleep and Epilepsy*. Cambridge: Cambridge University Press.
8. Song S, Sjöström P, Reigl M, Nelson S, Chklovskii D (2005) Highly nonrandom features of synaptic connectivity in local cortical circuits. *PLoS Biol* 3:e68.
9. Lefort S, Tómm C, Floyd Sarria JC, Petersen CCH (2009) The excitatory neuronal network of the C2 barrel column in mouse primary somatosensory cortex. *Neuron* 61:301–316.
10. van Vreeswijk C, Sompolinsky H (1996) Chaos in neuronal networks with balanced excitatory and inhibitory activity. *Science* 274:1724–1726.
11. Brunel N (2000) Dynamics of sparsely connected networks of excitatory and inhibitory spiking neurons. *J Comput Neurosci* 8:183–208.

12. Vogels TP, Abbott LF (2005) Signal propagation and logic gating in networks of integrate-and-fire neurons. *J Neurosci* 25:10786–10795.
13. Kumar A, Schrader S, Aertsen A, Rotter S (2008) The high-conductance state of cortical networks. *Neural Comput* 20:1–43.
14. Abbott LF (2008) Theoretical neuroscience rising. *Neuron* 60:489–495.
15. Teramae J, Fukai T (2011) A log-normal EPSP distribution accounts for the UP state, low-rate asynchronous firings, and precise firing sequences in cortical networks. *Society for neuroscience abstract* 552.15.
16. Softky W, Koch C (1993) The highly irregular firing of cortical cells is inconsistent with temporal integration of random EPSPs. *J Neurosci* 13:334–350.
17. Ecker AS, Berens P, Keliris GA, Bethge M, Logothetis NK, Tolias AS (2010) Decorrelated neuronal firing in cortical microcircuits. *Science* 327:584–587.
18. Renart A, et al. (2010) The asynchronous state in cortical circuits. *Science* 327:587–590.
19. Shu Y, Hasenstaub A, McCormick D (2003) Turning on and off recurrent balanced cortical activity. *Nature* 423:288–293.

On a Theory of Precise Neural Control in a Noisy System

Wenlian Lu, Shun-ichi Amari, Jianfeng Feng, and David Waxman

Abstract In this paper, we introduce a novel computational paradigm based on modern control and optimization theory and biological observations. We investigate the ‘minimum-variance principle’ of a controlled dynamical system with noise, assuming that the noise inherent to the control signal is sub-Poisson. In this case, we find that the optimal solution of the stochastic controller is not an explicit function but is composed of a parameterized measure. Moreover, in contrast to the supra-Poisson or Poisson noise, this sort of parameterized measure can achieve precise control performance even in the presence of noise.

1 Introduction

The purpose of this paper is to introduce a mathematical framework to realize precise neural control in a noisy system. The initial motivation of the paper comes from several biological observations. Noise is believed to be inevitable since it is an intrinsic component of the signal and furthermore its magnitude could also strongly depend on the signal magnitude [1]. However, as reported in [2], the movement error is believed mainly due to inaccuracies of the neural-sensor system,

W. Lu (✉)

Centre for Computational Systems Biology, Fudan University, Shanghai, China

Brain Science Institute, RIKEN, Wako-shi, Saitama, 351-0198, Japan

S. Amari

Brain Science Institute, RIKEN, Wako-shi, Saitama, 351-0198, Japan

J. Feng

Centre for Computational Systems Biology, Fudan University, Shanghai, China

Centre for Scientific Computing, Warwick University, Warwick, UK

D. Waxman

Centre for Computational Systems Biology, Fudan University, Shanghai, China

and not associated with the neural-motor system, which implies that the neural-motor system may be precisely controlled, even with randomness. A key feature of the neural signal is that it is locally distributed and likely to have only three states, namely inactive, excited, and inhibited. To make progress in understanding how precise movement control can be achieved in a noisy environment, we shall investigate theoretical relationships which may connect the observed activity of neurons with precise control performance.

In a mathematical form, the neural control problem can be expressed as minimizing the execution error caused by the noise inherent in the control signals [3]. One characteristic of the noise is the dispersion index, α , which relates the variance in the control signal to the mean control signal and hence describes the statistical regularity of the control signal. When the variance in the control signal is proportional to the 2α -th power of the mean control signal the dispersion index of the control noise is said to be α . It was shown in [1, 3] that an optimal solution of analytic form can be found when the stochastic control signal is supra-Poisson, i.e., when $\alpha \geq 0.5$. However, the resulting control is not precise and a non-zero execution error arises.

In the present work, thanks to an elegant theory developed by Young (Young measure) [4,5], we introduce some of mathematical principles linking the regularity of the control signal noise and the precision of the resulting control performance. We consider two examples of neural control: saccadic eye movement control and straight-trajectory arm movement control, where neural spikes act as control signals, which are formulated as Gaussian processes with signal dependent variances. Our results show that if the control signal is less random than a Poisson process (i.e., $\alpha < 0.5$) then the control optimization problem naturally involves solutions with a specific character (parameterized measure optimal solutions), which can achieve precise control.

2 Methods/Models

The purpose of our control task is to minimize the variance of the final ‘value’ of a dynamical system under a constraint on its average activity. That is,

$$\begin{cases} \min_{\lambda(t)} \int_T^{T+R} \text{var}[x(t)]dt, \\ \text{subject to : } \frac{dx}{dt} = a(x(t), t) + b(x(t), t)u(t) \\ x(0) = x_0; E[x(t)] = z, t \in [T, T + R]; \\ \lambda_i(t) \in [-M_Y, M_Y], t \in [0, T + R]. \end{cases} \quad (1)$$

Here, $\text{var}(\cdot)$ and $E(\cdot)$ represent variance and expectation respectively, $x(t)$ is a state vector while $u(t) = [u_1(t), \dots, u_m(t)]^\top$ is a controller vector, $a(x, t)$ denotes the uncontrolled dynamical system and $b(x, t)$ is the gain matrix with respect to u . Let $u_i(t) = \lambda_i(t) + \zeta_i(t)$, where $\lambda_i(t)$ denotes the mean control signal

and each $\zeta_i(t)$ is an independent white noise with the properties $E(\zeta_i(t)) = 0$ and $E(\zeta_i(t)\zeta_j(t')) = \sigma_i(t)\sigma_j(t')\delta(t - t')\delta_{ij}$, while $\delta(\cdot)$ is a Dirac delta function and δ_{ij} a Kronecker delta. The noise fluctuation $\sigma_i(t)$ explicitly depend on the magnitude of the signal: $\sigma_i = \kappa_i|\lambda_i(t)|^\alpha$, with $\kappa_i > 0$, and α is the dispersion index of the control process. The aim of control is to let $x(t)$ reach a target z at time $t = T$ and stay there for the period $[T, T + R]$.

Due to limited space, we cannot provide any details in the present paper, but give a summary of the main ideas. The mathematical contents can be found in our other papers. The abstract Hamiltonian minimum (maximum) principle (AHMP) [6] provides a necessary condition for the optimal solution, which is composed of the points that minimize the integrand function of the Hamiltonian (IFH). This principle indicates that the optimal solution should be a minimum of the given IFH for each t . If the control noise is supra-Poisson or Poisson, i.e., $\alpha \geq 0.5$, then the IFH is convex (or semi-convex), which implies that there is a unique minimum of the IFH for each t . Hence the optimal solution is an explicit function, in the sense that for each t , $\lambda(t)$ is the unique value that minimizes the IFH. If, however, the control signal is sub-Poisson, i.e., $\alpha < 0.5$, then no explicit function $\lambda(t)$ exists as the optimal solution, since the IFH is not convex. However, an optimal solution that is not an explicit function but a parameterized measure, $\{\eta_t(\cdot)\}$, exists. It is called ‘Young measure’ following [4, 5] and yields a set of values on which a measure (i.e., a weighting) $\eta_t(\cdot)$ is defined for each t . And, the optimal solution of Young measure has the form $\eta_t(\cdot) = \eta_{1,t}(\cdot) \times \cdots \times \eta_{m,t}(\cdot)$, with

$$\begin{aligned} \eta_{i,t}(ds) &= [\mu_i(t)\delta(s - M_Y) + v_i(t)\delta(s + M_Y) \\ &\quad + (1 - \mu_i(t) - v_i(t))\delta(s)]ds \end{aligned} \tag{2}$$

with $\mu_i(t)$ and $v_i(t)$ non-negative and $\mu_i(t) + v_i(t) \leq 1$, $\mu_i(t)v_i(t) = 0$. In addition, we can derive that

$$\min_{\eta} \sqrt{\int_0^T \text{var}[\phi(x, t)]dt} = O(1/(M_Y^{1/2-\alpha})), \tag{3}$$

as $M_Y \rightarrow \infty$. This implies the execution error approaches zero as M_Y goes to infinity if $\alpha < 0.5$. This is in clear contrast to the situation where the control signals are Poisson or more random than Poisson (i.e., $\alpha \geq 0.5$) where the optimal control signal is an ordinary function, not a parameterized measure, and the variance in control performance cannot approach zero.

3 Results

We consider two examples of neural controls, where the control signal is described as a Gaussian process: $\lambda(t) + \sigma(t)dW_t/dt$, with the noise depending on the

frequency $\lambda(t)$, that is $\sigma(t) = \kappa|\lambda(t)|^\alpha$ for some $\alpha > 0$, $\kappa > 0$. Then, the underlying dynamical system can be formulated as Itô diffusion.

First, we consider the model (4) of saccadic eyeball movements, which was studied in [7].

$$\ddot{x} = -\frac{1}{\tau_1\tau_2}x - \frac{\tau_1 + \tau_2}{\tau_1\tau_2}\dot{x} + \gamma \left[\lambda(t) + \kappa|\lambda(t)|^\alpha(t) dW_t/dt \right], \quad x(0) = 0, \quad \dot{x}(0) = 0. \quad (4)$$

Here x is the position of the eyeball, γ , $\tau_{1,2}$ are positive parameters of the oculomotor plant, and $\lambda(t) + \kappa|\lambda(t)|^\alpha dW_t/dt$ describes the control signal accompanying with signal-dependent noise [1]. The control object is to let $x(t)$ reach a target D at time $t = T$ and stay there for a period $[T, T + R]$. We revisit this problem via the idea of Young measure. As shown in Fig. 1A(a–c) with $\alpha = 0.25$ (< 0.5), one can see that the control signal is localized (Fig. 1A(b)) and the performance of control is precise (Fig. 1A(b)), in comparison to the case $\alpha > 0.5$ which cannot achieve a precise performance (Fig. 1A(c)).

Second, we consider a more complicated model of the arm movement related to biological signal control. The sensorimotor transformations are often formalized in terms of coordinate transformation. The nonlinearity arises from the geometry of the joints. For simplicity, we neglect gravity and viscous forces, and formulate the model as (5),

$$\begin{aligned} N(\theta_1, \theta_2) \begin{bmatrix} \ddot{\theta}_1 \\ \ddot{\theta}_2 \end{bmatrix} + C(\theta_1, \theta_2, \dot{\theta}_1, \dot{\theta}_2) \begin{bmatrix} \dot{\theta}_1 \\ \dot{\theta}_2 \end{bmatrix} &= \gamma_0 \begin{bmatrix} Q_1 \\ Q_2 \end{bmatrix}, \quad \theta_1(0) = -\frac{\pi}{2}, \quad \theta_2(0) = \frac{\pi}{2}, \\ \dot{\theta}_{1,2}(0) &= 0 \end{aligned}$$

$$\text{with } N = \begin{bmatrix} I_1 + m_1 r_1^2 + m_2 l_1^2 + I_2 + m_2 r_2^2 + 2k \cos \theta_2 & I_2 + m_2 r_2^2 + k \cos \theta_2 \\ I_2 + m_2 r_2^2 + k \cos \theta_2 & I_2 + m_2 r_2^2 \end{bmatrix},$$

$$C = k \sin \theta_2 \begin{bmatrix} \dot{\theta}_2 \dot{\theta}_1 + \dot{\theta}_2 \\ \dot{\theta}_1 \ 0 \end{bmatrix}, \quad Q_i = \lambda_i(t) + \kappa_0 |\lambda_i(t)|^\alpha dW_1/dt, \quad (5)$$

where $\theta_{1,2}$ are the angles between upper arm and horizontal direction, forearm and upper arm, respectively, $\lambda_{1,2}(t)$ are control signals to two directions accompanying with signal-dependent noises, and all other symbols ($m_{1,2}$, $I_{1,2}$, $r_{1,2}$ and κ_0) are constant parameters. The relation between the position of hand ($x(t)$, $y(t)$) and the angles $\theta_{1,2}$ is $\theta_1 = \arctan(y(t)/x(t)) - \arctan(l_2 \sin \theta_2 / (l_1 + l_2 \cos \theta_2))$ and $\theta_2 = \arccos[(x^2 + y^2 - l_1^2 - l_2^2) / (2l_1 l_2)]$. For the details of the model, please refer to [8]. We are to control the final hand position to reach the given target $H = [H_1, H_2]$. We can use a numerical approach to calculate an approximate solution, as shown in Fig. 1B(b). As it is shown in Fig. 1B(a), when $\alpha < 0.5$, the optimal localized solution has a precise control performance, in comparison to the case $\alpha > 0.5$,

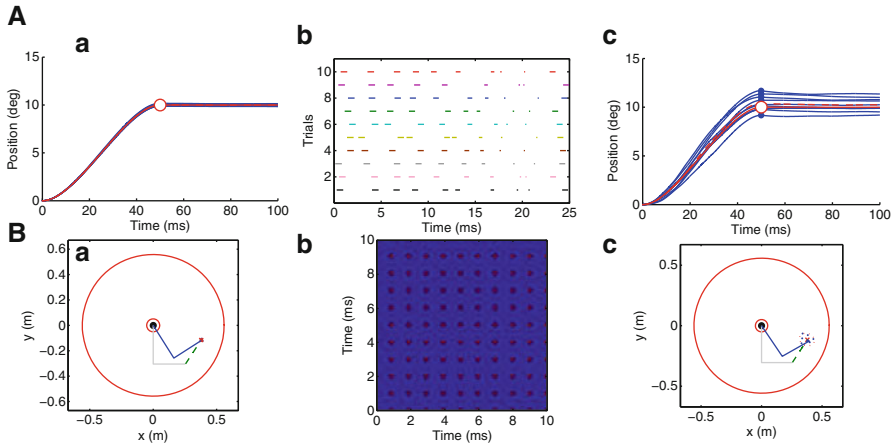


Fig. 1 Optimal control and performance. The ODE is numerically solved by the Euler method with a time step 0.01 ms. Panel A: Saccadic eye movement model with parameters $\tau_1 = 224$ ms, $\tau_2 = 13$ ms, $\gamma = 1e - 2$, $\kappa = 0.58$, $T = 50$ ms, $R = 50$ ms, $D = 10$ degree and $M_Y = 500$. (a) the dynamics of the position (in degree) under optimal control with $\alpha = 0.25$; the curves are plotted with ten overlaps (blue lines) by randomly picked initial values, the red line represents the mean over ten overlaps and the red circle is the pre-given position of the eye. (b) The localized sampling distributions of the value M_Y which is picked by the Young measure $\eta_t(\cdot)$ with ten overlaps (indicated by different colors). (c) the dynamics of the position (in degree) under the optimal control with $\alpha = 1$; the curves are plotted with ten overlaps (blue lines) by randomly picked initial values and the red line represents the mean over ten overlaps. Panel B: Straight-trajectory arm movement model with parameters $m_1 = 2.28$ kg, $m_2 = 1.31$ kg, $l_1 = 0.305$ m, $l_2 = 0.254$ m, $I_1 = 0.022$ kg·m², $I_2 = 0.0077$ kg·m², $r_1 = 0.133$ m, $r_2 = 0.109$ m, $T = 650$ ms, $R = 10$ ms, $\phi = 3\pi/4$ and $M_Y = 20,000$. (a) the movement of the arm in a platform under the optimal control with $\alpha = 0.25$. The red dash circle represents error region over ten overlaps and the gray line is the theoretical trajectory. (b) the local distribution of the optimal Young measure, where x and y axes represent the $\eta_{1,2}$ respectively, and the red points represent that $\eta_{1,2}$ are picked values at M_Y and otherwise in dark blue. (c) the movement of the arm in a platform under the optimal control with $\alpha = 1$ and the red dash circle represents error region over ten overlaps

which possess a deterministic solution but an unprecise performance as shown in Fig. 1B(c). The movement error also depends strongly on α and M_Y . The error decreases as M_Y increases and the logarithm of the standard deviation is linearly dependent on the logarithm of M_Y with a slope very near α . This relation can be described as Eq. (3) but is not shown in this paper.

References

1. Harris, C.M., Wolpert, D.M.: Signal-dependent noise determines motor planning. Nature **394** (1998) 780–784.
2. Osborne, L.C., Lisberger, S.G., Bialek, W.: Time course of information about motion direction in visual area MT. Nature **437** (2005) 412–416.

3. Harris, C. M.: On the optimal control of behaviour: a stochastic perspective. *Journal of Neuroscience Methods* **83** (1998) 73–88.
4. Young, L.C.: Generalized curves and the existence of an attained absolute minimum in the calculus of variations. *C. R. Soc. Sci. Letters de Varsovie, Cl, III* **30** (1937) 212–234.
5. Young, L.C.: Generalized surfaces in the calculus of variations. *Annals of Math.* **43** (1942) 84–103; 530–544.
6. Roubíček, T.: *Relaxation in Optimization Theory and Variational Calculus*. Berlin: Walter de Gruyter (1997).
7. Rossoni, E., Kang, J. Feng, J.F.: Controlling precise movement with stochastic signals. *Biol. Cybern.* **102:5** (2010) 441–450.
8. Winter, D.A. *Biomechanics and Motor Control of Human Movement*. Wiley-Interscience (2004).

Real-Time Wireless Sonification of Brain Signals

Mohamed Elgendi, Brice Rebsamen, Andrzej Cichocki, Francois Vialatte,
and Justin Dauwels

Abstract In this paper, an alternative representation of EEG is investigated, in particular, translation of EEG into sound; patterns in the EEG then correspond to sequences of notes. The aim is to provide an alternative tool for analysing and exploring brain signals, e.g., for diagnosis of neurological diseases. Specifically, a system is proposed that transforms EEG signals, recorded by a wireless headset, into sounds in real-time. In order to assess the resulting representation of EEG as sounds, the proposed sonification system is applied to EEG signals of Alzheimer's (AD) patients and healthy age-matched control subjects (recorded by a high-quality wired EEG system). Fifteen volunteers were asked to classify the sounds generated from the EEG of 5 AD patients and five healthy subjects; the volunteers labeled most

M. Elgendi (✉)

Institute for Media Innovation, Nanyang Technological University, Singapore, Singapore

School of Electrical and Electronic Engineering, Nanyang Technological University,
Singapore, Singapore

e-mail: elgendi@ntu.edu.sg

B. Rebsamen

Temasek Laboratories, National University of Singapore, Singapore, Singapore

e-mail: brice.rebsamen@gmail.com

A. Cichocki

Lab. ABSP, RIKEN Brain Science Institute, Wako-Shi, Japan

e-mail: cia@brain.riken.jp

F. Vialatte

ESPCI ParisTech, Paris, France

Lab. ABSP, RIKEN Brain Science Institute, Wako-Shi, Japan

e-mail: fvialatte@brain.riken.jp

J. Dauwels

School of Electrical and Electronic Engineering, Nanyang Technological University,
Singapore, Singapore

e-mail: jdauwels@ntu.edu.sg

sounds correctly, in particular, an overall sensitivity and specificity of 93.3% and 97.3% respectively was obtained, suggesting that the sound sequences generated by the sonification system contain relevant information about EEG signals and underlying brain activity.

1 Introduction

One of the interesting multidisciplinary applications of EEG is *sonification*, i.e., converting the brain waves into music.

As far as we know, sonification was for the first time attempted in 1965 by Alvin Lucier (composer) and Edmond Dewan (physicist); in their composition, called *Music for Solo Performer* [3], human brain waves control percussion instruments. Although several researchers and musicians tried to generate sound from EEG signals, there are still many open questions and challenges, and plenty of opportunities. For example, the recent advent of convenient wireless EEG headsets [4–8] may further stimulate and advance the area of EEG sonification.

In this study we design and implement a system that in real-time translates EEG signals, recorded from a wireless EEG headset, into sounds. We assess the sound representations in an offline fashion, by applying our sonification system to EEG collected from Alzheimer’s disease (AD) patients and from healthy subjects. The sounds generated from AD EEG should be distinct from sounds extracted from the EEG of healthy subjects. We investigate whether our EEG sonification system improves diagnosis of AD, following an approach proposed earlier by Vialatte et al. [9].

The paper is structured as follows. In the next section we explain our methodology. In Sect. 3 we evaluate our system *offline* by means of an EEG dataset of AD patients and control subjects. In Sect. 4 we discuss our results and offer concluding remarks.

2 Methods

The proposed sonification system has two operating modes: *offline* and *real-time* sonification. In the *offline* mode, the system extracts sounds from EEG signals that have been recorded earlier. In Sect. 3, we will apply our system to an EEG dataset from Alzheimer’s patients and control subjects, recorded by a wired high-performance EEG system. In *real-time* mode, EEG signals are acquired and immediately transformed into sounds. In the following, we will elaborate on the EEG signal acquisition. Next we will explain how we extract sounds from EEG.

2.1 Data Acquisition

The real-time EEG signals have been collected using a wireless EEG headset, specifically the Emotiv EPOC wireless headset [4] with a sampling frequency 128 Hz. The headset has 14 data collecting electrodes and two reference electrodes. The electrodes are placed approximately at the 10–20 locations AF3/4, F3/4, FC5/6, F7/8, T7/8, P7/8, and O1/2. We used the software package BCI2000 [10] to interface with the Emotiv EPOC wireless headset. The headset transmits encrypted data wirelessly to a laptop computer.

The Emotiv headset is mostly intended for entertainment (e.g., video games) rather than research or medical applications [4]. However, it is inexpensive and user-friendly, and with suitable signal processing, it may become suitable for research and clinical purposes. In particular, the device seems to be prone to various artefacts (such as eye blinking, ECG, EMG, body movements, power sources, etc.). In our ongoing work, we are developing real-time algorithms for removing artefacts, which is a crucial step towards reliable real-time EEG sonification.

2.2 Sonification

The system computes the *relative power* in three non-overlapping frequency bands (4–10, 10–20, and 20–30 Hz) and generates notes from the computed values. The EEG spectrum is known to depend on the mental state (e.g., relaxation, sleep); moreover, abnormal EEG spectra seem to be associated with neurological disorders, e.g., Alzheimer’s disease (AD) [11, 12]. We characterize the EEG spectrum by computing relative power in three different EEG frequency bands. Relative power is a simple measure that can readily be computed in real-time. In future work, we will experiment with other spectral measures as well.

We now provide more details on the sonification algorithm. The power spectrum P is calculated for each EEG channel; next *relative power* features f_1 , f_2 , and f_3 are calculated:

$$f_1 = \frac{P(4 - 10\text{Hz})}{P(4 - 30\text{Hz})} \quad f_2 = \frac{P(10 - 20\text{Hz})}{P(4 - 30\text{Hz})} \quad \text{and} \quad f_3 = \frac{P(20 - 30\text{Hz})}{P(4 - 30\text{Hz})}.$$

Those features are averaged across all channels. The averaged features are then mapped to music notes. To keep the generated sounds as simple and transparent as possible, we considered only notes from one octave (MIDI Octave -1) with pentatonic scale (five notes per octave); we limited ourselves to only one instrument (acoustic bass). Obviously, one could incorporate more music instruments and multiple octaves. However, the extracted sound easily becomes cacophonous and difficult to parse. In the future, we will explore alternative schemes to generate music from EEG relative power. We consider the following three notes and corresponding

MIDI note number: (C,48), (E,52), and (A,57). Those three notes will be played according to the three values of relative power (f_1, f_2, f_3): If feature f_i is above a certain threshold TH_i , note i is played. More precisely, the notes are generated as follows:

```
IF  $f_1 > TH_1$  THEN play bass note 48
IF  $f_2 > TH_2$  THEN play bass note 52
IF  $f_3 > TH_3$ . THEN play bass note 57.
```

The EEG is divided in consecutive segments of 1 s. In each segment the features (f_1, f_2, f_3) are computed, and notes are generated according to the above rule. Note that at most three notes can be generated for each EEG segment; that occurs when all three features are above threshold. Typically, however, one or two notes are played during each segment, which leads to simple sequences of notes. In future work, we hope to extract more melodic and harmonic compositions, perhaps by mapping features to multiple notes, music samples, natural sounds, etc.

We implemented our sonification system in Python (specifically, pyPortMidi [13] and Numpy [14]). The generated MIDI sequences are synthesized by SyFonOne [15] in conjunction with MIDI-YOKE [16]. The sound sequences are saved into MP3 files for further offline analysis.

3 Evaluation

Our sonification system translates EEG signals into sounds. It is important to verify whether the sounds are representative of EEG. To this end, we conducted a test: We asked several volunteers to use our EEG sonification system for diagnosing Alzheimer’s disease. The procedure is as follows. By means of our sonification system, we extract sounds from EEG signals of Alzheimer’s patients (AD) and age-matched control subjects. We ask the volunteers to label the generated sounds (AD vs. healthy). If the sounds reliably represent the EEG signals, it should be possible to distinguish sounds generated from AD EEG from sounds extracted from healthy EEG. Interestingly, the volunteers were indeed able to reliably classify the sounds. In the following, we describe our EEG data set; next we discuss the test procedure, and present our results.

3.1 EEG Dataset

We consider EEG data of mild-AD patients and age-matched control subjects. The EEG data set has been analyzed in previous studies [17–19]; the data was obtained using a strict protocol from Derriford Hospital, Plymouth, U.K., and had been collected using normal hospital practices [18]. This EEG dataset is composed of 24 healthy Ctrl subjects (age: 69.4 ± 11.5 years old; ten males) and 17 patients

with mild AD (age: 77.6 ± 10.0 years old; nine males). The EEG time series were recorded using 21 electrodes positioned according to Maudsley system, similar to the 10–20 international system, at a sampling frequency of 128 Hz. EEGs were band-pass filtered with digital third-order Butterworth filter (forward and reverse filtering) between 0.5 and 30 Hz. For each patient, an EEG expert selected by visual inspection one segment of 1920s artifact free EEG, blinded from the results of the present study. From each subject, one artifact-free EEG segment of 1920s was extracted and analysed.

3.2 Classification Procedure

A critical issue in our sonification system is the choice of thresholds TH_i . Depending on the application, we can determine the thresholds through various statistical principles. In the application at hand, we determine the thresholds TH_i with the aim of detecting AD EEG. We noticed that relative EEG power has substantially different values in AD patients than in healthy subjects. By appropriately choosing the thresholds, the generated sounds will differ as well. Following this reasoning, we have determined the thresholds as follows:

$$TH_1 = \frac{(\mu_A(f_1) - \sigma_A(f_1)) + (\mu_H(f_1) + \sigma_H(f_1))}{2},$$

$$TH_2 = \frac{(\mu_H(f_2) - \sigma_H(f_2)) + (\mu_A(f_2) + \sigma_A(f_2))}{2},$$

$$TH_3 = \frac{(\mu_H(f_3) - \sigma_H(f_3)) + (\mu_A(f_3) + \sigma_A(f_3))}{2}.$$

where μ_A and σ_A is the mean and standard deviation respectively of the features for AD EEG, and likewise μ_H and σ_H for healthy (control) EEG. Those choices of thresholds can be understood as follows. For example, relative power in the 4–10 Hz band is clearly larger in AD patients. Therefore, we choose the corresponding threshold TH_1 below the mean value (of relative power in the 4–10 Hz band) for AD EEG and above the mean value for control EEG. As a result, for AD EEG the threshold TH_1 will be reached more often, which will lead to more frequent low-pitch notes (bass note 48). Similarly, AD EEG will yield fewer high-pitch notes (E,52) and (A,57). Now we explain our survey in more detail. We asked 15 volunteers to listen to the generated sounds, and to guess whether they stem from AD patients or healthy subjects. Particularly, we asked each volunteer to classify sound sequences from ten different subjects (one sequence from each subject). Each volunteer was asked to score the sound sequences from 0 to 10 (0: certainly healthy, 5: unsure, and 10: certainly Alzheimer's). We did not provide any further details about the sound files.

Prior to this test, each volunteer was trained with sound sequences from four subjects (2 AD patients and two healthy subjects), so that they can learn to appreciate how the sounds generally differ in both subjects groups; we also briefly explained how the sounds were generated, and emphasized that, in our sonification scheme, AD EEG tends to generate more low-pitch notes.

4 Results

Overall, the volunteers were able to reliably label the sound sequences; they correctly classified 95% of the subjects, with *sensitivity* of 93.3% and *specificity* of 97.3%. Note that we tested just ten subjects out of 41, and classification on the entire database might be worse. Nevertheless, this experiment demonstrates that the proposed sonification system translates EEG into meaningful sounds, which can for example be used for detecting EEG abnormalities (as in, e.g., AD EEG).

As a benchmark, we conducted linear discriminant analysis (LDA) with the same features (f_1 , f_2 , f_3) for the same ten subjects; we average those features over the entire EEG segment of 1920s. In other words, we do not consider here individual EEG segments of 1 s. We compute classification rates through leave-one-out crossvalidation. It is noteworthy that through this approach, at most 90% of the subjects are correctly classified. In contrast, our sonification system yielded classification rates of 95%.

5 Discussion and Conclusion

In this study we have developed a system that translates EEG signals (acquired by a *wireless* headset) to *sounds* in *real-time*. The proposed sonification system has been validated *offline* by means of a small EEG data set, collected with high quality wired EEG headset.

Interestingly, the results show that the presented sonification algorithm can be used to differentiate *offline*, by listening to their sonified EEG, the subject with the mild Alzheimer's disease from control subjects with 95% accuracy (see samples on internet [20]), and therefore, it seems the *real-time* system can be used as a reliable AD diagnostic tool.

Acknowledgments Mohamed Elgendi and Justin Dauwels would like to thank the Institute for Media Innovation (IMI) at Nanyang Technological University (NTU) for partially supporting this project (Grant M58B40020).

References

1. Berger, H.: Über Das Elektrenkephalogramm Des Menschen. *Archiv für Psychiatrie und Nervenkrankheiten* 87 (1929) 527–570
2. Berger, H.: On the Electroencephalogram of Man. *Electroencephalography and Clinical Neurophysiology* (1969) 28:133
3. Lucier, A.: Statement on: music for solo performer. *Biofeedback and the Arts: Results of Early Experiments* (Vancouver, Canada: Aesthetic Research Centre of Canada) (1967)
4. EmotivSystems. Emotiv - brain computer interface technology. <http://emotiv.com>.
5. Imec: http://www2.imec.be/be_en/press/imec-news/imecEEGMWest.html.
6. NeuroFocus: <http://www.neurofocus.com/>.
7. MKS: <http://www.mks.ru/eng/Products/EEG/Neurobelt/>.
8. Biopac: <http://www.biopac.com/researchApplications.asp?Aid=23&AF=437&Level=3>.
9. Vialatte, F., Musha, T., Cichocki, A.: Sparse Bump Sonification: a New Tool for Multichannel EEG Diagnosis of Brain Disorders. *Artificial Intelligence in Medicine* (2010)
10. BCI2000 - General-Purpose System for Brain Computer Interface <http://www.bci2000.org/BCI2000/Home.html>.
11. Dauwels, J., Srinivasan, K., Reddy, R., Musha, T., Vialatte, F., Latchoumane, C., Jeong, J., Cichocki, A.: Slowing and loss of complexity in Alzheimer's EEG: Two sides of the same coin? *International Journal of Alzheimer's Disease*(in press) (2011)
12. Vialatte, F., Cichocki, A., Dreyfus, G., Musha, T., Rutkowski, T.M., Gervais, R.: Blind Source Separation and Sparse Bump Modelling of Time Frequency Representation of Eeg Signals: New Tools for Early Detection of Alzheimer's Disease. Paper presented at the IEEE Workshop on Machine Learning for Signal Processing, 28–28 Sept. 2005
13. <http://alumni.media.mit.edu/~harrison/code.html>.
14. <http://new.scipy.org/download.html>.
15. <http://www.synthfont.com/>.
16. <http://www.midiox.com/>.
17. Goh, C., Ifeachor, E., Henderson, G., Latchoumane, C., Jeong, J., Bigan, C., Besleaga, M., Hudson, N., Capotosto, P., Wimalaratna, S.: Characterisation of EEG at different stages of Alzheimer's disease (AD). *Clinical Neurophysiology* 117 (2006) 138–139
18. Henderson, G., Ifeachor, E., Hudson, N., Goh, C., Outram, N., Wimalaratna, S., Del Percio, C., Vecchio, F.: Development and assessment of methods for detecting dementia using the human electroencephalogram. *IEEE Transaction on Biomedical Engineering* 53 (2006) 1557–1568
19. Dauwels, J., Vialatte, F., Latchoumane, C., Jeong, J., Cichocki, A.: EEG synchrony analysis for early diagnosis of alzheimer's disease: A study with several synchrony measures and EEG data sets. Paper presented at the 31st Annual International Conference of the IEEE EMBS, Minneapolis, Minnesota, USA,
20. <http://sonification.webs.com/audio.htm>.

Part IV
Spatiotemporal Network Dynamics
and Biological Timing

Oscillator Cell Networks in the Hypothalamic Suprachiasmatic Nucleus, the Mammalian Circadian Clock

Sato Honma, Daisuke Ono, and Ken-ichi Honma

Abstract The master circadian clock of the mammals locates in the hypothalamic suprachiasmatic nucleus (SCN) which is composed of multiple oscillator cells. Cellular oscillators mutually synchronize to form several regional pacemakers which further couple to make-up the master circadian clock for coherent rhythm expression in physiology and behavior. In the present experiment, bioluminescent imaging of cultured SCN from mice carrying a *Per1* promoter-driven luciferase reporter revealed two separate pacemakers which locate in the anterior and posterior SCN, and regulate the onset and offset of behavioral activity, respectively. Thus the activity time is photoperiodically regulated depending on seasons. The neuronal and molecular mechanisms for forming the regional pacemakers are still poorly understood, however, *Per1* and *Per2* are suggested to have different roles in the photoperiodic clock. Furthermore, CRY1 and CRY2 seem to be involved in coupling between these oscillators.

1 Introduction

Mammalian circadian clock is located in the hypothalamic suprachiasmatic nucleus (SCN) which is composed of about 20,000 neurons in mice and rats. In the dispersed cell culture, about 70–80% SCN neurons with spontaneous firing show significant circadian rhythms in their firing rate, suggesting that most of SCN neurons possess an autonomous circadian oscillator. In addition, circadian periods of dispersed SCN

S. Honma (✉) • K.-i. Honma
Department of Chronomedicine, Hokkaido University Graduate School of Medicine,
Sapporo 060-8638, Japan
e-mail: sathonma@med.hokudai.ac.jp

D. Ono
Photonic Bioimaging Section, Research Center for Cooperative Projects,
Hokkaido University Graduate School of Medicine, Sapporo 060-8638, Japan

neurons followed Gaussian distribution in a relatively wide range from 20 to 30 h [1]. Therefore, synchronization among cellular oscillators is critical for circadian rhythm expression in physiological functions. In the organotypic slice culture of the SCN, the distribution of the circadian period in single neuronal rhythms became much narrower, between 22 and 26 h, but the average circadian periods were similar to that of dispersed cell culture. The result suggests that mutual coupling of single cell oscillators depends on cell architecture within the SCN. Circadian rhythms were also observed in the release of neuropeptides from cultured SCN slices. We previously reported synchronized circadian rhythms in the release of vasopressin (AVP) and Vasoactive intestinal polypeptide (VIP) [2]. However, two rhythms were desynchronized to each other by antimitotic treatment in the beginning of the culture, suggesting oscillatory cell networks form at least two regional pacemakers in the SCN.

Currently, an autoregulatory transcriptional and translational feedback loop is regarded as the intracellular molecular clock machinery. In the loop, heterodimeric transcription factors, CLOCK and BMAL1, activate transcription of *Period* (*Per*) 1, *Per*2, *Cryptochrome* (*Cry*) 1 and *Cry*2. The protein products PERs and CRYs translocate into the nucleus and bind CLOCK/BMAL1 heterodimers to suppress their own transcription, thus closing the feedback loop. A single turn of the feedback loop takes about 24 h. *Per*1 and *Per*2 are induced by phase-resetting light signals but with different kinetics. CRY1 and CRY2 are regarded as indispensable for the loop to turn and *Cry*1 and *Cry*2 double deficient (*Cry*1^{-/-}/*Cry*2^{-/-}) mice are regarded as “clock-less” mutants, because they become behaviorally arrhythmic immediately after they were exposed to constant darkness (DD). On the other hand, we previously reported that *Cry*1^{-/-}/*Cry*2^{-/-} mice exhibit behavior rhythms with circadian periodicity by chronic treatment with methamphetamine, a potent dopamine releaser in the central nervous system [3]. The finding suggested that *Cry*1^{-/-}/*Cry*2^{-/-} mice are not arrhythmic mutant but have an oscillatory system which can exhibit rhythms with circadian periodicity.

Recently firefly luciferase reporter genes are utilized for monitoring gene expression in living cells in real-time. In the present experiment, by using transgenic mice carrying a *Per*1 promoter driven-luciferase gene, we examined (1) location and functions of regional pacemakers which measure photoperiods and interface seasonal changes in the environments to bodily functions, and (2) coupling mechanisms within and between these regional oscillators in the SCN.

2 Methods

Animals: We used adult and newborn mice of C57BL/6J background carrying a *Per*1 promoter driven luciferase reporter gene (*Per*1-*luc*). We also used *Cry*1^{-/-}/*Cry*2^{-/-} mice carrying a *Per*1 reporter gene (*Cry*1^{-/-}/*Cry*2^{-/-}). They were housed in controlled environmental conditions, 12 h light-12 h dark condition (LD 12:12), lights-on 6:00–18:00, unless otherwise stated. All experiments were

conducted in accordance with the Guidelines for the Care and Use of Laboratory Animals in Hokkaido University.

Behavioral activity recording: Adult male mice were singly housed in a light-tight box. Spontaneous locomotor activity was measured every minute by an infrared thermal sensor in Experiment 1, and wheel-running activity rhythm was measured in Experiment 2.

SCN culture: For measuring *Per1-luc* rhythms, we made coronal SCN slices from adult mice kept in LD and measured bioluminescence either from the entire SCN slice using a photomultiplier or from single SCN cells by bioluminescence imaging with an EMCCD camera as described elsewhere [4].

For measuring neuronal activity, we made a coronal SCN slice of 200 μm thick from 2 to 5 day old pups and plated on a collagen precoated multi electrode array dish (MED) with 64 electrodes in the area of 0.56 mm^2 . They were cultured as described elsewhere with minor modification [5]. Spontaneous discharges of signal/noise >2.0 were simultaneously recorded from 10 to 19 electrodes.

Rhythm analysis: Significant circadian rhythmicity was evaluated by a chi-square periodogram using data of 5 consecutive days between 10.0 and 40.0 h with a significance level of 0.01.

Experimental protocols: In Experiment 1, we exposed adult male mice to one of following three different photoperiods for more than 3 weeks, LD 6:18, LD 12:12, and LD 18:6. After measuring behavior rhythms, brains were sampled for culturing two serial coronal SCN slices, anterior and posterior slices. We also made horizontal slices to further identify the regional pacemakers. In Experiment 2, we used *Cry1^{-/-}/Cry2^{-/-}* and control mice carrying a *Per1-luc* reporter. Adult mice kept in LD 12:12 were used for bioluminescence imaging, and 2–5 day old mice were used for MED recording.

3 Results

Experiment 1: The peak phase of *Per1-luc* rhythms always appeared earlier in the posterior SCN than in the respective anterior SCN. Irrespective of photoperiods, posterior peaks were phase-locked to the end of activity, suggesting the site of the pacemaker regulating the activity end, and the anterior peaks, to the activity onset, suggesting the site of the pacemaker regulating the activity onset. Under LD18:6, a bimodal *Per1-luc* pattern appeared only in the anterior SCN which gradually merged together in 5 days of culture. Single cell analyses by bioluminescence imaging revealed that the bimodal patterns are composed of two oscillating cell groups with the early and late peaks (Fig. 1). These findings indicate that there are three oscillating cell groups in the SCN which constitute regionally specific circadian pacemakers and regulate photoperiodic response of behavioral rhythm. The *Per1-luc* rhythms from horizontal slices further localized the site of three pacemakers in the SCN. However, *Per1-luc* rhythms are not always in phase with

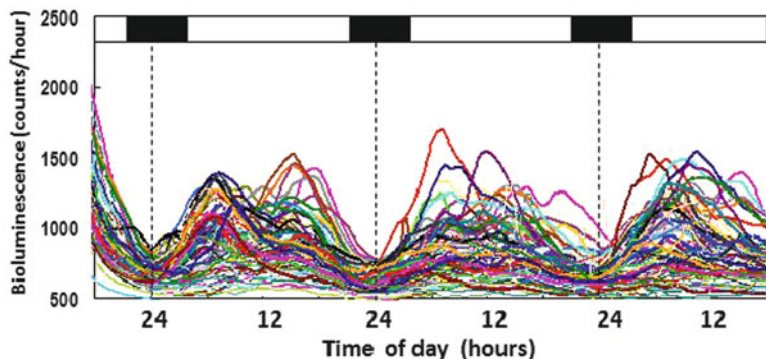


Fig. 1 *Per1-luc* rhythms in single cells of an anterior SCN from mice in LD18:6 revealed two regional oscillating cell groups. Dark horizontal bars indicate the subjective night

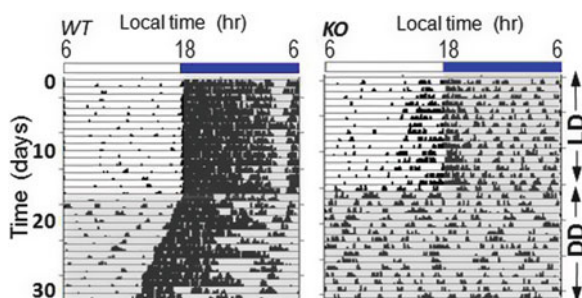


Fig. 2 Representative wheel-running activity records of a wild type mouse (WT) and *Cry1^{-/-}/Cry2^{-/-}* mouse (KO). Number of wheel revolutions in every 5 min was plotted as a histogram. Shaded areas indicate dark period. White and dark horizontal bars on the top indicate light and dark period under LD

Per2 rhythms, suggesting the different phase adjustment in *Per2* expression. In addition, the location of regional pacemakers was not coincided with the distribution of major neuropeptides, AVP and VIP, in the SCN.

Experiment 2: Behavioral rhythms of CRY deficient mice: *Cry1^{-/-}/Cry2^{-/-}* mice showed significant 24 h circadian rhythms under LD in their behavior activity, and became arrhythmic immediately after they were exposed to constant darkness (DD) (Fig. 2). However, the activity onset under LD was not always observed at the dark onset in *Cry1^{-/-}/Cry2^{-/-}* as in the wild type mice. The mean activity onset was located at 14.8 ± 2.7 h (\pm SD, $n = 14$) which was significantly advanced compared with that of wild type (18.0 ± 0.1 h). Among 14 *Cry1^{-/-}/Cry2^{-/-}* mice examined, the activity onsets of ten mice were located 2–10 h before the dark onset. These findings suggest that the circadian behavioral rhythm of *Cry1^{-/-}/Cry2^{-/-}* mice in LD is not due to simple masking by light but rather an expression of oscillatory entrainment to LD.

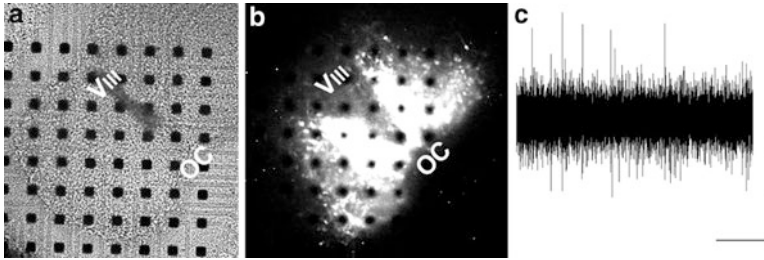


Fig. 3 A bright field image of SCN slice culture on an MED probe (a) and bioluminescence image of A (b). *Black squares* are electrodes. *OC* optic chiasm, *V_{III}* the third ventricle. Spontaneous discharges from the SCN were shown with scale bars (50 μ V, 0.5 s) (c)

In a cultured SCN slice of wild type mice, all SCN cells examined showed robust circadian bioluminescent rhythms. They were synchronized within a single SCN slice as demonstrated by the robust circadian rhythms in a whole SCN slices. The peak phases were located in the middle of the subjective day on the first day of culture similar to those *in situ*. In the SCN slices from *Cry1^{-/-}/Cry2^{-/-}* mice, most single SCN cells showed significant but less robust circadian bioluminescent rhythms. However, significant rhythms were not detected in a whole SCN, and the rhythms in a single SCN slices were desynchronized. The peak phases of cellular rhythms distributed in an extremely wide range even on the first day of culture, which markedly contrasted with the consolidated circadian peaks at the subjective noon in the control cells. These results indicate that individual SCN cells can exhibit circadian *Per1-luc* rhythms without CRYs, but they are desynchronized in a cultured SCN slice.

Robust and significant firing rhythms were also detected from all recorded electrodes in the wild type mice (Fig. 3). Interestingly, spontaneous firing of individual neurons exhibited robust and synchronized circadian rhythms in a cultured SCN slice of *Cry1^{-/-}/Cry2^{-/-}* mice.

4 Discussions

By monitoring *Per1-luc* rhythms, we demonstrated three regional pacemakers in the SCN. Two of them separately entrain to the light-on and light off signals and regulate the offset and onset of behavioral rhythms, thus change the activity time, the duration of active period in a day, depending of seasons. The long-lasting model for seasonal adaptation of behavioral rhythms is the two mutually coupled oscillators which separately respond to dawn (E-oscillator) and dusk (M-oscillator) and regulate the activity onset and end, respectively [6]. The two oscillating cell groups of synchronous *Per1* rhythms demonstrated the localization of the E and M oscillators within the SCN. The role of the third oscillator is not known, but seems

to relate dawn or dusk signals. The molecular mechanisms for the couplings within and between these regional oscillators are not known. VIP released from the ventral SCN and VIP receptors in the SCN are known to involve in oscillator networks in the SCN [7]. But other mechanisms may be involved in the present results. Since they are not photoperiodic, and VIP receptor deficient mice can exhibit behavioral rhythms in DD. The present study also suggested CRY1 and CRY2 are involved in the oscillatory network in the SCN. A lack of these proteins results in behavioral arrhythmicity in the constant condition, yet *Cry1*^{-/-}/*Cry2*^{-/-} mice still have some mechanism for entraining light-dark cycles.

In the SCN, there are different levels of oscillatory networks; multiple molecular networks within a single cells, networks among cellular oscillators within a regional pacemaker and those among regional pacemakers. The hierarchical multi-oscillator pacemaker system seems to be advantageous to adapt flexibly to a large variability of environmental cycles without losing stable and precise oscillation. Since there are different levels of networks in the SCN, disruption of oscillatory networks at any level would result in arrhythmicity in rhythm outputs.

References

1. Honma S et al. Diversity in the circadian periods of single neurons of the rat suprachiasmatic nucleus depends on nuclear structure and intrinsic period. *Neurosci. Lett.* **358**:173–176, 2004.
2. Shinohara et al. Two distinct oscillators in the rat suprachiasmatic nucleus *in vitro*. *Proc. Natl. Acad. Sci USA* **92**:7396–7400,1995.
3. Honma S et al. Circadian behavioral rhythms in *Cry1/Cry2* double deficient mice induced by methamphetamine. *J.Biol.Rhythms*, **23**:91–94, 2008.
4. Inagaki N et al. Separate oscillating cell groups in mouse suprachiasmatic nucleus couple photoperiodically to the onset and end of daily activity. *Proc Natl Acad Sci USA*, **104**:7664–7669, 2007.
5. Nakamura W et al. *Clock* mutation lengthens the circadian period without damping rhythms in individual SCN neurons. *Nature Neurosci.* **5**:399–400, 2002.
6. Pittendrigh C. and Daan S. A functional analysis of circadian pacemakers in nocturnal rodents. V. Pacemaker structure : a clock for all seasons. *J. Comp. Physiol. A.* **106**, 333–355, 1976.
7. Maywood ES. et al. Synchronization and maintenance of timekeeping in suprachiasmatic circadian clock cells by neuropeptidergic signaling. *Curr: Biol.* **16**, 599–605, 2006.

Oscillator Network Modeling of Circadian Rhythm in the Suprachiasmatic Nucleus

Isao Tokuda, Hirokazu Fukuda, and Naoto Hayasaka

Abstract Oscillator network model is presented for the simulation of phase waves observed in a cultured slice of the suprachiasmatic nucleus (SCN). The coupling matrix is obtained by partial synchronization analysis of the bioluminescence image data, which represent gene expression signals. Numerical simulations show that the coupling matrix itself is not sufficient for the network model to reproduce the phase waves. Our study implies that additional condition such as gradient distribution of the oscillation periods is necessary to reproduce the dynamics of the measurement data.

1 Introduction

Biological clocks, the generators of the circadian rhythm with a natural period of nearly 24 h, are ubiquitous in almost all living organisms. In mammals, the master circadian clock is located in the suprachiasmatic nucleus (SCN) of the brain. In the rat SCN, at least two subregions have been reported, i.e., the ventrolateral

I. Tokuda (✉)

Department of Mechanical Engineering, Ritsumeikan University, Kusatsu, Shiga, 525-8577, Japan

e-mail: isao@fc.ritsumei.ac.jp

H. Fukuda

Department of Mechanical Engineering, Graduate School of Engineering, Osaka Prefecture University, Sakai, Osaka, 599-8531, Japan

PRESTO, Japan Science and Technology Agency (JST), Kawaguchi, Saitama, 332-0012, Japan

N. Hayasaka

PRESTO, Japan Science and Technology Agency (JST), Kawaguchi, Saitama, 332-0012, Japan

Department of Neuroscience, Graduate School of Medicine, Yamaguchi University, Ube, Yamaguchi, 755-8505, Japan

Y. Yamaguchi (ed.), *Advances in Cognitive Neurodynamics (III)*,

DOI 10.1007/978-94-007-4792-0_26,

© Springer Science+Business Media Dordrecht 2013

SCN (vlSCN, core) and the dorsomedial SCN (dmSCN, shell). The SCN is a network of approximately 20,000 neurons. Within each individual neuron, clock genes and proteins compose interlocked regulatory loops that generate circadian oscillations on molecular level [1]. SCN neurons dispersed in cell cultures display cell-autonomous oscillation, with periods ranging from 20 to 28 h [2, 3]. Coupling and synchronization among SCN neurons are ensured by neurotransmitters and other factors. How such a network of heterogeneous circadian oscillators achieves a synchronous and coherent output rhythm has motivated extensive experimental and theoretical works [4–6]. Although anatomical studies provide a deep insight into the SCN physiology [7, 8], yet they are not enough to identify the core mechanism that maintains the synchronized neuronal rhythmicity in the SCN. Interestingly, recent technology of bioluminescence imaging has revealed synchronization of the SCN neurons and the robust temporal gradients in circadian clock gene expression in cultured SCN slices, which persist for weeks [9]. This kind of coordinated and recurring gradients, which we refer to as “phase wave,” potentially reflect unique and critical characteristics of the central circadian clock. Little is however known about the mechanism underlying the propagation of the phase wave and its biological significance.

In nonlinear physics, wave propagation in spatio-temporal system is usually induced by local diffusive coupling in the oscillatory media. This implies that the propagation of the phase wave in SCN is primarily due to local coupling among the neurons [10]. On the other side, it has been also speculated that there exists a monotonic gradient in the spatial distribution of the oscillation periods of the SCN neurons [11]. Such gradient may strongly contribute to the formation of the phase wave even under the global coupling. Towards understanding the mechanism underlying the phase wave, the present paper studies the effect of two factors, i.e., coupling function among the neurons and gradient distribution of the neuronal periods, on the formation of the phase wave observed in the SCN.

2 Experimental Data

Transgenic rats carrying a *Per2::Luciferase* reporter gene were generated [10]. Coronal brain slices including the SCN (300 μm thickness) were prepared from 2-week-old rat. Bioluminescence was measured with a luminescence microscope optimized for live cell imaging. The recording duration was 7 days.

To characterize the spatiotemporal dynamics of the circadian oscillations in the cultured SCN slices, phase of the bioluminescence oscillations in each pixel was computed by the peak picking technique, which defines inter-peak-interval as one cycle [12]. Moving images of the phase dynamics shows that the phase waves were initiated from the innermost dmSCN and traveled regularly from the dmSCN to the vlSCN with a velocity of about 0.2 mm/h [10].

3 Partial Phase Synchronization Analysis

In the SCN, neuronal oscillators are synchronized to achieve a coherent output rhythm. From such global coherence, it is important to distinguish direct and indirect dependencies among the neurons. To make such distinction, partial phase synchronization analysis [13] was carried out. This methodology has been developed based on the concept of graphical models and partialization analysis to phase signals of nonlinear synchronizing systems.

Consider phases of N neurons $\{\Phi_k(t)|k = 1, 2, \dots, N\}$. First, synchronization matrix is computed as

$$\mathbf{R} = \begin{pmatrix} 1 & R_{1,2} & \cdots & R_{1,N} \\ R_{1,2}^* & 1 & \cdots & R_{2,N} \\ \vdots & \vdots & \ddots & \vdots \\ R_{1,N}^* & R_{2,N}^* & \cdots & 1 \end{pmatrix}.$$

using pairwise synchronization indices of $R_{k,l} = \frac{1}{T} \sum_t \exp i[\Phi_k(t)\Phi_l(t)]$. $\Phi_k(t)$ represents phase of k -th neuron. The asterisk denotes complex conjugation. Then, the inverse $PR = R^{-1}$ of the synchronization matrix \mathbf{R} provides partial phase synchronization index

$$R_{k,l|Z} = \frac{|PR_{k,l}|}{\sqrt{PR_{k,k}PR_{l,l}}}$$

between k -th and l -th neurons conditioned on the remaining neurons $\{\Phi_Z(t)|Z = 1, \dots, N; Z \neq k, l\}$. If the phase synchronization index $R_{k,l}$ is considerably different from zero, while the corresponding partial phase synchronization index is close to zero ($R_{k,l|Z} \approx 0$), there is a strong evidence for an indirect coupling between k -th and l -th neurons.

From the bioluminescence image data, gene expression signals of 83 neuronal points were picked up at different locations ($N = 83$). The partial phase synchronization analysis was then applied. Since the oscillations of the SCN slice show strong coherent activity, the synchronization indices $R_{k,l}$ were all high. In contrast, partial phase synchronization index $R_{k,l|Z}$ were variable. Figure 1 shows the partial phase synchronization indeces $R_{k,l|Z}$ between the neuron located by white box and the neurons located by colored boxes. The red and purple colors indicate strong coherence associated with direct interaction, whereas blue colors indicate weak coherence with indirect interaction. We see that the neighboring neurons tend to exhibit a strong partial coherence, whereas strong coherences exist also in some of the long-range connections. Figure 2 shows dependence of the partial synchronization index $R_{k,l|Z}$ on the distance $d_{k,l}$ between k -th and l -th neuronal points. Although the distribution is rather noisy, the regression line of

Fig. 1 Partial phase synchronization indexes $R_{k,l|Z}$ between one neuron (*white box*) and another (*colored box*). The *red* and *purple* colors indicate strong partial coherence ($R_{k,l|Z} \approx 1$) associated with direct interaction, whereas *blue* colors indicate weak coherence ($R_{k,l|Z} \approx 0$) associated with indirect interaction

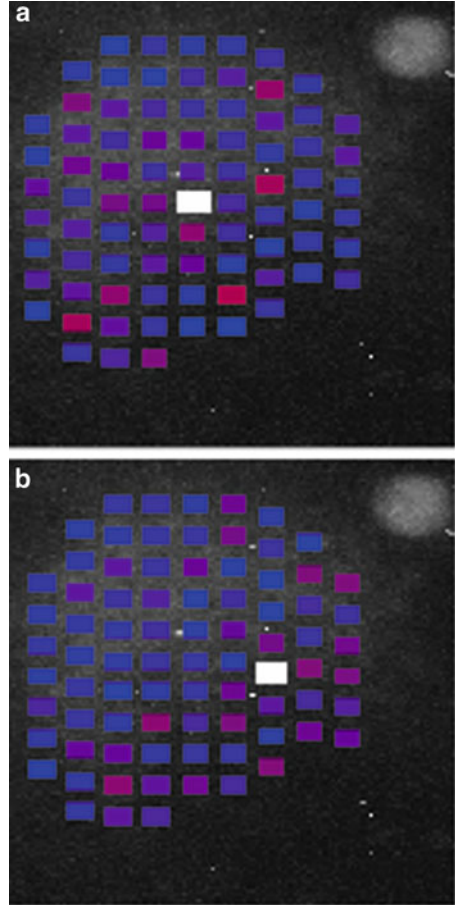
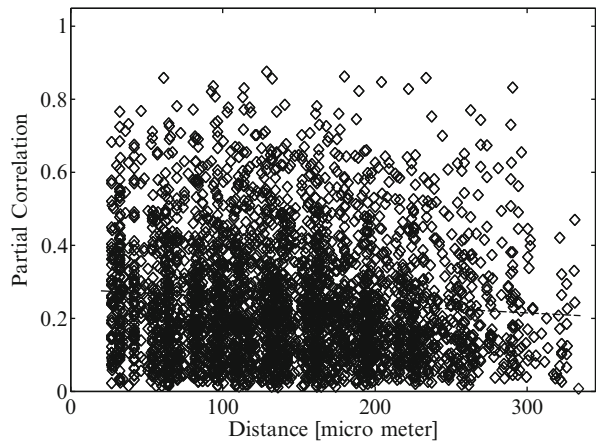


Fig. 2 Dependence of the partial phase synchronization index $R_{k,l|Z}$ on the distance $d_{k,l}$ between k -th and l -th neuronal points. The *dotted line* represents a regression line of $R_{k,l|Z} = -0.00022d_{k,l} + 0.28$



$R_{k,l|Z} = -0.00022d_{k,l} + 0.28$ indicates an abstract tendency that the partial coherence is weakened as the interaction range becomes longer. The noisy structure might be partially due to the estimation error caused by the limited duration of measurement and inaccurate extraction of the phase.

4 Modeling Study

4.1 Mathematical Modeling

Mathematical modeling based on Stuart-Landau equations was utilized for studying the synchronization-induced rhythmicity in the SCN.

$$\dot{z}_j = (\alpha_j + i\Omega_j - |z_j|^2)z_j + \frac{K}{N} \sum_{k=1}^N T_{k,j}(z_k - z_j),$$

where $j = 1, \dots, N$ ($N = 83$), the overdot means differentiation with respect to time t , z_j is the complex amplitude of the j th neuron, Ω_j is the natural frequency, K represents the coupling strength among the neurons, and Hopf parameter α_j determines whether j -th neuron is self-sustained or damped oscillator. In the numerical simulations, the Hopf parameter was randomly chosen as $\alpha_j \sim N(0, 0.1^2)$. As the coupling matrix, the partial phase synchronization indices were utilized ($T_{k,j} = R_{k,j|Z}$).

We test whether the coupling matrix \mathbf{T} , obtained by the partial phase synchronization analysis is sufficient to generate the phase waves or additional condition is necessary. Two conditions were examined. (A) Natural periods ($2\pi/\Omega_j$) of the neurons were randomly distributed as $\sim N(24, 1.5^2)$, while natural period was set to be 25 h only for the rightmost neurons next to vSCN (in accordance with experimental measurement [11]). (B) Natural periods ($2\pi/\Omega_j$) were monotonically increased from 23 to 25 h in the direction from the innermost dmSCN to vSCN.

4.2 Simulation Results

With a strong coupling K , mutual synchronization among all neurons was achieved for both conditions. In condition (A) with random setting of the natural periods, the phase wave was not observed. On the other hand, in condition (B) with gradient distribution of the natural periods, phase waves, which travel from the innermost dmSCN to vSCN, were clearly observed. Figure 3 shows the phase profiles observed in conditions (A) and (B). Condition (A) exhibits random ordering of the phases. Condition (B), on the other hand, gives rise to a monotonic decrease in the phase profile,

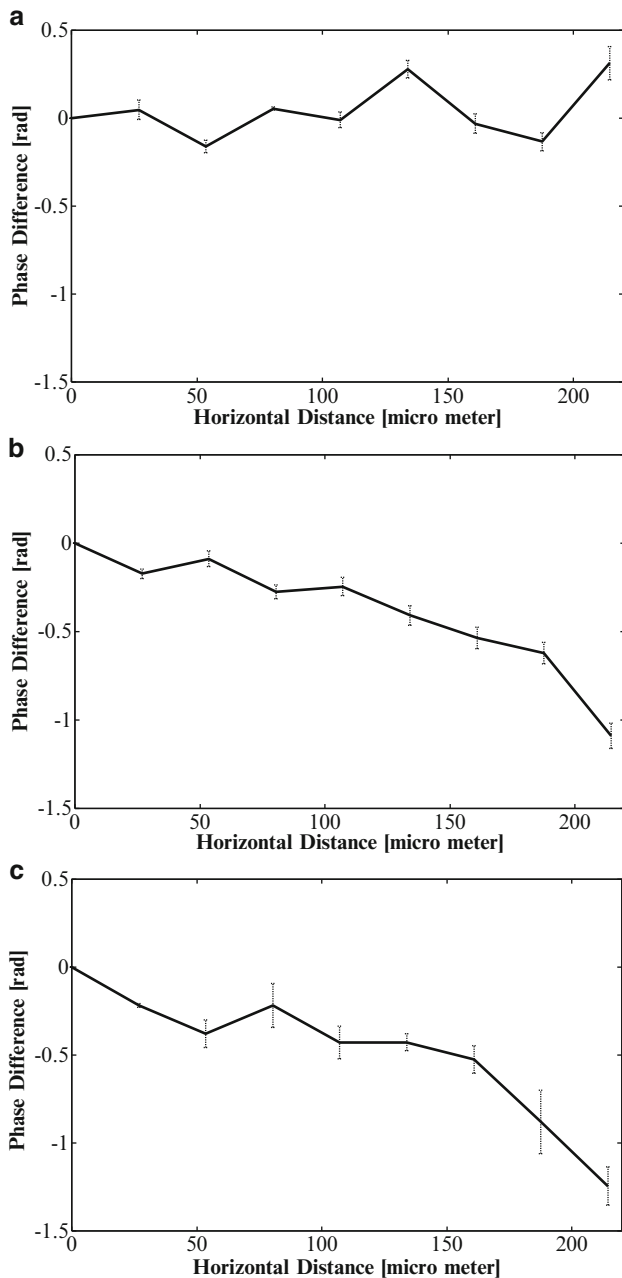


Fig. 3 Phase profile of neurons located from innermost dmSCN to outer dmSCN. (a) and (b) correspond to simulation conditions of (A) and (B), respectively, where (c) corresponds to real data from the bioluminescence imaging technique

which is quite similar to the measurement data. This implies that the coupling matrix itself is not sufficient to produce the phase wave and that gradient distribution of the oscillation periods is necessary to reproduce the measurement data.

5 Discussions

In summary, our quantitative analysis and mathematical model simulation of the phase wave propagation provided new insights into the network structure of the SCN neurons. The partial phase synchronization analysis revealed that the neurons are connected directly with neighboring neurons. Direct connections however exist also among distant neurons. Simulations of the oscillator network showed that the network structure itself could not well reproduce the phase wave. Additional condition such as the gradient distribution of the neuronal periods was necessary for the simulation of the phase waves. Our study needs further careful examination. In particular, limitation of the partial synchronization analysis due to short duration of the measurement data should be taken into account. It is of great interest to clarify possible functional roles of the phase waves from biological perspective.

References

1. Reppert, S.M., Weaver, D.R. *Nature* **418** (2002) 935.
2. Welsh, D.K., *et al.* *Neuron* **14** (1995) 697.
3. Honma, S., *et al.* *Neurosci. Lett.* **358** (2004) 173.
4. Aton, S.J., Herzog, E.D. *Neuron* **48** (2005) 531.
5. Kori, H., Mikhailov, A.S. *Phys. Rev. Lett.* **93** (2004) 254101.
6. Bernard, S., *et al.* *PLoS Comput. Biol.* **3** (2007) e68.
7. Pennartz, C.M.A., *et al.* *J. Physiol.* **506–3** (1998) 775.
8. Shirakawa, T., *et al.* *Chronobiology International*, **18–3** (2001) 371.
9. Yamaguchi, S., *et al.* *Science* **302** (2003) 1408.
10. Fukuda, H., *et al.* *PLoS ONE* **6** (2011) e23568.
11. Noguchi, T., *et al.* *Eur. J. Neurosci.* **20** (2004) 3199.
12. Pikovsky, A., *et al.* *Synchronization* (Cambridge: Cambridge University Press, 2001).
13. Schelter, B., *et al.* *Phys. Rev. Lett.* **96** (2006) 208103.

In Vivo Monitoring of Circadian Output in *Clock* Mutant Mice

Wataru Nakamura

Abstract It is well established that the suprachiasmatic nucleus (SCN) is the master circadian pacemaker in behavior and vice versa locomotor activity rhythm reflect SCN function as well. In this paper, we reported functional correlations between the SCN and locomotor activity in circadian systems by using direct read out of neuronal activity in the SCN and *Clock* mutant mice as effective tools. Further behavioral analysis revealed a possibility of unknown circadian oscillatory mechanism.

Keywords Circadian rhythm • Suprachiasmatic nucleus • Locomotor activity • Social interaction

1 Introduction

The master circadian clock in mammals is located in the suprachiasmatic nucleus (SCN) of the anterior hypothalamus, drives the daily circadian rhythms of the physiological and behavioral processes. The SCN functions as a self-sustained oscillator and is synchronized to the environmental 24-h light-dark (LD) cycles. Although circadian rhythm generation appears to be the property of individual SCN neurons, SCN tissue organization seems to be responsible for synchronizing the multiple oscillator neurons and producing an ensemble period that closely matches the period of the locomotor rhythm [1, 2]. Significant progress has been made in

W. Nakamura (✉)

Laboratory of Oral Chronobiology, Osaka University Graduate School of Dentistry, 1-8, Yamadaoka, Suita, Osaka 565-0871, Japan

PRESTO, Japan Science and Technology Agency (JST), 4-1-8 Honcho, Kawaguchi, Saitama 332-0012, Japan

e-mail: wataru@dent.osaka-u.ac.jp

manifesting the molecular mechanism underlying the mammalian circadian system. The core molecular circuitry of opposing interlocking transcriptional feedback loops has been defined as the fundamental basis of the circadian clock [3]; however, the network complexity of the clock system is becoming apparent [4–6]. Consequently, we are seeking how these cell-autonomous circadian oscillators interact in multicellular organisms to regulate physiology and behavior.

The mouse *Clock* mutation was identified in an N-ethyl-Nnitrosourea mutagenesis screen for circadian variants [7]. *Clock* is a semidominant mutation [8] that lengthens circadian period by 1 h in heterozygotes (*Clock/+*) and by 4 h in homozygotes (*Clock/Clock*). With prolonged exposure, *Clock* homozygotes fail to express persistent circadian rhythms in constant darkness. The lengthened-period and loss-of-rhythm phenotypes are the hallmarks of the original mutant allele.

The apparent complexity of the circadian control over the locomotor activity rhythms, drive us to monitor neuronal activity of the SCN in freely moving mice [9]. In the present study, we have used this technique to describe the characteristics of the SCN *in vivo*, the differences between the *Clock* mutant and wild-type combining with the detailed behavioral analysis. The purpose of this study is to elucidate the certain responses to environmental cues in behavioral circadian rhythms. Those results provide a new framework for understanding the regulation of locomotor rhythms in the circadian timing system.

2 Methods

Animals. Wild-type and *Clock* mutant mice were used in this study. Genotypes were determined for each individual by using a PCR mutagenesis method before surgery. The breeding colony was kept on a 12 h light: 12 h dark cycle (light on at 0800 h); food and water available ad libitum; light intensity of 200 lx at cage level.

Locomotor Activity recording. The mice were housed individually in standard cages (182 × 260 × 128 mm) placed in light-tight, ventilated boxes. Locomotor activity was detected with a passive infrared sensor (Biotex, Kyoto, Japan) positioned 30 cm above the center of the cage floor. Activity counts were monitored continuously by computer which can control light-dark cycle for each recording boxes and summed and stored at 1 min intervals. ClockLab (Actimetrics, IL) was used for analysis and display of activity data.

In Vivo Multiunit Neural Activity Recording. In vivo multiunit neural activity recording (MUA) from SCN was performed as previously described [9]. Simultaneously with neural activity monitoring, the locomotor activity in individual mice also was detected with a passive infrared sensor.

Social entrainment analysis. Pairs of female *Clock/+* and wild-type mice, 2 months old at the beginning of the experiment, were formed from animals previously kept in litter mate groups. Those pairs of mice were housed in cages and locomotor activity

was detected with a passive infrared sensor under constant darkness. After paired recording, each mouse was transferred to individual cages and monitored locomotor activity separately. Determination of the circadian period in individual records was obtained by the method of the chi square periodogram.

3 Results and Discussions

Light entrainment of the Clock/Clock mouse. The entrainment behavior of *Clock/Clock* mice to a light-dark cycle (LD) of 12 h: 12 h (LD12:12) appeared relatively normal. To determine whether photic entrainment may have been altered in *Clock/Clock* mice, we examined the phase relationship to the light cycle of LD 4:20, 2:22 and 1:23 (Fig. 1). The difference between the two genotypes was clearly seen when the durations of light period were shortened. Wild-type mice had negative phase angle of activity onset to the light off in all of 24 h light cycles. On the other hand, *Clock/Clock* mice showed positive phase angle under LD 4:20 and 2:22, consequently, the shortened light phases hit on those activity off. The LD 1:23 condition did not entrain *Clock/Clock* mice fully and we observed the “relative

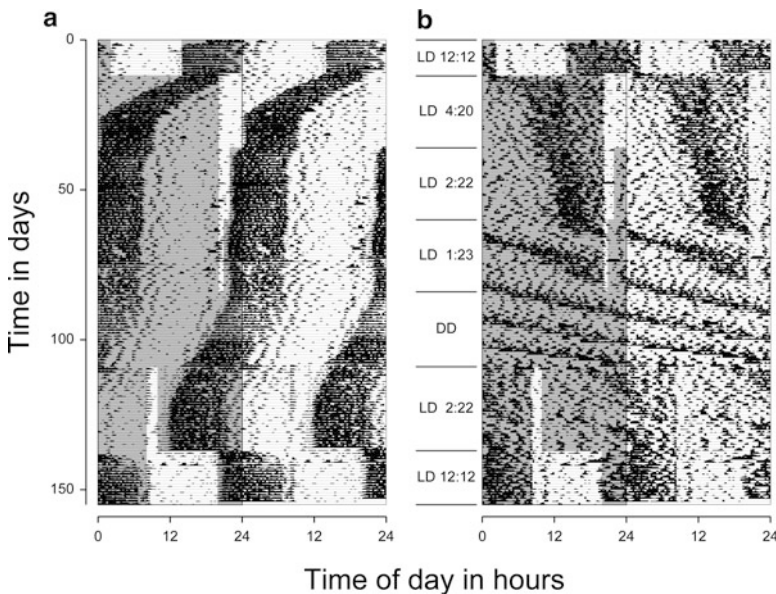


Fig. 1 Light entrainment to 24 h LD cycle in the locomotor activity rhythms of wild-type (a) and *Clock/Clock* (b) mice. Behavioral records are double-plotted. The gray and clear areas on the first part of actograms indicate the LD conditions denoting at the middle. The actograms show clear differences between the two genotypes in circadian property including free-run period and phase response to the lights

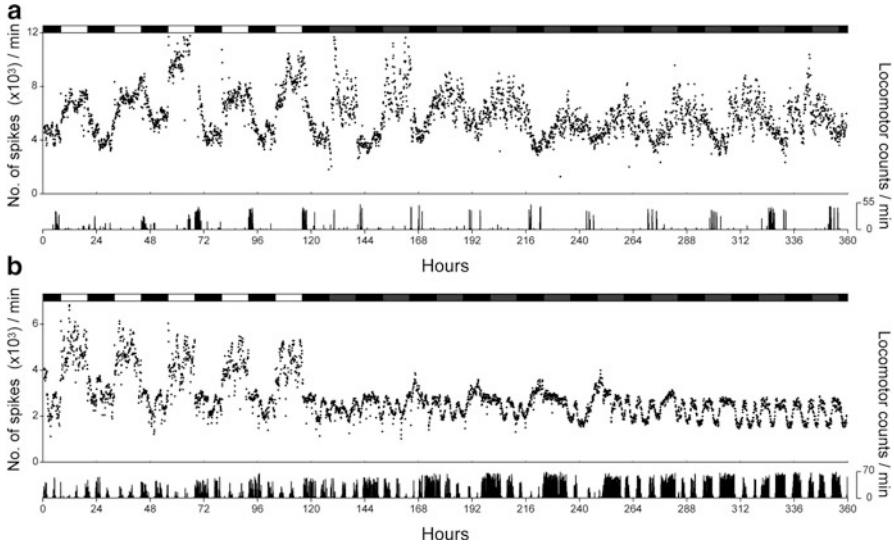


Fig. 2 Circadian rhythms of MUA in the Clock/Clock SCNs. Serial-plotted actograms of neural and locomotor activity show a long-lasting circadian rhythm (a) and a damping rhythm (b). Lighting condition is indicated at the top of the figure. Bottom trace represents simultaneous recorded locomotor activity. The number of spikes for MUA or activity counts for locomotor activity was counted every minute and integrated every 6 min

coordination” of lengthened circadian rhythms of the mutant mice. Under constant darkness (DD), the mutant mouse showed free-run rhythm with a period of 27.0 h. The wild-type mouse was entrained to LD 2:22 after several LD regimes with larger phase angle than before (Fig. 1a) and the *Clock/Clock* failed to be entrained to the 24 h cycle (Fig. 1b). Those suggest the “after effects” of circadian rhythms [10] in both genotypes.

Damping circadian rhythms of MUA in the Clock/Clock SCN. As previously reported [9] *Clock/Clock* mice exhibited elevated MUA during the day in the SCN under LD 12:12 (Fig. 2). After released in DD, one of homozygous mutants exhibited a long lasting free-running rhythm both in locomotor and MUA in the SCN (Fig. 2a). The peak in MUA occurred in the middle of the subjective day and in antiphase with locomotor activity. Another *Clock/Clock* mouse showed damping circadian locomotor rhythm for up to five cycles (Fig. 2b). When the mutant mouse showed the damping rhythm, a small elevation of MUA in the SCN occurred just before the onset of behavioral activity. That “anticipatory” elevation of MUA disappeared when the mouse got arrhythmic in locomotor activity except for an ultradian rhythm.

Functional input into the SCN. MUA in the SCN showed light response in circadian phase dependent manner. During the subjective day, the baseline discharge was relatively high and 1 h light pulse during this phase elicited only small responses

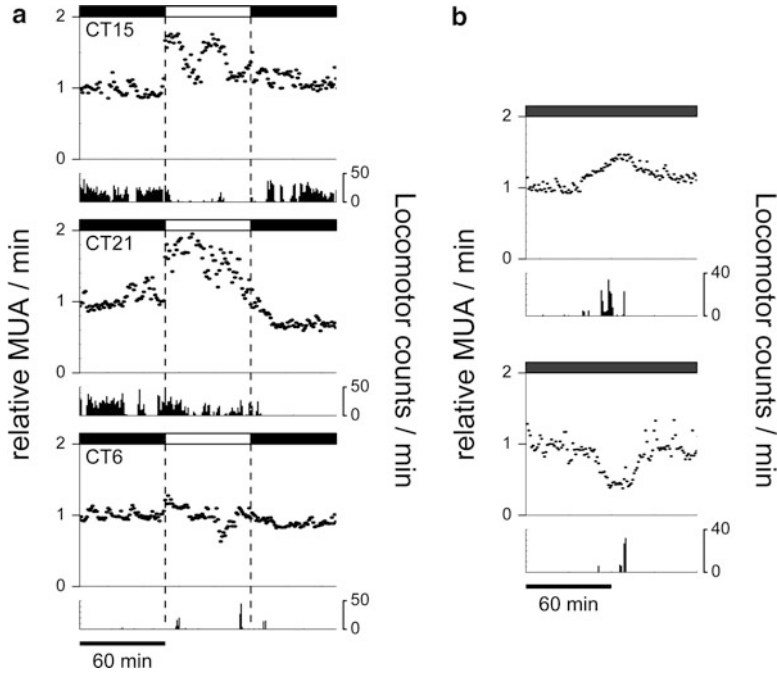


Fig. 3 Light response and correlation with locomotor activity of MUA in the wild-type SCN. Both MUA and locomotor activity were plotted in 1 min bins. MUA were normalized with the mean counts of pre- 60 min of light pulse (a). Positive (b, top) and negative (b, bottom) correlation were observed in different mice suggesting a regional heterogeneity within the SCN

(Fig. 3a bottom). During the subjective night, when baseline discharge was in its lower phase, large light responses were obtained for CT15 (Fig. 3a top) and CT21 (Fig. 3a middle). The MUA responses corresponded behavioral phase shift, phase delay of CT15, phase advance of CT21 and no phase shift of CT 6. Even though subtle light response during subjective day, certain correlation between MUA in the SCN and locomotor activity were observed (Fig. 3b). Because positive or negative correlations were consistent throughout the MUA recording, those directions might be dependent on the regional heterogeneity within the SCN. The functional effects of the behavioral feedback on the SCN remain to be elucidated.

Social interaction as a zeitgeber? By using of approximately 1 h difference of intrinsic circadian period between wild-type and *Clock*^{+/+} mice, we examined the effect of social interaction on circadian systems. The actograms from a pair of females showed two components of circadian rhythmicity (Fig. 4a, b). Those two components might attribute to each intrinsic circadian periods of the SCN in two genotypes because individual females showed their own period after separation (Fig. 4a, left for wild-type, right for *Clock*^{+/+} mice). We observed that some mice continued to show two circadian rhythmicities for several cycles after separation.

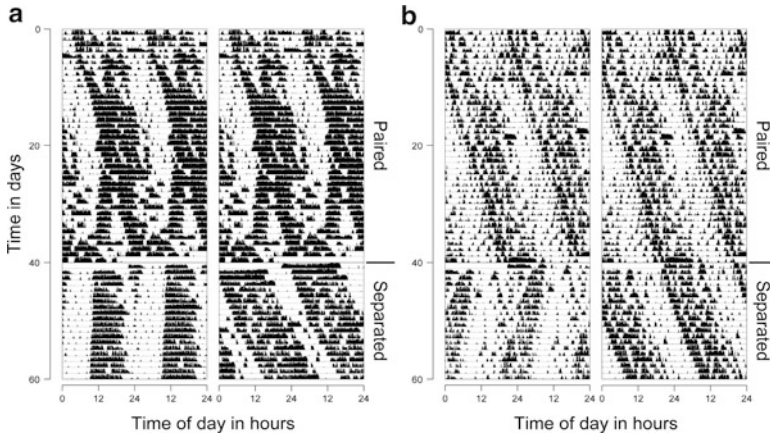


Fig. 4 Implication of a “social entrainable circadian pacemaker”. Two representative actograms of social interaction trials are shown (**a**, **b**). For the first 40 days, locomotor activity of paired wild-type and *Clock*/+ mice were monitored in a same cage under DD. Then the pair was separated and monitored in individual recording box. The first part of actograms were duplicated and followed to individual recordings, respectively. The lefts are for wild-type and the rights are for *Clock*/+ mice in either actograms (**a**, **b**)

One seems to be its own circadian period and the other was in accordance with the period of another genotype (Fig. 4b, left for wild-type). Although, the substantial to be determine, we propose that the second component might be controlled by social entrainable oscillator; SEO. Seeking the “SEO” circuit within and/or out of the SCN might be an intriguing challenge and we can extend our understandings of circadian systems beyond the SCN.

Acknowledgments This work was supported by Osaka University Life Science Young Independent Researcher Support Program through Special Coordination Funds for Promoting Science and Technology, and JST PRESTO program.

References

1. Nakamura, W. et al.: Clock mutation lengthens the circadian period without damping rhythms in individual SCN neurons. *Nat. Neurosci.* 5 (2002) 399–400.
2. Nakamura, W. et al.: Differential response of *Period 1* expression within the suprachiasmatic nucleus. *J. Neurosci.* 25 (2005) 5481–5487.
3. Ko, C.H. and Takahashi, J.S.: Molecular components of the mammalian circadian clock. *Hum. Mol. Genet.* 15 (2006) R271–R277.
4. Yamazaki, S. et al.: Resetting central and peripheral circadian oscillators in transgenic rats. *Science* 288 (2000) 682–685.
5. Abe, M. et al.: Circadian rhythms in isolated brain regions. *J. Neurosci.* 22 (2002) 350–356.
6. Liu, A.C. et al.: Intercellular coupling confers robustness against mutations in the SCN circadian clock network. *Cell* 129 (2007) 605–616.

7. Vitaterna, M.H. et al.: Mutagenesis and mapping of a mouse gene, *Clock*, essential for circadian behavior. *Science* 264 (1994) 719–725.
8. King, D.P. et al.: Positional cloning of the mouse circadian clock gene. *Cell* 89 (1997) 641–653.
9. Nakamura, W. et al.: In vivo monitoring of circadian timing in freely moving mice. *Curr. Biol.* 18 (2008) 381–385.
10. Pittendrigh, C.S. and Daan, S.: A functional analysis of circadian pacemakers in nocturnal rodents. *J. Comp. Physiol. A* 106 (1976) 223–252.

Modular Organization Enables Both Self-Organized Criticality and Oscillations in Neural Systems

Shengjun Wang, Claus C. Hilgetag, and Changsong Zhou

Abstract Neural networks in the brain display prominent hierarchical modular organization and complicated rhythmical oscillations. We systematically study the phenomenon of sustained activity in hierarchical modular networks, which are obtained by rewiring initially random networks. We find that a hierarchical modular architecture can generate sustained activity better than random networks. More importantly, the system can simultaneously support rhythmical oscillations and self-organized criticality, which are not present in the respective random networks. These results imply that the hierarchical modular architecture of cortical networks plays an important role in shaping the ongoing spontaneous activity, allowing the system to take the advantages of both the sensitivity of critical state and predictability and timing of oscillations for efficient information processing.

1 Introduction

Understanding the large-scale organization of the structure and dynamics in the brain from the viewpoint of complex networks has become a new frontier in neuroscience [1, 2], because the architecture of networks in brain always impacts neural system's dynamical behaviors and the dynamics underlie the mechanisms of the brain's functions.

One of the most prominent structural features in the neural system of the brain is the organization of modules, structured hierarchically from large-scale regions

S. Wang • C. Zhou (✉)

Department of Physics, Centre for Nonlinear Studies, Hong Kong Baptist University,
Kowloon Tong, Hong Kong
e-mail: cszhou@hkbu.edu.hk

C.C. Hilgetag

School of Engineering and Science, Jacobs University Bremen, Bremen, Germany

of the whole brain, via cortical areas and area subcompartments organized as structural and functional maps, to cortical columns, and finally circuits made up of individual neurons [3]. Meanwhile, the networks display self-organized sustained activity, which is persistent in the absence of external stimuli. At the systems level, such activity is characterized by complex rhythmical oscillations over a broadband background, such as α , θ , and δ oscillations [4]. While at the cellular level, neuronal discharges have been observed to display avalanches, indicating that cortical networks are at the state of self-organized criticality (SOC) [5]. Self-organized criticality is a concept proposed in physics that mimics the avalanche of sandpiles, and is an ubiquitous property of complex systems, such as piling of granular media, earthquakes, and forest fire, etc. [6–8]. The concept asserts that a system self-organized into a critical state is characterized by scale invariance. At such a critical state, signals and perturbations can efficiently propagate over broad spatio-temporal scales. Critical behavior in neural models has been shown to bring about optimal computational capabilities, optimal transmission, storage of information and sensitivity to sensory stimuli [9]. And SOC has been suggested playing an important role in human perceptual functions [10].

SOC is characterized by power-law distribution of the size of avalanches, indicating that there is no characteristic scale. On the contrary, rhythmic oscillations suggest that neural activity possesses typical scales and is predictable to certain extent. How these two apparently contradictory dynamical properties are unified in the neural dynamics is a question that has not been addressed in the studies of neurodynamics. In this work, we use numerical simulations to show that the modular network organization provides such a template to unify them.

Within the modules, the activity of the neural firing is characterized by SOC, while the weak interaction between the modules makes it possible that the avalanches of some modules can act as the weak input to other modules, leading to sustained activity without external stimulus.

2 Method/Models

We carried out intensive numerical simulations of a balanced neural network model [11]: there are 80% excitatory neurons and 20% inhibitory neurons. The dynamics of the membrane potential is described as

$$\tau \frac{dV}{dt} = (V_{rest} - V) + g_{ex}(E_{ex} - V) + g_{inh}(E_{inh} - V).$$

The value of the time constant is $\tau=20$ ms, the resting membrane potential is $V_{rest} = -60$ mV, reversal potentials of synapses for excitatory and inhibitory neurons are $E_{ex} = 0$ mV and $E_{inh} = -80$ mV. When an excitatory (or inhibitory) neuron fires, the synaptic variables g_{ex} (g_{inh}) of its postsynaptic targets are increased by Δg_{ex} (or Δg_{inh}). Otherwise, synaptic variables decay exponentially with the time constants $\tau_{ex} = 5$ ms and $\tau_{inh} = 10$ ms.

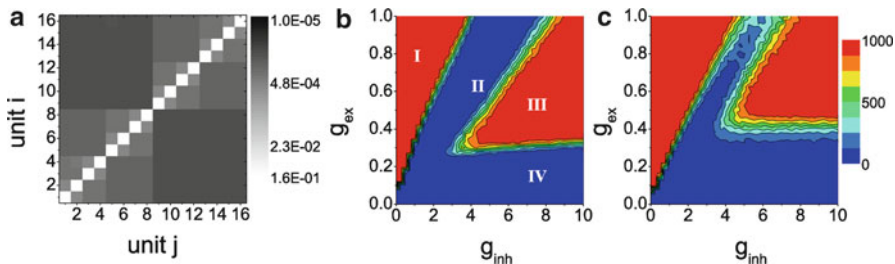


Fig. 1 (a) Connection density matrix of a 4-level HMN. Network size is $N = 10,000$, $R_{ex} = 0.99$. (b, c) Average duration of network activity in the parameter space (Δg_{inh} , Δg_{ex}). The results are averaged over 100 realizations of (b) random networks and (c) 4-level HMNs with $R_{ex} = 0.99$, respectively

The strengths of excitatory and inhibitory neurons are such that in a broad range, the average input current of a neuron from the excitatory pool is roughly canceled by that of the inhibitory pool; however, the fluctuations can be so large to exceed the firing threshold in sparse random networks with large enough number of neurons (10,000 neurons in our simulations). This will lead to sustained irregular activity in such a balanced random network of neurons. In our study, we introduced modular structure into the network connectivity. Beginning with random networks, the neurons are divided into groups and the connections between groups are moved into groups with a probability R . Then connections are denser within the group but much sparser between the groups, while maintaining the total connections the same as the original random networks. We can further divide the modules into sub-modules to obtain a hierarchical modular network (HMN). See Fig. 1 for an example of a 4-level HMN with 16 modules, each having $N/16 = 625$ neurons. Considering the fact that inhibitory couplings form local connections and excitatory couplings provide long-distance interactions, we rewire inhibitory inter-module connections with the probability $R_{ex} = 1$, and rewire excitatory inter-module connections with $0 < R_{ex} < 1$.

3 Results

In random networks, balance between excitation and inhibition exists in a region of the parameter space of the strength of the excitatory and inhibitory synapses (Δg_{inh} , Δg_{ex}), which allows the neural network to sustain irregular activity without external signals. In simulations, the networks were stimulated by noise in an initial period of time. Figure 1b and c show how long the activity sustained after noise is removed. The region III of the Fig. 1b represents the irregular sustained activity in random networks [12]. When the rewiring probability $R_{ex} = 0.99$, although modules are dense and small, the irregular sustained region is maintained in HMNs, as shown in Fig. 1c.

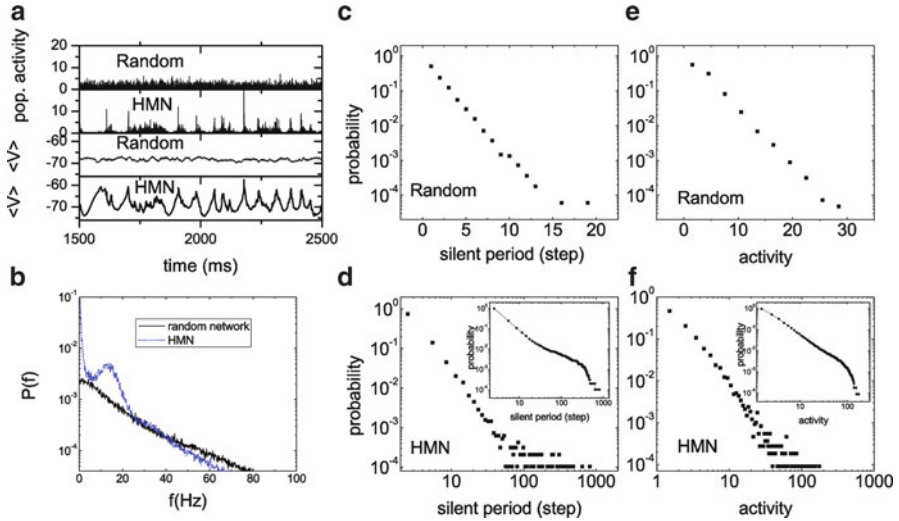


Fig. 2 (a) Population activity of an ensemble of neurons in a random network and of a module in the HMN rewired from the random network (*upper panels*), and corresponding average membrane potentials (*lower panels*). (b) Power spectrum density of average potentials in random networks (*black*) and HMNs (*blue*). (c) and (d) Distributions of the silent period in an ensemble of neurons in random networks and in a module of HMNs. (e) and (f) Distribution of the activity size in networks corresponding to (c) and (d). The insets in (d) and (f) show the cumulative distributions of silent period and activity size in modules of HMNs

However, different from quite homogeneous random activity in random networks, the activity patterns in modular networks is very heterogeneous. In Fig. 2a, we compare the activity of one module in a 4-level HMN obtained at $R_{ex} = 0.99$ and the activity of the corresponding ensemble of neurons in the random network before rewiring. The HMN displays intermittence with bursts of relatively strong activity separated by distinct silent periods, while the activity in the random network continues at a lower level, but without discernible silent intervals.

The intermittent activity of modules in the HMN exhibits the characteristics of avalanche dynamics. We analyzed the distribution of the size of each activity of a module and the lengths of the silent interval between two activities. In Fig. 2c and e, distributions of both the silent interval and the activity size in random networks are straight lines when plotted in log-linear form, showing that the distributions follow exponential functions. On the contrary, the distributions of modules in HMNs display straight lines in the log-log plot (Fig. 2d, f). Therefore in the HMN both the silent interval and the activity size are distributed according to the power-law functions.

Power-law distribution of avalanche size is the fingerprint of the self-organized criticality [9]. These results show that HMNs are close to critical states, while the random networks are not. The observation of critical states is consistent with experimental data which showed a power-law distribution of the neuronal avalanche size [5] or the intervals between large energy fluctuations [13].

Another significant effect of the intermittent dynamics in HMNs is the emergence of low frequency activity. In Fig. 2a one can see the fluctuation of the average potential of modules in HMNs is more significant than that of random networks and exhibits the characteristics of rhythmic oscillations. We perform an analysis by calculating the power spectrum density of the average potential of networks. Figure 2b shows that in random networks the power decays monotonically as the frequency increases. In the HMNs with $R_{ex} = 0.99$, a pronounced peak appears at low frequency around 15 Hz.

4 Conclusion/Discussions

We studied the effect of hierarchical modular structure on the dynamics of the sustained activity of neural networks with both excitatory and inhibitory neurons. The modular property can support the irregular sustained activity. More importantly, we found that the coexistence of SOC and oscillations could be realized in modular neural networks. Our results provide a new mechanism of sustaining activity and generating oscillations in cortex-like neural network that captures the most prominent structural features: the hierarchical modular organization and the coexistence of excitatory and inhibitory neurons.

Our further analysis shows that cutting SOC off at finite size due the limited number of neurons within the module could be one of the reasons that leads to the oscillations of the network collective activity. Currently we are exploring the implications of the combination of SOC and oscillations in information processing, which should shed light on the structure-function relationship in the brain. Further studies on the role and advantages of HMNs in information processing are interesting, and are potentially useful for understanding neural activities underlying perceptual functions.

Acknowledgments This work was partially supported by Hong Kong Baptist University and the Hong Kong Research Grants Council (HKBU 202710) and a grant from the Germany/Hong Kong Joint Research Scheme sponsored by the Research Grants Council of Hong Kong and the German Academic Exchange Service (Reference No. G-HK 006/08). This research was conducted using the resources of the High Performance Cluster Computing Centre, Hong Kong Baptist University.

References

1. Sporns, O., Chialvo, D., Kaiser, M., Hilgetag, C.: Organization, development and function of complex brain networks. *Trends Cogn. Sci.* 8 (2004), 418–425.
2. Bullmore, E., Sporns, O.: Complex brain networks: graph theoretical analysis of structural and functional systems. *Nat. Rev. Neurosci.* 10 (2009), 186–198.
3. Hilgetag, C., Burns, G., O’Neill, M., Scannell, J., Young, M.: Anatomical connectivity defines the organization of clusters of cortical areas in the macaque monkey and the cat. *Phil. Trans. R. Soc. Lond. B* 355 (2000), 91.

4. Buzsaki, G.: *Rhythms of the Brain*. Oxford University Press, USA. (2006)
5. Beggs, J., Plenz, D.: Neuronal avalanches in neocortical circuits. *J. Neurosci.* 23 (2003), 11167.
6. Bak, P.: *How nature works: the science of self-organized criticality*. Springer (1996).
7. Bak, P., Tang, C., Wiesenfeld, K.: Self-organized criticality: An explanation of the $1/f$ noise. *Phys. Rev. Lett.* 59 (1987), 381–384.
8. Jensen, H. J.: *Self-Organized Criticality: Emergent Complex Behavior in Physical and Biological Systems*. Cambridge University Press (1998).
9. Levina, A., Herrmann, J. M., Geisel, T.: Dynamical synapses causing self-organized criticality in neural networks. *Nat. Phys.* 3 (2007), 857–860.
10. Shimonono, M., Owaki, T., Amano, K., Kitajo, K., and Takeda, T.: Functional modulation of power-law distribution in visual perception. *Phys. Rev. E* 75 (2007), 051902.
11. Vreeswijk, C., Sompolinsky, H.: Chaos in neuronal networks with balanced excitatory and inhibitory activity. *Science* 274 (1996), 1724.
12. Vogels, T. P., Abbott, L. F.: Signal Propagation and Logic Gating in Networks of Integrate-and-Fire Neurons. *J. Neurosci.* 25 (2005), 10786–10795.
13. Worrell, G., Cranstoun, S., Echaux, J., Litt, B.: Evidence for self-organized criticality in human epileptic hippocampus. *Neuroreport* 13 (2002), 2017.

Traveling Waves in Locally Connected Chaotic Neural Networks and Their Phenomenological Modeling

Makito Oku and Kazuyuki Aihara

Abstract The emergence of traveling waves is a universal property of nervous systems. However, mechanisms of these waves and their functional roles have not yet been fully elucidated. Here, we numerically investigate traveling waves in a locally connected large-scale chaotic neural network (CNN) consisting of more than one million units. We simulate it by parallel computing and visualize the network output by using color images. If the refractoriness of neurons is sufficiently large, many local cell assemblies are generated and the boundaries between them move as traveling waves. We also develop a simplified phenomenological model for the CNN by adding a negative self-feedback mechanism to the Potts model. The proposed meso-scopic model can qualitatively reproduce complex wave patterns in the CNN. Because the model requires less computational resources, it may serve as a useful tool for investigating traveling waves in nervous systems.

1 Introduction

The emergence of traveling waves is a universal property of nervous systems. These waves have been widely observed experimentally in many organs such as the retina [1, 2], olfactory cortex [3], neocortex [4–6], hippocampus [7], and cerebellum [8].

M. Oku (✉)

Graduate School of Information Science and Technology, The University of Tokyo,
7-3-1 Hongo, Bunkyo-ku, Tokyo, 113-8656, Japan
e-mail: oku@sat.t.u-tokyo.ac.jp

K. Aihara

Graduate School of Information Science and Technology, The University of Tokyo,
7-3-1 Hongo, Bunkyo-ku, Tokyo, 113-8656, Japan

Institute of Industrial Science, The University of Tokyo, 4-6-1 Komaba, Meguro-ku,
Tokyo, 153-8505, Japan

Furthermore, theoretical and numerical analyses support the idea that traveling waves are easily generated in locally connected neural networks [9–13]. However, mechanisms of traveling waves and their functional roles have not yet been fully elucidated.

Detailed investigation of traveling waves requires large-scale simulations. This is because traveling waves are meso-scopic phenomena and involve a large number of neurons. Certain types of traveling waves are actually observable only in large-scale simulations [12].

Usually, the term “traveling waves” refers to the phenomenon of activation of some local region in the brain, and propagation of the activity to neighboring regions. However, not only the strength of neural activity but also higher-order properties may propagate in the actual brain. One such example of traveling waves is those of cell assemblies in a locally connected associative memory model [14, 15]. Here, cell assemblies refer to particular patterns of active and inactive neurons. Movement of boundaries between the assemblies results in alternation of local activity patterns.

In this study, we first numerically investigate traveling waves in a locally connected large-scale neural network. Then, we develop a simplified phenomenological model for the network.

2 Models

2.1 Chaotic Neural Network Model

In this study, we use the chaotic neural network (CNN) model [16, 17]. This network is composed of N units, each of which has two internal variables η_i and ξ_i and one output variable y_i . The units also receive a uniform and time-invariant external input. Let us adopt the vector representation $\boldsymbol{\eta} = \{\eta_1, \dots, \eta_N\}^T$, $\boldsymbol{\xi} = \{\xi_1, \dots, \xi_N\}^T$, and $\mathbf{y} = \{y_1, \dots, y_N\}^T$. Then, the model dynamics can be described by the following difference equations:

$$\boldsymbol{\eta}(t + 1) = k_f \boldsymbol{\eta}(t) + W \mathbf{y}(t), \quad (1)$$

$$\boldsymbol{\xi}(t + 1) = k_r \boldsymbol{\xi}(t) - \alpha \mathbf{y}(t) + \mathbf{a}, \quad (2)$$

$$\mathbf{y}(t + 1) = \mathbf{f}(\boldsymbol{\eta}(t + 1) + \boldsymbol{\xi}(t + 1)), \quad (3)$$

where $W = (w_{ij})$ denotes the $N \times N$ weight matrix; $0 \leq k_f, k_r \leq 1$, the decay constants; $\alpha \geq 0$, the strength of the refractoriness; and $\mathbf{a} = \{a, \dots, a\}^T$, the bias that includes the external input and the threshold. The activation function \mathbf{f} is an operation that applies the logistic function $f(x) = (1 + \exp(-x/\epsilon))^{-1}$ to each element of the argument vector, where ϵ denotes the steepness parameter.

Fig. 1 Four color images (256 × 256 pixels, 24-bit RGB mode) stored in the network



The weight matrix W is determined in the same manner as that in the conventional associative memory model [18]. This model defines the way in which the network memorizes some spatial patterns by changing its synaptic weights. The data here are K binary patterns $s^k = \{s_1^k, \dots, s_N^k\}^T$ ($k = 1, \dots, K, s_i^k \in \{-1, 1\}$). For simplicity, we assume that each pattern contains an equal number of 1's and -1's. Then, the weight matrix is determined by the autocorrelation matrix of the patterns as follows:

$$W = \frac{1}{K} \sum_{k=1}^K s^k (s^k)^T. \quad (4)$$

Now, we change the network's connectivity. Since many connections in the real brain are short-range ones, we restrict the connections in the neighborhood of each unit [14, 15]. Let us assume that the units are arranged in a two-dimensional lattice and let (u_i, v_i) denote the position of unit i . Its neighborhood N_i is defined as $N_i = \{(u, v) \mid \max(|u - u_i|, |v - v_i|) \leq d\}$. Within the area N_i , we select L units at random and connect them to unit i . Then, Eq. 4 is modified as follows. If there is a connection from unit j to unit i , $w_{ij} = K^{-1} \sum_{k=1}^K s_i^k s_j^k$. Otherwise, $w_{ij} = 0$.

To visualize the network's state, we use the color images shown in Fig. 1 and store them in the network. By using a method proposed in our previous study [19], we convert the color images to binary patterns so that the network can memorize them. The length of the binary patterns is $N = 24 \times 256^2 = 1,572,864$. We also adjust some statistics of the images so as to facilitate emergence of chaotic transitions among the patterns. Specifically, $\sum_i s_i^k = 0$, $\sum_i s_i^k s_i^l = 0.08N$ ($k \neq l$), and $\sum_i s_i^k s_i^l s_i^m = -0.08N$ ($k \neq l, l \neq m$, and $m \neq k$).

2.2 Phenomenological Model

Since large-scale simulations of the CNN are still computationally difficult, we develop a simplified phenomenological model based on the Potts model [20]. The Potts model is a generalization of the Ising model, which is a simple mathematical model of ferromagnetism in statistical physics. The Potts model is composed of spins that take discrete states $s_i \in \{1, \dots, Q\}$. The spins are arranged in a lattice and interact only with their nearest neighbors.

In our model, a single Potts spin represents the state of a small group of units in the CNN. Each state of the spin corresponds to the retrieval of a stored pattern within the local area. We also introduce the refractoriness variable h_i^q for each state q of each spin i . This variable intuitively shows to what extent spin i tends to avoid state q . The dynamics of h_i^q is described by the following difference equation:

$$h_i^q(t+1) = \gamma h_i^q(t) + c \delta(s_i, q), \quad (5)$$

where $0 \leq \gamma < 1$ denotes the decay constant and $c \geq 0$ denotes the strength of the refractoriness. $\delta(\cdot, \cdot)$ is the delta function. The size of the time step is the characteristic time in which every spin is updated once.

The refractoriness variable changes the form of the system's Hamiltonian H . It is then becomes as follows:

$$H = - \sum_{i,j} J_{ij} \delta(s_i, s_j) + \sum_i \sum_{q=1}^Q h_i^q(t) \delta(s_i, q), \quad (6)$$

where J_{ij} denotes the strength of the interaction between spin i and spin j . If these spins are neighbors, $J_{ij} = J > 0$. Otherwise, $J_{ij} = 0$. In this study, we use a two-dimensional lattice of size 100×100 and adopt the Moore neighborhood, that is, each spin has eight neighbors.

To investigate the model dynamics, we adopt the standard Monte Carlo method for the Potts model. In each step, we pick a spin i at random. Then, we update its state according to the following probability distribution:

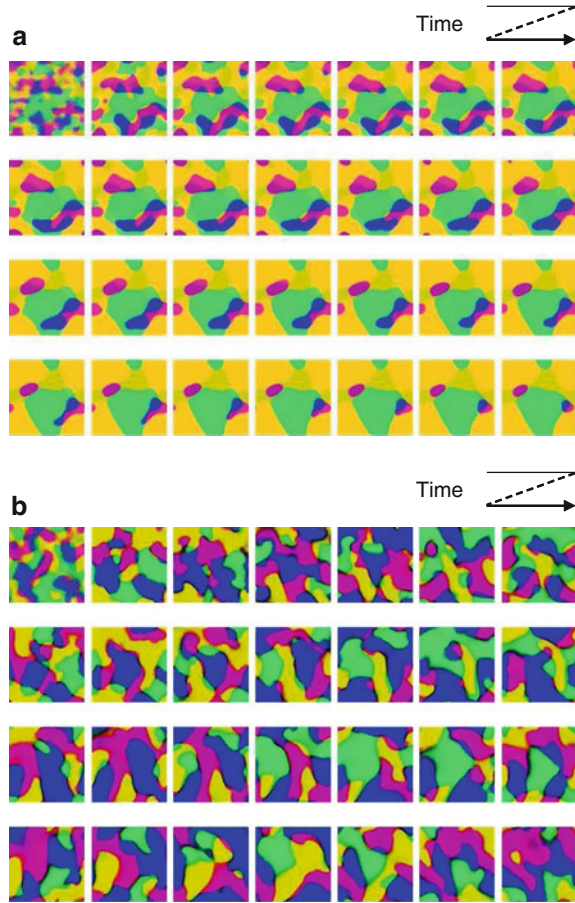
$$p(s_i \rightarrow q) = \frac{\exp(-\beta H(s_i = q))}{\sum_{q'=1}^Q \exp(-\beta H(s_i = q'))}, \quad (7)$$

where β denotes the inverse temperature. $H(s_i = q)$ denotes the value of the Hamiltonian when s_i is set to q with other spin states fixed. Because those terms that do not involve s_i can be canceled in the numerator and denominator, only the states of the nearest neighbors contribute to the probability distribution.

3 Results

In the following simulations of the CNN, we set $k_f = 0.7$, $k_r = 0.9$, $\epsilon = 0.015$, $d = 10$, and $L = 400$. As an initial condition, $\eta_i(0)$ takes a random value that is uniformly distributed in $[0, 1]$, and $\zeta_i(0) = 0$. The simulations are run on a cluster of four Linux server machines that have two 3.0-GHz dual-core processors and 8.0-GB RAM each. Computation of one step of the simulation takes approximately 1 s.

Fig. 2 Spatio-temporal patterns in the CNN displayed with ten-step intervals. (a) $\alpha = 0, a = 0$. (b) $\alpha = 20, a = 6.4$



First, we set $\alpha = 0$ and $a = 0$ so that the neurons have no refractoriness. In this case, the network is initially divided into many small clusters of different colors (see Fig. 2a). These clusters merge to become bigger ones with time and are not very mobile.

Next, we investigate the influence of the refractoriness by setting $\alpha = 20$ and $a = 6.4$. In this case, the network shows rich spatio-temporal dynamics (see Fig. 2b). The boundaries between clusters move as traveling waves. When two waves moving in different directions collide, rotating waves or spiral waves are sometimes generated temporarily.

Finally, we investigate the behavior of the phenomenological model. We set $J = 1, \beta = 3, Q = 4$, and $\gamma = 0.98$. Initially, s_i takes a random state and $h_i^q(0) = 0$. The model exhibits dynamics qualitatively similar to those of the CNN. If there is no refractoriness, i.e., $c = 0$, cluster merging is observed (see Fig. 3a). In contrast, with refractoriness ($c = 0.08$), complicated wave patterns are generated (see Fig. 3b).

4 Discussion and Conclusions

We have shown that a locally connected CNN exhibits rich dynamics of traveling waves (see Fig. 2b). These waves correspond to moving boundaries of local cell assemblies, and the waves disappear if the neurons have no refractoriness (see Fig. 2a). Therefore, refractoriness plays a key role in the emergence of traveling waves in the CNN. In the case of the real brain, the refractoriness—and possibly some other negative self-feedback mechanism such as spike-frequency adaptation and synaptic depression—could also contribute to the emergence of traveling waves.

Next, we showed that the proposed meso-scopic model can qualitatively reproduce complex wave patterns in the CNN (see Fig. 3b). Because the model requires less computational resources, it may serve as a useful tool for investigating traveling waves in nervous systems.

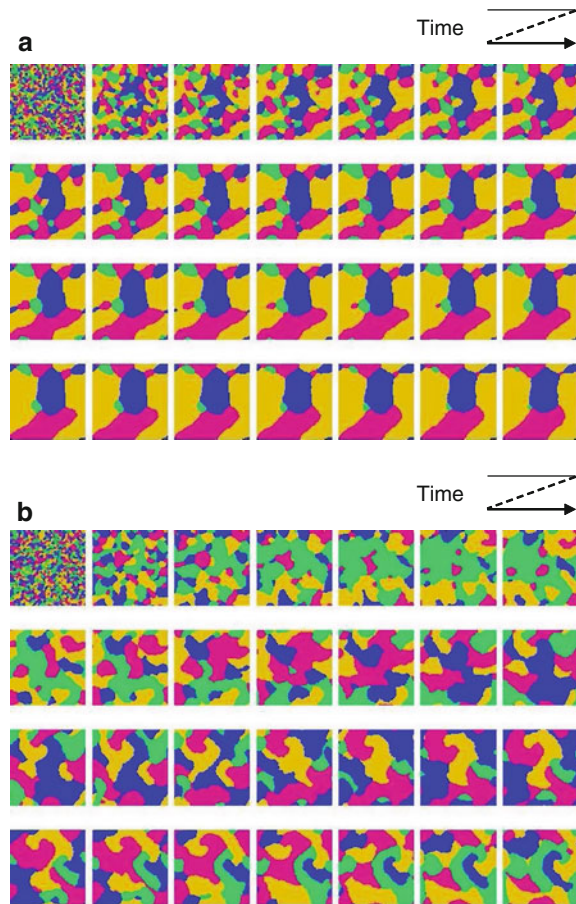


Fig. 3 Spatio-temporal patterns in the phenomenological model displayed with eight-step intervals. (a) $c = 0$. (b) $c = 0.08$

Furthermore, we found that rotating waves and spiral waves are often generated in both models. This seems to contradict the fact that such waves are rarely observed in experiments [21, 22]. Perhaps our model is not precise enough to reproduce real neuronal activity. However, some other numerical studies have also reported the emergence of rotating waves and spiral waves [12, 23, 24]. Thus, despite difficulty in detection of these waves, they may be actually generated in the brain.

Acknowledgements This research is partially supported by the Japan Society for the Promotion of Science, a Grant-in-Aid for JSPS Fellows (21-937) and the Aihara Project, the FIRST program from JSPS, initiated by CSTP.

References

1. M. Meister *et al.* *Science*, 252(5008):939–943, 1991.
2. R. O. Wong *Annu. Rev. Neurosci.*, 22:29–47, 1999.
3. D. Kleinfeld *et al.* *J. Neurophysiol.*, 72(3):1402–1419, 1994.
4. M. V. Sanchez-Vives, D. A. McCormick *Nat. Neurosci.*, 3(10):1027–1034, 2000.
5. A. Luczak *et al.* *Proc. Natl. Acad. Sci. U.S.A.*, 104(1):347–352, 2007.
6. I. Nauhaus *et al.* *Nat. Neurosci.*, 12(1):70–76, 2009.
7. E. V. Lubenov, A. G. Siapas *Nature*, 459(7256):534–539, 2009.
8. A. J. Watt *et al.* *Nat. Neurosci.*, 12(4):463–473, 2009.
9. H. R. Wilson, J. D. Cowan *Kybernetik*, 13(2):55–80, 1973.
10. S. Amari *Biol. Cybern.*, 27(2):77–87, 1977.
11. H. Liljenström *Int. J. Intell. Syst.*, 10(1):119–153, 1995.
12. N. F. Rulkov, I. Timofeev, M. Bazhenov *J. Comput. Neurosci.*, 17(2):203–223, 2004.
13. E. M. Izhikevich, G. M. Edelman *Proc. Natl. Acad. Sci. U.S.A.*, 105(9):3593–3598, 2008.
14. M. Oku *et al.* *IEICE Tech. Rep.*, 109(269):55–59, 2009. (in Japanese).
15. M. Oku, K. Aihara *NOLTA, IEICE*, 2011. (accepted).
16. K. Aihara, T. Takabe, M. Toyoda *Phys. Lett. A*, 144(6–7):333–340, 1990.
17. M. Adachi, K. Aihara *Neural Netw.*, 10(1):83–98, 1997.
18. J. J. Hopfield *Proc. Natl. Acad. Sci. U.S.A.*, 79(8):2554–2558, 1982.
19. M. Oku, K. Aihara in *Proc. NOLTA'10*, pp. 465–468, 2010.
20. F. Y. Wu *Rev. Mod. Phys.*, 54(1):235–268, 1982.
21. J. C. Prechtl *et al.* *Proc. Natl. Acad. Sci. U.S.A.*, 94(14):7621–7626, 1997.
22. X. Huang *et al.* *J. Neurosci.*, 24(44):9897–9902, 2004.
23. J. Milton, J. Cowan *Adv. Neural Info. Proc. Syst.*, 5:1001–1006, 1993.
24. M. Bazhenov *et al.* *Nat. Neurosci.*, 2(2):168–174, 1999.

Spatial Filtering by a Two-Dimensional Interconnected Network with Spike Timing Dependent Synaptic Plasticity Depending on Its Temporal Properties

Kazuhisa Fujita

Abstract In the present study, we investigated the dependence of characteristics of spatial filtering by the two-dimensional interconnected network with spike timing dependent plasticity (STDP) on its temporal properties. STDP has different temporal properties according to the area of a brain. The temporal properties are indicated by the form of learning window. In the previous study, we studied the response of an one-dimensional interconnected network with STDP in spatial processing using computer simulation and found that the one-dimensional network well responded to a particular spatial frequency component of the input. Here, we showed that the two-dimensional interconnected network with STDP provided two types of spatial filtering. One is spatial low-pass filtering using the learning rule of electric fish type. The other is spatial high-pass filtering using the learning rule of hippocampus type.

1 Introduction

Spike timing dependent synaptic plasticity (STDP) plays an important role in temporal processing because of dependence of synaptic modification by STDP on time differences between pre- and postsynaptic spike firing. Synaptic modification by STDP is found in various areas of various neural systems [3]. For example, STDP is found in the cultured hippocampus of rats [2], the visual cortex of cats [5], the electrosensory lobe of a weakly electric fish [1], etc. These STDP learnings have the individual temporal properties. The temporal properties are indicated by the form of learning window. Learning window is the function that indicates the relation between the intensity of synaptic modification and time difference of firings between pre- and postsynapse. In hippocampus, if time difference is negative, synaptic

K. Fujita (✉)

Tsuyama National College of Technology, 654-1 Numa, Tsuyama, Okayama 708-8506, Japan
e-mail: kazu@spikingneuron.net

efficacy is strengthened, whereas synaptic efficacy is weakened if time difference is positive [2], we call this learning “hippocampal type”. Meanwhile, the reversed learning rule is found in the electrosensory lobe of a weakly electric fish [1]. In this paper, we call this learning “electric-fish type”.

In the previous study, we studied the response of an one-dimensional interconnected network with STDP in spatial processing using computer simulation and found that the one-dimensional network well responses particular spatial frequency of input [6]. In the present study, we showed that the two-dimensional interconnected network with STDP worked as spatial filter. The function of spatial filtering depended on temporal properties of learning window. The network provided low-pass spatial filtering applying electric-fish type learning window. The network provided high-pass spatial filtering applying hippocampal type learning window. Furthermore we investigated the dependence of the filtering function on time constant τ of learning windows defined by Eq. 1.

2 Methods

Figure 1 shows the interconnected network using in this study. The structure of the network is two dimensional array. A neuron of the network has connection to neighbor neurons through synapses with STDP. The neuron i, j connects with neurons from $i - RF$ to $i + RF$ and from $j - RF$ to $j + RF$. RF is the size of connecting area. Each synapses were facilitated and depressed being subject to STDP learning rule.

2.1 Neuronal Model

The “leaky integrate and fire” neuron was used as a single neuron. The membrane potential $V(t)$ of a neuron is determined by $\tau_m \frac{dV(t)}{dt} = V_0 - V(t) + In(t)$, where τ_m is a time constant, $In(t)$ is the input voltage of the neuron. V_0 indicates resting potential. A neuron generates a spike and resets the membrane potential to V_0 when the membrane potential reaches threshold ϑ . Spike $S(t)$ is 1 if $V \geq \vartheta$. Otherwise,

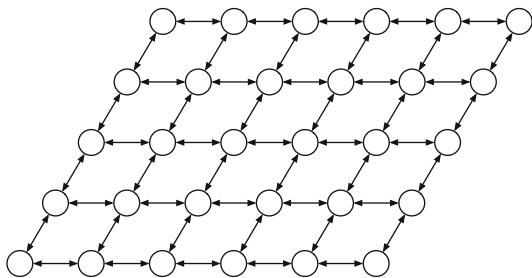


Fig. 1 Network model. A neuron on the network connects with neighbor neurons. The network received two-dimensional inputs

$S(t)$ is 0. A neuron is stimulated with input voltage and synaptic potential evoked by connected neurons. $In(t)$ is summed input voltage, synaptic potential, and noise. $In(t)$ is determined by $In(t) = I_c + g(t)(E_V - V) + \text{Noise}$, where I_c is input voltage and $g(t)$ is synaptic conductance. In the present study, I_c is voltage of a direct current. The noise is a uniform random number from 0 to 1 and is generated at each step.

2.2 Synaptic Model

We used the synaptic model proposed by Song and Abbott [7]. The synaptic conductance $g(t)$ is determined by $\tau_g \frac{dg(t)}{dt} = -g(t)$, where τ_g is a time constant. This model is based on a leaky integrator, thus synaptic conductance only decreases and comes to converge to 0. Synaptic conductance $g(t)$ increases when a presynaptic neuron generates a spike. If a presynaptic neuron generates a spike at t , synaptic conductance at $t + dt$ is determined by $g(t + dt) = g(t) + W(t)$, where $W(t)$ is synaptic efficacy. On STDP, synaptic efficacy changes when the spikes from pre- and postsynaptic neurons reach the synapse. Synaptic efficacy $W(t)$ is given by $W(t + \Delta t) = W(t) + F(t_{\text{pre}} - t_{\text{post}})W_{\text{max}}$, where F is the synaptic change rate that is called ‘‘learning window’’, t_{pre} is the time of presynaptic spike arrival, and t_{post} is the time of postsynaptic firing. The initial value of $W(t)$ is chosen W_0 . The synaptic change rate F is determined by

$$F(\Delta t) = \begin{cases} A_+ \exp(\Delta t/\tau) & \text{if } \Delta t > 0 \\ A_- \exp(\Delta t/\tau) & \text{otherwise} \end{cases}, \quad (1)$$

where Δt is $t_{\text{pre}} - t_{\text{post}}$. W is W_{max} when W is more than W_{max} . W is 0 when W is less than 0.

Temporal properties of STDPs are indicated by the form of learning windows of STDP. Learning window is defined by asymmetric exponential curves (Eq. 7). The temporal properties of learning window represents intensities of synaptic modification A_+ and A_- , and time constant τ in Eq. 1.

The values of parameters are: $\text{RF} = 8$, $\tau_m = 20$ msec, $V_0 = -70$ mV, $\vartheta = -54$ mV, $E_V = 0$ mV, $\tau_g = 5$ msec, $W_{\text{max}} = 0.005$, $W_0 = W_{\text{max}}/2$. $A_+ = 0.005$ and $A_- = -A_+$ when the learning is electric-fish type. $A_+ = -0.005$ and $A_- = -A_+$ when the learning window is hippocampal type.

2.3 Frequency Characteristics of the Network

To assess features of outputs of the network, we computed frequency characteristics FC. FC is defined by $\text{FC} = \sum_i P_i f_i / \sum_i P_i$, where f_i is frequency of component i of the input, P_i is power of the component in the frequency f_i . Simply, FC means weighted average of spatial frequency components of the input.

3 Results

3.1 Spatial Filtering by the Two-Dimensional Network

We investigated the response of the two-dimensional interconnected network with STDP learning. To address this issue, we calculated responses of the network. The network has 80×80 neurons. The synaptic connections between neurons are modified based on STDP. Here, time constant τ of the learning window is 20 msec.

Using the learning rule of electric-fish type, the network acted as spatial low-pass filter. Figure 2a, c show the input image that consists of a filled circle and spatial white noise. Figure 2b, d show the output of the network. The output image means firing counts of the neurons of the network from 9,000 to 10,000 msec. In this case, spatial high frequency noise was reduced and spatial low-frequency signal was represented in the output of the network. Thus the network functioned as spatial low-pass filter using the learning rule of electric-fish type.

Using the learning rule of hippocampal type, the network acted as spatial high-pass filter. Figure 2e, g show input image. Figure 2f, h show the output of the network. The output image means firing count of neurons of the network from 9,000 to 10,000 msec. In this case, firing counts of the neurons which were on the edge of the input image was higher than that of other neurons. Thus the network enhanced

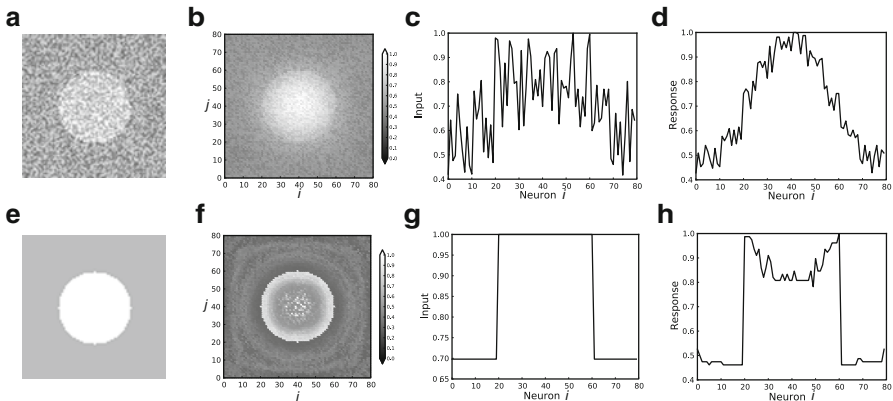


Fig. 2 Inputs and responses of the two-dimensional interconnected network. (a) The input image of the network with electric-fish type learning. Neurons on *white* and *grey area* received high and low intensity of input voltage, respectively. (b) Response of the network with electric-fish type learning. (c) Input intensity of the network at $j = 40$. This input intensity is a input voltage divided by the maximum input voltage that is 35 mV. (d) Response of the network at $j = 40$. Response is defined by a firing count of a neuron divided by the maximum firing count. (e) The input image of the network with hippocampal type learning. (f) Response of the network with hippocampal type learning. (g) Input intensity of the network at $j = 40$. This input intensity is a input voltage divided by the maximum input voltage that is 27 mV. (h) Response of the network at $j = 40$

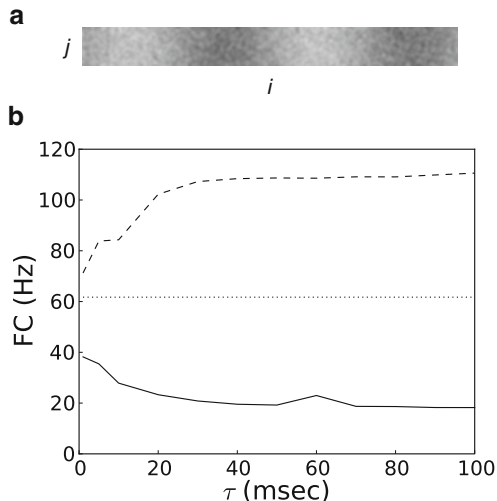


Fig. 3 (a) The input of the network to investigate frequency characteristics of the output of the network. The input consisted of 2 Hz spatial wave and *white noise*. (b) Frequency characteristics of the network. The *vertical line* indicates FC that means frequency characteristics of the network. The *horizontal line* indicates τ that is the time constants of learning window of STDP. The *solid line* shows frequency characteristics of the network with electric fish type STDP. The *broken line* shows frequency characteristics of the network with hippocampal type STDP. The *dotted line* shows weighted average of frequency components of the input

the edge of the input image. In other words, the network might function as spatial high-pass filter using the learning rule of hippocampal type because the edge of image consists of spatial high-frequency components.

3.2 Frequency Characteristics of an Output of the Network

We showed the response of the network depending on learning window mentioned above. In this subsection, we showed the dependence of frequency characteristics of the output of the network on time constant τ of learning window. The network using in this subsection has 200×20 neurons. The input of the network consisted of the signal that formed the 2 Hz wave and white noise shown in Fig. 3a. Here, one Hz as spatial frequency in this subsection has a spatial periodic interval 200 neurons. We calculated FC of the output of the network with changing time constant τ of learning window.

Figure 3b shows frequency characteristics FC of the output of the network with time constant τ of learning window. Solid line indicates the FC of the output of the network with electric-fish type learning. The FC decreased with τ from 0 to about 40 msec. From about 50 msec, the FC unchanged. The FC is lower than weighted

average of frequency components of the input. This result shows that the network with electric-fish type learning could work as spatial low-pass filter. Broken line indicates the FC of the output of the network with hippocampal type learning. The FC increased with τ from 0 to about 40 msec. From about 40 msec, FC unchanged. The FC is higher than weighted average of frequency components of the input. This result shows that the network with hippocampal type learning could work as spatial high-pass filter. The FC reached about 100 Hz at 40 msec. One hundred Hz means that spatial period is 2 neurons. This result shows spatial filtering of the network did not work. When time constant τ is around 20 msec, spatial filtering of the network works enough. The value of τ that is 20 msec is appropriate for experimental results [1, 4].

4 Discussion

The purpose of the present study is to investigate the function of a two-dimensional interconnected network with STDP and the change of the function according to temporal properties of learning window of STDP. We showed that the two-dimensional network could work as spatial low-pass and high-pass filter applying electric-fish type and hippocampal type learning, respectively. Furthermore, we showed that characteristics of filtering of the network depended on time constant τ of learning window and the value of τ is appropriate for experimental results when the network work as spatial filter enough.

References

1. Bell, C. C., Han, V. Z., Sugawara, Y., Grant, K.: Synaptic plasticity in a cerebellum-like structure depends on temporal order. *Nature* **387** (1997), 278–281.
2. Bi, G.-q., Poo, M.-m.: Synaptic modifications in cultured hippocampal neurons: Dependence on spike timing, synaptic strength, and postsynaptic cell type. *J Neurosci* **18** (1998) 10464–10472.
3. Dan, Y., Poo, M.-M.: Spike timing-dependent plasticity: From synapse to perception. *Physiol Rev* **86** (2006) 1033–1048.
4. Feldman, D. E.: Timing-based LTP and LTD at vertical inputs to layer II/III pyramidal cells in rat barrel cortex. *Neuron* **27** (2000) 45–56.
5. Fu, Y.-X., Djupsund, K., Gao, H., Hayden, B., Shen, K., Dan, Y.: Temporal specificity in the cortical plasticity of visual space representation. *Science* **296** (2002) 1999–2003.
6. Fujita, K.: Spatial feature extraction by spike timing dependent synaptic modification. *Lecture Notes in Computer Science* **6443** (2010) 148–154.
7. Song, S., Abbott, L. F.: Cortical development and remapping through spike timing-dependent plasticity. *Neuron* **32** (2001) 339–350.

Neural Model for Hierarchical Processing of Auditory Information in Mammal's Cortex

Yusuke Hara and Yoshiki Kashimori

Abstract In this paper, we present a model of auditory cortex, which performs a hierarchical processing of auditory information. We show that the aspects of spatiotemporal activity in the primary cortex are encoded by a combination of feature-detective neurons and then by a dynamical attractor in higher-ordered cortex. The present study provides a clue for understanding the mechanism of how the information of notes and syllables are constructed from the spatiotemporal activity of the primary auditory cortex.

1 Introduction

Animals utilize auditory information for survival and communications of conspecifics. Researchers have focused on several model systems to investigate the mechanism of auditory information processing. Studies on localization behaviors have demonstrated how auditory information of target is processed in animal brains. Bats have a specific brain maps for representing the features of target signal such as relative velocity and distance [1]. Barn owl also has the map structures in the brain, in which neurons respond selectively to interaural time difference and interaural

Y. Hara (✉)

Graduate School of Information Systems, University of Electro-Communications,
Chofu, Tokyo 182-8585, Japan
e-mail: pccpy430@yahoo.co.jp

Y. Kashimori

Graduate School of Information Systems, University of Electro-Communications,
Chofu, Tokyo 182-8585, Japan

Department of Engineering Science, University of Electro-Communication,
Chofu, Tokyo 182-8585, Japan

level difference [2]. Although mammalian auditory cortex has also frequency map structure in the primary auditory cortex, auditory information is encoded by a distributed pattern of neuronal activity.

A sequence of sound is analyzed in animals' brain as elementary components such as notes and syllables. Bird song has been a subject for investigating the neural mechanism underlying vocal learning. Studies on bird song revealed how birds are able to learn their own song in early period of life [3]. The reciprocal interaction between HVC and RA enables the song learning [4–6]. In contrast to the mechanism of the vocal learning, how auditory information about notes and syllables are represented in bird's auditory brain remains unclear.

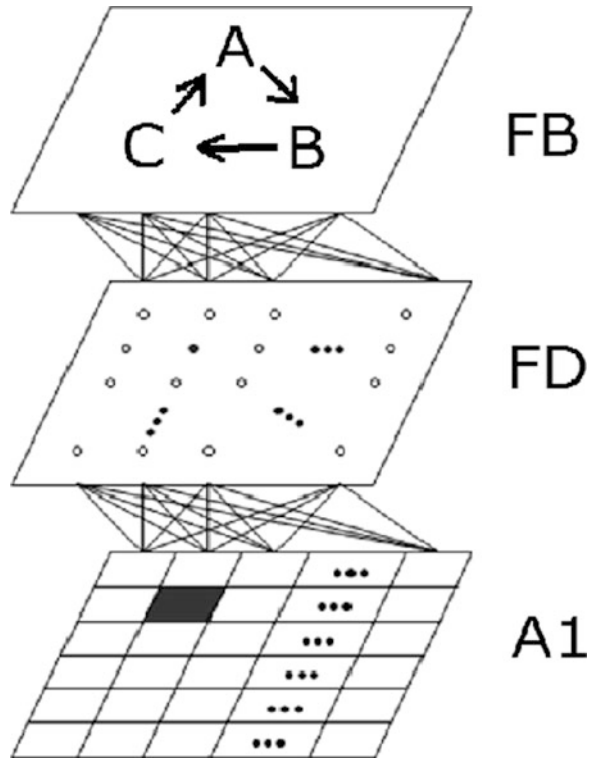
It has been reported that auditory information is represented by spatiotemporal activity of primary auditory cortex (A1) of mammals [7, 8]. The neural model of A1 has been proposed to account for the mechanism for generating the spatiotemporal activity in A1 neurons [10]. Recent study also showed that neural responses in the secondary auditory cortex mirror perception, showing categorical responses to continuous stimuli [11]. However, how the elementary components of sound are extracted from the spatiotemporal activity of neurons is poorly understood.

To address this issue, we present a model of auditory cortex, which performs a hierarchical processing of auditory information. The model consists of three layers of 2-dimensional networks. We show that the aspects of spatiotemporal activity in the primary cortex are encoded by a combination of feature-detective neurons and then by a dynamical attractor in higher-ordered cortex. The present study provides a clue for understanding the mechanism of how the information of notes and syllables are constructed from spatiotemporal activity of the primary auditory cortex.

2 Model

We propose a neural network model for hierarchical processing of auditory information, which consists of three networks, as shown in Fig. 1. The auditory information is encoded with spatiotemporal pattern of neuronal activity in the primary auditory (A1) cortex. The model of A1 was made based on the previous model by Yamaguchi et al. [10]. The network has a 2-dimensional array of A1 neurons, each of which is constructed with a pair of excitatory and inhibitory neurons. The balance in the excitatory and inhibitory connections between these neurons makes the spatiotemporal activity of A1 stabilize as a stationary pattern. The excitatory connections among the excitatory neurons enable propagation of stationary pattern across the network. Then the spatiotemporal aspect of the neuronal activity evoked in A1 is detected by the feature-detective (FD) neurons in the second layer. These FD neurons integrate the spatiotemporal pattern over a short time period, thereby enabling the second layer to represent the information about notes and about the correlation of notes. The FD neurons were organized by Kohonen's self-organized map [12]. Thus the FD neurons extract the features of the snapshot of the spatiotemporal activity, indicating the compression of spatiotemporal auditory information. The information encoded by the FD neurons is then combined as a linkage of attractors in the feature-binding

Fig. 1 The network model of auditory cortex. The model consists of three layers, primary auditory cortex (A1), feature-detective (FD) layer and feature-binding (FB) layer. "A", "B", and "C" in the FB layer indicate dynamical attractors. Each network has a 2-dimensional array of neurons. The auditory information is hierarchically processed by these three layers



(FB) layer, providing semantic information such as word. The network model of FB layer has a 2-dimensional array of neurons, each was based on the Leaky integrate-and fire neuron model [13]. The temporal correlation between attractors was formed with spike timing-dependent plasticity (STDP) learning [14].

3 Results

Figure 2 illustrates the snapshots of the neuronal activity of A1 and the activity of FD layer corresponding to the activity of A1 neurons, respectively, in response to the sound "a-b-c". The sound was represented as a spatiotemporal pattern of neuronal activity of A1. The balance of excitatory and inhibitory inputs to neurons enables the network to stabilize the propagation of A1 activity. The FD neurons integrated the spatiotemporal activity over a short time period, enabling the encoding of the features of the neuronal activity averaged over a short time period. The encoding by the FD neurons shapes the representation of a compressed, or a coarse-grained information of the spatiotemporal activity of A1.

Figure 3a and b illustrate the spatiotemporal activities of the FD neurons detecting the features of the note "a" of "a-b-c" and "a" of "c-b-a", respectively. The sound features were encoded by the population of FD neurons. The spatial activity



Fig. 2 Neural responses of A1 and FD layer to the sound “a-b-c”. Activated neurons are depicted by *white-colored clusters* in A1 and *filled circles* in FD layer, respectively. The snapshots are depicted every 20 ms

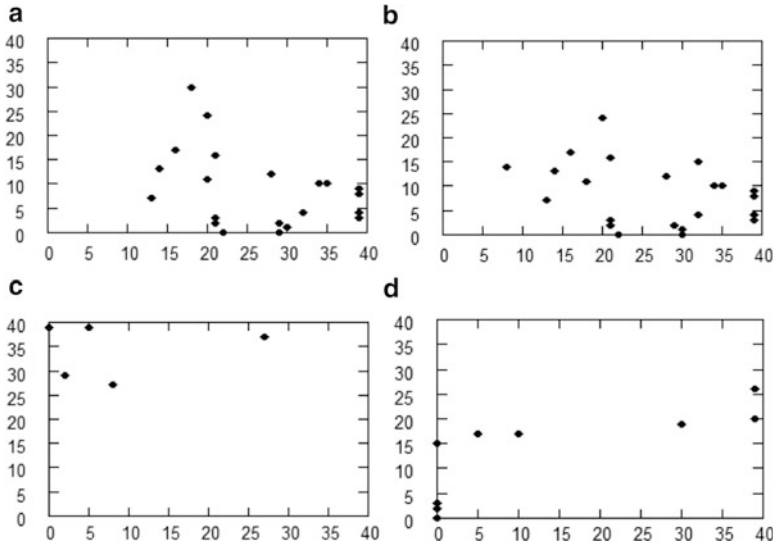
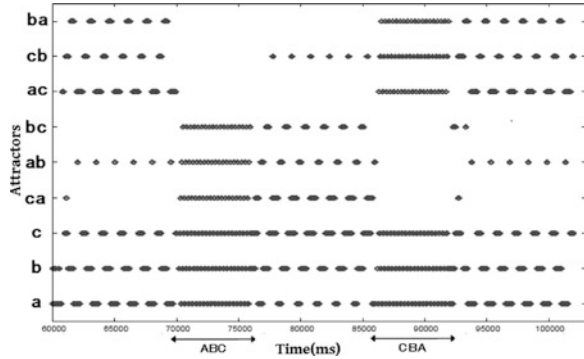


Fig. 3 Spatial activities of FD neurons in response to notes and their overlaps. Spatial activities of the FD neurons detecting the features of the notes, “a” of “a-b-c” (a) and “a” of “c-b-a” (b), and of the overlaps, “a-b” of “a-b-c” (c) and “b-a” of “c-b-a” (d). These patterns indicate the activated FD neurons during the presence of the notes and overlaps

of FD neurons in response to “a” in “a-b-c” exhibited the similar pattern to “a” in “c-b-a”. In contrast, FD neurons showed different patterns in response to “a-b” in “a-b-c” and “b-a” in “c-b-a”, as shown in Fig. 3c and d. Other notes and overlaps of them also had similar tendency to the patterns of the note “a” and the overlaps “a-b” and “b-a”. The FD neurons exhibited the similar spatial patterns in response to the notes, but did the different patterns for the overlap of the notes. This indicates that it is important for auditory perception to extract the features of the overlap between notes, besides the features of notes. Thus FD neurons encode the information about notes (“a”, “b”, and “c”) and the temporal correlation between the notes.

Figure 4 illustrates the network state of the FB layer during the perception of words, “a-b-c” and “c-b-a”. The spatiotemporal correlations among the attractors were formed by STDP learning. The information about notes and their correlations were combined as a linkage of dynamical attractors, enabling the network to represent the two words, “a-b-c” and “c-b-a”. After the perception of “a-b-c” or “c-b-a”, the network state was recovered to a background state, in which the network state exhibited an itinerant state between the attractor “a-b-c” and “c-b-a”.

Fig. 4 Temporal variation of the network state of binding layer. The short vertical bar means the attractor in which the network state stays



4 Discussions

We have shown a network model for hierarchical information processing in the auditory cortex, which consists of three layers. These layers encoded the information about different aspects of auditory features along the pathway from A1 to FB layer, enabling the system to percept a word in the FB layer. The present study provides an insight to understanding the information processing in auditory cortex.

In the present study, we have proposed the network models of the higher ordered areas beyond A1. The FD layer encodes the information about notes and syllables, which are extracted from the spatiotemporal activity of A1. The FB layer combines these features of notes and syllables and represents the information of a word as a linkage of dynamical attractors. The second auditory cortex neurons have been reported to exhibit categorical responses to continuous stimuli [11]. This might correspond to the function of the FD layer. It seems also reasonable that sound features are dynamically combined in a higher ordered area of auditory cortex. Further studies are needed to understand how semantic information such as words is constructed from spatiotemporal activity of A1.

References

1. Suga, N.: Biosonar and neural computation in bats. *Sci Am.* 262 (1990)60–68
2. Konishi, M.: Listening with two ears. *Sci Am.* 268 (1993) 66–73
3. Konishi, M.: The role of auditory feedback in the control of vocalization in white-crowned sparrow. *Z. Tierpsychol.* 22 (1962) 770–783
4. Doya, K., Sejnowski, T.J.: A computational model of avian song learning. Gazzaniga, M.S. (ed). In: *The New Cognitive Neurosciences.* (1999) Cambridge, MA, MIT press, pp. 469–482.
5. Troyer, T.W., Doupe, A.J.: An association model of birdsong sensorimotor learning. I. Efference copy and the learning of song syllables. *J Neurophysiol.* 84 (2000) 1204–1223
6. Troyer, T.W., Doupe, A.J.: An association model of birdsong sensorimotor learning. II. Temporal hierarchies and the learning of song sequence. *J neurophysiol.* 84 (2000) 1224–1239

7. Taniguchi I., Horikawa J., Moriyama T., Nasu M.: Spatio- temporal pattern of frequency representation in the auditory cortex of guinea pigs. *Neurosci Lett.* 146 (1992) 37–36
8. Horikawa, J., Hosokawa, Y., Kubota, M., Nasu, M., Taniguchi, I.: Optical imaging of spatiotemporal patterns of glutamatergic excitation and GABAergic inhibition in the guinea-pig auditory cortex in vivo. *J Physiol.* 497(1996) 629–638
9. Fukunishi, K., Murai, N. and Uno, H., Dynamical characteristics of the auditory cortex of guinea pig observed with multichannel optical recording, *Biol. Cybern.*, 67 (1992) 501–509
10. Yamaguchi, Y., Horikawa, J., Taniguchi, I.: Neural dynamics of vocal processing in the auditory cortex, *Biophysical Neural Network*, Mary Ann Liebert Inc, NY (2001), pp. 343–362
11. Chang, FF., Rieger, JW., Johnson, K., Berger, M.S., Barbaro, N.M., Knight, RT.: Categorical speech representation in human superior temporal gyrus. *Nat Neurosci.* 13 (2010)1428–1432.
12. Kohonen, T (1995) *Self-organized Maps*. Berlin, Springer-Verlag
13. Koch, C (1999) *Biophysics of Computation*. New York, Oxford University Press
14. Song, S., Miller, K.D., and Abbott L: Competitive Hebbian learning through spike-timing- dependent synaptic plasticity. *Nat Neurosci.* 3 (2000) 919–926

Modeling Dynamics of the Human Limbic System

Mark H. Myers and Robert Kozma

Abstract In this paper, we proposed a computational model of the limbic system in order to capture the spatio-temporal dynamics of abnormal/normal brain states. Power spectral density measurements of the abnormal seizure states are captured in order to differentiate from normal brain states. Electrical titration therapy is proposed through this model to demonstrate how the model can be utilized as an EEG simulator that demonstrates how external stimulation restores the model back to its normal chaotic operating state.

Keywords Power spectral density • Electroencephalograph • Seizure • Non-linear • Biological neural network

1 Introduction

Studies of the brain's electrical activity based on EEG analysis provide methods to differentiate among various cognitive states, i.e., sleep, awake, normal, or seizure [6]. Models of relatively large groups of interacting excitatory and inhibitory neural populations have been developed to exhibit abnormal/normal brain states and the effects of imbalanced excitatory and inhibitory neurons [12]. Tsakalis and Chakravarthy [2, 11] developed a neural mass model, with an internal feedback mechanism to maintain synchronous behavior within normal levels despite elevated coupling. Normal internal feedback quickly regulates an abnormally high coupling between the neural populations, whereas pathological internal feedback can lead to hyper-synchronization and the appearance of seizure-like high amplitude oscillations. Feedback decoupling is introduced [2] as a robust seizure control strategy. An

M.H. Myers (✉) • R. Kozma
Computational Neurodynamics Laboratory, University of Memphis,
Memphis, TN 38152, USA
e-mail: mhmyers@memphis.edu

external feedback decoupling controller is also introduced to maintain normal levels of synchronous behavior. Other internal feedback models featured closed-loop feedback control systems in epileptic seizures combining methods from seizure prediction and deep brain stimulation [7]. Periodic stimulation was also performed, with a reduction of seizure frequency in 33% of six rat modeling instances.

Clinical studies are often grouped by anatomical targets [1, 3, 8], but target-specific factors need to play a greater role in individualizing electrotherapy strategy and characterizing its mechanisms. Afferent connections throughout the different regions of the brain can influence the dynamics of neuronal populations and sensitivity to electrical stimulation.

2 Methods

High density arrays of electrodes were placed onto the surface of the scalp of four patients with medically intractable epilepsy, who are candidates for the Vagus Nerve Stimulator (VNS) surgical treatment. Features of normal/abnormal brain activity have been monitored for 60–90 min. EEG evoked response potentials are captured at a sampling rate of 250 points/s. Power spectral density analysis was performed on the EEG data sets. Due to the identified spatio-temporal dynamics of EEG signals, the power spectral density (PSD) often exhibits a linearly decreasing behavior over log-base10 coordinates considering frequency and amplitude of PSD or spectral power. This is called in the literature “power law” or scale-free behavior “ $1/f^{-\alpha}$ ”, where cognitive processing states varied by “ α ” [6]. The power law relation is seen on the example of Fig. 1 over the whole range of frequencies from 10 to 100 Hz, i.e., the beta-gamma range. Power law behavior is attributed to the brain structural connectivity and dynamical properties.

The PSD of the states of sleep, awake, seizure, and VNS dampened seizure conform to the power law relation, $1/f^{-\alpha}$, where $\alpha = -3$ when the patient is at rest, $\alpha = -3$ to -2 during the awake state, $\alpha = -2$ during cognitive tasks and intentional behaviors [5]. The case $\alpha = -2$ is mathematically referred to as brown noise, $1/f^2$,

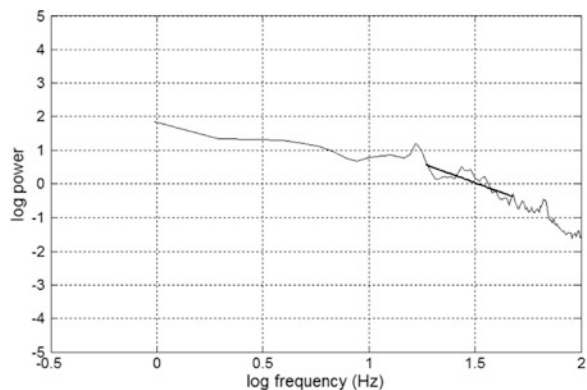
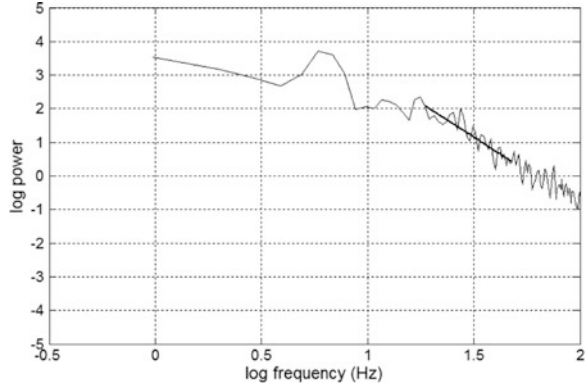


Fig. 1 The EEG of the normal state depicted as the slope of the PSD where $\alpha = -2.16$

Fig. 2 The EEG of a seizure state depicted as the slope of the PSD here $\alpha = -3.68$



whereas $\alpha = -3$ is called sometimes as black noise. The calculated PSD linear regression values during the seizure state will have $\alpha < -4$. Figure 1 exhibits low alpha values signifying the normal EEG state, while Fig. 2 exhibits alpha values in the seizure range.

The KIV model is a biologically inspired neural network [10]. The K-set family includes hierarchy of K models of increasing complexity. They represent different aspects of the vertebrate brain. It has the functionality of sensory perception and action selection. The fundamental building block of the KIV model is the dynamics corresponding to the K0 set which is governed by a point attractor. This means that, over time, a non interacting population of neurons will converge to the point zero. The K0 set is the basic unit of the K models, upon which the rest of the hierarchy is based on. The dynamics of the K0 set are given by the following second order ODE (ordinary differential equation).

$$\frac{1}{ab} \left[\frac{d^2 p(t)}{dt^2} + (a + b) \frac{dp(t)}{dt} + abp(t) \right] = X(t) + I(t)$$

where ‘a’ and ‘b’ are rate constants determined based on physiological experiments, $p(t)$ is the pulse density at time t and $X(t)$ is the internal input, and $I(t)$ is the external input at time t . The KIV model architecture is represented by three major parts; the KIII cortex, KIII hippocampus and the KII amygdala. Hippocampus models include navigation functions. The cortex models sensory processing and pattern recognition in various sensory modalities. The amygdala is the unit where the activations from the cortex and hippo-campus are projected and decision is made concerning the next action, based on the fusion of the signals from other brain areas.

The KIV model is used as an EEG simulator to exhibit similar attributes found in the analysis of human EEGs. In order to exhibit the ‘normal’ chaotic state of human EEGs, the KIV model was adjusted to exhibit the same ‘noisy’ attributes through the input of random variables throughout the network. Low coupling between the networks enabled low feedback to occur and therefore diminish the influence of the three networks onto each other.

Fig. 3 The simulated EEG of the normal state depicted as the slope of the PSD where $\alpha = -2.73$

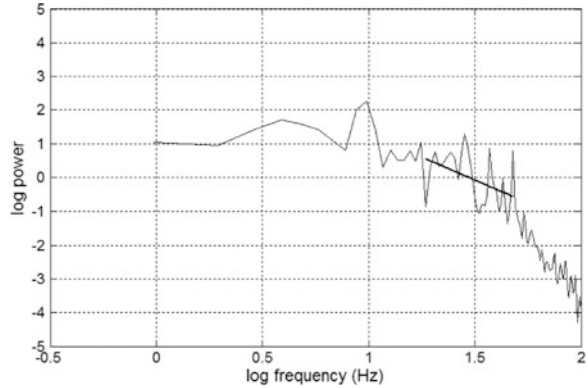
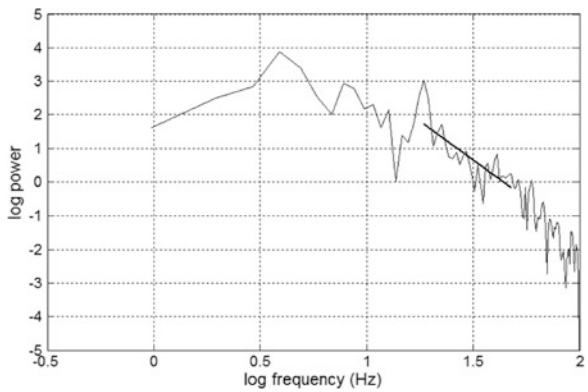


Fig. 4 The simulated EEG of the seizure state depicted as the slope of the PSD where $\alpha = -3.88$



We have utilized the seizure parameterized KIII and incorporate this model into the KIV model [4]. Due to the increased energy in the theta brain state frequency range, the calculated alpha value, derived by the slope of the PSD is much steeper than the alpha value of the PSD of the normal state. The epilepto-genesis created in the KIII is due to the imbalance of inhibitory nodes/neurons in the delayed feedback connections of the KIII causing runaway inhibitory behavior.

Figure 3 shows normal simulated normal EEG behavior. Figure 4 displays abnormal simulated EEG behavior using the KIV model.

3 Results

The PSDs of four human patients EEGs were analyzed to find the differing alpha values found between the normal and seizure states, as seen in Tables 1 and 2. These behaviors are modeled in the KIV network. The PSD values found during seizure activity exhibited high power in both the low and high theta ranges, corresponding to the 3/s wave that dominated the EEG [6].

Table 1 PSD- EEG – normal state

	Patient 1 (25)	Patient 2 (25)	Patient 3 (25)	Patient 4 (25)
Ave	2.38	2.53	2.46	2.51
Std	0.24	0.29	0.25	0.24
Min	2.02	2.01	2.04	2.15
Max	2.91	2.93	2.86	2.89

Table 2 PSD-EEG – seizure state

	Patient 1 (25)	Patient 2 (25)	Patient 3 (25)	Patient 4 (25)
Ave	3.65	3.68	3.72	3.64
Std	0.16	0.14	0.11	0.10
Min	3.41	3.39	3.54	3.42
Max	3.89	3.91	3.88	3.81

Table 3 PSD-KIV – normal state

	A1 (25)	A2 (25)	A3 (25)	A4 (25)	A5 (25)
Ave	2.40	2.40	2.50	2.67	2.70
Std	0.28	0.26	0.24	0.22	0.16
Min	2.04	2.06	2.12	2.32	2.41
Max	2.86	2.88	2.92	2.95	2.96

Table 4 PSD-KIV – abnormal state

	A1 (25)	A2 (25)	A3 (25)	A4 (25)	A5 (25)
Ave	3.61	3.65	3.74	3.77	3.77
Std	0.18	0.17	0.13	0.11	0.11
Min	3.31	3.33	3.44	3.57	3.60
Max	3.96	3.91	3.95	3.97	3.98

Additionally, the KIV normal and seizure state exhibited the same alpha value range. The role of noise in the KIV is illustrated in Table 3 and 4 Five simulated patients are constructed through the KIV by varying the levels of noise throughout the KIV by 5%, whereas patient A1 is a KIV with full input noise, and patient A5 has 20% less noise than A1. Noise is applied to the external input I(t) of the second order ODE of the K0 set. These simulated ‘patient’ EEGs illustrate how noise affects the alpha values collected from their respective EEGs. The lessening of noise from patient A1 to A5 seems to increase the PSD alpha values from the normal to abnormal KIV time series. The rise of PSD values found in the theta frequency bands of 3–8 Hz causes the slope of the PSD to rise sharply, causing the higher frequency bands to diminish due to the reduction of noise in the system [9]. Takeshita et al. have proposed that noise is still present in the seizure state as well as the normal state and may contribute to seizure initiation within neural populations where transitions between bistable states (epileptic and nonepileptic) are caused by noise [12].

The simulation using noise in the KIV requires temporal filtering to give 1/f amplitude spectra of temporal frequencies. This method of simulation is based on the premise that EEG activity is due to near-white noise generated by immense numbers of interacting pyramidal cells, whose activity episodically undergoes transient increases in spatial coherence [5]. Noteworthy are the steepened slope of

Table 5 PSD – KIV restored state

	A1 (25)	A2 (25)	A3 (25)	A4 (25)	A5 (25)
Ave	2.47	2.52	2.61	2.69	2.77
Std	0.18	0.17	0.17	0.17	0.16
Min	2.13	2.17	2.28	2.36	2.44
Max	2.65	2.70	2.78	2.89	2.95

1/f PSD in the seizure state compared with the normal EEG state, which is simulated in the KIV model. PSD values found during the EEG time series and the simulated EEG time series exhibit low standard deviation during the seizure states per patient. This activity may be due to the entrainment of large scale neural population whose power per frequency is limited to the theta range. High theta activity causes the slope of the PSD to rise sharply, and diminishes any other brain activity state, i.e., the carrier wave in the rest state, active state and sleep state which seems to be diminished or lost during the seizure [6].

Additionally, KIV network is able to simulate behavior characteristic to the so-called ‘restoration’ state that mimics the external stimulation of the VNS therapy onto the brain to restore the effects of the seizure state back to the brain’s normal neural chaotic behavior. The ‘seizure to restore’ state is accomplished through the input of Brain Stimulator Interface (BSI) object. The de-synchronizing external signal is a KII signal with the original internal node values. In this manner, we are adding a KII network to the KIV network to overcome the semi-periodic neural abnormal firings of an ‘abnormal firing’ KII network due to runaway inhibitory neuron hyper-excitation. The KII object also consists of an amplitude reduction signal which is a sample of the seizure state time period increased by 1%. The BSI added input restore the signal back to its normal state (Table 5). This technique mirrors the approach from Tsakalis [11] Decoupling Control mechanism.

The previous PSD values show that the restoration state also exhibits small standard deviation across the simulated patient EEGs, while maintaining the alpha range of 2–3. The external signal that restores the KIV model back to its initial state causes the runaway inhibitory signal to become ‘rebalanced’, since the external signal may provide the excitatory signal needed to restore the signal.

4 Discussions

Measurement of the slope of the PSD of human EEG data provides α values in the range of 2–3 for normal brain states, and values approaching four near the seizure location. Changes of the power law index alpha values are successfully modeled by the KIV network. Injection of KII object as a BSI object onto the simulated seizure state restores the normal simulated EEG state, which is of potential modeling benefit to titration therapies.

Acknowledgments The data for this study are due to Dr. James W. Wheless, MD, Professor and Chief of Pediatric Neurology, LeBonheur Chair in Pediatric Neurology, University of Tennessee Health Science Center. IRB permit # E04-199 University of Memphis.

References

1. Bertram, E. (2007) The relevance of kindling for human epilepsy. *Epilepsia*, 48(2), 65–74.
2. Chakravarthy, N., Sabesan, S., Iasemidis, L.D., Tsakalis, K. (2007) Controlling Synchronization in a Neuron-Level Population Model, *Journal: International Journal of Neural Systems - IJNS*, vol. 17, no. 2, pp. 123–138.
3. Ellis, T.L., Stevens, A. (2008) Deep brain stimulation for medically refractory epilepsy. *Neurosurg Focus*. 25(3), E11.
4. Freeman, WJ (1986) Petit Mal Seizure Spikes in Olfactory Bulb and Cortex Caused by Runaway Inhibition After Exhaustion of Excitation, *Brain Research Reviews*, 11, 259–284
5. Freeman W.J. (2006). Origin, structure, and role of background EEG activity. Part 4. Neural Frame Simulation. *Neurophysiol.*, 117, 572–589
6. Freeman WJ, Holmes MD, West GA, Vanhatalo S. (2006) Dynamics of human neocortex that optimizes its stability and flexibility. *Journal of Intelligent Systems* 21, 1–21
7. Good, L.B., Sabesan, S., Marsh, S.T., Tsakalis, K., Treiman, D., Iasemidis L., (2009) Control of synchronization of brain dynamics leads to control of epileptic seizures in rodents. *Int J Neural Syst.*, 19(3):173–96.
8. Halpern, C.H., Samadani, U., Litt, B., Jaggi, J.L., Baltuch, G.H. (2008) Deep Brain Stimulation for Epilepsy. *Neurotherapeutics*, 5, 59–67.
9. Kozma, R. (2003). On the Constructive Role of Noise in Stabilizing Itinerant Trajectories in Chaotic Dynamical Memories. *Chaos, Special Issue on Chaotic Itinerancy*, 13(3), 1078–1090.
10. Kozma R, Freeman WJ, Erdi P (2003), The KIV Model Nonlinear Spatio-temporal Dynamics of the Primordial Vertebrate Forebrain. *Neurocomputing*, 52–54, 819–826.
11. Tsakalis, K., Chakravarthy, N., & Iasemidis, L., (2005). Control of Epileptic Seizures: Models of Chaotic Oscillator Networks, *Proc. 44th IEEE Conf. Decision & Control, & European Control Conference*, Seville, Spain, December 2005.
12. Takeshita, S., Sato, Y. Bahar S., (2007) Transitions between multistable states as a model of epileptic seizure dynamics, *Phys. Rev. E*. 75, 051925.

Part V
Dynamic Patterns of Neural Activity
in Human Information Processing

Infant's Primitive Walking Reflex from the Perspective of Learning in the Uterus

Hiroki Mori and Yasuo Kuniyoshi

Abstract Recently, researchers have found that preterm infants' walking starts later than term infants, epidemiologically. In previous study, we have discussed about fetal development in uterus from a perspective of learning and self-organization in the uterine environment and hypothesized that the fetal experience affects an infant's walking ability because fetuses learn reflexive alternating foot stepping relative to primitive walking. We conducted a fetal development simulation and analyzed the feet trajectories by canonical correlation analysis to detect legs' alternating coordinated movements. The results of the analysis show the appearance of alternating feet movements through the uterine experience. Finally, we conducted primitive walking experiments out of the uterine environment with learned neural connectivity and random neural connectivity. In conclusion, the behavior such as primitive walking is acquired through the uterine experience in the simulation and we show the possibility that uterine experience contributes to walking development after birth.

1 Introduction

Even just after birth, term infants can perform walking-like leg movements when one holds them to stand on a floor. Researchers have considered that the reflexive leg movements, which are called walking reflex or primitive walking, facilitate

H. Mori (✉)

Department of Adaptive Machine Systems, Graduate School of Engineering,
Osaka University, Osaka, Japan
e-mail: hiroki@ams.eng.osaka-u.ac.jp

Y. Kuniyoshi

Department of Mechano-Informatics, Graduate School of Information
Science and Technology, The University of Tokyo, Tokyo, Japan
e-mail: kuniyosh@isi.imi.i.u-tokyo.ac.jp

the development of walking. Thelen and Smith had implied that infants' nervous system for walking does not disappear, based on results from a primitive walking experiment in water with 2 months old infants, which do not perform walking reflex above ground. They concluded that the stepping behavior at birth continuously contributes to walking development around 1 year old of age.

A recent epidemiological study revealed delay in the walking development of preterm infants. According to Jeng et al. [1], preterm infants start to stand and walk 2 months later than term infants do, on average. We have discussed the effects of fetal experiences in the uterus for fetal motor development from the perspective of the self-organization of dynamical system of the nervous system, the body, and the uterus, based on a whole body fetal computer simulation. From that aspect, we considered that the duration of the fetal experience in the uterus affects walking development after birth.

In this research, we proposed the scenario of shaping the reflex neural circuit for primitive walking through experience in uterus and the proposal was examined by a computer simulation of a fetal whole body musculoskeletal model and a spinobulbar system with tactile cells.

2 Methods

To study fetal sensori-motor development, we previously developed a fetal whole body musculoskeletal model (Fig. 1) with 198 muscles, 22 joints, 1,542 tactile cells, an uterine wall and amniotic fluid [2]. The distribution of the tactile cells depends on two-point discrimination lengths, so there are many cells on the face, the hands and the feet whereas there are fewer cells on the arms, the thighs, calves and the body trunk (Fig. 2).

The spinal cord model, including inter-neurons, α motor neurons and γ motor neurons, is based on He et al. [3] while a neural oscillator model, modeling neurons in medulla to generate general movements [4], is based on Asai et al. [6]. The neural oscillator is embedded in a one-to-one manner for each muscle, implementing a Coupled Chaotic System [5].

The proposed nervous system is illustrated in Fig. 3. The nervous system model has totally-coupled connectivity from tactile cells to the α motor neurons and the neuronal oscillators. The connectivity weights from the tactile cells to the motor neurons change depending on a modified Hebbian learning (Covariance rule) [8].

In previous work, we proposed a scenario that fetal motor developments, including isolated arm/leg movements and hand/face contacts [7], emerges from tactile experiences with complex and smooth movements, which are regarded as general movements [2]. The scenario had been validated based on the fetal computer simulation. In this paper, we hypothesized the scenario that stepping behaviors emerge from an interaction between leg movements and the uterine response

Fig. 1 A fetal whole body simulation with uterus



Tactile points on right or left side
(Whole tactile points: 1542)

Head	Neck	Chest	Abdomen	Hip
365	6	32	45	22
Shoulder	Upper arm	Forearm	Hand	
15	17	14	173	
Thigh	Calf	Foot		
22	17	43		

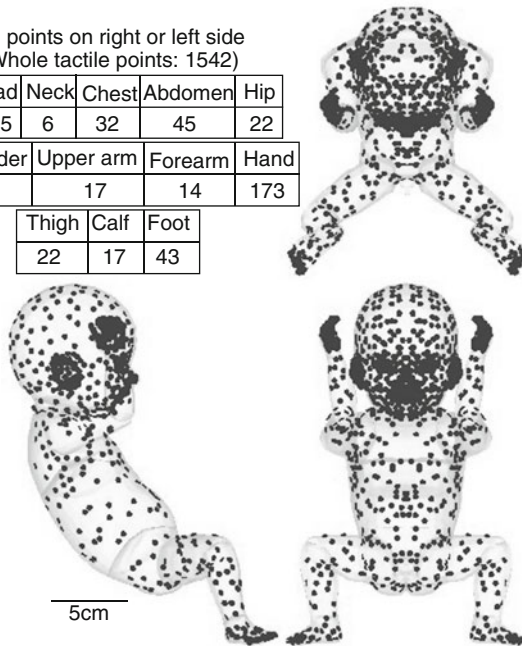
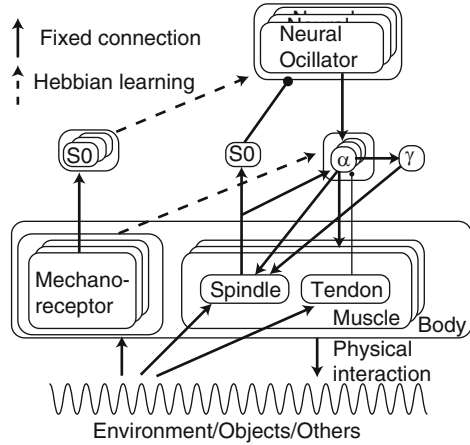


Fig. 2 A simulation model of fetus with tactile cells

through tactile signals before birth, and from an interaction between leg movements and the floor response through tactile signals after birth, since a little biased tactile pattern on right or left foot due to the body trunk's squirm and kicking womb is gradually strengthened by Hebbian learning in the uterus.

Fig. 3 A nervous system model with tactile cells



To validate our scenario in which the fetal experiences facilitate the construction of the neuronal circuit to induce primitive walking, we conducted the fetal computer simulation in uterus with learning for 10,000 s, and primitive walking experiments on a floor without learning for 1,000 s with the following three conditions.

1. Randomized(initial) connectivity, on the floor.
2. Learned connectivity, above the floor.
3. Learned connectivity, on the floor.

Condition 1. corresponds to preterm infants without the experience in uterus. Condition 2. corresponds to term infants without interaction with the environment. Condition 3. corresponds to term infants with environment interaction experience.

The result is analyzed by three aspects. One of them is correlation of distances between both fetal model's feet and its groin. The feet perform stepping movements if the correlation was a negative value. The second is the weight from the feet to the motor neurons which indicate the effect of tactile signals for the behavior. Finally, canonical correlation analysis (CCA) is used to detect the most coordinated feet movement patterns as the first canonical vectors.

3 Results

In the fetal simulation experiment in the uterus model, the leg movements gradually change from random to alternating or stepping, qualitatively.

For the quantitative account, the change of correlation between both feet is illustrated in Fig. 4. The result indicates the stepping behavior increases while the value became negative by 10,000 s.

The weights from tactile cells on both feet to α motor neurons for muscles in both legs at 10,000 s is displayed in Fig. 5 The weight values to the right and the left

Fig. 4 The change of correlation of distances between both feet and groin

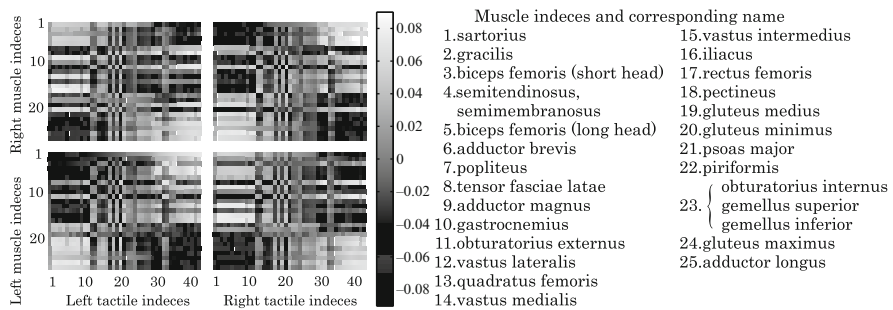
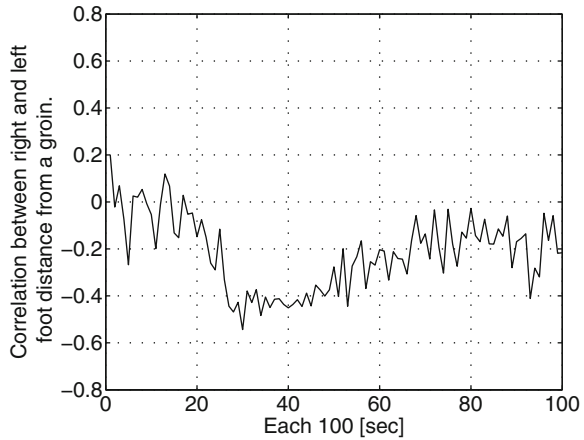


Fig. 5 The weight of connectivity from foot tactile cells to leg muscles

leg muscles are inverted, which means that the neuronal circuit induces alternating leg movements by inverted signals to muscles in the right and the left leg through tactile signals.

To demonstrate the most coordinated leg movement pattern, the results of CCA at the first 1,000 s and the last 1,000 s of the simulation are displayed in Figs. 6 and 7. The canonical correlation increases along with the increase of experience in uterus. The first canonical vectors change from simultaneous forward or backward kicking Fig. 7a to stepping to right or left Fig. 7b.

After the learning period, the fetal model was located on the floor without the uterine model. In Condition 1 (Fig. 8a) and Condition 2 (Fig. 8b), the leg movements did not perform stepping movements. In Condition 3 (Fig. 8c), the leg movements perform stepping movements which are similar to primitive walking by term infants.

Finally, we show the appearance of the primitive walking experiment in Condition 3 in Fig. 9. The fetal model appears to move right and left legs alternatively, such as primitive walking by real infants.

Fig. 6 The change of canonical correlation between right and left foot

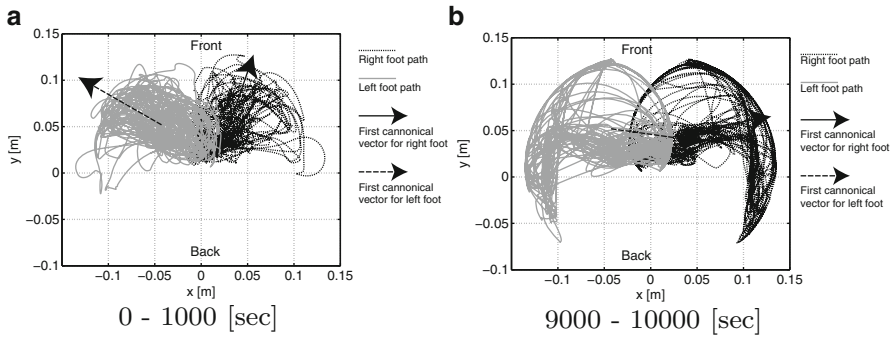
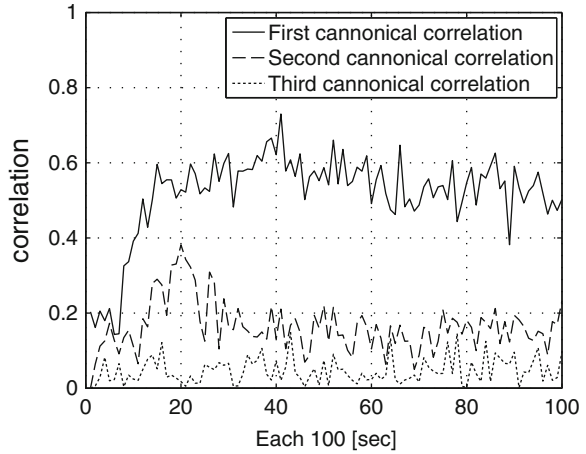


Fig. 7 Feet coordination at the first and the end of learning. Foot paths are illustrated for 100 s in each time duration. First canonical vectors are calculated from the both feet paths for 1,000 s. (a) 0–1,000 s; (b) 9,000–10,000 s

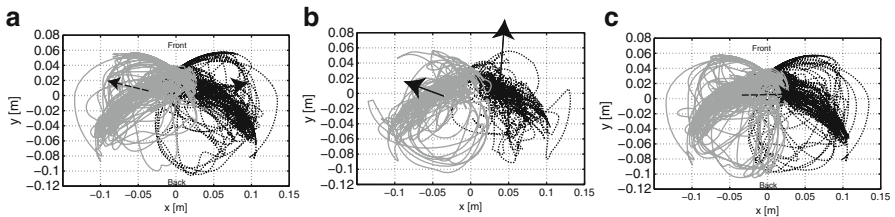


Fig. 8 Results of CCA for a primitive walking experiment (1,000 s) with three conditions. (a) The fetal model on a floor with random connectivity. (b) The fetal model above a floor with learned connectivity. (c) The fetal model on a floor with learned connectivity

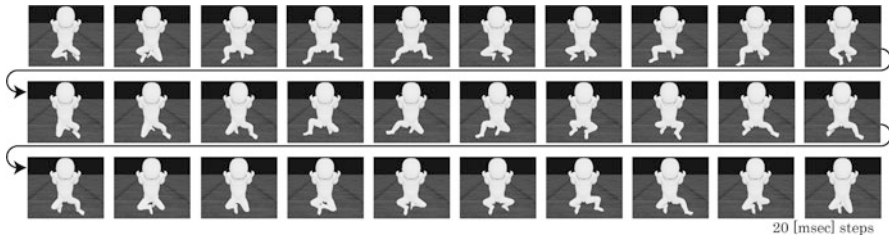


Fig. 9 Primitive walking experiment with neural connectivity experienced in uterus

4 Discussion

The traditional perspective of development is that human development is scheduled along with a built-in time clock, whereas the traditional perspective of learning, such as reinforcement learning, is that learning is adapted to only a certain purpose in the here and now. However, we do not think that the above two perspectives can describe the human development efficiently.

According to the computer simulation in this paper, fetal intrauterine experiences do not only shape intrauterine behavioral development but also primitive walking on the ground, which contributes to walking development after birth. It is plausible that the structure of a body and a nervous system under a dynamics for cognition and behaviors is shaped (or prepared) through the interaction among the nervous system, the body, and the surrounding environment in a self-organizing way before a certain cognitive or behavioral development appear. This concept for human development is similar to “pre-adaptation” in the field of evolutionary study.

It is a problem that the simulation duration, which is 10,000 s, is too short to validate the model to explain the real fetal developments. A simple way to solve the problem is that the gain from merkel cells to motor neurons and the learning coefficient are identified from observation data of fetal behaviors. Finally, we should execute “lifelong” simulations with realistic parameters.

We believe that this scenario contributes to novel therapy methods for preterm infants to help with their walking development.

References

1. S. Jeng et al. “Development of walking in preterm and term infants: Age of onset, qualitative features and sensitivity to resonance,” *Gait and Posture*, **27** (2008) 340–346.
2. H. Mori and Y. Kuniyoshi, “A human fetus development simulation: Self-organization of behaviors through tactile sensation,” *International Conference on Development and Learning* **9** (2010).
3. J. He et al. “Learning from biological systems: Modeling neural control,” *Control Systems Magazine* **21(4)** (2001) 55–69.

4. H. F. R. Prechtl, "State of the art of a new functional assessment of the young nervous system. An early predictor of cerebral palsy," *Early Human Development*, **50** (1997) 1–11.
5. Y. Kuniyoshi and S. Suzuki, "Dynamic emergence and adaptation of behavior through embodiment as coupled chaotic field," *Proceedings of 2004 IEE/RSJ International conference on intelligent robots and systems* (2004) 2042–2048.
6. Y. Asai et al. "Emergence of oscillation in a model of weakly coupled two Bonhoeffer-van der Pol equations," *BioSystems*, **58** (2000) 239–247.
7. J.I.P. de Vries et al. "The emergence of fetal behavior. I. Qualitative aspects," *Early human development* **7** (1982) 301–322.
8. P. dayan and L. F. Abbott, "Theoretical neuroscience: Computational and Mathematical modeling of neural systems," The MIT Press, (2001)

Socially Developmental Robot based on Self-Induced Contingency with Multi Latencies

Hideobu Sumioka, Yuichiro Yoshikawa, Masanori Morizono,
and Minoru Asada

Abstract Early social development is a process that a human infant and his/her caregiver adapt to each other. This paper presents a learning mechanism to find the contingency of human-robot interaction in the real world, which is intended to enable similar process to the mutual adaptation in the infant-caregiver interactions. A contingency measure based on information theory is applied not only to acquire behavior rules but also to find suitable latency to observe the found contingency. Experimental results show that a robot can acquire a series of social behavior such as gaze following and utterance to a human subject through 20 min interaction. Mutual adaptation between them is discussed in terms of transition and synchronization of their behavior, based on the analysis of the interaction data.

H. Sumioka (✉)

Department of Informatics, University of Zurich, Andreasstrasse 15, CH-8050, Zurich,
Switzerland

e-mail: sumioka@ifi.uzh.ch

Y. Yoshikawa

Department of Engineering Science, Graduate School of Osaka University, Machikaneyamacho
1-3, Toyonaka, 560-8531, Osaka, Japan

M. Morizono

Department of Adaptive Machine Systems, Graduate School of Osaka University, Yamadaoka
2-1, Suita, 565-0871, Osaka, Japan

M. Asada

JST ERATO Asada Synergistic Intelligence Project, Osaka University, Osaka, Japan

Department of Adaptive Machine Systems, Graduate School of Osaka University, Yamadaoka
2-1, Suita, 565-0871, Osaka, Japan

1 Introduction

Human infants acquire a variety of social behavior and gradually socialize through various interactions with their caregivers [1]. For example, they become to follow the gaze of an adult and then begin to show gaze alternation, i.e., successive looking between a caregiver and an object, and pointing. However, it remains unclear how these abilities are acquired through multimodal sensorimotor association with their caregivers.

When we try to understand such a learning process, we need to consider not only the information processing for learning in an infant but also dynamics of the interaction with a caregiver because the caregiver adapts himself/herself to infant development. In other words, it is necessary to model mutual adaptation of dynamics among cognition and actions of both an infant and a caregiver. However, it seems difficult to study such adaptation and to understand how an infant adapts itself to its caregiver. A simple computational model might miss key elements such as response time to a caregiver.

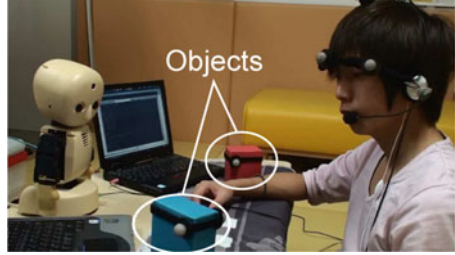
We approach to reveal a basic mechanism underlying the dynamics of early social development from a viewpoint of the cognitive developmental robotics [2]. As a learning principle of an infant, we focus on contingency that refers to a rule of environmental changes caused by a certain action given a certain context. Finding contingencies in the interaction with another person is supposed to be the most fundamental for early social development [3]. Synthetic studies have reported that such ability allows a robot to acquire a social skill such as gaze following [4] and detection of responses from another person [5]. Although some mechanisms based on contingency or similar principles have been proposed for learning several motor skills or social ones [6–8], computation time was unrealistic [8] or time interval to find contingencies in the interactions was fixed [6–8].

In this paper, we build and examine a robot that extracts contingencies from the interaction with a person and utilizes them as behavior rules for realizing mutual adaptation with the person. A contingency measure proposed in [8] is applied not only to find the behavior rules but also to improve them online in order to refine the robot's behavior during the interaction. It is also used to find suitable time intervals between robot's actions to highlight the found rules. Experimental results show that a robot can acquire a series of social behavior such as gaze following and utterance to the human subject through 20 min interaction.

2 Methods

We assume a scene of human-robot interaction where a person sits across from a robot and tries to teach it colors of objects on a table between them (see Fig. 1). We also assume that the robot detects the following information: locations of objects, orientation of the human's head, human's utterance, and its own posture. The robot

Fig. 1 An experimental setup



executes actions such as gaze shift and vowel utterance. These senses and actions are represented and processed in a discrete manner. The robot has no knowledge about relations among them at the beginning.

Let s_i^t and a_j^t be a state of sense S_i and a motor command for act A_j at time t , respectively. Contingency among s_k^t , a_j^t , s_i^t , and $s_k^{t+\Delta t}$, is measured as the reliability of the transition rule from s_k^t to $s_k^{t+\Delta t}$ caused by a_j^t given s_i^t . We refer to a combination $(S_k | S_i, A_j)$ as an *event*. The task of the robot is to find several events with larger expected values of contingencies than other possible events. The found values are then exploited for learning behavior rules and for tuning time interval Δt between its actions so as to highlight the contingencies.

We use the information theoretic measure proposed by Sumioka et al. [8], called C-saliency, to evaluate contingencies in each event. C-saliency of an event $(S_k | S_i, A_j)$ is given by:

$$\begin{aligned}
 C_{i,k}^j &= T_{(S_i, A_j) \rightarrow S_k} - (T_{S_i \rightarrow S_k} + T_{A_j \rightarrow S_k}) \\
 &= \sum_{s_i^t, s_k^t} p(s_k^t, s_i^t) \sum_{s_k^{t+\Delta t}, a_j^t} e(s_k^{t+\Delta t}, a_j^t | s_k^t, s_i^t),
 \end{aligned}$$

where $T_{Y \rightarrow X}$ shows transfer entropy [9] representing the dependency of a process X on a process Y , and $e(s_k^{t+\Delta t}, a_j^t | s_k^t, s_i^t)$, called an element of C-saliency, indicates the reliability of the contingency among $s_k^{t+\Delta t}$, s_k^t , a_j^t , and s_i^t . A behavior rule is defined as selecting an action with the highest element of C-saliency.

The robot incrementally acquires behavior rules based on the extended mechanism of the previous method proposed in [8] (Fig. 2). The mechanism includes a prediction evaluator to ignore doubtful behavior rules and a timing adjuster to tune time interval for each rule to highlight the found contingencies, in addition to four existing modules: (1) a contingency detector; (2) contingency reproduction modules (CMs) that output motor commands according to behavior rules; (3) reactive behavior modules (RMs) that output ones according to pre-defined rules; and (4) a module selector.

RMs and CMs output motor commands to be executed and the reliability values that are computed based on elements of C-saliency. The reliabilities are used by the module selector to decide robot's actions after they are modified by the prediction evaluator. The history of the state and the selected motor command are stored with

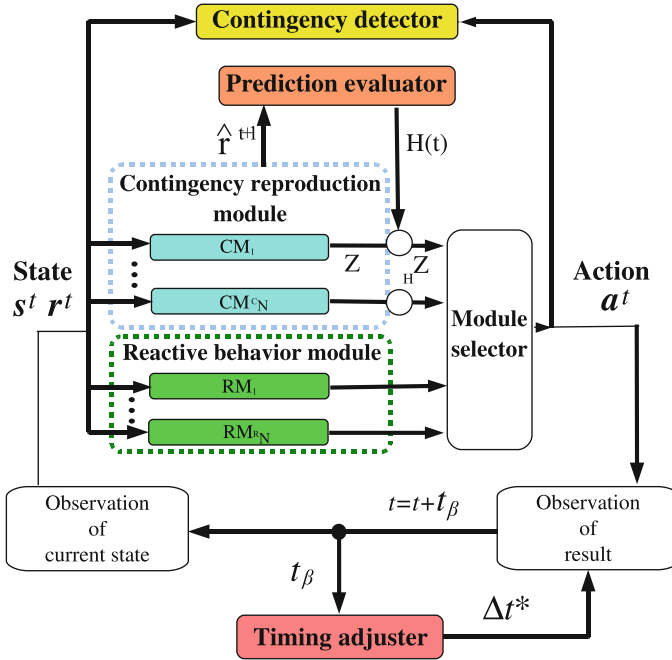


Fig. 2 The proposed mechanism

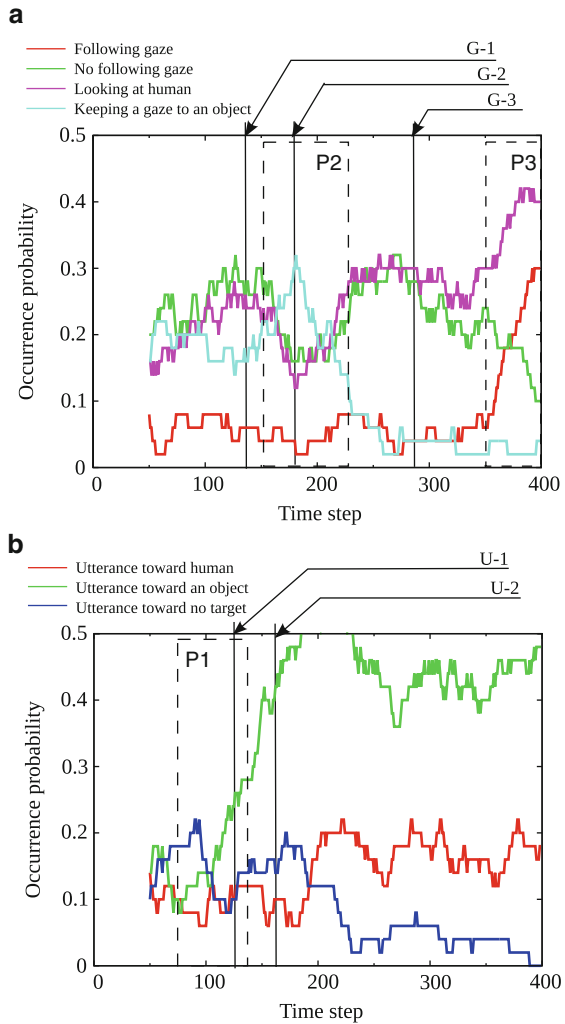
the resultant state in the contingency detector to find a contingent event and to generate subsequent CM based on it. A behavior rule in the CM is updated online so that the C-saliency of the contingent event increases, while it was fixed in [8].

Although a robot and its caregiver were assumed to alternately act at a fixed time interval in the previous model [8], it is not likely in the real world interaction. The timing adjuster finds an appropriate time interval to observe contingent change caused by the last action of the robot, based on the prediction of the change. This module allows the robot to take its next action at different interval.

3 Results

We implemented the proposed mechanism into a humanoid robot and observed its interaction with a person during about 20 min. In the interaction, the person responded to its behavior and tried to draw its attention to an object. The robot's senses and acts were given and represented by six sensory variables, allowing the duplicated definitions for the same property, and two action ones: orientation of person's head (S_1), a state of an object (S_2), person's utterance (S_3), person's frontal face (S_4), person's profile (S_5), own posture (S_6), gaze shift (A_1), vowel utterance (A_2).

Fig. 3 Change of robot's behavior in face-to-face interaction. **(a)** change in gaze shift **(b)** change in utterance. One step in the horizontal axis indicates an action selection of the robot. The vertical one indicates the moving average of the occurrence rate of each behavior among the last 50 steps. The timing of generating new CMs is shown as arrows at the top of the graphs



The robot was able to acquire various behavior rules with different time intervals, although their types, orders, and intervals depended on the history of the interaction. We pick up and analyze a case where it acquired some social skills. Fig. 3 shows the change of its behavior through the interaction. The robot found a rule in $(S_3|S_2, A_2)$ that its utterance to an object causes human's utterance (U-1) and then often chose to utter a vowel when looking at an object (green line in Fig. 3b). Then, it became to often keep its gaze on an object due to the next rule found in $(S_2|S_6, A_1)$ at G-1 (cyan line in Fig. 3a). After that, the utterance during looking at the person (red line in Fig. 3b) and shifting its gaze to the person given human utterance (magenta line in Fig. 3a) increased from U-2 and G-2, respectively. Finally, it became to follow the person's gaze by using the rule found in $(S_2|S_1, A_1)$ at G-3 (red line in Fig. 3a).

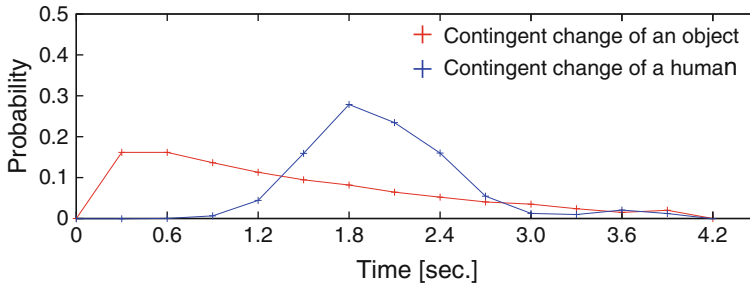


Fig. 4 Examples of probability distributions of the contingent changes observed during 4.5 s after the last robot's action. The *red* and *blue* lines show the case of contingent change for an object (G-1) and one for a human (U-1), respectively

An analysis of time intervals found by the robot revealed different tendencies between events concerning objects and those concerning the person (Fig. 4). The time interval for objects had a peak immediately after the last robot's action while one for the person was observed a few seconds later which is considered to correspond to the duration between a robot's action and a human response. As a result, longer interval was observed when a contingent change concerning the person was expected, compared to one concerning an object.

We observed changes of the dynamics of person's behavior as well as ones of the robot (see Fig. 5). The person increased the utterance to an object (blue line in P1 of Fig. 5b) as the robot increased its utterance to an object (green line in P1 of Fig. 3b). The person's utterance to the robot was often observed when the robot kept its gaze on an object (aqua line in P2 of Fig. 3a and red one in P2 of Fig. 5b). When the robot became to follow the person's head (red line in P3 of Fig. 3a), the person often uttered a vowel to an object (blue line in P3 of Fig. 5b). Since the changes in the person seem to synchronize with ones in the robot, mutual adaptation between them might cause the transition of interaction patterns.

The synchronization between the person and the robot was also observed in terms of the timing of their actions. They took actions alternatively as the interaction develops: the ratio in Fig. 5c approached to one. The time interval between their actions seemed to get shorter (data not shown).

4 Discussion and Conclusion

The proposed mechanism allowed a robot to acquire a series of social behavior through interaction with a person. Moreover, mutual adaptation between the person and the robot was observed in terms of transition and synchronization of their behavior. Although similar tendencies were observed among some of persons, there

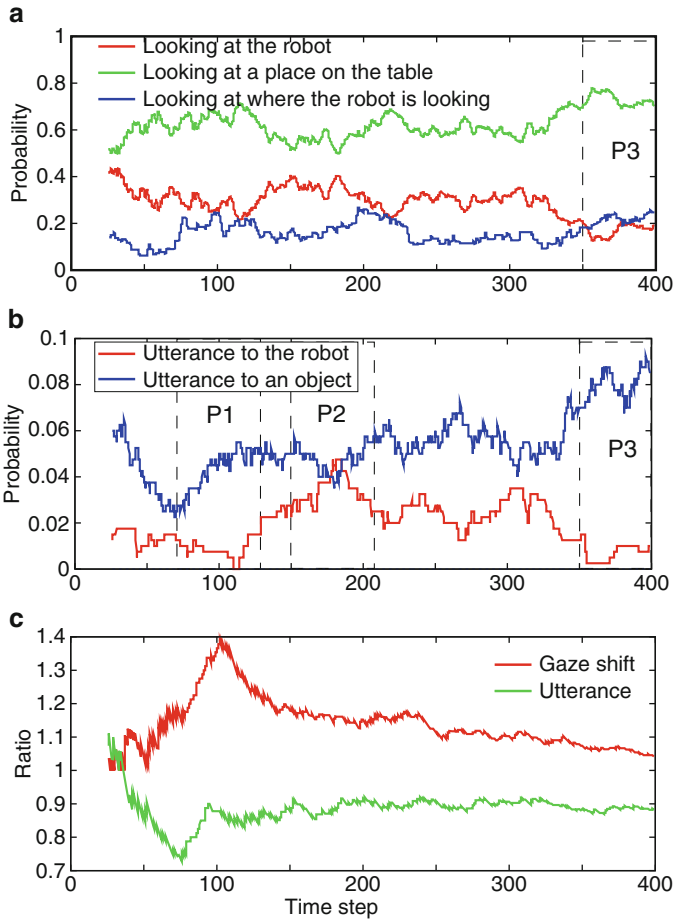


Fig. 5 Changes of human’s behavior. (a) Change in gaze shift of the human. (b) Change in human’s utterance. (c) Transition of the ratio of the number of actions to a robot’s action. A step in the *horizontal axis* shows the robot’s action selection. The *vertical one* shows the moving average among the last 2 min before robot’s action

was a diversity of their behavior patterns. Further analysis on the influence of person’s behavior on learning of the robot will shed light on how the behavior of a caregiver facilitates early social development.

It is noteworthy that the changes in the robot and the person were observed through the 20 min interaction. By virtue of the shorter time scale necessary for mutual adaptation, the proposed system is expected to provide a new research field where early social development can be synthesized and examined through human-robot interaction.

References

1. Moore, C. and Dunham, P., Eds., *Joint Attention: It's Origins and Role in Development* Erlbaum, (1995).
2. Asada, M., Hosoda, K., Kuniyoshi, Y., Ishiguro, H., Inui, T., Yoshikawa, Y., Ogino, M., and Yoshida, C., "Cognitive developmental robotics: A survey," *IEEE Trans. on Auton. Ment. Dev.* **1(1)**, (2009), 12–34.
3. Rochat, P. R., "Social contingency detection and infant development", *Bulletin of the Menninger Clinic*, **65**, (2001), 347–360.
4. Nagai, Y., Hosoda, K., Morita, A., and Asada, M., "Constructive model for the development of joint attention", *Conn. Sci.*, **15(4)**, (2003), 211–229.
5. Movellan, J.R., "An Infomax Controller for Real Time Detection of Social Contingency", *Int. Conf. on Dev. and Learning*, (2005).
6. Oudeyer, P.Y., Kaplan, F., and Hafner, V.V., "Intrinsic motivation systems for autonomous mental development", *IEEE Trans. on Evo. Comp.*, **11(1)**, (2007), 265–286.
7. Kuriyama, T. and Kuniyoshi, Y., "Co-creation of human-robot interaction rules through response prediction and habituation/dishabituation", In *Proc. of the Int. Conf. on Intel. Rob. and Sys.*, (2009), 4990–4995.
8. Sumioka, H., Yoshikawa, Y., and Asada, M., "Reproducing Interaction Contingency Toward Open-Ended Development of Social Actions: Case Study on Joint Attention", *IEEE Trans. on Auton. Ment. Dev.*, **2(1)** (2010), 40–50.
9. Schreiber, T., "Measuring information transfer", *Phy. Rev. Let.*, **85** (2000), 461–464.

On the Brain's Dynamical Complexity: Coupling and Causal Influences Across Spatiotemporal Scales

Emmanuelle Tognoli and J.A. Scott Kelso

Abstract The goal of this paper is to reflect on how neural ensembles affect one another, that is, to characterize their causal influences. The work is based on the tenets that function emerges at several levels of organization between micro- and macro-scale and unfolds on multiple time scales. Such dynamical context creates the condition for complexity and blurs the classical Shannonian definition of transmission upon which causality can be unambiguously established. Our arguments are supported by analysis of models of and empirical support for spatiotemporally metastable brain dynamics: a scale-independent self-sustained regime in which integration (tendencies for the parts to act in a coordinated manner) and segregation (tendencies for independent behavior) are simultaneously realized in space and time.

1 Introduction

Function is a fundamental concept for biological systems. It rests on two foundations. The first one is *coordination* between parts of the system. As a matter of fact, it is difficult to imagine any function produced by just one biological entity: a single thing “is” but does not “do”. In effect, exchange of information, energy or matter between parts creates functional coupling or synergies, from which

E. Tognoli (✉)

Human Brain and Behavior Laboratory, Center for Complex Systems and Brain Science,
Florida Atlantic University, 777 Glades Road, Boca Raton, FL, USA
e-mail: tognoli@ccs.fau.edu

J.A.S. Kelso

Human Brain and Behavior Laboratory, Center for Complex Systems and Brain Science,
Florida Atlantic University, 777 Glades Road, Boca Raton, FL, USA

Intelligent System Research Centre, University of Ulster, Derry, Northern Ireland, UK
e-mail: kelso@ccs.fau.edu

function emerges [1]. The second foundation is *dynamics*: for the system to adapt to ever changing external and internal milieu, it is proscribed that interactions between its parts would be fixed. This is most evident when studying the cognitive brain. If spatiotemporal patterns of brain activity ever freeze rather than perpetually change, thinking, memory, perception, emotion, action and consciousness vanish hopelessly. Within the framework of Brain Coordination Dynamics, and its key concept, metastability [1–3], here we explore how functionally meaningful neural ensembles influence each other. After a theoretical discussion of concepts (Sect. 2), we will consider two types of informational paths, that of synaptic coupling of neurons (Sects. 3 and 4), and that of extracellular neuromodulation of neural ensembles by global neural fields (Sect. 5).

2 Functional Coupling: Irregular Contours in Space ~ Time

The brain exhibits organized activity at many spatial and temporal scales, in which neural ensembles couple and uncouple dynamically. This complex spatiotemporal patterning has been demonstrated empirically, both at rest and during interaction with the environment. The fact that change in spatiotemporal organization arises spontaneously (and with it, associated itinerancy of the mind) imposes specific constraints on our theories of the brain: a plausible theory should explain changing spatiotemporal patterns from within, without resort to inexplicit control mechanisms, the brain's *deus-ex-machina*. Theories have proposed that the brain's dynamically coordinated behavior is accomplished under the rule of attractors [1, 4, 5] or more flexible attractor remnants [1, 3, 6] or both [2]; in the presence of attractors, spontaneous changes in brain coordination dynamics are obtained from multistability on one end, and noise (rest) or incoming energy (stimulation) on the other; in the absence of attractors, spontaneous changes naturally occur as attractor remnants are successively visited and escaped from. A model of coupled oscillators that exhibit simultaneous phase-locking (attractors) and metastability (attractor remnants) is that of Kuramoto and Battogtokh [7]. In this model, oscillators that do escape phase-locking were initially described as following an "incoherent" behavior [7]. We have demonstrated that their dynamics exhibited dwell ~ escape patterns of relative phase behavior that is characteristic of metastability [8]. Study of this model revealed that integrative tendencies exist within irregular space ~ time contours (Fig. 1). Over time, larger or smaller ensembles integrate their activity, and from the complementary spatial standpoint, oscillators join collective behavior for longer or shorter periods of time. The resulting space-time portrait of this behavior (in the Minkowski sense) reveals irregular contours: a challenge for separate spatial or temporal approaches (see boxes, Fig. 1) that if not addressed, limits our understanding of brain complexity.

By relaxing the constraints on spatial and temporal order simultaneously (Fig. 2), spatiotemporal metastability also presents the joint possibility for integrative behavior and information flows. It offers a compromise between two radical views in which the brain is deemed to function in terms of information propagation (in the

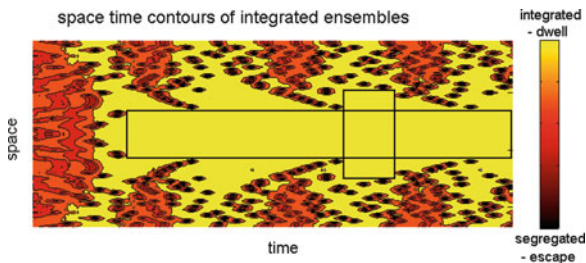
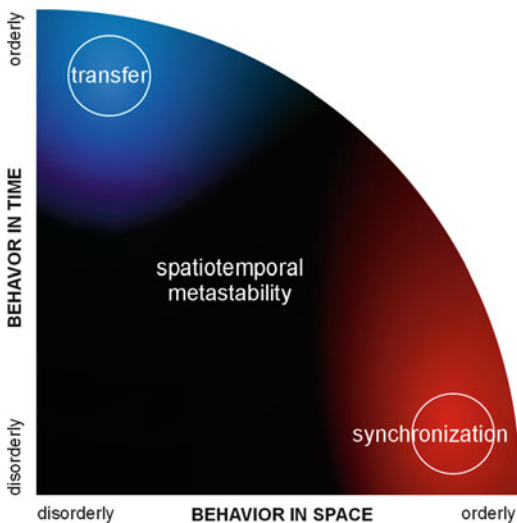


Fig. 1 From Kuramoto and Battogtokh's chimera model [7], a space \sim time portrait of integration is shown. Oscillators are represented on the vertical axis and their partaking in collective behavior over time (*horizontal axis*) is encoded following the color scale on the right (integrative tendencies in *yellow*; segregative in *dark red*). Integrative behavior emerges in a space \sim time domain that has irregular contours (*yellow surface*) which are not properly captured by techniques that follow only a spatial or temporal approach: as black rectangles suggest, only a fraction of the integrative behavior is expressed in such partial approaches, namely those with less complex and dynamical coordination behavior

Fig. 2 A conceptual view of the spatial and temporal order in the behavior of neural ensembles. Concepts of order in time (*blue*, "transfer") and space (*red*, "synchronization") have been most studied. In their pure form, each hampers the meaningful expression of the other. Complexity lives in the dark areas of this diagram (spatiotemporal metastability) -with its mixture of integrative and segregative tendencies in space \sim time



strict Shannonian sense) or coupled oscillations [e.g. 1, 4, 5, 9]. Yet, metastability creates difficulties with the interpretation of the direction of information flow which emerge at multiple levels of description and become dependent on spatial and temporal scales, as we further discuss in Sect. 3.

3 Causality in Simple and Complex Systems

Coupling is a concept more akin to spatial order (Sect. 2), whereas causality relates more closely (albeit not exclusively) to temporal order. In this latter respect, a substantial part of today's neuroscience paradigm draws from Shannon's

“Mathematical Theory of Communication” (1948) [10]. This seminal paper describes transfer of information between emitter and receiver in telecommunication networks, and implies two fundamental boundaries: discrete communication acts, and well-defined direction for the transfer of information in unique channels. In a single channel of communication with emitter and receiver as defined by Shannon [10], to define causality, it suffices to track the temporal ordering of information to determine the system’s causal flows. The paradigm’s success in Neuroscience owes much to the fact that it works sufficiently well insofar as only two brain components are isolated: with their directional interactions, a pair of neurons immediately comes to mind as an ideal substratum for Shannonian transmission. Even in a more complicated system composed of multiple components and reciprocal connectivity, if the system is initially silent and then subjected to external stimulation, its transmission path(s) can readily be identified. But the brain as a whole is operating in a self-sustained nonequilibrium regime [1, 6, 11–13], and is not amenable to such formalism: if observed for sufficient time especially at meso- and macro-levels, it is clear that parts of the brain “talk” continuously and simultaneously to each other: they are self-organized. When there is energy input coming in (for instance, a stimulus entering the system through sensory receptors), what happens is not the recruitment of mute regions that suddenly enter into action -each at their turn- and return to rest. What happens instead is that the ongoing coordination is “perturbed” and ripples across the many spatial and temporal scales at which brain self-organization lives. The “event” is woven into the brain’s ongoing activity. In this (general) case, causal influences between brain parts are much less straightforward to define. Since information flows cannot be described as departure from equilibrium states, well-defined causality is restricted to narrow spatiotemporal windows in the vicinity of a particular “input” or “event” (see also fig. 5 from Izhikevich and Edelman [14] for related account). And because observation windows are finite, empirical quantifications of information flows are restricted: lack of information about the system’s past prevents accurate characterization of ongoing dynamics and its coupling with incoming information (see Sect. 4).

4 Entangled Precedence

We have argued that spatiotemporal metastability prevents stagnation of information flow, while simultaneously allowing for collective (coordinated) behavior (Fig. 2). The challenge becomes to determine which brain parts influence which others, through space and time, and across their respective scales of observation (Fig. 3). When emitter and receiver are not *a priori* defined, a useful concept is that of precedence (Sect. 3). However, even in the simpler case of the resting brain transiently removed from external input, its intrinsic dynamics includes continuous exchange of information between the parts (A-causes-B-causes-A . . .), and salient “causes” to any neural event exist at multiple times in the history of the system’s

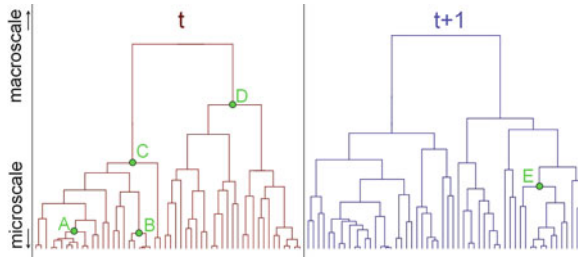


Fig. 3 Functional nodes across spatial scales shown at two successive time points t and $t+1$: the dendrograms link microscopic parts (*bottom*) according to their momentary coupling. Every node influences every other at all times, with a finite strength $k(i_i, j_j)$. A few nodes are marked to exemplify upward and downward causation (e.g. influence of B on C , and vice-versa), instantaneous (e.g. A on B) and delayed (D on E) causality. An important challenge is to discover key causal nodes in this system: which set of relationship is strongest across spatial scales, within and across time [15]

self-organized dynamics: causes are entangled over continuous and reciprocal information exchange. To understand spatiotemporal influences between brain parts requires one to confront this “entangled precedence”: that is, to incorporate precedence and causality from Shannonian systems (Sect. 3) with ongoing coupling expressed at multiple time scales (Sect. 2), which, under metastable regimes of coordination, fluctuates over time.

Rather than attempting to identify causality in a time-independent manner, a solution consists of quantifying its manifold expression across temporal and spatial scales (which are interrelated: see e.g. Fig. 1). Figure 3 shows a dendrogram that clusters phase similarity of neural ensembles over spatial scales at different times. Each node of the dendrogram speaks of a transient neural ensemble, which exerts a finite influence k on each of the other nodes. The strongest directional couplings between pairs of nodes in the system reveal key causal relationships.

5 Beyond Synapses: Dendritic Sensing of the Extracellular Field

So far, we have only explored (slow) information exchange via synaptic coupling. This scheme of information exchange suffers delays of several tens of milliseconds for the communication of information between most distant neural groups. Dendritic trees however are exposed to two types of information: that delivered through their synaptic contacts and that due to local fluctuations in the ionic composition of extracellular space. This raises the theoretical possibility that neurons attune themselves to specific aspects of extracellular fields, using their spatially extended dendritic branches to appreciate extracellular gradients and to sense the global patterning of the brain near-instantaneously. According to this suggested mechanism, the brain

would be endowed with two ways to exchange information, one global and fast, the other local or selective and slow. Such a mechanism could have a profound impact on the definition and quantification of coupling and causality in the brain.

6 Conclusion

Identifying information flows in the brain constitutes an important challenge with significant consequences: for instance, with such knowledge, ideal functional nodes for therapeutic intervention could be discovered and operationalized. We have stressed that brain complexity constitutes an obstacle to the unambiguous and unique definition of causal paths in the brain. We discussed whether causality : (1) is uniquely defined by the structural network; (2) is context-dependent; (3) flows in an identical manner across spatial scales of description; and (4) is expressed in a similar manner across different temporal scales. These considerations point toward the importance of spatiotemporally metastable dynamics for understanding the workings of the brain.

Acknowledgments This work was supported by NIMH Grant MH080838, NSF BCS0826897, the US ONR N00014-09-1-0527 and the Davimos Family Endowment for Excellence in Science. Discussions with G.C. de Guzman are gratefully acknowledged.

References

1. Kelso, J.A.S. (1995). *Dynamic Patterns: the Self-organization of Brain and Behavior*. Cambridge, MIT Press.
2. Kelso, J.A.S., Tognoli, E. (2007). Toward a Complementary Neuroscience: Metastable Coordination Dynamics of the Brain. In R. Kozma & L. Perlovsky (Eds.) *Neurodynamics of Higher-level Cognition and Consciousness*. Springer, Heidelberg.
3. Tognoli E., Kelso J.A.S. (2009). Brain Coordination Dynamics: True and False Faces of Phase Synchrony and Metastability. *Prog. Neurobiol.*, 87(1): 31–40.
4. Freeman, W.J. (1975). *Mass Action in the Nervous System*. New York: Academic Press.
5. Bressler, S.L., Tognoli, E. (2006). Operational Principles in Neurocognitive Networks. *Int. J. Psychophysiol.*, 60: 139–148.
6. Tsuda, I. (1992), Dynamic Link of Memory– Chaotic Memory Map in Nonequilibrium Neural Networks. *Neural Networks*, 5: 313–326.
7. Kuramoto, Y., Battogtokh, D. (2002). Coexistence of Coherence and Incoherence in Nonlocally Coupled Phase Oscillators: a Soluble Case. *Nonlin. Phenom. Complex Syst.* 5: 380–385.
8. Kelso, J.A.S., Tognoli, E. (*in prep*). *The Metastable Brain*.
9. Hebb, D.O. (1949). *The Organization of Behavior*. New York: John Wiley.
10. Shannon, C.E. (1948). A Mathematical Theory of Communication, *Bell System Technical Journal*, 27, 379–423, 623–656.
11. Fuchs, A., Kelso, J.A.S., Haken, H. (1992). Phase transitions in the human brain: spatial mode dynamics. *International Journal of Bifurcation and Chaos*, 2(4): 917–939.

12. Kelso, J.A.S., Bressler, S.L., Buchanan, S., De Guzman, G.C., Ding, M., Fuchs, A., Holroyd, T. (1992). A phase transition in human brain and behavior. *Phys Lett A*, 169:134–144.
13. Chialvo, D. (2010). Emergent Complex Neural Dynamics. *Nature Phys.* 6: 744–750.
14. Izhikevich, E.M., Edelman, G.M. (2008). Large-scale Model of Mammalian Thalamocortical Systems. *Proc Natl Acad Sci USA*, 105: 3593–3598.
15. Sporns, O. (2011). *Networks of the Brain*. Cambridge: MIT Press.

Formulating a Cognitive Branching Task by MTRNN: A Robotic Neuroscience Experiments to Simulate the PFC and Its Neighboring Regions

Fady Alnajjar, Yuichi Yamashita, and Jun Tani

Abstract The foremost objective of our research series is to construct a neuro-computational model that aims to achieve a Large-Scale Brain Network (LSBN), and to offer a better insight of how the macro-level anatomical structures, such as the connectivity between the frontal lobe regions and their dynamic properties, can be self-organized to obtain the higher order cognitive mechanisms. To address this issue, this paper focuses in proposing a model that intends to understand the mechanisms underlying the cognitive branching function, a higher order cognitive mechanism, in which a delaying to the execution of an original task occurs until the completion of a subordinate task. The model is constructed by a hierarchical Multi-Timescale Recurrent Neural Network (MTRNN) and conducted on a humanoid robot in a physical environment. Experimental results suggest possible neural activities and network's layout at the investigated regions that act as an important factor to accomplish such a task.

1 Introduction

Defining the functional organization of the frontal lobes and its neighboring regions in the human brain remains a significant challenge for cognitive neuroscience. The importance of such areas is its responsibility to operate higher cognitive functions and controls [1]. Although many studies have provided various assumptions of how the neurons on the frontal cortex are organized, connected, functioning and/or communicating, through neuropsychological, and neuroimaging studies [1, 2], these assumptions are still in a very abstract level [1]. The common argument is mainly that the frontal regions along the rostro-caudal axis interact with one another

F. Alnajjar (✉) • Y. Yamashita • J. Tani
Lab. for Behavior and Dynamic Cognition, RIKEN Brain Science Institute,
Saitama 351-0198, Japan
e-mail: fady@brain.riken.jp; yamay@brain.riken.jp; tani@brain.riken.jp

hierarchically [3]. The more anterior regions on the brain influence processing in the more-posterior regions to a greater extent than vice versa. Although this issue has been so far generally formulated in phenomenological terms, their functional organization remains controversial. The question is how such hierarchal connectivity between the frontal lobes and the dynamic properties of each of its local region, can be self-organized to obtain the higher order cognitive mechanisms, such as planning, reasoning, cognitive branching, etc.

Neurocomputational models attempt to establish detailed links between biology and cognition in a way that is consistent with established neural information processing principles. Their main advantages are being able to describe functional principles of how the simulated neural system in the brain operates in a relatively comprehensible set of equations, which makes it a powerful tool for studying mechanisms of neural systems. MTRNN model has been considered as a suitable candidate to simulate, to some extent, the brain activities [3]. It has been proven to achieve the function hierarchy through a form of self-organization that is not only based on the spatial connection between neurons but also on multi distinct types of neuron activities, each with different time properties. Through such various neuron activities, continuous sequences of any set of behavior are segmented into reusable primitives which in turn are flexibly integrated into diverse sequential behaviors. The biological observation of such a type of hierarchy has been discussed in details by Badre [1], who suggested that levels of abstraction might gradually reduce along the rostro-caudal axis in the frontal cortex of the monkey and human brain. Others have also addressed that the rostral part is considered to be more integrative in processing information than the caudal part due to its slower timescale dynamics, which result in such a formation of functional hierarchy in the frontal cortex.

The purpose of this paper, therefore, is to construct a neurocomputational model of the frontal lobes based on anatomical and functional image data collected from the brain of monkey and human [1, 2]. The proposed model will aim to pave the way to achieve a large-scale brain network, and to offer a better insight of how macro-level anatomical structures can be self-organized to obtain the higher order cognitive mechanisms. More precisely, we are trying to understand how the dorsolateral prefrontal cortex (BA9/46) with its neighboring regions, such as the lateral frontopolar cortex (BA10), the premotor cortex (BA8&6), and the primary motor cortex (BA4) are structured and linked to ruling the cognitive branching task, in particular (Fig. 1a).

The validity of the resulted model is examined and analyzed through a variety of robotic experiments. We believe that this proposed study can be considered as a joint research between the synthetic and the empirical studies, which can open a new era for better understanding of brain mechanisms.

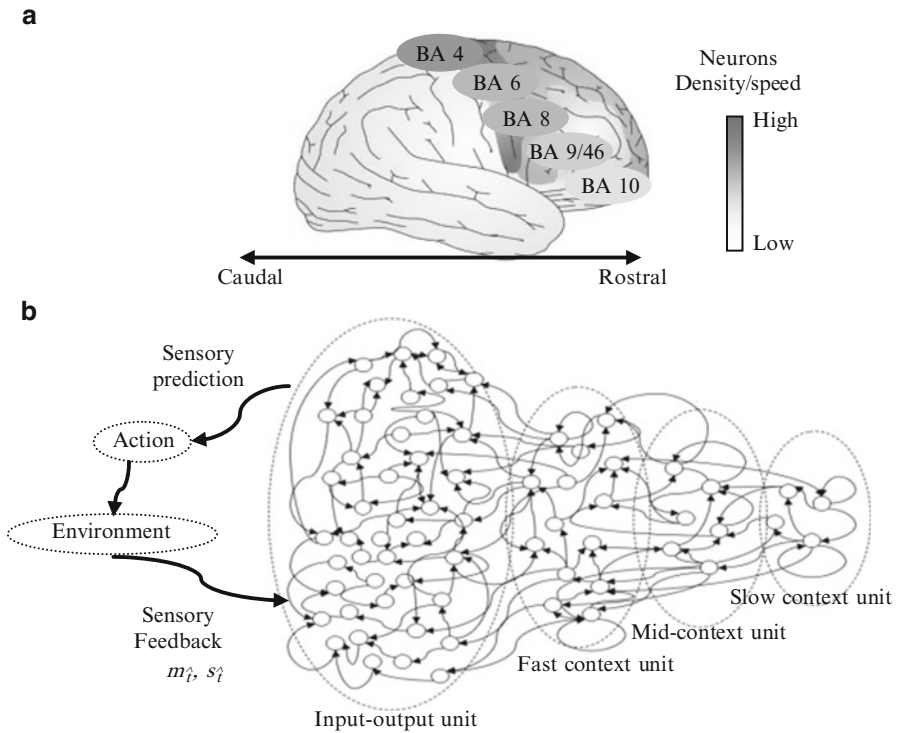


Fig. 1 (a) Anatomical sites of area of focus on the human brain. (b) The proposed MTRNN model

2 Methods

2.1 Task Design

A small humanoid robot was used in the role of a physical body interacting with the actual environment Fig. 2. The robot was fixed to a stand, with tasks involving movement of the head and the right arm of the robot. The arm moves with 4° of freedom $m_{\hat{t}}$ (4 dimensional vectors representing the angles of the arm joints), and the head motor moves with 2° of freedom $s_{\hat{t}}$ (2 dimensional vectors representing the stimulus position (a red mark)). The joints of the robot have rotation ranges which are mapped to values [0.0 ~ 1.0]. Encoder values of these arm joint sensors are received as the current proprioceptive sensory feedback and sent to the network. A vision system mounted on the robot’s head was programmed to locate a red mark on the workspace. The direction of the robot’s head, indicated by encoder values of two neck joints, expressed the object position in the visual field relative to the robot. This relative location of the object was treated as visual input to the system to observe the stimulus status.

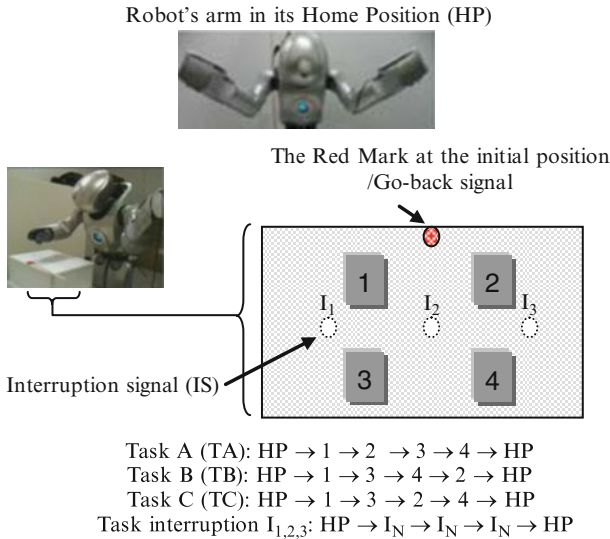


Fig. 2 The workspace and the robot tasks

For the workspace, a workbench was set up in front of the robot. A sheet of a white paper, which shows four numbers and moveable red mark, was placed on the workbench to conduct the experiment Fig. 2. The robot's task was to autonomously reproduce a cognitive branching behavior: (1) Start an original task: dialing a certain sequence of numbers by clicking on these numbers using its right arm index finger whenever the red mark is replaced on the initial position. (2) When an external stimulus appears, i.e. the red mark is placed to one of the interruption positions (I_1 , I_2 , I_3), the robot should suspend working on its original task until accomplishing the interruption subtask (clicking directly on the red mark). (3) When the red mark is returned to its initial position, which is a Go-Back signal, the robot should resume its outstanding original task starting always from the arm in its Home-Position (Fig. 2).

2.2 System Overview

The main component of the current model is borrowed from a Continuous Time RNN (CTRNN) [4]. CTRNN is a type of RNN that implements a feature of biological neurons, thus the activities of neurons are determined not only by the current synaptic inputs but also by the history of neural states. Due to these characteristics, CTRNN can reproduce complex dynamics, and continuous sensorimotor sequences.

To construct a hierarchy structure of CTRNN, we adopted the model of the MTRNN (Fig. 1b). The functional hierarchy in MTRNN is made possible through the use of three distinct types of neurons, each with different temporal properties.

The first type of neurons is the “fast” unit, whose activity change quickly over the short term. The second type of neurons is the “mid” unit, whose activity change over time between the fast and the slow unit, which in turn represents the third type of neurons “slow unit”.

In the model, inputs to the system were the proprioception $m_t^{\hat{}}$ and the vision sense $s_t^{\hat{}}$. Based on the current $m_t^{\hat{}}$ and $s_t^{\hat{}}$, the model generated predictions of proprioception m_{t+1} for the next time step (vision is not predictable since it is randomly occurring). The prediction of the proprioception m_{t+1} was then sent to the robot in the form of target joint angles, which acted as motor commands for the robot in generating movements and interacting with the environment. For the initial teaching signal, the experimenter guided the robot’s right hand along the trajectory of each task sequences. These trajectories were then recorded and used, in an off-line manner, as teaching sequences to the model using the conventional Back-Propagation Through Time (BPTT). The learning target was to find optimal values of synaptic weights that minimizing the error between teaching sequences and the model output.

Neural activity in the model can be described by the following differential equation [3]:

$$\tau_i \dot{u}_{i,t} = -u_{i,t} + \sum_j w_{ij} x_{j,t} \quad (1)$$

where $u_{i,t}$ is the membrane potential, $x_{i,t}$ is the neural state of the i th unit, and w_{ij} is synaptic weight from the j th unit to the i th unit. The second term of the equation corresponds to synaptic inputs to the i th unit. The time constant τ is defined as the decay rate of the unit’s membrane potential, analogous to the leak current of membrane potential in real neurons. When the τ value is large, the activation of the unit changes slowly, because the internal state potential is strongly affected by the history of the unit’s potential. On the other hand, when the τ value of a unit is small, the effect of the history of the unit’s potential is also small, and thus it is possible for activation of the unit to change quickly.

The network that was used in the current model consisted of input-output and a context unit. Context unit was divided into three groups based on the value of time constant τ . The overall connection between the units in the model is as shown in Fig. 1b. The setting of neuron initial states are self-organized through the learning process [5], thus the initial values which correspond to the same behavior are very close to each other in the state space of initial values.

2.3 Training

Through the training process, the network learns gradually to predict the motor feedback for the next time step. After teaching the network in a closed-loop manner, the robot in turn will be able to reproduce the learned movements.

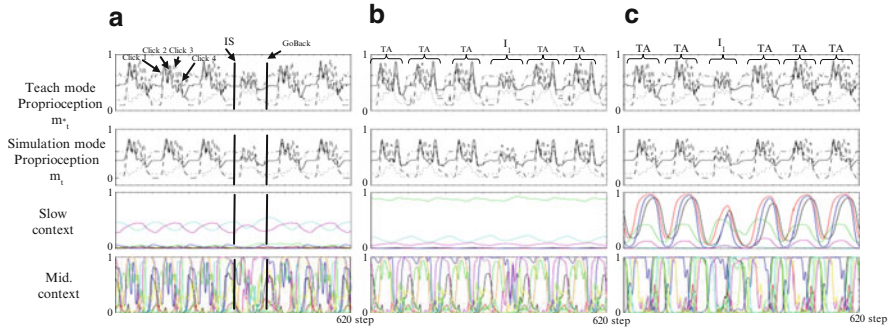


Fig. 3 Example of behavior sequences for (a) multi task TA with an interruption (I_1), (b) multi TB with I_1 , and (c) multi TA with I_1 (different initial synaptic weights). The trained networks reproduced target behavior sequence successfully (teach mode = trained network output (simulation mode)). In this example, fast-unit ($\tau = 3$), mid-unit ($\tau = 8$), and slow unit ($\tau = 40$). Due to different initial synaptic weights, different neural representations that can affect long-term memory stability have been observed during the experiments

Three learning trials were conducted with randomized initial synaptic weights. Optimal trained weights were then tested through the interaction of the robot in the simulation and the physical environment. Figure 3 illustrates an example of the trained model generated by mental simulation while performing Task A and Task B. In our experiment, both in mental simulation and in the actual robot interacting with a physical environment, the trained network reproduced the desired behavior successfully.

2.4 Results

In the first example, Fig. 3a and b, when the robot reproduces the movements of a task, the slow context unit changes gradually and systematically without showing the details of the motor moving patterns (represents a very abstract manner). Accordingly, no significant discrimination between the original and the interruption task can be observed in this unit.

The mid-unit, in contrast, shows better the distinction between these tasks. The repetitions of similar patterns, e.g., click 1, click 2, etc., are also observed partially in the mid-unit activities, and in more details in the fast-unit (results are not shown). These results suggest that the robot, in this example, has indeed encoded the memory of the original task in the slow unit, forming a role similar to that of the parametric bias [3]. Such a memory formation build a static-type memory, which helped the robot to have stability when dealing with a multi and/or long term interruption task, as has been experimentally observed.

In the second example, Fig. 3c, on the other hand, the slow context unit seems to be much involved in encoding both the original and the interruption tasks, which

in turn leads to form a dynamic-type memory that decreases the robot memory stability. If the interruption task occurs for a longer period, for instance, all the units, including the slow unit, will gradually tuned to fit with the interruption task making returning to the original task impossible. This phenomenon has also been experimentally observed.

3 Conclusions and Future Directions

In this study, the proposed model successfully situated itself to perform properly the desired behavior; suspending an original task up to the time of the completion of the extraneous subtask. The result analyses outlined how both the mid- and the slow units could work to form the memory by delaying the outstanding task. The memory formation (static or dynamic), however, seems to be highly affected by the randomized initial synaptic weights. From the results, we believe that this work could contribute as a possible neural implementation for a better insight of how macro-level anatomical nodes in the frontal lobe are dynamically structured and organized to obtain such a higher order cognitive mechanism. An important issue for the future directions will be to scale both the model and the task into a further complex level: as for the model, it is important to look at the direction and the strength of connection between the local units. While as for the task, we are planning to conduct an additional switching task and compare between its neural dynamics and the reported dynamics from the current task. It will be also interesting to try to enhance the interruption task to occur not only in the HP period but also in between the task sequences itself.

Acknowledgments Use of the robot was made possible through a collaboration with SONY Corporation.

References

1. D. Badre, et al., Is the rostro-caudal axis of the frontal lobe hierarchical? *Nature reviews. Neurosci.*, 10(9), 2009, pp. 659–669.
2. P. Hagmann et al. Mapping the Structural Core of Human Cerebral Cortex, *PLoS Comp. Bio.*, 6(7), 2008, 0060159.
3. Y. Yamashita, et al., “Emergence of functional hierarchy in a multiple timescale neural network model: a humanoid robot experiment”, *PloS Comp. Bio.*, 4(11), 2008, e1000220.
4. J Elman: Finding structure in time. *Cogn. Sci.* 14, 1990, 179–211.
5. R. Nishimoto, et al.: Learning multiple goal-directed actions through self-organization of a dynamic neural network model, *Adapt. Behav.*, 16, 2008, 166–181.

Neurodynamical Account for Altered Awareness of Action in Schizophrenia: A Synthetic Neuro-Robotic Study

Yuichi Yamashita and Jun Tani

Abstract We hypothesize that altered awareness of action in schizophrenia may arise from disturbance of the forward model originating in functional disconnection in a hierarchical neural network. The proposed idea was tested through a neuro-robotic experiment using a hierarchical neural network model connected to a humanoid robot interacting with a physical environment. The results demonstrate that not only top-down forward dynamics, but also bottom-up regression processes driven by prediction error are important mechanisms for flexible adaptation to unpredictable changes in environment. In the simulated functional disconnection, in contrast to the normal condition, it turns out that this bottom-up regression process generates unnecessary modulatory signals which may induce altered awareness of action in patients. These results suggest that the proposed hypothesis may provide novel insight for understanding the pathological mechanisms of schizophrenia.

Keywords Prediction error • Neural networks • Hierarchy • Disconnection • Motor control

1 Introduction

It is generally thought that complex and diverse behavior of animals result from functional hierarchy of the neural systems [1, 2]. In such hierarchical neural systems, *top-down* and *bottom-up* interactions play an important role for flexible

Y. Yamashita (✉)

ERATO, Okanoya Emotional Information Project, Japan Science Technology Agency,
Saitama 351-0198, Japan
e-mail: yamay@brain.riken.jp

J. Tani

Department of Electrical Engineering, Korea Advanced Institute of Science and Technology,
Daejeon 305-701, Republic of Korea
e-mail: tani1216jp@gmail.com

adaptation to the environment. For example, in a cognitive task such as the Wisconsin card sorting test, a subject selects a response based on an internally represented task context (i.e. a current appropriate matching rule) in a top-down manner. During the course of the test, the matching rules could be switched by the experimenter with unpredictable timing, resulting in a discrepancy between top-down prediction and the actual feedback. Based on this discrepancy signal, the task context should be modulated so as to match with the current appropriate rule (bottom-up regression). This interaction between top-down and bottom-up processes in a hierarchical network could allow animals to produce skillful behavior and to achieve flexible adaptation to changes in environment.

However the underlying neural mechanisms governing the interactions between top-down and bottom-up processes in hierarchical neural systems have not yet been clarified. In the previous studies, Tani [3] showed that a robot can produce adaptive behavior through the top-down prediction and bottom-up regression processes using a simple computational principle of minimizing prediction error. Based on a similar idea of minimizing prediction error, but using a statistical formulation, Friston [4] also proposed a computational model as a general principle of brain functions. In the current study, we test these hypotheses through examining a pathological symptom of neuropsychiatric disease as a failure in the interaction of top-down and bottom-up processes in hierarchical neural systems. Specifically, we focus on a symptom of altered awareness of action (delusion of control) in schizophrenia.

Delusion of control is one of the characteristic symptoms of schizophrenia, where a patient feels that his actions are generated not by himself but by some outside force, even though his action itself is basically intact. Some biological observations suggest that delusion of control is associated with abnormal functionalities in the prefrontal cortex and the parietal cortex [5]. However, there is little evidence for the anatomical abnormalities in those local regions. Based on this fact, Friston proposed a hypothesis that basic pathology of schizophrenia may be associated with functional disconnectivity between prefrontal and posterior brain regions (i.e. “disconnectivity syndrome hypothesis” [6]).

This pathological phenomenon is also considered from the aspect of motor control theory. Frith [7] hypothesized that delusion of control arises due to a failure to form the sensory prediction of action (“forward model hypothesis”). According to this hypothesis, the *sense of agency* (awareness that one executes and controls one’s own action) is based on the sensory attenuation which occurs when the forward prediction of action consequences matches the actual sensory feedback. In schizophrenic patients, due to the impairment of forward model, mismatch between the forward prediction and actual sensory feedback would arise. As a result, altered awareness of action may be induced, even though patient’s action itself is intact [7].

In the current study, we unite these two lines of theory. We hypothesize that delusion of control may arise from disturbance of the forward model originating in functional disconnectivity in a hierarchical network. In order to test this idea, we developed a hierarchical neural network model connected to a humanoid robot interacting with a physical environment.

2 Methods

The task for the robot was to repeatedly reproduce the following series of sequential behavior associated with positioning an object: (1) move the object up and down three times at the position L, (2) move the object from the position L to the position R, (3) move the object left and right three times at the position R, (4) move the object from the position R to the position L. This sequence is described by the state transition diagram in Fig. 1a. In addition to producing the periodic behavior sequences, the robot was also required to adapt to unpredictable sensory perturbation. Specifically, during execution of task behavior, the position of the object was switched by an experimenter with unpredictable timing.

Figure 1b shows an overview of the system. Inputs to the system were the proprioception and the vision senses. Based on the current input, the system generates predictions of proprioception and the vision senses for the next time step. The forward prediction of the proprioception was sent to the robot in the form of target joint angles, which acted as motor commands for the robot in generating movements.

The main component of the system was modeled by a “multiple timescale recurrent neural network (MTRNN)” [2] which is a type of a continuous time recurrent neural network. The model of neurons is a conventional firing rate model, in which each unit’s activity represents the average firing rate over a group of neurons. The continuous time characteristics of the MTRNN are described as follows,

$$\tau_i \dot{u}_{i,t} = -u_{i,t} + \sum_j w_{ij} x_{j,t} \tag{1}$$

where $u_{i,t}$ is the membrane potential and $x_{i,t}$ is neural state of the i th unit at time t . The MTRNN is made up of two different types (*fast* and *slow*) of context units, each type with its own distinct time constant τ (multiple timescale). Through the introduction of the multiple timescales, functional hierarchy, within which the slow units represents task context states as a higher level and the fast units represents sensori-motor interaction as a lower level, can be self-organized [2].

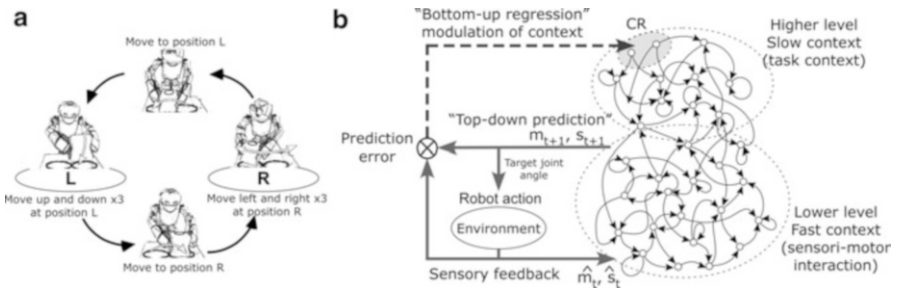


Fig. 1 (a) Robot task and (b) system overview

A network was trained by means of supervised learning (back-propagation through time algorithm (BPTT)) using teaching sequences obtained through tutoring by the experimenter. The objective of training was to find optimal values of connective weights minimizing sensory prediction error.

In order to achieve quick adaptation to environmental changes, we also introduced a bottom-up regression process [3], in which task context states were modulated so as to minimize prediction error (Fig. 1b). In the current model, we introduced *conflict resolver* (CR) units which modulate activities of the slow context through the bottom-up regression process. The role of CR units is similar to a “parametric bias” [3], in the sense that activity of the CR unit can be modified only through the regression process, not by external inputs. Update of CR activity is calculated as follows,

$$pe_t = \sum_{s=t-l}^t \sum_{i \in O} \hat{y}_{i,s} \log \left(\frac{\hat{y}_{i,s}}{y_{i,s}} \right) \quad (2)$$

where pe_t is prediction error within time window l at time step t , error is determined as a KL-divergence between the prediction of the network y_t and actual feedback \hat{y}_t . Membrane potential of the CR unit is updated in a direction opposite to that of the gradient $\partial pe / \partial u$, which is calculated using BPTT algorithm. Interested readers could find details of the calculation as described in our previous work [3].

In order to simulate disconnection syndrome, connective weights between the slow (task context level) and fast (sensori-motor level) context units were slightly modified by adding random noise.

3 Results

As a result of training, the proposed network successfully reproduced learned task behavior with the interaction of robot’s body and a physical environment. Moreover, the robot successfully adapted to unpredictable sensory perturbation, through the bottom-up modulation of task context. Figure 2 illustrates an example of sensori-motor sequences and changes in the activities of the trained network during robot’s task execution. Due to the unpredictable switch of the object’s position, prediction error was temporally increased. This increase of prediction error induced the activation of CR units resulting in the modulation of task contexts represented in the slow units.

In the simulation of disconnection syndrome, despite no external sensory perturbation, intermittent increases of the prediction error were observed (Fig. 3). This indicates that functional disconnection in a hierarchical network led to impairment of forward prediction. However, the increase in prediction error induced the activation of CR units resulting in the context states of the higher level of the network

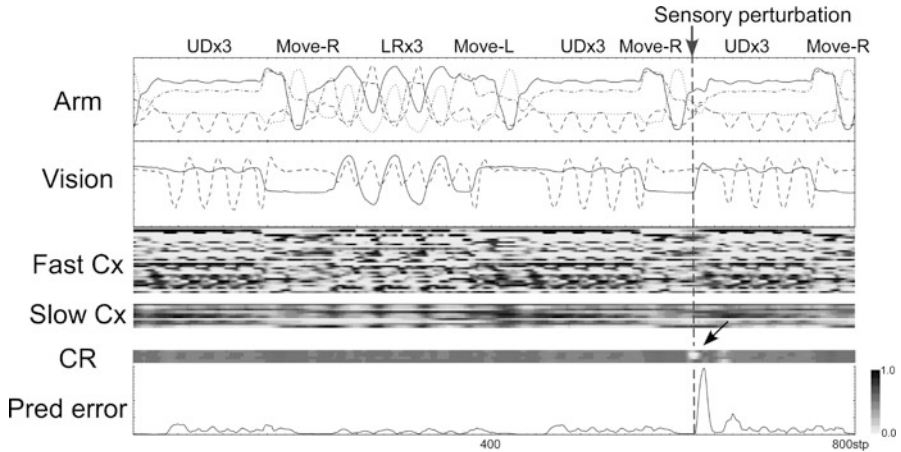


Fig. 2 Example of behavior sequence with sensory perturbation by experimenter. *Arm*: 4 dimensional joint angles, *Vision*: relative position of the object (x–y axis), *Pred error*: prediction error accumulating for past ten steps. A long sideways rectangle indicates the single unit activity of fast, slow, and CR units over many time steps. Activation level was indicated by the intensity of grey scale

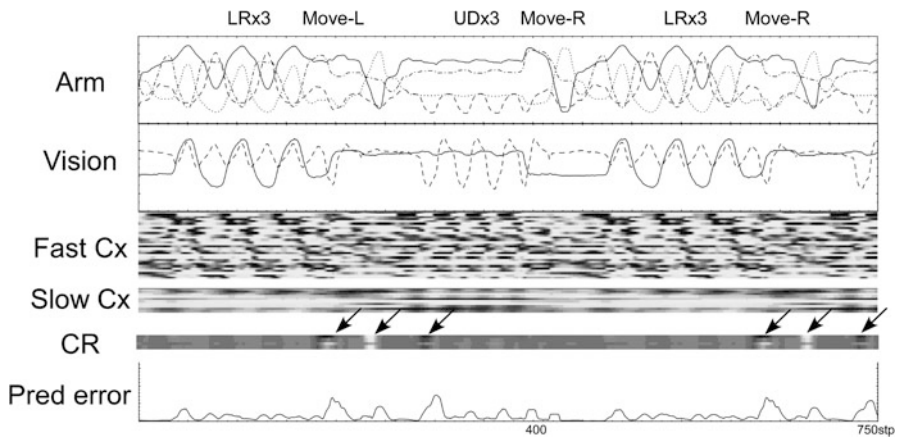


Fig. 3 Example of behavior sequence with simulated functional disconnection

being automatically modulated so as to minimize prediction error. As a result of this top-down and bottom-up interaction, the robot was able to generate seemingly normal behavior. Modulatory signals resulting from the functional disconnection were equivalent to those from external sensory perturbations. These observations suggest that, the modulation signal induced by internally generated prediction error might account for the feeling that the patient’s action is affected by some outside force.

4 Discussions

We demonstrated that not only top-down forward dynamics, but also bottom-up regression processes driven by prediction error are important mechanisms for flexible adaptation to unpredictable changes in environment. In contrast to the healthy condition, in the simulated disconnection syndrome, this bottom-up regression process generates unnecessary modulatory signals even in the predictable environments. This unnecessary modulatory signal may induce altered awareness of action in patients. These results of the robot experiments support the hypothesis of the impaired forward model resulting from functional disconnection in a hierarchical network and may provide novel insight for understanding the pathological mechanisms of schizophrenia.

The current study also showed that production of sequential behavior and flexible adaption to changes in environment can be realized based on a simple computational principle of minimizing prediction error. This result is consistent with the idea that minimizing prediction error may act as a general principle of the computation of the brain conducted in different levels and various modalities [3, 4].

Acknowledgments Use of the robot was made possible through the collaboration with SONY Corporation. This work was partially supported by KAKENHI (#23700279).

References

1. Fuster, JM.: The prefrontal cortex—an update: time is of the essence. *Neuron* 30 (2001) 319–333.
2. Yamashita, Y., and Tani, J.: Emergence of functional hierarchy in a multiple timescale neural network model: a humanoid robot experiment. *PLoS Comput Biol* 4 (2008) e1000220.
3. Tani, J.: Learning to generate articulated behavior through the bottom-up and the top-down interaction processes. *Neural Networks* 16 (2003) 11–23.
4. Friston, K.: The free-energy principle: a rough guide to the brain? *Trends Cogn Sci.* 13 (2009) 293–301.
5. Spence SA, Brooks DJ, Hirsch SR, Liddle PF, Meehan J, Grasby PM.: A PET study of voluntary movement in schizophrenic patients experiencing passivity phenomena (delusions of alien control). *Brain* 120 (1997) 1997–2011.
6. Friston KJ. The disconnection hypothesis. *Schizophr Res* 10 (1998) 115–125.
7. Frith, CD., Blakemore, SJ., Wolpert, DM.: Abnormalities in the awareness and control of action. *Philos Trans R Soc Lond B.* 355(2000)1771–1788.

Self-Organizing Dynamic Neural Fields

Nicolas P. Rougier and Georgios Is. Detorakis

Abstract In this paper, we propose a model of cortical self-organization based on the dynamic field theory. Learning is made through the modification of feed-forward connections using a time invariant learning rule that allows for dynamic (or life-long) learning. This preliminary model suggests that cortical plasticity may be conveyed through feed-forward connections only while cortico-cortical connections role would be to ensure dynamic competition among cortical columns.

1 Introduction

We introduced in [1] the dynamic self-organized map architecture that is a variation of the self-organizing map algorithm [2] where the original time-dependent (learning rate and neighborhood) learning function has been replaced by a time-invariant learning rule. This modification allows the network to support life-long learning and may explain to some extent cortical plasticity. However, current implementation is not biologically plausible since it requires a central supervisor (to designate the winning unit) and the neighborhood influence is computed using a function.

This article introduces preliminary results concerning a biologically plausible implementation using numerical, distributed and local computations, based on the original dynamic neural field definition [3].

The concept of self-organization using lateral connections is well-known and well-investigated, especially by Sirosh and Miikkulainen [4] and Bednar et al. [5]. In those works authors provide an algorithm for self-organization learning lateral weights using a Hebbian-like learning rule. On the other hand, we put forward a new approach of self-organization using a combination of a dynamic neural field

N.P. Rougier (✉) • G.Is. Detorakis
INRIA Nancy-Grand Est, 615 rue du Jardin Botanique, 54600 Villers-lès-Nancy, France
e-mail: Nicolas.Rougier@inria.fr; Georgios.Detorakis@inria.fr

and a Hebbian-like learning rule. Thus, self-organization can be achieved, learning only the feed-forward weights. Because of that property our model is quite simple, straightforward to implement and it does not require any outlandish handling.

2 Model

The neural field theory has been introduced by Wilson and Cowan [6, 7] and latter formalized by Amari [3] and Taylor [8]. This theory introduces a model at the level of a population of neurons in the form of an integro-differential equation describing the *spatio-temporal evolution of coarse-grained variables such as synaptic or firing rate value* [9]. We will use notations introduced by Amari and consider the membrane potential to be governed by the following equation:

$$\tau \frac{\partial V(\mathbf{x}, t)}{\partial t} = -V(\mathbf{x}, t) + h + I(\mathbf{x}, t) + \int_M W(|\mathbf{x} - \mathbf{y}|) f(V(\mathbf{y}, t)) d\mathbf{y} \quad (1)$$

where $V(\mathbf{x}, t)$ designates the membrane potential at position \mathbf{x} and time t , $W(|\mathbf{x} - \mathbf{y}|)$ is the lateral connection weight function between position \mathbf{x} and \mathbf{y} (we assume here that the system is spatially homogeneous and isotropic), f is the mean firing rate function, $I(\mathbf{x}, t)$ is the input at position \mathbf{x} and h is the resting potential.

2.1 Fitting Input

Depending on the firing rate function f , the lateral connectivity function W and the input I , such fields are known to exhibit a range of dynamic behaviors going from spatially and/or temporally periodic patterns to localized regions of activity. This latter case has been extensively used in a number of work to model visual attention [10], motor control [11], working memory [12], etc. In the following, we will consider the lateral connectivity function to be a Difference of Gaussians (DoG) of the form:

$$W(x) = Ae^{-x^2/2\sigma_A^2} - Be^{-x^2/2\sigma_B^2}$$

and the firing rate function to be a simple positive linear function:

$$f(x) = \begin{cases} x & \text{if } x > 0 \\ 0 & \text{if } x \leq 0 \end{cases}$$

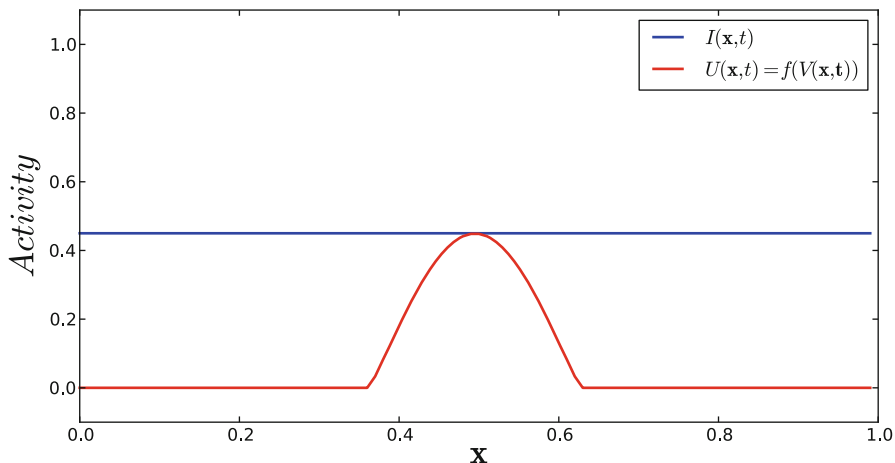


Fig. 1 One dimensional neural field using $n = 100$, $\tau = 10$, $A = 1.5$, $\sigma_A = 0.1$, $B = 0.75$, $\sigma_B = 1.0$. For any uniform and positive input level I , the neural field maximum activity is approximately equal to I after convergence

The numerical simulation of such fields requires the spatial discretization of the domain M into n spatial elements while the temporal integration can be made using classical integration schemes. Considering $M = [0..1]$ and $h = 0$, we can thus rewrite Eq. 1 as:

$$\tau \frac{\Delta V(\mathbf{x}_i, t)}{\Delta t} = -V(\mathbf{x}_i, t) + I(\mathbf{x}_i, t) + \sum_{j=0}^n W(|\mathbf{x}_i - \mathbf{x}_j|) f(V(\mathbf{x}_j, t))$$

with $\mathbf{x}_i = i/(n - 1)$. In the following, we will use the forward Euler integration scheme. Under these assumptions, we have been studying a set of parameters for the lateral weight connection that exhibit the following property: *for any uniform and positive input I , the neural field converges towards a single localized packet of activity whose maximum is approximately equal to I* . We do not have yet the formal proof of such behavior but we found the property to be very consistent over a wide set of numerical simulations using different parameters (n , I , Δt). We report in Fig. 1 such a simulation where the field is able to fit a constant input of level 0.45 after convergence. Instead of a stereotyped packet of activity with a constant maximum, the field activation represents a measure of the input. We will now explain how to use such property to ensure self-organization.

2.2 Self-Organization

Let us now consider the slightly modified equation:

$$\begin{aligned} \tau \frac{\partial V(\mathbf{x}, t)}{\partial t} = & -V(\mathbf{x}, t) + 1 - \int_M |I(t) - W_F(\mathbf{x})| d\mathbf{x} \\ & + \int_M W_L(|\mathbf{x} - \mathbf{y}|) f(V(\mathbf{y}, t)) d\mathbf{y} \end{aligned} \quad (2)$$

where I is now considered to be uniform over M while a set of feed-forward weights W_F has been added such that the actual input for any position \mathbf{x} is $1 - |I(t) - W_F(\mathbf{x})|$.

Considering the set of parameters given in the previous subsection and considering a given input I , if we have $W_F(\mathbf{x}) = I$, the actual input of the field would be 1. In such a case, we explained that the field maximum activity would match this value (1). However, it is not possible to have such equality for any value of I because it would mean to change all feed-forward weights at once. Nonetheless, we can restrict this equality to the support of the localized packet of activity at the equilibrium point. Said differently, it is sufficient to have $W_F(\mathbf{x}) = I$ for \mathbf{x} such that $V(\mathbf{x}, t)$ is not null at the equilibrium point. The goal of the learning rule is thus to reach such a state.

We considered the learning rule introduced in [1] that reflect two main ideas:

- If a neuron is *close enough* to the data, there is no need for others to learn anything: the winner can represent the data.
- If there is no neuron close enough to the data, any neuron learns the data according to its own distance from the data.

To achieve such behavior, we propose to consider the following learning rule:

$$\frac{\partial W_F(\mathbf{x}, t)}{\partial t} = \eta L_e(\mathbf{x}, t) (I(t) - W_F(\mathbf{x}, t)) \quad (3)$$

where $L_e(\mathbf{x}, t) = \int_M W_L(|\mathbf{x} - \mathbf{y}|) f(V(\mathbf{y}, t)) d\mathbf{y}$ denotes the excitatory part of the lateral interaction such that $W_L = W_{L_e} - W_{L_i}$ and η is a constant learning rate. The modification of feed-forward weights is thus directly correlated with the closeness of weights to the input and this is modulated by the amount of lateral excitation. Since we know the final state of the model is a localized Gaussian-shaped packet of activity, learning occurs maximally in this vicinity.

3 Results

3.1 Experimental Setup

A set S_k of samples is generated by drawing k evenly spaced values in the interval $[0..1]$ with special case S_∞ whose values are drawn uniformly from the interval $[0..1]$. A sample is randomly chosen from S_k and presented to the network which has been previously reset. The network is then simulated and learning occurs until ε -convergence has been reached, i.e. $\forall \mathbf{x}, |V(\mathbf{x}, t + dt) - V(\mathbf{x}, t)| \leq \varepsilon$. Another sample is then drawn and the procedure is repeated for a given number of epochs.

3.2 Learning Discrete Values

We trained a network of 100 neurons for 2,500 epochs and using as parameters, $\tau = 10, A = 1.5, \sigma_A = 0.1, B = 0.75, \sigma_B = 1.0$, self-organization was obtained. In Fig. 2 is illustrated the results of the simulation. The feed-forward weights were randomly initialized (the red line) and after 2,500 epochs the feed-forward weights were organized (the blue line), as the network learned the three input values $(0, \frac{1}{2}, 1)$. Hence, that step-like shape of feed-forward weights is because the first 20 neurons learned the value 0, the 20 middle neurons learned the value $\frac{1}{2}$, and the last 20 neurons learned the value 1. Moreover, the rest of the neurons learned different values from the input and may be that provide a smooth drift from one batch of neurons to another one.

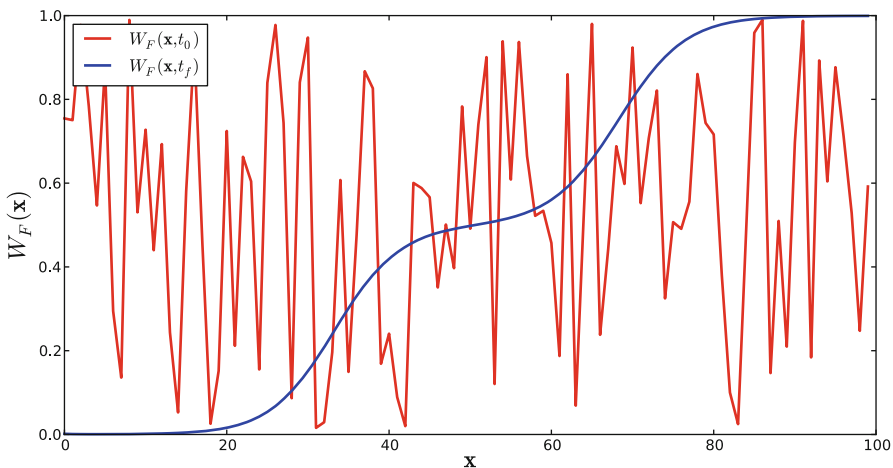


Fig. 2 A neural field has been trained for 2,500 epochs on S_3 $(0, \frac{1}{2}$ and $1)$. Blue and red curves respectively show initial and final set of weights

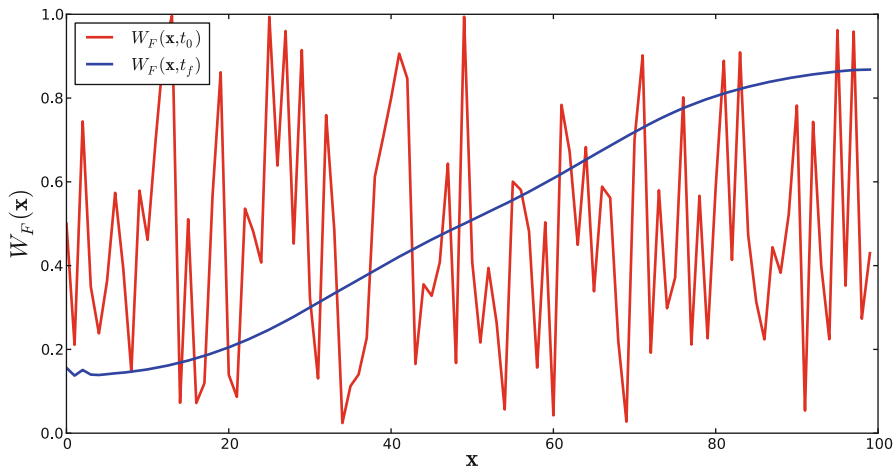


Fig. 3 A neural field has been trained for 2,500 epochs on S_∞ . *Blue and red curves* respectively show initial and final set of weights

3.3 Learning Continuous Values

We used the same network architecture as in introduced in previous paragraph but it has been trained on the S_∞ set. After 2,500 epochs the network has learned the feed-forward weights. In addition, the so-called step-like shape of feed-forward weights was substituted by an almost linear shape. That's because of the continuous nature of the input. It is to be noted that almost all values are represented but the bounds due to the non-toric nature of the network. This side effect is well-known in the case of Kohonen's map. Results are depicted in Fig. 3 while Fig. 4 shows the evolution of the receptive fields of unit #50 that slowly drifts from a weak and random response to a sharp localized one.

4 Discussion

We introduced a one dimensional dynamic neural field that can continuously and dynamically self-organize itself around a set of one-dimensional discrete or uniform values by modifying its feed-forward connections and using the lateral weighted sum of excitation as a modulation signal for learning. We are currently investigating the two-dimensional case, due to obtain a more biological plausible model since the cortex can be modeled as a two-dimensional sheet of neurons. In this context, we would like to investigate meta-plasticity and/or homeostatic plasticity as it has been reported in [13].

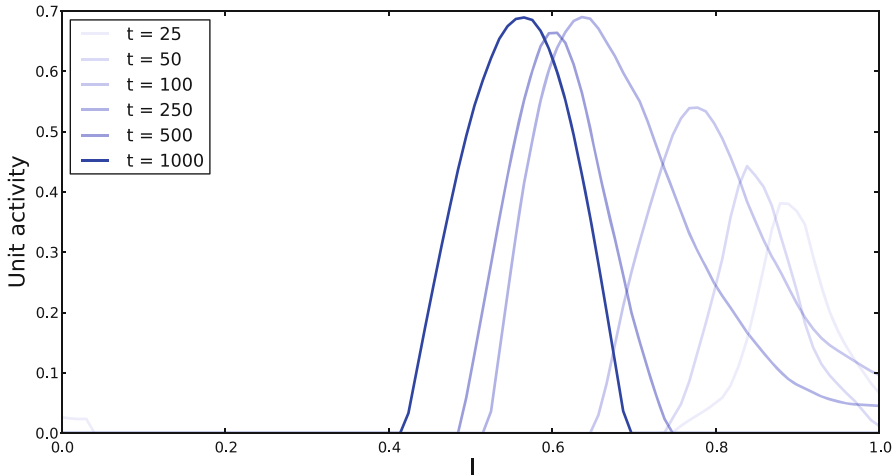


Fig. 4 Evolution through time (t) of the receptive field of unit #50 from a network learning S_{∞} . At each record time, learning is frozen and the network is presented successively with values ranging from 0 to 1 with step of 0.01. Activity level of unit #50 is recorded (after convergence) for each of these input values and is plotted for each record time

Finally, we would like to examine the properties of cortical reorganization under the presence of a lesion. Such lesions have been extensively investigated by Kaas [14] and others from a neurophysiological point of view and there is consequently a strong and detailed experimental background providing significant data which could feed our computational model.

References

1. N. Rougier and Y. Boniface, "Dynamic self-organising map," *Neurocomputing*, vol. In Press, Corrected Proof, pp. –, 2011.
2. T. Kohonen, "Self-organized formation of topologically correct feature maps," *Biological Cybernetics*, vol. 43, pp. 59–69, 1982.
3. S.-I. Amari, "Dynamic of pattern formation in lateral-inhibition type neural fields," *Biological Cybernetics*, vol. 27, pp. 77–88, 1977.
4. J. Sirosh and R. Miikkulainen, "Self-organizing feature maps with lateral connections: Modeling ocular dominance," in *Proceedings of the 1993 Connectionist Models Summer School. Hillsdale, NJ: Erlbaum, Citeseer*, 1994.
5. J. Bednar, J. De Paula, and R. Miikkulainen, "Self-organization of color opponent receptive fields and laterally connected orientation maps," *Neurocomputing*, vol. 65, pp. 69–76, 2005.
6. H. Wilson and J. Cowan, "Excitatory and inhibitory interactions in localized populations of model," *Biophysics*, vol. 12, pp. 1–24, 1972.
7. H. Wilson and J. Cowan, "A mathematical theory of the functional dynamics of cortical and thalamic nervous tissue," *Kybernetik*, vol. 13, pp. 55–80, 1973.
8. J. Taylor, "Neural bubble dynamics in two dimensions: foundations," *Biological Cybernetics*, vol. 80, pp. 5167–5174, 1999.

9. S. Coombes, "Neural fields," *Scholarpedia*, vol. 1, no. 6, p. 1373, 2006.
10. N. Rougier and J. Vitay, "Emergence of attention within a neural population," *Neural Networks*, vol. 19, no. 5, pp. 573–581, 2006.
11. W. Erlhagen and E. Bicho, "The dynamic neural field approach to cognitive robotics," *Journal of Neural Engineering*, 2006.
12. J. P. Spencer and G. Schöner, "An embodied approach to cognitive systems: A dynamic neural field theory of spatial working memory," in *Proceedings of the 28th Annual Conference of the Cognitive Science Society (CogSci 2006)* Society (CogSci 2006), (Vancouver, Canada), pp. 2180–2185, 2006.
13. D. Buonomano and M. Merzenich, "Cortical plasticity: from synapses to maps," *Annual review of neuroscience*, vol. 21, no. 1, pp. 149–186, 1998.
14. J. Kaas, "Plasticity of sensory and motor maps in adult mammals," *Annual review of neuroscience*, vol. 14, no. 1, pp. 137–167, 1991.

Spontaneous EEG Activity and Biases in Perception of Supra-Threshold Stimuli

Andrey R. Nikolaev, Sergei Gepshtein, and Cees van Leeuwen

Abstract Human perception of oriented visual stimuli is biased: some orientations are seen more often than others. We studied how the orientation bias is represented in the electrical brain activity that preceded presentation of ambiguous supra-threshold visual stimuli. We examined scalp EEG over the parieto-occipital regions during 1 sec before stimulus presentation. The alpha activity of pre-stimulus EEG was associated with the orientation bias: the preference for vertical orientation in most observers corresponded to low pre-stimulus alpha power. The results indicate that the orientation bias is encoded in intrinsic properties of ongoing cortical dynamics, forming spontaneous orientation-specific patterns of activity.

Keywords EEG • Spontaneous alpha activity • Perceptual organization • Perceptual bias

1 Introduction

The perception of a stable and continuous world is mediated by neural mechanisms that are adept at resolving ambiguities of stimulation. One factor that helps to resolve the ambiguities is expectation of stimuli from prior experience in similar perceptual situations. Perception can therefore be viewed as a *competition* of two

A.R. Nikolaev (✉)

RIKEN Brain Science Institute (BSI), 2-1, Hirosawa, Wako-shi, Saitama 351-0198, Japan
e-mail: nikolaev@brain.riken.jp

S. Gepshtein

RIKEN Brain Science Institute (BSI), 2-1, Hirosawa, Wako-shi, Saitama 351-0198, Japan
Salk Institute for Biological Studies, La Jolla, San Diego, CA, USA

C. van Leeuwen

RIKEN Brain Science Institute (BSI), 2-1, Hirosawa, Wako-shi, Saitama 351-0198, Japan

forces: current stimulus and stimulus expectation. Unnoticeable in regular viewing conditions, the competition comes to the fore in the perception of multistable stimuli [1, 2].

Gepshtein and Kubovy experimentally measured and modeled the competition in ambiguous visual stimuli [3]. They explicitly separated the factors extrinsic to the brain (called “stimulus support”) from intrinsic factors (“perceptual bias”) in grouping by proximity. The authors showed how perception depends on both factors, and how stimulation controls perception when it overcomes the intrinsic perceptual bias.

Gepshtein and Kubovy proposed that the intrinsic factor depends on ongoing brain activity [3]. Supporting this notion, previous studies found that the power [4] and phase [5] of ongoing electrical brain activity (EEG) affected perception of the upcoming stimuli. These studies mainly used stimuli near the threshold of detection. Here we asked whether ongoing activity may also affect perception of supra-threshold stimuli.

We studied perceptual grouping in ambiguous dot lattices, each of which can be seen as strips of dots in different orientations. Perception of these stimuli is an outcome of competition between stimulus factors that support several orientations, and intrinsic orientation bias that presumably originates in ongoing brain activity. We looked for associations between electrical brain activity that precedes stimulus presentation and the perception of subsequent dot lattices.

2 Methods

Thirteen healthy participants took part in the experiment. The stimuli were dot lattices which are spontaneously perceived as strips of dots [6]. The shorter the distance between the dots in a certain orientation, the more likely the dots group along that orientation. According to the pure distance law [7], grouping in dot lattices depends on their aspect ratio (AR), which is the ratio of two shortest inter-dot distances. We used dot lattices with four values of AR: 1.0, 1.1, 1.2, and 1.3. The lattices were presented at four orientations, such that the orientation of the shortest distance was rotated counterclockwise from the horizontal for 22.5°, 67.5°, 112.5°, or 157.5° (Fig. 1).

Each trial consisted of four phases: fixation, stimulus, blank screen, and response screen. During fixation, observers were instructed to look at a small circle at the screen center for a duration that varied randomly according to a uniform distribution on the interval of 1,200–1,500 ms. The durations of stimulus and blank-screen were both fixed at 300 ms. A response screen was presented until a response was received. The task was to report the orientation of the perceived dot grouping by choosing one of the four response icons (shown as white insets in Fig. 1) on the response screen.

EEG was recorded using a 256-channel Geodesic Sensor Net (Electrical Geodesics Inc., USA). Data were digitized at 250 Hz. All channels were referenced to the vertex electrode (Cz). Further details of stimulus, procedure, and EEG recordings are available in [8].

Fig. 1 A dot lattice presented at four orientations. The orientations of 22° and 157° are close to the horizontal, and the orientations of 67° and 112° are close to the vertical. The aspect ratio of this lattice is 1.3

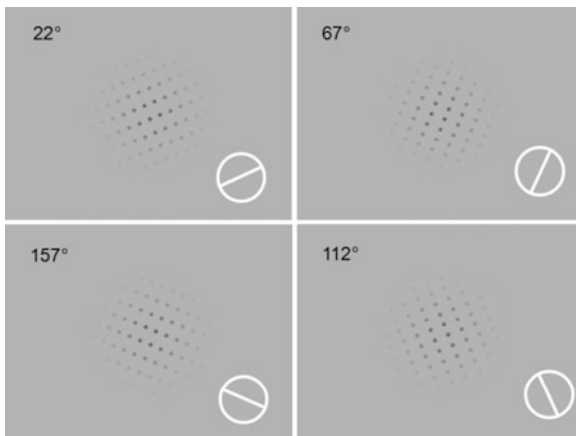
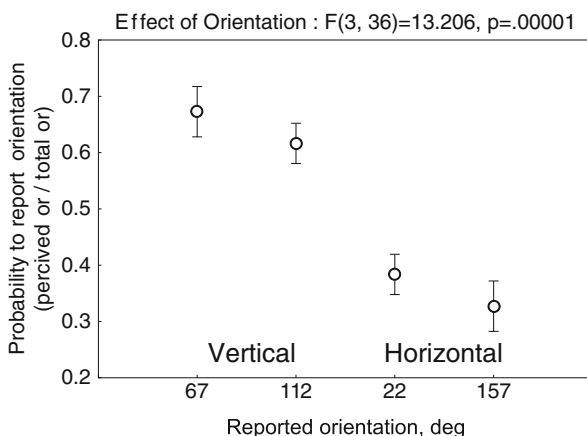


Fig. 2 Behavioral results: orientation bias. Reports of the close-to-vertical percepts were more common than reports of the close-to-horizontal percepts



We estimated the power of alpha-band activity (8–13 Hz) during a 1-s interval prior to stimulus presentation (i.e., during fixation). The alpha power was computed using FFT in 59 electrodes selected over the parieto-occipital regions. Electrodes were sorted by alpha power in descending order. We selected 29 electrodes with highest power and averaged their alpha power. The power values were log-transformed so the distribution of values approached the normal distribution.

3 Results

All other factors being equal, observers preferred vertical over horizontal dot groupings (Fig. 2). We estimated the strength of this *orientation bias* by measuring the difference in frequency of reports of “vertical” and “horizontal” groupings.

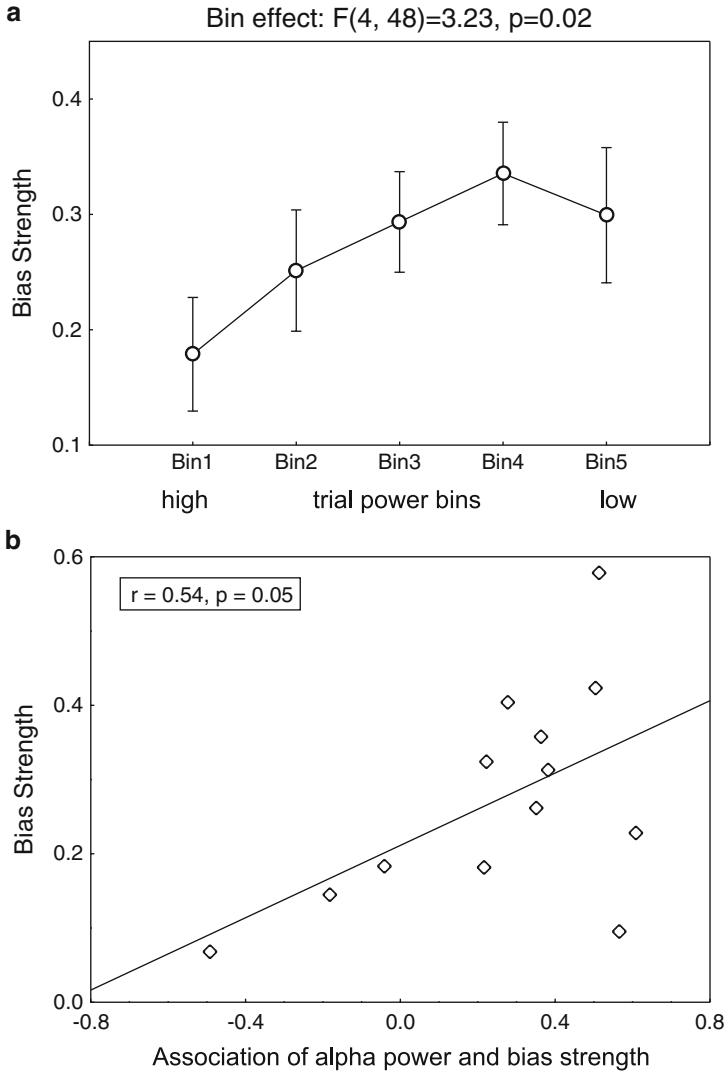


Fig. 3 (a) Strengths of orientation bias within bins of trials for different levels of pre-stimulus alpha power. Alpha power decreases from left to right. (b) Association of bias strength and pre-stimulus alpha power. Each point represents a different observer. The association of alpha power and bias strength was more pronounced in those trials where perception was dominated by bias

We sorted trials by alpha power in descending order, divided them into five bins, and calculated the strength of orientation bias for trials within each bin. Pre-stimulus alpha activity was associated with orientation bias: the bias for vertical orientation occurred more often in trials with low pre-stimulus alpha power (Fig. 3a). This effect was modulated by bias strength: the higher the bias the more it was associated with pre-stimulus alpha power (Fig. 3b).

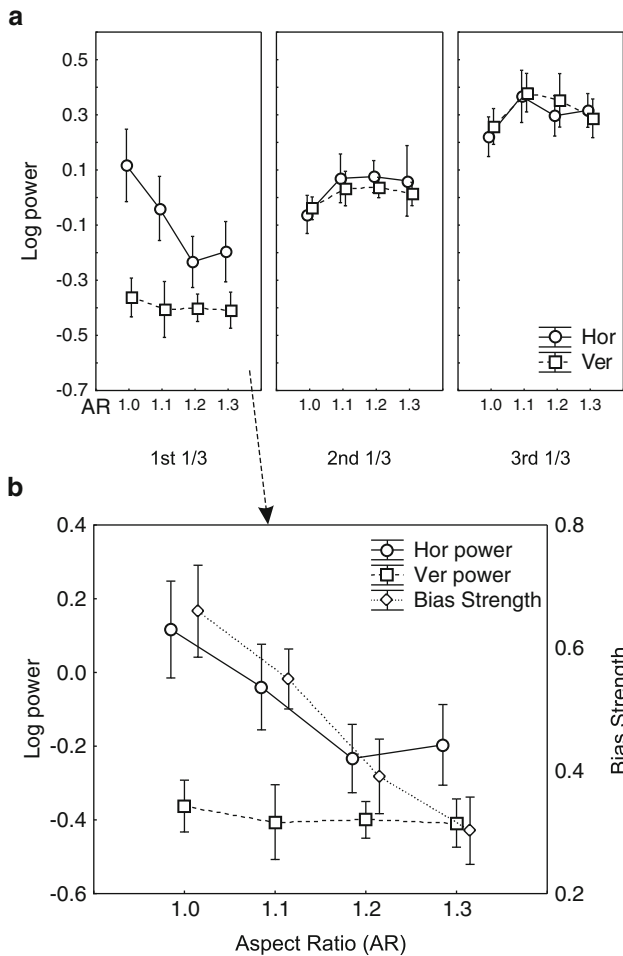


Fig. 4 (a) Log alpha power as a function of AR plotted separately for trials in which horizontal and vertical groupings were seen. The three panels represent three sequential parts a session, each part containing one third of trials. The association of alpha power and AR was present only in the first third of session, and only when horizontal groupings were reported. (b) Log alpha power for reports of horizontal and vertical grouping in the first third of session (*left ordinate*), and behavioral bias strength (*right ordinate*). Both alpha power and bias strength decreased with AR in trials where horizontal groupings were seen. The data are shown for ten observers whose performance was the highest

Next we asked whether the effect of alpha power depended on stimulus ambiguity (controlled by lattice aspect ratio, AR). We found that alpha power was not associated with AR when all trials were analyzed together. But when trials from different parts of experimental sessions were studied separately, it turned out that the strength of orientation bias was high in the beginning of the session, and gradually

decreased toward the end. We therefore divided the session in three equal parts, each about 200 trials long, and studied associations of alpha power in each part separately. We found that alpha power significantly increased during session time course ($F(2,18) = 20.3$; $p = .00003$) (Fig. 4a), suggesting that observers became more relaxed toward the session's end.

Alpha power was significantly higher in trials with reports of horizontal than vertical grouping ($F(1, 9) = 8.1$, $p = .02$), consistent with an effect of alpha power on orientation bias (Fig. 3a). In the first third of trials, alpha power was associated with AR. Alpha power gradually decreased with AR in trials with reports of horizontal grouping ($F(3, 27) = 3.2$, $p = .039$). This decrease was consistent with the decrease of bias strength as a function of AR (Fig. 4b). That is, the association of pre-stimulus alpha power with perception was largest in the most ambiguous dot lattices ($AR = 1.0$).

4 Discussion

Studies of perceptual organization suggested that perception of ambiguous figures depends on two competing factors: extrinsic (stimulus support) and intrinsic (perceptual bias) to the brain [3]. Here, we found in ongoing electrical brain activity a correlate of the intrinsic bias in the perception of supra-threshold visual stimuli. Alpha power of pre-stimulus cortical activity correlated with the degree to which intrinsic bias affected perception (Fig. 3a). This relationship was most prominent in the trials where grouping was inconsistent with the proximity principle (Fig. 4b). Since high alpha power is considered an indicator of cortical inhibition [9], the association of low alpha power with large perceptual bias suggests that the bias is an intrinsic property of the visual system manifested during its active state. Previous studies showed that ongoing cortical activity can spontaneously generate patterns that correspond to certain stimulus orientations, in absence of stimulation [10]. Our results show how this spontaneous activity affects perception.

Analyzing the event-related potentials in the same data set we previously found that orientation of dot lattices is reflected in early C1 component of the stimulus-evoked activity: C1 amplitude gradually changes with orientation [8]. Alpha activity correlates with early components of the evoked potentials [9]. This may indicate the mechanism of influence of pre-stimulus brain state on subsequent perception of orientation.

References

1. Julesz, B., Chang, J.J.: Interaction between pools of binocular disparity detectors tuned to different disparities. *Biol. Cybern.* 22 (1976) 107–119
2. Kanizsa, G., Luccio, R.: Multistability as a research tool in experimental phenomenology. In: Kruse P, Stadler M (eds) *Ambiguity in mind and nature*. Springer, Berlin, Heidelberg, New York (1995) 47–68

3. Gepshtein, S., Kubovy, M.: Stability and change in perception: spatial organization in temporal context. *Exp. Brain Res.* 160 (2005) 487–495
4. Linkenkaer-Hansen, K., Nikulin, V.V., Palva, S., Ilmoniemi, R.J., Palva, J.M.: Prestimulus oscillations enhance psychophysical performance in humans. *J. Neurosci.* 24 (2004) 10186–90
5. Mathewson, K.E., Gratton, G., Fabiani, M., Beck, D.M., Ro, T.: To see or not to see: prestimulus alpha phase predicts visual awareness. *J. Neurosci.* 29 (2009) 2725–32
6. Kubovy, M.: The perceptual organization of dot lattices. *Psychon. Bull. Rev.* 1 (1994) 182–190
7. Kubovy, M., Holcombe, A.O., Wagemans, J.: On the lawfulness of grouping by proximity. *Cognitive Psychol.* 35 (1998) 71–98
8. Nikolaev, A.R., Gepshtein, S., Kubovy, M., van Leeuwen, C.: Dissociation of early evoked cortical activity in perceptual grouping. *Exp. Brain Res.* 186 (2008) 107–122
9. Klimesch, W., Sauseng, P., Hanslmayr, S.: EEG alpha oscillations: the inhibition-timing hypothesis. *Brain Res. Rev.* 53 (2007) 63–88
10. Kenet, T., Bibitchkov, D., Tsodyks, M., Grinvald, A., Arieli, A.: Spontaneously emerging cortical representations of visual attributes. *Nature* 425 (2003) 954–956

Functional Roles of Corticofugal Plasticity in Detecting a Moving Target in Bat's Auditory System

Yoshitaka Muto, Yoshihiro Nagase, and Yoshiki Kashimori

Abstract In the present paper, we present a neural model for detecting Doppler-shifted frequency of echo sound reflecting from a target. We present here the neural mechanism by which the centripetal and centrifugal best frequency (BF) shifts are elicited. These BF shifts come from the modulations of the receptive field of cortical neurons elicited by short-term synaptic learning, depending on the stimulus context. This synaptic learning enables the system to follow a rapid frequency modulation, leading to detection of a moving target.

1 Introduction

Animals usually receive complex sensory signals in external world. To perform sensory perception, they must select actively the sensory information relevant to their behavior. To extract such information from complex signals, the feedback signals from cortex to subcortical and peripheral regions are needed. However, it is not yet clear how the feedback signals contribute to the selection of sensory information. The behavioral characteristics of the sound selection determine that

Y. Muto (✉)

Department of Engineering Science, University of Electro-Communications, Chofu,
Tokyo 192-8585, Japan
e-mail: mutoh1117@live.jp

Y. Nagase

Graduate School of Information Systems, University of Electro-Communications, Chofu,
Tokyo 182-8585, Japan

Y. Kashimori

Department of Engineering Science, University of Electro-Communications, Chofu,
Tokyo 192-8585, Japan

Graduate School of Information Systems, University of Electro-Communications, Chofu,
Tokyo 182-8585, Japan

the underlying neuronal substrate must be a back projection system and is able to implement selective sound processing based on auditory information already registered in the higher auditory processing levels. To address the issue of sound selection, we study echolocation of mustached bats, because the physiological properties of neuronal activities modulated by the feedback signals have been actively investigated [1–4], and the functions of the cortical areas have been well characterized [5].

Mustached bats emit ultrasonic pulses and listen to returning echoes for orientation and hunting flying insects. The bats analyze the correlation between the emitted pulses and their echoes and extract the detailed information about flying insects based on the analysis. This behavior is called echolocation. The neuronal circuits underlying echolocation detect the velocity of target with accuracy of 1 cm/s and the distance of target with accuracy of 1 mm. To extract the various information about flying insects, mustached bats emit complex biosonar that consists of a long-constant frequency (CF) component followed by a short frequency-modulated (FM) component. Each pulse contains four harmonics and so eight components represented by (CF1, CF2, CF3, CF4, and FM1, FM2, FM3, FM4) [6]. The information of target distance and velocity are processed separately along the different pathways in the brain by using four FM components and four CF components, respectively [5].

In natural situation, large natural objects in environment, like bushes or trees, produce complex stochastic echoes, which can be characterized by the echo roughness. The echo signal reflecting from a target insect is embedded in the complex signal. Even in such a environment, bats can detect accurately the detailed information of flying insect. To extract the information about insects, the feedback signals from cortex to subcortical areas are needed.

To investigate the role of feedback signals in extracting the information about insect, we consider the neural pathway for detecting velocity of target, which consists of cochlea, inferior colliculus (IC), and Doppler-shifted constant frequency (DSCF) area. The IC and DSCF area are located in subcortical and cortical area, respectively. The cochlea is remarkably specialized for fine-frequency analysis of the second harmonic CF component (CF2) of Doppler-shifted echoes. The information about echo CF2 (ECF2) is transmitted to IC, and the relative velocity of target insect is detected in DSCF area by analyzing the Doppler-shifted frequency [7]. Xia and Suga [4] have shown on intriguing property of feedback signals that the electric stimulation of DSCF neurons evokes the best frequency (BF) shifts of IC neurons away from the BF of the stimulated DSCF neuron (centrifugal BF shift) and bicuculline (an antagonist of inhibitory GABA receptors) applied to the stimulation site changes the centrifugal BF shifts into the BF shifts towards the BF of stimulated DSCF neurons (centripetal BF shift). Although these BF shifts are generated by the feedback signals from DSCF neurons to IC neurons, it is not yet clear how the feedback signals determine the direction of BF shift.

To address this issue, we present a neural model for detecting Doppler-shifted frequency of echo sound reflecting from a target. We present here the neural mechanism by which the centripetal and centrifugal BF shifts are elicited. These BF shifts come from the modulations of the receptive field of cortical neurons elicited

by short-term synaptic learning, depending on the stimulus context. This indicates that the tuning properties of subcortical neurons change on-line. This synaptic learning enables the system to follow a rapid frequency modulation, leading to detection of a moving target.

2 Model

We propose a network model for detecting the Doppler-shifted frequency, as shown in Fig. 1. The model consists of cochlea (Ch), inferior colliculus (IC), and Doppler-shifted constant frequency (DSCF) area, each of which has a linear array of frequency-tuned neurons. Each of the three layers contains a tonotopical map, in which the neurons in each layer are tuned in to specific echo frequency ranging from 60.0 to 63.0 kHz, corresponding to the frequency range of the second harmonics. The bat uses the Doppler-shifted frequency of echo sound to detect the relative velocity of target. The neuron was modeled with the Leaky integrate-and-fire neuron model [8], because temporal information may play an important role in auditory information processing. The neurons in the three layers are reciprocally connected with each other, with on center-off surrounding connections. The neurons in different layers are connected with an excitatory and inhibitory synapse, whose weights are updated with learning with short-term dynamics.

3 Results

Figure 2a shows the modulation of tuning property of IC neurons in the case where electric stimulus (ES) was applied to a DSCF neuron. The ES evoked the BF shift away from that of the electrically stimulated DSCF neuron, that is, centrifugal BF shift. Before the ES, the IC neurons maximally responded to 60.6 kHz (vertical

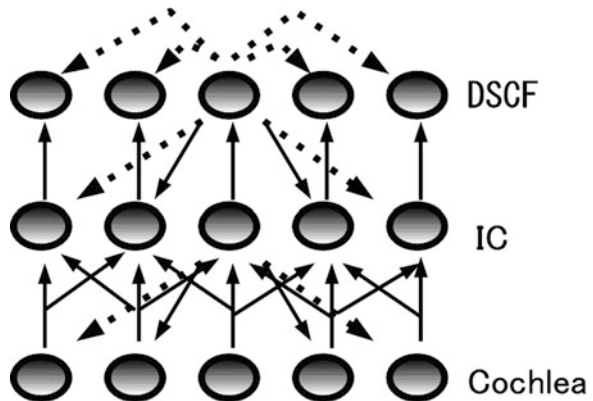


Fig. 1 Neural model for detecting Doppler-shifted frequency of echo sound. The excitatory and inhibitory synaptic connections are depicted by the *solid* and *dashed lines*, respectively

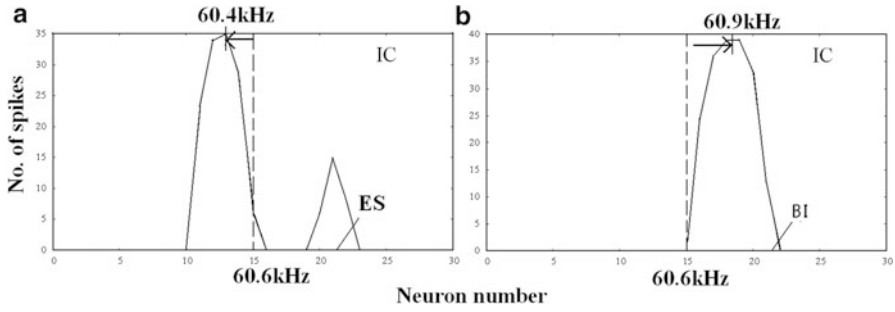


Fig. 2 Two types of BF shifts. (a) centrifugal and (b) centripetal BF shifts. The *dashed line* indicates the frequency tuned in control condition. *ES* and *BI* mean electric stimulation and bicuculline injection, respectively

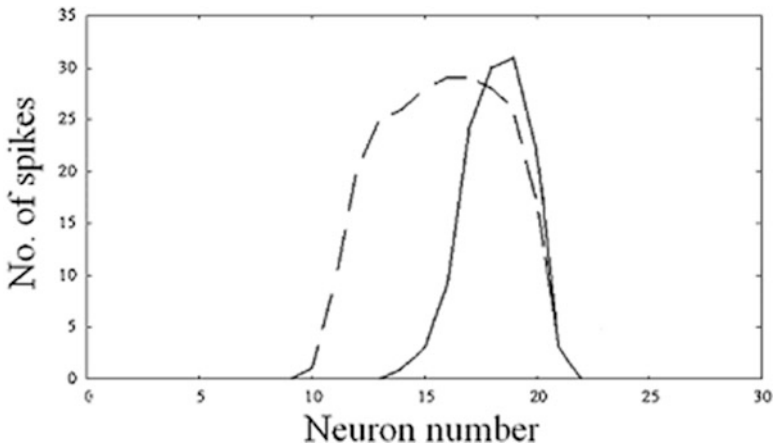


Fig. 3 Effect of synaptic plasticity on centripetal BF shift. The *solid* and *dashed lines* indicate the centripetal BF shifts elicited by IC neurons with and without synaptic plasticity, respectively

dashed line). When DSCF neuron tuned to 60.9 kHz was electrically stimulated, the BF of IC neuron was shifted from 60.6 to 60.4 kHz. That is, the IC neurons showed a centrifugal shift. Our model reproduced also centripetal BF shift evoked by the application of bicuculline, an antagonist of GABA, as shown in Fig. 2b. The inhibition of GABA by bicuculline led to the BF shift of the IC neuron towards the BF of the bicuculline-injected DSCF neuron. The BF of IC neurons shifts from 60.6 to 60.9 kHz. That is, the IC neurons showed a centripetal BF shift. These BF shifts come from the modulation of receptive field of top-down from DFCF to IC neurons.

Figure 3 shows the centripetal BF shifts of IC neurons with and without synaptic changes. The synaptic changes modulated the receptive field of top-down signals,

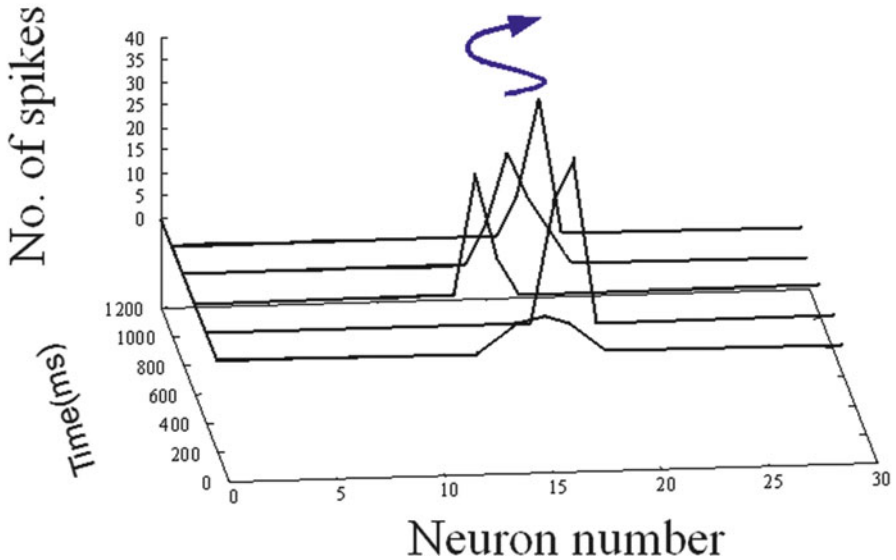


Fig. 4 Time course of the firing patterns of DSCF neurons in response to a moving target

leading to a rapid BF shift to the echo signal. IC neurons without synaptic changes exhibited a broad firing in response to echo signal and did not cause a significant BF shift, as shown in Fig. 3.

Figure 4 shows the response of DSCF neurons for a moving target. The target was oscillated with the frequency of 2 Hz. The DSCF neurons could follow rapidly the frequency change of the moving target. The system without the synaptic changes failed to follow the frequency modulation induced by the moving target. Thus the detection ability of DSCF neurons is due to fast synaptic changes of top-down connections from DSCF to IC neurons. The synaptic plasticity modulates the balance of excitatory and inhibitory signals to IC neurons, producing the responses of IC neurons depending on stimulus context.

4 Discussions

We have presented a network model of the Doppler shifted frequency. The model well reproduced the two types of BF shifts observed by Xiao and Suga [4]. The synaptic weights rapidly changed, enabling DSCF neurons to detect the temporal varying stimuli such as echo signals reflecting from a moving target.

The balance of excitatory and inhibitory inputs to neurons has been reported to play important roles in sensory coding. Recent study has demonstrated that detailed balance of excitation and inhibition can efficiently gate the propagation of firing rate [9]. The balance between excitation and inhibition appears also in short-term

synapses, responsible for a temporal filtering of sensory signals [10]. Similarly to the functions of short-term synaptic plasticity, the synaptic plasticity used in our model also modulates rapidly the receptive field of DSCF neurons, enabling the rapid adaptation for temporal-varying signal induced by a moving target. Thus the short-term synaptic change may play a crucial role in extracting desired information depending on stimulus context.

References

1. Ma, X., Suga, N.: Long-term cortical plasticity evoked by electric stimulation and acetylcholine applied to auditory cortex. *Proc Natl Acad Sci, USA* 102 (2005) 9335–9340
2. Sakai, M., Suga, N.: Plasticity of cochleotopic (frequency) map in specialized and nonspecialized auditory cortices. *Proc Natl Acad Sci, USA* 98 (2001) 3507–3512
3. Suga, N., Ma, X. : Multiparametric corticofugal modulation and plasticity in the auditory system. *Nat. Rev. Neurosci.* 4 (2003) 783–794
4. Xiao, Z., Suga, N. : Reorganization of the cochleotopic map in the bat's auditory system by inhibition. *Proc Natl Acad Sci, USA* 99 (2002) 15743–15748
5. Suga, N.: Cortical computational maps for auditory imaging, *Neural networks.* 3(1990) 3–21
6. O'Neill, W.E., Suga, N.: Encoding of target range and its representation in the auditory cortex of the mustached bat. *J. Neurosci.* 2 (1982) 17–31
7. Suga, N., Manabe, T.: Neural bases of amplitude–spectrum representation in auditory cortex of the mustached bat. *J Neurophysiol.* 47 (1982) 225–255
8. Koch, C (1999) *Biophysics of Computation.* New York, Oxford University Press
9. Vogel, T.P., Abbott, L.F.: Gating multiple signals through detailed balance of excitation and inhibition in spiking networks, *Nat Neurosci* 12 (2009) 483–491
10. Abbott, L.F., Regehr, W.G.: Synaptic computation. *Nature* 431 (2004) 796–803

The Origin of the Spatial Pattern of Amplitudes in Trial-Averaged MEG

David M. Alexander, Peter Jurica, Andrey R. Nikolaev, Mikhail Zvyagintsev, Klaus Mathiak, and Cees van Leeuwen

Abstract We analysed the spatial pattern of trial-averaged MEG time-series over the whole scalp. The contributions of both signal phase and amplitude to these spatial patterns were assessed. While a substantial proportion of the pre-stimulus time-series is explained by the amplitude component in the alpha/beta range, most of the post-stimulus evoked response is explained by averaging of the phase-only component. We suggest that the whole scalp pattern of evoked responses is akin to an interference pattern produced by trial averaging.

1 Introduction

The origin of event-related brain signals and the role phase therein is subject to debate [1]. We distinguish the effects of cross-trial phase locking and single trial amplitudes on the trial-averaged signal [2]. Understanding the relationship between the signals underlying whole scalp patterns of event-related fields (ERFs) is important for at least three reasons. First, whole scalp ERFs are typically used

D.M. Alexander (✉)

Perceptual Dynamics Laboratory, RIKEN Brain Science Institute, Wako, Saitama, Japan

Laboratory of Experimental Psychology, University of Leuven, Leuven, Belgium

e-mail: David.Alexander@psy.leuven.be

P. Jurica • A.R. Nikolaev • C. van Leeuwen

Perceptual Dynamics Laboratory, RIKEN Brain Science Institute, Wako, Saitama, Japan

M. Zvyagintsev

Department of Psychiatry and Psychotherapy, RWTH Aachen University, Aachen, Germany

K. Mathiak

Department of Psychiatry and Psychotherapy, RWTH Aachen University, Aachen, Germany

INM-1, Research Center Jülich, Jülich, Germany

Y. Yamaguchi (ed.), *Advances in Cognitive Neurodynamics (III)*,

DOI 10.1007/978-94-007-4792-0_41,

© Springer Science+Business Media Dordrecht 2013

in source localization techniques. A reasonable alternative, though technically challenging, would be to fit the equivalent current dipole to individual trial data and then average these fits. So it matters what, exactly, is being localized when *averaged* signal is fit to an equivalent current dipole [3]. Second, a wealth of evidence links various stages of cognition to evoked responses in the EEG and MEG. However, the relative effects of phase and amplitude on evoked responses are usually considered at individual recording sites [1]. If there are global relationships in the way phase and amplitude interact, they may be missed when only sites with maximum ERF amplitude are considered. Third, inter-trial coherence has become a standard tool for understanding large-scale network interactions in the cortex [4, 5]. The present work has implications for the relationship between evoked response measures and measures of inter-trial coherence. We show that the bulk of the ERF amplitude variation over the scalp is due to the degree of inter-trial phase coherence.

2 Methods

2.1 Subjects and Task

Twenty human subjects (age range 22–36 years, mean age 27.1; 12 females) engaged in an audio-visual perceptual task, while their brain activity was recorded via MEG. All the subjects were right-handed, had no audiological abnormalities, and had normal or corrected-to-normal vision. Written informed consent was obtained from all subjects prior to participation in the study. The study was approved by the ethics committee of the University of Tübingen. The task required the subject to choose the direction of motion of an audio-visual apparent motion stimulus. The visual component was located on the horizontal with the distance of 15° of visual angle at either side of the screen center. The apparent motion illusion was elicited by presenting the stimuli for 67 ms at the one side, and then after 67 ms delay, for 67 ms at the opposite side. The auditory stimuli were the white noise bursts presented in such a way that the sound was spatially perceived at the position of the visual stimuli ($+15^\circ$ or -15°). Subjects were instructed to press buttons in random order either by the left or right index finger. The stimulus moved from the side indicated by the subject and then to the other side (i.e. either ‘left to right’ or ‘right to left’; this was the ‘predictable’ condition). In some blocks of trials the direction of stimulus motion was randomized and not due to the subject’s choice (i.e. ‘unpredictable’ condition). We applied analyses only on the trials in which the side of first stimulus coincided with the button pressed: all trials in the predictable and approximately half of trials in the unpredictable condition. Further details of the experiment can be found elsewhere [6].

2.2 MEG Recording

Subjects were seated comfortably in a dimly-lit room. Neuromagnetic responses were recorded in a magnetically shielded booth using a 151-sensors whole-head gradiometer (CTF Systems Inc., Vancouver, Canada). The MEG signals were sampled at 312.5 Hz.

2.3 Analysis

MEG data were low-pass filtered with a cut off at 39 Hz. Artifact removal and trial selection criteria are described in detail elsewhere [6]. Source modeling revealed three consistent dipole patterns: a lateralized motor dipole at the time of stimulus initiation, bilateral auditory activity at around 80 ms and a lateralized visual dipole at around 150 ms [6]. In the present analyses we focused on the former activity.

We sought to analyse the composition of the ERF signal, considered as a spatio-temporal pattern over all recording sites and over one cycle at the frequency of interest e.g. 100 ms at 10 Hz. In order to see how the band-pass signal predicted the ERF, we made a trial average of the band pass signal and correlated this with the ERF, including values from all sites and over an entire cycle. The amount of variance explained by this predictor signal was simply the correlation squared. The same procedure was used to see how well the phase-only signal (as cosine of phase) predicted the ERF.

The Fourier components, X , of the MEG signal, x , were estimated over a range of frequencies, f , (0.5 to 32.0 Hz in N_f steps), about each sample, t , using two cycle Morlet wavelets. MEG time-series were averaged over all trials, N_t , (for each subject and condition), $\bar{T} = \langle x \rangle_{N_t}$ and the pattern of \bar{T} over sensors compared to a predictor signal. One predictor signal was constructed by averaging the amplitude normalized signal $\bar{P} = \langle Re(X/X) \rangle_{N_t}$. We calculated the fit of \bar{P} , at frequency, f , to \bar{T} over all sensors s ($N_s = 151$), and over one cycle c , about the centre sample, t .

$$R_{N_t \times N_f}^2(\bar{T}, \bar{P}) = \rho(\bar{T}_{N_t \times N_f \times N_c \times N_s} - \langle \bar{T}_{N_t \times N_f \times N_c \times N_s} \rangle_{N_c} U_{1 \times 1 \times N_c \times 1}, \bar{P}_{N_t \times N_f \times N_c \times N_s})^2$$

where ρ denotes the correlation of two vectors, here length $N_s N_c$ and U is the unitary matrix; $c \in (t - 1/2f, t + 1/2f)$; and, $N_c \approx 1000/3.2f$. A second predictor signal was constructed by averaging the band-pass signal $\bar{B} = \langle Re(X) \rangle_{N_t}$; and analogously we calculated $R_{t,f}^2(\bar{T}, \bar{B})$.

3 Results

The result of the analysis is given in Fig. 1, as a time/frequency plot of $R_{t,f}^2(\bar{T}, \bar{P})$ and $R_{t,f}^2(\bar{T}, \bar{B})$. For this experimental task, a pattern of time-locked responses on these measures begins with a theta band component at the time of the button press, related to the motor dipole previously characterized [6]. The audio-visual stimulus evokes a series of events in the alpha band from around 100 ms onwards, also consistent with previous dipole modeling [6].

Consistent with previous studies [9, 10], the amplitude pattern of the cross-trial average is a function of both single-trial phase and single-trial amplitudes. The pattern of trial-averaged MEG across sensors in the pre-stimulus alpha/beta signal contained a large contribution from single trial amplitudes, seen in the $R_{t,f}^2(\bar{T}, \bar{B})$ plot. Indeed this effect is almost as large as the evoked portion of the plot. When this component is compared to the pre-stimulus alpha/beta component of $R_{t,f}^2(\bar{T}, \bar{P})$, it can be seen that about 30% additional explained variance in \bar{T} is explained by the band-pass compared to the phase-only signal.

By contrast, the peaks in $R_{t,f}^2(\bar{T}, \bar{P})$ at post-stimulus latencies are considerably larger than the $R_{t,f}^2(\bar{T}, \bar{P})$ pre-stimulus alpha/beta component. Additionally, the evoked peaks in $R_{t,f}^2(\bar{T}, \bar{P})$ were of the same order as the evoked peaks in $R_{t,f}^2(\bar{T}, \bar{B})$, with about 70% of the variance in the pattern of ERF amplitudes—at

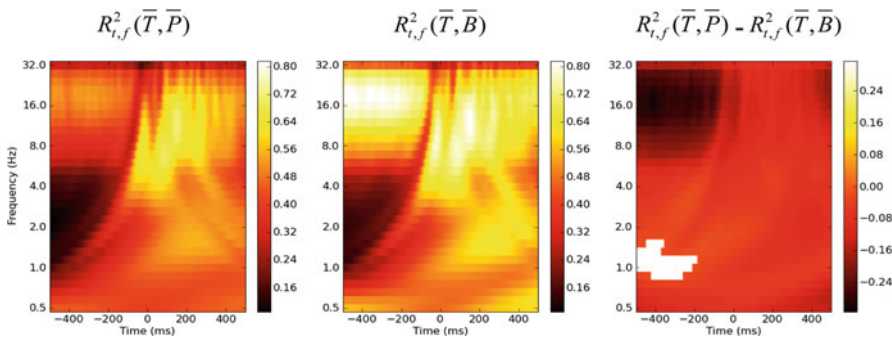


Fig. 1 The relative contributions of phase and amplitude to the spatial pattern of ERFs. *The first panel* shows the grand-average values of $R_{t,f}^2(\bar{T}, \bar{P})$, for all times and frequencies evaluated. The values from 20 subjects, and each of four experimental conditions ('predictable' vs. 'unpredictable' and 'left to right' vs. 'right to left'), were averaged together here. *The second panel*, likewise, shows the grand-average values of $R_{t,f}^2(\bar{T}, \bar{B})$. *The third column* shows the difference between these two grand-averages, and the results of pixel-wise t-tests, comparing each subject's mean score for the two statistics ($n = 20$, $p < 0.05$ shown in non-white). Since almost all points are significantly different, i.e. there is only one cluster, correction for multiple comparisons was not necessary. Throughout the event-related region of the plot ($t > -100$), the subjects show a small ($\sim 8\%$) but significant difference in mean values of variance explained in the ERFs by the two predictor signals. For $t < -100$, in the alpha/beta bands, the difference is larger ($\sim 30\%$)

event-related peaks in the $R^2_{r,f}(\overline{T}, \overline{P})$ spectrum—explained by the phase-only signal. The single trial phase plus amplitude signal only contributed about 8% additional explained variance to the ERFs.

While the band-pass signal contributes substantially to the pre-stimulus trial-averaged time-series, it does not contribute the major proportion of the evoked signal. The evoked signal, considered as a global spatio-temporal pattern, is mainly due to cross-trial averaging of phase.

4 Discussion

The results in this paper clarify the relationship between dynamical approaches to brain function and approaches that emphasize localized sources. Most of the variance in the evoked components of this task is explained as the average of single-trial dynamics with spatially *uniform* amplitudes, \overline{P} . This component is distinct from a signal in which amplitude declines as the inverse-square of distance from a localized source. This raises the possibility that the ERFs have a component that is akin to an interference pattern, where that interference pattern results from cross-trial averaging during numerical analysis. This possibility arises when we put together the present results with those on traveling waves in the EEG/MEG.

A growing literature relates coherent traveling waves to mental states [11, 12], cognitive function [8, 13] and clinical deficits [14–16]. These waves are typically of long wavelength and can traverse large distances across the EEG/MEG recording array. They also can travel in a variety of directions during the same (i.e. stimulus locked) task-related windows [16], and their preferred direction changes on a developmental time-scale [15, 16]. Traveling wave components have been related to the P2 and N2 auditory evoked potentials, as well as the P3b ERP [8, 17]. They share common frequency and latency characteristics, as well as a shared task-dependency [8, 16]. The results in the present study shed further light on the relationship between evoked responses and these global phase dynamics. Phase is the main ingredient in the global pattern of ERFs. If amplitude were the main ingredient, this would make it more difficult to reconcile ERFs/ERPs with globally coherent traveling waves.

When the phase dynamics have coherent motion, static ‘sources’ in the trial-average can be understood as a kind of interference pattern. The resultant pattern of activity has maximum amplitude over the localized brain region that is critical for the execution of the task—and so this framework is consistent with the wealth of data collected on specialization of cortical function. However, the present results suggest that inter-trial measures may not directly reflect the ongoing activity pattern. Rather, these measures reflect the consistency in timing of brain activity, at particular sites, across trials. Localized regions with consistent timing across trials, while conveying important information about *timing*, do not necessarily imply localized *sources* of brain activity. This can be easily demonstrated by making

an analogy with Moiré patterns—the component images (analogous to individual trials) of these interference patterns do not have the same amplitude maxima as the Moiré pattern itself (analogous to the inter-trial measure).

In conclusion, the fields generated by brain activity exist at the single trial level, whereas repeated experimental trials are solely a convenience for the experimenter. The subject's brain has no *direct* access to the cross-trial measures. This point is important because recent findings have shown network coupling effects via endogenous fields in hippocampal and cortical neurons [18–21]. These findings are consistent with a growing literature on the effects of trans-cranial stimulation [22, 23]. In both these cases, the fields play a causal role in network activity. It is therefore timely to uncover differences between the properties of single-trial activity and inter-trial quantities. Here we show that single-trial *phase* dynamics contribute more to the global pattern of ERF *amplitudes* than do single-trial *amplitudes*. This result garners support for the importance of another property that cross-trial measures often disguise (c.f. [24]), namely, coherent activity with non-zero velocity—traveling waves. Cross-trial averages of both ERPs and traveling waves typically have mean velocity close to zero [16, 17].

References

1. P. Sauseng, W. Klimesch, W. R. Gruber, S. Hanslmayr, R. Freunberger, and M. Doppelmayr, "Are event-related potential components generated by phase resetting of brain oscillations? A critical discussion," *Neuroscience*, vol. 146, no. 4, pp. 1435–1444, Jun. 2007.
2. J. Fell, "Cognitive neurophysiology: Beyond averaging," *NeuroImage*, vol. 37, no. 4, pp. 1069–1072, Oct. 2007.
3. A. Mouraux and G. D. Iannetti, "Across-trial averaging of event-related EEG responses and beyond," *Magnetic Resonance Imaging*, vol. 26, no. 7, pp. 1041–1054, Sep. 2008.
4. J. P. Lachaux, E. Rodriguez, J. Martinerie, and F. J. Varela, "Measuring phase synchrony in brain signals," *Human Brain Mapping*, vol. 8, no. 4, pp. 194–208, 1999.
5. J. F. Hipp, A. K. Engel, and M. Siegel, "Oscillatory Synchronization in Large-Scale Cortical Networks Predicts Perception," *Neuron*, vol. 69, no. 2, pp. 387–396, 2011.
6. M. Zvyagintsev, A. R. Nikolaev, K. A. Mathiak, H. Menning, I. Hertrich, and K. Mathiak, "Predictability modulates motor-auditory interactions in self-triggered audio-visual apparent motion," *Experimental Brain Research. Experimentelle Hirnforschung. Expérimentation Cérébrale*, vol. 189, no. 3, pp. 289–300, Aug. 2008.
7. D. Rubino, K. A. Robbins, and N. G. Hatsopoulos, "Propagating waves mediate information transfer in the motor cortex," *Nat Neurosci*, vol. 9, no. 12, pp. 1549–1557, Dec. 2006.
8. D. M. Alexander, C. Trengove, J. J. Wright, P. R. Boord, and E. Gordon, "Measurement of phase gradients in the EEG," *Journal of Neuroscience Methods*, vol. 156, no. 1–2, pp. 111–128, Sep. 2006.
9. R. J. Barry, "Evoked activity and EEG phase resetting in the genesis of auditory Go/NoGo ERPs," *Biological Psychology*, vol. 80, no. 3, pp. 292–299, Mar. 2009.
10. B.-K. Min et al., "The best of both worlds: phase-reset of human EEG alpha activity and additive power contribute to ERP generation," *International Journal of Psychophysiology: Official Journal of the International Organization of Psychophysiology*, vol. 65, no. 1, pp. 58–68, Jul. 2007.

11. M. Massimini, R. Huber, F. Ferrarelli, S. Hill, and G. Tononi, "The Sleep Slow Oscillation as a Traveling Wave," *The Journal of Neuroscience*, vol. 24, no. 31, pp. 6862–6870, 2004.
12. J. Ito, A. R. Nikolaev, and C. van Leeuwen, "Dynamics of spontaneous transitions between global brain states," *Human Brain Mapping*, vol. 28, no. 9, pp. 904–913, Sep. 2007.
13. P. Sauseng, W. Klimesch, W. Gruber, M. Doppelmayr, W. Stadler, and M. Schabus, "The interplay between theta and alpha oscillations in the human electroencephalogram reflects the transfer of information between memory systems," *Neuroscience Letters*, vol. 324, no. 2, pp. 121–124, May. 2002.
14. D. M. Alexander et al., "The contribution of apolipoprotein E alleles on cognitive performance and dynamic neural activity over six decades," *Biological Psychology*, vol. 75, no. 3, pp. 229–238, Jul. 2007.
15. D. M. Alexander et al., "Event-related wave activity in the EEG provides new marker of ADHD," *Clinical Neurophysiology: Official Journal of the International Federation of Clinical Neurophysiology*, vol. 119, no. 1, pp. 163–179, Jan. 2008.
16. D. M. Alexander et al., "Spatio-temporal EEG waves in first episode schizophrenia," *Clinical Neurophysiology*, vol. 120, no. 9, pp. 1667–1682, Sep. 2009.
17. P. Anderer, H. V. Semlitsch, and B. Saletu, "Multichannel auditory event-related brain potentials: effects of normal aging on the scalp distribution of N1, P2, N2 and P300 latencies and amplitudes," *Electroencephalography and Clinical Neurophysiology*, vol. 99, no. 5, pp. 458–472, Nov. 1996.
18. C. A. Anastassiou, R. Perin, H. Markram, and C. Koch, "Ephaptic coupling of cortical neurons," *Nat Neurosci*, vol. 14, no. 2, pp. 217–223, Feb. 2011.
19. J. K. Deans, A. D. Powell, and J. G. R. Jefferys, "Sensitivity of coherent oscillations in rat hippocampus to AC electric fields," *The Journal of Physiology*, vol. 583, no. 2, pp. 555–565, Sep. 2007.
20. F. Fröhlich and D. A. McCormick, "Endogenous electric fields may guide neocortical network activity," *Neuron*, vol. 67, no. 1, pp. 129–143, Jul. 2010.
21. T. Radman, Y. Su, J. H. An, L. C. Parra, and M. Bikson, "Spike Timing Amplifies the Effect of Electric Fields on Neurons: Implications for Endogenous Field Effects," *The Journal of Neuroscience*, vol. 27, no. 11, pp. 3030–3036, Mar. 2007.
22. L. Marshall, H. Helgadottir, M. Molle, and J. Born, "Boosting slow oscillations during sleep potentiates memory," *Nature*, vol. 444, no. 7119, pp. 610–613, Nov. 2006.
23. A. Floel and L. G. Cohen, "Contribution of noninvasive cortical stimulation to the study of memory functions," *Brain Research Reviews*, vol. 53, no. 2, pp. 250–259, Feb. 2007.
24. G. Nolte et al., "Robustly Estimating the Flow Direction of Information in Complex Physical Systems," *Physical Review Letters*, vol. 100, no. 23, p. 234101, Jun. 2008.

Rhythm Matters: A Case in Attentional Blink

Chie Nakatani and Cees van Leeuwen

Abstract For processing a fast train of visual stimuli, their timing is an effective cue. This paper reports that EEG phase of parietal activity to the timing of the stimuli has critical importance for target detection in an Attentional Blink (AB) task. When the phase was locked to the stimuli before and during target presentation, but shifted backward immediately afterwards, the AB phenomenon was avoided. On the other hand, when the phase acutely advanced after the second target presentation, the target was missed even in the Lag 7 condition. These results suggest that the phase shift is a potential control signal for working memory processes.

1 Introduction

When two target stimuli are embedded in a stream of nontargets, people often miss the second target when it lags 200–500 ms from the first one. The phenomenon is called attentional blink (AB) [1, 2]. In a typical AB task, the stimulus sequence is presented at a constant rate of about 10 Hz. The constant rate could be utilized as a cue to prepare the perceptual system for upcoming targets. Previous studies, however, are not in accord with this intuition: Steady-state visual evoked potential (ssVEP) in 10 Hz EEG did not differ in amplitude between hits and misses of the second target [3]. However, rather than amplitude, the phase the 10-Hz activity may be relevant to the AB. The 10-Hz phase synchrony among MEG dipoles in various brain areas did not differ between hits and misses [4]. However, in their study, only

C. Nakatani (✉) • C. van Leeuwen
RIKEN Brain Science Institute (BSI), 2-1, Hirosawa, Wako-shi, Saitama 351-0198, Japan
e-mail: cnakatani@brain.riken.jp

phase locking between 10 Hz components of pairs of dipoles was examined (using phase synchrony level index which was proposed in [5]), not whether, across trials, the 10 Hz activity has a preferred phase-locking to the stimuli.

In the current study, therefore, we investigated whether there is a 10-Hz subcomponent which is phase-locked to the stimuli and, if so, whether it is relevant to the AB. We analyzed human EEG during an AB task to separate such ‘rhythm keeper’ activity from target driven components.

2 Methods

Thirteen observers (11 women, 2 men) with normal/corrected-to-normal vision participated. They were asked to observe 17–20 stimuli which were presented at a 10 Hz rate. The stimuli were single letter or digit in white on a gray background, except for one in blue. The blue stimulus was the target of the first task (T1). The participants were asked to judge category (letter or digit) of T1. The second task was to report the presence or absence of the letter ‘O’, which is the second target (T2) (See Fig. 1). T1 precedes T2 in 100, 300 or 700 ms (T1-T2 Lags 1, 3, or 7).

EEG was recorded using a commercial EEG recording system (EEG1100, Nihon Kohden, Tokyo, Japan) from 19 electrodes, which were placed according to the international 10–20 system. Horizontal and vertical EOG electrodes were also attached. Data were digitized at 500 Hz (0.1–100 Hz analogue bandwidth).

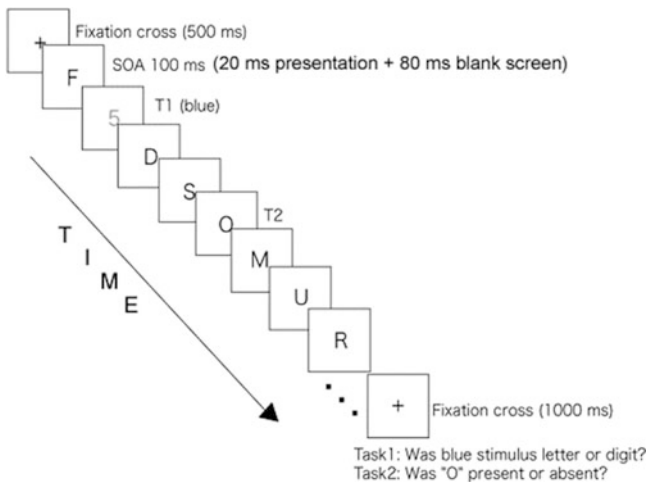


Fig. 1 Illustration of the attentional blink task

3 Results

3.1 Behavioral Results

T2-hit rate was the lowest in the Lag 3 (i.e., the AB phenomenon), followed by the Lag 1 (the so-called Lag-1 sparing phenomenon [6]), and was highest in the Lag 7 condition. Thus, our results reproduce the behavioral pattern typically observed in an AB task.

3.2 EEG Processing

The InfoMax algorithm [7] was applied to the EEG signals taking the 19 electrodes as factors. About 17 components were obtained for each participant. Two of these components, one spread over parietal regions and the other located in the right temporal region, commonly appeared amongst all participants. Both components showed peak power at 10 Hz. Another peak appeared in the theta band. We band passed the signal around 10 Hz (9.345–10.625 Hz), and theta band (4.00–8.00 Hz). The Hilbert transform was applied to the band-passed signals to compute instantaneous amplitude and phase. Amplitude and phase time series were segmented -500 and $+1,300$ ms from T1 onset. Note that in this segment stimuli were presented every 100 ms. The segments were collated based on three T1-T2 lags and two T2 results (hit or miss). This yielded six trial categories. In all categories, trials with incorrect T1 report were excluded from analyses.

3.3 10 Hz Activity

Average amplitude was computed for the 10 Hz segments in each trial category. Grand mean amplitude, however, did not yield significant difference between hit and miss trials in any of the lags; neither in the parietal, nor in the right temporal component.

Similar to amplitude, mean phase angle was computed for the hit and miss trials within each lag. Grand mean angles of the parietal component are shown in Fig. 2a. In the Lag 1 condition, the grand mean phase advanced smoothly with respect to the stimulus onsets across the rapid serial visual presentation (RSVP) episode. Angular velocity slowly increased and phase was shifted about a half cycle per second. However, the phase shift was not smooth in the Lag 3 condition. When T2 was correctly detected (hit trials), the phase did not shift until about the 600 ms from T1 onset (300 ms from T2 onset), then angular velocity abruptly *decreased*. As a result, phase was shifted about half a cycle within a 200 ms period. On the other hand,

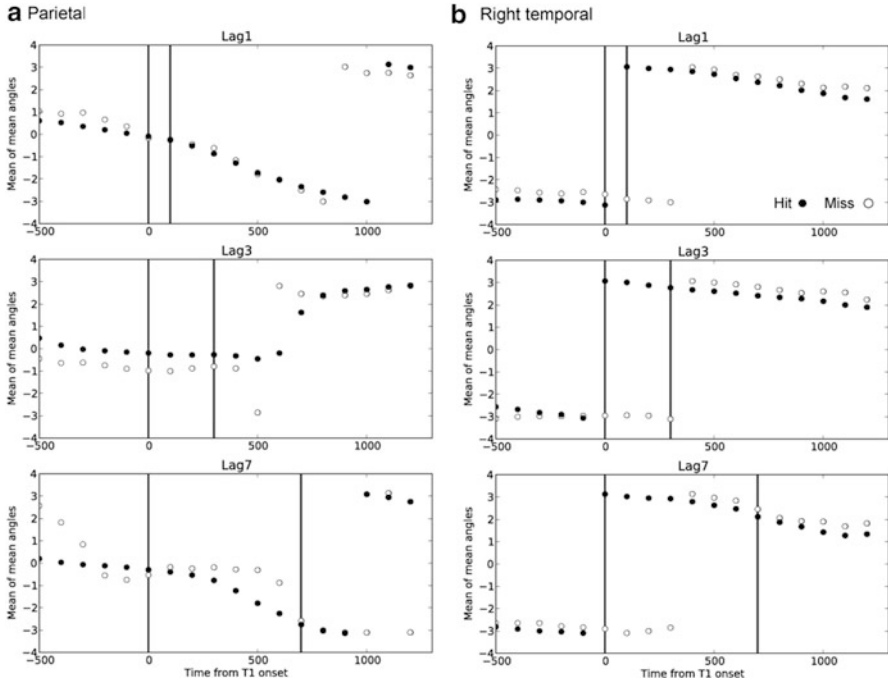


Fig. 2 Grand mean angles of 10 Hz activity at the onset of each stimulus in the parietal (**a**) and right temporal (**b**) components. The angles are plotted for the hit (*black dots*) and miss (*white dots*) trials. T1 and T2 onsets are shown in *black vertical lines*

when T2 was missed, the phase shift took place earlier and occurred in the opposite direction: about 400 ms from T1 onset (100 ms from T2 onset), angular velocity *increased* and advanced the phase about half a cycle within a 100 ms period. In the Lag 7 condition, phase smoothly shifted in the hit condition, while it advanced half a cycle about before T1 and T2 onsets in the miss trials.

The grand mean phase of the right temporal component, on the other hand (Fig. 2b), did not indicate any such shift. Instead, the phase was more-or-less time-locked to the RSVP stimuli for all lags and equally for hit and miss trials.

3.4 *Theta Band Activity*

Average amplitude of the theta band segments did not yield any significant difference between the T2 hit and miss trials in all lags; neither in the parietal, nor in the right temporal component.

Grand mean phase of the theta band activity did not reveal any consistent pattern between the T2 hit and miss trials. This was mostly because mean angles varied

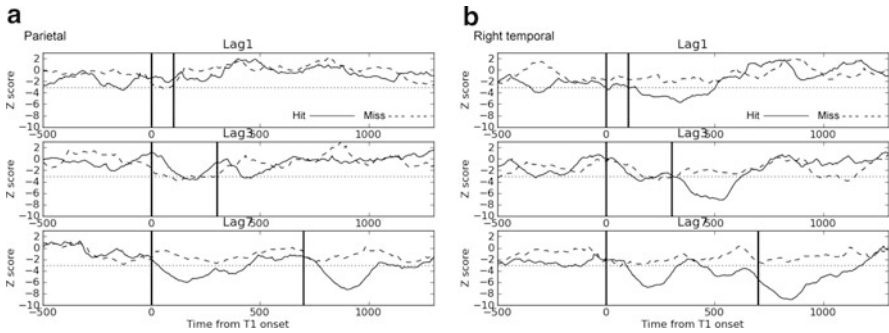


Fig. 3 Z score for the combined probability of phase uniformity. The parietal (*top*) and right temporal components (*bottom*). The hit (*solid line*) and miss (*broken line*) trials are shown in each lag. T1 and T2 onsets are shown by *black vertical lines*. *Dotted line* indicate z score for Prob.(uniform) = 0.001

across individuals. To test phase locking in the theta band activity in individuals, we took two steps: First, phase locking across trials was tested within each participant using the Rayleigh test. The test provides the probability of instantaneous phase being uniform (i.e. random). Second, the individual probabilities were combined over all participants. In this way, phase locking can be assessed independently from individual differences in the mean phase angles. Figure 3 shows the Z-score for the combined probability in each lag for the parietal and temporal components. In the hit trials, the phase was less uniform (i.e., less random) than that in the miss trials. This was most clearly in evidence in the right temporal component after T1 and T2 onsets (Fig. 3b).

4 Discussion

In an Attentional Blink task, a constant rate of stimulus presentation rate might be a useful cue for our perceptual system to synchronize to the rapid sequence of stimuli. The current study showed that, whereas, 10-Hz activity of the right temporal component was uniformly time locked to the stimuli, phase locking of the parietal 10-Hz brain activity to the 10-Hz stimuli had critical importance for successful detection of T2 in the most difficult AB condition.

In the Lag 1 and 7 conditions, on the other hand, the phase of the parietal 10 Hz activity advanced smoothly with respect to the stimulus onsets across the RSVP episode, except for the miss trials in the Lag 7 condition. Thus the phase at onset uniquely represents each stimulus within the RSVP. Such information is useful to control post-stimulus processing, such as working memory operations. For example, working memory operations could be intensified when an acute phase shift occurs. Absence of an acute phase shift in the Lag 1 condition indicates

that, presumably, pre-working memory processes, such as stimulus selection, have more critical effect for T2 detection than working memory operation in the Lag 1 condition, as suggested in previous studies (e.g., [8]). The phase reset even harms T2 detection in the Lag 7 condition. When T2 was missed, the phase advanced acutely. This was the same as in the miss trials in the Lag 3 condition. Such acute phase advance might upset working memory operations (for example, it might increase an inter-item interference in working memory [9]). These results indicate a potential role of the phase shift, which is a control signal for working memory operations.

Phase locking of the theta band activity in the right temporal component suggests that working memory operations are modulated by 10 Hz activity. The relationship between theta and 10 Hz activity is currently under investigation. The current study, at least, present a neural candidate for a ‘rhythm keeper’ function and specifies its role to control of post-target selection, i.e., working memory, processes in the AB task.

References

1. D. E. Broadbent & M. P. Broadbent (1987). From detection to identification: Response to multiple targets in rapid serial visual presentation. *Perception & Psychophysics*, *42*, 105–113.
2. J. E. Raymond, K. L. Shapiro, & K. M. Arnell (1992). Temporary suppression of visual processing in an RSVP task: an attentional blink? *Journal of Experimental Psychology: Human Perception & Performance*, *18*, 849–860.
3. A. Keil, N. Ihssen, & S. Heim (2006). Early cortical facilitation for emotionally arousing targets during the attentional blink. *BMC Biology*, *4*. DOI:10.1186/1741-7007-4-23.
4. J. Gross, F. Schmitz, I. Schnitzler, K. Kessler, K. Shapiro, B. Hommel, & A. Schnitzler (2004). Modulation of long-range neural synchrony reflects spatiotemporal limits of visual attention in humans. *Proceedings of the National Academy of Sciences, U.S.A.*, *101*, 13050–13055.
5. M. Le Van Quyen, J. Foucher, J. P. Lachaux, E. Rodriguez, A. Lutz, J. Martinerie, & F. J. Varela (2001). Comparison of Hilbert transform and wavelet methods for the analysis of neuronal synchrony. *Journal of Neuroscience Methods*, *111*, 83–98.
6. M. C. Potter, A. Staub, & D. H. O’Connor (2002). The time course of competition for attention: attention is initially labile. *Journal of Experimental Psychology: Human Perception & Performance*, *28*, 1149–1162.
7. S. Makeig, A. J. Bell, T.-P. Jung, & T. J. Sejnowski (1996). Independent component analysis of electroencephalographic data. In D. S. Touretzky, M. C. Mozer, & M. E. Hasselmo (Eds.). *Advances in information processing systems* 8. MIT Press: Cambridge, MA.
8. V. Di Lollo, J. Kawahara, S. M. Shahab Ghorashi & J. T. Enns (2005). The attentional blink: resource depletion or temporary loss of control? *Psychological Research*, *69*, 191–200.
9. K. L. Shapiro, J. E. Raymond, & K. M. Arnell (1994). Attention to visual pattern information produces the attentional blink in rapid serial visual presentation. *Journal of Experimental Psychology: Human Perception and Performance*, *20*, 357–371.

Complex Network Topology and Dynamics in Networks Supporting Precisely-Timed Activity Patterns

Chris Trengove, Cees van Leeuwen, and Markus Diesmann

Abstract We study the relationship between structure and activity in a system of synfire chains with random couplings. Ongoing activity is regulated by noise feedback, which, due to variability in the strengths of chains or couplings, creates an activity-dependent family of *effective* digraphs. We find that the distribution of activity across chains is well-correlated with the activity level at which they are recruited into the giant out component.

1 Introduction

Synfire chains, fine-grained structures of diverging and converging feedforward connections that link successive pools of neurons in a sequential manner and support waves of propagating activity packets [1, 2], have been proposed as building blocks, which can be coupled to form more complex network structures [3–5]. In large-scale systems of chains, we will consider the effect of including a broad class of functional recurrent connectivity on the variety of ongoing activity patterns. We are interested in how network structure determines the distribution of ongoing activity.

C. Trengove (✉)

RIKEN Computational Science Research Program, 2-1, Hirosawa, Wako-shi, Saitama 351-0198, Japan
e-mail: ctrengove@brain.riken.jp

C. van Leeuwen

RIKEN Brain Science Institute (BSI), 2-1, Hirosawa, Wako-shi, Saitama 351-0198, Japan

M. Diesmann

RIKEN Computational Science Research Program, 2-1, Hirosawa, Wako-shi, Saitama 351-0198, Japan

RIKEN Brain Science Institute (BSI), 2-1, Hirosawa, Wako-shi, Saitama 351-0198, Japan

Institute of Neuroscience and Medicine, Computational and Systems Neuroscience (INM-6), Juelich, Germany

We will consider an abstract model, in which the state of the system is a set of active pools. The pools are ordered into chains. The transmission of activity from one pool to the next reflects wave propagation. Global activity feedback is considered in the model as a noise source.

Couplings between synfire chains are pairwise, unidirectional, forming a sparse, random globally recurrent network. The coupling connects a subset of pools in one chain to a subset in the other in a one-to-one fashion. This permits a wave of activity in the first chain to activate one in the second, with a specific temporal alignment between the two. We will study the effect of introducing heterogeneity to either the strengths of the chains, or the strengths of the couplings.

2 Methods

2.1 Models

We set the number of chains to $N = 1,000$. We specify a sigmoidal feedback function P_0 as follows:

$$P_0(h, J) = \sigma(J_c(J - J_0) - h_c(h - h_0)). \quad (1)$$

where $\sigma(x) = 1/(1 + \exp(-x))$. The function P_0 gives the probability that a wave successfully propagates over a chain of standard length and strength J , given that h waves are present over the duration of the propagation. The units of J are arbitrary, so without loss of generality we set $J_c = 1$. J_0 is a reference strength, and h_0 represents the activity level at which wave propagation on a chain of reference strength will be *marginally stable*, i.e. where $P_0 = 0.5$.

Wave propagation occurs in discrete time steps, from one pool to the next. The probability of successful propagation per time step is given by:

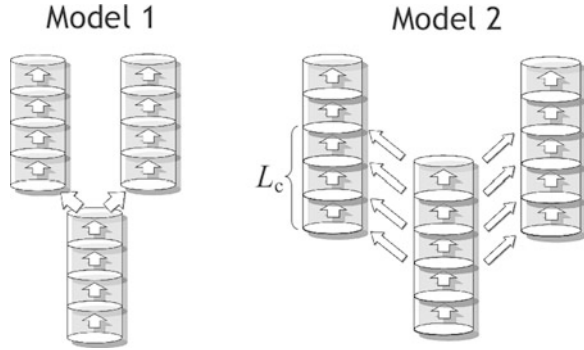
$$P(h, J) := P_0(h, J)^{1/L_0},$$

where L_0 is the number of pools in the standard length chain. We use $h_0 = 10$, and $h_c = 5$ which results in a fairly sharp transition relative to h . In order to avoid artificial wave alignment downstream of a source chain, their lengths vary with a uniform distribution on $[L_0 - \Delta L/2, L_0 + \Delta L/2]$ with $L_0 = 20$ and $\Delta L = 10$.

Chains and between-chain couplings constitute, respectively, the nodes and edges of a directed random graph G_0 , with a fixed out-degree of 2. We will formulate two specific versions (Models 1 and 2)

In Model 1, chains vary in *strength* according to a normal distribution with mean $J_\mu = J_0$ and standard deviation J_σ . We set $J_\sigma = h_c h_\sigma$. The parameter h_σ expresses the variation in chain strength in units of h . This means that a chain of strength

Fig. 1 Pools are coupled to form chains (vertical arrows); two ways of coupling chains used (diagonal arrows); global feedback (not shown) is also present



$J = J_0 \pm J_\sigma$ will be marginally stable when $h = h_0 \pm h_\sigma$. We consider $0 \leq h_\sigma \leq 5$. Couplings between chains are strictly sequential: a link from the last pool of one chain to the first pool of another. Their strength is the same as that of the links within the source chain.

In Model 2, wave propagation within chains is governed by the same survival dynamics as in Model 1, but chain strengths are uniformly fixed above the reference: $J = J_0 + h_c h_0$. This means, according to Eq. (1), that propagation becomes marginally stable at $h = 2 h_0$. Coupling comprises a cascade of L_c weak cross-links between two chains (see Fig. 1). We set $L_c = 10$, which is less than the shortest chain length. Coupling strength varies according to a normal distribution with mean $J_\mu^c = J_0$, and standard deviation $J_\sigma^c = h_c h_\sigma$. We set $J_\mu^c = J_0$ so that a coupling of strength J_μ^c becomes marginally effective at initiating a wave, i.e. $P_0(h, J_\mu^c) = 0.5$, when $h = h_0$. As before, $0 \leq h_\sigma \leq 5$. $P_0(h, J_{ij})$ represents the probability that a wave on chain j will initiate a wave on chain i , given the former traversed all the cross-linked pools. The source wave fails to initiate a wave on chain i if and only if it fails at each of the cross-linked pools. Therefore $P_c(h, J_{ij}) = 1 - (1 - P_0(h, J_{ij}))^{1/L_c}$ is the probability per time step that one wave activates another. If two or more waves from different source pools converge on the same target pool simultaneously, any of them can initiate a wave on the target chain.

2.2 Analysis

For Model 1, we consider node i to be effective at activity h if $h < h_{th}(i)$, where $h_{th}(i)$ is the point of marginal stability of the i -th chain given by $P_0(h_{th}, J_i)^{L_i/L_0} = 0.5$. Likewise, for Model 2, an edge (i, j) is effective if $h < h_{th}^c(i, j)$, the latter defined by $P_0(h_{th}^c, J_{ij}) = 0.5$.

Given their respective strengths, whereas in Model 1 the effectiveness of the chains determines activity propagation, in Model 2 it is the effectiveness of the edges. Therefore, for Model 1, we create a subgraph $G(h)$ of G_0 by removing

all the nodes of the graph corresponding to chains which are ineffective given the activity level. For Model 2, we create $G(h)$ by removing all the edges which are ineffective at that activity level. For each subgraph $G(h)$ we determine the largest strongly connected component, $SC(G)$, and its out-component $OC(G)$ [6]. These track the emerging giant strong and out components, respectively for h between 0 and 20 at a sampling resolution of 0.1.

Each node x in G_0 is characterized by a function $\hat{h}_{SC}(x)$, the largest h -value for which node x still belongs to SC , and likewise $\hat{h}_{OC}(x)$ for the OC . For Models 1 and 2, we generated ten different structures; for each, we estimate $A(x)$, the mean number of wave activations per chain x from ten runs of 10^5 time steps initialized with h waves in randomly selected pools ($h = h_0$), discarding a 2,000 steps initial transient.

3 Results

In both models, ongoing activity fluctuates rapidly around a mean value close to h_0 without external input for long periods of time. The first two columns of Fig. 2 depict the behavior of Model 1 for five values of h_σ . The leftmost column shows $A(x)$ versus $\hat{h}_{SC}(x)$ and $\hat{h}_{OC}(x)$. Chains which more robustly belong to the largest out-component tend to be more active. This trend is less prominent for the largest strong component. The second column plots versus h , firstly: the number of vertices in $G(h)$ relative to G_0 (green dot-dashed), secondly: the relative size of $OC(G(h))$ (red dashed), and thirdly: $\sum A(x)$ over all x for which $\hat{h}_{OC}(x) < h$ (blue, solid). The green curve directly reflects the normal distribution of $h_{th}(x)$. The red curve shows, as theoretically expected [6], the emergence of the giant OC at $h \approx h_0$, where half the nodes of G_0 are in $G(h)$, which implies the average degree of $G(h_0) = 1$ (that of G_0 being 2). The blue curve shows that the activity is mainly concentrated on the few chains that remain in the out-component around this point. The vertical dotted lines indicate the grand mean of activity \pm the SD. The bounds are remarkably independent of h_σ ; the upper stays around h_0 . Finally, the inset shows the cumulative activity of chains ordered by activity (lowest to highest). The striking non-uniformity of ongoing activity increases with strength variability. The last two columns of Fig. 2 similarly describe Model 2. (The green curve becomes the number of *edges* in $G(h)$ relative to G_0 .) The critical point for emergence of the giant component is the same but mean activity is higher, with the *lower* bound consistently around h_0 . This may be, firstly, because chain propagation is robust even when edge propagation is not, and secondly, because in Model 2 coupled chains are active in parallel.

Figure 3 shows the rank correlations between $A(x)$ and $\hat{h}_{OC}(x)$ and between $A(x)$ and $\hat{h}_{SC}(x)$ over chains in $OC(G_0)$ versus h_σ for Models 1 and 2, respectively. They are consistently high for $h_\sigma > 1$, but drop towards zero as $h_\sigma \rightarrow 0$. This is

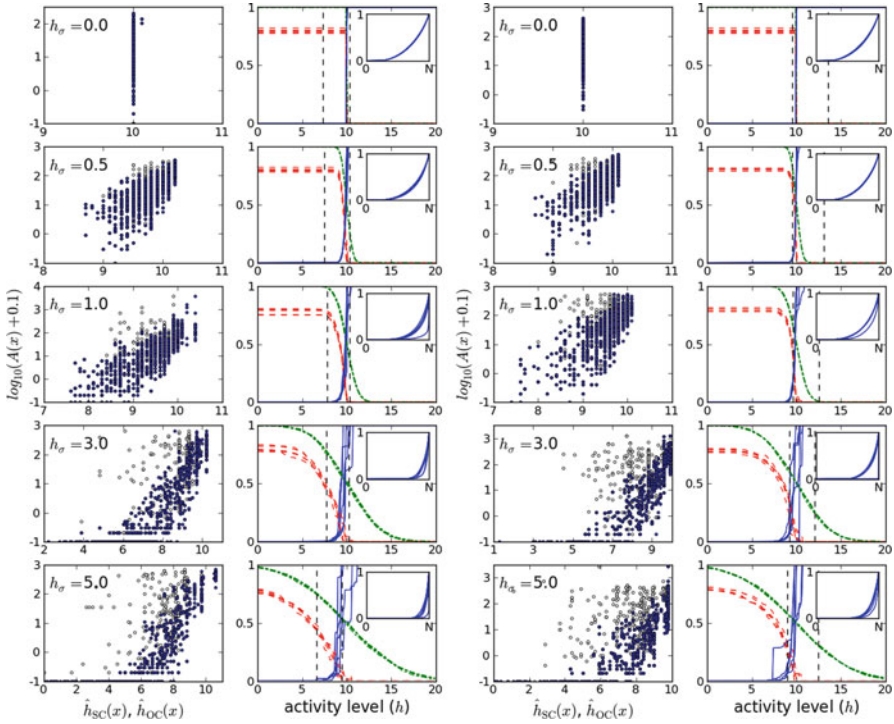


Fig. 2 First two columns: Model 1 for five values of chain strength variability h_σ . First column: mean number of activations per chain $A(x)$ versus the highest h -value for which the chain belongs to the strong component $\hat{h}_{SC}(x)$ – open circles, or the out component, $\hat{h}_{OC}(x)$ – filled circles. Second column: for five network instances, number of nodes in $G(h)$ relative to G_0 (green dot-dashed), relative size of $OC(G(h))$ (red dashed), cumulated average activity $\sum A(x)$ of all chains x for which $\hat{h}_{OC}(x) < h$ (blue, solid). Inset: normalized cumulative plot of activity versus chains ranked by activation. Last two columns: Corresponding results for Model 2, with number of edges in $G(h)$ relative to G_0 (green dot-dashed) (Color figure online)

because in the limit of uniform chain thresholds ($h_{th}(x) \rightarrow h_0$), the giant component abruptly drops from $OC(G_0)$ to \emptyset at $h = h_0$ rather than decreasing gradually with h . Residual variability in $h_{th}(x)$ due to the variability in chain lengths leads to a small positive correlation even at $h_\sigma = 0$ in Model 1, while in Model 2 it is undefined at $h_\sigma = 0$ because $h_{th}^c(i, j)$ is uniform. The rank correlation between $h_{th}(x)$ and $A(x)$ for Model 1, Fig. 3 is consistently below the previous, indicating that $\hat{h}_{OC}(x)$ and $\hat{h}_{SC}(x)$ characterize the distribution better. Exceptions are chains of relatively low $\hat{h}_{OC}(x)$ with a high frequency of activity. These chains usually are both strong and strongly self-coupled, forming loops on which waves can circulate robustly, despite being isolated from the giant component.

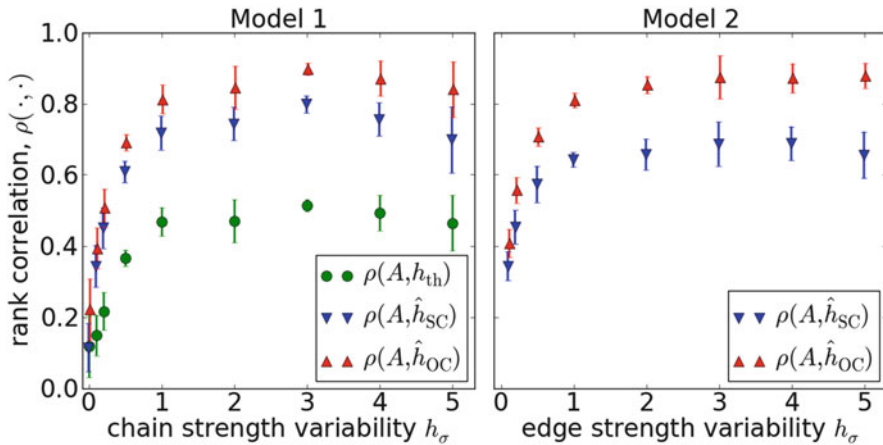


Fig. 3 Rank correlations between $A(x)$ and $\hat{h}_{SC}(x)$, $\hat{h}_{OC}(x)$ respectively and, for Model 1, between $A(x)$ and $h_{th}(x)$, for chains x in $OC(G_0)$

4 Discussion

The propagation of activity in our models exhibits a wandering dynamics. The activity level (h) modulates the *effective* connectivity of the network: the effectiveness of chains (Model 1) or couplings (Model 2); activity fluctuations dynamically create a range of effective graph structures $G(h)$ near the threshold for the emergence of the giant components ($OC(h)$ and $GC(h)$). Activity tends to concentrate on chains that remain in the giant components at higher activity levels. Variability in strength controls the uniformity of activity: the larger the variability the more restricted is the percolation of activity. To serve memory functions, in future developments combinations of wave activity may be selectively reinforced, using dynamic coupling, giving rise to more complex topologies.

References

1. Abeles, M.: Local Cortical Circuits: An Electrophysiological Study. Springer, Berlin (1982).
2. Diesmann, M., Gewaltig, M. O., Aertsen, A.: Stable propagation of synchronous spiking in cortical neural networks. *Nature* **402**, (1999) 529–533.
3. Bienenstock, E. Composition.: In: A. Aertsen and V. Braitenberg (eds), *Brain Theory – Biological Basis and Computational Theory of Vision*. Elsevier (1996) 269–300.
4. Abeles, M., Hayon, G. and Lehmann, D.: Modeling compositionality by dynamic binding of synfire chains. *J. Computational Neuroscience*, **17** (2004) 179–201.
5. Hanuschkin, A., Herrmann, J., Morrison, A., Diesmann, M.: Compositionality of arm movements can be realized by propagating synchrony. *J. Computational Neuroscience*, (2010) DOI [10.1007/s10827-010-0285-9](https://doi.org/10.1007/s10827-010-0285-9).
6. Barbosa, V. C, Donangelo, R., Souza, S. R.: Directed cycles and related structures in random graphs: I – Static properties. *Physica A*, **321** (2003) 381–397.

Part VI
Toward Understanding of Intelligence:
Collaboration Between Neuroscience
and Robotics

Neural Synchrony for Expert Memory in Shogi (Japanese Chess) Players

Hironori Nakatani and Yoko Yamaguchi

Abstract Experts in most domains show superior memory performances for domain-specific stimuli. Psychological studies proposed that chunk-based processing is a key mechanism of cognitive expertise and superior memory performances of experts are natural consequences of chunk-based processing. A neuroimaging study has shown that chunks are stored in the temporal lobe. On the other hand, brain dynamics underlying chunk-based processing is poorly understood. With shogi (Japanese chess), we investigated neural synchrony underlying working memory of shogi players. We found that neural phase synchrony between the frontal and the temporal areas was associated with memory retention of expert players. The result indicates that synchronized interaction between frontal executive area and temporal chunk area realizes chunk-based processing.

1 Introduction

Experts have domain-specific superior cognitive ability [1–3]. For example, expert chess players can memorize a number of chess positions from real game records [4–6] and can rapidly find superior moves [6]. Psychological studies proposed that a key mechanism underlying cognitive expertise is chunk-based processing [7]. Chunks are long-term memory (LTM) information about stereotyped patterns of piece positions [4, 5]. As chunks are perceptual units and are associated with chess strategy, recognition of chunks in chess positions reduces mental load and also retrieves moves from knowledge about chess strategy.

H. Nakatani (✉) • Y. Yamaguchi
Laboratory for Dynamics of Emergent Intelligence, RIKEN Brain Science Institute,
Saitama, 351-0198, Japan
e-mail: hnakatani@brain.riken.jp; yokoy@brain.riken.jp

Recent neuroimaging studies have identified brain areas underlying superior cognitive process of chess experts. Campitelli et al. showed that chunks are stored in the temporal lobe [8]. With shogi (Japanese chess), Wan et al. showed that the precuneus in the parietal lobe is responsible for perception of piece positions and the caudate nucleus of basal ganglia is responsible for quick generation of the move [9]. On the other hand, brain dynamics underlying superior cognitive ability is poorly understood.

We assumed that phase synchronization of brain activity between the frontal area and the temporal area realized chunk-based processing and it, therefore, characterized high level of expertise. Phase synchronization of neural activity has been proposed as a mechanism to integrate neural processes that are distributed across the brain [10, 11]. If the chunk-based processing is a key mechanism underlying cognitive expertise [7], phase synchronization would mediate a formation of dynamic links between frontal executive area and temporal chunk area.

In this study, we carried out working memory experiments with shogi. As chess studies reported that working memory performances were closely correlated with chess expertise [4–6], brain activity underlying working memory would reflect expert's cognitive process. We compared phase synchronization of the electroencephalogram (EEG) activity between brain areas across different levels of shogi expertise.

2 Methods

Thirty participants with normal or corrected-to-normal vision participated in this study. They were professional players, amateur players, and non-playing participants. Participants were classified into following four groups: professional group ($n = 12$), high-ranked amateur group ($n = 6$), low-ranked amateur group ($n = 6$), and non-playing group ($n = 6$). Participants gave their written informed consent. The Research Ethics Committee of the RIKEN approved our experiments.

In our working memory experiments, each trial consisted of four periods: 3 s of fixation period, 5 s of encoding period, 3 s of retention period, and self-paced retrieval period. In the encoding period, a shogi position was presented visually on a monitor. In the retrieval period, a shogi board and pieces were presented on the monitor. Participants then reconstructed the piece positions based on their memory. There were two stimulus conditions. One was a game condition, in which piece positions were from game records. Shogi players recognized game positions as chunks of pieces, not as individual pieces. The other was a random condition, in which piece positions were created by random replacement of piece positions in the game condition. We used 50 stimuli in the game condition and 50 stimuli in the random condition. The stimuli were presented with randomized order.

We measured the EEG activity with 19 Ag/AgCl electrodes that were placed on the scalp in accordance with the international 10/20 system. Reference and ground electrodes were placed on the left ear and forehead, respectively. Electrooculogram (EOG) was also recorded.

In order to evaluate the synchronized brain activity between brain areas, we used phase synchronization index (PSI). The index is a statistic for phase-locking between two signals [11, 12]. After we reduced blink and EOG-related artifacts from EEG recordings with independent component analysis [13, 14], we calculated the PSI. The details of the calculation were shown in [15].

3 Results

Phase synchrony spectra systematically changed according to levels of shogi expertise (Fig. 1).

During the retention period, the professional and the high-ranked amateur groups showed enhanced phase synchronization in the alpha band between the frontal activity (Fz-site) and the left temporal activity (T5-site). The high-ranked amateur and the low-ranked amateur groups showed enhanced phase synchronization in the beta band between the frontal activity (Fz-site) and the parietal activity (Pz-site). These results indicate that phase synchronization between the frontal area and the temporal area characterizes high level of expertise and phase synchronization between the frontal area and the parietal area characterizes intermediate level of expertise.

On the other hand, during the encoding period, the low-ranked amateur and the non-playing groups showed enhanced phase synchronization in the beta band between the frontal activity (Fz-site) and the left temporal activity (T5-site) without enhanced alpha band phase synchronization during the retention period. Phase synchronization between the frontal area and the temporal area, thus, also characterizes low level of expertise.

Interestingly, waveforms of phase synchrony spectra in the random condition were similar those in the game condition (Fig. 1).

4 Discussion

As chunks are LTM representations about stereotyped patterns of piece positions [4, 5], chunk-based processing [7] would temporarily activate LTM representations to process domain-specific information. In our study, participants with high level of shogi expertise showed enhanced phase synchronized EEG activity between the frontal and the temporal areas during memory retention (Fig. 1). The result suggests that the frontal executive function accessed LTM representations about chunks in the temporal area [8] to maintain internal representations about presented piece positions.

Waveforms of phase synchrony spectra in the random condition were similar to those in the game condition (Fig. 1). The similar spectra suggests that similar cognitive dynamics were applied for both meaningful game positions and meaningless random positions. According to chess study, expert players did find some chunks

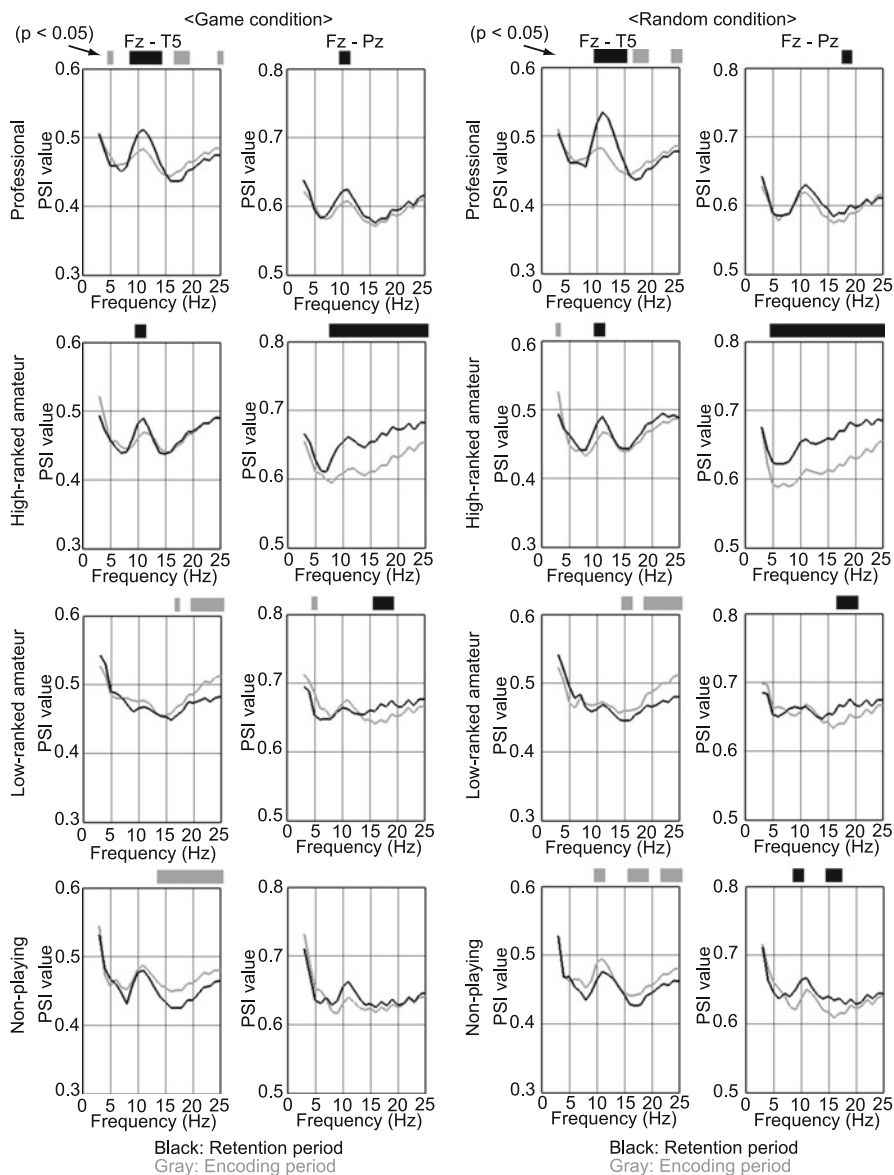


Fig. 1 Waveforms of phase synchrony spectra were systematically associated with levels of shogi expertise. Values of PSI between the Fz-site and the T5-site and between Fz-site and Pz-site in the encoding and the retention periods were shown

even in randomized positions [16]. As stronger players have larger repertoires of chunks in LTM [7, 16, 17], they are more likely to find rare patterns in LTM than weaker players. The effect of chunk-based processing in the random condition was confirmed by computer simulations [17].

Thus, we propose that a key neural dynamics underlying chunk-based processing is alpha band phase synchronized brain activity between the frontal and the temporal areas.

Intermediate level of expertise were characterized by enhanced phase synchronization between the frontal and the parietal areas. A fMRI study reported that training of working memory task increased the frontal and the parietal areas [18]. Phase synchronization between the frontal and the parietal areas might reflect some aspects of training in shogi regarding working memory function such as manipulation of internal representation about shogi-related information.

From waveforms of phase synchrony spectra (Fig. 1), we can infer how brain dynamics change during skill development. The frontal area first cooperates with the parietal area at the early stage of skill development, and then it cooperates with the temporal area when we attain high level of expertise with long-term, intensive training.

Acknowledgements This study has been supported by Fujitsu, Fujitsu Laboratories, and Japan Shogi Association.

References

1. Ericsson, K.A., Lehmann, A.C: Expert and exceptional performance: evidence of maximal adaptation to task constraints. *Annu. Rev. Psychol.* **47** (1996) 273–305
2. Ericsson, K.A., Charness, N., Feltovich, P.J., Hoffman, R.R: The cambridge handbook of expertise and expert performance. Cambridge University Press. (2006)
3. Ross, P.E: The expert mind. *Sci. Am.* **295** (2006) 64–71
4. Gobet, F., Lane, P.C., Croker, S., Cheng, P.C., Jones, G., Olier, I., Pone, M: Chunking mechanisms in human learning. *Trends. Cogn.* **5** (2001) 236–243
5. Gobet, F., Clarkson, G: Chunks in expert memory: evidence for the magical number four ... or is it two?. *Memory.* **12** (2004) 732–747
6. Gobet, F., de Voogt, A., Retschitzki, J: Moves in mind: the psychology of board games. Psychology Press. Hove and New York. (2004)
7. Chase, W.G., Simon, H.A: Perception in chess. *Cogn. Sci.* **4** (1973) 55–81
8. Campitelli, G., Gobet, F., Head, F., Buckley, M., Parker, A: Brain localization of memory chunks in chessplayers. *Int. J. Neurosci.* **117** (2007) 1641–1659
9. Wan, X., Nakatani, H., Ueno, K., Asamizuya, T., Cheng, K., Tanaka, K: The neural basis of intuitive best next-move generation in board game experts. *Science.* **331** (2011) 341–346
10. Engel, A.K., Singer, W: Temporal binding and the neural correlates of sensory awareness. *Trends. Cogn. Sci.* **5** (2001) 16–25
11. Varela, F., Lachaux, J.P., Rodriguez, E., Martinerie, J: The brainweb: phase synchronization and large-scale integration. *Nat. Rev. Neurosci.* **2** (2001) 229–239
12. Lachaux, J.P., Rodriguez, E., Martinerie, J., Varela, F.J: Measuring phase synchrony in brain signals. *hum. Brain Mapp.* **8** (1999) 194–208
13. Hyvärinen, A., Oja, E: A fast fixed-point algorithm for independent component analysis. *Neural Comput.* **9** (1997) 1482–1492
14. Hyvärinen, A., Oja, E: Independent component analysis: algorithms and applications. *Neural Netw.* **13** (2000) 411–430

15. Nakatani, H., van Leeuwen, C: Transient synchrony of distant brain areas and perceptual switching in ambiguous figures. *Biol. Cybern.* **94** (2006) 445–457
16. Gobet, F., Simon, H.A: Recall of rapidly presented random chess positions is a function of skill. *Psychonomic. Bull. Rev.* **3** (1996) 159–163
17. Gobet, F., Simon, H.A: Recall of random and distorted chess positions: implications for the theory of expertise. *Memory & Cognition.* **24** (1996) 493–503
18. Olesen, P.Oj., Westerberg, H., Klingberg, T: Increased prefrontal and parietal activity after training of working memory. *Nat. Neurosci.* **7** (2004) 75–79

Neuronal Synchrony During the Planning and Execution Period in the Prefrontal Cortex

Kazuhiro Sakamoto, Katsutoshi Yamamoto, Naohiro Saito, Kazuyuki Aihara, Jun Tanji, and Hajime Mushiake

Abstract We analyzed synchronous firing in lateral prefrontal cortex (IPFC) neurons while monkeys were performing a path-planning task that required them to perform multiple related cursor movements. A synchronous group of neuronal pairs showed enhanced synchrony at each cursor-movement step. This enhanced synchrony, which preceded the execution period for the first cursor movement, was significantly correlated with cursor-movement selectivity as defined by the firing rate during the planning period. Information about the behavioral plan represented by the firing rate may be transformed from the “planned state” into the “execution state” by neuronal synchrony within the IPFC.

K. Sakamoto (✉)

Research Institute of Electrical Communication, Tohoku University, 2-1-1 Katahira, Aoba-ku, Sendai 980-8577, Japan
e-mail: sakamoto@riec.tohoku.ac.jp

K. Yamamoto

Department of Physiology, Tohoku University School of Medicine, 2-1 Seiryō-cho, Aoba-ku, Sendai 980-8575, Japan

N. Saito

Department of Clinical Neuroscience, Yamagata University Graduate School of Medical Science, 2-2-2 Iida-Nishi, Yamagata 990-9585, Japan

K. Aihara

Institute of Industrial Science, University of Tokyo, 4-6-1 Komaba, Meguro-ku, Tokyo 153-8505, Japan

J. Tanji

Brain Science Center, Tohoku University, 2-1-1 Katahira, Aoba-ku, Sendai 980-8577, Japan

H. Mushiake

Department of Physiology, Tohoku University School of Medicine, 2-1 Seiryō-cho, Aoba-ku, Sendai 980-8575, Japan

CREST, Tokyo, Japan

Y. Yamaguchi (ed.), *Advances in Cognitive Neurodynamics (III)*,

DOI 10.1007/978-94-007-4792-0_45,

© Springer Science+Business Media Dordrecht 2013

Keywords Neuronal synchrony • Monkey • Prefrontal cortex

1 Introduction

The lateral prefrontal cortex (IPFC) is involved not only in maintaining behaviorally relevant information internally but also in planning multiple actions that are executed subsequently [1]. Several studies have reported that during such execution periods, enhanced synchronous neuronal firing precedes each action (e.g. [2]). However, the functional role of such synchrony is unclear.

We previously observed transient synchronous firing among a group of IPFC neurons in monkeys during the planning period of a path-planning task that required them to plan multiple cursor movements to reach a goal [3]. This synchrony seemed to coincide with a shift from the “instructed final goal” state to the “planned cursor movement” state as represented by the firing rate, suggesting that neuronal synchrony is involved in a state shift in the IPFC.

In this study, we examined whether transient synchrony is observed during the task execution period and, if so, what the behavioral relevance is, particularly its relationship to neuronal representation of cursor movements.

2 Methods

The details of the experimental and analytical procedures are described in [1, 3, 4].

2.1 Behavioral Procedures

Two monkeys (*Macaca fuscata*) were trained to perform a path-planning task that required planning multiple cursor movements, controlled with manipulanda, to reach a goal within a maze (Fig. 1). Animals were cared for in accordance with the Guiding Principles for the Care and Use of Laboratory Animals of the NIH and our institution. To begin the trial, the animals were required to hold the two manipulanda in a neutral position for 1 s (Initial Hold). Subsequently, a cursor was presented at the center of the maze (Start Display). One second later, the position of a goal cursor was presented for 1 s (Final Goal Display). After a delay (Delay 1 or Delay 2), the color of the cursor was changed from green to yellow, which served as an initiation signal (1st GO). After a 1-s hold period, the next GO signal was presented (2nd GO). When the cursor reached the final goal position, the animal received a reward (Reward). To dissociate arm and cursor movements, the arm-cursor assignments were altered on completion of a block of 48 trials.

We used conventional electrophysiological techniques to obtain *in vivo* single-cell recordings from the IPFC.

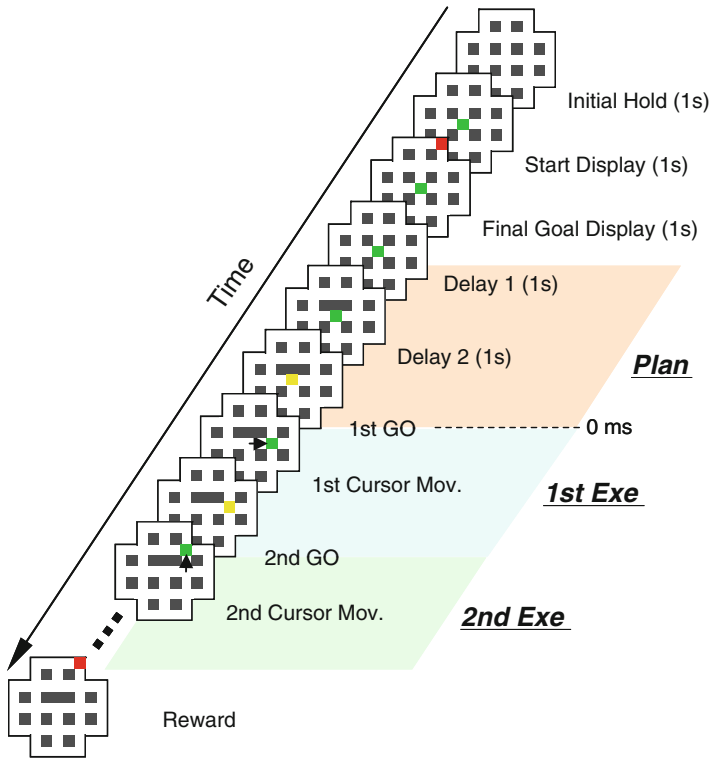


Fig. 1 Temporal sequence of events in the path-planning task. *Green, red and yellow squares* denote current cursor positions, the positions of the final goal and GO signals, respectively (Color figure online)

2.2 Analysis of Single-Unit Activity

We examined the time course of firing-rate selectivity for each cursor movement during the entire task period. First, spike counts within 100-ms time frames were assessed using multiple regression analysis. Then, the *F*-values of regression coefficient for in successive 100-ms time frames were normalized to the predicted value of each neuron at $P = 0.05$ and smoothed using a sliding average for 500-ms time frames.

To evaluate the extent to which PFC neuronal activity predicted information associated with cursor movements within each 100-ms time frame, we calculated the predictive information carried by the occurrence of spikes by quantifying the decrease in entropy in the cursor directions [1].

The normalized *F*-values and information within a pair of neurons were averaged and used to assess the statistical significance of the pair.

2.3 Analysis of Neuronal Synchrony

We used the time-resolved cross-correlation method [3, 5] to assess changes in the synchrony of neuron pairs independently of changes in the firing rate of individual neurons by using the instantaneous firing-rate (IFR) estimate to correct for firing-rate modulation.

A time-resolved cross-correlation (TCC) histogram was obtained by cross correlating the spike times of two neurons of pair. Namely, this histogram is a plot for spike timing of one neuron within ± 200 ms of when the other neuron fires. The predictor (time-resolved cross-predictor; TCP) used to estimate false synchrony caused by fluctuations in firing rate was estimated by cross correlating IFRs. The IFR at each time was defined from the reciprocal of the interspike interval. Thus, the IFR was obtained for each trial, avoiding the detection of false synchrony caused by intertrial fluctuations. The TCP was subtracted from the TCC at each data point, and this value was summed over the task period to create the standard cross-correlation histogram (CCH).

The CCH was used to select significantly synchronous pairs based on the following criteria: more than 2,000 spikes contributed to the cross-correlation estimate, the CCH had a positive peak of more than 4.41 SDs above baseline ($P < 0.00001$), and the significant peak was within ± 25 ms of the center of the CCH [6].

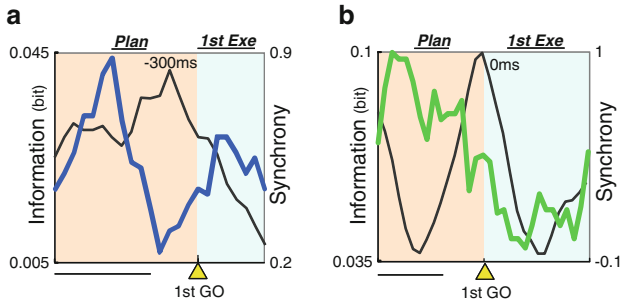
To examine synchrony in the significantly correlated pairs of spikes over time, we first calculated raw synchrony (RS) by averaging synchrony magnitudes in the TCC, taken from the half-width area around the peak in the CCH. Similarly, we calculated the firing-rate-dependent synchrony (FRDS) as a reference or a predictor for synchrony estimated from the firing rate. Then, we calculated the difference between RS and FRDS (divided by the SD of the latter for normalization) and plotted the values as normalized synchrony. In the following, we used the term synchrony in place of normalized synchrony for simplicity.

3 Results

Among 456 neuronal pairs (458 neurons) recorded simultaneously, 23 pairs (45 neurons) showed significant synchronous firing during the entire task period (synchronous pairs). In this report, we focused on the selectivity of these pairs for the first and second cursor movements during the planning and execution periods.

Transient synchrony seemed to follow the increase in cursor movement selectivity during the planning period. In the example pair indicated in Fig. 1a, a synchrony peak was observed near the transition time between the planning and execution periods (-300 ms from the first GO signal). Before this peak, information predicting the first cursor movement, calculated from the firing rate of the neurons of the pair, exhibited a prominent peak during the planning period. A comparable result for information associated with the second cursor movement was obtained in another pair indicated in Fig. 2b.

Examples



Population

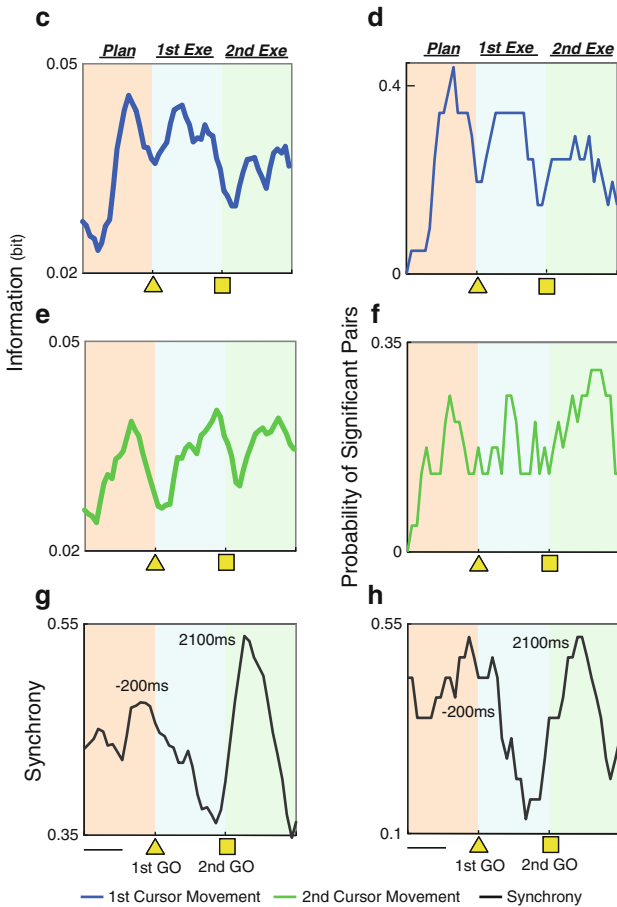


Fig. 2 Time course of synchrony and information for the first and second cursor movements within the synchrony-pair population. The time course of the probabilities for the significant pairs within this population is also shown. (a, b) Examples. (c–h) Averages of the synchronous pairs. The times of significant peak synchrony are indicated in (a, b, c, and h) ($P < 0.05$)

At the population level of the synchrony pairs ($n = 23$), broad peaks of predictive information about the first cursor movement were observed not only during the execution periods but also during the planning period (Fig. 2c). This result was supported by the plot of the probability of pairs that showed significant selectivity for the first cursor movement (Fig. 2d). Corresponding figures for the second cursor movement are presented in Fig. 2e and f. These results were consistent with our previous study [1].

Enhanced synchrony at the transition time between the planning and execution periods was also observed at the population level. Figure 2g and h indicate the time course of the averaged synchrony and probability of significant synchrony. A significant broad peak in synchrony was observed near the first GO signal (-200 ms; $P < 0.05$, binominal test). We called this broad peak “synchrony-at-transition”. We also observed another significant broad synchrony peak during the execution period (2,100 ms; $P < 0.05$, binominal test) and called it “synchrony-during-execution”.

To examine the physiological relationship between these two synchronous peaks and the information for the first and second cursor movements, we analyzed the correlations between the magnitude of synchrony and the predictive information in the planning and execution periods across the population pairs (Fig. 3). The results revealed that synchrony-at-transition was more correlated with information for the first cursor movement than for synchrony-during-execution (Fig. 3a). In particular, synchrony-at-transition was significantly correlated with the predictive information during the planning period ($r = 0.48$, $P < 0.05$). The correlations between the synchronous peaks and predictive information about the second cursor movement were quite similar (Fig. 3b).

4 Discussion

We investigated the role of synchronous firing in the IPFC as monkeys performed a path-planning task that required multiple cursor movement steps to reach goals. We detected two different types of neuronal synchrony, which were enhanced transiently at different phases of the trial (Fig. 4). The first broad synchronous peak was detected near the transition period from the planning to the execution phase (synchrony-at-transition), and the second synchronous peak was detected during the execution period (synchrony-during-execution). Synchrony-at-transition was significantly correlated with predictive information about cursor movements during the planning period. In contrast, synchrony-during-execution was not correlated with planned actions.

Our findings suggest different functional roles for each type of synchrony. Synchrony-at-transition may involve a state transition between simultaneous planning and serial execution of intended actions within the IPFC. In contrast, Synchrony-during-execution did not reflect information about planned actions and

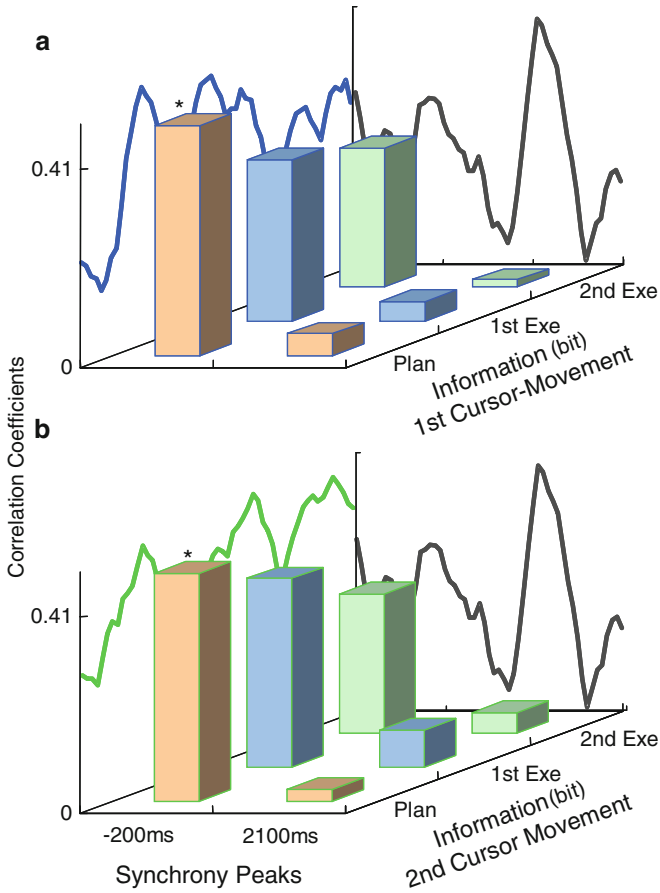
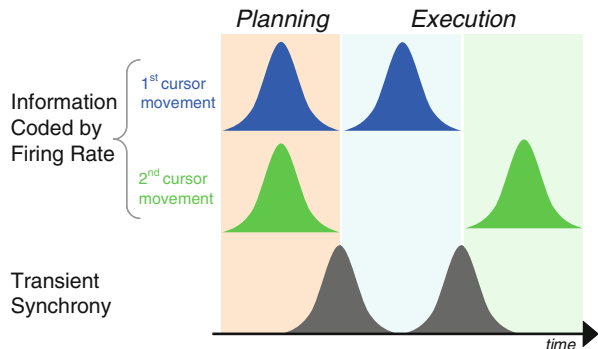


Fig. 3 Correlation between broad synchrony peaks and predictive information for the first and second cursor movements. The maximum correlation coefficients for each of the three periods are shown. **(a)** First cursor movement. **(b)** Second cursor movement. Plan, planning period; *1st Exe* first execution period, *2nd Exe* second execution period. Each period was 1,800 ms in length. Asterisks, $P < 0.05$

Fig. 4 A schematic summary of the findings. Two types of transient synchrony and their relationship with a representation of sequential actions



appeared to be incidental in nature. The physiological implications of this newly detected synchrony-during-execution remains to be further studied.

Acknowledgments This research is supported by the Ministry of Education, Culture, Sports, Science, and Technology of Japan (#22120504).

References

1. Mushiake, H., Saito, N., Sakamoto, K., Itoyama, Y., Tanji, J.: Activity in the lateral prefrontal cortex reflects multiple steps of future events in action plans. *Neuron*. 50 (2006) 631–641.
2. Riehle, A., Grün, S., Diesmann, M., Aertsen, A. Spike synchronization and rate modulation differentially involved in motor cortical function. *Science* 278 (1997) 1950–1953.
3. Sakamoto, K., Mushiake, H., Saito, N., Aihara, K., Yano, M., Tanji, J.: Discharge synchrony during the transition of behavioral goal representations encoded by discharge rates of prefrontal neurons. *Cerebral Cortex*. 18 (2008) 2036–2045.
4. Saito, N., Mushiake, H., Sakamoto, K., Itoyama, Y., Tanji, J.: Representation of immediate and final behavioral goals in the monkey prefrontal cortex during an instructed delay period. *Cerebral Cortex*. 15 (2005) 1535–1546.
5. Baker, S.N., Spinks, R., Jackson, A., Lemon, R.N.: Synchronization in monkey cortex during a precision grip task. I. Task-dependent modulation in single-unit synchrony. *J. Neurophysiol.* 85 (2001) 869–885.
6. Constantinidis, C., Franowicz, M.N., Goldman-Rakic, P.S.: Coding specificity in cortical microcircuits: a multiple-electrode analysis of primate prefrontal cortex. *J. Neurosci.* 21 (2001) 3646–3655.

A Constructive Approach for Investigating the Emergence of Role Division in Social Interactions

Kenichi Minoya, Takaya Arita, and Takashi Omori

Abstract This paper attempts to demonstrate the emergence of role division in a short time scale where agents dynamically determine their roles based on the estimated intention of others. To do this, we use a *Functional Parts Combination* (FPC) model, which regards the brain at a functional level as composed of a set of functional parts and activation signals specifying selectively activated patterns. We conduct computer simulations in which the activation signals are learned using a hunter task as a problem to be solved by the agents. The simulation demonstrates a scenario for bootstrapping *Theory of Mind* (ToM) as the emergence of the partial-networks of functional parts in the brain based on the interactions between the recursive levels of intentionality in ToM. It also shows that appropriate behaviors suited for others interacting for the first time can be swiftly acquired simply by reusing the acquired partial-networks.

1 Introduction

In social interactions human can behave cooperatively by estimating the intention of others and determining own roles. Understanding of others as having intentional states such as beliefs and desires is called *Theory of Mind* (ToM) [1]. We model a human communication based on the mind-reading as follows: (1) humans estimate

K. Minoya (✉) • T. Arita

Graduate School of Information Science, Nagoya University, Furo-cho, Nagoya 464-8601, Japan
e-mail: kenichiminoya@alife.cs.is.nagoya-u.ac.jp; arita@nagoya-u.jp

T. Omori

College of Engineering, Tamagawa University, 6-1-1 Tamagawa Gakuen, Machida,
Tokyo 194-8610, Japan
e-mail: omori@lab.tamagawa.ac.jp

the intention of others from his/her behavior by simulating it based on their own action decision process as if they were in the same situation [2]; (2) humans interactively determine own behaviors in accordance with the estimated intention of others. Unlike the static environment where certain rules that agents have to learn were permanent, these processes are too dynamic to be explained by the traditional action learning methods through a trial and error because it is necessary to cope promptly with the change of the intention of others in its dynamic environment.

This paper attempts to demonstrate the emergence of role division in social interactions among agents estimating the intention of others based on a *Functional Parts Combination* (FPC) model [3]. The FPC model is based on the neuroscientific fact that each cerebral cortical area has a different role and is selectively activated depending on the task.

Several studies in agent-based computational modeling have been made on the emergence of role division in social interactions on the basis of ToM [4, 5]. However, functions of ToM in these studies are procedurally defined a priori. This paper focuses on the emergence of a ToM without defining it a priori by modeling the brain at the functional level.

2 The Model

2.1 Functional Model of the Brain

Figure 1 shows a functional model of the brain based on the FPC model [6]. There are modules M_i in the brain, which constitute a module network. A set of modules in the network is activated by a set of activation signals represented as a vector of binary values 0 and 1: $A = (a_0, \dots, a_i, \dots, a_{k-1})$, where k is the number of

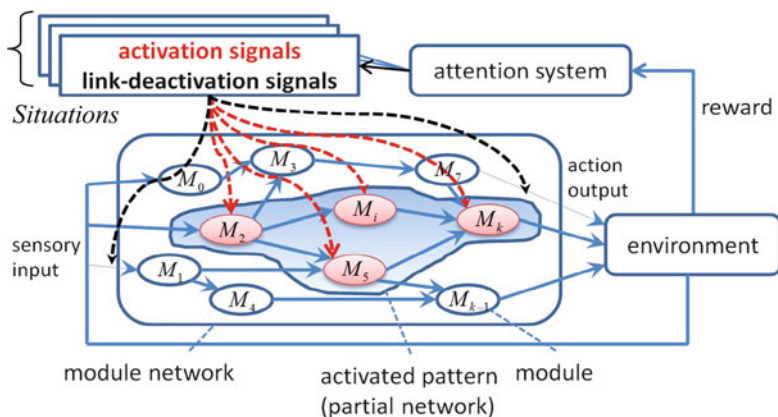


Fig. 1 Functional model of the brain

(continued)

M_8 (intention formation): intention $G_s (\neq G_o)$ is formed.

M_9 (action selection): action $a_s = \operatorname{argmax}_a P(a | s_s, G_s)$.

M_{10} (action-selection function): it is the one based on soft-max reinforcement learning.

M_{11} (Q-Table): it is an evaluation value acquired by reinforcement learning.

d_{24}, d_{34}, d_{88} (link-deactivation signals): $d_{24} = d_{88}$, and $d_{24} \neq d_{34}$.

The brain searches for a setx of activation and link-deactivation signals: $Solution = (A, D)$ responding to the current task (or social situation). The searching system alternates between the two modes: searching for a new $Solution$ and switching among the acquired $Solutions$, evoked by the change of environmental nature [9]. In searching mode, it searches for a new $Solution$ for the current (social) situation. When a solution which forms a new partial network containing sensory input and action output is obtained, it is registered in the $Situations$. The system changes into switching mode when the evaluation keeps lower than a threshold for a certain period of time. In switching mode, an adequate $Solution$ continues to be used while the evaluation is stable. However, if there are no suited solutions in the $Situations$ for the current environment, which means that it is a novel environment, the system returns into searching mode. The evaluation is updated per unit time:

$$E_{p+1} = \alpha_e \cdot reward + (1 - \alpha_e) \cdot E_p, \quad (1)$$

where α_e is a parameter which coordinates the update rate and $reward$ is an evaluation of the present partialnetwork. The threshold is also updated per unit time:

$$T_{p+1} = \alpha_t \cdot T_{max} + (1 - \alpha_t) \cdot T_p, \quad (2)$$

where α_t is a parameter which coordinates the update rate and T_{max} corresponds to a threshold value of the model. The sensitivity to change of the environmental nature is regulated by T_{max} . In order to prevent the frequent mode change, T_p is set to T_{min} after the mode change.

2.2 Task

This paper focuses on the emergence of activation and link-deactivation signals for forming ToM partial-networks with a specific recursion level to achieve cooperative behavior in a hunter task. Two hunters cooperatively capture the two prey in a 20×20 a two-dimensional grid folded to a torus in the task. Each hunter moves one

cell per step to the left, right, up or down, or stays in the current cell according to its own strategy, while each prey moves one cell per step stochastically. When starting the task, all four agents are randomly located in the grid, and each hunter selects the closer prey as an initial target. Each *episode* ends when each hunter captures the different prey or the number of time steps exceeds the upper limit $step_{max}$.

The task is solved several times using the current solution in each *period*. Averaged time steps to solve the task, which is used to evaluate the solution:

$$reward = 100/step. \tag{3}$$

The *reward* is shared between cooperators, and then E_p (expression (1)) and T_p (expression (2)) are updated.

3 Experiments

3.1 Experimental Setup

We conducted simulations in which each agent learned the activation and link-deactivation signals in parallel on the basis of tabu search [10]. First, N agents were created, each with a randomly generated initial solution: $Solution_0 = (s_0, \dots, s_i, \dots, s_{k-1}, s_k)$, where s_i ($i = 0, \dots, k-1$) corresponds to the activation signal a_i for module M_i , and s_k represents the link-deactivation signal (d_{34}), respectively. Each agent solved the hunter task $N - 1$ times, each with a different agent in a round robin manner. Table 1 shows the experimental setup of the experiments.

4 Results

Figure 3a shows the transition of $Solution_p$, *reward*, E_p and T_p of a hunter during learning (7 rounds). In the following account, we call the focal hunter ‘Ken’. Figure 3b shows the transition of those of Ken’s 7 different partners each round.

Table 1 Experimental setup

Population size: N	8	T_{max}	2
$Period_{max}$	1,000	T_{min}	-1
$Episode_{max}$	10	α_e, α_t (in searching mode)	0.02
$Step_{max}$	500	α_e, α_t (in switching mode)	0.005
Neighbor size: n	13	History size: H	5
Mutational rate: p	0.15	Temperature: β	1
<i>Tabu tenure</i>	7		

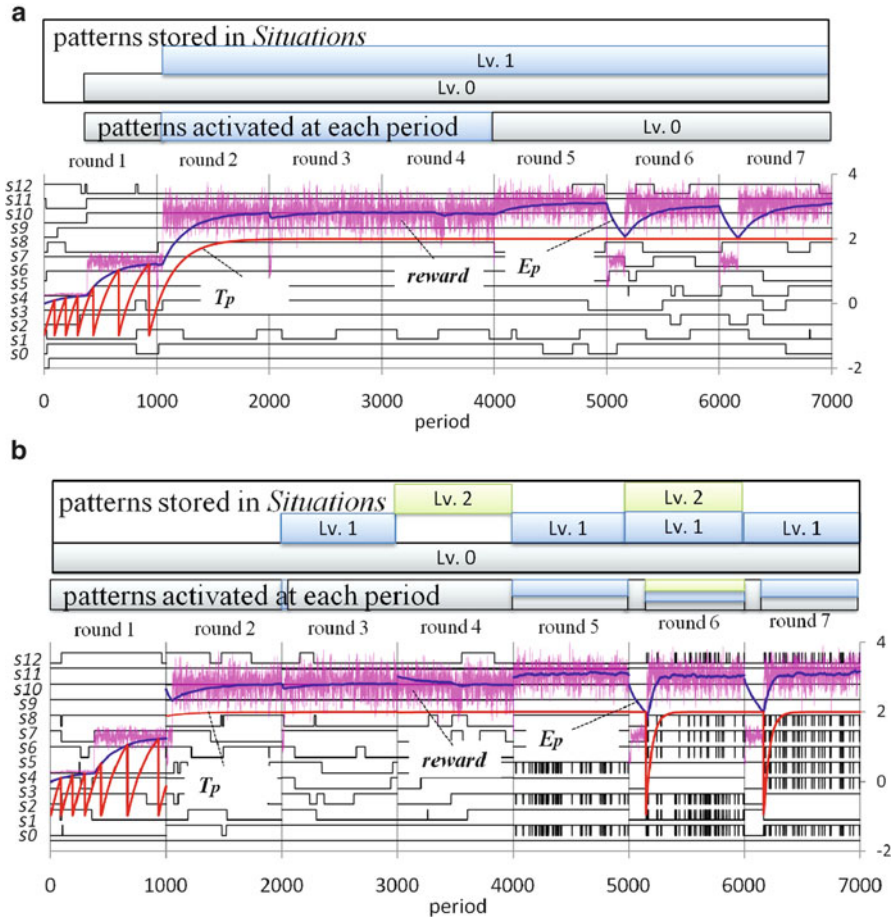


Fig. 3 The transition of the $Solution_p$ (black lines), reward (pink line), E_p (blue line) and T_p (red line). (a) A certain hunter (named ‘Ken’). (b) Ken’s partners which changed per 1,000 periods (Color figure online)

The bars in Fig. 3a and b represent the patterns stored in *Situations* (Fig. 1) and those activated at each period. We have found the emergence and adaptive switching of partial networks for processing higher-order estimation of other’s intention in terms of intentional stance developed by Dennett [8] as shown in Fig. 4, which shows the networks for processing level 0, level 1 and level 2 ToM, respectively.

In the 1st round, the initial solutions of Ken and his partner that were randomly generated were (0, 0, 1, 0, 0, 0, 0, 1, 0, 0, 0, 1, 1) and (1, 0, 1, 0, 0, 0, 1, 1, 1, 1, 1, 1, 0), respectively (see Sect. 3.1). Note that $M_9 = 0$, in other words, there were no output (Fig. 1) in the Ken’s network while the activated pattern for level 0 ToM was

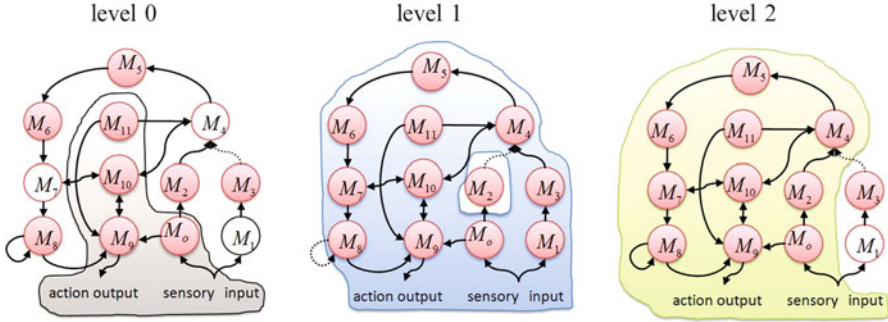


Fig. 4 The emerged partial-networks for processing level 0, level 1 and level 2 ToM. The red circles represent activated modules

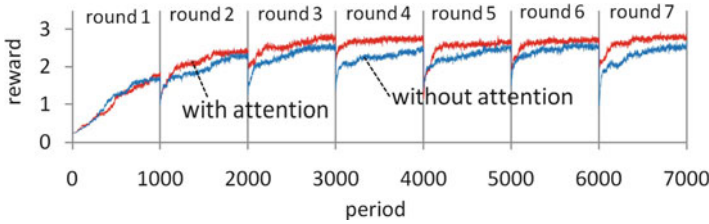


Fig. 5 The transition of the average *rewards* of *N* agents with and without the attention system, averaged over ten trials

already included in his partner’s network. The *reward* increased suddenly at around 400th period, when the solution of the Ken became (1, 1, 0, 1, 0, 0, 1, 1, 0, 1, 1, 1, 0), in other words, he acquired the network for level 0 ToM. In the second round, Ken and his new partner behaved using level 0 ToM at first. The *reward* increased at around 1050th period in parallel with the activation of Ken’s M_4 . It is because by then Ken had acquired the activated pattern for level 1 ToM.

Between third and fifth rounds the *reward* remained stable thanks to the adaptive interactions between the levels of ToM. However, it decreased in the early stage in the sixth round. At that time Ken and his new partner behaved competitively using level 0 ToM. After that, E_p of the partner became less than T_p , and the *reward* increased. This is because the partner shifted into switching mode and reused the adequate activated patterns for the current environment.

Next, we compared the performance with those without the attention system [6] to evaluate the introduction of the mechanism for switching among the kept *Solutions* in *Situations*. Figure 5 shows the transition of the average *rewards* of *N* agents with and without the attention system, averaged over ten trials. It is shown that the *rewards* with the system in the early stage of each round were clearly higher than those without it. This indicates that the appropriate partial-network could be swiftly acquired by using the attention system even when interacting a new partner.

5 Conclusions

We constructed a functional model of the brain based on a functional parts combination (FPC) model to investigate the emergence of the role division in social interactions. The simulation demonstrated a scenario for emergence of role division based on estimating the intention of others as the acquisition of the partial-networks formed by the cooperative interactions between the recursive levels of intentionality in ToM. It was also shown that even when interacting a new partner the appropriate partial-network could be swiftly acquired simply by reusing the acquired partial-networks. These results imply that efficient social behaviors were attained not only by the individual cognitive components but also the appropriate combinations of these modules, which has much in common with the neuroscientific facts about autism [11]. The next step would be to investigate the acquisition of not only the activation signals but also the connections between modules.

Acknowledgments This work was supported by the Grant-in-Aid for Scientific Research on Innovative Areas from the Ministry of Education, Culture, Sports, Science and Technology (No. 21120010), and by the Sasakawa Scientific Research Grant from The Japan Science Society.

References

1. Premack, D., Woodruff, G.: Does the chimpanzee have a theory of mind? *The Behavioral and Brain Sciences* 1 (1978) 515–523
2. Gallese, V., Goldman, A.: Mirror neurons and the simulation theory of mind-reading. *Trends in Cognitive Sciences* 2 (1998) 493–501
3. Omori, T., Ogawa, A.: Two hypothesis for realization of symbolic processing in brain. *Proc. of the 9th International Conference on Neural Information Processing* (2001)
4. Yokoyama, A., Omori, T.: Model based analysis of action decision process in collaborative task based on intention estimation (in japanese). *The Transactions of the Institute of Electronics, Information and Communication Engineers. A*, J92-A (11) (2009) 734–742
5. Nagata, Y., Ishikawa, S., Omori, T., Morikawa, K.: Computational model of cooperative behavior based on dynamical selection of intention based action decision strategy (in japanese). *Cognitive studies* 17(2) (2010) 280–286
6. Minoya, K., Arita, T., Omori, T.: An artificial life approach for investigating the emergence of a Theory of Mind based on a functional model of the brain. *Proc. of the 2011 IEEE Symposium on Artificial Life* (2011) 108–115
7. Trealeven, P. C., Hopkins, R. P., Rautenbach, P. W.: Combining data flow and control flow computing. *Computer Journal* 25(2) (1982) 207–217
8. Dennett, D.: *The Intentional Stance*. MIT Press, Cambridge (1987)
9. Takahashi, H., Ishikawa, S., Omori, T.: Modeling of dynamical cognitive control mechanism that supports social interaction. *Cognitive Studies* 15(1) (2008) 202–215
10. Glover, F., M. Laguna: *Tabu Search*. Kluwer, Norwell, MA (1997)
11. Happe, F., Ronald, A., Plomin, R.: Time to give up on a single explanation for autism. *Nature Neuroscience* 9 (2006) 1218–20

Estimating Similarity Judgment Processes Based on Neural Activities Measured by Near-Infrared Spectroscopy (NIRS)

Yoshihiko Suzuki and Shohei Hidaka

Abstract Similarity takes a crucial role in various kinds of cognitive processes. In the present study, we investigated the neural activities during similarity judgments on 1,225 pairs of images using the near-infrared spectroscopy. The predictability of similarity judgments were analyzed with a hierarchical Bayesian framework applied on the neural activities. It revealed that the neural activities located in a prefrontal region had a sharp increase prior to onsets of subjects' responses. Given the findings, we discussed about a key process, information integration of various domains, underlying similarity judgments.

1 Introduction

Semantic judgments such as association, similarity, and categorization are fundamental capability that appears in any contexts. In past works, it has been empirically studied in two approaches: One is subjective method in which it relies on common trends in multiple subjects' association, similarity or category judgments [1], and the other is relatively more objective method in which brain activities measured by advanced techniques, such as EEG, MEG, and fMRI, are analyzed in behalf of subjective judgments [2]. In order to bridge and integrate findings in the two empirical approaches, it is crucial to take advantage of theoretical models on semantic cognition. In particular, here we focus on similarity judgment. Similarity judgment has been generally accepted as a key piece of computation in theoretical approaches (e.g., mathematical models [3] and neural network models [1]) with massive empirical supports.

Y. Suzuki (✉) • S. Hidaka

Japan Advanced Institute of Science and Technology (JAIST), 1-1, Asahidai, Nomi-shi, Ishikawa 923-1291, Japan
e-mail: s1050028@jaist.ac.jp; shhidaka@jaist.ac.jp

The goal of the present study is to understand relationship among subjective rating, neural signals, and computational models on similarity judgments. Specifically, our question here is whether there exists neural basis which correlates with similarity *regardless* of various kinds of stimuli. In order to answer the question, we asked subjects to answer similarity of various pairs of images. Subjects had no specific criterion about “similarity” –they can evaluate similarity by visual features such as color, shape, and texture or they may also evaluate similarity of associated properties such as monkey from a picture of a banana. Here we report a first step of research showing that particular patterns in neural activity may reflect “similarity computation” invariant to various kinds of visual stimuli.

2 Methods

2.1 Subjects

Ten subjects (six males and four females) were recruited from graduate students in Japan Advanced Institute of Science and Technology in Japan. The mean age of subjects is 26.1 (S.D. = 4.33). All the subjects were right-handed and had good corrected or non-corrected visual acuity.

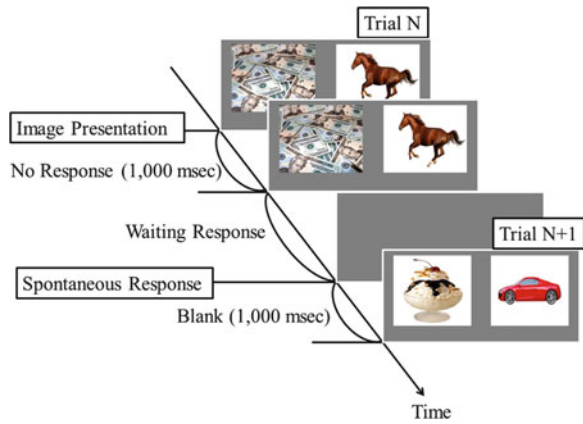
2.2 Experiment Procedure

The subjects were instructed to answer, by pressing one of five keys (“1”, “2”, “3”, “4”, and “5”) that are mapped on scales, “very similar” to “very dissimilar”, similarity of two images presented on the screen in one trial of the experiment. We have two sets of mapping between keys and similarity codes, “1” as “very similar” or “1” as “very dissimilar”, and each subject was assigned one of either randomly. The experiment consists of 1,225 trials. In each trial, subjects were presented a pair of two images drawn from the unique 1,225 combinations (pairs sampled from 50 categories without a pair of an identical category). The presentation order was randomized and counterbalanced across subjects.

The time course of each trial is shown in Fig. 1. Each trial starts with presentation of a pair of two images at left and right boxes with a beep sound, and took no response during the first 1 s. After the first second, subject could make a response by pressing a key in his/her own timing. During 1 s right after the subject’s response, the blank screen was presented, and it was followed by the next trial with another pair of images.

During the experiment, we measure the relative changes in oxy-hemoglobin concentrations of frontal lobe using a near-infrared spectroscopy (NIRS) (ETG-4000, the Hitachi Medical). The probes were attached with a cap on subject’s scalp

Fig. 1 The time course of each trial



which was located based on the International 10–20 system. The Probe 1 (3 by 5) covered the prefrontal area, and the Probe 2 (two separate 3 by 3 sets) covered the left and right lateral area next to the Probe 1.

2.3 Noun Categories

The 50 categories were selected from a normative list of 300 English nouns that typical 3-year-olds have learned [4]. Specifically, 50 nouns are as follows: *butterfly, cat, fish, frog, horse, tiger, arm, eye, hand, knee, tongue, boots, gloves, jeans, shirt, banana, egg, ice cream, milk, pizza, salt, toast, bed, chair, door, refrigerator, table, rain, snow, stone, tree, water, camera, cup, keys, money, paper, scissors, plant, balloon, book, doll, glue, airplane, train, car, bicycle, truck, and bird.*

2.4 Images

Five images for each of 50 nouns were collected [5]. All the pictures have a still and real object on the center (see also Fig. 1 for examples).

2.5 Sparse Regression Analysis

We employed a hierarchical Bayes model for analysis of neural signals obtained from NIRS measurements in similarity judgments. We assume that a prototypical pattern of neural signals over channels and time emerges when a subject judges similarity between a given pair of stimuli. The present hierarchical Bayes model is

inspired by the hierarchical linear regression model proposed by Nambu et al. [6]. Nambu et al. have proposed the *sparse linear regression* in which the regression coefficients with non-zero values are penalized by the sparseness prior distribution on them. In the sparse linear regression, only few parameters can be non-zeros due to the presumed sparseness of parameters, and this may solve the over-fitting problem which a typical NIRS experimental setting tends to have. In the present analysis, we employed the logistic regression with the sparseness prior distribution for the regression coefficients. The likelihood of binary responses (binomial distributions) and the sparseness prior distribution forms the posterior distribution of parameters which is sampled by the Monte Carlo Markov Chain.

3 Results

The average reaction time across the subjects is 1.70 s (S.D. 0.54). The similarity judgments on 1,225 pairs (50 categories) average over the subjects were visualized with hierarchical clustering (Fig. 2). The overall patterns were consistent to the previous experiment with a similar procedure [5]: several superordinate categories such as vehicles, animals, cloths, and household objects were clustered.

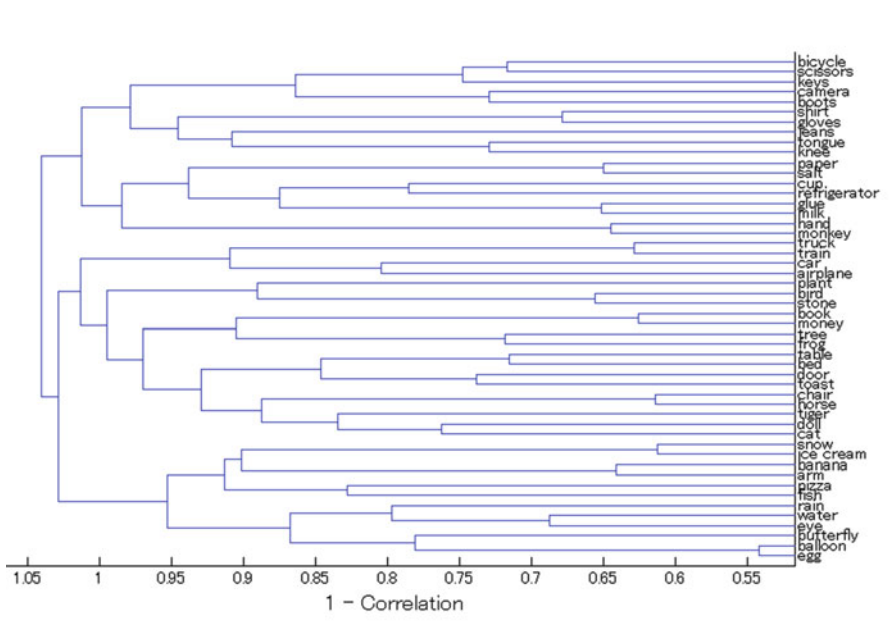


Fig. 2 Clustering tree of the similarity judgements

In the experiment, the timing of similarity judgment was up to subjects' decision. The present experimental design allows us to analyze the temporal structure of subject's similarity judgments. Therefore, we applied the sparse logistic regression model to the similarity judgment dataset in eight different conditions (2 by 4) which have the neural signals obtained in different time intervals. In *stimulus-trigger* condition, we analyzed the similarity judgments based on the neural signals from the stimulus onset (i.e., image presentation as the trigger) to 1, 2, 3, and 4 s. In *response-trigger* condition, we analyzed them based on the neural signals from 1, 2, 3, and 4 s prior to the response onset. In each condition, we evaluated four models with different set of regression coefficients (over the interval 0–1, 2, and 4 s) using Deviance Information Criterion (DIC; [7]). We found that, for the majority of subjects, the model on the 1-s interval after stimulus or before response was the best model (five (stimulus-trigger) and seven (response-trigger) out of ten subjects). In the best models for all the subjects, the odds ratios of the correct prediction of subjective similarity judgment from the neural signals¹ were better than the baseline model² in which no neural signals is available for prediction. ($p < 0.01$). The result confirmed that the sparse logistic regression captured the neural signals with significant predictive power for similarity judgments.

Next we analyzed the regression coefficients (averaged over subjects and the posterior distribution) in the best model in each of stimulus-trigger and response-trigger conditions. Figure 3 showed the topographic map of the absolute regression coefficients of the sparse logistic regression analysis based on the neural signals in (a) 1 s from stimulus onset and in (b) one interval to response onset. In both Fig. 3a and b, we found a sharp peak in prefrontal area. Moreover, the peak tends to become strong at the end of the intervals which is right before subject's responses.

4 Discussions

In the present study, we investigated the spatio-temporal neural activities in similarity judgments on presented paired images drawn from 50 basic categories. The Bayesian hierarchical model has revealed that subjects' similarity judgment can be significantly predicted with the neural activities in the prefrontal area prior to their decision making.

The peak was located in Inferior prefrontal region. This region is close to the ventromedial prefrontal cortex (VM), which is supposed to take a key role in decision making in a gambling task [8], although the NIRS is limited to capture the neural activities in only surface areas. In the previous study, it has been considered

¹The odds ratio is $P_{correct} / (1 - P_{correct}) \bar{P}_{correct} / (1 - \bar{P}_{correct})$, where $P_{correct}$ and $\bar{P}_{correct}$ are correct prediction of the best model and the baseline model.

²The base line model has two parameters, slope and intercept, for baseline-frequency of response.

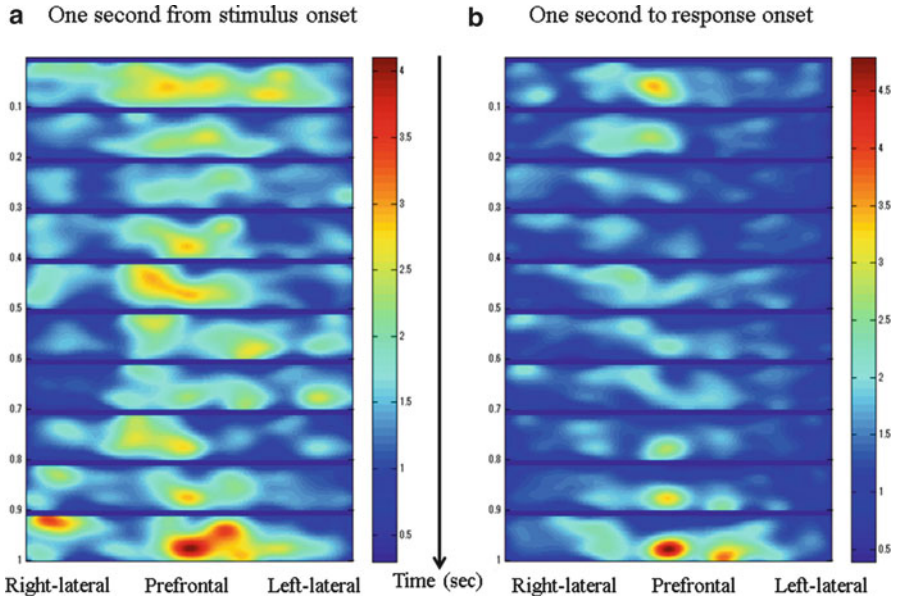


Fig. 3 The topographic map of the average absolute coefficients in (a) 1 s from stimulus onset and in (b) 1 s to response onset (10 Hz)

that the VM takes a crucial role in integration of a wide range of information. It leads us to hypothesize that integration of multiple types of attributes (i.e., visual, associative, and semantic attributes) may be crucial to the timing of decision making in similarity judgments.

Acknowledgments This work was supported by Grant-in-Aid for Research Activity Start-up No. 22800028.

References

1. Rogers, T. T., McClelland, J. L.: *Semantic Cognition: A Parallel Distributed Processing Approach*, MIT Press, Cambridge, MA (2005)
2. Kutas, M., Federmeier, K. D.: Language comprehension and the N400, *Trends in Cognitive Sciences*. 4(12) (2000) 463–470
3. Nosofsky, R. M.: Attention, similarity, and the Identification-Categorization Relationship, *Journal of experimental Psychology: General*. 115(1) (1986) 39–57
4. Fenson, L., Dale, P., Reznick, J. S., Bate, E., Hartung, J., Pethick, S., and Reilly, J.: *MacArthur Communicative Development Inventories*. CA: Singular Publishing, San Diego, (1993)
5. Hidaka, S.: Development of the Semantic Network: From a random to a complex network, In *proceedings of The Thirty Second Annual Meeting of Cognitive Science Society* (2010)

6. Nambu, I., Osu, R., Sato, M.A., Ando, S., Kawato, M., Naito, E.: Single-trial reconstruction of finger-pinch forces from human motor-cortical activation measured by near-infrared spectroscopy (NIRS). *Neuro Image*. 47(2) (2009) 628–63
7. Claeskens, G., Hjort, N.L.: *Model Selection and Model Averaging*. Cambridge. 3(5) (2008)
8. Bechara, A., Damasio, H., Damasio, A.R.: Emotion, Decision Making and the Orbitofrontal Cortex. *Cereb*. 10(3) (2000) 295–307

Autonomous Robot with Internal Topological Representation

Pitoyo Hartono and Thomas Trappenberg

Abstract In this study, we implement the Map Initialized Perceptron (MIP), which is a hierarchical model of neural network with a Self-organizing map in the internal layer, as a trainable controller for autonomous robot. Our objective is to empirically investigate the correlation between the fidelity of internal representation and the learning ability of the robot in the physical environment. We believe that a well organized internal representation will enable better artificial learning systems and knowledge representation, which than can be utilized for designing better learning mechanisms, morphologies and environments. We support this hypothesis in this paper with some empirical experiments.

Keywords Self-organizing map • Autonomous robot • Hierarchical neural network

1 Introduction

In recent years, many studies have been dedicated to the realizations of autonomous robots operating in physical environments. Because of the difficulty of hand-coding the controller of such kind of robots, machine learning methods are the natural choices to be used for controllers. While the utilization of the machine learning methods brings significant success and open interesting fields that bring together machine learning, neuroscience and robotic technologies, there is one unavoidable drawback. In the human-designed robots, the designers have good understanding

P. Hartono (✉)

Department of Mechanics and Information Technology, Chukyo University, Toyota, Japan
e-mail: hartono@sist.chukyo-u.ac.jp

T. Trappenberg

Faculty of Computer Science, Dalhousie University, Halifax, NS, Canada
e-mail: tt@cs.dal.ca

Y. Yamaguchi (ed.), *Advances in Cognitive Neurodynamics (III)*,

DOI 10.1007/978-94-007-4792-0_48,

© Springer Science+Business Media Dordrecht 2013

of the behavior of the robots, while in adaptive robotics, it is often prohibitively difficult to relate the internal characteristics and the physical functionality of the robots. This lack of “internal plausibility” often limits the utilization of adaptively trained robots to the critical areas, such as medical and welfare fields that should benefit most from these technologies. Furthermore, we believe that a well organized internal representations, as increasingly found in the brain, is essential for building advanced systems.

In this study we implement our previously proposed model of hierarchical neural network, namely the Map Initialized Perceptron (MIP) [1] as a controller for a robot. MIP is a variety of Multilayered Perceptron where the hidden or internal layer is a two dimensional Self-Organizing Map (SOM) [2]. The learning characteristic of MIP ensures the formation of relation between the internal topology of the model with the physical actions of the robots. In this extended abstract we presented some of our preliminary experimental results.

2 Map Initialized Perceptron

As shown in Fig. 1, in this study, we implement MIP as a trainable controller for a small mobile robot called e-puck [3], which is trained to acquire a strategy of obstacle avoidance while randomly walking in a physical environment as shown in Fig. 2. Initially, MIP is trained to form an internal map according to the conventional learning of SOM. The data for this initial learning are the sensory values acquired by e-puck while executing a hand-designed obstacle avoidance strategy. After the map

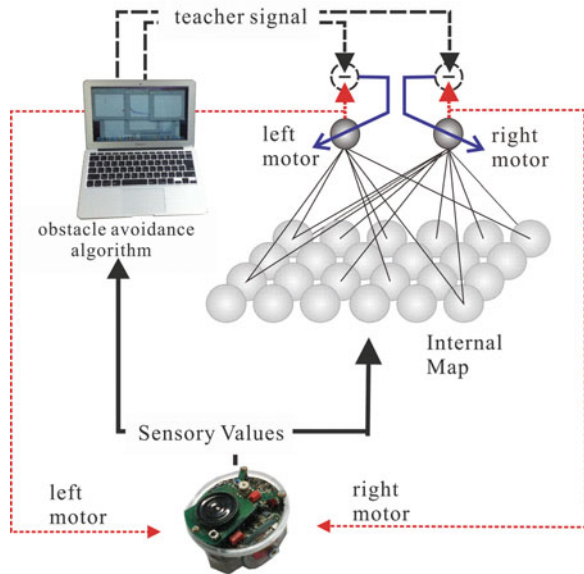


Fig. 1 Implementation of MIP

Fig. 2 Learning environment



formation phase, the robot is trained to acquire a strategy for obstacle avoidance. In this supervised training phase, the robot acquires a sensory vector from its eight proximity sensors at time t , $\mathbf{X}(t) \in R^8$. This input vector is then compared to all of the code vectors which are aligned as neurons in the two-dimensional internal map as in Eq. (1).

$$w(t) = \arg \min_i |\mathbf{X}(t) - \mathbf{W}_i| \quad (1)$$

Here, $\mathbf{W}_i \in R^8$ is the i -th code vector in the internal map, while $w(t)$ is the index of the code vector with the minimum distance to the input $\mathbf{X}(t)$.

The next step is to calculate the output of the neurons in the map as follows.

$$M_j(t) = \exp\left(-\left(\frac{|\mathbf{X}(t) - \mathbf{W}_j|}{|\mathbf{X}(t) - \mathbf{W}_{w(t)}| + \varepsilon} - 1\right)\right) \quad (2)$$

Here, $M_j(t)$ is the output of the j -th neuron in the internal map and ε is empirically set constant to avoid calculation overflow.

From Eq. (2) it is obvious that the winning neuron, $w(t)$, produces the largest output. Because of the topological characteristics of the internal map, it can be expected that other neurons in the vicinity of the winner also produce large output while neurons that are located far from the winner produce small outputs. This indicates that similar input vectors will produce similarly unique firing patterns in the map, while different input vectors will create different firing patterns. The outputs of the neurons in the internal map will then be propagated to the output layers containing two neurons to produce motor action for the robot as follows.

$$\begin{aligned} O_l(t) &= f(\mathbf{V}_l^t(t) \cdot \mathbf{M}(t) - \theta_l(t)) \\ O_r(t) &= f(\mathbf{V}_r^t(t) \cdot \mathbf{M}(t) - \theta_r(t)) \end{aligned} \quad (3)$$

Here, O_l and O_r are the speed of the left motor and the speed of the right motor, respectively. $V_l^i(t)$, V_r^i , θ_l , θ_r are the vector connecting the neurons in the internal map with the output neuron associated with the left motor, vector to the output associated with the right motor and the threshold values of the output neurons, respectively, while \mathbf{M} is the vector, which elements are the outputs of the neurons in the internal map.

In the supervised training phase, the connection weight vector $V = \begin{bmatrix} V_l \\ V_r \end{bmatrix}$ is modified as in the conventional Delta Rule as follows.

$$\mathbf{V}(t+1) = \mathbf{V}(t) - \eta \frac{\partial E(t)}{\partial \mathbf{V}(t)}$$

$$E(t) = \frac{1}{2} |\mathbf{O}(t) - \mathbf{T}(t)|^2 \quad (4)$$

Here, \mathbf{O} is a vector which components are the value of the output neurons associated with the left motor and the one associated with the right motor, while \mathbf{T} is the teacher signal produced by the hand coded obstacle avoidance strategy as depicted in Fig. 1.

As opposed to the conventional Delta Rule where the topological order of the neurons that are forwarding their outputs to the output layer does not have any influence, here the topological structure of the internal map plays an important role. In this learning mechanism, the weights that are intensely modified are the ones that are connecting the internal neurons which have large values and the output neurons. Since the internal neurons are topologically structured, and thus the internal layer produces a topologically clustered firing pattern, the weights modifications are also executed in a clustered manner. This will lead to generate a strong correlation between the localities in the internal map and the actions of the robot. This locality-action correlation will give us a better understanding on the relation between internal structure of the adaptive controller model and the functionality of the robot. This “internal plausibility” potentially leads to our ability to understand the encoding and formation of knowledge into artificial learning systems.

3 Experiments

In the experiment, we first collect sensory data by running the robot in a physical environment with several obstacles as shown in Fig. 2. Here, we collect 5,000 input vectors from the proximity sensors of the robot. The data are then utilized to form an internal map with various sizes.

Figure 3 shows the Self-Organizing process of internal maps with the sizes of 4×4 neurons, 25×25 neurons and 40×40 neurons over 50 training epochs, where the vertical axis shows the average distortion between the winning neurons and the

Fig. 3 Self-organization of internal map

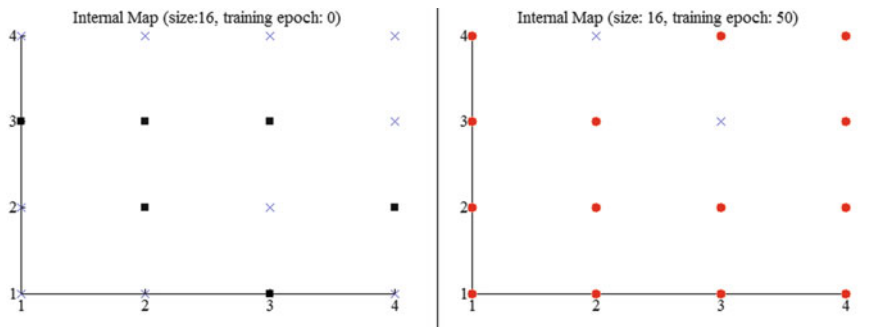
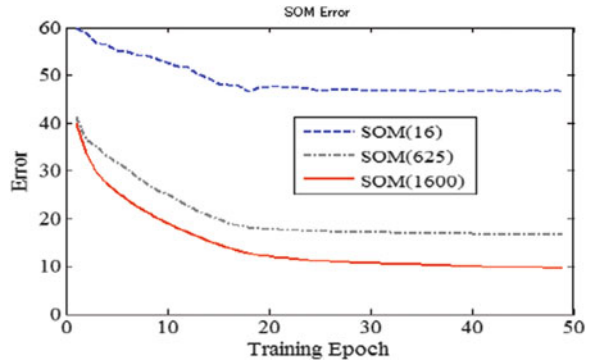


Fig. 4 Internal map (4 × 4 neurons)

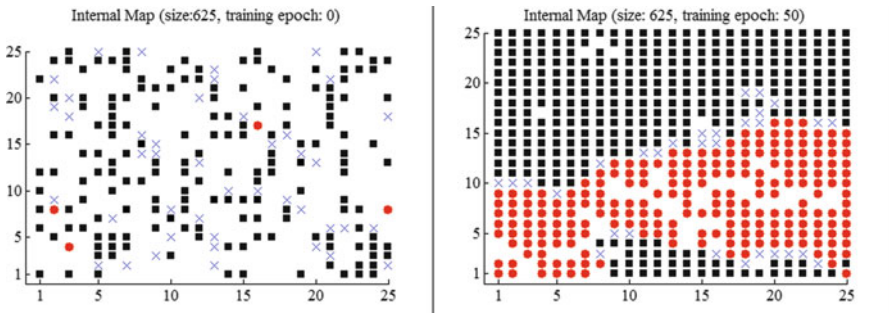


Fig. 5 Internal map (25 × 25 neurons)

input vectors. This figure shows that internal maps with various sizes are able to topologically organize the internal representations of sensory stimuli, but naturally the capacity of the maps influences the distortion level.

The topographical organization of internal maps with three different sizes are shown in Figs. 4, 5 and 6. In the respective figure, graph on the left shows the

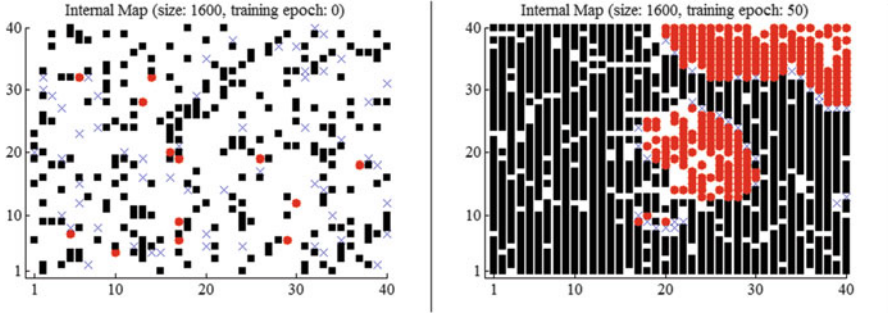


Fig. 6 Internal map (40 × 40 neurons)

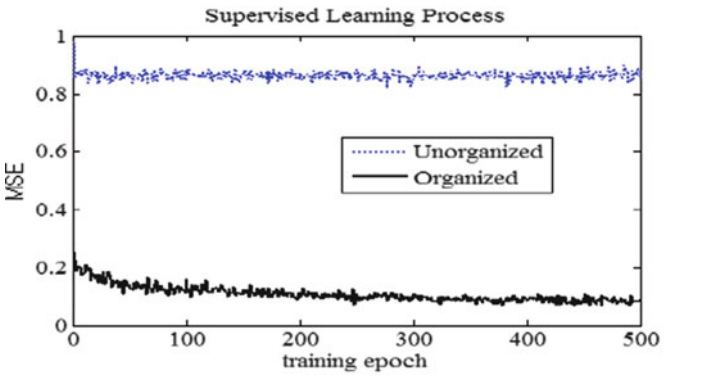


Fig. 7 Supervised training

activations of the neurons in the internal map responding to the sensory stimuli for an internal map that is not topologically, while the right graph shows the activations of the neurons in the internal map that was trained in 50 epochs. Neurons shown as ■ indicate neurons that are activated whenever the robot is located safely far from the obstacles. Neurons shown as ● indicate neurons that are activated whenever the robot is located dangerously close to the obstacles, while × indicate a neuron which is activated for both conditions.

It is obvious from these figures, that there is no topological order in the untrained map, while there are clear topological organizations in the trained internal maps. This topological organization can be considered as an internal representation of the physical world for the robot.

After the formation of internal map, we utilized this map as a hidden layer in training the robot to acquire a strategy for obstacle avoidance. The training process is shown in Fig. 7 which clearly indicates that MIP with an organized map learns significantly better than the one without topological order. Figure 8 shows the

Fig. 8 Activation of an unorganized map

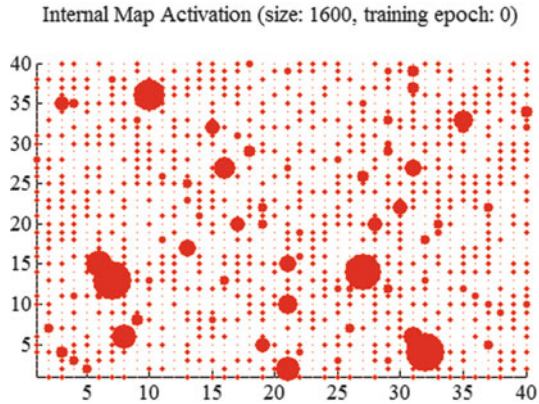
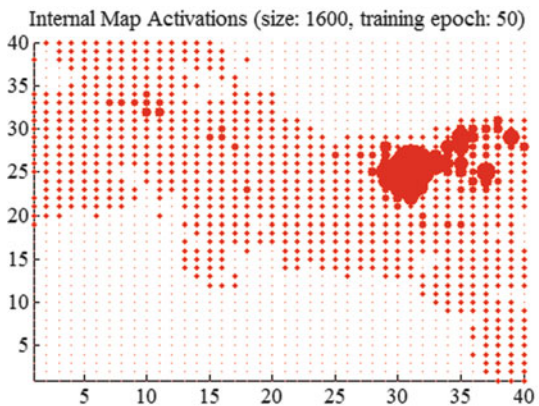


Fig. 9 Activation of a topographical map



activation of the neurons in the internal map with regards to 5,000 sensory stimuli after the termination of the supervised training process in MIP with a map with no topological order.

It is clear that no locality pattern can be observed from this map. Figure 9 shows the activation of the neurons in the internal map with respect to the same stimuli in MIP with a topologically organized map. It is clear that there are dominant neurons that form clustered activation patterns. Figures 7, 8 and 9 indicate that there is a strong correlation between the degree of internal organization with the learning ability of the controller. Figure 10 shows one example of the relation between the locality of the map with the motory action of the robot. This figure shows the activation pattern for the stimuli that caused the robot to execute “turn right” action in the robot, with the left graph showing the activations of an unorganized map, while the right graph shows the activations of the organized one.

A clustered pattern in the organized map shows a strong correlation between the locality of the map and the functionality of the robot. We believe that this

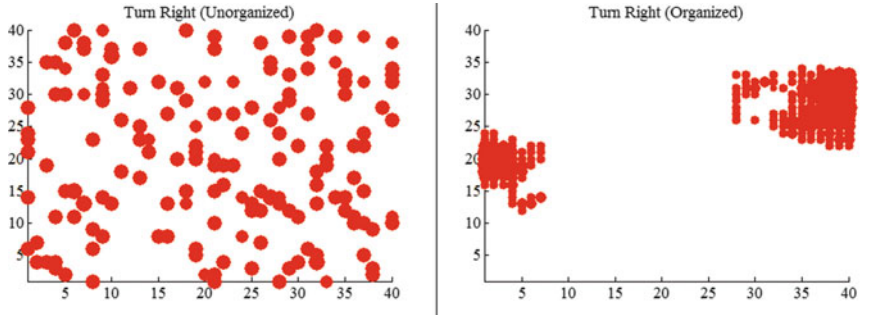


Fig. 10 Activation pattern for “Turn Right”

locality-functionality characteristic may help us to better understand the nature of the artificial learning systems that interact with physical environment. This understanding can potentially help us in designing better learning mechanisms, morphologies, sensory systems, and the learning environment for this kind of systems, especially robots.

4 Conclusions

In this study we implemented MIP as the controller for physical robot, e-puck. From the initial results we found that there is a strong correlation between the internal organization with the learning ability and the physical functionality of the robot. The visual accessibility of the internal representation helps us in analyzing and understanding the relation between the internal representations that are formed in the map with the physical functionality of the robot. In this preliminary study we only implement a top down control scheme where the internal representations control the physical outputs. However, we are also interested in understanding how the physical functionality and the partial defect in it influence the original internal representation. This understanding will be important in designing a good learning strategy and environment for artificial learning systems but also in understanding re-learning strategy in the face of internal and environmental changes, conditions that are often encountered by autonomous robots.

References

1. Hartono, P., Trappenberg, T.: Learning Initialized by Topologically Correct Map, Proc. IEEE SMC 2009 (2009) 2802–2806.
2. Kohonen, T.: Self-Organized Formation of Topologically Correct Feature Maps, Biological Cybernetics. 43 (1982) 59–69.
3. Mondada, F. et al.: The e-puck, A Robot Designed for Education in Engineering, Proceedings of the 9th Conference on Autonomous Robot Systems and Competitions, 1(1) (2009) 59–65.

SUDOKU Puzzle: The Neurodynamics of Intelligence to Choose the Right Solution from Many Possible Options in a Hypothetical Reasoning

Hiroaki Wagatsuma

Abstract This report is devoted to analyzing of mental arithmetic procedures in SUDOKU puzzles and exploring a possible hypothesis of how multiple brain regions are coordinated when solving the puzzle in a form of neurodynamics. We presented here an idea of integrative modeling related to the hippocampal-amygdala-prefrontal network and the prefrontal-parietal network, which is mediated by a coupling of theta and beta/gamma frequencies. This hypothesis may afford a clue to recursive calculation abilities that we have due to the brain.

1 Introduction

Human intelligence is severely difficult to measure by examining the physical organization of the brain structure, as is noted in the evolutionary psychology to differ the human mind from animals [1], and therefore theoretical researchers are taking notice of the idea that a phenomenological modeling of the neurodynamics, or information flow elucidates a link between the comprehensive ability exhibited in a form of intelligence and a coordination among multiple brain functions. Non-linear dynamics such as neural synchronizations [2] and chaotic dynamical systems [3] are candidates as modeling and those dynamics are examined to investigate how intelligent capabilities are emerged in the collective neural activities beyond the stimulus-response paradigm. Recently computer power increases as overwhelming us by the speed of arithmetic calculation, and some parallel processing methods

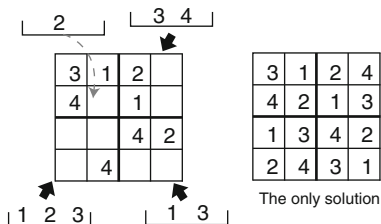
H. Wagatsuma (✉)

Department of Brain Science and Engineering, Graduate School of Life Science and Systems Engineering, Kyushu Institute of Technology, Kitakyushu 808-0196, Japan

RIKEN Brain Science Institute, Wako, Saitama, Japan

e-mail: waga@brain.kyutech.ac.jp

Fig. 1 A 4×4 grid Sudoku example and its only solution. Numbers in *baskets* represent options to be able to put empty cells according to Sudoku rules



are practically used for solving board games, such as chess and shogi, so that the performance comes close to matching a level of semiprofessional players. A question arises as to whether these computer algorithms of board games would be a key to understand how the brain works in solving a complicated and high degree-of-freedom problem so called ill-posed problem. Or, the brain process in solving games may completely different from the computer algorithm. Interestingly, a recent neuroimaging study [4] revealed a clear difference of activated brain regions of professional shogi players from amateurs when solving shogi mating problems, suggesting the existence of automatic processes of board-pattern perception and next-move generation in the experts for serving as a high-speed, yet accurate, decision-making process in board games. This fact indicates that information flows and its brain usage is not unique even in solving the same problem and the usage gives rise to differentiations of the performance how fast and accurate the subject solves the problem. Measuring the performance in board games, analyzing the brain process and specifying the routes if it is a cascade process are possible ways to investigate the human intelligence in viewpoints of how we can measure the intelligent level, improve it and treat it if there are some impairments of brain functions.

Sudoku puzzle is a popular puzzle to enter a number from 1 to 9 in each cell of a Sudoku grid, most frequently a 9×9 grid made up of 3×3 subgrids, as the standard type. It basically contains 81 cells, nine rows and nine columns. The game begins with numbers already printed in some cells. The player must fill in the empty cells with the numbers 1 to 9 in a way that no digit appears twice in the same row, column or subgrid. To be “Sudoku,” each puzzle must have one unique solution. In mathematicians, in fact, the Sudoku grid is known to be a special case of Latin squares, which are $n \times n$ matrices that are filled with n symbols in the way that the same symbol never appears twice in the same row or column. Why do people in the world arouse enthusiasm in solving the Sudoku? As Latin squares to be a kind of Sudoku, the most simplest case is a 4×4 grid with 2×2 subgrids, as shown in Fig. 1. This type has Sudoku properties so that subgrids, rows and columns must use the numbers 1 to 4 for each cell uniquely. However, in the 4×4 grid version, we can easily get deterministic steps without any hesitations. It is not attractive as games. On the other hand, a further complex version can be formed as a 16×16 grid with 4×4 subgrids, but it is too much complicated to be solved by ordinary human abilities. The typical 9×9 version may fit for our levels of intelligence and enhance motivations to solve the puzzle. Depending on

the pre-configured numbers in cells, the level of the complexity can be controlled even in the same 9×9 version. Some cases are deterministic, but others require speculative and hypothetical considerations.

This report is devoted to analyzing of mental arithmetic procedures in the puzzle and exploring a possible hypothesis of how multiple brain regions are coordinated when solving the puzzle in a form of neurodynamics, which may afford a clue to recursive calculation abilities that we have due to the brain.

2 A Possible Brain Process

In the first place, necessary arithmetic procedures should be overviewed. Figure 1 shows an example of the simplest version with 4×4 grid and the only solution. Solvers find a deterministic step, such as the empty cell in the top-left subgrid, in which the remaining number is the only one option. In this case, solvers can find a route, or cascade process, to solve the whole solution by following deterministic steps to put the only one option in each step (Fig. 2). Indeed, 4×4 Sudoku supplies mostly trivial cases with less motivation for solving the puzzle. In 9×9 Sudoku, there are not only simple cases but also complex cases having routes to solve (Fig. 3). The solution cannot be obtained deterministically and step-by-step, and the complex case must require a speculative or hypothetical selection of the number in a branching point. The temporal selection is verified in following steps by exhibiting a deadlock due to a contradiction with rules, not allowed any more steps.

Secondary, a minimum set of representations and operations of numbers, as information space and flow, should be considered. A well-known approach to solve the Sudoku is backtracking algorithms to seek a solution by tracing routes in the tree

Fig. 2 A procedure to solve the Sudoku puzzle. Steps 1–3 are deterministic by following Sudoku rules as unique in subgrids (rule 1), rows (rule 2) and columns (rule 3)

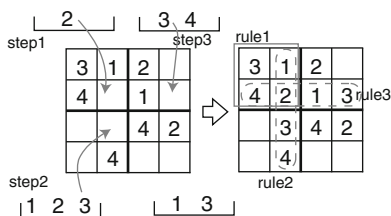


Fig. 3 A possible process for solving the puzzle. Solvers require at least tables for knowing the fixed configuration without any contradiction with rules and for thinking temporally about possible next steps

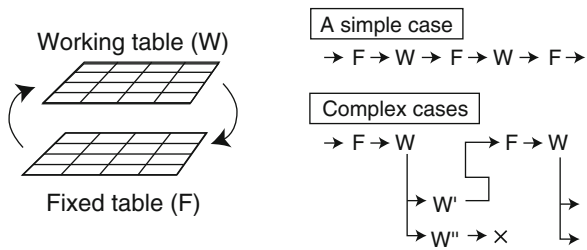
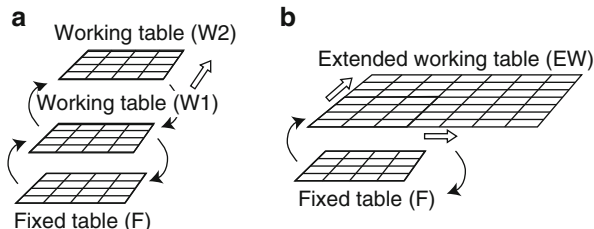


Fig. 4 (a) Recursive working table development (*RW*). (b) Extending working memory area (*EW*)



of the problem space until the dead-end and going back to the nearest branching point if it is not a solution. This is a simple recursive procedure, which is useful in trees with a low depth. Another procedure is to extend the working table. Many human solvers use empty cells for writing remaining options down, checking it out and eliminating an option if it is inconsistent with rules in the current configuration of numbers.

The two ways can be considered as recursive working table development (*RW*) and extending working memory area (*EW*) as schematically shown in Fig. 4. Theoretically, the *RW* certainly provides a solution in the problem space; however, the method cannot guarantee the completion under finite-time in combinatorial explosion. Making a consistent table, or map, like *EW* provides an overview of item relationships, which may enhance the checking speed to eliminate inconsistent options in empty cells. Meanwhile, questions of how the table can be manipulated and how the size is regulated to be as small as possible remain unsolved. For applying of the extended table to complex cases even with hypothetical steps, a flexibility and dynamics in management of representations and operations in the number plate is expected to emerge from the brain research especially focusing on dynamical process.

3 Hypothesis

We have proposed a robotic model for solving a cross maze task that is used for rat navigation studies and for investigating the hippocampal on-going neuronal activity in solving the maze [5]. The cognitive map of the whole environment in which the rat explores is represented by hippocampal collective activities known as place cells. The pattern of place cell activities is flexibly reorganized depending on the situational changes on visual cues, the environmental shape, and task requirements. In our previous model, we hypothesized that the decision-making process in a branching point of the maze arms requires three minimal brain regions, which are the hippocampus for spatial representation and storing episodic memory of past experiences, the prefrontal cortex for determining to go according to pre-learned rules applying to the current spatial situation (context) in the hippocampus, and the amygdala for judgments and evaluations that mediates hippocampal and prefrontal functions [5].

Fig. 5 A complex case facing a branching point in the problem space. There are three subgrids to have two (minimum) options. The solver has to proceed to the next step without certainty in the current stage by choosing either one of the two options hypothetically

1	7				6	8		
4	5			2				8
8	2				5	4	3	
9	3	6				2	5	7
4	5			9				2
6	2			5				1
		8	9				2	5
2	8			3	5			9
5	6				3	2	4	
3	9	4	2	5				6

In an extended model to the human intelligence to be able to solve the puzzle, consideration of issues concerning the working memory is necessary. The working memory refers to a brain system that provides temporary storage and manipulation of the information for complex cognitive tasks, and it requires the simultaneous storage and processing of information that can be divided into subcomponents: (i) the central executive, including an attentional-controlling system, is necessary for skills of chess, (ii) the visuospatial sketch pad, which manipulates visual images and (iii) the phonological loop in speaking, or transformation of perceptions and mental representations into a set of motions, which stores and rehearses action-based information [6]. In recent evidence [7], a contribution of the prefrontal-parietal network for mathematical reasoning within working memory is highlighted. In addition, a review of Savant Syndrome [8] suggests a deficit of the left frontotemporal area involving rule-based information, or logical reasoning, uncurbs the suppression of extending of the working table, providing procedural high-speed calculation.

A theoretical prediction is that (i) a coupling between the fixed and working tables (Fig. 3) is maintained in the prefrontal-parietal network, (ii) the parietal representation is simply extended to a large area if the frontal regulation is absent (Fig. 4), and (iii) a high-speed operation and well-learned skills are provided by this network, presumably involving the basal ganglia if it reaches an automatic level [4]. A brain process to dynamically generate hypothetical steps, or recursive procedures, for solving a complex case such as Fig. 5 is still unclear, but we note a significant contribution of the hippocampal map reorganization providing the contextual information to the prefrontal cortex [5], and propose a model that combines the prefrontal-parietal network with our previous hippocampal-amygdala-prefrontal network. An interesting evidence [9] for bridge between the two reported a cross-frequency coupling of theta and beta/gamma frequencies during a multi-item working memory task by using the human subjects, supporting neural representations using phase information in oscillation. The theoretical implementation of multi-frequency phase coding is further, yet urgent, work.

4 Discussions

We analyzed the arithmetic procedures in SUDOKU puzzles in the viewpoint of working memory usage, and explored possibilities of cooperative relationships among multiple brain regions, which may be related to the hippocampal-amygdala-prefrontal network and the prefrontal-parietal network. In EEG studies, arithmetic operations are used for increasing of subjects' concentration in cognitive tasks, and some report suggests a desynchronization of alpha amplitude coinciding with an increase in theta amplitude prior to a correct solution of Sudoku in healthy adults [10], as a possible relation to the right temporal cortical alpha and the frontal theta [11]. The relevance to brain activities in dreams subsequent to solving puzzles is of interest [12] to further investigations of the relationship between the cortico-hippocampal memory consolidation and the working memory usage.

Acknowledgments This work was supported in part by JSPS KAKENHI (22300081).

References

1. Arnold B. Scheibel, A.D., Schopf, J.W.: The origin and evolution of intelligence. Jones & Bartlett Pub (1997)
2. Yamaguchi, Y., Shimizu, H.: Pattern recognition with Figure-Ground Separation by generation of coherent oscillations. *Neural Networks* 7 (1) (1994) 49–63
3. Tsuda, I.: Toward an interpretation of dynamic neural activity in terms of chaotic dynamical systems. *Behav Brain Sci.* 24(5) (2001) 793–848
4. Wan, X., Nakatani, H., Ueno, K., Asamizuya, T., Cheng, K., Tanaka, K.: The neural basis of intuitive best next-move generation in board game experts. *Science* 331(6015) (2011) 341–346
5. Wagatsuma, H., Yamaguchi, Y.: Context-dependent adaptive behavior generated in the theta phase coding network. *LNCS.* 4985 (2008) 117–184
6. Baddeley, A.: Working memory. *Science* 255(5044) (1992) 556–559
7. Bor, D., Owen, A.M.: A common prefrontal-parietal network for mnemonic and mathematical recoding strategies within working memory. *Cereb Cortex* 17(4) (2007) 778–786
8. Hughes, J.R.: A review of Savant Syndrome and its possible relationship to epilepsy. *Epilepsy and Behavior* 17(2) (2010) 147–152
9. Axmacher, N., Henseler, M.M., Jensen, O., Weinreich, I., Elger, C.E., Fell, J.: Cross-frequency coupling supports multi-item working memory in the human hippocampus. *PNAS* 107(7) (2010) 3228–3233
10. Sobolewski, R., Reilly, R.B.: Monitoring of cognitive processes in older persons. *Proc 4th Int IEEE EMBS Conf on Neural Engineering (NER'09)* (2009) 132–135
11. Marzano, C., Ferrara, M., Mauro, F., Moroni, F., Gorgoni, M., Tempesta, D., Cipolli, C., De Gennaro, L.: Recalling and forgetting dreams: theta and alpha oscillations during sleep predict subsequent dream recall. *J Neurosci.* 31(18) (2011) 6674–83.
12. Stickgold, R., Malia, A., Maguire, D., Roddenberry, D., O'Connor, M.: Replaying the game: hypnagogic images in normals and amnesics. *Science* 290(5490) (2000) 350–353.

Part VII
Dynamic Brain Forum

Heterogeneity-Induced Pulse Generators

Yasumasa Nishiura, Takashi Teramoto, and Masaaki Yadome

Abstract Heterogeneity is one of the most important and ubiquitous types of external perturbations. We study a spontaneous pulse generating mechanism caused by the heterogeneity of jump type. Such a pulse generator (PG) has attracted much interest in relation to potential computational abilities of pulse waves in physiological signal processing. Exploring the global bifurcation structure of PGs as periodic solutions, we find firstly the conditions under which they emerge, i.e., the onset of PGs, secondly a candidate for the organizing center producing a variety of PGs.

1 Introduction

Pulse wave is the main carriers of information and the effect of heterogeneity in the media is of great importance for the understanding of signaling processes in biological and physiological systems. The role of heterogeneity in the media does not remain a perturbative effect, in fact it influences a lot over the concerned system and even produces a qualitatively new dynamics. It is known that heterogeneities produce various types of ordered patterns called heterogeneity-induced patterns [1, 2], which sometimes work as blockers for propagation waves. There is, however, another aspect of heterogeneity-induced dynamics, namely it creates a

Y. Nishiura (✉) • M. Yadome

Research Institute for Electronic Science, Hokkaido University, Kita12 Nishi7, Kita-ku,
Sapporo, 060-0812, Japan
e-mail: nishiura@nsc.es.hokudai.ac.jp

T. Teramoto

Research Institute for Electronic Science, Hokkaido University, Kita12 Nishi7, Kita-ku,
Sapporo, 060-0812, Japan

Chitose Institute of Science and Technology, Chitose, Hokkaido, 066-8655, Japan

spontaneous generator of pulses without any triggers and external forces. We present a representative example of such a pulse generator (PG) and try to clarify the underlying mathematical mechanism from dynamical system view point. Our model takes the following 1D three-component reaction diffusion (RD) system:

$$\begin{cases} u_t = d_u u_{xx} + f(u) - k_3 v - k_4 w + k_1, \\ \tau v_t = d_v v_{xx} + u - v, \\ \theta w_t = d_w w_{xx} + u - w, \end{cases} \quad (1)$$

where $d_u, d_v, d_w > 0$ are diffusion coefficients. We specify the nonlinearity as $f(u) = k_2 u - u^3$, which allows us to regard (1) as a generalized version of the FitzHugh-Nagumo equations by adding the second inhibitor w . Here we employ the following parameters: $k_1 = -5.7, k_2 = 2.0, k_3 = 1.0, k_4 = 8.5, (d_u, d_v, d_w) = (0.9 \times 10^{-4}, 1.0 \times 10^{-3}, 0.6 \times 10^{-2}), \tau = 52, \theta = 1$. The model (1) is a typical example of one-activator-two-inhibitor system, which was first proposed as a qualitative model of gas discharge phenomena [3]. The heterogeneity is introduced to the controllable parameter k_1 that corresponds to the applied voltage or external stimulus in neural tissues.

We consider the situation of $\tau \gg \theta$, that is, the response of v component is much slower than that of w . In particular, the third equation can be easily solved with respect to w for $\theta = 0$, by using the inverse Fourier transform of $\mathcal{F}^{-1}[1/(1 + d_w k^2)] = \exp[-|x|/\sqrt{d_w}]/2$. Substituting that into the first equation of (1), we have

$$\begin{cases} u_t = d_u u_{xx} + f(u) - k_3 v \\ \quad - \frac{k_4}{2\pi} \int_{-\infty}^{\infty} e^{-\frac{|x-y|}{\sqrt{d_w}}} u(y) dy + k_1, \\ \tau v_t = d_v v_{xx} + u - v. \end{cases} \quad (2)$$

This type of integro-differential equations like (2) have been used as continuum field models of neural activity in a population of interacting neurons [4]. The wave behaviors observed in the neural field models were studied in connection with the physiological functions in brain.

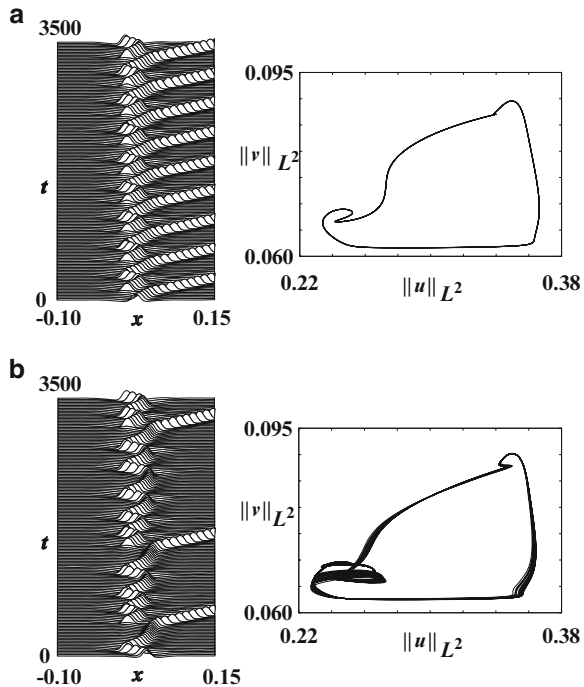
A precise form for the spatial heterogeneity of jump type for k_1 is given by

$$k_1 = k_{1L} + \epsilon \chi(x), \quad \chi(x) = \frac{1}{1 + e^{-\gamma x}}.$$

The height of jump ϵ is taken as the bifurcation parameter. The parameter γ controls the steepness of the slope around the jump point, but we fix it to be 100. Due to the jump from k_{1L} to $k_{1L} + \epsilon$, we lose the translation invariance and constant homogeneous state.

Figure 1 shows how the jump heterogeneity can produce traveling pulses spontaneously without any triggers or external forces. Note that our PG is quite different from the pulse emission phenomena reported in [5, 6] in the sense that our PGs are robust, exist on intervals, and have variety of generating manners. On

Fig. 1 Heterogeneity-induced pulse generators for (a) $\epsilon = 0.29$ and (b) 0.3022 . The *left* figures show the spatio-temporal patterns of u -component and their behaviors projected to an appropriate two dimensional space are shown in the *right*



the other hand the pulse-emission discussed in [7] is close to ours, however its underlying structures for the onset and generating mechanism remains completely open. Here we report on how such a PG emerges depending on the height and try to understand the generating mechanism from bifurcational view point.

2 Methods

The pulse generators (PGs) shown in Fig. 1 can be regarded as time-periodic heteroclinic orbits of (1) connecting the left homogeneous state to the wave train far right, in fact the emitted pulses eventually could form a wave train far from the jump point. There are, however, no systematic numerical methods to detect and trace those generalized heteroclinic orbits to our best knowledge.

We first develop a new numerical framework to detect those PGs as periodic solutions, then trace them globally with respect to the height parameter. Global behaviors of those branches allow us to find a candidate of organizing center which produces a variety of PGs as discussed in the next section.

A key idea here is to compactify the problem on infinite domain to the one on a finite interval by adopting the following pulse-sink boundary condition at the right boundary. That is, when the emitted pulse reaches an appropriate point distanced

from the jump heterogeneity, then it is eliminated, i.e., that is replaced by a uniform rest state with the timing of the pulse generating interval T . It is numerically checked that the such an elimination does not influence the pulse behaviors near the jump point as far as the location of right boundary is far enough.

We rewrite (1) into the following generalized form of RD systems and change the scale as $s = t/T$ by using the generation interval T which is unknown.

$$U_s = T(DU_{xx} + F(U; k_1(x, \epsilon))), \quad (3)$$

where $U(s, x) \in \mathbf{R}^N$, $D = \text{diag}(d_1, \dots, d_N)$ and $F : \mathbf{R}^N \times \mathbf{R} \rightarrow \mathbf{R}^N$. The T -periodic solution satisfies the periodic boundary condition $U(0, x) = U(1, x)$ for any x . Let $\Psi_T^\epsilon(s, x, U(0, x))$ be the solution of (3) at time s with initial state $U(0, x)$, then what we have to solve is the following.

$$\Phi_T^\epsilon(1, x, U(0, x)) - U(0, x) = 0. \quad (4)$$

The system (4) is solved by using the Newton method, in which the Jacobian matrix can be obtained using the shooting method, i.e, we integrate numerically (3) with respect to time imposing the pulse-sink boundary condition described above.

3 Results

Pulse generators (PGs) as shown in Fig. 1 display a variety of spatio-temporal patterns depending on the jump height ϵ ranging from time-periodic to even chaotic emission of pulses. For the onset of PGs, it is closely related to the “disappearance regime” of stable heterogeneity-induced ordered patterns, namely PGs start to emerge in the region where all the stable patterns induced by the heterogeneity, including standing pulses (SPs) and breather (SB), disappear. In fact such a regime exists in between $\epsilon = 0.2960$ and $\epsilon = 0.3025$. The SPs lose their stabilities via Hopf bifurcations and the period-doubling (PD) bifurcation occurs on the SB branch as shown in Fig. 2 denoted by H1, H2, and PD. It is remarked here that we found a new type of unstable standing pulse named by SP2, which turns out to be the destination of PGs as its period goes to infinity.

By using the numerical method described in the previous section, we have succeeded to detect the PG in between H1 and PD in Fig. 2. We trace the PG branch as a periodic solution and find that it persists robustly as in Fig. 3 for the wide range of ϵ values. As ϵ is increased or decreased, the PG branch turns back via saddle-node (SN) bifurcations. It is numerically suggested that both arms of unstable branches are eventually terminated at the homoclinic orbits of SP2 as the period $T \rightarrow \infty$. In fact each periodic orbit spends most of time around SP2 and approaches into the homoclinic orbit as indicated in the insets of Fig. 3.

Moreover, an intensive numerical global bifurcation analysis shows that the PG behaviors emerge almost exactly at the point where the stable SP and SB cease to exist. Two typical types of time-periodic PG patterns are depicted in Fig. 4.

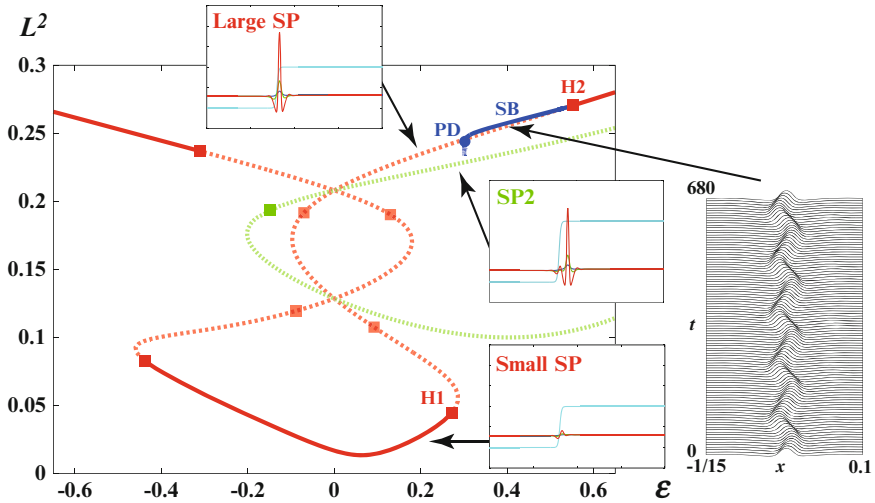


Fig. 2 Global bifurcation diagram for SPs and SB. The vertical axis indicates the L^2 -norm. The solid and dashed line indicate the stable and unstable branch, respectively. The squares and circle show the Hopf and period doubling bifurcation points, respectively

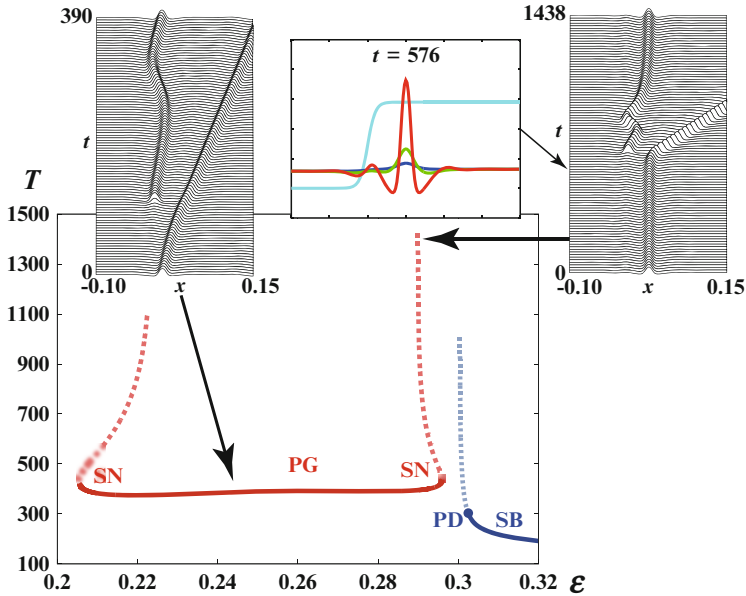


Fig. 3 Global bifurcation diagram for PG and SB. The vertical axis indicates the time interval T of a periodic motion. The insets show the spatio-temporal patterns of the one-cycle for pulse generation with $T = 390$ and $1,438$, respectively

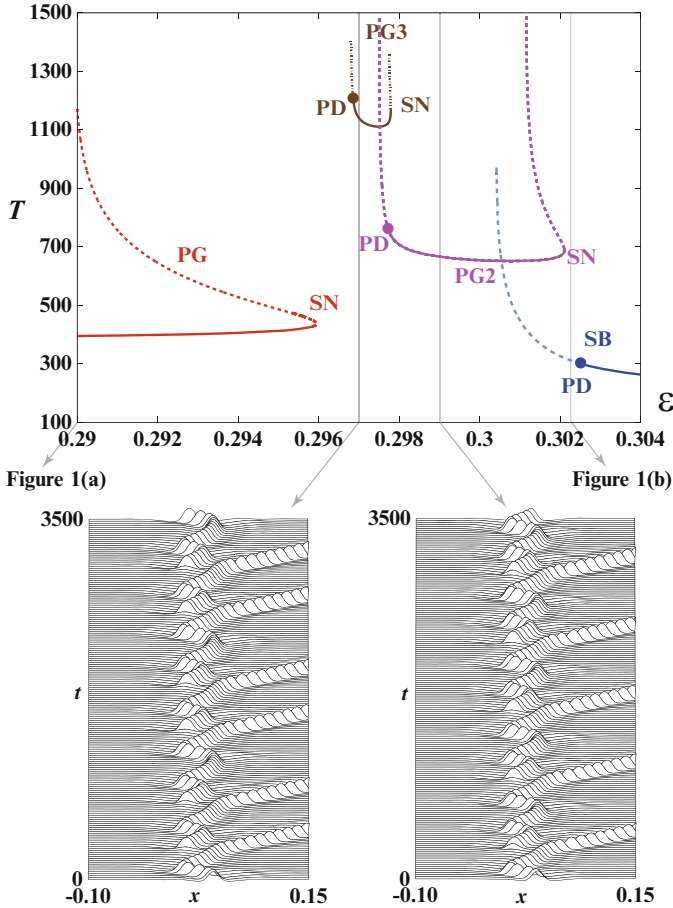


Fig. 4 Global bifurcation diagram for PG2 and PG3. The lower figures show their spatio-temporal patterns for $\epsilon = 0.297$ and 0.299 , respectively

For PG2 (resp. PG3) a generated pulse oscillates one time (resp. two times) near the jump point, then travels to the right direction. Both PG2 and PG3 lose their stabilities via PD bifurcations as ϵ is decreased, while the SN bifurcations occur when ϵ is increased. It is worth noting that all four unstable branches of PG2 and PG3 terminate at homoclinic bifurcations of SP2. This implies that the onset of various types of PGs could be characterized via unfoldings of multi-homoclinic structure of SP2.

4 Discussion

We present 1D heterogeneity-induced pulse generators arising in the three-component RD system. The simplest jump heterogeneity is employed here and the resulting PGs are robust against the change of the height. The traveling pulses are produced spontaneously around the jump point and they are emitted in one direction. The pulse-sink boundary condition allows us to reduce the PGs to periodic solutions so that we can trace their global behaviors as the height of the jump varies. Exploring the parameter space, we find various types of PGs, i.e., pulse-emitting manner has a variety as in Figs. 1 and 4. Nevertheless there seems to exist a hidden organizing center producing those PGs inspired by the common features shared among the global behaviors of PG branches. For instance the PG branches terminate at the same unstable stationary pattern SP2 shown in Figs. 2 and 3 when PG's periods tend to infinity. Also their manner of destabilization is quite similar as depicted in Fig. 4. These observations indicate that there exists a hierarchical structure of bifurcating branches of PGs originated in a multi-homoclinic-loop structure at SP2. For this purpose we are currently investigating the orientabilities for homoclinic center manifolds and searching for singularities of higher codimension in the extended parameter space.

Acknowledgements This work was partially supported by the Grant-in-Aid for Scientific Research under Grant No. 21120003 and B21340019.

References

1. Yuan, X., Teramoto, T., and Nishiura, Y.: Heterogeneity-induced defect bifurcation and pulse dynamics for a three-component reaction-diffusion system. *Phys. Rev. E*. **75** (2007) 036220
2. Teramoto, T., Yuan, X., Bär, M., and Nishiura, Y.: Onset of unidirectional pulse propagation in an excitable medium with asymmetric heterogeneity. *Phys. Rev. E*. **79** (2009) 046205
3. Schenk, C. P., Or-Guil, M., Bode, M., and Purwins, H. -G.: Interacting Pulses in Three-Component Reaction-Diffusion Systems on Two-Dimensional Domains. *Phys. Rev. Lett.* **78** (1997) 3781–3784
4. Amari, S.: Dynamics of Pattern Formation in Lateral-Inhibition Type Neural Fields. *Biol. Cybernetics*. **27** (1997) 77–87
5. Ermentrout, G. B., and Rinzel, J.: Reflected waves in an inhomogeneous excitable medium. *SIAM J. Appl. Math.* **56** (1996) 1107–1128
6. Cytrynbaum, E. N., and Lewis, T. J.: A Global bifurcation and the appearance of a one-dimensional spiral wave in Excitable media. *SIAM J. Appl. Dyn. Syst.* **8** (2009) 348–370
7. Prat, A., Li, Y. -X., and Bressloff, P.: Inhomogeneity-induced bifurcation of stationary and oscillatory pulses. *Physica D*. **202** (2005) 177–199

Balancing Robustness with Plasticity Through Evolution and Learning

Kunihiko Kaneko

Abstract Biological systems are robust to external perturbations, in order to function under noisy environment, while they should also be plastic to adapt to novel environment. Considering slower (evolutionary) changes in faster developmental dynamics, we show that optimal noise level is necessary for the compatibility between the robustness and plasticity. We will also discuss relevance of the results to learning process where robust and plastic neural dynamics are shaped under an appropriate noise level.

1 Introduction

Biological systems in general have to adapt to a variety of environmental conditions, whereas they have to be robust against disturbances applied into the system. For the former, the system has to sensitively respond to changes in the external conditions. This is plasticity. For the latter, the system should be insensitive against variation imposed into the system. This is robustness. Now, how can a biological system strike a balance between these two seemingly conflicting properties [1–4]?

Previously we studied the evolution of robustness, by postulating that a dynamical system should generate a functional phenotype, and examining if the system is insensitive to perturbations introduced by noise, environmental and genetic changes [5]. Through simulations of a simple stochastic gene expression network that undergoes mutation and selection, we showed that in order for a system to acquire robustness, it maintains a global attraction to an attractor. We then demonstrated that such system has structural stability also, that is robustness against

K. Kaneko (✉)

Department of Basic Science and Research Center for Complex Systems Biology,
University of Tokyo, Komaba 3-8-1, Meguro-ku, Tokyo, Japan
e-mail: kaneko@complex.c.u-tokyo.ac.jp

genetic change to modify the equations of dynamical systems. The results reveal how noise encountered during developmental process shapes system' robustness to stochasticity in gene expression, which in turn shapes robustness to mutation. Furthermore we found there is a transition such that the system loses robustness as the noise amplitude is decreased below a certain critical value. On the other hand, for a system that achieved robustness through evolution, the variance of phenotypic fluctuations due to noise and that due to genetic changes decrease through evolution, keeping the proportionality between the two [6, 7]. Hence, robustness of the phenotype increases, and the plasticity decreases through evolution. Still, in nature, neither phenotypic fluctuations nor potentiality in evolution is vanished. How are phenotypic fluctuations or plasticity are sustained in nature?

One possible cause for preservation of plasticity or fluctuation is the environmental fluctuation. Plasticity of a biological system will be relevant to cope with the environmental change that alters the condition for the fitness. Here, as a simple illustration of environmental change, we carry out some numerical experiments to switch the fitness condition, and examine how the phenotypic fluctuations are changed accordingly. For this numerical evolution, we selected a dynamical system so that it can adapt to a fitness conditions that vary over generations. We will show that a system near the critical noise level in which the robustness is lost, both the plasticity and robustness are compatible. When the external condition is changed, the system can first adapt rapidly by phenotypic changes, and later by genetic changes. We then discuss briefly that a certain noise level is also relevant to neural dynamics to achieve robust learning process.

2 Model

As a specific example, we have adopted a simple model for gene expression dynamics with a sigmoid input–output behavior [5–7], although several simulations in the form of biological networks will give essentially the same result. In this model, the dynamics of a given gene expression level, x_i , is described by the following:

$$dx_i/dt = \gamma \{ \tanh[\beta \sum_{j>k}^M J_{ij} x_j] - x_i \} + \sigma \eta_i(t), \quad (1)$$

where $J_{ij} = -1, 1, 0$, and $\eta_i(t)$ is a Gaussian white noise given by $\langle \eta_i(t) \eta_j(t') \rangle = \delta_{i,j} \delta(t - t')$. M is the total number of genes, and k is the number of target genes that determine fitness.

The amplitude of noise strength is given by σ that determines stochasticity in gene expression. The initial condition is given by $(-1, -1, \dots, -1)$; i.e., all genes are “off” – none of them are expressed. The fitness F is determined by whether the expressions of “target” genes are matched with a prescribed pattern after a sufficient

time. First, this fitness condition is given such that all the target genes should be “on” (expressed), i.e., $x_i > 0$ for $i = 1, 2, \dots, k < M$, represented by ++. . . ++. Because the model includes a noise component, the fitness can fluctuate at each run, which leads to a distribution in the fitness F and x_i , even among individuals sharing the same gene regulation network. For each network, we compute the average fitness \bar{F} over L runs, and also the variance of the fitness over runs. This variance V_{ip} represents the fluctuation of the fitness over isogenic individuals (isogenic phenotype variance).

Now, at each generation, there are N individuals with slightly different J_{ij} . Since there are N individuals having different gene regulation networks, the fitness \bar{F} differs by each. Among the networks, we select those with higher fitness values. From the selected networks, J_{ij} is “mutated,” i.e., J_{ij} for a certain pair i, j selected randomly with a certain fraction is changed among $\pm 1, 0$. Each of the $N_s (< N)$ networks with higher \bar{F} values are selected which produce N/N_s mutants. We repeat this selection-mutation process over generations. We chose $N = L = 200$, and $N_s = N/4$, while the conclusion to be shown below does not change as long as these values are sufficiently large. We use $\beta = 7$, $\gamma = .1$, $M = 64$ and $k = 8$, and initially chose J_{ij} randomly with equal probability for $\pm 1, 0$.

Now we have two types of variances. Besides V_{ip} , V_g is defined as the variance of \bar{F} over the N individuals having different genes (gene regulation networks). This gives the variance due to genetic change. As V_g is decreased, the fitness becomes insensitive to the genetic change, i.e. robustness to mutation is increased. On the other hand, as V_{ip} is decreased, robustness to noise is increased, since V_{ip} measures the variance due to noise in developmental process.

Previously, we showed that when the noise is beyond a certain threshold value $\sigma_c \sim 0.01$, both V_{ip} and V_g through evolution, as each individual achieves the highest fitness value to match the target pattern. Hence, the evolution of robustness to noise and mutation is achieved when the noise amplitude is larger than σ_c . When the noise level σ is less than σ_c , these two variances remain rather high. Even though some individuals achieve the highest fitness value. Some other mutants remain to take much lower fitness values. Robustness to mutation (and to noise) did not evolve in this case.

3 Evolution of Plasticity and Robustness

To discuss the environmental change, we altered the fitness condition at some generation in the following way: After evolving gene expression dynamics with the fitness to prefer $x_i > 0$ for the target genes $i = 1, 2, \dots, k (= 8)$ as adopted already, then at a certain generation we changed the fitness condition so that the genes $i = 1, 2, \dots, k/2$ are on and the rest are off (i.e., the fittest gene expression pattern is ++++—, instead of ++++++++). Here we switched the fitness after a sufficiently large number of generations when the fittest networks were evolved

already (i.e., with $x_i > 0$ for target genes). By this switch, the fitness was then decreased, but after a few dozens of generations, the networks evolved to adapt to the new fitness condition. Again for $\sigma > \sigma_c$, almost all the population took the highest fitness, implying the increase in robustness to mutation.

To see the evolution of phenotypic plasticity, we have computed the variances of the fitness, V_{ip} and V_g . After the switch of the fitness condition, both of them first start to increase. During this increase, the proportionality between the two was roughly preserved [6]. The locus of (V_{ip}, V_g) over generations through the evolution followed reversely the course experienced through the decrease in V_{ip} and V_g . At later generations, both of them decreased again following the proportionality. The proportionality law between genetic and epigenetic variances was satisfied both in the evolution to increase and decrease the plasticity.

Right after the switch in the fitness, gene expression levels were no longer rigidly fixed, and can vary sensitively to the noise and mutation. With this sensitivity, the gene expression dynamics regained plasticity, which allows for the switch of the target genes after further generations in evolution. Then networks with higher fitness were selected, so that the adaptation to new condition was achieved. Later, the decrease in fluctuations progressed, to increase the robustness to noise and mutation.

When environmental changes were continuously repeated, the decrease and increase processes of the variances V_{ip} and V_g were repeated. Note that it takes more generations to adapt to a new fitness condition, if the phenotypic variances is smaller. In our model, if the noise level in development is larger, the phenotypic variances already became small during the adaptation to one fitness condition.. Hence in this case, it takes more generations to adapt to a new fitness condition. On the other hand, if the noise level σ is smaller than σ_c , robust evolution does not progress. Hence for continuous environmental change, there will be an optimal noise level both to adapt sufficiently fast to a new environment and to evolve robustness of fitness for each environmental condition. In Fig. 1, we have plotted the time course of the average fitness in population when the fitness condition is switched per 20 generation. If the noise level is large, the system cannot follow the frequent environmental change and the fitness did not increase. If the noise level is small, the fitness increased, but if it is smaller than σ_c , fitness of some individuals remained low. Indeed, if the noise level is near σ_c , the average fitness increased for each condition. In Fig. 2, the average fitness over generations is plotted against the noise level σ . It shows a maximum at around $\sigma \sim \sigma_c$.

Then we have plotted the variances V_{ip} and V_g over generations (see Fig. 3). When $\sigma < \sigma_c$, $V_g > V_{ip}$ and both the variances remain rather large, demonstrating that robustness did not evolved at all. For $\sigma > \sigma_c$, $V_g < V_{ip}$ and the variances remain small. The robustness has evolved, but the system cannot adapt to an environmental change as the variances became too small. In contrast, for $\sigma \sim \sigma_c$, V_{ip} and V_g vary between low and high values over generations, keeping proportionality between the two variances with V_g slightly less than V_{ip} .

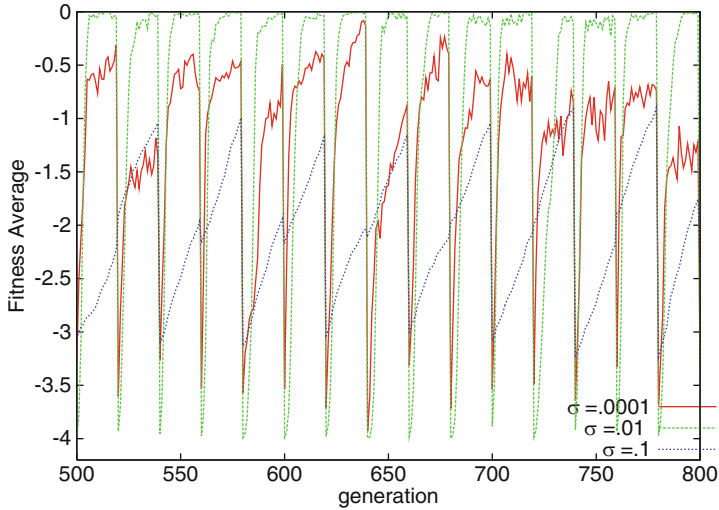


Fig. 1 The average of fitness plotted per generation, where the fitness condition is switched per 20 generations between ++++++ and ++++—. The average of the mean fitness \bar{F} of each individual (over $L = 200$ runs) is computed over the total population ($N = 200$) at each generation. The noise level σ is 0.0001 (red), 0.01 ($\sim \sigma_c$; green) and 0.1 (blue)

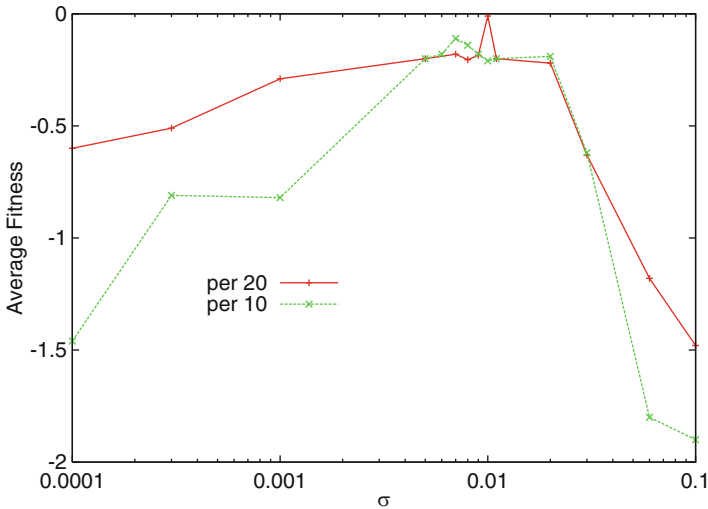


Fig. 2 The temporal mean of the average fitness. After computing the average fitness over total populations as in Fig. 1 at each generation, its temporal mean over 200–700 generations is computed, which is plotted against the noise level σ . Here, the fitness condition is switched per 10 (green) and 20 (red) generations, between ++++++ and ++++—. This mean fitness takes a maximum around $\sigma_c \sim 0.01$

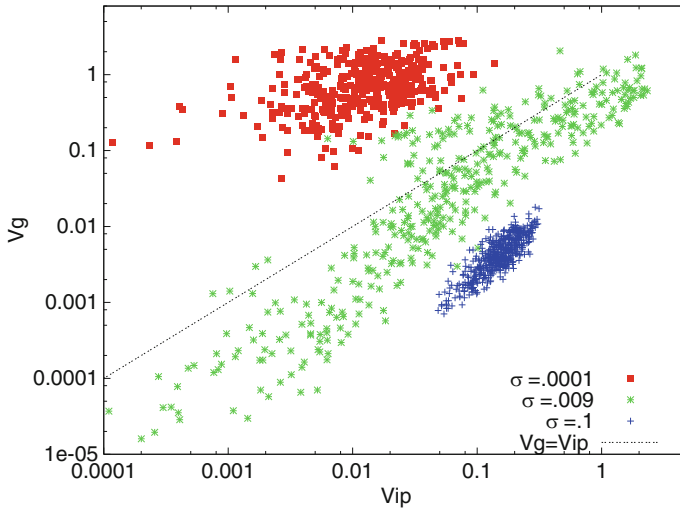


Fig. 3 Variances of the fitness, (V_{ip} , V_g). The *X-axis* denote V_{ip} , i.e., the variance due to noise, and *Y-axis* denote V_g , the variance due to mutation. Each point is a result of one generation, and the plot is taken over 500–800 generations with changing the fitness condition as mentioned in the caption of Fig. 1. The noise level σ is .0001 (*red*), 0.009 (slightly below σ_c ; *green*) and 0.1 (*blue*)

4 Learning with Plasticity and Robustness

When the plasticity and robustness are compatible, the system we studied here has two distinct time scales; fast adaptation to new environment by using the plasticity, and slower fixation of genetic changes to stabilize the adopted phenotypes. This embedding of fast dynamic changes into slower genetic changes is regarded as genetic assimilation proposed by Waddington [1].

The embedding of changes of variables with faster time scales onto network structure with a slower time scale is not restricted to the evolution of phenotypes, but is also relevant to learning process in the brain [8]. Here faster changes in neuronal activity are later embedded into neural network structure through slower changes in synaptic connections. By using dynamical systems of neural activity akin to Eq. (1), and assuming that its time scale (rate constant) depends on the “fitness”, i.e., the degree of matching between output neural activity and the target activity postulated by a learning task, and introducing Hebbian and anti-Hebbian changes in the synaptic connection J_{ij} , we studied if learning of input/output relationship is possible under noise in neural activity dynamics. We found that an appropriate noise level is required to achieve robust learning. Noise-induced attractor selection [9] and shaping of dynamical systems with such attractor(s) by synaptic change support this robust learning.

Acknowledgements This work was supported by a Grant-in-Aid for Scientific Research on Innovative Areas “The study on the neural dynamics for understanding communication in terms of complex hetero systems (No. 4103)” of MEXT, Japan.

References

1. C. Waddington, *The Strategy of the Genes* (George Allen & Unwin, 1957)
2. A. Wagner, *Robustness and Evolvability in Living Systems* (Princeton Univ. Press, 1957)
3. M. West-Eberhard, *Developmental Plasticity and Evolution* (Oxford Univ. Press, 2003)
4. K. Kaneko, *Life: An Introduction to Complex Systems Biology* (Springer, 2006)
5. K. Kaneko, PLoS One **2**, e434 (2006)
6. K. Kaneko, BMC Evol. Biol. **11**, 27 (2011)
7. K. Kaneko, Chaos **18**, 026112 (2008)
8. T. Kurikawa, K. Kaneko, PLoS ONE **6**, e17432 (2011)
9. A. Kashiwagi, I. Urabe, K. Kaneko, T. Yomo, PLoS One **1**, e49 (2006)

Influence of the Endogenous Acetylcholine on STDP Induction

Takeshi Aihara, Eriko Sugisaki, Yasuhiro Fukushima, and Minoru Tsukada

Abstract Cholinergic inputs from the medial septum are projected to pyramidal neurons in hippocampal CA1 and release acetylcholine (ACh) from their terminals. The cholinergic inputs are considered to be integrated with sensory inputs and to play a crucial role in learning and memory. Meanwhile, it has been reported that the relative timing between pre- and post-synaptic spiking determines the direction and extent of synaptic changes in a critical temporal window, called Spike Timing-Dependent Plasticity (STDP). The positive and negative pairing-timing of a post-synaptic spike for pre-synaptic spikes induce long-term potentiation (LTP) and long-term depression (LTD), respectively.

To investigate influence of muscarinic activation by cholinergic inputs on synaptic plasticity, STDP induction-protocol was applied during the muscarinic induction of a slow excitatory postsynaptic potential (slow EPSP) following by a repetitive stimulation in the stratum oriens. As a result, LTP induced with the positive timing was facilitated and LTD induced with the negative timing was abolished by the muscarinic activation, respectively. Furthermore, interestingly, LTD was switched to LTP, depending on the intensity of ACh changed by

T. Aihara (✉)

Graduated College of Engineering, Tamagawa University, 6-1-1 Tamagawagakuen, Machida, Tokyo 194-8610, Japan

Brain Science Institute, Tanagawa university, 6-1-1 Tamagawagakuen, Machida, Tokyo 194-8610, Japan

e-mail: aihara@eng.tamagawa.ac.jp

E. Sugisaki

Graduated College of Engineering, Tamagawa University, 6-1-1 Tamagawagakuen, Machida, Tokyo 194-8610, Japan

Y. Fukushima • M. Tsukada

Brain Science Institute, Tanagawa university, 6-1-1 Tamagawagakuen, Machida, Tokyo 194-8610, Japan

application of eserine, a cholinesterase inhibitor. It suggests that synaptic plasticity is modulated depending on cholinergic inputs. The modulation of synaptic plasticity by muscarinic activation may show one important stage of the integration of top-down and bottom-up information integration in hippocampal CA1 neurons.

Keywords STDP • Hippocampus • CA1 • Muscarinic receptor

1 Introduction

The cholinergic neuron projecting to hippocampus is coming from medial septum to CA1 pyramidal neuron and interneuron via fimbria [7]. Stimulating cholinergic neurons projecting to hippocampus release ACh and enhance LTP [6, 9]. ACh seems to be more involved in attentional processes than in learning and memory processes [3, 10]. While, Spike-timing dependent plasticity (STDP), one of the protocols used to induce synaptic plasticity, is characterized by temporal coincidence of excitatory postsynaptic potential (EPSP) induced by electrical stimulation of the CA3-CA1 Schaffer collaterals and back-propagating action potential (BPAP) from postsynaptic neuron firing [1, 5, 8]. Stimulation on pre synapse following BPAP of the post neuron induces LTP, while the opposite timing induces LTD. Therefore, STDP is a protocol that can induce both LTP and LTD by timing dependency by changing the relative timing of spikes. As STDP is consisted of neuron firings in coincidence, the induced synaptic plasticity is elicited under moderate condition.

Repetitive stimulation of cholinergic axons projecting to the hippocampus at 40 Hz for 0.5 s was reported to induce short (2 s) inhibitory postsynaptic potential (IPSP) and then consequent small and long-lasting EPSP, called “slow EPSP” [4]. Shinoe et al. [11] reported that a long EPSP activated muscarinic acetylcholine receptors (mAChR) through repetitive stimulation of cholinergic neurons and ACh released in hippocampal slices enhanced LTP induced by tetanic stimulation. On the other hand, it is unclear that the effects of ACh on induction of LTD. Therefore, it is not investigated how mAChR activated by ACh influence the both induction of LTP and LTD.

In order to evaluate synaptic plasticity with the activation of mAChR through cholinergic inputs, the STDP protocol was applied either with slow EPSP induced by muscarinic activation following electrical stimulation of the oriens or with an change in ACh concentration following application of eserine, a cholinesterase inhibitor. As a result, the effect of ACh on the plasticity induced by STDP was shown under physiological condition. Furthermore, the effect of mACh activation to the synaptic plasticity was investigated in detail by controlling the intensity of ACh. The influence of muscarinic activation not only on LTP but also on LTD was estimated using STDP protocol, and we demonstrate that synaptic plasticity in the CA1 area is modulated by mACh activation depending on the amount of cholinergic inputs.

2 Methods

All procedures were approved by Tamagawa University Animal Care and Use Committee. Hippocampal slices (400 μm thick) were prepared from Wistar rats (2–3 weeks old) according to the standard procedure reported by Tsukada et al. [12].

Picrotoxin at 25 μM (Sigma, St. Louis, USA) was added to the aCSF in order to block GABAA-R related response. Atropine (1 μM) and eserine (0.6, 2, 20 μM) (Sigma, St. Louis, USA) were also added when needed. Extracellular stimulation of 50–100 μs in duration at 10 μA to Schaffer collaterals was made by stimulating electrode (glass pipette filled with aCSF, glued to silver rod) to induce EPSPs (Fig. 1a). The elicited EPSPs were adjusted to the amplitude of 2–4 mV as a control. STDP protocol (modified from protocols by Nishiyama et al. [8]) was used. An action potential during STDP protocol was induced by 2–2.5 nA current injection to the soma (2 ms in duration at). In STDP protocols, positive timing was defined as EPSP precedes the post-synaptic action potential ($\Delta t = 12$ ms), while the opposite,

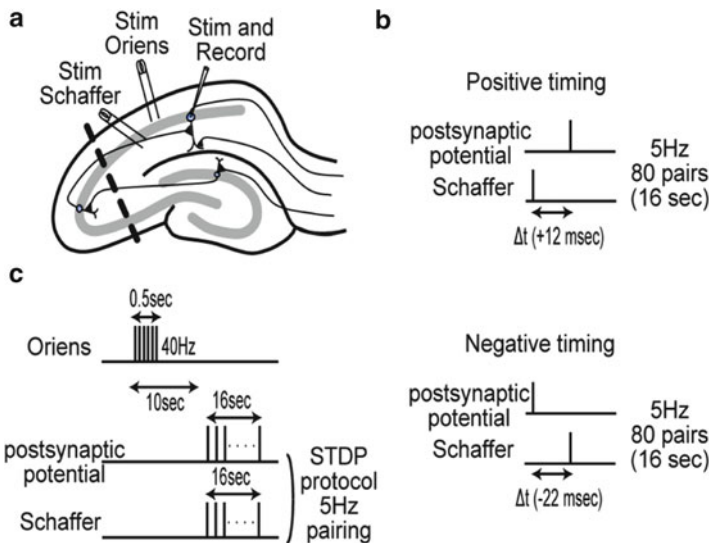


Fig. 1 Experimental procedure and stimulation pattern. (a) Schematic drawing of hippocampal slice removed from CA3. One stimulating electrode was placed extracellularly in the Schaffer collaterals, and the other was placed in stratum Oriens. Whole cell patch clamp was made for current injection and recording recordings in CA1 pyramidal neurons. (b) Two STDP inducing protocols. LTP-timing protocol (*upper*): a stimulation to Schaffer collaterals was applied before a postsynaptic action potential at a positive timing ($\Delta t = +12$ ms). LTD-timing protocol (*lower*): Stimulation to Schaffer collaterals was applied after postsynaptic action potential at a negative timing ($\Delta t = -22$ ms). Each STDP protocol was applied at 5 Hz for 16 s. (c) A stimulation pattern for investigation for the influence of Ach on STDP induction. A STDP protocol was applied at 10 s after the repetitive stimulation (40 Hz for 0.5 s) to stratum Oriens

negative timing was defined as an action potential follows EPSP ($\Delta t = -22$ ms) (Fig. 1b). Pairing stimulus was provided at 5 Hz for 16 s. To release ACh, another stimulating electrode was placed in stratum Oriens to stimulate at 40 Hz for 0.5 s with 80–300 μ s in duration at the strength of 80 V [4, 11] (Fig. 1a, c). In order to clarify the effect of ACh on STDP, STDP protocol was applied 10 s after the stimulation in stratum Oriens (Fig. 1c) because the peak latency of slow EPSP was around 10 s. EPSP (0.05Hz) was applied before and after a set of the STDP protocol with stimulation in stratum Oriens. The magnitude of the plasticity was defined as (averaged EPSP slopes obtained from 20 to 30 min after STDP-inducing stimulus)/(averaged baseline EPSP slopes). ANOVA and post-hoc was used for statistical analysis ($p < 0.05$).

3 Results

Slow EPSP: Repetitive stimulation in the stratum oriens induced an inhibitory post-synaptic potential followed by a small slow EPSP that last approximately 60 s. The slow EPSP was enhance by 2 μ M eserine, a cholinesterase inhibitor, and completely blocked by 1 μ M atropine, a nonselective mAChR antagonist (Fig. 2a, b).

The effect of ACh to STDP: To investigate the effect of ACh to synaptic plasticity, cholinergic input or eserine were applied to CA1 neurons during STDP induction. In positive timing of STDP protocol, the magnitude of LTP was significantly enhanced with slow EPSP or eserine. On the other hand, LTD induced by negative timing was not seen with slow EPSP and was changed to LTP with eserine. ACh effected synaptic plasticity to changed into the direction from depression to potentiation. Applying both slow EPSP and eserine to lead excessive ACh effect, it did not show LTP enhancement in the positive or negative timing, respectively (Fig. 2c, d)

4 Discussions

The cholinergic neuron projecting from the medial septum to the hippocampus extends its axon to terminate on the pyramidal neurons and inter neurons in CA1 via the fimbria, and ACh is released from the synaptic terminals by repetitively stimulating the axon of the cholinergic neuron [4, 7]. The present study focused on the modulation of plasticity in CA1 pyramidal neurons by the release of ACh from the synaptic terminals. Our results indicate that the priming effect of endogenous ACh was mediated by mAChR and modulated STDP, both LTP and LTD, in which LTP was facilitated and LTD was abolished by slow EPSPs, which is close to the physiological condition of mAChR activation (Fig. 2a, b). We also found an interesting feature of ACh as the modulating system for shifting the plasticity in the potentiating direction (Fig. 2c, d), following the BCM rule [2]. Thus, our results suggest that ACh may regulate learning and memory performance, indicating a new

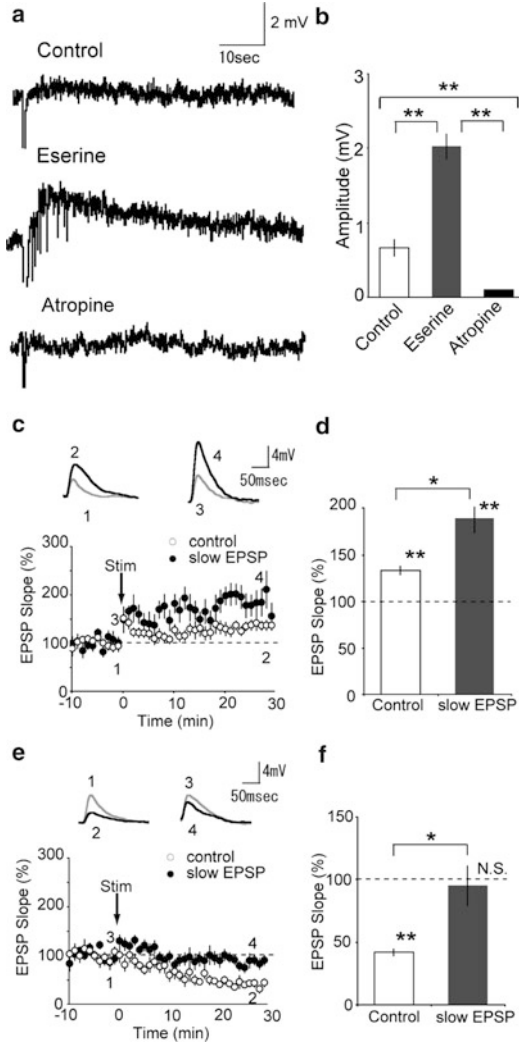


Fig. 2 The influence of slow EPSP on STDP Induction. **(a)** Slow EPSP elicited by a repetitive stimulation. Slow EPSPs due to the excitability of the pyramidal cell were elicited by the release of endogenous ACh following repetitive stimulation of the oriens. Representative traces show typical examples of slow EPSPs in the absence (*top*) and presence of 2 μ M eserine (*middle*), and the presence of 1 μ M atropine (*bottom*). Membrane potential was maintained at -53 mV. **(b)** Summary of slow EPSP amplitudes. The peak amplitudes in the absence (control), presence of eserine, and presence of atropine were measured, respectively. **(c)** The influence of slow EPSP on STDP induction at positive timing ($\Delta t = 12$ ms). STDP, LTP induced by LTP-timing protocol, was enhanced by the slow EPSP. EPSP slopes in absence (*open circle*) and presence (*filled circle*) of slow EPSP were presented in percentages, respectively. Upper EPSP traces were measured at the time corresponding to numbers indicated in the time course of EPSP slopes. **(d)** Summary of influences of slow EPSP on STDP induction at positive timing. **(e)** The influence of slow EPSP on STDP induction at negative timing ($\Delta t = -22$ ms). STDP, LTD induced by LTD-timing protocol, was abolished by the slow EPSP. **(f)** Summary of influences of slow EPSP on STDP induction at positive timing. * $p < 0.05$, ** $p < 0.01$ in Student's *t*-test; *N.S* not satisfied

aspect of learning and memory in the hippocampus. We conclude that ACh plays a critical role as a modulator for spatial-temporal information processing in the hippocampus, and thus attention modulates learning and memory at cell level.

Acknowledgments This work was supported by the 21st Century Center of Excellence (COE) Program and the Global COE Program at Tamagawa University and Grants-in-Aid for Scientific Research on Innovative Areas 21120006 from the Ministry of Education, Culture, Sports, Science and Technology of Japan.

References

1. Bi G.Q., Poo M.M., 1998, Synaptic modifications in cultured hippocampal neurons: dependence on spike timing, synaptic strength, and postsynaptic cell type. *J Neurosci.* 18 (24), 10464–72.
2. Bienenstock E.L., Cooper L.N., Munro P.W., 1982, Theory for the development of neuron selectivity: orientation specificity and binocular interaction in visual cortex. *J Neurosci.* 2 (1), 32–48.
3. Blokland A., Acetylcholine: a neurotransmitter for learning and memory? *Brain Res Brain Res Rev.* 21 (3), 285–300.
4. Cole A.E., Nicoll R.A., 1984. Characterization of a slow cholinergic post-synaptic potential recorded in vitro from rat hippocampal pyramidal cells. *J Physiol.* 352, 173–88.
5. Magee J.C., Johnston D., 1997. A synaptically controlled, associative signal for Hebbian plasticity in hippocampal neurons. *Science.* 275 (5297), 209–13.
6. Nakao K., Ikegaya Y., Yamada M.K., Nishiyama N., Matsuki N., 2003. Fimbrial control of bidirectional synaptic plasticity of medial perforant path-dentate transmission. *Synapse.* 47 (3), 163–8.
7. Nicoll R.A., 1985. The septo-hippocampal projection: a model cholinergic pathway. *Trends Neurosci.* 8, 533–536.
8. Nishiyama M., Hong K., Mikoshiba K., Poo M.M., Kato K., 2000. Calcium stores regulate the polarity and input specificity of synaptic modification. *Nature.* 408 (6812), 584–8.
9. Ovsepian S.V., Anwyl R., Rowan M.J., 2004. Endogenous acetylcholine lowers the threshold for long-term potentiation induction in the CA1 area through muscarinic receptor activation: in vivo study. *Eur J Neurosci.* 20 (5), 1267–75.
10. Parent M.B., Baxter M.G., 2004. Septohippocampal acetylcholine: involved in but not necessary for learning and memory? *Learn Mem.* 11 (1), 9–20.
11. Shinoe T., Matsui M., Taketo M.M., Manabe T., 2005. Modulation of synaptic plasticity by physiological activation of M1 muscarinic acetylcholine receptors in the mouse hippocampus. *J Neurosci.* 25 (48), 11194–200.
12. Tsukada M., Aihara T., Kobayashi Y., Shimazaki H., 2005. Spatial analysis of spike-timing-dependent LTP and LTD in the CA1 area of hippocampal slices using optical imaging. *Hippocampus.* 15 (1), 104–9.

Transition Dynamics in Spatial Choice

Hiroshi Nishida, Muneyoshi Takahashi, Jin Kinoshita, and Johan Lauwereyns

Abstract Previous research has provided abundant evidence that negative as well as positive reinforcers can elicit operant responding in rats. Less is known, however, about the relative impact of positive versus negative reinforcers on the dynamics of spatial choice in a complex setting, including old and new stimuli. To study such dynamics, we devised a behavioral paradigm consisting of an initial learning phase, followed by a “transition test,” which included a novel stimulus. In the initial learning phase, rats acquired an operant nose-poke response to a visual (LED) onset at the central hole in the front wall of a Skinner box. We trained two groups of rats, with different types of reinforcement; Group 1 (appetitive learning) obtained a food pellet as reinforcement for correct responding, whereas Group 2 (appetitive *and* avoidance learning) obtained a food pellet and avoided a foot shock as reinforcement for correct responding. Once both groups had established similar, near-perfect levels of performance, we introduced a first transition test, in which a second visual (LED) onset was presented simultaneously with the visual onset at the center. The rats were free to continue responding to the central hole (with the same reinforcement schedule for central responding as during the initial learning). However, the rats obtained three instead of only one food pellet for responding to the peripheral hole (Group 1 and Group 2) as well as avoiding a foot shock (Group 2). Overall, as compared to rats in Group 1, the rats that underwent both appetitive and avoidance learning showed more efficient transition, switching to peripheral responding. These data cannot easily be accommodated by operant conditioning models, according to which the rats in Group 2 should have been particularly motivated to continue responding at the central hole. Instead, we propose that their spatial choice was modified by a complex interaction of classic and operant learning.

H. Nishida • M. Takahashi • J. Kinoshita • J. Lauwereyns (✉)
Graduate School of Systems Life Sciences, Kyushu University, Fukuoka 819-0395, Japan
e-mail: jan@sls.kyushu-u.ac.jp

Keywords Rat • Operant learning • Reward • Punishment • Transition dynamics

1 Introduction

As our daily life is filled with a plethora of stimuli, successful behavior requires us to pick out and process the relevant ones (e.g., signals associated with a large amount of reward or with the impending arrival of an aversive event). The stimulus selection and processing allows us to compute the appropriate response (e.g., approach or run away). The trick, of course, is to know which are the relevant stimuli, and which the most beneficial responses. Learning may be the classic answer to the problem, but how and when do we engage in learning? In real life, we generally face novel stimuli or unfamiliar happenings with some frequency, yet they are often embedded in contexts with familiar patterns, including well-learned statistical regularities between objects and events, actions and outcomes. Thus, we can choose to explore the new or to exploit the familiar.

Here, we aim to develop a behavioral paradigm that allows us to investigate, in precise and systematic ways, the various factors that determine the tendency to engage in exploration. We ask under which circumstances (in which contexts) an animal prefers exploring an unfamiliar stimulus over exploiting a familiar stimulus. It is well-known that both positive and negative reinforcers can shape an animal's behavior with respect to a particular stimulus [1, 2]. However little is known about how the presence of such reinforcers (i.e., the potential to obtain familiar outcomes) impacts on the dynamics of exploration in an environment with a novel (newly introduced) stimulus.

The reaction to the uncertainty and the potential risk associated with the new stimulus may vary as a function of the context. To approach or to avoid the novel stimulus, then, can be thought of as a context-dependent decision-making process [3]. Given that novel stimuli can elicit such diametrically opposed behaviors, it is crucial to investigate the effect of context in a systematic, hypothesis-driven manner. Particularly, we aimed to contrast a hypothesis on the basis of “motivational significance” (compatible with traditional models of operant conditioning [4]) versus a hypothesis on the basis of “information value” (compatible with models of operant learning that reserve a specific role for cognitive factors [5]). Consider a situation in which a novel stimulus is presented concurrently with a familiar stimulus of a particular motivational value (i.e., associated with a particular action outcome). Here, the likelihood of exploring the novel stimulus might depend on the motivational value of the familiar stimulus, such that highly valued familiar stimuli would result in less exploratory behavior than moderately valued familiar stimuli. We call this the “motivational significance hypothesis.”

Now consider a situation in which a novel stimulus is presented concurrently with a familiar stimulus of a particular level of information complexity. In this case,

the information value of new stimuli (as a potential predictor of events, or a possible source to reduce the complexity of the situation) should be higher when the familiar stimulus implies complex, and therefore potentially “ambiguous” associations than when the familiar stimulus provides a clear and simple implication. By this view, familiar stimuli with complex associations should produce more exploratory behavior than familiar stimuli with simple implications. We refer to this proposal as the “information value hypothesis.”

In the present study, we devised a nose-poke task for rats that puts the two hypotheses in opposition.

2 Methods

Twenty-four experimentally naïve male Sprague Dawley rats served as subjects. Each rat was assigned to one of two groups (each with $n = 12$). Four identical nine-hole nose-poke chambers (ENV-NPW-9L; Med Associates Inc.) were used to conduct the experimental procedure.

In the initial learning phase, rats acquired an operant nose-poke response to a visual (LED) onset at the central hole in the front wall of a Skinner box. The duration of central illumination was gradually decreased from 60 to 5 s according to the performance during 45 min of daily training session. We trained two groups of rats, with different types of reinforcement; Group 1 (appetitive learning; App-only) obtained a food pellet as reinforcement for correct responding, whereas Group 2 (appetitive *and* avoidance learning; App-Av) obtained a food pellet and avoided a 0.18 mA of scrambled foot shock as reinforcement for correct responding.

Once both groups had established similar, near-perfect levels of performance, we introduced a first transition test, in which a second visual (LED) onset was presented simultaneously with the visual onset at the center. The rats were free to continue responding to the central hole. However, the rats obtained three instead of only one food pellet for responding to the peripheral hole (Group 1 and Group 2) as well as avoiding a foot shock (Group 2).

To assess the effect of reinforcement context on the transition behavior, we measured the peripheral preference rate (PPR) as follows:

$$PPR = \frac{N(\textit{peripheral})}{N(\textit{peripheral}) + N(\textit{center})}$$

$N(\textit{peripheral})$ denoted the number of correct peripheral choices and $N(\textit{center})$, the number of correct center choices. This index ranged from 0, if the rats always chose the central hole, to 1, if their preference had completely shifted to the peripheral option. The effect of Context and Day was assessed using two-way ANOVA, with Day as a within-subjects variable (Fig. 1).

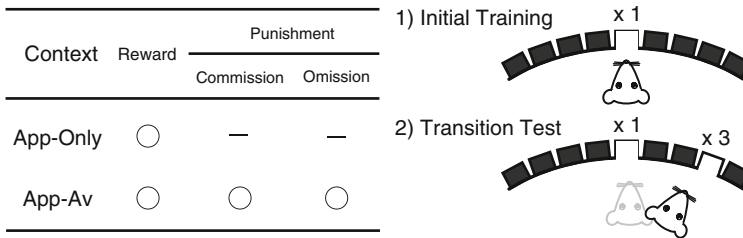


Fig. 1 Experimental design for the transition test

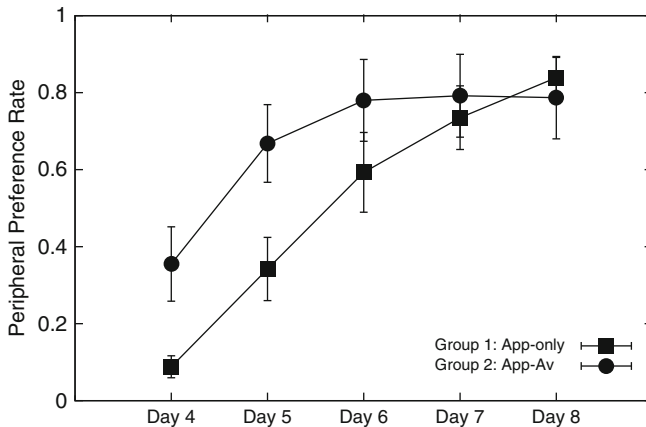


Fig. 2 The 5-day dynamics of the average peripheral preference rates in the transition test

3 Results

After 30 days of training, all 24 rats (from both Group 1, App-only and Group 2, App-Av) were able to perform more than 120 correct nose-poke responses to the central hole when the LED was illuminated, at a correct performance rate of more than 80% during a 45-min session. Our analyses showed similar trends for absolute numbers of correct trials as for correct performance rates. Thus, we concentrated all analyses on rates of responding.

In the first transition test, the average peripheral preference rate gradually increased over the course of 5 days, both for Group 1, App-only (0.09 ± 0.10 , 0.34 ± 0.28 , 0.59 ± 0.36 , 0.74 ± 0.29 , and 0.84 ± 0.18 ; mean \pm SD) and for Group 2, App-Av (0.36 ± 0.33 , 0.67 ± 0.35 , 0.78 ± 0.37 , 0.79 ± 0.37 , 0.79 ± 0.37 ; mean \pm SD) (Fig. 2). A two-way repeated measures ANOVA, with the factors Context (App-only, App-Av) and Day (4–8), revealed a significant main effect of Day ($F(4, 88) = 56.09$, $MSE = 0.03$, $p < 0.001$) but not of Context ($F < 2$). However, there was a significant interaction between Day and Context

($F(4, 88) = 5.76$, $MSE = 0.03$, $p < 0.001$). Post hoc pair-wise comparisons (with Bonferroni correction) revealed that there were statistically significant differences between Contexts on Day 4 ($p < 0.05$) and Day 5 ($p < 0.05$). On Days 4 and 5, which were the first and second day of the transition test 1, rats that had been trained with a complex reinforcement schedule, involving both appetitive and avoidance learning, were able to achieve higher peripheral responding rates (0.36 on Day 4 and 0.67 on Day 5) than rats that had been trained in the alternative context (0.09 on Day 4 and 0.34 on Day 5). This result clearly suggested that the preference shift occurred more rapidly in Group 2, App-Av, than in Group 1, App-only.

4 Discussion

In the present study, we introduced a new behavioral paradigm to investigate the impact of positive and negative reinforcers on the dynamics of exploratory behavior. The rats were trained initially on a nose-poking task to an illuminated central nose-poke hole either using positive reinforcers only (i.e., Group 1, App-only) or using positive and negative reinforcers (i.e., Group 2, App-Av). For the subsequent transition test, we introduced an alternative peripheral nose-poke hole in the same experimental chamber, extending the paradigm to a free-choice task. If the rat chose the peripheral hole, it received a larger reward than for a response at the central hole (where the reinforcement schedule remained unchanged). We found that rats in Group 2, App-Av, shifted their preference to the peripheral hole faster than rats in Group 1, App-only.

The data cannot easily be accommodated by traditional operant conditioning models [6, 7], which predicted that rats in Groups 2 should be motivated more strongly than their counterparts to continue responding at the central hole. We suggest that the information value hypothesis provides a better fit with the data. By the latter view, the exploratory behavior depended on the complexity of information present in the given context. In an ambiguous context, when the familiar stimulus implied two different associations, the rats were more likely to explore the new alternative than in an unambiguous context, when the familiar stimulus offered only one straightforward association. The present data are consistent with recent models that leave an explicit role for cognitive processing in the organization of behavior [5, 8, 9], and agree with recent findings suggesting that context may serve to resolve ambiguity (i.e., temporal ambiguity [10]). Indeed, several researchers have suggested that complex settings tend to increase exploratory behavior [11, 12]. Similarly, animals often prefer variable over fixed reinforcement ratios, even when the fixed ratio provides a better payoff [13], again connecting exploratory behavior with complexity or uncertainty. From a cognitive perspective, such tendencies suggest that the exploratory behavior may be driven by a need for information as a potential source of disambiguation.

By this reading, information would serve as an intrinsic attractor, particularly in complex or ill-understood settings. The notion that information may be desirable in

and of itself was illustrated recently in a study by Bromberg-Martin and Hikosaka (2009), in which monkeys chose to obtain cues that provided reliable advance information about future events rather than cues that provided random information, even though the information changed nothing with respect to the actual amounts of reward that could be obtained in the experiment [14]. Apparently, the monkeys valued the advance information. Similarly, in our current experiments, rats that were faced with a complex setting may have been particularly responsive to the attraction of new information that might shed light on the relationship between different stimulus features and outcomes.

Future studies can build on the current paradigm to systematically investigate the role of information complexity, and the role of different types of reinforcers, in the dynamics of exploration. Arguably the principal merit of the current paradigm is that it offers a clear and easy rat model of exploration dynamics in a way that will be compatible with neurophysiological recording. Nose-poke paradigms for freely moving rats are already successfully combined with large-scale neuronal ensemble recording techniques using several tens of microelectrodes [15]. To explore the neural mechanisms of exploration, then, we propose that the present rodent model offers a unique opportunity to conduct experiments with a large subject sample (e.g., recording only 5–10 daily sessions per subject, from groups of 12 or 24 rats). Targeting rats and mice as animal models, this approach will be suitable not only for neurophysiological recording, but also for anatomical, pharmacological and genetic approaches, to advance our understanding of the neural mechanisms of exploration.

Acknowledgments This work was supported by Human Frontier Science Program award RGP0039/2010.

References

1. Ilango, A., Wetzel, W., Scheich, H., Ohl, F.W.: The combination of appetitive and aversive reinforcers and the nature of their interaction during auditory learning. *Neuroscience* 166 (2010) 752–762
2. Kobayashi, S., Nomoto, K., Watanabe, M., Hikosaka, O., Schultz, W., Sakagami, M.: Influences of rewarding and aversive outcomes on activity in Macaque lateral prefrontal cortex. *Neuron* 51 (2006) 861–870
3. Simon, N.W., Gilbert, R.J., Mayse, J.D., Bizon, J.L., Setlow, B.: Balancing risk and reward: A rat model of risky decision-making. *Neuropsychopharmacology* 34 (2009) 2208–2217
4. Dickinson, A., Balleine, B.: Motivational control of goal-directed action. *Anim Learn Behav.* 22 (1994) 1–18
5. Blaisdell, A.P.: Cognitive dimension of operant learning. In Menzel, R. (Ed.), *Learning theory and behavior*. Vol. 1 of *Learning and memory: A comprehensive reference*. 4 vols, (2008) 173–195, Oxford: Elsevier
6. Bindra, D., Palfai, T.: Nature of positive and negative incentive-motivational effects on general activity. *J Comp Physiol Psychol.* 63 (1967) 288–297
7. Dinsmoor, J.A.: Stimuli inevitably generated by behavior that avoids electric shock are inherently reinforcing. *J Exp Anal Behav.* 76 (2001) 311–333
8. Foote, A.L., Crystal, J.D.: Metacognition in the rat. *Curr Biol.* 17 (2007) 551–555

9. Kepecs, A., Uchida, N., Zariwala, H.A., Mainen, Z.F.: Neural correlates, computation and behavioural impact of decision confidence. *Nature* 455 (2008) 227–231
10. Molet, M., Urcelay, G.P., Míguez, G., Miller, R.R.: Using context to resolve temporal ambiguity. *J Exp Psychol Anim Behav Process.* 36 (2010) 126–136
11. Berlyne, D.E.: Curiosity and exploration. *Science* 153 (1966) 25–33
12. Catania, A.C.: Freedom and knowledge: An experimental analysis of preference in pigeons. *J Exp Anal Behav.* 24 (1975) 89–106
13. Field, D.P., Tonneau, F., Ahearn, W., Himeline, P.N.: Preference between variable-ratio and fixed-ratio schedules: Local and extended relations. *J Exp Anal Behav.* 66 (1996) 283–295
14. Bromberg-Martin, E.S., Hikosaka, O.: Midbrain dopamine neurons signal preference for advance information about upcoming rewards. *Neuron* 63 (2009) 119–126
15. Takahashi, M., Lauwereyns, J., Sakurai, Y., Tsukada, M.: A code for spatial alternation in rat hippocampal CA1 neurons. *J. Neurophysiol.* 102 (2009) 556–567

Perseveration of Response Sequences as a Mechanism Underlying 3,4-Methylenedioxymethamphetamine (MDMA or ‘Ecstasy’) Induced Memory Impairments

David N. Harper

Abstract At doses above 3.0 mg/kg i.p. MDMA shares a number of features in common with other drugs of abuse in terms of the specific behavioral processes that lead to task disruption as well as an overlapping neurochemical basis. Converging evidence suggests that much of the behavioral disruption caused by acute exposure to MDMA emerges because of an increased tendency to perseverate with learned response sequences even when those tendencies reduce access to reinforcement. We believe that this behavioral feature of MDMA may be linked to increased brain dopamine activity at sufficiently high enough doses. The current work has theoretical implications for understanding the actual behavioral locus for the learning and memory impairments that arise following exposure to a range of dopamine agonist drugs.

Keywords MDMA • Perseveration • Memory • Concurrent schedule

1 Introduction

Exposure to the stimulant-based recreational drug (+/–)3,4-methylenedioxy-methamphetamine (MDMA, or ‘Ecstasy’) is associated with impairments in a range of conditional discrimination tasks that reflect memory function, decision making and self-control [1–3]. Recent studies with rats using the delayed matching-to-sample (DMTS) paradigm [4, 5] have shown that MDMA’s acute effects are qualitatively very similar to the disruption produced by classic stimulant-type drugs such as *d*-amphetamine and cocaine in terms of an overall impairment to accuracy across all delays.

D.N. Harper (✉)

School of Psychology, Victoria University of Wellington, Wellington 6140, New Zealand
e-mail: david.harper@vuw.ac.nz

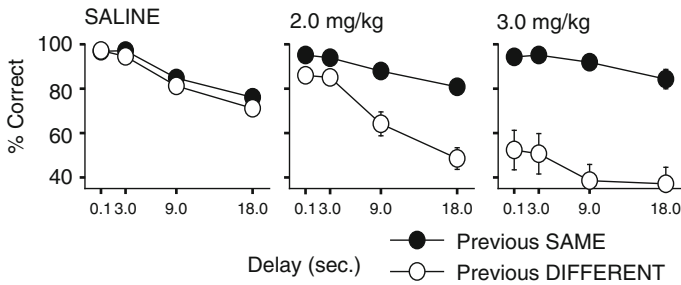


Fig. 1 Accuracy in DMTS task divided into trials in which the response made in the immediately preceding trial was the same (*filled symbols*) versus different (*unfilled symbols*) from the correct response required on the current trial across doses of MDMA

However, the actual behavioral process by which MDMA alters performance in these tasks is not clear. One interpretation of such findings has been that overall stimulus control is impaired (i.e., rats have trouble discriminating between response options and/or which reinforcers were associated with which stimulus-response option). Such a possibility lies at the heart of many explanations based on problems with attention or retention of information. This interpretation also leads to the expectation that rats should display reduced molar sensitivity to changes in reinforcer ratios arranged across concurrently available response alternatives.

Explanations based on impaired stimulus control are, however, hard to reconcile with a re-analysis of the original data from a study by Harper et al. [4] which reveals that this overall impairment is a direct result of increased susceptibility to the confounding influence of responses made in the immediately preceding trial on current trial performance (*'proactive interference'*). For example, after choosing a LEFT lever on Trial 'n-1' there was a greater tendency to respond LEFT again on Trial 'n' (irrespective of whether the correct lever on the current trial was LEFT or RIGHT); an effect which becomes more extreme at doses above 1.5 mg/kg i.p. of MDMA (see Fig. 1).

Therefore, an alternate interpretation is that poorer discrimination arises because there is a localized perseverative tendency in responding which effectively interferes with appropriate responding. Experiment 1 was an attempt to elucidate the extent to which MDMA produces response perseveration vs. impairments to stimulus control at doses that impair DMTS task performance. Experiment 2 investigated whether the resulting memory impairments were related to MDMA's neurochemical actions as a dopamine agonist.

2 Experiment 1

Experiment 1 examined the effects of acute exposure to MDMA on sensitivity to reinforcement and response perseveration in a concurrent choice arrangement by using Davison & Baum's (2000) concurrent choice procedure [6]. At a molar level

Table 1 Variable Interval (VI) reinforcement schedules arranged for responding across two concurrently available levers

Pair	Left lever	Right lever	Reinforcer ratio
1	VI 32 s	VI 480 s	15:1
2	VI 36 s	VI 180 s	5:1
3	VI 60 s	VI 60 s	1:1
4	VI 180 s	VI 36 s	1:5
5	VI 480 s	VI 32 s	1:15

Numerical values for each VI refer to average time between the availability of successive reinforcers (see [5] for details)

his paradigm examines the degree to which an organism (a rat in this experiment) will allocate its responding across two response options (operant levers in the current case) that differ in terms of the ratio of reinforcement available on each option. At a more molecular level this paradigm allows the assessment of ‘*preference pulses*’ (the tendency to make a response on the same lever as the last response was made; a preference that increases following successive reinforcers presented for responding on that option). The expectation is that if MDMA is causing an increase in response perseveration then rats will tend to make more responses (preference pulses) on the lever associated with the current highest rate of reinforcement; this, in turn, should drive an increase in overall molar sensitivity (because rats are more likely to continue responding on the lever associated with the richest reinforcement). In contrast, an impairment to stimulus control should result in lower overall sensitivity to the reinforcer ratios.

2.1 Methods

Seven Norway Hooded rats were trained to respond on two levers in an operant chamber for food reinforcement (45 mg sugar pellets delivered via a hopper) in which the ratio of reinforcement available for responding across two concurrently available levers varied within a 60 min session.

Each reinforcer schedule pair was presented once for 12 min in random order within each session. Rats were administered MDMA (0–3.0 mg/kg i.p.) 15 mins prior to a session once stable performance was achieved. Three sessions were conducted per dose, with 2–3 washout days between drug days. Statistical analyses were conducted using repeated-measures analyses of variance (ANOVAs) (Table 1).

2.2 Results

Overall molar-level analysis was conducted by using the Generalized Matching Law [7]. This analysis plots changes in response ratios across the two response options as a function of changes in the obtained reinforcer ratio for individual subjects.

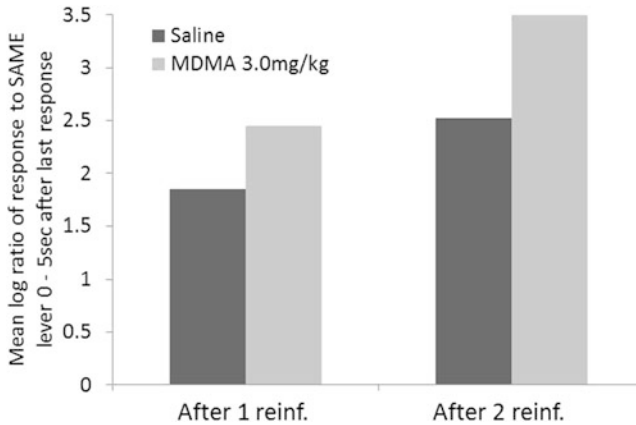


Fig. 2 Mean ratio of current response (n) being made to the ‘same’ vs. ‘opposite’ lever as the immediately preceding response (n–1) presented as a function of number of preceding reinforcers delivered for responding to the ‘same’ lever. Data shown for saline control vs. highest dose of MDMA tested (3.0 mg/kg)

This analysis revealed that there was a systematic increase in sensitivity (from 0.38 to 0.57) to the reinforcer ratios as dose of MDMA increased ($p < 0.01$). That is, as the dose of MDMA increased, the ratio of response allocation across the two concurrently available choice alternatives came to more closely match the arranged reinforce ratio across those two alternatives.

Figure 2 shows the outcome from a molecular analysis of individual responses [5] that examined the degree to which rats made a response to the same lever as the one they had just responded to (within the last 5 s). This analysis revealed the expected ‘preference pulse’ effect. Specifically, rats were twice as likely to emit a response to the same lever as they were to switch levers following a response to a given lever (e.g., rats were twice as likely to respond LEFT followed by LEFT again than they are LEFT followed by RIGHT). The more reinforcers gained on a given lever in succession, the greater the preference pulse. MDMA significantly increased this effect ($p < 0.01$) in a dose dependent manner.

3 Experiment 2

The proactive interference effects observed in previous studies [4, 5] and enhanced preference pulses observed in Experiment 1 become obvious at doses between 2.0 and 3.0 mg/kg i.p. of MDMA. Interestingly, at doses less than 2.0 mg/kg MDMA’s main neurochemical action is via an enhancement of 5-HT activity, whereas at doses greater than 2.0 mg/kg, MDMA also results in high extracellular levels of dopamine [8]. Therefore, one prediction is that MDMA is having its

effects on response perseveration (and hence memory function in the DMTS task) primarily via its enhancement of dopamine activity. Such a possibility would also be consistent with the observed similarity in terms of the pattern of disruption seen to DMTS performance between MDMA and drugs such as amphetamine and cocaine [4] which are known to have many of their behavioral effects via dopamine [9, 10].

3.1 Methods

The same DMTS procedure used in previous studies to examine the effects of MDMA on memory-task performance was used in the current experiment [4, 5]. After 18 rats were showing stable performance they were administered MDMA (at a target dose of 3.0 mg/kg i.p.) on its own or in combination with the D1 antagonist SCH23390 (0.0–0.02 mg/kg) or the D2 antagonist eticlopride (0.0–0.1 mg/kg). Statistical analyses were conducted using ANOVAs.

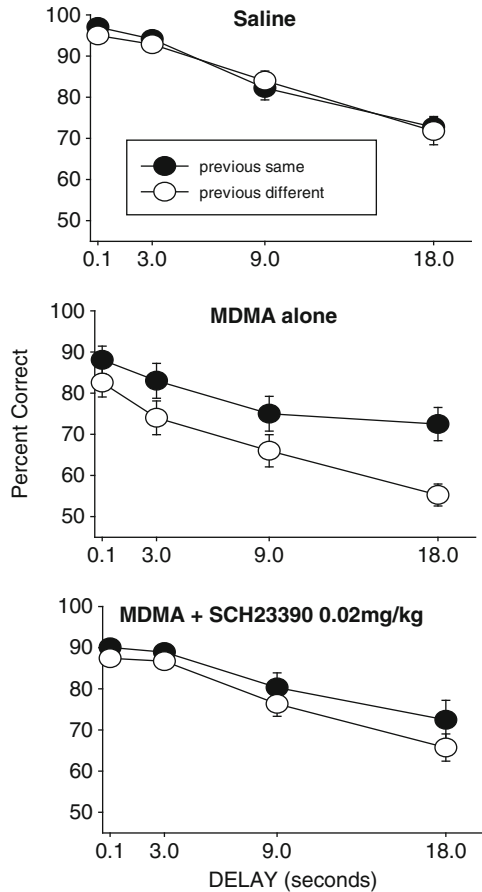
3.2 Results

As seen in previous studies, MDMA at 3.0 mg/kg produced a significant overall decrease in accuracy ($p < 0.01$) and an obvious increase in proactive interference (see Fig. 3). Only the D1 antagonist SCH23390 at the 0.02 dose significantly ameliorated this effect of MDMA ($p < 0.01$).

4 Discussion

Across different paradigms it appears that MDMA can induce an increase in response perseveration (effectively returning to a previously emitted response option). This localized tendency to repeat individual responses (in the case of the concurrent schedule task) or sequences of responses (in the case of the DMTS and other memory tasks [e.g. 3–5]) can account for a variety of more molar level changes in performance. Somewhat counter-intuitively, increased responding on the more richly reinforced lever in the concurrent schedule arrangement produces an apparent increase in sensitivity to changes in the reinforcer ratios. This phenomenon arises because generally rats, like other species, tend to under-match in such procedures in control conditions (i.e., respond less extremely than the ratio of reinforcers obtained across response options [7]). Such a finding is not easily reconciled with an account of MDMA's actions purely in terms of an impairment to stimulus control processes (at least at the doses of MDMA examined in the current research).

Fig. 3 DMTS accuracy divided into trials in which the response made in the immediately preceding trial was the same (*filled symbols*) vs. different (*unfilled symbols*) from the correct response required on the current trial for saline vs. MDMA 3.0 mg/kg vs. MDMA 2.0 mg administered concurrently with SCH23390 at 0.02 mg/kg



It should be noted that although response perseveration serves as a description of the behavioral changes observed here, the actual behavioral process by which it arises still needs to be elucidated. Future research needs to explicitly identify whether an MDMA-induced perseveration arises because the drug acts to increase relative reinforcer value (i.e. organisms persist with previously reinforced responses because the reinforcers for design so are now relatively more valuable) or whether the underlying mechanism relates more to inflexible motor control programs independent of reinforcement.

Although initial evidence suggests MDMA may produce the current behavioral effects via dopamine at the D1 receptor site, a possible role played by 5-HT cannot be dismissed, especially because of the inter-dependent nature of dopamine and 5-HT activity [10]. However, a possible role of dopamine suggests that the proposed mechanism by which MDMA is impairing memory-task accuracy can be applied to a wide range of other stimulant-based drugs of abuse.

References

1. Kalechstein, A.D., et al: MDMA use and neurocognition: a meta-analytic review. *Psychopharmacology* 189 (2007) 531–537
2. LeSage, M., Clark, R., Poling, A: MDMA and memory: the acute and chronic effects of MDMA in pigeons performing under a delayed-matching-to-sample procedure. *Psychopharmacology* 110 (1993) 327–332.
3. Kay C., Harper D.N., Hunt, M: Differential effects of MDMA and scopolamine on working versus reference memory in the radial-arm maze task. *Neurobiology of Learning and Memory* 93 (2010) 151–156
4. Harper, D.N., Wisniewski, R., Hunt, M., Schenk, S: MDMA, d-amphetamine and cocaine impair delayed matching-to-sample performance via an increase in susceptibility to proactive interference. *Behav Neurosci* 119 (2005) 455–463.
5. Harper, D.N., Hunt, M., Schenk, S: Attenuation of the disruptive effects of (+/–)3,4-methylenedioxymethamphetamine (MDMA) on delayed matching-to-sample performance in the rat. *Behav Neurosci* 120 (2006) 201–205
6. Davison, M.C., Baum, W.M: Choice in a variable environment: every reinforcer counts. *J Exp Anal Behav* 74 (2000) 1–24
7. Baum, W.M: On two types of deviation from the matching law: Bias and undermatching. *J Exp Anal Behav* 22 (1974) 231–242
8. Baumann, M.H., Clark, R.B., Rothman, R.D: Locomotor stimulation produced by 3,4-methylenedioxymethamphetamine (MDMA) is correlated with dialysate levels of serotonin and dopamine in rat brain. *Pharm Biochem Behav* 90 (2008) 208–217
9. Ushijima, I., Carino, M.A., Horita A: Involvement of D1 and D2 dopamine systems in the behavioral effects of cocaine in rats. *Pharm Biochem Behav* 52 (1995) 737–741
10. Gudelsky, G.A., Yamamoto, B.K: Actions of 3,4-methylenedioxymethamphetamine (MDMA) on cerebral dopaminergic, serotonergic and cholinergic neurons. *Pharm Biochem Behav* 90 (2008) 198–207

Multiple Neural Circuits in Value-Based Decision-Making

Masamichi Sakagami

Abstract Valuation is an essential function in decision-making. To understand the nature of the distinct neural systems used in such valuation, we performed monkey single-unit recording experiments and a human fMRI experiment using (1) a perceptual discrimination task with asymmetric reward, and (2) a reward inference task. The results suggest that both the primate and human brain have, at least, two distinct valuation systems: one in the nigro-striatal circuit (the stimulus-based valuation system) and the other in the PFC circuit (the knowledge-based valuation system). We propose that the stimulus-based valuation system calculates values based on the empirical and probabilistic relation between an event and its outcome. The knowledge-based valuation system generates values by further extension of directly-experienced association through categorical processes and rules, thereby enabling animals to predict the outcome of an inexperienced event.

1 Introduction

The brain is an organ able to select an appropriate behavior in an ever-changing environment. Although a smaller brain would effectively work as a “relay machine,” a larger brain seems able to select more appropriate behaviors among available choices, depending on the context of the stimulus environment. Such function is termed “decision-making.” Decision-making does not involve a single process. For example, Rangel et al. suggested that value-based decision-making is composed of five processes: (1) state representation, (2) valuation, (3) action selection, (4) outcome evaluation, and (5) learning [1]. Among these, the valuation process is critical in decision-making because the evolution of the animal brain has developed

M. Sakagami (✉)

Brain Science Research Institute, Tamagawa University, Tamagawa-gakuen, 6-1-1,
Machida, Tokyo 194-8610, Japan
e-mail: sakagami@lab.tamagawa.ac.jp

multiple valuation systems, and the divergence of decision-making mainly depends on the variation of valuation systems. In this paper, we will see some evidence bearing on the diverse contributions of cortical and subcortical neural circuits in both the non-human and human primate brain, and also discuss the nature of the decision-making function.

2 Methods

2.1 *Perceptual Discrimination Task*

We recorded brain activity during the performance of a random dot motion discrimination task using an asymmetric reward schedule in both human fMRI (BOLD signal) and monkey neurophysiology (single unit recording from midbrain dopamine neuron) experiments [2, 3]. The subject was presented with random dot motion, and required to report its motion direction (rightward or leftward). In a given block, while one direction of motion stimuli was associated with more valuable reward, the other direction was associated with less valuable reward. To manipulate discrimination difficulty, several levels of coherence were used. Although small details of the task were adapted to work well with different species, the task structure was basically the same. Whereas the stimulus-based valuation system shows reward prediction based on the motion stimulus itself, the knowledge-based valuation system shows reward prediction based on the subject's reported perceptual discrimination. Dissociation between these two systems is discernable in error trials.

2.2 *Reward Inference Task*

We recorded single unit activity from the lateral PFC (LPFC) and striatum of monkeys performing a sequential paired association task with an asymmetric reward schedule [4]. In this task, the monkeys first learned two stimulus-stimulus association sequences (here denoted: $A1 \rightarrow B1 \rightarrow C1$ and $A2 \rightarrow B2 \rightarrow C2$, where $A1$, $B1$, $C1$, $A2$, $B2$, and $C2$ were six different visual stimuli), in sequential paired association trials (SPATs). After having mastered the task, the monkeys were taught the asymmetric reward schedule using reward instruction trials, in which one stimulus ($C1$ or $C2$) was paired with a large reward (0.4 ml of water) and another stimulus ($C2$ or $C1$) with a small reward (0.1 ml of water). Reward instruction trials were followed by SPATs in one block. In the SPATs, the amount of reward at the end of correct trials was also asymmetric: if $C1$ had been paired with the large reward, and $C2$ with the smaller, in the reward instruction trials, the sequence $A1 \rightarrow B1 \rightarrow C1$ would lead to the larger reward, while the sequence $A2 \rightarrow B2 \rightarrow C2$ would lead to the smaller reward, and vice versa. Our question was

whether the monkeys would transfer the reward information associated with C1 and C2 to the first visual stimuli, A1 and A2, in the SPATs. Stimuli A1 and A2 were not directly paired with the different amount of reward, but if the monkeys could generate the stimulus–reward relation (C with reward amount), and stimulus–stimulus ($A \rightarrow B \rightarrow C$) associations, we could expect them to predict reward amount at the time of the first stimulus presentation of A1 or A2 in a SPAT, just after reward instruction with C1 and C2.

3 Results

3.1 *Perceptual Discrimination Task*

Human fMRI experiment. We were able to show that the striatum (caudate nucleus) and the medial prefrontal cortex (MPFC) are involved in distinct reward predictions. Whereas the caudate activity shows stimulus-based reward prediction, the MPFC activity is consistent with the knowledge-based reward prediction. The activity in the caudate nucleus predicted reward based on the sensory input of cues (direction and coherence of the motion stimuli), irrespective of the subjects' perceptual decision on the motion direction. In contrast, the MPFC seemed to use the output of perceptual decision to predict reward, especially in the low-coherence trials, where the sensory input of the cue stimuli was limited. These results suggest that the striatum generates a stimulus-driven reward value based on the probabilistic relation between stimulus input and reward, whereas the MPFC incorporates the output of the stimulus processes (i.e., the percept), to compensate for weak sensory-dependent prediction by the striatum.

Monkey single unit recording experiment. Midbrain dopamine neurons provide abundant projections to the striatum [5]. In agreement with previous findings [6], dopamine neurons responded to reward-indicative cues (i.e., direction of motion stimuli) and showed reward-predictive activity based on the stimulus-based system [3]. Importantly, dopamine responses in the small-reward error trials are similar to those in the small-reward correct trials, even if perceptual decisions were in the opposite direction, suggesting that dopaminergic responses were not consistent with reward prediction associated with behavioral reports. Rather, dopaminergic responses reflected reward prediction associated with actual motion stimuli. These results suggest that dopaminergic activity reflects external stimulus-based reward prediction, irrespective of the monkey's report. Accordingly, dopaminergic neurons may influence the stimulus-based striatal activity through dopaminergic projections to the striatum.

Our results demonstrate that two distinct systems are differently involved in reward prediction under stimulus ambiguity. The caudate activity reflected reward prediction based on the physical properties of external stimuli in a probabilistic manner. This is consistent with previous studies [7]. Moreover, we found that

dopamine-reward-predictive activity was also based on the motion stimulus itself, but not on behavioral report. Given that the striatum receives massive dopaminergic inputs [5], these subcortical structures collaboratively provide reward prediction on the basis of the external stimulus-based system. Unlike this subcortical circuit, the MPFC activity was correlated with perceptual judgment on motion direction. We observed this feature only for the lower coherence level. This suggests that knowledge-based reward prediction by the MPFC is particularly effective when the external stimulus is weak, or stimulus input is limited. In the context of perceptual decision-making, a previous study has shown that the MPFC holds predictive codes for perceptual categorization [8]. Thus, our results suggest that the MPFC activity supplements limited stimulus information with reward prediction based on perceptual judgment. This would entail that the coding of the MPFC is consistent with the knowledge-based system (single unit study [9] and human fMRI study [10]).

3.2 Reward Inference Task

Our results showed that the monkeys and LPFC neurons discriminated the large reward condition from the small reward condition from the first SPATs [4]. In particular, we found that a group of LPFC neurons predicted reward information specific to a group of relevant visual stimuli that required the same behavioral response (e.g., the A1-group including A1, B1, and C1, and the A2-group including A2, B2, and C2). These neurons responded to each stimulus from the preferred group in the preferred reward condition (large or small), and showed no response to the stimuli from the non-preferred group, irrespective of the reward condition. Thus, these neurons (category-reward neurons) likely coded both the category information of visual stimuli (either the A1 or A2 groups), and reward information (either large or small), simultaneously. The monkeys might group the relevant stimuli according to intended behavior requiring the same matching response, together as a functional category through extensive training with the paired association task. When the monkeys learned that C1 (or C2) was paired with a large reward, category-reward neurons combined the stimulus–reward relation and the category information to relay the reward information to other category members, which would allow the monkeys to predict reward on the basis of A1 (or A2) just after the reward instruction of C1 or C2. Even in the perceptual decision task, LPFC neurons showed categorical coding [11].

The results are consistent with the predictions from the model-based process proposed by Daw et al., which stands on higher order computations that allow simulations to predict outcomes using internal models [12]. Daw et al. also suggest that the striatum codes for stimulus–outcome relations through direct experiences, as a result of a model-free process, which is different from the prefrontal model-based process. To investigate this difference, we simultaneously recorded neural activity from the LPFC and striatum of the third monkey in the reward-instructed

sequential paired association task. We found that many striatal neurons showed reward-predictive activity to the first cue stimuli (A1 and A2), and that the activity was independent of the visual properties of the stimuli (as in the reward neurons studied in [4]). However, careful analysis revealed that the reward neurons in the striatum showed different response patterns when compared to those in the LPFC. After reward instruction with C1 and C2, the striatal neurons showed no differential activity between the large and small reward conditions in the first SPAT. In other words, these neurons were unable to predict the reward based on the first cue stimuli in the first trials, but could do so from the second SPATs. The results suggest that the striatal neurons, unlike the LPFC neurons, cannot transfer reward information associated with C1 and C2 to the first cues, A1 and A2, in the SPATs without direct experience. Therefore, there may be different mechanisms in the LPFC and striatum for reward prediction. Thus, we propose that the LPFC represents the category of a relevant stimulus as knowledge or an internal model, and predicts reward for the stimulus based on its category membership without requiring the direct experience of stimulus-reward associations. Furthermore, the striatum appears to predict reward for stimuli after directly experiencing each stimulus-reward relation.

4 Discussions

Valuation is a key function in decision-making. Variety and organization of valuation systems appear to be essential to decision-making. In this paper, we have suggested, by showing experimental data from our laboratory, that the primate brain has at least two distinct valuation systems that cooperate in one situation but compete in another. One of these systems is a part of the nigro-striatal circuit (the stimulus-based valuation system); and the other, a part of the PFC circuit (the knowledge-based valuation system). The nigro-striatal circuit appears to calculate values based on the empirical and probabilistic relation between an event and the ensuing reward or punishment. On the other hand, the PFC circuit appears to generate reward values in a more elaborate process that applies categorical information and rules to previously experienced association in order to make reward predictions, and thereby enabling an animal to predict the outcome of an inexperienced event. To reach single final decision, the two valuation systems may compete against each other in a certain occasion, but may cooperate in the other. Although some groups have proposed ideas on how the brain integrates values from different valuation systems [13, 14], not much is known about the relationship between these systems.

Acknowledgments Our research was supported by the twenty-first Century Center of Excellence (COE) program (Integrative Human Science Program, Tamagawa University) and the global COE program (Origins of the Social Mind, Tamagawa University) from the Japan Society for Promotion of Science (JSPS), and Grants-in-Aid for Scientific Research on Priority areas from the Ministry of Education, Culture, Sports, Science and Technology, Japan.

References

1. Rangel, A., Camerer, C., Montague, P.R.: A framework for studying the neurobiology of value-based decision-making. *Nat. Rev. Neurosci.* 9 (2008) 545–556
2. Yamamoto, M., Okuda, J., Samejima, K., Sakagami, M.: Differential reward prediction on salient and uncertain perception as revealed by random dot motion stimuli and fMRI. *Soc. Neurosci. Abstr.* (2007) 311.12
3. Nomoto, K., Schultz, W., Watanabe, T., Sakagami, M.: Temporally extended dopamine responses to perceptually demanding reward-predictive stimuli. *J. Neurosci.* 30 (2010) 10692–10702
4. Pan, X., Sawa, K., Tsuda, I., Tsukada, M., Sakagami, M.: Reward prediction based on stimulus categorization in primate lateral prefrontal cortex. *Nat. Neurosci.* 11 (2008) 703–712
5. Haber, S.N.: The primate basal ganglia: parallel and integrative networks. *J. Chem. Neuroanat.* 26 (2003) 317–330
6. Schultz, W., Dayan, P., Montague, P.R.: A neural substrate of prediction and reward. *Science*, 275 (1997) 1593–1599
7. Tobler, P.N., O’Doherty, J.P., Dolan, R.J., Schultz, W.: Reward value coding distinct from risk attitude-related uncertainty coding in human reward systems. *J. Neurophysiol.* 97 (2007) 1621–1632
8. Summerfield, C., Egner, T., Mangels, J., Hirsch, J.: Mistaking a house for a face: neural correlates of misperception in healthy humans. *Cereb. Cortex*, 16 (2006) 500–508
9. Hayden, B.Y., Pearson, J.M., Platt, M.L.: Fictive reward signals in the anterior cingulate cortex. *Science*, 324 (2009) 248–250
10. Yoshida, W., Seymour, B., Friston, K.J., Dolan, R.J.: Neural mechanisms of belief inference during cooperative games. *J. Neurosci.* 30 (2010) 10744–10751
11. Kim, J., Shadlen, M.N.: Neural correlates of a decision in the dorsolateral prefrontal cortex of the macaque. *Nat. Neurosci.* 2 (1999) 176–185
12. Daw, N.D., Niv, Y., Dayan, P.: Uncertainty-based competition between prefrontal and dorsolateral striatal systems for behavioral control. *Nat. Neurosci.* 8 (2005) 1704–1711
13. Behrens, T.E., Hunt, L.T., Rushworth, M.F.: The computation of social behavior. *Science*, 324 (2009) 1160–1164
14. Hare, T.A., Camerer, C.F., Rangel, A.: Self-control in decision-making involves modulation of the vmPFC valuation system. *Science*, 324 (2009) 646–648

Towards Understanding of Neural Dynamics in Communicating Brains

Ichiro Tsuda

Abstract We present a mathematical model to describe interacting processes of model neural networks. A model consists of several subsystems, each of which describes each different function. An overall dynamics of the whole model stems from the interactions between different areas of the brain, influenced by the incoming dynamics of the other brains. In particular, the interactions of slow and fast dynamics through mediating dynamics can create meaning of behavior. One of subsystems is a memory system, where new activity patterns can be learned without destroying all memories by novelty-induced learning. This subsystem can be applied to itinerant behaviors of searching animals such as vicarious try and error (VTE). One of the other subsystems works as a copy-and-identification unit, which is necessary for mimicking the others' behaviors. This unit also provides a model of mirror neuron systems.

1 Introduction

Communication can be characterized from various aspects. In our research project, it is considered to be a process of creating new meaning by the verbal and/or nonverbal interactions of individuals, and then sharing meaning, understanding the other logics and emotions, and sympathizing with others. Each brain is originally isolated in meaning space from others and/ or environment. In spite of this solipsism, an individual tries to adapt to the other meaning space, interprets the signals emitted from such a space, judges in which way one should behave and then actually behaves. This type of adaptation belongs to instinct, and follows the evolutionary principle. Thus, the necessity of communication stems from solipsism of each brain [1].

I. Tsuda (✉)

Research Institute for Electronic Science, Kita-12, Nishi-6, Kita-ku, Sapporo,
Hokkaido 060-0812, Japan

e-mail: tsuda@es.hokudai.ac.jp; tsuda@math.sci.hokudai.ac.jp

Y. Yamaguchi (ed.), *Advances in Cognitive Neurodynamics (III)*,

DOI 10.1007/978-94-007-4792-0_56,

© Springer Science+Business Media Dordrecht 2013

The purpose of our research is to extract a fundamental dynamical system which underlies the neural mechanism for communication, and to analyze its dynamics. There are many important factors of communication. Among others, we are interested in genesis of meaning, symbols and rules from dynamics, namely “creation of new states, while keeping old states.” Consistency in meaning space can be described in low-dimensional phase space. One can describe the transition from an old state of consistency to its new state through chaotic itinerancy [2–7] in high-dimensional phase space. However, in a new stage of dynamics after the transition, an old state of consistency should be kept. This situation is prerequisite for evolution of memory, thinking, and judgment in the communication process. Thus evolutionary dynamics and dynamics by hetero-interactions will provide the necessary mathematical tools for the studies of genesis of meaning and rules, and also hybrid-harnessing systems for the studies of symbol grounding and de-grounding and analog-digital matching. There are at least two levels of mathematical models: a model for intra-brain mechanism for cooperation and entrainment of brain activity by means of say, mirror-neuron systems, and a behavioral model for cooperation via mutual understanding and role sharing.

2 Methods

The model equations which are supposed to describe an overall dynamics of a concerned brain interacting with the other ones are as follows:

$$\tau_s \frac{ds_i}{dt} = G_{\gamma_1} \left(\sum_j k_{ij} s_j + I(x)H(c_i) \right) + eF(s, c) \quad (1)$$

$$\tau_c \frac{dc_i}{dt} = G_{\gamma_2} \left(\sum_j l_{ij} c_j + I(x)H(s_i) \right) + \bar{e}B(s, c) \quad (2)$$

$$I(x) = \sum_{i=1}^n a_i / m^i, \quad \text{if } x \text{ rep. } (a_1, a_2, \dots, a_n), \quad \text{where } a_i = 0, 1, \dots, m-1 \quad (3)$$

$$I(x) = 0, \text{ otherwise}$$

where

$$G_\gamma(z) = (1 + \tanh(\gamma z)) / 2 \quad (4)$$

$$H(s_i) = \sum_j v_{ij} s_j \quad (5)$$

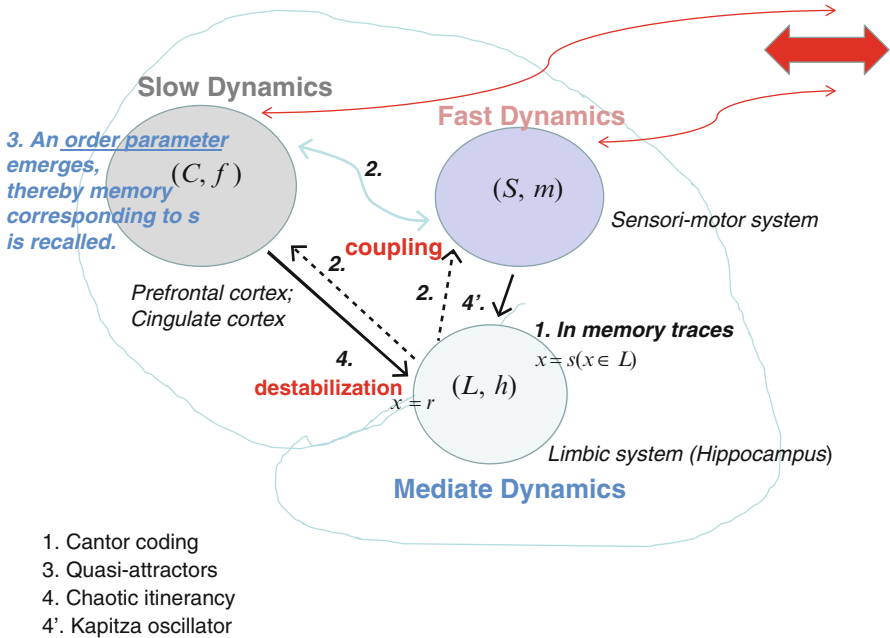


Fig. 1 Schematic drawing of an overall dynamics of the brain which interact with other brains

$$H(c_i) = \sum_j w_{ij} c_j \tag{6}$$

$$\tau_c \gg \tau_s \tag{7}$$

The overall dynamics consists of three special dynamics: fast, slow and mediate dynamics, which are represented by the dynamical variables, s , c , and x , respectively, and obey the dynamical laws, (1), (2), and (3), respectively (See also Fig. 1).

The dynamics proceeds in the following way. We assume Cantor coding [8–12] in memory systems, which act here as a mediate dynamics. The external inputs come from the other interacting brains, which are represented as sensori-motor signals. If the memory state lies in some specific subsets of Cantor set, which means the internal representation of some specific episode, then such a memory state mediates the interactions between fast and slow dynamics. An order parameter emerges in slow dynamics, thereby memory corresponding to the state s is recalled, which is represented by a quasi-attractors such as a Milnor attractor. Then, slow dynamics destabilizes the mediate dynamics, whereby the state changes from the previous s to a new one, say, r , according to its own dynamics. This state change can occur, using chaotic itinerancy or Kapitza oscillators.

3 Results

Within the framework described in Sect. 2, we have investigated several subsystems to clarify the mechanism of communication from nonlinear dynamical systems viewpoint.

In communication, we have to maintain memory associated with continuation of a specific episode, provided that recent own memories are attended and retrieved. How can it be accomplished? We will refer to this system as a subsystem-dynamic memory (DM).

We consider the γ -band of neural activity as the fast dynamics, through which all kinds of sensory information are carried. The slow dynamics is here considered as δ - and θ -bands of activity, thereby the working memory, memory retrievals, and also the process of judgment can be represented. Here, one of the main issues is γ - θ or γ - δ interactions. This system will be here called a subsystem-multiple time scales of interactions (MTSI).

In this subsystem, various interactions such as amplitude-amplitude, phase-phase, and amplitude-phase interactions play a role in creation of information necessary for the emergence of chaotic itinerancy in the slow system. This subsystem also acts for deliberative decision-making [13], which may be related to the behavioral signals like vicarious try-and-error (VTE).

It is well-known that a mirror-neuron system acts in communication. We developed a mathematical model for a mirror-neuron system [14]. A system called a mirror-neuron system [15], which is active for the voluntary movements, becomes active when such voluntary movements are mimicked by others, where several remote areas of the brain interact with each other. It has been highlighted in neuroscience research fields, and been also investigated a detail of its mechanism from the aspect of neuroscience. The mechanism has not, however, been clarified so far. It is expected that a mathematical modeling can provide a promising way to clarify the mechanism. In this circumstance of research, motivated by clarifying the mechanism of mirror-neuron systems, we tried to extract the essence of function of mirror-neuron systems, developed its mathematical model from the aspect of nonlinear dynamical systems, and investigated the dynamical behaviors of the model. This is also a subsystem within our present framework, which is here called a subsystem-mirror-neuron system (MNS). This subsystem works within the slow dynamics.

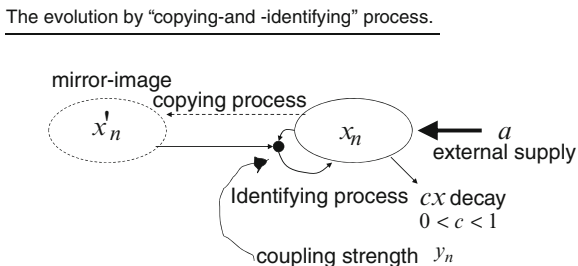
Our model equations are as follows (see also Fig. 2).

$$x_{n+1} = cx_n + bx_n x'_n y_n + a \quad (8)$$

$$y_{n+1} = y_n + dx_n - bx_n x'_n y_n \quad (9)$$

$$x'_{n+1} = f(x'_n, x_n) \quad (10)$$

Fig. 2 The evolution by copying-and-identifying process (See text)



where x is a system’s variable, x' a mirror image of the system, x, y a coupling strength acting for the process of identification of x' with x , c a decay constant, a an external supply, and n a discrete time, namely a step for evolution.

In the model, a mimicking process is supposed to be divided into two processes: a copying and an identifying process, thereby a dynamical model for the mimicking process is developed. We performed the dynamical systems analyses and also conducted its computer simulations. The model shows various interesting phenomena, in particular, a single dynamical orbit in a mimicking process starts to trace various types of bifurcations including period-doubling bifurcations, saddle-node bifurcations, and even Hopf bifurcations. After a while, such an orbit converges to a moving fixed point and eventually to the fixed point, which is an actual and unique fixed point of the system. This final state implies the complete success of mimicking behaviors. In such a way, the present study is successful to represent the potential dynamics of mirror-neuron systems, though the present model does not explicitly contain the typical equations of neurons.

In this identification process, the system x commits or entrusts itself to understand the other’s behaviors by making its mirror-image, x' . The feedback process is assumed to be nonlinear via a new variable representing a feedback gain, y . One can choose a function f , which changes the details of the bifurcations to a final state, but does not change the final state. After itinerant behaviors appear via various bifurcations, the system goes to a fixed point by “entrainment”, that is, $x'_n = x_n$ holds. However, the value of this fixed point moves because identification process still proceeds. Finally, self-identification is established by the appearance of the true fixed point $x' = x$.

4 Discussions

Deliberative decision-making has been investigated within the framework of rats’ T-maze tasks (see, for example, [16]). This has not been observed in a final stage of learning, but observed in the process. Thus, it is plausible to think that deliberation is necessary for understanding an environment. In this respect, deliberation occurs also in communication as an itinerant process that is necessary for understanding

the meaning of others' behaviors. Thus deliberation in communication can be considered to be a hermeneutic process [17, 18] of determining the hypotheses on the meaning of others' behaviors. The relationship between deliberative decision-making and the dynamic process in communication will be studied elsewhere.

Acknowledgments This work was partially supported by a Grant-in-Aid for Scientific Research on Innovative Areas "The study on the neural dynamics for understanding communication in terms of complex hetero systems (No.4103)" (21120002) of The Ministry of Education, Culture, Sports, Science, and Technology, Japan, and also partially supported by HFSP0 (HFSP: RGP0039).

References

1. Freeman, W. J.: *How Brains Make up Their Minds*. (Weidenfeld & Nicolson, London, 1999); Japanese translation is to appear from Sangyo-tocho, 2011.
2. Ikeda, K., Otsuka, K., and Matsumoto, K.: Maxwell-Bloch turbulence, *Progress of Theoretical Physics, Supplement*, 99 (1989) 295–324.
3. Kaneko, K.: Clustering, coding, switching, hierarchical ordering, and control in network of chaotic elements. *Physica D* 41 (1990) 137–172.
4. Tsuda, I.: Chaotic itinerancy as a dynamical basis of Hermeneutics of brain and mind. *World Futures* 32 (1991) 167–185.
5. Tsuda, I.: Dynamic link of memories-chaotic memory map in nonequilibrium neural networks. *Neural Networks* 5 (1992) 313–326.
6. Kaneko, K. and Tsuda, I., eds.: *Focus Issue on Chaotic Itinerancy*. *Chaos* 13 (2003) 926–1164.
7. Tsuda, I.: Hypotheses on the functional roles of chaotic transitory dynamics. *Chaos* 19, 016113 (2009) 1–10.
8. Tsuda, I.: Toward an interpretation of dynamic neural activity in terms of chaotic dynamical systems. *Behavioral and Brain Sciences* 24 (2001) 793–847.
9. Tsuda, I. and Kuroda, S.: Cantor coding in the hippocampus. *Japan J. Indust. Appl. Math.* 18 (2001) 249–258.
10. Fukushima, Y., Tsukada, M., Tsuda, I., Yamaguti, Y., and Kuroda, S.: Cantor-like coding in hippocampal CA1 pyramidal neurons. *Cogn. Neurodyn.* 1 (2007) 305–3167.
11. Kuroda, S., Fukushima, Y., Yamaguti, Y., Tsukada, M., and Tsuda, I.: Iterated function systems in the hippocampal CA1. *Cogn. Neurodyn.* 3 (2009) 205–222.
12. Yamaguti, Y., Kuroda, S., Fukushima, Y., Tsukada, M., and Tsuda, I.: A mathematical model for Cantor coding in the hippocampus. *Neural Networks* 24 (2011) 43–53.
13. Redish, A. D. et al.: HFSP 2010 Deliberative Decision-Making.
14. Kang, H. and Tsuda, I.: Dynamical analysis on copying-and-identifying process: toward the understanding of mirror-neuron systems. Submitted to *Physica D* (2011).
15. Rizzolatti, G. and Craighero, L.: The Mirror-neuron system. *Annu. Rev. Neurosci.* 27 (2004) 169–192.
16. Redish, A. D.: *Beyond the Cognitive Map—from the place cells to episodic memory*. A Bradford Book The MIT Press, Cambridge, Massachusetts, London, England, 1999.
17. Tsuda, I.: A hermeneutic process of the brain. *Prog. Theor. Phys. Suppl.* 79 (1984) 241–259.
18. Erdi, P. and Tsuda, I.: Hermeneutic approach to the brain: Process versus device. *Theoria et Historia Scientiarum* VI(2) (2002) 307–321.

The Organization of Neuronal Discharge on Timescales of Milliseconds and Seconds Is Related to the Spatial Response Properties of Hippocampal Neurons

Eduard Kelemen and André A. Fenton

Abstract According to a widely held view, the neuronal discharge underlying cognition is structured into temporally and functionally organized cell assemblies. What timescale(s) this dynamic organization operates on, is an open question. We analyze the relationship between the timing of the discharge amongst hippocampus neurons and the information they process that is manifest in the spatial response properties of these cells. On timescales of tens of milliseconds and seconds, we observed that the firing of cells with similar response properties is positively correlated, while the firing of cells with distinct response properties is uncorrelated or negatively correlated. Our results show that neuronal discharge is organized on a range of timescales, which may serve distinct functions.

Keywords Place cell • Hippocampus • Neural coordination • Cell assembly • Functional grouping

Place cells are hippocampal neurons in rodents that have spatially tuned activity. The firing rate of a place cell increases when an animal is in a particular location of an environment – called the cell’s firing field, while in other locations of the environment the place cell does not discharge action potentials. Accumulating

E. Kelemen

Department of Physiology and Pharmacology, State University of New York Downstate Medical Center, Brooklyn, NY, USA

A.A. Fenton (✉)

Center for Neural Science, New York University, New York, NY, USA

The Robert F. Furchgott Center for Neural and Behavioral Science, State University of New York Downstate Medical Center, Brooklyn, NY, USA

Department of Physiology and Pharmacology, State University of New York Downstate Medical Center, Brooklyn, NY, USA

e-mail: afenton@nyu.edu

evidence shows that hippocampal place cells process information as organized, coordinated coalitions of cells called cell assemblies [1–3]. There has been a focus on the temporal organization of cell assemblies at the timescale of ~ 40 Hz gamma oscillations, but because the mechanisms of gamma generation are believed to be localized [4], it is doubtful that gamma oscillations can organize neural discharge beyond small regions of tissue [5]. While it remains unknown how cell assemblies organize in time, it is even unclear on what timescales cell assemblies operate. Here we report our novel observations on the temporal organization of hippocampal activity on different timescales.

Theories about information processing in the nervous system suggest that action potentials emitted by neurons that participate in the same representation of information should be coordinated in time [6, 7]. In the hippocampus, the field potential oscillations with frequency of 6–12 Hz (theta rhythm) are implicated in organizing neuronal discharge [8–11], and facilitating activity-dependent synaptic plasticity [12–15]. We studied whether different spatial representations are organized on the physiologically relevant timescale of the hippocampal theta rhythm.

1 Temporal Organization of Activity on the Timescale of the Theta Rhythm

We characterized the temporal organization of hippocampal firing in an active place avoidance task, in which a rat has to retrieve food pellets from the surface of a circular arena, while it is avoiding a 45° shock zone [16]. Cross-correlations of action potentials from pairs of hippocampal pyramidal cells were computed and often showed a tendency of one cell to discharge with a characteristic time delay after another cell (Fig. 1a). The cross-correlation for the same cell pairs was stable across two subsequent recording sessions during the place avoidance task (Fig. 1b).

2 Cells Firing Together on the Theta Timescale Have Similar Response Properties

We studied whether the characteristic timing of cell pair discharge was related to the signal that the cells presumably represent. The cell pairs were divided into two groups based on the preferred phase of modulation in the theta timescale cross-correlogram. One group included those cells that discharged together on the same phase of theta and the other group included cell pairs that fired separately. The similarity between the firing fields of each cell pair was assessed by the correlation of the individual spatial firing rate maps. We observed, that the cell pairs that fired close together in time had more similar firing fields ($t_{50} = 2.78$, $p < 0.01$; Fig. 1c). This observation is consistent with the notion that cells participating in the same representation have a stronger tendency to fire together and cells coding

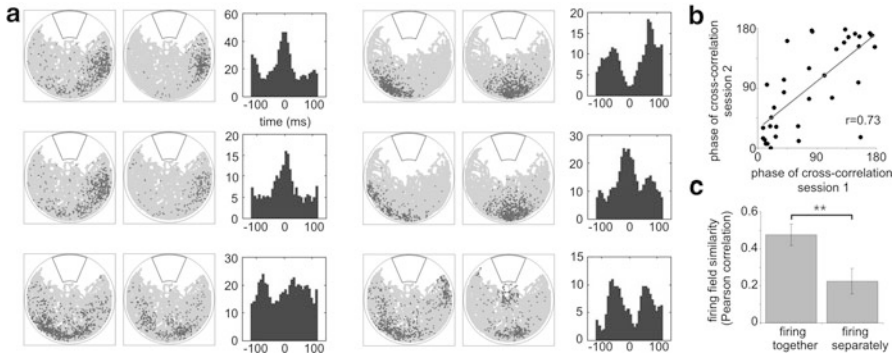


Fig. 1 Organization of place cell firing at the timescale of theta oscillations during a place avoidance task. **(a)** Examples of cross-correlations for pairs of cells are shown together with spike maps of the two cells. Spike maps show the trajectory of the rat in gray and locations of place cell discharge in black. Strong modulation by the theta rhythm is seen for most cell pairs. Some cells discharge close in time, as is indicated by a cross-correlation peak close to zero, other cells discharge with a characteristic time delay. **(b)** The cross-correlation was typical for a cell pair and was preserved between experimental sessions ($r^2 = 0.53$, $p < 0.001$). **(c)** Cells firing closer together in time have more similar firing fields. If the cross-correlation had strong theta modulation and the preferred phase was between 0° and 45° the cells were classified as firing together. If the preferred phase was between 135° and 180° the cells were classified as firing separately. The similarity of firing fields was assessed by correlation of the pair of firing rate maps. The tendency of cells firing together to have more similar firing fields was significant ($t_{50} = 2.78$, $p < 0.01$)

for different mental objects should have firing separated in time [2, 17]. Notice, that in spite of this overall tendency of cells with more overlapping fields to fire together on the theta timescale, cell pairs with similar spatial overlap could have quite different cross-correlation plots (see top two cell pairs in the right column of Fig. 1a). Examples like this strongly suggest that the similarity between firing fields is not the only determinant of temporal coordination of cell activity.

Our previous study revealed that the temporal separation of activity on the timescale of tens of milliseconds could help organize the processing of two different categories of information [18]. In a two-frame place avoidance task the rats had to process two sets of spatial landmarks simultaneously [16]. They were put on a slowly rotating arena (1 rpm) and had to avoid two shock-zones. One shock zone was stationary, defined relative to room landmarks, and the other was rotating, defined relative to arena landmarks. Hippocampal place cells signal the rat's location by discharging in firing fields. During the rotation, about half the cells preferentially signaled the rat's location in the stationary room frame, the other half preferentially signaled the rat's location in the rotating arena frame. Thus for each cell a room or arena spatial frame preference could be defined.

The cross-correlations were analyzed separately for concordant and discordant cell pairs. Concordant cell pairs were pairs of cells that had the same spatial frame preference. Cells with a different spatial frame preference were designated discordant cell pairs. The cells with concordant responses were likely to fire close

together in time. This tendency was not observed in cells with discordant responses. These results indicate that groups of cells with the same frame preference have discharge that is temporally coordinated on the theta timescale [18].

3 Coordination of Discharge at the Timescale of Seconds

Mental phenomena that include selective attention, motor planning, and multistable perception of ambiguous images occur at the timescale of seconds [19, 20]. The modulation of hippocampal activity at this timescale has been documented in prior studies [18, 21–23]. During place avoidance on a stationary arena we analyzed cell pairs with overlapping firing fields. Five-second intervals of data were analyzed, which corresponds approximately to the time it takes a rat to traverse the firing field of a place cell [24]. Intervals were only studied if both cells were expected to fire at least one spike per second during the interval, which is above the average firing rate of hippocampal complex-spike cells.

The first step of our analysis is trivial but preparatory. We observed that the correlation between the firing rates of cells was positively related to the similarity between their firing rate maps ($r = 0.56$, $p < 0.001$, Fig. 2A1). Cells with highly

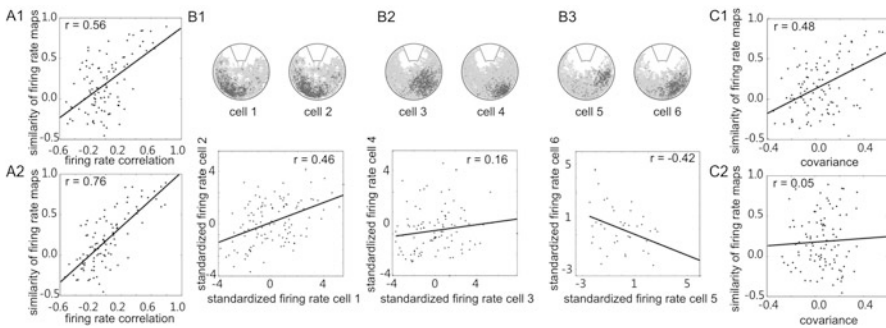


Fig. 2 Characterizing temporal coordination of cell firing on the timescale of seconds. (a) Relationship between firing rate of cells during five-second intervals and the firing field similarity. (A1) The more similar firing fields are, the stronger the correlation in the firing of the two cells. (A2) The same analysis as in A1 was performed using simulated data that preserved the firing rate maps of place cells, but removed any extra-positional temporal organization of firing. (b) Covariance in firing deviations of three example cell pairs. *Cells 1 and 2* had strong positive covariance in firing deviations, when one cell fired more than expected the other cell also had a tendency to fire more than expected. *Cells 3 and 4* had lower covariance in their firing deviations, suggesting they fired independently and the covariance in the firing deviations of *cells 5 and 6* was strongly negative, when *cell 5* fired more than expected, *cell 6* fired less than expected. (c) The relationship between covariance of firing deviations and firing field similarity. (C1) The more similar firing fields were, the higher the covariance of the firing deviations. (C2) The same analysis as in (C1) was performed using simulated data in which the average firing rates and firing field locations of the cells were preserved and any extra-positional temporal organization in their discharge was removed. The covariance in the firing deviations of cells with overlapping fields was no longer present

overlapping firing fields will fire together more often than cells with less overlap. A similar (even stronger) tendency was observed when the same analysis was performed with simulated data ($r=0.76$, $p < 0.001$). In the simulation the firing of a cell during each time interval was determined by the inhomogeneous Poisson process set by the rate at the current location in the firing rate map [24]. Thus the simulation removed any fine temporal organization of discharge that was in the recorded data while preserving the firing rate maps that were observed (Fig. 2A2).

4 Covariance of Firing Deviations in Place cell Firing

Fenton and Muller [24] demonstrated an excess variance in cell discharge during different visits of a rat to the cell's firing field. During one visit to the firing field a cell can discharge many action potentials; while during a different visit with a very similar trajectory the cell may not fire at all. The statistical structure of this overdispersion in place cell discharge was studied by Olypher et al. [18]. We asked whether the excess variance in place cell firing between different visits to a firing field is related for pairs of cells, whether the activity of cells co-varies on the timescale of the seconds it takes the rat to pass through a firing field.

We standardized the firing rates at each time interval by the average firing rate that was characteristic for the rat's locations during that time interval. This standardized firing signifies how much more or less a cell fired during each time interval compared to its expected firing based on the average firing rate at a given location. We asked whether the deviation of firing from the expectation correlates for a pair of cells. If one cell fired more than expected, did the other cell also fire more than expected; and vice versa? Figure 2b shows examples of three pairs of cells with overlapping firing fields. The scatter plots of standardized firing for pairs of cells are shown on the bottom. Each dot on these scatter plots represents a single five-second interval when both cells were expected to discharge at a rate higher than 1 spike/s. We use the term 'covariance of firing deviations' (abbreviated as 'covariance' below) to describe the correlation coefficient that characterizes the tendency for the variability of location-specific discharge to co-vary between a pair of cells.

We studied whether the covariance of firing deviations is related to the similarity between representations coded for by the two cells. We observed that the covariance in the firing deviations of neurons is positively related to the similarity between their firing fields ($r=0.48$, $p < 0.001$, Fig. 2C1). The relationship between the covariance of firing deviations and firing field similarity was not present in the simulated data ($r=0.05$, $p=0.61$, Fig. 2C2) that preserved the location-specific firing rate maps but removed extra-positional temporal organization. These analyses indicate that the relationship between the covariance in firing deviations and firing field similarity is a result of the temporal organization of cell discharge that cannot be directly predicted from the location-specific firing rate maps alone. It supports the notion that place cell ensemble firing is organized in time on the timescale of seconds [23].

Cells with similar average spatial responses tend to fire together, this was observed on the timescale of tens of millisecond and seconds. We studied the relationship between the correlations of cell pair discharge on these two timescales. The time of the cross-correlation peak was related to the covariance of the cell pair's firing deviations ($r = -0.51$); the better the firing of a pair of cells is coordinated on the theta timescale the better the firing is coordinated on the timescale of seconds. This relationship is particularly interesting because by itself, the organization of activity on one timescale cannot explain the organization on the other timescale. The theta-scale organization of firing must be lost when activity is averaged over several seconds; and the organization observed in five-second intervals should provide no prediction about the organization on the timescale of tens of milliseconds. Dragoi and Buzsáki [2] made a somewhat similar observation in rats running on a linear track.

Our analyses provide evidence that the discharge amongst functionally related groups of hippocampal cells is organized in time. We showed that the activity of cells is organized on different timescales and that the temporal coordination of cell discharge is related to the similarity between the response properties of the cells. It remains an open question whether the different timescales of organization of neuronal assemblies serve the same or different functional roles.

Acknowledgments Supported by National Science Foundation grant IOS-0725001; and NIH grant R01MH084038-01.

References

1. Harris KD, Csicsvari J, Hirase H, Dragoi G, Buzsáki G. 2003. Organization of the cell assemblies in the hippocampus. *Nature* 424 (6948): 552–556
2. Dragoi G, Buzsáki G. 2006. Temporal encoding of place sequences by hippocampal cell assemblies. *Neuron* 50: 145–157
3. Fenton AA, Kao HY, Neymotin SA, Olypher A, Vayntrub Y, Lytton WW, Ludvig N. 2008. Unmasking the CA1 ensemble code by exposure to small and large environments: More place cells and multiple, irregularly arranged place fields in the larger space. *J Neurosci.* 28(44): 11250–11262
4. Whittington MA, Traub RD, Jefferys JG. 1995. Synchronized oscillations in interneuron networks driven by metabotropic glutamate receptor activation. *Nature* 373(6515): 612–615
5. Ray S, Maunsell JH. 2011. Differences in gamma frequencies across visual cortex restrict their possible role in computation. *Neuron* 67(5): 885–896
6. Abeles M. 1991. *Corticonics*. Cambridge University Press, Cambridge.
7. Von der Malsburg C. 1981. The correlation theory of brain function. MPI Biophysical Chemistry, internal report 81–82. Reprinted in *Models of neural networks II*. 1994. (E Domany, JL van Hemmen, and K Schulten, eds.) Springer, Berlin
8. Buzsáki G, Eidelberg E. 1983. Phase relations of hippocampal projection cells and interneurons to theta activity in the anesthetized rat. *Brain Res.* 266: 334–339
9. Fox SE, Wolfson S, Ranck JB Jr. 1986. Hippocampal theta rhythm and the firing of neurons in walking and urethane anesthetized rats. *Exp Brain Res.* 62: 495–508

10. O'Keefe J, Recce ML. 1993. Phase relationship between hippocampal place units and the EEG theta rhythm. *Hippocampus*. 3: 317–330
11. Klausberger T, Magill PJ, Márton LF, Roberts JDB, Cobden PM, Buzsáki G, Somogyi P. 2003. Brain-state- and cell-type-specific firing of hippocampal interneurons *in vivo*. *Nature* 421: 844–848
12. Pavlides C, Greenstein YJ, Grudman M, Winson J. 1988. Long-term potentiation in the dentate gyrus is induced preferentially on the positive phase of theta rhythm. *Brain Res.* 439: 383–387
13. Otto T, Eichenbaum H, Wiener SI, Wible CG. 1991. Learning-related patterns of CA1 spike trains parallel stimulation parameters optimal for inducing hippocampal long-term potentiation. *Hippocampus*. 1: 181–192
14. Hölscher C, Anwyl R, Rowan J. 1997. Stimulation on the positive phase of hippocampal theta rhythm induces long-term potentiation that can be depotentiated by stimulation on the negative phase in area CA1 *in vivo*. *J Neurosci*. 17: 6470–6477
15. Hyman JM, Wyble BP, Goyal V, Rossi CA, Hasselmo ME. 2003. Stimulation in hippocampal region CA1 in behaving rats yields long-term potentiation when delivered to the peak of theta and long-term depression when delivered to the trough. *J Neurosci*. 23: 11725–11731
16. Fenton AA, Wesierska M, Kaminsky Y, Bures J. 1998. Both here and there: simultaneous expression of autonomous spatial memories in rats. *PNAS USA* 95(19): 11493–11498
17. Itskov V, Pastalkova E, Mizuseki K, Buzsaki G, Harris KD. 2008. Theta-mediated dynamics of spatial information in hippocampus. *J Neurosci*. 28(23): 5959–5964
18. Kelemen E, Fenton AA. 2010. Dynamic grouping of hippocampal neural activity during cognitive control of two spatial frames. *PLoS Biology*. 8(6): e1000403 doi:[10.1371/journal.pbio.1000403](https://doi.org/10.1371/journal.pbio.1000403)
19. Struber D, Basar-Eroglu C, Hoff E, Stadler M. 2000. Reversal-rate dependent differences in the EEG gamma-band during multistable visual perception. *Int J Psychophysiol*, 38: 243–252
20. Nakatani H, van Leeuwen C. 2005. Individual differences in perceptual switching rates; the role of occipital alpha and frontal theta band activity. *Biol Cybernetics*. 93:343–354
21. Olypher AV, Lánský P, Fenton AA. 2002. Properties of extra-positional signal in hippocampal place cell discharge derived from the overdispersion in location-specific firing. *Neurosci*. 111: 553–566
22. Jackson J, Redish AD. 2007. Network dynamics of hippocampal cell-assemblies resemble multiple spatial maps within single tasks. *Hippocampus* 17: 1209–1229
23. Fenton AA, Lytton WW, Barry JM, Lenck-Santini PP, Zinyuk LE, Kubík Š, Bureš J, Poucet B, Muller RU, Olypher AV. 2010. Attention-like modulation of hippocampus place cell discharge. *J Neurosci*. 30(13): 4613–25
24. Fenton AA, Muller RU. 1998. Place cell discharge is extremely variable during individual passes of the rat through the firing field. *PNAS USA*. 95(6): 3182–3187

An Animal Model of Decision Making: Vicarious Trial-and-Error in Tasks Requiring Memory for Visual Associations or Spatial Locations

Paul A. Dudchenko, David Bett, Elizabeth Allison, Karola Kaefer,
and Emma R. Wood

Abstract To assess the neural substrates of deliberative decision-making, it is useful to have a tractable animal model of this cognitive process. In this chapter we describe one potential marker of deliberative decision making in rodents: the back-and-forth head movements of the animal as it makes a decision, also referred to as vicarious trial-and-errors (VTEs). We quantify these in a spatial reversal task and a visual discrimination task, and observe that they exhibit different patterns in these tasks. This result indicates that there may be at least two types of VTEs: exploratory and deliberative.

Keywords Decision-making • Learning • Vicarious trial-and-error

1 Introduction

In the hippocampus, individual principal neurons often show firing that is tuned to a specific location in the animal's environment [1]. Recent work has revealed that the firing of these neurons, referred to as place cells in the rodent, can also anticipate future destinations at a critical junction on a maze [2], or at the start of the maze [3]. In the former experiment, this anticipatory neural activity was related to a back-and-forth movement of the rat's head. Such activity may be a behavioural index of deliberative decision-making. To substantiate this, and as a first step in assessing the

P.A. Dudchenko (✉) • D. Bett
Psychology, School of Natural Sciences, University of Stirling, Stirling, UK

Centre for Cognitive and Neural Systems, University of Edinburgh, Edinburgh, UK
e-mail: p.a.dudchenko@stir.ac.uk

E. Allison • K. Kaefer • E.R. Wood
Centre for Cognitive and Neural Systems, University of Edinburgh, Edinburgh, UK

neural substrates of decision making, we sought to identify memory tasks in which this back-and-forth head movement could be observed.

Although the neural substrates of decision-making are of current experimental interest, the behaviours associated with animal choice have been described in several early studies. For example, Robert Yerkes in his 1907 work, *The Dancing Mouse* [4], described a hesitant, back-and-forth movement of the mouse as it faces a choice between two doorways. One doorway led to a chamber in which the mouse would receive a shock, while the other led to a passageway that would take the animal to a nest site with food. Experiencing the shock caused the mouse

... to hesitate before the entrances to the boxes, to run from one to the other, poking its head into each and peering about cautiously, touching the cardboards at the entrances, apparently smelling of them, and in every way attempting to determine which box could be entered safely. I have at times seen a mouse run from one entrance to the other twenty times before making its choice; now and then it would start to enter one and, when halfway in, draw back as if it had been shocked. (pg. 130)

In rats, back-and-forth movement of the head at a decision point was described by Meunzinger [5], Tolman [6], and others (for reviews see [7–10]). Meunzinger termed this behaviour “vicarious trial-and-error”. Since the 1950s, vicarious trial-and-error (VTE) has received only sporadic attention (e.g., [11–14]). The purpose of the current experiments was to see whether VTE behaviour occurred robustly in a visual discrimination task and in a spatial memory task, and to relate this behaviour to learning.

2 Experiment 1: Visual Task VTEs

2.1 Method

Eight Lister Hooded rats were trained on a black-white visual discrimination task, as illustrated in Fig. 1. The apparatus comprised of three black boxes (each 52 cm high, 49 cm wide). One box served as the start box, and it contained two doorways, one covered with a white curtain and one with a black curtain, each leading to another

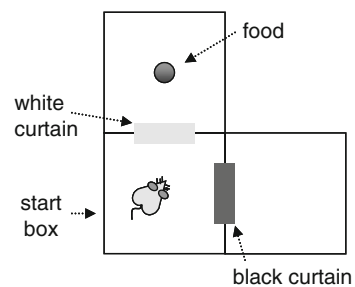


Fig. 1 Schematic of the visual discrimination task

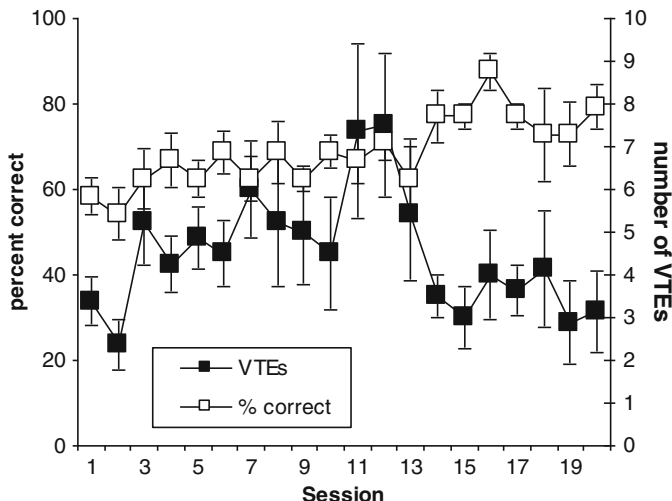


Fig. 2 Percent correct (*left axis*) and VTEs (*right axis*) during acquisition of the visual discrimination task

box. For half of the rats, a food bowl was located in the box behind the white curtain; for the other half, the food bowl was found in the box behind the black curtain. For each session, the positions of the black curtained box and the white curtained box were switched.

Rats received six trials per session. After being placed in the start box, a choice was recorded if the animal moved its head through a curtain. If the animal entered the box containing the food (Weetos chocolate cereal loops), it was allowed to eat for 10 s. If the rat chose the empty box, it was permitted to explore the box for 10 s, and was then replaced in the holding bucket.

In addition to the choices made by the animals, we recorded their behaviour prior to making a choice. Rats often oriented towards one curtain (A) and then turned to face the other curtain (B). In agreement with Goss and Wischner [9], we counted these A-B or B-A shifts as VTEs.

2.2 Results and Discussion

Over 20 sessions of training, the rats learned to select the curtained doorway that led to the food (Fig. 2). In the first 12 sessions, VTE behaviour increased. Thereafter, even though performance continued to improve, the number of VTEs decreased.

These observations were borne out statistically. Across sessions, there was a significant increase in the percentage of responses to the correct curtain (linear trend: $F(1,7) = 9.9$, $p < 0.016$). For VTEs, the increase followed by a decrease across sessions approached, but did not reach, significance ($F(19,114) = 1.62$, $p = .063$).

These results confirm the patterns of findings that Tolman [6] obtained in work with a jumping stand. In both the current results and Tolman's study, VTEs appeared to increase during learning, but as the discrimination was acquired, this behaviour became less prevalent. It is possible that, as Tolman [10] suggested, VTE behaviour aids learning. However, the current findings only show the concomitant changes over sessions; it remains possible that learning and VTE behaviour are independent.

3 Experiment 2: Spatial Task VTEs

Our ultimate interest is in the neural substrates of decision-making, and thus we wished to assess VTE behaviour in a task known to require the hippocampus. To that end, we chose a spatial reversal task which requires the hippocampus [15], and in which hippocampal place cells show anticipatory firing [3].

Early work by Jackson [16] suggested that VTEs served different roles in different tasks. He argued that in a visual discrimination task, like the one described in Experiment 1, VTEs contribute to learning because both VTEs and correct responding increase together. However, in a spatial maze task, they reflect the rat's uncertainty, as VTEs decrease while performance increases.

Thus, the aim of the current experiment was to see whether robust VTEs are observed in a spatial task, and, if so, to see whether they differ from those seen in the previous experiment.

3.1 Method

Five Lister hooded rats, different from those used in Experiment 1, were used in this experiment. These rats were participants in a larger, ongoing experiment (to be reported elsewhere), and thus received sham lesions. They were first trained to find the single reward location on an elevated double-Y maze (Fig. 3). The reward, chocolate cereal loops, was located in a bowl in one of the four terminal goal boxes. The other three goal boxes likewise contained a bowl, but no reward.

In this initial version of the task, alleyways connected the terminal goal boxes to the nearest choice point. The rat's task was to move from the start box to one

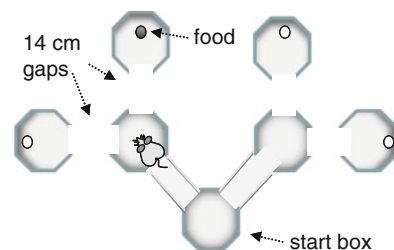


Fig. 3 Schematic of the spatial memory task. To obtain food, rats had to move from the start box to one of the two choice points, and then jump to one of the goal boxes

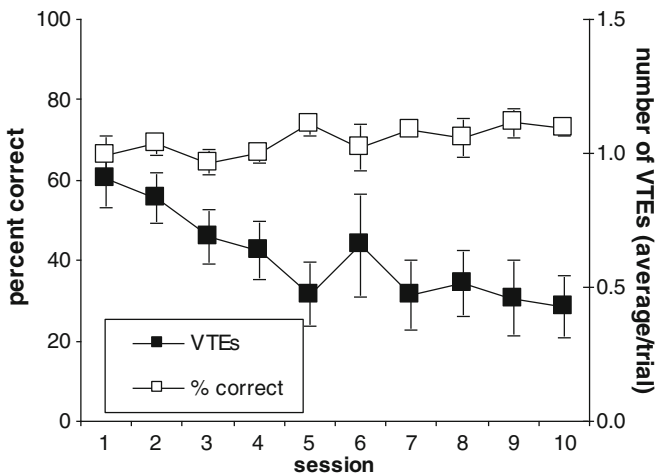


Fig. 4 Percent correct (*left axis*) and VTEs (*right axis*) during the spatial memory task

of the goal boxes. If it selected the correct box it was permitted to consume the loops for ~ 10 s before being removed by the experimenter. If the animal chose an unrewarded goal box, it was confined to the box with a wooden barrier for ~ 10 s before being removed by the experimenter.

Once the reward was found, the rat received nine more trials with food in the same goal box. The food was then moved to a different goal box, and the process was repeated. The location of the reward was changed in this way up to two times in a daily session, and rats were trained until they chose the reinforced box on 80% of the trials following the discovery of the reward on two consecutive days.

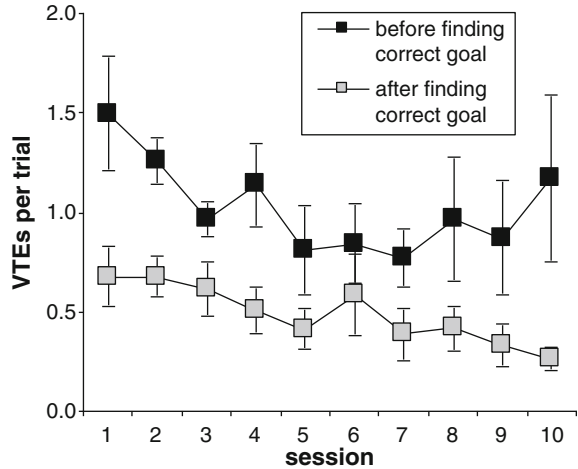
After this initial training, rats received sham lesions. After a recovery period, the rats were returned to the maze. To encourage VTE behaviour, the alleyways between the last decision point and the goal boxes were removed. Thus the rat had to make a short jump over a 14 cm gap to get to the goal boxes. The data we present are from the first ten sessions with these gaps.

3.2 Results

On the spatial task, rats selected the correct location readily, even from the first session with the gaps (Fig. 4). Their performance was at or around 70% correct across sessions, and this high level was likely due to their initial training on the task rule prior to the introduction of the gaps. As evident in Fig. 4, performance did not differ across sessions ($F(9,36) = 1.2, p = .33$).

VTE behaviour, in contrast, showed a significant decrease over sessions ($F(9,36) = 2.18, p < 0.05$). We also looked at the average number of VTEs before the animal found the rewarded goal box, and the average number of VTEs on

Fig. 5 Rats exhibited more VTEs on trials before they discovered the location of the food, compared to trials after they had found the food



trials after the rat found the goal box. As is evident in Fig. 5, the rats showed a significantly higher number of VTEs on the trials prior to locating the rewarded goal box compared to the trials after they'd found the food (which, for the most part, consisted of returns to the correct goal box) ($F(1,4) = 15.17$, $p < 0.02$).

4 General Discussion

In this chapter we describe two situations in which vicarious trial-and-error behaviour, the back and forth movement of rats at a decision point, is observed. On a black-white visual discrimination, VTE behaviour appeared to increase as the animal acquired the discrimination, and then decreased. On the spatial memory task, VTEing decreased across sessions. In this task, more VTEs were observed on trials before the animal found the rewarded goal box, compared to the trials after it had found the food.

Previous work has suggested that VTEs in a visual discrimination are associated with learning, while VTEs in a spatial task reflect the animal's uncertainty at a choice point [16, 17]. Our results do not clearly endorse either of these interpretations. We found that VTEs decreased when the accuracy of performance continued to increase (in the later sessions of the visual discrimination), but they also decreased when performance was stable (in the spatial switching task). This raises the possibility that VTEs are not directly related to performance, but instead occur when aspects of the environment, like the black and white curtains, or the gaps in the Y-maze, are unfamiliar.

In closing, we speculate animals may exhibit VTE behaviour for different reasons at different points in the acquisition and performance of a decision task. During acquisition, animals may exhibit *exploratory* VTEs, which may, nonetheless, be

centred at decision points. These decrease as the environment and its contingencies become familiar. Later in training, when the environment is familiar but the animal is faced with a difficult discrimination or a change in the reinforcement contingencies, it may exhibit *deliberative* VTEs, a reflection of the anticipation of alternatives. This distinction may be supported by the greater amount of VTEing observed in the spatial task on trials before the rat finds the food, compared to trials after it has found the food. After identifying this location, deliberation is no longer necessary, and the rat simply returns to the correct location repeatedly until the reward location is changed.

Acknowledgements This work was supported by a grant from the Human Frontiers Science Program (HFSP; grant: RGP0039/2010).

References

1. O'Keefe J (1976) Place units in the hippocampus of the freely moving rat. *Experimental Neurology*, 51: 78–109.
2. Johnson A and Redish AD (2007). Neural ensembles in CA3 transiently encode paths forward of the animal at a decision point. *Journal of Neuroscience*, 27, 12176–12189.
3. Ainge JA, Tamosiunaite M, Woergoetter F, Dudchenko PA (2007) Hippocampal CA1 place cells encode intended destination on a maze with multiple choice points. *Journal of Neuroscience*, 27, 9769–9779.
4. Yerkes YM (1907) *The Dancing Mouse* The Macmillan Company: New York
5. Meunzinger KF (1938) Vicarious trial and error at a point of choice. I. A general survey of its relation to learning efficiency. *Journal of Genetic Psychology*, 53: 75–86.
6. Tolman EC (1939) Prediction of vicarious trial and error by means of the schematic sowbug. *Psychological Review*, 39: 318–336.
7. Taylor JG, Reichlin B (1951) Vicarious trial and error. *Psychological Review*, 58(6): 389–402.
8. Meunzinger KF (1956) On the origin and early use of the term vicarious trial and error (VTE). *Psychological Bulletin*, 53(6): 493–494.
9. Goss AE, Wischner GJ (1956) Vicarious trial and error and related behaviour. *Psychological Bulletin*, 53(1): 35–53.
10. Tolman EC (1938). The determiners of behavior at a choice point. *Psychological Review*, 45, 1–41.
11. Kemble ED, Beckman GJ (1970) Vicarious trial and error following amygdaloid lesions in rats. *Neuropsychologia*, 8: 161–169.
12. Amsel A (1993) Hippocampal function in the rat: cognitive mapping or vicarious trial and error? *Hippocampus*, 3: 251–256.
13. Hu G, Amsel A (1995) A simple test of the vicarious trial-and-error hypothesis of hippocampal function. *Proceedings of the National Academy of Sciences USA*, 92: 5506–5509.
14. Bimonte HA, Dennenber VH (2000) Sex differences in vicarious trial-and-error behaviour during radial arm maze learning. *Physiology and Behavior*, 68(4): 495–499.
15. Stevenson C (2010) Investigating the role of the hippocampal formation in episodic and spatial memory. Ph.D. thesis, Biomedical Sciences, University of Edinburgh.
16. Jackson LL (1943) VTE on an elevated T-maze. *Journal of Comparative Psychology*, 36(2): 99–107.
17. Tolman EC, Ritchie BF (1943) Correlation between VTE's on a maze and on a visual discrimination apparatus. *Journal of Comparative Psychology*, 36(2): 91–98.

Correlated Brain Activations During Formation of Memory for Future Plans

Jiro Okuda, Maki Suzuki, and Toshikatsu Fujii

Abstract We used functional magnetic resonance imaging (fMRI) and performed trial-by-trial activity correlation analyses to examine behavioral significance of regional correlations of brain activities during formation of memory for future action plans. Activities in several brain regions during formation of future action plans could differentiate performances of remembering the plans in a later retrieval phase. Among these, activity in the ventromedial prefrontal area showed significant correlations with that in the medial temporal and sensory areas according to later performances of remembering the plans, suggesting functional significance of activity correlations across specific brain regions during formation of robust memory for future plans.

Keywords Prospective memory • Memory formation • Regional correlation • Ventromedial prefrontal cortex • Medial temporal lobe

1 Introduction

Forming, maintaining, and remembering future action plans (termed collectively as “prospective memory” [1–3]) are fundamental cognitive activities supporting our normal daily life. Accumulating studies suggest that processes involved in this kind of memory for future plans is supported by the functioning of multiple brain areas including medial temporal memory systems and frontal executive systems.

J. Okuda (✉) • M. Suzuki
Faculty of Computer Science and Engineering, Khoyama Centre for Neuroscience,
Kyoto Sangyo University, Kamigamo Motoyama, Kita-ku, Kyoto 603-8555, Japan
e-mail: jokuda@cc.kyoto-su.ac.jp

T. Fujii
Kansei Fukushi Research Institute, Tohoku Fukushi University, 6-149-1 Kunimigaoka,
Aoba-ku, Sendai 981-8522, Japan

For example, functional neuroimaging studies using positron emission tomography (PET) and functional magnetic resonance imaging (fMRI) have consistently identified activations in lateral and medial prefrontal cortices covering Brodmann's area (BA) 10 [4–8], as well as that in medial temporal lobe (MTL) structures [4], while human subjects were required to maintain and remember to perform specific action plans during any other ongoing tasks unrelated to the plans. A more recent study investigating formation of prospective memory has indicated that magnitude of activations in the frontal and MTL regions during formation of memory for future plans potentially predict later performances of remembering the plans [9]. While these studies are useful in identifying brain systems participating in prospective memory processes, however, a question remains about the way how these multiple brain systems interact and communicate with each other to form, store, and later remember the future plan.

A growing body of recent studies on brain's functional connectivity has gradually disclosed that context-dependent correlations across distinct brain areas are related to effective functioning of our cognitive systems [10]. Taking advantage of recent development of sophisticated signal decomposition methods applicable to fMRI data, these studies have demonstrated, for instance, that changes in activity correlations among regions within the frontal executive systems reflect proactive preparation for subsequent task performances [10], or that trial-by-trial correlations between the frontal areas and posterior sensory areas were related to successful detection and resolution of sensori-motor conflicts during a Stroop interference task [11]. Despite such increasing attempts in the domain of cognitive control, however, no studies have yet examined functional significance of correlation of activities across multiple brain regions supporting prospective memory processes.

In the present study, we explored cross-areal correlations of brain activities during formation of future action plans. Specifically, we examined whether activity correlations across specific brain regions during the plan formation were related to later performances of remembering the plans.

2 Methods

To examine a series of processes involved in memory for future plans under a laboratory situation, we developed a behavioral task in which subjects were asked to make specific action plans to visual stimuli (a planning phase) and to spontaneously retrieve and perform the planned action after a delay (a retrieval phase). Twenty-five healthy volunteers (13 males, mean age 23.0 years old) participated in the study after giving informed consent.

During the planning phase, the subjects were presented with a picture (a natural scene of flowers or animals, a manmade tools, building, or vehicles) for 4 s in each trial, followed by a plan-for-action cue (a red question mark) on the picture for 4 s (Fig. 1a). The subjects held a joystick with their left hand, and were asked to

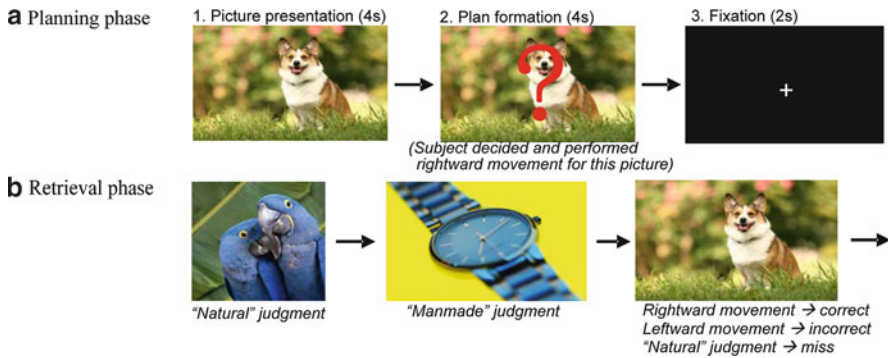


Fig. 1 Schematic illustration of task procedures. **(a)** A sequence of one trial in a planning phase. Subjects were presented with picture stimuli to which they determined and performed joystick movements (left, right, up, or down; rightward for this example) in response to presentation of a plan-for-action cue (*a question mark*). **(b)** In a retrieval phase, subjects continuously made manmade or natural judgments about presented pictures. Upon occasional presentation of specific pictures to which they had determined the action plan of joystick movement in the planning phase, they had to spontaneously remember and carry out the planned joystick movement instead of the manmade or natural judgment. The same joystick movement that the subjects had planned and performed in the planning phase was classified as “correct”. A different movement from that of the planning phase was classified as “incorrect”. No joystick movement to the specific picture was classified as “miss”

determine a left-hand movement (joystick control toward the right, left, up, or down) to each picture stimulus. As soon as they decided the movement, they carried out it so that the experimenter could record the decided direction. The subjects were also told to memorize an action plan of the joystick movement to the picture so that they could remember and carry out it if they would encounter that particular picture in later part of the experiment. A total of 24 pictures were presented.

In the retrieval phase after approximately 20-min delay, the subjects were presented with a series of pictures about which they made manmade or natural judgments by a button press with their right hand (Fig. 1b). In addition, they were also asked to spontaneously retrieve and perform planned joystick movement with their left hand upon occasional appearance of specific pictures presented in the planning phase. The task was subject-paced without any feedback on each response. The specific pictures were presented approximately every 28 pictures.

We classified subjects’ actions of the joystick movement into three categories: (1) “correct”, when the subjects carried out the same movement as they planned in the planning phase, (2) “incorrect”, when they carried out a movement that they did not plan, and (3) “miss”, when they did not move the joystick.

We used fMRI (1.5T Siemens Sonata) to scan subjects’ brain activity during the planning phase. In the fMRI data analyses, we adopted a trial-by-trial event-related hemodynamic modeling procedure [12] that allowed us to estimate separate effect size data (a statistical measure approximating magnitude of brain activations) for each individual event in each individual trial for each individual subject. In the first

level analysis for each individual subject, we separately modeled fMRI activations at picture presentation (i.e., a preparation period just before plan formation) and at the plan-for-action cue (plan formation period) on a trial-by-trial basis.

In the second level, random effect analyses treating each subject data from the first level analyses as a random sample, we constructed a general linear model (GLM) that consisted of contrast images corresponding to average of each later correctly remembered, incorrectly remembered, and missed plan, separately for picture presentation and plan formation period. In this GLM, we examined brain regions whose activities could differentiate later correct, incorrect, and missed retrieval of the plans by using appropriate linear contrasts across the trial categories (e.g., later correctly remembered plans minus later missed ones). Significance level was set $P < 0.001$, uncorrected for multiple comparison.

After identifying the regions differentiating the three trial categories according to the later retrieval performances, we calculated voxel-by-voxel correlation matrices (Pearson's correlation coefficient, r) of the effect sizes (drawn from each event-related, single-trial contrast image in the first level analyses) across these regions, separately for each category of later performances of remembering the plans. By using Fisher's r -to- z transformation, we compared correlation coefficients across the three categories, and examined the voxel pairs that showed differential correlations between the categories (e.g., significantly higher correlations for later correctly remembered plans than for missed ones, $P < 0.05$).

3 Results

Across subjects, mean percentage of the correct, incorrect, and miss responses to specific pictures at the retrieval phase were 43.9%, 15.4%, and 40.7%, respectively.

A number of brain regions were identified whose activities during the planning phase differed across three categories of later performances of remembering the plans. For the plan formation period (at the time of the plan-for-action cue), significantly greater activation for later correctly remembered plans (hereafter described as "later-correct") than for later missed ones ("later-miss") was found in the right parahippocampal gyrus (peak MNI coordinates and Z -score; $x = 33$, $y = -30$, $z = -24$, $Z = 3.53$, Fig. 2a). This region also showed greater activation for later incorrectly remembered plans ("later-incorrect") than for the "later-miss" ($x = 33$, $y = -33$, $z = -24$, $Z = 3.20$). Extensive areas covering bilateral visual cortices showed greater activations for the "later-incorrect" than for the "later-correct" and "later-miss". On the other hand, activity in the ventromedial prefrontal (subcallosal) area ($x = 3$, $y = 15$, $z = -12$, $Z = 3.29$, Fig. 2b) was significantly decreased for the "later -incorrect" relative to the "later-miss".

For the picture presentation period just before the plan formation, the ventromedial prefrontal area revealed exactly opposite activation pattern to that for the plan formation period; greater activation for the "later-incorrect" relative to the

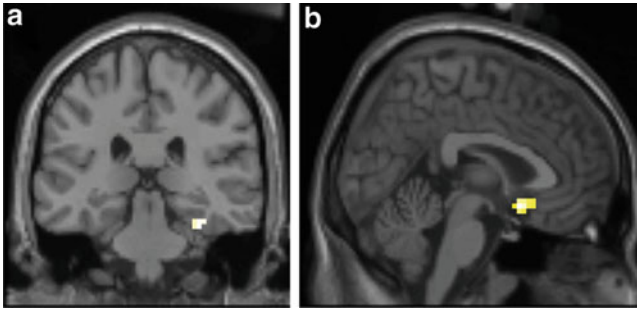


Fig. 2 Brain areas whose activities during the plan formation period differentiated performances of later remembering of the plans. **(a)** Right parahippocampal gyrus showing greater activations for the later correctly remembered plans than for the later missed ones. **(b)** Ventromedial prefrontal area showing decreased activity for the later incorrectly remembered plans relative to the later missed ones

“later-miss” ($x = 3, y = 12, z = -12, Z = 4.52$) and “later-correct” ($x = 3, y = 15, z = -12, Z = 3.96$). In a similar manner, bilateral visual cortices showed a reversed pattern of activation to that for plan formation period; decreased activity for the “later -incorrect” relative to the “later-miss” and “later-correct”.

Further correlation analyses revealed that activity correlation between the ventromedial prefrontal and the visual areas was significantly negative for the “later-incorrect” plans as compared to the “later-correct” ones, during both the picture presentation and plan formation periods. We also found a significant negative correlation specific to the “later-incorrect” plans between the ventromedial prefrontal and MTL activities only during the picture presentation period.

4 Discussions

The present results revealed that activation levels in multiple brain regions including ventromedial prefrontal, medial temporal, and sensory areas during formation of memory for future action plans could differentiate later performances of remembering the plans. In addition to this finding, the later performances of remembering the plans were related to characteristic regional correlation patterns during the task, suggesting possible roles of activity correlations, as well as the activation levels themselves, in signifying successful formation of the future action plans. In particular, activity correlation between the ventromedial prefrontal area and other areas (the MTL and visual areas) showed differential patterns during the course of the planning task. Therefore, multiple networks that commonly involve the ventromedial prefrontal area may play specific roles in multiple processes underlying formation of robust memories of future action plans.

Acknowledgments This study was supported by Grant-in-Aid for Scientific Research on Innovative Areas (The study on the neural dynamics for understanding communication in terms of complex hetero systems), MEXT, Japan.

References

1. Meacham, J.A., Singer, J.: Incentive effects in prospective remembering. *J. Psychol.* 97 (1977) 191–197
2. Dalla Barba, G.: Prospective memory: a ‘new’ memory system? In F. Boller, J. Grafman (Eds.), *Handbook of Neuropsychology*, Amsterdam: Elsevier Science (1989) pp. 239–251
3. Brandimonte, M., Einstein, G.O., McDaniel, M.A.: *Prospective Memory: Theory and Applications*. Mahaw, New Jersey: Lawrence Erlbaum Associates (1996)
4. Okuda, J., Fujii, T., Yamadori, A., Kawashima, R., Tsukiura, T., Fukatsu, R., et al.: Participation of the prefrontal cortices in prospective memory: evidence from a PET study in humans. *Neurosci. Letters* 253 (1998) 127–130
5. Burgess, P.W., Quayle, A., Frith, C.D.: Brain regions involved in prospective memory as determined by positron emission tomography. *Neuropsychologia* 39 (2001) 545–555
6. Burgess, P.W., Scott, S.K., Frith, C.D.: The role of the rostral frontal cortex (area 10) in prospective memory: a lateral versus medial dissociation. *Neuropsychologia* 41 (2003) 906–918
7. Okuda, J., Fujii, T., Ohtake, H., Tsukiura, T., Yamadori, A., Frith, C.D., Burgess, P.W.: Differential involvement of regions of rostral prefrontal cortex (Brodmann area 10) in time- and event-based prospective memory. *Int. J. Psychophysiol.* 64 (2007) 233–246
8. Okuda, J., Gilbert, S.J., Burgess, P.W., Frith, C.D., Simons, J.S.: Looking to the future: automatic regulation of attention between current performance and future plans. *Neuropsychologia* 49 (2011) 2258–2271
9. Poppenk, J., Moscovitch, M., McIntosh, A.R., Ozcelik, E., Craik, F.I.M.: Encoding the future: successful processing of intentions engages predictive brain networks. *NeuroImage* 49 (2010) 905–913.
10. Sakai, K., Passingham, R.E.: Prefrontal interactions reflect future task operations. *Nat. Neurosci.* 6 (2003) 75–81
11. Morishima, Y., Okuda, J., Sakai, K.: Reactive mechanism of cognitive control system. *Cer. Cortex* 20 (2010) 2675–2683
12. Rissman, J., Gazzaley, A., D’Esposito, M.: Measuring functional connectivity during distinct stages of a cognitive task. *NeuroImage* 23 (2004) 752–763

Cognitive Modeling of Human-Robot Interaction Estimating Other's Internal State

Takashi Omori, Ayami Yokoyama, Kasumi Abe, and Takayuki Nagai

Abstract Various types of action decision strategy are used to realize a smooth interaction with others. We can estimate intention of others and determine own action accordingly, or can induce intention and actions of others' as we intend. In this study, a computational model of the action decision has been constructed based on an intention estimation of others and is evaluated its effectiveness by 'a robot-child play' experiment. For the model construction, the human adult behavior in the game play with child has been analyzed.. As a result, a necessity of "Meta-strategy" such as a choice of action decision strategy is suggested.

Keywords Mental state • Estimation • Model • Action decision • Robot-child play

1 Introduction

Communication is a result of interaction between one's self and others, and includes a dynamic brain processes which includes an observation of other's behavior as well as an estimation of other's intention from the observation result [1]. The analysis and modeling of the process is important for a computational understanding of the brain dynamics underlining communicative interaction.

In our previous study, a computational model of collaborative action decision process between two subjective agents had been constructed. In the model, we

T. Omori (✉) • A. Yokoyama
Brain Science Institute, Tamagawa University, 6-1-1, Tamagawagakuen, Machida-shi, Tokyo
194-8610, Japan
e-mail: omori@lab.tamagawa.ac.jp

K. Abe • T. Nagai
Graduate School of Informatics and Engineering, The University of Electro Communications,
1-5-1 Chofugaoka, Chofu-shi 182-8585, Japan

assumed different strategies of Level.0, 1, 2 and Level.0* for the depth of intention estimation, found necessity of a meta-strategy that manages a strategy change to adapt other's strategy, and established a method of human behavior analysis based on the model[2]. However, it is not yet clear on how the human strategies appear in real scenes and what information become to be the key to cause the change of the strategies. In this study, we aim a computational modeling of more realistic human interaction scene through a play experiment between a child and an adult.

2 Model of Action Decision Based on the Estimation of Other's Intention

2.1 Computational Principle of Intention Estimation

During the play with fickle children, we observe their behavior and try various interaction methods or plays to keep their enjoying state. In the process of activity above, we estimate internal state of children [3] and predict effects of own action repertoires on them, then choose an action, such as praising, talking or proposing a new game, to keep their interest. It is obvious that a model of child is necessary in order to predict the effect of our action. But not limited to the model of child, there are plenty of factors that affect performance of the interaction. The clarification of those factors is a key for understanding human communication. But in real interaction scene, the interaction between adults is too complex. So in this study, we focus on a play between a child and an adult as we expect the process to be much simpler.

In order to understand the brain dynamics of communication in wider situations, the computational modeling is a method. For the basic model of human-human interaction, we assume an existence of the model of other in our mind. Current question lies on how the model is made of use in the realistic interactive scenes?

Figure 1 shows the basic assumption of our study. We assume that every human behavior can be described by a triad of a state of the moment s , an action a of the moment and an internal state G , the intention or goal, of the person. When a relation of the three parameters is expressed by a combinative probability $P(s, a, G)$, we are

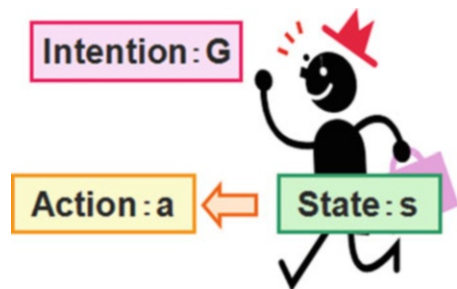


Fig. 1 Human behavior can be expressed by a triad of State, Action and Intention $P(s, a, G)$

able to estimate one of the parameters from other two. Thus, we can estimate other's intention G_o when we observe a state s_o and an action a_o of the person. This is the computational principle of the intention estimation.

2.2 Estimation Level of Action Decision

On the other hand, we consider an intention of self G_s at first in the active strategy, and search for an action a_s that can be most easily observed by the other agent referring to the knowledge of action decision for self. Then the action is observed by the other agent and affects its intention decision. When the other agent makes a collaborative decision, the decided intention should be one that is also convenient for the self agent [4]. The intention is expected to appear through the action of the other agent.

The passive strategy and the active strategies can be classified in more detail. For instance, the passive strategy is the one directional action decision from the others to the self. A typical behavior we imagine will be a strategy that estimates the intention from the others' behavior, and decides its' own behavior based on it. We call such an action, decision strategy Level 1 (Lv.1). Here, the level means a depth of intention estimation.

The passive strategy is not limited to Lv.1. Another method is that the self agent estimates one more step deeper, such as "How the self is estimated by the others", and chooses its own behavior to match with the one that the other agent expected on self. We call such an action, decision strategy Level 2 (Lv.2). Another most basic strategy is that the self agent doesn't consider others' intention and just pursuits its own goal. We call such an action decision strategy Level 0 (Lv.0).

A feature of Lv.1 and Lv.2 strategy is adapting to the other's decision. In contrast, the active strategy decides its own intention at first, and expects the other agent to take Lv.1 strategy. The intention is demonstrated to the other agent explicitly, made sure that the other estimates self intention as desired and influences the others intention decision to induce an others' action that is convenient to the self. We call this action decision strategy level zero star (Lv.0*). As Lv.0* strategy expects the others to estimate intention of self and adjust its intention, Lv.0* agent doesn't observe others behavior and change the intention of self. The strategy is same as Lv.0 strategy in a sense of not estimating others' intention. So the level of this strategy is considered to be zero [5].

2.3 Computation for Action Decision

The action decision process of these strategies were formulated [4]. We assumed that human intention could be described by a simultaneous occurrence probability distribution $P(a,s,G)$ of an action a , a state s , and an intention G . It's natural to

think that we have acquired the knowledge $P(a,s,G)$ from an accumulation of past experiences. In this paper, we do not refer to the learning of knowledge.

When the two values among these three variables are known, we can calculate a conditional probability distribution of one remaining variable. For instance, we can estimate the probability distribution $P(G|a,s)$ of other's intention from the other's action and the state of the moment. The same calculation applies for the estimation of a and s by $P(a|s,G)$ and $P(s|a,G)$ [5].

In the Lv.1 strategy, the self agent estimates the goal of the other agent \dot{G}_o by applying the observed others situation s_o and action a_o to the goal estimation function (1). Once the goal of the other agent is estimated, the corresponding self goal G_s can be decided by a task requirement, or the game rule in this paper, and the self agent decides its own action as the Eq. (2).

$$\dot{G}_o = \operatorname{argmax}_G P(G|a_o, s_o) \quad (1)$$

$$a_s = \operatorname{argmax}_a P(a|s_s, \dot{G}_s) \quad (2)$$

The Lv.2 agent assumes that the other agent is also under estimation of its own goal using Lv.1 strategy. Estimating the others estimation can be realized by substituting the other's state s_o and action a_o by its own state s_s and action a_s in its own goal estimation function (1) as the Eq. (3). And then, the self decides its own action a_s according to the estimated goal \dot{G}_s of self by others so that the self action a_s is consistent to the others' action a_o . The calculation is expressed by the Eq. (4).

$$\dot{G}_s = \operatorname{argmax}_G P(G|a_s, s_s) \quad (3)$$

$$a_s = \operatorname{argmax}_a P(a|s_s, \dot{G}_s) \quad (4)$$

On the other hand, the strategy of Lv.0 is unconscious of the others intention. The action decision process can be expressed by the Eq. (5)

$$a_s = \operatorname{argmax}_a P(a|s_s, G_s) \quad (5)$$

In contrast to the passive action decision of Lv.1 and Lv.2, the self decides its action that expresses its intention most explicitly to the other in the strategy Lv.0*. This requirement is realized by searching an action that maximizes a difference of the action probability between the aiming goal and the other goals. The calculation is expressed by the Eq. (6).

$$a_s = \operatorname{argmax}_a \{ \operatorname{argmin}_{\dot{G} < G_s} (P(G_s | s_s, a) - P(\dot{G} | s_s, a)) \} \quad (6)$$

Formulation of the decision making process based on the intention estimation is expected to be effective for an understanding of human behavior in social interaction scenes. In the next section, the action decision strategy of human in the scene of play between child and adult is evaluated.

3 Human Model Construction from an Adult-Child Play Observation

An nursery nurse more than 10 years experience was instructed to play with a child of first sight for 30 min (Fig. 2). Six years old children, one boy and one girl, played with her. We recorded their play by a video camera, and analyzed her action strategy for keeping the child's interest using our model. At first, we assumed the child taking Lv.0 strategy and the nurse taking Lv.1 strategy. In the play process, we focused on a dynamics of child's mental state toward the plays, a variety of nurse's playing and interacting action choices, their timing, and change of the child's mental state by her actions.

At the beginning of the experiment, the child was strained by meeting a new person in a new environment. After a few minutes of interactions with the nurse, the child became relaxed and then began to focus on the games that the nurse worked on to play together. But after a while, the child became bored of the game, and the nurse tried to keep the attention of the child as long as possible. In order to do so, the nurse tried various interactions to keep the attention level of the child high.

From the verbal report of the nurse while watching the video record after the experiment, we confirmed that the nurse was conscious of having the mental model of children. She intentionally classified the character of the child, and choose her action by consulting her mental model of the child. In this process, she estimated an internal state of the child from its behavior and facial expression. She applied the estimation result and other observations to the child model, and chose the most effective action for keeping the interest of the child.

From this result, we figured out the state flow of child's internal state and corresponding possible internal system model of the nurse. Figure 3 shows the structure and signal flow of the process we estimated. This is a case that the nurse



Fig. 2 A nursery nurse played with a child to keep interest of the child longer

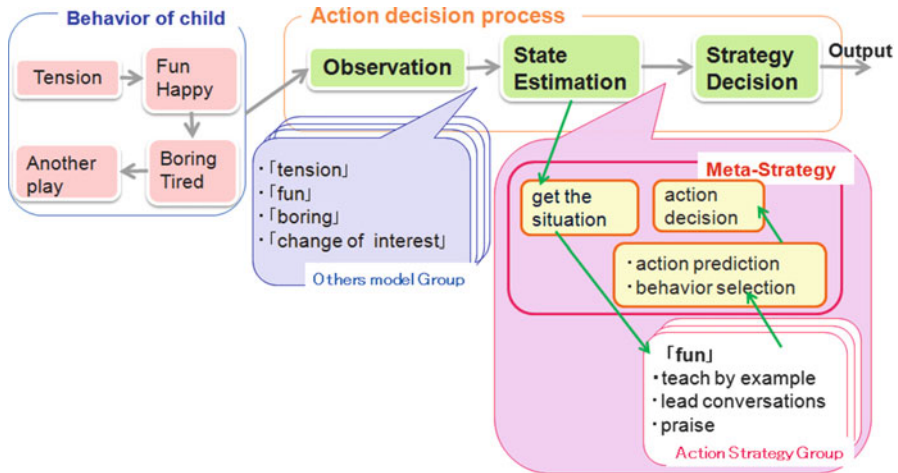


Fig. 3 Under the child’s state observation, the nurse selected a child model and sought for a proper action of the moment by predicting its effect to the child’s state

took Lv.1 strategy assuming the child taking Lv.0. But we observed the child taking Lv.1 action to wait and observe the nurse’s action a couple of times, and the nurse followed it by Lv.2 or Lv.0* strategy.

4 Playmate Robot Model

To evaluate the model from the behavior observation, we realized a robot that can play with a child. The robot was 135 cm height, 70 kg weight [6]. We constructed an action decision model described by a set of features and actions observed (Fig. 4). We adopted a state transition model in which states represent degree of child’s internal state for a play of the moment.

In Fig. 4, the state of the child’s interest changes from the initial nervous state to the bored one through the familiarizing and enjoying state along time. This is the basic flow of the states. But when any proper input is given by the nurse, it causes a change of state to keep the interest. Though the child’s internal interest state can’t be observed directly, it generates corresponding characteristic behaviors that can be observed from outside. So, the state can be estimated by observing the child’s behavior.

The nursery nurse observes the child’s behavior and estimates the internal state that represents child’s degree of interest to the play. Then, the nurse decides her action whether to keep or move the child’s state to a desirable one by consulting her knowledge on the child. This is a kind of inverse use of a forward model.

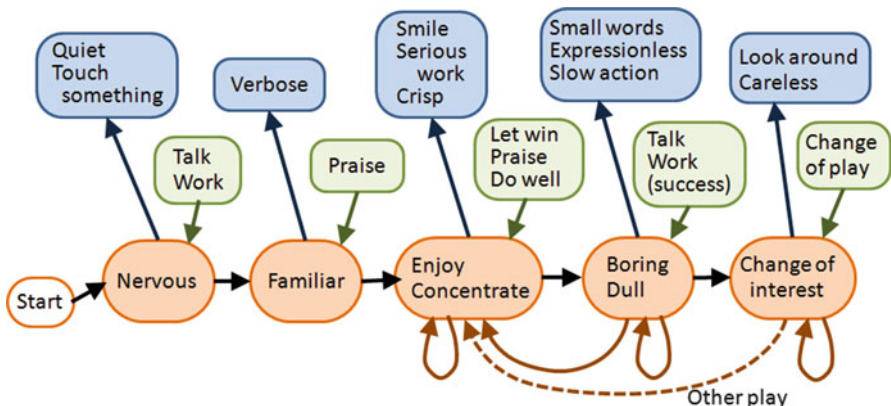


Fig. 4 State model of child with input and output

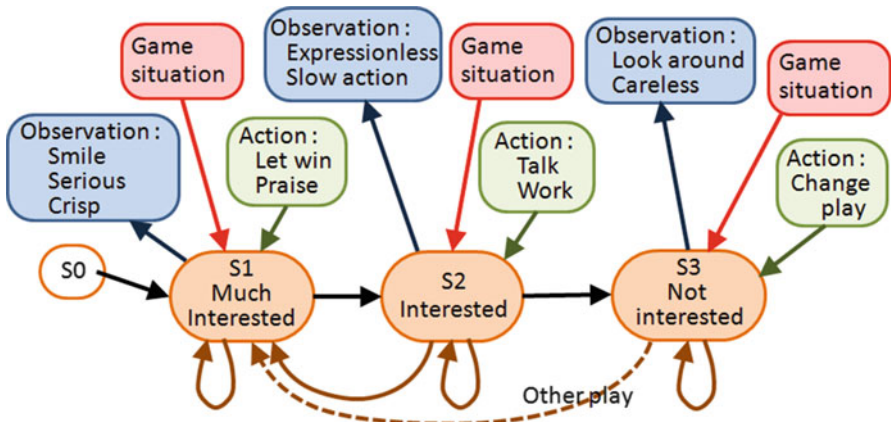


Fig. 5 Implemented action decision model for the robot based on the estimated interest index of a child

Given the model of child state transition in Fig. 4 and the strategy of nurse action decision in Fig. 3, we reconstructed a simpler model of nurse action decision in which each of the feature observations and actions are realizable by our robot system (Fig. 5). In the model, we used an interest value as the internal state of the child, and we estimated the interest value from their facial expressions while they are playing games with our robot.

For the facial expression observation, a measurement of face direction, gaze direction and smile index using facial image processing software (OKAO VISION, OMRON Corp.) was taken. The degree of interest is acquired by the linear sum of these indices. The number of state was three and the action choice probability of the robot is designed to express the nurse behavior. As a control condition in the

following experiment, we used uniform choice of possible actions corresponding to a game situation. The game situation is designed by the human designer of the game and the choice timing is designated by a human operator.

5 Robot-Child Play Experiment

A play experiment between a robot and a child using the action decision model shown in Fig. 5 was placed. Participants were 6 years old children (three boys, three girls) and it was the first time for the participants to meet the robot. Each of the children confronts to the robot. Mother of the child was in the room. We asked her to do nothing and keep quiet. After 5 min of interaction practice, the child played a card game and scissors-paper-rock game for 25 min. Four participants played for 25 min, of which two played with the nurse model robot and the other two participants played with the control model robot, that choose its action uniformly from a set of possible actions in each of the game situations (Fig. 6).

To evaluate the degree of children's interest towards the game and robot, we asked three well experienced nursery caregivers to evaluate the interest by watching video record of the robot-child play. We also asked the caregivers to fill out questionnaire about the change of child's interest before and after the play. By analyzing the reply, we found an interest to the robot used for the play increased through the interaction with robot.

By comparing the gaze direction of children between the nurse model condition and the control uniform condition, we found a tendency that the children who played with the nurse model robot looked at the face of robot longer than the control condition when the card game or the scissors-paper-rock game had finished. The child's interest moves on to the next phase when the game ends and he/she looks at the robot face asking for the next play. The child's tendency of looking robot face expresses a child's stance to think the robot a target of communication. The stance suggests a robot-child relation became more alike to the relation between human.



Fig. 6 Play experiment of the robot with the children

6 Discussion

One major conclusion from a series of researches is the necessity of the strategy to switch and manage the action decision strategies, so called "Meta strategy". Communication is quite a complex behavior between two or more agents. The reason for this complexity is that the agents decide their own action goal and action decision strategy, and they often change them without noticing the change to the other. So, in communication with the others, we must estimate what goal the other is aiming for, what strategy the other choice is, and what strategy we should take in order to take proper action that fits well to the others intention. And what makes it even more complex is that both of the agents do the same thing simultaneously and independently.

Thus far in our study, we couldn't find a single action decision strategy that can solve all the possible situations of interaction, but found a set of strategies of Lv.1, Lv.2, Lv.0 or Lv.0* that can decide action in limited situations. Therefore, we must choose the strategies and change it dynamically depending the situation of the moment. In our experiment, we observed change of strategy level in both of the nurse and child behavior. And the proposed nurse model includes change of strategy depending on the internal state of the child. So, the strategy change is suggested to be necessary. But we haven't clarified a condition that causes the level change. The process that select the level is the phenomenon of meta strategy that we should pursuit next.

7 Conclusion

In this study, a computational model of the nursery nurse action decision strategy is proposed and the model is evaluated by implementing on a robot that can play with a child. The robot could keep interest of the child longer when it used the nurse model for its action decision than the control condition. From the result, we discussed necessity of meta-strategy model that select action decision strategy depending on the situation.

Acknowledgments This work was supported by a Grant-in-Aid for Scientific Research on Innovative Areas 'The study on the neural dynamics for understanding communication in terms of complex hetero systems' (21120010).

References

1. Makino, T., Aihara, K.: Multi-agent reinforcement learning algorithm to handle beliefs of other agents' policies and embedded beliefs, In Proceedings of the 5th International Joint Conference on Autonomous Agents and Multiagent Systems (AAMAS'06), p 789–791, 2006.

2. Nagata Y., ishikawa S., Omori T., and Morikawa K.: Computational Model of Cooperative Behavior: Adaptive Regulation of Goals and Behavior, Proceeding of the Second European Cognitive Science Conference (EuroCogSci 07), 202–207, (2007).
3. Omori T., Yokoyama A., and Okada H.: Computational modeling of human-robot interaction based on active intention estimation, ICONIP2007, 2007.
4. Yokoyama A., Omori T., Ishikawa S., and Okada H.: Modeling of action decision process based on intention estimation, SCIS & ISIS2008, TH-F3-1, 2008.
5. Omori T., Yokoyama A., Nagata Y., and Ishikawa S.: Computational Modeling of Action Decision Process including Other's Mind - A Theory toward Social Ability -, Keynote Talk, IEEE International Conference on Intelligent Human Computer Interaction (IHCI 2010), Allahabad, India, Jan. 16, 2010.
6. Attamimi M., Mizutani A., Nakamura T., Sugiura K., Nagai T., Iwahashi N., Okada H., Omori T.: Learning Novel Objects Using Out-of-Vocabulary Word Segmentation and Object Extraction for Home Assistant Robots, pp.745–750, 2010.

Symbol Communication Systems Integrate Implicit Information in Coordination Tasks

Takeshi Konno, Junya Morita, and Takashi Hashimoto

Abstract In order to study the formation of communication systems through interactions, we conducted an experiment in which pairs of participants attempted to complete a coordination task through an exchange of messages composed of a set of abstract figures. At the beginning of the interaction, there was no shared rule for the meanings and usage of the figures as symbols. We observed that the participants completed the coordination task by forming communication systems. We suggested that communication systems can be developed effectively if participants have implicit behavioral tendencies, such as using small number of symbols, meeting at a usual place, and smooth turn taking.

1 Introduction

Humans express and share many meanings using symbols in communication. Meanings change according to situations, contexts, and intentions even if the symbols used are the same [1]. Much information is also expressed implicitly by behavioral patterns, such as gaze, gestures, and turn taking. It is important to clarify the correlation between implicit information and explicit symbol usage in order to understand symbolic communication systems [2]. However, it is difficult to conduct a controlled experiment that reveals this correlation because the existing symbol system, namely, language, is so established and complex that it becomes difficult to observe the formation process of a linguistic communication system.

Galantucci [3] conducted an experiment to observe the formation of symbol communication systems in which participants communicated through a medium that restricted the use of standard communication means such as utterances and letters.

T. Konno (✉) • J. Morita • T. Hashimoto

School of Knowledge Science, Japan Advanced Institute of Science and Technology (JAIST),
Asahidai 1-1, Nomi-Si, Ishikawa, 923-1292 Japan
e-mail: t-konno@jaist.ac.jp; j-morita@jaist.ac.jp; hash@jaist.ac.jp

He observed that implicit information was conveyed through routine behavior and the temporal order of messages were built into communication systems. This indicates an advantage of the experimental approach with the design of an artificial communication medium [4, 5]. We can observe the effects of implicit, that is, non-linguistic, behavior on the formation of symbol communication systems under a restricted communication medium.

However, this previous research failed to provide adequate and clear evidence for the effectiveness of behavior that conveys implicit information on the formation of symbol communication systems. Therefore, we designed an experiment to analyze implicit behavior quantitatively and to verify its effectiveness with regard to the formation of symbol communication systems. In this experiment, a pair of participants engaged in a coordination task through an exchange of messages composed of a set of abstract figures, where no rule regarding their usage was shared. We expect a significant correlation between task performance and certain behaviors to identify whether implicit information is conveyed.

2 Task

We used a coordination game that was modified from the previous study [3] to obtain quantitative data concerning implicit behavior such as using symbols, forming routine behavior, and the temporal structure of message exchange. The game environment contained two agents, each controlled by two players, and 2×2 intercommunicating rooms (Fig. 1). The agents could not move to diagonal rooms. The game was composed of several repeated rounds. At the beginning of each round, the agents were randomly located in two different rooms. Each player, who was unaware of the location of the other, aimed to bring her/his agent to the same room. To accomplish this, each player could send a symbolic message to the other before moving the agent.

In Galantucci's experiment, players exchanged handwritten distorted graphics as messages, and they could exchange the messages as many times as needed in a round. This design makes the frequency of symbol use and the correlation between messages and behavior unclear. In the coordination game, we assumed that implicit

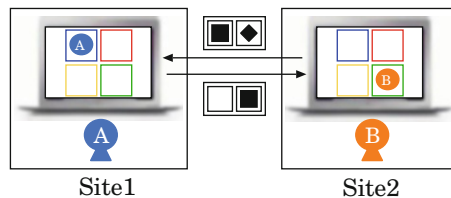









Fig. 1 Experimental environment. The player controls her/his own agent using laptop computers located at different sites. She/he coordinates with the agents to bring them into the same room

information would be conveyed with some behavioral tendencies, such as a bias toward using a specific set of symbols, a bias toward moving to a specific room, and smooth turn taking. To measure the behavioral tendencies quantitatively, we designed the following task procedure.

First, a message was created by composing two figures, such as , using six alternatives, , , , , , and . The meanings and usage of the figures were not shared among participants in advance.

Second, the players exchanged each message once per round. After the exchange, they separately decided the destination of the agents' moves, including keeping the agents in the rooms they originally were in. The initial location and the result of the movement of each agent were displayed on the both players' screens at the same time. This design connected the messages clearly with the behavior.

Finally, the messages were displayed on the partners' screen immediately after they were sent. Therefore, the second sender could see the first sender's message and manage turn taking. Temporal differences in the message exchange indicated a degree of smooth turn taking.

3 Method

Participants: Twenty-one dyads, consisting of graduate students and university researchers, voluntarily participated in this study. They were aged between 22 and 37 years (*mean age* = 25.5, *SD* = 3.0).

Apparatus: The dyads engaged in a coordination game from different sites using interconnected laptop computers¹ (Fig. 1).

Procedure: The experimental procedure consisted of one trial session and three test sessions. In the trial session, the participants attempted to develop a communication system within a time limit of 1 h. If they moved to the same room, the players got two points or else they lost one point, but the scores did not drop below zero. When the score reached 50 points, the trial session was interrupted.

The test sessions were conducted subsequently. TEST1 restricted any message exchanges. In TEST2, messages were displayed on the partners' screens after both the players had sent their messages. Thus, turn taking was prevented in this test session. TEST3 was conducted under the same condition as the trial session. From the difference in performances between TEST1 and TEST3, we confirmed the effectiveness of symbol use. We also confirmed the effectiveness of turn taking from the difference between TEST2 and TEST3. Each test had 12 rounds that contained all combinations of two agents' locations. The order of appearances were set at random.

¹ Each laptop computer exchanged information through a server, using a web browser (Firefox). The server-client system was a web application with SQL database and PHP.

4 Results

4.1 Performances in the Trial Session

In the trial session, 14 of 21 pairs (66.7%) scored 50 points within 1 h. A number of rounds averaged 54.8 ($SD = 25.1$). An average of the time was 40 min 41 s ($SD = 16$ min 25 s). Figure 2 shows the concordance rate of destinations of each pair in the last 12 rounds in the trial session ($mean = 0.72$, $SD = 0.22$). We assume that this rate reflects the performance of the communication system each pair built. We measured the performances of the communication systems by the concordance rate of the moves coordinated thereafter. Almost all participants successfully completed the coordination task because the performances surpassed the expectation value of this game, which was 0.22 (two times match in nine rounds).

4.2 Performances in the Test Session

Figure 3 indicates the average performance scores of the three tests. We conducted a one-way within-subject analysis of variance (ANOVA) using test type as an independent variable to assess the features of the formed communication systems² and found the significant main effect of the task ($[F(2, 19) = 31.66, p < .01]$). Furthermore, multiple comparisons (Tukey’s HSD test) revealed significant differences between TEST1 and other test scores ($p < .01$), suggesting that the players could form communication systems with effective symbol usage. We also found a difference between TEST2 and TEST3 ($p < .05$), confirming that players developed communication systems including an effective management of turn taking.

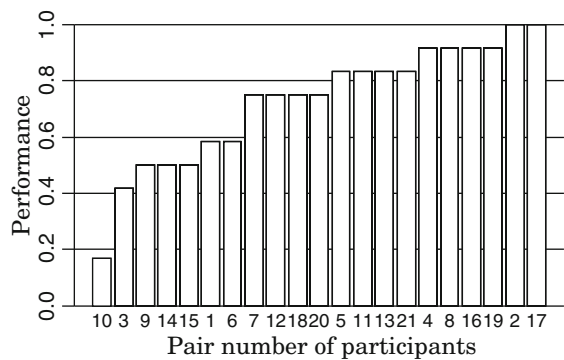


Fig. 2 Performances measured by the concordance rate of the moves in the last 12 rounds in the trial session

² Pair 5 was excluded for failure in the test session because a player of the pair unilaterally changed the rules from the trial session.

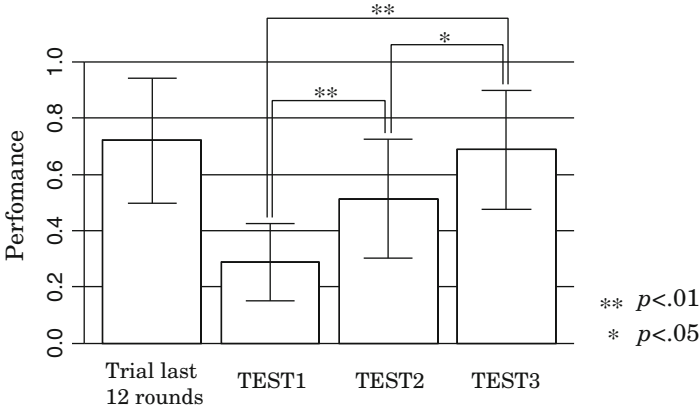


Fig. 3 Averages of concordance rates of the moves in the trial and test sessions. Error bars show the standard deviation

4.3 Correlations Between Implicit Behavior and Performances

We investigated correlations between the performances of the three tests and the behavioral indexes of the trial session to detect implicit information related to the formation of symbol communication systems. We analyzed three behavioral indexes: bias towards using a specific set of symbols, B_{Sym} , bias towards moving to a specific room, B_{Pos} , and temporal differences in message exchange, TD_{Mes} .

The former two indexes were calculated by the geometric mean of two Kullback–Leibler divergences between two probability distributions P and E .

$$B = \sqrt{D_{\text{KL}}(P_1||E) \cdot D_{\text{KL}}(P_2||E)},$$

$$D_{\text{KL}}(P_i||E) = \sum_{n=1}^N P_i(n) \log \frac{P_i(n)}{E}, \tag{1}$$

where P_i was the probability distribution of symbol use or the destination rooms of the player i ; E was the uniform distribution, and N was the number of bins of the probability distributions.³ If the distribution P deviated from the uniform distribution, the index would increase.

The latter index, TD_{Mes} , was calculated as follows.

$$TD_{\text{Mes}} = \frac{1}{N_r} \sum_{r=1}^{N_r} |t_{m_1}(r) - t_{m_2}(r)|, \tag{2}$$

³ For the distribution of symbol use, $E = 1/6, N = 6$. For the distribution of destination rooms, $E = 1/4, N = 4$.

Table 1 Correlation results of the performances with three behavioral indexes

Index	TEST1	TEST2	TEST3
B_{Sym}	.005	.479*	.292
B_{Pos}	.620*	.441^	.307
TD_{Mes}	-.367	-.602*	-.222

Note. $\hat{p} < .1$; * $p < .05$ indicates significant correlations

where N_r denoted the number of rounds and t_m denoted the time that had elapsed since a message was sent to the partner from the beginning of the round. This index measured temporal differences between the first and the second transmission of messages.

We calculated Pearson's product-moment correlations between the three indexes and the performances in the three tests (Table 1). Consequently, first, we found significant correlations between the performance in TEST1 and B_{Pos} . The index indicated that the players had a bias of routine movement behavior such as moving upward or to the left side. If the players had this bias, they would move to the same room without an exchange of messages. Second, we found significant correlations between the performance in TEST2 and the three behavioral indexes. Third, these behavioral indexes did not correlate with the performance in TEST3. We discuss these results in the next section.

5 Discussion

The three indexes, which showed the bias towards using a specific set of symbols, the bias towards moving to a specific room, and the temporal differences in message exchange, indicated a significant correlation with the performance in TEST2, in which turn taking was prevented.

This result provides the basis for three general conclusions. First, the bias toward using a specific set of symbols indicates that both the players' messages are composed of small number of symbols. This bias implies that the messages would not convey excess information, thus causing a misunderstanding. Second, the index of the bias toward moving to a specific room indicates that both the players move to a usual place. The behavioral tendency will probably convey implicit information to help inference in a situation where turn taking is restricted in TEST2. Finally, the index concerning a temporal structure of messaging negatively correlated with the performance in TEST2. This indicates the relation between immediate responses and the formation of a symbol communication system.

Surprisingly, we could not find any correlation between the performance in TEST3 and the three behavioral indexes. To achieve the best performance in TEST3, participants need to divide roles in communication. For example, in the case of pair 2, one player sent a message representing her/his current position and the other decided on a destination where both of them could meet. We need to consider the

type of behavior that contributes to form a communication system integrating the role-sharing strategy. The results presented in Table 1 suggest that the development of the role-sharing strategy in communication is independent from the three implicit behaviors we examined.

6 Conclusions

This study explored how people initiated coordination by forming communication systems under a condition where no rule on symbol usage was shared. The results suggest that communication systems can develop effectively if participants have implicit behavioral tendencies, such as using small number of symbols, meeting at the usual place, and smooth turn taking. However, these behavioral tendencies did not contribute to the division of roles using turn taking. In the future, we will explore factors influencing role division in communication systems.

Acknowledgements This work was supported by a Grant-in-Aid for Scientific Research on Innovative Areas “The study on the neural dynamics for understanding communication in terms of complex hetero systems (No.4103)” (21120011) of The Ministry of Education, Culture, Sports, Science, and Technology, Japan.

References

1. J. Barwise and J. Perry, *Situations and attitudes*, MIT Press, 1983.
2. M. Tomasello, *The cultural origins of human cognition*. Harvard University Press, Cambridge, 2000.
3. B. Galantucci, An experimental study of the emergence of human communication systems. *Cognitive Science. A Multidisciplinary Journal*, 29(5): 737–767, 2005.
4. B. Galantucci, Experimental semiotics: A new approach for studying communication as a form of joint action. *Topics in Cognitive Science*, 1(2): 393–410, 2009.
5. T. Scott-Phillips and S. Kirby, Language evolution in the laboratory. *Trends in Cognitive Sciences*, 14(9): 411–417, 2010.

Intermittent Brain Motor Control Observed in Continuous Tracking Task

Yutaka Sakaguchi

Abstract In the present study, the author analyzed the hand movement in one-dimensional visuo-manual tracking task. When the target moved slowly or unpredictably, the hand velocity contained many bell-shaped components lasting several-hundred milliseconds. When the target moved fast and sinusoidally, on the other hand, subjects seemed to adjust the movement by a unit of cycle. These findings suggest that our brain divides temporal axis into discrete segments and plans/adjusts motor commands for each segment. This “intermittent motor control” may be the brain’s fundamental strategy for achieving good motor performance with slow sensorimotor system.

1 Introduction

Brain motor control system contains many delay/lag elements in the control loop, such as neural transmission, neural calculation and muscle activation. A fundamental question here is how our brain performs a given motor task in a real-time fashion with such a slow system. Computational theory gave an answer of “feed-forward control,” that is, our brain makes a motor plan in advance and executes it without sensory feedback. The validity of this framework has been discussed mainly in relation to reaching movement. Meanwhile, the requirement of real-time control must be more serious in performing a continuous task (such as tracking) compared to a ballistic task (such as reaching), because brain has to obtain task-related sensory information, to design/adjust motor plans and to monitor the performance in a seamless manner. How does our brain handle this situation? One possible answer

Y. Sakaguchi (✉)

Human Informatics Laboratory, Graduate School of Information Systems, University of Electro-Communications, Tokyo 182-8585, Japan
e-mail: sakaguchi@is.uec.ac.jp

is that brain divides the time axis into discrete segments and executes feed-forward control in each time segment (i.e., “intermittent control”). Actually, our body movement contains discontinuous components even in a continuous tracking task [1–3]. The present study investigates the nature of such discontinuities in a visuo-manual tracking task. Especially, the author aims to analyze the hand movement in time domain while most previous analyses were done in frequency domain.

2 Method

The experimental setup was as follows. A subject sat in front of a table with his/her chin rested on a chin rest. He/she put his/her right hand on an air-floating slider moving along a linear rail in a front-back direction. The position of the slider was monitored by an optical sensor and sampled by 200 Hz. The hand position was displayed as the vertical position of a red laser spot on a front screen (2.2 m apart from the subject head), where forward hand motion brought upward spot motion. Hand motion was magnified two times on the screen (i.e., 10 mm hand move brought 20 mm (or 0.5° in visual angle) spot move). On the screen, another green laser spot (“target”) was presented whose vertical position was controlled by the experimental program. The task was to move the right hand so that the red spot (i.e., hand) tracked the green spot (i.e., target) as accurately as possible.

Two types of target motion were used: One was sinusoidal motion (frequency was 0.3–1.2 Hz), and the other was pseudo-random motion where target position was given by a linear summation of three sinusoids with different frequencies and amplitudes.

Hand position data were fitted by fifth-order spline curves whose node interval was 100 ms (i.e., 20 data points). Velocity, acceleration, jerk and snap were calculated using the derivatives of the spline function. Three subjects participated in the experiment, but the data from one subject was introduced below.

3 Results

3.1 Pseudo Random Target Motion

Figure 1 shows a typical example of hand trajectory in the pseudo-random condition. The top panel shows the hand and target positions and their difference (i.e., tracking error: magnified ten times), and the middle panel shows the hand and target velocities. The bottom panel shows the hand acceleration and jerk.

Position profile of hand motion clearly shows its discontinuous behavior, in contrast to the continuous target behavior. Error profile consists of a number of humps with 0.3–0.7 s lengths, implying that our brain may correct hand

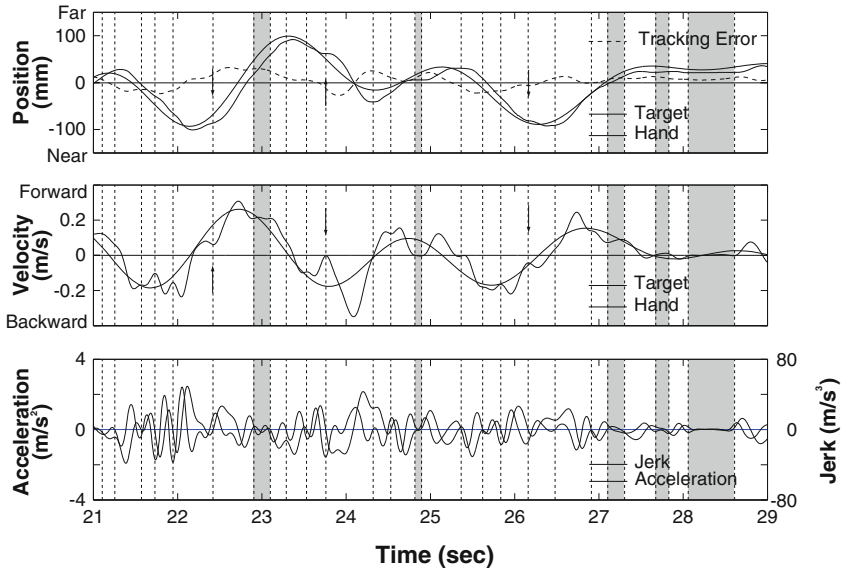


Fig. 1 Typical trajectory observed in pseudo random condition

movement with a unit of several hundred milliseconds (i.e., “intermittently”). The discontinuities were observed either around the turning points or in the mid-course of the motion (as indicated by arrows).

Intermittent structure could be also found in the velocity profile: It consisted of a number of bell-shaped components, suggesting that subjects might perform the tracking task as a series of reaching-like ballistic movements.

Interestingly, the subjects sometimes stood still for a while until starting a new movement. This can be found around 25 and 27–29 s in Fig. 1 (indicated by hatchings), where both acceleration and jerk remained low. This “moratorium period” can be regarded as the time while the brain is prepared for catching a clue to identifying the nature of target motion in the next few seconds. In other words, the brain is waiting for upcoming events which can be used for planning the next action.

The author tried to extract the segmental structure from the trajectory data, and found that the following method worked fairly well (a different method will be reported elsewhere). First, onsets of bell-shaped velocity components are detected based on the zero-crossing of acceleration and the direction (or sign) of jerk. Second, the valleys of acceleration profile are detected by the zero-crossing of jerk and the sign of snap. Moratorium periods are determined based on the acceleration and jerk levels. Finally, the detected epochs are merged and adjusted manually.

The extracted segment boundaries are indicated by vertical broken lines in Fig. 1. The left panel of Fig. 2 shows the histogram of lengths of the extracted segments. They distributed mainly over the range of 0.2–0.8 s.

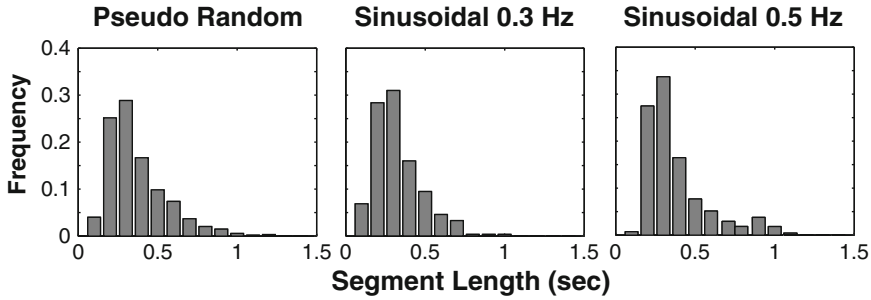


Fig. 2 Distribution of segment lengths

3.2 Sinusoidal Target Motion

For sinusoidal target motions, the nature of hand motion depended largely on the target frequency. Figure 3 shows the movement profiles in the cases of 0.3 and 1.2 Hz.

When the frequency was low (~ 0.5 Hz), the hand motion contained unequally-segmented components, similar to the pseudo random case. Different from the pseudo random case, however, bell-shaped velocity humps were superimposed on the baseline sinusoidal curve. Thus, the segmental structure could be more clearly observed in the acceleration profile: Whilst the target motion was sinusoidal (and its acceleration was also sinusoidal), the acceleration of hand motion consisted of a number of irregular humps.

When the segment boundaries were extracted by the above algorithm, the resultant segment lengths distributed over 0.2–0.9 s (Fig. 2, center and right panels), similar to the pseudo-random case. We should note that segment boundaries were observed almost uniformly over all motion epochs in 0.3 Hz case, but in higher frequency cases, they were more often observed around the turning points (Fig. 4). This suggests that the turning points may have special meaning for brain's motor control. This point will be discussed later.

When the target frequency was above 1 Hz, in contrast, the hand motion became quite rhythmic and its acceleration profile approached sinusoids (Fig. 3 lower panel). This implies that subjects performed the task by the cycle unit, rather than faithfully pursuing the target.

Two points should be noted here. First, when the target frequency was higher than 1 Hz, the phase of the hand motion tended to precede that of the target motion. Interestingly, the magnitude of phase precedence varied according to the motion epoch and was minimized in the backward movement. Figure 5 shows the histograms of phase difference between the target and hand motions at four epochs. Values inside the plots indicate the average phase differences (a positive value means that the hand preceded the target). When the target frequency was 0.3 Hz, the hand phase tended to be behind the target phase at all epochs, implying that the hand

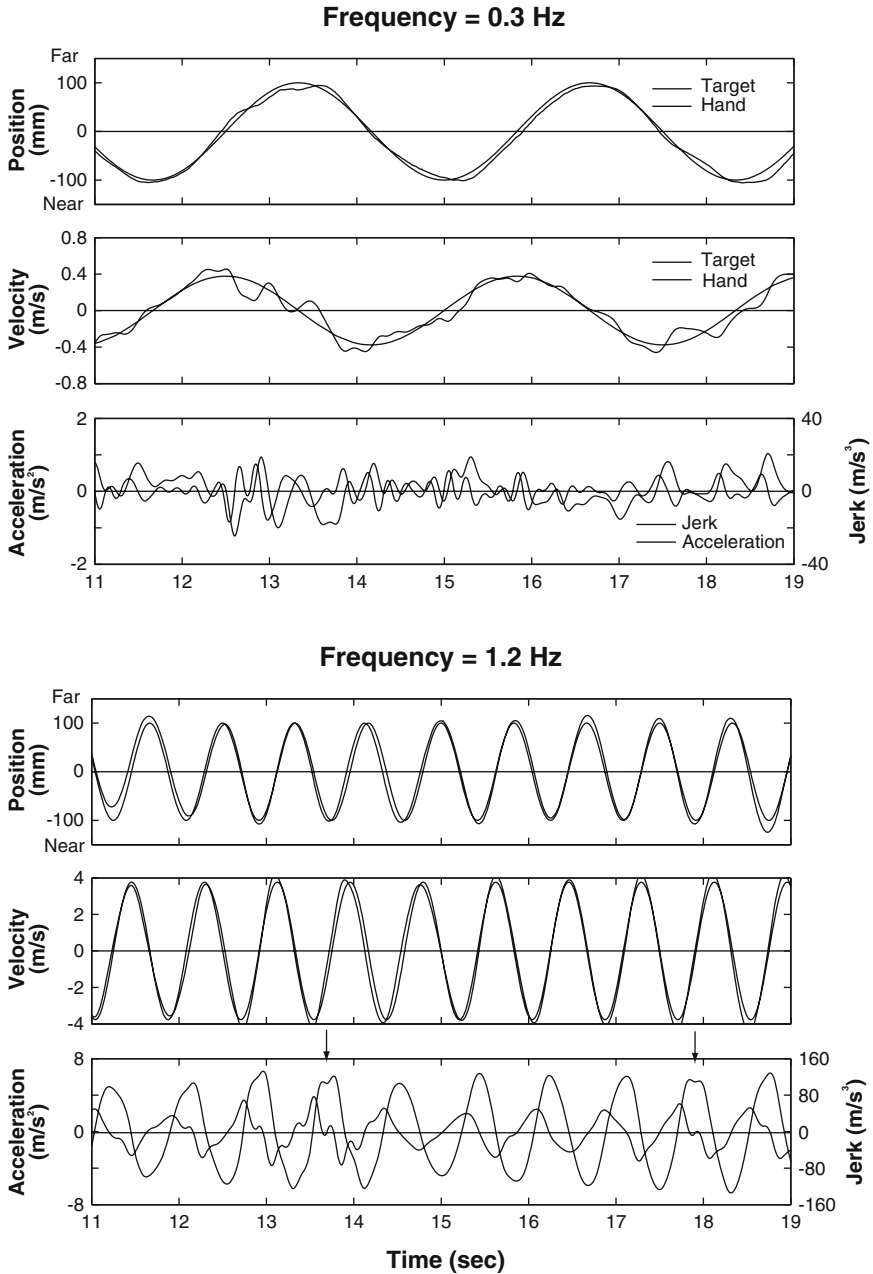


Fig. 3 Typical trajectory in sinusoidal condition

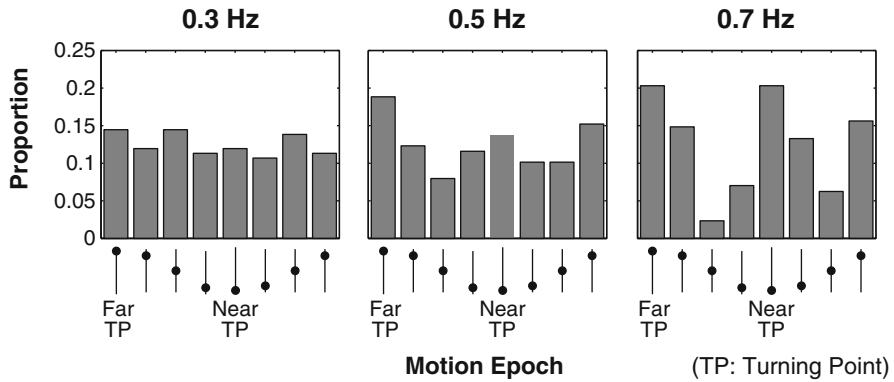


Fig. 4 Distribution of segment boundary positions in low-frequency sinusoidal tracking

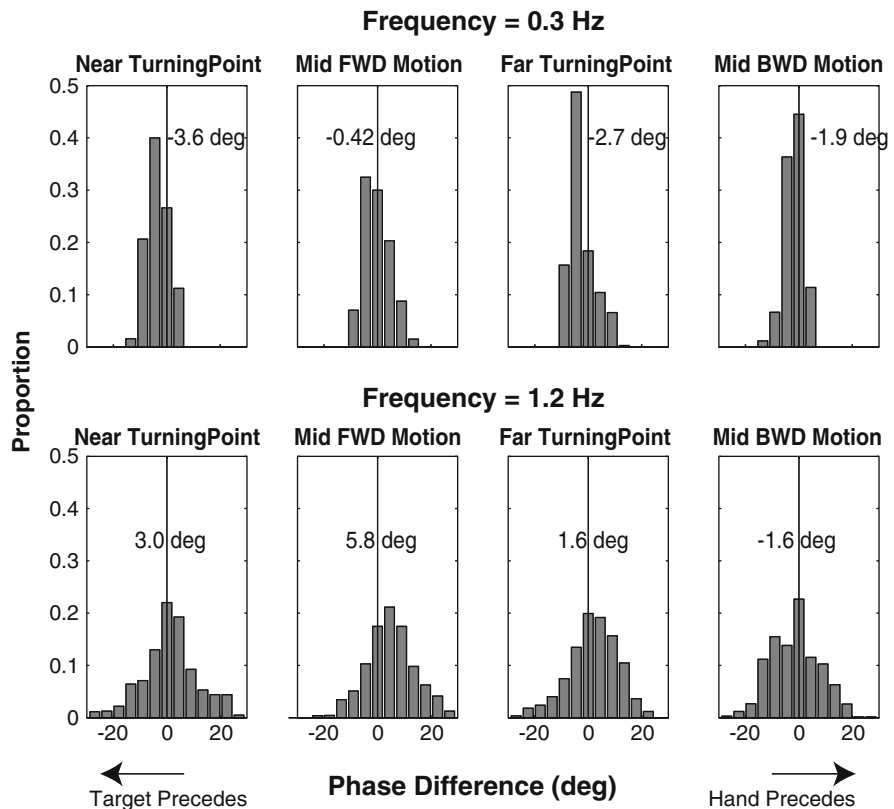


Fig. 5 Distribution of target-hand phase difference at four epochs in fast sinusoidal tracking

basically followed the target. When the frequency was 1.2 Hz, however, the hand phase tended to precede the target phase except for the backward movement. This suggests that the subject might adjust the movement so that the hand phase matched the target phase at a specific epoch.

Second, we see some valleys in the acceleration profile (indicated by arrows in Fig. 3) though acceleration varied almost regularly. It is noteworthy that these valleys were exclusively observed around the turning points. This indicates that the subjects adjusted the movement around the turning points.

Therefore, these observations together suggest that our brain may segment a continuous sinusoidal motion at/near the turning points and adjust the movement intermittently. A possible reason why the turning points were chosen as segment boundary is that they may be appropriate places for monitoring the target and hand positions and for catching the timing (or rhythm) of target motion.

4 Discussions

The present study examined the nature of intermittent motor control of human brain using a tracking task. Intermittent behavior in the tracking task itself has been already reported by other researchers [1–3].

Miall, et al. [1] ran behavioral experiments similar to the present study (but they used lower-frequency motion) and discussed the meaning of intermittency in human motor control. Using frequency analysis, they showed that intermittent components were around 0.8–1.8 Hz. This frequency range roughly coincided with the segment lengths (0.2–1 s) obtained in the present study (Fig. 4). Furthermore, Miall, et al. examined the amount of tracking error at the onsets of velocity humps and argued that corrective movements were evoked when the positional error exceeded a certain threshold (“error deadzone”). Based on these results, they proposed a view that intermittent motor behavior was caused by nonlinear characteristics of brain control mechanism owing to error deadzone and temporal constraints (such as feedback delay and refractory period).

This view is quite persuasive and the author partially agrees with it. Actually, Gawthrop, et al. [4] built a computational model of intermittent control based on the error deadzone idea and showed that the system marked good control performance even with a large sensory delay. However, there is an essential difference between their view and the author’s view. The “error deadzone view” is fundamentally based on an assumption that our brain invokes movement in order to recover the error caused in the *past*. That is, it regards the intermittent movements as “corrective reaction” to the error occurred in the past.

In contrast, the author stands on a view that the brain plans movement so as to maximize the task performance (i.e., minimize tracking error) in the *future*. Concretely, the author assumes that brain predicts the target motion in the near future and designs an appropriate motor plans for tracing the predicted motion. This process is driven by the visual feedback, but the point is that the visual feedback

is mainly utilized for sensing the target/hand motions and estimating/updating their internal models, rather than for producing corrective movements *per se*. Thus, the intermittent control process may not simply depend on the amount of error: An important factor may be what epoch (or timing) is appropriate to acquire visual information for updating the hand and target models. This could explain why the segment boundaries tended to be located around the turning points for high-frequency sinusoidal targets: Presumably, our visual system can estimate target and hand positions most accurately (because motion speed is lowest) and detect the onset of new cycle of movement most sensitively (because motion direction is switched) around the turning points.

Therefore, the author would like to propose that the intermittency is our brain's fundamental control strategy that it predicts the near future and determines the motor plans adaptively so as to achieve a good performance with our slow sensorimotor system. The validity of this view should be examined in the future experimental and computational studies.

Acknowledgments This work was supported by a Grant-in-Aid for Scientific Research on Innovative Areas "The study on the neural dynamics for understanding communication in terms of complex hetero systems (No.4103)" (21120012) of MEXT, Japan.

References

1. Miall, R.C., Weir, D., J. Stein, J.F.: Intermittency in human manual tracking tasks. *J Motor Behavior*, 25 (1993) 53–63.
2. Doeringer, J.A., Hogan, N.: Intermittency in preplanned elbow movements persists in the absence of visual feedback. *J Neurophysiol* 80 (1998) 1787–99.
3. Kakei, S., Lee, J., Kagamihara, Y.: Identification of two parallel controllers for tracking movement of the wrist. *SfN Annual Meeting*, (2010), 582.7.
4. Gawthrop, P., Loram, I., Lakie M. & Gollee, H.. Intermittent control: a computational theory of human control, *Biol. Cybern.*, 104 (2011), 31–51.

Molecular and Neural Mechanisms for Behavioral Choice Between Two Conflicting Alternatives in *C. elegans*

Takeshi Ishihara

Abstract Animals facing conflicting sensory cues make a behavioral choice through the integration of sensory cues. This kind of sensory processing is important even for simple organisms. We studied the molecular and neuronal mechanisms of such behavioral choice by using nematode *C. elegans* as a model organism. Our genetic analyses revealed that the information about two conflicting sensory cues is processed in a pair of interneurons, in which two signaling pathways regulate the sensory integration independently.

Keywords Decision making • *C. elegans* • Behavior

1 Introduction

Animals sense many environmental stimuli simultaneously, and process the information within the central nervous system to generate proper behavioral responses. For example, animals often sense two conflicting stimuli simultaneously, and so they have to choose one of the two stimuli to respond to. This kind of behavioral choice in invertebrates, or decision making in vertebrates, is important for animals to adapt to their environments. Furthermore, the proper regulation of such behavioral choice is important to survive in continuously changing environments. Indeed, the behavioral choice reflects the relative preference between the contradictory sensory cues [1, 2]; hence, the choice can be altered depending on an animal's status. However, the molecular and neuronal mechanisms underlying the behavioral choice remain to be revealed.

T. Ishihara (✉)

Department of Biology, Graduate School of Sciences, Kyushu University, 6-10-1, Hakozaiki, Higashi-ku, Fukuoka 812-8581, Japan
e-mail: takeiscb@kyushu-u.org

Caenorhabditis elegans has a simple nervous system with 302 neurons in adult hermaphrodites and is well described [3]. In addition, behavioral, genetic, and imaging analyses can be used for the study of the nervous system in *C. elegans*. For example, genetic and behavioral studies revealed the mechanisms of sensory transduction at the molecular level, and the functions of the sensory neurons at the level of neural circuits. These studies promise *C. elegans* to be an ideal model organism to study sensory processing involved in behavioral choice.

2 Behavioral Paradigm to Study Behavioral Choice

The responses of *C. elegans* show attraction or aversion to various kinds of chemicals. For example, wild type animals show chemotaxis to an odorant, diacetyl (butter flavor chemical), which is sensed by a pair of sensory neurons, AWA [4]. On the other hand, they avoid heavy metal ions including Cu^{2+} ion, which is sensed in two pairs of sensory neurons, ASH and ADL [5]. To study behavioral choice between two conflicting sensory cues, we devised an assay paradigm, which is named “interaction assay”, by using diacetyl and Cu^{2+} ion as sensory cues. In this assay, animals must cross the Cu^{2+} barrier to reach the attractive diacetyl (Fig. 1a). For quantitative analysis, we defined an index on the basis of the percentage of animals on the odorant side relative to the total number of animals.

In the interaction assay, the index depends on the concentration of diacetyl and Cu^{2+} . The chemotaxis to diacetyl is suppressed by the presence of Cu^{2+} , whereas the avoidance of Cu^{2+} is suppressed by the presence of diacetyl (Fig. 1b, c). Since Cu^{2+} and diacetyl are sensed in distinct sensory neurons, this observation suggested that information about Cu^{2+} and diacetyl is integrated in the neuronal circuit. Therefore, this interaction assay enables us to study the sensory processing involved in the behavioral choice between diacetyl and Cu^{2+} .

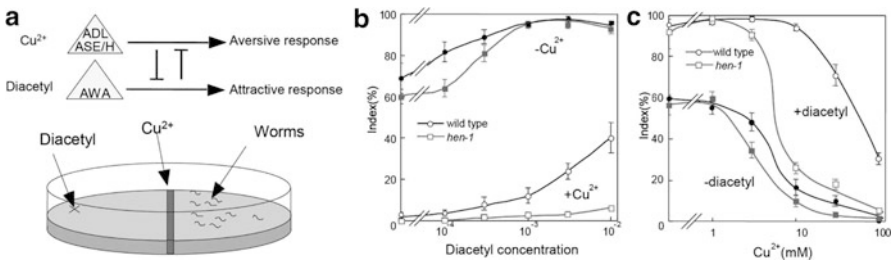


Fig. 1 (a) Interaction assay to evaluate the sensory integration in *C. elegans*. (b) Chemotaxis in response to diacetyl in wild type and *hen-1* with or without Cu^{2+} [1]. (c) Avoidance in response to Cu^{2+} in wild type and *hen-1* with or without diacetyl [1]

3 Molecular Mechanisms for the Behavioral Choice

By using this assay, we found a mutant defective in the behavioral choice. We named this mutant *hen-1* after *hesitation*. The *hen-1* mutant animals, compared with wild type animals, prefer the avoidance of Cu^{2+} to the approach response to diacetyl, although their sensory responses to each of these stimuli are indistinguishable to those of wild type animals. This result suggested that the *hen-1* gene responsible for the phenotype in the interaction assay is involved in the behavioral choice. To elucidate the molecular basis of the behavioral choice, we identified the *hen-1* gene by positional cloning. The *hen-1* gene encodes a secretory protein with an LDL receptor motif A, which is involved in protein interaction and is most similar to the Jeb protein in *Drosophila*.

To determine where the HEN-1 protein functions, we analyzed its expression pattern by a specific antibody, and found that it is expressed in two types of neurons, ASE and AIY. The expression of HEN-1 not only in ASE or AIY but in other neurons is sufficient to restore the phenotype. This result suggested that HEN-1 functions as a secretory protein. Next, we studied when HEN-1 functions for the behavioral choice. Accordingly, the expression of HEN-1 in the adult stage was sufficient to rescue the phenotype, although the expression in larval stage could not restore the phenotype. This result suggested that HEN-1 is not involved in neuronal development but regulates the behavioral choice at the adult stage.

To elucidate the mechanisms of the regulation of the behavioral choice, we searched a receptor for HEN-1. Since in *Drosophila* *Jeb*, which is most similar protein to HEN-1, functions through a receptor tyrosine kinase DALK [6], we analyzed mutants defective in *SCD-2*, which is an ortholog of DALK in *C. elegans*. The *scd-2* mutant animals showed a phenotype similar to *hen-1*, preferring the avoidance of Cu^{2+} over the approach to diacetyl. To determine whether HEN-1 and *SCD-2* function in the same genetic pathway, we made double mutants and analyzed their behavior [7]. The *scd-2;hen-1* double mutants showed the same phenotype as each of the single mutants, suggesting that *hen-1* and *scd-2* function in the same genetic pathway. Taken together, *SCD-2* may be a receptor for HEN-1 to regulate the behavioral choice. Since *SCD-2* is expressed in many neurons, we examined where *SCD-2* functions. The genetic analyses revealed that *SCD-2* in a pair of interneurons AIA is sufficient for the proper regulation of the behavioral choice.

For further investigation of the molecular mechanisms, we screened another mutant defective in the behavioral choice, and identified a mutant in which the receptor type guanylyl cyclase GCY-28 is mutated [7]. Since *gcy-28;scd-2* double mutants showed a more severe phenotype than each of the single mutants in the interaction assay, it appears that *gcy-28* and *scd-2* function in parallel pathways.

To identify neurons involved in the behavioral choice, we analyzed *gcy-28* mutant expressing wild type GCY-28 in various sets of neurons, and found that the expression of GCY-28 in AIA interneurons is also essential for the proper regulation of behavioral choice. These results suggested that, in AIA interneurons, the two signaling pathways regulate the sensory processing in parallel.

4 Neural Circuit for the Behavioral Choice

Our genetic analyses revealed that the signaling pathways in the AIA interneurons are important for the proper regulation of the behavioral choice. In *C. elegans*, diacetyl is mainly sensed in a pair of sensory neurons AWA, whereas Cu^{2+} is mainly sensed in two pairs of sensory neurons ASH. ASH is activated by the stimulation of Cu^{2+} [8], whereas we found that AWA is influenced by the stimulation of diacetyl. According to electron microscopic analyses [3], AIA neurons are connected with AWA by gap junctions and received chemical synapses from ASH. Our analyses suggested that this wiring diagram also supports the idea that AIA interneurons are important for the behavioral choice.

To elucidate the function of AIA interneurons, we used two mutant ion channels MEC-4(d) and UNC-103(gf). MEC-4(d) is a mutant epithelial sodium channel (ENaC)/degenerin channel, which is constitutively active, and thereby the expression of MEC-4(d) in neurons causes degeneration of the neurons [9]. UNC-103(gf) is a mutant ERG-like K^+ channel, which has a gain of function mutation, and thereby the expression of UNC-103(gf) in neurons causes inactivation of the neurons [10]. We made wild type animals expressing MEC-4(d) or UNC-103(gf) only in the interneurons. These animals do not have functional AIA neurons.

Firstly, we examined whether these animals can normally respond to the sensory stimuli, diacetyl and Cu^{2+} . As shown in Fig. 2a and b, animals expressing MEC-4(d) or UNC-103(gf) in AIA interneurons showed normal avoidance of Cu^{2+} and normal approach to diacetyl, suggesting that AIA interneurons are not necessary for the behavioral response to each of the stimuli.

Next, we examined the behavioral phenotype in the interaction assay. Animals expressing MEC-4(d) or UNC-103(gf) in AIA interneurons preferred the avoidance of Cu^{2+} over the approach to diacetyl, like *hen-1* animals (Fig. 2c), suggesting that AIA interneurons are crucial for the proper behavioral choice between Cu^{2+} and diacetyl [7].

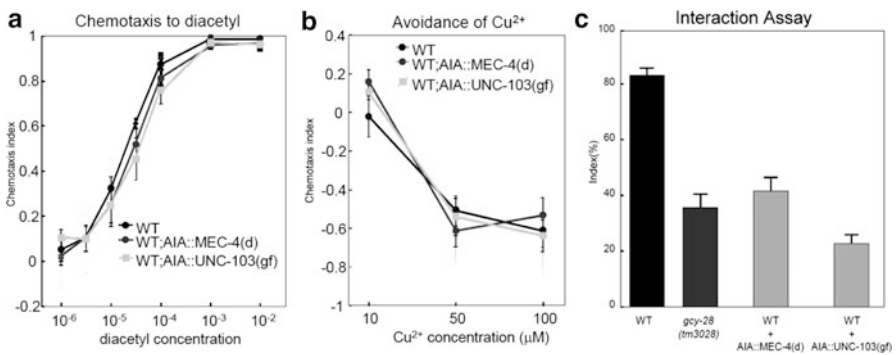
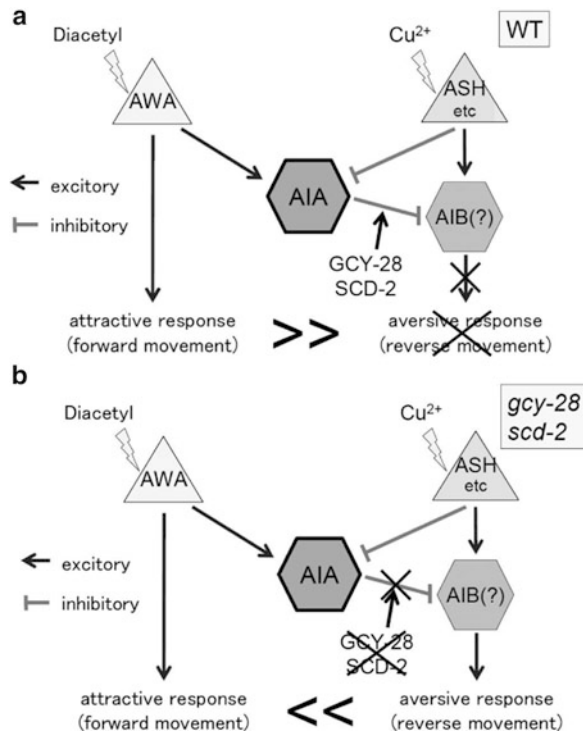


Fig. 2 (a) Chemotaxis in response to diacetyl of animals without functional AIA interneurons [7]. (b) Avoidance response to Cu^{2+} of animals without functional AIA interneurons [7]. (c) Animals without functional AIA neurons prefer the avoidance of Cu^{2+} over the approach to diacetyl [7]

Fig. 3 (a) In wild type animals, AIA interneurons inhibit AIB interneurons, and thereby the aversive response to Cu^{2+} is suppressed. (b) In the mutants, AIA neurons cannot inhibit AIB, and hence the animals prefer the avoidance response



Our genetic analyses revealed that the sensory processing for the behavioral choice in *C. elegans* is regulated by a simple neural circuit (Fig. 3). Cu^{2+} is sensed by ASH sensory neurons, which make inhibitory synapses to AIA interneurons. Diacetyl is sensed by AWA sensory neurons, which are connected with AIA interneurons by gap junctions. ASH sensory neurons make synapses to AIB interneurons, of which the activation induces backward movement, suggesting that AIB is responsible for the avoidance of Cu^{2+} . In our model, depending on the balance of these conflicting signals from AWA and ASH/ADL, AIA interneurons may inhibit the function of AIB through GCY-28 and HEN-1/SCD-2 pathways, and thereby they prefer the approach response to diacetyl over the avoidance of Cu^{2+} (Fig. 3a). On the other hand, in *gcy-28* or *scd-2* mutant animals or wild-type animals without functional AIA sensory neurons, AIA cannot inhibit AIB, and thereby AIB stimulates the avoidance of Cu^{2+} (Fig. 3b). Therefore, these animals may behave in the interaction assay as if the worms sensed a higher ratio of Cu^{2+} relative to diacetyl than wild-type animals. To elucidate the functions of AIA interneurons, we plan to visualize the activity of the neural circuit by Ca^{2+} imaging.

Interneurons play an important role in the sensory processing in vertebrates and invertebrates. This study of the sensory processing underlying behavioral choice is important to understand the molecular and neuronal basis of behavioral choice in invertebrates and decision making in vertebrates.

Acknowledgments This review is based on our studies [1, 7]. We are very grateful to our collaborators, especially to Prof. Bargmann, Prof. Iino, and Prof. Katsura. This work was supported by a Grant-in-aid for Scientific Research, by Asahi Glass Foundation, and by the Naito Foundation.

References

1. Ishihara, T. et al.: HEN-1, a secretory protein with an LDL receptor motif, regulates sensory integration and learning in *Caenorhabditis elegans*. *Cell*.109 (2002) 639–649
2. Kristan, W.B.: Neuronal decision-making circuits. *Curr Biol*.18(2008) R928–R932
3. White, J.G. et al.: The structure of the nervous system of the Nematode *Caenorhabditis elegans*. *Philos Trans R Soc Lond B Biol Sci*.314(1986) 1–340
4. Bargmann, C.I. et al.: Odorant-selective genes and neurons mediate olfaction in *C. elegans*. *Cell*. 74 (1993) 515–527
5. Sambongi, Y. et al.: Sensing of cadmium and copper ions by externally exposed ADL, ASE, and ASH neurons elicits avoidance response in *Caenorhabditis elegans*. *Neuroreport*.10(1999) 753–757
6. Englund, C. et al.: Jeb signals through the Alk receptor tyrosine kinase to drive visceral muscle fusion..*Nature*.425(2003) 512–516
7. Shinkai, Y. et al.: Behavioral choice between conflicting alternatives is regulated by a receptor guanylyl cyclase, GCY-28, and a receptor tyrosine kinase, SCD-2, in AIA interneurons of *Caenorhabditis elegans*..*J Neurosci*.31(2011) 3007–3015
8. Hilliard, M.A. et al.: In vivo imaging of *C. elegans* ASH neurons: cellular response and adaptation to chemical repellents..*EMBO J*.24(2005) 63–72
9. Harbinder, S. et al.: Genetically targeted cell disruption in *Caenorhabditis elegans*..*Proc Natl Acad Sci U S A*.94(1997) 13128–13133
10. Reiner D.J. et al.: Behavioral genetics of *Caenorhabditis elegans* unc-103-encoded erg-like K(+) channel. *J Neurogenet* 20(2006)41–66

Modulating the Phase Coherence of Neuronal Population Oscillations in the Gamma Band

B. Sancristóbal, R. Vicente, A.J. Pons, G. Pipa, and J. Garcia-Ojalvo

Abstract Control of the phase coherence between oscillatory neuronal populations has been proposed as a key mechanism to gate neuronal communication. Here we investigate the emergence of phase coherence, at the level of both LFP and MUA, between two neuronal areas that exhibit population oscillations in the gamma band. To that end we simulate two large interacting recurrent networks of Hodgkin-Huxley neurons. We observe that changes in the strength and topology of inter-areal synaptic projections can effectively modulate the phase coherence at gamma frequencies.

1 Introduction

Neurons in cortical, subcortical, and cerebellar areas have been observed to engage in oscillatory activity at different frequency bands. In particular, upon sensory stimulation many cortical regions exhibit oscillations at the neuronal population level, as measured by local field potentials (LFP), in the beta (12–30 Hz) and gamma (30–90 Hz) range [1]. While individual neurons are found to spike irregularly and at much lower rate than the population oscillations, their action potentials can be

B. Sancristóbal (✉) • A.J. Pons • J. Garcia-Ojalvo
Departament de Física i Enginyeria Nuclear, Universitat Politècnica de Catalunya,
08222 Terrassa, Spain
e-mail: belen.sancristobal@upc.edu

R. Vicente
Department of Neurophysiology, Max-Planck Institute for Brain Research, Frankfurt, Germany
Frankfurt Institute for Advanced Studies (FIAS), Frankfurt, Germany

G. Pipa
Department of Neuroinformatics, Institute of Cognitive Science, University of Osnabrück,
Osnabrück, Germany

precisely locked to a narrow phase of the recorded LFP. The mechanisms generating gamma-band oscillations rely on local recurrent inhibitory networks that modulate the excitability of neurons in a periodic manner [2]. Such fluctuating excitability makes the spiking probability of a neuron be correlated with the global oscillation phase [3].

Given the rhythmic susceptibility of an oscillatory area to incoming input, we can expect the strength of interaction between coupled neuronal populations to be modulated by their phase difference: incoming action potentials arriving at the high excitability phase will have a higher probability of triggering a spike in the post-synaptic neuron, in comparison with those arriving within the low excitability window. In that way, an efficient and dynamic gating of neuronal communication can occur by modulating the phase difference and/or the phase coherence between oscillatory populations. This is known as the *communication through coherence* hypothesis [4]. Experimental evidence for phase-sensitive responsiveness of neuronal populations has been demonstrated in peripheral structures [5]. However, whether the nervous system actively uses such mechanisms for routing and processing information is currently a topic of intensive research.

In this work, we investigate how the phase coherence between neuronal oscillations depend on the architectural properties of the coupled neuronal populations. To that end, we have conducted extensive simulations of two interacting recurrent networks of Hodgkin-Huxley neurons. The interaction is unidirectional, and each network is subjected to sensory-like input that sustains a local gamma rhythm at each population. To quantify these rhythms we use the LFP, which captures the summed synaptic activity of the network, and the multiple-unit activity (MUA), which measures the joint spiking behavior of a subset of neurons within the network. In particular, we explore the frequency dependency of LFP-LFP, MUA-MUA and MUA-LFP phase coherence, and possible mechanisms for its dynamic modulation in terms of the coupling architecture between the populations.

2 Methods

We model two neuronal populations (representing cortical areas) each composed by 2,000 neurons, with each neuron connecting randomly with 400 other neurons of the same area. Eighty percent of the cells in each network are excitatory. Inter-areal connectivity is uni-directional and purely excitatory, and is defined by the percentage of projecting cells and by a divergence factor (expressing the percentage of cells contacted by a single long-range projecting neuron). For those long-range connections, we assume an axonal conduction delay of 10 ms.

Each neuron is defined by its membrane potential and several channel gating variables, described by Hodgkin-Huxley equations. Excitatory and inhibitory synaptic currents are mediated by AMPA and GABA_A receptors, with an elicited conductivity time-course of an alpha function. Rise and decay time of inhibitory

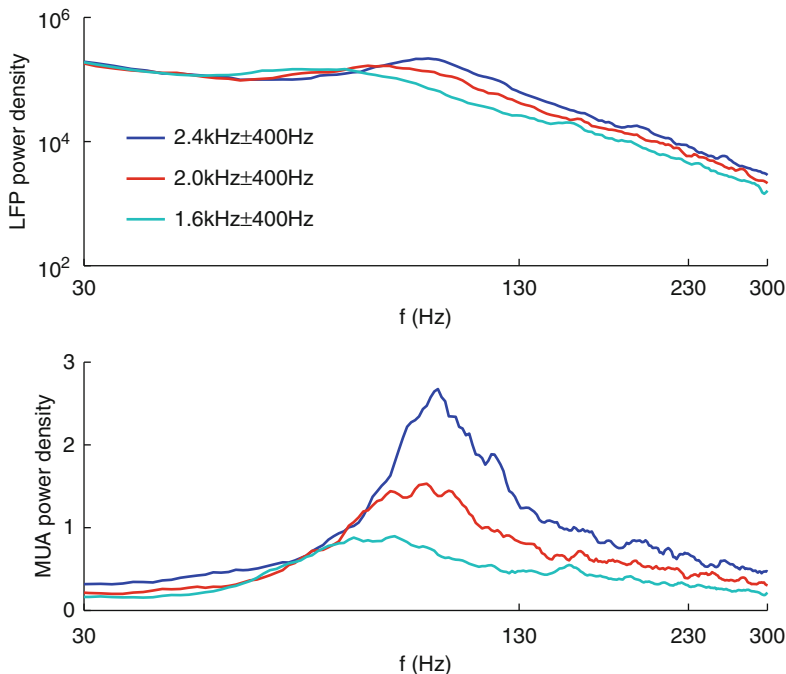


Fig. 1 LFP (*top panel*) and MUA (*bottom panel*) power spectra for different values of the external rate

synapses controlled the frequency of gamma oscillations. Here, we set a rise time of 0.1 ms and a decay time of 5 ms, leading to oscillations in the range of 80–90 Hz. Feedforward connections to each population from lower cortical or subcortical areas is mimicked by external input. This is modeled as a non-homogeneous Poisson train of incoming excitatory post-synaptic potentials (EPSPs). The instantaneous rate of this input is generated by an Ornstein-Uhlenbeck process, which fits the basic features of naturalistic stimuli driving the cortex. The non-homogeneous Poisson-train stimulation induces low frequency activity and contributes to the $1/f$ power spectral profile of the simulated LFPs (top panel of Fig. 1).

We calculate the LFP from the sum of the absolute value of the excitatory $|I_{\text{AMPA}} + I_{\text{ext}}|$ and inhibitory $|I_{\text{GABA}}|$ synaptic currents impinging on excitatory (pyramidal) neurons [6]. The MUA was estimated from the spiking histogram of a subset of 500 neurons of each population. A typical trial consisted of a 3-s realization of the dynamics of both networks. During the first second the two populations remained uncoupled and only driven by the same external stimulus (inhomogeneous Poisson process, mean = 2,200 Hz, variance = 400 Hz). For the next 2 s the two networks were simulated to interact unidirectionally accompanying a rate increase of the external input at the projecting area. Note that concomitantly

with the rate increase, the gamma peak of the LFP spectrum shifts to higher frequencies. The results shown below correspond to average over 400 trials. Power spectra and phase coherence were computed from 500 ms windows using a multitaper estimator with a spectral concentration of ± 6 Hz.

3 Results

In our simulations recurrent excitation and inhibition in each network produce a gamma rhythm at a frequency determined mainly by the rise time of the GABAergic synapses. The strength of the synapses can also modify the frequency content of the LFP power spectrum, since the discharge rates of neurons vary accordingly. Slower oscillations emerge for slower inhibitory synapses (results not shown). The power spectra of the LFP and MUA signals are plotted in Fig. 1 for different values of the external input rate. Lower stimulus intensities produce slower oscillations. In addition, the bump in the gamma-band of the LFP power spectrum is relatively broad and therefore, the associated oscillations are far from harmonic.

Before considering the effect of coupling between the two populations, we study the relation between LFP and MUA signals from a single population. Our results show that the LFP and the MUA activities are phase coherent across trials (Fig. 2), which indicates that spikes in a population are phase-locked to its LFP. The phase-coherence between MUA and LFP can be sustained for an extensive range of frequencies (Fig. 2, top). Moreover, the phase difference between the two signals as a function of frequency shows a linear relationship (Fig. 2, bottom). This suggests that the relation between MUA and LFP consists of a constant temporal lag, which is in turn translated to a bigger phase difference as the frequency increases. Indeed, the troughs of the LFP are observed to coincide with the peaks of the MUA (Fig. 3).

When the networks are coupled, the EPSPs elicited at the receiving population by the spikes coming from the sending population can affect the timing of action potential generation. This, in turn, is reflected as a change of the LFP phase. Figure 4 shows that the interacting networks also exhibit LFP-LFP, MUA-MUA and MUA-LFP phase coherence with a preferential range in the gamma-band. In all simulations the strength of the AMPA intra-area synapses was considered equal to the AMPA inter-area synapses. Increasing the conductance of the AMPA intra-area synapses increases the effect of the sending on the receiving area, and the phase coherence increases accordingly (results not shown).

We have also studied how inter-area connectivity affects the phase coherence. Two structural coupling parameters are considered, the convergence (percentage of neurons in the sending area connecting to the receiving area) and divergence (number of affected neurons in the postsynaptic area). Above a minimum convergence value the phase coherence (most notably LFP-LFP) starts to increase with increasing divergence in the beta and gamma range, around the frequency peak of the LFP power spectrum of the projecting area (Fig. 4). If the convergence is low, on the other hand, no phase coherence emerges regardless of the divergence (results not

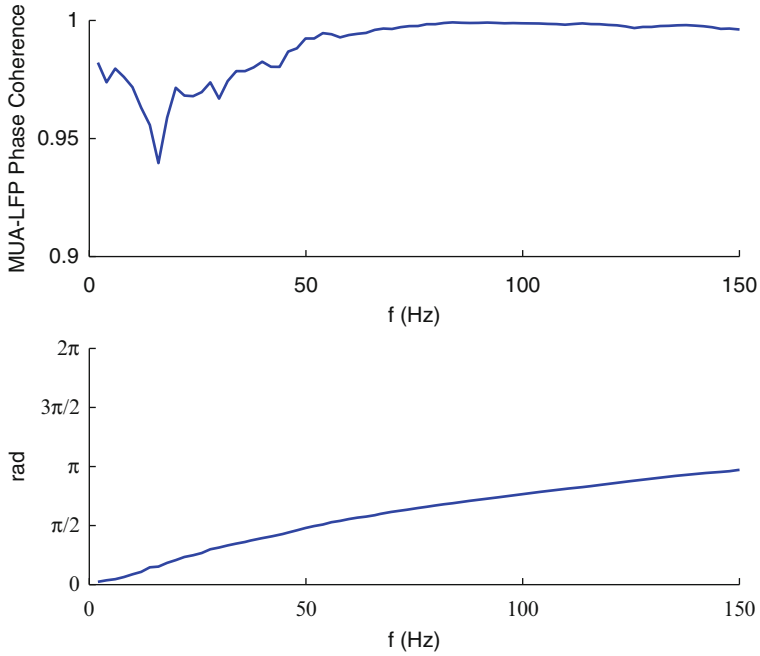


Fig. 2 MUA-LFP phase coherence (*top panel*) and MUA-LFP phase difference (*bottom panel*) for a single population as a function of frequency

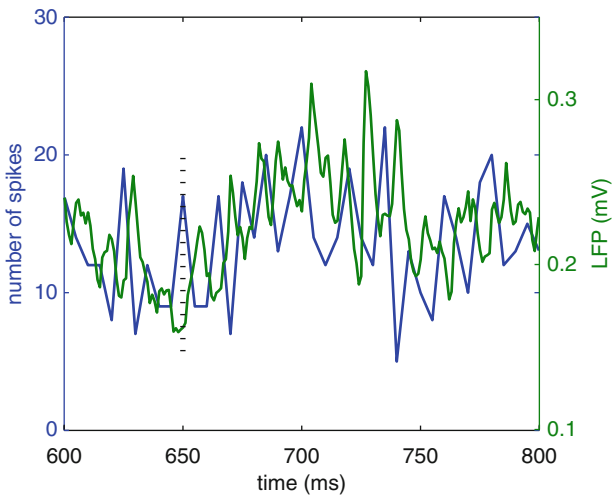


Fig. 3 LFP trace (*green*) and MUA (*blue*) of one population showing how the minima of the inhibitory current (LFP) matches with the maxima of the spike histogram (MUA)

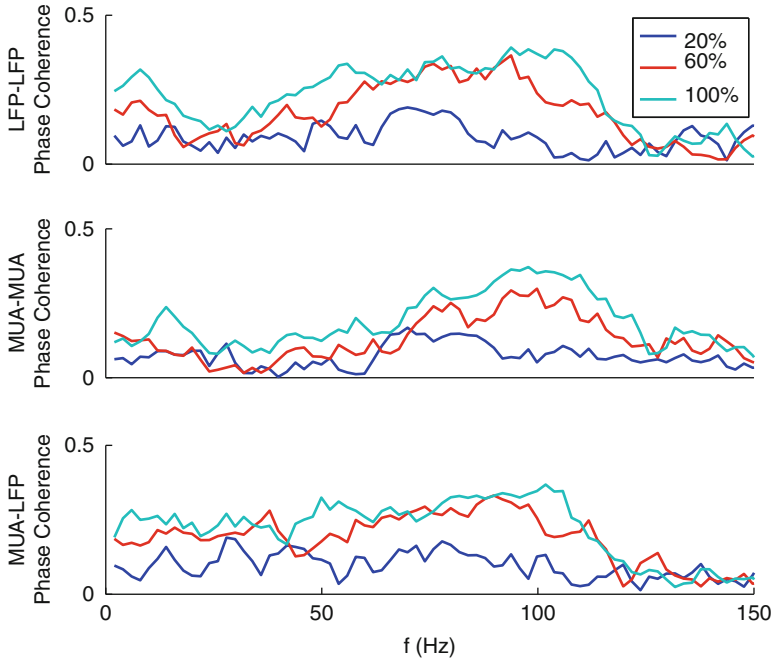


Fig. 4 LFP-LFP (*top*), MUA-MUA (*middle*) and MUA-LFP (*bottom*) phase coherence between two coupled populations. Convergence is set to 60 % while divergence is varied (see legend)

shown). There is also a transition from no phase coherence to a high coherence in a wide range of frequencies as the connectivity is varied from weak to strong synaptic strength (results not shown).

4 Discussion

We have built recurrent networks with sparse connectivity to investigate the establishment and modulation of phase coherence between two neuronal populations exhibiting global oscillations, at the level of both LFP and MUA signals. Previous experimental work has shown that MUA-MUA and MUA-LFP phase coherence between two different visual cortical areas concentrates in the gamma band [7]. This specificity of phase coherence may be a mechanism of controlling the communication between areas: on the one hand the phase relation is robust to the noise coming from different biological sources as it remains constant across trials (phase coherence), and on the other hand this situation is only achieved in a narrow frequency band, which can be viewed as a channel for information transmission control. Our simulations suggest that recurrent inhibition is responsible for the locking between MUA and LFP signals in single populations. For two coupled

populations, the interaction between incoming EPSPs and local activity can shift the timing of action potentials, leading to phase locking between LFP-LFP, MUA-MUA and MUA-LFP signals.

The strength and connectivity of the inter-area synaptic projections are main determinants of the phase-coherence. If the percentage of neurons of the sending area (convergence) is low the phase relation between any two signals (LFP or MUA) is random and inconsistent over trials. As the divergence increases the phase coherence is enhanced around the frequency peak of the LFP power spectrum of the sending area and in the beta band. These results reproduce qualitatively the behavior of the phase coherence obtained experimentally [7]. Further research is oriented to investigate the phase locking of reciprocally connected areas, as well as considering the interaction between frequency mismatched oscillatory populations.

Acknowledgements We thank Pascal Fries for useful discussions. Funding provided by the Ministerio de Ciencia e Innovación (Spain, project FIS2009-13360) and the ICREA Academia programme.

References

1. Buzsáki, G., Draguhn, A. Neuronal oscillations in cortical networks. *Science* **304** (2004) 1926–1929.
2. Brunel, N., Wang, X.-J.: What determines the frequency of fast network oscillations with irregular neural discharges? I. Synaptic dynamics and excitation-inhibition balance. *J Neurophysiol* **90** (2003) 415–430.
3. Volgushev, M., Chistiakova, M., Singer, W.: Modification of discharge patterns of neocortical neurons by induced oscillations of the membrane potential. *Neuroscience* **83** (1998) 15–25.
4. Fries, P. A mechanism for cognitive dynamics: neuronal communication through coherence. *Trends Cogn Sci* **9** (2005) 474–480.
5. van Elswijk, G., Maj, F., Schoffelen, J.-M., Overeem, S., Stegeman, D. F., Fries, P. Corticospinal beta-band synchronization entails rhythmic gain modulation. *J Neurosci* **30** (2010) 4481–4488.
6. Mazzoni, A., Panzeri, S., Logothetis, N. K., Brunel, N.: Encoding of naturalistic stimuli by local field potential spectra in networks of excitatory and inhibitory neurons. *PLoS Comp Biol* **4** (2008) e1000239.
7. Womelsdorf, T., Schoffelen, J.-M., Oostenveld, R., Singer, W., Desimone, R., Engel, A. K., Fries, P.: Modulation of neuronal interactions through neuronal synchronization. *Science* **316** (2007) 1609–1612.

The Phase Space of Lateral Thought

Eleonora Russo and Alessandro Treves

Abstract While others prefer to engage in deliberative decision-making, our mind is mostly absorbed in speculative lateral thought. Can it be modeled in a precise mathematical framework? In the attractor network putatively realized in any cortical patch, memory representations are not artificially stored as prescribed binary patterns of activity as in the Hopfield model, but self-organize as continuously graded patterns induced by afferent input. Recordings in macaque indicate that such cortical attractor networks may express retrieval dynamics over cognitively plausible rapid time scales, shorter than those dominated by neuronal fatigue. A cortical network comprised of many local attractor networks, and incorporating a realistic description of adaptation dynamics, may then be captured by a Potts model. This network model has the capacity to engage long-range associations into sustained iterative attractor dynamics at a cortical scale, in what may be regarded as a mathematical model of spontaneous lateral thought. We describe the phase space of the model, which presents a number of phase transitions dependent on a set of critical parameters, which can be related to cortical quantities.

Keywords Associative network • Adaptation • Latching dynamics

1 From Local to Global Latching

Self-organizing attractor networks may comprise the building blocks for cortical dynamics, endowing it with the basic operations of categorization, including analog-to-digital conversion, association and auto-association, which are then expressed as components of distinct cognitive functions depending on the contents of the neural codes in each region.

E. Russo • A. Treves (✉)
Cognitive Neuroscience sector, SISSA, via Bonomea 265, 34136 Trieste, Italy
e-mail: ale@sissa.it

Braitenberg and Schüz [1] and others have put forward the conception that the whole cortex be regarded as a memory machine, in which self-similar local modules of pyramidal cells, densely connected by synapses mainly on their Basal dendrites, are also sparsely connected across modules by synapses mainly on their Apical dendrites [2]. These A and B systems would both be associatively modifiable with some variant of ‘Hebbian’ plasticity, endowing the modular network with the capability to function as a two-tier associative memory [3], at the local and at the global level. A rigid subdivision into distinct modules is not essential, but it simplifies rendering this theoretical notion with a well-defined mathematical model. The core idea made salient from such a perspective is that all cortical information processing, at the local level, may be expressed through the fundamental associative memory operation of self-organized categorization (as modeled by competitive networks), pattern association (as modeled by hetero-associative networks) and pattern completion and retrieval (as modeled by auto-associative networks). A number of studies have shown, over the years, that the quantitative description of such fundamental operations offered by simplified abstract models, such as the Hopfield recurrent network [4] extends without major qualitative changes to biologically more realistic models [5]. A number of issues in the mapping between the Hopfield model and a plausible cortical scenario have been discussed in our review paper with Athena Akrami [6].

In a single auto-associative memory network in which the firing rate of individual units adapts, one observes, as mentioned in [6], *latching* dynamics, i.e. the tendency to jump from one attractor to the next, in a potentially indefinite sequence. Latching occurs if either the uncorrelated, that is, non-memory state is unstable – and then a very small random fluctuation, correlated with one of the memory patterns, can be amplified and cue its retrieval in an unpredictable manner – or else, when the uncorrelated state is stable and has a finite basin of attraction of its own, if the memory patterns are however correlated with each other, so that the decaying pattern itself cues the next one. While the first type of transition can be regarded as induced by noise, the second type explicitly reflects the correlational structure of the stored memories. For both types, the first units to change state in a self-reinforcing manner are some among the inactive ones, which are activated by the latching cue [6].

Similar latching dynamics have been described for the Potts auto-associative network introduced by Kanter [7] and later extended to include a rough model of firing rate adaptation [8]. A Potts unit may in fact be interpreted as an effective model of a local auto-associative network in the cortex. It reduces the local network to a single unit of a particular type, a Potts graded response variable, which can take graded activation values $0 < \sigma^k < 1$ in S different states, $k = 1, \dots, S$, as well as remain in the inactive state to a degree $\sigma^0 = 1 - \sum_k \sigma^k$. Such a reduction offers the advantage of simplifying the analysis of auto-association mechanisms by removing local dynamics, and focusing attention on global dynamics. A global cortical activity pattern is interpreted by the model as the composition of several active states in a subset of the cortical patches, while the internal or local dynamics are not described, except by means of the collective variables σ^k . The complementary subset of local networks is taken to be in the inactive state, i.e. $\sigma^0 \approx 1$. When endowed with a

model of firing rate adaptation, the Potts network does exhibit latching dynamics with the same types of transitions, between randomly correlated as well as between explicitly correlated memory patterns, as seen in a model of a single cortical patch [9]. In addition, the Potts network can exhibit “pathological” oscillations between highly correlated patterns, what can also be observed in models of a single local network.

2 Reduction to Potts Parameters

The retrieval capacity of a non-adapting version of the Potts model that has stored p randomly correlated global attractors has been analyzed in detail [10], showing that the upper limit on p is

$$p_c \approx C_M S^2 / [4a \ln(2S/a)] \tag{1}$$

where a is the fraction of Potts units in an active state, and C_M is the connectivity among units, ie among the M modules. Since each of these connections entails a tensor of S^2 adjustable values, the storage process is equivalent to one that spans a total of $M C_M S^2$ ‘synapses’. If each module is taken to represent a local network of N real neurons, the total $M N$ real neurons would receive each $C_L = C_M S^2 / N$ long-range synapses, on average. The number of local states S , on the other hand, can be related to the number C_S of short range synapses among real neurons, by assuming that each local module is at most loaded close to capacity, so that [5]

$$S \approx k C_S / [a_M \ln(1/a_M)] \tag{2}$$

where $k \approx 0.1$ and a_M is the sparseness of the representation within each module. For example, one might consider $N \approx 10^5$, $C_L \approx C_S \approx 10^4$, and $S \approx C_M \approx 10^3$ for the human cortex.

To introduce firing rate adaptation in a network in which single neuron-like units are not represented, two distinct processes are summarily described as activity dependent thresholds. One, driven with time constant τ_2 by the activation σ^k of each state, represents fatigue specifically in the neurons active in that state; the input activation feeding into that state is then compared to that specific threshold. The other, driven with time constant τ_3 by the summed activation $\sum_k \sigma^k$ across states, represents overall resource consumption at the local patch level, as well as slow non-specific inhibition; a general activity-dependent term is then added to the fixed (activity-independent) common threshold U of each Potts unit. Neuronal dynamics is taken to evolve more rapidly than adaptation effects, at a characteristic time scale τ_1 , at which input activation are reflected into the corresponding activation values of each state. It is at this rapid time scale that, as discussed above, attractor dynamics take place.

In the Potts auto-associative model, the positive feedback inherent to local attractor dynamics is replaced by a self-reinforcing term, of strength w , with which each activation σ^k feeds into itself. What does w really stand for? In a standard Hopfield model, the overlap m with a given memory, in the attractor state, satisfies an equation of the type [11]

$$m = \tanh[\beta(m + h^{\text{ext}})] \quad (3)$$

where $T = 1/\beta$ is an effective temperature, parametrizing the effects of noise or firing irregularity, and h^{ext} is an external cue, or signal, adding to the feedback in the direction of the retrieved memory. Also in graded response networks, the local feedback signal enters the analog of Eq. (3) with added the external signal. Obviously in such models the scale of the external signal is arbitrary. In the Potts network, the total signal received by a unit in one of its states σ^k is $w\sigma^k + m_G$, where m_G is a global overlap parameter of maximum value 1. The parameter w therefore represents the relative weight of the local over the global signal. Its value is expected to reflect the ratio of the number of local to long distance connections each unit receives, C_S/C_L , which is estimated to be of order 1 in the cortex [12].

3 Distinct Free Association Phases

When $\tau_1 \ll \tau_2 < \tau_3$, several different phases characterize latching dynamics [13]. If w is small (and T not too small), no latching occurs, unless the inactive state of each Potts unit is artificially made unstable by low or even negative thresholds, in which case latching is among uncorrelated states. As w grows, the network enters a narrow phase of *phasic* latching, in which it latches for only a few transitions, between correlated memories, followed by a *tonic* phase in which it latches until the generic thresholds prevent further transitions, hence for a time of order τ_3 . If w is even larger, latching can be sustained for an indefinitely long time, as the generic thresholds become ineffective to stop it. Several other parameters affect latching duration, and in particular a higher memory load leads to longer latching.

As for a local auto-associative network, each latching transition in the global Potts network is initiated by the self-reinforcing activation of some of the units previously in the quiescent state [9]. It can be shown that these units are those with the lowest threshold to be activated into the next global pattern, and their activation triggers a cascade of positive feedback that culminates into the “flip” into another attractor state – although in practice the transition can be much messier than a clean flip, as Fig. 1 illustrates. There is a limit, however, to how much the self-coupling w facilitates latching: when it crosses a further critical value, which depends on the temperature T , it stabilizes indefinitely any attractor state irrespective of adaptation, and the network is stuck (to the right of the blue curve in Fig. 2). Latching then occurs between the red and the blue curves, and indefinite latching to the right of the dashed curve in Fig. 2.

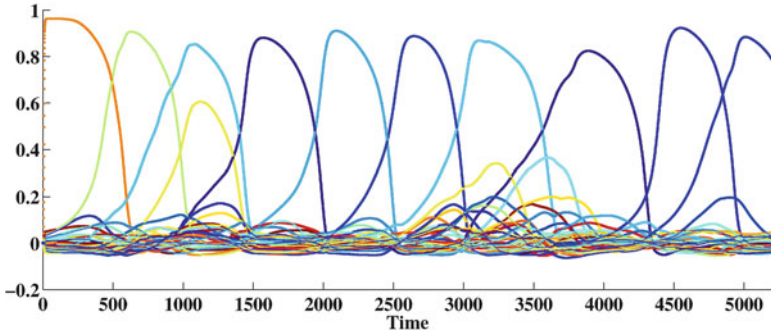


Fig. 1 Latching dynamics in the Potts network

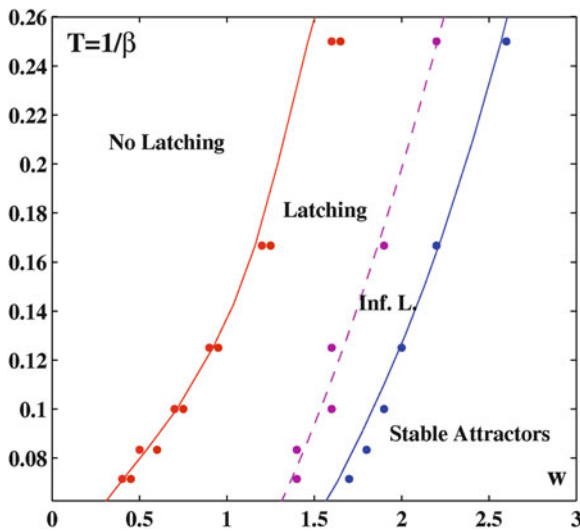


Fig. 2 Schematic Potts latching phase diagram, in the w - T plane, for uncorrelated patterns. Latching does not start above a critical temperature that grows rapidly with the self-coupling w (red curve). Beyond a lower critical temperature, latching goes on indefinitely (dashed curve). When the self-coupling is too strong, however (to the right of the blue curve) attractor states are stable, as firing rate adaptation fails to destabilize them. The data points are the results of numerical simulations, while the red and blue curves are derived semi-analytically [13] and the dashed curve is just to guide the eye (Color figure online)

4 The Role of Correlations

Crucially, the distance between the red and the blue curves grows with the mean variance Δ^2 in the interference, at retrieval, due to other stored patterns [13]. With randomly generated, and on average uncorrelated, patterns, $\Delta^2 \approx pa/(C_M S^2)$; when

instead patterns are generated with a multifactorial algorithm intended to reproduce plausible correlations among semantic representations [8]

$$\Delta^2 \approx p^2 S^{-2\gamma} \quad (4)$$

with $\gamma > 1$ (and sometimes the power law in Eq. (4) has to be replaced by an exponential). This implies that for any value of the effective temperature $T = 1/\beta$, to be beyond the dashed curve in Fig. 2 and hence to show indefinite latching, the network needs to have stored more patterns than a critical value p_l , which is roughly independent of C_M and scales supra-linearly with S .

This result, to be reported in full elsewhere, revises what had been extrapolated from early numerical simulations of the Potts network [8], and suggests the following scenario for the evolution of the cortical parameters underlying free associations and the capacity to sustain indefinite latching dynamics. Expansion in body weight and, particularly in humans, in pyramidal cell numbers [14] is accompanied by a much more moderate expansion in the cortical connectivity parameters C_S and C_L [15] which allows a parallel gradual increase in the number of distinct attractor states in a cortical patch, S , and, through C_M , in the number of global attractor states p , still compatible with associative memory operations [1, 5], ie $p < p_c$. When p crosses the lower critical latching value p_l , the correlations naturally arising from semantic data storage endow the cortex, which continues to operate as an associative memory machine, with the capacity for lateral thought. Such a scenario has to be corroborated by further analysis and ultimately to be submitted to experimental falsification.

References

1. Braitenberg, V., Schüz, A.: *Anatomy of the Cortex*. Berlin: Springer-Verlag (1991)
2. O’Kane, D., Treves, A.: Short and long range connections in autoassociative memory. *J. Phys. A* 25 (1992) 5055–5069
3. O’Kane, D., Treves, A.: Why the simplest notion of neocortex as an autoassociative memory would not work. *Network*. 3 (1992) 379–384
4. Hopfield, J.J.: Neural networks and physical systems with emergent collective computational abilities. *Proc. Natl. Aca. Sci. USA*. 79 (1982) 2554–2558
5. Rolls, E.T., Treves, A.: *Neural Networks and Brain Function*. Oxford: Oxford UP (1998)
6. Akrami, A., Russo, E., Treves, A.: Lateral thinking, from the Hopfield model to cortical dynamics. *Brain Research*, 1434 (2012) 4–16
7. Kanter, I.: Potts-glass models of neural networks. *Phys. Rev. A*. 37 (1988) 2739–2742
8. Treves, A.: Frontal latching networks: a possible neural basis for infinite recursion. *Cogn. Neuropsych.* 21 (2005) 276–291
9. Russo, E., Nambodiri, V.M.K., Treves, A., Kropff, E.: Free association transitions in models of cortical latching dynamics. *New J. Phys.* 10(1) (2008) 015008
10. Kropff, E. and Treves, A.: The storage capacity of Potts models for semantic memory retrieval. *J. of Statistical Mechanics: Theory and Experiment* (2005) P08010
11. Amit D.J., Gutfreund, H., Sompolinsky, H.: Storing infinite numbers of patterns in a spin-glass model of neural networks. *Phys. Rev. Lett.*, 55(14) (1985) 1530–1533

12. Abeles, M., 1982. *Local Cortical Circuits*. New York: Springer
13. Russo, E., Treves, A.: Cortical free-association dynamics: Distinct phases of a latching network. *Phys. Rev. E*. 85 (2012) 051920
14. Herculano-Houzel, S.: The human brain in numbers: a linearly scaled-up primate brain. *Front. Hum. Neurosci.* 3 (2009) art. 31, 1–11
15. Elston, G.N.: Pyramidal cells of the frontal lobe: All the more spinous to think with. *Journal of Neuroscience* 20 (2000) RC95 1–4

Learning and Decisions as Functional States of Cortical Circuits

José M. Delgado-García, Raudel Sánchez-Campusano, and Agnès Gruart

Abstract The complexity of brain functions can only be approached by a multidisciplinary and complementary approach. The availability of genetically manipulated mammals (mostly mice) and of sophisticated electrophysiological techniques, susceptible of being applied in behaving animals during the acquisition of different learning paradigms, has largely facilitated this approach. Our group has studied for years the contribution of hippocampal, motor, premotor, and prefrontal circuits to different types of associative and non associative learning paradigms. For this, we have recorded activity-dependent changes in strength in cortical and subcortical synapses during the acquisition process. Until now, we have studied the contribution of many different neurotransmitters and related receptors in selected transgenic and knock-out animals, as well as using *in vivo* si-RNA injection procedures. The main output of our studies is that learning is the result of the activity of wide cortical and subcortical circuits activating particular functional properties of involved synaptic nodes. Collected data indicate that many synaptic sites within cortical circuits modulate their synaptic strength across the successive stages of the acquisition of new motor and cognitive abilities. In addition, in this paper we elucidated the theoretical prediction of the relationships among different synaptic-learning states and the comparison between learning and performance.

Keywords Mice • Hippocampus • Associative learning • Classical conditioning • Synapses • Synaptic strength • Multisynaptic state functions

J.M. Delgado-García (✉) • R. Sánchez-Campusano • A. Gruart
Division of Neurosciences, Pablo de Olavide University, Seville, Spain
e-mail: jmdelgar@upo.es

1 Introduction

The study of neuronal mechanisms underlying learning and memory processes has been approached traditionally with the help of molecular, histological, *in vitro* electrophysiological procedures and other limited neurophysiological approaches [1]. Beside their evident advantages, those technical procedures use to generate profound alterations of the nervous system. In this regard, learning and related cognitive and motor processes should be studied at live, – i.e., at the very moment in which learning is taking place.

In addition, if we consider that the neuron is the basic functional element characterizing the nervous tissue, we would need to know the specific functional properties of each neural type present in a given neural circuit and its contribution, moment to moment, to the global process of learning, forgetting and remembering. Thus, each neuronal type in this circuit should play a specific role that can only be determined by the use of experimental models allowing its study in the best physiological conditions and during the acquisition of new motor or cognitive abilities [2–4]. We have developed the basic technology for the study of activity-dependent changes in synaptic strength at a given relay site [2].

In this paper, we have extended this information to many different synapses at the hippocampal and prefrontal circuits (see Fig. 1) during the acquisition and storage of associative and non-associative learning tasks in alert behaving wild-type mice.

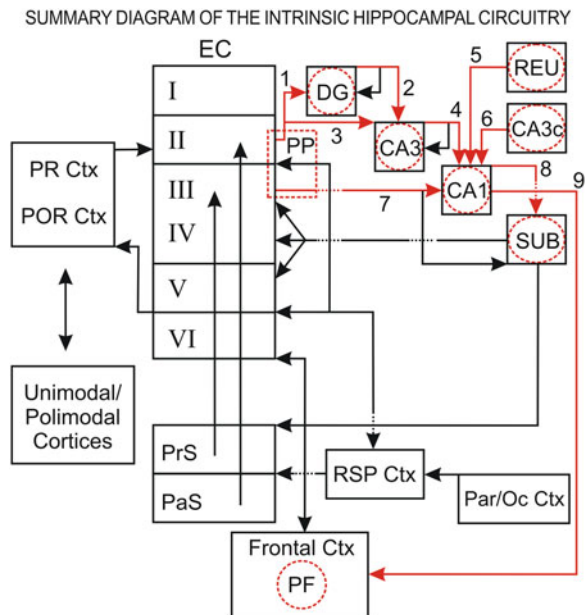


Fig. 1 Main synaptic pathways at the hippocampus, indicating input and output physiological connections. The synapses included in this study are indicated in red color with their corresponding numbers (e.g., 1, 2, 3, . . . , 9) (Color figure online)

2 Methods

Animals were prepared for the chronic recording of the electromyographic activity of orbicularis oculi muscle and of synaptic activity from the indicated neural synaptic sites (see Fig. 1). Animals were trained with a pavlovian training protocol (i.e., a classical eyeblink conditioning). The simultaneous recording of synaptic activities at different neural sites offers a still unknown picture of the specific functional states taking place at hippocampal and prefrontal circuits during the actual acquisition process. Synaptic relay sites included in this study were further characterised with the help of input/output curves, double-pulse tests, and by the experimental induction of long-term potentiation (LTP) or depression (LTD) [2, 4].

We used here mathematical tools developed in our laboratory to obtain the state functions characterizing the acquisition of new motor and/or cognitive skills [5]. For a specific behavioral/conditioning learning task, we can propose a synaptic-learning states matrix of the type:

$$\left\{ \begin{array}{ccc} S_{Nss,1}[t, x(t)] & \dots & S_{Nss,Nsy}[t, x(t)] \\ \vdots & \ddots & \vdots \\ S_{1,1}[t, x(t)] & \dots & S_{1,Nsy}[t, x(t)] \end{array} \right\} \uparrow$$

$i = 1, \dots, Nss$ (sessions); $j = 1, \dots, Nsy$ (synapses)

$S_{i,j}[t, x(t)] \mapsto$ Synaptic – learning states function

The states function comprised $i \times j$ components, each of which characterized the average of the synaptic strengths (taken trials by trials from i th session of all the experimental subjects) that were denoted here by the variable $x(t)$. The functional vector of the synaptic state (the rows in the matrix representation) is analogous to a precise picture of a specific pathway (e.g., the polysynaptic pathways at hippocampus – inputs and outputs connections) while the animal learns the task. A mathematical formulation of this state functions is the following:

$$S_{i,j}[t, x(t)] = \sum_{k=1}^{i-1} v_{i-k,j}(t) S_{i-k,j}[t, x(t)] + \sum_{n=1}^{j-1} \sum_{k=1}^i v_{k,n}(t) S_{k,n}[t, x(t)] + \xi_t$$

The first term to the right of the above equation represents the relations among the state $S_{i,j}[t, x(t)]$ and the previous learning states of the same synapse $S_{i-k,j}[t, x(t)]$ using the weight function $v_{i-k,j}(t)$. The second term to the right characterizes the functional couplings among the state $S_{i,j}[t, x(t)]$ and the

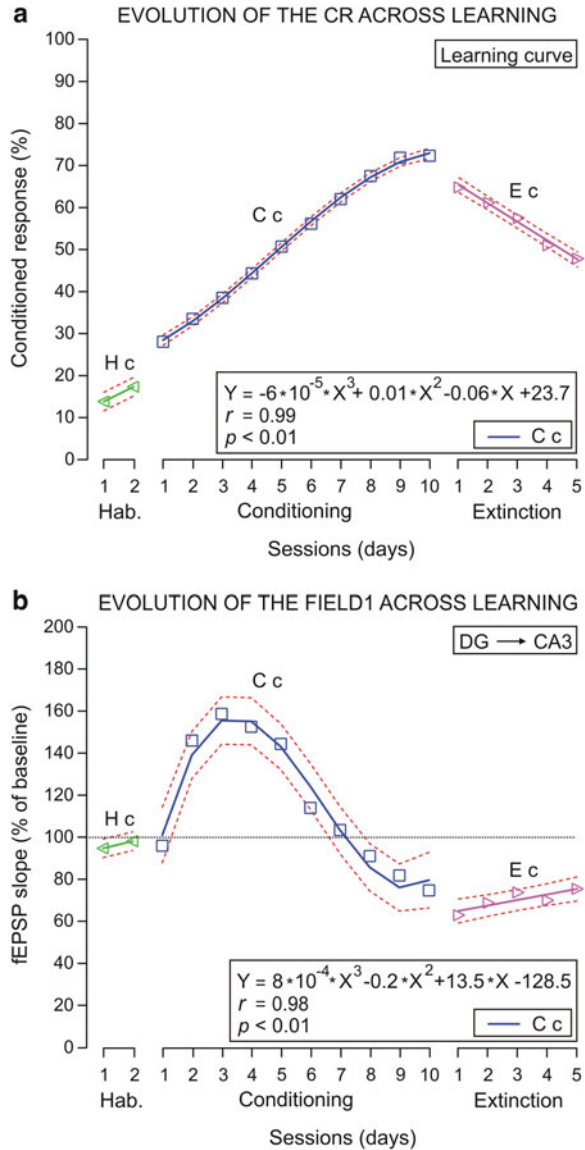
previous synaptic-learning states $S_{k,n}[t, x(t)]$ by means of the weight function $v_{k,n}(t)$. The time-dependent weights functions determine the strength (strong or weak) and type (linear or nonlinear) of interdependences among states as well as the timing-causality (time delays and correlation code) relationships among them (for details see [5]). The parameter ξ_t (the prediction error) estimates the uncertainties associated with the model and depends on the past values of all the synaptic-learning states (see the above equation). The programs/scripts used here were developed by one of us (R.S.-C.) with the help of MATLAB routines.

3 Results

In a study from our laboratory [2] we have shown that hippocampal synapses (specifically the CA3 \rightarrow CA1 synapse) changes in strength during the acquisition of an associative learning task – namely, the classical conditioning of eyelid responses. This learning-dependent change in synaptic strength was shown to be linearly related with the learning curve indicating a direct relationship between the acquisition of a new motor ability and the underlying synaptic plastic change. In the past few months we have been checking if all synapses in hippocampal and prefrontal circuits behave in the same way, that is, if all of them present similar changes in strength during this type of associative task. As illustrated in Fig. 2, the DG \rightarrow CA3 behaves in a quite different way presenting a complex evolution across the successive conditioning sessions. Thus, it was clear that each synapse in those cortical circuits contributes in a different way to the acquisition process.

As illustrated in Fig. 3, the functional complexity of cortical circuits during a simple type of associative learning becomes evident. The analytical and representational approaches (see the above equation and Fig. 3) enables a better determination and definition of functional states involved in the acquisition of new motor and cognitive abilities [5]. A precise vector (corresponding to a given functional state) will eventually be defined in quantitative terms describing the situation of multiple synapses – i.e., neurally generated kinetic commands (e.g., the synaptic strengths) and the level of the expression of learned responses – i.e., the kinematic (e.g., the eyelid biomechanical and electrical muscle activities) for a given training session. In the present study, the time-dependent weights functions allowed us to determine, in quantitative terms, the relationships among the different synaptic-learning states (e.g., the mathematical differences among the mean values of the color intensities in Fig. 3) – i.e., the quantitative and qualitative characterization of the changes in synaptic strength. The proposed experimental design also allows the incorporation of further kinetic and kinematic variables, with the sole condition that the same experimental conditioning situation is reproduced. Finally, this experimental approach will allow comparison between learning and performance in different experimental situations. In a recent study [5] we present a meta-analysis revealing future directions for the understanding of functional states during motor and cognitive learning.

Fig. 2 An example of the quantitative analysis for changes in synaptic strength taking place in the dentate gyrus (*DG*) → CA3 synapse during the acquisition of a classical eyeblink conditioning. **(a)** The typical learning curve calculated from the *orbicularis oculi* muscle activity. Animals were classically conditioned using a short tone as a conditioned stimulus and an electrical shock applied to the trigeminal nerve as an unconditioned stimulus. **(b)** The dynamic evolution of the synaptic strength (*DG* → CA3 synapse) during this associative learning process. Note that this synapse presents a complex polynomial evolution across the sessions (Color figure online)



4 Discussion

We hope that the present experimental approach will help to offer, for the very first time, a complete and quantifiable picture of synaptic events taking place in cortical circuits directly involved in the acquisition, storage, and retrieval of different types of associative and non-associative learning tasks. Indeed, our experimental

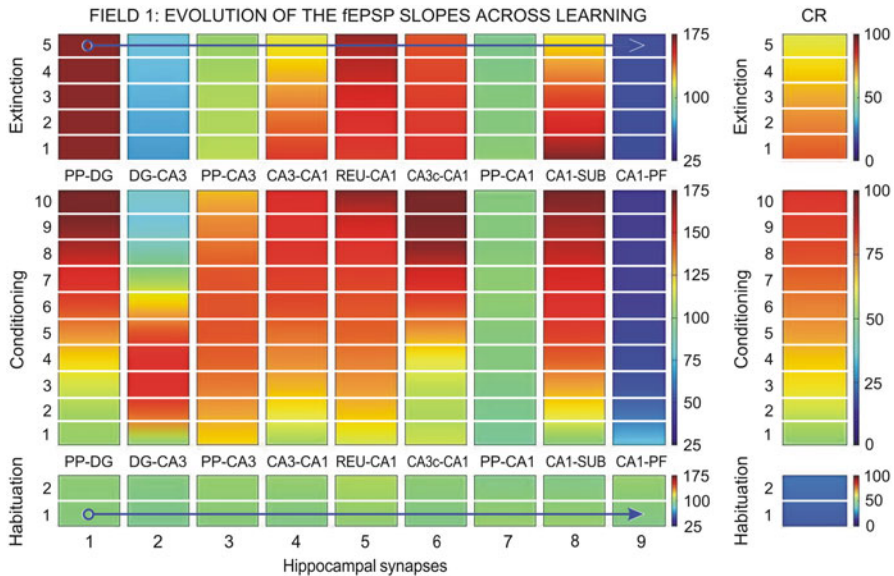


Fig. 3 A color map representation of the dynamic evolution of field excitatory postsynaptic potentials (*fEPSP*) collected across classical eyeblink conditioning sessions from alert behaving mice. Selected synapses were: perfortant pathway (*PP*) → dentate gyrus (*DG*); *DG* → *CA3*; *PP* → *CA3*; *CA3* → *CA1*; thalamic reuniens nucleus (*REU*) → *CA1*; contralateral *CA3* (*CA3c*) → *CA1*; *PP* → *CA1*; *CA1* → subiculum (*SUB*); and *CA1* → prefrontal cortices (*PF*). The selected synapses are indicated with the *corresponding numbers* (e.g., 1, 2, 3, . . . , 9). At the diagram are illustrated activity-dependent changes in synaptic strength taking place at the indicated synapses across the successive habituation ($n = 2$), conditioning ($n = 10$), and extinction ($n = 5$) sessions. The evolution of evoked conditioned eyelid responses (*CR*) is illustrated at the right diagram. Note that some synapses increased in learning-dependent strength across training (i.e., *PP* → *DG*, *CA3* → *CA1*), other did not present any significant change in this type of associative learning (*PP* → *CA1*), and finally, others decreased in their synaptic strength (*CA1* → *PF*) (see the quantitative *color bar* to the right of each panel) (Taken from Fernández-Guizán, A., Sánchez-Campusano, R., Gruart, A., and Delgado-García, J.M., in preparation) (Color figure online)

approach is susceptible of being used in different types of associative learning as instrumental [1] and classical conditioning [2], as well in other types of learning as spatial orientation [3], object recognition [4], etc. The main output of these types of study will be the precise definition of the functional state of large cortical synaptic circuits during the very moment at which learning is taking place. In this regard, we expect that a specific map (as the one illustrated in Fig. 3 for classical eyeblink conditioning – delay paradigm) will be offered in the near future for the different types of learning tasks.

In order to better understand the contribution of the cortical system to learning and memory processes, the same experimental protocols could also be applied to genetically manipulated mice or in animals receiving selective injections of si-RNA and other molecular approaches. Our laboratory is presently actively involved in these types of approaches.

References

1. Thompson, R.F., Patterson, M.M., Teyler, T.J. The neurophysiology of learning. *Annu. Rev. Psychol.* (23) (1972) 73–104.
2. Gruart, A., Muñoz, M.D. and Delgado-García, J.M. Involvement of the CA3-CA1 synapse in the acquisition of associative learning in behaving mice. *J. Neurosci.* (26) (2006) 1077–1087.
3. Diba, K., and Buzsáki, G. Hippocampal network dynamics constrain the time lag between pyramidal cells across modified environments. *J. Neurosci.* (28) (2008) 13448–13456.
4. Clarke, J.R., Cammarota, M., Gruart, A., Izquierdo, I., Delgado-García, J.M. Plastic modifications induced by object recognition memory processing. *Proc. Natl. Acad. Sci. U.S.A.* (107) (2010) 2652–2657.
5. Sánchez-Campusano, R., Gruart, A. and Delgado-García, J.M. Dynamic changes in the cerebellar-interpositus/red-nucleus-motoneuron pathway during motor learning. *Cerebellum* (10) (2011) 702–710. doi: 10.1007/s12311-010-0242-1.

Causal Effects for Prediction and Deliberative Decision Making of Embodied Systems

Nihat Ay and Keyan Zahedi

Abstract This article deals with the causal structure of an agent's sensori-motor loop and its relation to deliberative decision making. Of particular interest are causal effects that can be identified from an agent-centric perspective based on in situ observations. Within this identification, an optimal world model of the agent plays a central role. Its optimality is characterized in terms of prediction quality.

1 Introduction

Evaluating different possibilities and deliberately choosing among them is an important ability in humans and animals. In order to be intentional, such a choice has to be based on knowledge about causal consequences of individual brain dynamics. Within dynamical systems theory, a plausible model to describe switching between different dynamics is based on chaotic attractors [2]. However, in this framework the study of causality remains a challenge. In this paper, we address causal effects in the sensori-motor loop (SML) within a coarse-grained level of description where transitions are modelled in terms of stochastic maps.

We use the formalism of Bayesian networks to study the causal relations in the SML (see previous work [3] and [1] in this context). A Bayesian network consists of two components, a directed acyclic graph Γ and a set of stochastic maps describing

N. Ay (✉)

MPI for Mathematics in the Sciences, Inselstrasse 22, 04103 Leipzig, Germany

Max Planck Research Group Information Theory of Cognitive Systems, Santa Fe Institute,
1399 Hyde Park Road, Santa Fe, 87501 NM, USA

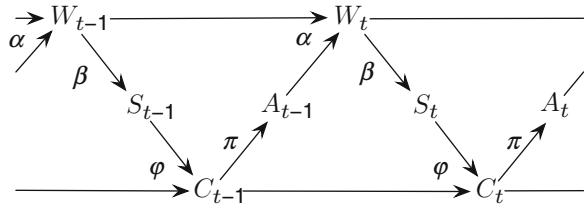
e-mail: nay@mis.mpg.de

K. Zahedi

Max Planck Research Group Information Theory of Cognitive Systems,
MPI for Mathematics in the Sciences, Inselstrasse 22, 04103 Leipzig, Germany

e-mail: zahedi@mis.mpg.de

Fig. 1 Causal diagram of the sensori-motor loop



the individual mechanisms of the nodes in the graph. More precisely, Γ is assumed to have no directed cycles (see Fig. 1 as an example). Given a node Y with state set \mathcal{Y} , we write $X := pa(Y)$ for the set of nodes X_i with an edge from X_i to Y . The mechanism of Y is formalized in terms of a stochastic map $\kappa : \mathcal{X} \times \mathcal{Y} \rightarrow [0, 1]$, $(x, y) \mapsto \kappa(x; y)$, where \mathcal{X} denotes the state set of X . The stochasticity of κ refers to $\sum_y \kappa(x; y) = 1$ for all x .

The Fig. 1 shows the general causal diagram for the SML, where W_t, S_t, C_t, A_t denote the world, sensor, controller (memory), and action at some time t . We denote their state sets by $\mathcal{W}, \mathcal{S}, \mathcal{C}, \mathcal{A}$, respectively. The stochastic maps α, β, φ , and π describe the mechanisms that are involved in the sensori-motor dynamics. Here, φ and π are intrinsic to the agent. They are assumed to be modifiable in terms of a learning process. The mechanisms α and β are extrinsic and encode the agent’s embodiment which sets constraints for the agent’s learning (for details, see [3, 5]).

Pearl [4] proposes the concept of intervention to capture causal relationships between random variables in a given Bayesian network. We will show that the formalization of the SML allows to determine causal relations solely observational without any experimental intervention, although its derivation is based on the concept of intervention (see Sect. 2). In this identification of causal effects, the optimal world model plays a central role. It is given as the conditional probability $p(s|c, a)$ of observing the next sensor state s as a result of the current controller state c and the current action a of the agent.

2 Causal Effects in the Sensori-Motor Loop

Figure 1 illustrates the causal structure of the SML. This representation has been used in [1, 3].

Pearl’s formalism [4] allows to define and study causal effects in the SML, for instance the effect of actions on sensor inputs. Here, a fundamental understanding is that in order to reveal causal effects one has to test the system in experimental situations (ex situ). In this context, intervention is an operation that serves as an important building block in corresponding experiments. However, it is not always possible for an agent to perform an intervention. Therefore, it is important to know whether a particular causal effect can be identified purely based on in situ observations of the agent. In the proposition below, we list three causal effects in

Fig. 2 Reduction procedure of the causal diagram

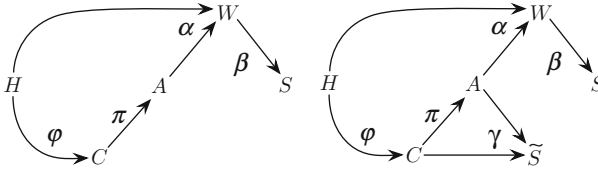
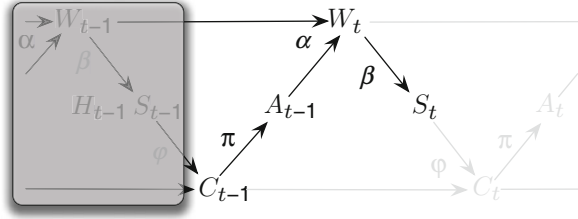


Fig. 3 *Left*: Reduced causal diagram for one time step. *Right*: Causal diagram with world model γ

the SML that are identifiable by the agent without actual intervention. In order to be more precise, we have a closer look at the causal diagram of the transition from time $t - 1$ to t .

Here, as shown in Fig. 2, we consider the future sensor value of only one time step and summarize the past process by a variable H_{t-1} . We focus on the resulting causal diagram of Fig. 3 (left-hand side). The joint distribution in the reduced diagram is given as

$$p(h, c, a, w, s) = p(h)\varphi(h; c)\pi(c; a)\alpha(h, a; w)\beta(w; s). \tag{1}$$

Given such a factorization of the joint distribution, one can define the intervention in a subset, which is referred to as *do*-operation. It is simply given by the corresponding truncation of the product, which formalizes the idea that the mechanisms of the intervened variables are changed from outside. As an illustration, we consider the product (1) and set the value A to a , that is we do a . The result of this conditioning is given as

$$p(h, c, w, s | do(a)) = p(h)\varphi(h; c)\alpha(h, a; w)\beta(w; s).$$

Summing over the variables h, c, w , for example, gives us the probability of observing s after having set a . The corresponding stochastic map is referred to as the *causal effect* of A on S :

$$p(s | do(a)) = \sum_{h,c,w} p(h, c, w, s | do(a)).$$

Note that, in general, we do *not* have $p(s | do(a)) = p(s | a)$, which is an important property of causal effects. Applying the described procedure, one can compute various other causal effects. The following question plays a central role in Pearl's causality theory: Is it possible for an observer, such as an autonomous agent considered in this paper, to reveal a causal effect based on observations only? At first sight, this so-called identifiability problem appears meaningless, because causal effects are based on the concept of intervention. However, having some structural information sometimes allows to identify causal effects from observational data.

The following causal effects can be identified by the agent without any actual intervention.

Proposition 1. *Let the joint distribution (1) be strictly positive. Then the following equalities hold:*

- (a) $p(s | do(a), c) := \frac{p(s, c | do(a))}{p(c | do(a))} = p(s | c, a)$
- (b) $p(s | do(a)) = \sum_c p(s | c, a) p(c)$
- (c) $p(s | do(c)) = \sum_a p(a | c) \sum_{c'} p(s | c', a) p(c')$.

The proof of Proposition 1 is given in the appendix. In all three causal effects of this proposition, the conditional distribution $p(s | c, a)$ turns out to be essential as building block for the identification of the causal effects. Note that in the strictly positive case, according to Proposition 1 (a), it is not dependent on the agent's policy. In the next section, this distribution will be studied in more detail.

3 World Model and Prediction

The causal effects of Proposition 1 involve the conditional distribution $p(s | c, a)$. In this section we derive an interpretation of this conditional distribution as optimal world model that allows for the best possible prediction. In order to do so, we extend the causal diagram of Fig. 3 by a world model γ which assigns a probability of observing s as a result of the action a in the context of the internal state c , formally $\gamma : (\mathcal{C} \times \mathcal{A}) \times \mathcal{S} \rightarrow [0, 1]$. The world model is a model of the agent's expectation, which can be used for a prediction \tilde{S} of the next sensor input S . We obtain the diagram of Fig. 3 (right-hand side).

The distribution of \tilde{S} given C is derived as

$$\begin{aligned} \tilde{p}(s|c) &:= \text{Prob}\{\tilde{S} = s | C = c\} \\ &= \sum_{a'} \pi(c; a') \gamma(c, a'; s). \end{aligned}$$

(Here, **Prob** stands for probability.) In order to measure the quality of the world model γ , we use the entropic distance, also known as KL divergence, between $\tilde{p}(s|c)$ and $\beta(w; s)$:

$$D(\beta \parallel \tilde{p}) := \sum_{c,w} p(c, w) \sum_s \beta(w; s) \ln \frac{\beta(w; s)}{\tilde{p}(s|c)}.$$

The following proposition identifies the conditional probability $p(s|c, a)$ as best world model in terms of this deviation measure.

Proposition 2. *If a world model $\hat{\gamma}$ satisfies $\hat{\gamma}(c, a; s) = p(s|c, a)$ whenever $p(c, a) > 0$ then it minimizes the distance $D(\beta \parallel \tilde{p})$:*

$$\begin{aligned} \inf_{\gamma} \sum_{c,w} p(c, w) \sum_s \beta(w; s) \ln \frac{\beta(w; s)}{\sum_{a'} \pi(c; a') \gamma(c, a'; s)} \\ = \sum_{c,w} p(c, w) \sum_s \beta(w; s) \ln \frac{\beta(w; s)}{\sum_{a'} \pi(c; a') p(s|c, a')}. \end{aligned}$$

This implies that the minimal distance coincides with the conditional mutual information $I(W; S | C)$.

The proof of Proposition 2 is a straightforward application of the Lagrange multiplier method.

4 Deliberative Actions

In the previous sections, we referred to a reactive interpretation of actions (see [4], p. 108). The corresponding reactive policy π assigns an action a to the agent’s state c , formalized in terms of a stochastic map $\pi : \mathcal{C} \times \mathcal{A} \rightarrow [0, 1]$, $(c, a) \mapsto \pi(c; a)$. In order to have a deliberative interpretation of a given policy, we decompose the internal state c into a memory state m and a goal state g , that is $c = (m, g)$ and $\mathcal{C} = \mathcal{M} \times \mathcal{G}$. We assume that the goal variable G only depends on the memory variable M , which leads to the causal diagram of Fig. 4.

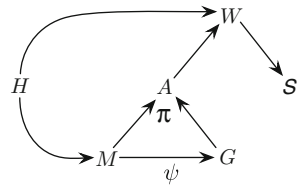


Fig. 4 Causal diagram with goal map ψ and deliberative policy π

The map ψ models the process of choosing a goal. Studying intentionality, we hypothesize that the causal effect $p(s | do(g))$ of the goal g on the sensor input s plays an important role. A simple calculation, similar to the one in the proof of Proposition 1(b), yields

$$\begin{aligned} p(s | do(g)) &= \sum_m p(s | m, g) p(m) \\ &= \sum_m \sum_a p(s | m, a) \pi(m, g; a) p(m). \end{aligned}$$

In particular, the causal effect of the goal variable G on the sensor variable S is identifiable. This implies that intentionality is identifiable through M, G, A, S , a conceptually interesting observation. Note, however, that this is only valid in the case of strict positivity of the underlying distribution.

Acknowledgements Both authors thank Ralf Der, Daniel Polani, and Bastian Steudel for valuable discussions on causal effects in the sensori-motor loop. This work has been supported by the Santa Fe Institute.

Appendix

Proof of Proposition 1:

$$\begin{aligned} \text{(a)} \quad p(h, c, w, s | do(a)) &= p(h) \varphi(h; c) \alpha(h, a; w) \beta(w; s). \end{aligned}$$

This implies

$$\begin{aligned} p(s, c | do(a)) &= \sum_{h,w} p(h) \varphi(h; c) \alpha(h, a; w) \beta(w; s) \end{aligned}$$

$$\begin{aligned} p(c | do(a)) &= \sum_s \sum_{h,w} p(h) \varphi(h; c) \alpha(h, a; w) \beta(w; s) \\ &= p(c) \end{aligned}$$

$$\begin{aligned}
 & p(s \mid do(a), c) \\
 &= \frac{p(s, c \mid do(a))}{p(c \mid do(a))} \\
 &= \sum_{h,w} \frac{p(h)}{p(c)} \varphi(h; c) \alpha(h, a; w) \beta(w; s) \\
 &= \sum_{h,w} p(h \mid c) p(w \mid h, a) p(s \mid w) \\
 &= \sum_{h,w} p(h \mid c, a) p(w \mid h, a, c) p(s \mid w, h, a, c) \\
 &\quad \text{(conditional independence, see diagram in Fig. 3)} \\
 &= p(s \mid a, c).
 \end{aligned}$$

The second and third equations of the proposition follow from the general theory (see [4], Theorem 3.2.2 (Adjustment for Direct Causes, and Theorem 3.3.4 (Front-Door Adjustment)). For completeness, we prove them directly.

(b)

$$\begin{aligned}
 & p(s \mid do(a)) \\
 &= \sum_{h,c,w} p(h, c, w, s \mid do(a)) \\
 &= \sum_{h,c,w} p(h) \varphi(h; c) \frac{\pi(c; a)}{p(a \mid c)} \alpha(h, a; w) \beta(w; s) \\
 &= \sum_{h,c,w} \frac{p(h, c, a, w, s)}{p(c, a)} p(c) \\
 &= \sum_c p(s \mid c, a) p(c).
 \end{aligned}$$

(c)

$$\begin{aligned}
 & p(s \mid do(c)) \\
 &= \sum_{h,a,w} p(h, a, w, s \mid do(c)) \\
 &= \sum_a \pi(c; a) \sum_{h,w} p(h) \alpha(h, a; w) \beta(w; s) \\
 &= \sum_a p(a \mid c) \sum_{h,w} \left(\sum_{c'} p(c') p(h \mid c') \right) \\
 &\quad \times p(w \mid h, a) p(s \mid w)
 \end{aligned}$$

$$\begin{aligned}
&= \sum_a p(a|c) \sum_{c'} p(c') \\
&\quad \times \sum_{h,w} p(h|c') p(w|h, a) p(s|w) \\
&= \sum_a p(a|c) \sum_{c'} p(c') \\
&\quad \times \sum_{h,w} p(h|c', a) p(w|h, a, c') p(s|w) \\
&= \sum_a p(a|c) \sum_{c'} p(c') p(s|c', a). \quad \square
\end{aligned}$$

References

1. N. Ay and D. Polani. Information flows in causal networks. *Advances in Complex Systems*, 1(11):17–41, 2008.
2. K. Kaneko and I. Tsuda. *Complex Systems: Chaos and Beyond*. Springer, 2001.
3. A. S. Klyubin, D. Polani, and C. L. Nehaniv. Tracking information flow through the environment: Simple cases of stigmergy. *Proceedings of Artificial Life IX*, 2004.
4. J. Pearl. *Causality: Models, Reasoning, and Inference*. Cambridge University Press, 2000.
5. K. Zahedi, N. Ay, and R. Der. Higher coordination with less control – a result of information maximization in the sensori-motor loop. *Adaptive Behavior*, 18(3–4):338–355, 2010.

Part VIII
Widespread of Cognitive Neurodynamics
Modeling

Ongoing Global Phase Pattern and Visual Signal Detection

Daisuke Shimaoka, Keiichi Kitajo, Kunihiro Kaneko, and Yoko Yamaguchi

Abstract When a stimulus is present on the threshold, it appears that we perceive it by chance. Previous electroencephalogram (EEG) studies have reported that the prestimulus phase and amplitude of alpha band activity at a single channel were correlated with visual perception. However, these factors cannot explain a major portion of fluctuations in perception. We hypothesized that another activity in the prestimulus period should predict the success/failure of perception. This would be phase coherence across cortical areas. We conducted a simple visual discrimination task in which subjects reported whether they had perceived a tiny flash of light by pressing one of two keys. We calculated inter-trial coherence (ITC) of the alpha band phase for the hit and miss trials, respectively. We found that the peak ITC times between hit and miss trials were 250–400 ms apart. These results imply that

D. Shimaoka (✉)

Department of Basic Science, The University of Tokyo, Komaba, Meguro-ku,
Tokyo 153-8902, Japan

Lab for Dynamics of Emergent Intelligence, RIKEN BSI, Hirosawa, Wako-shi,
Saitama 351-0198, Japan
e-mail: shimaoka@complex.c.u-tokyo.ac.jp

K. Kitajo

Lab for Cognitive Brain Mapping, RIKEN BSI, Hirosawa, Wako-shi, Saitama 351-0198, Japan

Rhythm-Based Brain Computation Unit, RIKEN BSI - Toyota Collaboration Center,
Hirosawa, Wako-shi, Saitama 351-0198, Japan

PRESTO, Japan Science and Technology Agency, 4-1-8 Honcho, Kawaguchi,
Saitama 332-0012, Japan

K. Kaneko

Department of Basic Science, The University of Tokyo, Komaba, Meguro-ku,
Tokyo 153-8902, Japan

Y. Yamaguchi

Laboratory for Dynamics of Emergent Intelligence, RIKEN Brain Science Institute,
Wako City, Japan

spontaneous formation of coherent alpha band activity and its timing are crucial in the processing of visual perception. These results suggest the importance of neural dynamics in the form of coherent alpha band activities in the frontal and occipital regions for the processing of visual perception.

1 Introduction

When an external stimulus is present on the threshold, it appears that we perceive it by chance. This fluctuation of perception has been assumed to derive from intrinsic neuronal noise. Recent experimental studies have revealed that such neuronal noise indeed possessed spatio-temporal organization instead of what had been originally assumed (called spontaneous or prestimulus activity). In addition, it has been revealed that fluctuation of prestimulus activity is associated with the processing of external stimuli [1]. In particular, previous electroencephalogram (EEG) studies reported that the prestimulus phase [2–4] and/or amplitude [5–7] of alpha band activity at a single channel were correlated with visual perception. However, when we assume that deterministic dynamics lead to perception, not only do amplitude and/or phase at a particular time prior to stimulus appear, their timing may also differ. We then hypothesized that timing of coherence provides crucial clues to determine whether subjects saw the light (hit trials) or not (miss trials). In this study, we conducted a simple visual discrimination task in which subjects reported whether they perceived a tiny flash of light by pressing one of two keys. We focused on the timing of respective prestimulus phase coherence for the hit and miss trials.

2 Methods

2.1 Subjects

Ten volunteers performed a discrimination task in which subjects reported whether they had perceived a flash by pressing one of two keys in 80 trials in 15 blocks. One participant was excluded from analysis due to excessive eye movements throughout the experiment. Another subject was excluded because of unstable behavioral performance. All participants had normal or corrected-to-normal vision. The RIKEN research ethics committee approved the study, and the experiment was undertaken with written informed consent.

2.2 Stimuli and Behavioral Task

Visual stimuli were presented on a gray background on a 150-Hz cathode ray tube monitor (FlexScan, Eizo, Japan). Subjects were instructed to pay covert attention

to the site indicated by peripheral markers (7° visual angles to the right of the fixation point), where the target flash (0.7° in size) might appear. The target was presented in 80% of the trials (the remaining 15% were flash-absent “catch” trials and 5% were trials with a high-luminance flash that subjects could easily perceive). The flash onset was randomly drawn from 2,200 to 2,500 ms after the onset of central fixation. The flash intensity for each subject was controlled with a staircase procedure so that the detection rate of the flash matched 50%. During the task, 64-channel scalp EEG signals and 4-ch electro-oculography (EOG) signals were recorded with a BrainAmp MR plus amplifier (Brain Products, Germany), and eye movement was recorded with a video-based eye-tracker (EyeLink CL, SR Research, Canada).

2.3 Data Analysis

EEG signals were first high-pass filtered at 1 Hz to correct linear trend. Then, the EEG record from 2,000 ms before to 500 ms after the flash was extracted as a record of a single trial. To remove artifacts derived from eye blinks, we excluded trials that contained EEG signals exceeding $\pm 100 \mu\text{V}$ or horizontal EOG signals exceeding $\pm 150 \mu\text{V}$. To remove artifacts derived from myoelectric signals, we also excluded trials that included EEG signals deviating in a -100 – $+25$ dB range at 20–40 Hz. In addition, using the data from the video-based eye-tracker, we excluded trials in which the eye position on the display deviated more than 2.5° of visual angles. EEG signals were decomposed into instantaneous phase ($\varphi(t)$) and amplitude at 10 Hz using wavelet transformation, where a Morlet wavelet of three cycles was used as the mother wavelet. We obtained inter-trial coherence (ITC) to quantify phase coherence across trials. ITC is defined as:

$$ITC(t) = \frac{1}{N} \left| \sum_{k=1}^N e^{-i\varphi_k(t)} \right|,$$

where N indicates the number of trials for each subject and perception condition. $\varphi_k(t)$ indicates the instantaneous phase at the k -th channel at time t . $ITC = 1$ indicates perfect phase coherence across trials, whereas $ITC = 0$ indicates that the phases are completely randomized over trials.

To study region specificity of the phase coherence, we classified the recording channels into four groups according to their locations on the scalp, namely, left frontal (Fp1, AF3, AF7, F1, F3, F5, F7, FC1, FC3, FC5, FT7), right frontal (Fp2, AF4, AF8, F2, F4, F6, F8, FC2, FC4, FC6, FT8), left occipital (CP1, CP3, CP5, TP7, P1, P3, P5, P7, PO3, PO7, O1, O9), and right occipital (CP2, CP4, CP6, TP8, P2, P4, P6, P8, PO4, PO8, O2, O10). A two-tailed t -test was conducted for each time step and group, where one sample was drawn from one channel in one group. This test examined whether ITC in one condition significantly deviated from that in another condition.

3 Results

3.1 Difference in ITC Peak Time Between Hit and Miss Trials

A study by Busch et al. [2] reported that the alpha band prestimulus phase was contrary in hit and miss conditions within 400–0 ms before the target presentation. We thereby investigated the ITC in this time range. Figure 1 indicates how different the ITC of hit and miss trials are at each time step as obtained from the data of two representative subjects. In one subject (Fig. 1a), significant ITC time for hit trials alternated with that for miss trials by 250 ms in the left frontal region. This alteration was more obvious in the result from the other subject (Fig. 1b). Here, the alteration was observed in all four regions. We also found that the peak time of the

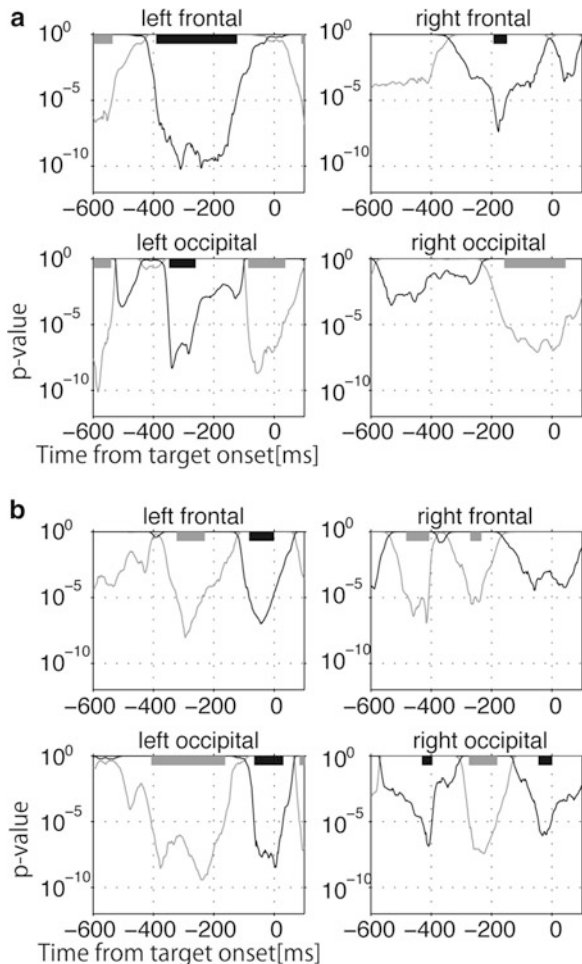


Fig. 1 Difference in prestimulus ITC between hit and miss trials. The recording channels are divided into four groups according to their location on the scalp. Using one sample as a datum from one channel, a t -test statistic is calculated for each group at each time. Y-axis indicates p -value that is transformed from a corresponding t -value. *Black line* indicates the p -value of whether the ITC distribution in the hit condition is larger than that in the miss condition. *Gray line* indicates the p -value of whether the ITC distribution in the miss condition is larger than that in the hit condition. The bars above each figure indicate the period where p -values are within $p < 0.05$ (Bonferroni corrected) (a) hit: 107 trials, miss: 99 trials, (b) hit: 178 trials, miss: 187 trials

prestimulus ITC nearest to target onset was for the hit condition in the left frontal region in six of eight subjects, although the peak times between subjects were not consistent.

3.2 Cross Correlation Between ITC of Hit and Miss Trials

Does this alteration of ITC appear only near the onset of the target, or hold for much longer? To verify this, we calculated the cross-correlation between the time courses of hit trial ITC and that of miss trials from 1,500 to 0 ms before target onset. We found that all the eight subjects exhibited significant negative correlation in the left occipital region (Spearman rank correlation, $p < 0.05$), whereas four of them also exhibited significant negative correlation in the left frontal region. Only two subjects exhibited significant negative correlation in the right frontal and occipital regions. These results indicate that ITC alteration of the hit and miss trials was maintained for at least 1,500 ms, mainly in the left occipital region.

4 Discussion

Busch et al. [2] reported that the prestimulus alpha band phase was correlated with perception. The study was based on the assumption that the coherent timing for hit and miss trials was identical (200 ms before the stimulus). In our study, however, the timing of ITC right before the target stimulus was associated with whether subjects perceived the flash. This means that the (absolute) phase of a particular timing plays a key role in whether we perceive the flash or not. In this sense, our findings are an extension of the previous report. Prediction of behavioral performance based on the timing of phase information remains to be explored.

Our cross-correlation analysis suggests that the alteration of peak ITC time could be observed for a long time before the target stimulus. One possible interpretation of this result is that an unknown coupling exists between the alpha band oscillation phase and that of a slower oscillation, such as theta and delta oscillations. It has occasionally been reported that coherent phase activity (mainly in gamma band) appears intermittently [8–10]. The findings of these studies and our results may be comparable in that coherent phase activity appeared intermittently in a few 100-ms intervals. Thus, there might be a common principle governing these processes. The relationship between our findings and that of prestimulus alpha band phase and amplitude previously reported should be investigated in a future study. In particular, it will be important to study the phase coherence in the frontal region, where significant prestimulus phase effects on perception were observed by Busch et al. [2]. Single-trial-based analysis will also be required to better predict perception and clarify the mechanism of prestimulus activity on perception.

Acknowledgments We thank H. Nakatani and J. Ito for helpful discussion. This study was partially funded by MEXT Grant-in-Aid for scientific research (No. 21120004: K Kaneko, No. 21120005: K Kitajo and YY), JST PRESTO program (K Kitajo) and by JSPS Fellows (DS).

References

1. S. Wakisaka, Y. Gunji, H. Ohta, K. Kitajo and Y. Yamaguchi, Binocular rivalry between patterns and visual noises: Way to 'see' your spontaneous activity in the early visual system by yourself, *Perception* **37** (2008)
2. N.A. Busch, J. Dubois and R. VanRullen, The phase of ongoing eeg oscillations predicts visual perception., *J Neurosci* **29** (2009) 7869–7876.
3. N.A. Busch and R. VanRullen, Spontaneous eeg oscillations reveal periodic sampling of visual attention., *Proc Natl Acad Sci U S A* **107** (2010) 16048–16053.
4. K.E. Mathewson, G. Gratton, M. Fabiani, D.M. Beck and T. Ro, To see or not to see: Prestimulus alpha phase predicts visual awareness., *J Neurosci* **29** (2009) 2725–2732.
5. T. Ergenoglu, T. Demiralp, Z. Bayraktaroglu, M. Ergen, H. Beydagi and Y. Uresin, Alpha rhythm of the eeg modulates visual detection performance in humans., *Brain Res Cogn Brain Res* **20** (2004)376–383.
6. H. van Dijk, J.M. Schoffelen, R. Oostenveld and O. Jensen, Prestimulus oscillatory activity in the alpha band predicts visual discrimination ability., *J Neurosci* **28** (2008)1816–1823.
7. S. Hanslmayr, A. Aslan, T. Staudigl, W. Klimesch, C.S. Herrmann and K.H. Bäuml, Prestimulus oscillations predict visual perception performance between and within subjects., *Neuroimage* **37** (2007)1465–1473.
8. S. Doesburg, K. Kitajo and L. Ward, Increased gamma-band synchrony precedes switching of conscious perceptual objects in binocular rivalry., *Neuroreport* **16** (2005)1139–1142.
9. H. Nakatani and C. van Leeuwen, Transient synchrony of distant brain areas and perceptual switching in ambiguous figures., *Biol Cybern* **94** (2006) 445–457.
10. E. Rodriguez, N. George, J. Lachaux, J. Martinerie, B. Renault and F. Varela, Perception's shadow: Long-distance synchronization of human brain activity., *Nature* **397** (1999) 430–433.

Model on Visualization and Analysis for Peripheral Drift Illusion

Keiichiro Inagaki and Shiro Usui

Abstract The peripheral drift illusion yields rotating motion on our peripheral vision. It has been reported that the order of four different luminance regions is essential for this illusion (black, blue (dark gray), yellow (light-gray), and white). Moreover, it has been suggested that luminance or contrast dependent latency of V1/MT direction selective cells contributes on induction of the rotating illusory motion. In the present work, we modeled V1 and MT as a retinotopic map of those direction selective cells and investigated whether the illusory rotating motions in peripheral drift illusion can be reproduced. In our simulation, the illusory rotating motions are represented in the transition of neuronal responses in both V1 and MT when the responses are visualized in contrast domain, but not in luminance domain, suggesting that the contrast is key information for induction of the rotating motion in the peripheral drift illusion.

Keywords Illusory motion • Primary visual cortex • Middle temporal • Model simulation

1 Introduction

Most people perceive an impressive illusory motion in the static image called peripheral drift illusion (e.g. Fraser and Wilcox [8], Rotating snake [12]). The peripheral drift illusion composed of luminance defined patterns with four different

K. Inagaki (✉)

Computational Science Research Program, RIKEN, Saitama 351-0198, Japan

e-mail: kay@brain.riken.jp

S. Usui

Laboratory for Neuroinformatics, RIKEN Brain Science Institute, Saitama 351-0198, Japan

Computational Science Research Program, RIKEN, Saitama 351-0198, Japan

adjacent luminance patches: black, blue (dark gray), white, and yellow (light gray); where illusory rotating motion is perceived in this order. Recently these illusory images are regarded as an art and attract a great deal of interest [15]. In contrast, the scientific studies for perception of the illusion were minority [1, 2, 6, 7, 12, 13, 16]. So far, several lines of evidence have been proposed for the perceptual mechanism of the peripheral drift illusion. Faubert and Herbert have suggested that the apparent motion was induced by difference latency among different luminance [7]. Kitaoka and Ashida have also proposed that the order of the four different luminance regions is essential for the illusion perception [12]. Namely, the illusory rotating motion depends on the fact that contrast of black and white are higher than blue (dark gray) and yellow (light gray), and the apparent motion was produced from high contrast to low contrast. In fact, contrast dependent latency of the neuronal responses was reported in bipolar cell [3], amacrine cell [4], and retinal ganglion cell [5]. Moreover, Conway et al. have experimentally revealed contrast dependent difference of the neuronal response in V1 and MT by using stimuli involved with the rotating snake, and found that the peak responses of V1 and MT direction selective cells for white or black bars were earlier than that for blue (dark gray) and yellow (light gray) [6]. Backus and Oruç have reported that the rotating snake and the Fraser and Wilcox illusion result from contrast or luminance adaptation [1]. They proposed that fast and slow changes over time in the neuronal representation of contrast or luminance gradually deform the representation of stimulus image. Thus, the contrast dependent latency was thought to be related with the peripheral drift illusion; however, how this contributes on the induction of illusion is still unknown.

In the present work, we modeled V1 and MT as a retinotopic map using those direction selective cells [6] for visualization of the peripheral drift illusion, and analyzed its perceptual mechanisms. In our simulation, the rotating motions were represented in the transition of neuronal responses in both V1 and MT when the responses were visualized in contrast domain, but not in luminance domain. This suggests that contrast is a key information for reproducing the rotating motion in the peripheral drift illusion.

2 Methods

2.1 The Model of V1/MT

Both V1 and MT models were constructed as retinotopic maps consisted of 133,225 (365×365) direction selective cells each (Fig. 1). The temporal response of V1 and MT direction selective cells for each luminance input (black, dark gray, light gray, and white) was modeled by the following equation.

$$\begin{aligned} F(s) &= X(s) \cdot G(s) \\ &= X(s) \cdot g \cdot e^{-\tau s} / (\alpha s^2 + \beta s + \gamma) \end{aligned} \quad (1)$$

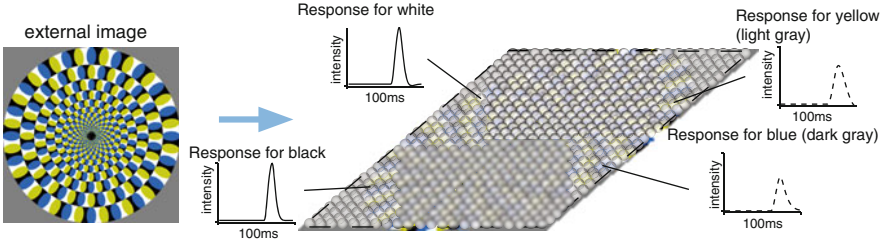


Fig. 1 Retinotopic model of V1 or MT. The model configured from 133,225 (365×365) direction selective cells of V1 or MT. In each model, an external image was directly projected onto the cells, and the response of each cell was computed as impulse response for the luminance (contrast)

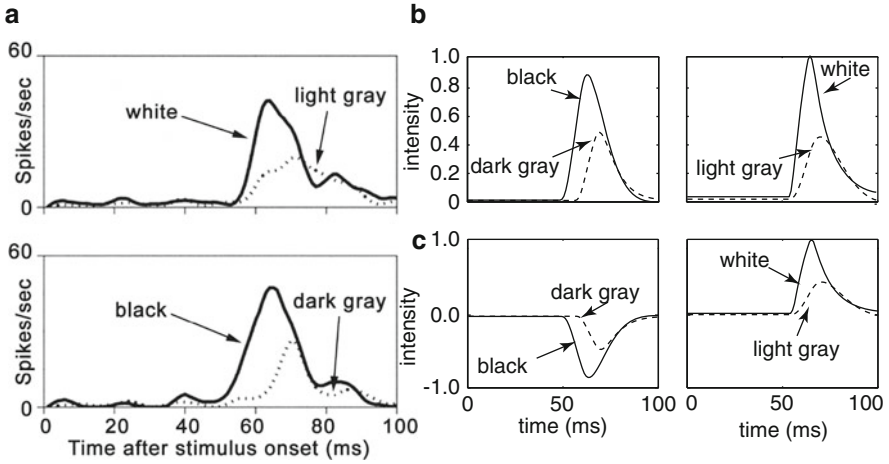


Fig. 2 Neuronal response of V1 direction selective cell for the four types of luminance input (*black, dark gray, light gray, and white*): experimental data [12] (a) and the model response parameterized for luminance (b) and for contrast (c). In each panel, *solid line* indicates response for *black or white*, and *dashed line* indicates response for *dark gray or light gray*

where, s denotes Laplace operator, and $X(s)$ is the Laplace transform of absolute value of difference between luminance and gray ($|I_{in} - I_{gray}|/I_{gray}$). τ denotes delay time of a neuronal response. The parameter α, β, γ , and g were estimated by fitting the model output to temporal response of V1 or MT reported by Conway et al. [6], while τ was globally searched between 40 and 65 ms in 1 ms steps. Parameter estimation was carried out in MATLAB. After determined the model parameter, response of the model was parameterized for either luminance or contrast (Figs. 2, and 3) for visualization. In the parameterization for the luminance (Figs. 2, and 3b), the model output was normalized to take a range from 0.0 (black) to 1.0 (white). For the contrast (Figs. 2, and 3c), low and high contrast were defined to be negative and positive value, respectively, and the model output was normalized (0 (gray) to 1.0 (white) or -1.0 (black)).

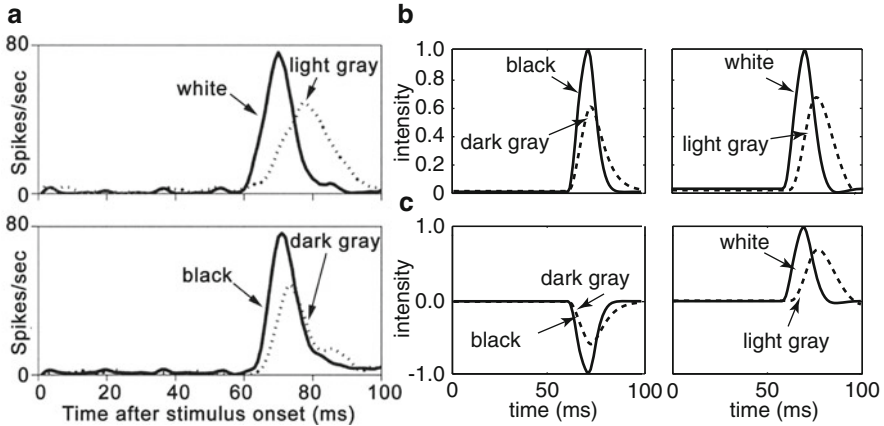


Fig. 3 Neuronal response of MT direction selective cell for the four types of luminance input. The format is the same as Fig. 2

3 Results

We used the rotating snake and control stimulus (Fig. 4) as the model input, where the order of color unit (black-blue-white-yellow) was arranged in the same direction for the former, but reversed between every unit for the later.

In agreement with experimental study [12], similar rotating motions were observed as the transition of neuronal responses in both the V1 and the MT model were visualized in contrast domain. On the other hand, opposite directional rotating motion was found in both model responses when visualized in luminance domain. For the control stimulus, no rotating motion was observed for both contrast and luminance.

To quantify the reproduced motion, we analyzed the transition of the neuronal response of V1 and MT using optical flow. The optical flows were calculated every five pixel using Lucas-Kanade algorithm [14]. Note that the counter clockwise flows correspond to direction of rotating illusion.

Figure 5 illustrates an example of the optical flows (indicated by red lines) in MT neuronal response for the rotating snake (a) and the control stimulus (b).

The counter clockwise flows were mostly found in the peripheral region of V1 (data not shown) and MT when those responses were visualized in contrast domain (Fig. 5a). For the control stimulus, the flows for both clockwise and counter clockwise rotation were detected (Fig. 5b), thus canceling the perception of rotating motions.

The number of clockwise and counter clockwise flows is summarized in Table 1. When the neuronal responses were visualized in contrast domain, almost all detected flows in both V1 and MT were counter clockwise for the rotating snake. For the control stimulus, the number of the counter clockwise flows was smaller than the

Fig. 4 Rotating snake (*left*) and control (*right*) stimulus. Color unit defined by *black*, *blue*, *white*, and *yellow* is repeated every unit for the rotating snake while it is reversed every unit for the control (Color figure online)

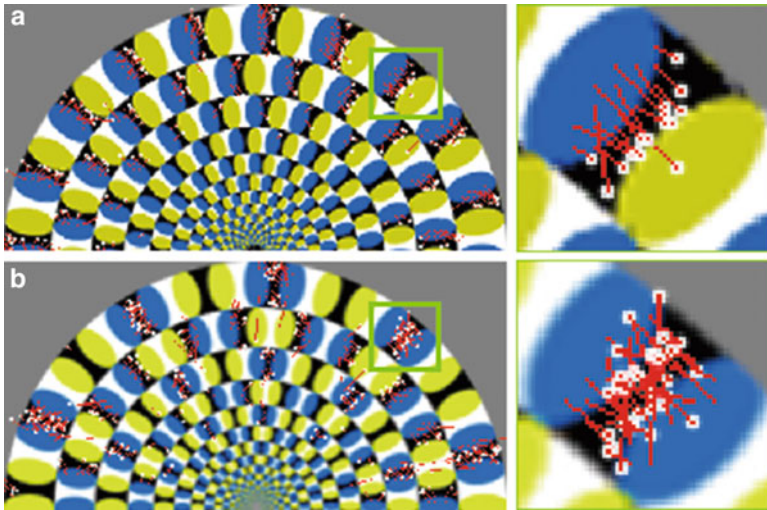
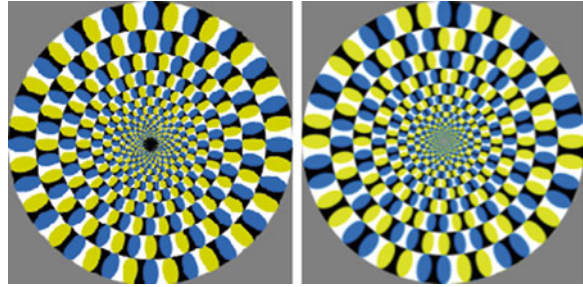


Fig. 5 Simulation of the MT responses for the rotating snake (a) and the control stimulus (b). The model response was visualized in contrast domain. *Right image* shows enlarged image of green region in *left image*. *Red lines* and *white boxes* indicate detected optical flows and those starting points (Color figure online)

Table 1 Summary of detected optical flow

	Condition	Stimulus	Percentage of detected flow	
			Clockwise	Counter clockwise (rotating motion)
V1	Luminance	Rotating snake	99.7%	0.3%
		Control	60.4%	39.6%
MT		Rotating snake	75.6%	24.4%
		Control	59.9%	40.1%
V1	Contrast	Rotating snake	1.6%	98.4%
		Control	64.6%	35.4%
MT		Rotating snake	0.2%	99.7%
		Control	62.4%	37.6%

clockwise one in both V1 and MT. When the neuronal response was visualized in luminance domain, mostly clockwise flows were detected in both V1 and MT for the rotating snake.

4 Discussions and Conclusion

In the present study, we modeled the V1 and MT direction selective cells based on those single unit data [6], and constructed the retinotopic map of both cells. In agreement with experimental study [12], similar rotating motion was observed in both the V1 and the MT model in which the neuronal responses were parameterized in contrast domain. By analyzing the V1 and MT response transition by optical flow, the flows accompanied with the rotating illusory motion were represented peripherally in those maps for the rotating snake, while the flows countervailing the perception of rotating illusion were observed in the control stimulus. The results indicated that the signal source for the perception of rotating snake were represented in both V1 and MT, and suggested that the contrast is a key signal to drive an illusory motions in the peripheral drift illusion as reported by previous studies [1, 6, 12].

Several lines of evidence indicated the involvement of fixation instability (microsaccades and drift) for the generation of rotating illusion [1, 16]. Recently, we have developed the model that can generate the fixation instability [9] and will integrate the present model to evaluate the contribution of fixation instability on the induction of illusory rotating motions. Furthermore, we recently put forward to aid in uncovering various neuronal mechanisms on our vision including those for attention, illusion, and subconscious perception [10, 11, 17]. In future studies, we will integrate the present model on the whole visual system model and analyze the perceptual mechanisms of the peripheral drift illusion.

Acknowledgments We thank to Drs. T. Kannon and H. Sasaki for valuable discussions, and Mr. N.L. Kamiiji for comments on earlier version of manuscript. This research was supported by “The Next-Generation Integrated Simulation of Living Matters”, part of the Development and Use of the Next Generation Supercomputer Project of the MEXT.

References

1. Backus, B.T., Oruc, I. Illusory motion from change over time in the response to contrast and luminance. *J. Vis.*, 5 (2005), 1055–1069.
2. Beer, A.L., Heckel, A.H., Greenlee, M.W. A motion illusion reveals mechanisms of perceptual stabilization. *PLoS one*, 3 (7) (2008), 1–7.
3. Burkhardt, D.A., Fahey, P.K. Contrast enhancement and distributed encoding by bipolar cells in the retina. *J. Neurophysiol.*, 80(3) (1998), 1070–1081.
4. Burkhardt, D.A., Fahey, P.K. Contrast rectification and distributed encoding by ON-OFF amacrine cells in the retina. *J. Neurophysiol.*, 82(4) (1999), 1676–1688.

5. Burkhardt, D.A., Fahey, P.K., Sikora, M. Responses of ganglion cells to contrast steps in the light-adapted retina of the tiger salamander. *Vis Neurosci.* 15(2) (1998), 219–29.
6. Conway, B.R., Kitaoka, A., Yazdanbakhsh, A., Pack, C.C., Livingstone, M.S. Neural basis for a powerful static motion illusion. *J. Neurosci.*, 25(23) (2005) 5651–5656.
7. Faubert, J., Herbert, A.M. The peripheral drift illusion: A motion illusion in the visual periphery. *Perception*, 28 (1999), 617–621.
8. Fraser, A., Wilcox, K.J.: Perception of illusory movement. *Nature* 281 (1979) 565–566.
9. Inagaki, K., Kannon, T., Kamiyama, Y., Satoh, S., Kamiji, N., Hirata, Y., Ishihara, A., Shouno, H., Usui, S. Environment for an integrative model simulation: PLATO. *Frontiers in Neuroscience*, abstract: Neuroinformatics 2010, (2010) P91.
10. Inagaki, K., Hirata, Y., Usui, S. A model-based theory on the signal transformation for microsaccade generation. *Neural networks*, submitted.
11. Kannon, T., Inagaki, K., Kamiji, N., Makimura, K., Usui, S.. PLATO: Data-oriented approach to collaborative large-scale brain system modeling. *Neural networks*, submitted.
12. Kitaoka, A., Ashida, H.: Phenomenal characteristics of the peripheral drift illusion, *Vision*, 15 (4) (2003), 261–262.
13. Kuriki, I., Ashida, H., Murakami, I., Kitaoka, A. Functional brain imaging of the Rotating Snakes illusion by fMRI. *J. Vis.*, 8(10):16 (2008), 1–10.
14. Lucas, B.D., Kanade, T.: An iterative image registration technique with an application to stereo vision.. *Proc. of Image understanding workshop*, (1981), 121–130.
15. Martinez-Conde, A., Macknik, S.L., *Art as Visual Research: Kinetic Illusions in Op Art*, *Scientific american*, (2010), 48–55.
16. Murakami, I., Kitaoka, A., Ashida, H. A positive correlation between fixation instability and the strength of illusory motion in a static display. *Vision Res.*, 46 (2006), 2421–2431.
17. Usui, S., Inagaki, K., Kannon, T., Kamiyama, Y., Satoh, S., Kamiji, N.L., Hirata, Y., Ishihara, A., Shouno, H. A next generation modeling environment PLATO: Platform for collaborative brain system modeling. *Lecture Notes in Computer Science*, 5863 (2009), 84–90.

Differentiation Through Symbolic Communication

Takuma Torii and Takashi Hashimoto

Abstract We explore the manner in which a neuro-symbolic hybrid system differentiates through symbolic communication. The hybrid system consists of a recurrent neural network and a rewriting rule system. It is shown that the differentiation comes from the asymmetric structure of the symbol system, i.e., usage of different rules in deriving and accepting the same symbolic message. The dynamics of symbolic communication depends on the phase space structure of the neural system. The asymmetric structure is realized by generalization, and it must be ubiquitous in adaptive symbol systems such as human language.

1 Introduction

In human communication, a symbolic message is often differently understood by different people. It is often speculated that this difference in understanding stems from their physical, neural, and experiential differences. This speculation raises the following question: can the differentiation of systems be possible from completely identical physical and neural systems? Further, for such cases, if it is the case, what is the mechanism of differentiation?

Kaneko and Yomo [1] studied cell differentiation from the dynamical viewpoint. They showed that very similar cells can be differentiated after cell division due to chaotic dynamics. In contrast to their focus on the chaotic nature of cells, we concentrate on the symbolic nature of human communication, where a sequence of symbols referring to something are interchanged.

T. Torii (✉) • T. Hashimoto

School of Knowledge Science, Japan Advanced Institute of Science and Technology,
1-1 Asahidai, Nomi, Ishikawa 923-1292, Japan
e-mail: tak.torii@jaist.ac.jp; hash@jaist.ac.jp

2 Model

We construct a model of symbolic communication between two agents, a speaker and a hearer (see [2] for details). Each agent $\mathbf{p/q}$ consists of a symbol system \mathbf{S} and a neural system \mathbf{N} . The symbol system \mathbf{S} is a rewriting rule system consisting of a set of rules mapping expressions e and internal representations r . The rules are generalized by rule-generalization algorithms. The neural system \mathbf{N} is a recurrent artificial neural network.

Communication is defined as the interchange of expressions e between the speaker and the hearer. The internal process of the agents consists of three phases: (1) *Acceptance*: The symbol system \mathbf{S} transforms an expression e^A received from the other agent (the speaker) into an internal representation r^A ; (2) *Sensemaking*: The neural system \mathbf{N} converts the internal representation r^A into a new internal representation r^D ; (3) *Derivation*: The symbol system \mathbf{S} transforms the new internal representation r^D into an expression e^D to be sent to the other agent. Since the symbol system \mathbf{S} cannot always map between expressions e and representations r , two additional processes are required: (1) *Instruction*: When the acceptance fails, the speaker communicates to the hearer the speaker's internal representation r^A by some other means, e.g., pointing to an object to which r^A refers. (2) *Invention*: When the derivation fails, an expression e^D is randomly produced. We call the internal process from acceptance to derivation a *turn*. The actual communication between two agents is a series of turns (Fig. 1).

2.1 Symbol System

A symbolic rule “ $k / r \leftrightarrow e$ ” is a mapping between a representation r and an expression e , discriminated by a label k , where both r and e are sequences of characters (examples are shown in Fig. 3). The rule can contain labeled variables, which will be substituted by another rule discriminated by the same label in the acceptance and derivation processes. Rules can be learned with generalizations (see [2]), which are operations involving the creation of a generalized rule by replacing different or common parts of two rules with a labeled variable. In this model, the rules are chosen on predefined priorities and not in a probabilistic manner. Thus, differentiation cannot occur due to rule selection. Two types of characters are assigned to e and r , respectively.

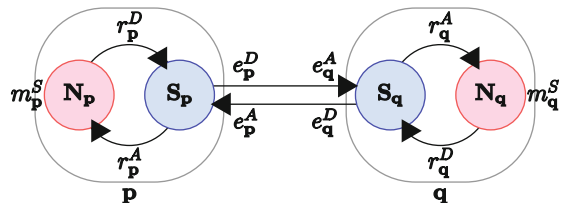


Fig. 1 Model of symbolic communication

2.2 Neural System

The neural network consists of sets of 2 input, 2 output, and 6 hidden neurons denoted by \mathbb{I} , \mathbb{O} , and \mathbb{H} , respectively. The numbers of input and output neurons are determined by the method of converting a character sequence r into an input to the neural system.¹ In this model, we adopt the winner-take-all coding scheme, and there are two different types of characters. The i -th neuronal state y_i^t at time t ($= \{1, 2, \dots, T\}$) changes according to the equation

$$y_i^{t+1} = \sum_j w_{ji}^t z_j^t + \alpha I_i^t + \beta O_i^t,$$

where w_{ij} ($= [-8, 8]$) denotes a constant connection weight from the j -th to i -th neuron, z_j ($= [0, 1]$) indicates the firing rate of the j -th neuron updated by $z_j = 1/(1 + \exp(-y_j))$, $O_{i \in \mathbb{I}}$ ($= [-1, 1]$) denotes linear transformation of an output $z_{l \in \mathbb{O}}$ ($= [0, 1]$) of the other agent's neural network, and $I_{i \in \mathbb{I}}$ denotes the input to the i -th neuron from the symbol system determined by the equation

$$I_i^k = \begin{cases} R_{ik} & \text{if } 1 \leq k \leq |r| \\ 0 & \text{otherwise} \end{cases}.$$

In accordance with the winner-take-all coding, each character is represented as a sequence of binary values. Thus, R_{ik} ($= \{-1, 1\}$) is the i -th binary value of the k -th character of a representation r . The terms α ($= 8.0$) and β ($= 8.0$) represent constant parameters.

The agents interchange a total of U ($= 1,000$) expressions in simulation. The neural networks are updated T ($= 100$) times for every turn u ($= \{1, 2, \dots, U\}$), in which the speaker and the hearer process r^A and r^D , respectively. The term τ ($= \{1, 2, \dots, TU\}$) hereafter denotes the time after t updates in the u -th turn.

3 Results

The neural systems are identical initially; these identical systems include not only w_{ij} but also y_i and z_i . Due to the reduced size of the present model, generalization in the symbol system usually stops when the symbol system is able to transform any representations produced by the coupled neural system.

¹We decided on the number of hidden neurons by examination of the smallest system with chaotic behavior.

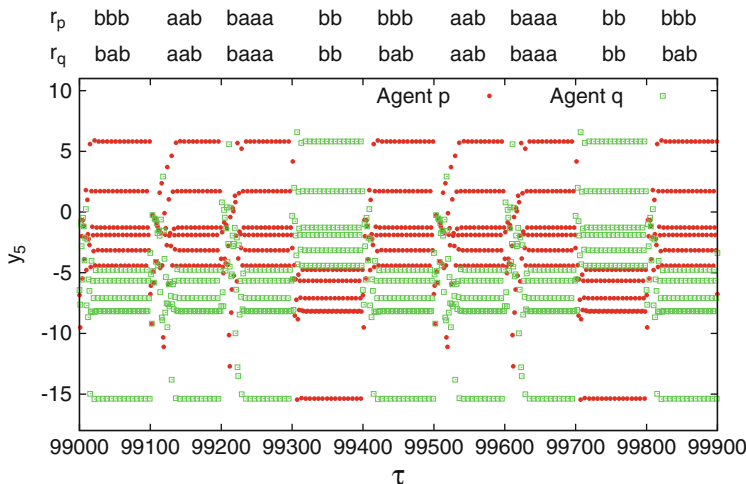


Fig. 2 The neuronal dynamics of hidden neurons and the representations formed (r_p/r_q). Their neural systems transit the two alternative attractors (period-six) driven by the inputs R_{ik} given every $T (= 100)$ steps

$S / b x^N \leftrightarrow A x^N$	(1)
$S / a x^N \leftrightarrow A x^N$	(2)
$N / b \leftrightarrow B$	(3)

Fig. 3 An example of a symbol system with DA-asymmetry. ‘S’ and ‘N’ are labels, ‘x’ is a variable, ‘a’ and ‘b’ are characters for representation r , ‘A’ and ‘B’ are those for expression e

Figure 2 shows a converged periodic time-evolution of symbolic communication where differentiation in neural dynamics is observed. The agents evolve to exhibit different dynamics although they start as completely identical systems.

The differentiation only happens when the agents’ identical symbol systems have different paths of rule substitution in the derivation and acceptance processes of an expression. We call this property “derivation-acceptance asymmetry” (DA-asymmetry). If the agents have this property, the agents have different representations for the same expression.

Figure 3 is an example of a symbol system with DA-asymmetry. An agent with the symbol system in Fig. 3 performs the derivation from the representation $r^D = ‘b b’$ to the expression $e^D = ‘A B’$ by substituting rule (3) into the variable x^N in rule (1). On the other hand, the agent can possibly accept the received expression $e^D = ‘A B’$ via two paths of acceptance, namely, as the representation $r^A = ‘b b’$ by substituting rule (3) into rule (1) and $r^A = ‘a b’$ using rule (2) instead of (1). Actually, in the present model, a path is selected deterministically based on predefined priorities without multiple possibilities. It is noteworthy that the agent may use different paths in derivation and acceptance under any rule selection strategy. This is the case of differentiation, where the speaker and the

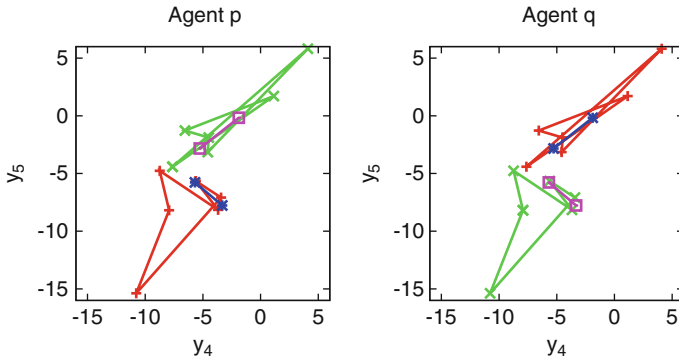


Fig. 4 Four coupling attractors of the coupled neural system, corresponding to Figs. 2 and 5. A coupling attractor is a pair of individual attractors (e.g., '+' in the figures on the left and right

hearer processing identical symbol systems may have different representations for the same expressions, so that their neural systems receive different inputs, thereby causing differences in the dynamics of their neural systems.

Generalization of a rewriting rule system usually causes DA-asymmetry. Further, it can be brought about by invention when an expression that is randomly produced falls into the same rule system as an existing rules.

As described in Sect. 2, two neural systems of both agents are coupled via their inputs and outputs. We call the attractor of the coupled dynamical system of the two neural systems a *coupling attractor*. In contrast, an attractor of a neural system is called an *individual attractor*. Here, the two neural systems are coupled with each other as dynamical systems; however, they are separated as distinct individual agents.

There are three types of coupling attractors for neural systems of identical weights:

1. On the same individual attractor with the same phase;
2. On the same individual attractor with different phases;
3. On different individual attractors.

The types 2 and 3 are regarded as differentiated.

The phase space structure of a neural system determines the possible types of coupling attractors to which the neural systems converge after the symbol systems attain different representations for the same expressions. Figure 4 shows the coupling attractors corresponding to Fig. 2. There are four kinds of coupling attractors; all of them occur due to the various combinations of the couplings of the different individual attractors. In this case, there are only type 3 coupling attractors, and the neural systems inevitably differentiate if the symbol systems form different representations. On the other hand, neural systems never differentiate when there are only type 1 coupling attractors even if the symbol systems attain DA-asymmetry.

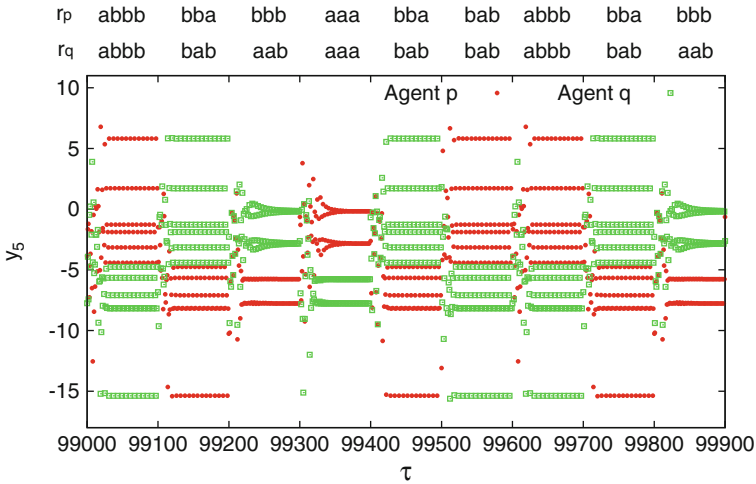


Fig. 5 Neuronal dynamics after the convergence of symbolic communication. The neural systems used are identical to those in Fig. 2

The symbol system and neural system mutually regulate each other. Figure 5 shows a converged time-evolution of symbolic communication in which the neural systems have coupling attractors identical to those shown in Fig. 2; these coupling attractors are shown in Fig. 4. In Figs. 2 and 5, it is observed that different symbol systems develop with identical neural systems. The different symbol systems produce different expressions/representations; consequently, the neural systems transit through different types of attractors in different ways. The representations $r^{\mathcal{D}}$ to be input to the symbol systems are formed based on the dynamics of individual attractors. Consequently, the symbol system regulates the pattern of attractor transitions, and the neural system regulates the pattern of interchanging expressions. Symbolic communication is an interaction between the mutual regulation systems.

4 Discussion

The asymmetry between forms and meanings, which is a type of derivation-acceptance asymmetry, is inevitable because of the difference between the cardinalities of forms and meanings. In our model, DA-asymmetry is attained by generalization learning and word invention. Therefore, the mechanism of differentiation that we showed in this study must be ubiquitous in any system whose sub-part deals with symbols; in particular, this is true in an adaptive symbol system that performs generalization or invention.

Since we have focused on the mechanism of differentiation that relies on a symbol system, we have introduced a few unusual settings in our model.

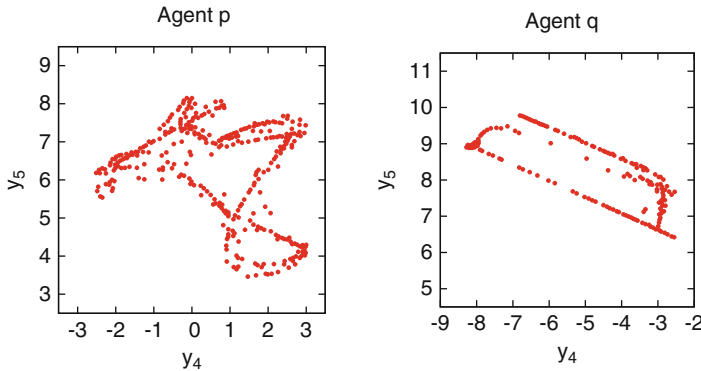


Fig. 6 An example of type 3 with chaotic-chaotic coupling. The figures on the *left* and *right* show the individual attractors of each agent, respectively. One coupling attractor is drawn from several attractors

We introduced a fixed order in the rule selection in the symbol system. If we use probabilistic or dynamic selection, as in the general model of a formal language system, differentiation will be more frequent. We did not introduce supervised learning in the neural system using the other agent’s output as teacher signals; this is different from usual communication models. Although agents in such supervised learning models are likely to be identical as coupling attractors, the agent as an individual system may be differentiated.

In the present model, the dynamics of neural networks in differentiated systems can be chaotic, as shown in Fig. 6. This indicates that neuro-symbolic hetero systems may show not only differentiation by symbol system but also by sensitivity under initial conditions [1]. Furthermore, the hetero system may develop through mutual regulation, or positive feedback, between the neuronal chaotic dynamics and the symbolic DA-asymmetry if we introduce learning in the neural systems.

The mechanism of differentiation in our model can be seen as that of self-other differentiation. The key idea in the theory of self-other differentiation [3] is that one comes to recognizes the ‘self’ from the viewpoint of ‘other’ after identifying the other with the self. Our model of symbolic communication before differentiation can be regarded as reflective dialogue since the two agents are completely identical. The ‘self’ and the ‘other’ could differentiate through DA-asymmetry; consequently, the ‘other’ stands as one producing different interpretations of expressions from the ‘self.’

5 Conclusion

We showed that it is possible for identical symbol systems and neural systems to differentiate in symbolic communication. The differentiation comes from the asymmetric structure of the symbol system, i.e., different rules in the derivation

and acceptance of the same symbolic expression. The dynamics of symbolic communication depend on the types of the attractors of the neural system as a coupled dynamical system. The asymmetric structure that is brought about by generalization learning must be ubiquitous in adaptive symbol system (human language may be considered as a typical example).

Acknowledgements This work is supported by a Grant-in-Aid for Scientific Research (No. 21120011) on Innovative Areas, “The study on the neural dynamics for understanding communication in terms of complex hetero systems,” (No. 4103) of the Japan Society for the Promotion of Science (JSPS).

References

1. Kaneko, K. & Yomo, T. Isologous diversification: a theory of cell differentiation. *Bulletin of Mathematical Biology*, vol.59 (1997) 139–196.
2. Torii, T. & Hashimoto, T. Modelling generation and sharing of novel expressions and meanings in symbolic communication. *Int. J. Bio-Inspired Computation* (in press).
3. Tomasello, M. *The cultural origins of human cognition*. Harvard University Press (1999).

Theoretical Analysis of Phase Resetting on Matsuoka Oscillators

Kazuki Nakada, Yasuomi D. Sato, and Kiyotoshi Matsuoka

Abstract In this paper, we consider functional roles of phase resetting of the piecewise linear oscillator model known as the Matsuoka oscillator, which widely applied in the field of robotics, particularly, in the design of central pattern generator (CPG) units for controlling robotic rhythmic motion. The oscillator can be regarded as a fast-slow system composed of a fast membrane potential dynamics and a slow recovery dynamics. Firstly, we show phase response curves (PRCs) for both the dynamics based on the phase reduction approach, and plausibility of phase resetting through the slow dynamics as well as the fast dynamics during periodic motion. Secondly, we show plausibility of feedback inputs to the slow dynamics rather than the fast dynamics by using a singular perturbation approach. Our results will bridge the gap among theoretical analysis, design principle, and practical and efficient implementation for applications in robotics and biomedical engineering.

K. Nakada (✉)

Advanced Electronics Research Division, INAMORI Frontier Research Center,
Kyushu University, 744 Motoooka, Nishi-ku, Fukuoka 819-0395, Japan
e-mail: k.nakada@ieee.org

Y.D. Sato

Graduate School of Life Science and Systems Engineering, Kyushu Institute of Technology,
2-4 Hibikino, 808-0196, Wakamatsu-ku, Kitakyushu, Japan

Frankfurt Institute for Advanced Studies, Johann Wolfgang Goethe University,
Ruth-Moufang-Str. 1, 60438, Frankfurt am Main, Germany
e-mail: sato-y@brain.kyutech.ac.jp

K. Matsuoka

Graduate School of Life Science and Systems Engineering, Kyushu Institute of Technology,
2-4 Hibikino, 808-0196, Wakamatsu-ku, Kitakyushu, Japan
e-mail: sato@fias.uni-frankfurt.de

1 Introduction

During the past quarter century, from the findings in neuroscience [1, 2], a piecewise linear oscillator model known as the Matsuoka oscillator [3–5], has been studied in diverse research fields including robotics [6–10]. The oscillator model is composed of a fast membrane potential dynamics and a slow recovery dynamics [3–5].

From a biological point of view, its inhibitory interconnection is consistent with the conceptual model of half-center oscillators [1] that constitute the central pattern generator (CPG), which is a central nervous system responsible for generating rhythmic movements of animals [1, 2]. Based on the perspective, such a network configuration has been widely used in the design of CPG units for controlling robotic rhythmic motion [6–10] because of the scalability to stationary inputs and robust entrainment properties to periodic inputs.

In previous works, several theoretical approaches have been proposed for analyzing such entrainment properties: (1) the linear stability analysis [3, 4], (2) the describing function method [11], and (3) the harmonic balance method [5]. These works were carried out only in the cases for stationary or periodic inputs with the harmonic order. Little is known on the effects of timing of perturbation on the dynamics, despite of the significance of the perturbation as inputs, which play a key role in phase resetting during periodic motion including walking [12–14].

In the past, dealing with interactions through the fast dynamics of the Matsuoka oscillator has been assumed naturally, and thus systems with interactions through the slow recovery dynamics have not been well studied. In contrast, Sato et al. implies rather more plausibility of the interaction through the recovery dynamics in the oscillator by using a singular perturbation approach [17].

In this study, we consider plausibility of phase resetting through the slow recovery dynamics as well as the fast membrane potential dynamics by using the phase reduction method [15]. Based on the results, we demonstrate specific features of phase response properties of the oscillator. Finally, we will discuss its possible functional roles of the phase resetting through both the dynamics of the oscillator on controlling rhythmic motion.

2 Model

Let us begin with by explaining coupled piecewise linear oscillators known as the Matsuoka oscillator, which is given by the general form:

$$\frac{d\mathbf{X}^{(i)}}{dt} = \mathbf{F}^{(i)}(\mathbf{X}^{(i)}) + \epsilon \mathbf{G}^{(i)}(\mathbf{X}^{(\bar{i})}), \quad (i = 1, 2), \quad (1)$$

where \bar{i} represents a counterpart of the i -th unit and $\mathbf{X}^{(i)} = (V_1^{(i)}, W_1^{(i)}, V_2^{(i)}, W_2^{(i)}) \in \mathfrak{R}^4$ the state vector. We assume that the coupling strength ϵ is weak. The baseline vector field $\mathbf{F}^{(i)}(\mathbf{X}^{(i)})$:

$$\mathbf{F}^{(i)}(\mathbf{X}^{(i)}) = \begin{pmatrix} -V_1^{(i)} + s - bW_1^{(i)} - ag(V_2^{(i)}) \\ (-W_1^{(i)} + g(V_2^{(i)}))/P \\ -V_2^{(i)} + s - bW_2^{(i)} - ag(V_1^{(i)}) \\ (-W_2^{(i)} + g(V_1^{(i)}))/P \end{pmatrix}, \quad (2)$$

where the nonlinear transfer function is given by $g(x) \equiv \max(0, x - \theta)$, V and W represent the fast membrane potential dynamics and slow recovery dynamics, respectively, θ a certain threshold, and P the time scale parameter.

We can consider both the cases of the V - and W -couplings for the coupling vector $\mathbf{G}^{(i)}(\mathbf{X}^{(i)})$ as in our previous works [16]. We focus on the dynamics of the oscillator as a fast-slow system with the time scale parameter P :

$$\frac{d\mathbf{X}}{dt} = \mathbf{F}(\mathbf{X}, P), \quad (3)$$

as a specific case in the following simulations.

3 Previous Approaches

Let us briefly summarize theoretical and practical approaches for studies on the Matsuoka oscillator in previous works.

3.1 Theoretical Approaches

We here briefly review at least three conventional theoretical approaches proposed for analyzing the entrainment properties of the Matsuoka oscillator:

1. The linear stability analysis on the sustained oscillations in mutually inhibitory networks, in which the necessary and sufficient conditions for a stable sustained oscillation have been proven [3, 4],
2. The describing function method to determine an optimal parameter set for generating a required periodic motion in a plant control system, in which feedback inputs are approximately represented as sinusoidal signals [11],
3. The harmonic balance method, in which both the frequency and amplitude of the oscillation are approximately calculated as the functions of the coupling parameters and the time constants [5].

These approaches provide valuable information to determine the parameters of the oscillators for controlling physical systems including feedback loops. In fact, we can estimate the entrainment frequency of the systems in addition to the natural frequency and amplitude of the oscillation.

3.2 *Practical Approaches*

We review practical approaches for controlling robotic rhythmic movements using the Matsuoka oscillator as CPG units. For instance, Taga et al. have used a CPG model in simulating for biped locomotion [6], and Taga proposed the concept of the global entrainment, which emerges as a limit cycle through interactions among, a CPG system, a physical system, and an environment. Based on the concept, Kimura et al. designed CPG-based controllers for quadruped robot locomotion on rough terrain [7]. Williamson applied a CPG unit for controlling rhythmic arm movements of a humanoid robot [8]. Kotosaka and Schall built a drumming robot with a CPG controller unit [9]. Berthouze implemented a CPG controller for humanoid robots [10].

These works have proven the effectiveness of the global entrainment in controlling robotic rhythmic motion. The results imply the advantages of the Matsuoka oscillator for practical implementation of the global entrainment on robotic platform.

4 Our Approaches

The previous theoretical works were carried out only in the cases for stationary or periodic inputs with the harmonic order. Still little is known on the effects of timing of perturbation as inputs to systems with the Matsuoka oscillators. However, perturbation as feedback with impact is naturally apparent at the ground contact and plane impact in controlling practical robotic platforms [8–10]. In addition, the perturbation as feedback at the ground contact is related with phase resetting for stable walking [12–14].

From the standpoint, we here clarify the effects of perturbation as inputs on phase resetting based on the phase reduction method. We further show plausibility of the perturbation inputs to the slow recovery dynamics rather than the fast membrane potential dynamics based on the results from the singular perturbation method [17].

5 Results

Firstly, by using the phase reduction method, we computed phase response curves (PRCs) for the fast and slow dynamics of the Matsuoka oscillator, as shown in Fig. 1. We found that the PRCs of the Matsuoka model are qualitatively similar to those of

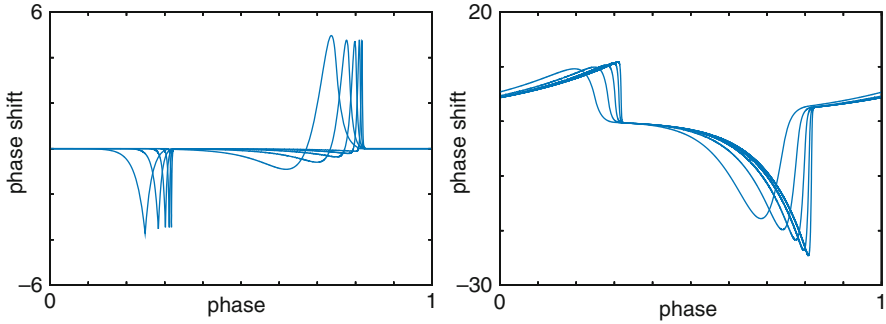


Fig. 1 Phase response properties of the Matsuoka oscillator, where *left* and *right* figures represent phase response curves with regard to the fast and slow dynamics, respectively. We here set the parameters as: $a = 2.0$, $b = 2.5$, $s = 2.0$, and $\theta = 0.0$, and set the time scale parameter as: $P = 12.5, 25.0, 50.0, 100.0$, and 200

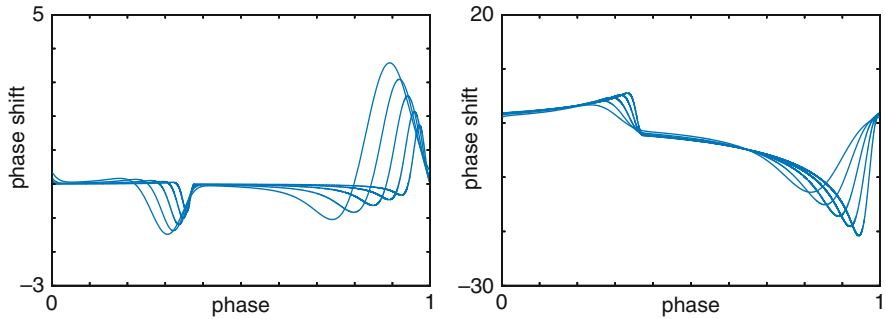


Fig. 2 Phase response properties of the FitzHugh Nagumo model, where *left* and *right* figures represent phase response curves with regard to the fast and slow dynamics, respectively [16]. We here used the standard parameter set, and set the time scale parameter as: $P = 12.5, 25.0, 50.0, 100.0$, and 200 for comparison with Fig. 1

the FitzHugh-Nagumo (FHN) model, as shown in Fig. 1, which are quite different from those of the Morris-Lecar (ML) model [16]. In particular, with increasing the time scale parameter P , the PRCs of the both models become qualitatively equivalent.

These results may indicate different functional roles in timing of perturbation inputs to the fast and slow dynamics. In fact, such specific features of the PRCs are reasonable for regulating phase advance and delay in the phase resetting control during periodic motion [12–14].

To support this, we have previously proven that the Matsuoka oscillator is close to the specific type of integrate-and-fire model, taking limit of the time scale parameter, using the singular perturbation approach [17]. This shows the plausibility of inputs to the slow recovery dynamics rather than the fast dynamics (Fig. 2).

6 Conclusions

In this paper, we have investigated the effects of perturbation inputs to both the dynamics of the Matsuoka oscillator by using the phase reduction method. We computed the phase response curves of the oscillator, and discussed the plausibility of phase resetting through both the dynamics.

Our research viewpoint will bridge the gap among theoretical analysis, design principle, and practical and efficient implementation for the phase resetting control in robotics and biomedical engineering. We are going to apply our approach to designing and controlling on practical platforms.

Acknowledgements This work was supported by the Grant-in-Aid for Young Scientist (B) No. 22700237. One of the authors Y.D.S. have partially participated in the “Bernstein Focus: Neurotechnology through research grant 01GQ0840” founded by the German Federal Ministry of Education and Research (BMBF).

References

1. Brown, TG: *Proceedings of the Royal Society of London. Series B, Containing Papers of a Biological Character*, 84, 572, (1911) 308–319
2. Delcomyn., F: *Foundations of Neurobiology*, WH Freeman, New York (1997)
3. Matsuoka, K: (1985) *Biol. Cybern.* 52 367–376
4. Matsuoka K: *Biol. Cybern.* 56 (1987) 345–366
5. Matsuoka K: *Biol. Cybern.* 104 (2011) 297–304
6. Taga G, Yamaguchi Y, Shimizu H: *Biol. Cybern.* 65 (1991) 147–159
7. Kimura H, Fukuoka Y, Cohen AH: *Int. J. Robotics Research*, 22, 3–4, (2003) 187–202.
8. Williamson, MM: PhD Thesis (1999)
9. Kotosaka S and Schaal S: *Journal of the Robotics Society of Japan*, 19, 1 (2001) 116–123.
10. Berthouze L and Lungarella M: *Adaptive Behavior*, 12, 1, (2004) 47–63
11. Katayama, O: PhD Thesis (1997)
12. Nomura T, Kobayashi M, Nakashima T, Sato S: *Proceedings of ICONIP 1998* (1998) 1196–1199
13. Yamasaki T, Nomura T, and Sato S: *Biol. Cybern.* 88, 6 (2003) 468–496
14. Nakanishi, J., Morimoto, J., Endo, G., Cheng, G., Schaal, S., and Kawato, M.: *Robotics and Autonomous Systems*, 47, 2–3, (2004) 79–91
15. Kuramoto, K.: *Chemical oscillations, waves, and turbulence*, Springer (1984)
16. Sato YD, PhD Thesis (2005)
17. Sato Y.D., Nakada K., Matsuoka K.: *Proceedings of ICANN*, 6792 (2011) 269–276

“Memories as Bifurcations”: A Simple Model

Tomoki Kurikawa and Kunihiro Kaneko

Abstract In this paper, we propose a simple neural network on the basis of the “memories as bifurcations,” by extending construction of synaptic connection by Hopfield. In the scheme of “memories as bifurcations,” an input is given as a bifurcation parameter, while in the traditional neural network models it is given as an initial state. By analyzing this model, we find that memory capacity defined as ability that distinguishes the target pattern to be recalled from others in the presence of a given input is $\sim 0.7 N$ and that the spontaneous activity in the absence of the inputs exhibits periodic or chaotic oscillation where the activity approaches and departs from some of targets.

1 Introduction

In traditional neuroscience, one has focused on responses to stimuli for understanding function of the brain: By measuring response neural activities to sensory stimuli and cognitive task by various methods, e.g., functional magnetic resonance imaging (fMRI), electroencephalogram (EEG) and magnetoencephalogram (MEG), regions of executing the corresponding function have been identified. In this scheme, the spontaneous activity in the absence of stimuli has been ignored as noise. In most of neural network studies[1–3], furthermore, a memory of input-output mapping is considered to be included in one of the attractors in neural dynamical systems, depending on the initial neural state specified by an input, where the spontaneous activity is not taken into account seriously. Recent studies [4–7], however, revealed that the spontaneous activity is not simple noise, but has some spatio-temporal pattern. Furthermore, it is revealed that these spontaneous activities

T. Kurikawa (✉) • K. Kaneko
Department of Basic Science, University of Tokyo, Komaba 3-8-1, Meguro-ku, Tokyo, Japan
e-mail: kurikawa@complex.c.u-tokyo.ac.jp

show some structure similar to the response activities. We have proposed [8] a novel memory scheme in which the change in the flow structure of neural dynamics upon application of an input is represented as bifurcation of the neural activity state, in contrast to the traditional studies where the input is represented as the initial condition of the neural dynamics. In this paper, we study a simple model on this picture of “memories as bifurcations,” by modifying from Hopfield-type neural network, and analyze the relation between the evoked dynamics (the response activities) and the spontaneous dynamics. We find that memory capacity is $\sim 0.7 N$ and that the spontaneous activity is formed so that it comes closer to target patterns in time, while a fixed-point attractor matching a given target pattern is generated in the presence of the corresponding input.

2 Models

We design a recurrent neural network in which input and output pattern (I/O) mappings are embedded on the basis of “memories as bifurcations.” In other words, we design a dynamical system in which an attractor matching the target output pattern is generated in the presence of the corresponding input. For implementing such system, we modify the Hopfield-type neural network [3]. We consider a recurrent neural network model with N neurons and all-to-all connections J_{ij} , and generate an ensemble of M mappings of input pattern (termed as $\eta^\mu (\mu = 1, 2, \dots, M)$) and target pattern (termed as $\xi^\mu (\mu = 1, 2, \dots, M)$) which are N -dimensional vectors whose components are set at -1 or 1 randomly. Synaptic connection J_{ij} which represents a connection from the j -th neuron to the i -th neuron is generated by

$$J_{ij} = \sum_{\mu=1}^M (\xi_i^\mu - \eta_i^\mu)(\xi_j^\mu + \eta_j^\mu)/N. \quad (1)$$

In our model, the synaptic connections are composed of the target and the input patterns, while in the original Hopfield neural network, the connections are composed of the only target patterns. The i -th neuronal activity x_i evolves by the equation

$$\dot{x}_i = \tanh(\beta(\sum_{j \neq i} J_{ij} x_j + \alpha \eta_i^v)) - x_i. \quad (2)$$

We can find that behavior of this model satisfies the perspective of “memories as bifurcations” by the following simple discussion; When the neural activity x is near a target pattern ξ^σ , the term of the input current through the synaptic connection in Eq. 2, $\sum_{j \neq i} J_{ij} x_j$, is estimated as follows:

$$\sum_{j \neq i} J_{ij} x_j = \sum_{\mu} (\xi_i^{\mu} - \eta_i^{\mu})(\delta^{\mu\sigma} + (2 - \delta^{\mu\nu})O(1/\sqrt{N})) \tag{3}$$

$$= (\xi_i^{\sigma} - \eta_i^{\sigma}) + O(\sqrt{(M/N)}), \tag{4}$$

here, we use that ξ^{μ} and ξ^{ν} are assumed to be uncorrelated and that the two N -dimensional uncorrelated vectors satisfy $\sum_j \xi_j^{\mu} \xi_j^{\nu} / N = \delta^{\mu\nu} + (1 - \delta^{\mu\nu})O(1/\sqrt{N})$. Therefore, in the presence of the external input η^{ν} ($\alpha = 1.0$) and with M much smaller than N , it is expected that neural activity pattern near the target ξ^{ν} corresponding to the imposed input is a fixed point and the other targets ξ^{μ} ($\mu \neq \nu$) are not fixed points. In the following part, we set $N = 100, \beta = 4.0$.

3 Results

First, we show that in this model I/O mappings are embedded on the basis of “memories as bifurcations”, i.e., in the presence of a input, the corresponding target pattern is generated as a stable fixed point. In Fig. 1, typical dynamics in the presence and absence of a input is plotted by measuring overlap of the neural activity with the first target, that with the first input, and that with the second target. We can find that

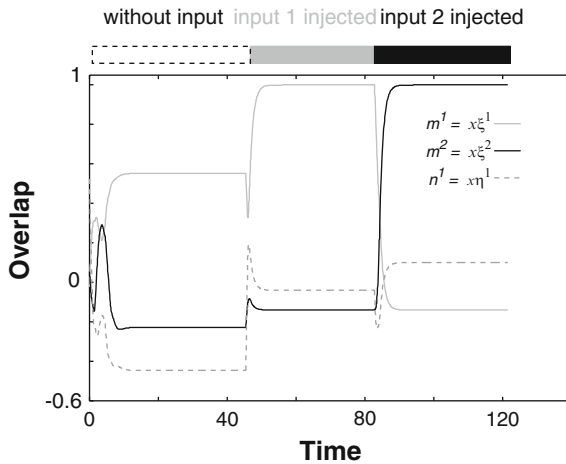


Fig. 1 Example of the dynamics in the presence and absence of the input. Overlap of the neural activity with the 1st target pattern (gray full line) and the 2nd target pattern (black full line), as well as that with the 1st input (black dotted line). These overlaps are plotted in the absence of the input (up to time 45) and the presence of the 1st input (up to time 85) and of the 2nd input. We set $M = 5$

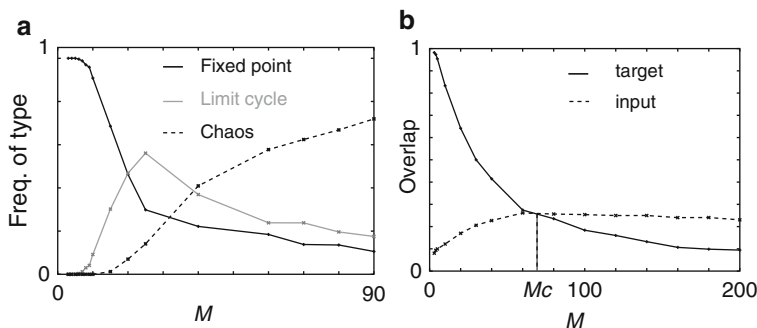


Fig. 2 (a) Frequency of each type of attractor of the evoked dynamics plotted. Fixed point, cycle and chaotic attractor are represented as *black full*, *gray full* and *black dotted lines* respectively. To discriminate each type, we measured the first Lyapunov exponent of the evoked dynamics in the presence of each of five different input, sampled over 100 networks. (b) The overlaps between the neural activity in the evoked dynamics and the target corresponding to the injected input (*black full line*) and the input (*gray full line*) are plotted as a function of M

the activity converges to a pattern that is matched almost completely with the first target in the presence of the first input ($45 < t < 85$ in Fig. 1) and then converges to another pattern matched with the second target in the presence of the second input ($85 < t < 120$ in Fig. 1). In the contrast, in the absence of the input, the activity converges to a pattern that are matched neither with the first nor the second target. Overlap between the activity and another target is not high in the absence of the input (data not shown here).

Next, we analyze the dynamical system in the presence of the input statistically. As a result, we find that the fixed-point attractor that is matched with the corresponding target is generated in small M (Fig. 2). Overlap between the neural activity and the target pattern corresponding to the injected input is very high, i.e., the neural activity is almost matched with the target pattern. The basin for this fixed point attractor is very large and from almost all initial points the neural dynamics converges to it. As M is larger, the type of attractor changes from the fixed point to a limit cycle or chaotic one, and the overlap decreases rapidly (Fig. 2). However, the overlap between the output dynamics and the corresponding target is larger than that between the output and another pattern and that between the output and the input pattern, so that the corresponding target is distinguishable by measuring the overlap. As M is further increased, the overlap of the neural activity with the corresponding target decreases to the level of the overlap with a different pattern or the input. At $M \sim 0.7 N$, the overlap of the neural activity with the corresponding target and that with the input crosses over, where we can no longer distinguish the corresponding target by measuring the overlap (Fig. 2).

Here, we analyze how the evoked dynamics changes depending on the parameters β and N . When β is changed, the type of the attractors is changed significantly, however, the overlaps are changed a little. In the case of small M , as β is larger, the frequency of fixed point attractors decreases and those of limit cycle and chaotic

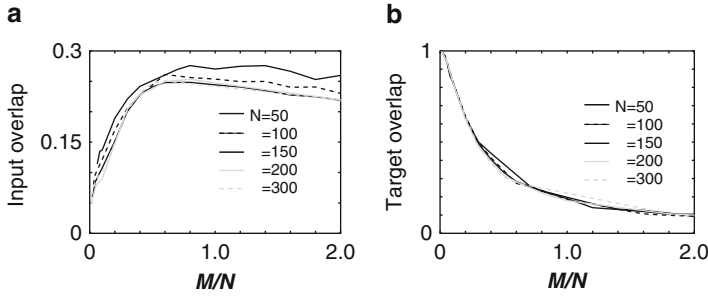


Fig. 3 Dependence of the overlap on the number of the neurons. **(a)** Curves of the overlap with the injected input are plotted as a function of the number of embedded mappings M scaled by the number of neurons N . **(b)** Curves of the overlap with the corresponding target are plotted. Different colored curves represent the overlaps with different number of the neurons N respectively

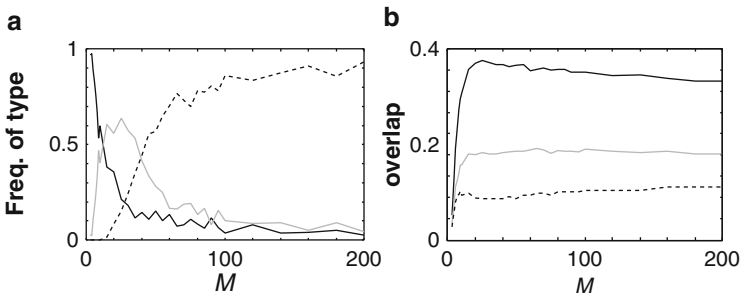


Fig. 4 Dependence of the type of attractors and the overlap of the evoked dynamics on the number of embedded I/O mappings. The frequencies of each type of the spontaneous attractors, fixed point (black full line), limit cycle (gray full line) and chaotic attractors (black dotted line) as a function of the number of the mappings are plotted in **(a)** in the same way as that in Fig. 2. **(b)** The maximum (black full line) and average (gray full line) overlaps with the target are plotted. The overlap with the input are plotted as black dotted line

attractor increase. The oscillation of the limit cycle and chaotic attractor bifurcated through β larger is around the original fixed point and its amplitude remains rather small. Thus, the target pattern is well retrieved so that the abovementioned capacity is little changed by changing β . Then, we study the dependence of the capacity on the number of the neurons N . In Fig. 3, curves of the overlap with the injected input pattern and that with the corresponding target pattern are plotted. Here, the curves are plotted as a function of M/N , the number of the embedded mappings scaled by that of the neurons. We can find that these curves converge to a curve with N increased, so that the cross over points M_C/N of the curves of the overlap of the input and that of the target with each N are scarcely different ($M_C/N \sim 0.7$). As a result, the memory capacity is estimated as $\sim 0.7 N$ from the cross over point.

Finally, we analyze the spontaneous dynamics in the absence of the input (Fig. 4). We find that the spontaneous activity has a single or a few fixed-point attractors in

small M , while chaotic attractors are dominated in large M . Spontaneous neural activity of the chaotic and limit cycle attractors in the absence of inputs repeats approach and departure from the some targets, while the attractors in the presence of an input take the trajectories stretched along the direction only of the corresponding target. In fact, the overlap between the spontaneous activity and the target averaged over all targets takes a larger value than that between the activity and the input and that between the activity and the random pattern.

4 Conclusion

To understand relationship between the memories of I/O mapping and “memories as bifurcations”, we introduced a simple Hopfield-type neural network. In this paper, we analyzed the neural dynamics in the absence and presence of the input. For small M , a fixed point attractor matched with the corresponding target is generated in the presence of the input. The frequency of the networks in which the fixed point attractor is generated decreases as M is increased and, at the same time, the overlap of the neural activity with the target decreases. On the other hand, the overlap with the input increases. Memory capacity is defined as the cross over point between these two curves, where the target pattern is no longer distinguished from another pattern by measuring the neural activity under input. From this point, memory capacity is estimated at $M_c \sim 0.7 N$. In the absence of the input, high frequency of networks generates the chaotic attractors. Considering that the overlap with the target is higher than the overlap against the other pattern, it is shown that these spontaneous neural activity itinerates over some of targets selectively, by exploiting chaotic dynamics.

Acknowledgements This work was supported by a Grant-in-Aid for Scientific Research on Innovative Areas “The study on the neural dynamics for understanding communication in terms of complex hetero systems (No. 4103)” (No. 21120004) of MEXT, Japan and by JSPS Fellows (No. 233744).

References

1. D.J. Willshaw, C. von der Malsburg, Royal Society of London Proceedings Series B **194**, 431 (1976)
2. T. Kohonen, Biological Cybernetics **43**(1), 59 (1982)
3. J.J. Hopfield, Proceedings of the National Academy of Sciences of the United States of America **81**(10), 3088 (1984)
4. A. Arieli, A. Sterkin, A. Grinvald, A. Aertsen, Science **273**(5283), 1868 (1996)
5. T. Kenet, D. Bibitchkov, M. Tsodyks, A. Grinvald, A. Arieli, Nature **425**(6961), 954 (2003)
6. A. Luczak, P. Bartho, K.D. Harris, Neuron **62**(3), 413 (2009)
7. A. Luczak, P. Barthó, S.L. Marguet, G. Buzsáki, K.D. Harris, Proceedings of the National Academy of Sciences **104**(1), 347 (2007)
8. T. Kurikawa, K. Kaneko, PLoS ONE **6**(3), e17432 (2011). DOI 10.1371/journal.pone.0017432

Biologically Inspired Closed-Loop Model of Precision Grip Lifting Task

Ankur Gupta, Manikanta Avinash, Deepa Kandaswamy, Muthu Kumar, Suresh Devasahayam, K. Srinivasa Babu, and V. Srinivasa Chakravarthy

Abstract We study precision grip performance (PGP) in human subjects with wide intrinsic variation in skin friction (μ). Two types of subjects (with high and low friction) are considered. Furthermore, change in PGP is studied under transiently varied conditions of μ (dry and wet). The experimental study is also supported by a computational model of PGP involving a nonlinear, closed-loop control scheme. Models of human PGP often deal with performance at a single μ value. However, studies on the effect of intrinsic friction (IF) as opposed to transient changes in friction on PGP are nearly non-existent, which forms the motivation for the present study.

A. Gupta

Department of Biotechnology, Indian Institute of Technology Madras, Chennai, Tamil Nadu 600036, India

M. Avinash

Department of Electrical Engineering, Indian Institute of Technology Madras, Chennai, Tamil Nadu 600036, India

D. Kandaswamy • M. Kumar • K.S. Babu

Neurophysiology Laboratory, Department of Neurosurgical Sciences, Christian Medical College, Vellore, Tamil Nadu 632004, India

S. Devasahayam

Department of Bioengineering, Christian Medical College, Vellore, Tamil Nadu 632004, India

V.S. Chakravarthy (✉)

Department of Biotechnology, Indian Institute of Technology Madras, Chennai, Tamil Nadu 600036, India

e-mail: schakra@ee.iitm.ac.in

1 Introduction

Napier (1956) first defined precision grip as gripping an object between index finger and thumb [1]. Experiments based on grip force alone are incapable of explaining the motor control since the process is entirely feed-forward. To overcome this limitation and to understand the role of feedback control, grip-lift tasks were designed [2, 3]. A successful lift requires planning [4], motor command execution and fine motor control of the involved muscles [2, 5] for force production. Before an initial contact with the object, an internal model is formed based on visual estimate of the object's weight [5, 6], size [7], surface curvature [8] and friction [9]. Post internal model generation, an appropriate motor command in the form of lift force (F_L) and grip force (F_G) is generated to lift the object. A successful lift is only possible when the F_G is sufficiently large to prevent the object from slipping [10] and the F_L is more than the weight of the object. During lift, F_G is kept sufficiently large to prevent accidental slips from internal (accelerations in arm motion) [11] and external [12] (random perturbation in load) perturbations. In a prehensile grip, friction plays a prominent role in coupling the hand to the object [3, 13]. F_L and F_G translate into frictional force, which in turn lifts the object. In case of a faulty internal model, the error signal generated are used to correct the on-going lift [14] and to update the internal model [15].

Now let us examine the role of the IF in PGP. Studies on friction and PGP are limited to experiments involving F_G generation with a fixed μ [9, 10]. Thus, these studies fail to account for the role of IF.

Recent study by Muthukumar et al. (manuscript submitted) [16] suggest that subjects with different IF follow different strategies for F_G generation. In subjects with low IF, steady state grip force (SGF) exceeds peak grip force (PGF), whereas in subjects with high IF $SGF < PGF$ [16].

In the proposed model, classical PID controllers and friction-based plant model are used for F_G and F_L generation. F_G binds the hand to the object and F_L is required for lifting the object. The effect of transiently varying friction (reducing friction by wetting fingers) on PGP and its role in the strategies involved in grip force generation is studied. Thus four cases emerge: (1) high IF, dry condition, (2) high IF, wet condition, (3) low IF, dry condition, (4) low IF, wet condition. Results suggest that the model is able to reproduce the F_G profiles of the experimental data for SGF with $< 1\%$ error for μ_{hd} (high IF, dry condition); $< 18\%$ for μ_{hw} (high IF, wet condition) and $< 2\%$ for μ_{ld} (low IF, dry condition); $< 5\%$ for μ_{lw} (low IF, wet condition).

2 Materials and Methods

Subjects and procedure: The study was conducted on 16 healthy right-handed subjects (12 male, 4 female) with mean age 33 ± 5.95 years, Range 26–50 years). Subjects washed their hands with soap and water. The hands were air dried until

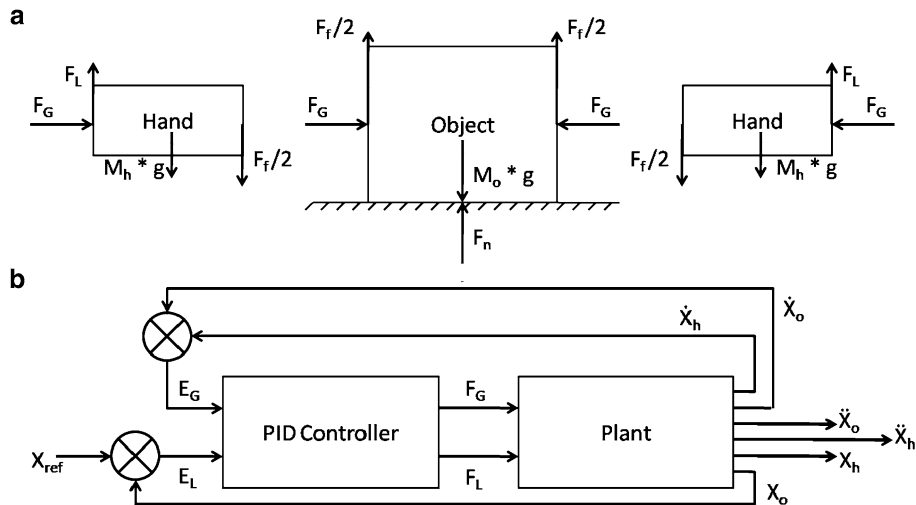


Fig. 1 (a) Free body diagram showing forces acting on hand and object, (b) the overview of the model for grip force and lift force generation

visible traces of water were absent. Subjects sat on a chair in a comfortable position with their forearm flexed in the anterior direction. Subject was required to lift his/her hand off the touch pad, grip and lift the object to a height of 12 cm and allow it to slip after holding the object in stable F_G for 6 s (which was verbally conveyed to the subject). Slip force is the F_G at which the object slips out of the grip. The data was acquired at 1 KHz in LABVIEW 8 and analysed in MATLAB 7. Six consecutive trials were carried out for a load force of 1.274 N in both dry and wet condition. Wet condition was achieved by immersing the finger in water for 2 s between trials and performing the task immediately. Standard load force – slip force ratio [9] was used to determine μ for each trial. An average of six trials was used to determine μ_{hd} , μ_{hw} , μ_{ld} and μ_{lw} . The subjects were classified as high IF when $\mu_{dry} > 0.75$ and low IF when $\mu_{dry} < 0.75$. Informed written consent of the subject was obtained before the study.

Test object: The device comprised of an object (0.117 Kg) with a load cell (having four strain gauges) mounted on a steel plate for measuring the grip force. Object has a provision of manually loading it from the top. The object was loaded from the top to make the total mass of the object (M_o) 0.130 Kg.

Model: The free-body diagram for individual components (object and hand) is shown in Fig. 1a. The model (Fig. 1b) consists of a nonlinear controller and a nonlinear plant in closed loop configuration. The controller generates F_G and F_L , which interact with the object due to friction.

The net forces acting on the object and hand are

$$F_o = F_f + F_n - M_o g \quad (1)$$

$$F_h = F_L - F_f - M_h g \quad (2)$$

Where, F_o = net force acting on object tangential to object's surface; F_f = frictional force; F_n = force normal to the table surface; M_o = mass of the object; M_h = mass of the hand/finger; F_h = net force acting on hand tangential to object's surface; F_L = lift force.

The assumptions for the model are $g = 9.8 \text{ m/s}^2$ and $M_h = M_o/10$. F_{noslip} (3) is the frictional force required to have no slip. Whereas, F_{slip} (4) is the frictional force (assumed to follow a nonlinear square law) expressed as a function of F_G .

$$F_{noslip} = \frac{M_o M_h}{M_o + M_h} * \left(\frac{F_L}{M_h} + \frac{F_n}{M_o} \right) \quad (3)$$

$$F_{slip} = 2\mu F_G^2 \quad (4)$$

F_f and F_n are given in Eqs. (5) and (6)

$$F_f = \begin{cases} F_{noslip}, & \text{if } F_{noslip} < F_{slip} \\ F_{slip}, & \text{else} \end{cases} \quad (5)$$

$$F_n = \begin{cases} M_o g - F_f, & \text{if } X_o = 0 \wedge M_o g > F_f \\ 0, & \text{else} \end{cases} \quad (6)$$

Here, X is the position and \dot{X} represent the velocity (Fig. 2).

The controller consists of two modules which are two PID controllers, one each for F_G and F_L . The errors for F_L and F_G are given in Eqs. (7) and (8). When E_L (E_G) is substituted for E on the right side of Eq. (9), we obtain F_L (F_G) on the left.

$$E_L = X_{ref} - X_o \quad (7)$$

$$E_G = (\dot{X}_h - \dot{X}_o)^2 \quad (8)$$

$$F = K_p E + K_I \int_0^t E(\tau) d\tau + K_D \frac{dE}{dt} \quad (9)$$

Here X_{ref} = reference position to which the object is lifted (0.12 m); X_h = position of hand; X_o = position of object; \dot{X}_h = hand velocity; \dot{X}_o = object velocity; K_p , K_I and K_D are proportional, integral and derivative gains respectively.

The controller was optimised for dry condition while keeping the F_L fixed and varying F_G . Stochastic gradient ascent algorithm [17] and genetic algorithm [18] were used for determining the optimal controller parameters. The fitness function (\mathcal{F}) was defined as

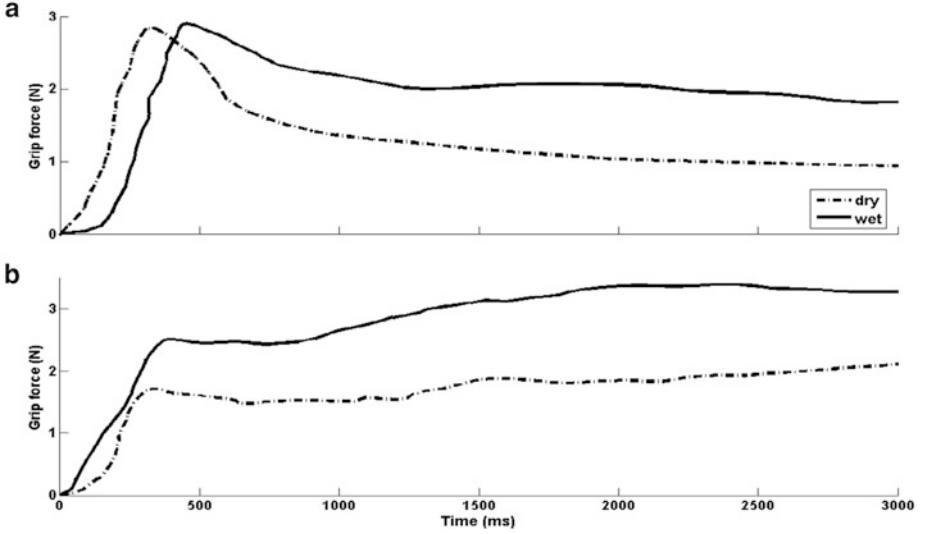


Fig. 2 Single trial experimental grip force profiles for (a) high IF subject, (b) low IF subject

$$\mathcal{F} = \frac{|PGF_M - PGF_E|}{PGF_E} + \frac{|SGF_M - SGF_E|}{SGF_E} + |dis| \quad (10)$$

Here, subscript M and E denote the model and experimental values respectively and *dis* denotes the distance between the hand and the object.

The wet condition was simulated by fixing the optimal PID parameters for dry case and changing μ to the experimentally determined wet μ value.

3 Results

Experimental data: The PGF is defined as the point of maximum slope in first 500 ms of lift and the SGF is the average grip force exerted between 3,500 ms and 4,500 ms after the lift onset. For a high IF subject $PGF > SGF$, whereas an opposite trend was seen in the low IF subjects. Slip force for μ_{hd} , $F_{slip} = 0.73$ N & for μ_{hw} , $F_{slip} = 1.19$ N and μ_{ld} , $F_{slip} = 1.19$ N & μ_{lw} , $F_{slip} = 1.60$ N. The safety margin employed was μ_{hd} , $F_{slip} = 0.25$ N & μ_{hw} , $F_{slip} = 0.63$ N and μ_{ld} , $F_{slip} = 0.99$ N & μ_{lw} , $F_{slip} = 1.45$ N. The ratio PGF/SGF for $\mu_{hd} = 2.64$ & $\mu_{hw} = 1.45$ and $\mu_{ld} = 0.71$ & $\mu_{lw} = 0.83$.

PGF_{dry}/PGF_{wet} ratio for high IF subject was 0.98 and for low IF subject it is 0.68. SGF_{dry}/SGF_{wet} ratio for high IF subject was 0.54 and for low IF subject it is 0.79.

Simulation: Simulation results (Fig. 3) for the dry case were obtained by using the optimal controller parameters for a given μ and the wet case was simulated by

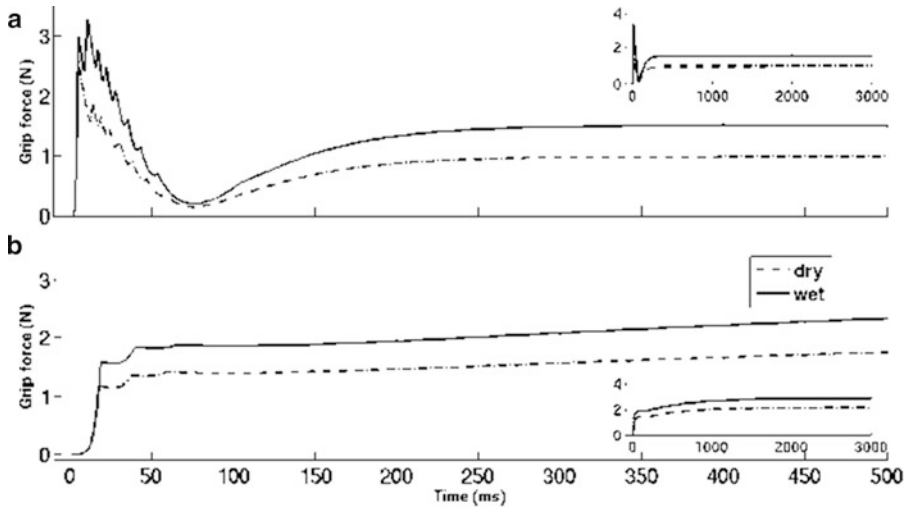


Fig. 3 Simulated single trial 0 to 500 ms grip force profile for (a) high IF subject, (b) low IF subject. Inset shows 3-s long profile of the corresponding plot

Table 1 Comparison of experimental and model PGF and SGF for 1 high IF and 1 low IF subject

μ	Experimental (N)		Model (N)		Error (%)	
	PGF	SGF	PGF	SGF	PGF	SGF
$\mu_{hd} = 1.2$	2.58	0.97	2.57	0.98	0.39	0.51
$\mu_{hw} = 0.45$	2.64	1.82	3.28	1.50	24.24	17.58
$\mu_{ld} = 0.45$	1.54	2.18	1.40	2.14	19.09	1.83
$\mu_{lw} = 0.25$	2.28	2.75	1.87	2.87	17.98	4.36

changing μ with the controller parameters remaining unaltered. The simulation was carried out for both the high IF and low IF cases. A comparison is drawn between the experimental and simulated data in Table 1.

PGF_{dry}/PGF_{wet} ratio for high IF case was 0.78 and for low IF case it is 0.65. SGF_{dry}/SGF_{wet} ratio for high IF case was 0.75 and for low IF case it is 0.75. The safety margin employed for dry and wet cases were 0.25 N and 0.31 N for high IF case and 0.95 N and 1.27 N for low IF case.

4 Discussions

The grip force profiles obtained for high and low friction subjects were in accordance of the findings of Muthukumar et al., (submitted) [17]. The strategy employed for F_G generation ($SGF > PGF$ or $PGF > SGF$) remains unaltered with the change in μ . This result suggests that the internal model formed is not updated when μ is changed from dry to wet condition. The safety margin employed increases with

decrease in IF; this may be because of an increase in slip probability in case of smaller μ .

Simulation studies suggest that the subject does not re-train for a changing μ . The closeness of the experimental and model data supports the plausibility of the model. In future, we propose to extend the present study to precision grip performance in Parkinson's patients.

Acknowledgments The authors acknowledge support of the Department of Biotechnology, India.

References

1. Napier, J.R.: The prehensile movements of the human hand. *J Bone Joint Surg Br* Nov38-B(4) (1956) 902–13.
2. Forssberg, H., Eliasson, A.C., Kinoshita, H., Johansson, R.S., Westling, G.: Development of human precision grip. I: Basic coordination of force. *Exp Brain Res* 85(2) (1991) 451–7.
3. Westling, G., Johansson, R.S.: Factors influencing the force control during precision grip. *Exp Brain Res* 53(2) (1984) 277–84.
4. Flanagan, J.R., Vetter, P., Johansson, R.S., Wolpert, D.M.: Prediction precedes control in motor learning. *Curr Biol* Jan 21 13(2) (2003) 146–50.
5. Johansson, R.S., Westling, G.: Coordinated isometric muscle commands adequately and erroneously programmed for the weight during lifting task with precision grip. *Exp Brain Res* 71(1) (1988) 59–71.
6. Forssberg, H., Kinoshita, H., Eliasson, A.C., Johansson R.S., Westling G., Gordon, A.M.: Development of human precision grip. II. Anticipatory control of isometric forces targeted for object's weight. *Exp Brain Res* 90(2) (1992) 393–8.
7. Gordon, A.M., Forssberg, H., Johansson, R.S., Eliasson, A.C., Westling, G.: Development of human precision grip. III. Integration of visual size cues during the programming of isometric forces. *Exp Brain Res* 90(2) (1992) 399–403.
8. Jenmalm, P., Goodwin, A.W., Johansson, R.S.: Control of grasp stability when humans lift objects with different surface curvatures. *J Neurophysiol* 79(4) (1998) 1643–52.
9. Forssberg, H., Eliasson, A.C., Kinoshita, H., Westling, G., Johansson, R.S.: Development of human precision grip. IV. Tactile adaptation of isometric finger forces to the frictional condition. *Exp Brain Res* 104(2) (1995) 323–30.
10. Johansson, R.S., Westling, G.: Roles of glabrous skin receptors and sensorimotor memory in automatic control of precision grip when lifting rougher or more slippery objects. *Exp Brain Res* 56(3) (1984) 550–64.
11. Werremeyer, M.M., Cole, K.J.: Wrist action affects precision grip force. *J Neurophysiol* 78(1) (1997) 271–80.
12. Eliasson, A.C., Forssberg, H., Ikuta, K., Apel, I., Westling, G., Johansson, R.S.: Development of human precision grip. V. anticipatory and triggered grip actions during sudden loading. *Exp Brain Res* 106(3) (1995) 425–33.
13. Cadoret, G., Smith, A.M.: Friction, not texture, dictates grip forces used during object manipulation. *J Neurophysiol* 75(5) (1996) 1963–9.
14. Johansson, R.: Dynamic use of internal models in the control of dexterous manipulation. *Acta Physiol Scand* 167(2) (1999) A10.
15. Nowak, D. A., Glasauer, S., Hermsdörfer, J.: How predictive is grip force control in the complete absence of somatosensory feedback? *Brain* 127(Pt 1) (2004) 182–92.
16. Muthukumar M., Babu K.S., Deepa K., Devasahayam S: Correlation of Skin Friction with Precision Grip under Dry and Wet Conditions. (manuscript submitted)

17. Doya, K., Sejnowski, T.J: A novel reinforcement model of birdsong vocalization learning. *Advances in Neural Information Processing Systems 7*, MIT Press, (1995) 101–108.
18. Varsek A., Urbacic T., Filipic B: Genetic Algorithms in Controller Design and Tuning, *IEEE Trans. Sys.Man and Cyber.* 23 (5) (1993) 1330–1339.

A Communicative Model: Can We Interpret Neural Dynamics of Understanding?

Yongtao Li and Ichiro Tsuda

Abstract In this paper, a communicative model with two nonequilibrium neural networks is proposed to emulate the dynamical process of how we can understand each other. A novelty-induced learning process is introduced to realize memory transmission between heterogeneous neural network models. The simulation results suggest that the communicative model could subserve to interpret the underlying neural mechanism of understanding.

1 Introduction

Communication with the surroundings is an instinctive ability for animals to survive adaptively in ever-changing environmental circumstances. However, how we can understand each other is still an open question because it is quite difficult to deal with the highly complicated spatiotemporal dynamics which is emerging in neural systems while communicative behaviours occur.

In the present study, we are concerned about whether or not we can construct a communicative model to investigate the underlying neural mechanism of communicative behaviors. Specially, it is expected that more knowledge about the relation between mutual understanding and neural dynamics can be obtained. Recent experiments of mirror neurons has suggested that mirror neurons could be involved in mutual understanding [1]. In particular, recent experiments in fMRI have shown “resonate” firing phenomenon in communicators when one guesser saw a

Y. Li (✉)

Research Center for Integrative Mathematics, Hokkaido University, Sapporo 060-0810, Japan
e-mail: yongtaoli@es.hokudai.ac.jp

I. Tsuda

Research Center for Integrative Mathematics, Hokkaido University, Sapporo 060-0810, Japan
Research Institute for Electronic Science, Hokkaido University, Sapporo 060-0812, Japan

gesture of a gesturer [2] and synchronous firing in communicating brains when one listener has understood a story from a speaker [3]. These findings have brought us an important implication that similar spatiotemporal dynamics could emerge in heterogeneous brains when two people understood each other.

Motivated by the above findings, let us consider a typical communication scenario.

*There are two interactive individuals who are named as agent **A** and agent **B**, respectively. **A** is introducing new things to **B** who has no a prior knowledge about the things. Finally, agent **B** must learn the state of **A** so as to understand **A**.*

In this case, the dynamics emerging in the brain of agent **B** can be supposed to be a learning process such that the transition from the “*I do not know*” state to the “*I know*” state can occur. In the earlier Freeman’s works, he shows that chaotic activities work as a novelty filter, namely, an “*I do not know*” state [4]. Remarkably, various experiments and theories have suggested that chaos is crucial to learning in brain [4, 5]. Therefore, we here take the following working hypotheses.

1. Attractor dynamics is emerging in the brain of agent **A** due to the requirement for memory retrieval of the concerned things.
2. Chaotic dynamics is emerging in the brain of agent **B** as **B** has no prior knowledge about the thing.
3. After agent **B** learned such things, attractor dynamics similar to those of agent **A** is emerging in the brain of agent **B** because the memories in **A** about the things have been transmitted into the brain of agent **B**.

In order to clarify the truth and false of these working hypotheses, we propose a preliminary idea to emulate the process of memory transmission that two neural networks with different memories learn each other through a communicating process between them. From the viewpoint of dynamic brain, which emphasizes the important functional roles of complex dynamics emerging in brain, we propose a communicative model consisting of two nonequilibrium neural networks [5, 6] which satisfy two characteristic properties of communicative process. First, each nonequilibrium neural network performs a dynamic process in which a successive memory retrieval can be obtained. Second, novelty-induced learning algorithm is introduced so that selective learning can be implemented into the two networks. We hypothesize a scenario in which one can understand another by memory transmission. The results of simulation show that unidirectional and bidirectional memory transmission can be implemented successfully.

2 Communicative Model

A nonequilibrium neural network model adopted here is shown in Fig. 1 which is based on the model proposed by Tsuda [5, 6]. The network consists of two kinds of probabilistic neurons: N pyramidal neurons (denoted by **S**) and N stellate neurons (denoted by **R**), which are the most important types of neurons in neocortical

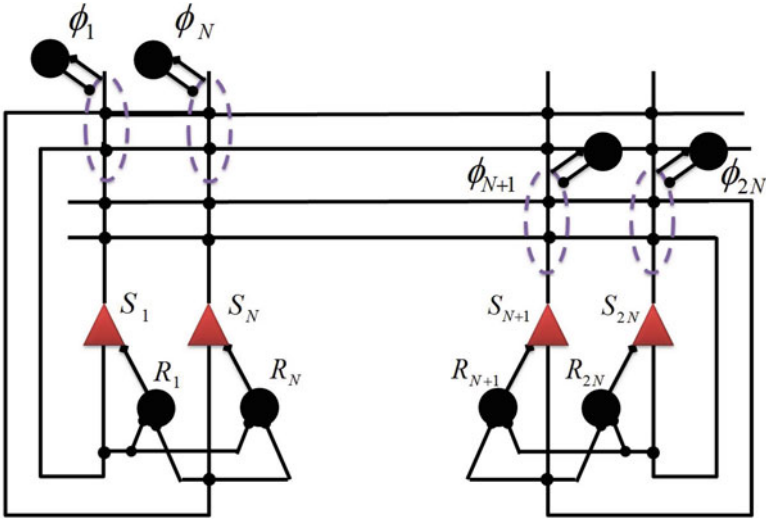


Fig. 1 A nonequilibrium neural network model

columns. All pyramidal neurons are supposed to form a fully interconnected recurrent neural network, whereas each stellate neuron is supposed to receive input from all pyramidal neurons and send output to only one corresponding pyramidal neuron. We assume that memories are only embedded in synaptic connections between pyramidal neurons. Each memory is a N dimensional vector consisting of firing states of pyramidal neurons, each of which is encoded into two values $+1$ (when firing) or -1 (when non-firing). The state of each neuron has analog values from -1.0 to $+1.0$. The neural dynamics of each neuron is defined as follows.

$$S_i(t + 1) = f^p \left(\sum_{j=1}^N W_{ij} S_j(t) + d_i R_i(t) - \delta_i \Phi_i(t) \right), \tag{1}$$

$$R_i(t + 1) = f^p \left(\sum_{j=1}^N e_j S_j(t) \right), \tag{2}$$

where $\Phi(t) = x(t_1)$, $t_1 = \max_{t>s} \{s | x(s) = x(s - 1)\}$, where $x(t)$ is given by

$$x(t) = \sum_{j=1}^N W_{ij} S_j(t),$$

and the activation functions of pyramidal neurons S_i and those of stellate neurons R_i are independently determined by the following probabilistic law.

$$y(t+1) = f^p(x) = \begin{cases} \tanh(\gamma x) & \text{with probability } p \\ y(t) & \text{with probability } 1-p, \end{cases}$$

where the parameter γ describes the steepness of the function. The results of our simulation show that larger γ is easier to produce a dynamic associative process in the network. We have employed a larger $\gamma = 10$.

2.1 Embedded Memories

M memories are initially embedded in the network by the following well-known Hebbian algorithm,

$$W_{ij}(0) = \sum_{\mu=1}^M \xi_i^{(\mu)} \xi_j^{(\mu)}, \quad (3)$$

where $1 \leq i, j \leq N$ and N dimensional vector ξ^μ ($1 \leq \mu \leq M$) denotes the μ -th memory of M embedded memories.

In contrast to the typical Hopfield neural network, the nonequilibrium neural network includes two subsystems that can lead the system either to convergent dynamics or to divergent dynamics. First, recurrent connections W_{ij} of pyramidal neurons $S(t)$ enable the network to perform attractor dynamics like a Hopfield network, whereas the presence of the feedback $\phi_i(t)$ leads the network to be unstable. The feedback $\phi_i(t)$ originates from the temporal states of pyramidal neurons and works only when pyramidal neurons reach a steady state, namely, $S(t) = S(t-1)$. Thus, the network shows a successive retrieval of embedded memories instead of a gradually converging dynamics.

2.2 Dynamics Measure

Since evolutionary dynamics of the nonequilibrium neural network show a successive retrieval of embedded memories, a direction cosine as an appropriate dynamics measure is required, which is defined as follows.

$$D^\mu(t) = \frac{\mathbf{S}(t) \cdot \xi^\mu}{\|\mathbf{S}(t)\| \cdot \|\xi^\mu\|}, \quad (4)$$

where memories $\{\xi^\mu\}$ ($1 \leq \mu \leq M$) are equivalent to the coordinates of state pattern $\mathbf{S}(t)$ in the state space, and $D^\mu(t)$ is a temporal variable with values from -1.0 to $+1.0$. While $D^\mu(t)$ of $\mathbf{S}(t)$ is -1.0 or $+1.0$, a memory or its negative pattern is retrieved. We identify these two patterns. By virtue of this measure, we can clearly trace the dynamical processes of the nonequilibrium neural network.

2.3 Novelty-Induced Learning

Since many experiments imply that novelty can enhance memory and learning [7], novelty-induced learning is introduced into our communicative model. When one network in our model is showing a steady state which can be regarded as a memory retrieval, the steady pattern is applied to the other network that will learn based on the novelty of the input pattern. Mathematically, the novelty of one incoming pattern relative to an existing memory can be estimated by its direction cosine to the extent of which one pattern mismatches the memory. If a message is sent by a sender at time τ , the message as one incoming pattern is denoted by $S^I(\tau)$. At the same time, the receiver has M memories η^α ($1 \leq \alpha \leq M$). Then, the novelty measure $H(\tau)$ for the incoming pattern is defined by

$$H(\tau) = \max \{1 - F_\alpha(\tau) | 1 \leq \alpha \leq M\} \quad (5)$$

$$F^\alpha(\tau) = \left| \frac{S^I(\tau) \cdot \eta_\alpha}{\|S^I(\tau)\| \cdot \|\eta_\alpha\|} \right|, \quad (6)$$

Note that $H(\tau) \leq 1.0$. By means of the novelty measure $H(\tau)$, we replace the Hebbian learning rule by the following modified one, which we call a novelty-induced learning.

$$W_{ij}(t+1) = W_{ij}(t) + \Delta W_{ij}(t) \quad (7)$$

$$\Delta W_{ij}(t) = \epsilon S_i(t) S_j(t) H(t) \quad (8)$$

When the incoming pattern is quite novel, the novelty measure $H(t)$ gives a value approximating 1.0 so that the learning rate is kept. On the other hand, when the incoming pattern is not too novel, the novelty measure gives a value approximating 0.0, which can weaken the learning rate. In particular, $H(t) = 0.0$ means that the receiver has learned the incoming pattern, so the learning process is terminated. Using this novelty-induced learning rule, a selective learning process can be implemented in our model.

3 Results and Discussions

By means of the novelty-induced learning, we have investigated two typical examples as metaphor scenarios where communicative behaviors occur. First, only unidirectional learning is introduced, namely, one network is regarded as a sender and the other as a receiver. Second, bidirectional learning means that the two networks learn each other in an interactive way. By virtue of the method of dynamics

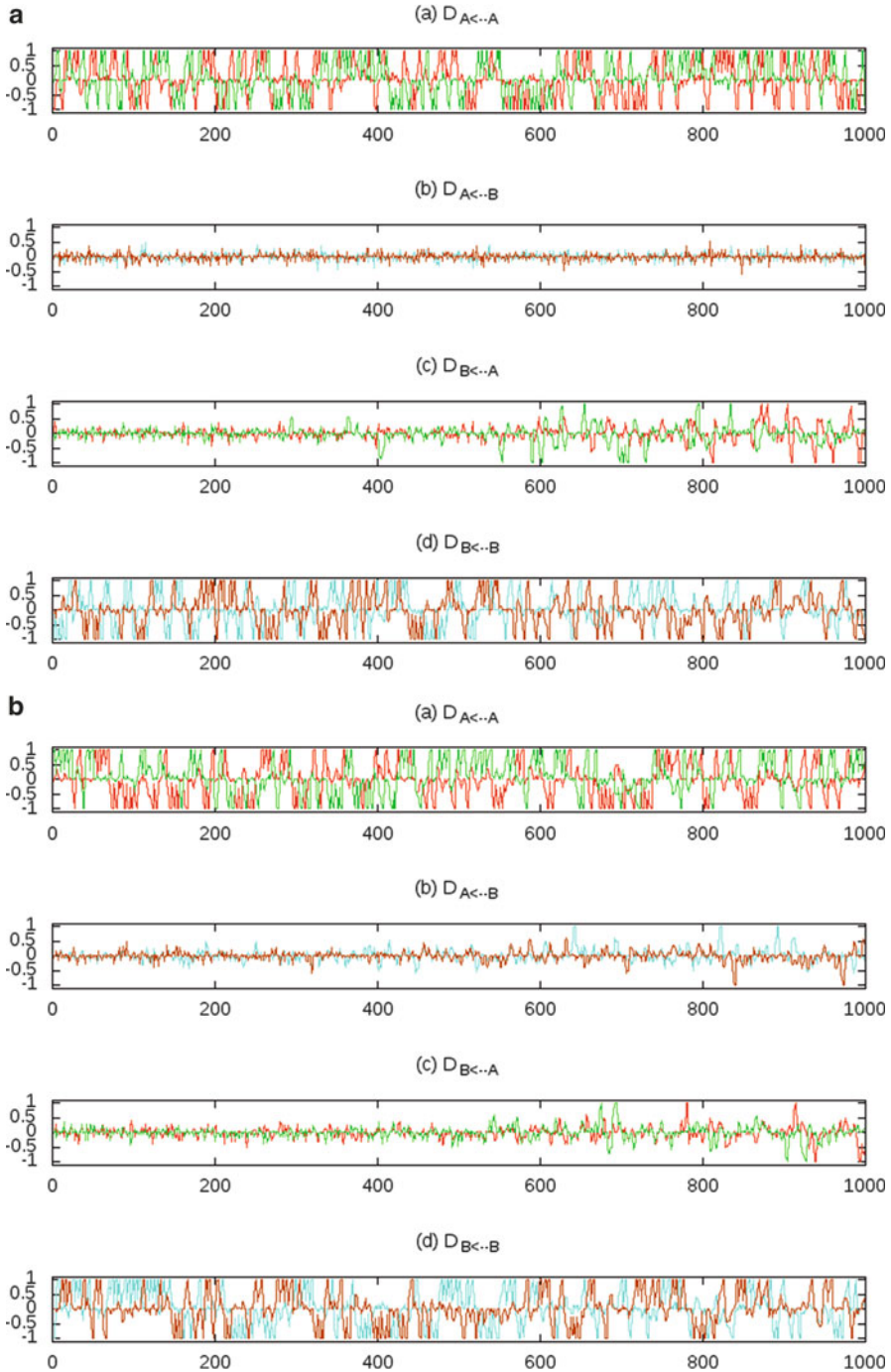


Fig. 2 Unidirectional and bidirectional learning. **(a)** Unidirectional. **(b)** Bidirectional

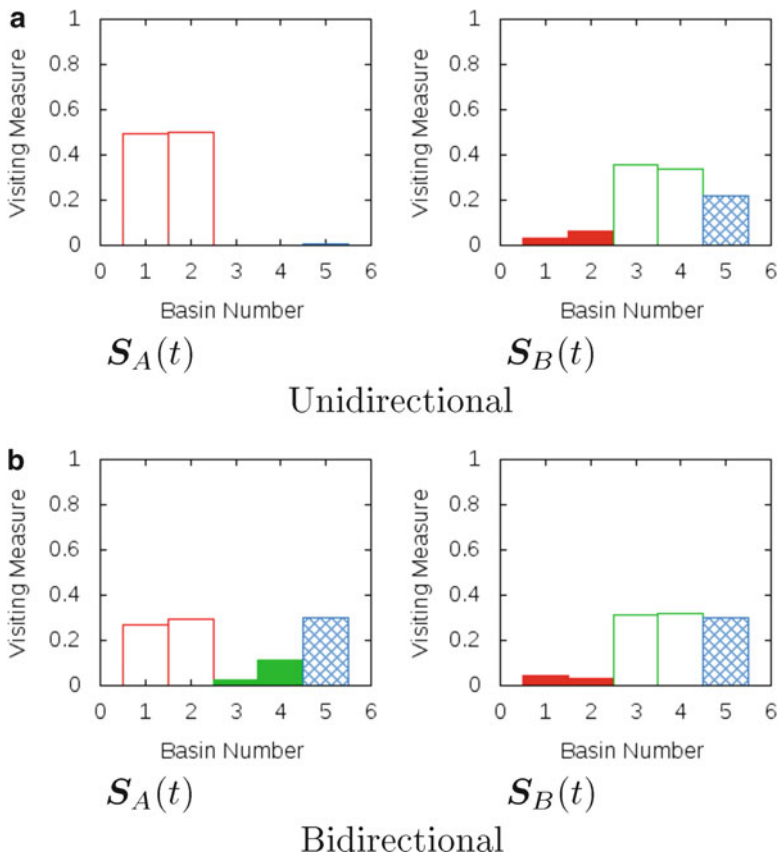


Fig. 3 Basin visiting measure of dynamical trajectories of unidirectional (a) and bidirectional learning (b)

measure proposed above, we can trace the changes of dynamical behaviors in the two networks. Corresponding to unidirectional and bidirectional learning, two examples are shown in Fig. 2a, b where the upper two figures correspond to $S_A(t)$ and the lower two figures, $S_B(t)$. Comparing the second and third column of Fig. 2a, we can find that, after some time learning, some memories of agent A are retrieved by agent B , but agent A has no memories of agent B , as means that agent B is only learning agent A in an unidirectional way. Obviously, bidirectional learning results in interactive memory retrieval of agent A and agent B , which is shown in Fig. 2b.

Interestingly, when the two networks have learned each other, a new “landscape” gradually formed in the phase space but maintain the old “landscape” which is formed by old memories. This is confirmed by a statistical investigation of basin visiting measure, which is used to estimate the visiting distribution of a dynamical trajectory in phase space. Corresponding to two scenarios in Figs. 2 and 3a, b show the changes of basins of $S_A(t)$ and $S_B(t)$, respectively. In these figures, different

types of color are used to mark different basins, such as A (red) and B (green). The basins of learned memories are filled, but self basins are blank. In the case of unidirectional learning, the dynamical trajectory of $S_B(t)$ has passed through not only private basins, but also the basins corresponding to embedded memories in system A . Furthermore, the dynamical trajectories of both $S_A(t)$ and $S_B(t)$ have passed through the whole basins corresponding to all embedded memories in two systems by bidirectional learning.

4 Conclusions

A communicative model with two nonequilibrium neural networks is proposed to emulate the dynamical process of how we can understand each other. The model is quite simple, but successful memory transmission has brought us an important implication that it is likely to construct a neural model to interpret the underlying neural mechanism of understanding.

Acknowledgements This work was partially supported by a Grant-in-Aid for Scientific Research on Innovative Areas (No.4103)(21120002) from MEXT in Japan and partially supported by HFSPO(HFSP:RGP0039).

References

1. Christian Keysers and Valeria Gazzola. Social neuroscience: Mirror neurons recorded in humans. *Current biology*, 20(8):353–354, 2010.
2. Marleen B. Schippers, Alard Roebroek, Remco Renken, Luca Nanetti, and Christian Keysers. Mapping the information flow from one brain to another during gestural communication. *Proceedings of the National Academy of Sciences*, 107(20):9388–9393, 2010.
3. Greg J. Stephens, Lauren J. Silbert, and Uri Hasson. Speaker-listener neural coupling underlies successful communication. *Proceedings of the National Academy of Sciences*, 2010.
4. C. A. Skarda and W. J. Freeman. Brains make chaos to make sense of the world. *Behavioral and Brain Sciences*, 10(2):161–173, 1987.
5. I. Tsuda, E. Koerner, and H. Shimizu. Memory dynamics in asynchronous neural networks. *Progress of Theoretical Physics*, 78(1):51–71, 1987.
6. Ichiro Tsuda. Dynamic link of memory–chaotic memory map in nonequilibrium neural networks. *Neural Networks*, 5(2):313–326, 1992.
7. L. Nyberg. Any novelty in hippocampal formation and memory? *Current Opinion in Neurology*, 18(4):424–428, 2005.

Mechanisms for Generating Intermittency During Manual Tracking Task

Tetsumasa Asano, Jun Izawa, and Yutaka Sakaguchi

Abstract Intermittent velocity peaks of movement trajectory are commonly observed when subjects perform manual tracking task. However, the underlying mechanism of such intermittency has not been revealed yet. Focusing on the process of updating the internal target of movement, we proposed a computational model of “motor intermittency” in which a choice between two internal models, “dynamic target model” and “stable target model” might generate intermittent update of target, causing intermittency in the sequence of motor commands. To examine this model, we ran a behavioral experiment using a simple manual tracking task. In the experiment, we tested how the uncertainty of the prior knowledge of the target speed affected the nature of intermittency. The results showed that properties of intermittency were modulated by prior uncertainty of the target speed, which suggests that the brain might use a stochastic computational process to generate “motor intermittency”.

1 Introduction

To achieve the task in ever-changing environment, our brain must plan and generate motor commands in limited time. As appreciated from that it takes some time (latency) from obtaining the motion cue to beginning the movement, it takes little time for calculating motor command. Moreover, there is a few tens of milliseconds time delay until muscle produces contractive force after receiving motor command. Therefore, the brain must decision and generate appropriate

T. Asano (✉) • J. Izawa • Y. Sakaguchi
Laboratory for Human Information Science, The University of Electro-Communications,
Tokyo 182-8585, Japan
e-mail: asano@hi.is.uec.ac.jp

movement in appropriate timing under the nervous and musculoskeletal system having time lag. Then these restrictions in physical or information processing should compose computational principle.

For instance, feed-forward control play more important role than feedback control in fast reaching movements [1, 2]. These computational principles should be more precise in continuous tasks which is hard on time restriction (i.e. the subject must generate motor command continuously in response to the variable object) like tracking movements than sporadic tasks like reaching movements. For example, in the task of tracking a slowly moving target by the arm or the finger, the velocity profile of hand position commonly shows peaks [3–8]. Many ideas are discussed as cause of this “intermittency”: Time delay of visual feedback and noise, etc. If these movement properties found in continuous tasks could be due to computational principle of motor planning and control, the movement mechanism in the brain could be revealed by focusing to the mechanism of intermittency.

On the other hand, many of computation principles of motor control in the brain proposed by previous works were attending to smoothness of the movement trajectory especially in reaching movement. For example, Wolpert et al. focused on signal dependent noise (SDN) included in motor command, and proposed that the criterion by minimizing the effect of SDN is a factor of which generates movement smoothness [2, 9]. In the present model, the internal target was updated by minimum variance estimation, on the assumption that the internal target to generate motor command must be updated intermittently even though the target is moving continuously.

As described later, our model predicts that the property of the movement intermittency changed by the uncertainty of target movement. To examine this prediction, we performed behavioral experiment of manual tracking task. In the following, first, we present a motor control model on manual tracking task.

2 Model

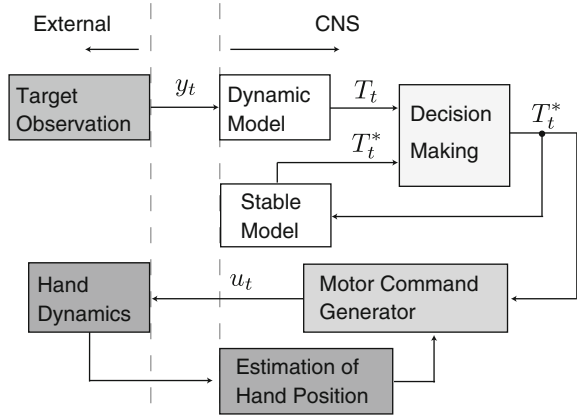
2.1 Model Structure

The scheme of our model which generates movement intermittency during a tracking movement is shown in Fig. 1. Proposed motor control system is composed of (1) two internal models on target motion and a decision making mechanism for switching these models, (2) the mechanism which estimates hand position in tracking movement and (3) the feedback controller that generates motor command for tracking the target.

Motor command u was generated by following equation using hand position and target position (gathered into state variable \hat{x}):

$$u_t = L_t \hat{x}_t$$

Fig. 1 Model structure



where subscript t is a time. In the following discussion, we focus on the mechanism of estimating the target position assuming that hand state is estimated appropriately due to internal model for hand dynamics, somatosensory feedback and visual feedback.

The process of updating target representation in the brain (T^*) is composed of two models, (1) updating target position T_t by measurement y_t and (2) maintaining conventional T_t^* , in addition to the process of doing decision making whether the target might be updated or not.

2.2 Updating Target Position in Uniform Motion

In the ballistic movements as reaching movements, once target representation is set up in the brain as P (with the exception of anomalous case as double step task) keep on $T^* = P$. In this paper, we assume that target representation is not kept but updated repeatedly. Additionally, we assume that target position is represented with a probabilistic model. Furthermore, we assume that the subject established the model for a motion of target position through experience of manual tracking tasks.

Here, the probability distribution of target position at $t-1$ is given by $P(T_{t-1}|Y_{t-1})$. Where Y_{t-1} is the set of measurements of target position until time $t-1$. When the transition probability of target position is described as $P(T_t|T_{t-1}; Q_D)$ (Q_D : noise). The probability distribution of target position at one time step later is shown as follows:

$$P(T_t|Y_{t-1}) = \int P(T_{t-1}|Y_{t-1})P(T_t|T_{t-1}; Q_D)dT_{t-1} \cdots (1)$$

Then if the visual information of target position is received at time t , probability distribution integrated the transition model and visual information is $P(T_t|Y_t) = P(T_t|Y_{t-1})h(y_t|T_t; R)/P(y_t)$.

Where $h(y_t | T_t; R)$ is observation model or likelihood and R is observation noise. The brain estimates the target position as the updated expected value of T : $E[T_t | Y_t]$. According to this model, the estimation of target position is updated continuously and smoothly during movement.

As another possibility, there is a way that internal target position is updated intermittently and updated position is maintained a certain time.

Consequently, we suggest that the brain has two models: “the model that target position is updated” and “the model that target position is maintained”, and switches target representation between these models by using decision making mechanism. In the model that target position T^* is maintained, internal representation of target position is not changed spatially over time, but updated by the following formula:

$$T_t^* = T_{t-1}^* + n_S (n_S \approx N(0, \sigma_S^2)).$$

Hereby, the uncertainty of target position increases with time. When above-mentioned procedure is shown as the update equation of probability part

$$P(T_t^*) = \int P(T_{t-1}^*)P(T_t^*|T_{t-1}^*; Q_S)dT_{t-1}.$$

In our model, T_t^* updates to T_t^* when the ratio of posterior probability of these two target representations exceed a certain threshold γ ,

$$P(T_t|Y_t)/P(T_t^*) > \gamma.$$

2.3 Numerical Simulation

Figure 2 shows the numerical simulation result. The target reaches $x=0$ at time 100 steps, and moves to the position $x=0.096$ at a constant speed. simulation was on two different variances of internal noise for dynamic model ($\sigma_S < \sigma_L$). Each probability distribution is assumed to be normally distributed. These conditions are the same as the behavioral experiment described later. Vibration component (in period 0.5–2 s) is seen in velocity waveform, and the frequency of target updating depends on the uncertainty of target motion (Fig. 2a). Figure 2b shows velocity power spectra. The power between 1–2 Hz was larger when the uncertainty of target motion was larger. In the case that target velocity changed at start position (add ± 0.9 ; also see Sec. 3 for the detail), difference in hand velocities between increased and depressed target velocity could be regarded as the response in terms of target velocity perturbation (Fig. 2c). The uncertainty of target motion affects a peak of the response.

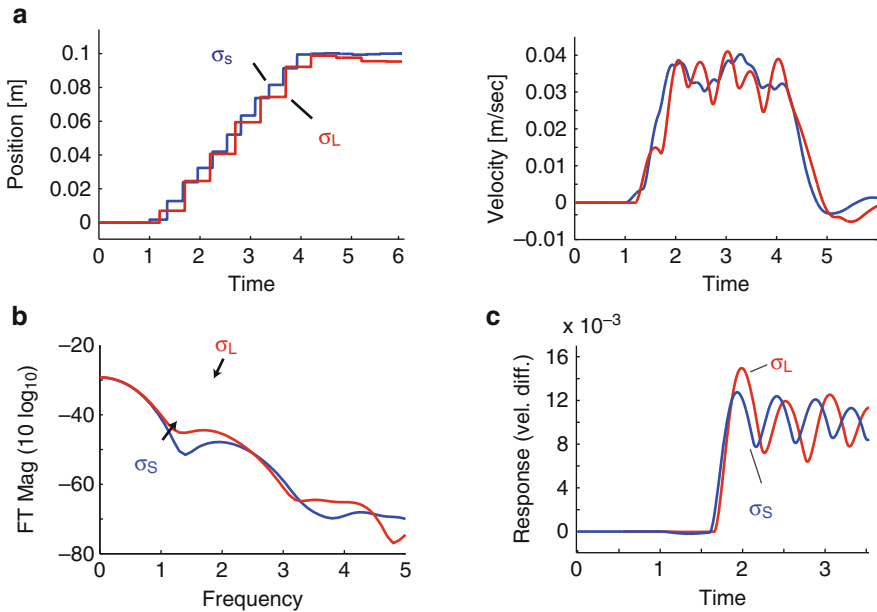


Fig. 2 Result of numerical simulation ($\gamma = 12.0, \sigma = 0.0001$). Initial values of standard deviations of internal target position for dynamic model and for stable model are 0.003 and 0.0001, respectively. Standard deviation of observation noise is 0.003. **(a)** Time variations of target representation and hand velocity. **(b)** Velocity power spectra. **(c)** Response of velocity difference

3 Experiments

According to our model, the timing of updating the internal target of movement T^* was determined by the transition of the variance in target representation (distribution). To verify this, we examined the effects of the velocity variance (i.e., uncertainty) in visually presented target motion on motor intermittency.

3.1 Method

Nine subjects participated in this experiment. Experimental procedures were approved by the local review board and all subjects signed a consent form. The experimental apparatus is shown in Fig. 3. The subjects were asked to keep their chin on the pedestal and to seat in front of the table. The subjects were asked to keep their right hand on the slider and asked to control it in back and forth direction. The air pressure floated the slider to avoid the frictional force and the PSD camera measured their hand position with 200 Hz in the refresh rate. The target position

Fig. 3 Experimental apparatus

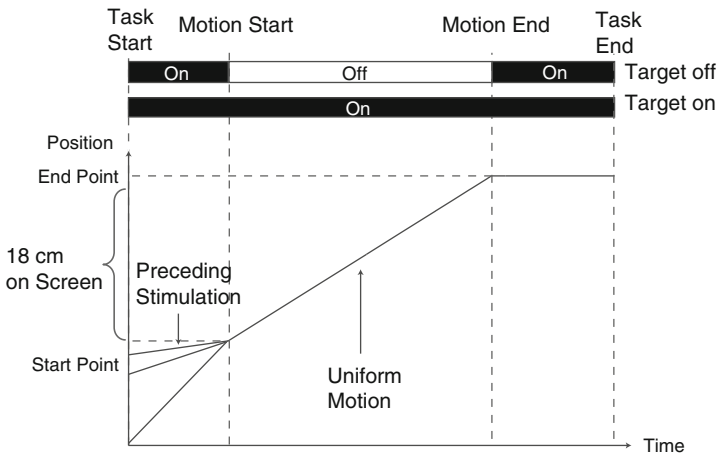


Fig. 4 Task assignments

and the cursor indicating subjects' hand were projected on the vertical screen by green and red laser spots. The target moved 18 cm (4.7° in visual angle), and this was 9.6 cm in the hand coordinate system.

Figure 4 shows task assignments. After the subjects positioned the cursor at the start position, three consecutive beeps were provided to subjects. The target was appeared at the bottom side of the start position and started to move upward. When the target crossed the start position, subjects initiated to track the target. The visual information of the target provided before it crossed the start position was called 'prior information'. In order to control uncertainty about target motion, the target speeds were randomly selected from three possibilities [Slow (3.6 cm/s), Medium (6.3 cm/s), and Fast (9.0 cm/s)]. Furthermore, we controlled the variance of visual noise injected in the prior information so that it changed every trial randomly from three different standard deviations: σ_S^2 , σ_M^2 , σ_L^2 ($\sigma_S < \sigma_M < \sigma_L$). Thus, the subjects estimated the speed of the moving target taking advantage of the prior

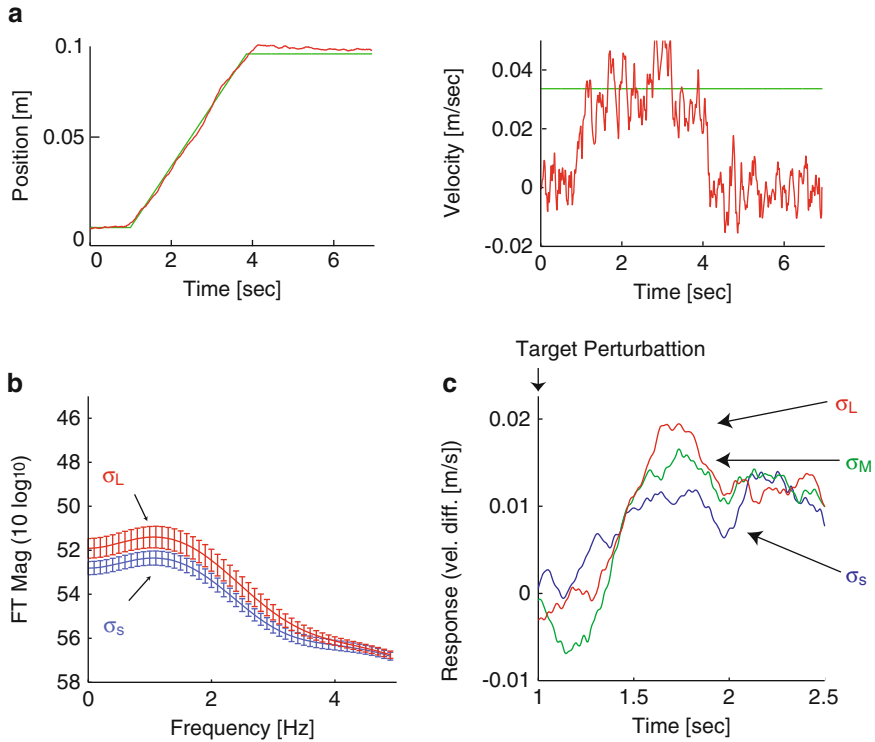


Fig. 5 Experimental results. (a) Typical orbital of hand position and velocity in the target visible condition. (b) Frequency analysis of hand velocity. (c) Velocity difference between the cases that the target speed was increased and decreased at the start point

information. Furthermore, in some trials, the target was turned off after the target crossed the start point so that the subjects had to achieve the task without visual feedback of the target and simply based on the prior information. In addition, in 60% of all trials, the target speed after start point was equal to average of prior information, and in 40% of trials, was added ± 0.9 cm/s to prior information.

3.2 Result

Figure 5a shows a typical orbital of hand position and velocity in case when target was visible. As seen from this figure, hand trajectory changed discontinuously, and meticulous vibration component (in period 0.5–2 s) was seen in velocity waveform.

Figure 5b shows the power spectral density in range of 0–5 Hz. Strong spectral component can be found at 0.5–2.0 Hz. In addition, the magnitude of the power

spectral density depended on the velocity variance of prior information. This means that vibration components were affected by probabilistic information about target motion obtained before movement start.

Figure 5c shows the subjects' response in terms of target velocity perturbation. The magnitude of the velocity variance in prior information significantly affected the peak of brain's response.

4 Discussion and Conclusion

In previous computational models of motor control, computation principles of motor control in a brain was considered to generate smooth movement as the result of the optimization based on minimum variance estimation of movement-related states (e.g., hand position) and minimization of variance of task-related variables (e.g., endpoint and viapoint). On the other hand, intermittency can be observed in hand movements when the hand speed is slow and constant. This behavior seemingly contradicts above computational principle, but we established that intermittency in tracking movement could be explained by assuming the decision making process using the posterior probability ratio of the minimum variance estimate contributed by two different target transition models. It was revealed that the intermittency in motion is not due to only the delay in visual feedback [5] and noise [6] but also characteristics of the motor control in the brain. In addition, it was revealed that the response to target speed variation changed by the uncertainty of prior information. This shows that updating the estimated position of the target is probabilistic, and our model supports that.

References

1. Kawato M, Wolpert D (1998) Internal models for motor control. *Novartis Found Symp* 218: 291–304; discussion 304–297
2. Wolpert DM, Kawato M (1998) Multiple paired forward and inverse models for motor control. *Neural Netw* 11: 1317–1329
3. Doeringer JA, Hogan N (1998) Intermittency in preplanned elbow movements persists in the absence of visual feedback. *J Neurophysiol* 80: 1787–1799
4. Doeringer JA, Hogan N (1998) Serial processing in human movement production. *Neural Netw* 11: 1345–1356
5. Miall RC, Weir DJ, Stein JF (1993) Intermittency in human manual tracking tasks. *J Mot Behav* 25: 53–63
6. Hogan N, Sternad D (2007) On rhythmic and discrete movements: reflections, definitions and implications for motor control. *Exp Brain Res* 181: 13–30
7. Neilson PD, Neilson MD, O'Dwyer NJ (1988) Internal models and intermittency: a theoretical account of human tracking behavior. *Biol Cybern* 58: 101–112
8. Slifkin AB, Vaillancourt DE, Newell KM (2000) Intermittency in the control of continuous force production. *J Neurophysiol* 84: 1708–1718
9. Todorov E, Jordan MI (2002) Optimal feedback control as a theory of motor coordination. *Nat Neurosci* 5: 1226–1235

Multi-dynamics Learning Algorithm Based on SOM²

Satoshi Matsushita, Takashi Ohkubo, and Tetsuo Furukawa

Abstract The purpose of this work is to develop a learning algorithm for multiple dynamical systems, which is referred to as the Multi-Dynamics Learning Algorithm (MDLA). The MDLA is necessary when one develops robots which learn various motion patterns, and which act adaptively depending on the context or the environment. The MDLA is also expected to be the theoretical abstraction of the dynamics learning ability of human or animal. In this paper, it is shown that the MDLA can be realized by employing the higher-rank of self-organizing map, namely, SOMⁿ.

1 Introduction

Human learns a vast number of action patterns during the development, and we can execute the acquired actions adaptively depending on the context and the environment. This ability, which is provided by the brain, is also required when engineers design autonomous intelligent robots. The purpose of this work is to develop such a learning algorithm that enables us to deal with a group of dynamical systems. Here let us refer the algorithm as Multi-Dynamics Learning Algorithm (MDLA). The MDLA is expected to have the abilities to learn, represent, estimate, quantize, interpolate, and classify a class of dynamics. The destination of this work is to discover the theoretical principle of MDLAs as well as the implementations of the algorithms. In this presentation we focus on an implementation of MDLA by using higher-rank of self-organizing map, namely SOMⁿ [1, 2].

S. Matsushita • T. Ohkubo • T. Furukawa (✉)
Department of Brain Science and Engineering, Kyushu Institute of Technology 2-4 Hibikino,
Wakamatsu-ku, Kitakyushu, 818-0196, Japan
e-mail: furukawa@brain.kyutech.ac.jp

2 What Is MDLA?

First of all, let us clarify what we expect from the Multi-Dynamics Learning Algorithm. Suppose that we have a set of N dynamical systems represented by N difference equations $\mathbf{z}_n(t + 1) = f(\mathbf{z}_n(t); \theta_n)$ or differential equations $\dot{\mathbf{z}}_n(t) = f(\mathbf{z}_n(t); \theta_n)$. Here $\mathbf{z}_n(t)$ is the state variable, while θ_n is the parameter vector which determines the n -th dynamics. The dynamics dealt with by the MDLA is assumed to be altered continuously when θ_n is changed continuously. It is further supposed that the dynamics set $\{f_n(\mathbf{z})\}$ and the parameter set $\{\theta_n\}$ are unknown, whereas a part of the state variable $\mathbf{z}(t)$ is assumed to be observable. Thus $\mathbf{z}(t)$ consists of the observable part $\mathbf{x}(t)$ and unobservable part $\mathbf{y}(t)$, such as $\mathbf{z} = (\mathbf{x}(t), \mathbf{y}(t))$ (Fig. 1). Therefore N time sequences $X(t) = \{\mathbf{x}_1(t), \dots, \mathbf{x}_N(t)\}$ are available to use for training of MDLA.

With this framework, the MDLA is expected to have the following abilities.

1. The MDLA estimates the dynamics which generated the given sequences $X = \{\mathbf{x}_n(t)\}$. It means that MDLA needs to estimate both $\{f_n(\mathbf{z})\}$ and the latent variable $\{\mathbf{y}_n(t)\}$.
2. The MDLA measures the distances or similarities between the estimated dynamics. It also means the MDLA can sort, classify and quantize the given dynamics if it is needed.
3. By giving an intermediate θ , the MDLA represents the intermediate dynamics between given sequences.
4. If a new sequence $\mathbf{x}_{\text{new}}(t)$ is observed after training, the MDLA identifies the corresponding parameter θ_{new} of the sequence, and classifies the dynamics.

3 Naive Algorithm

For this purpose, modular network architectures have often been adopted traditionally. One of the representative one is MODular Selection And Identification for Control (MOSAIC) [3]. Sometimes SOM is combined with the modular network

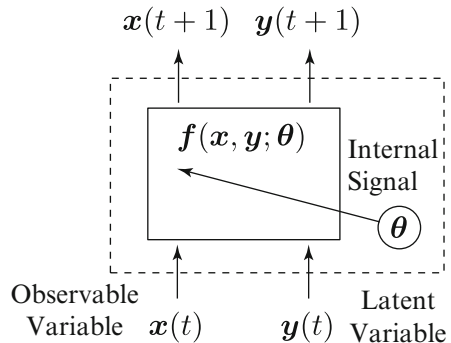


Fig. 1 Thime-series generation model in the framework for learning of multiple dynamics

[4–6]. An alternative architecture is Jordan’s plan unit or its modifications, such as the Parametric Bias (PB) methods [7, 8]. The common principle of these methods is that the best matching module or the best matching parameter is most responsible for each dynamics, and the network is trained by mixing the given sequences according to the responsibility.

Unfortunately it has been shown that such naive algorithms are effective only in some simple cases, in which the distance between two dynamics can be defined as [2, 9],

$$L^2(f_1, f_2) \triangleq \int \|f_1(\mathbf{x}, \mathbf{y}) - f_2(\mathbf{x}, \mathbf{y})\|^2 p(\mathbf{x}, \mathbf{y}) d\mathbf{x}d\mathbf{y} \quad (1)$$

Here \mathbf{x} and \mathbf{y} are the observable and the latent state variables, and f_1, f_2 represents the function of the differential/difference equations. To apply this distance measure, the probability density function (PDF) $p(\mathbf{x}, \mathbf{y})$ should be equal to both dynamics, but it is uncommon in many realistic cases. To make the situation worse, the probability density of the latent variable $\mathbf{y}(t)$ is underspecified, because there is always arbitrariness of the scale and the bias of \mathbf{y} . Therefore such naive algorithm based on the mixture learning is not appropriate for the task (Fig. 2). Thus we need another strategy to develop the MDLA which works in more generalized situations.

4 Theory for Natural Algorithm

To solve the arbitrariness problem of the latent variable $\mathbf{y}(t)$, let us employ the embedded representation.

$$\tilde{\mathbf{x}}_n(t) \triangleq (\mathbf{x}_n(t), \mathbf{x}_n(t-1), \dots, \mathbf{x}_n(t-L+1)) \quad (2)$$

Since $\tilde{\mathbf{x}}(t)$ means a short trajectory for the period of T , $\tilde{\mathbf{x}}_n$ distributes differently for each sequence and forms a individual subspace. Thus we obtain N subspaces from N observed sequences. If the subspaces are linear, then they can be represented by the autoregressive (AR) model. Here we assume that these subspaces are nonlinear for generality. It means that our task becomes to identify, classify and interpolate a set of nonlinear manifolds. In such situation, the dynamics is represented by

$$\tilde{\mathbf{x}}_n(t+1) = \tilde{f}_n(\tilde{\mathbf{x}}_n(t)). \quad (3)$$

It is worth noting that these manifolds are all isomorphic. If they are not isomorphic, then those dynamics are heterogeneous, and no comparison between dynamics can be made.

Now let us introduce the concepts of *intrinsic variable* and *intrinsic dynamics*. The intrinsic variable ξ indicating the position in each manifold, while the intrinsic dynamics can be represented as

$$\xi(t+1) = f(\xi(t)). \quad (4)$$

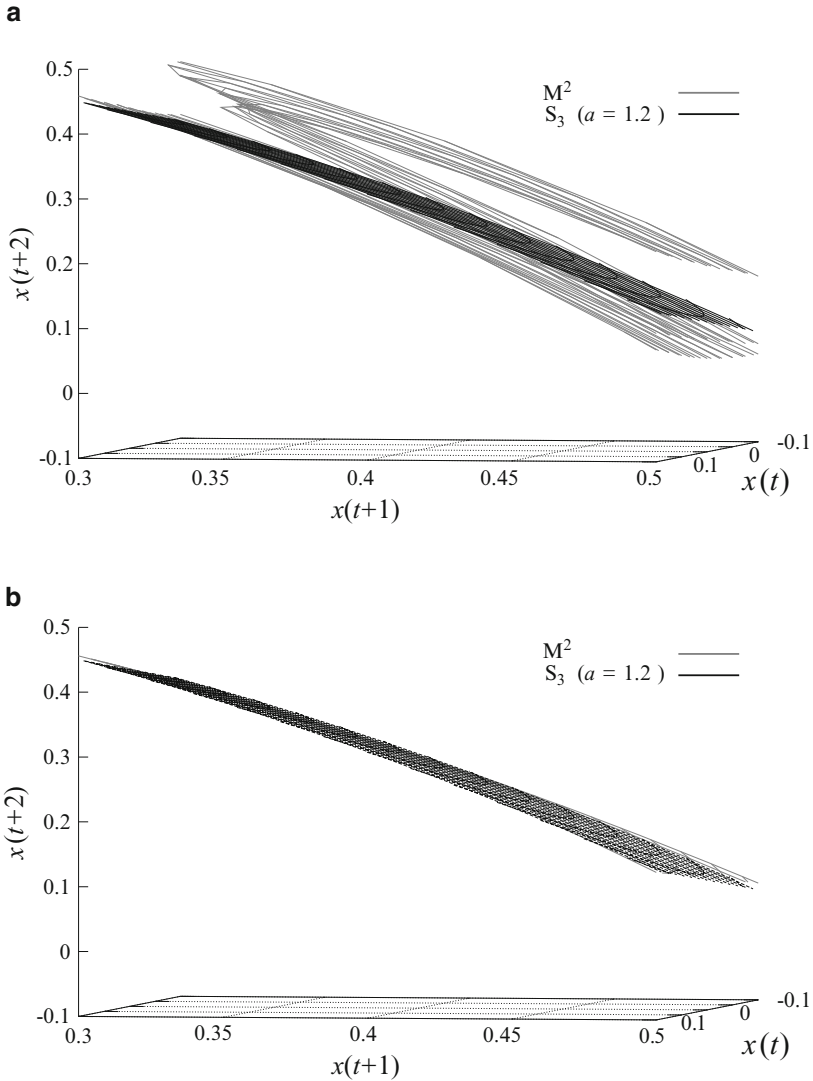


Fig. 2 Single RNN is trained by two time-series of Henon map with different parameters, $a = 1.4$ and $a = 1.0$. The *gray surface* of each panel represents the dynamics expressed by the RNN, while the *black surface* represents the desired dynamics when an intermediate parameter is used, i.e., $a = 1.2$. **(a)** The result of the naive algorithm. **(b)** The result of the natural algorithm

The intrinsic variable ξ should be carefully determined so that the intrinsic dynamics are common for all given sequences. Thus the maps from the intrinsic space to the observed embedded space depends on the sequences so that

$$\tilde{\mathbf{x}}_n = g_n(\xi) = g(\xi, \theta_n). \tag{5}$$

Under this formulation, the distance measure between two dynamics is defined by

$$L^2(g_1, g_2) \triangleq \int \|g(\xi; \theta_1) - g(\xi; \theta_2)\|^2 p(\xi) d\xi. \quad (6)$$

To measure the distance, we have to estimate both $g_n(\xi)$ and $\xi_n(t)$ for $\tilde{\mathbf{x}}_n(t)$. It is worth noting that the estimation of ξ_1 and ξ_2 should be made simultaneously so that the same value of ξ means the same intrinsic state. Therefore the essence of this task is to estimate the homotopy $g(\xi, \theta)$ from a family of dataset. The higher-rank of self-organizing map SOMⁿ is designed for this purpose. In this case, the 2nd rank of SOM, i.e., SOM² is most suited algorithm [1].

5 Natural Algorithm

To solve this problem, the following three steps are necessary. (1) Estimating each nonlinear manifold M_n , which consists of the dataset $\tilde{X}_n = \{\tilde{\mathbf{x}}_n(t)\}$. (2) Homologizing the estimated manifolds so that the intrinsic variable ξ becomes common for all dynamics. (3) Comparing between homologized manifolds, and sorting, interpolating and quantizing them. These tasks cannot be made by one-pass process, and we need to solve them iteratively. The higher-rank SOM (SOMⁿ) is developed for the very purpose. The second rank of SOM, i.e., SOM² has a hierarchical structure consisting of the 1st SOMs and the 2nd SOM. The task of the 1st SOMs is to model a set of manifolds, while 2nd SOM models the relation between the maps organized by the 1st SOMs (Fig. 3).

The algorithm is described as follows [1]. First, each manifold M_n is estimated by the 1st SOM.

$$M_n(\tau) := \mathcal{S}_{1st}[\tilde{X}_n, M_n(\tau - 1)] \quad (7)$$

Here the symbol \mathcal{S} is the SOM operator, which means a single step of SOM algorithm. τ is the calculation step, and $M_n(\tau - 1)$ is used as the initial condition of the estimation. In SOM² $M_n(\tau)$ is represented by a tensor, and it can be dealt with as an ordinary vector. Second, the meta-map Q is estimated by the 2nd SOM.

$$Q(\tau) := \mathcal{S}_{2nd}[\{M_n(\tau)\}, Q(\tau - 1)] \quad (8)$$

The 2nd SOM homologizes the given manifold set by making interpolation. As the result, the intrinsic variable ξ are gradually aligned for all dynamics.

As the result, the 2nd SOM organizes a map of the manifolds. Then finally, the winner unit of the 2nd SOM is copied back to the corresponding 1st SOM.

$$M_n(\tau) := \mathbf{q}_n^*(\tau) \quad (9)$$

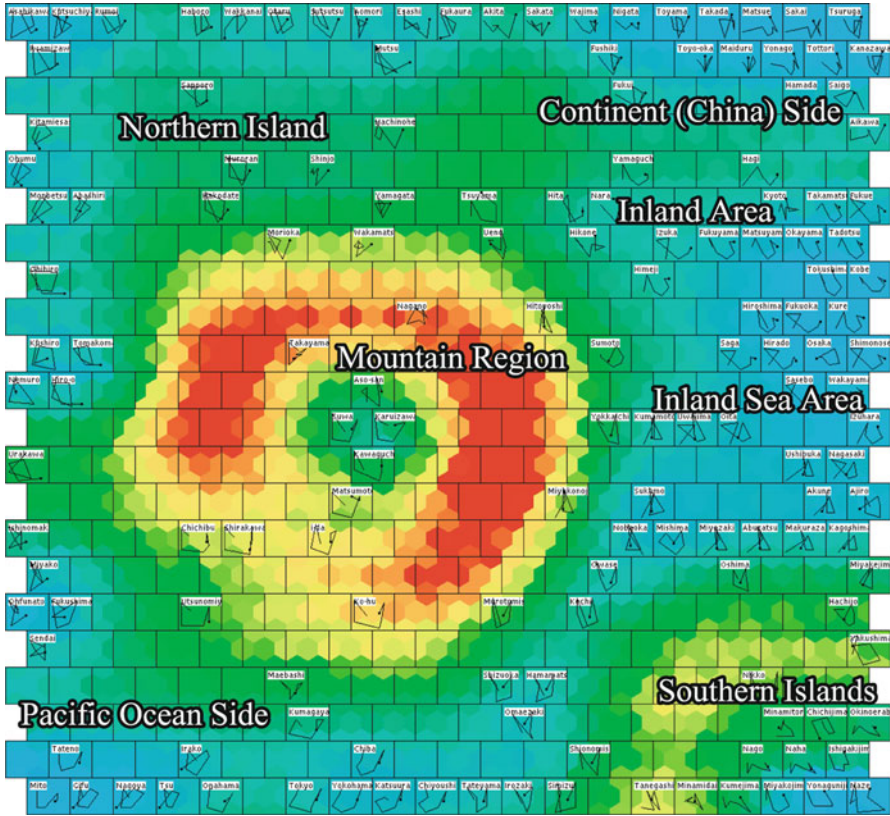


Fig. 3 A map of weather dynamics organized by a SOM². Weather trajectories during 1 week for 153 cities are indicated in the winner node

Here \mathbf{q}_n^* is the winner unit of M_n within the units of the 2nd SOM. The third step is essentially important, because the homologized manifolds become the initial state of the next iteration.

6 Simulation and Result

To examine this algorithm, the SOM² based algorithm was applied to the weather data observed at 153 cities in Japan. In the weather dynamic case, the intrinsic variable ξ means the essential representation of the weather state which usually features the pressure pattern and so on. In this simulation we assumed that the observation dates are unknown, and thus it was impossible to compare the weather data of the same day between different cities.

The result is shown in Fig. 2. In the organized map, the cities belonging to the similar weather classes are located nearer and the entire map represents the continuous representation of weather features of the cities. Unlike the ordinary Kohonen's SOM, each nodal unit of SOM² represents a self-organizing map of the 1st SOMs. Thus we can see a single dynamics in each unit of the SOM², while a map of dynamics can be seen in the entire SOM². In Fig. 2, weather trajectory during 1 week of 153 cities are also indicated in the corresponding (i.e. the winner) unit.

7 Discussion

In this presentation, we proposed a novel method of self-organizing map of a set of dynamics based on SOM². It should be stressed that SOM is not essential in the algorithm, and one can replace SOM by other type of subspace learning algorithms. The most essential point of the algorithm is the hierarchical estimation of the 1st and the 2nd levels, and the simultaneous estimation of the intrinsic variable and the map from the intrinsic space to the observed data space. Homologizing between different dataset is not easy, and one-pass naive algorithm is only effective in simple and lucky cases.

Theoretical viewpoint, several issues are expected to be clarified further. First, the algorithmic structure of SOM² should be described in terms of probabilistic learning such like Bayesian theory. Second, the concepts of the intrinsic dynamics and the intrinsic variable should be more clarified in terms of dynamics. Third, the issue of the metrics of dynamics is important but still remained.

Acknowledgements This work is supported by Grant-in-Aid for Scientific Research on Innovative Areas 22120510, *The study on the neural dynamics for understanding communication in terms of complex hetero systems*.

References

1. T. Furukawa, *Neural Networks*, **22**, 463–478, 2009.
2. T. Ohkubo, K. Tokunaga, T. Furukawa, *IEICE Trans. Inf. & Sys.*, **E92-D**, 1388–1396, 2009.
3. D.M. Wolpert, M. Kawato, *Neural Networks*, **11**, 1317–1329, 1998.
4. K. Minamino, *In: Developing Intelligence (Intelligence Dynamics Series Vol.3)*, Springer-Japan, 73–111, 2008 (in Japanese).
5. T. Minatohara, T. Furukawa, *IJICIC*, **7**, 2011 (in press).
6. K. Tokunaga, T. Furukawa, *Neural Networks*, **22**, 82–90, 2009.
7. M.I. Jordan, *ICS Report*, 8604, 1986.
8. J. Tani, *IEEE Trans. SMC Part A*, **33**, 481–488, 2003.
9. T. Ohkubo, K. Tokunaga, T. Furukawa, *Int. Congress Series*, **1301**, 168–171, 2007.

Saccade Dynamics in Error Trials During Visual Search

Atsushi Fujimoto, Satoshi Nishida, and Tadashi Ogawa

Abstract We recorded behavioral properties of a monkey performing visual search task and analyzed erroneous trials by classifying them into three error types depending on the saccade trajectory. In spite of common motor requirements and feedbacks, we observed distinctly different patterns in the reaction times and the peak eye velocity. These results suggest different causes and neuronal substrates underlying different error types.

1 Introduction

We sometimes make mistakes, even when we make a well-learned response following instructions. This phenomenon has been commonly observed in animal studies. A visual search task is a simple task and it is widely used in animal studies. Nevertheless, animal subjects sometimes make error responses, even after they have been well trained and they fully recognized a task sequence [1, 2].

Although the reasons that cause erroneous responses may differ from trial to trial (e.g. memory loss, failure in motor planning, and lack of attention or motivation), few studies separately analyzed erroneous responses depending on the cause of them. The purpose of the present study was to classify erroneous responses into subgroups depending on the cause that elicits erroneous responses and to elucidate the response-property differences among the different types of erroneous responses.

Here, we required a monkey to perform a visual search task and analyzed saccadic eye movements obtained from the erroneous trials. By classifying erroneous trials into three types depending on the trajectory of the first saccade in visual search,

A. Fujimoto • S. Nishida • T. Ogawa (✉)
Graduate School of Medicine, Kyoto University, Yoshida-Konoe-chou, Sakyo-ku,
Kyoto 606-8501, Japan
e-mail: togawa@brain.med.kyoto.ac.jp

we demonstrated that the response properties substantially differed among the three types of erroneous responses, implicating different causes underlying different types of erroneous responses.

2 Methods

Data were collected from one female Japanese monkey (*Macaca fusucata*) weighing 7.0 kg. A head holder and a scleral search coil were surgically implanted before the experiments. All animal care procedures and experimental protocols were in accordance with the National Institutes of Health Guidelines for the Care and Use of Laboratory Animals (1996) and were approved by the Animal Care and Use Committee of Kyoto University.

The monkey was trained to perform a target-tracking visual search task (Fig. 1). Eye movements during experimental sessions were measured using the electromagnetic search coil technique. Each trial began with the appearance of a fixation point and the monkey was required to fixate on that spot within a square window of ± 1.5 – 1.7 deg. After fixation for 1,200–1,500 ms, an array of six colored elements (red, orange, yellow, green, blue, and magenta) appeared in a circle around the fixation point. The color order of an array was randomly changed from trial to trial. After fixation for an additional 600–1,000 ms, the fixation point disappeared (Go signal) and the monkey was required to make a saccade to one of the elements. One color was defined in advance as the behaviorally relevant target. Immediately after saccade onset, the array stimulus disappeared. If the monkey made a single saccade landing inside a square window of ± 2 deg centered on the target, another fixation point appeared at the target position. After fixation to this point for 600 ms, the monkey received a juice reward accompanied by a high-pitched tone, indicating a successful trial.

If the monkey made a saccade to a non-target-color element or to another location outside the target window, the trial was terminated and only a low-pitched tone was delivered, indicating an erroneous trial. If the gaze position deviated from the fixation window before the Go signal, the trial was immediately aborted without reward or sound feedback. The trial was also aborted if the saccade reaction time was too short (<130 ms) because that saccade may have been initiated before the Go signal.

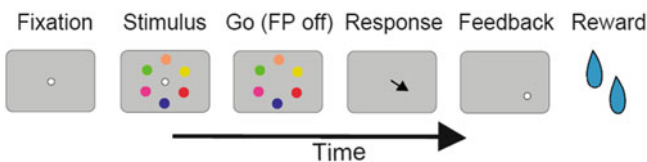


Fig. 1 Target-tracking visual search task

The target color remained the same within a block of 20–40 successful trials, and then changed unexpectedly. This task design required the monkey to find the target color on the corresponding block by trial and error and then repetitively select the relevant color in the subsequent trials within the block. In this study, we focused on only the trials following the first successful trial after a color change. On these trials, the monkey presumably recognized the relevant color of the block and could select it in a stereotypical manner.

To characterize the behavioral response properties during the task, we calculated the success rate and two kinds of reaction times. The success rate was calculated as the ratio of the number of the successful trial to the summed number of the successful and erroneous trials. The reaction time of the fixational eye movements toward the fixation point (RTFP) was defined as the interval between the fixation point appearance and the time at which the gaze position shifted into the central eye window. The RTFP was set to 800 ms when the RTFP was larger than 800 ms, and set to 0 ms when the gaze position already located in the central eye window before the appearance of the fixation point. Saccadic reaction time (SRT) was defined as the interval between the fixation point disappearance and saccade initiation. The peak eye velocity (PEV) was defined as the maximum eye velocity during the first saccade following Go signal. Trials in which it was lower than 180 deg/s were excluded from data analysis (0.7%). For the statistical comparisons, the median value of RTFP and SRT and the mean value of PEV were calculated for each session, then the average and standard deviation (SD) were calculated across all sessions for each result state.

3 Results

The data obtained from 504 blocks (39 sessions) were used in all of the following analyses. On average, the monkey performed 12.9 ± 3.4 (mean \pm SD) blocks in each session. The average number of the erroneous trials (trial-and-error searches) before first successful trial after a color change was 5.0 ± 1.1 trials. Once the monkey accidentally made a saccade to the target color of the currently-executing block (first successful trial), the success rate immediately increased and then kept at a high-performance level ($82.9 \pm 4.8\%$), indicating that the monkey fully recognized the relevant target color and selected a color element depending on the knowledge about it (knowledge-based searches). In the current study we only analyzed the trials following the first successful trial after a color change.

We classified erroneous trials into three types depending on the landing point of the first saccade (Fig. 2). The most frequent erroneous type (62.7%) was ‘Distracter-selected’ type, in which the monkey selected a non-target stimulus with a single saccade. Secondary one (18.3%) was ‘Non-selected’ type, in which the first saccade did not reach any of the color elements. Third one (17.7%) was ‘Target-selected’ type, in which the monkey successfully selected the target element but failed to keep the post-saccade fixation until the reward delivery.

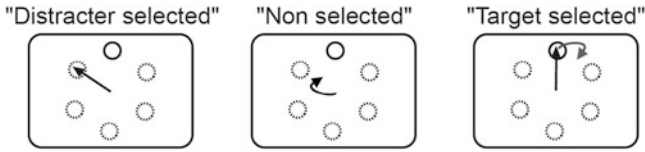


Fig. 2 Three types of erroneous saccade responses. The target (*solid circle*) and distracters (*dashed circles*) are shown. *Arrows* indicate schematic saccade trajectories

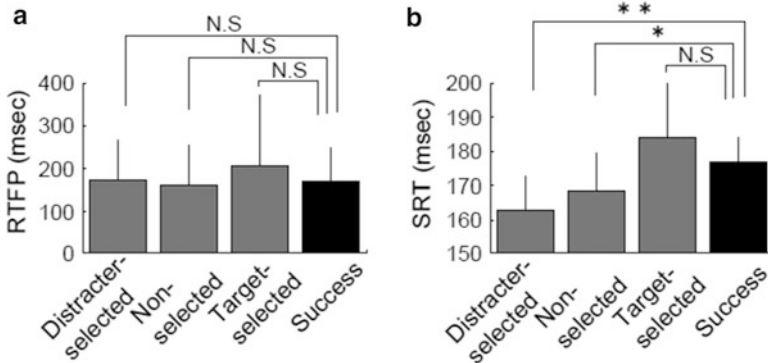


Fig. 3 Error-type-dependent differences in RTFP (**a**) and SRT (**b**). *Asterisks* over the bars indicate statistical significances (rank-sum test, ** $p < 0.01$; * $p < 0.05$; N.S., $p > 0.05$)

We first compared the RTFP values among the three error types and the successful trials (Fig. 3a). We found that there was no significant difference in the RTFP values across the three erroneous types (distracter-selected, 164.4 ± 81.2 ms; non-selected, 152.2 ± 98.5 ms; target-selected, 181.1 ± 122.7 ms; one-way ANOVA, $p = 0.46$, $F = 0.77$). In addition, the RTFP values in the three erroneous types were not significantly different from that in the successful trials (164.4 ± 77.7 ms) (rank-sum test, $p > 0.05$). Thus, RTFP was not linked with the erroneous type and the result state (successful or erroneous trials).

We next compared the SRT values among the three error types and the successful trials. We found significant differences among the three error types (distracter-selected, 165.7 ± 8.7 ms; non-selected, 170.8 ± 18.7 ms; target-selected, 179.5 ± 16.1 ms; one-way ANOVA, $p < 0.001$, $F = 8.2$). The SRT values in both the distracter-selected and non-selected error types were significantly shorter than that in the successful trials (176.1 ± 7.0 ms; rank-sum test, $p < 0.01$, distracter-selected vs. success; $p < 0.05$, non-selected vs. success). But there was no significant difference between the target selected error type and successful trials (rank-sum test, $p > 0.05$).

Finally, we compared the PEV of the first saccade after Go signal among the erroneous and successful trials. Because the saccade amplitude affects the PEV, we used only the trials with saccade amplitude was within $6\text{--}7^\circ$. There were significant differences among three error types (distracter-selected, 381 ± 19.0 deg/s;

non-selected, 348 ± 21.5 deg/s; target-selected, 313 ± 38.5 deg/s; one-way ANOVA, $p < 0.001$, $F = 58.9$). The PEV was significantly larger in the distracter-selected erroneous trials and in the non-selected erroneous trials than in the successful trials (312 ± 24.3 deg/s) (rank-sum test, $p < 0.01$). It was also significantly different between the distracter-selected and non-selected types ($p < 0.01$). Thus, the non-selected type erroneous trials had fastest PEV among three error types.

Taking together, the SRT and the PEV values in the distracter-selected and non-selected erroneous trials significantly differed from those in the successful trials. In contrast, there was no such difference between the target-selected-erroneous and successful trials.

4 Discussions

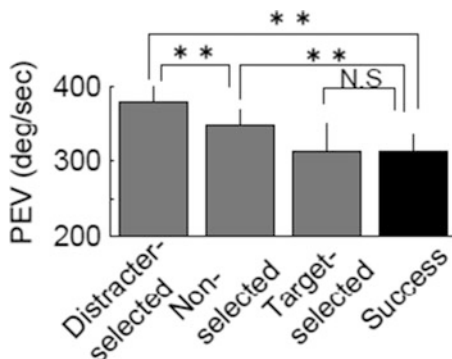
In this study, we compared the behavioral response profiles (RTFP, SRT, and PEV) among the different-type erroneous (distracter-selected, non-selected and target-selected error types) and successful trials when a monkey performed a visual search task. We found that changes in the response profiles between the erroneous and successful trials were not the same but instead largely varied depending on the error type.

Previous studies reported that RTFP could reflect the motivational state of an animal subject on the individual trials [3, 4]. Okada et al. (2009) gave the different amount of reward after successful responses. The magnitude of reward was instructed in advance by the shape of the fixation point so that the monkey could expect that. The mean RTFP value increased on the trials in which the monkey anticipated a large reward, whereas it decreased when the monkey anticipated a small reward [3]. Although it is expected that internal motivation may differ between the successful and erroneous trials, we found that RTFP did not depend on either the error type or the result state (Fig. 3a). Thus, there may be no difference in motivational state among different result state, or if any, they were not reflected in RTFP in our visual search task.

The present study demonstrated that reaction times in the target-selected erroneous trials did not significantly differ from that in the successful trials. (Fig. 3). In this type of erroneous trials, visual saccade selection processes may be adequately advanced, and the monkey only failed to maintain post-saccade fixation until reward delivery. Therefore, in the following discussion, we mainly focused on neural mechanisms that produce erroneous saccades in the distracter-selected and non-selected error types.

SRT in the distracter-selected and non-selected error types were significantly shorter than that in the successful trials (Fig. 3b). Previous studies suggested that an unusual neuronal pathway resulted in short SRT and erroneous response. Yoshida et al. (2008) investigated saccade profiles in the monkey with unilateral lesion in the primary visual cortex. They reported shortened SRT and compensative activation of the superior colliculus (SC) when the monkeys made a saccade to the affected

Fig. 4 Error-type-dependent differences in the peak eye velocity



visual field [5], suggesting that the amount of the time to generate a saccade might be shortened due to shortcutting in the processing through the neocortex. However, because SC neurons are poorly selective for stimulus features [6], such a by-passed process might elicit incorrect responses in visual search in which the target was defined with stimulus features. Gold et al. (2007) suggested that the accumulation of sensory evidence in the lateral intra-parietal area (LIP) is crucial to execute a correct response [7, 8]. Imperfect accumulation of the sensory evidence may elicit an immature saccade with short SRT and result in an erroneous response. Taking together, the present finding that the SRT values in the distracter-selected and non-selected erroneous trials significantly decreased suggest that the accumulation of sensory evidence may be insufficient in the distracter selected and non-selected erroneous trials compared to the target-selected erroneous and successful trials in this study.

The PEV was significantly higher in the distracter-selected erroneous trials and in the non-selected erroneous trials compared to that in the successful trials. Moreover, distracter-selected type was faster than the non-selected type (Fig. 4). Previous studies reported that the saccadic peak velocity varies depending on the task conditions. Van, Gelder et al. (1997) trained monkeys to perform both visually-triggered and memory-guided saccade tasks and found that the peak velocity in saccadic eye movements decreased in the memory-guided saccade task [9]. The existence of a visual stimulus at the location of a saccade end point may facilitate the saccade initiation processes in a stimulus-driven manner and generate a faster saccade in a visually-triggered saccade task. In contrast, in the lack of the visual guidance, such stimulus-driven facilitation cannot work and generate a slower saccade in a memory-guided saccade task. Based on the expansion of this view, we infer that the relatively slower saccadic eye velocity in the non-selected erroneous trials observed in this study may be due to the lack of stimulus-driven facilitation, because the monkey shifted gaze to the blank region (no stimulus at the saccade end point) in this type of erroneous trials.

In a memory-guided saccade task, the information about the target position should be maintained in working memory and the motor plan should be made under the top-down control. The fact that the PEV of a memory-guided (top-down control) saccade is slower than that of a visually-triggered saccade suggest that the emergence of top-down control has an effect so that the eye velocity becomes slower. In other words, if the saccade initiation process is only based on stimulus-driven manner and free from any top-down control, the saccade eye velocity could be faster. In the present study, we found that the PEV was significantly higher in the distracter-selected erroneous trials than that in the successful trials. We think that less top-down control (reflective) may produce a faster saccade observed in this type of erroneous trials.

Thus, the lack of the top-down control presumably elicits a fast erroneous saccade (distracter-selected erroneous type), whereas the lack of stimulus-driven facilitation causes a slow and miss-localized saccade (non-selected erroneous type). The emergence of the markedly different types of erroneous saccades suggests the importance of the balance of top-down control and stimulus-driven facilitation in producing a correct saccade response during visual search.

References

1. Schall, J.D., Sato, T.R., Thompson, K.G., Vaughn, A.A., Juan, C.H: Effects of search efficiency on surround suppression during visual selection in frontal eye field. *J Neurophysiol* 91 (2004) 2765–2769
2. Sato, T., Murthy, A., Thompson, K.G., Schall, J.D: Search efficiency but not response interference affects visual selection in frontal eye field. *Neuron* 30 (2001) 583–591
3. Kobayashi, Y., Inoue, Y., Yamamoto, M., Isa, T., Aizawa, H: Contribution of pedunculopontine tegmental nucleus neurons to performance of visually guided saccade tasks in monkeys. *J Neurophysiol.* 88(2) (2002) 715–31
4. Okada, K., Toyama, K., Inoue, Y., Isa, T., Kobayashi, Y: Different Pedunculopontine Tegmental Neurons Signal Predicted and Actual Task Rewards. *Journal of Neuroscience* 29 (2009) 4858–4870
5. Yoshida, M., Takaura, K., Kato, R., Ikeda, T., Isa, T: Striate cortical lesions affect deliberate decision and control of saccade: implication for blindsight. *J Neurosci.* 28(42) (2008) 10517–10530
6. McPeck, R.M., Keller, E.L: Saccade target selection in the superior colliculus during a visual search task. *J Neurophysiol.* 88(4) (2002) 2019–2034
7. Gold, J.I., Shadlen, M.N: The neural basis of decision making. *Annu Rev Neurosci.* 30 (2007) 535–574
8. Kiani, R., Hanks, T.D., Shadlen, M.N: Bounded integration in parietal cortex underlies decisions even when viewing duration is dictated by the environment. *J Neurosci.* 28(12) (2008) 3017–3029
9. Van, Gelder, P., Lebedev, S., Tsui, W.H: Peak velocities of visually and nonvisually guided saccades in smooth-pursuit and saccadic tasks. *Exp Brain Res.* 116(2) (1997) 201–215

Design and Dynamics of Active-Touch Sensory Model

Tatsuo Yanagita

Abstract An active sensory system is designed using the Markov chain Monte Carlo (MCMC) method. The system is a feedback circuit comprising four parts: receptors, sensory, motor, and internal neurons. The neurons are modeled using excitable cellular automata. The neural connections between them are determined by the MCMC method so as to minimize a given sensing error. Several modes of sensing motions have been found depending on the optimization level, and a logical interpretation of an optimized neural network is obtained.

1 Introduction

In general, haptic (touch) perception entails the exploration and recognition of object surfaces through active touch. Numerous studies have been conducted in this regard [1–4]. Perception via active sensing is more effective than perception via passive sensing [1, 4]. Our objective is to determine how such an effective sensing can be achieved by sensing environment patterns via input neurons and computing motor outputs using neural networks. From a mathematical point of view, finding similarities among algorithms for the different types of touch is an interesting task. For this purpose, first, we design a mathematical model of an active sensory system. Then we optimize the neural networks using the Markov chain Monte Carlo (MCMC) technique, and we analyze the types of logic that can be embedded in the optimized neural networks.

T. Yanagita (✉)

Osaka Electro-Communication University, Neyagawa Osaka 572-8530, Japan
e-mail: yanagita@isc.osakac.ac.jp

2 Models and Methods

The system considered herein is a neural feedback circuit with several components, i.e., sensory neurons, motor neurons, interneurons, and receptors, as shown in Fig. 1. The output signals of sensor neurons are activated by receptors and transmitted to motor neurons via interneurons. The excitation of motor neurons induces the motion of the receptor part, and stimuli to these receptors change as a result of this motion. Thus, the system is a feedback circuit between the input signals to the receptors and the self-generated sensing motion controlled by the neural network.

For simplicity, we use an excitable cellular automaton (ECA) as a model neuron, i.e., the excitable neuron has n states $s_i \in \{0, \dots, n\}$, ($i = 1, \dots, N$), $s_i = 0$ is the resting state; $s_i = 1$ corresponds to excitation, and the remaining states $s_i = 2, \dots, n - 1$ are refractory states. When the sum of the input signals to the i -th neuron exceeds a threshold, it goes from state $s_i = 0$ to 1. Time is discrete and the dynamics, after excitation, are deterministic: if $s_i = 1$, in the next time step, its state changes to $s_i = 2$ and so on until the state $s_i = n - 1$ leads to the $s_i = 0$ resting state. Thus, the element is a cyclic cellular automaton.

In the following, we consider an ensemble of ECA neurons $\mathcal{N} = \{\mathcal{N}_S \cup \mathcal{N}_L \cup \mathcal{N}_R \cup \mathcal{N}_I\}$, where \mathcal{N}_S denotes sensor neurons, which receive signals from receptors, \mathcal{N}_L and \mathcal{N}_R denote motor neurons, which control the left and right motions of the receptor part, respectively, and \mathcal{N}_I denotes interneurons. The sensorimotor system contains a feedback loop between the signals from the receptors and the autonomously generated sensing motion.

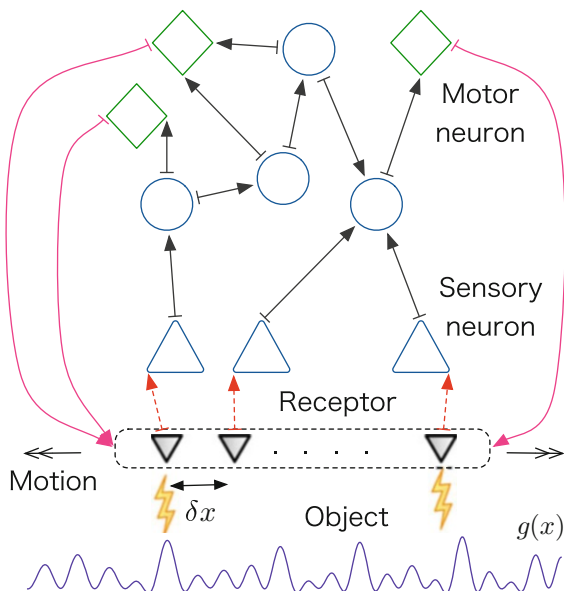


Fig. 1 Schematic figure of mathematical model for active touch sensory system. Sensory neurons, interneurons, motor neurons, and receptors are represented by triangles, circles, diamonds, and inverted triangles, respectively

When a sensory neuron i connects to a set of receptors \mathcal{R}_i , it receives the following inputs from \mathcal{R}_i depending on the positions at which the receptors are located, i.e., the signal to the sensory neuron i from the receptors is

$$I_i^r = \sum_{j \in \mathcal{R}_i} g(x_j),$$

where $g(\cdot)$ is a given function that determines the profile of an object, and x_j is the position of receptor j . We assume that all the receptors are attached to a single base at equal intervals, and thus, the positions of the receptors are

$$x_k = X + \delta x(k-1) - \frac{(N_r-1)\delta x}{2}, \quad (k = 1, \dots, N_r),$$

where N_r is the number of receptors, δx is the interval between receptors, and X is the position of the center of the base. The neuron i receives the following input signal from the connected neurons and receptors,

$$I_i = \sum_j w_{j,i} \delta_{1,s_j^n} + I_i^r, \quad (1)$$

where $\mathbf{w} = \{w_{i,j}\}$ is the connection matrix between the neurons. $\delta_{i,j}$ is Kronecker's delta. If $i = j$, $\delta_{i,j} = 1$; otherwise, $\delta_{i,j} = 0$.

In this paper, we consider the one-dimensional motion of the receptor part. The governing equations of motion obey the following Newtonian dynamics with external forces f ,

$$M \frac{d^2 X}{dt^2} = f(\mathcal{N}_L, \mathcal{N}_R) \exp(-|\dot{x}|/v_{max}), \quad (2)$$

where $f(\mathcal{X}, \mathcal{Y})$ is external force acting on the receptor part, which is controlled by motor neurons \mathcal{N}_L and \mathcal{N}_R , v_{max} denotes the maximum speed, and M is the total mass of the receptor part. For simplicity, we set $f(\mathcal{X}, \mathcal{Y}) = \#\mathcal{X} - \#\mathcal{Y}$, where $\#\mathcal{X}$ denotes the number of firing neurons in \mathcal{X} , i.e., $\#\mathcal{X} = \sum_{i \in \mathcal{X}} \delta_{s_i,1}$; thus, the sensing motion is controlled by the difference in the number of firing neurons of \mathcal{N}_L and \mathcal{N}_R .

An artisan can grind and polish a designed structure elaborately, e.g., telescope lenses and perfectly flat mirrors are polished manually by a skilled craftsmen. They can actively detect the slightest roughness and polished it off. On this basis, we assign the following task. The time-averaged signals from the receptors

$$Q = \sum_{i=1}^{N_r} \frac{1}{T} \sum_{t=0}^T g(x_i(t)) dt, \quad (3)$$

i.e., the sensorimotor system tries to detect a tiny hollow in a given surface profile $g(x)$ by self-generated sensing motion, where T is the time interval in haptic perception. For this purpose, we employ a MCMC method to design a neural network, which has been previously applied to dynamical systems [5]. In the actual implementation, we use the replica exchange Monte Carlo (REMC) algorithm, which provides an efficient method to investigate systems with rugged free-energy landscapes, specifically at low temperatures (see [5] for details).

3 Numerics

For each Monte Carlo step, since we have to estimate Q by time evolution of the model equation, systems with the number of neurons $N = 4, 8, 16$ are investigated in this paper. Initially, the center of the receptor part is $X = 0$, for all the neurons, $s_i = 0$, ($i = 0, 1, \dots, N$), and a random matrix is used as the initial $w_{i,j}$. The interval between the receptors is $\delta x = 0.2$. The total number of links between the neurons is fixed at L . For time averaging, intervals of length $T = 200$ and 500 were typically used. The results did not significantly depend on T when sufficiently large values of T were taken. Using Q , networks \mathbf{w} were sampled by the REMC optimization method. Simultaneously, the evolution of K replicas with inverse temperatures $\beta_m = \delta\beta \times m$, $m = 0, 1, \dots, K - 1$, was performed (with $K = 16$ and $\delta\beta = 10$). For display and statistical analysis, sampling was carried out every 50 mcs after a transient of 5,000 mcs has been undertaken. In the following, we consider $g(x) = \exp(-x^2)$ and $g(x) = \cos^2(2\pi x)$ as profile of objects.

First, we consider a trivial task, i.e., $g(x) = \exp(-x^2)$. In this case, the best strategy to sense the tiny hollow is that the receptor part should try to get away from the original position $X = 0$, as quickly as possible. In fact, such motion is observed in optimized neural networks. Here, we use “optimizing” in the following sense. Many networks are sampled by the aforementioned algorithm, and their performances are dependent on β , i.e., replicas with larger β usually sample better networks. We divide all the sampled networks into K sets, $\{\mathbf{w}\}_k = \{\mathbf{w} | Q_k < Q(\mathbf{w}) < Q_{k-1}\}$ ($k = 0, 1, \dots, K - 1$), where $Q_k = Q_{\min} + \frac{(Q_{\max} - Q_{\min})k}{K}$, and Q_{\min} and Q_{\max} are the minimum and maximum performances for sampled networks, respectively. Decreasing the index k , the mean performance of the set $\{\mathbf{w}\}_k$ increases. We regard these sets as different optimized levels, and the set $\{\mathbf{w}\}_0$ denotes optimized networks.

The best sensing motion can be realized in $\{\mathbf{w}\}_0$ by a simple network structure, as shown in Fig. 2(a-ii). Because there is no uncertainty regarding the initial condition of the system, only a symmetry-breaking connection from a sensory neuron to a motor neuron is required to induce such unidirectional motion. In fact, as shown in Fig. 2(a-ii), unidirectional motion can be realized by this simple asymmetrical neuronal connection.

When we set the profile $g(x) = \cos^2(2\pi x)$, it is obvious that such a unidirectional motion cannot give the best performance. One may expect that it is difficult for

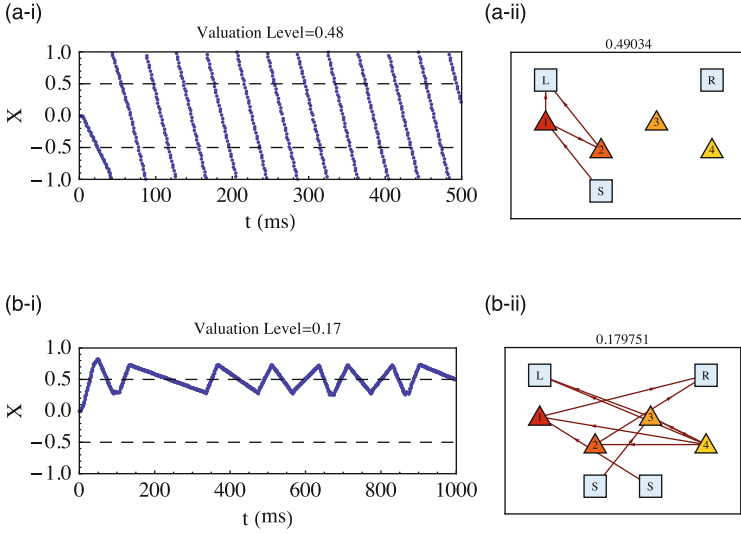


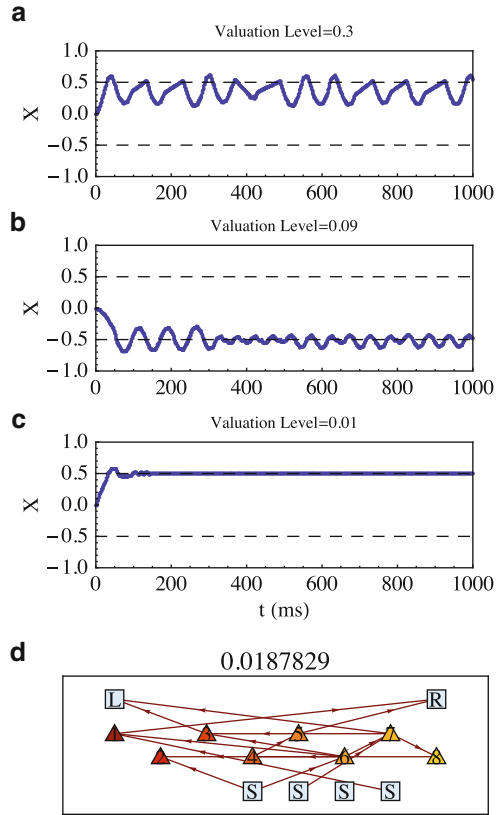
Fig. 2 Typical realization of sensing motion. *Left:* The position of the center of the receptor part X as a function of time. The *broken lines* indicate the positions at which the external stimulus $g(x) = \cos^2(2\pi x)$ takes minimal values. *Right:* The corresponding networks. The numbers on the top of the figures show the Q value. (a) $N_r = 1, L = 4$ (b) $N_r = 2, L = 10$, and the other parameters are $N = 4$ and $M = 1$

the system with only one receptor to generate any motion except for unidimensional motion, and it cannot perform the task. In fact, the system with $N_r = 1$ exhibits only unidirectional motion if the number of neurons is small.

When we increase the number of receptors, several types of autonomous sensing motions are found, i.e., unidirectional, periodic, damping, aperiodic, and convergent motions, depending on the optimization level (typical styles are shown in Fig. 3). These modes can be interpreted as follows. The periodic sensing motion shown in Fig. 3a is a result of the simple logical connection between a sensory neuron and a motor neuron as follows. Signals from the left (right) side receptor excite the motor neurons $\mathcal{N}_R(\mathcal{N}_L)$ through sensor and internal neurons, and this circuit causes oscillatory sensing motion.

The convergent motion to the position of the hollow $\hat{x} = \arg \min_x g(x)$ appears in such a way that after generating left (right) motion, this motion is counterbalanced by generating forces resulting from the excitations of the opposite motor neurons when the receptor part is in the vicinity of the minimum point (see Fig. 3c). This means that there exists a delay circuit in the network; however, we cannot determine the explicit logical interpretation in the network. It may be seen that the convergent motion is one of the “best” sensing motions minimizing Q . However, this mode can be seen as an “over-fitting” in the sense that the optimized network does not give good performance when we change the object’s profile in time. In fact, when the profile varies stepwise as $g(x, t) = \cos[2\pi(x - \Delta(t))]$, $x(t) = 0.5 \sum_{i=1}^3 \Theta(t - t_i)$,

Fig. 3 Typical styles of sensing motion depending on Q level. **(a)** Oscillatory mode ($Q \sim 0.3$) **(b)** Dumping mode ($Q \sim 0.09$) **(c)** Over dumped mode ($Q \sim 0.01$) **(d)** Network that generates over dumped mode (e). The parameters are $N_r = 4$, $N = 8$, and $L = 40$



where $\Theta(\cdot)$ is the Heaviside function, the convergent sensing motion does not appear. Thus, this mode is a “good” strategy for a given (well-known) static object, however, it is not robust against time variation of an object.

As the number of receptors and neurons increases, more complex sensing motions are realized, e.g., dumping motions and aperiodic oscillatory motions emerge. Typically, these motions are realized with the intermediate Q levels, as shown in Fig. 3b. Furthermore, in contrast to convergent motion, the dumping and aperiodic motions are robust against the time variation of an object, and the performances of the designed system is stable for many types of given objects.

4 Summary and Discussion

We designed an active-touch sensory system equipped with an excitable cellular automaton network. Considering an artisan’s polishing skills, which are known to be actively acquired, we assigned the task of detection of a tiny hollow on a surface

defined by a given profile function $g(x)$. To design a neural network that perform the task, we used the Markov chain Monte Carlo method.

Many styles of sensing motions of the receptor part emerged depending on the optimized levels, and the number of neurons and receptors. For small networks, we could identify the algorithm/logic of the sensorimotor system by a direct comparison with the neural network; however, exploration of such a relationship may require statistical analysis for larger networks. Since it is difficult, in general, to derive logic/algorithm from a dynamical system, even if it is a small network consisting of simple dynamical elements presented in this study, we may have to reconsider how to understand a functional dynamical system. The interpretation of a dynamical system via logic/algorithm may be inadequate for understanding the system.

It is also interesting to elucidate how dumping and aperiodic motions are produced by designed neural network, e.g., how the time scales of dumping and fluctuation are reflected by the neural networks. Since we detected aperiodic sensing motion for larger neural networks, it is important to consider the role of fluctuation and chaos in sensing.

Acknowledgements This study has been partially supported by the Ministry of Education, Culture, Sports, Science and Technology (MEXT, Japan) , Grant-in-Aid for Scientific Research (Grant No. 21540376, 22120501), and the Volkswagen Foundation (Germany).

References

1. Gibson, J.J.: Observations on active touch. *Psychol. Rev.* **69** (1962) 477–491
2. Diamond M. E., Prescott, T. J. and Wing, A. M.: Active touch sensing. *Phil. Trans. R. Soc. B* **366** (2011) 2989–2995
3. Bajcsy, R.: Active perception. *Proceedings of the IEEE*, **76(8)** (1988) 966 –1005
4. Robles-De-La-Torre, G., and Hayward, V.: Force can overcome object geometry in the perception of shape through active touch. *Nature* **412** (2001) 445–448
5. Yanagita, T and Mikhailov, A. S.: Design of easily synchronizable oscillator networks using the Monte Carlo optimization method. *Phys. Rev. E* **81** (2010) 056204–056212

Human Object Recognition Based on Internal Models of the Human Hand

Masazumi Katayama and Tatsuya Kurisu

Abstract In this study, we have assumed that tools to use by hand are recognized based on the internal model of the hand. In the first step to validate the hypothesis, we investigated whether internal model influences the size that participants recognize as the tool. In the experiments, by repeatedly grasping while looking an object and a geometrically transformed hand shape that were displayed on a monitor, each participant acquired the internal model that corresponds to the transformation hand shape. By the measurement experiments after the training, we found that the cognitive judgment of the size was affected by the geometrical transformation of the hand shape. This result indicates that the internal model is closely related to the object recognition.

1 Introduction

When you feel a thirst, you can immediately find a drinking cup even from the complicated environment, although there are many kinds of cups. Here, we emphasize that such a cognitive process closely relates to sensorimotor experiences for object manipulation of tools. For example, the size that we look like a drinking cup may depend on the size of our own hand because a larger object of a cylinder type looks like a vase. Thus, object recognition for graspable tools may be closely related to the size of the human hand. From this point of view, in this study, we have made a hypothesis that we search and recognize tools such as a drinking cup by using an internal model of the human hand [1, 2]. According to this hypothesis, by

M. Katayama (✉) • T. Kurisu

Department of Human and Artificial Intelligent Systems, Graduate School of Engineering,
University of Fukui, 3-9-1 Bunkyo, Fukui, 910-8507, Japan
e-mail: kata@u-fukui.ac.jp

using the internal model, we can easily recognize a drinking cup by judging whether we can grasp and manipulate the object or not, although various kinds of memories such as a declarative memory for tools are also important.

In this study, for the first step to evaluate the biological plausibility of the hypothesis, we built an experimental paradigm to learn internal models of the human hand and then we investigate a relationship between the internal models and object recognition.

2 Methods

As shown in Fig. 1, we built a experimental system in a dark room that constructed by using a hand-shape measurement device (CyberGlove, Immersion Corp.), a three dimensional motion measurement device (OPTOTRAK3020, Northern Digital, Inc.), a mirror, a display (U2711, DELL), an experimental chair using an ergonomically designed car seat (Keiper Recaro GmbH and Co), a 4-point seat belt to fix participant's body, and a chin rest to fix participant's head. Infrared light-emitting diodes (IR LED markers) were attached to each fingertip in order to accurately measure the fingertip positions by OPTOTRAK at 200 Hz. Hand shape of the right hand of each participant was also measured by CyberGlove (22 joint-angles) at 120 Hz and the hand shape were displayed on the display. Before the experiments, a right hand and a forearm were displayed on a monitor and then we calibrated the position, size and hand shape of the displayed hand in order that each participant looks like own hand.

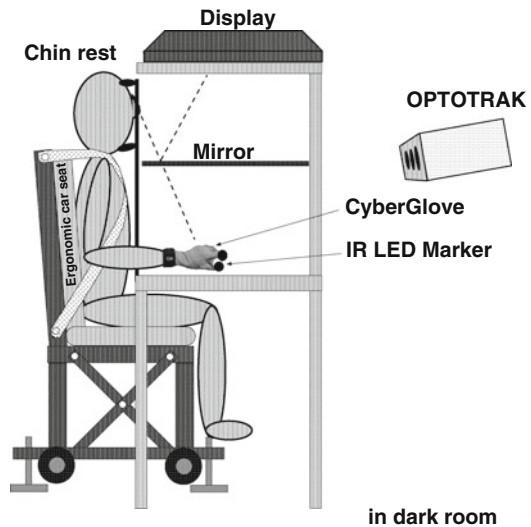


Fig. 1 Experimental environment

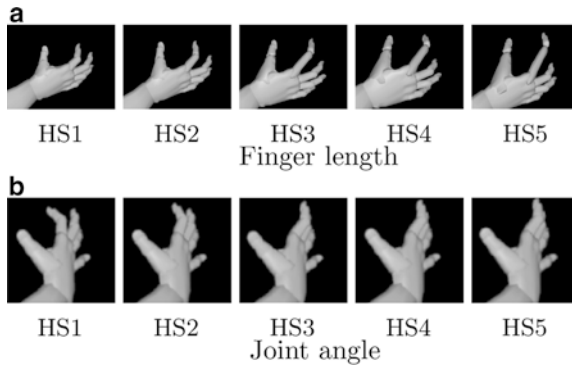
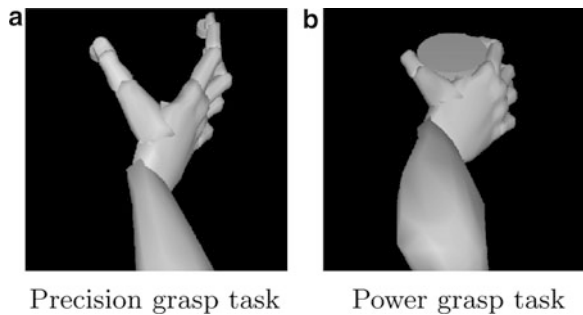


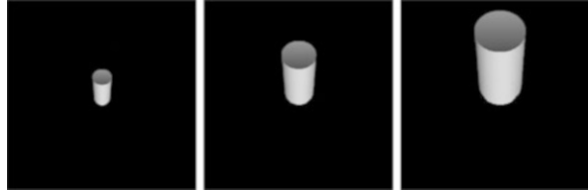
Fig. 2 Geometrically-transformed hand shapes displayed on a monitor. Both of HS2 are the same hand shape, size and position as each participant’s hand. (a) HS1 is the case of shorter finger length and HS3–HS5 are the longer cases. (b) HS1 is the case of narrow grip aperture and HS3–HS5 are the wider cases. For all the hand shapes in each of (a) and (b), the participant’s hand shape is the same as HS2

Fig. 3 Displayed image on an monitor. Grasping task to train the internal model that corresponds to the geometrical transformation of the displayed hand shape. (a) Precision grasp task. (b) Power grasp task



In the experiments, the hand shape of participant’s hand was geometrically transformed and the transformed hand shape was displayed on a monitor. We used two kinds of the transformation for finger length and joint angle. For finger length, the geometrical transformation was to change the length of each first link of the thumb and the index finger. There are five hand shape types from HS1 to HS5: 0.6, 1.0, 1.4, 1.8 and 2.2 times, as shown in Fig. 2a. For joint angle, the transformation was to shift angle of each first joint of the two fingers. There are also five hand shape types from HS1 to HS5: -5 , 0 , 5 , 10 and 15 degrees, as shown in Fig. 2b. Eight participants joined the experiments (eight male, right-handed, aged 21–26) and were divided into two groups for the finger-length condition and the joint-angle condition. In each group, cognitive judgment for tool size was examined after learning a grasping task described in the below. The learning and measurements for each hand shape type were executed in the order of HS2, HS1, HS4, HS3 and HS5 on different days (Fig. 3).

Fig. 4 Examples of the displayed objects



2.1 Learning Phase of the Internal Model

A right hand and a forearm were displayed on a monitor and moreover two small circles were also displayed as shown in Fig. 4. The displayed hand and forearm could be moved in synchronization with participant's hand-movement measured by CyberGlove. In order to train the internal model, participants repeatedly executed the grasping task that positioned each fingertip to each small circle and the positions of two circles were randomly changed every trial. Whether the learning had finished was judged after each set (one set was 20 trials). If the learning had not finished then participant executed trials of one set. When the learning had finished, it is indicated that participants trained a new internal model that corresponded to the transformed hand shape.

2.2 Measurement Phase of the Cognitive Judgment

After they completely trained the grasping task for each hand shape type, we examined cognitive judgment of tool size. For the measurement phase, the hand and forearm were not displayed and an object (cylinder) was only displayed as shown in Fig. 4. We used 11 objects of different diameters: the diameters were 24, 38, 52, 66, 80, 94, 108, 122 and 136 mm. The aspect ratio of the diameter and the height of the objects was constant. Only one object (cylinder) was selected and displayed on a monitor at each trial. Participant answered whether they recognized the displayed object as a drinking cup or not: When they recognized as a drinking cup, they answered "Yes". The measurements were 20 trials for each object size (the total were 180 trials).

3 Results

The results of cognitive judgment for object size were shown in Fig. 5. The probabilities of "Yes" for the displayed objects in each hand shape type were almost distributed as a normal distribution. For each hand shape type, the object

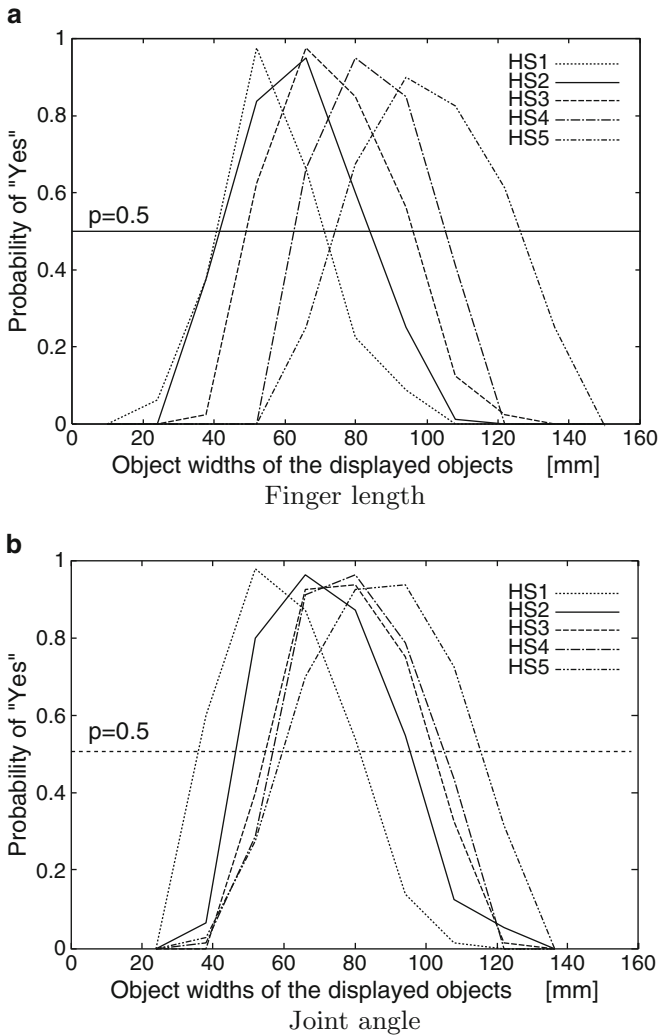
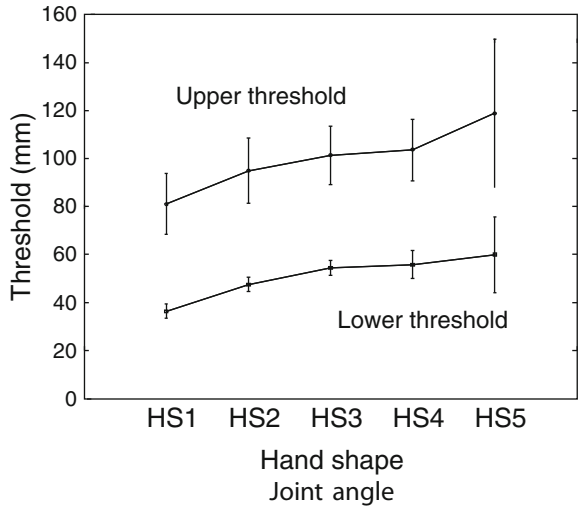
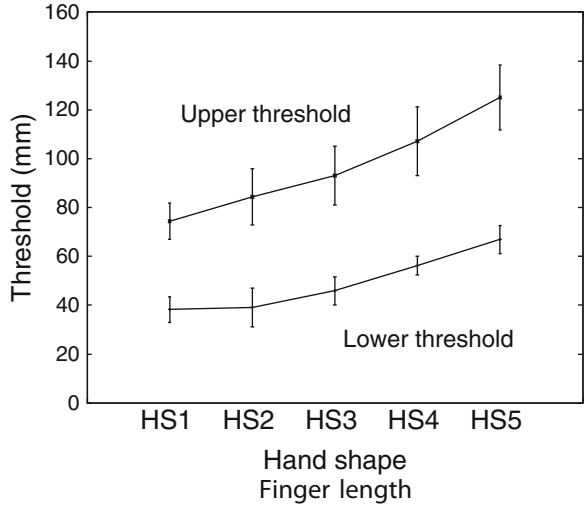


Fig. 5 Averaged results of cognitive judgment for all participants. Participants answered “Yes” when they looked like a drinking cup. The values when the probability is 0.5 express cognitive thresholds. (a) Finger length. (b) Joint angle

widths at two intersection points that the probability is 0.5 are the lower and upper thresholds for object recognition. These thresholds are shown in Fig. 6. Both of the lower and upper thresholds for each hand shape type increase in almost proportion to the amount of change of grip aperture of the transformed hand shape. These thresholds for each condition were significantly different except the combinations of the lower values of HS1 and HS2 in the finger length condition and the values

Fig. 6 Averaged thresholds for all participants. The object size between the lower and upper thresholds for each hand shape type are recognized as a drinking cup. The vertical line for each plot expresses the standard deviation. (a) Finger length. (b) Joint angle



of HS3 and HS4 in the joint angle condition ($p < 0.05$, Turkey-kramer method). These results show that when cylinders of width from the lower threshold to the upper threshold were displayed, participants recognized as a drinking cup. Table 1 shows the ratio between changes in cognitive judgment and changes in grip aperture of the transformed hand shape. These values of the ratios are almost 1 although the values are smaller than 1. Thus, these results show that the ranges that participants recognize as a drinking cup increase in almost proportion to the amount of change of grip aperture of the transformed hand shape.

Table 1 Ratio between changes in cognitive judgment and changes in grip aperture of the transformed hand shape. Change in grip aperture, ΔC , was an amount of change from the grip aperture of HS2. Change in cognitive judgment, ΔG , was also an amount of change from the threshold of HS2. The ratio is $\Delta C / \Delta G$. The threshold is an average of the lower and upper values. The lower column is the standard deviation

	HS1	HS3	HS4	HS5	Average
Ratio	0.94	0.95	0.88	0.89	0.92
Std.	0.06	0.08	0.07	0.14	0.08

4 Discussion

In this research, we found that the sizes that we recognize as a drinking cup depend on the geometrical transformation of the displayed hand shape. These results indicate that we recognize the displayed object (cylinder) as a drinking cup by using the trained internal model of the geometrically transformed hand.

In our experimental paradigm, some of the readers may have a question that the internal models were not learned. In our previous experiments, however, we ascertained that the learning effect of the right hand did not translate to the left hand [2]. Moreover, we have reported that the learning effect does not influence the image memory of a familiar cup used in daily life [2]. Those results indicate that the internal models that correspond to the transformed hand shapes were acquired by using the experimental paradigm we built.

In previous psychological studies, from the viewpoint of the affordance theory [3], some researchers have supposed that observation of tools used by the hand activates an internal simulation of action such as grasping because observation of an tool activates it's related action [4–6] and action-related brain areas [7]. In order to perform such an internal simulation for action, the human hand should be internally represented in the brain, that is the internal model. One of the possible reasons to explain that in this study the trained internal model of the transformed hand shape affect cognitive judgment for object size, is to perform the internal simulation using the internal model. Thus, our results also indicate an internal simulation of action in cognitive process of graspable tools, using the internal model of the human hand.

Acknowledgements This research was partially supported by MEXT, KAKENHI (20500235).

References

1. Katayama M., Kawato M.: A neural network model Integrating visual information, somatosensory information and motor command. *Journal of The Robotics Society of Japan* **8** (1990) 757–765 in Japanese
2. Katayama M.: Internal models of the human hand affect object recognition. *Proceedings of the 7th International Conference on Cognitive Science* (2010) 355–356

3. Gibson J. J.: *The Senses Considered as Perceptual System*. Boston: Houghton Mifflin (1966)
4. Grezes J., Decety J.: Functional anatomy of execution, mental simulation, observation, and verb generation of actions: a meta- analysis. *Hum. Brain Mapp.* **12** (2001) 1–19
5. Borghi, A. M.: Object concepts and action. In D. Pecher, R. A. Zwaan (eds.), *Grounding Cognition: The Role of Perception and Action in Memory, Language, and Thinking*, Cambridge: Cambridge University Press (2005) 2–34
6. Creem-Regehr, S. H., Lee, J. N.: Neural representations of graspable objects: are tools special?. *Cognitive Brain Research* **22** (2005) 457–469
7. Chao L. L., Martin A.: Representation of manipulable man-made objects in the dorsal stream. *Neuroimage* **12** (2000) 478–484

Estimation of Children's Interest Dynamics While Communicating with Robots

Takayuki Shimotomai, Kasumi Abe, Ayami Yokoyama, Takayuki Nagai, and Takashi Omori

Abstract The purpose of this study is to develop a communicative robot that estimates other's mental state, and to elucidate a computational principle of brain dynamics that realizes a mental level interaction. As the first step for the perspective, we had constructed robots that can observe and estimate child's internal states, such as boring or enjoying. As the experiment, we observed a child playing a card game with a robot that we had developed, and talking with the robot. After the experiments, the children's mental states were evaluated by other participants by watching videos. The results showed high correlation with an index calculated by a face recognition system in the robot. This result suggests that it is possible for the robot to recognize human interest and to make an action inducing human-like interaction.

1 Introduction

An important point to build a communicative robot is to consider dynamic interaction. The important aspect in this study is to find the best way for evaluation of dynamic interest change on communication in face-to-face dialog. Recently robotic technologies are on the verge of becoming possible to talk and interact with humans. In fact, there are growing evidences on how human interacts with robots [1, 2]. From a psychological view, Tanaka et al. [1] observed interaction of children and

T. Shimotomai (✉) • T. Omori
Brain Science Institute, Tamagawa University, 6-1-1 Tamagawa Gakuen, 194-8610, Tokyo, Japan
e-mail: shimotomai@lab.tamagawa.ac.jp; omori@lab.tamagawa.ac.jp

K. Abe • T. Nagai
The University of Electro-Communications, 1-5-1 Chofugaoka, 182-8585, Tokyo, Japan

A. Yokoyama
Tamagawa Gakuen, 6-1-1 Tamagawa Gakuen, 194-8610, Tokyo, Japan

a robot. They showed a correlation between interaction strategies and children’s interactive actions. From an engineering view, Castellano et al. [2] developed chess player system with emotional face interface and observed interaction during playing chess with children.

The purpose of this study is to develop a communicative robot that estimates other’s mental state and to elucidate a computational principle of brain dynamics that realizes a mental level interaction. As the first step, we had constructed robots that can observe and estimate child’s internal mental states, such as boring, enjoying.

In the experiment, we observed children playing a card game and talking with robots. To estimate the internal ‘interest’ dynamics of the children, we used an observed face expression sequence, and evaluated the result by comparing it with the estimation by human adults. And we proposed a rating model for child’s interest and evaluated the model.

2 Model and System

We have developed a humanoid robot system [3, 4]. The robot has verbal interface and two arms, vision system such as two cameras like human eyes, and a 3D sensor (SR4000, Mesa Imaging AG, Zurich). The robot system uses the Scale-Invariant Feature Transform (SIFT) based vision system for the object detection [4], and a face recognition system (OkaoVision, OMRON Corp., JAPAN). The experimental sessions were recorded by a camera in the robot system for analysis after the experiments (Fig. 1).

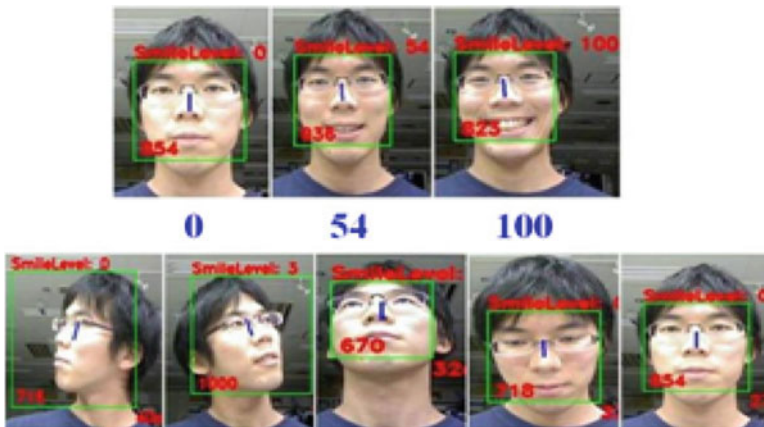


Fig. 1 Face recognition for direction (lower) and smiling value (upper): white rectangles means recognized face area, and black bars means recognized nose position and face angle

Fig. 2 A child playing card game with the robot



The robot can talk and play a card game ‘concentration’ (Fig. 2). We aimed finding a child’s behavioral index that represents the child’s internal states for their emotion or interest, and its dynamics.

In the game, the player knows the game state and decides their own actions. In order to construct the mental model, we precisely observed the child’s behavior, and compared robot’s observation and human evaluation for the child’s states during the card game.

3 Methods

Participants were two kindergarten children (a 6 years old boy and a 5 years old girl). Each child talked (talking session) and played the concentration game with the robot (game session). The robot behaved autonomously and the assistant did not operate the robot during the experiment.

In the game session, at first, cards were flipped and arrayed on the table by the assistant. The child or robot then finds pairs from the flipped cards. On the robot’s turn, the robot points at one of the cards and the assistant turns it up.

In the talking session, a human who is not the assistant operated the robot from a distant place that the child could not see. The session consisted of three phases, PHASE1, 2 and 3. In PHASE1 the robot talked according to a pre-programming without any interactions. In PHASE2 the robot talked with the child using a chatterbot algorithm that is a simple one of the natural language processing systems. The algorithm uses keywords included in what the counterpart said. In PHASE3, the human typed what the robot should talk in real time. PHASE2 and PHASE3 have an interaction between the robot and child, but not in PHASE1.

The index of child's interest is defined as a linear sum of the face direction toward the robot and the smiling value (Fig. 1). To evaluate the degree of interest during the play, adult participants rated the child's interest. By watching the video the participants scaled the child's interest using 2-point or 5-point rating.

Since PHASE3 is the most interactive and the PHASE1 is the least, we hypothesize that the child's interest increases according to PHASE 1–3.

4 Results

4.1 2-Point Rating

The adult participants evaluated the child's internal interest by 2-point scale (Figs. 3 and 4 lower). The index of interest $f(t)$ from the robot (Figs. 3 and 4 upper) was calculated as follow:

$$f(t) = \beta_h h(t) + \beta_s s(t) \quad (1)$$

Here, t is a discrete time variable corresponding to each of the video frame, $h(t)$ is the face direction, $s(t)$ is the smiling value and β_h, β_s are coefficients. The robot index showed the 92% agreement between the smiling value and that of human. Examples of index for a session is shown in Fig. 3 for the talking session and Fig. 4 for the game session. This supports the validity of the interest rating methods. But an explicit difference for talking algorithm was not observed. As the

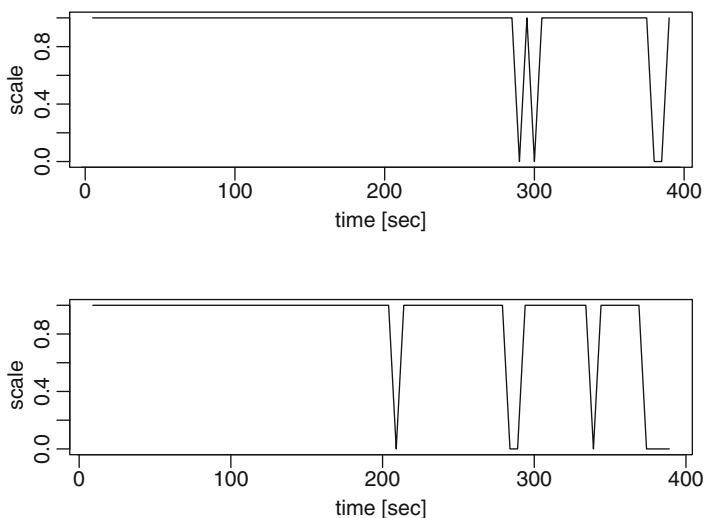


Fig. 3 Human and robot evaluation of interest in the game session (boy): robot estimation (*upper*) and human evaluation (*lower*)

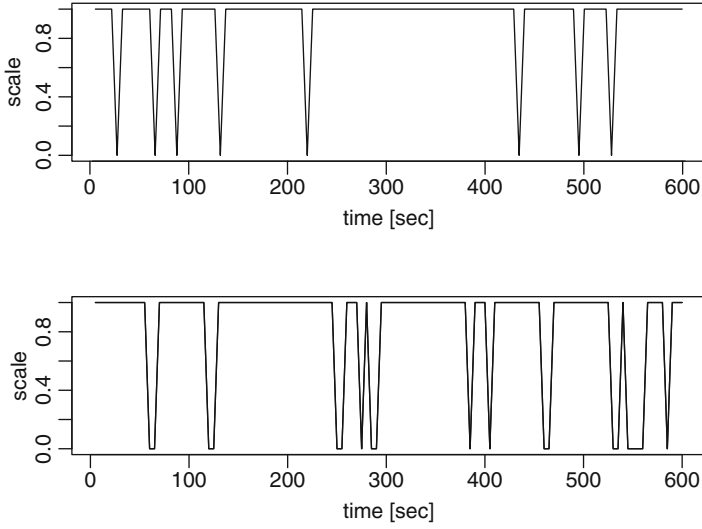


Fig. 4 Human and robot evaluation of interest in the game session (girl): robot estimation (*upper*) and human evaluation (*lower*)

furthermore analysis, we performed 5-point rating for the videos because the 2-point rating analysis was too simple to analyze the dynamics of interest for human robot interaction.

4.2 Interest Dynamics

The participants scaled 5-point rating while watching videos of each child talking with the robot in the experiment (Fig. 5). First, we assumed an interest value $u(t)$ for each time t during the rating process. The observed scores $y_j(t)$ of j -th participants is defined as discrete probabilistic variables in time frame t ,

$$y_j(t) = \begin{cases} 2 & (a_{j,3} < u(t)) \\ 1 & (a_{j,2} < u(t) < a_{j,3}) \\ 0 & (a_{j,1} < u(t) < a_{j,2}) \\ -1 & (a_{j,0} < u(t) < a_{j,1}) \\ -2 & (u(t) < a_{j,0}), \end{cases} \quad (2)$$

where $a_{j,i}$ means the threshold variables of j -th participants. In the rating process, we considered that thresholds could differ for inter/intra participants. We assumed that the threshold $a_{j,i}$ was estimated as probabilistic variables.

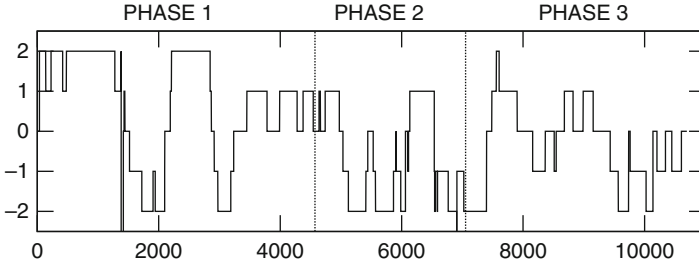


Fig. 5 The rating data example of subject 1 (15 fps)

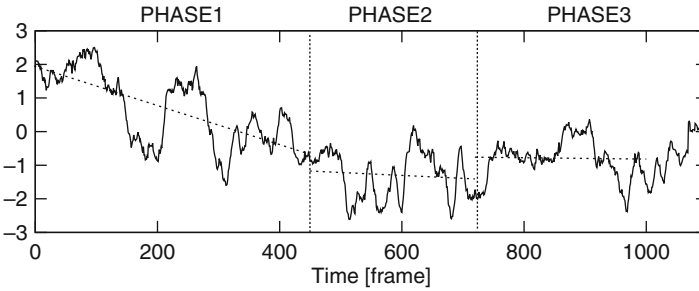


Fig. 6 An estimated interest line during talking with the robot (1.5 fps)

We used the ordered probit model to estimate the child’s interest sequence. In this formulation, we describe the interest $u_j(t)$ is a value with a Gaussian noise of variance $\sigma(t)$.

$$u_j(t) = \alpha x(t) + \epsilon \tag{3}$$

where $x(t)$ is a continuous hidden variables representing child’s internal interest, and α is a scaling parameter, which was set to 1 in this estimation. This assumes that a human rating process should includes fluctuation.

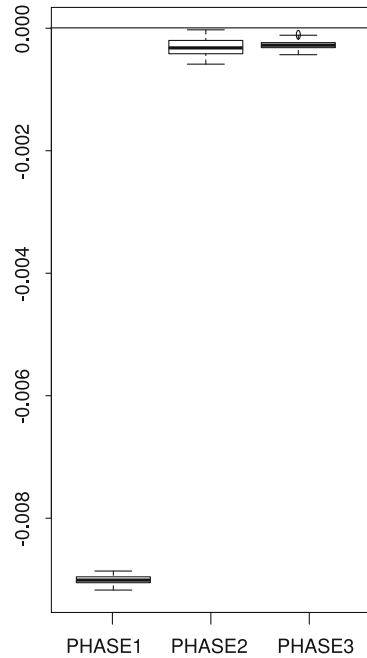
$$x(t) - x(t - 1) \sim N(0, \eta^2)(\forall t) \tag{4}$$

To prevent divergence, $a_{j,i}$ has a restriction as follow:

$$a_{j,i} \sim N(0, \alpha^2)$$

The interest value $x(t)$, variance $\sigma(t)$ and threshold $a_{j,i}$ were estimated by the Bayesian estimation method, called Markov Chain Monte Carlo (MCMC). The video sampling rate was 15 frame per second (fps), and in the estimation we performed down-sampling to 1.5 [fps]. First, the estimated interest line is shown in Fig. 6. We used the maximum a posterior probability (MAP) estimation calculated by the Metropolis-Hasting method.

Fig. 7 The change in slope of interest line: This is a box-and-whisker plot about slope value. The boxes mean lower and higher quartiles and the center lines mean median



A trend of interest $x(t)$ was calculated in each phase as shown in Fig. 7. The slope coefficients of PHASE1 showed significantly low value than others. The median and quartile values were calculated by sampling data obtained by MCMC.

5 Discussion

In the result, the strategy used in PHASE1 depressed interest $x(t)$ as we predicted. According to the estimated interest line, other strategies succeeded at maintaining the interest in spite of the previous depression. We predicted that the interest trend in PHASE3 should be larger than others. The interval of the conversation in PHASE3 was significantly longer than PHASE1. We suppose this long interval might have the wrong effect on the interaction.

These results shows that interactive talking algorithms have an important role for child’s interest dynamics while talking with the robot. The result also suggests that it is possible for the robot to recognize human interest from visual features as human do. Our next step will be developing a strategy planner that decides robot action, such as praising or talking to child, and to keep up child’s interest by consulting a child interest dynamics model.

Tanaka et al. [1] also showed the correlation between haptic sensor data and evaluation through the video. Our result is consistent with the result.

6 Conclusion

In this study, we developed the robot which plays with children, and evaluated change in child's interests by the statistical method. Using the model estimation method, we found a significant difference between communication algorithms, suggesting effectiveness of our experimental paradigm.

Acknowledgements This work was supported by a Grant-in-Aid for Scientific Research on Innovative Areas (21120010) from the Ministry of Education, Culture, Sports, Science, and Technology, JAPAN and supported by a Grant-in-Aid for Young Scientists (B) (22700225) from JAPAN Society for the Promotion of Science.

References

1. F. Tanaka, A. Cicourel, and J. R. Movellan. Socialization between toddlers and robots at an early childhood education center. *Proceedings of the National Academy of Sciences of the United States of America*, 104(46):17954–8, 2007.
2. G. Castellano, A. Pereira, I. Leite, A. Paiva, and P.W. McOwan. Detecting user engagement with a robot companion using task and social interaction-based features. In *Proceedings of the 2009 international conference on Multimodal interfaces*, pages 119–126, 2009.
3. T. Nakamura, K. Sugiura, T. Nagai, N. Iwahashi, T. Toda, H. Okada, and T. Omori. Learning novel objects for extended mobile manipulation. *Journal of Intelligent and Robotic Systems*, pages 1–18, 2011.
4. M. Attamimi, A. Mizutani, T. Nakamura, K. Sugiura, T. Nagai, N. Iwahashi, H. Okada, and T. Omori. Learning novel objects using out-of-vocabulary word segmentation and object extraction for home assistant robots. In *Proceedings of the IEEE International Conference on Robotics and Automation*, pages 745–750, 2010.

Robotic Motion Coach: Effect of Motion Emphasis and Verbal Expression for Imitation Learning

Tetsunari Inamura and Keisuke Okuno

Abstract In this paper, a robotic motion coaching system that coaches human beings is proposed. The purpose of this robotic system is to have subjects imitate and learn imitation target motions effectively and well. By applying the Mimesis model, we integrated qualitative and quantitative evaluation of player's imitated motion patterns, as well as introduced a method to synthesize emphatic motion patterns and to integrate verbal attention that corresponds to the degree of emphasis. Series of experiment, coaching how to perform forehand-tennis-swing, showed the feasibility of the proposing method and confirmed that emphatic motions with verbal attention improved the imitation learning of motion patterns.

1 Introduction

To develop effective and intelligent human-robot interaction systems that use whole body gestures and verbal expressions, verbal expression and gesture expression should be strongly connected according to given tasks and current situation. Additionally not only fixed expressions but also modification of the expressions such as emphasis of motions and changing speech words is also an important function to achieve tasks smoothly according to reaction from users. Analysis of the connection between gestures and speech act often discussed in the field of psychology; however synthesis and emphasis of gestures and speech from engineering point of view is not discussed well. Since synthesis of motion and speech also requires recognition of current situation such as reaction of users, we therefore should integrate (1) recognition of reaction, (2) planning to achieve tasks, (3) synthesis and emphasis of motions and speech, and (4) keeping interaction loop consists of (1)–(3).

T. Inamura (✉) • K. Okuno
National Institute of Informatics, The Graduate University for Advanced Studies,
Tokyo, 101-8430, Japan
e-mail: inamura@nii.ac.jp

In this paper, we focus on a robotic system that coaches human beings how to modify their motions to discuss the above issue. The robotic coaching system should include all of the four elements. (1) recognition of reaction: The robot should evaluate humans' performance and analyze similarities and differences between the performance and target. (2) planning to achieve tasks: The robot should let the human subject to make better performance based on feedback consists of motion and speech expressions. (3) synthesis and emphasis of motion and speech: The robot should modify and emphasize motion demonstrations and speech expressions based on the result of (1)'s analysis. (4) The robot repeats above three processes not to let the subjects tired and bored.

With regard to researches on binding of motion patterns and verbal expressions in imitation learning frameworks, there are researches of systematic binding taking advantage of interaction, such as [1, 2]. However, these do not consider how they could be used for establishing a continuous loop of interaction between robots and human beings.

We think a common problem not being considered in above related works is that the four required elements were separated. Since each element is complex, we propose a simple framework to integrate those elements that uses sole parameter to connect all of the processes. In motion coaching tasks, considerable factors can be evaluated by scalar parameter such as similarity of performed motion between target motion, degree of emphasis of motion, variety of verbal expression using adverb for feedback. In this paper, we propose a method to evaluate and control those factors. Furthermore we show feasibility and effectiveness of robotics motion coaching systems based on the proposed method through experiments of real sports training tasks for beginners.

2 Method

2.1 Abstract of Motions as Parameter

To abstract motion patterns, continuous Hidden Markov Models(HMM) with left-to-right model are used. HMM consists of a set of parameter $\lambda = \{\mathbf{Q}, \mathbf{A}, \mathbf{B}\}$, where $\mathbf{Q} = \{q_1, \dots, q_N\}$ is a finite set of states, $\mathbf{A} = \{a_{ij}\}$ is a state transition probability matrix from i -th state q_i to j -th state q_j , and $\mathbf{B} = \{b_i\}$ is set of output probabilities of joint angle $\theta[t]$, at the state q_i when time is t . HMM abstracts motion patterns $\mathbf{M} = [\theta_1, \dots, \theta_n]^T$, where θ_i are time series joint angles, of humans and humanoid robots. To parameterize motion patterns, distance between two motions is measured by calculation of distance between two HMMs based on Bhattacharyya Distance. The distances among motion patterns introduce a phase space structure that indicate relationship among the motion patterns. It is called as the *proto-symbol space* [3] that convert a motion pattern into a static point in the phase space. Each motion

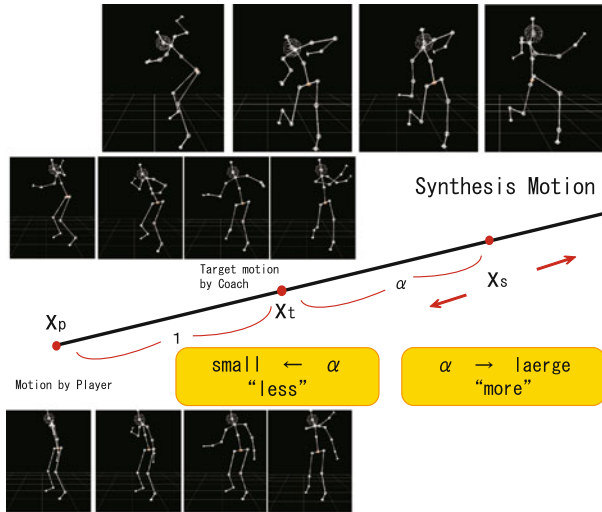


Fig. 1 Example relationship between the weight α , adverbially expression and synthesis motion

pattern, that is static point, can be identified by a base motion (base point) and scalar parameter which indicates distance from base motion (base point).

Since let x a position vector of a motion pattern in the proto-symbol space, the phase space can interpolate/extrapolate any motion patterns with

$$x_s = c_i x_i + c_j x_j, \tag{1}$$

where c_i, c_j are weight coefficients. Addition of vectors are translated into interpolation/extrapolation of HMMs; then a motion pattern is reproduced from the synthesized HMM[4]. Using this function, the robot easily convert any motion patterns into parameters such as c_i ; and convert the parameters into motion pattern without consideration of heterogeneous time length of each motions.

2.2 Flow of the Coaching with Emphatic Motions and Adverbially Expressions

In the robotic motion coaching system, motion pattern performed by both of the robot and the user are abstracted by the position vector in the proto-symbol space. The robot performs emphatic motion to make effective coaching according to observation result of the user’s performance as shown in Fig. 1.

The experiment of the motion coaching task was executed as follow (As depicted in Fig. 2).

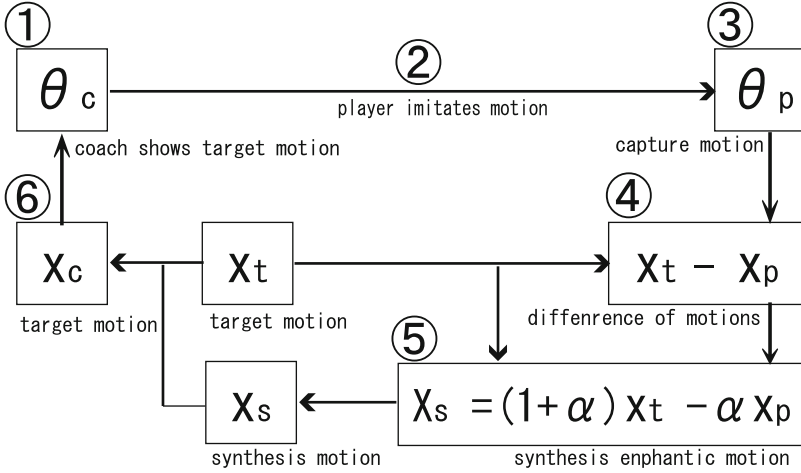


Fig. 2 Flow of the motion coaching

1. The coach (an agent in a virtual environment in this paper) demonstrates a motion pattern θ_c as an imitation target motion.
2. The human player watches the motion θ_c and imitates it.
3. The coach observes the player's imitated motion θ_p and converts it to a static point x_p .
4. If the x_p is not close to x_t , then it is interpreted that the player's imitated motion is imperfect. The coach calculate the missing elements in the imperfect imitation of the player by $x_t - x_p$.
5. The coach calculate the external dividing point x_s by adding the missing elements ($x_t - x_p$) to the target motion (x_t), using

$$x_s = (1 + \alpha)x_t - \alpha x_p \quad (2)$$

where α is a weight coefficient for extrapolation.

6. θ_c is generated from the x_c . Use the point x_s as the x_c , which corresponds to the re-demonstration motion pattern θ_c for the next trial.

Repeat a loop 1–6 as needed. One loop is considered as one trial in the experiment.

As it is depicted in Fig. 1, this weight coefficient α corresponds to the degree of emphasis of the synthesis motion. In addition, we can assign different adverbially expression to the weight coefficients such as “a little more” to $\alpha = 1.5$, “more” to $\alpha = 2.0$, and “much more” to $\alpha = 2.5$.

In this way, with one parameter α , it is possible to control both degree of emphasis of synthesized motion and choice of adverbially expression. In this paper, we focus on the effectiveness of emphasis of synthesized motion and inquiry about the presence of adverbially expression as the first step.

3 Experiment

We conducted series of experiments, in which a forehand tennis swing was coached to males by the robotic system. All of the subjects were beginners of the tennis, never played before. The proposed method and the flow of the coaching system explained in the previous section was used with conditions below.

3.1 Experiment Conditions

The coaching agent demonstrates motion pattern θ_t as the imitation target motion and it was displayed on a large screen. The given instruction to subjects was “please imitate this”. Five swings were used to abstract each player’s swing to *HMM* at each trials.

In the experiment, 13 subjects attended the motion coaching test. The adverbially expressions such as “more like this” were used. Following four kinds of experimental cases were performed to evaluate how the emphatic motion and the adverbially expression contributed. All the subjects attended to the all cases with counter balanced order.

Case 1: The coaching agent repeated demonstrating imitation target motion θ_t only, In other words, coached using motions with $\alpha = 0.0$ and no adverbially expression was used.

Case 2: Coached using motions with $\alpha = 0.0$ and adverbially expression.

Case 3: The coaching agent re-demonstrated with emphatic motion patterns θ_s synthesized by the proposed method. In other words, coached using motions with $\alpha = 2.0$ and no adverbially expression.

Case 4: Coached using motions with $\alpha = 2.0$ and adverbially expression.

The cases are summarized in Table 1. The order of conducting each experimental cases were randomly shuffled for each subjects.

3.2 Result

To evaluate the results, the following measures were used. Average ratio of error in imitation at l -th trial is:

$$\bar{R}_l = \frac{\sum_{i=1}^m \frac{d_{il}}{d_{i1}}}{m}, \tag{3}$$

Table 1 Cases in Experiment 2

	$\alpha = 0.0$	$\alpha = 2.0$
Without verbal exp.	Case 1	Case 3
With verbal exp.	Case 2	Case 4

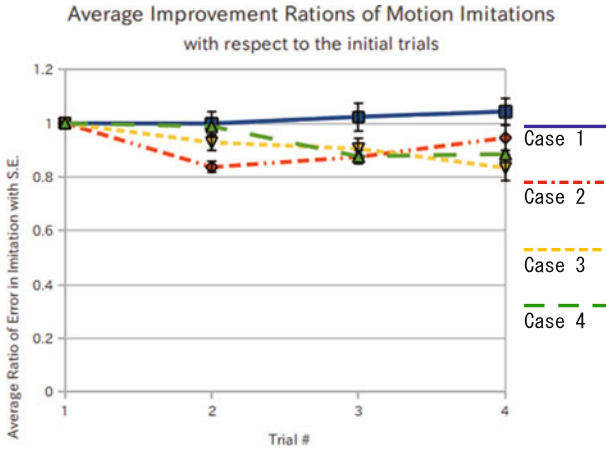


Fig. 3 Average ratio of imitation error: \bar{R}_l in Eq. (3)

Table 2 One-tailed T-test with \bar{R}_l in Eq. (3) for Exp.2

–	2nd trial	3rd trial	4th trial
Case 1 vs. Case 2	0.0025**	0.0012**	0.00091**
Case 1 vs. Case 3	0.000042**	0.000024**	0.0000079**
Case 1 vs. Case 4	0.000095**	0.000067**	0.000031**
Case 2 vs. Case 4	0.061 ⁺	0.084 ⁺	0.061 ⁺
Case 3 vs. Case 4	0.41	0.43	0.48

Note: **($p < 0.01$), +($p < 0.10$)

where m is the number of subjects ($m = 13$) and d_{ij} is distance between the target motion and the j -th trial of the i -th subject. If the imitation error is smaller compared to the initial trial in the same case, the \bar{R}_l will be less than 1.0. If the imitation error is larger compared to the initial trial in the same case, the \bar{R}_l will be more than 1.0. When imitation is almost perfect, \bar{R}_l approaches to zero.

From Fig. 3 and Table 2, it would be able to say that emphatic motions contributed somehow to improve the motion learning of the players. However, we would not able to say if the adverbially expression contributed or not. It is because that between case 2 and case 4, p is $0.05 < p < 0.10$, and no significant difference found between case 3 and case 4.

4 Conclusion and Discussion

To develop effective and intelligent human-robot interaction systems that use whole body gestures and verbal expressions, verbal expression and gesture expression should be strongly connected according to given tasks and current situation.

To discuss the open problem, we developed and focused on a motion coaching robot that coaches human being to modify insufficient motions. We integrated (1) recognition of reaction, (2) planning to achieve tasks, (3) synthesis and emphasis of motions w/ and w/o speech, and (4) keeping interaction loop consists of (1)–(3). The common problem not being considered in existing works was that the four required elements were separated. Thus, we proposed a method to evaluate and control – (1) similarity of performed motion between target motion, (2) degree of emphasis of motion, and (3) presence of verbal expression using adverb for feedback – by one scalar parameter.

We have also proposed estimation of others' sensorimotor pattern based on imitation and verbal communication based on the Mimesis model [5]. Estimation of the user's sensor pattern and getting feedback for the user are important functions to realize sophisticated coaching system. We plan to integrate the Mimesis model and the proposed method in this paper to construct a whole system that estimate other's inner state, generate suitable motion performance and verbal utterance, based on the Mimesis model which is inspired by mirror neuron systems. Additionally, we also plan to analyze coaching behavior of real sports trainers to extract coaching skill. This skill would be represented by relation between usage of emphatic motion/verbal expression and distance between beginner's performance and the target motion that is a certain type of communication. Another advantage of the proposed method is being able to be exploited in such an analysis.

References

1. N. Iwahashi. Robots that learn language: Developmental approach to human-machine conversations. In N. Sanker et al., editor, *Human-Robot Interaction*, pp. 95–118. I-Tech Education and Publishing, 2007.
2. W. Takano and Y. Nakamura. Integrating whole body motion primitives and natural language for humanoid robots. In *IEEE-RAS Int'l Conf. on Humanoid Robots*, pp. 708–713, 2008.
3. T. Inamura, H. Tanie, and Y. Nakamura. From stochastic motion generation and recognition to geometric symbol development and manipulation. In *Int'l Conf. on Humanoid Robots*, 2003. (CD-ROM).
4. T. Inamura and T. Shibata. Geometric proto-symbol manipulation towards language-based motion pattern synthesis and recognition. In *IEEE/RSJ Int'l Conf. on Intelligent Robots and Systems*, pp. 334–339, 2008.
5. K. Okuno and T. Inamura. A research on motion coaching for human beings by a robotics system that uses emphatic motion and verbal attention. In *Humanoids 2010 Workshop on Humanoid Robots Learning from Human Interaction*, 2010.

Synthetic Approach to Understanding Meta-level Cognition of Predictability in Generating Cooperative Behavior

Jun Namikawa, Ryunosuke Nishimoto, Hiroaki Arie, and Jun Tani

Abstract We propose that “predictability” is a meta-level cognitive function that accounts for cooperative behaviors and describe this from a dynamical systems perspective based on a neuro-robotic experiment. In order to bring about cooperative behaviors among individuals, individuals should attempt to predict the behavior of their partners by making internal models of them. However, the behaviors of partners are often unpredictable because individuals possess free will to generate their own independent actions. Thus, acquiring internal models which attempt to completely predict the actions of others seems to be intractable. In the current study we suggest that, when learning internal models for interacting with the partners, cooperative agents should maintain predictability monitoring mechanisms by which attention is oriented more toward predictable segments in spatio-temporal sensory input space.

1 Introduction

This study represents an attempt to understand the nature of cooperative behaviors in terms of abstract models of perceptual inference and learning. The concept of cooperative behavior has been widely investigated in the fields of distributed intelligence [1–4] and social psychology [5, 6]. Except for interactions among individuals having no internal states, the individuals should make internal models of them in order to predict behaviors of partners. However, acquiring internal models to be able to completely predict behaviors of others seems to be intractable because individuals are capable of generating voluntary actions. An important point is that when achieving cooperative behaviors, an individual only needs to predict the

J. Namikawa (✉) • R. Nishimoto • H. Arie • J. Tani
Laboratory for Behavior and Dynamic Cognition, RIKEN Brain Science Institute,
Saitama 351-0198, Japan
e-mail: jnamika@brain.riken.jp

behaviors of their partner that relate to their own actions. Therefore, we propose an artificial neural network model possessing predictability monitoring mechanisms by which they can focus on predictable segments in spatio-temporal input sequences. We hope to show that predictability as the meta-level cognition is indispensable in achieving cooperative behaviors.

In addition, we try to describe that the problems of how attention works can be resolved using exactly the same principle. Attention, defined broadly as the cognitive process in which processing resources are allocated to one aspect by ignoring other things, is a ubiquitous feature in information processing [7–10]. For example, learning performance of a mixture of RNN experts was improved by adding a mechanism by which each expert network selectively concentrates on a primitive pattern in spatio-temporal time series [11]. It has been suggested that attention can be understood as inferring the level of precision during hierarchical perception in a Bayesian fashion [12]. We pursue these attempts to understand attention in terms of dynamical systems perspective.

The work in the current paper is related to temporal sequence learning problems for artificial neural networks. Artificial neural networks have been widely applied to learning problems for various kinds of temporal sequences [13–17]. However, in spite of the considerable accounts carried out since the mid-1980s, it has been thought that neural networks could not be scaled so as to be capable of learning complex sequence patterns, especially when the sequence patterns to be learned contain long-term dependencies. This is due to the fact that the error signal cannot be propagated effectively in long time windows of sequences using the gradient descent method, because of the potential nonlinearity of the neural dynamics [17]. This paper will claim that the predictability monitoring mechanism improves learning performance because it avoids the unreasonable interference of the error signal corresponding to unpredictable parts in spatio-temporal sequences.

2 Methods

This section explains an artificial neural network model together with how the model is applied to a specific robotic experiment. The network received two different modality inputs, proprioceptive somato-sensory input and vision input. These different modality sensations came together in the network to generate predictions of the future states. The next visuo-proprioceptive states which were predicted from the current states were used to control the robot. In addition, the network also predicted the prediction errors between visuo-proprioceptive inputs and predicted values, as “prediction of prediction errors”. The dynamics of the network is described by the following differential equation:

$$\tau \dot{\mathbf{u}}(t) = -\mathbf{u}(t) + W^u \langle \hat{\mathbf{x}}(t - \xi), f(\mathbf{u}(t)) \rangle + \mathbf{I}^u, \quad (1)$$

$$\mathbf{x}(t) = f(W^x f(\mathbf{u}(t)) + \mathbf{I}^x), \quad (2)$$

$$\mathbf{v}(t) = g(W^v f(\mathbf{u}(t)) + \mathbf{I}^v), \quad (3)$$

where \mathbf{u} is membrane potential of internal context neurons (in experiments the number of neurons is 50), $\hat{\mathbf{x}}$ is sensory-motor input, \mathbf{x} is sensory-motor output, \mathbf{v} is variance as described below, and ξ is the feedback time delay of the controlled robot. The functions f and g denote component-wise application of \tanh and \exp , respectively. $\langle \mathbf{a}, \mathbf{b} \rangle$ denotes the concatenation of vectors \mathbf{a} and \mathbf{b} .

To perform given tasks of cooperative behaviors, the network learned to predict sensory feedback for the next time step through training processes. The network was trained by means of supervised learning using teaching sequences obtained using the robots. The training of the network is defined as maximizing (or integrating over) the likelihood P as follows:

$$P = \prod_t \prod_i \frac{1}{\sqrt{2\pi v_i(t)}} \exp\left(-\frac{(x_i(t) - \hat{x}_i(t))^2}{2v_i(t)}\right), \quad (4)$$

where $x_i(t)$ and $v_i(t)$ are generated by the network, and $\hat{x}_i(t)$ is training data representing visuo-proprioception. A notable point in this scheme is that the network generates the prediction of prediction error as the variance vector \mathbf{v} . Since the variance $v_i(t)$ works to be a weighting factor for the mean square error $(x_i(t) - \hat{x}_i(t))^2$ [11], the network is able to control the importance of sensations via the variances and, as such, this control might play a role of the “attention”. Maximizing P is achieved using the back propagation through time (BPTT) method [15].

3 Results

Two small humanoid robots, A and B, interact with each other in a physical environment. In cooperative mode, robot B will periodically move the object it holds and robot A must attempt to track it with its hand. Robot B will enter uncooperative mode 50% of the time and will randomly move the object, in defiance of its partner. The task for robot A is to learn at which times it is possible to cooperate with robot B and to do so when feasible. In the experiment, robot B is controlled by the experimenter and robot A is controlled by the neural network.

Three experiments were carried out, each consisting of a training and a testing phase. During training, the switching of robot B’s cooperative/uncooperative behaviors was either deterministic or random, depending on the experiment. During testing, the switching of robot B’s behavior was deterministic for *all* experiments.

In experiment 1, during training and testing, robot B switched its behavior in a deterministic fashion. Figure 1 displays an example of network dynamics during testing, where robot A learned to predict robot B’s behaviors that changed from cooperative to uncooperative actions in a deterministic manner. Through training, the robots were able to reproduce the object manipulation cooperatively, and they also generated uncooperative actions. It can be seen here that the variance corresponding to the vision sensor increased when the partner moved the object randomly.

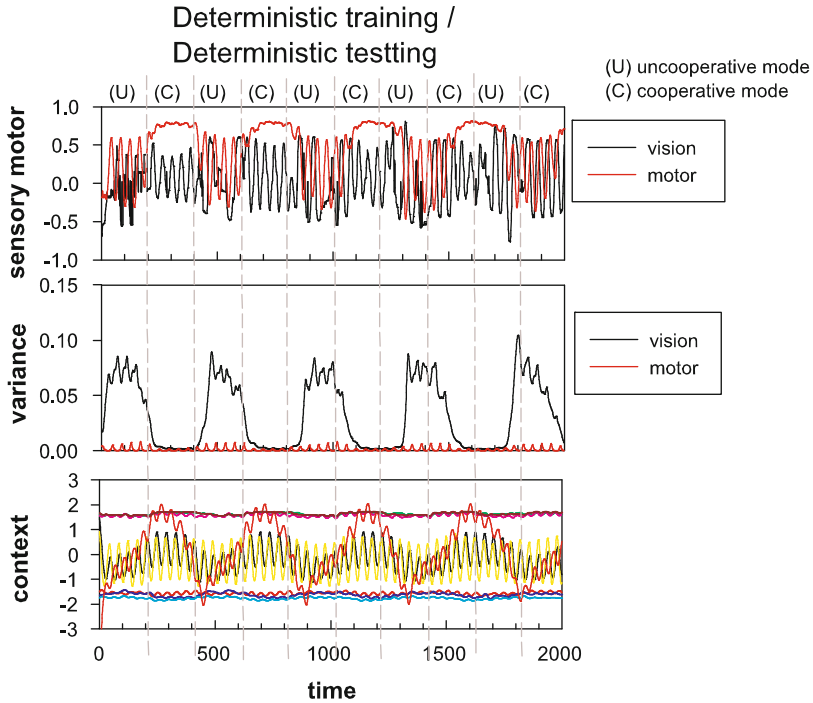


Fig. 1 Example of behavior sequence generated by a trained network. The network learned behaviors in which cooperative actions and uncooperative actions are switched in a deterministic manner. In the case of sensory-motor, 2 out of a total of 8 dimensions were plotted (vision: vertical axis of object position captured by the vision sensor, motor: *left* arm pronation). In variance, two lines corresponding to the relative sensory-motor were depicted. In context, first 8 neural units were plotted (a total of dimensions is 50)

In experiment 2, robot B switched its cooperative/uncooperative behaviors randomly during training. Figure 2 depicts robot A's network dynamics during testing when robot B switched its behaviors deterministically. Although, the variance plot initially appears to show the correct switching between cooperative/uncooperative modes, ultimately robot A always migrates towards an uncooperative behavior.

The difference between these experiments is attributed to the difference of predictability in behaviors during training. In the case of Fig. 1, switching between cooperative/uncooperative behaviors is periodic, and so the network was able to attend to this temporal cue even though ignoring sensations of the uncooperative behavior. In experiment 2, there was no temporal cue available during training, therefore during testing the network could not exploit this during the absence of predictable input. Thus, if some cues which indicate change of partner's behaviors are presented, the network will be able to generate both cooperative/uncooperative actions.

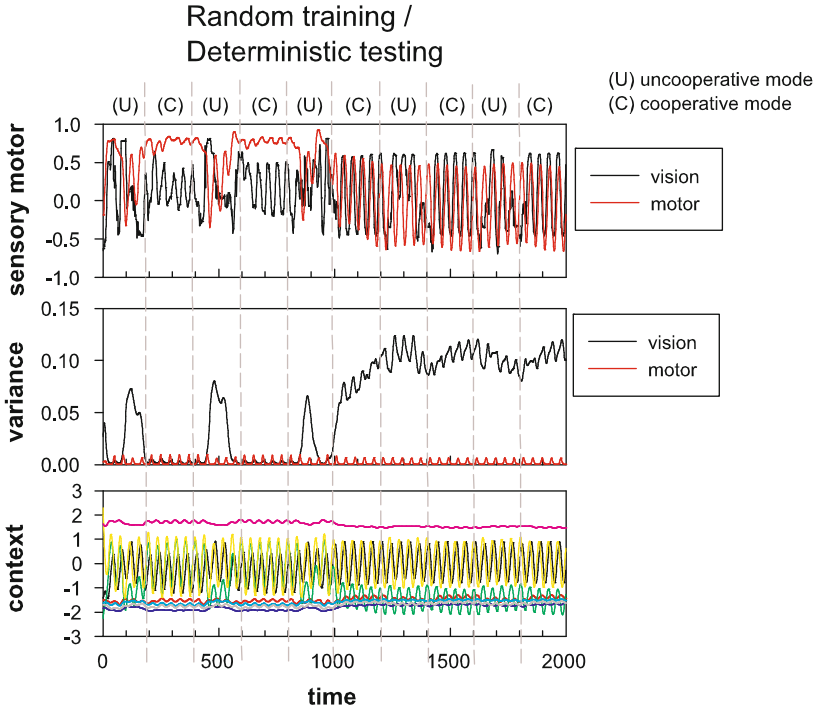


Fig. 2 This figure uses the same format as Fig. 1 but shows the result when cooperative/uncooperative actions are switched randomly in training

In experiment 3, again robot B switched its cooperative/uncooperative behaviors randomly during training but this time an additional cue was added to indicate the switching to cooperative behavior. The cue took the form of a key press from the experimenter. Figure 3 shows the network dynamics of robot A during deterministic testing containing both sensory-motor and cue inputs.

In this case, the trained network was able to switch from uncooperative behaviors to cooperative one by means of cueing. However, even though the timing of the cue was not predictable, the network could recognize when robot B is in uncooperative mode and activities of variance were initiated before cueing in Fig. 4. It can be inferred that the trained robot A prepared mentally for the coming cue by predicting prediction errors.

4 Conclusion

As shown by the robotics experiments, cooperative/uncooperative behaviors of the robots appeared to be controlled by the variances, the so-called “prediction of prediction errors”. The results revealed that the predictability in terms of “prediction

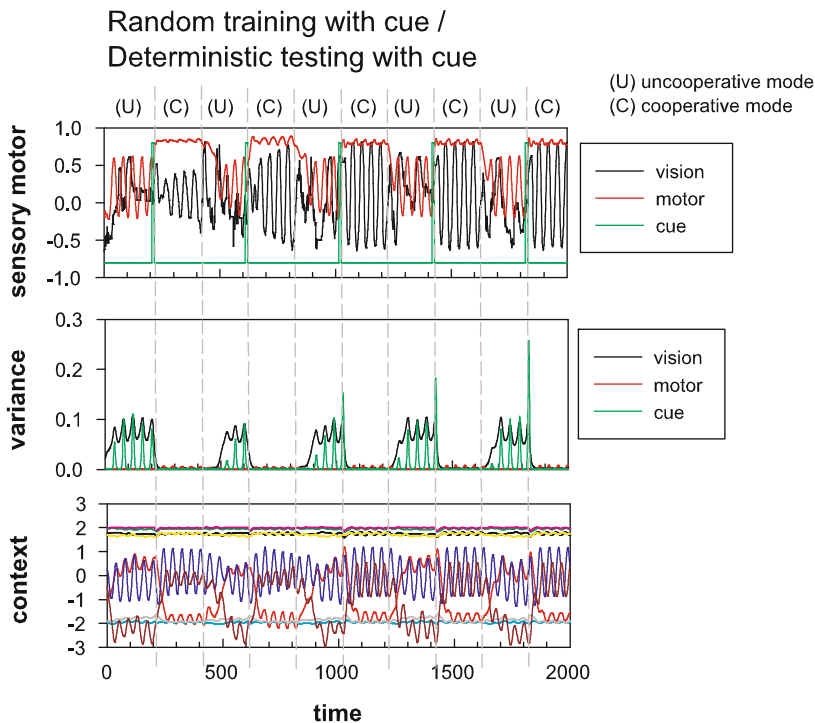


Fig. 3 This figure uses the same format as Figs. 1 and 2 but reports the result when both sensory-motor and cue are presented simultaneously

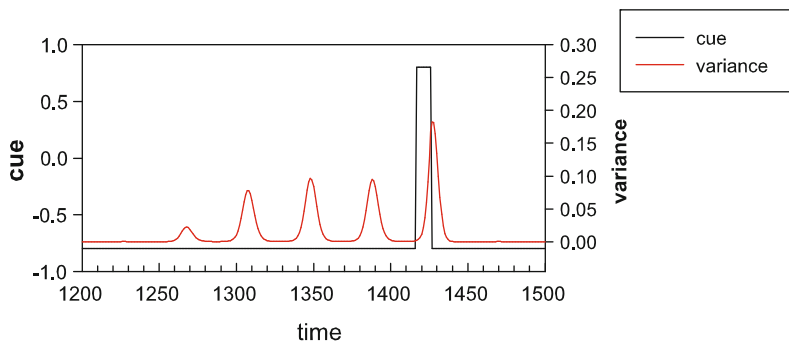


Fig. 4 This figure demonstrates how networks generate variances corresponding to unpredictable inputs

of prediction errors” enables the attention of agents to be focused on predictable parts in the sensory sequences through learning of prediction models for partners’ actions. It is also suggested that “prediction of prediction errors” as the meta-level cognition is indispensable in achieving autonomous mechanisms of joint attention in cooperative behaviors.

Acknowledgments The present study was supported in part by a Grant-in-Aid for Scientific Research on Innovative Areas “The study on the neural dynamics for understanding communication in terms of complex hetero systems” from the Japanese Ministry of Education, Culture, Sports, Science and Technology.

References

1. Reynolds, C.W.: Flocks, herds and schools: A distributed behavioral model. *ACM SIGGRAPH Comp. Graph.* **21(4)** (1987) 25–34
2. Asada, M., Uchibe, E., Hosoda, K.: Cooperative behavior acquisition for mobile robots in dynamically changing real worlds via vision-based reinforcement learning and development. *Artif. Intell.* **110(2)** (1999) 275–292
3. Yamaguchi, H.: A cooperative hunting behavior by mobile-robot troops. *Int. J. Robot. Res.* **18(9)** (1999) 931
4. Kube, C.R., Bonabeau, E.: Cooperative transport by ants and robots. *Robot. Auton. Syst.* **30(1–2)** (2000) 85–101
5. Brothers, L.: The social brain: a project for integrating primate behavior and neurophysiology in a new domain. *Concept Neurosci.* **1** (1990) 27–51
6. Frith, U., Frith, C.: The social brain: allowing humans to boldly go where no other species has been. *Philos. T. Roy. Soc. B* **365(1537)** (2010) 165–175
7. Posner, M.I.: Orienting of attention. *Q. J. Exp. Psychol.* **32(1)** (1980) 3–25
8. Treisman, A.M., Gelade, G.: A feature-integration theory of attention. *Cognitive Psychol.* **12(1)** (1980) 97–136
9. Duncan, J., Humphreys, G.W.: Visual search and stimulus similarity. *Psychol. Rev.* **96(3)** (1989) 433
10. Spratling, M.W.: Predictive coding as a model of biased competition in visual attention. *Vision Res.* **48(12)** (2008) 1391–1408
11. Namikawa, J., Tani, J.: A model for learning to segment temporal sequences, utilizing a mixture of RNN experts together with adaptive variance. *Neural Netw.* **21(10)** (2008) 1466–1475
12. Feldman, H., Friston, K.J.: Attention, uncertainty, and free-energy. *Frontiers in Human Neurosci.* **4** (2010)
13. Jordan, M.I.: Indeterminate motor skill learning problems. *Attention and Performance XIII* (1989)
14. Elman, J.L.: Finding structure in time. *Cognitive Sci.* **14(2)** (1990) 179–211
15. Rumelhart, D.E.: Learning internal representations by error propagation. *DTIC Document* (1985)
16. Jaeger, H., Haas, H.: Harnessing nonlinearity: Predicting chaotic systems and saving energy in wireless communication. *Science* **304(5667)** (2004) 78
17. Schmidhuber, J., Gers, F., Eck, D.: Learning nonregular languages: A comparison of simple recurrent networks and LSTM. *Neural Comput.* **14(9)** (2002) 2039–2041

Neural Correlates of Cognitive Dissonance and Decision Conflict

Keise Izuma, Madoka Matsumoto, Kou Murayama, Kazuyuki Samejima, Sadato Norihiro, and Kenji Matsumoto

Abstract Research in social psychology has shown that after making a difficult choice between two equally preferred items, individuals come to reduce their preferences for the item they rejected. This phenomenon was explained as “cognitive dissonance,” an uncomfortable feeling induced by simultaneously holding two or more contradictory cognitions (e.g., “I like it” and “I rejected it”). While previous neuroimaging studies indicated that the anterior cingulate cortex (ACC) was involved in cognitive dissonance, it is not known whether the ACC area involved in a type of complex conflict of cognitive dissonance overlaps with areas involved in other types of conflict (i.e., decision-conflict). Our results suggest that the ACC area involved in cognitive dissonance reliably overlapped with areas which were positively correlated with subjects’ trial-by-trial reaction times during a binary choice task, suggesting that the same ACC area is involved in cognitive dissonance and decision conflict.

K. Izuma (✉) • M. Matsumoto • K. Samejima • K. Matsumoto
Brain Science Institute, Tamagawa University, 6-1-1, Tamagawa-gakuen, Machida,
Tokyo 194-8610, Japan
e-mail: izuma@caltech.edu

K. Murayama
Department of Psychology, University of Munich, Leopoldstrasse 13 (PF 67),
Munich 80802, Germany

S. Norihiro
Division of Cerebral Integration, Department of Cerebral Research, National Institute
for Physiological Sciences (NIPS), 38 Myodaiji-cho, Okazaki, Aichi 444-8585, Japan

1 Introduction

According to modern economic theories, actions simply reflect an individual's preferences, whereas a psychological phenomenon called "cognitive dissonance" claims that actions can also create preference [1]. For more than five decades, social psychological studies have repeatedly shown that rejecting individual's favorite item, such as music CD and poster, reduces his/her preference for it [2–4]. This phenomenon is explained by cognitive dissonance theory [5] which states that holding two or more contradictory cognitions simultaneously (e.g., "I like the item" and "I rejected it") causes a psychological discomfort called "cognitive dissonance," and individuals are motivated to reduce it by changing their original preferences.

While the cognitive dissonance theory is one of the most influential and extensively-studied theories in social psychology [6], only a few studies investigated neural mechanisms underlying this phenomenon. Harmon-Jones [7] argued that since it has been shown that the anterior cingulate cortex (ACC) is involved in monitoring the presence of response conflict [8, 9] and that dorsal ACC (dACC) activity increases when behavior conflicts with self-concept [10], higher-level conflict such as cognitive dissonance might also engage the ACC. Consistent with the prediction, two recent studies using functional magnetic resonance imaging (fMRI) converged to show that the ACC is involved in cognitive dissonance [11, 12]. However, it remains unclear whether the same ACC area plays a role both in cognitive dissonance and other types of conflict.

The present study aims to investigate whether the area in the ACC involved in higher cognitive conflict of cognitive dissonance overlaps with areas involved in decision-conflict (i.e., conflict related to choice between equally desirable options) [13].

2 Methods

The current study involved an analysis of the same data set as that collected in our previous study [11]. Twenty subjects underwent fMRI scanning while they followed the experimental procedure called a "free-choice paradigm" [2]. Subjects performed following three tasks inside the fMRI scanner: (1) Preference task 1, (2) Choice task, and (3) Preference task 2. After these tasks, subjects also performed the Post-Experimental Choice task outside the scanner. This last task was intended to control the effect of "preference revealed by choices" [14].

In the two Preference tasks, subjects were presented with food items one by one (e.g., chocolate, snack, etc) and asked to rate their preference for each item. In the Choice task, subjects were asked to make a choice between two food items. Pairs of foods varied systematically so that choices were sometimes made between two equally liked items (Self-Difficult trials), and other times between one liked item and one disliked item (Self-Easy trials). In still other trials, choices were made randomly by a computer (Computer trials). During the second Preference task,

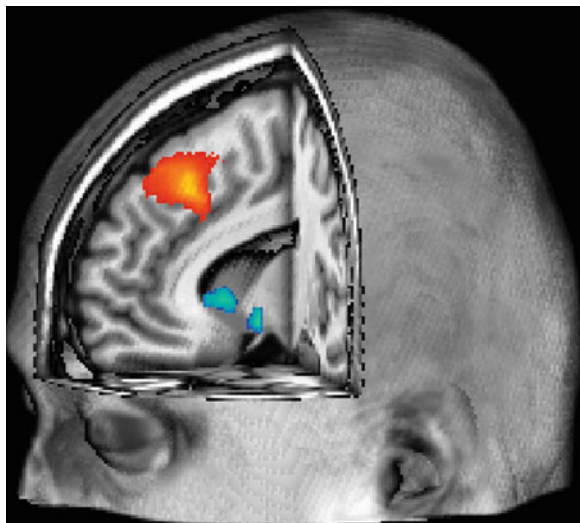
subjects were also presented with decisions they had made during the Choice task (e.g., “You chose it” or “You rejected it”). According to cognitive dissonance theory [5], subjects’ perceived cognitive dissonance should be higher when their past decisions contradict with their preferences (e.g., rejecting favorite foods, choosing unfavorable foods).

Decision conflict-related brain areas were defined as the areas whose activities were significantly positively correlated with subjects’ reaction times (RTs) during the Choice task. The previous research consistently showed that the degree of decision conflict are reflected in subjects’ RTs in the binary choice task (i.e., the closer two options in value, the longer RTs) [15, 16]. Furthermore, Knutson and his colleagues showed that the ACC activity was actually positively correlated with RTs during the financial decision task [17], and in another study [18], the same ACC area was correlated with the index of conflict as well as RTs during the buying and selling decision task. Only the data from the choice task were estimated by a general linear model (GLM). The model included following three regressors; (1) Self trials, (2) Self trials modulated by reaction time, and (3) Computer trials. See [11] for more details about methods.

3 Results

We first found that consistent with cognitive dissonance theory, subjects’ self-reported preferences decreased after they rejected their favorite foods, and the same pattern was also observed as the change in the activity of the ventral striatum, areas which codes subjects’ preference (Fig. 1, cyan; see [11] for more details about results of preference change in self-report as well as brain activities).

Fig. 1 The ventral striatum (cyan) activity was significantly reduced from the first to the second Preference tasks for the items subjects initially liked but rejected during the Choice task. The dACC (red) was positively correlated with cognitive dissonance (Color figure online)



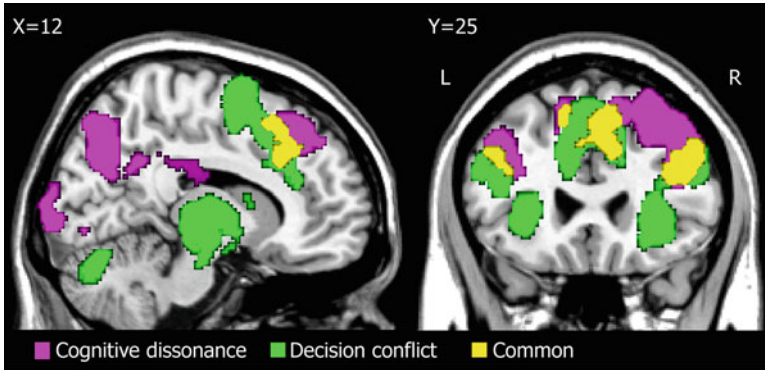


Fig. 2 A sagittal slice (*left panel*) and a coronal slice (*right panel*) showing areas correlated with the degree of cognitive dissonance during Preference task 2 (*magenta*), areas correlated with RTs during Self trials of the Choice task (*green*), and their overlap (*yellow*). A statistical threshold was set at $p < 0.001$ (uncorrected) (Color figure online)

Our data also showed that the dACC (Fig.1, red) was significantly positively correlated with the degree of cognitive dissonance on trial-by-trial basis (see [11] for more fMRI results and how we quantified the degree of cognitive dissonance in each trial). It should be noted that subjects' trial-by-trial RTs during the Preference tasks were also included in the GLM, and thus, it is highly unlikely that the dACC activity just reflected the level of response or decision conflict.

In the present paper, we next addressed whether the ACC area involved in cognitive dissonance overlaps with the area related to decision conflict. RT data for the Choice task revealed that RTs for both the Self-Difficult and Self-Easy trials were significantly longer than those in the Computer trials (vs. the Self-Difficult condition, $t(19) = 12.80$, $p < 0.001$; vs. the Self-Easy condition, $t(19) = 16.63$, $p < 0.001$), indicating that the higher decision conflict in the Self-Difficult condition. During the Self trials, subjects took significantly longer to choose when two alternatives were close in preference (Self-Difficult trial) than when they were far apart (Self-Easy trial; $t(19) = 3.74$, $p = 0.001$, see [11]).

We next estimated the fMRI data from the Choice task with RTs as a parametric modulator to identify decision conflict related brain regions. As predicted, the dACC showed the significant positive correlation with RTs during the Self trials (both Self-Easy and Self-Difficult trials) in the Choice task ($p < 0.001$, uncorrected). Other areas positively correlated with RTs included anterior insula, dorsolateral prefrontal cortex (DLPFC), thalamus, and left primary motor cortex (precentral gyrus), and these results are largely consistent with the previous report [18]. Then, it was found that the dACC area correlated with RTs during Self trials of the Choice task overlapped with the area correlated with cognitive dissonance during the Preference task 2 (Fig. 2, yellow), suggesting that the dACC area involved in relatively simple decision conflict also plays an important role in the more complex conflict of cognitive dissonance. Other areas showing the same overlap included only bilateral DLPFC (see Fig. 2) and left superior parietal lobule.

4 Discussions

Although previous fMRI studies have reported that the ACC is involved in cognitive dissonance, the present study extended them and further showed that within the dACC, the area correlated with cognitive dissonance largely overlapped with the area correlated with the degree of decision conflict during the binary choice task. This result indicates that while Festinger [5] distinguished between pre-decisional conflict and post-decisional dissonance, they are represented in the same brain area. That is, the same dACC area plays a pivotal role in not only decision conflict, but a complex cognitive conflict such as cognitive dissonance, which supports the hypothesis by Harmon-Jones [7].

The overlapped area in dACC identified in the present study seems to correspond to the area involved in processing various types of negative outcome (pain, monetary loss, response error, response conflict) as reported in a recent meta-analysis [19]. However, it should be tested further in the future research how the dACC area involved in cognitive dissonance is related to areas involved in error detection, pain recognition and response conflict. Furthermore, it should be noted that as seen in Fig. 2, our data also showed decision conflict related dACC area extends more posteriorly, whereas cognitive dissonance related dACC extends to anteriorly. Then, it would be interesting to see whether there is any functional specialization within the ACC region for these different types of conflicts, and if so whether there is any individual difference in such specialization.

Acknowledgments This study was supported by a Grant-in-Aid for JSPS Fellows to K. Izuma, a Grand-in-Aid for Scientific Research on Innovative areas #22120515 to K. Matsumoto and Tamagawa University Global COE grant from the MEXT, Japan.

References

1. Ariely D., Norton M.I. How actions create—not just reveal—preferences. *Trends Cogn Sci* 12 (2008) 13–16.
2. Brehm J.W. Post-decision changes in the desirability of choice alternatives. *J Abnorm Soc Psychol* 52 (1956) 384–389.
3. Gerard H.B., White G.L. Post-decisional reevaluation of choice alternatives. *Pers Soc Psychol B* 9 (1983) 365–369.
4. Shultz T.R., Leveille E., Lepper M.R. Free choice and cognitive dissonance revisited: Choosing “lesser evils” versus “greater goods”. *Pers Soc Psychol B* 25 (1999) 40–48.
5. Festinger L. *A Theory of Cognitive Dissonance*. Stanford: Stanford University Press. (1957).
6. Harmon-Jones E., Mills J. *Cognitive Dissonance: Progress on a pivotal theory in social psychology*. Washington DC: Braum-Brumfield. (1999).
7. Harmon-Jones E. Contributions from research on anger and cognitive dissonance to understanding the motivational functions of asymmetrical frontal brain activity. *Biol Psychol* 67 (2004) 51–76.
8. Botvinick M., Nystrom L.E., Fissell K., Carter C.S., Cohen J.D. Conflict monitoring versus selection-for-action in anterior cingulate cortex. *Nature* 402 (1999) 179–181.

9. Carter C.S., Braver T.S., Barch D.M., Botvinick M.M., Noll D., Cohen J.D. Anterior cingulate cortex, error detection, and the online monitoring of performance. *Science* 280 (1998) 747–749.
10. Amodio D.M., Harmon-Jones E., Devine P.G., Curtin J.J., Hartley S.L., Covert A.E. Neural signals for the detection of unintentional race bias. *Psychol Sci* 15 (2004) 88–93.
11. Izuma K., Matsumoto M., Murayama K., Samejima K., Sadato N., Matsumoto K. Neural correlates of cognitive dissonance and choice-induced preference change. *Proc Natl Acad Sci U S A* 107 (2010) 22014–22019.
12. van Veen V., Krug M.K., Schooler J.W., Carter C.S. Neural activity predicts attitude change in cognitive dissonance. *Nat Neurosci* 12 (2009) 1469–1474.
13. Pochon J.B., Riis J., Sanfey A.G., Nystrom L.E., Cohen J.D. Functional imaging of decision conflict. *J Neurosci* 28 (2008) 3468–3473.
14. Chen M.K., Risen J.L. How choice affects and reflects preferences: revisiting the free-choice paradigm. *J Pers Soc Psychol* 99 (2010) 573–594.
15. Lebreton M., Jorge S., Michel V., Thirion B., Pessiglione M. An automatic valuation system in the human brain: evidence from functional neuroimaging. *Neuron* 64 (2009) 431–439.
16. Tom S.M., Fox C.R., Trepel C., Poldrack R.A. The neural basis of loss aversion in decision-making under risk. *Science* 315 (2007) 515–518.
17. Kuhnen C.M., Knutson B. The neural basis of financial risk taking. *Neuron* 47 (2005) 763–770.
18. Knutson B., Wimmer G.E., Rick S., Hollon N.G., Prelec D., Loewenstein G. Neural antecedents of the endowment effect. *Neuron* 58 (2008) 814–822.
19. Shackman A.J., Salomons T.V., Slagter H.A., Fox A.S., Winter J.J., Davidson R.J. The integration of negative affect, pain and cognitive control in the cingulate cortex. *Nat Rev Neurosci* 12 (2011) 154–167.

Cantor Coding of Song Sequence in the Bengalese Finch HVC

Jun Nishikawa and Kazuo Okanoya

Abstract Cantor coding has been theoretically proposed as an excellent way to encode sequential information in the brain. Empirical verification has been successfully given for the dynamical nature of the Cantor coding in experiments using hippocampal slice preparations. However, because these studies adopted artificial electrical stimulation for inputs, it remains unanswered as to whether brain really uses this coding scheme. In this study, we examined the Cantor coding in vivo in HVC (a song nucleus) of Bengalese finches, as the HVC is responsible for processing complex sequence of song syllables. We recorded multiple single-unit responses to acoustic stimuli that were composed of randomized sequences of syllables. Analyses of neuronal activities revealed that auditory responses of single HVC neurons coded sequences of multiple syllables (3 or more), suggestive of the hierarchical dependency that is a necessary condition of the Cantor coding. Further studies will shed light on how the Cantor coding could be implemented in biological system.

J. Nishikawa (✉)

RIKEN Brain Science Institute, Saitama 351-0198, Japan

Graduate School of Frontier Biosciences, Osaka University, Osaka 565-0871, Japan

e-mail: j_kohaku@sc5.so-net.ne.jp

K. Okanoya

RIKEN Brain Science Institute, Saitama 351-0198, Japan

Department of Cognitive and Behavioral Sciences, University of Tokyo, Tokyo 153-8902, Japan

Japan Science Technology Agency, ERATO Okanoya Emotional Information Project,
Saitama 351-0198, Japan

e-mail: cokanoya@mail.ecc.u-tokyo.ac.jp

Y. Yamaguchi (ed.), *Advances in Cognitive Neurodynamics (III)*,

DOI 10.1007/978-94-007-4792-0_84,

© Springer Science+Business Media Dordrecht 2013

1 Introduction

How the brain encodes complex sequential signals is one of the important topics in neuroscience. For an example, sophisticated communication by language in human being is based on the abilities for cognition, processing, and generation of complex sound sequence. One possible mechanism could be Cantor coding, which is an excellent way to encode sequential information into the brain proposed by theorists [1]. Recently, this dynamical encoding scheme was verified experimentally in the hippocampus slice preparation [2, 3]. However, obtained results have not been reached whether the brain really utilizes it or not, because they used artificial electrical stimulations as input elements with the *in vitro* experiment.

Bengalese finches, one of songbirds, might be great help for *in vivo* experimental verification of Cantor coding. Because they have a complex learned vocalization which is composed of various sound elements with a typical sequential rule, and utilize it for courtship behavior from male to female birds [4]. In addition, they have a specialized brain area (song system) for song production, learning, and cognition [5]. Especially, in the brain nucleus HVC (equivalent to cortex in mammals [6]), there are neurons selectively respond to typical song element sequence [7]. It means that HVC are responsive for sequential information processing.

In the present study, we analyze the trajectories constructed from multiple single-unit recording from HVC in the Bengalese finch driven by random sequence stimulus of song elements, and try to verify the Cantor coding *in vivo* using biologically plausible stimuli.

2 Methods

Six adult Bengalese finches (>180 days post-hatch) were used in this study. All experimental procedures were performed according to established animal care protocols approved by the animal care and use committee at RIKEN.

Undirected songs were recorded in a quiet soundproof box using a microphone and amplifier connected to a computer with a sampling rate of 44.1 kHz and 16-bit resolution. We calculated sonograms from the recorded song using sound analysis software (SASLab Pro; Avisoft, Berlin, Germany). A birdsong consists of a series of discrete song elements with silent intervals among them. Song elements were divided into distinct types by visual inspection of the spectro-temporal structure of each sonogram. Then, we constructed a random sequence of all song elements (random sequence stimulus) in pre-recorded subject's song (Fig. 1).

Before electrophysiological recording sessions, birds were anesthetized with 4–7 doses of 10% urethane (40 μ l per dose) at 20-min intervals. The birds were restrained in a custom-made chamber on a stereotaxic device (Narishige, Tokyo, Japan). The birds were fixed with ear-bars and a beak-holder that positioned the

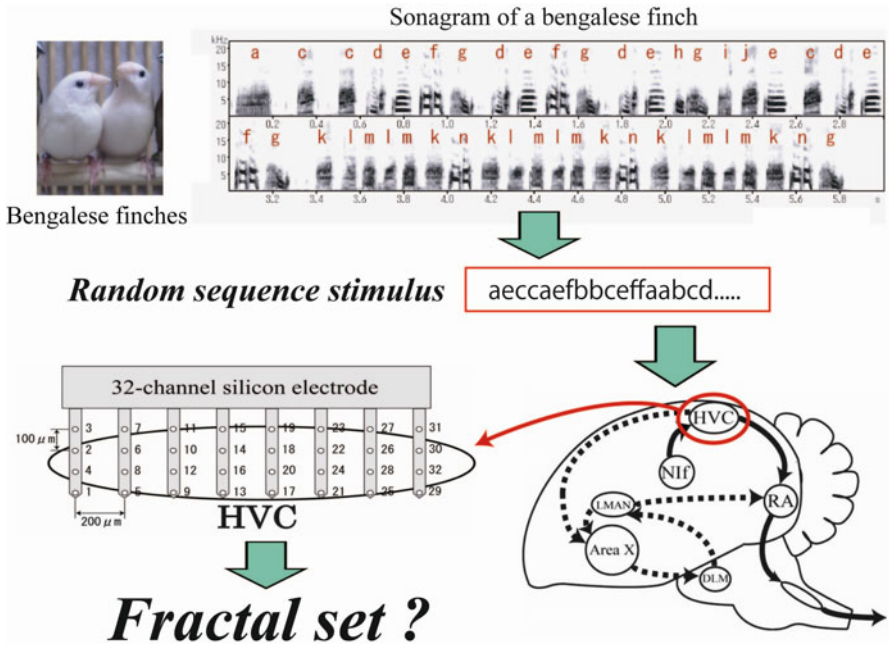


Fig. 1 Schematic diagram of the present study. Random sequence stimuli were constructed from each song elements which is previously recorded from each subject. We try to verify Cantor coding *in vivo* to record neural activities from the Bengalese finch HVC to the random sequence stimuli

beak tip at an angle of 45° below the horizontal plane. The head was treated with Xylocaine gel and the feathers and skin were removed. A custom-made three-point fixation device was attached to the rostral part of the skull surface with dental cement. Small holes were made in the skull just above the HVC. Finally, the dura was removed, and a high-density silicon electrode (8 × 4 = 32-ch; NeuroNexus, Dallas, USA) were set on the surface.

The stereotaxic device with anesthetized birds was moved into an electromagnetically shielded sound-attenuation box for neural recording. The ear-bars were removed before making physiological recordings. The electrodes were lowered into the brain using a micro-positioner (SM-25; Narishige, Tokyo, Japan), and extracellular signals from HVC were recorded. The signals from the electrodes were amplified (gain 1,000–2,000) and filtered (100 Hz–10 kHz bandpass) using an extracellular multi-unit recording system (MAP system; Plexon, Dallas, USA). The data were digitized at 40 kHz with 16-bit resolution using associated software RASPUTIN. During neural recording, random sequence stimuli or other sound stimuli were presented at a peak sound pressure of 70 dB.

We calculated the time course of average firing rate of each neuron, and analyzed its sequential dependency from the perspectives of Cantor coding.

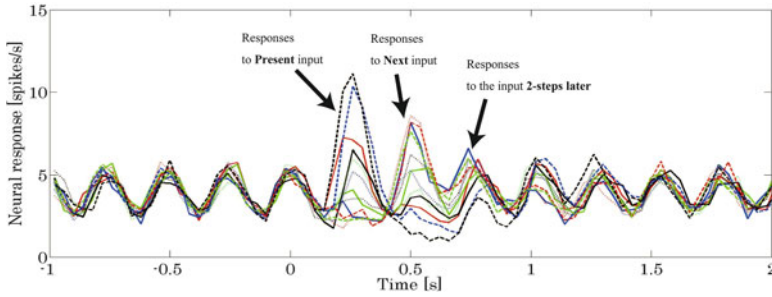


Fig. 2 A typical auditory response of random song element sequence in the Bengalese finch HVC in anesthetized condition. Each color of traces is averaged firing rate trace with same present input. There is the evidence of long-term dependency with at least three elements, which is the necessary condition of Cantor coding

3 Results

We recorded auditory responses in multiple single-units from six urethane anesthetized adult Bengalese finches HVC using 32-ch high-density silicon electrodes. In average, we obtained 10–30 single units simultaneously from one recording session. We analyzed these data from the perspective of Cantor coding.

We calculated average firing rate in each present input from the obtained data as shown in Fig. 2. There are oscillatory traces with about 0.25 s cycle, which is the cycle of sound element (~ 0.05 s) plus inter-stimulus interval (0.20 s). Therefore, each peak is the result of auditory response of each sound element. It is natural that we can observe large difference in the responses to present inputs according to each color. In addition of that, we can observe clear difference in the responses to next inputs according to each color. This dependency was also valid in the responses to the inputs 2-steps later. These results revealed the long-term dependency of song sequence in HVC.

4 Discussions

In summary, we showed that the long-term dependency in auditory responses in the Bengalese finch HVC at least three time steps. This hierarchical dependency is one of the necessary conditions of Cantor coding. Therefore, the present study have an important meaning to have a first step to verify Cantor coding *in vivo* with biologically plausible input units.

However, we couldn't complete the experimental verification, because we haven't show the fractal set in the neural dynamics in HVC. For that purpose, we have to analyze its spatial clustering property with hierarchical structure and

self-similarity in the neural phase space. Some useful index, “spatial clustering index” and “self-similarity index” will be helpful for the future study [2]. Linear discriminant analysis (LDA) will also help us for further analysis [8].

In the analysis in this study, we only calculate the average firing rate in each individual cell. However, Kuroda et al. reported the performance of Cantor coding in CA1 hippocampal slice experiment is remarkably improved at population level [3]. Therefore, we should analyze the dynamics in multi-dimensional phase space with multiple single-unit data set as well as single unit based analysis. After these analyses have done, we will try to compare each sequential rule to the clustering configuration in the corresponding fractal set in neural phase space. These analyses will be shed light on the biological plausibility of Cantor coding.

Although we analyzed auditory responses in the anesthetized birds, these results still give an insight to understand the sequential processing during singing. Because singing-related and hearing-related activities in songbird HVC is identical in some cases, known as auditory-vocal mirror neurons [9]. In general, Cantor coding have infinite hierarchy to represent long sequences, because this coding is implemented on the continuous multi-dimensional neural phase space. We expect that this feature has considerable advantage to represent flexible sequence compared to the coding with higher-order Markov chain.

Acknowledgments This study was partially supported by Grant-in-Aid for Young Scientists (B) (No. 18700303, 20700278) and Grant-in-Aid for Scientific Research on Innovative Areas “The study on the neural dynamics for understanding communication in terms of complex hetero systems” (No. 22120521) to J.N. from The Ministry of Education, Culture, Sports, Science and Technology of Japan, and ERATO Okanoya Emotional Information Project to K.O. from Japan Science Technology Agency.

References

1. Tsuda, I.: Toward an interpretation of dynamic neural activity in terms of chaotic dynamical systems. *Behavioral and Brain Sciences* 24 (2001) 793–847
2. Fukushima, Y., Tsukada, M., Tsuda, I., Yamaguti, Y., Kuroda, S.: Spatial clustering property and its self-similarity in membrane potentials of hippocampal CA1 pyramidal neurons for a spatio-temporal input sequence. *Cognitive Neurodynamics* 1 (2007) 305–316
3. Kuroda, S., Fukushima, Y., Yamaguti, Y., Tsukada, M., Tsuda, I.: Iterated function systems in the hippocampal CA1. *Cognitive Neurodynamics* 3 (2009) 205–222
4. Okanoya, K.: The Bengalese finch: a window on the behavioral neurobiology of birdsong syntax. *Annals of the New York Academy of Sciences* 1016 (2004) 724–735
5. Stokes, M., Leonard, C.M.: Central control of song in the canary, *Serinus canarius*. *Journal of Comparative Neurology* 165 (1976) 457–486
6. Reiner, A., Perkel, D.J., Bruce, L.L., Butler, A.B., Csillag, A., Kuenzel, W., Medina, L., Paxinos, G., Shimizu, T., Striedter, G., Wild, M., Ball, G.F., Durand, S., Gütürkün, O., Lee, D.W., Mello, C.V., Powers, A., White, S.A., Hough, G., Kubikova, L., Smulders, T.V., Wada, K., Dugas-Ford, J., Husband, S., Yamamoto, K., Yu, J., Siang, C., Jarvis, E.D.: Revised nomenclature for avian telencephalon and some related brainstem nuclei. *Journal of Comparative Neurology* 473 (2004) 377–414

7. Nishikawa, J., Okada, M., Okanoya, K.: Population coding of song element sequence in the Bengalese finch HVC. *European Journal of Neuroscience* 27 (2008) 3273–3283
8. Yamaguti, Y., Kuroda, S., Fukushima, Y., Tsukada, M., Tsuda, I.: A Mathematical Model for Cantor Coding in the Hippocampus. *Neural Networks* 24 (2011) 43–53
9. Prather, J. F., Peters, S., Nowicki, S., Mooney, R.: Precise auditory–vocal mirroring in neurons for learned vocal communication. *Nature* 451 (2008) 305–310

Inhibitory Network Dependency in Cantor Coding

Yasuhiro Fukushima, Yoshikazu Isomura, Yutaka Yamaguti, Shigeru Kuroda, Ichiro Tsuda, and Minoru Tsukada

Abstract Cantor coding provides an information coding scheme for temporal sequences of events. In this paper, we analyzed an inhibitory network dependency in Cantor coding from hippocampal CA1 neurons of rat acute slice preparation by using GABA_A receptor blocker (gabazine). After gabazine application, clustering index was lower under subthreshold condition and higher at suprathreshold condition. Our results suggest the tendency that inhibitory network enlarges the difference between responses under sub- and supra-threshold conditions.

1 Introduction

Contextual information is thought to be temporarily stored in the hippocampus in the form of short-term memory. It is important for the investigation of memory systems to clarify how information is coded and represented in hippocampal network. There are roughly three areas in hippocampus: dentate gyrus, CA3, and CA1. Input from entorhinal cortex is sent to dentate gyrus. Dentate gyrus is connected through a circuit with CA3 to CA1. CA3 area is characterized by a distinct biological

Y. Fukushima (✉)

Brain Science Institute, Tamagawa University, 6-1-1, Tamagawagakuen, Machida 194-8610, Japan

Department of Social Work, Kawasaki University of Medical Welfare, 288, Matsushima, Kurashiki 701-0193, Japan

e-mail: fukushima@mw.kawasaki-m.ac.jp

Y. Isomura • M. Tsukada

Brain Science Institute, Tamagawa University, 6-1-1, Tamagawagakuen, Machida 194-8610, Japan

Y. Yamaguti • S. Kuroda • I. Tsuda

Research Institute for Electronic Science, Hokkaido University, Kita 20 Nishi 10, Kita-ku, Sapporo 001-0020, Japan

neural network, which has a recurrent (feedback) connection. On this subject, Nakazawa et al. [1] have reported that after knocking out feedback in CA3 of mice using genetic techniques, an extremely large number of cues were required to accomplish one action. According to these observations, it can be hypothesized that the hippocampal CA3 network forms a context of time sequence, while CA1 maps the spatio-temporal context to its synaptic weight space [2–5]. In the CA1 area of the hippocampus, the magnitude of LTP depends not only on the frequency of applied stimuli, but also on time sequences [2, 6, 7]. However, experimentally, the coding property of spatial clustering and its self-similarity has been less reported in the sequence of input–output relation in hippocampal CA3-CA1 system.

Theoretically, Tsuda predicted the possibility of Cantor coding in CA3-CA1 network [8–10]. Cantor coding provides an information coding scheme for temporal sequences of events. It forms a hierarchical structure in state space of neural dynamics. In this model, it is assumed that the CA3 state is wandering around quasi-attractors, each of which represents a single episodic event, and that CA3 outputs a temporal sequence of events, which should be encoded in CA1 network, especially in temporal dimensions. Input-dependent distribution of CA1 state is hierarchically clustered in the vector space.

In order to show the physiological evidence for Cantor coding, we have been reported some papers. Our previous study showed the Cantor coding-like property in rat hippocampal CA1 pyramidal neurons, where the clustering property was dependent on the size of EPSP and NMDA-type glutamate receptor [11]. Furthermore, the relation between input pattern and recorded responses was proved to be described as iterated function systems, which provides a direct evidence of the presence of Cantor coding, and also the coding quality was drastically improved by a newly invented virtual reconstruction method using data from plural neurons [12]. In addition, in order to clarify the detailed property of Cantor coding, we showed that the performance of Cantor coding sensitivity is dependent on interval of input sequence theoretically by using two-compartment modeled neurons [13] and physiologically in pyramidal CA1 neurons (in preparation).

There are many kinds of inhibitory neurons in hippocampus [14]. Many previous study showed the importance of inhibitory network on control for pyramidal neurons in hippocampal CA1 area. GABAergic interneurons and their inhibitory synapses play a major role in oscillatory patterns [15]. In relation to temporal coding, inhibitory network in CA1 changes the timing sensitivity in spike timing dependent plasticity of hippocampal CA1 system [16]. However, inhibitory network dependency of Cantor coding for sequential input is not clear. In this study, we estimated GABAergic control dependency of Cantor coding in hippocampal CA1. Our previous study showed that the performance of Cantor coding is best when interval of input sequence is 30 ms. The time course of GABA_A receptor response is more similar to those of GABA_B receptor, so we first applied GABA_A blocker to CA1 neurons.

2 Methods

Acute rat slice preparation including hippocampal CA1 area was made and electrical stimulation was applied pyramidal neurons in CA1 as in our previous study [12]. Two stimulating electrodes were set to the Schaffer collaterals, proximal and distal sites to the soma (Fig. 1). The four input spatial patterns were as follows: (1) electrical stimulation through both electrodes (“11”), (2) electrical stimulation through one electrode (“10”), (3) electrical stimulation through the other electrode (“01”), and (4) no electrical stimulation (“00”). Successive ten electrical pulses (33 Hz), randomly selected from one of four patterns, was applied at 10 s intervals for 20 min. Membrane potentials from soma were recorded by patch clamp methods.

Five minutes after adding gabazine (antagonist for GABA_A receptor) to the bath solution, membrane potentials were recorded by electrical stimulation with same input sequence.

To evaluate the accuracy of cantor coding with/without inhibitory network, the following two measures were used as in our previous study [11]. A “spatial clustering index” indicates how well the distribution of responses is clustered by the patterns of electrical stimulation. A “self-similarity index” indicates a measure of hierarchical self-similarity in time-history.

(1) Spatial clustering index

First, each response was classified into four groups (G_{ij} ($ij = 11, 10, 01, 00$)) with regard to the spatial input pattern. The mean amplitude of each group was calculated and defined as the “weighted-center” of each group ($W_{00}, W_{01}, W_{10},$ and W_{11} , cross in Fig. 2). The difference between an amplitude (V_{ij} , $i, j = 0$ or 1 , where ij is stimulus pattern) and “weighted-center” except its own value ($W_{00}, W_{01}, W_{10}, W_{11}$) was defined as distances ($D_{00}, D_{01}, D_{10}, D_{11}$).

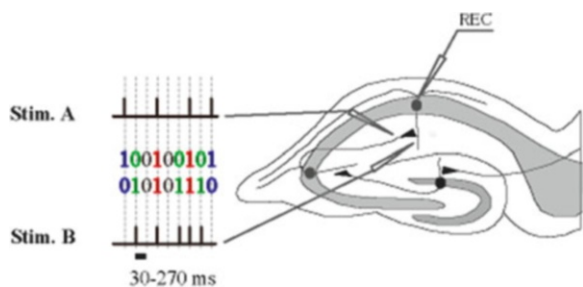


Fig. 1 Experimental procedure

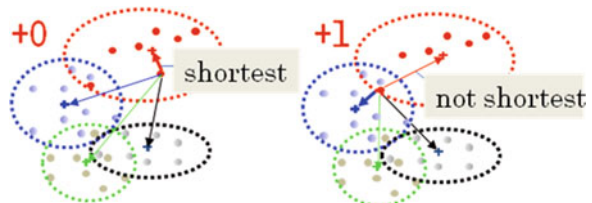


Fig. 2 How to calculate clustering index. Spatial clustering index get large when the counting number (i.e. overlapping of cluster) is large

If the shortest distance (D_{\min}) when V_{ij} was given belonged to the identical group (G_{ij}) of its own input pattern (ij), the “cluster point” (C_{ij}) was assigned a zero ($C_{ij} = C_{ij} + 0$; Fig. 2 left). If not, the “cluster point” was assigned one ($C_{ij} = C_{ij} + 1$; Fig. 2 right). This procedure was applied to all values of V_{ij} . The cluster points were normalized by the number of responses belonging to G_{ij} and divided by 0.75. “Spatial clustering index” was defined as the averaged value from four patterns. The value ranged from 0 (non-overlapping state; the highest performance) to 1 (randomly overlapping; no effect).

(2) Self-similarity index

A self-similarity index indicates a measure of hierarchical self-similarity between time-history steps ($\#$; i.e. the effect after $\#$ input pattern). The four weighted centers (W_{00} , W_{01} , W_{10} , and W_{11}) for each time-history step of the spatial input pattern forms an observed pattern in amplitudes. The self-similarity measure (PN) is the necessary number of neighboring permutations to get a target-ordered pattern to correspond with the standard pattern (the ordered pattern of 1st time history step). The self-similarity index is obtained by normalizing the measure PN for the chance level (3). The value ranged from 0 (same order) through 1 (random order) to 2 (completely opposite order).

3 Results

First, we calculated the spatial clustering index. Under subthreshold conditions, spatial clustering index after gabazine application was smaller than before at history #3, and did not show significant difference at history #1 and #2 (Fig. 3, left). Under suprathreshold conditions, spatial clustering index was larger than before at history #1 and #2, and did not show significant difference at history #3 (Fig. 3, right). These results suggest the tendency that inhibitory network enlarges the difference of spatial clustering property between under sub- and supra-threshold conditions.

In self similarity index, gabazine dependency was not observed between under sub- and supra-threshold conditions (Fig. 4).

4 Discussions

In general, inhibitory network suppresses the EPSP size and decrease the ratio of action potential induction. If the property of inhibitory network in CA1 is simply shifting the condition from suprathreshold to subthreshold, spatial clustering index under suprathreshold condition show no difference between before and after gabazine treatment and spatial clustering index after gabazine treatment under subthreshold is similar to those under suprathreshold conditions. However, in our results, spatial clustering index under suprathreshold condition

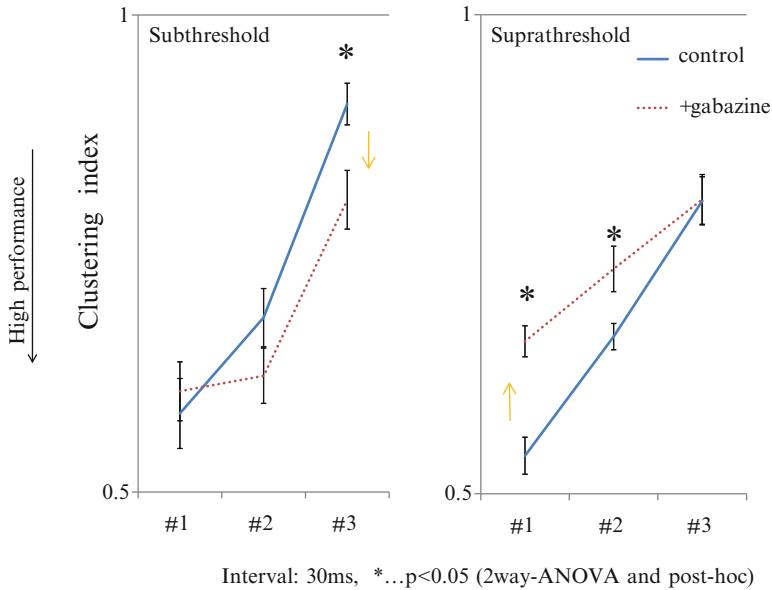


Fig. 3 Spatial clustering index with/without gabazine

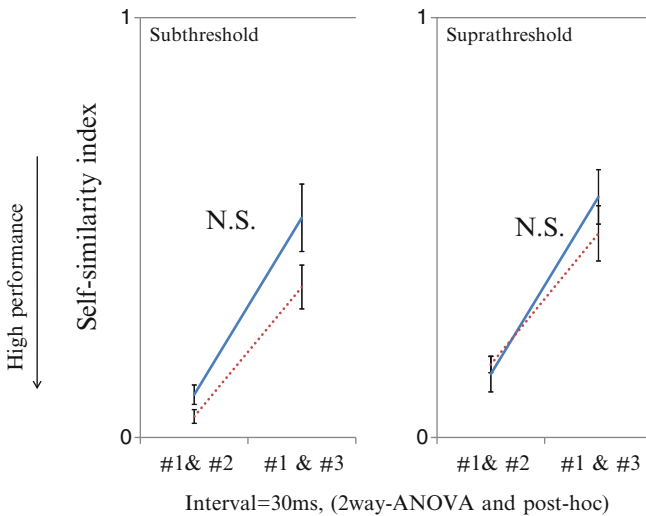


Fig. 4 Self-similarity index with/without gabazine

after gabazine treatment was larger than before. These results show that the role of inhibitory network does not simply decrease the size of EPSP and ratio of action potential induction. Our previous results show that the difference between under sub- and supra-threshold conditions were mainly dependent on NMDA type

glutamate receptor [11]. Both NMDA-receptor and GABAergic synapse enlarges the difference of Cantor coding performance between under sub- and supra-threshold conditions, but the mechanism was different between them.

Acknowledgments This work was supported by the Global COE Program at Tamagawa University and Grant-in-Aid for Scientific Research 22120520 from Ministry of Education, Culture, Sports, Science and Technology of Japan.

References

1. Nakazawa K., Quirk M.C., Chitwood R.A., Watanabe M., Yeckel M.F., Sun L.D., Kato A., Carr C.A., Johnston D., Wilson M.A., Tonegawa S.: Requirement for hippocampal CA3 NMDA receptors in associative memory recall. *Science* 297 (2002) 211–218
2. Tsukada M., Saito H.A., Aihara T., Kato H.: Hippocampal LTP depends on spatial and temporal correlation of inputs. *Neural Netw* 9 (1996) 1357–1365
3. Tsukada M., Pan X.: The spatiotemporal learning rule and its efficiency in separating spatiotemporal patterns. *Biol Cybern* 92 (2005) 139–146
4. Tsukada M., Yamazaki Y., Kojima H. Interaction between the Spatio-Temporal Learning Rule (STLR) and Hebb type (HEBB) in single pyramidal cells in the hippocampal CA1 Area. *Cogn Neurodyn* 1(2) (2007) 157–167
5. Tsukada M., Fukushima Y.: A context-sensitive mechanism in hippocampal CA1 networks. *Bull Math Biol* 73(2) (2011) 417–435
6. Tsukada M., Aihara T., Mizuno M., Kato H., Ito K.: Temporal pattern sensitivity of long-term potentiation in hippocampal CA1 neurons. *Biol Cybern.* 70(6) (1994) 495–503
7. Aihara T., Tsukada M., Crair M.C., Shinomoto S.: Stimulus-dependent induction of long-term potentiation in CA1 area of the hippocampus: experiment and model. *Hippocampus.* 7(4) (1997) 416–26
8. Tsuda I.: Toward an interpretation of dynamic neural activity in terms of chaotic dynamical systems. *Behav Brain Sci* 24(5) (2001) 793–847
9. Tsuda I., Kuroda S.: Cantor coding in the hippocampus. *Japan J Indust Appl Math* 18 (2001) 249–258
10. Tsuda I., Kuroda S.: A complex systems approach to an interpretation of dynamic brain activity II: Does Cantor coding provide a dynamic model for the formation of episodic memory. P Erdi et al. (Eds.): *Cortical dynamics, LNCS 3146* (2004) 129–139
11. Fukushima Y., Tsukada M., Tsuda I., Yamaguti Y., Kuroda S.: Spatial clustering property and its self-similarity in membrane potentials of hippocampal CA1 pyramidal neurons for a spatio-temporal input sequence. *Cogn. Neurodyn.* 1 (2007) 305–316
12. Kuroda S., Fukushima Y., Yamaguti Y., Tsukada M., Tsuda I.: Iterated function systems in hippocampal CA1. *Cogn Neurodyn* 3 (2009) 205–222
13. Yamaguti Y., Kuroda S., Fukushima Y., Tsukada M., Tsuda I.: A Mathematical Model for Cantor Coding in the Hippocampus. *Neural Netw* 24(1) (2011) 43–53
14. Freund T.F., Buzsáki G.: Interneurons of the hippocampus. *Hippocampus.* 6(4) (1996) 347–470
15. Buzsáki G. Hippocampal GABAergic interneurons: a physiological perspective. *Neurochem Res* 26 (2001) 899–905
16. Tsukada M., Aihara T., Kobayashi Y., Shimazaki H.: Spatial analysis of spike-timing-dependent LTP and LTD in the CA1 area of hippocampal slices using optical imaging. *Hippocampus* 15(1) (2005) 104–9

Sequential Memory Retention by Stabilization of Cell Assemblies

Timothee Leleu and Kazuyuki Aihara

Abstract The concept of Hebbian cell assemblies is exploited to illustrate how sequential memory robust to noise and lags between inputs can be formed in analog neural networks. The processing of a sequence is modeled by a succession of shifts between stable attractors induced by the symbols of the sequence. The learning is unsupervised and achieved after a single presentation of the stimuli, by creating the succession of attractors. Analyses and simulations of the dynamics enable a better understanding of the effects of generalized Hebbian learning. The conditions under which these assemblies can form and retain sequential memory are clarified.

1 Introduction

Sequence learning is probably a fundamental issue in the global understanding of cognition, and remains highly controversial. A multitude of models have been proposed for the past 50 years. Perhaps the first attempt was initiated with Hebb's assumptions [7], stating that the encoding of memories is assured by cell assemblies, i.e. groups of neurons exhibiting higher activity. Early models of this persistent activity, known as auto-associative models [8], have then been applied to sequence learning [12]. In these, successive items are chained by associations (typically using a correlation rule) occurring at a slower time scale, so that sequences can be replayed.

The concept of time in neural networks has also been widely spread by Elman's simple recurrent network [5], and several supervised learning rules such as back-propagation through-time [18], in which the memory of past symbols is encoded in the phase space of the neural system. In these cases, each successive symbol shifts

T. Leleu (✉) • K. Aihara

The University of Tokyo, 4-6-1 Komaba, Meguro-ku, Tokyo, 153-8505, Japan
e-mail: timothee@sat.t.u-tokyo.ac.jp

the dynamics in the phase space, allowing dynamical computation. These models introduced the idea to use the dynamics in the phase space to account for complex computation [16].

To allow more realistic dynamics, the framework of reservoir computing, such as liquid-state machines [13] and echo-state networks [10], proposed that the preservation of the separation of trajectories due to inputs would be sufficient to achieve computation, if a reader mechanism could decode instantaneous states. Lastly, it has been argued that neural dynamics could be better modeled by transient trajectories, itinerant between Milnor attractors [20].

All these models have in common that sequence learning should integrate two time scales: a rapid time scale of neural dynamics, and a slower one during which each symbol is retained active in memory, long enough to be temporally overlapped with the next input.

Simultaneously to these developments, Hebb's assumptions were partially challenged, after the discovery of STDP [3], and development of spiking neuron models. STDP has notably been applied to sequence acquisition in a hierarchical model [11]. Effects which cannot be described with the firing rates only may be at the basis of sequence processing, and may capture more biologically relevant mechanisms of sequence acquisition [6]. Nevertheless the analysis of the effects of STDP remains difficult [14], and it is unclear whether or not increasing model complexity will help in the understanding of sequence processing. This is particularly true when analyzing cognition at the macroscopic scale (EEG and MEG recordings), where Hebb's hypothesis of assemblies processing seems plausible [17].

There are probably the very large differences in scales (milliseconds for STDP [14], to seconds for neural recordings (during language tasks [17])), and a lack of precision in the definition of Hebbian assemblies [4] which make the development of a unifying model difficult. Understanding how information separated from more than seconds to ten of seconds can combine to generate sequential memory may require a mesoscopic level viewpoint.

We extend our models of rate-based networks with the recent developments in Hebbian cell assemblies, LTP/LTD¹ and dynamical systems theory to provide an intermediate level viewpoint. In this framework, the mathematical analysis of effects of Hebbian learning is more tractable. We assume the central role of cell assemblies, and show with a very simplified model how a realistic learning rule can self-organize the neural connectivity to allow the creation of successive attractors. During sequence processing, neural dynamics remain in these attractors during a slower time scale, until the next input is fed to the network. We describe how these assemblies can interact and eventually combine, via Hebbian-like learning rules, in order to produce a realistic, robust and scalable mechanism for sequence learning.

¹LTP: long-term potentiation, LTD: long-term depression.

2 Model

For the current analysis, a model of neurons which can exhibit chaotic dynamics is exploited [1]. The dynamics of M neurons are described by the following equations:

$$y_i(n+1) = F_i(y(n)), \quad (1)$$

$$F_i(y(n)) = ky_i(n) + V_i(n) - \alpha x_i(n) + \theta_i + a_i, \quad (2)$$

$$V_i(n) = \sum_{i \neq j} \omega_{ij}(m)x_j(n), \quad (3)$$

$$x_j(n) = f(y_j(n)), \quad (4)$$

where y_i is the internal state of the neuron i , y the vector of internal states, $V_i(n)$ the local interaction term, $\omega_{ij}(m)$ the connection weight from neuron j to i , $\alpha > 0$ the refractoriness, θ_i the threshold, x_i the activity of neuron i , f the activation function, and a_i the external inputs. The map f used here is the cumulative distribution function of the standard normal law. Finally, the activity of the neuron i is $x_i(n) = f(y_i(n))$.

The weights $\omega_{ij}(m)$ are updated via a learning rule, acting on a slower time scale m . Each time-unit m is subdivided into N intervals, each representing the faster time-unit n . The following generalized learning is considered, taking into account both LTP/LTD:

$$\omega_{ij}(m+1) = \omega_{ij}(m) + \frac{\lambda}{M} \text{sgn}(m_i(m))h(m_j(m)), \quad (5)$$

$$m_i(m) = \frac{1}{N} \sum_{n=0}^N x_i(n) - d_i, \quad (6)$$

where d_i is the threshold for LTP/LTD, h the Heaviside step function, and sgn the sign function. When neurons i and j are both firing strongly in average, then the change is positive (long-term potentiation). When j is firing, but not i , it is negative (long-term depression). It is equal to zero otherwise. Moreover, a saturation level s_j for weights ω_{ij} is assumed to be $|\omega_{ij}| < s_j$. Similar rules, modeling LTP/LTD [2, 9], and using a longer time scale for the change in synaptic efficacy [19] exist in the literature.

3 Proposed Mechanism

In line with reservoir computing, we propose that the separation of trajectories after each input symbol is sufficient to encode a sequence. However, the dynamics between each symbol is supposed persistent, i.e. each intermediate state encoding

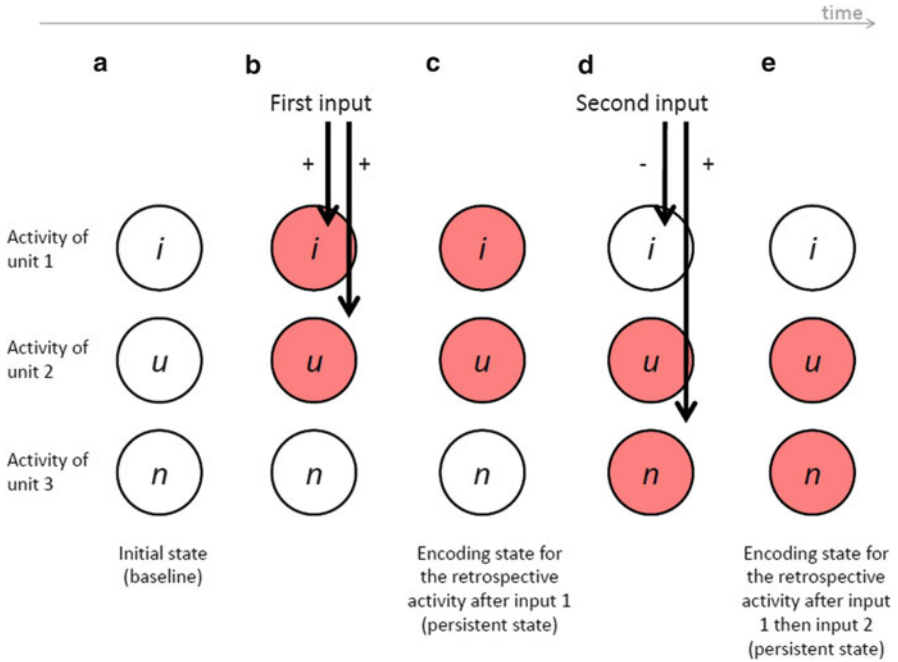


Fig. 1 Dynamics of sequence processing with time. Units in *gray* are active. Inputs can excite (arrow with +) or inhibit (arrow with -) each unit. **(a)** Baseline state, all units are silent. **(b)** Effect of the first input. Populations i and u are active. **(c)** The assembly composed of i and u acquires persistent activity with Hebbian learning. **(d)** Effect of the second input. Population i is inhibited and n is active. Population u is unaffected by the second input. **(e)** This assembly acquires stable firing by Hebbian learning

for a symbol is an attractor, and learning occurs with LTP and LTD. Each attractor encoding a retrospective activity must be unique, in order to respect the separation of trajectories. Contrarily to chained auto-associative models, each attractor is not associated with the following one. The transition between attractors is achieved by the effect of the external inputs (see Fig. 1).

The changes in weights depend on the history of activities. To simplify further the analysis, we consider only the populations i and u of Fig. 1, without loss of generality. During the first input, both populations are firing. Thus, the synaptic efficacies between these are strengthened by LTP, and they can sustain their activity by reverberation (see Fig. 2, left). The second input inhibits the population i , and therefore LTD reduces the synaptic efficacies from population u to i (see Fig. 2, right). The weights, from population u to itself, are strengthened by LTP. Other connections remain unchanged.

By modeling these two populations by simply two neurons connected to each other, by means of a mean field approximation, the dynamical analysis of the

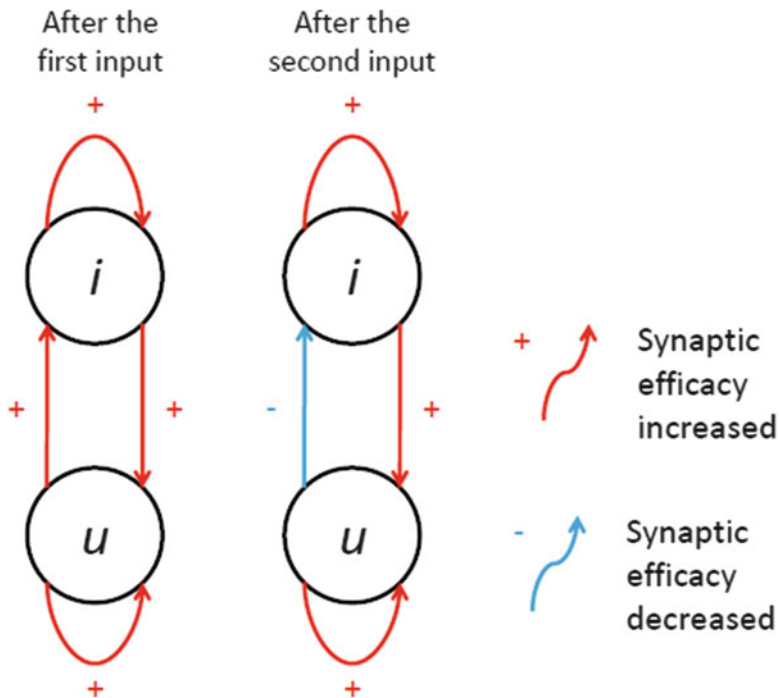


Fig. 2 Change in synaptic efficacies during learning. (*left*) After the first input, all connections have stronger synaptic efficacies. (*right*) After the second input, connections from populations u to i have reduced synaptic efficacies

resulting system can be studied. For certain values of synaptic efficacies, the case described in Fig. 3 can occur. The steady states of the two variables system $\{y_i, y_u\}$, corresponding to the internal states of populations i and u respectively, noted $y_i = F_i(y_i, y_u)$ and $y_u = F_u(y_i, y_u)$, show that there are five fixed points, three stable and two unstable. Their basins of attraction (Fig. 3, bottom) show that this system can process sequences as described previously in Fig. 1.

4 Results

We consider the activity of the two populations i and u during the recognition of a sequence of two symbols. In Fig. 4, the learned sequence has unique successive attractors for each symbol.

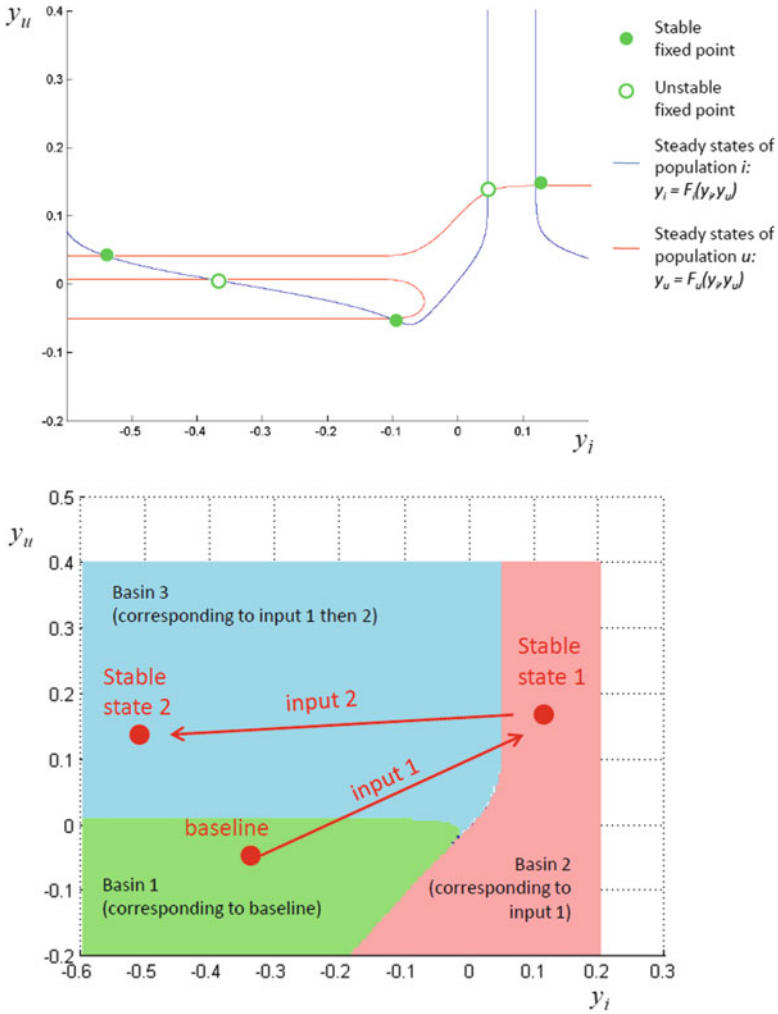


Fig. 3 Dynamical analysis of the two populations. (top) Steady states of the system $\{y_i, y_u\}$ intersect in five locations. Three are stable fixed points, two unstable. (bottom) The basins of attraction of the stable fixed points are described: (1) when populations i and u are excited, they retain this state, (2) if population i is then inhibited, it remains in this state. This dynamic corresponds to the recognition of the sequence

5 Conclusion

After successive inputs, due to the hysteresis effect described above, the changes in weights can depend on the history of inputs, and maintain the dynamics in successive stable dynamical regimes. Because of this dynamical stability, the time lag between successive inputs is not a sensitive parameter, and the retention of information is robust to noise.

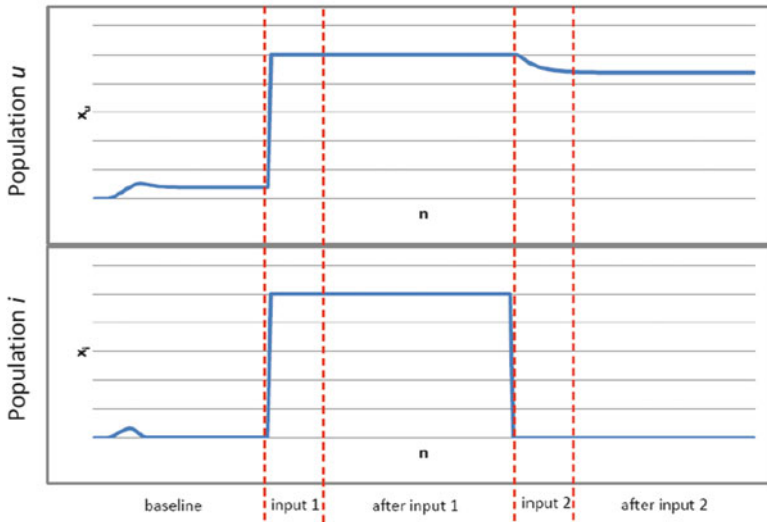


Fig. 4 Trajectory of the activities x of the populations i and u during sequence recognition

A mechanism similar to Fig. 1 has been experimentally observed in vivo [15]. During sequential motor actions in the prefrontal cortex of monkeys, a parallel activation of the encoding units first occurs. Subsequent events inhibit all neurons except those encoding for the current step in the sequence.

Acknowledgments This research is supported by the Global Center of Excellence (G-COE) “Secure-Life Electronics” sponsored by the Ministry of Education, Culture, Sports, Science and Technology (MEXT), and partially by the Aihara Project, the FIRST program from the Japan Society for the Promotion of Science (JSPS), Japan.

References

1. K. Aihara, T. Takabe, and M. Toyoda. Chaotic neural networks. *Physics Letters A*, 144(6-7):333 – 340, 1990.
2. A. Artola and W. Singer. Long-term depression of excitatory synaptic transmission and its relationship to long-term potentiation. *Trends in neurosciences*, 16:480 – 487, 1993.
3. G. Bi and M. Poo. Synaptic modification by correlated activity: Hebb’s postulate revisited. *Annual review of neuroscience*, 24(1):139–166, 2001.
4. G. Buzsaki. Neural syntax: Cell assemblies, synapsembles, and readers. *Neuron*, 68(3):362–385, Nov. 2010.
5. J. L. Elman. Finding structure in time. *Cognitive Science*, 14:179–211, 1990.
6. P. Foldiak. Learning invariance from transformation sequences. *Neural Comput.*, 3:194–200, June 1991.
7. D. Hebb. *The Organization of Behavior*. Wiley: New York, 1949.

8. J. J. Hopfield. Neural networks and physical systems with emergent collective computational abilities. *Proceedings of the National Academy of Sciences of the United States of America*, 79(8):2554–2558, Apr. 1982.
9. F. C. Hoppensteadt and E. M. Izhikevich. *Weakly connected neural networks*. Springer-Verlag New York, Inc., Secaucus, NJ, USA, 1997.
10. H. Jaeger. The hecho stateh approach to analysing and training recurrent neural networks. *German National Research Institute for Computer Science*, 148, 2001.
11. D. James and A. Maida. Sequential hierarchical recruitment learning in a network of spiking neurons. volume 0, pages 1407–1413, jun. 2009.
12. D. Kleinfeld and H. Sompolinsky. Associative neural network model for the generation of temporal patterns. theory and application to central pattern generators. *Biophys J*, 54(6):1039–1051, Dec. 1988.
13. W. Maass, T. Natschlager, and H. Markram. Real-time computing without stable states: A new framework for neural computation based on perturbations. *Neural Computation*, 02:2531–2560, 2002.
14. A. Morrison, M. Diesmann, and W. Gerstner. Phenomenological models of synaptic plasticity based on spike timing. *Biol. Cybern.*, 98:459–478, 2008.
15. H. Mushiake, N. Saito, K. Sakamoto, Y. Itoyama, and J. Tanji. Activity in the lateral prefrontal cortex reflects multiple steps of future events in action plans. *Neuron*, 50(4):631–641, 2006.
16. J. B. Pollack. The induction of dynamical recognizers. In *Machine learning*, volume 0, pages 227–252. Kluwer Academic Publishers, 1991.
17. F. Pulvermiller. Hebb’s concept of cell assemblies an the psychophysiology of word processing. *Psychophysiology*, 33(4):317–333, 1996.
18. D. E. Rumelhart, G. E. Hinton, and R. J. Williams. Learning internal representations by error propagation. *Nature*, 323:533–536, 1986.
19. B. Siri, H. Berry, B. Cessac, B. Delord, and M. Quoy. A mathematical analysis of the effects of hebbian learning rules on the dynamics and structure of discrete-time random recurrent neural networks. *Neural Comput.*, 20(12):2937–2966, 2008.
20. I. Tsuda. Toward an interpretation of dynamic neural activity in terms of chaotic dynamical systems. *Behav. Brain Sci.*, 24:793–810, 2001.

Statistical Estimation of Non-uniform Distribution of Dendritic Membrane Properties

Toshiaki Omori, Toru Aonishi, and Masato Okada

Abstract We propose a statistical method for estimating the spatial distribution of membrane properties that are non-uniformly distributed over dendrites from partially observable noisy data. We employed the Bayesian statistical approach to extract the hidden but substantial information about the distribution of membrane properties over the dendrites. Simulated data showed that the proposed method can simultaneously estimate the distribution of membrane properties and the distribution of membrane potentials, even from partially observable noisy data.

1 Introduction

Experimental findings such as dendritic spikes and back-propagating action potentials suggest that dendrites contribute more to neural computation than previously thought [1–3]. Since information arriving at a dendrite tends to differ in a spatially segregated manner [4], the heterogeneity of the dendritic membrane properties determines how different kinds of information are processed in neural systems

T. Omori (✉)

Department of Electrical and Electronic Engineering, Graduate School of Engineering, Kobe University, 1-1 Rokkodai-cho, Nada-ku, Kobe, Hyogo 657-8501, Japan

RIKEN Brain Science Institute, Saitama, 351-0198, Japan

e-mail: omori@eedept.kobe-u.ac.jp

T. Aonishi

Department of Computational Intelligence and Systems, Interdisciplinary Graduate School of Science and Engineering, Tokyo Institute of Technology, 4259 Nagatsuta-cho, Midori-ku, Yokohama, Kanagawa 226-8502, Japan

M. Okada

Department of Complexity Science and Engineering, Graduate School of Frontier Sciences, The University of Tokyo, 5-1-5 Kashiwanoha, Kashiwa, Chiba 277-8561, Japan

RIKEN Brain Science Institute, Saitama, 351-0198, Japan

[4–6]. However, it is unclear how the membrane properties are distributed over a dendrite due to the difficulty in performing direct measurement; observable data in imaging experiments has a low spatial resolution and is noisy.

To overcome this difficulty, we propose a method for statistically estimating the non-uniform membrane properties. Based on Bayesian statistics, we derive an algorithm to simultaneously extract the spatial distribution of membrane properties and the spatiotemporal distribution of membrane potentials from partially observable noisy data.

2 Methods

We developed a method for estimating the non-uniform distribution of the membrane properties over a dendrite (Fig. 1). Since dendrites are partially observable, we first need to estimate the distribution of membrane potentials $\{v_{x,t}\}$ over the dendrite. We developed a distributed constant-type Kalman filter (DCKF) from a multi-compartment model, which estimate the distribution of membrane potential over the dendrite $\{v_{x,t}\}$ from partially observable noisy data $\{y_{x,t}\}$. Next, we employed an EM algorithm to estimate the distribution of the membrane properties Θ that govern dendritic spatiotemporal dynamics but are a hidden feature of dendrites. Using the derived DCKF and the EM algorithm, we simultaneously extract the distribution of membrane potentials $\{v_{x,t}\}$ and membrane properties Θ from partially observable noisy data.

2.1 State Space Model for Dendrite

We first derive the DCKF from a differential equation governing the spatiotemporal dynamics of dendrites. The spatiotemporal dynamics of the true membrane potentials over a dendrite, $v(x, t)$, obeys the following cable equation [2]:

$$\frac{\partial v}{\partial t} = \tilde{D} \frac{\partial^2 v}{\partial x^2} + \tilde{f}(v(x, t), x) + \tilde{u}(x, t) + \tilde{\sigma}s(x, t), \tag{1}$$

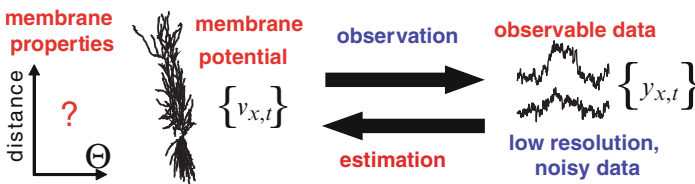


Fig. 1 Illustration of method for statistically and simultaneously estimating non-uniform distribution of membrane properties Θ and membrane potentials $\{v_{x,t}\}$ from partially observable noisy data $\{y_{x,t}\}$

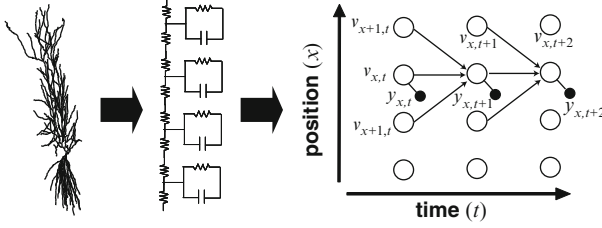


Fig. 2 Distributed constant-type Kalman filter (DCKF) for dendrites. (*left*) Dendritic structure with complex morphology, (*center*) multi-compartment model, (*right*) the derived DCKF. An *open circle* shows true membrane potential $v_{x,t}$, whereas a *filled circle* shows partially observable noisy data $y_{x,t}$

where \tilde{D} expresses an intracellular resistance, \tilde{f} is a membrane current, \tilde{u} is an input current, and $\tilde{\sigma}s$ is a white Gaussian noise with variance $\tilde{\sigma}^2$. By discretizing this differential equation, we obtain the system model:

$$v_{x,t+1} = D(v_{x-1,t} - 2v_{x,t} + v_{x+1,t}) + f_x(v_{x,t}) + u_{x,t} + \sigma s_{x,t}. \tag{2}$$

As illustrated in Fig. 2, dendrites are described as distributed constant-type circuit; the true membrane potentials, $v_{x,t+1}$ at position x and time $t + 1$ (Fig. 2, open circle) depend not on all compartments but on neighboring compartments $x - 1, x,$ and $x + 1$ for the preceding time t . By formulating the system model using this property, we can reduce calculations in Kalman filter. The system model is expressed by using probabilistic model $P(v_{x,t+1}|v_{x-1,t}, v_{x,t}, v_{x+1,t}, u_{x,t})$ as

$$P(v_{x,t+1}|v_{x-1,t}, v_{x,t}, v_{x+1,t}, u_{x,t}) \propto \exp \left[-\frac{1}{2\sigma^2} \left(v_{x,t+1} - D(v_{x-1,t} - 2v_{x,t} + v_{x+1,t}) - f_x(v_{x,t}) - u_{x,t} \right)^2 \right]. \tag{3}$$

In this study, we put $f_x(v_{x,t}) = a_x v_{x,t} + b_x = (\Delta t \tilde{a}_x + 1)v_{x,t} + \Delta t \tilde{b}_x$.

The observable data $y_{x,t}$ (Fig. 2, filled circles) are assumed to be partially observable, and are set to be the sum of the true membrane potential $v_{x,t}$ and noise η as

$$y_{x,t} = c v_{x,t} + \eta s_{x,t}, \tag{4}$$

where $s_{x,t}$ is a white Gaussian noise and c and η are constants. The observation model is expressed by using the following probabilistic model:

$$P(y_{x,t}|v_{x,t}) \propto \exp \left[-\frac{(y_{x,t} - c v_{x,t})^2}{2\eta^2} \right]. \tag{5}$$

2.2 Estimation of Membrane Potential

We derive a framework to extract the distribution of membrane potentials $\{v_{x,t}\}$ over the dendrite from the partially observable noisy data $\{y_{x,t}\}$. By considering the probabilistic path (Fig. 2, right), we see that the membrane potential at position x depends on the membrane potentials of neighboring position $x - 1$, x and $x + 1$ at one preceding time. Using Bayes' theorem, we obtain the recursive relation among posterior distributions $P(v_{x,t}|y_{x,t})$ as

$$\begin{aligned} & P(v_{x,t+1}|y_{x,t+1}) \\ & \propto P(y_{x,t+1}|v_{x,t+1}) \int dv_{x-1,t} dv_{x,t} dv_{x+1,t} \\ & \times P(v_{x,t+1}|v_{x-1,t}, v_{x,t}, v_{x+1,t}, u_{x,t}) \\ & \times P(v_{x-1,t}|y_{x-1,t}) P(v_{x,t}|y_{x,t}) P(v_{x+1,t}|y_{x+1,t}). \end{aligned} \quad (6)$$

Substituting the system model (Eq. (3)) and the observation model (Eq. (5)) into Eq. (6), we derive a recursion equation for an average of membrane potential $\bar{v}_{x,t}$ as

$$\begin{aligned} \bar{v}_{x,t+1} &= D(\bar{v}_{x-1,t} + \bar{v}_{x+1,t}) + (a_x - 2D)\bar{v}_{x,t} \\ & \quad + u_{x,t} + b_x + G_{x,t+1}(y_{x,t+1} - \hat{y}_{x,t+1}), \end{aligned} \quad (7)$$

where $G_{x,t+1}$ is a Kalman gain, and $\hat{y}_{x,t+1}$ is a predicted value for observation expressed by

$$\begin{aligned} \hat{y}_{x,t+1} &= c[D(\bar{v}_{x-1,t} + \bar{v}_{x+1,t}) + (a_x - 2D)\bar{v}_{x,t} \\ & \quad + u_{x,t} + b_x]. \end{aligned} \quad (8)$$

We can derive a recursion equation for the variance of membrane potential in a similar way.

2.3 Estimation of Membrane Properties

Here, we estimate hyperparameters $\Theta = \{a_x, b_x, c, D, \sigma, \eta\}$ by using the EM algorithm. The EM algorithm is an iterative method consisting of the E-step and the M-step [7]. In the E-step, we calculate the following Q function:

$$Q(\Theta|\Theta_n) = \langle \log L(\{v_{x,t}\}, \{y_{x,t}\}|\Theta) \rangle, \quad (9)$$

where $L(\{v_{x,t}\}, \{y_{x,t}\}|\Theta)$ is expressed using the system model and observation model, as

$$\begin{aligned}
 &L(\{v_{x,t}\}, \{y_{x,t}\}|\Theta) \\
 &= \prod_{x,t} P(y_{x,t+1}|v_{x,t+1})P(v_{x,t+1}|v_{x-1,t}, v_{x,t}, v_{x+1,t}).
 \end{aligned}
 \tag{10}$$

The Q function is expressed by the average $\langle v_{x,t} \rangle$ and correlation $\langle v_{x,t+1}v_{x+i,t} \rangle$ ($i = -1, 0, 1$). In the M-step, we find the hyperparameters that maximize the Q function.

$$\Theta_{n+1} = \arg \max_{\Theta} Q(\Theta|\Theta_n)
 \tag{11}$$

The hyperparameters Θ are estimated by performing the E step and the M step alternatively.

The estimation using the proposed method is performed in two steps. First, we estimate the membrane potential: using the DCKF, we derive the average $\langle v_{x,t} \rangle$ and correlation $\langle v_{x,t}v_{x+i,t+1} \rangle$. Second, we estimate the membrane properties: we obtain the hyperparameters Θ that maximize the Q function using $\langle v_{x,t} \rangle$ and $\langle v_{x,t}v_{x+i,t+1} \rangle$. We perform these two steps alternatively until the estimated distribution converges. Through this procedure, the mathematical model assimilates the observable data.

3 Results

To evaluate the effectiveness of the proposed method, we investigated using simulated data whether the hidden feature of dendrite, namely, the distribution of membrane properties Θ can be estimated from the partially observable noisy data $\{y_{x,t}\}$. We used simulated data from a multi-compartment model with 11 compartments (Fig. 3a). External input was assumed to be injected to compartment 1.

We first assumed that the distribution of membrane properties was *uniform*. Here, we estimated a distribution of membrane potentials over the dendrite $\{v_{x,t}\}$ from partially observable noisy data $\{y_{x,t}\}$. Figure 3b shows the estimation result using observable data at every other point ($x = 1, 3, 5, \dots, 11$). We found that the distribution of membrane potentials $\{v_{x,t}\}$ were successfully estimated. We also found that the distribution $\{v_{x,t}\}$ could be estimated when observable data was obtained at every two and every three points (data not shown). This demonstrates that the proposed method is effective for low spatial resolution data such as the imaging data. We also showed that six kinds of hyperparameters $\Theta = \{a_x, b_x, c, D, \sigma, \eta\}$ were simultaneously and accurately estimated from partially observable data [data not shown].

Next, we assumed that the distribution of membrane properties was *non-uniform* and that membrane resistance \tilde{a}_x^{-1} (closely related to a_x) obeyed a sigmoid function [6]:

$$\tilde{a}_x^{-1} = R_1 + \frac{R_0 - R_1}{1 + \exp[-\beta(x - \theta)]},
 \tag{12}$$

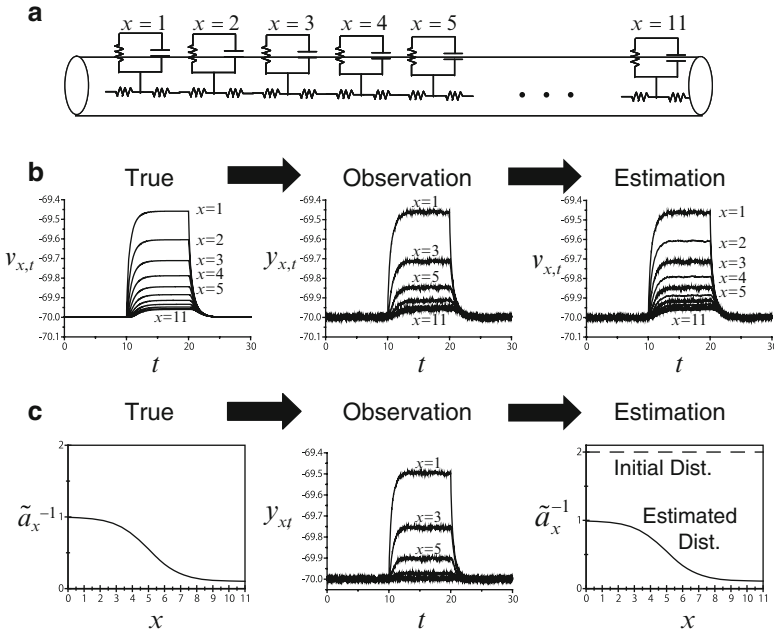


Fig. 3 Estimation result. (a) Multi-compartment model, (b) Estimation of membrane potentials $\{v_{x,t}\}$ from partially observable noisy data $\{y_{x,t}\}$. This example shows an estimation result from data with low spatial resolution. (c) Estimation of non-uniform membrane property $\{\tilde{a}_x^{-1}\}$ from partially observable data $\{y_{x,t}\}$. Using partially observable data, the non-uniform distribution of membrane properties was accurately estimated even when a uniform distribution was used as the initial distribution

where R_0 and R_1 are constants and β and θ determine the steepness and the threshold, respectively. Using partially observable noisy data shown in Fig.3c (center), we estimated the distribution of membrane properties as shown in Fig.3c (right). We found that the estimated distribution of membrane properties was similar to a true distribution, even when a uniform distribution was used as the initial distribution. The estimated distribution of membrane potentials was also similar to the true distribution of membrane potentials. These results demonstrate that the non-uniform dendritic membrane properties and membrane potentials over the dendrite can be estimated even from partially observable noisy data.

4 Discussion

We proposed a method for statistically estimating the non-uniform distribution of dendritic membrane properties. We showed using simulated data that the non-uniform membrane properties over the dendrite can be estimated from partially

observable noisy data. This suggests that our method would be effective for estimation of non-uniform membrane properties from voltage imaging data.

Previous studies by using simulations with compartment models [5, 6] estimated the distribution of membrane resistance in hippocampal CA1 pyramidal neurons from voltage imaging data. We leave a statistical estimation of membrane properties by using the proposed method from voltage imaging data as one of future works.

Acknowledgments This work was partially supported by a Grant-in-Aid for Scientific Research on Innovative Areas “Neural Creativity for Communication (Project No.4103)” [Grant No. 22120506] from MEXT, Japan.

References

1. Häusser M.: Diversity and dynamics of dendritic signaling. *Science* **290** (2000) 739–744
2. Stuart G., Spruston, N., Häusser M.: *Dendrites* (2nd Ed.) Oxford University Press (2007)
3. Spruston N.: Pyramidal neurons: dendritic structure and synaptic integration. *Nat. Rev. Neurosci.* **9** (2008) 206–221
4. Shepherd G.M.: *The synaptic organization of the brain*. Oxford University Press (2003)
5. Omori T., Aonishi T., Miyakawa H., Inoue M., Okada M.: Estimated distribution of specific membrane resistance in hippocampal CA1 pyramidal neuron. *Brain Res.* **64** (2006) 199–208
6. Omori T., Aonishi T., Miyakawa H., Inoue M., Okada M.: Steep decrease in the specific membrane resistance in the apical dendrites of hippocampal CA1 pyramidal neurons. *Neurosci. Res.* **64** (2009) 83–95
7. Bishop C.M.: *Pattern Recognition and Machine Learning*, Springer-Verlag (2006)

Context-Dependent Call Variation in the Male Bengalese Finch

Midori Osada and Tetsu Okumura

Abstract The Bengalese finches live in group and emit several types of calls (such as alarm, distance, distress, begging, and courtship calls). These calls are frequently observed, and these may have an important role in social interactions. This study was performed to elucidate in detail the functions of calls of Bengalese finches. We observed the calling behavior of male birds presented movies of other male and female birds with and without their calls. We also evaluated the influence of other conspecific birds' calls on male calling behavior. Detailed sound analysis shows that several types of calls were produced by males. Our data also suggested that males have an ability to discriminate between other individuals, and that they are able to produce different types of calls in a context-dependent manner.

1 Introduction

Many avian species are known to produce long and complicated songs; their calls, in comparison, are shorter, acoustically less complex, and monosyllabic. All bird species, however, have a repertoire of calls that are produced in a context-dependent manner [1]. Bird's calls have the following functions: predator alarm [2, 3],

M. Osada
Faculty of Comprehensive Informatics, Shizuoka Institute of Science and Technology,
Toyosawa 2200, Fukuroi 437-8555, Japan

Graduate School of Science, Shizuoka University, Ohya 830, Suruga-ku, Shizuoka
422-8529, Japan

T. Okumura (✉)
Faculty of Comprehensive Informatics, Shizuoka Institute of Science and Technology,
Toyosawa 2200, Fukuroi 437-8555, Japan

RIKEN Brain Science Institute, 2-1, Hirosawa, Wako 351-0198, Japan
e-mail: tetsuok-tmdu@umin.ac.jp

announcement and exchange of food, signaling of aggression, and maintenance of social interactions [4]. Understanding the brain mechanisms underlying adaptation to a social context requires a multidisciplinary approach. To make a beginning with such an approach we asked the following 2 questions in this study: How many types of calls are present in the male Bengalese finch's call repertoire? If several types of calls are present, does the male Bengalese finch produce them in a context-dependent manner? To address these questions, we observed the vocal behavior of male birds presented movies of other male and female birds with and without their calls. We also evaluated the influence of other birds' calls on their vocal behavior.

2 Methods

2.1 *Subjects and Recordings of Vocalizations*

This study used one female and three male Bengalese finches, aged over 180 days. The birds were supplied by a local pet shop and did not have any experimental history. Birds were kept under a fixed 13:11 h light-dark cycle and given *ad libitum* access to food and water. Of these, two male birds (Bird 1 and Bird 2) were used as subjects. They were housed in a breeding cage (width \times depth \times height = 30 \times 15 \times 20 cm) and isolated in a sound-attenuated box for at least 30 days. They were allowed to move freely within the cage, and all their daytime vocalizations (calls and songs) were recorded on a hard disk drive. A microphone (ECM-MS957, Sony), microphone amplifier (AT-MA2, audio-technica), computer, and digital recording software (Avisoft-Recorder, Avisoft Bioacoustics, Berlin) were used for these recordings. The other two birds, one male and one female, were used for shooting auditory and visual stimuli.

2.2 *Stimulus and Experimental Procedures*

Four sets of 30-min movies of conspecific male and female birds were captured with and without vocal behavior using a high-resolution digital video camera (HDR-CX170, Sony). The recordings were shown to the caged birds on an LCD (TFT) monitor that was placed in the sound-attenuated box [5]. These movies were of both a female and a male, with and without calls. The size of the birds displayed on the monitors was set equal to the size of real birds.

These 30-min movies of other birds were presented once per hour during nine consecutive hours each day during a total of 3 days, and no movies or sounds were presented during inter-trial-intervals (ITI) those last 30 min. The first 5 min of vocalizations of the caged birds directly after playback started were analyzed, because vigorous behavioral change was observed consistently during these periods.

These auditory and visual stimulations and audio recordings were performed during 3 days for all five conditions (four movies and ITI [no movie, no call]).

The numbers of songs and calls produced were counted, and the phonetic parameters (sound pressure level, first and second formant frequency, and duration) of all calls were analyzed using sound analysis software (Avisoft-SAS Lab Pro, Avisoft Bioacoustics). The recorded calls were plotted on Formant 1 (F1) vs. Formant 2 (F2) plots (Fig. 2). For these formant analyses, we applied linear predictive coding (LPC).

3 Results

3.1 Call Repertoire and Context-Based Call Production

As seen in Fig. 1, six call types (A–F) were emitted by Bird 1. In the F1 vs. F2 plots of bird 1's calls (Fig. 2), most of the analyzed calls could be classified into 6 major clusters (A–F in Fig. 2). Calls belonging to the same cluster showed similar acoustic features on the spectrogram, and could be distinguished from calls in other clusters sound. However, border of the clusters B and C could not be defined clearly in our preliminary cluster analysis (K-means and EM clustering). Observed difference in acoustic feature may be attributed to difference in expiratory pressure pattern.

The calls in each cluster were produced in different context-dependent distributions. For example, call “B” was produced frequently when a male was presented to the bird, whereas call “F” was produced primarily when a female was presented (See histogram insets in Fig. 2). These kinds of differential distributions were also observed for Bird 2.

The pie charts in Fig. 3 show the frequency distributions of each call of Bird 1 (A–F) under four stimulus conditions and ITI (no movie, no call). These

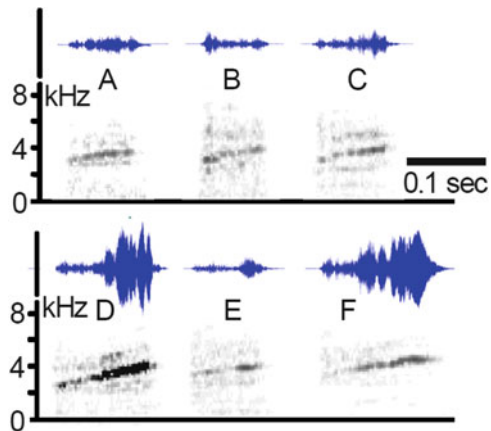


Fig. 1 Waveforms (*upper rows*) and sound spectrograms (*lower rows*) of Bird 1's calls (A–F). Calls “A” to “F” correspond to clusters “A” to “F” in Fig. 2, respectively

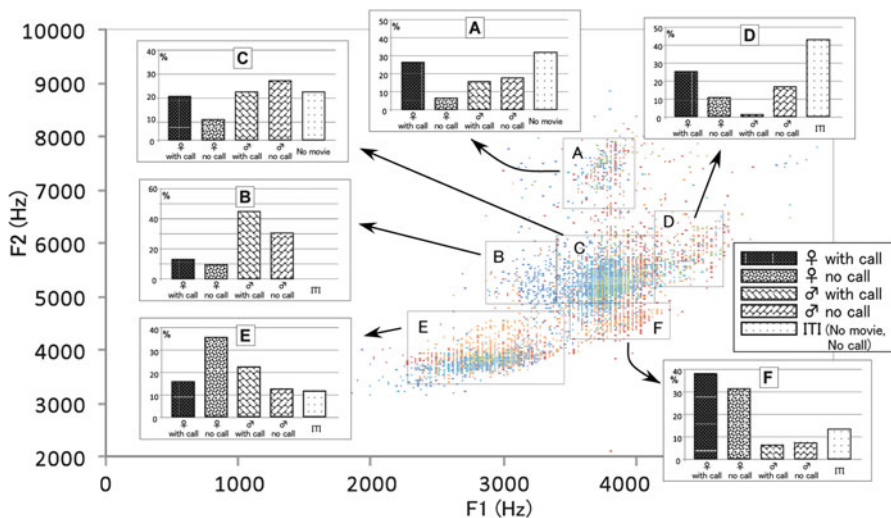


Fig. 2 F1-F2 plot of calls. The 8,557 calls plotted here were emitted by Bird 1 in the first 5 min of each of 5 conditions (movies of females with and without calls, movies of males with and without calls, ITI: The total analyzed duration of each condition was 135 min). A–F are the call clusters. The inset histograms show the conditions under which the calls in these clusters were produced

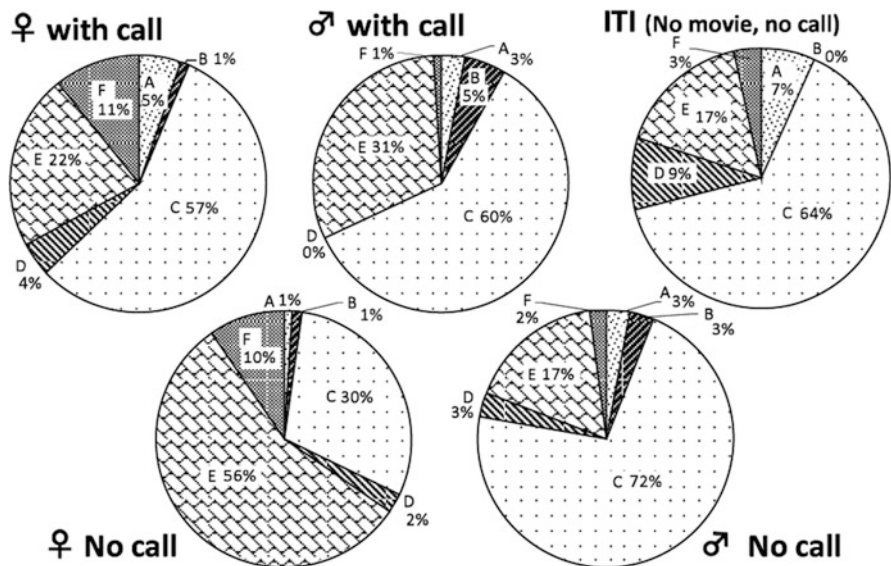


Fig. 3 Frequency distribution of each call (A–F) under five stimulus conditions. A–F indicate frequencies of calls A–F in Fig. 1, respectively

distributions of produced calls differ according to stimulus conditions. For example, calls F were emitted with higher frequencies when the subject bird was presented with movies of a female, rather than a male. Notable deviations were observed in comparison to female presentation with and without calls. When a movie of a female with its call was presented to Bird 1, a lower frequency of call E was observed. In contrast, the percentage of call C diminished when a female movie without call was presented to the bird.

3.2 Number, Average Duration, and Sound Pressure Level of Songs and Calls Produced Under Each Condition

The average numbers of songs by Bird 1 and Bird 2 produced in 1 h when presented with the movie of the female bird (♀) without call stimulus were 21.3 and 47 times/h, respectively. These were much higher frequencies than those produced when presented with the movie of a female with call stimulus (6.4 [Bird 1] and 28 [Bird 2] times/h). In contrast, as seen in Fig. 4, the number of calls produced when presented with the movie of a female without the call stimulus (776 [Bird 1] and 152 [Bird 2] times/h) were less than half those produced when presented with the movie of a female with the call stimulus (1,718 [Bird 1] and 977 [Bird 2] times/h). Taken together, besides the ITI periods, the song occurrence ratio in birds' vocal behavior ($\frac{\#songs}{\#songs + \#calls}$) was maximum when the birds were presented with movies of a conspecific female bird without call stimulus, and the call occurrence probability was maximum when the birds were presented with a female bird with call stimulus. In addition, the average sound pressure levels and call durations were higher when the subject birds were presented with movies of female birds, than when presented with movies of male birds (data not shown).

4 Discussion

Bengalese finches have sufficient visual [6, 7] and auditory [8–10] capacity to be used for discrimination of other conspecific individuals. Most previous research applied operant conditioning techniques. Such techniques have certain advantages in the evaluation of an animal's capability to discriminate between various types of stimuli. However, when researchers want to elucidate spontaneous animal responses in a natural social context, intensive observation of spontaneous behavior under various conditions could be a good alternative. The present study shows that male Bengalese finches altered their pattern of calling behavior in response to different types of auditory and visual stimuli of other conspecific individuals without any rewards and punishments. We established here that our experimental setup can be used to switch the mode of a bird's vocal behavior according to social context in a

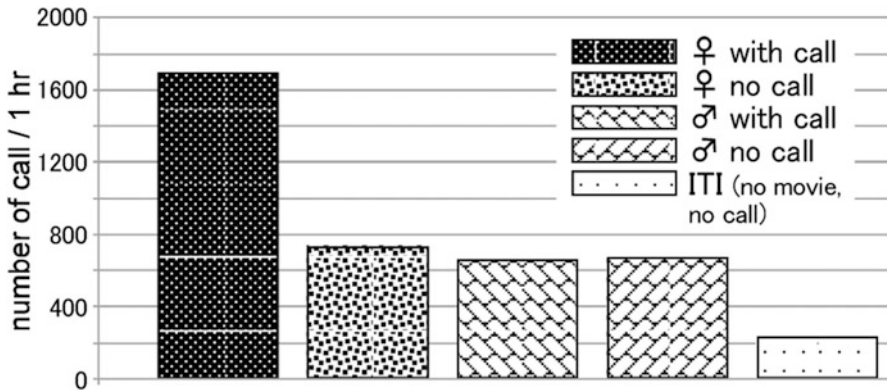


Fig. 4 Number of calls/h under five kinds of stimulus conditions. These numbers are the average number of calls/h of Bird 1. It was calculated based on the average number of calls in the first 5 min of each stimulus condition

more natural manner. In addition, present results also suggest that male Bengalese finches are able to discriminate between male and female by their appearance. These abilities of gender estimation and context discerning are fundamentals of their social behavior including mating. We next intend to elucidate the dynamic brain mechanisms that underlie context-based vocal behavior by using this setup.

Acknowledgments The authors thank Mr. T. Otsuka and Mr. Y. Yamazaki for their technical assistance. We also thank an anonymous reviewer for helpful comments. This study was supported by a Grant-in-Aid for Scientific Research on Innovative Areas “Neural creativity for communication (No.4103)” (22120516) of MEXT, Japan and Brainscience Grant on Creativity from NPO Neurocreative Laboratory to T.O.

References

1. Marlar, P. et al. (ed.): Nature’s music. The science of birdsong. Elsevier, Amsterdam (2004) 132–177
2. Griesser, M.: Referential calls signal predator behavior in a group-living bird species. *Cur. Biol.* 18 (2008) 69–73
3. Suzuki, T.: Parental alarm calls warn nestlings about different predatory threats. *Cur. Biol.* 21 (issue 1) (2011), R15–R16
4. Freeberg TM. & Harvey EM.: Group Size and Social Interactions Are Associated With Calling Behavior in Carolina Chickadees (*Poecile carolinensis*). *J. Comp. Psychol.* 122 (2008) 312–318
5. Ikebuchi, M. & Okanoya, K.: Male zebra finches and Bengalese finches emit directed songs to the video images of conspecific Females Projected onto a TFT display. *Zool. Sci.* 16 (1999), 63–70
6. Watanabe, S. and Jian, T.: Visual and Auditory Cues in conspecific discrimination learning in Bengalese Finches. *J. Ethol.* 11 (1993), 111–116

7. Watanabe, S., Yamashita, M., & Wakita, M. Discrimination of video image of conspecific individuals in Bengalese finches. *J. Ethol.* 11, (1993) 67–72
8. Okanoya, O. and Kimura T.: Acoustical and perceptual structure of sexually dimorphic distance calls in Bengalese finches (*Lonchura striata domestica*). *J. Comp Psychol.* 107 (1993) 386–394
9. Okanoya, K., Tsumaki, S., & Honda, E. (2000). Perception of temporal properties in self-generated songs by Bengalese finches (*Lonchura striata* var. *domestica*). *J. Comp Psychol.* 114, 239–245.
10. Ikebuchi, M., & Okanoya, K. (2000). Limited auditory memory for conspecific songs in a non-territorial songbird. *Neuroreport.* 27, 3915–3919

Capturing the Global Behavior of Dynamical Systems with Conley-Morse Graphs

Zin Arai, Hiroshi Kokubu, and Ipei Obayashi

Abstract We present a computational machinery for describing and capturing the global qualitative behavior of dynamical systems (Arai et al. *SIAM J Appl Dyn Syst* 8:757–789, 2009). Given a dynamical system, by subdividing the phase space into a finite number of blocks, we construct a directed graph which represents the topological behavior of the system. Then we apply fast graph algorithms for the automatic analysis of the dynamics. In particular, the dynamics can be easily decomposed into recurrent and gradient-like parts which allows further analysis of asymptotic dynamics. The automatization of this process allows one to scan large sets of parameters of a given dynamical system to determine changes in dynamics automatically and to search for “interesting” regions of parameters worth further attention. We also discuss an application of the method to time series analysis.

The method presented in Sects. 1–4 below is given in [1] for the first time, which is based on and combines a number of theoretical results as well as computational software packages developed earlier. For the details, see the original paper [1].

1 Conley-Morse Decompositions

Throughout the paper, we assume that the system is given by a family of continuous maps

$$f: \mathbb{R}^n \times \mathbb{R}^d \ni (x, \lambda) \mapsto f_\lambda(x) \in \mathbb{R}^n.$$

Z. Arai (✉)

Creative Research Institute, Hokkaido University, Sapporo, 001-0021, Japan

JST CREST, 5, Sanbancho, Chiyoda-ku, Tokyo, 102-0075, Japan

e-mail: arai@cris.hokudai.ac.jp

H. Kokubu • I. Obayashi

Department of Mathematics, Kyoto University, Kyoto, 606-8502, Japan

JST CREST, 5, Sanbancho, Chiyoda-ku, Tokyo, 102-0075, Japan

Y. Yamaguchi (ed.), *Advances in Cognitive Neurodynamics (III)*,

DOI 10.1007/978-94-007-4792-0_89,

© Springer Science+Business Media Dordrecht 2013

We are interested in the analysis of global dynamics generated by f as the parameter λ is varied over \mathbb{R}^d . In most situations, only some bounded regions $R \subset \mathbb{R}^n$ and $\Lambda \subset \mathbb{R}^d$ have physical meaning for the analyzed model. If both R and Λ are rectangular regions then one can easily introduce finite rectangular grids \mathcal{H} and \mathcal{L} in both of them.

A *Morse decomposition* of a dynamical system is a finite collection of disjoint isolated invariant sets S_1, \dots, S_n (called *Morse sets*) with strict partial ordering $<$ on the index set $\{1, \dots, n\}$ such that for every x in the phase space there exist indices $i < j$ such that the α - and ω -limit sets of x is contained in S_j and S_i , respectively. A Morse decomposition can be represented in terms of a directed graph $G = (V, E)$ where $V = \{S_1, \dots, S_n\}$ and $(S_i, S_j) \in E$ iff $j < i$. This graph is called a *Morse graph*. If each Morse set is assigned its Conley index [3, 4] then such a structure is called a *Conley-Morse decomposition*, and the corresponding graph is called a *Conley-Morse graph* [1].

Note that a Morse decomposition of X is not unique. In particular, if i, j are such indices that $i < j$ but there is no other index k such that $i < k < j$ then one can create a coarser Morse decomposition by replacing S_i and S_j with $S_i \cup S_j \cup C(i, j)$, where $C(i, j)$ denotes the union of the images of all the complete orbits such that $\gamma(t) \rightarrow S_i$ and $\gamma(-t) \rightarrow S_j$ as $t \rightarrow \infty$.

2 Graph Representation

Given a formula for f_λ and some grid \mathcal{H} in the region $R \subset \mathbb{R}^n$, for each parameter set $L \in \mathcal{L}$ one can use the interval arithmetic directly to compute a combinatorial representation $\mathcal{F}_L: \mathcal{H} \rightarrow \mathcal{H}$ for f_λ , which then will be represented by a directed graph $G = (V, E)$ where $V = \mathcal{H}$ and $(v, w) \in E$ iff $w \in \mathcal{F}(v)$. It turns out that the analysis of the graph G can easily provide meaningful information on the asymptotic dynamics of f_λ represented by \mathcal{F}_L . For example, each *combinatorial invariant set* defined as a set $S \subset \mathcal{H}$ for which $S \subset \mathcal{F}(S) \cap \mathcal{F}^{-1}(S)$ covers an isolated invariant set with respect to f_λ . More precisely, if S is a combinatorial invariant set then $|S|$ is an isolating neighborhood, and if S is an isolated invariant set with respect to f_λ for some $\lambda \in L$ then its minimal cover S is a combinatorial invariant set. Another example is a *combinatorial attractor* defined as a set $\mathcal{A} \subset \mathcal{H}$ such that $\mathcal{F}(\mathcal{A}) \subset \mathcal{A}$ which covers a real attractor for f_λ . In fact, if \mathcal{A} is a combinatorial attractor then $|\mathcal{A}|$ is an isolating neighborhood whose invariant part $A := \text{Inv}|\mathcal{A}|$ is stable in the sense of Conley, that is, every positive semitrajectory starting in some open neighborhood of A tends to A . In particular, if there exist two combinatorial attractors for \mathcal{F}_L then this implies the existence of two disjoint attraction basins for f_λ for every $\lambda \in L$. See [2] for detail.

Extensive analysis of the dynamics can be obtained by computing the *strongly connected components* of G . It is known that all the strongly connected components of G form isolating neighborhoods for the union of all the chain recurrent sets of

the dynamical system, and thus can serve as a *combinatorial Morse decomposition* $\{\mathcal{M}_i : i = 1, \dots, k\}$, for some $k > 0$, which represents a family of isolating neighborhoods $|\mathcal{M}_i|$. The sets \mathcal{M}_i are called *combinatorial Morse sets*. A partial order $<$ between the computed combinatorial Morse sets can be determined by the analysis of paths in G connecting those sets.

3 Continuation and Bifurcations

If two adjacent sets of parameters $L_1, L_2 \subset \Lambda$, with $L_1 \cap L_2 \neq \emptyset$, are considered, and the combinatorial Morse decompositions computed for L_1 and L_2 are equivalent then we talk about *continuation* of combinatorial Morse decompositions. More precisely, let $(\mathcal{M}_1^1, \dots, \mathcal{M}_{k_1}^1, <^1)$ be a combinatorial Morse decomposition for \mathcal{F}_{L_1} and let $(\mathcal{M}_1^2, \dots, \mathcal{M}_{k_2}^2, <^2)$ be a combinatorial Morse decomposition for \mathcal{F}_{L_2} . We say that these decompositions are *equivalent* if $k := k_1 = k_2$ and there exists a bijection b of the set $\{1, \dots, k\}$ onto itself such that $\mathcal{M}_i^1 \cap \mathcal{M}_j^2 \neq \emptyset$ iff $j = b(i)$, and b does not violate the order defined by the relations $<^1$ and $<^2$, that is, for no i, j one has $i <^1 j$ and $b(j) <^2 b(i)$.

This definition provides a very weak kind of continuation; it is, in fact, the continuation of isolating neighborhoods in the sense of Conley (see [3]). In particular, the lack of continuation *suggests* a substantial change in dynamics. It *implies* such a change only if one ignores spurious Morse sets in the comparison of combinatorial Morse decompositions. One can use the Conley index to determine which combinatorial Morse sets are *not* spurious, and the lack of continuation between those sets with nontrivial Conley indices implies that a bifurcation is taking place. The type of bifurcation can be determined to certain extent by analyzing failures of continuation; for example, a bifurcation that resembles the saddle-node bifurcation at the scale of isolating neighborhoods can be detected as a series of two failures of continuation: first, a combinatorial Morse set with a trivial index appears from nothing, and second, this set splits into two combinatorial Morse sets with non-trivial indices, one corresponding to a stable fixed point or periodic orbit, and the other one corresponding to an unstable fixed point or periodic orbit, respectively.

4 Applications

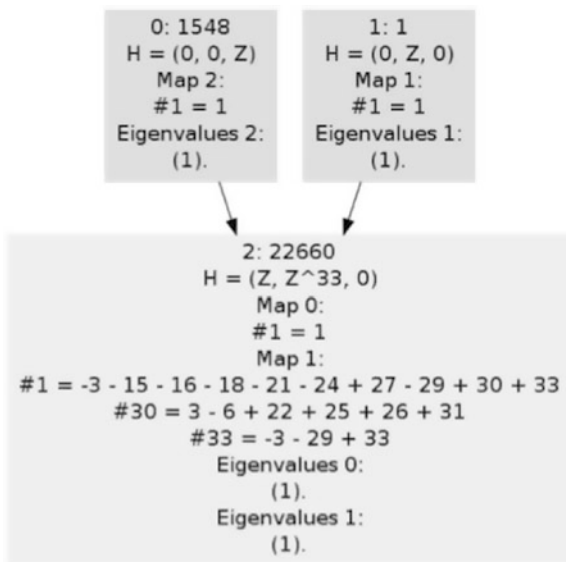
The practicality of the method is illustrated in [1] with the application to the 2-dimensional non-linear Leslie population model $f: \mathbb{R}^2 \times \mathbb{R}^4 \rightarrow \mathbb{R}^2$, which is given by

$$f(x, y; \theta_1, \theta_2, \kappa, p) = ((\theta_1 x + \theta_2 y) e^{-\kappa(x+y)}, px).$$

Fig. 1 Morse decomposition for $\theta_1 = \theta_2 = 32.0$



Fig. 2 Conley-Morse graph for $\theta_1 = \theta_2 = 32.0$

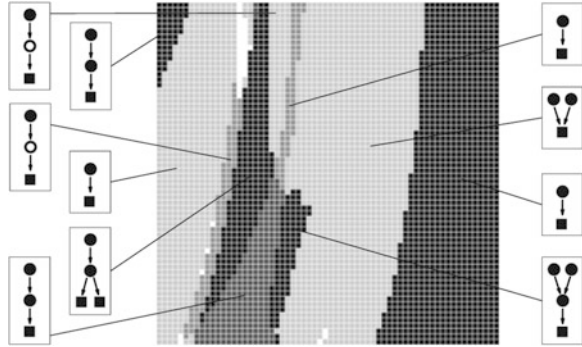


The numerical studies in [5] indicate that this system exhibits a wide variety of different dynamical behavior, and thus is considered a meaningful test for the usefulness of our method. In particular, the coexistence of multiple chaotic attractor, a very important behavior from a practical point of view, is observed for some parameter values [5]. However, the computation in [5] is done only for a limited set of parameters and therefore, we would like to ask when this coexistence happens for a larger parameter region.

The parameter κ is just a rescaling factor, so it is arbitrarily set to 0.1, as in [5]. The parameter p is fixed to 0.7, also the same as in [5].

By applying our method to the nonlinear Leslie model with $\theta_1 = \theta_2 = 32.0$, we obtain Figs. 1 and 2. Figure 1 shows resulting three Morse sets: the fixed point at

Fig. 3 “Bifurcation” diagram



the origin, the oval-shaped region in the middle and the largest one surrounding oval one. Figure 2 is the Conley-Morse graph. The numbers inside the vertices carry the information of Conley indexes of associated Morse sets. From this graph, we can read the coarse gradient behavior of the dynamics: the origin and the oval invariant set are relative repellers and there exist connecting orbits from these repellers to the attractor.

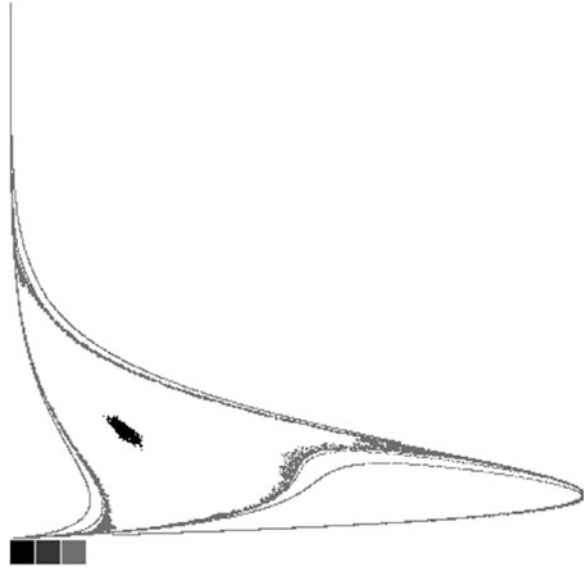
The result of the continuation analysis of the previous section is illustrated in Fig. 3. For simplicity, the parameter space $(\theta_1, \theta_2) \in [10, 35]^2$ is subdivided into 64×64 equal squares here. The bounded region R in the phase space is subdivided into 4096×4096 rectangles of the same size and a combinatorial Conley-Morse decomposition is computed for each parameter box using this grid. In the picture, adjacent boxes in the parameter space (θ_1, θ_2) with equivalent Morse decompositions are plotted in the same shade of gray and white squares correspond to parameter boxes for which no continuation could be found to any adjacent box. The transitive reduction of the Morse graph is illustrated for some regions; a square indicates an attractor, a filled circle corresponds to a Morse set with a nontrivial Conley index, and a hollow circle indicates a Morse set with the trivial Conley index. From the figure, we can easily identify the parameter region with multiple attractors. We want to emphasize here that this computation is fully automatic and no a priori knowledge is required. Therefore our method can also be applied for higher dimensional problems where it is difficult to answer the number of attractors from simple numerics.

One can interactively explore computational results explained in this section at the project web site <http://chomp.rutgers.edu/database/>.

5 Time Series Analysis

In practical applications, the data of the system of our interest is often provided as a time series coming from experiments. In this section, we thus present some preliminary computations towards the application of Conley-Morse graph method to time series analysis.

Fig. 4 From a time series of length $30 \times 2,000$



We remark that in real experiments, the size of the data is always finite. Therefore even if we know that the system is driven by a continuous dynamical system, its behavior can not be entirely reconstructed from the data. Hence, our goal would be to reconstruct a coarse-grained system as close to the original one as possible. Since the Conley-Morse graph method explained in previous sections involves a procedure of coarsening, namely, fixing a grid-size on the phase space and ignoring the behavior of the system smaller than this grid size, it is natural to apply this method to time series analysis.

For this purpose, we need to notice that due to practical restrictions on experiments, a time series is usually not fully distributed on the phase space or attractors of the system. That is, the information of the system may be missing on significantly large parts of the phase space. And furthermore, a times series may contain unknown experimental noise. Therefore, we muse discuss the robustness of the Conley-Morse graph computation under the existence of noise and deficits.

Figure 4 illustrates the result of a Morse decomposition for a time series of length $30 \times 2,000$ (the data of 2,000 orbits of length 30) generated by the non-linear Leslie model with $\theta_1 = \theta_2 = 32.0$. Compared with Morse sets in Fig. 1 where we constructed them directly from the dynamics, we find that Morse sets reconstructed here from the time series miss some parts while their rough geometric shapes are similar.

Figure 5 is the same as Fig. 4, but for a time series of length 30×500 . Notice that although the size of the series is one-fourth of the first figure, we still have a qualitatively similar decomposition of the invariant set.

Figure 6 shows the Morse decomposition obtained for a noisy time series. The parameter of the system is the same as before, but here we put Gaussian noise of

Fig. 5 From a time series of length 30×500

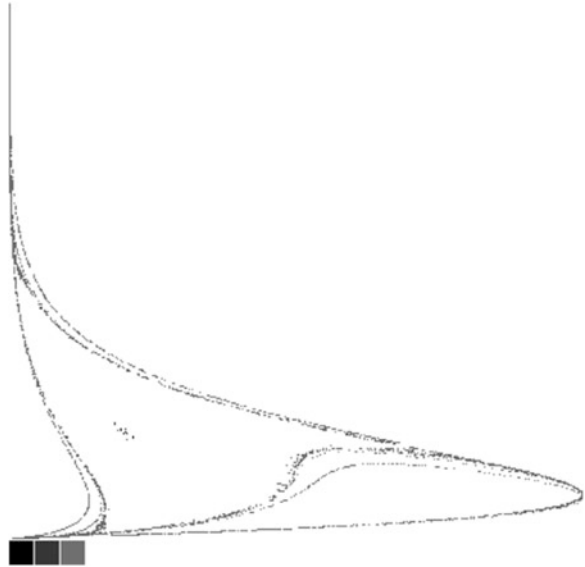
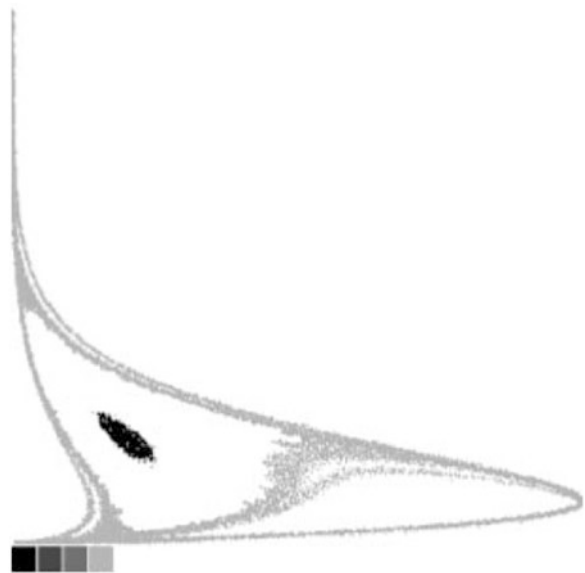


Fig. 6 From a noisy time series



standard deviation 0.15. Notice that the shape of Morse sets now blurs to some extent but still keeps the essential structure of the original decomposition.

These computations advocate a vague kind of robustness of Conley-Morse graph and possible application to times series analysis. To obtain mathematically meaningful results, we need a more detailed study on it taking the dependency of Conley-Morse graph on noise and deficits into account. This will be discussed elsewhere.

References

1. Arai, Z., Kalies, W., Kokubu, H., Mischaikow, K., Oka, H. and Pilarczyk, P., *SIAM Journal on Applied Dynamical Systems*, **8** (2009), 757–789.
2. Arai, Z., Kokubu, H. and Pilarczyk, P., *Japan Journal of Industrial and Applied Mathematics*, **26** (2009) 393–417.
3. Conley, C., *Isolated Invariant Sets and the Morse Index*, CBMS Regional Conference Series in Math., **38**, Amer. Math. Soc., Providence, RI, 1978.
4. Mischaikow, M. and Mrozek, M., Conley index, *Handbook of dynamical systems*, Vol. 2, North-Holland (2002), 393–460.
5. Ugarcovici, I. and Weiss, H., *Nonlinearity* **17** (2004) 1689–1711.

A Heuristic Model of Intra-brain Communications Using Chaos in Artificial Neuron Systems

Yu Arai, Ryota Mori, Fuyuki Aoto, and Shigetoshi Nara

Abstract To show a functional role of chaos in brain, a heuristic model to consider mechanisms of intra-brain communications is proposed. The key idea is to use chaos in firing pattern dynamics of artificial neuron networks as propagation medium of pulse signals. The two kinds of networks, one consisting of two-state neuron model, and the other, pseudo-neuron device model using opto-electronic technology, are employed to evaluate signal transport characteristics by calculating correlation functions between sending elements and receiving elements of pulse signals.

1 Introduction

Rapid progress in studying biological information and control processing, particularly brain functions, suggests that they might be based on novel *dynamical mechanisms* which result in excellent functioning of brain [1–4]. Associated with these ideas, the other new approaches, for example, “neural network processing”, “self-organization” and so on, have been appearing in the last few decades. In these approaches, complex dynamics including chaos in systems with large but finite degrees of freedom are considered from the viewpoint that they would play important roles in complex functioning and controlling of biological systems including brain. Particularly, Nara and Davis have been considering, “What is the role of chaos in functioning or controlling?”, in other words, “Can we show that chaos works effectively as a dynamic machine under various environments?” [5]. Along these ideas, in their functional experiments, chaotic dynamics was applied to solving a memory search task or an image synthesis task set in ill-posed context [5]. Furthermore, the idea has been extended to challenging applications of chaotic

Y. Arai • R. Mori • F. Aoto • S. Nara (✉)

Department of Electrical and Electronic Engineering, Graduate School of Natural Science and Technology, Okayama University, Okayama, 700-8530, Japan
e-mail: nara@elec.okayama-u.ac.jp

dynamics to control. Chaotic dynamics in a recurrent neural network model was applied to control tasks, for example, a task in which an object solves a two-dimensional maze to catch a target [6, 7], or to capture a target moving along different trajectories [8]. From the results of computer experiments, we concluded that chaotic dynamics could be useful not only in solving ill-posed problems but also in controlling systems with many degrees of freedom.

In this paper, we develop this idea to show phenomena of synchronization of firing patterns between far distant neurons, which are observed in physiological-, fMRI-, and EEG-experiments on brains, associated with advanced functioning (for example, see [9]). The important point of the observed synchronization phenomenon is that there does not appear to be any strongly correlated activity in the intermediate neurons located between the synchronized neurons. We consider that intermediate neurons may be chaotic. In our work, the key idea is to use chaos in firing pattern dynamics of artificial neuron networks as propagation medium of neuron signals. So, to show a functional role of chaos in intra-brain communications, two kinds of heuristic model are proposed. One is a recurrent neural network consisting of two-state neuron model, and the other is a network consisting of pseudo-neuron device model to be made using opto-electronic technology. To evaluate signal transport characteristics, correlation functions between sending elements and receiving elements of pulse signals are calculated and they exhibit that chaos can work as a transport medium of pulse signals which is robust to local defects of neurons.

2 A Recurrent Neural Network Model

Employing a two-state neuron model, let us consider a recurrent neural network shown in Fig. 1 and define the updating rule of firing patterns (state vectors) as $x_i(t+1) = \text{sgn}\left[\sum_j^N w_{ij}x_j(t) - \theta_i\right]$, where $\{x_i = \pm 1 | i = 1 \sim N\}$ and $\text{sgn}(u) = 1(-1); u \geq 0(u < 0)$. $\{w_{ij} | i, j = 1 \sim N\}$ is a synaptic strength matrix and can be determined so as to embed intended patterns as attractors (memories) in state updating. θ_i is threshold and is taken to be 0 without loss of generality. N is the number of neurons and is 400 or 900 in the present paper. The embedded patterns in our computer experiments are shown in Fig. 2.

3 Pseudo Neuron Device

In our previous works [10, 11] *SEED Device* (Fig. 3) *DSEED (Dynamic Self Electro-optic Effect Device)* (Fig. 4) was proposed, where the device consist of seriesly coupled *pin* diode (*p*-type semiconductor, ~ 10 nm intrinsic semiconductor layer made from multi-quantum wells (abbreviated as *i*), and *n*-type semiconductor) (Fig. 5). As shown in Fig. 10, when incident light with having appropriately chosen

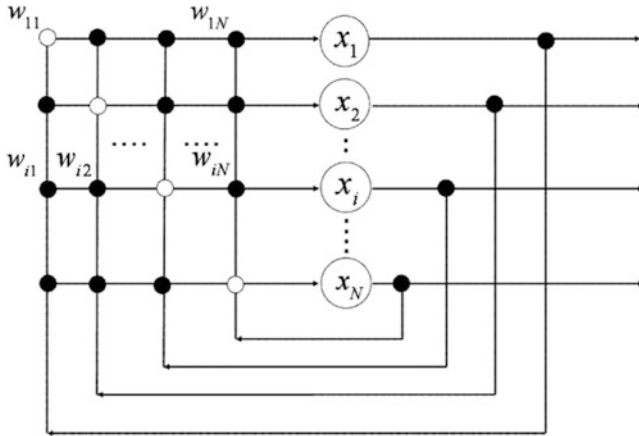
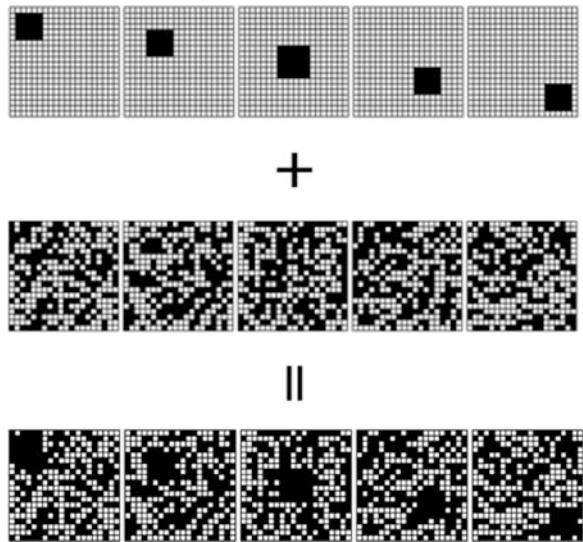


Fig. 1 A recurrent neural network model

Fig. 2 Propagation of fired block pattern in a recurrent neural network model (The initial five patterns in a cycle attractor consisting of 30 patterns)



power (P_{in}) and wave length (frequency ω), with feedback light from lower device as well, is given, pulse oscillation of photo-current occurs in the circuit, as shown in Fig. 6.

The rate equations of the photocarrier densities $\{n_{ij} | i, j = 1 \sim \sqrt{N}\}$ about both the *upper* device and the *lower* device indicated by the suffixes u and l are written as follows, $\frac{dn_{i,j}^{u(l)}}{dt} = -\frac{n_{i,j}^{u(l)}}{\tau_{u(l)}} + \frac{\alpha_{u(l)}(P_{in} + m_l n_{i,j}^l + (-m_u n_{i,j}^u))\Omega_{u(l)}}{\{\omega - \omega_{u(l)} + \beta_{u(l)}(V_{u(l)} - \eta_{u(l)} R_{u(l)} n_{i,j}^{u(l)})^2 + (\Omega_{u(l)}/2)^2\}}$, where the detailed discussion was given in our previous works [12]. Hereafter, the position index $\{(i, j) | i, j = 1 \sim \sqrt{N}\}$ in two dimensional configuration will be replaced $\{i | i = 1 \sim N\}$ in one dimensional rearranged configuration without explicit noting.

Fig. 3 Single SEED

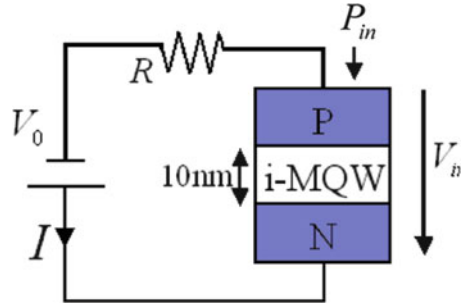
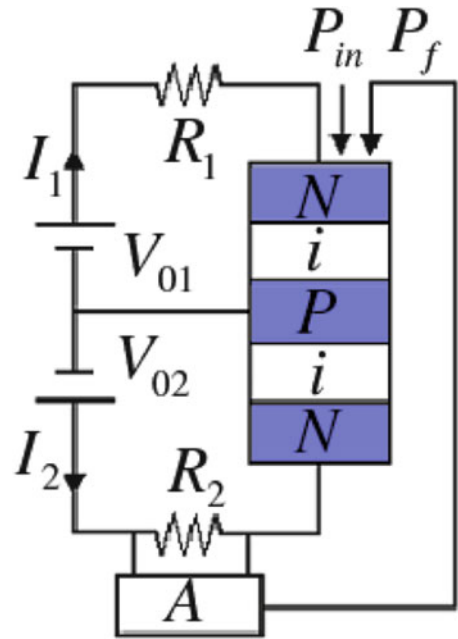


Fig. 4 Serially connected SEEDs with feedback



4 Small World Network and Signal Propagation via Chaos

In connecting between elements in our network model (400 or 900 elements), we employed the Barabasi-Albert (BA) connections that is one of the small world network models, where it has both scale free and small world properties, but does not have cluster property [13]. The connections are shown in Fig. 7, where each element is put on circle array configuration and connections are represented by lines. Blue color represents sending elements and connecting lines from them and red color represents receiving elements and connecting lines from them (Fig. 8).

In the case of the coupled two state neuron network with the given synaptic connection strength $\{w_{ij}\}$ that is determined so as to embed cycle attractor(s), the definite connections are put vanished except the connections resulting from BA

Fig. 5 Stationary solutions of D-SEED. Note that there exists light power region which gives only unstable fixed point

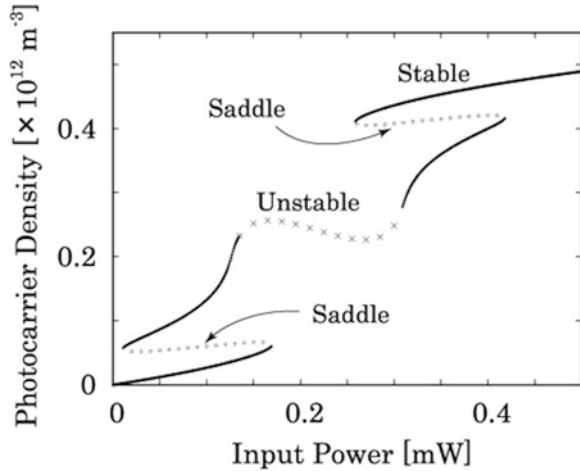
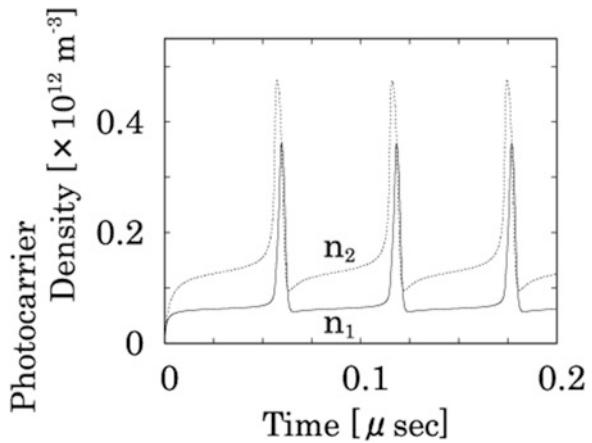


Fig. 6 Pulse oscillation (limit cycle) around unstable fixed point



connecting processes, and then the updated patterns show chaotic dynamics (Fig. 9). In this paper, let us give weight to the results of DSEED-experiments, and the results of the two-state neural network with small world property will be reported elsewhere.

In the case of DSEED network, we introduce diffusive coupling of photocARRIER densities between elements with BA connections. Time developments of this network also show chaotic dynamics when we solve the set of coupled $2 \times (400 \text{ or } 900)$ rate equations by numerical methods starting from arbitrarily given initial conditions. Let us consider the case, $N = 900$, and set a group for sending elements to emit pulse signals and a group for receiving elements of them, where the both group contain a certain number of elements about one order of magnitude less than N . Discarding the detailed explanation about the selecting method, actually chosen numbers of elements are 37 for sending elements and 20 for receiving

Fig. 7 Small world network made by BA method

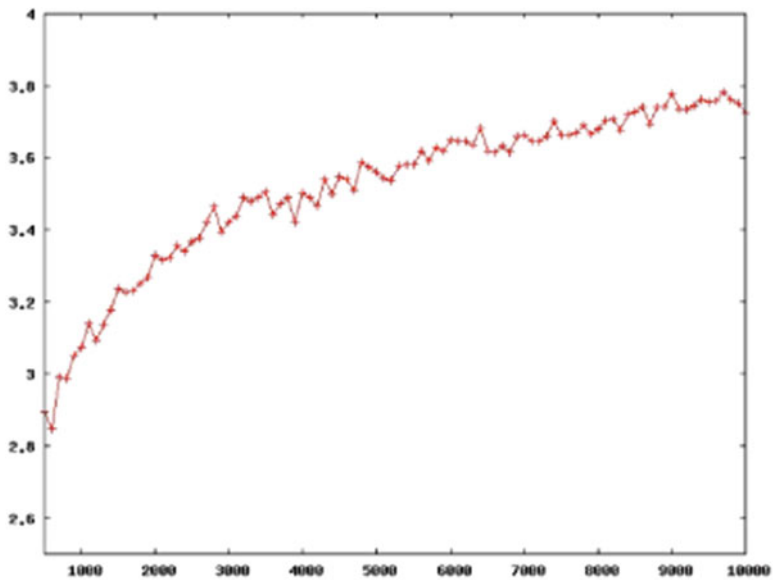
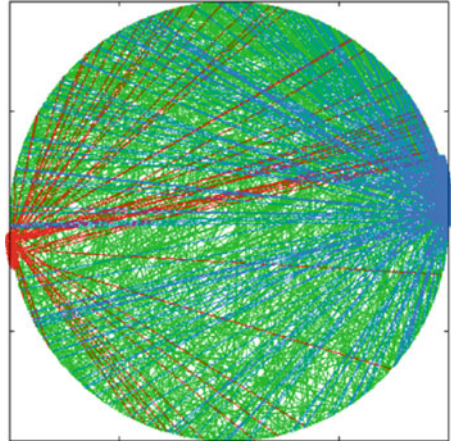


Fig. 8 Averaged minimum path length vs. the total number of elements. Note that it is well represented by $\sim \log N$

elements, which are shown in Figs. 7 and 10. It should be noted that there is *no direct connection* between the sending elements and the receiving elements in the present case, and the averaged minimum path length between sending elements and receiving elements is 4.52.

Fig. 9 A snap shot of firing pattern in our binary neuron network model

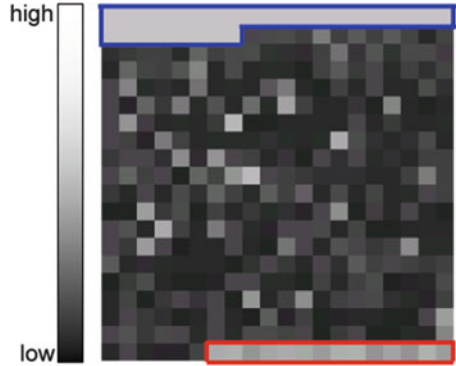
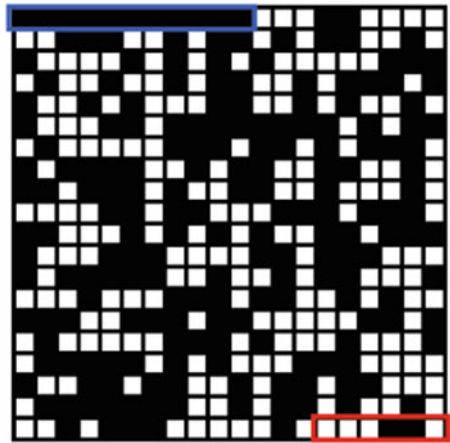


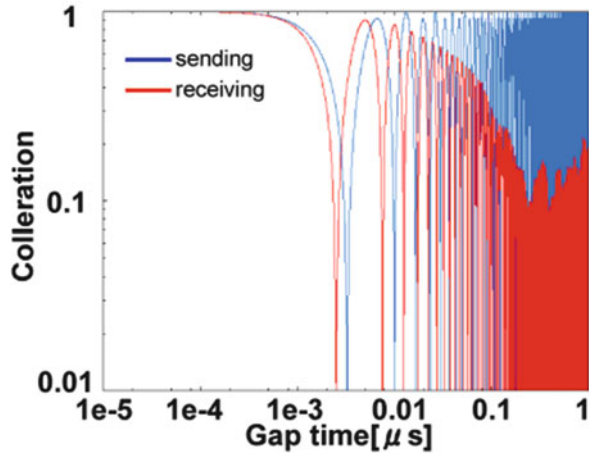
Fig. 10 A snap shot of network pattern in *gray scale*



5 Results

To compare mutual correlations with the sending elements, we have chosen the five elements having the averaged minimum path length, 2.81, 3.89, 4.38, 4.51, and 5.59, respectively. So, in this choice, receiving elements are located at about middle (averaged) distance from sending elements. We choose 0.210 mW of the incident light power for the both sending and receiving elements because this light power leads the elements to synchronizing when there is no external disturbance. To all of the other elements, the incident light power is kept to be 0.155 mW, which results in chaos. When the receiving elements are exposed to chaos generated by the other elements via diffusive coupling terms, $D \sum_l (n_l - n_i)$, and under the condition that the sending elements do not emit pulse signals, then the receiving elements are also in chaotic state. To evaluate these dynamical properties more accurately, it is appropriate to calculate correlation functions defined as

Fig. 11 Auto correlation of sending and receiving elements in the case of no signal from sending elements



$$f_{n_i n_j}(\tau) = \frac{\frac{1}{T} \sum_{t=1}^T \{n_i(t) - \bar{n}_i\} \{n_j(t + \tau) - \bar{n}_j\}}{\sqrt{\frac{1}{T} \sum_{t=1}^T \{n_i(t) - \bar{n}_i\}^2} \sqrt{\frac{1}{T} \sum_{t=1}^T \{n_j(t) - \bar{n}_j\}^2}} \quad (1)$$

$$\bar{n}_i = \frac{1}{T} \sum_{t=1}^T n_i(t), \quad \bar{n}_j = \frac{1}{T} \sum_{t=1}^T n_j(t), \quad (2)$$

where $n_i(t)$ is photo-carrier density of the i -th elements (either upper or lower). The result of calculation about an auto correlation function of the sending elements indicates that they are synchronizing according to a cooperative effect between them. Now, under the condition that the sending elements are not connected to the outer elements, so pulses are not emitted to the network, the result of calculation about an auto correlation function of receiving elements shown in Fig. 11 (left) indicates a power law decaying depending on time shift τ . It means that the dynamic state is surely chaos but weak dynamical characteristics remains even in chaos. The mutual correlation functions between the sending elements and the other elements including the receiving elements are calculated and they indicate that there are no correlation between them.

On the other hand, once pulses from the sending elements are emitted to the outer elements, the autocorrelation function of the receiving elements and the mutual correlation between the receiving elements and the sending elements drastically change as shown in Figs. 12–14.

Fig. 12 Auto correlation of sending and receiving elements with existence of pulse signals from sending elements

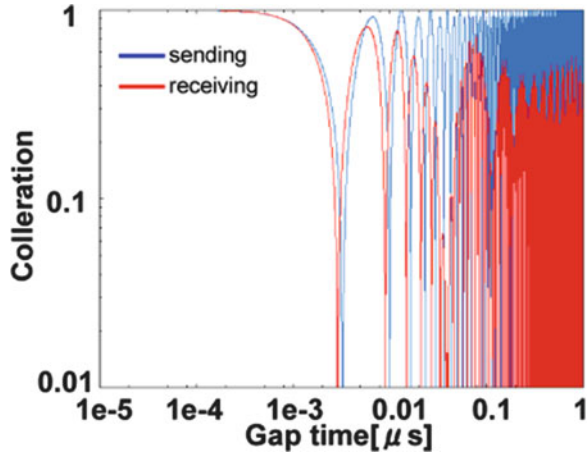
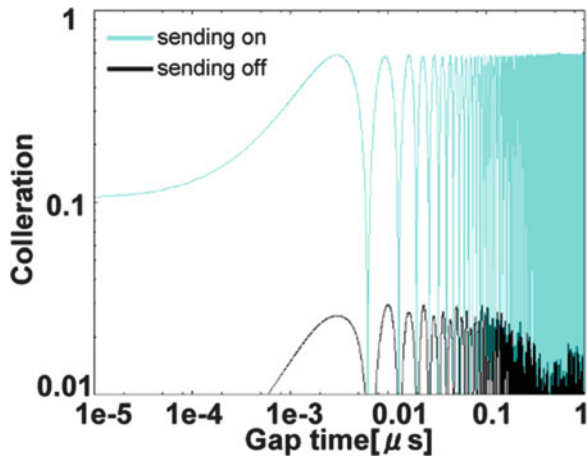
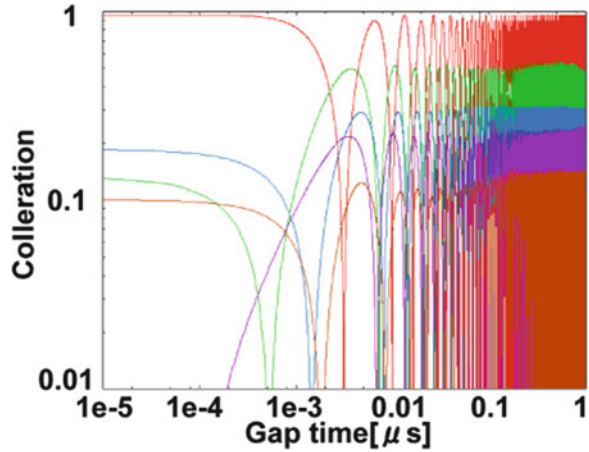


Fig. 13 Correlation between sending and receiving elements in the case of no signal from sending elements and with signal. Note that correlation increases from ~ 0.02 to ~ 0.6



First, the autocorrelation function indicates that the receiving element is almost synchronizing because the power law decaying vanishes and a stationary oscillatory behavior is kept depending on time shift τ . Second, about the mutual correlation function between the receiving elements and the sending elements, the amplitude becomes more than one order of magnitude bigger than the case with no influence via the sending elements. The mutual correlations between the other elements and the sending elements increases, however, it should be noted that the increasing about the receiving element exceeds that of the other elements having the same averaged minimum path length to the sending elements. This means that the receiving elements sensitively respond to small signal fragments from the sending elements via chaos, and the fragments stimulate synchronization of the receiving elements.

Fig. 14 Correlation between sending and chaos elements under the existence of sending signals



6 Conclusion

1. Without emitting of pulse signals from the sending elements to the surrounding ones, the receiving elements are in chaos under the strong influence of chaotic driving from surrounding elements.
2. Once pulse signals are emitted from the sending elements, then the receiving elements synchronize with the sending elements stimulated by arrived very small fragments of synchronous pulses from the sending elements propagated through the sea of chaos.

References

1. I. Tsuda Behavioral and Brain Sciences, Vol. 24, pp. 793–847 (2001).
2. H. Fujii, H. Itoh, K. Aihara, N. Ichinose, and M. Tsukada, Neural Networks, 9 (1996) p. 1303
3. M. Adachi and K. Aihara, Neural Networks 10(1997) pp. 83–98.
4. C. A. Skarda and W. J. Freeman, Behavioural and Brain Sciences, **10** (1987) pp. 161–195
5. S. Nara, P. Davis, Prog. Theor. Phys. **88** (1992) 845–855, and S. Nara, Chaos **13**(3) (2003) 1110–1121
6. Y. Suemitsu, S. Nara, Neural Computation, **16**(9) (2004)1943–1957
7. Y. Li, S. Kurata, S. Morita, S. Shimizu, D. Munetaka and S. Nara : Biological Cybernetics, **99**, p. 185 (2008)
8. Y. Li and S. Nara, Cognitive Neurodynamics, vol. 2, pp. 39–48, 2008.
9. Y. Yamaguchi, Lect. Notes Comput. Sci. 5286: 1–12 (2008).
10. S. Nara, Y. Tokuda, Y. Abe, M. Yasukawa, N. Tsukada, and H. Totsuji, J. Appl. Phys **75**(8) April, pp. 3749–755(1994)
11. Y. Ohkawa, T. Yamamoto, T. Nagaya, S. Nara Appl. Phys. Lett. **86**, p. 111107(2005)
12. T. Yamamoto, Y. Ohkawa, T. Kitamoto, T. Nagaya, and S. Nara: Int. Journal of Bifurcation and Chaos, **16**, p. 3717(2006)
13. A.-L. Barabasi, R. Albert, and H. Jeong, Physica A, **272**, p.173 (1999)

Transitory Memory Retrieval in the Neural Networks Composed of Pinsky-Rinzel Model Neurons

Hiromichi Tsukada, Yutaka Yamaguti, Hiroshi Fujii, and Ichiro Tsuda

Abstract It has been proposed an abstract memory model of cortex that the recurrent network with inhibitory interneurons shows the successive retrieval of memories. It has not, however, been clarified whether such behavior appears in the realistic network model with the Hodgkin-Huxley type of neuron. By using the realistic model that consists of excitatory neurons and inhibitory interneurons, we here show that the successive retrieval of memories is also observed in the network of biologically-plausible model neurons.

Biologically, there is evidence for the involvement of acetylcholine (ACh) in attentional modulation and cholinergic projection decreases IPSPs in pyramidal neurons in layer 2/3 of the cerebral cortex.

Our simulation result shows that the coupling strength of inhibitory interneurons is very crucial for controlling the states of memory retrieval; all firing state, memory completion state and successive memory retrieval state. The field potential of the network in each state of memory retrieval has a specific frequency band. In this paper, we discuss the effects of the coupling strengths of inhibitory interneurons, the states of memory retrieval and the characteristics of frequency band in relation to the neurophysiological experimental data.

H. Tsukada (✉)

Department of Mathematics, Graduate School of Science, Hokkaido University,
Sapporo 060-0810, Japan
e-mail: tsukada@math.sci.hokudai.ac.jp

Y. Yamaguti • I. Tsuda

Research Institute for Electronic Science, Hokkaido University, Sapporo 060-0812, Japan

H. Fujii

Department of Intelligent Systems, Kyoto Sangyo University, Kyoto 603-8555, Japan

1 Introduction

In the layer 2/3 of the cerebral cortex, pyramidal cells are reciprocally connected by recurrent connections and GABAergic neurons are locally connected to the pyramidal cells. Such an abstract network model has the ability to retrieve memories from incomplete sets of cues, which is a pattern completion in memory systems. It has been proposed an abstract model that the recurrent network with inhibitory interneurons shows a successive retrieval of memory [1, 2]. It has not, however, been clarified whether such behavior appears in realistic network with the Hodgkin-Huxley type of neuron.

Biologically, inhibitory interneurons in the cortex have been assumed to provide stability to the pyramidal cell activity by feedback and feedforward inhibitions. The firing pattern of pyramidal cells is modulated and coordinated by a diverse population of GABAergic interneurons [3, 4]. In addition, there is evidence for the involvement of acetylcholine (ACh) in attentional modulation in cortical areas [5]. The activation of muscarinic receptors reduces the release of GABA, hence decreases IPSPs in pyramidal neurons in layer 2/3 of cerebral cortex [6, 7]. On the other hand, the cortical input from the basal forebrain corticopetal cholinergic projection induces cortical gamma-frequency activity [8–10]. The direct application of muscarinic cholinergic agonists induces gamma oscillations in both hippocampal and neocortical slices [11, 12]. It is not yet clear how cholinergic modulation contributes to the genesis of gamma rhythms, and what is a role of gamma rhythms in attentional processing.

In this work, we propose such a realistic model of memory dynamics and investigate the effects of the coupling strength of inhibitory interneurons, the state of memory retrieval and the characteristic of frequency band.

2 Methods

The network model studied in this paper consists of a population of pyramidal cells and GABAergic fast-spiking interneurons.

We employ a two-compartment model for pyramidal cells proposed by Pinsky and Rinzel [13]. It consists of a somatic and a dendritic compartment comprising different active ion-currents and synaptic inputs. The soma compartment has two voltage-dependent currents, the fast sodium current I_{Na} and the delayed rectifier potassium current I_{K-DR} . The dendritic compartment has three voltage-dependent current, which are calcium current I_{Ca} , Ca-activated potassium current I_{K-C} and potassium after-hyperpolarization current I_{K-AHP} . The compartments were electrically connected via conductance g_c . The interneuron model consists of a single compartment with a sodium current I_{Na} and a potassium current I_K [14]. Interneurons project via GABA_A synapses to pyramidal cells, and the pyramidal cells project via AMPA synapses to other pyramidal cells forming recurrent network and also project via AMPA synapses to interneurons. We did not include NMDA or GABA_B receptors in the present model. The network architecture is shown in Fig. 1.

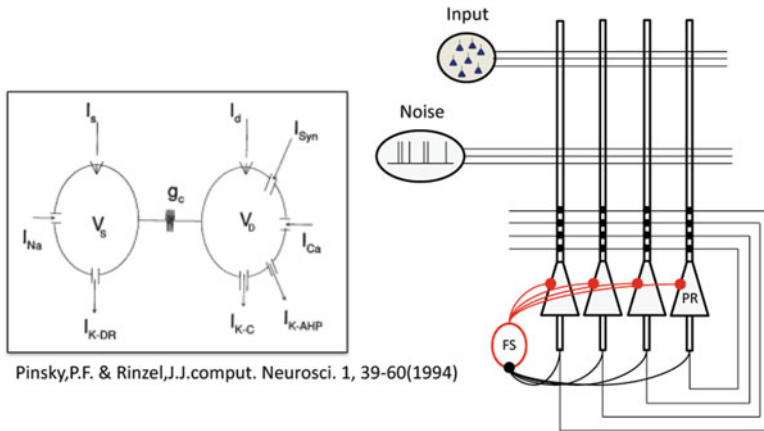


Fig. 1 A schematic diagram of Pinsky-Rinzel neuron (*left*) and network architecture (*right*)

The spatial memory patterns are embedded to the recurrent excitatory synaptic connections by Hebbian learning and Poisson spike trains are included in this model as a background noise.

3 Results

The performance of memory retrieval was estimated for the coupling strength g_{IE} of inhibitory neurons to the pyramidal neurons. Figure 2 shows spike trains of pyramidal neurons when the coupling strength g_{IE} is varied. We can classify the state of memory retrieval depending on the coupling strength g_{IE} . Without inhibition the firing activity of pyramidal cells in the network are enhanced by recurrent connections (Fig. 2a). In the case that g_{IE} is weaker, the spike trains of pyramidal neurons behave as an associative memory (Fig. 2b). In the case that g_{IE} is stronger, the spike trains of pyramidal neurons show transitory behavior (Fig. 2c). We calculate the direction cosine (DC) between stored memory and retrieval memory, which is shown in Fig. 2. Each state of memory retrieval is named as following state I–III.

The orbit of memory retrieval is shown in Fig. 3. The result implies that the dynamics of memory retrieval changes to the transitory behavior with an increase in the connection strength g_{IE} .

We estimate the stability of memory retrieval when incomplete sets of cues are input in this system. The performance of memory retrieval in state II and state III are shown Fig. 4. Horizontal axis represents Hamming distance between an input pattern and a stored memory pattern. The result in the case of state II indicates that when the input pattern is different from the stored memory pattern by several bits, the memory retrieval is completed such as an associative memory. This indicates

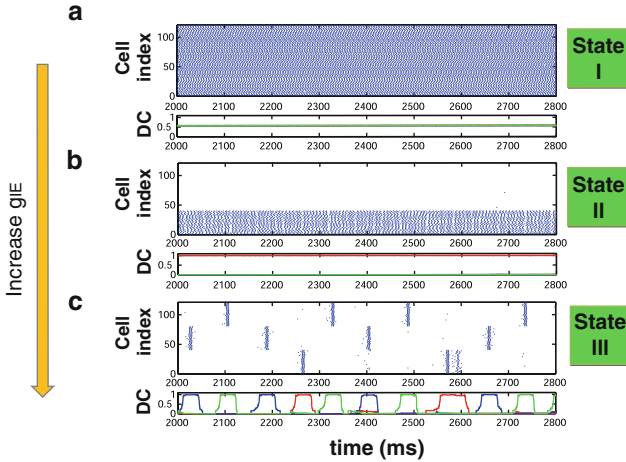


Fig. 2 Spike rastergram of pyramidal neurons (*top*) and DC (*bottom*). (a) The case of zero-coupling strength between excitatory neurons and inhibitory interneurons. (b) The case of weak coupling. (c) The case of strong coupling. Different memory retrieval is indicated by different color in DC (Color figure online)

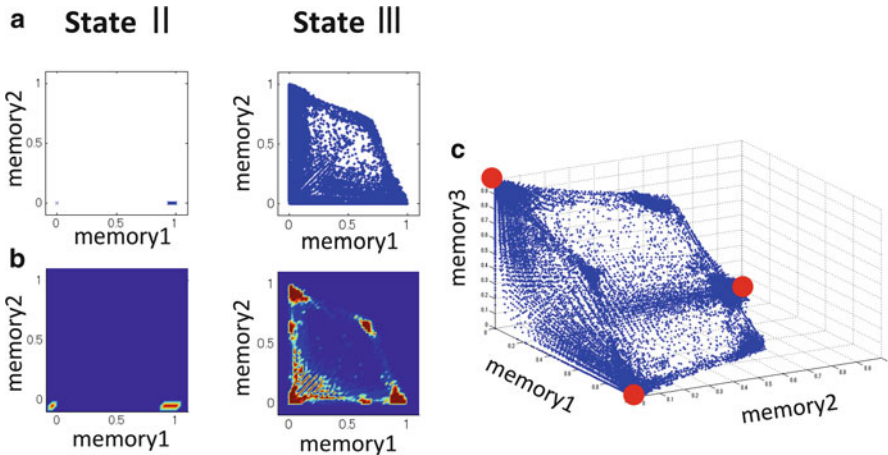


Fig. 3 Direction Cosine of state II and state III. (a) Trajectories of DC. (b) Frequency distribution of the DC trajectory. (c) Trajectories of DC (state III)

the presence of attractors. The memory retrieval depends on the initial condition and the basin structure of embedded memory looks very complicated. In the case of state III, the state of memory retrieval becomes temporarily unstable. These results indicate that the landscape of basin is varied by the strength of g_{IE} .

We examine the power spectrum of each process of memory retrieval. The frequency bands of each state are shown in Fig. 5. The peak frequency is shifted from

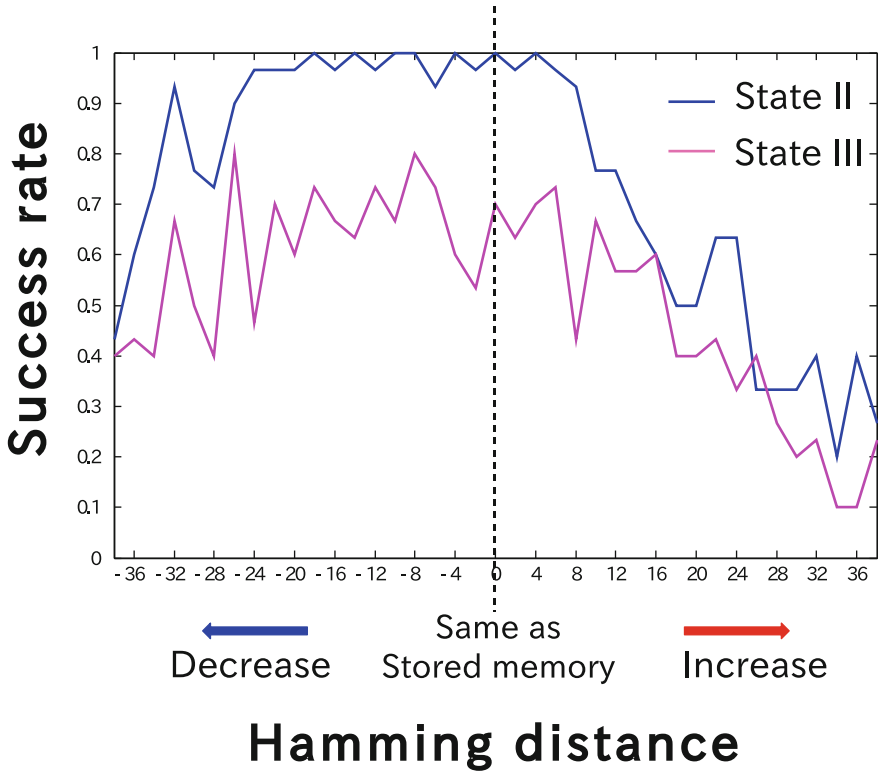


Fig. 4 The success rate of memory retrieval in state II and state III. The success rate calculated from direction cosine

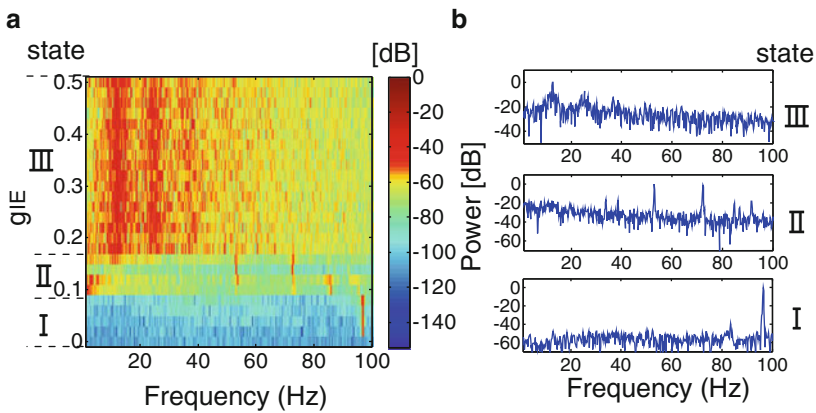


Fig. 5 (a) Power spectrum of soma potentials of pyramidal neurons. The y-axis denotes the coupling strength g_{IE} , and the x-axis frequency (Hz). (b) Typical power spectrum for each state is shown. $g_{IE} = 0.14$ (upper frame), $g_{IE} = 0.2$ (middle frame), $g_{IE} = 0.02$ (lower frame)

high frequency range to low frequency range with an increase of the connection strength g_{IE} . Figure 5 shows that the characteristic of power spectrum is also related with each state of memory retrieval. When the memory retrieval is completed (state II), the activity with the gamma band frequency (30–100 Hz) appears. The parameter g_{IE} is increased more (state III), the peak frequencies are switched from the gamma band to the theta band (4–12 Hz). The frequencies converge to around 10 Hz when the parameter g_{IE} is much stronger. The state of memory retrieval is crossly related to the frequency band.

4 Discussions

The successive retrieval of memories is observed in the network of biologically-plausible model neurons. The coupling strength of inhibitory interneurons is very crucial for controlling the retrieval of memories.

In the biological sense, there is ample evidence for the involvement of acetylcholine (ACh) in attentional modulation. The activation of muscarinic receptors reduces the release of GABA, hence decreases IPSPs in pyramidal neurons in layer 2/3 of the cerebral cortex. These effects indicate that acetylcholine projection reduces the coupling strength of inhibitory neurons g_{IE} . Our simulation results imply that when g_{IE} is reduced, the state of memory retrieval is changed, and the frequency bands also shift to the gamma band from theta or alpha band.

Acknowledgments This work was supported by a Grant-in-Aid for Scientific Research on Innovative Areas “The study on the neural dynamics for understanding communication in terms of complex hetero systems (No.4103)” (21120002) of The Ministry of Education, Culture, Sports, Science, and Technology, Japan.

References

1. Tsuda, I., Koerner, E., & Shimizu, H. (1987). Memory dynamics in asynchronous neural networks. *Progress of Theoretical Physics*, 78, 51–71.
2. Tsuda, I. (1992). Dynamic link of memory: chaotic memory map in nonequilibrium neural networks. *Neural Networks*, 5, 313–326.
3. Klausberger, T., Marton, L.F., Baude, A., Roberts, J.D.B., Magill, P. & Somogyi, P. (2004). Spike timing of dendrite-targeting bistratified cells during hippocampal network oscillations in vivo. *Nat Neurosci*, 7, 41–47.
4. Csicsvari, J., Hirase, H., Czurkó, A., Mamiya, A. & Buzsáki, G. (1999). Oscillatory coupling of hippocampal pyramidal cells and interneurons in the behaving rat. *J. Neurosci*, 19, 274–287.
5. Herrero, J.L., Roberts, M.J., Delicato, L.S., Gieselmann, M.A., Dayan, P. & Thiele, A. (2008). Acetylcholine contributes through muscarinic receptors to attentional modulation in V1. *Nature* 454, 1110–1114.
6. Toth, K., Freund, T. F. & Miles, R. (1997). Disinhibition of rat hippocampal pyramidal cells by GABAergic afferents from the septum. *J. Physiol*, 500, 463–474.

7. Salgado, H., Bellay, T., Nichols, J.A., Bose, M., Martinolich, L., et al. (2007). Muscarinic M2 and M1 receptors reduce GABA release by Ca²⁺ channel modulation through activation of PI3K/Ca²⁺ + - independent and PLC/Ca²⁺ + - dependent PKC. *J. Neurophysiol.*, 98, 952–965.
8. Cape, E.G. & Jones, B.E. (1998). Differential modulation of high-frequency gamma - electroencephalogram activity and sleep-wake state by noradrenaline and serotonin microinjections into the region of cholinergic basal ganglia neurons. *J. Neurosci.*, 18, 2653–2666.
9. Dringenberg, H.C. & Vanderwolf, C.H. (1997). Neocortical activation: modulation by multiple pathways acting on central cholinergic and serotonergic systems. *ExpBrain Res.*, 116, 160–174.
10. Rodriguez, R., U. Kallenbach, W. Singer & M.H.J. Munk. (2004). Short- and long-term effects of cholinergic modulation on gamma oscillations and response synchronization in the visual cortex. *J. Neurosci.*, 24, 10369–10378.
11. Fisahn, A., Pike, F.G., Buhl, E.H. & Paulsen, O. (1998). Cholinergic induction of network oscillations at 40 Hz in the hippocampus in vitro. *Nature*, 394, 186–189.
12. Buhl, E.H., Tamás, G. & Fisahn, A. (1998). Cholinergic activation and tonic excitation induce persistent gamma oscillations in mouse somatosensory cortex in vitro. *J. Physiol (London)*, 513, 117–126.
13. Pinsky, P. F. & Rinzel, J. (1994). Intrinsic and network rhythmogenesis in a reduced Traub model for CA3 neurons. *Journal of Computational Neuroscience*, 1, 39–60.
14. Wang, X.-J. & Buzsáki, G. (1996). Gamma oscillation by synaptic inhibition in a hippocampal interneuronal network model. *J. Neurosci.*, 16, 6402–6413.

Dynamic Information Processing in the Frontal Association Areas of Monkeys During Hypothesis Testing Behavior

Norihiko Kawaguchi, Kazuhiro Sakamoto, Yoshito Furusawa, Naohiro Saito, Jun Tanji, and Hajime Mushiake

Abstract Top-down visual search is based on subjective knowledge about the target, which is updated with behavioral consequences. To establish whether the frontal association areas (FAAs) are involved in the knowledge-based visual search, we introduced a new oculomotor task requiring monkeys to search for a valid pair of targets among four visual stimuli where the valid pair of targets changed without instruction. This result indicated that the FAA neurons of the monkeys showed a gradual shift of representation when the valid pair was changed. Our result suggests that the FAAs are involved in dynamically updating subjective knowledge of the search for targets based on behavioral consequences.

1 Introduction

Visual searching is believed to be a combination of the bottom-up and top-down cognitive processes [1, 2]. In everyday life, especially when the visual salience of objects is not a reliable cue for searching a target, we often conduct visual searches based on our previous knowledge of the target. When we expected to find the target, we maintain our previous knowledge. But when our search fails, we need

N. Kawaguchi • Y. Furusawa • N. Saito • H. Mushiake
Department of Physiology, Tohoku University School of Medicine, 2-1 Seiryō-cho, Aoba-ku,
Sendai 980-8575, Japan

K. Sakamoto (✉)
Research Institute of Electrical Communication, Tohoku University, 2-1-1 Katahira, Aoba-ku,
Sendai 980-8577, Japan
e-mail: sakamoto@riec.tohoku.ac.jp

J. Tanji
Brain Science Center, Tohoku University, 2-1-1 Katahira, Aoba-ku, Sendai 980-8577, Japan

to update our knowledge of the targets and search continually until the target is found. Therefore, it is plausible to consider a serial searching process as a series of hypothesis-testing behaviors. This top-down searching often manifests as sequential eye movements.

The frontal association areas (FAAs) are considered to be neural substrates for the control of visual searching process because they are involved in controlling actions in various contexts and monitoring behavioral outcomes [3–7]. FAAs are also anatomically connected with higher-order motor areas [7, 8]. To investigate the neural mechanisms underlying the knowledge-based searching process, we introduced an oculomotor target pair search task, and studied how the FAA neurons are involved in this task.

2 Methods

2.1 Behavioral Procedures

Three Japanese monkeys (*Macaca fuscata*) were trained to perform an oculomotor target pair search task (Fig. 1). The monkeys were required to select two stimuli from four identical visual stimuli (white dots: top left [TL], bottom left [BL], top right [TR], bottom right [BR]) by making a saccade to, and fixating on, each of the two stimuli, alternately. We defined four pairs, each consisting of two adjacent stimuli as follows: pair L (TL and BL), pair R (TR and BR), pair T (TR and TL), and pair B (BR and BL). The trial event sequences are illustrated in Fig. 1a. Each trial began with the appearance of a central fixation point on the display. When the monkey had fixated on this fixation point, it turned red. After 500 ms, it turned green. After a further 500 ms of fixation, four stimuli were presented at 8.5° of visual angle from the fixation point. Following a further 500 ms after the four stimuli presentation, the fixation point disappeared, serving as a go signal for the monkey to make a saccade to one of the four stimuli. The monkey had to maintain fixation on the stimulus for 1,000 ms and at this point the stimulus turned green if it was valid (correct trial). In the correct trials, 500 ms after the stimulus turned green, the four stimuli disappeared, and a reward was given. Following a saccade to an invalid stimulus (error trial), the four stimuli were turned off and the trial was aborted, and the same trial repeated. Once a trial was completed, the cycle was repeated and the monkey had to fixate on the central fixation point again. After predetermined number of correct trials (6 or 10 trials), the valid pair was switched to a new pair without explicit instruction in a pseudorandom manner (Fig. 1b). Eye positions and movements were monitored with an infrared corneal reflection monitoring system. We recorded neuronal activities from the bilateral frontal association areas from two monkeys. We used conventional electrophysiological techniques using single electrodes and multiple electrode arrays.

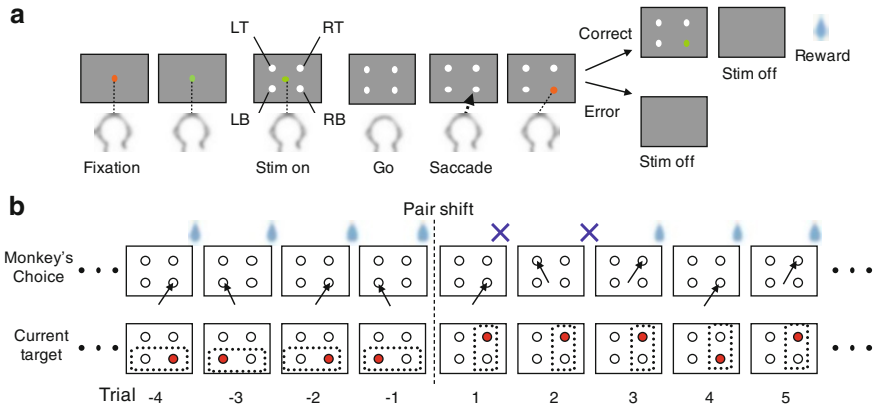


Fig. 1 (a) Temporal sequence of events in the task. (b) A series of behaviors across a shift from one pair (*pair B*) to another (*pair R*)

2.2 Data Analysis

To examine changes in firing rates (FR) associated with task events, we defined seven behavioral periods related to the events (*central fixation point on, fixation point color change, stimuli on, Go signal, target point color change, stimuli off, reward*), and calculated firing rates for 500 ms after each event. To determine the selectivity for the behavioral periods, we carried out one-way analysis of variance (ANOVA) using factors of the behavioral periods, followed by *post-hoc* pairwise comparison using the Bonferroni test. If the neural activities in at least one behavioral period were significantly different from other intervals ($p < 0.01$), we classified the neurons as task-related.

To assess how the regression parameters were related to neuronal activity, we performed multiple linear regression analysis using the following equations:

$$FR = \alpha_0 + \alpha_1 \times (\text{current pair}) + \alpha_2 \times (\text{previous pair})$$

$$FR = \beta_0 + \beta_1 \times (\text{current target}) + \beta_2 \times (\text{previous target})$$

FR is the firing rate calculated from the number of spikes within a 100 ms time frame, α_0 and β_0 are the intercepts, α_1 and β_1 are the coefficients for the current pair or targets, and α_2 and β_2 are the coefficients for the previous pair or targets. The categorical factors for the targets were TL, TR, BL, and BR, and the factors for pairs were T, B, L, and R. The F values derived from the regression coefficients were normalized by dividing them by the F values of the significance level ($p < 0.01$). If the normalized F value for pair or target of a neuron was significant during consecutive two bins, the neuron was regarded as pair- or target-related.

To quantify the selectivity for the current or previous pair and targets, we calculated the selectivity index of FAAs. The Pair index (PI) was defined as $(P_c - P_p)/(P_c + P_p)$, where P_c and P_p were the normalized F values for the current and previous pairs derived from regression analysis using the first formula, respectively. The Target index (TI) was defined as $(T_c - T_p)/(T_c + T_p)$, where T_c and T_p were the normalized F values for the current and previous targets derived from regression analysis using the second formula, respectively. F values were calculated using the corresponding bin-by-bin data using 100 ms time windows, and the mean indices were calculated using the overall average of each trial (Fig. 4).

3 Results

3.1 Behavioral Analysis

The two monkeys performed the oculomotor target pair search task with success rates of more than 90% after two valid targets were found. (Monkey G: 95%, Monkey K: 91%.) The two monkeys showed a similar series of eye movements after a valid pair was shifted (Fig. 1b). The oculomotor search patterns were classified into three types and time courses were plotted (Fig. 2). When the monkey made saccades alternately to a previous pair of targets in consecutive trials, we classified the movements as a “previous pair” pattern. When the monkey made saccades alternately to the current pair of targets, we defined the movements as a “current pair” pattern. The remaining search patterns were classified as “other” patterns. In the first trial after a valid pair was shifted, the monkey tried to search the previous pair of targets, and received an error signal. In the second trial, the monkey often

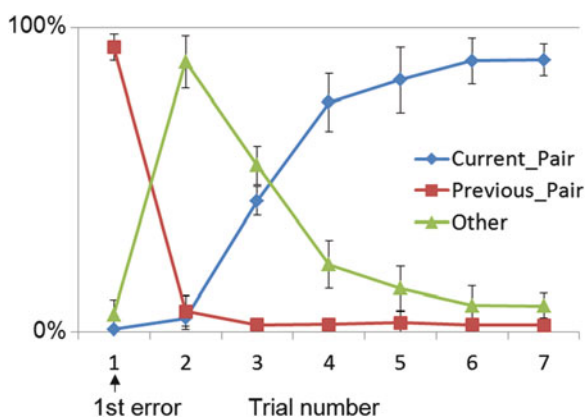


Fig. 2 Oculomotor search pattern. After a pair shift, the monkey changed the search pattern in order to search a new valid pair and found it within four trials

made a saccade to the target diagonal to the target chosen in the first trial in order to search a new valid target. In the third trial, the monkey often tried to search the adjacent target, and half of the targets were included in the current pair. Within four trials after the pair was shifted, the monkey usually found the current valid pair of targets. This behavioral analysis suggests that the monkeys were able to efficiently update their knowledge about valid pairs of targets based on the consequences of actions.

3.2 *Neuronal Analysis*

We obtained 504 neurons from the two monkeys. Among 254 task-related neurons, we analyzed how the neuronal activities reflected the current pair and targets. The regression analysis revealed that 101 neurons were pair-related, 54 neurons were target-related, and 75 neurons were both pair- and target-related. Among the task-related neurons, an illustrative example is shown in Fig. 3a, where a neuron exhibited activity preferentially for the saccades to targets belonging to pair B. The neuron showed sustained activity after the saccade to the target BR and preceding the saccadic eye movement to the target BL. For the remaining pair, this neuron showed weak activity for pair L and pair T and moderate activity for pair R, and these were termed non-preferred pairs.

We analyzed whether the previous information about the pair and targets after a valid pair was shifted. Figure 3b shows the changed in pair-selective activity change after the valid pair was shifted from the preferred pair B to the non-preferred pair R. In the first trial, the monkey made a saccade to BR and the neuron showed distinct activity after the stimuli was turned off. Interestingly, in the second trial, the monkey made a saccade to the target diagonal to the previous target, and the neuron showed distinct activity again preceding the saccade to target TL although this target belonged to the non-preferred pair. This suggests that the information of the previous pair (pair B) and target (target BL) was maintained even after the pair had changed.

To examine quantitatively how the previous and current information were represented in the frontal association areas, we calculated the PI and TI (Fig. 4). In the first and second trials, both PI and TI were both negative, indicating that the neuron reflected the knowledge of the previous pair and targets more than the current one. Interestingly, in the second trial, the neuronal activity and selecting behavior were often dissociated. However, the PI and TI turned positive in later trials (trials 3–6), indicating that the neuronal activity reflects knowledge about the current pair and targets. These results demonstrate that the neural representation shows a gradual shift from the previous to current knowledge about the valid pair and target.

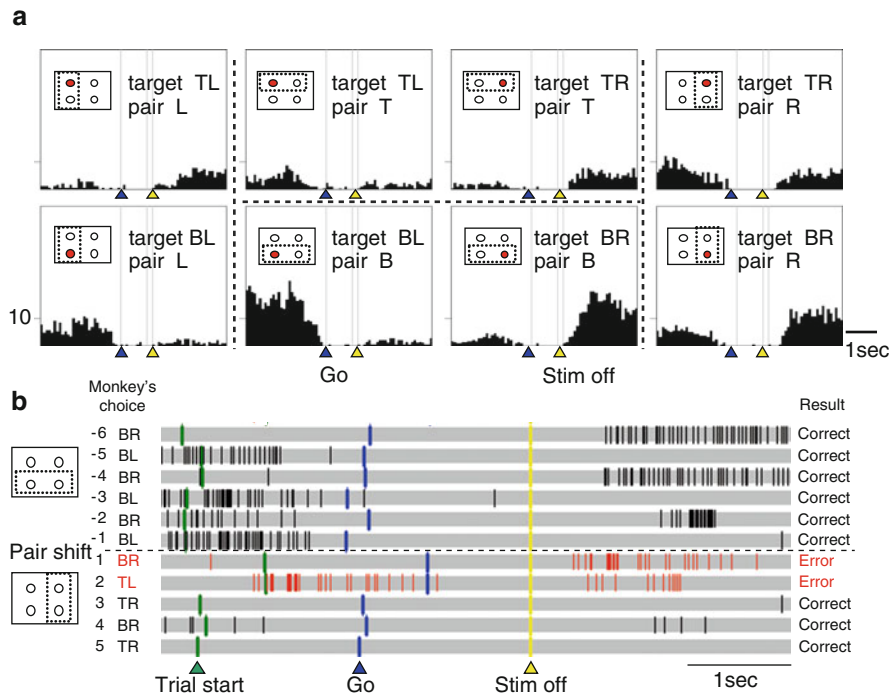
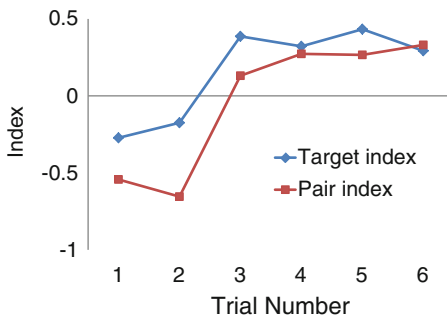


Fig. 3 (a) An example of the neurons with selectivity of pair and target. (b) The activity changes of the neuron before and after the shift of target-pair

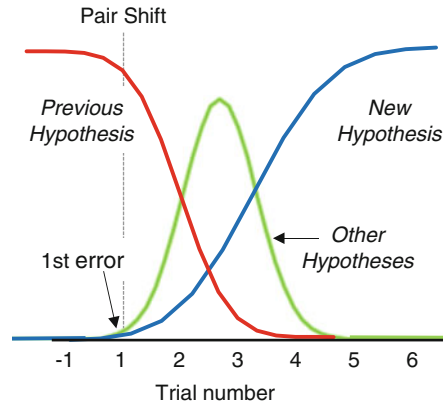
Fig. 4 Time course of the pair and target indices. Both indices turned from negative to positive within a few trials



4 Discussions

We found that the monkeys were able to search valid pairs of targets based on the consequences of their actions in the oculomotor target pair search task. The FAA neurons represented the information about the previous and current pair in the course of the task. Moreover, after a pair was shifted, the neural representation of the knowledge about the task condition changed dynamically from the previous to

Fig. 5 Scheme of hypothesis-testing behavior represented in the neuronal activity



the current. These results were consistent with the view that the FAAs are involved in the higher-order control of actions [9–11].

Based on our findings, we interpreted the function of the FAAs from the viewpoint of hypothesis-testing behavior (Fig. 5). We assumed FAA neurons hold a subjective possibility of the current hypothesis relating to the current valid pair. Immediately after a valid pair was shifted, the FAAs still maintained the subjective possibility of the previous hypothesis. However, when the monkey received an error signal in the first trial, the subjective possibility of the previous hypothesis decreased. At the same time, possibilities of various other hypotheses transiently increased (Fig. 5). After a couple of trials of active searches, the subjective probability of a new hypothesis reached the level of acceptance, and the previous hypothesis was replaced by the new hypothesis. Thus, the FAAs are involved in the knowledge-based searching process by dynamically updating the subjective probability of the current status of knowledge.

Acknowledgments This research is supported by the Ministry of Education, Culture, Sports, Science, and Technology of Japan (#22120504).

References

1. Wolfe, J. M.: Guided Search 2.0: A revised model of visual search. *Psychon Bull Rev.* 1(2) (1994) 202–238.
2. Treisman, A.: Search, similarity, and integration of features between and within dimensions. *J Exp Psychol Hum Percept Perform.* 17(3) (1991) 652–676.
3. Johnston, K., Everling, S.: Neurophysiology and neuroanatomy of reflexive and voluntary saccades in non-human primates. *Brain Cogn.* 68(3) (2008) 271–283.
4. Pierrot-Deseilligny, C., Müri, R.M., Rivaud-Pechoux, S., Gaymard, B., Ploner, C.J.: Cortical control of spatial memory in humans: the visuoculomotor model. *Ann Neurol.* 52(1) (2002) 10–19.

5. Isoda, M., Tanji, J.: Contrasting neuronal activity in the supplementary and frontal eye fields during temporal organization of multiple saccades. *J Neurophysiol.* 90(5) (2003) 3054–3065.
6. Schall, J.D., Stuphorn, V., Brown, J.W.: Monitoring and control of action by the frontal lobes. *Neuron.* 36(2) (2002) 309–322.
7. Amiez, C., Petrides, M.: Anatomical organization of the eye fields in the human and non-human primate frontal cortex. *Prog Neurobiol.* 89(2) (2009) 220–230.
8. Pierrot-Deseilligny, C., Milea, D., Müri, R.M.: Eye movement control by the cerebral cortex. *Curr Opin Neurol.* 17(1) (2004) 17–25.
9. Miller, E.K., Cohen, J.D.: An integrative theory of prefrontal cortex function. *Annu Rev Neurosci.* 24 (2001) 167–202.
10. Duncan, J.: An adaptive coding model of neural function in prefrontal cortex. *Nat Rev Neurosci.* 2(11) (2001) 820–829.
11. Tanji, J., Shima, K., Mushiake, H.: Concept-based behavioral planning and the lateral prefrontal cortex. *Trends Cogn Sci.* 11(12) (2007) 528–534.

Simple Dynamical Models to Understand the Mechanisms of Drug Addiction

Takashi Tateno

Abstract Drug addiction is a chronically relapsing disorder characterized by a compulsion to seek and take a drug despite harmful consequences. We have developed a model to examine the molecular, neuropharmacological, and neuro-circuitry changes that mediate the transition from controlled drug use to the loss of behavioral control over drug seeking and taking. The neurotransmitter dopamine (DA) is thought to play a central role in drug addiction. The mesolimbic DA system provides the neural basis of the rewarding effects of certain drugs. In addition, an opponent process or allostasis contributes to the persistence of drug addiction. Here, we propose a model of drug addiction consisting of an opponent process, DA-gated learning, and an action selection module. The results indicate that interplay between DA-gated learning and the opponent process plays a significant role in the development of addictive behaviors.

Keywords Action selection modeling • Dopamine • Opponent process • Reinforcement learning

1 Introduction

Drug addiction is a chronically relapsing disorder characterized by a compulsion to seek and take a drug despite harmful consequences. Understanding drug addiction requires evaluation of the dynamics of molecular, neuropharmacological, and neuro-circuitry changes that mediate the transition from controlled drug use to the loss of behavioral control over drug seeking and taking. DA-gated learning and an opponent process may play significant roles in the development of addictive behaviors [1]. DA-dependent reinforcement learning, however, does not always account for the

T. Tateno (✉)

Graduate School of Information and Technology, Hokkaido University, Kita 14, Nishi 9, Kita-ku, Sapporo, 060-0814 Japan

e-mail: tateno@ist.hokudai.ac.jp

Y. Yamaguchi (ed.), *Advances in Cognitive Neurodynamics (III)*,

DOI 10.1007/978-94-007-4792-0_93,

© Springer Science+Business Media Dordrecht 2013

persistence of addictive behaviors [2], whereas the opponent process theory does not provide a computational mechanism for how addiction is acquired [3]. Hedonic, positive affective, or negative affective emotional states were hypothesized to be modulated automatically by the central nervous system with mechanisms that reduce the intensity of the emotional state. Counteradaptation hypotheses have long been proposed to explain tolerance and withdrawal and the motivational changes associated with the transition to addiction [1]. Counteradaptive processes such as the opponent process that are part of the normal homeostatic limitation of reward function are hypothesized to fail to return to the normal homeostatic range and thus produce the reward deficits that are prominent in addiction. Moreover, although models of each process have been individually proposed, few studies have integrated the two concepts; reinforcement learning and opponent processes [4]. In this paper, we propose a relatively simple computational model incorporating both processes. The model of action selection includes effects of various receptors—e.g., nicotinic acetylcholine receptors (nAChRs)—on a dopaminergic neuronal population and learning. In particular, we have focused on slow adaptation in the opponent process as addictive behaviors are acquired. The results provide insights into the mechanisms that drive the development of addiction.

2 Methods

2.1 *Allostasis*

To simulate the opponent process of activity in a dopaminergic neuronal population, we developed the model shown in Fig. 1A. Although our approach was based on a modeling concept proposed by Gutkin et al. [3] and has three similar components—namely, the acute response, upregulation, and adaptation—many of the mathematical details are different. In particular, a long-term adaptation process was incorporated into the model as the third process (Fig. 1Bd), an approach that was not directly considered in the previous model [4]. The adaptation process plays a key role in the switch between persistence and amelioration of addictive behaviors in the model (see “Results”).

2.2 *Action Selection*

We used the simple network shown in Fig. 2 as an action selection model. The model is based on the example proposed by Gurney et al. [5]. The principle substructures of the basal ganglia (BG) include the striatum (STR), the subthalamic nucleus (STN), the internal and external globus pallidus (GPi and GPe), and the substantia nigra pars reticulata and compacta (SNr and SNc). In addition, the model includes the cortex and thalamus, which have bidirectional and autoregressive connections,

Fig. 1 Allostasis model. **(A)** Block diagram of the three components with different time scales. **(B)** Drug injection (*a*, black rectangles) produced characteristic responses in the output from the total system (*b*), the upregulation process (*c*), and the adaptation process (*d*)

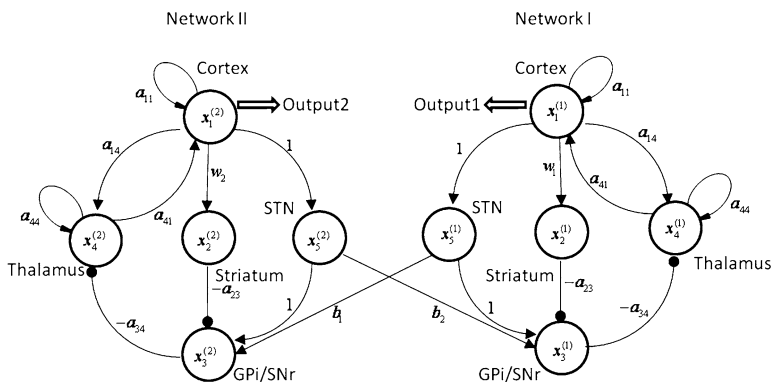
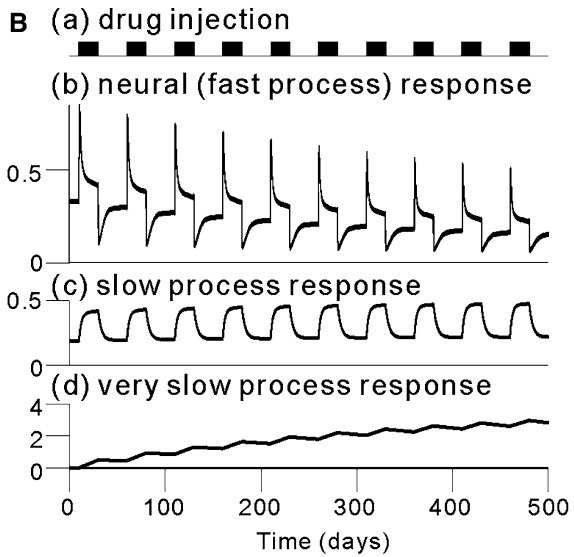
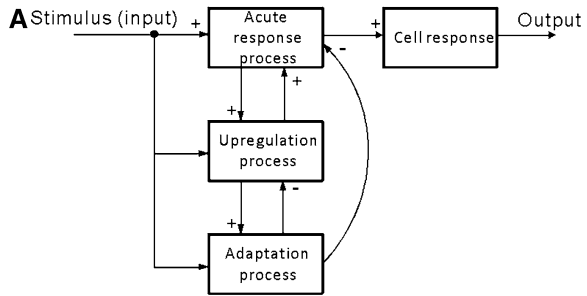


Fig. 2 A simple network model for action selection. Two identical networks (Networks 1 and 2) are interconnected by projections from the STN to the GPI/SNr

respectively (Fig. 2). The components of Networks 1 and 2 are all represented by single state variables and the evolution of the variables over time is described using five differential equations (see “Appendix”). The main projection from the BG to the thalamus is inhibitory (filled circles in Fig. 2), whereas the connections from the cortex to the BG (STR and STN) are excitatory projections (arrows). When performing the action selection (i.e., taking drugs or not), two symmetrical substructures are interconnected from one side of the STN to the other side of the GPI/SNr. We hypothesized that the thalamocortical and corticostriatal loops cause recurring excitation in the behavioral choice circuit. Moreover, the resetting following each trial may reflect rapid clearing of the motor/cognitive command representation from the cortical working memory store. When each component ($x_1^{(i)}$, $i = 1, 2$) corresponding to the cortex converged to a fixed point with a high value (e.g., $x_1^{(i)} = a_i$; $i = 1, 2$) from a randomly selected set of initial parameters, the state of the cortex is defined as active; otherwise, the state is defined as passive (e.g., $x_1^{(i)} = p_i$; $p_i < a_i$; $i = 1, 2$). Furthermore, if $(x_1^{(1)}, x_1^{(2)}) = (a_1, p_2)$, the selected action is taking drugs, whereas, otherwise, not taking drugs is selected.

2.3 DA Signaling and DA-Gated Learning

In this study, a simple first-order model was used to represent DA population activity. Neuronal activity in the substructure is described by the firing rate x_{DA} for $[0, 1]$.

$$\frac{dx_{DA}}{dt} = -\lambda_{DA}x_{DA} + f_{DA} \left(\sum_i A_i(t), R(t) \right) \quad (1)$$

where f_{DA} is a sigmoid input–output function that is described by the following relationship:

$$f_{DA} \left(\sum_i A_i(t), R(t) \right) = 0.5 \times \left(1 + \tanh \left(R(t) \sum_i A_i(t) - \theta_{DA} \right) \right) \quad (2)$$

Here, $A_i(t)$ is the effect of an action i on the dopaminergic signal and the selection of -1 (aversive), 0 (no selection), or $+1$ (appetitive). $R(t)$ reflects receptor activation in response to a drug with a gain modulatory effect on x_{DA} . Additionally, θ_{DA} is the threshold level for the dopaminergic neurons. Plasticity is modeled as changes in the synaptic weights (w_1 and w_2) from the cortex to the STR. Therefore, for learning during action selection, the dynamics of the excitatory weights is given by the following equations for $i = 1, 2$ and $j \neq i$:

$$\begin{aligned} \frac{dw_i}{dt} = & -\lambda_w \left(w_i - w_0^{(i)} \right) \\ & + K (< x_{DA} >, < R >) H(x_{DA} - \theta_{DA}) U \left(\left| x_1^{(i)} - x_e^{(i)} \right| < \theta_C^{(i)} \right) \\ & - K (< x_{DA} >, < R >) H(x_{DA} - \theta_{DA}) U \left(\left| x_1^{(j)} - x_e^{(j)} \right| < \theta_C^{(j)} \right) \end{aligned} \quad (3)$$

In Eq. (3), λ_w and w_0 are both constants and the factor K is a smooth increasing function of short-period averages of the phasic dopaminergic activity x_{DA} and activation R of certain receptors (e.g., nAChRs). $x_e^{(j)}$ ($j = 1, 2$) represents equilibrium points of $x_1^{(j)}$, and θ_{DA} and $\theta_C^{(j)}$ ($j = 1, 2$) are the threshold for dopaminergic activity and the results of action selection, respectively. $H(x)$ is 0 when x is negative and is equal to the x otherwise. $U(x < y)$ is 1 when $x < y$ is satisfied and is equal to 0 otherwise. The weight w_i increases when x_{DA} is above the threshold and the conditions for $x_1^{(i)}$ are satisfied. In contrast, the weight w_i decreased when both x_{DA} and $x_1^{(i)}$ are not satisfied. Therefore, one of the weights increases while the other decreases, if both $x_1^{(i)}$ and x_{DA} are over the threshold and the condition is detected in one of the networks. No phasic DA activity causes the weights decrease to the initial level (w_0).

In the following simulation, two conditions were considered: chronic use or self-administration of a drug in the presence and absence of the opponent process. For chronic drug use, the model ran continuously and action selection was not performed, while drug was applied externally. In contrast, for self-administration of a drug, a single trial consisted of 100–200 self-administration sessions with action selection. To calculate response probabilities, we averaged 200 trials for initial conditions distributed normally around $X = (x_1^{(1)}, x_1^{(2)}) = (0.95, 0.95)$ with standard deviations $(\sigma_1^{(1)}, \sigma_1^{(2)}) = (0.1, 0.1)$ in the cortical blocks of the network (for more details, see “Results”). After one session, the action selection module was reset to the initial conditions.

3 Results

3.1 *Allostasis Model*

In the allostasis model, we simulated long-lasting drug effects in dopaminergic neurons (Fig. 1B). Each time the drug was delivered (Fig. 1Ba), a fast transient decayed to a sustained level. After drug delivery stopped, the DA response decreased, producing a putative signature of withdrawal. The mean response level for each drug administration shifted downward owing to negative feedback from the adaptation process.

3.2 *Action Selection Model*

During action selection, behavioral choices derived from the network result from symmetry breaking (Fig. 3), and neural activity reflecting one action plan wins over the others because of strong competitive interactions. In the model, fixed points correspond to single action selection. Before analyzing the entire network model, we examined bifurcation of individual parameters (w_1 or w_2) in the individual

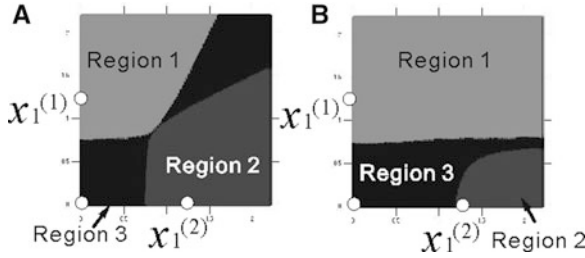


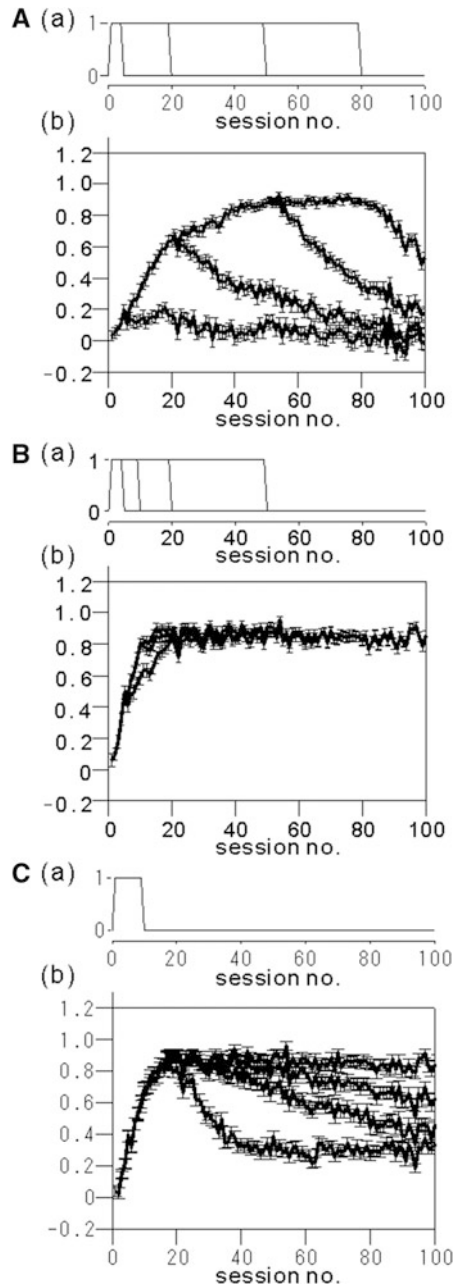
Fig. 3 Attraction domains of the action selection model for different values of w_1 and w_2 . For initial points $(x_1^{(1)}, x_1^{(2)})$ located in each region, state points converged to the same fixed points (white circles). (A), $(w_1, w_2) = (0.505, 0.505)$; (B), $(w_1, w_2) = (0.577, 0.433)$

subnetworks (Network 1 or 2). The subsystem had only one stable fixed point before the saddle-node bifurcation point at $w_0^{(i)} = 0.505$ ($i = 1, 2$). Thereafter, each subsystem has two stable fixed points ($x_1^{(i)} = a_i$, $i = 1, 2$) and one unstable one ($x_1^{(i)} = p_i$, $p_i < a_i$, $i = 1, 2$). After combining the two subnetworks, the maximum number of stable fixed points increased from two to four. For the same two substructures, however, the number decreased to three because the symmetrical weights changed in opposite directions (Eq. 3). When the cortical state was represented by $X = (x_1^{(1)}, x_1^{(2)})$, these fixed points were denoted by X_1^* , X_2^* , and X_3^* . For the initial condition $X_0 = (x_1^{(1)}(t=0), x_1^{(2)}(t=0))$ at time $t = 0$, the attraction domains for the fixed points X_1^* , X_2^* , and X_3^* are respectively named Regions 1, 2 and 3. The attraction domains for two sets of parameter values— w_i ($i = 1, 2$)—are illustrated in Fig. 3.

3.3 The Combined Model

First, for each trial under the control conditions (no drug), the action selection network has three steady states ($X = X_i^*$, $i = 1, 2, 3$), which correspond to one of three decisions: taking the drug ($X = X_1^*$), not taking the drug (X_2^*), and no decision (X_3^*). The probabilities of taking or not taking the drug were nearly equal ($45.7 \pm 4.5\%$ vs. $46.3 \pm 5.1\%$ for $n = 100$ trials). Under chronic drug administration, the average level of dopaminergic neural activity (x_{DA}) increased to +1 and saturated after 50 sessions (Fig. 4Ab). Similarly, the weight w_1 from the cortex to the striatum in Network 1 saturated after 50 sessions ($w_1 \approx 1.1$). After a period of drug administration, x_{DA} gradually decreased to a consistent level. Second, for self-administration of the drug with no opponent process, the selected action rapidly moved to taking the drug (Fig. 4Bb). The initial period of chronic administration (5, 10, 20, and 50 sessions) had little effect on changes in decision making, although the slope of the initial phase was different. Third, under self-administration conditions with the opponent process, the adaptation time parameters affected the persistence of drug seeking. As the adaptation parameter decreased, action selection fluctuated and the average level decreased.

Fig. 4 Simulated dopaminergic activity and self-administration of a drug. **(A)** Dopaminergic activity was simulated for four different periods (5, 20, 50, or 80 sessions) of chronic drug administration. **(B)** For the self-administration condition with no opponent process, the probability of taking the drug in a session vs. the number of sessions is shown for four initial periods (5, 20, 50, or 80 sessions) of external drug application. **(C)** The plots are as described for B, but with a different opponent adaptation time constant ($\tau = 5, 20, 40,$ or 200 sessions)



4 Discussion

To examine the mechanisms of drug addiction, we created a computational model of drug-induced neuroadaptation and DA-gated learning for striatocortical action selection. The model can mimic short-term drug effects and accelerate behavioral motor activation, such that the preferentially selected actions reflect addiction (Fig. 4B). In addition, the model showed that interplay between action selection and the slow opponent process cement drug-related behaviors despite reduced DA responses. In this model, the decay rate of the probability of taking the drug was slower than that of the dopaminergic activity (Fig. 4C). After learning and a shift in the attraction domain to the case shown in Fig. 3B, self-administration of the drug continued and became difficult to extinction. The model, however, is based on a number of assumptions about the effects on single cells and larger networks. Thus, our approach requires additional testing and experimental data for validation.

Acknowledgments This work was supported by Funding Program for Next Generation World-Leading Researchers (NEXT program), PRESTO, JST, and a Grant-in-Aid for Scientific Research on Innovative Areas, Scientific Research (B), and Exploratory Research, MEXT.

A.1 Appendix

A.1.1 Introduction

To construct a drug addiction model, we propose four simple parts as the components: (1) an opponent-process (allostasis) model, (2) an action selection model, (3) a DA signaling model, and (4) a population activity model of DA neurons. The four models are all described by ordinary differential equations and the details of the opponent process and action selection models are written in the following two sections.

A.1.2 Opponent Process

For the opponent-process model, three state variables (x_1 , x_2 , x_3) of the fast, slow, and very slow processes are respectively described by the following equations:

$$\tau_1 \frac{dx_1}{dt} = -\beta_1(x_2)x_1 + \alpha_1(d_t, x_3)(1 - x_1) \quad (1a)$$

$$\tau_2 \frac{dx_2}{dt} = -\beta_2x_2 + \alpha_2(d_t, x_1)(1 - x_2) \quad (1b)$$

$$\tau_3 \frac{dx_3}{dt} = -\beta_3x_3 + d_t \quad (1c)$$

Table A.1 Opponent-process model parameters

Parameters	Values
τ_1	0.2
τ_2	10
τ_3	5, 20, 40, or 100
β_2	2.0
β_3	0.1
a_1	1.7
a_2	2.0
b_1	1.3
b_2	0.9
θ_1	1.2
θ_2	0.9
c_1	2.0
e_1	6.0
η_1	0.35

where τ_i ($i = 1, 2, 3$) are time constant, β_i ($i = 2, 3$) are decay constant, and d_t is time-varying drug input to the system. The functions α_i ($i = 1, 2,$) and β_1 in Eqs. (1a-c) are all sigmoid functions and written by

$$\alpha_i(d, x) = \frac{a_i}{2} [1 + \tanh(b_i(d + x - \theta_i))] \quad (1d)$$

and

$$\beta_1(x) = \frac{c_1}{2} [1 + \tanh(e_1(x - \eta_1))] \quad (1e)$$

The parameter τ_3 determines adaptation of the very slow process. All parameters are listed in Table A.1.

A.1.3 Action Selection

For the action selection model, two substructures are described by two identical sets of five differential equations. For the five state variables (x_1, \dots, x_5) corresponding to activity levels of the five brain regions in Network 1, the equations are described as

$$\frac{dx_1}{dt} = -\lambda_1 x_1 + a_{11} x_1 + a_{41} f_1(x_4) \quad (2a)$$

$$\frac{dx_2}{dt} = -\lambda_2 x_2 + w_1 f_2(x_1) \quad (2b)$$

Table A.2 Action-selection model parameters

Parameters	Values
λ_1	1.0
λ_2	1.0
λ_3	5.0
λ_4	1.0
a_{11}	0.1
a_{13}	2.0
a_{14}	1.0
a_{23}	1.0
a_{34}	2.0
a_{41}	1.0
a_{44}	0.1
b_1	0.2
b_2	0.2
w_1	0.505 (initial value)
w_2	0.505 (initial value)
$\sigma_i (i = 1, \dots, 6)$	0.1

$$\frac{dx_3}{dt} = -\lambda_3 x_3 + a_{13} f_3(x_1) - a_{23} f_4(x_2) + b_2 g(y_5) \quad (2c)$$

$$\frac{dx_4}{dt} = -\lambda_4 x_4 + a_{44} x_4 + a_{14} f_5(x_1) - a_{34} f_6(x_3) \quad (2d)$$

$$\frac{dx_5}{dt} = \frac{dx_1}{dt} \quad (2e)$$

where a_{ij} ($i, j = 1, \dots, 4$), w_i ($i = 1, 2$), and b_i ($i = 1, 2$) are all constant values and the values are listed in Table A.2.

The functions $f_i(x)$ and $g(x)$ are sigmoid functions and are written by

$$f_i(x) = 0.5(\tanh(2\sigma_i(x - 0.6)) + 1) \quad (2f)$$

$$g(x) = 0.5(\tanh(x - 0.6) + 1) \quad (2g)$$

The variable x_5 is different from x_1 only in an initial value. Similarly, For Network 2, the equations are described as

$$\frac{dy_1}{dt} = -\lambda_1 y_1 + a_{11} y_1 + a_{41} f_1(y_4) \quad (3a)$$

$$\frac{dy_2}{dt} = -\lambda_2 y_2 + w_2 f_2(y_1) \quad (3b)$$

$$\frac{dy_3}{dt} = -\lambda_3 y_3 + a_{13} f_3(y_1) - a_{23} f_4(y_2) + b_1 g(x_5) \quad (3c)$$

$$\frac{dy_4}{dt} = -\lambda_4 y_4 + a_{44} y_4 + a_{14} f_5(y_1) - a_{34} f_6(y_3) \quad (3d)$$

$$\frac{dy_5}{dt} = \frac{dy_1}{dt} \quad (3e)$$

When performing the action selection (i.e., taking drugs or not), two symmetrical substructures are interconnected from one side of the STN to the other side of the GPi/SNr. We hypothesized that the thalamocortical and corticostriatal loops cause recurring excitation in the behavioral choice circuit. Moreover, the resetting following each trial may reflect rapid clearing of the motor/cognitive command representation from the cortical working memory store. When each component ($x_1^{(i)}$, $i = 1, 2$) corresponding to the cortex converged to a fixed point with a high value (e.g., $x_1^{(i)} = a_i$; $i = 1, 2$) from a randomly selected set of initial parameters, the state of the cortex is defined as active; otherwise, the state is defined as passive (e.g., $x_1^{(i)} = p_i$; $p_i < a_i$; $i = 1, 2$). Furthermore, if $(x_1^{(1)}, x_1^{(2)}) = (a_1, p_2)$, the selected action is taking drugs, whereas, otherwise, not taking drugs is selected.

To calculate response probabilities, we averaged 200 trials for initial conditions distributed normally around $X = (x_1^{(1)}, x_1^{(2)}) = (0.95, 0.95)$ with standard deviations $(\sigma_1^{(1)}, \sigma_1^{(2)}) = (0.1, 0.1)$ in the cortical blocks of the network (for more details, see “Results”). After one session, the action selection module was reset to the initial conditions.

References

1. Koob, G.F., Le Moal M.: Drug addiction, dysregulation of reward, and allostasis“ Neuropsychopharmacology 24 (2001) 97-129.
2. Redish, A. D.: Addiction as a computational process gone awry. Science 306 (2006) 1944–1947.
3. Peper, A.: A theory of drug tolerance and dependence I: a conceptual analysis. J. Theor. Biol. 229 (2004) 477–490.
4. Gutkin, B. S., Dehaene, S., Changeux, J. P.: A neurocomputational hypothesis for nicotine addiction. Proc. Natl. Acad. Sci. USA 103 (2006) 1106-1111.
5. Gurney, K., Prescott, T. J., Redgrave, P.: A computational model of action selection in the basal ganglia. I. A new functional anatomy. Biol. Cybern. 84 (2001) 401-410.

Toward an Animal Model of Spatial Hemineglect: Preliminary Investigation

Masatoshi Yoshida

Abstract In this paper, I summarized current findings about brain regions responsible for spatial hemineglect in human patients and about studies that intend to induce spatial hemineglect in macaque monkeys. To establish an animal model of spatial hemineglect, the fibers that connect the posterior parietal cortex and the prefrontal cortex was transected in one macaque monkey. A histological analysis showed that the site of the lesion was as intended, centered on the second branch of the superior longitudinal fasciculus (SLFII). There was no damage in the internal capsule, the damage of which will induce motor deficits. By combining with computational models, I expect that an animal model of spatial hemineglect will be established in the future experiments.

1 Introduction

Spatial hemineglect is a cognitive deficit in which the patients have difficulty in responding to the space contralateral to the brain damage and is caused mainly by damage in the right cerebral cortex [1].

Growing evidence suggests that spatial hemineglect is a deficit in the brain network including parietal and frontal cortex [2] (Fig. 1). For example, analysis of the hemineglect patients without hemianopia indicates that the center of the damage was the white matter beneath the brain area such as temporoparietal junction (TPJ) and the superior temporal gurus [3]. Direct electrical microstimulation of the SLFII

M. Yoshida (✉)

Laboratory of Behavioral Development, Department of Developmental Physiology,
National Institute for Physiological Sciences, National Institutes of Natural Sciences,
Okazaki 444-8585, Japan

School of Life Science, The Graduate University for Advanced Studies (SOKENDAI),
Hayama 203-0193, Japan
e-mail: myoshi@nips.ac.jp

Fig. 1 Neural network that is proposed to be involved in spatial hemineglect in human. *FEF*, frontal eye field; *IPS*, intraparietal sulcus; *VFC*, ventral frontal cortex; *TPJ*, temporoparietal junction; *SLFII*, the second branch of the superior longitudinal fasciculus

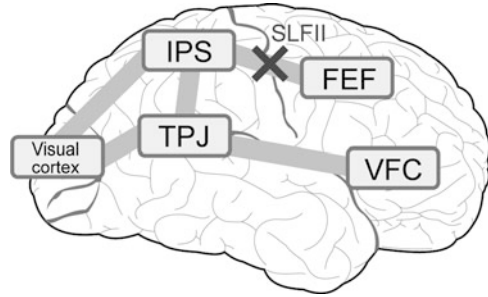
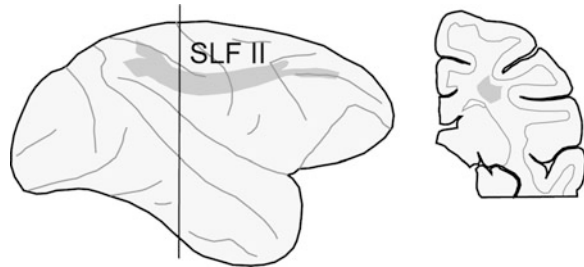


Fig. 2 Target lesion site in the brain of a macaque monkey. *Left*, lateral view of the right brain. *Right*, coronal view of the brain. *Grey portion*: the second branch of the superior longitudinal fasciculus (*SLFII*)



fibers of the patients during awake craniotomy induces similar symptoms to those of spatial hemineglect [4]. A functional MRI study revealed that disconnection of FEF and IPS was associated with lowered functional connectivity of the ventral frontal cortex (VFC) and the temporoparietal junction (TPJ) (Fig. 1) [5].

Despite of clinical significance, an animal model of spatial hemineglect is not established yet. An animal model of hemineglect has to satisfy the following behavioral criteria. (1) Sustained deficits in localizing or detecting sensory stimuli have to be observed. (2) The deficit cannot be simply explained by sensory loss. (3) The deficit cannot be simply explained by motor deficits. Here I concentrate on studies using macaque monkeys, which have similar visual systems with those of human. Ablation or pharmacological inactivation of the posterior parietal cortex or the prefrontal cortex alone in macaque monkeys is not sufficient to cause behavior similar to spatial hemineglect [6, 7]. Combined ablation of the posterior parietal cortex or the prefrontal cortex leads to a deficit in visually guided saccades but the deficit recovers within 1 week [6]. One exception is a study published in 15 years ago, using monkeys with transection of the SLFII, in which showed sustained deficits in a memory-based symbol search task [8]. However, the study did not describe details such as the time course of the deficit and did not record eye and head movements, which is necessary to establish an animal model of spatial hemineglect.

As a first step of an ongoing project to establish an animal model of spatial hemineglect, I made a lesion in a monkey's brain to disconnect the prefrontal cortex and the posterior parietal cortex (Fig. 2).

2 Methods

All experimental procedures were performed in accordance with the National Institutes of Health Guidelines for the Care and Use of Laboratory Animals and approved by the Committee for Animal Experiment at National Institute of Natural Sciences.

Surgery. Under anesthesia, a craniotomy was made on the right parietal cortex in one Japanese monkey (*Macaca fuscata*). The dura was flapped to expose the parietal cortex (Fig. 3). A part of the right inferior parietal lobule was removed by aspiration with a small-gauge metal suction tube [9–12] to expose the white matter at the fundus of the intraparietal sulcus (IPS). The white matter was sectioned by aspiration, along the line of the IPS and towards the lateral ventricle, until the lateral ventricle appeared [8] (Fig. 4).

Fig. 3 Surgery. Before the lesion. CS, central sulcus; IPS, intraparietal sulcus; LF, lateral fissure; LS, lunate sulcus. Orientation: top, medial; right, anterior

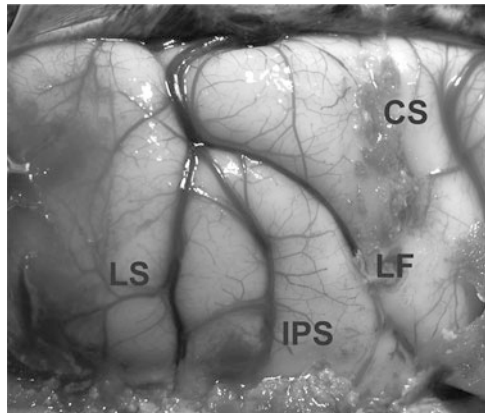
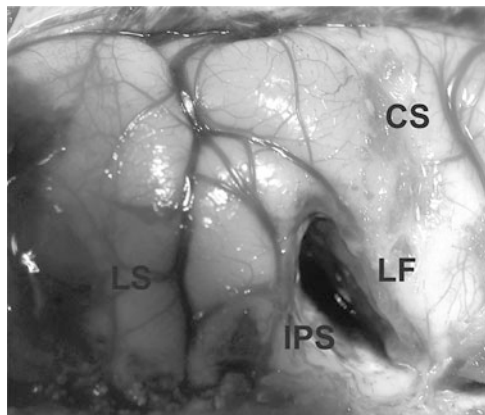


Fig. 4 Surgery. After the lesion. See Fig. 3 for abbreviations



Histology. After the surgery, the animal was killed with Nembutal (100 mg/kg) and perfused with 4% paraformaldehyde via the arterial line. The brain was cut into coronal slices (50 μ m thickness) and was processed for Nissl stain to identify the site of the lesion.

3 Results

The surgery: The surgery was completed without fatal bleeding or other problems (Fig. 4). This is important to note because numerous blood vessels run around the lesion site, including the veins on the ventral lip of the IPS and the branches of the middle cerebral artery around the lateral fissure (Fig. 3), the damage of which causes spatial hemineglect in human patients after stroke.

The site of the lesion: The lesion was centered on the white matter between the lateral ventricle and the fundus of the IPS (Fig. 5). Anatomically the fibers damaged by the lesion are estimated to be the superior longitudinal fasciculus (SLF II), which connects the prefrontal cortex and the posterior parietal cortex. On the other hand, neighboring brain structures were kept intact. For example, the internal capsule, which contains the fibers projecting from the primary motor cortex to the spinal cord and thus is indispensable for limb and body movements, was undamaged.

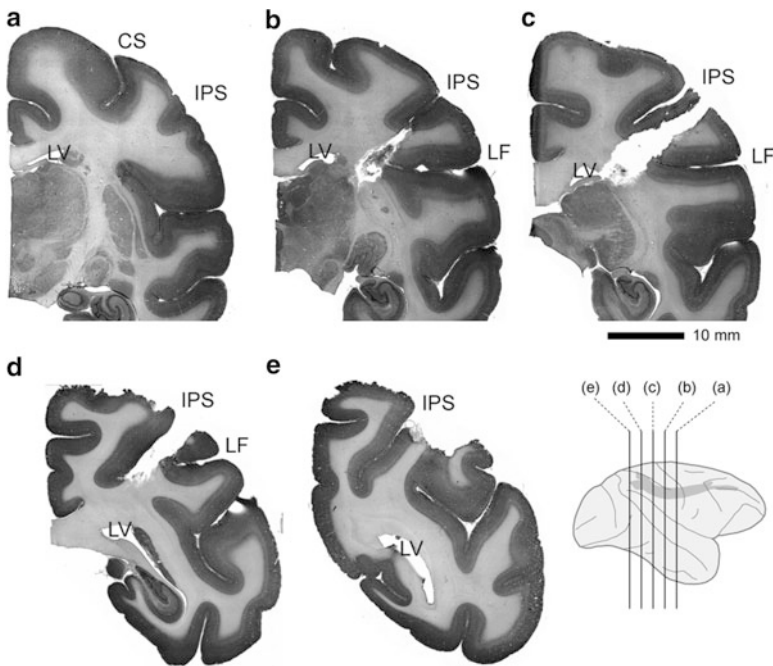


Fig. 5 Histological sections of the lesioned brain. *CS*, central sulcus; *IPS*, intraparietal sulcus; *LF*, lateral fissure; *LV*, lateral ventricle

4 Discussions

In this study, I established the method of making lesioned monkeys to test for spatial hemineglect. What kind of behavioral results will be expected by the lesion? Because both the early visual cortex and the internal capsule are spared, visual deficits and motor deficits will be less likely to occur, which is the behavioral criteria (2) and (3) in Introduction. According to the previous report [8], the lesion is likely to induce visual neglect (criteria 1). The question is whether the deficits will be transient or sustained and visual or multimodal. By combining with a computational model for bottom-up attention and free-viewing experiments, which proved to be effective for evaluating attention in monkeys with blindsight [13], I expect that an animal model of spatial hemineglect will be established by the future experiments.

Acknowledgments This work was supported by Grant-in-Aid for Scientific Research on Innovative Areas: The study on the neural dynamics for understanding communication in terms of complex hetero systems.

References

1. Karnath, H-O., Milner, D., Vallar, G. (ed.): The cognitive and neural bases of spatial neglect. Oxford University Press. (2002)
2. Bartolomeo, P. et.al. *Cereb Cortex*. 17 (2007) 2479–2490.
3. Doricchi and Tomaiuolo. *Neuroreport*. 14 (2003) 2239–2243.
4. Thiebaut de Schotten et.al. *Science*. 309 (2005) 2226–2228.
5. He et.al., *Neuron*. 53 (2007) 905–918.
6. Lynch and McLaren. *J Neurophysiol*. 61 (1989) 74–90.
7. Wardak et.al., *J Neurosci*. 22 (2002) 9877–9884.
8. Gaffan, D., Hornak, J. *Brain*. 120 (1997) 1647–1657.
9. Yoshida, M. et.al. *Journal of Neuroscience*. 28 (2008) 10517–10530.
10. Takaura et.al., *J. Neurosci*. 31 (2011) 4233–4241.
11. Ikeda et.al., *J. Cogn. Neurosci*. 23 (2011) 1160–1169.
12. Kato et.al., *Eur. J. Neurosci*. 33 (2011) 1952–1960.
13. Yoshida, M., et.al. *Journal of Vision*. 10 (2010) 140, 140a [Abstract]

Prestimulus Neural Oscillations Contribute to Recollection and Familiarity

Florence Kleberg, Keiichi Kitajo, Masahiro Kawasaki, and Yoko Yamaguchi

Abstract Humans may experience qualitatively different memory retrieval when recognizing a previously encountered stimulus, such as recollection and familiarity. We present evidence for differences in theta and alpha oscillation amplitude during encoding and during the preparatory period before encoding of the later recognized stimulus. Additionally, fronto-posterior phase locking in theta frequency was increased right before encoding recollection. We suggest that oscillatory activity and coordination during the prestimulus period may already influence the qualitative nature of stimulus encoding in memory.

F. Kleberg (✉)

RIKEN Brain Science Institute (BSI), Saitama, Japan

Department of Systems Science, Graduate School of Engineering, University of Tokyo, Tokyo, Japan

e-mail: kleberg@brain.riken.jp

K. Kitajo

RIKEN Brain Science Institute (BSI), Saitama, Japan

PRESTO, Japan Science and Technology Agency (JST), Saitama, Japan

Rhythm-based Brain Computation Unit, RIKEN BSI-TOYOTA Collaboration Center, Saitama, Japan

M. Kawasaki

RIKEN Brain Science Institute (BSI), Saitama, Japan

Rhythm-based Brain Computation Unit, RIKEN BSI-TOYOTA Collaboration Center, Saitama, Japan

Y. Yamaguchi

Laboratory for Dynamics of Emergent Intelligence, RIKEN Brain Science Institute, Wako City, Japan

1 Introduction

When judging whether an item has been encountered before, one may experience recollecting the episodic context in which it was first encountered, or one may simply know that it has been encountered before, but nothing about when or where. These phenomena are termed recollection and familiarity, respectively [18]. There is mounting evidence that these subjective experiences may result from two distinct retrieval mechanisms in human recognition memory. The differences are already apparent in psychophysical paradigms. For instance, if subjects are instructed to make speeded responses, recollection at retrieval is significantly diminished, while familiarity is spared [11]. Retrieval by recollection does seem to include associative memory, whereas retrieval by familiarity does not [33]. Additionally, BOLD responses in fMRI studies have shown that medial temporal lobe and prefrontal areas are engaged in encoding of familiarity and recollection, respectively [14], and within the MTL, additional distinctions have been shown [4, 6], as well as in the parietal cortex [34]. However, some studies show that both retrieval processes are at least partly supported by the same structures [10, 15].

Both recollection and familiarity are associated with different event-related potential (ERP) responses during memory encoding and retrieval [8, 30]. A recent ERP study additionally suggests that parietal areas may be specifically involved in signaling the subjective memory experience [1].

Although numerous behavioural, fMRI or ERP recording-based studies have tackled the issue of familiarity and recollection, the operational role of oscillatory synchrony remains largely uninvestigated. In EEG recordings, we have access to the high temporal-resolution oscillations that are spatial averages of the brain's internal signals between neurons and between neuronal groups. Changes in amplitude of these oscillations at a recording site indicate either local changes in neuronal firing rates or changes in synchronization within a local area, while analyses targeting 'phase locking' can show synchronization, or desynchronization, between oscillations at distant recording sites. This 'locking' of oscillations may be important for providing a window for communication between neuronal groups [32], as it can be regulated at a shorter timescale than anatomical changes [9]. It has been shown that neural synchrony plays a likely functional role in human cognition, for instance in the binding of visual features in a coherent percept [27] and in working memory maintenance [24]. Indeed, particular neural oscillatory states may support various cognitive processes, even during the prestimulus period [19]. Importantly, prestimulus brain states are shown to influence the evoked response after stimulus onset [3]. In turn, evoked [23] and induced [28] oscillations in memory tasks are associated with memory processing. In other words, from these findings we may hypothesize that the state of prestimulus synchrony is decisive at least in part for successful memory processing, and that this is achieved by prestimulus oscillations preparing or increasing the oscillations operating during stimulus perception or encoding.

Theta oscillations (in the range of 4–7 Hz in humans) are believed to be involved in executing task-driven goals by long-range synchronization [16]. In human recognition memory, theta oscillations regulate memory by phase-lock on a single neuron level [20, 22] and scalp-recorded theta is involved in working memory load management [12, 24] and encoding of recognition memory tasks [20]. Alpha oscillations (8–12 Hz) are also involved in working memory processes, possibly for local memory module execution and retrieval [13, 25], although they may play a role of inhibiting task-irrelevant processing [26].

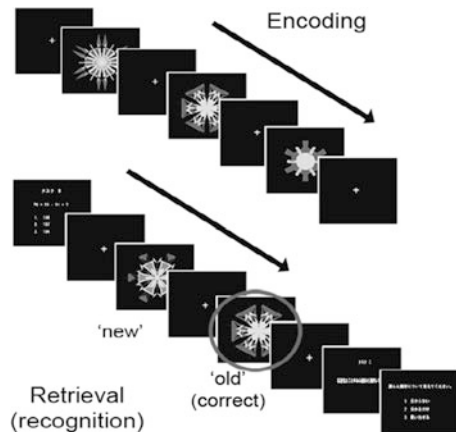
We therefore investigated the role of alpha and theta oscillations in the prestimulus period and the stimulus presentation period, during the ‘encoding stage’ of a memory task, and in particular their relation to subsequent familiarity and recollection.

2 Method

Recognition memory was assessed with a two-alternative forced-choice paradigm, in which participants (n = 11) were required to encode and retrieve abstract kaleidoscope-like images (Fig. 1; [30, 31]). We chose abstract images over word stimuli because they can create new familiarity and recollection experiences, which are not as much associated with a participant’s well established verbal memory as word stimuli. Abstract images also allow us to assess the purely perceptual side of recognition memory and limit interference from verbal rehearsal, such as in natural scene recognition paradigms, which cannot readily be controlled in the paradigm.

Participants perceived a sequence of kaleidoscopic stimuli and fixation crosses while fixating the centre of the screen. Each kaleidoscopic stimulus was presented for 2,000 ms. A mental arithmetic task was performed after the sequence to prevent bridging of encoding and retrieval by active rehearsal in working memory.

Fig. 1 Task design. Participants fixated the screen centre while viewing a sequence of abstract images, after which they performed a brief distracter task. During retrieval, participants selected either of the images as being ‘old’, and reported on their subjective recognition experience [5]. The abstract images were presented for 2,000 ms



Participants retrieved item memory by selecting the previously seen image from a pair of images shown in a sequence. Importantly, after each retrieval trial, participants reported their subjective recognition experience by selecting one answer out of “Remember”, “Know”, and “Don’t Know (guess)” where the first two choices refer to recollection and familiarity, respectively [29]. The two-stimulus retrieval stage was repeated ten times to account for all non-buffer stimuli from the encoding phase. Participants performed 16 blocks with each ten trials, yielding a total of 160 trials per participant.

During encoding and retrieval of the images, scalp EEG was recorded with 60 cap-embedded electrode channels with a temporal resolution of 500 Hz. Artifacts related to ocular movements were removed with Second Order Blind Identification (SOBI) type Blind Source Separation, in MATLAB EEGLab [7]. Epochs that still contained artifacts after the SOBI were manually rejected. The raw signal was filtered with a FIR band-pass filter for 2-45 Hz. Frequency amplitude and frequency phase were estimated with the Hilbert Transform method. The phase was then used to compute the phase-locking value (or PLV: [17]) per frequency, timepoint and channel (Eq. 1).

$$PLV_{f,t} = N^{-1} \left| \sum_{n=1}^N e^{i(\phi_1(f_n,t_n) - \phi_2(f_n,t_n))} \right|$$

Eq. 1: The PLV value is a measure for the consistency of phase difference in frequency f at any timepoint t for the channel pair 1 and 2, across N trials. If the phase difference is similar across trials, the PLV approaches the value 1, however if the phase difference is variable across trials, the PLV approaches 0.

We did not use the prestimulus period (1,000 ms) as a baseline to normalize activity after image onset, as this period may contain important information about how different brain states lead to variations in memory processing. If used as a baseline for normalization, activity in the prestimulus period vanishes from our results. Therefore, the results shown here do not represent event-related synchronization (ERS). Instead, we normalized amplitude and PLV by computing a common mean and standard deviation for “Remember” and “Know” trials put together.

To then find significant differences in z-values between the conditions of familiarity and recollection, we performed a non-parametric permutation test [5] with $\alpha = 0.05$, and controlled for multiple comparisons with the False Discovery Rate procedure [2].

3 Results

Behavioural results suggest that participants had above chance performance overall ($78.8\% \pm 7$, $p < 0.05$), as well as above chance performance on “Know” trials ($81.1\% \pm 11$, $p < 0.05$) and “Remember” trials ($96.2\% \pm 07$, $p < 0.025$). Accuracy

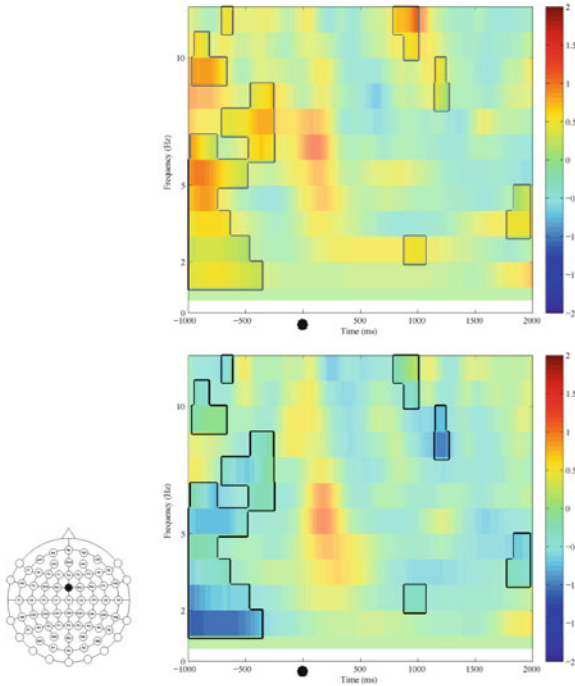


Fig. 2 Prestimulus differences in 2–12 Hz power at frontal channel FCz between Remember and Know trials. The scalp graph shows the location of the channel in the scalp cap. Time-frequency plots show the average z-values for Remember (*top*) and Know (*bottom*) encoding trials at FCz from –1,000 ms prestimulus to 2,000 ms after stimulus onset, for frequencies 2–12 Hz. *The black rectangles delineate the increases in power for “Remember” compared to “Know” after the permutation test. Because of multiple comparisons we cannot assume that all of these areas are significantly different. Statistically significant points must however lie within these areas. The black dots indicate the time of stimulus onset*

on “Don’t Know” trials was not different from chance ($59.6\% \pm 09$, $p > 0.25$). These results suggest that participants could, on average, accurately encode and retrieve the items in familiarity and recollection trials.

We then compared the “Remember” and “Know” trials during encoding with stimuli that were later associated with a correct response at retrieval, to investigate the subsequent memory effects. We found that the slow oscillation (3 Hz) and theta (6 Hz) amplitude before stimulus onset was higher for subsequent “Remember” stimuli than for subsequent “Know” stimuli, at the midfrontal channel FCz (Fig. 2, permutation test result; Fig. 3, statistical significance). Another prestimulus increase for Remember could be seen at occipital channel PO7, in 4 Hz (Fig. 4, permutation test result; Fig. 5, statistical significance).

No significant decreases in power were found for Remember compared to Know trials in the prestimulus period.

Fig. 3 Prestimulus differences in 3 and 6 Hz power at frontal channel FCz between Remember and Know trials. The scalp graph shows the location of the channel in the scalp cap. Time-frequency plots show the average z-values for Remember (*top*) and Know (*bottom*) encoding trials at FCz from $-1,000$ ms prestimulus to $2,000$ ms after stimulus onset, for frequencies 2–12 Hz. The *black rectangles* delineate the statistically significant increase in power for “Remember” compared to “Know”, after correcting for multiple comparisons by FDR. The *black dots* indicate the time of stimulus onset

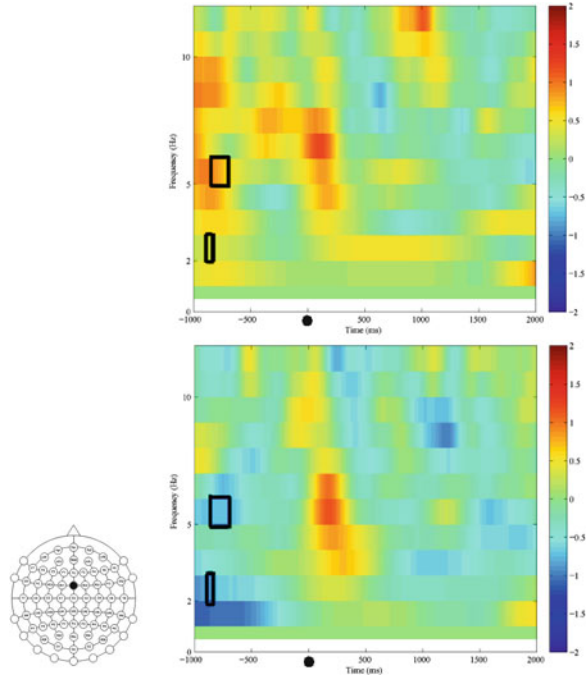
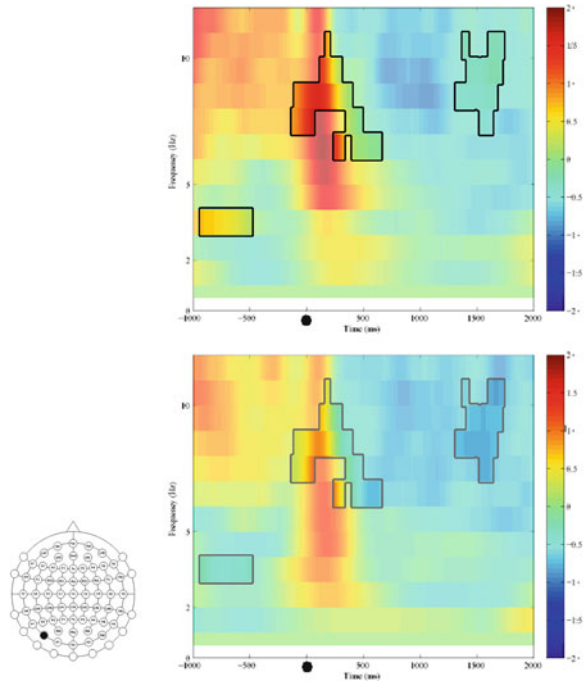


Fig. 4 Pre- and poststimulus differences in 4 and 7–11 Hz power at frontal channel FCz. The scalp graph shows the location of the channel in the scalp cap. Time-frequency plots show the average z-values for Remember (*top*) and Know (*bottom*) encoding trials at PO7 from $-1,000$ ms prestimulus to $2,000$ ms after stimulus onset, for frequencies 2–12 Hz. The *black rectangles* delineate the increases in power for “Remember” compared to “Know” after the permutation test. Because of multiple comparisons we cannot assume that all of these areas are significantly different. The *black dots* indicate the time of stimulus onset



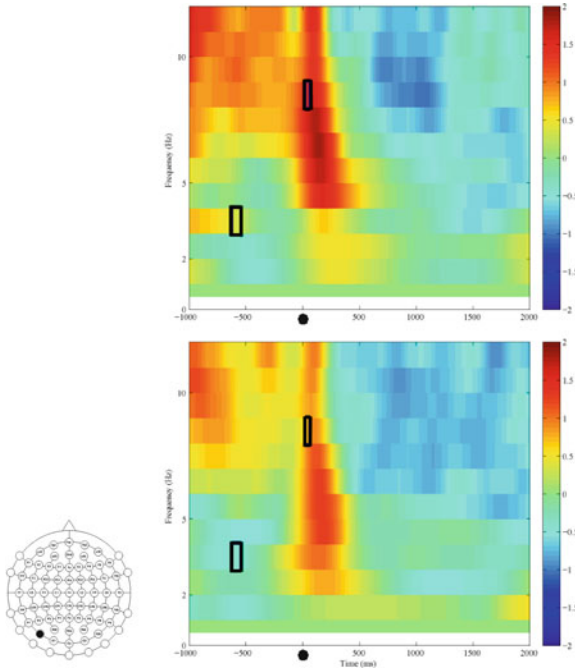


Fig. 5 Pre- and poststimulus increases in theta and alpha range power at occipital channel PO7, for “Remember” and “Know” trials. The scalp graph shows the location of the channel in the scalp cap. Time-frequency plots show the average z-values for frequencies 2–12 Hz for Remember (*top*) and Know (*bottom*) encoding trials at PO7 from –1,000 ms prestimulus to 2,000 ms after stimulus onset. *The black rectangles delineate the statistically significant increase in power for “Remember” compared to “Know” trials, after correcting for multiple comparisons. At this channel, increases for Remember are evident before stimulus onset in the 4 Hz range, and after stimulus onset in the 9 Hz range. The black dots indicate the time of stimulus onset*

We performed a PLV analysis to investigate the synchronization in the 3–6 Hz frequency range, and showed that there is significantly higher PLV for Remember compared to Know trials in the 4 Hz range between channels FCz and PO7 (Fig. 6). This effect appears approximately –550 ms before stimulus onset.

After stimulus onset, the Remember trials during encoding were characterized by poststimulus increases in higher frequencies compared to the Know trials, notably at occipital channel PO7 (Figs. 4 and 5), occipital channel PO8, and lateral-parietal channel C3 in 7–8 Hz, respectively.

We investigated the PLV values between channels PO7, PO8 and C3 in the 7–11 Hz frequency range, and found a significantly higher PLV for Remember compared to Know trials between PO8 and C3 in 10 Hz around 300 ms after stimulus onset, and a later increase again for Remember compared to Know between C3 and PO7, in 9 Hz around 500 ms after stimulus onset (figures not shown).

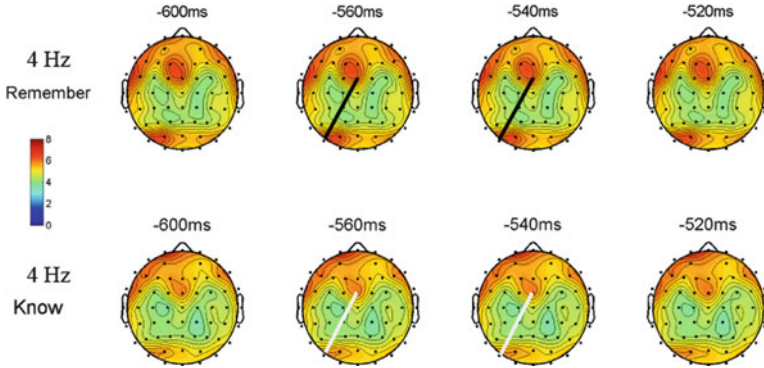


Fig. 6 Scalp distributions of average raw 4 Hz amplitude in μV , for Remember trials (*top*) and know trials (*bottom*), with a significant difference in phase-locking between channels FCz and PO7, in 4 Hz, occurring around -550 ms before stimulus onset. This significance is found after correction by FDR. The difference indicates a higher PLV for Remember (*black line*) compared to Know trials (*dark gray line*). Centres of increased raw amplitude can clearly be seen around the two channel locations

4 Discussion

We showed that qualitatively different brain states in the prestimulus period and the period during stimulus presentation are associated with subsequently different subjective memory experiences. Importantly, we showed that alpha and theta range oscillations in widespread cortical areas may support the encoding of an item that is later recollected with context as opposed to an item that is later judged familiar. Theta oscillations appear before stimulus onset and may be supporting later increase in alpha, possibly for enhanced processing of the visual stimulus or binding contextual elements into one episode.

Depending on the attentional state of the subject the network may be receptive to encoding the episode in the moment, or it may be merely receptive to increased localized processing for a single stimulus. These theta oscillations may be indicative of this attentional state. It will be of great interest to next investigate (1) the trial-predictive power of the current findings, (2) cross-frequency coupling between theta and alpha, and (3) whether the fluctuating theta-state and its subsequent metamemory type is under voluntary control.

Acknowledgments This work was supported by a Grant-in-Aid for Scientific Research of The Ministry of Education, Culture, Sports, Science, and Technology, Japan (21120005).

References

1. Ally B.A., Simons J.S., McKeever J.D., Peers P.V., Budson A.E. (2008) *Neuropsychologia* **46**: 1800–1812
2. Benjamini Y, Hochberg Y. (1995) *J. R. Statist. Soc. B* **57**: 289–300
3. Brandt M.E., Jansen B.H., Carbonari J.P. (1991) *Electroencephalogr. Clin. Neurophysiol.* **80**: 16–20
4. Bowles B., Crupi C., Mirsattari S.M., Pigott S.E., Parrent A.G., Pruessner J.C., Yonelinas A.P., Koehler S. (2007) *Proc. Natl. Acad. Sci. USA*, **104**:16382–16387
5. Burgess A, Gruzelier J. (1999) *Handbook of electroencephalography and clinical neurophysiology, revised series*, **6**: 139–158. Pfurtscheller G, Lopes da Silva FH (eds.) Amsterdam: Elsevier Science.
6. Davachi L., Mitchell J.P., Wagner A.D. (2003) *Proc. Natl. Acad. Sci. USA*, **100**:2157–2162
7. Delorme A, Makeig S. (2004) *J Neurosci Methods*. **134**:9–21
8. Duarte A., Ranganath C., Winward L., Hayward D., Knight R.T. (2004) *Cogn. Brain Res.* **18**: 255–272
9. Fries, P. (2005) *Trends Cogn. Sci.* **9**: 474–480
10. Gold JJ, Smith CN, Bayley PJ, Schragger Y, Brewer JB, Stark CEL, Hopkins RO, Squire LR. (2006) *PNAS* **103**: 9351–9356
11. Hintzman DL, Curran T. (1994) *J. Mem. Lang.* **33**:1–18
12. Jensen O, Tesche C (2002) *Eur. J. Neurosci.* **15**:1395–1399
13. Kawasaki, M. Kitajo K, Yamaguchi Y. (2010) *Eur. J. Neurosci.* **31**:1683–1689
14. Kirwan C.B., Wixted J.T., Squire L.R. (2008) *J. Neurosci.* **28**: 10541–10548
15. Kirwan C.B., Wixted J.T., L.B.Squire (2010) *PNAS* **107**: 344–348.
16. Klimesch, W., Freunberger, R., Sauseng, P. & Gruber, W. (2008) *Brain Res.* **1235**: 31–44
17. Lachaux J, Rodriguez E, Martinerie J, Varela FJ. (1999) *Hum. Brain Mapp.* **8**: 194–208
18. Mandler, G. (1980) *Psychol. Rev.* **87**: 252–271
19. Mathewson K.E., Gratton G., Fabiani M., Beck D.M., Ro T. (2009) *J. Neurosci.* **29**: 2725–2732
20. Osipova, D, Takashima A, Oostenveld R, Fernandez G, Maris E, Jensen O. (2006) *J. Neurosci.* **26**:7523–7531
21. Rizzuto D.S., Madsen J.R., Bromfield E.B., Schulze-Bonhage A., Kahana M.J. (2006) *NeuroImage* **31**:1352–1358
22. Rutishauser U, Ross i.B, Mamelak A.M, Schuman E.M. (2010) *Nature* **464**:904–909
23. Sanquist T.F., Rohrbaugh J.W., Syndulko K., Lindsley D.B. (1980). *Psychophysiol.* **17**:568–576
24. Sarnthein J, Petsche H, Rappelsberger P, Shaw GL, Von Stein A (1998) *PNAS* **95**:7092–7096
25. Sauseng P, Klimesch W, Gruber W, Doppelmayr M, Stadler W, Schabus M. (2002) *Neurosci. Let.* **324**:121–124
26. Sauseng P, Klimesch W., Heise K.F., Gruber W.R., Holz E., Karim A.A., Glennon M., Gerloff C., birbaumer N., Hummel F.C. (2009) *Curr. Biol.* **19**: 1846–1852
27. Singer W, Gray CM. (1995) *Annu. Rev. Neurosci.* **18**: 555–586
28. Tallon-Baudry C., Bertrand O., Peronnet F., Pernier J. (1998) *J. Neurosci.* **18** :4244–4254
29. Tulving, E. (1985) *Can. Psychol.* **26**:1–12
30. Voss JL, Paller KA. (2009a) *NeuroImage* **46**: 280–289
31. Voss JL, Paller, KA. (2009b) *Nat. Neurosci.* **12**: 349–355
32. Womelsdorf T, Schoffelen J, Oostenveld R, Singer W, Desimone R, Engel AK, Fries P. (2007) *Science* **316**: 1609–1612
33. Yonelinas, AP. (1997) *R Memory Cognit.* **25**, 747–763
34. Yonelinas A. P., Otten L. J., Shaw K.N., Rugg, M.D. (2005) *J. Neurosci.* **25**: 3002–3008

Contribution of the Cholinergic Innervation to Early Memory Development in the Neonate Para-Hippocampal System

Alexandre Pitti and Yasuo Kuniyoshi

Abstract Newborns present impressive developmental changes during the first year in almost all domains marked by memory categorization and variability. We propose that one important actor of this developmental shift is the gradual influence of the cholinergic system in the cortico-hippocampal circuits. Based on neurological observations and developmental studies, we model how the neuromodulator acetylcholine could be gradually released in the hippocampal system from the fetal period till the first year to support the detection of novel signals and the encoding of memories. By doing so, we suggest that the cholinergic system realizes the functional reorganization of the cortico-hippocampal system as a working memory for novelty.

1 Introduction

Among the principal neuromodulators, acetylcholine (ACh) plays a particular role during brain development for the acquisition of cognitive capabilities. During early postnatal development, ACh regulates critical aspects of maturation and plasticity of the neocortex, hippocampus and cerebellum for memory and learning [2–4]. For instance, converging evidences attribute a developmental and cognitive role to ACh that may involve changes to the hippocampal cholinergic system [5, 6], although

A. Pitti (✉)

Laboratoire ETIS, UMR 8051, Université de Cergy-Pontoise, St-Martin 1, 2, avenue Adolphe-Gauvin F-95302 Cergy-Pontoise, France
e-mail: alexandre.pitti@ensea.fr

Y. Kuniyoshi

Laboratory for Intelligent Systems and Informatics, Department of Mechano-Informatics, University of Tokyo, Tokyo, Japan
e-mail: kuniyosh@isi.imi.i.u-tokyo.ac.jp

the mechanism by which choline influences learning and memory remains unclear. In this paper, we propose that ACh operates as a kind of “order parameter” for memory development to reorganize functionally the cortico-hippocampal system into a working memory for novelty.

The cholinergic system is composed of two chemical families with different genes expressions that have high affinity either with nicotine or muscarine via nicotinic acetylcholine receptors (nAChRs) and muscarinic acetylcholine receptors (mAChRs). Current researches in pharmacology focus their attention especially on nAChRs because of its high sensitivity with nicotine which can exert neurotoxic effects on development [7]. This is particularly detrimental because innervation of nicotinic receptors nAChRs in the cerebral cortex and hippocampus is very early and rapid as it falls within the first 6 months of life [1, 7, 8].

In contrast, the binding of muscarinic acetylcholine receptors mAChRs tends to rise significantly after birth till the first year and particularly within the entorhinal cortex, the gating pathway to hippocampus, to reach 80% density relative to the childhood period [1, 8]. The role of mAChRs differs from nAChRs’ one but they are both equally important since mAChRs regulate the maturing entorhinal system to detect and to support the encoding of novel signals into the hippocampus [9]. Taken together, these findings suggest that understanding the innervation timeline of the cholinergic system into the different brain regions, and particularly in the hippocampal region, can provide us a better comprehension of the developmental changes occurring during the first year.

From a cognitive viewpoint, the cholinergic system is known to regulate the balance between memory storage and renewal depending on its concentration level and the brain regions where it is released [10]. In the cerebral cortex, ACh modulates the synaptic plasticity by enhancing long-term potentiation depending on its concentrate rate [11]. In the hippocampal system, ACh acts as a working memory for novel information [4, 9]; high concentration level of ACh sets the circuit dynamics for attention and encoding of new memory whereas low level of ACh regulates the consolidation of older memories [12]. More precisely, mAChRs are involved in the persistent firing of individual entorhinal neurons for the maintenance of novel information [13–15] and nAChRs are involved in synaptic plasticity of the hippocampal cells for learning memory patterns.

Interestingly, the period of cholinergic maturation in the hippocampal system coincides with the period when infants enrich their motor repertoire with novel actions [16], categorize novel objects into new classes [17, 18], shift from an egocentric representation of space to an allocentric one [19] which are all features attributed to hippocampal processing. Furthermore, this chronology of the hippocampal changes agrees with Nelson’s proposal that the operative brain does not come ‘online’ until the second half of the first year when the hippocampus is fully functional [20].

We can hypothesize therefore that the cholinergic system plays the key role to activate the learning capabilities of the hippocampal system rapidly (through

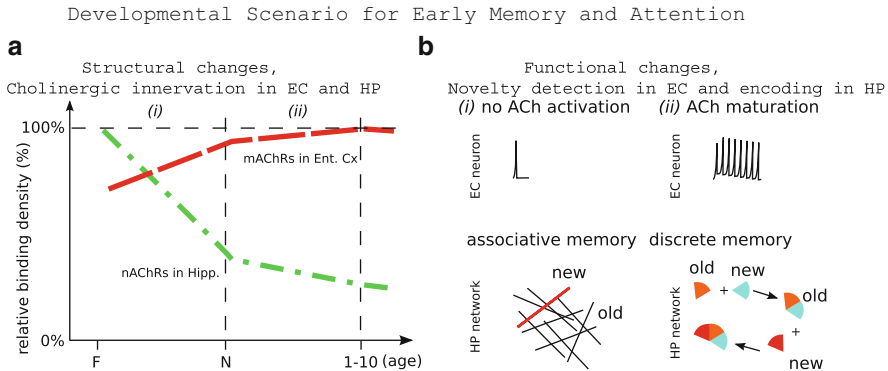


Fig. 1 Structural and functional changes in the hippocampal system and its contribution for early development of memory and attention. Graph (a) describes the evolution of the cholinergic levels in the entorhinal cortex (EC) and in the hippocampus (CA3 and CA1) during the first year; adapted from [1]. Figure (b) presents how the maturation of the cholinergic system would activate the functioning of the hippocampal structure. During the period (i), ACh in EC is not active enough to detect and support novel signals, HP works as an associative memory. When ACh is active during the period (ii), entorhinal neurons can detect and sustain novel signals, while HP favors their learning. HP works then as a discrete memory

fast nAChRs binding) while augmenting slowly the filtering capabilities of the entorhinal system for novelty detection (through slow mAChRs binding), see Fig. 1.

The paper is organized as follows. In the first part we define the parahippocampal networks associated with the neuromodulatory mechanism of acetylcholine. The good balance between the cholinergic rules controls the overall stability and plasticity of the system; i.e., to maintain the hippocampal signals and/or to sustain the novel ones coming from the entorhinal system. It follows that, without ACh, the cortico-hippocampal system behaves as a classical associative memory that extracts the statistical features from the inputs whereas the gradual activation of ACh changes the cortico-hippocampal system into a self-organizing discrete map that rewards the novel signals over the familiar patterns. The new system acquires then the emerging functionalities of a working memory which can deal with novelty by categorizing the novel patterns and by maintaining them active during encoding. We suggest that this feature could support a mechanism for delayed-response tasks to novel stimuli located in the hippocampus [9], complementary to those located in the prefrontal cortex, also based on ACh [21]. Moreover, since hippocampal theta waves have been observed during the Piagetian A-not-B error experiment [22, 23], which is a delayed-response task for novel stimuli that has served also as a touchstone for many theories of cognitive development [24–26], we propose to examine this experience in the light of the cholinergic activation in this area.

2 Neuromodulators and Neural Circuits

We describe in this section the models defined for the hippocampus and the entorhinal cortex with their respective networks architecture and regulatory mechanisms. The EC network consists of uncoupled, bistable neurons and feeds forward to the HP network, which is fully recurrent and receives an oscillating current in the theta band.

2.1 Stellate Cells of Entorhinal Neurons

In contrast with the most common types of neurons in the neo-cortex, the stellate cells of entorhinal neurons possess some specific *internal* currents, cholinergic-dependent, which permit them to sustain long-lasting bursting even if inputs fade away [27]. Moreover, the entorhinal neurons possess very few recurrent connections so that the entorhinal cortex can be modeled as a segregated network of isolated neurons with *no* synaptic connections between them. According to Hasselmo, it is the muscarinic cholinergic receptors that enable persistent spiking to continue after the sample stimulus [4, 9]. We formalize them with the neuron model proposed by Izhikevich [28] which is a resonator cell whose bursting frequency increases depending on the input current I :

$$\begin{cases} C v' = k(v - v_r)(v - v_t) - u + I \\ u' = ab(v - v_r) - u \end{cases} \quad (1)$$

where I is the external input bound in the interval $[0; 2,000 \mu A]$, v represents the membrane potential of the neuron and u represents a membrane recovery variable (cf., [28, 29]); v' and u' their temporal derivate. The voltage threshold level v_t is set to -45 mV and the resetting voltage level V_r to -60 mV. We set also the constants $C = 2,000$ and $k = 0.75$. The after-spike resetting is done with

$$\text{if } v \geq +v_{peak}, \text{ then } \begin{cases} v \leftarrow c \\ u \leftarrow u + d. \end{cases} \quad (2)$$

with $v_{peak} = 30$ mV. The variables set $\{a, b, c, d\}$ defines the neurons attributes $(a; b) = (0.01; 15.0)$ and $(c; d) = (-50; 200)$.

2.2 Hippocampal Neurons

The hippocampal neurons are defined with the model proposed by Colliaux [30] that realizes a up- and down-states where up-states are associated with firings and

down-states with silences. Up- and down-states occur at each theta cycle – which is the natural rhythm of the hippocampal neurons between 6 and 10 Hz – and the up-state firings trigger in advance or in retard to it, before and after the peak.

The phasic (temporal) information from all the neurons represent then one memory pattern. Theta oscillations are modelled by the two variables, S and ϕ , such that an oscillation component $\cos \phi$ produces the intrinsic oscillation of the membrane potential S for which the phase ϕ depends on its level of depolarization. In a network of N units, the state of the cell i is defined by $\{S_i, \phi_i\} \in \mathfrak{R} \times [0, 2\pi[$, for ($i \in [1, N]$) and evolves according to the dynamics:

$$\begin{cases} S'_i = -S_i + \frac{1}{N} \sum_{j=1}^N w_{ij} R(S_j) + \Gamma(\phi_i) + I_i \\ \phi'_i = \omega + (\beta - \Lambda(S_i)) \sin \phi_i \end{cases} \quad (3)$$

with w_{ij} , the synaptic weight between cells i and j . $R(S_j)$ is the spike density of the cell j and I_i represents the driving stimulus which enables to selectively activate a cell. In the second equation, ω and β are respectively the frequency and the stabilization coefficient of the internal oscillation.

The spike density is defined by a sigmoid function:

$$R(x) = \frac{1}{2}(\tanh(g(x - 0.5)) + 1). \quad (4)$$

The coupling between the two equations, Γ and Λ appear as follows:

$$\begin{cases} \Gamma(\phi_i) = \sigma(\cos \phi_i - \cos \phi_0) \\ \Lambda(S_i) = \rho S_i \end{cases} \quad (5)$$

where ρ and σ modulates the coupling between the internal oscillation and the membrane potential, and ϕ_0 is the equilibrium phase obtained when all cells are silent ($S_i = 0$); i.e., $\phi_0 = \arcsin(-\omega/\beta)$. We used the following parameters in our experiments: $\omega = 1$, $\beta = 1.2$ and $g = 10$. Accordingly, $\cos \phi_0 \approx -0.55$. ρ , σ are adjusted respectively to 1 and 0.96, and external voltages I are normalized below 0.1 to not saturate the hippocampal dynamics.

The coupling to the entorhinal system is done as follows. The entorhinal neurons receive the membrane voltage S from their respective hippocampal neurons, which is originally comprised between $(-0.5 \text{ V}; 1.5 \text{ V})$ and renormalized to $[0 \text{ mA}; 2,000 \text{ mA}]$, such that any up-state oscillation entrains the entorhinal neuron to increase its firing rate.

The system behaves as follows. For a hippocampal network of eighty units ($N = 80$) regrouped into ten clusters with initial synaptic weights, the system transits freely from one pattern to another without external inputs, see the raster plot in Fig. 2; same conditions as in [30]. The small perturbations pull up one pattern (up-state) and pull down the others (down state) at each theta cycle. Under these

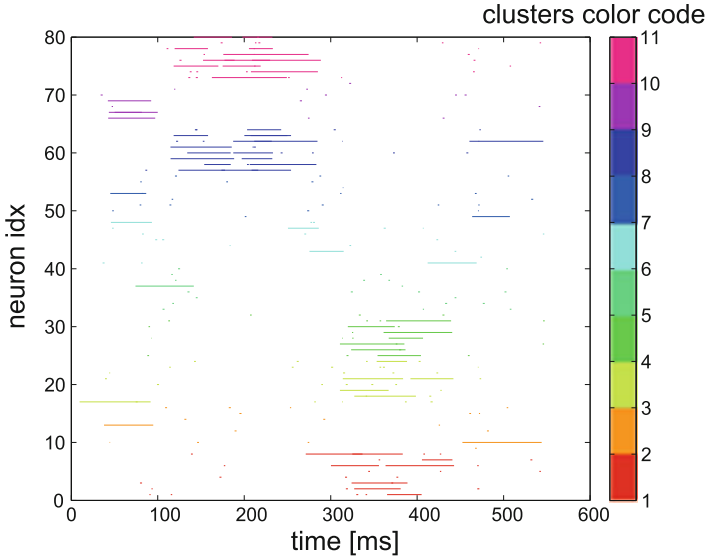


Fig. 2 Raster plot of the hippocampal dynamics without external drive. The network dynamics stabilize or switch from one cluster to another at each theta cycle

conditions, the coupled system has an interesting stability-plasticity trade-off as it can recall rapidly its already learnt patterns but cannot maintain easily the new ones.

2.3 Hebbian Learning

Memory patterns in the hippocampal system are associated with the respective up-state of the active cells, see Fig. 2. The robustness of one particular neural pattern depends then on the strength of the neurons' synaptic weights. The regulation of these weights are done by aHebb-like rule that strengthens the links of two contingent neurons i and j by a small fraction Δw (long-term potentiation) computed by

$$\Delta w = \epsilon I_i I_j, \quad (6)$$

with learning rate $\epsilon = 10^{-5}$. The weights' updating rule is then:

$$w_{ij}(t+1) = w_{ij}(t) + \Delta w. \quad (7)$$

The hippocampal system behaves as a classical associative memory which follows the probability distribution of the imposed external inputs.

2.4 Cholinergic Neuromodulation

Acetylcholine levels control the balance between memory storage and memory update at both the cellular and the circuits levels [9]. In the hippocampus, nAChRs modulate the synapses' plasticity at the circuit level whereas mAChRs modulate the neurons firing at the cells level in the entorhinal cortex: on the one hand, when a novel input is exposed, high cholinergic levels make the entorhinal cells to generate spikes and favor hippocampal plasticity; i.e., plasticity to afferent input, on the other hand, when a familiar input is exposed, low cholinergic levels do not affect the entorhinal cells and reinforce the hippocampal network; i.e., robustness against afferent input.

The concentration level of ACh can be defined then as the relative novelty index of one input pattern I to the embedded hippocampal patterns. The novelty distance can be computed from the hippocampal weights w of dimension N^2 ($w_{i,j} \in [1, \dots, N] \times [1, \dots, N]$). For an input I of N elements ($I_{i \in [1, \dots, N]}$), the novelty index `ACh_level` is defined as:

$$\text{ACh_level} = 1 - \frac{1}{N(N-1)} \sum_i \sum_j I_i \cdot w_{ij}, \text{ for } i \neq j. \quad (8)$$

with `ACh_level` comprised between $[0, 1]$ for which a low value corresponds to a familiar pattern and a high value corresponds to a novel one.

Its action on the networks is as follows. In the entorhinal network, input currents are sustained for any concentration rates above a specified level `novelty_threshold`. One simple rule to relate the entorhinal neurons' resonance to `ACh_level` is:

if `ACh_level` > `novelty_threshold`, then
sustain input current intensity I .

This condition applies for the first time the input is above the threshold and its value stays fixed during the whole period when `ACh_level` > `novelty_threshold`. In the hippocampal network, the plasticity of the hippocampal weights is adjusted proportionally to `ACh_level` which functions as a variable learning rate [31]. The updating rule in Eq. 7 is changed in:

$$w_{ij}(t+1) = w_{ij}(t) + \text{ACh_level} \Delta w. \quad (9)$$

To understand better the effect of neuromodulation on the networks, we conduct a priming task experiment when the EC-HP networks are exposed to a novel input, see Fig. 3. We recall that HP and EC have 80 units each with intra-map connections for HP (not for EC) and unidirectional connections from EC units to their respective HP units.

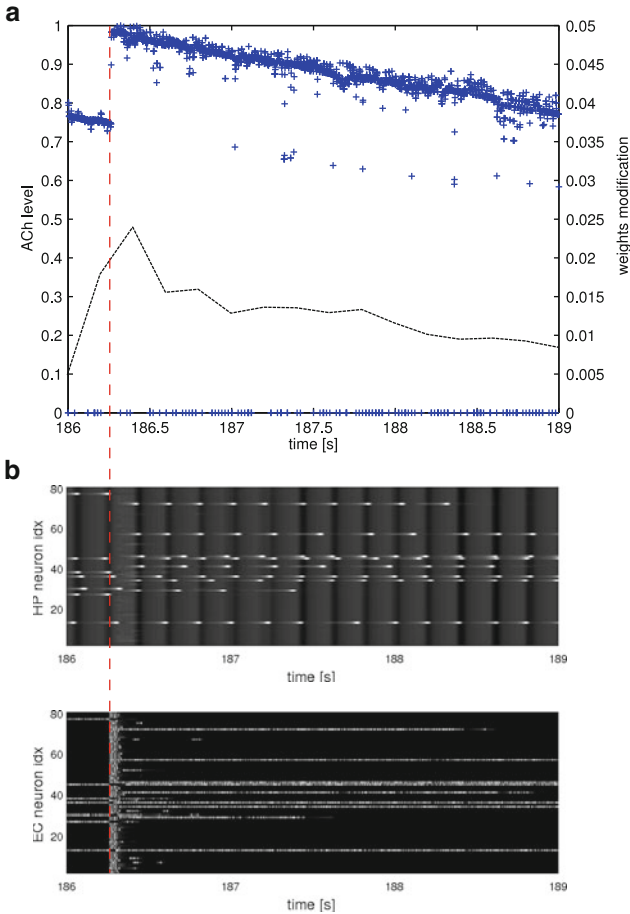


Fig. 3 Effect of cholinergic activation on the hippocampal and entorhinal dynamics after presentation of a novel input. The exposure of a novel input (*red line*) rises ACh level to its highest value (*blue crosses* in **a**), which contributes to sustain the dynamics in both networks and to enhance its learning. While the pattern is being learnt, ACh level slowly decreases as a counter-effect

The presentation of a novel input to the entorhinal cortex at $t = 186.25$ s (see Fig. 3b) automatically rises ACh_level to a high value (see the blue crosses in Fig. 3a). It has for net effect to keep the entorhinal neurons firing for several seconds and to enhance the hippocampal encoding of the novel memory with respect to Eq. 9, see the black line in Fig. 3a. Therefore, the more novel a pattern is, the higher ACh_level (ascending phase). In return, the hippocampus strengthens more its synaptic links to the novel pattern, which makes it less novel and reduces accordingly $\langle \Delta w \rangle$ and ACh_level (descending phase). In other words, the cholinergic system plays the role of a ‘retainer’ for novel signals that can be used further for attentional tasks.

3 Simulations

3.1 Developmental Timeline of Cholinergic Innervation

In this section, we simulate the progressive cholinergic innervation of the hippocampal system. On the one hand, muscarinic binding in the entorhinal cortex, which is responsible for sustaining novel signals, is slow to mature and reaches its highest level at 1 year-old period [1].

On the other hand, nicotinic binding in the hippocampus, which is responsible for the reinforcement learning of older memories, is very fast to mature as it drastically falls with age during the fetal and post-natal period [1, 32]. We model the gradual mAChRs binding in EC with the variable `activation_ratio` that augments continuously within the range $[0, 1]$: `activ_ratio` = 0 corresponds to the fetal period when there is no muscarinic binding and `activ_ratio` = 1 corresponds to the period when the infant reaches its first year and when the hippocampus is fully operational.

To simplify our experimental setup, the maturational parameter `activ_ratio` augments linearly with a step of 10^{-4} per iteration (1 ms), starting at the simulation time $t = 50$ s. The variables `ACh_level` and `novelty_threshold` are weighted to `activ_ratio` so that they reach progressively their maximal value when `activation_ratio` = 1. As a rule, the initial level of `novelty_threshold` is set to 0.85 to filter as much as possible novel signals in the beginning of the simulation whereas its value is decreased progressively to allow more novel signals to pass. We impose this ad hoc rule in order to replicate the functional acceleration observed during cholinergic innervation in brain development.

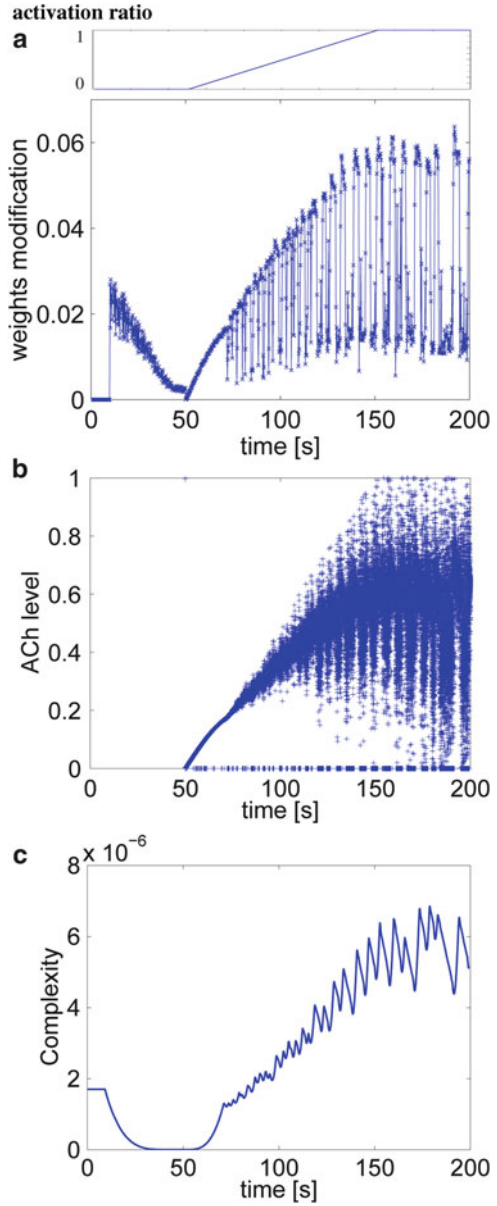
The equations set for the cholinergic activation is then:

$$\begin{cases} \text{ACh_level}(t + 1) = \text{activ_ratio} \times \text{ACh_level}(t) \\ \text{novelty_threshold}(t + 1) = \\ \quad \text{activ_ratio} \times (0.85 - 0.25 \text{activ_ratio}), \end{cases} \quad (10)$$

where `activ_ratio` stands for `activation_ratio`. We present in Fig. 4 the results of this developmental scenario when the hippocampal system is exposed to random inputs, starting at $t = 50$ s, when `activ_ratio` increases linearly to 1.

Figure 4a plots the weights modification $\langle \Delta w \rangle$ averaged over all the weights at each time step, Fig. 4b plots the evolution of `ACh_level` during cholinergic activation and Fig. 4c displays the overall complexity inside the hippocampal network computed from the synaptic weight matrix. The complexity measure $C(w)$ of the system's weight matrix w is defined as the difference between the integration level $I(w)$ considered as a whole and the average integration for small subsets within, following [33]: $C_N(w) = \sum_{k=1}^n [(k/n)I(w) - \langle I(w_j^k) \rangle]$. Low complexity levels reflect a randomly or a uniformly organized network with low memory

Fig. 4 Weight modification for Hebbian learning with gradual activation of ACh modulation starting at $t = 50$ s resp. **(a)** and **(b)**. Complexity measures computed from the connection matrix of the hippocampal network relative to cholinergic activation rate **(c)**



capacity whereas high complexity levels reflect functional connectivity within the network and higher memory capacity.

The situation before ACh activation, when $activ_ratio = 0$ ($t < 50$ s), corresponds to the case described in Sect. 2.3 when the learning system encodes continuously the external inputs and converges to its probabilistic distribution.

The weights rapidly stabilize themselves within a minimal fluctuation regime and the system behaves as a classical associative memory. The complexity level decreases continuously indicating that the hippocampus continuously adapts its structure to the novel inputs while it forgets at the same time the older memories (poor stability/plasticity ratio).

This situation drastically changes at $t = 50$ s when the binding process begins to start. Here, the variable `ACh_level` starts to oscillate between low and high states with bigger amplitudes as `activ_ratio` augments: the learning system becomes more and more sensitive to the inputs' novelty and scaffolds its memory capacity by embedding one at a time a novel input : a phase transition is at work within the neural dynamics. The ascending phases (i.e., the crests) correspond to the encoding periods and the descending phases (i.e., the troughs) correspond to the continued encoding of established CA3/CA1 patterns.

Moreover, this capability produces within the system some new emergent functionalities. For instance, since the new patterns do not overlap with the old memories, the hippocampal system tends to be sparsely organized, which rise in fine its complexity level. In other words, it enables the hippocampal system to categorize on the fly new memories while preserving the old ones. The result is the emergence of a 'working memory for novelty' – i.e., a memory that can support the detection and the learning of novel and non-novel patterns – that scaffolds over time the memory organization.

3.2 \overline{AB} Experiment

The experiment in the previous section described how the good balance between the cholinergic rules permits to control the overall stability and plasticity of the system in order to maintain hippocampal signals or to sustain the entorhinal signals.

This is particularly critical during the first year when infants exploit these attentional skills for cognitive processing. For instance, the development of a working memory for novelty endows the infant to succeed delayed-response tasks, which are also correlated with high theta rhythm [23]. Besides, there is substantial evidences that cholinergic innervation is a necessary component for the development of such a working memory since ACh levels in the hippocampus and cerebral cortex correlate also to behavioral performance in spatial attention and memory [6, 15, 34–36]. Based on these evidences, we propose that the hippocampal cholinergic system plays an important functional role for succeeding the Piagetian A-not-B task [22], along the prefrontal cortex. We envision therefore the prefrontal cortex to be complementary to the hippocampus in this task and not to be the most important as it is prevailed in most developmental theories [25, 37–39].

The classic Piagetian A-not-B error witnesses the developmental changes occurring during the first year, see Fig. 5. A tantalizing object is presented to an infant and put in a box at a location *A* hidden from his sight for several trials, then the object is lastly set at a new location *B*. A peculiar mistake occurs for infants of 7–8 months

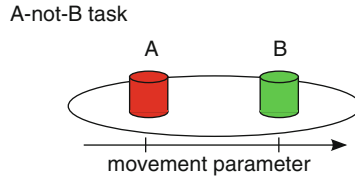


Fig. 5 A-not-B experiment with a protocol similar to [42]. The localized peaks of activation in the neural system respect the spatial topology of the environment such that location *A* is represented by neurons of low-ranked indices and location *B* by those of high rank

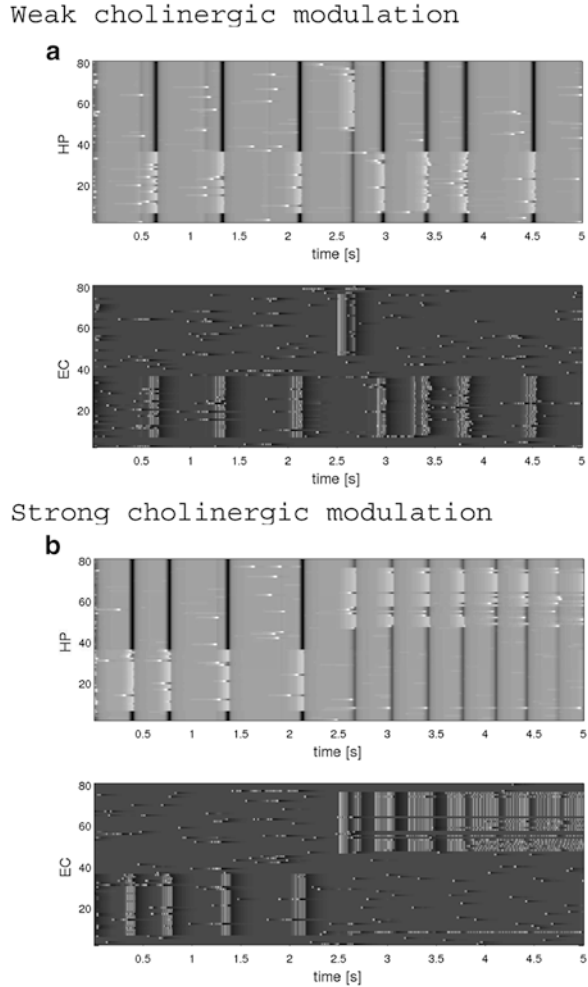
of age which is to perseverate searching at the *A* location when a delay to reach is imposed. For 10–12 months old infants, the error however disappears and most infants succeed to reach the object at its correct location independently to the delay-interval duration. Hence, the presence of the delay is critical to exhibit the error [40] whereas the error still persists even when the object is not hidden at all [41].

Our experimental protocol is similar to the one proposed by [42] where the spatial coordinates along a unidimensional space are assimilated to the topology of the neurons indices, see Fig. 5: low-ranked indices neurons are associated to the location *A* in the left-side and the high-ranked indices neurons are associated to location *B* in the right-side. We employ the same neural circuits used in the previous sections (each network is composed of 80 units) and initialize its weights probability distribution corresponding to the location *A* only – i.e., we skip the learning phase. The neurons with lower indices comprised in the interval between [5, . . . , 35] are set with the weights distribution $w = 0.05$ and the other weight coefficients are set to zero. We present the behavior of the cortico-hippocampal system before and after cholinergic innervation when a novel pattern *B* is presented for a short period of time, see Fig. 6. Figure 6a displays the raster plot of a weakly innervated network and Fig. 6b displays the raster plot of a matured network.

For the case of a weak cholinergic activation in Fig. 6a, which corresponds to the situation described in Sects. 2.3 and 2.4 for `activation_ratio` < 0.22, the network does not get easily perturbed by novel inputs and it remains mostly insensitive to external exposure; the system has a strong stability-versus-plasticity ratio. As a result, the hippocampal system stays only for one theta cycle at the *B* pattern presented at $t = 25$ s but then perseverates to the learnt pattern *A*, even if the pattern *B* was exposed for several tens of milliseconds. The neural system displays the properties of a reinforcement learning system without attentional mechanism which strongly bias the familiar patterns against the new ones. In contrast, the cholinergic activation of the hippocampal ensemble detects and holds the novel pattern *B* in regard to the embedded memory *A* and even if the former has exposed for a very short period, see Fig. 6b.

The dual mechanism of ACh can permit then to sustain inputs dynamically without interference and competition between memories. We speculate that its nonlinear effect on the maturing hippocampus could be one factor contributing to the U-shaped curve of development discovered with the A-not-B error, showing

Fig. 6 A-not-B task before and after cholinergic activation, resp. **(a)** and **(b)**. Without cholinergic neuromodulation, the short exposure of an object placed at a novel location *B* for several hundreds of milliseconds does not influence the dynamics of the entorhino-hippocampal system whereas the novel pattern is sustained for several seconds for the situation with cholinergic activation



increases in perseveration before showing decreases [43]. ACh allows the cortico-hippocampal system to encode and manipulate flexibly discrete patterns during environmental changes which are then as such categories for the cortical maps to learn progressively the overall structure, see Fig. 7.

4 Conclusion

In this paper, we proposed to model the cholinergic system innervation in the hippocampal system and its influence for learning, attention and memory development. Acetylcholine is involved in the structural and functional adjustments of the hippocampus, transforming it into an attentional system; i.e., a working memory for

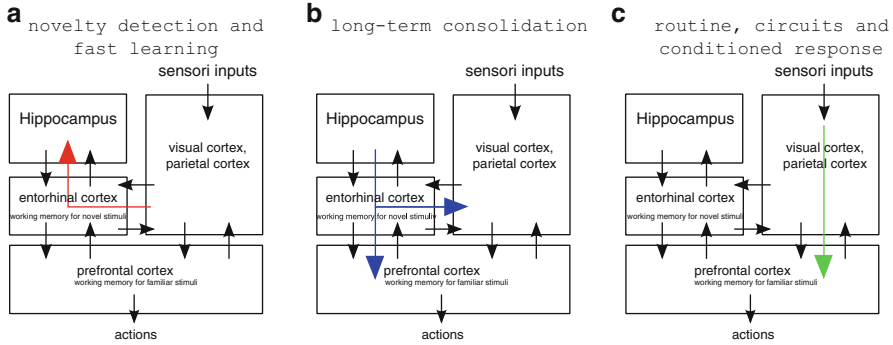


Fig. 7 Cognitive architecture for memory retention, transfer and consolidation

novel information. Under its action, the entorhinal cortex sustains and facilitates the learning of novel stimuli relative to the old patterns already present in the hippocampus. We show in our experiments how this dual mechanism may generate simply some emergent properties necessary for cognitive development. For instance, it limits the interference between memories which has for effect to scaffold the memory organization and to discretize the memory space into separated categories in the same time.

Moreover, our cholinergic hypothesis may give some partial answers to the paradoxes that pose the hippocampus and other subcortical structures that appear to function at birth but show some evidence of slow development and/or functional reorganization. Here, we propose that the neurotransmitter acetylcholine may play the role of a “catalyst” that activates the functional organization of the cortico-hippocampal system (i.e., detecting and holding stimuli, preserving and acquiring memories).

Although ACh is generally known to regulate the structural maturation of the central nervous system [2] – e.g., the growth, differentiation, and plasticity of the neurons – the precise timing of cholinergic innervation to the cortex appears to be crucial also for the normal development of cognitive functions. Its action is even broader since ACh has been identified for mediating the propagation of slow waves of electrical activity in the developing neocortex [3, 44], which are associated with long-term memory and categorization performances [17, 18]. In our model, we show how theta waves could slowly shape the neocortical maps into coherent patterns (rhythmical theta/gamma activity). Hence, the modeling of the cholinergic system in the para-hippocampal system is not only critical for understanding development during the first year [1] but also for understanding memory transfer, attention processes and retrieval task [4].

Since acetylcholine is highly associated with hippocampal performances and that hippocampal theta rhythm is involved in spatial processing [6] and in working memory tasks such as the Piagetian A-not-B task [23], any serious developmental theories should be considered in the light of it.

Acknowledgments The authors would like to thank professor Ichiro Tsuda for his valuable comments and remarks.

References

1. J. Court, S. Lloyd, M. Johnson, M. Griffiths, N. Birdsall, M. Piggott, A. Oakley, P. Ince, E. Perry, and R. Perry, "Nicotinic and muscarinic cholinergic receptor binding in the human hippocampal formation during development and aging," *Developmental Brain Research*, vol. 101, pp. 93–105, 1997.
2. J. Lauder and U. Schambra, "Morphogenetic roles of acetylcholine," *Environmental Health Perspectives*, vol. 107, pp. 65–69, 1999.
3. L. Descarries, N. Mechawar, N. Aznavour, and K. Watkins, "Structural determinants of the roles of acetylcholine in cerebral cortex," *Progress in Brain Research*, vol. 145, pp. 45–58, 2004.
4. M. Hasselmo, "The role of acetylcholine in learning and memory," *Current Opinion in Neurobiology*, vol. 16, pp. 710–715, 2006.
5. M. Matsukawa, M. Ogawa, T. Nakadate, K. Maeshima, Y. Ichitani, N. Kawai, and N. Okado, "Serotonin and acetylcholine are crucial to maintain hippocampal synapses and memory acquisition in rats," *Neuroscience Letters*, vol. 230, pp. 13–16, 1997.
6. W. Meck, C. Williams, J. Cermak, and J. Blusztajn, "Developmental periods of choline sensitivity provide an ontogenetic mechanism for regulating memory capacity and age-related dementia," *Front. Integr. Neurosci.*, vol. 1, no. 7, pp. 1–11, 2008.
7. J. Dwyer, S. McQuown, and F. Leslie, "The dynamic effects of nicotine on the developing brain," *Pharmacology & Therapeutics*, vol. 122, pp. 125–139, 2009.
8. J. Court, E. Perry, M. Johnson, M. Piggott, J. Kerwin, R. Perry, and P. Ince, "Regional patterns of cholinergic and glutamate activity in the developing and aging human brain," *Developmental Brain Research*, vol. 74, pp. 73–82, 1993.
9. M. Hasselmo and C. Stern, "Mechanisms underlying working memory for novel information," *Trends in Cognitive Sciences*, vol. 10, no. 11, pp. 487–493, 2006.
10. P. Gold, "Acetylcholine modulation of neural systems involved in learning and memory," *Neurobiology of Learning and Memory*, vol. 80, pp. 194–210, 2003.
11. K. Doya, "Metalearning and neuromodulation," *Neural Networks*, vol. 15, p. 495506, 2002.
12. M. Hasselmo and J. McGaughy, "High acetylcholine levels set circuit dynamics for attention and encoding and low acetylcholine levels set dynamics for consolidation," *Progress in Brain Research*, vol. 145, pp. 207–231, 2004.
13. R. Knight, "Contribution of human hippocampal region to novelty detection," *Nature*, vol. 383, pp. 256–259, 1996.
14. R. Klink and A. Alonso, "Ionic mechanisms of muscarinic depolarization in entorhinal cortex layer ii neurons," *J. Neurophysiol.*, vol. 77, pp. 1829–1843, 1997.
15. D. Kumaran and E. Maguire, "Novelty signals: a window into hippocampal information processing," *Trends in Cognitive Sciences*, vol. 13, no. 2, pp. 47–54, 2009.
16. K. Adolph and A. Joh, *Multiple learning mechanisms in the development of action*. New York: Oxford University Press, 2009.
17. L. Smith and L. Samuelson, "Perceiving and remembering: Category stability, variability and development," In K. Lamberts & D. Shanks (Eds.), *Knowledge, Concepts and Categories*. Psychology Press, East Sussex, UK, pp. 161–195, 1997.
18. P. Quinn, A. Westerlund, and C. Nelson, "Neural markers of categorization in 6-month-old infants," *Psychological Science*, vol. 17, pp. 59–66, 2006.
19. N. Newcombe and J. Huttenlocher, "Development of spatial cognition," *Handbook of Child Psychology*, vol. 5, no. 2, pp. 734–776, 2006.

20. C. Nelson, "The ontogeny of human memory: A cognitive neuroscience perspective," *Developmental Psychology*, vol. 31, pp. 723–738, 1995.
21. A. Yu and P. Dayan, "Acetylcholine in cortical inference," *Neural Networks*, vol. 15, no. 4-6, pp. 719–730, 2002.
22. J. Piaget, *The construction of reality in the child*. New York: Basic Books, 1954.
23. K. Cuevas and M. Bell, "Eeg and ecg from 5 to 10 months of age: Developmental changes in baseline activation and cognitive processing during working memory task," *Int. J. of Psy.*, vol. 80, no. 2, pp. 119–128, 2011.
24. A. Diamond, "Development of the ability to use recall to guide action, as indicated by infants' performance on a-not-b," *Child Development*, vol. 74, pp. 24–40, 1985.
25. Y. Munakata, "Infant perseveration and implications for object permanence theories: A pdp model of the a-not-b task," *Developmental Science*, vol. 1, no. 2, pp. 161–211, 1998.
26. L. Smith and E. Thelen, "Development as a dynamic system," *Trends in Cognitive Sciences*, vol. 7, no. 8, pp. 343–348, 2003.
27. R. Klink and A. Alonso, "Muscarinic modulation of the oscillatory and repetitive firing properties of entorhinal cortex layer ii neurons," *J. Neurophysiol.*, vol. 77, pp. 1813–1828, 1997.
28. E. M. Izhikevich, "Simple model of spiking neurons," *IEEE Transactions on Neural Networks*, vol. 14, pp. 1569–1572, 2003.
29. E. Izhikevich, "Polychronization: Computation with spikes," *Neural Computation*, vol. 18, pp. 245–282, 2006.
30. D. Colliaux, C. Molter, and Y. Yamaguchi, "Working memory dynamics and spontaneous activity in a flip-flop oscillations network model with a milnor attractor," *Cogn. Neurodyn.*, vol. 3, pp. 141–151, 2009.
31. M. Hasselmo, "Neuromodulation and cortical function: modeling the physiological basis of behavior," *Current Opinion in Neurobiology*, vol. 67, pp. 1–27, 1995.
32. J. Court, C. Martin-Ruiz, A. Graham, and E. Perry, "Nicotinic receptors in human brain: topography and pathology," *Journal of Chemical Neuroanatomy*, vol. 20, pp. 281–298, 2000.
33. G. Tononi, O. Sporns, and G. Edelman, "A measure for brain complexity: Relating functional segregation and integration in the nervous system," *Proc. Natl. Acad. Sci.*, vol. 91, pp. 5033–5037, 1994.
34. W. Meck, R. Smith, and C. Williams, "Pre- and postnatal choline supplementation produces long-term facilitation of spatial memory," *Dev. Psychobiol.*, vol. 21, pp. 339–353, 1988.
35. S. Ikegami, "Behavioral impairment in radial-arm maze learning and acetylcholine content of the hippocampus and cerebral cortex in aged mice," *Behavioral and Brain Research*, vol. 65, pp. 103–111, 1994.
36. M. Sarter and V. Parikh, "Choline transporters, cholinergic transmission and cognition," *Nat. Rev. Neurosci.*, vol. 6, pp. 48–56, 2005.
37. A. Diamond and P. Goldman-Rakic, "Comparison of human infants and rhesus monkeys on piaget's a-not-b task: Evidence for dependence on dorsolateral prefrontal cortex," *Experimental Brain Research*, vol. 74, pp. 24–40, 1989.
38. S. Dehaene and J. Changeux, "A simple model of prefrontal cortex function in delayed response tasks," *Journal of Cognitive Neuroscience*, vol. 1, pp. 244–261, 1989.
39. S. Marcovitch and P. Zelazo, "A hierarchical competing systems model of the emergence and early development of executive function," *Developmental Science*, vol. 12, no. 1, pp. 1–25, 2009.
40. A. Diamond, "A model system for studying the role of dopamine in the prefrontal cortex during early development in humans: Early and continuously treated phenylketonuria," *Handbook of Developmental Cognitive Neuroscience*. Edited by Charles A. Nelson and Monica Luciana, pp. 433–472, 1998.
41. L. Smith, E. Thelen, R. Titzer, and D. McLin, "Knowing in the context of acting: The task dynamics of the a-not-b error," *Psychological Review*, vol. 106, pp. 235–260, 1999.

42. G. Schöner and E. Dineva, "Dynamic instabilities as mechanisms for emergence," *Developmental Science*, vol. 10, no. 1, pp. 69–74, 2007.
43. L. Gershkoff-Stowe and E. Thelen, "U-shaped changes in behavior: A dynamic systems perspective," *Journal of Cognition and Development*, vol. 1, no. 5, pp. 11–36, 2004.
44. A. Peinado, "Traveling slow waves of neural activity: a novel form of network activity in developing neocortex," *J. Neurosci.*, vol. 20, no. RC54, pp. 1–6, 2000.

Unintentional Synchronization of Behavior in Japanese Monkeys

Yasuo Nagasaka, Zenas C. Chao, Naomi Hasegawa, Tomonori Notoya, and Naotaka Fujii

Abstract The human studies in perception and action in social context revealed that social interaction facilitated behavioral synchronization. To understand brain mechanisms for the synchronization in details, studies in animal model are required. However, little is known about the behavioral synchronization in animals. Here we examined an unintentionally synchronized behavior in monkeys. The unintentional synchronization was quantified by changes in button-pressing behavior while two monkeys were seated facing each other. Different experimental conditions were applied to explore interferences of visual information on the speed and the timing of the button-pressing. The changes in behavior were observed when the subject was paired with another monkey, suggesting that social bonds play an important role in synchronization through visuo-motor or auditory-motor coupling to other's behaviors.

1 Introduction

In social environment, one has to coordinate his or her actions with another in order to establish smooth joint actions. Several studies demonstrated that humans intended to coordinate their actions by predicting others' knowledge and action goals, and by understanding environmental constraints [1]. However, in some cases, the coordination has to be achieved rapidly, where intentional coordination might be unsuitable or impossible, and spontaneous coordination might take place.

Several human studies demonstrated that socially or visually coupled dyad showed spontaneous synchronization in moving a finger, swinging pendulum,

Y. Nagasaka (✉) • Z.C. Chao • N. Hasegawa • T. Notoya • N. Fujii
RIKEN Brain Science Institute, Saitama 351-0198, Japan
e-mail: nyasuo@brain.riken.jp

stepping, rocking chair, and facial expressions [2–6]. Those studies suggested that the synchronized behaviors were the results of unintentional cognitive functions, which might be facilitated by social bonds.

Coordination of actions was also found in non-human social animals, such as flash synchronization of fireflies, movement of shoaling fish, and flying of flocking birds [7–9]. However, most of animal studies were field studies and did not focus on whether the animal changed the behavior on purpose (intentionally) or not (unintentionally). There are a few studies under laboratory setting focused on spontaneous entrainment, however, all of them focused on contagious yawning in animals [10–12]. It is still unclear whether animals show unintentional behavioral changes during voluntary action. Furthermore, animal model is required for further understanding of brain mechanisms underlying coordination, which has not been established yet.

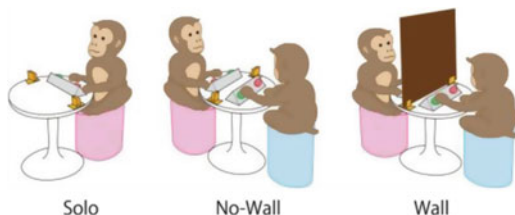
In the present study, we first explored whether monkeys show unintentional synchronization in social environment during a rhythmic behavior: button-pressing action. Furthermore, we examined the importance of visual cues to create corresponding social bond that could lead to unintentional synchronization.

2 Methods

Subjects and materials: Three male Japanese monkeys (*Macaca fuscata*; monkeys B, C, and T) participated in the present study. These monkeys did not have kinship or any preceding interaction consolidating social rank among them. The monkey was seated in a primate chair with his head, chest, and arms free. Through infrared-reflectable markers on a custom jacket, the subject's shoulders, elbows, and wrists positions were recorded by a motion capture system (Vicon Motion Systems, CA, USA) with 120 Hz sampling rate. In each experiment, two monkeys were seated across the table (60 cm diameter) facing each other, each with a button box placed in front of him. The box had two buttons, with LEDs inside, aligned horizontally separated with a distance of 50 cm. Six video cameras were used for recording the whole experimental environment. The experimental session was controlled by iMac (Apple Inc., Cupertino, CA, USA) and was programmed with MATLAB (MathWorks Inc., Natick, MA, USA) using the Psychophysics Toolbox extensions [13]. All procedures were approved in advance by the RIKEN Animal Committee (H20-2-307).

Solo condition: Each monkey was trained individually to press the two buttons alternately. At the outset of each trial, both buttons were illuminated and the monkey could start pressing button from either side. When an illuminated button was pressed, a short note was presented followed by an immediate turnoff of the LED. A trial was considered as successful when a criterion was achieved: a randomly assigned number of pressing (from 30 to 36, $M = 33$) was achieved without pausing for more than 5 s. At the end of each trial, both LEDs were turned off. The following

Fig. 1 Schematics of experimental conditions



trial was started after an inter-trial-interval (ITI; 5 to 10s randomly assigned). After each successful trial, a chime was presented, and the monkey was rewarded with a small piece of apple or nuts during the ITI. After ten consecutive successful trials, the motion capture system and a video recorder were used to record the monkey's button-pressing behavior (Fig. 1, Solo).

No-Wall condition: Two of the three monkeys were seated facing each other while performing the button-pressing task (Fig. 1, No-Wall). The procedure was the same as in *Solo* condition, except that the trial was considered successful when (1) both monkeys satisfied the criteria, and (2) the monkey reached the criterion earlier continued pressing until another monkey reached his.

Wall condition: In order to investigate effects of the visual of another on the individual's button-pressing behavior, a board was placed between two monkeys (Fig. 1, Wall).

In a daily session, three test blocks were conducted. Each block consisted of ten trials in No-Wall condition and 10 trials in Wall conditions, conducted in a random order. A total of 300 trials in five sessions was obtained for each monkey pair.

Quantification of behavioral synchronization: We defined that behavioral synchronization occurred when the timings of button-pressings between paired monkeys were time-locked. Assume the series of button-pressing timings for monkeys B and C in a single trial were $\mathbf{b} = \{b_1, b_2, \dots, b_N\}$ and $\mathbf{c} = \{c_1, c_2, \dots, c_M\}$, respectively, where N and M represent the corresponding numbers of total button-pressings. Then all the possible delays between \mathbf{b} and \mathbf{c} could be represented by:

$$\text{Delays}_{b-c} = \{b_n - c_m | n = 1, 2, \dots, N; m = 1, 2, \dots, M\}$$

In order to identify delays that occurred more frequently than by chance, we compared Delays_{b-c} to its shuffled version. Each b_n in \mathbf{b} was replaced by b'_n , a randomly selected value within the interval of $[(b_{n-1} + b_n)/2, (b_n + b_{n+1})/2]$. This is equivalent to adding a jitter, a value between $(b_{n-1} - b_n)/2$ and $(b_{n+1} - b_n)/2$, to b_n . By repeating this process for all elements in \mathbf{b} and \mathbf{c} , a shuffled set $\mathbf{b}' = \{b'_1, b'_2, \dots, b'_N\}$ was created, and the corresponding delays, $\text{Delays}_{b'-c}$, were measured. This process was repeated 100 times. Then the histogram of Delays_{b-c} (H_{org}), and the histograms of 100 different $\text{Delays}_{b'-c}$ ($H_{sh1}, H_{sh2}, \dots, H_{sh100}$) were created by 200 ms window with 20 ms step. The significant differences in histograms, i.e. H_{org} vs. $\{H_{sh1}, H_{sh2}, \dots, H_{sh100}\}$, indicated the delays that occurred more frequently than by chance (time-locked), which further implied that synchronization occurred.

3 Results

By comparing the button-pressing behavior between when the monkey was *alone* (Solo) and when the monkey was *paired* with another (Wall and No-Wall), we evaluated whether behavioral synchronization occurred.

3.1 Difference in Speed of Button-Pressing Between Alone and Paired Conditions

For each monkey, significant differences in speed of button-pressing were found between Solo and Wall conditions ($p < 0.05$, Wilcoxon signed-rank test), and between Solo and No-Wall conditions ($p < 0.05$). For monkeys B and C, the speed of button-pressing in Wall and No-Wall conditions was significantly slower than the speed in Solo condition. For monkey T, the speed of button-pressing in Wall and No-Wall conditions was significantly faster than the speed in Solo condition (Fig. 2). Furthermore, for monkey C, the speed of button-pressing in No-Wall condition was significantly slower than in Wall condition when paired with monkeys B or T ($p < 0.05$, Wilcoxon signed-rank test). For monkey T, the speed of button-pressing in No-Wall condition was significantly slower than in Wall condition when paired with monkey C ($p < 0.05$) but not with monkey B (Fig. 2). For monkey B, no significant difference in speed was found between No-Wall and Wall conditions when paired with either monkey C or T. Those results indicated that the speed of button-pressing was affected by the visual of the paired monkey's behavior. Also, the influence of the visual was partner-dependent.

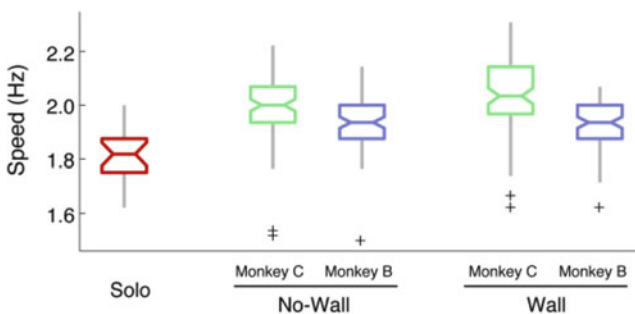


Fig. 2 The change of speed in button-pressing. One representative example (monkey T) of the speed of button-pressing in Solo condition and paired with monkeys B or C in each experimental condition. +: outlier. See text for details of statistical difference between conditions

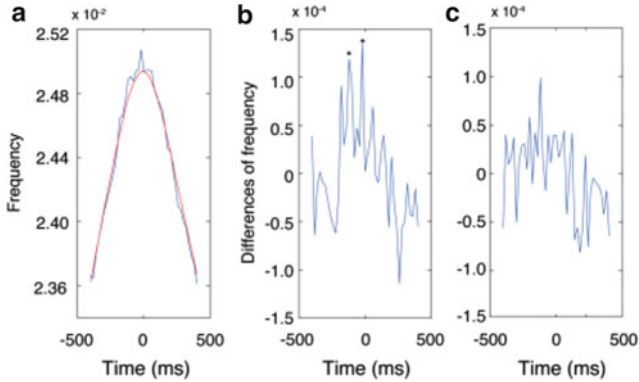


Fig. 3 Quantification of behavioral synchronization between monkeys B and T. (a) One representative example of H_{org} and H_{sh} in monkey B calculated by aligning the button-pressing of monkey T in No-Wall condition; the blue line represents H_{org} and the red line represents H_{sh} . (b) The difference of histograms between H_{org} and H_{sh} . (c): The difference of histograms between H_{org} and H_{sh} . for the same monkeys in Wall condition. * $p < 0.01$, Wilcoxon signed-rank test (one-tailed)

3.2 Synchronization in Button-Pressing

To explore the synchronization of button-pressing behavior in paired monkeys, a histogram created from the original data (H_{org}) was compared with histograms created from the shuffled data ($\{H_{sh1}, H_{sh2}, \dots, H_{sh100}\}$) (Fig. 3a). If the timings of button-pressings in the original data contain specific temporal structures, then those structures are likely destroyed in the shuffled data (see Methods). Thus, the values significantly greater in H_{org} than in $\{H_{sh1}, H_{sh2}, \dots, H_{sh100}\}$ represent the time-locked delays in the timings of button-pressings in the original data. Time-locked delays were found in all pairs of monkeys in No-Wall condition ($p < 0.01$, Wilcoxon signed-rank test, one-tailed). A representative example between Monkeys B and T in No-Wall condition is shown in Fig. 3b, where time-locked delays at -120 and -20 ms were found. This indicated that Monkey B pushed a button before Monkey T more frequently with 20 or 120 ms delays.

Those results indicated that the timing of button-pressing was time-locked with a monkey was paired with another. Furthermore, no significant time-locked delay was found in all pairs of monkeys when visuals of partners were absent (Wall condition, Fig. 3c). Those results further suggested that visuals of the partner played a crucial role in synchronization in button-pressing behavior.

4 Discussions

In summary, we found that the speed of button-pressing in monkeys was affected by social bonds, which were partner-dependent. Furthermore, the synchronization of button-pressing occurred when social bonds were formed.

To ensure the synchronization was induced by unintentional factors, instead of intentional factors, such as learning, we trained each monkey separately. During training, the monkeys were never differentially reinforced to change the speed of button-pressing. Furthermore, when the monkeys were paired, food rewards were presented to both monkeys at the same time when the monkeys reached the criteria (see Methods). This procedure was unlikely to reinforce competition for food, change of speed, nor synchronization. Therefore, the change of the monkeys' behavior was, at least, not due to learning process. Furthermore, the monkeys did not need to synchronize their behavior with another to get food; the synchronization of behavior in the present study was fruitless for the monkeys. For this reason, the monkeys were likely to coordinate their behavior unintentionally, not intentionally. To our knowledge, this is the first demonstration of unintentional synchronized voluntary behavior in non-human animals under laboratory settings.

We further demonstrated that the synchronization could be disrupted by the absence of visual cues. Other information, such as auditory cues, might also involve in creating social bonds that lead to the observed synchronization. However, the effect of the sound was not investigated in the present study. In Wall condition, the monkey could not see the partner, but could hear the sound corresponding to button-pressing of the partner. We showed that the sound cue affected the speed of button-pressing in Wall condition (Fig. 2), however, the sound did not induce the synchronization (Fig. 3). Therefore, the sound might have a little effect for forming social bonds, but it was not enough for causing synchronization.

During synchronization, a subject's behavior was affected not only by his partner's behavior, but also his own previous behavior. That is, changes in the subject's behavior could affect his partner's behavior, which would be perceived and then consequently affect the subject's own behavior. In order to dissociate this complex feedback and to understand how coordination could occur in a one-way manner, our future plan is to investigate synchronization when a monkey is paired with a virtual monkey (video-recorded monkey).

The brain areas responsible for the unintentional behavioral synchronization remain undiscovered. In monkey studies, "mirror system", including the ventral premotor cortex and the rostral region of the inferior parietal lobule, was activated during the monkey's performing an action and also during the monkey's observing the same action [14]. Therefore, it is likely that those areas also involve in the unintentional coordination of actions. Our future plan is to record neural activities in multiple brain areas in the subjects presented in this work, and to identify neural correlates underlying the unintentional behavioral synchronization.

Acknowledgments This study is partly supported by Grant-in-Aid for Scientific Research on Innovative Areas 'Neural creativity for communication' (22120522) of MEXT, Japan

References

1. Sebanz, N., Bekkering, H., Knoblich, G.: Joint action: bodies and minds moving together. *Trends Cogn Sci* 10 (2006) 70–76
2. Oullier, O., de Guzman, G. C., Jantzen, K. J., Lagarde, J., Kelso, J. A.: Social coordination dynamics: measuring human bonding. *Soc Neurosci* 3 (2008) 178–192
3. Richardson, M. J., Marsh, K. L., Schmidt, R. C.: Effects of visual and verbal interaction on unintentional interpersonal coordination. *J Exp Psychol Hum Percept Perform* 31 (2005) 62–79
4. Honma, M., Kumada, T., Osada, Y., Nagai, M.: The synchronized stepping -Automatic imitation behavior between persons-. *The Japanese Journal of Psychonomic Science* 27 (2008) 127–128
5. Richardson, M. J., Marsh, K. L., Isenhower, R. W., Goodman, J. R., Schmidt, R. C.: Rocking together: dynamics of intentional and unintentional interpersonal coordination. *Hum Mov Sci* 26 (2007) 867–891
6. Sato, W., Yoshikawa, S.: Spontaneous facial mimicry in response to dynamic facial expressions. *Cognition* 104 (2007) 1–18
7. Copeland, J., Moiseff, A.: The occurrence of synchrony in the North American firefly *Photinus carolinus* (Coleoptera: Lampyridae). *Journal of Insect Behavior* 8 (1994) 381–394
8. Pitcher, T. J., Parrish, J. K. (1993). Functions of shoaling behavior in teleosts. In T. J. Pitcher (Ed.), *Behaviour of Teleost Fishes* (pp. 363–439).
9. Iztok, L. B., Frank, H. H.: Organized flight in birds. *Animal Behaviour* 78 (2009) 777–789
10. Anderson, J. R., Myowa-Yamakoshi, M., Matsuzawa, T.: Contagious yawning in chimpanzees. *Proc Biol Sci* 271 Suppl 6 (2004) S468–70
11. Paukner, A., Anderson, J. R.: Video-induced yawning in stump-tail macaques (*Macaca arcoides*). *Biol Lett* 2 (2006) 36–38
12. Harr, A. L., Gilbert, V. R., Phillips, K. A.: Do dogs (*Canis familiaris*) show contagious yawning? *Anim Cogn* (2009)
13. Kleiner M., B. D., Pelli D.: What's new in Psychtoolbox-3? *Perception* 36 (2007) ECVF Abstract Supplement
14. Gallese, V., Fadiga, L., Fogassi, L., Rizzolatti, G.: Action recognition in the premotor cortex. *Brain* 119 (1996) 593–609

Effects of Medial Amygdala Lesions upon Social Behaviour in Mice

Yu Wang, Yuki Takayanagi, and Tatsushi Onaka

Abstract The medial amygdala has been suggested to be involved in social behaviour. However, detailed roles of the medial amygdala in the control of social behaviour remain unknown in mice. Here, we examined effects of excitotoxic destruction of the medial amygdala upon social behaviours in mice. Mice whose medial amygdala was lesioned showed no biting behaviour towards intact young intruder mice and showed less direct contact behaviour. The present data are consistent with a view that the medial amygdala is essential for social behaviour in mice.

1 Introduction

The amygdala has been suggested to be involved in social behaviour [1]. The amygdala is activated during social behavior. Lesions of the amygdala have been shown to affect social behaviour. Activation of the amygdala affects social behavior. Amygdala-lesioned monkeys have been shown to become less aggressive and to initiate more affiliative behaviors towards unfamiliar partners than do control animals [2]. Amygdalectomized animals have been shown to be associated with hypersexuality and impaired maternal behaviours.

Studies with patients have also suggested involvement of the amygdala in the control of social behavior. Patients with bilateral damages [3, 4] to the amygdala display inappropriate social behaviours or show deficits in making social judgement of trustworthiness from faces of unfamiliar people [5]. Damage to the amygdala has also been shown to yield deficits in recognition of facial expression with negative emotional signals, such as fear. The amygdala is activated during evaluation of

Y. Wang • Y. Takayanagi • T. Onaka (✉)
Division of Brain and Neurophysiology, Department of Physiology, Jichi Medical University,
Tochigi 329-0498, Japan
e-mail: tonaka@jichi.ac.jp

faces with negative emotions [6]. All these data suggest that the amygdala plays an important role in the cognitive evaluation of facial expression in humans.

The amygdala has also been implicated in the generation of the defensive behaviors such as freezing and avoidance behaviours towards potentially dangerous stimuli. Amygdala-lesioned animals showed less fearful behaviours. Lesioned monkeys blunt fear and avoidance of snakes. Social behaviors are largely affected by emotions, and thus impaired social behaviors observed in lesioned animals might have been due to the changes in emotions following amygdala lesions.

The amygdala contains several sub nuclei, including medial amygdala, central amygdala and basolateral amygdala. Anatomical studies have shown that there are three major functional systems associated with the amygdala [7]; the olfactory systems, autonomic system and fronto-temporal cortices-system associated with basolateral amygdala nuclei. The olfactory system plays a pivotal role in the control of social behavior in rodents. Olfactory information enters into the medial amygdala. It is thus possible the medial amygdala plays an important role in social behavior in rodents.

In fact, a variety of social stimuli activate the medial amygdala [8, 9]. Laboratory rats or hamsters with lesions of the medial amygdala show impairment in copulation [10], maternal behavior [11] and aggression [12, 13]. Axon-sparing lesions of the medial amygdala decrease male parental behavior in the highly social prairie vole. In male prairie voles, lesions of the medial amygdala decrease affiliative behaviors towards pups [14].

However, detailed roles of the medial amygdala in the control of social behaviour in mice remain unknown. Here, we examined effects of excitotoxic destruction of the medial amygdala upon social behaviours in mice.

2 Methods

Adult male mice (C57BL6J) were used. Mice at the age of 9 weeks were anaesthetized with Avertin (tribromoethanol 250 mg/kg bw) and positioned in a stereotaxic frame. N-methyl-D-aspartate (NMDA) solution or the vehicle was microinjected via cannulae into both sides of the medial amygdala in order to destroy neuronal cell bodies in the medial amygdala. NMDA solution (1.6 μg) at a volume of 0.08 μl was infused at following two points bilaterally: 0.8 mm caudal to bregma, ± 2.6 mm lateral to the midline and 5.4 mm below the skull and 1.4 mm caudal to bregma, ± 2.6 mm lateral to the midline and 5.4 mm below the skull. More than two weeks after the injections, mice were examined for social behaviour. Injection sites were verified histochemically after completion of experiments.

In a social behaviour test with an intact young male, one intact young male mouse (3 weeks old) was introduced into the home cage of the resident mouse (14–16 weeks old) that had been injected with NMDA or the vehicle into the medial amygdala. Behaviour towards the young mice during 4-min test was recorded [15].

In another series of experiments with a social behaviour test, two NMDA-treated mice or two vehicle-treated mice were placed together in a cage (29 \times 18 \times 12 cm)

and their behaviours were video-monitored. Social behaviors in the social interaction test were hand-scored [16]. Behaviors were recorded on digital video and social behaviors of two mice were observed during the first 5 min following placement of the two mice into the test cage. Total duration of social behaviors (approaching, following, anogenital sniffing, nose-to-nose sniffing, crawling over and under, grooming each other, sleeping together, and fighting) were counted. Behaviour of the two mice was also recorded with a system that automatically analyzes behaviour in home cages [16, 17]. The system consisted of a cage and a filtered cage top containing an infrared video camera and infrared light emitting diodes. Images from each cage were captured at a rate of one frame per second. Social interaction was measured by counting the number of particles in each frame; two particles indicated that the mice were not in contact with each other, and one particle indicated that mice were in contact with each other. The percentages of time spent for direct contact behavior during a period (15:30-16:30) 270 min following placement of the tow mice into the test cage were calculated. Total locomotor activity of the paired mice was also measured.

Data were presented as means \pm SEM, and were analyzed using a Mann–Whitney *U* test.

3 Results

3.1 Medial Amygdale Lesions

Injections of NMDA solution into the medial amygdala destroyed cell bodies of the medial amygdala.

3.2 Social Behaviours Towards Intact Young Mice After Medial Amygdala Lesions

Vehicle-treated resident mice showed aggressive behavior towards young male intruders (Fig. 1). On the other hand, no medial amygdala-lesioned resident mice showed aggressive behaviour. Lesioned animals showed mounting behaviours towards young male intruders, while no control animals showed mounting behaviour.

3.3 A Social Behaviour Test with the Identically Treated Mouse

Social behaviours observed between pairs of lesioned mice or those of control animals were analyzed for the first 5 min of the first encounter. Lesioned mice spent more time for social behaviours than did the control mice.

Fig. 1 Aggressive behaviour towards intact young mice. Control mice showed aggressive behaviour towards young intruders, while mice whose medial amygdala was lesioned showed no fighting behavior

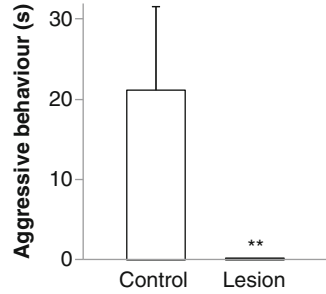


Fig. 2 The percentage of time spent in contact in the social interaction test. Amygdalarectomized mice spent less time in contact with each other ($p < 0.05$) as compared with control mice

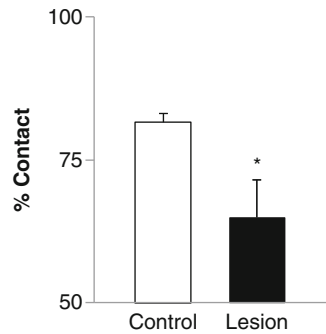
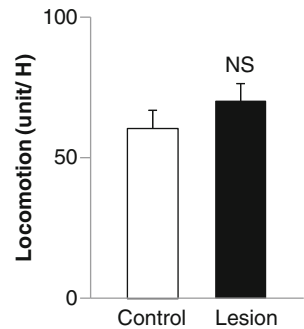


Fig. 3 Total locomotor activity in the social interaction test. Total locomotor activity did not significantly change following bilateral medial amygdala lesions



In the light period, vehicle-treated mice spent majority of time staying still in contact with each other. On the other hand, the NMDA-treated mice spent less time in contact with each other (Fig. 2). There was no significant difference in locomotor activity between sham and lesioned animals during 15:30-19:30 (Fig. 3).

4 Discussions

In the present studies, medial amygdala lesion reduced aggressive behaviour towards young intruders, consistent with previous data that amygdala-lesioned animals show reduced aggressiveness, and further suggest involvement of the

medial amygdala in aggression in mice. In the present data, amygdala-lesioned animals showed increased social behavior such as 'following' behaviour. However, direct contact behavior was significantly reduced in lesioned animals, suggesting that involvement of the medial amygdala in social behaviours is dependent upon social behavior observed. All these data are consistent with a view that the medial amygdala is essential for social behaviour in mice.

Acknowledgments This work was supported by KAKENHI (22120512, 22659050, 23390052) from MEXT and JSPS.

References

1. Bachevalier J. The amygdala, social behavior, and autism. In J P Aggleton (ed) *Amygdala 2000*, pp 509–544.
2. Emery NJ, Capitanio JP, Mason WA, Machado CJ, Mendoza SP, Amaral DG. The effects of bilateral lesions of the amygdala on dyadic social interactions in rhesus monkeys (*Macaca mulatta*). *Behav Neurosci*. 2001; 115: 515–544.
3. Tranel D, Hyman BT. Neuropsychological correlates of bilateral amygdala damage. *Arch Neurol*. 1990; 47: 349–355.
4. Nahm FK, Tranel D, Damasio H, Damasio AR. Cross-modal associations and the human amygdala. *Neuropsychologia*. 1993; 31: 727–744.
5. Adolphs R, Tranel D, Damasio AR. The human amygdala in social judgment. *Nature*. 1998; 393: 470–474.
6. Morris JS, Frith CD, Perrett DI, Rowland D, Young AW, Calder AJ, Dolan RJ. A differential neural response in the human amygdala to fearful and happy facial expressions. *Nature*. 1996; 383: 812–815.
7. Swanson LW, Petrovich GD. What is the amygdala? *Trends Neurosci*. 1998; 21: 323–331.
8. Curtis JT, Wang Z. Forebrain c-fos expression under conditions conducive to pair bonding in female prairie voles (*Microtus ochrogaster*). *Physiol Behav*. 2003; 80: 95–101.
9. Cushing BS, Mogekwu N, Le WW, Hoffman GE, Carter CS. Cohabitation induced Fos immunoreactivity in the monogamous prairie vole. *Brain Res*. 2003; 965: 203–11.
10. Kondo Y, Sakuma Y. The medial amygdala controls the coital access of female rats: a possible involvement of emotional responsiveness. *J Physiol*. 2005; 55: 345–353.
11. Fleming AS, Vaccarino F, Luebke C. Amygdaloid inhibition of maternal behavior in the nulliparous female rat. *Physiol Behav*. 1980; 25: 731–743.
12. Takahashi LK, Gladstone CD. Medial amygdaloid lesions and the regulation of sociosexual behavioral patterns across the estrous cycle in female golden hamsters. *Behav Neurosci*. 1998; 102: 268–275.
13. Vocteloo JD, Koolhaas JM. Medial amygdala lesions in male rats reduce aggressive behavior: interference with experience. *Physiol Behav*. 1987; 41: 99–102.
14. Kirkpatrick B, Carter CS, Newman SW, Insel TR. Axon-sparing lesions of the medial nucleus of the amygdala decrease affiliative behaviors in the prairie vole (*Microtus ochrogaster*): behavioral and anatomical specificity. *Behav Neurosci*. 1994; 108: 501–13.
15. Takayanagi Y, Yoshida M, Bielsky IF, Ross HE, Kawamata M, Onaka T, Yanagisawa T, Kimura T, Matzuk MM, Young LJ, Nishimori K. Pervasive social deficits, but normal parturition, in oxytocin receptor-deficient mice. *Proc Natl Acad Sci U S A*. 2005; 102: 16096–16101.
16. Sato Y, Takayanagi Y, Onaka T, Kobayashi E. Impact of cyclosporine upon emotional and social behavior in mice. *Transplantation*. 2007; 27; 83: 1365–1370.
17. Takayanagi Y, Fujita E, Yu Z, Yamagata T, Momoi MY, Momoi T, Onaka T. Impairment of social and emotional behaviors in *Cadm1*-knockout mice. *Biochem Biophys Res Commun*. 2010; 396: 703–708.

Theta-Burst Stimulation Induces Long-Term Potentiation During Beta Oscillation, but Not During Epileptic Discharges, in Rat Hippocampal Slices

Motoshi Nishimura and Kiyohisa Natsume

Abstract Rats exhibit several physiological rhythms— θ , β , and γ rhythms, sharp waves, and ripples—that are related to memory processing. They also exhibit pathological epileptic discharges, and these discharges suppress memory processes. What is the difference between rhythms and discharges? The θ , β , and γ rhythms are reproduced in hippocampal slices. Long-term potentiation (LTP) was easily induced during the generation of carbachol-induced β oscillations, whereas it was suppressed during the generation of gabazine-induced epileptic discharges. These results suggest there is a difference in the mechanism of LTP induction between physiological β oscillations and the pathological rhythm of epileptic discharges. Synaptic plasticity is necessary for induction of the rhythm. It is therefore suggested that synaptic plasticity is not supported during epileptic discharges whereas it can be occurred during the physiological rhythm. This difference could differentiate the memory processes of the two rhythms in vivo.

1 Introduction

The rat hippocampus has several rhythms: θ , β , and γ rhythms, sharp waves, and ripples. Theta and gamma rhythms are related to spatial learning in the rat [1]. The beta rhythm is related to odor discrimination learning [2], as well as spatial learning. Sharp waves and ripples relate to the consolidation of associative memory [3]. These rhythms are related to the memory process, and they are referred to as physiological rhythms [4]. The rat hippocampus often also exhibits a pathological rhythm, such as epileptic discharges. During epileptic discharges, the memory process is suppressed, and the discharges induce amnesia [5]. Synaptic plasticity is a

M. Nishimura • K. Natsume (✉)

Kyushu Institute of Technology, 2-4 Hibikino, Wakamatsu-ku, Fukuoka 808-0196, Japan
e-mail: natume@brain.kyutech.ac.jp

basic phenomenon underlying the learning process. The results described above, on the relationship between learning and physiological rhythms, suggest that during the generation of these physiological rhythms, synaptic plasticity (for example, long-term potentiation [LTP]) is induced; on the other hand, pathological rhythms (for example, epileptic discharges) correlate with the suppression of LTP.

The θ , β , and γ rhythms and epileptic discharges are reproduced in an *in vitro* system by using the cholinergic agent carbachol and the GABA_A receptor antagonist SR95531 (gabazine) [6–9]. We showed differences in synaptic plasticity between the physiological rhythm and the pathological rhythm using carbachol-induced β oscillations (CIBO) and gabazine-induced epileptic discharges (GIED) in rat hippocampal slices. One of the authors previously reported that LTP is better facilitated during the generation of carbachol-induced θ activity, more so than the rest of CIBO [10]. Whether LTP is induced during the other rhythms has not yet been studied. We therefore applied LTP induction stimuli at several phases of the CIBO and GIED rhythms.

2 Method

The present data were obtained from 406 hippocampal slices (thickness, 450 μm) from 140 male Wistar rats, aged 3–5 weeks. The experiments were carried out in compliance with the Guide for the Care and Use of Laboratory Animals at the Graduate School of Life Science and Systems Engineering of the Kyushu Institute of Technology. The rats were anaesthetized by diethyl ether and decapitated. The brains were rapidly removed and placed in ice cold artificial cerebrospinal fluid (ACSF) of the following composition: 124 mM NaCl, 5 mM KCl, 1.25 mM NaH₂PO₄, 2 mM MgSO₄, 2 mM CaCl₂, 26 mM NaHCO₃, and 10 mM glucose, which was saturated with 95% O₂/5% CO₂.

Transverse hippocampal slices were prepared using a microslicer (ZERO-1; Dosaka Co., Kyoto, Japan). The slices were transferred to a holding chamber containing continuously oxygenated ACSF, and incubated for recovery for at least 1 h in ACSF at 33°C. For electrophysiological recordings, the slices were transferred to an interface recording chamber, where they were continuously perfused with ACSF (1.5 ml/min) and bubbled with 95% O₂/5% CO₂ at 33°C. CIBO and GIED were induced by the application of carbachol and gabazine to the hippocampal slices, respectively. The rhythmic phenomena were recorded from the stratum pyramidale of CA3 by using a glass pipette (2 M NaCl; 1–2 M Ω). In the LTP experiment, Schaffer collaterals were stimulated using the concentric stimulation electrode antidromically, and population excitatory postsynaptic potentials (pEPSP) were measured at the recurrent CA3 synapse and at the synapse between Schaffer collaterals and CA1 pyramidal cells, using the glass pipette (internal solution 2 M NaCl; 1–2 M Ω), at the stratum radiatum in CA3 and CA1 (A and C in Fig. 1).

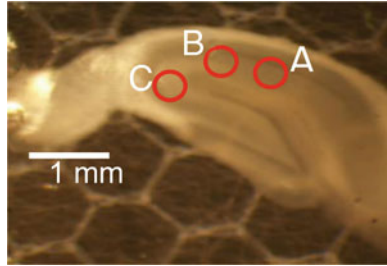
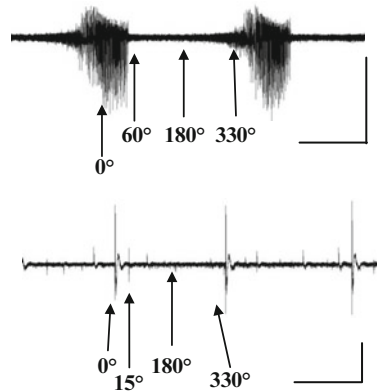


Fig. 1 Stereo microscope photograph of a hippocampal slice, indicating the sites of the electrodes. Sites where the recording electrodes (*A* and *C*) and the stimulation electrode (*B*) were placed are shown. The pEPSP and the rhythmic phenomena, CIBO and GIED, were recorded at sites *A* and *C*. pEPSPs at 40 min were compared to those at -1 min by using Student's *t*-test

Fig. 2 The stimulation phase of TBS is defined by the time of onset of the stimulation in the interburst interval of CIBO (*above*) and GIED (*below*). Scale bars indicate 2 mV and 10 s



Theta-burst stimulation (TBS), consisting of five bursts separated by 200 ms, was used to induce LTP. Each burst consisted of five rectangular current pulses (0.1 ms in duration) at 100 Hz.

CIBO was induced in an intermittent burst form with an interburst interval of 20–30 s. GIED occurred with a regular interval of 10–20 s. TBS was delivered in several phases of the interval, during the burst or discharges (0° phase), just after CIBO (60° in CIBO, and 15° in GIED), during the resting period of CIBO or GIED (180°), and just before CIBO or GIED (330°) (Fig. 2). In the case of CIBO, the 0° phase was positioned 3 s after the beginning of CIBO.

3 Results

When TBS was delivered at the 0° phase during CIBO, the slope of the pEPSP significantly increased, and this increased slope was maintained for at least 40 min at the CA3 recurrent synapse (CA3 in Fig. 3); LTP was thus induced. At the CA1

Fig. 3 The synaptic changes induced by TBS at the 0° phase of CIBO. In the figure, the representative pEPSPs 1 min before TBS (pre) and 40 min after TBS (post) are shown. LTP was induced at the CA3 recurrent synapse (** $p < 0.01$; $n = 6$), and was not induced at the CA1 synapse ($n = 3$). The scale bars indicate 2 mV and 10 ms

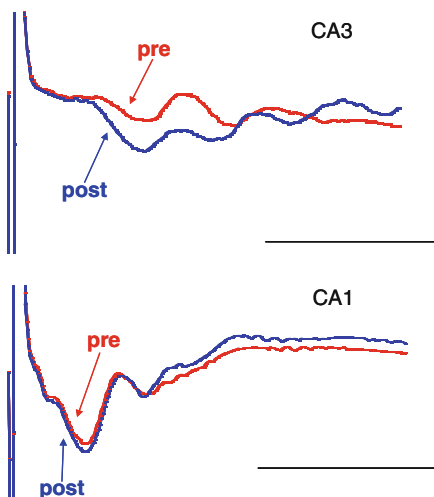
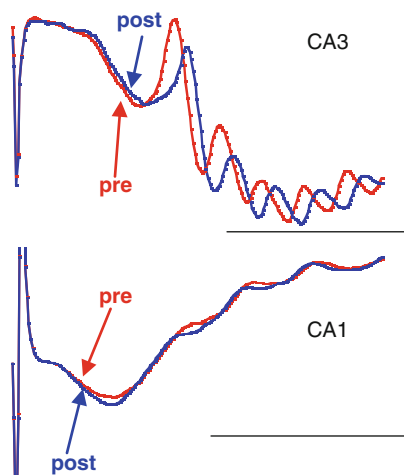


Fig. 4 The synaptic changes by TBS at the 0° phase of GIED. LTP was induced at neither CA3 nor CA1. CA1 data were obtained from four slices. The scale bars indicate 2 mV and 10 ms



synapse, TBS induced only short-term potentiation, and did not have any long-term effect (CA1 in Fig. 3). On the other hand, LTP was not induced when TBS was performed at the 0° phase during GIED, at either the CA3 or CA1 synapse (Fig. 4). TBS induced LTP in all phases of CIBO at the CA3 recurrent synapse (Table 1). The potentiation at phases of 180° and 330° was particularly significant. At the CA1 synapse, TBS induced significant LTP in phases of 180° and 330°. In GIED, LTP was not induced in any phase at the CA3 synapse; LTD was induced only at phases of 330° (Table 1).

Table 1 The synaptic changes induced by TBS in several phases of CIBO and GIED

		0°	15° or 60°	180°	330°
CIBO	CA3	LTP**	LTP*	LTP**	LTP**
	CA1	–	–	LTP**	LTP*
GIED	CA3	–	–	–	LTP**
	CA1	–	–	LTP*	LTP**

The table indicates LTP, LTD, or no change (–). pEPSPs at 40 min after TBS were compared with those at 1 min before TBS. LTP was induced at all phases of CIBO, and LTD was induced in the 330° phases of GIED at the CA3 recurrent synapse. LTP was only induced in the late phases (180° and 330°) of CIBO and GIED at the CA1 synapse. (* $p < 0.05$; ** $p < 0.01$)

4 Discussion

LTP was easily induced during CIBO, whereas it was not induced in GIED at the CA3 synapse. At the CA1 synapse, LTP was induced during both CIBO and GIED in the late stimulation phases (180° and 330°), and the magnitude of LTP induced during CIBO was greater than that induced during GIED (data not shown). These results suggest the presence of a difference in the mechanism by which LTP is induced between the conditions of physiological β oscillation and pathological epileptic discharges.

CIBO is generated in CA3, and GIED may be generated in CA3 or CA1 [11]. The CA3 recurrent synapse is required for the generation of epileptic discharges [12]. In the generation of GIED, synaptic potentiation of the CA3 recurrent synapse could be induced [13]. It is therefore suggested that there is no potential for synaptic plasticity in GIED, and LTP cannot be induced. On the other hand, there is room for synaptic plasticity in CIBO, and plasticity can be induced during the oscillation. This differentiates the physiological rhythms and the pathological rhythm, and also differentiates the mechanism of the memory process during the two rhythms *in vivo*. A clear difference in CA3 LTP induction was observed between CIBO and GIED. CA3 plays a significant role in the memory process, and the results obtained here are consistent with this.

In addition, in the 180° and 330° phases of CIBO, a greater magnitude of LTP could be induced at the CA3 and CA1 synapses; however, in the 60° phases, the magnitude was smaller. Therefore, LTP was suppressed at this refractory stage, and possibly others, during CIBO.

The ease with which LTP was induced depended on the phase of the generation of CIBO. CIBO was generated intermittently with an interval of 20–30 s. A slow rhythm, the period of which underlies the generation of CIBO, is present. The slow rhythm that induces the generation of CIBO may control how the induction of LTP in CA3 and CA1 is facilitated; however, further study is needed to confirm this.

References

1. Lisman, J, Redish, A.D.: Prediction, sequences and the hippocampus. *Philos Trans R Soc Lond B Biol Sci.* 364(1521) (2009) 1193–201.
2. Martin, C., Beshelf, J., Kay, L.M.: An olfacto-hippocampal network is dynamically involved in odor-discrimination learning. *J Neurophysiol.* 98(4) (2007) 2196–205.
3. Ramadan, W., Eschenko, O., Sara, S.J.: Hippocampal sharp wave/ripples during sleep for consolidation of associative memory. *PLoS One* 4(8) (2009) e6697.
4. Schnitzler, A. and Gross, J.: Normal and pathological oscillatory communication in the brain. *Nature Rev. Neurosci.* 6 (2005) 285–296.
5. Gallassi, R.: Epileptic amnesic syndrome: an update and further considerations. *Epilepsia* 47 Suppl 2 (2006) 103–5.
6. MacIver, M.B., Harris, D.P., Konopacki, J., Roth, S.H., Bland, B.H.: Carbachol induced rhythmical slow wave activity recorded from dentate granule neurons in vitro. *Proc West Pharmacol Soc.* 29 (1986) 159–61.
7. Arai, J., Natsume, K.: The properties of carbachol-induced beta oscillation in rat hippocampal slices. *Neurosci Res.* 54(2) (2006) 95–103.
8. Fisahn, A., Pike, F., Buhl, E. H. & Paulsen, O.: Cholinergic induction of network oscillations at 40 Hz in the hippocampus in vitro. *Nature* 394 (1998) 186–189.
9. Sokal, D.M., Mason, R., Parker, T.L.: Multi-neuronal recordings reveal a differential effect of thapsigargin on bicuculline- or gabazine-induced epileptiform excitability in rat hippocampal neuronal networks. *Neuropharmacology* 39(12) (2000) 2408–17.
10. Natsume, K., Kometani, K.: Theta-activity-dependent and -independent muscarinic facilitation of long-term potentiation in guinea pig hippocampal slices. *Neurosci. Res.* 27 (1997) 335–41.
11. Nishimura, M., Hashimoto, A., Natsume, K.: Carbachol-induced beta oscillation and the epileptic discharges in rat hippocampal slices. *Neurosci. Res.* 65 Suppl 1 (2009) P3–n12.
12. Bains, J.S., Longacher, J.M. & Staley, K.J.: Reciprocal interactions between CA3 network activity and strength of recurrent collateral synapses. *Nat Neurosci* 2 (1999) 720–726.
13. Ogata, G., Natsume, K.: The synaptic efficacy modulates the frequency of interictal discharges induced by bicuculline in guinea-pig hippocampal slices. *SFN Abstracts* (2007) 165.14.

Integration of Hetero Inputs to Guinea Pig Auditory Cortex Established by Fear Conditioning

Yoshinori Ide, Muneyoshi Takahashi, Johan Lauwereyns, Minoru Tsukada, and Takeshi Aihara

Abstract The present study used an optical imaging paradigm to investigate plastic changes in the auditory cortex induced by fear conditioning, in which a sound (Conditioned Stimulus, CS) was paired with an electric foot-shock (Unconditioned Stimulus, US). We report that, after conditioning, auditory information could be retrieved on the basis of an electric foot-shock alone. Before conditioning, the auditory cortex showed no response to a foot-shock presented in the absence of sound. In contrast, after conditioning, the mere presentation of a foot-shock without any sound succeeded in eliciting activity in the auditory cortex. Additionally, the magnitude of the optical response in the auditory cortex correlated with variation in the electrocardiogram. The area activated in the auditory cortex, in response to the electric foot-shock, also showed a considerable correspondence to that elicited by the CS sound. These results suggest that integration of different sensory modalities in the auditory cortex was established by fear conditioning.

1 Introduction

Sensory cortices are defined by responses to physical stimuli in specific modalities. Recently, however, human neuroimaging studies have shown auditory cortex activation without sound. Little is known about how the brain produces such

Y. Ide (✉) • M. Tsukada

Brain Science Institute, Tamagawa University, Tokyo 194-8610, Japan

e-mail: yide@lab.tamagawa.ac.jp

M. Takahashi • J. Lauwereyns

Brain Science Institute, Tamagawa University, Tokyo 194-8610, Japan

Graduate School of Systems Life Sciences, Kyushu University, Fukuoka 819-0395, Japan

T. Aihara

Brain Science Institute, Tamagawa University, Tokyo 194-8610, Japan

Faculty of Engineering, Tamagawa University, Tokyo 194-8610, Japan

Y. Yamaguchi (ed.), *Advances in Cognitive Neurodynamics (III)*,

DOI 10.1007/978-94-007-4792-0_100,

© Springer Science+Business Media Dordrecht 2013

activity. Here we study this topic with an entirely different paradigm, based on fear conditioning, using optical imaging with a voltage-sensitive dye [1] in the guinea pig auditory cortex. Our data show that foot shocks, through conditioning, can activate the auditory cortex in the absence of sound.

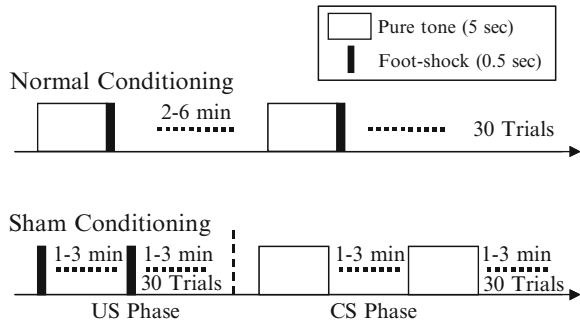
The traditional view that auditory cortex neurons are only activated by sound stimuli required revision when functional magnetic resonance imaging in humans showed blood flow changes in auditory cortex during silence [2–4]. It was confirmed that mental imagery [2] and stimulus expectancy [3] create virtual acoustic representations, which may be responsible for the perception of sounds that are physically absent, as when subjects report hearing a familiar song continue even if the music has stopped. The latter finding was obtained when subjects were given no specific instructions, suggesting that the phenomenon had an obligatory aspect [4]. We reasoned that if auditory cortex activation can occur autonomously as a consequence of over learning (e.g., a familiar song), then similar results might be obtained with nonhuman animals in a conditioning paradigm. To investigate effects of conditioning on auditory cortex activity, we used a fear-conditioning paradigm in guinea pigs, pairing pure tones with foot shocks. Fear conditioning and other behavioral and pharmacological paradigms have induced plasticity in various aspects of mammalian auditory cortical representations, but the possibility of signals in the absence of sound, elicited through auditory fear conditioning, remained unexplored.

In this work, to investigate whether auditory information could be retrieved by electric foot-shock after the conditioning or not, the auditory response to a foot-shock was investigated in three groups: normal conditioning, sham conditioning, and naïve.

2 Methods

The experiments were performed in accordance with the guidelines of the Animal Experiments Committee of Tamagawa University. Nineteen guinea pigs of 250–450 g, 3–6 weeks old females were used as experimental subjects. Three groups (normal conditioning, sham conditioning and naïve) were prepared. Six guinea pigs in each normal/sham conditioning group were fear-conditioned while they were awake in the test cage, through a grid shock floor. Fear conditioning was carried out by using a pure tone (CS) and an electric foot-shock (US). The normal/sham conditioning protocols is shown in Fig. 1. After the conditioning, the animals were anesthetized and underwent surgery for optical recording. The auditory cortex was stained for 40–60 min with a voltage-sensitive dye, RH795 (0.125 mg/ml, dissolved in saline; molecular Probes). While a pure-tone (duration: 5 s, frequency: 4–16 kHz, acoustic pressure: 65 dB SPL) was presented to the right ear or an electric shock (duration: 0.5 s, current intensity: 0.5–1.5 mA) was applied to hind legs, response from the left auditory cortex was recorded. 100 × 100 ch MOS imaging

Fig. 1 Normal and sham conditioning protocol



device (MiCAM ULTIMA-L, Brainvision Inc., Tokyo) was used for recording the fluorescent signals from the cortex. The wavelengths of excitation and emission were 540 ± 30 nm and > 600 nm, respectively.

3 Results

Figure 2 shows the comparison of the ΔRR value measured before and after normal/sham conditioning under anesthesia, where ΔRR is the variation of the R-R interval in the electrocardiogram (ECG). There was a significant difference between pre and post in the normal conditioning group ($P < 0.01$), suggesting that the guinea pigs in the normal conditioning group were fear conditioned. On the other hand, there was no significant difference between pre and post in the sham conditioning group. Moreover, there was also a significant difference between normal and sham conditioning groups after the conditioning ($P < 0.05$).

Next, the neural responses in the auditory cortex to electric foot-shocks alone were investigated. Figure 3a shows the optical responses to foot-shock alone in the three groups. The neural responses in the auditory cortex could be clearly observed in both the normal and the sham conditioning groups, but no response could be observed in the naïve group. Figure 3b shows the time course of the optical response to foot-shock alone in the three groups. No response was observed in the naïve group, whereas responses were observed in both the normal and sham conditioning groups. ECG data show that the guinea pigs of the sham conditioning group were not statistically significantly conditioned. However there was a tendency of a difference between pre and post conditioning, implying that some level of conditioning might have occurred. The time course of the normal tone response (gray line) shows a peak onset latency of approximately 40 ms and an offset latency of approximately 100 ms. However, the time course of the neural responses in the auditory cortex to electric foot-shock alone (black lines) shows an onset latency of 120 ms and a very long duration of over 500 ms, suggesting that the time course of the optical response to electric foot-shock was very different from that of the responses to pure tones.

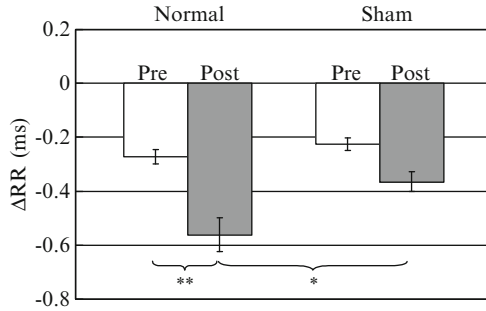
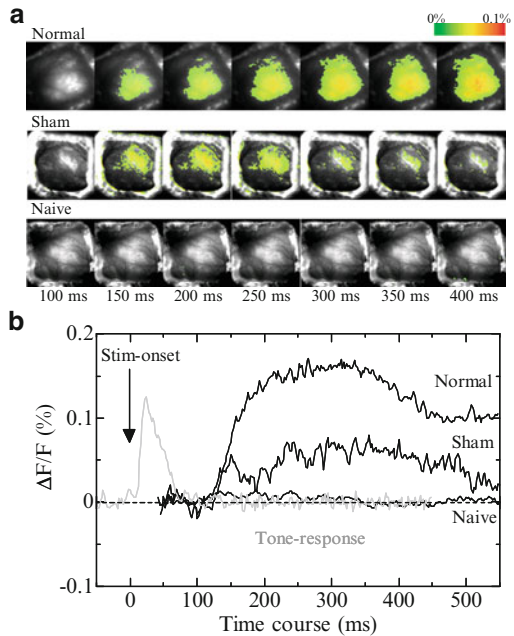


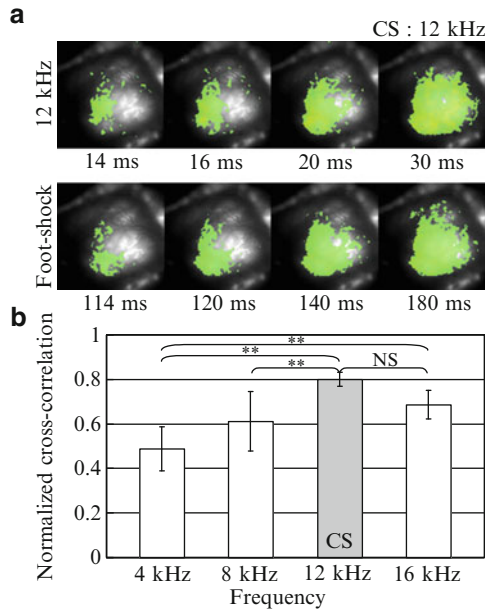
Fig. 2 Comparison of the ΔRR value measured before and after the normal/sham conditioning. White and gray color bars represent the ΔRR measured before and after the conditioning, respectively. The four bars represent the mean value of the ΔRR measured for 10 s after CS onset. Error bar is SEM. Normal: $n = 6$, Sham: $n = 6$, * $P < 0.05$, ** $P < 0.01$

Fig. 3 (a) The cortical responses to foot-shock alone in the normal/sham conditioning and naïve groups. **(b)** The time course of the cortical responses to foot-shock alone (black lines). Gray line represents the cortical response to 12 kHz pure tone



In order to confirm the correlation between the ΔRR and the optical response, we calculated correlation coefficient. The correlation coefficient R amounted to -0.68 , $P < 0.01$, implying that there was a significant negative correlation between the ΔRR and the optical responses. Next, the areas of the cortical responses to the CS sounds and the electric foot-shocks were compared. As shown in Fig. 4a, there

Fig. 4 (a) The cortical responses to the CS sound and the electric foot-shock. (b) The normalized cross-correlation between the activated area in response to the CS/non-CS sounds and that to the electric foot-shock. Error bar is SD. n = 6, **P < 0.01, NS: no significant differences



seemed to be a correlation between the shape and location of the activated area in response to the CS sound and electric foot-shock, although there was a large difference in time scale. In order to compare quantitatively, the normalized cross-correlation between the activated area in response to the CS/non-CS sounds and that to the electric foot-shock was calculated. The normalized cross-correlation R was defined as:

$$R = \frac{\sum_{j=1}^N \sum_{i=1}^M (f_{i,j} - \bar{f}) (g_{i,j} - \bar{g})}{\sqrt{\sum_{j=1}^N \sum_{i=1}^M (f_{i,j} - \bar{f})^2} \sqrt{\sum_{j=1}^N \sum_{i=1}^M (g_{i,j} - \bar{g})^2}}$$

where $f_{i,j}$ and $g_{i,j}$ are the (i, j) th element of the matrix F and G. The matrix F and G represent 100×100 ch optical imaging data in response to electric foot-shock and CS/non-CS tone stimuli, respectively. Thus, $N, M = 100$ in the above formula. In the matrix F and G, the numerical values of $f_{i,j}$ and $g_{i,j}$ were converted into 0 or 1 from the real optical imaging data $\Delta F/F$ (%) according to the following rule: $f_{i,j}$ and $g_{i,j} = 0$ when $\Delta F/F \leq 3SD$, and $f_{i,j}$ and $g_{i,j} = 1$ when $\Delta F/F > 3SD$ (standard deviation) of the baseline. \bar{f} and \bar{g} are mean value of $f_{i,j}$ and $g_{i,j}$, respectively. Figure 4b shows that the activated area in response to electric foot-shock statistically significantly had a larger cross-correlation value for tone response to the CS sound compared to the non-CS sounds.

4 Discussions

It has been reported that neural circuits involving the medial geniculate body, the amygdala, the basal forebrain (BF) and the auditory cortex are very important for fear conditioning using sound and foot-shock, and that the plastic changes in the auditory cortex are induced by acetylcholine (ACh) released from the basal forebrain to the cortex during conditioning [5]. ACh affects pyramidal neurons and promotes plastic changes in the auditory cortex [6]. We propose the following hypothesis about neural mechanisms of auditory fear conditioning. Figure 5 shows a schematic diagram of the hypothesized neural circuit including the auditory cortex, the thalamus, the amygdala and the basal forebrain based on Weinberger’s model [7]. First, CS (tone) information is directly transferred to the auditory cortex by way of MGv (the ventral subdivision of the medial geniculate body) in the thalamus, such that pyramidal neurons in layers II and III produce EPSP (normal tone response). Next, US (foot-shock) information is transferred to the amygdala by way of MGM in thalamus, and ACh is released from BF to the auditory cortex. As a result, LTP and/or LTP-like plastic changes occur in MGm (the magnocellular subdivision of the medial geniculate body) and in the pyramidal neurons in layers II and III of the auditory cortex, where EPSP is induced in response to CS. Then, after conditioning, when US alone is presented, learning-dependent increase in ACh release from BF occurs and US information is transferred to the auditory cortex by way of MGm, eliciting EPSP in the pyramidal neurons where LTP and/or LTP-like plastic changes were induced by conditioning. This, in turn, would result in the emergence of the neural responses in the auditory cortex to a foot-shock alone, and might explain

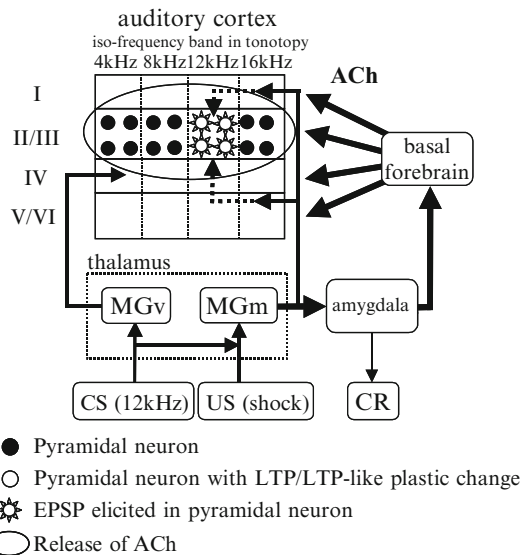


Fig. 5 A neural model of CS-specific tuning plasticity in the primary auditory cortex according to associative learning

the correlation between the auditory activated area in response to CS sound and US foot-shock. We conclude that integration of different sensory modalities in the auditory cortex was established by fear conditioning.

Acknowledgments This work was supported by the twenty-first Century Center of Excellence (COE) Program and the Global COE Program at Tamagawa University and Grants-in-Aid for Scientific Research (A) 19200014, Young Scientists (B) 21700435 and Scientific Research on Innovative Areas 21120006 from MEXT in Japan.

References

1. Hosokawa, Y., Sugimoto, S., Kubota, M., Taniguchi, I., Horikawa, J. (2004) Optical imaging of binaural interaction in multiple fields of the guinea pig auditory cortex. *Neuroreport*, 15, 1093–1097.
2. Kraemer, D.J., Macrae, C.N., Green, A.E., Kelley, W.M. (2005) Musical imagery: sound of silence activates auditory cortex. *Nature*, 434, 158.
3. Voisin, J., Bidet-Caulet, A., Bertrand, O., Fonlupt, P. (2006) Listening in silence activates auditory areas: a functional magnetic resonance imaging study. *J. Neurosci.*, 26, 273–278.
4. Zatorre, R.J. & Halpern, A.R. (2005) Mental concerts: Musical imagery and auditory cortex. *Neuron*, 47, 9–12.
5. Kilgard, M.P. & Merzenich, M.M. (1998) Cortical map reorganization enabled by nucleus basalis activity. *Science*, 279, 1714–1718.
6. Bandrowski, A.E., Moore, S.L., Ashe, J.H. (2001) Cholinergic synaptic potentials in the supragranular layers of auditory cortex. *Synapse*, 41, 118–130.
7. Weinberger NM, Bakin JS (1998) Learning-induced physiological memory in adult primary auditory cortex: Receptive field plasticity, model, and mechanisms. *Audiology & Neuro-Otology* 3: 145–167.

The Theta Cycle and Spike Timing During Fixation in Rat Hippocampal CA1

Muneyoshi Takahashi, Yoshio Sakurai, Yoshikazu Isomura, Minoru Tsukada, and Johan Lauwereyns

Abstract In this paper, we report the first evidence that the spikes of CA1 neurons shift approximately half of the theta cycle: The shift occurs from the positive peak of the cycle recorded in the CA1 cell layer at the beginning of fixation, to the negative trough at the end of fixation. This happens during a one-second period of immobile fixation, while the rat is fully alert and waits for the next event. It is known that the strongest input from entorhinal cortex occurs at the positive peak of the CA1 cell layer theta, whereas the strongest input from CA3 is associated with the trough of the theta. We hypothesize that CA1 pyramidal cells perform a function as an adaptive filter between entorhinal cortex and CA3, propagating relevant information depending on task requirements.

1 Introduction

The theta rhythm in hippocampus is thought to play an important role in learning and memory. Many rodent studies have focused on the hippocampal theta rhythm that can be observed during translational movements (i.e., Type 1 theta [1].) However, less is known about the function of the theta rhythm during alert immobility (i.e., Type 2 theta [1].) Several studies pointed out that the hippocampus involves

M. Takahashi (✉) • J. Lauwereyns
Graduate School of Systems Life Sciences, Kyushu University, Fukuoka 819-0395, Japan

Brain Science Institute, Tamagawa University, Tokyo 194-8610, Japan
e-mail: taka@sls.kyushu-u.ac.jp

Y. Sakurai
Department of Psychology, Graduate School of Letters, Kyoto University, Kyoto 606-8501, Japan
Core Research for Evolutional Science and Technology (CREST), Japan Science and Technology Agency, Kawaguchi 332-0012, Japan

Y. Isomura • M. Tsukada
Brain Science Institute, Tamagawa University, Tokyo 194-8610, Japan

intensive information processing during the delay period when the subject stays immobile while being fully alert [2]. Therefore, to understand the neural basis of learning and memory it is essential to elucidate the hippocampal mechanisms during this period.

During the period of active exploration, hippocampal place cells exhibit a phenomenon called “theta phase precession,” firing spikes late in the ongoing theta cycle when a rat first enters the place field of the cell, but firing spikes earlier in the theta cycle as the rat progresses through the field [3, [4]. Some theoretical studies claimed an importance of this phenomenon to the hippocampal information processing [4–8]. Here we investigated the relationship between the theta rhythm in the local field potentials (LFPs) and the spike timing of the CA1 area during immobile fixation when Type 2 theta oscillation can be observed [9].

2 Methods

Four male adult Wistar/ST rats were trained to perform a delayed (memory-guided) spatial alternation task using a nose-poking paradigm (Fig. 1) [9, 10]. A hyperdrive assembly with 14 tetrodes was chronically implanted on the right CA1 (AP -3.6 mm, ML 2.2 mm) of each animal. We recorded CA1 neural activity (multi-unit activity and LFPs) with position tracking (Cheetah 160 Data Acquisition System, Neuralynx Inc., Bozeman, MT, USA) during task behavior (60 min sessions) on several days.

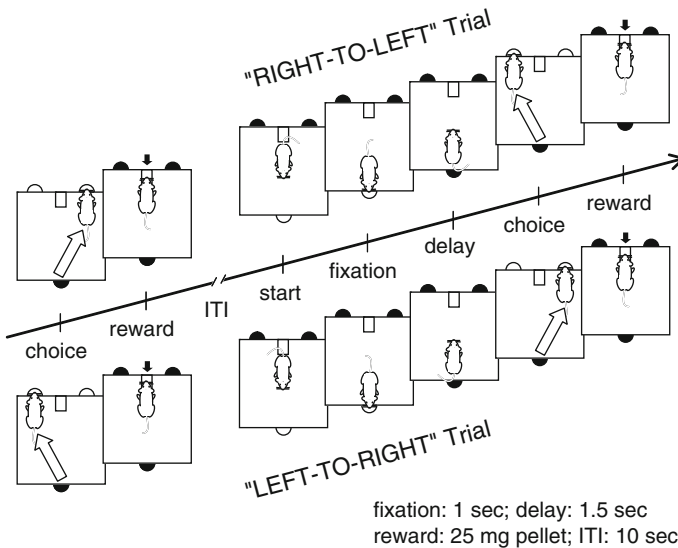


Fig. 1 Experimental design of the memory-guided spatial alternation task. The sequence shown on top represents a *RIGHT-TO-LEFT* trial; the one below represents a *LEFT-TO-RIGHT* trial. Open half circles indicate illuminated nose-poke holes whereas filled ones indicate the light is out

Multi-unit activity was spike-sorted by standard methods [11, 12]. Well-isolated putative pyramidal neurons were used for further analyses. Neurons whose activity during fixation was significantly higher than the average firing rate throughout the session were considered to be “fixation-related.” The differential firing rate of these neurons between RIGHT-TO-LEFT (RL) and LEFT-TO-RIGHT (LR) trials during fixation (i.e., sequence dependency) was statistically evaluated by Mann–Whitney *U*-test ($\alpha = 0.05$). Firing characteristics of fixation-related units were categorized in several types using the following indices:

$$I_{pre} = \frac{fr(PRE)}{fr(PRE) + fr(FIX)}$$

$$I_{post} = \frac{fr(POST)}{fr(POST) + fr(FIX)}$$

Where $fr(X)$ denotes the firing rate during period X , *PRE* denotes the pre-fixation period (1 s before), *FIX* denotes the fixation period, *POST* denotes the post-fixation period (1 s after) [11]. We focused on the “fixation only type” ($I_{pre} < 0.5$ AND $I_{post} < 0.5$) in the present study (i.e., “fixation unit”).

LFPs were filtered offline to extract their theta-band rhythms (6–10 Hz). The instantaneous filtered LFP phase was calculated by Hilbert transformation. Fixation units that showed more than 100 spikes in total during the fixation periods in a single recording session were selected, and the circular correlation between the LFP phase (recorded from the corresponding tetrode) and spike timing during fixation was statistically evaluated ($p < 0.05$) [13]. Data from all significant sequence-dependent fixation units in this analysis were merged and we conducted a population analysis to elucidate the general trends of CA1 activity during alert immobility.

3 Results

We recorded 248 putative CA1 pyramidal neurons from a total of 18 task sessions. Forty neurons showed fixation-specific increase in their firing (i.e., fixation units) and 28 of these showed sequence dependency, meaning the firing rate during fixation was statistically different between RL and LR trial sequences. We further analyzed 24 of these, which showed more than 100 spikes in total during the fixation periods in a single session. Sixteen (66%) showed a significant circular correlation between spike-timing and the ongoing theta cycle during fixation.

First, we investigated the relationship between spike timing and spiking phase of the theta cycle on a trial-by-trial basis (Fig. 2) and confirmed the theta phase precession-like phase shift occurred during fixation in several trials. Interestingly, there seemed to be a consistent trend such that the spikes mainly occurred at the positive peaks of the theta cycles recorded around the CA1 cell layer at the

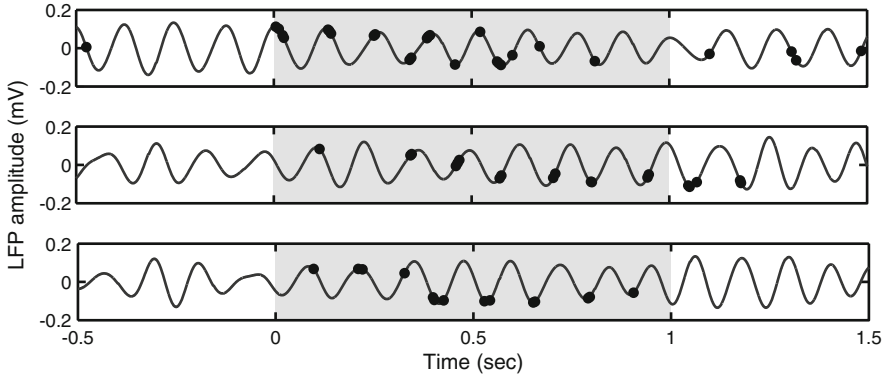


Fig. 2 Examples of filtered (6–10 Hz) LFP traces and spike timings (*dots*) of a single neuron in a single trial. The shaded duration (*grey*) indicates 1 s of fixation

beginning of the fixation period whereas they shifted and occurred at the negative trough at the end of fixation.

To investigate this profile more systematically, we next drew histograms of the 2-D colored map of spike timing versus spiking phase for each neuron during a single recording session. Several examples are shown in Fig. 3. The relationships between spike timing and spiking phase differed from neuron to neuron and depended on the trial sequence. However, in many cases, we confirmed a trend such that the spikes mainly occurred at the positive peaks of the theta cycles (0° in the figure) at the beginning of the fixation period whereas they shifted and occurred at the negative trough (-180°) at the end of fixation.

Finally, for these cells, we drew population histograms of the 2-D colored map of spike timing versus spiking phase (Fig. 4a) and the mean values for each 0.1 s bin (Fig. 4b). Again, the data clearly showed the phase shift trend described above. This trend was more prominent for the “preferred-sequence” trials, in which the cell showed the highest firing rate.

4 Discussion

Several recent studies showed that a theta phase precession can be observed while the subject is located in the same position but continuing the movements (e.g., a running wheel [14], a head-fixed treadmill [15]) or during a transitional stage in jumping or dropping to avoid foot shocks that included a certain freezing period [16]. In contrast to these reports, we found theta phase precession-like activity during an immobile fixation period while the rat is fully alert and waits for the next event (i.e., under Type 2 theta). However, the properties of the phenomenon were quite different from those reported in previous studies that concentrated

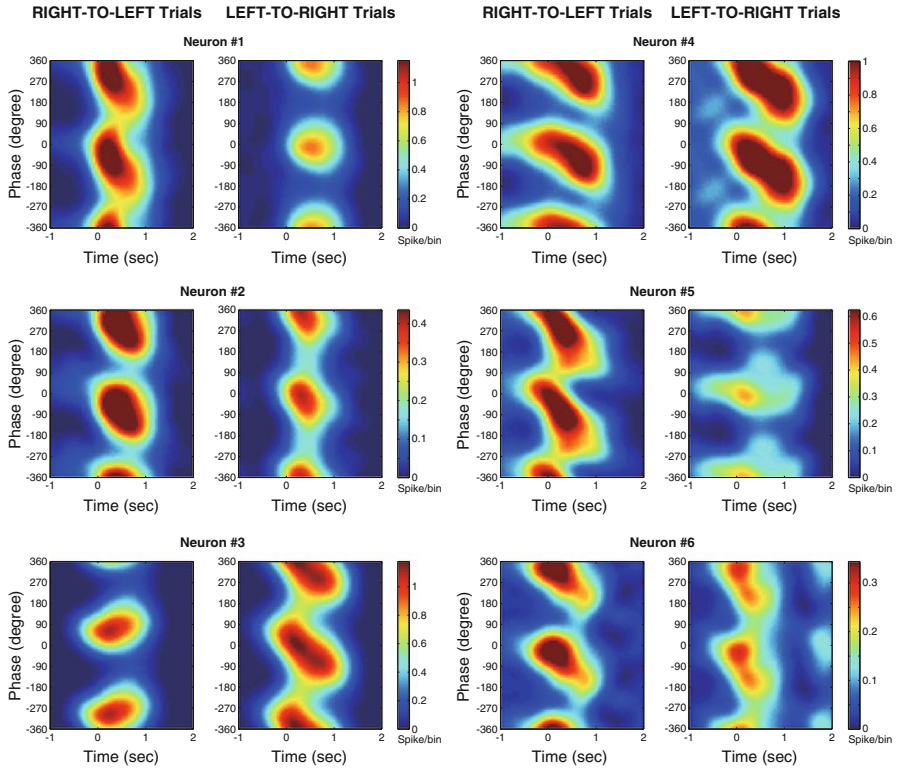


Fig. 3 Activity of six example neurons on the 2-D colored map of spike timing versus spiking phase. The trends of each neuron are shown separately for RIGHT-TO-LEFT and LEFT-TO-RIGHT sequences. The fixation period is from 0 to 1 s

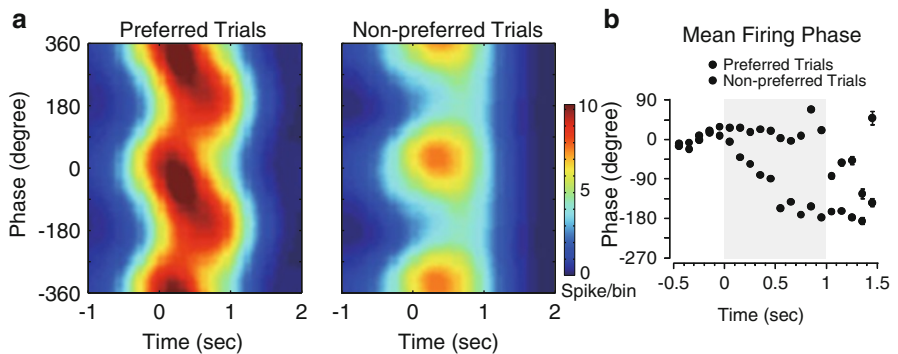


Fig. 4 (a) Population trends of theta phase shift during the fixation period for their preferred versus non-preferred sequence. (b) The mean spiking phase for each 0.1 s bin. The fixation period is from 0 to 1 s

on mobile periods. First, the phase shift advanced only half of the theta cycle. Yamaguchi et al. (2002) pointed out that the theta phase precession during mobile periods consists of two independent components and each of them covers either the first or the second 180° of precession [17]. This theoretical prediction is now confirmed by several lines of empirical evidence [18, 19]. Our results also support this perspective, suggesting that the phase precession cannot advance more than half of a theta cycle (i.e., 180°). Second, the initial spike timings were highly phase-locked to the positive peaks of the theta cycle. This indicates that the variation of the initial spiking phase in the traditional phase precession observed during translational movement might be modulated by physical factors such as variance of movement velocity, sensory inputs, and so forth.

An important question is why the theta phase shift occurs during fixation in memory-guided spatial alternation. What could be the functional significance of this phenomenon for the information processing in hippocampal CA1? It is known that two major, mutually exclusive streams of input reach CA1: from entorhinal cortex (EC) and from CA3, corresponding to the peak and trough of the theta cycle [7]. Thus, CA1 spikes at different LFP phases may propagate different types of information toward downstream structures for further processing. According to this perspective, the theta phase shift during fixation should always advance 180° (i.e., from EC to CA3) regardless of the fixation duration. Future studies should verify the hypothesis that CA1 performs a function as an adaptive filter between EC and CA3, passing on relevant information from EC to CA3 depending on task requirements.

Acknowledgments This work was supported by Human Frontier Science Program award RGP0039/2010, and Tamagawa Global Center of Excellence (COE) Program.

References

1. Kramis, R.C., Vanderwolf, C.H., Bland, B.H.: Two types of hippocampal rhythmical slow activity in both the rabbit and the rat: Relations to behavior and effects of atropine, diethyl ether, urethane, and pentobarbital. *Exp. Neurol.* 49 (1975) 58–85
2. Ainge, J.A., van der Meer, M.A., Langston, R.F., Wood, E.R.: Exploring the role of context-dependent hippocampal activity in spatial alternation behavior. *Hippocampus* 17 (2007) 988–1002
3. O'Keefe, J., Recce, M.L.: Phase relationship between hippocampal place units and the EEG theta rhythm. *Hippocampus* 3 (1993) 317–330
4. Skaggs, W.E., McNaughton, B.L., Wilson, M.A., Barnes, C.A.: Theta phase precession in hippocampal neuronal populations and the compression of temporal sequences. *Hippocampus* 6 (1996) 149–172
5. Hasselmo, M.E., What is the function of hippocampal theta rhythm? – Linking behavioral data to phasic properties of field potential and unit recoding data. *Hippocampus* 15 (2005) 936–949
6. Jensen, O., Lisman, J.E.: Hippocampal sequence-encoding driven by a cortical multi-item working memory buffer. *Trends Neurosci.* 28 (2005) 67–72
7. Buzsáki, G.: *Rhythms of the brain.* (2006) Oxford University Press

8. Yamaguchi, Y., Sato, N., Wagatsuma, H., Wu, Z., Molter, C., Aota, Y.: A unified view of theta-phase coding in the entorhinal-hippocampal system. *Curr. Opin. Neurobiol.* 17 (2007) 197–204
9. Takahashi, M., Lauwereyns, J., Sakurai, Y., Tsukada, M.: A code for spatial alternation during fixation in rat hippocampal CA1 neurons. *J. Neurophysiol.* 102 (2009) 557–567
10. Takahashi, M., Lauwereyns, J., Sakurai, Y., Tsukada, M.: Behavioral state-dependent episodic representation in rat CA1 neuronal activity. *Cogn. Neurodyn.* 3 (2009) 165–175
11. Redish, A.D., et al.: <http://redishlab.neuroscience.umn.edu/MClust/MClust.html>
12. Harris, K.D.: <http://klustakwik.sourceforge.net/>
13. Zar, J.H.: *Biostatistical Analysis* (2009) Pearson Higher Education
14. Pastalkova, E., Itskov, V., Amarasingham, A., Buzsaki, G.: Internally generated cell assembly sequences in the rat hippocampus. *Science* 321 (2008) 1322–1327
15. Harvey, C.D., Collman, F., Dombeck, D.A., Tank, D.W.: Intracellular dynamics of hippocampal place cells during virtual navigation. *Nature* 461 (2009) 941–946
16. Lenck-santini, P.P., Fenton, A.A., Muller, R.U.: Discharge properties of hippocampal neurons during performance of a jump avoidance task. *J. Neurosci.* 28 (2008) 6773–6786
17. Yamaguchi, Y., Aota, Y., McNaughton, B.L., Lipa, P.: Bimodality of theta phase precession in hippocampal place cells in freely running rats. *J. Neurophysiol.* 87 (2002) 2629–2642
18. Schmidt, R., Diba, K., Leibold, C., Schmitz, D., Buzsaki, G.: Single-trial phase precession in the hippocampus. *J. Neurosci.* 29 (2009) 13232–13241
19. Hafting, T., Fyhn, M., Bonnevie, T., Moser, M.B., Moser, E.I.: Hippocampus-independent phase precession in entorhinal grid cells. *Nature* 453 (2008) 1248–1252

Reactivation Hypothesis in Episodic Memory: From the Findings of Neuroimaging Studies

Aya Ueno, Jiro Okuda, and Toshikatsu Fujii

Abstract Memory traces of an event include various types of information about the content of the event and the circumstances under which the individual experienced it. How these various types of information are stored and later retrieved, however, is poorly understood. The reactivation hypothesis postulates that retrieval of specific event information reactivates cortical regions that were active during the encoding of the information, with the aid of binding functions in the medial temporal lobe (MTL) structures. In this paper, we describe our two PET studies on reactivation hypothesis, and then review previous neuroimaging studies relevant to this hypothesis.

1 Introduction

Episodic memory is memory that allows one to remember past events in one's life [1]. It is widely accepted that memory traces of an event include various types of information about the content of the event and about the circumstances in which the individual experienced the event [2] [3, 4]. However, how these various types of information are stored and later retrieved is poorly understood. One hypothesis postulates that retrieval of a specific event information reactivates cortical regions that were active during the encoding of the information [5] (the cortical

A. Ueno (✉) • T. Fujii

Department of Behavioral Neurology and Cognitive Neuroscience, Tohoku University School of Medicine, 2-1, Seiryomachi, Aoba-ku, Sendai 980-8575, Japan
e-mail: uenoaya@med.tohoku.ac.jp

J. Okuda

Khoyama Center for Neuroscience, Department of Intelligent Systems, Faculty of Computer Science and Engineering, Kyoto Sangyo University, Kamigamo-Motoyama, Kita-Ku, Kyoto 603-8555, Japan

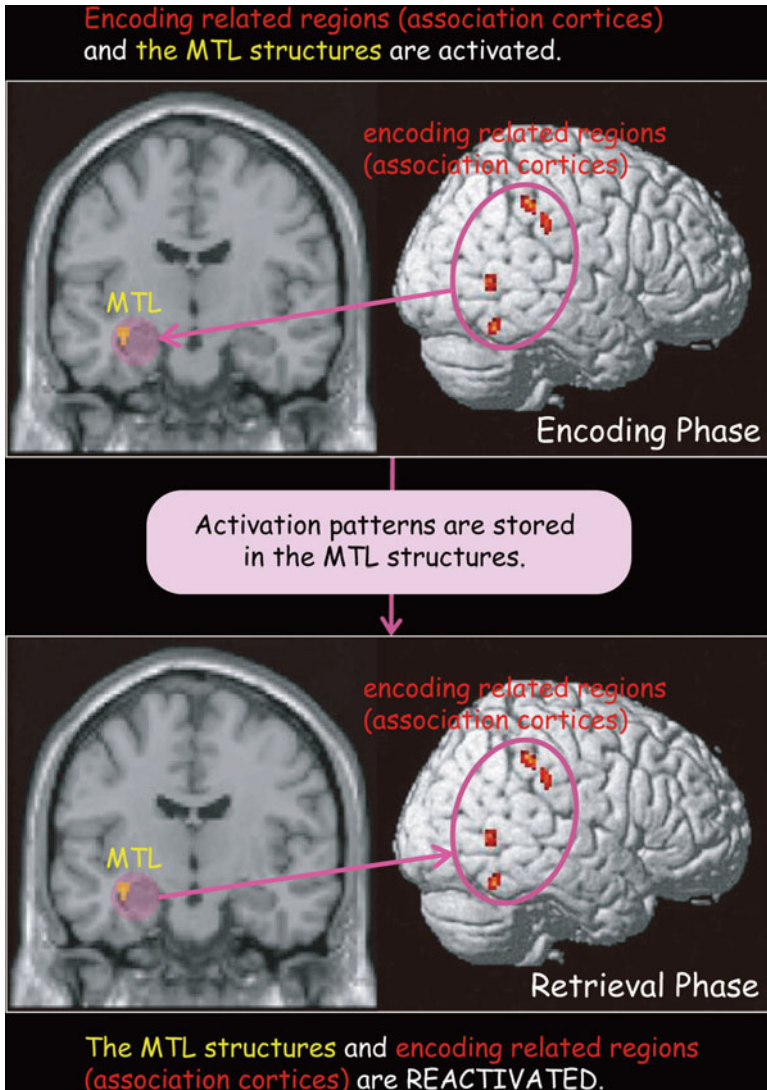


Fig. 1 Reactivation hypothesis

reinstatement hypothesis), with the aid of binding functions of the medial temporal lobe (MTL) structures [6]. In this paper, by the “reactivation” hypothesis, we refer to the reactivation of both cortical regions and the MTL structures (see Fig. 1). To date, however, only a relatively small number of neuroimaging studies have directly assessed whether the neural activity elicited during encoding is reactivated during retrieval of the encoded information.

2 Our Two Studies on Reactivation Hypothesis

We used positron emission tomography (PET) to identify brain regions related to the encoding and retrieval of two different types of visual information (i.e., color and motion).

In Study 1 [7], subjects were asked to encode colored (red or green) and achromatic random shapes. At subsequent testing, subjects were presented with only achromatic shapes, which had been presented with or without colors during encoding, and were engaged in retrieval tasks of shapes and colors. Overlapping activity was found in the MTL and occipital lobe (the lingual and inferior occipital gyri) in the right hemisphere during the encoding and retrieval of meaningless shapes with color information compared with those without color information (Fig. 2a).

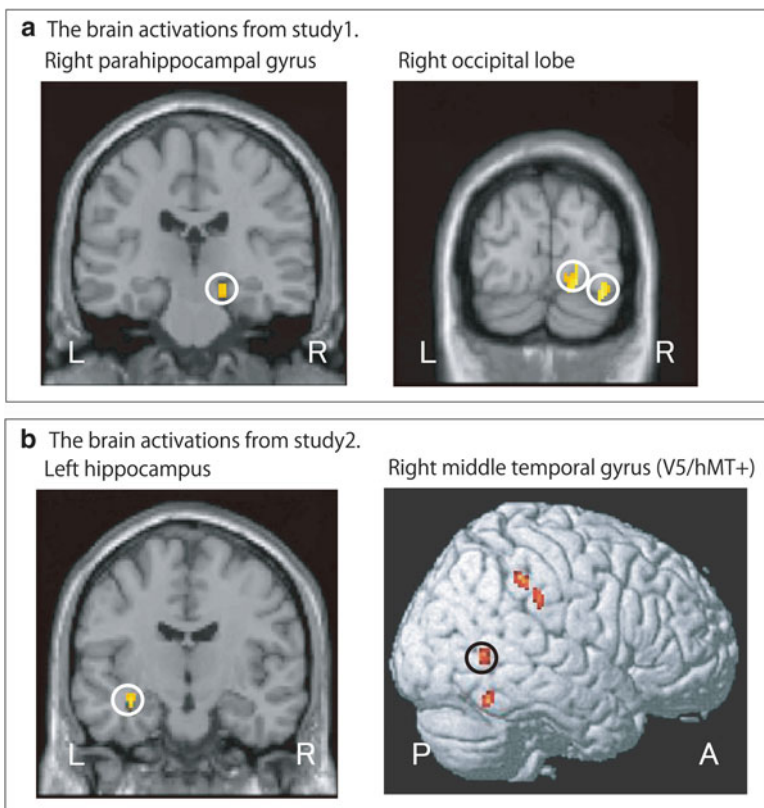


Fig. 2 Brain activations in our two PET studies. **(a)** Brain activations common to the encoding and retrieval of color information: the right lingual gyrus (18, -88, -6), the right inferior occipital gyrus (34, -88, -16), and the right parahippocampal gyrus (18, -22, -16). **(b)** Brain activations common to the encoding and retrieval of motion information: the right middle temporal gyrus (46, -58, 2) and the left hippocampus (-34, -12, -14)

In Study 2 [8], subjects were asked to encode moving (turning around to the right or the left) and static random shapes. At subsequent testing, subjects were presented with only static shapes, which had been presented with or without motion during encoding, and were engaged in retrieval tasks of shapes and motion. Overlapping activity was found in the left MTL and the right middle temporal gyrus (V5/human MT+) during the encoding and retrieval of shapes with motion compared with those without motion (Fig. 2b).

These two studies demonstrated that, regardless of the type of the information, both the MTL and the higher-order visual cortex were consistently reactivated. These results indicate that memory contents are stored in the relevant cortices of the brain, and medial temporal lobe (MTL) structures bind these constituents to each other and to event-specific contextual information. Thus, these findings seem to support the view that the retrieval of specific event information is associated with reactivation of both the MTL structures and the regions involved in encoding the information (i.e., the reactivation hypothesis).

3 Previous Neuroimaging Studies Relevant to the Reactivation Hypothesis

We found five PET studies, including our two studies, and 12 fMRI studies relevant to the reactivation hypothesis. Several studies employed blocked experimental designs (Ueno et al. [7], Ueno et al. [8], Nyberg et al. [9], Nyberg et al. [10], Persson and Nyberg [11], Vaidya et al. [12]). The results of these studies have shown cortical reinstatement effects, but the blocked designs of these studies leave open the possibility that the material-specific retrieval effects reflect the attempt to retrieve targeted memories, rather than the consequence of successful retrieval.

Some other studies employed event-related design with fMRI (Wheeler et al. [13], Wheeler et al. [14], Wheeler and Buckner [15], Khader et al. [16], Wheeler and Buckner [17], Gottfried et al. [18], Kahn et al. [19], Woodruff et al. [20], Johnson and Rugg [21], Johnson et al. [22], Vannini et al. [23]). However, only four studies have directly assessed whether the neural activity elicited during encoding is reactivated during retrieval of the encoded information. The remaining seven studies reported brain activity only during the retrieval phase.

Another contaminating factor is a repeated encoding procedure in several studies including ours. Most of the studies asked subjects to learn associations between plural components of stimuli. The difficulty in associative learning requires the repeated encoding in several studies. This multiple encoding procedure makes it impossible to determine whether memories assessed are episodic or semantic in nature.

As for the brain activations reported in the studies that assessed both encoding and retrieval phases, some of the sensory-processing brain regions (i.e., posterior association cortices) activated during encoding are reactivated during retrieval.

The findings with regard to MTL are, however, inconsistent with each other; five studies have reported MTL reactivation (Ueno et al. [7], Ueno et al. [8], Nyberg et al. [9], Johnson et al. [22], Vannini et al. [23]), but the others have not (Nyberg et al. [10], Persson and Nyberg [11], Vaidya et al. [12], Wheeler et al. [13], Johnson and Rugg [21]). We do not know the precise reason for this inconsistency, but one possible explanation is that these studies differed from one another in terms of experimental paradigms such as the stimuli and tasks involved. Therefore, in the future studies, it is worthwhile investigating what circumstances lead to overlapping activation in the MTL and other association cortices during both encoding and retrieval.

Acknowledgments This work was supported by the Grant-in-Aid for Scientific Research on Innovative Areas (The study on the neural dynamics for understanding communication in terms of complex hetero systems), MEXT, Japan.

References

1. Tulving, E. Episodic memory and common sense: how far apart? *Philos. Trans. R. Soc. Lond. B Biol. Sci.* **356** (2001) 1505–1515.
2. Fujii T. et al. Neural correlates of context memory with real-world events. *Neuroimage* **21**(2004) 1596–1603.
3. Nadel, L. and Moscovitch, M. consolidation, retrograde amnesia and the hippocampal complex. *Curr. Opin. Neurobiol.* **7** (1997) 217–227.
4. Squire, L.R. and Alvarez, P. Retrograde amnesia and memory consolidation: a neurobiological perspective. *Curr. Opin. Neurobiol.* **5** (1995) 169–177.
5. Rugg MD. et al. Encoding-retrieval overlap in human episodic memory: a functional neuroimaging perspective. *Progress in Brain Research* **169** (2008) 339–352.
6. Norman KA. and O'Reilly RC. Modeling hippocampal and neocortical contribution to recognition memory: A complementary-learning-systems approach. *Psychol. Rev.* **110** (2003) pp. 611–646.
7. Ueno A. et al. Reactivation of medial temporal lobe and occipital lobe during the retrieval of color information: a positron emission tomography study. *Neuroimage* **34** (2006) 1292–1298.
8. Ueno A. et al. Reactivation of medial temporal lobe and human V5/MT+ during the retrieval of motion information: a PET study. *Brain Research* **1285** (2009) 127–134.
9. Nyberg L. et al. Reactivation of encoding-related brain activity during memory retrieval. *PNAS.* **97** (2000) 11120–11124.
10. Nyberg L. et al. Reactivation of motor brain areas during explicit memory for actions. *Neuroimage* **14** (2001) 521–528.
11. Persson J. and Nyberg L. Conjunction analysis of cortical activations common to encoding and retrieval. *Micrisc. Res. Tech.* **51** (2000) 39–44.
12. Vaidya CJ. et al. Evidence for cortical encoding specificity in episodic memory: memory-induced re-activation of picture processing areas. *Neuropsychologia* **40** (2002) 2136–2143.
13. Wheeler MA. et al. Memory's echo: vivid remembering reactivates sensory-specific cortex. *PNAS.* **97** (2000) 11125–11129.
14. Wheeler MA. et al. Evidence for Separate Perceptual Reactivation and Search Processes during Remembering. *Cerebral Cortex* **16** (2006) 949–959.
15. Wheeler MA. and Buckner RL. Functional Dissociation among Components of Remembering: Control, Perceived Oldness, and Content. *The Journal of Neuroscience* **23**(9) (2003) 3869–3880.

16. Khader P. et al. Content-specific activation during associative long-term memory retrieval. *Neuroimage* **27** (2005) 805–816.
17. Wheeler MA. and Buckner RL. Functional-anatomic correlates of remembering and knowing. *Neuroimage* **21** (2004) 1337–1349.
18. Gottfried JA. et al. Remembrance of odors past: human olfactory cortex in cross-modal recognition memory. *Neuron* **42** (2004) 687–695.
19. Kahn I. et al. Functional–Neuroanatomic Correlates of Recollection: Implications for Models of Recognition Memory. *The Journal of Neuroscience* **24**(17) (2004) 4172–4180.
20. Woodruff CC. et al. Content-specificity of the neural correlates of recollection. *Neuropsychologia* **43** (2005) 1022–1032.
21. Johnson JD. and Rugg MD. Recollection and the reinstatement of encoding-related cortical activity. *Cerebral Cortex* **17** (2007) 2507–2515.
22. Johnson JD. et al. Recollection, familiarity, and cortical reinstatement: a multivoxel pattern analysis. *Neuron* **63** (2009) 697–708.
23. Vannini P. et al. What goes down must come up: role of the posteromedial cortices in encoding and retrieval. *Cerebral Cortex* **21**(1) (2011) 22–34.

Model-Based Analysis of Functional Connectivity During Associative Learning in Schizophrenia

Mihály Bányai, Vaibhav Diwadkar, and Péter Érdi

Abstract Schizophrenia is often regarded as a set of symptoms caused by impairments in the cognitive control in macro-networks of the brain. To investigate this hypothesis, an fMRI study involving an associative learning task was conducted with schizophrenia patients and controls. A set of generative models of the BOLD signal generation were defined to describe the interaction of five brain regions (Primary Visual Cortex, Superior Parietal and Inferior Temporal Cortex, Hippocampus and Dorsal Prefrontal Cortex) and the experimental conditions. The models were fitted to the data using Bayesian model inversion. The comparison of different model connectivity structures lead to the finding that in schizophrenia, there are significant impairments in the prefrontal control of hippocampal memory formation in patients.

1 Introduction

Schizophrenia is a complex disorder with diverse related impairments in the central nervous system. Specifically, altered interaction of prefrontal cortex and hippocampus is hypothesized to be a central aspect of its pathophysiology [1]. Here we investigated impaired functional macro-network interactions in schizophrenia by applying Dynamic Causal Modelling (DCM) [2] to the analyses of fMRI data collected during an object-location paired-associate learning paradigm [6]. The aim

M. Bányai (✉) • P. Érdi

KFKI Research Institute for Particle and Nuclear Physics of the Hungarian Academy of Sciences, Budapest, Hungary

Center for Complex Systems Studies, Kalamazoo College, Kalamazoo, MI, USA
e-mail: perdi@kzoo.edu

V. Diwadkar

Wayne State University School of Medicine, Detroit, MI, USA

of modeling interactions of brain areas using DCM is to characterize: (a) the intrinsic connectivity of the network and (b) the contextual modulation of the intrinsic connections by psychological aspects of the task.

1.1 *Associative Learning: Behavioral Task and Data*

We adopted a paired-associate learning paradigm in which subjects are required to learning arbitrary associations between locations (in space) and objects (with unique identities). The two kinds of memoranda (“where” and “what”) are processed by the two components, i.e. spatial (dorsal) and object (ventral), of the forward visual pathway [3]. It is assumed that these information streams converge in the hippocampus, with potential supervisory inputs from the prefrontal cortex. Through the repeated alternation between learning and retrieval epochs using a block design, we were able to capture learning dynamics in controls and patients over time (see Fig. 1).

2 Methods

2.1 *Dynamic Causal Modelling*

DCM provides a complete phenomenological model framework for the analysis of fMRI data. For a detailed description see [2]. The model structure consists of two components: a neural state equation and a hemodynamic model. The neural component describes the time evolution of the neural state variables, x , which refer to the neural activity of the brain areas. This is a bilinear formula of the state variables themselves and the input variables, u , which are the conditions defined by the experiment (Eq. 1). The connectivity parameters of the neural model are the elements of the three matrices, $\theta_n = \{A, B, C\}$. A contains the intrinsic coupling parameters, the causal effects of the areas on each other, B contains the modulatory parameters, the effects of the inputs on the intrinsic connections, and C contains the direct effects of the inputs on the areas.

$$\dot{x} = \left(A + \sum_{i=1}^N u_i B^i \right) x + C u \quad (1)$$

$$y = \lambda(x, \theta_h) \quad (2)$$

The hemodynamic component describes the nonlinear mapping from the neural activity to the fMRI signal, y , actually measured in the brain areas (Eq. 2). For the details of the hemodynamic model see [4]. We need to estimate the values of

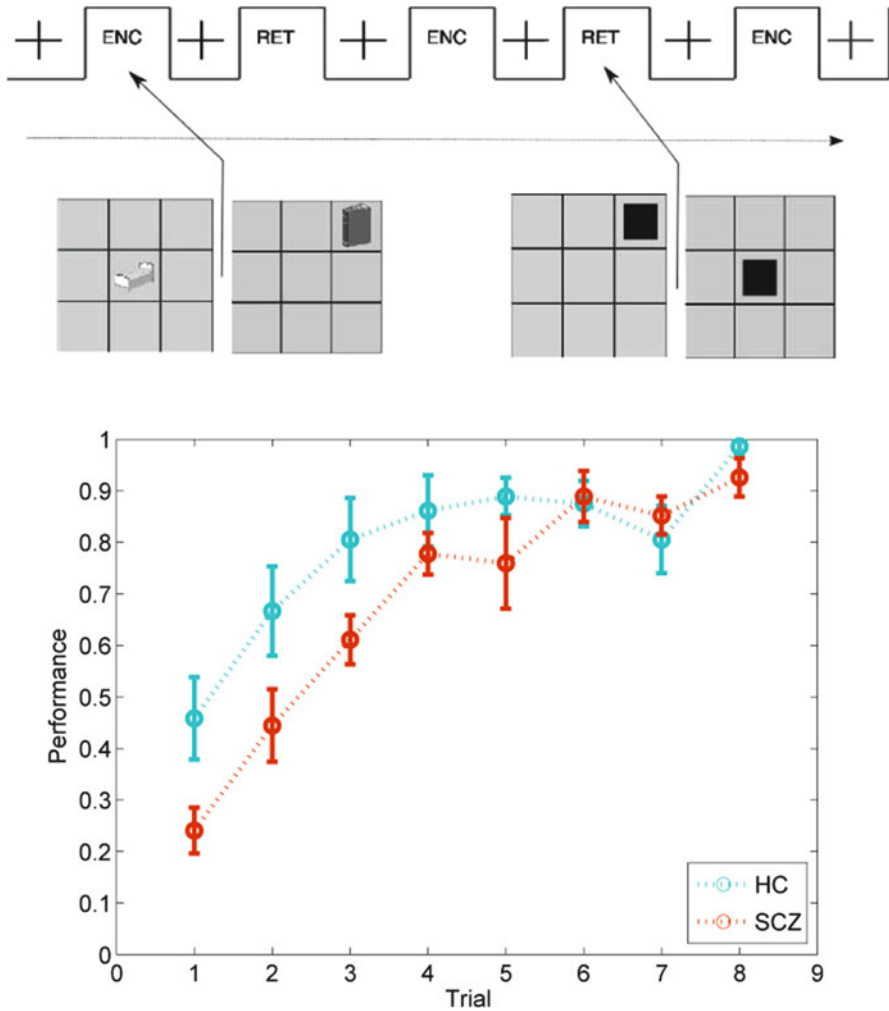
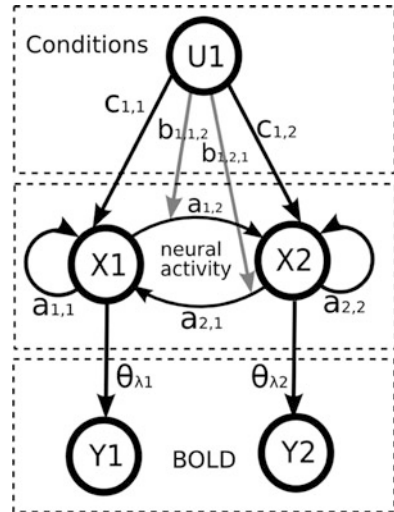


Fig. 1 *Top*: structure of the experimental paradigm is depicted with two examples of associations presented during encoding/consolidation (“bed” and “book”) and examples of those locations cued during recall/retrieval. *Bottom*: learning dynamics in the associative memory task in controls and schizophrenia patients over time. The data provide evidence of generally asymptotic learning in both groups, with reduced learning rates in patients compared to controls

the parameter set, $\theta = \{\theta_h, \theta_n\}$ best fitting to measurement data. One possible procedure to do so is the Bayesian maximum a posteriori (MAP) estimation technique defined by Eq. 3, where M denotes the specific connectivity pattern of the model.

$$p(\theta | y, M) = \frac{p(y | \theta, M)p(\theta | M)}{p(y | M)} \tag{3}$$

Fig. 2 Schematic diagram of a generative DCM of an fMRI study



For all probability distributions in (3), we assume that both the prior ($p(\theta | M)$) and posterior ($p(\theta | y, M)$) distributions are Gaussians, and the MAP estimation is defined as the mean of the posterior distribution. To compare models with different connectivity patterns, we can set the prior probability of having certain connections is a certain model to zero (Fig. 2).

2.2 Comparison of Models

We can compare models with different connectivity patterns in a Bayesian way by estimating their model evidence:

$$p(y | M) = \int p(y | \theta, M)p(\theta | M) d\theta \tag{4}$$

The model evidence is the probability of obtaining the actual measurement conditioned on the model form, integrated on the whole parameter space of the model. The computation of the evidence is usually not feasible, so we approximate it by a variational Bayesian method. To obtain the expected posterior probabilities of all models in a model set, we assume a hierarchical model of data generation. We can invert this model using a variational Bayesian method that requires only the estimates of the log-evidences for each subject-model pair. This way we obtain the expected posterior probability of each model regarding the subject group. For a complete description of the comparison method see [5].

Fig. 3 The model space for varying intrinsic connections. Connections marked by *dashed line* are varied

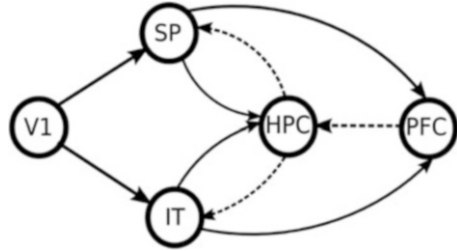


Table 1 Posterior model probabilities for the patient and control groups

No.	Additional connections	SCZ	HC
1	None	0.099	0.079
2	PFC→HPC	0.145	0.106
3	HPC→IT	0.099	0.079
4	HPC→IT, PFC→HPC	0.172	0.101
5	HPC→SP	0.158	0.081
6	HPC→SP, PFC→HPC	0.095	0.116
7	HPC→SP, HPC→IT	0.136	0.081
8	HPC→SP, HPC→IT, PFC→HPC	0.095	0.357

2.3 Model Definitions

A set of causal models of fMRI signal generation (with the mathematical structure described above) were defined to evaluate connections between five regions material to the task (Primary Visual Cortex (V1), Superior Parietal (SP) and Inferior Temporal Cortex (IT), Hippocampus (HPC) and Dorsal Prefrontal Cortex (PFC)). To model the information processing in the associative learning task, we assumed the presence of two streams connecting the five brain regions. The “forward” or “data” stream propagates sensory information at different levels of processing from the low-level sensory areas towards high-level cognitive areas. The “backward” or “control” stream propagates control signals from the high-level areas towards the lower-level ones. In this paper we examine impairments in cognitive control, so the focus of the investigations is the control stream.

Multiple models were evaluated by varying hypothesis-related intrinsic connections between regions, while fixing other connections (*A* matrix). We included the intrinsic connections of the data stream to all models. Based on the hypothetical control stream we defined three additional connections that may extend the basic model in different combinations. The eight possible combinations of these connections constitute the model class. All possible intrinsic connections are visualized in Fig. 3 and described in Table 1.

3 Results

3.1 Model Selection

The results show that in the control group (HC) there is a clear winner for the intrinsic connection patterns, the model that contains the full control stream. In the schizophrenia group (SCZ), there is no clear winner, there are several more probable models, and the differences are smaller between model probabilities. It can also be seen that while the winning model in the HC group contains all the connections defined, while the most probable models in the SCZ group lack more or less connections. This result implies that the information processing network of schizophrenia patients is fundamentally different than the one of controls. Results are shown in Table 1. However, the model selection does not provide the specific pathways being impaired, so the parameter level analysis is also necessary.

3.2 Effective Connectivities

In the next step of the analysis, we give a more detailed quantitative characterization of the results. At the parameter level, we look for significant differences in the effective connectivity in the models fit to the data of the two subject groups, assuming fixed model structure. To do so, we selected a reference model for comparison by running the model selection for all subjects, no distinction by group.

The winning model is the one containing all hypothesized connections. The means and standard deviations of the intrinsic coupling and modulatory parameters are depicted in Fig. 4.

The significant differences between groups are in the strength of intrinsic connections between prefrontal cortex and hippocampus and between hippocampus and inferior temporal cortex. All these connections are weakened in the SCZ group, supporting the hypothesis about impaired effective connectivity in the control

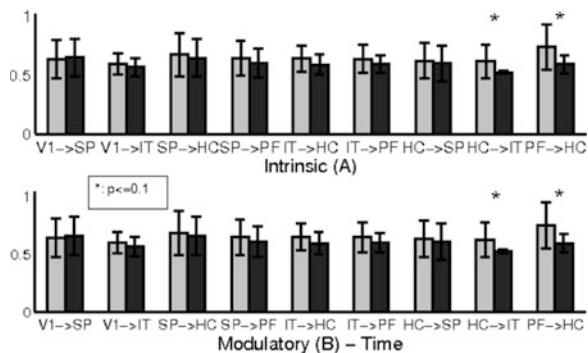


Fig. 4 Average connectivity parameters for HC and SCZ (dark) groups. The significant differences are in the prefronto-hippocampal and hippocampo-inferior temporal pathways

stream in schizophrenia. Both these connections are playing important roles in the cognitive control of the associative memory formation. Furthermore, we see the reduced effects of Time on these causal links meaning reduced excitatory contextual modulation by learning. This can be seen as reduced task-related plasticity of a pathway in the illness.

4 Discussion

Learning impairments have been considered good markers of hippocampal impairment in schizophrenia [7], and computational models of hippocampal function have been applied to study this cognitive impairment in the disorder [6, 8]. However, the basis of these impairments in terms of network interactions has not been known. Our results (the first based on in vivo fMRI data) provide evidence of impaired frontal inputs to the hippocampus, and reduced learning related plasticity of fronto-hippocampal coupling in the disorder.

Acknowledgments We are thankful to the National Institutes of Mental Health, the Children's Research Center of Michigan, the Elizabeth Elser Doolittle Investigator-ship and the Henry Luce foundation.

References

1. Harrison, P.J.: The neuropathology of schizophrenia. A critical review of the data and their interpretation. *Brain* 122 (1999) 593–624
2. Friston, K.J., Harrison, L., Penny, W.D.: Dynamic causal modelling. *NeuroImage* 19 (2003) 1273–1302
3. Buchel, C., Coull, J.T., Friston, K.J.: The predictive value of changes in effective connectivity for human learning. *Science* 283 (1999) 1538–1541
4. Friston, K.J., Mechelli, A., Turner R., Price, C.J.: Nonlinear responses in fmri: The balloon model, volterra kernels and other hemodynamics. *NeuroImage* 12 (2000) 466–477
5. Stephan, K.E., Penny, W.D., Daunizeau, J., Moran R., Friston K.J.: Bayesian model selection for group studies. *NeuroImage* 46 (2009) 1004–1017
6. Diwadkar, V., Flaughner, B., Jones, T., Zalányi, L., Ujfalussy, B., Keshavan, M.S., Érdi, P.: Impaired associative learning in schizophrenia: Behavioral and computational studies. *Cognitive Neurodynamics* 2(3) (2008) 207–219
7. Wood et al.: Visuospatial memory and learning in first-episode schizophreniform psychosis and established schizophrenia: a functional correlate of hippocampal pathology? *Psychological medicine* 32 (2002) 429–438
8. Siekmeier, P.J., Hasselmo, M.E., Howard, M.W., Coyle, J.: Modeling of context-dependent retrieval in hippocampal region CA1: implications for cognitive function in schizophrenia. *Schizophrenia research* 89 (2007) 177–190

Neuronal Activity in the Prefrontal Cortex During Performance of a Dual Task Consisting of a Main- and An Interrupting-Task

Atsushi Miyazaki, Toshi Nakajima, Keisetsu Shima, and Hajime Mushiake

Abstract To investigate the neuronal mechanism of multi-tasking, we recorded neuronal activity in the prefrontal cortex (PFC) and the dorsal premotor cortex (PMd) while monkeys performed a dual task consisting of a main-task and an interruption. We found PFC neurons responded selectively to either the interruption or resumption to the main-task. PMd neurons showed sustained activity related to preparation for the main-task. Accordingly, we hypothesized a model in which the PFC controls a dual task by providing biasing signals to downstream systems.

1 Introduction

In order to cope in a dynamically changing environment, we often manage interruptions even while performing certain main-tasks. Obviously, multi-task performance requires not only a system to select action in response to immediate sensory input but also an executive system that controls behavior to obtain a certain behavioral goal. The prefrontal cortex (PFC) has been known to be crucially involved in executive control of behavior [1, 2]. Human clinical studies have demonstrated that frontal lesion, including the PFC, causes impairment of dual task performance [3]. Neurophysiological studies have revealed that single-neuron activity in the PFC reflects behavioral goals [4], rules to select action [5], the category of visual objects and the category of behavioral sequences [6, 7]. In contrast, the dorsal premotor cortex (PMd) has been implicated in rule-based action selection and motor preparation and execution [8]. However, how these areas are involved in multi-tasking is poorly understood on the single-neuron level. To address the neuronal mechanism of multi-tasking, we trained monkeys to perform a dual task;

A. Miyazaki (✉) • T. Nakajima • K. Shima • H. Mushiake
Department of Physiology, Tohoku University School of Medicine, 2-1, Seiryō-cho Aoba-ku,
Sendai, Miyagi 980-8575, Japan
e-mail: a-miyazaki@med.tohoku.ac.jp

while the animals repeated a memorized motor sequence, an interrupting signal instructed the animals to perform a separate movement, independent of the motor sequence. The animals were required to reproduce the original motor sequence after the interruption. We recorded neuronal activity in the PFC and PMd while they performed the dual task.

2 Methods

We used two monkeys (*Macaca fuscata*, 6.5 and 5.8 kg), cared for in accordance with the Guidelines for Institutional Animal Care and Use published by our institute. We trained these monkeys to perform a dual task consisting of a main- and an interrupting-task. During the experiment, each animal sat in a primate chair, facing a computer display.

Experimental sessions were divided into blocks of six consecutive trials. Fig. 1a illustrates time course of an example experimental block. The temporal structure of the block was as follows: (1) Main-task with visual guidance: the animals had to perform a sequence of two movements (main sequence) in response to colored cues presented one after the other with an intervening delay. The red, blue, yellow or green cues indicated either of four movements shown in Fig. 1b. The animals had to memorize the particular main sequence while performing it twice. (2) Main-task before interruption: the memorized main sequence was repeated for two trials. (3) Interrupting-task: the animals had to execute a movement

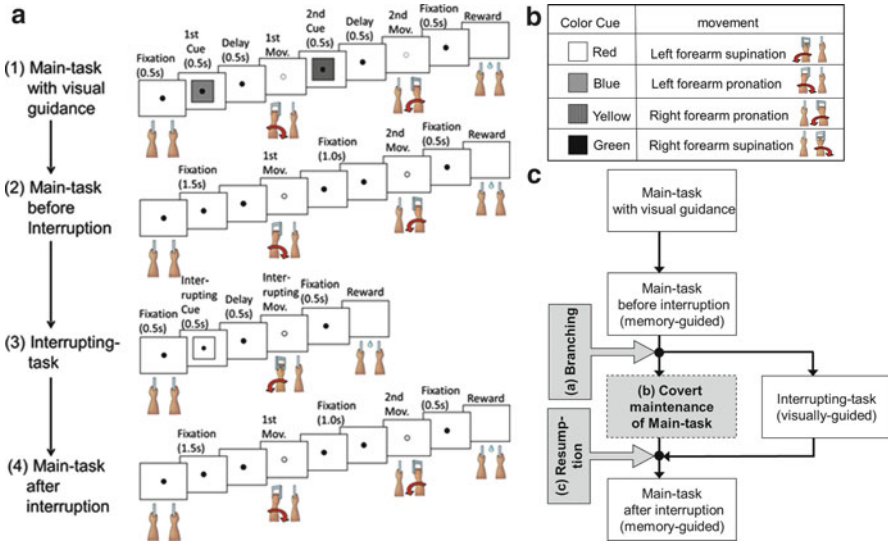


Fig. 1 Behavioral task. (a) Temporal sequence of behavioral events. (b) Four possible movements. (c) A schematic drawing of a behavioral task

(interrupting movement) indicated by a colored cue, branching from the main-task. The relationship between colored cues and movements was the same as (1). (4) Main-task after interruption (resumption trial) the animals were required to recall and perform the main sequence once without visual guidance. A new main sequence with an interruption combination was selected pseudorandomly and alternated for each block. Fig. 1c illustrates cardinal processes for performance of the dual task: (a) branching from the main- to the interrupting-task, (b) covert maintenance of the information for the main-task during the interruption, and (c) resumption to the main-task after interruption.

We recorded neuronal activity in the PFC and PMd of both monkeys. In this report, we focus our analysis on neuronal activity related to the interruption and resumption to the main task. If neuronal activity was significantly stronger in the interrupting task than in the initial trial of the main-task where the main sequence was instructed (one-tailed t -test, $P < 0.05$), the activity was classified as interruption-selective. Similarly, if neuronal activity became significantly stronger in the main-task after interruption (i.e., resumption trials) than before the interruption (one-tailed t -test, $P < 0.05$), the activity was classified as resumption-selective. We computed the index for the aforementioned selectivity with the following formula: $-\log_{10}(P \text{ value})$.

3 Results

For both monkeys, the correct rates in the interrupting-task and main-task after interruption were $> 98\%$ and $> 80\%$, respectively. We recorded activity of 270 PFC neurons and 214 PMd neurons in two monkeys. Of these, 131 PFC and 104 PMd neurons were classified as interruption-selective, whereas 102 PFC and 62 PMd neurons were found to be resumption-selective.

Interruption selective activity in the PFC: We found PFC neurons exhibiting distinct cue response in the interrupting-task, not in the main-task. An example neuron is shown in Fig. 2a, b. We divided a trial period into consecutive 250-ms periods and estimated interruption selectivity for each period. For this neuron, interruption selectivity was the strongest at the early-cue period (Fig. 2c).

Interruption related activity in the PMd: Unlike PFC neurons, a typical PMd neuron exhibited sustained precue activity in the interrupting-task. The activity ceased after cue onset (Fig. 2d, e). Accordingly, interruption selectivity of this neuron was significantly high before cue presentation but diminished in the early-cue period (Fig. 2f).

Comparison of interruption-related activity in the PFC and PMd: We performed a population analysis of interruption-selective neurons (Fig. 3). During the trial-start and precue periods, interruption selective neurons were found more frequently in

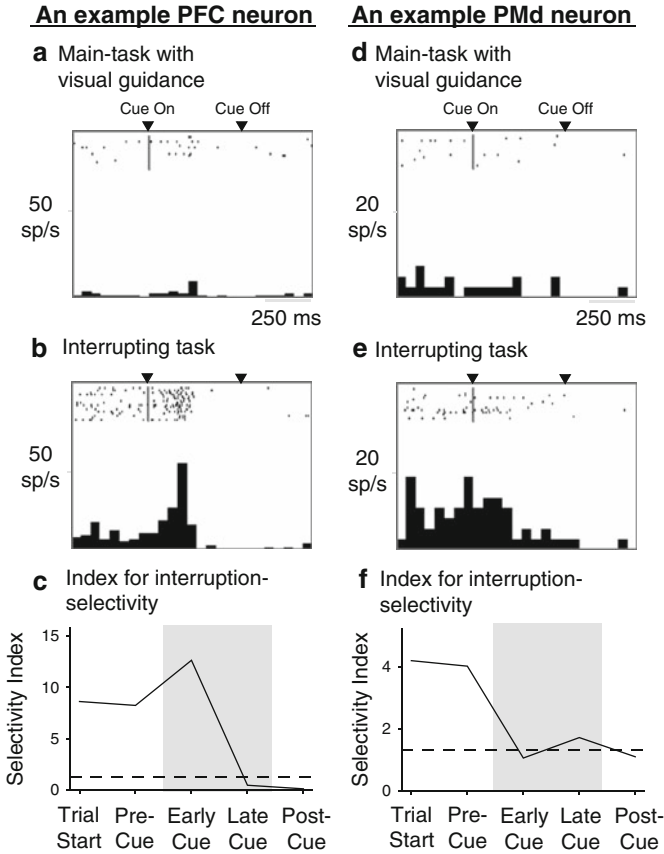
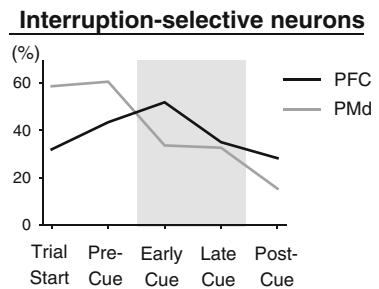


Fig. 2 Activity of a PFC and a PMd neuron during main-task with visual guidance (**a, d**) and interrupting task (**b,e**). Each raster and histogram is aligned with 1st cue onset. Time course of interruption selectivity of the neuron (**c,f**). The shaded areas indicate the 500-ms interval for cue presentation. Dashed lines indicate significance level ($P = 0.05$)

Fig. 3 The fractions of interruption selective neurons in the PFC (black line) and PMd (gray line) in each analytic period



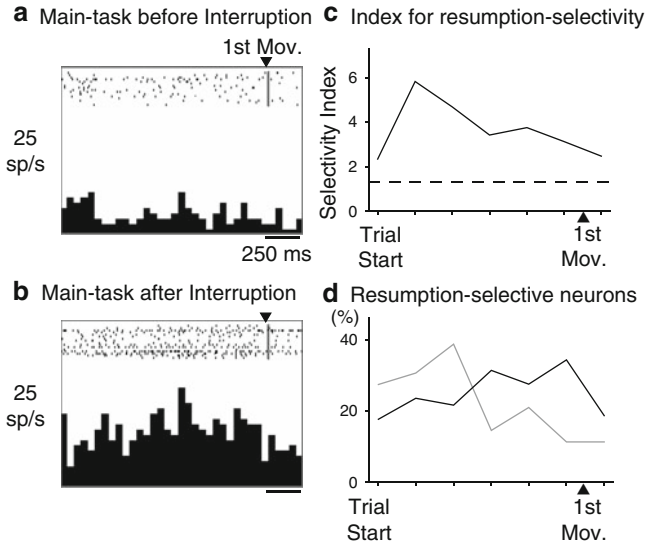


Fig. 4 (a, b) Comparison of activity of a PFC neuron in the main-task before interruption with the main-task after interruption (resumption trial). Activity is aligned with 1st movement onset. (c) Resumption selectivity of the neuron. (d) The fractions of resumption-selective neurons in the PFC and PMd. The other display formats are the same as in Fig. 2, 3

the PMd than in the PFC. This relationship reversed after cue presentation. The fraction in the PFC peaked at the early-cue period and decreased thereafter, whereas the fraction in the PMd continuously decreased.

Resumption selective activity in the PFC: Activity of PFC neurons tends to be enhanced after an interruption. We found that a neuron became continuously active during motor preparation in the main-task after interruption (Fig. 4a, b). Resumption selectivity of this neuron was significant throughout the analytic periods (Fig. 4c). Population analysis revealed gradual increment of resumption selective neurons in the PFC until the onset of the 1st movement (Fig. 4d). The opposite trend was observed in the PMd.

4 Discussions

We found interruption- or resumption-selective activity in the PFC and PMd while monkeys performed a dual task. PFC neurons preferentially responded to interrupting cues (Fig. 2) and showed enhanced activity on motor initiation after an interruption (Fig. 4). PMd neurons showed sustained activity until cue presentation; thereafter, activity decreased (Fig. 3).

3. Baddeley, A., Della, Sala. S.: Working memory and executive control. *Philos Trans R Soc Lond B Biol Sci.* 351(1346) (1996) 1397–403
4. Mushiake, H., Saito, N., Sakamoto, K., Itoyama, Y., Tanji, J.: Activity in the lateral prefrontal cortex reflects multiple steps of future events in action plans. *Neuron.* 50(4) (2006) 631–41
5. Wallis, J.D., Anderson, K.C., Miller, E.K.: Single neurons in prefrontal cortex encode abstract rules. *Nature.* 411(6840) (2001) 953–6
6. Freedman, D.J., Riesenhuber, M., Poggio, T., Miller, E.K.: Categorical representation of visual stimuli in the primate prefrontal cortex. *Science.* 291(5502) (2001) 312–6
7. Shima, K., Isoda, M., Mushiake, H. Tanji, J.: Categorization of behavioural sequences in the prefrontal cortex. *Nature.* 445(7125) (2007) 315–8
8. Hoshi, E., Tanji, J.: Distinctions between dorsal and ventral premotor areas: anatomical connectivity and functional properties. *Curr Opin Neurobiol.* 17(2) (2007) 234–42
9. Sakai, K.: Task set and prefrontal cortex. *Annu Rev Neurosci.* 31 (2008) 219–45
10. Schneider, D.W., Logan, G.D.: Task Switching. *Encyclopedia of Neuroscience* 9 (2009) 869–874
11. Sakai, K., Rowe, J.B., Passingham, R.E.: Active maintenance in prefrontal area 46 creates distractor-resistant memory. *Nat Neurosci.* 5 (2002) 479–484
12. Koehlin, E., Summerfield, C.: An information theoretical approach to prefrontal executive function. *Trends Cogn Sci.* 11 (2007) 229–235
13. Shallice, T.: Specific impairments of planning. *Philos Trans R Soc Lond B Biol Sci.* 298(1089) (1982) 199–209

Functional Analysis of the Hippocampus Using Opto-fMRI

Yoshihumi Abe, Masaki Sekino, Yugo Fukazawa, Hiromu Yawo, Hiroyuki Ohsaki, and Tatsuhiro Hisatsune

Abstract A new technique ‘opto-fMRI’ combined optogenetics and fMRI (functional magnetic resonance imaging) was born in 2010. We investigated hippocampal network and activity using opto-fMRI. We stimulated the dentate gyrus expressing channelrhodopsin2 (ChR2) by optic light. As a result, we observed activation of the CA3 region and in the hippocampus. In this paper, we succeeded in measuring opto-fMRI BOLD (blood oxygenation level-dependent) signals of the hippocampus.

1 Introduction

In recent years the technique of optogenetics has been thoroughly developed. By inducing the expression of light-gated cation channel channelrhodopsin2 (ChR2) in neuronal cells, we can operate the activity of neurons by using light. ChR2 has become an important tool in neuroscience.

Y. Abe (✉) • T. Hisatsune

Department of Integrated Biosciences Graduate School of Frontier Science, The University of Tokyo, 5-1-5 Kashiwanoha, Kashiwa, Chiba 277-8562, Japan
e-mail: 106303@ib.k.u-tokyo.ac.jp

M. Sekino • H. Ohsaki

Department of Advanced Energy Graduate School of Frontier Science, The University of Tokyo, 5-1-5 Kashiwanoha, Kashiwa, Chiba 277-8562, Japan

Y. Fukazawa

Division of Cerebral Structure, National Institute for Physiological Sciences, 5-1 Higashiyama, Myodaiji Okazaki 444-8787, Japan

H. Yawo

Department of Developmental Biology and Neuroscience, Tohoku University Graduate School of Life Sciences, 2-1-1 Katahira, Aoba-ku, Sendai 980-8577, Japan

It is well known that functional magnetic resonance imaging (fMRI) based on the blood oxygenation level-dependent (BOLD) signal can be used to measuring brain activity and neural network.

In recent papers, optogenetics and fMRI were combined [1, 2]. This new technique was called opto-fMRI (ofMRI). The response of brain stimulated by the light to neuronal cells expressing ChR2 can be measured by fMRI. Opto-fMRI was enabled to observe the entire brain activity and network noninvasively. This allows us to perform two experiments. One was to investigate neuronal networks. The other was to investigate the function of neurons.

As reports until now, Lee et al. demonstrated opto-fMRI and reported a BOLD response in the thalamus during local primary motor cortex (M1) stimulation [1]. Also, Desai et al. reported the same in the sensory cortex [2]. Both reports investigated the networks of cerebral cortex.

Our study focused on the hippocampal network. The hippocampus plays important role in neurogenesis and memory formation. Knowing the hippocampal network has contributed to understanding how memory is formed and where memory is accumulated. Also, this knowledge has contributed to the studies of dementia and amnesia in memory impairment disorders.

It is well known that the stimulation from the entorhinal cortex (EC) inputs into the dentate gyrus (DG) in the hippocampus and the signals from the DG are sent to the CA3 and CA1 regions [3, 4].

In this study, we investigated how the dentate gyrus of the hippocampus responds when it is stimulated by light. Also, we confirmed whether the response of hippocampus by opto-fMRI was similar to already-known hippocampal network.

2 Methods

Animal. Transgenic rats used in our study were Wistar-Thy-1.2 promoter-ChR2-Venus rats (12–13 weeks old) [5]. To perform opto-fMRI, animals were anesthetized with an alpha-chloralose (80 mg/kg) i.p. injection. All experiments were carried out in accordance with animal experimentation protocols approved by the Animal Care and Use Committee of the University of Tokyo, Japan.

fMRI. fMRI scans were conducted with 4.7 T MRI scanner (Varian technologies). We obtained BOLD fMRI data using fast low-angle shot (FLASH) sequence with the following parameters: $tr = 156.2$ ms, $te = 15$ ms, flip angle = 20 deg, field of view = 30×30 mm, acquisition matrix = 128×128 , slice thickness = 1.5 mm, slice number = 6. Structural images were obtained by spin echo (SE) sequence using the following parameters: $tr = 3,000$ ms, $te = 80$ ms, field of view = 30×30 mm, acquisition matrix = 128×128 , slice thickness = 1.5 mm, slice number = 20. We also obtained structural images by diffusion weighted image (DWI) with following parameters: $tr = 3,000$ ms, $te = 50$ ms, b value = $1,496$ s/mm², field of view = 30×30 mm, acquisition matrix = 128×128 , slice thickness = 1.0 mm.

Optical stimulation. A nonmagnetic cannule was inserted through craniotomy into the dentate gyrus (DG: -1.5 mm AP, -3.3 mm ML, -2.8 mm DV) of animals subjected to fMRI. We performed 10 Hz, 10 ms pulsewidth stimulation with 473 nm light (Shanghai Laser). Optical fibers were used with the optical fiber output power level at about 10 mW.

Analysis of fMRI data. We used spm5 software (Wellcome Trust Center Neuroimaging) for pre-processing, including slice realignment, spatial normalization, and smoothing. Statistical analysis was also conducted using spm5. We determined the brain regions displaying significant BOLD changes by student's *t*-test. For making T-contrast images, we analyzed regions showing significant activation ($p < 0.05$, $p < 0.01$, uncorrected) [6].

Immunocytochemistry. Animals were perfused by 4% paraformaldehyde (PFA) after being subjected to fMRI. The brains were removed, post-fixed overnight with 4% PFA at 4°C , and placed in 30% sucrose in phosphate-buffered saline (PBS) for 3 day at 4°C and then frozen at -80°C . The frozen brains were sliced using a cryostat (MICROM, Walldorf) into $40\text{-}\mu\text{m}$ -thick coronal sections. Sections were washed in TBS and stained with DAPI (Sigma, 1/1000). Then, the sections were coverslipped in ImmuMount (Shandon, Pittsburgh). Stained sections were examined using confocal laser scanning microscopy (TCS SP2; Leica, Mannheim). Obtained image data were processed using image processing software (LCS; Leica).

3 Results

We examined the expression of ChR2-Venus in the transgenic rat brain. We identified the expression in the dentate gyrus (DG) and hilus of the hippocampus (Fig. 1a). Also, ChR2-Venus was expressed in the granule cells of granule cell layer (GCL) (Fig. 2b).

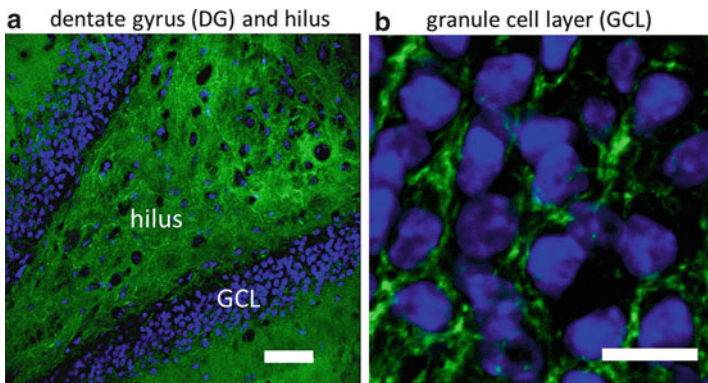


Fig. 1 Expression of ChR2-Venus in the hippocampus. **(a)** Expression of ChR2-Venus in dentate gyrus (DG) and hilus of the hippocampus. *green* : ChR2-Venus, *blue*: DAPI (nucleus), scale bar = $50\ \mu\text{m}$. **(b)** The expression of ChR2-Venus in granule cell layer (GCL). Scale bar = $10\ \mu\text{m}$ (Color figure online)

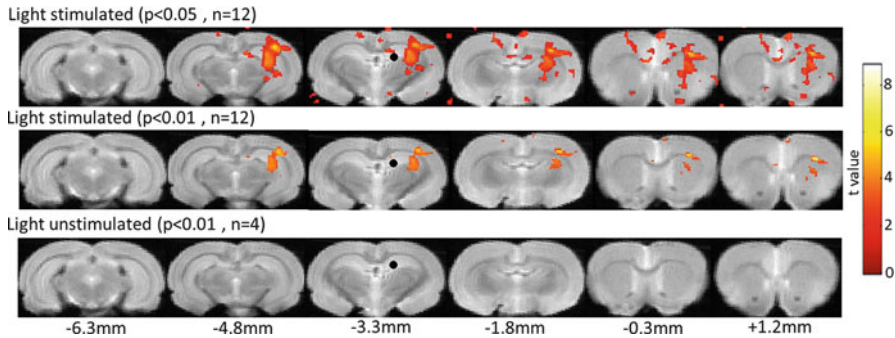


Fig. 2 Response of the hippocampus after light stimulation at DG. A significant BOLD signal change of the hippocampus after light stimulation at DG was observed. Above: light stimulated ($p < 0.05$, $n = 12$), middle : light stimulated ($p < 0.01$, $n = 12$), below : the optic fiber was inserted to the DG but light was not stimulated ($p < 0.01$, $n = 4$). Distance from the bregma is shown as numbers below the figure. The each sections were constituted of 1.5 mm thickness and had ± 0.75 mm thickness as the center in the below number. For example, the section of -3.3 mm from the bregma was constituted of the thickness from -3.96 to -2.64 mm. The black spot is the tip of the optic fiber. Color bar is t-value (Color figure online)

Next, we performed opto-fMRI in the DG of the hippocampus. fMRI BOLD data were obtained by fast low-angle shot (FLASH) sequence. As structural images, we used T2 weighted image (T2WI) by spin echo (SE) sequence and diffusion weighted image (DWI). We confirmed where the location of the canule in the DG using the structural images obtained T2WI. fMRI data was analyzed statistically by spm5. Analyzed data was overlaid on the structural image by DWI and we identified the activated region after light stimulating at DG. As a result, we observed activation of the CA3 region in the hippocampus, when the DG was stimulated by light (Fig. 2). In another region, we observed the activation region in cerebral cortex (visual cortex, somatosensory cortex, and motor cortex), thalamus, and CPu (caudate putamen) (Fig. 2a). We indicate that the thalamus was stimulated by the light of the optic fiber, and the signals from the thalamus were sent to cerebral cortex, because it is under hippocampus and expressed Chr2. Also, we indicate that the signals of the cerebral cortex from the thalamus were projected to CPu.

4 Discussions

In the studies until now, optogenetics and fMRI have been fitted together. We used opto-fMRI and investigated the activity and networks of the hippocampus. As a result, we observed activation of the CA3 region in the hippocampus.

In already-known networks of the hippocampus, the perforant path from the entorhinal cortex (EC) extends to the molecular layer of hippocampus and project to the granule cells of GCL. The granule cells activated by EC pass through mossy

fibers of the granule cells to send the signals to CA3 pyramidal cells [7]. The CA3 pyramidal cells extend the axon called ‘Schaffer collateral’ to CA1 pyramidal cells and project to the region of CA1. The signal of the CA1 pyramidal cells are returned again to EC. Also, the axons of the CA3 pyramidal cells have the property of excitatory feedback to enhance the signals of the CA3 region.

In our study, after the DG was stimulated by light, the region of CA3 was the most activated area. The result indicates that the signals from DG were sent to the region of CA3, and the CA3 pyramidal cells were activated and enhanced by excitatory feedback. In a part of the CA1 region, a little activation was observed. It indicates that the region of CA1 was projected by the activated region of CA3, or directly activated by light due to being located above the DG.

In this study, we succeeded in measuring opto-fMRI BOLD signals of hippocampus. We suggest that this technique is very valuable for measuring the brain activity and network. However, the hippocampal activity is suppressed under anesthesia condition. Therefore, we will need to perform opto-fMRI without the use of anesthesia in order to prevent the reduction of hippocampal activity.

Acknowledgments We thank Drs. Tsurugizawa and Yahata for technical assistance with spm5.

References

1. Lee KM, Durand R, Gradinaru V, Zhang F, Goshen I, Kim DS, Fenno LE, Ramakrishnan C, and Deisseroth K. Global and local fMRI signals driven by neurons defined optogenetics by type and wiring. *Nature* 465: 788–792, 2010.
2. Desai M, Kahn I, Knoblich U, Bernstem J, Atallah H, Yang A, Kopell N, Buckner RL, Graybiel AM, Moore CI, and Boyden ES. Mapping brain networks in awake mice using combined optical neural control and fMRI. *J Neurophysiol*, 2010.
3. Burwell RD. The parahippocampal region: corticocortical connectivity. *A N Y Acad Sci*. 911:25–42, 2000.
4. Claiborne BJ, Amaral DG, Cowan WM. A light and electron microscopic analysis of the mossy fibers of the rat dentate gyrus. *J Comp Neurol*. 22:246(5): 435–58, 1986.
5. Tomita H, Sugano E, Fukazawa Y, Isago H, Sugiyama Y, Hiroi T, Ishizuka T, Mushiake H, Kato K, Hirabayashi M, Shigemoto R, Yawo H, and Tamai M. Visual properties of transgenic rats harboring the channelrhodopsin-2 gene regulated by the thy-1.2 promoter. *PLOS ONE* 4(11): e7674, 2009.
6. Tsurugizawa T, Uematsu A, Ueyama H and Torii K. Effects of isoflurane and alpha-chloralose anesthesia on BOLD fMRI responses to ingested L-glutamate in rat. *Neuroscience* 165: 244–251, 2010.
7. Henze DA, Urban NN, Barrionuevo G. The multifarious hippocampal mossy fiber pathway: a review. *Neuroscience*. 98(3): 407–27, 2000.

Modulation of Cortico–Hippocampal EEG Synchronization with Visual Flicker: A Theoretical Study

Naoyuki Sato

Abstract Visual flicker is known to induce electroencephalography (EEG) at the frequency of the flicker. An induced EEG on the scalp reflects neural synchronization of a number of brain regions, thus it can be expected that visual flicker can be used to probe the synchronization network of multiple regions. In this study, a neural network model is proposed to analyze EEG synchronization in the cortico–hippocampal network in relationship to the flicker. According to results, it is predicted that the flicker phase–locking to the frontal EEG on the scalp can modulate EEG synchronization in the cortico–hippocampal network.

1 Introduction

Visual flicker is known to induce a scalp electroencephalogram (EEG) at the frequency of the flicker [1]. Interestingly, the power of the induced EEG is not fixed but, rather, it depends on the functional state of the subject, such as attention [2] or binocular fusion [3]. This indicates that the connectivity of cortical regions in terms of neural oscillation changes according to the task demands. Thus the visual flicker is expected to be a probe for the functional synchronization network of multiple brain regions.

The dynamics of flicker–induced EEG have been studied with models using nonlinear oscillators [1] of which activity can be phase–locked to periodic inputs in a few oscillation cycles. Unlike neurophysiologically based models [4–6], the description of the nonlinear oscillators does not directly correspond with parameters of real neural networks. However, it has an advantage in qualitatively describing

N. Sato (✉)

Future University Hakodate, 116-2 Kamedanakano, Hakodate, Hokkaido 116-2, Japan
e-mail: satonao@fun.ac.jp

EEG properties by using a small number of parameters. The description of nonlinear oscillators can be used to evaluate the influence of visual flicker on the network of multiple brain regions, such as the cortico–hippocampal network.

In this study, a computational model of the cortico–hippocampal network is proposed to evaluate the ability of visual flicker to of the synchronization network of multiple brain regions. Since it is known that both theta–band (4–8 Hz) EEG power on the scalp [7] and theta–band EEG coherence in the medial temporal lobe [8] are associated with successful memory encoding, we focused on theta–band dynamics in the cortico–hippocampal network.

2 Model

Neural synchronization between brain regions activating at the upper theta band (8 Hz) is modeled. The EEG of each region is modeled by a population of nonlinear oscillators that are assumed to be spontaneously activated in the theta band. Each of the oscillators in a region is inhibitory connected each other and receives the same input from other regions. Next, the population activity shows larger amplitudes for larger inputs in the theta band. The dynamics of the oscillators is described by a phase variable as used in a network model of the hippocampus [9]. EEG of the k -th region, $E^k(t)$, is given by

$$E^k(t) = \sum_{i=1}^N \cos \phi_i^k \quad (1)$$

with

$$\begin{aligned} \frac{1}{\omega} \frac{d\phi_i^k}{dt} = & 1 - (C_F I_k(t) + C_w \sum_{l=1}^M w_{kl} E^l \\ & - C_I E^k + C_e e_i(t)) \sin \phi_i^k \end{aligned} \quad (2)$$

where ϕ_i^k is phase of the i -th oscillator in the k -th region, $I_k(t)$ is input of the flicker, $e_i(t)$ is a perturbation, w_{kl} is the connection strength from the l -th to the k -th region where $\sum_{l=1}^M w_{kl}$ is given to be proportional to the size of each of the cortical regions, and other capital letters denote constants.

In computational experiments, these network structures are used to compare the network dynamics with experimental data. First, a single region is used to evaluate the temporal response of the region to the flicker input. The constants, C_F , C_I , and C_e are determined to show facilitation phenomena during the receipt of flicker input where the EEG power saturates in a half of second [1, 2]. Second, a network consisting of sequentially connected regions is evaluated where flicker input is introduced to one of the network terminals. The constant C_w is determined

to propagate the induced EEG along the connected regions without divergence of the activation in the network. Finally, a cortico–hippocampal network consisting of 35 regions ($M = 35$) with 337 pathways based on anatomical structure [10] is analyzed. The flicker is given to the V1 region and the transmission of the induced EEG is evaluated in relation to the state of the cortico–hippocampal network.

3 Results

3.1 Facilitation of Induced EEG

Figure 1a shows a result of the EEG in a single region. During the introduction of flicker, the amplitude of the EEG gradually increases and saturates over several oscillation cycles. This is in agreement with experimental phenomena [1, 2]. When the global inhibition (C_I) is smaller, the timescale of the induced EEG becomes larger. Without flicker input, as shown in Fig. 1b, the amplitude of the EEG shows a waxing and waning pattern that appears similar to the result of neurophysiological model of EEG [4].

3.2 Transmission of Induced EEG

Figure 2a shows the network structure where flicker input is introduced to Region 1 (R1). Figure 2b shows temporal development of induced EEG power in each region. The induced EEG power appears quickly decrease in relationship to the distance of

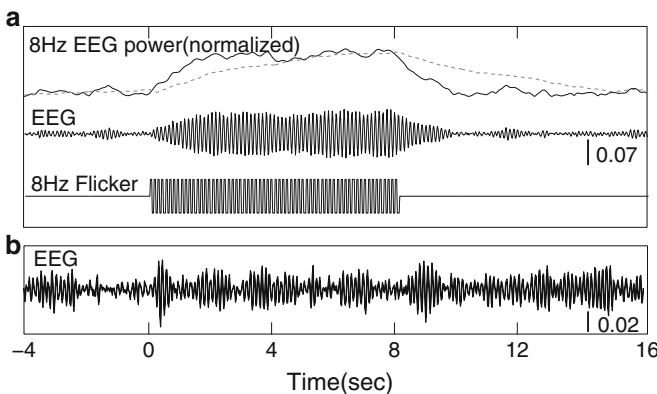
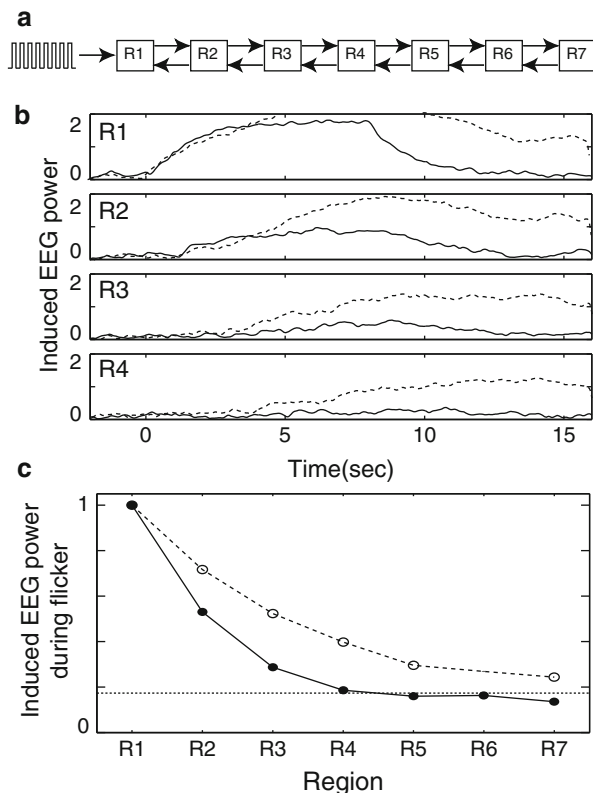


Fig. 1 Temporal evolution of EEG of a single region. (a) Flicker–induced EEG. *Dotted line* indicates a flicker–induced EEG in the case of smaller value of global inhibition, C_I . (b) Spontaneous EEG pattern

Fig. 2 (a) A network of sequentially connected regions. (b) Temporal evolutions of induced EEG powers in Regions R1–R4. *Broken line* indicates induced EEG powers with larger connection strength, C_w . (c) Induced EEG powers during flicker period in each region. *Broken line* indicates the power for larger connection strength (C_w)



each region with R1, as also shown in Fig. 2c. In the case of a larger connection strength (C_w), the induced EEG sustains longer after the offset of the flicker. Such a long duration of induced EEG does not correspond with experimental observations, thus the connection weights between regions were determined to be sufficiently weak in the following experiments.

3.3 EEG Synchronization in Cortico–Hippocampal Network

Figure 3 shows results of induced EEG in the cortico–hippocampal network for three flicker conditions. First, in the case of the introduction of flicker to the V1 region, the induced EEG widely propagates over visual areas and those amplitudes steeply decrease in relationship to the distance of each region with V1 (gray plot in Fig. 3). Such dominance of V1 region in the induced EEG is consistent with the results of source estimation of induced MEG signals [11].

Second, in the case of the introduction of flicker to the entorhinal cortex (ER) that models memory–dependent theta enhancement in the hippocampus, the induced

Fig. 3 Temporal development of induced EEG power of each region in the cortico–hippocampal network. *Filled gray, white, black* plots respectively indicate the EEG power during receiving the flicker only in V1, only in the entorhinal cortex (*ER*) and only in V1 and ER

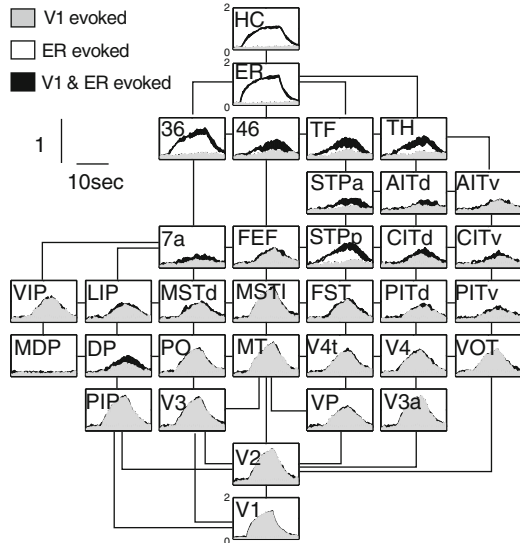
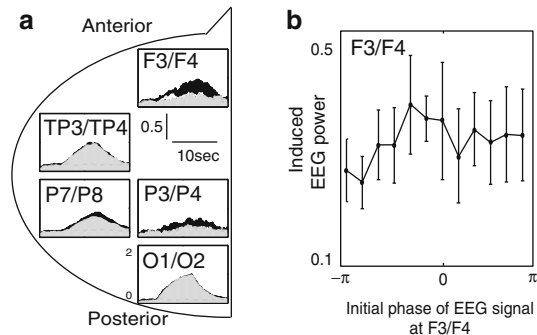


Fig. 4 (a) Induced EEG on the scalp. *Gray, white and black* plots respectively indicate the EEG power during receiving the flicker to V1, ER and both of V1 and ER. (b) Induced EEG power as a function of phase difference between flicker and frontal EEG at the F3/F4 electrode



EEG propagates in a limited region in the medial temporal lobe (white plot in Fig. 3). This could agree with evidence from cats where the oscillation of regions in the medial temporal lobe are closer than those of the neocortex [12].

Third, in the case of the introduction of a synchronous flicker to the V1 and the entorhinal cortex, the resultant induced EEG appears stronger than those of the cases above mentioned. In this case, induce EEG in the regions between V1 and the entorhinal cortex, such as BA46, TF, TH, STP and BA7a, increases. When the induced EEG on the scalp is calculated based on scalp electrode locations with cortical regions [13], these increases of induced EEG power dominantly appear at the frontal and parietal regions on the scalp as shown in Fig. 4a.

What timing of visual flicker can enhance cortico–hippocampal EEG synchronization? By applying asynchronous flicker to V1 and the entorhinal cortex, we evaluated the relationship between induced EEG power and the timing of the flicker to V1. Figure 4b shows our results dealing the induced EEG power as a function of

the flicker's phase with the frontal EEG (at F3/F4 electrode). It shows that the flicker at a specific phase with the frontal EEG can effectively induce the frontal EEG. This prediction can be easily evaluated by using scalp EEG experiments as a verification of the current model.

4 Discussions

Visual flicker is considered to dominantly induce EEG in the primary visual cortex [2], while its effect on the other cortices is still under discussion [3, 11]. The current study showed that the primary visual cortex is a dominant source of the induced EEG on the scalp and the other regions can be also sources under a specific temporal relationship between EEG in these regions and the flicker (Fig. 4b). Such effects can produce an index of EEG synchronization in the network of multiple brain regions. However, it is necessary to further evaluate the ambiguity of the mapping from cortical EEG to scalp EEG during flicker.

Theta synchronization in the hippocampus is theoretically necessary for encoding of the spatio-temporal pattern of behavioral input [9]. During the encoding of the complex environment in the hippocampus, the neocortex is also considered to cooperate with the hippocampus through theta synchronization [14, 15]. The current study predicts that the specific relationship between scalp EEG and the flicker can modulate EEG synchronization in cortico-hippocampal network.

Acknowledgments This work was supported by a Grant-in-Aid for Scientific Research on Innovative Areas "Neural creativity for communication (No.4103)" (20120511) of MEXT, Japan.

References

1. Harada, K., Nishifuji, S., Kai, S., Hirakawa, K. Response of alpha wave to flicker stimulation. *IEICE Transactions* **E74** (6) (1991) 1486–1491.
2. Muller, M.M., Teder-Salejarvi, W., Hillyard, S.A.: The time course of cortical facilitation during cued shifts of spatial attention. *Nat Neurosci* **1**(7) (1998) 631–634.
3. Srinivasan, R., Russell D.P., Edelman G.M., Tononi, G.: Increased synchronization of neuro-magnetic responses during conscious perception. *J Neurosci* **19**(13) (1999) 5435–5448.
4. Jansen, B.H. and Rit V.G.: Electroencephalogram and visual evoked potential generation in a mathematical model of coupled cortical columns. *Biol Cybern* **73** (1995) 357–366.
5. Valdes, P.A., Jimenez, J.C., Riera, J., Biscay, R., Ozaki, T.: Nonlinear EEG analysis based on a neural mass model. *Biol Cybern.* **81** (5-6) (1999) 415–424.
6. David, O., Friston, K.J.: A neural mass model for MEG/EEG: coupling and neuronal dynamics. *Neuroimage.* **20**(3) (2003) 1743–1755.
7. Sato, N., Yamaguchi, Y.: Theta synchronization networks emerge during human object-place memory encoding. *NeuroReport* **18**(5) (2007) 419–424.
8. Fell, J., Klaver, P., Elfadil, H., Schaller, C., Elger, C.E., Fernández, G.: Rhinal-hippocampal theta coherence during declarative memory formation: interaction with gamma synchronization? *Eur J Neurosci.* **17**(5) (2003) 1082–1088.

9. Yamaguchi, Y.: A theory of hippocampal memory based on theta phase precession. *Biol. Cybern.* **89** (2003) 1–9.
10. Felleman, D.J. and Van Essen, D.C.: Distributed hierarchical processing in the primate cerebral cortex. *Cerebral Cortex* **1** (1991) 1–47.
11. Kamphuisen, A., Bauer, M., van Ee, R.: No evidence for widespread synchronized networks in binocular rivalry: MEG frequency tagging entrains primarily early visual cortex. *Journal of Vision* **8** (5) (2008) 1–8.
12. Collins, D.R., Lang, E.J., Pare, D.: Spontaneous activity of the perirhinal cortex in behaving cats. *Neuroscience*. **89**(4) (1999) 1025–1039.
13. Homan, R.W., Herman, J., Purdy, P.: Cerebral location of international 10-20 system electrode placement. *Electroencephalogr Clin Neurophysiol.* **66**(4) (1987) 376–382.
14. Sato, N., Yamaguchi, Y.: On-line formation of a hierarchical cognitive map for object-place association by theta phase coding. *Hippocampus* **15** (2005) 963–978.
15. Sato, N., Ozaki, J.T., Someya, Y., Anami, K., Ogawa, S., Mizuhara, H., Yamaguchi, Y.: Subsequent memory–dependent EEG theta correlates to parahippocampal blood oxygenation level–dependent response. *NeuroReport* **21** (2010) 168–172.

Transition of Firing Patterns in a CA1 Pyramidal Neuron Model

Dan Ma, Shenquan Liu, and Lei Wang

Abstract This paper considered a one-compartment and conductance-based model of CA1 pyramidal neuron. The InterSpike Interval(ISI) bifurcation diagrams were employed to demonstrate the transition modes of different firing patterns. The numerical results show that period-doubling and period-adding bifurcation phenomenon are exist in pyramidal cells in CA1 region.

1 Introduction

Pyramidal neurons are a type of neuron found in areas of the brain including cerebral cortex, the hippocampus, and in the amygdala. The intrinsic discharge mode of individual cortical pyramidal cells varies along a spectrum of “burstiness” from regular firing evoked by depolarization of the neuron to spontaneous bursting unprovoked by any extrinsic stimuli [1, 2]. And a large body of evidence indicates that the propensity of a neuron to burst depends on a large number of internal and external factors, such as the type of ions channel, the ions concentration, the activation of ions channel, depolarizing currents and membrane capacitance etc.

Literatures about pyramidal neuron models and its behaviors are very rich, such as: Durstewitz et al. analyzed the irregular spiking in prefrontal cortex pyramidal neurons [3], Saraga et al. studied the spiking in the rodent hippocampus regulated by inhibitory synaptic plasticity [4], Royeck et al. made a good analysis of NaV1.6 sodium channels in action potential initiation of CA1 pyramidal neurons [5]. Nowadays, except for a larger number of neural electrophysiological experiments, there are many literatures which numerically simulated and analyzed the theoretical neuron models. Rinzel and Terman got abundant of firing patterns and the

D. Ma • S. Liu (✉) • L. Wang

Department of Mathematics, South China University of Technology, Guangzhou 510640, China
e-mail: mashqliu@scut.edu.cn

transmission modes between different neuron models [6, 7]. Izhikevich used the fast and slow bifurcation analysis to classify the various patterns of action potential bursting in detail [8]. The bifurcation patterns of neuronal firing sequences are also interested by other literatures.

With the aid of InterSpike Intervals(ISI) bifurcation diagram, we give a detailed analysis of the variety of firing patterns in this model, and make a further analysis of period bifurcation phenomenon in the transitions of different firing patterns. The simulation results show the complex firing behaviors in CA1 pyramidal cells.

2 Model and Method

The somatic, single-compartment model was represented by coupled differential equations according to the Hodgkin-Huxley-type scheme [9]. The model here was constructed in two stages. In the first stage, we introduced only the ionic currents that are involved in firing dynamics in zero $[Ca^{2+}]_o$, at which it is simpler to analyze. In the second state, we added voltage-gated Ca^{2+} and Ca^{2+} -activated K^{+} currents, to explore their influence on bursting behavior. In this article we only discuss the property of zero $[Ca^{2+}]_o$.

The model includes the currents that are known to exist in the soma and proximal dendrites: the transient sodium current (I_{Na}) and the delayed rectifier potassium current (I_{Kdr}) that generate spikes, and the muscarinic-sensitive potassium current (I_M) that contributes the slow variable necessary for bursting [10, 11]. A model with these three currents only is the minimal model that allows bursting. We added the persistent sodium current (I_{NaP}) because we wanted to focus on its contribution to bursting [1]. The A-type potassium current (I_A) and the leak current (I_L) are included as well. The kinetics equations and parameters are listed in Table 1. The cell model for zero $[Ca^{2+}]_o$ has five dynamical variables: V, h, n, b and z .

Table 1 Kinetics equations and parameters for the zero $[Ca^{2+}]_o$ model

Current, variable	Kinetics/Time Constant, ms	Parameters
I_{Na}, m	$m = m_{\infty}(V)$	$\theta_m = -30 mV, \sigma_m = 10.5 mV$
I_{Na}, h	$dh/dt = \phi_k [h_{\infty}(V) - h] / \tau_k (V)$ $\tau_k(V) = 0.1 + 0.75$ $\times \{1 + \exp[-(V - \theta_{k2}) / \sigma_{k2}]\}^{-1}$	$\theta_k = -45 mV, \sigma_k = -7 mV$ $\theta_{k2} = -40.5 mV, \sigma_{k2} = -6 mV,$ $\phi_k = 1$
I_{NaP}, p	$p = p_{\infty}(V)$	$\theta_p = -45 mV, \sigma_p = 3 mV$
I_{Kdr}, n	$dn/dt = \phi_n [n_{\infty}(V) - n] / \tau_n (V)$ $\tau_n(V) = 0.1 + 0.5$ $\times \{1 + \exp[-(V - \theta_{n2}) / \sigma_{n2}]\}^{-1}$	$\theta_n = -35 mV, \sigma_n = 10 mV$ $\theta_{n2} = -27 mV, \sigma_{n2} = -15 mV,$ $\phi_n = 1$
I_A, a	$a = a_{\infty}(V)$	$\theta_a = -50 mV, \sigma_a = 20 mV$
I_A, b	$db/dt = [b_{\infty}(V) - b] / \tau_b, \tau_b = 15$	$\theta_b = -80 mV, \sigma_b = -6 mV$
I_M, z	$dz/dt = [z_{\infty}(V) - z] / \tau_z, \tau_z = 75$	$\theta_z = -39 mV, \sigma_z = 5 mV$

The current balance equation is:

$$C \frac{dV}{dt} = -I_L - I_{Na} - I_{NaP} - I_{Kdr} - I_A - I_M + I_{app} \quad (1)$$

where $C = 1\mu F/cm^2$, $g_L = 0.05mS/cm^2$, $V_L = 70mV$, and I_{app} is the applied current. The ionic currents are:

$$\begin{aligned} I_{Na}(V, h) &= g_{Na} m_{\infty}^3(V) h (V - V_{Na}), \\ I_{Kdr}(V, n) &= g_{Kdr} n^4 (V - V_K), \\ I_m(V, z) &= g_M z (V - V_K), \quad I_A = g_A a_{\infty}^3(V) b (V - V_K) \\ I_{NaP}(V) &= g_{NaP} p_{\infty}(V) (V - V_{Na}), \quad I_L = g_L (V - V_L) \end{aligned}$$

The activation and inactivation curves $x_{\infty}(V)$ are determined by the equation $x_{\infty}(V) = \{1 + \exp[-(V - \theta_x)/\sigma_x]\}^{-1}$.

Where $x = m, h, p, n, a, b, z$.

3 Simulation Results and Analysis

3.1 The Influence of Membrane Capacitance and External Stimulus

Since neuron membranes are composed of double-membrane phospholipid, the thickness and cytoplasm component are similar, so difference of C for different neurons is not large, but the little distinction always exists as to a variety of neurons. Thus in this section we give an analysis of the influence of C to the generation and conduction of neural action potential sequences and obtains various bifurcation patterns in the model. See Fig. 1a, b for details.

External stimulus is an important factor which can influence neuronal firing activities obviously. See Fig. 1c for more information.

From diagram a~b we can see that with the increasing of C, the firing pattern of CA1 pyramidal neuron changes from period firing modes to period complex bursting, and the spikes in the bursting are increasing too. The firing sequences show a clear period adding phenomenon. In diagram b, with the increasing of C from 0.7 to 1.2, ISIs sequence changes from period-1 firing doubling to period-2 bursting, continues after another period doubling bifurcation turns into period-4 bursting, then turns into period-3 bursting through a complex region, after that turns into period adding bifurcation phenomenon.

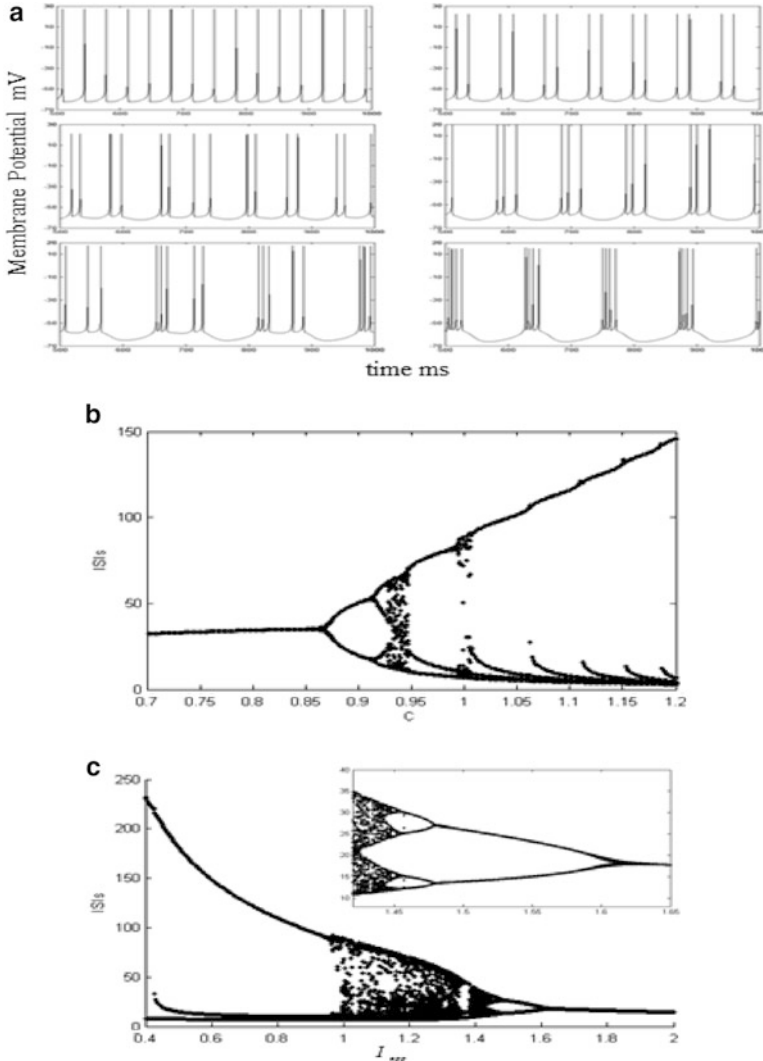


Fig. 1 Firing patterns in the model. (a) Under the stimulation of $I_{app} = 1.0nA$, period adding firing sequences of membrane potential from period-1 to 5 for $C = 0.8, 0.9, 0.93, 0.95, 1.0$ and 1.05 respectively. (b) Corresponds to diagram a, the bifurcation diagram of C vs. ISIs. (c) The bifurcation diagram of I_{app} vs. ISIs, the diagram on the top right corner is the enlargement of diagram c

From the analysis of diagram c, we know that with the decreasing of dc stimulus from 2 to 0.4, the ISIs sequence of this neuron model change from period-1 firing doubling to period-2 bursting, continue after two period doubling bifurcations reach to period-8 bursting, then turn into period-3 bursting through a complex region.

3.2 *The Influence of the Transient Sodium Current*

In the description of the classical HH model, the change of sodium ion conductance and potassium ion conductance are determined by three variables: m , h and n , where the change of m and h determine the amplitude of sodium ion current, and the change of n determine the amplitude of potassium ion current. The change speed of these variables determine ion channel current's amplitude at different time, and then influence the firing pattern of action potential, so the perturbation of ion channel variable is critical in the activities of neuron. In this part, we make a simple discussion about the variables m , h of the transient sodium current. See Fig. 2a, b, c for details.

At present, there is still a lot of literature in which the influence of ions channel conductance and ions equilibrium potential to neuron activity were investigated. In this section, by changing the ion conductance and ion equilibrium potential of transient sodium current, rich bursting patterns and the bifurcation phenomenon in the switching between different patterns of firing are obtained. See Fig. 2d.

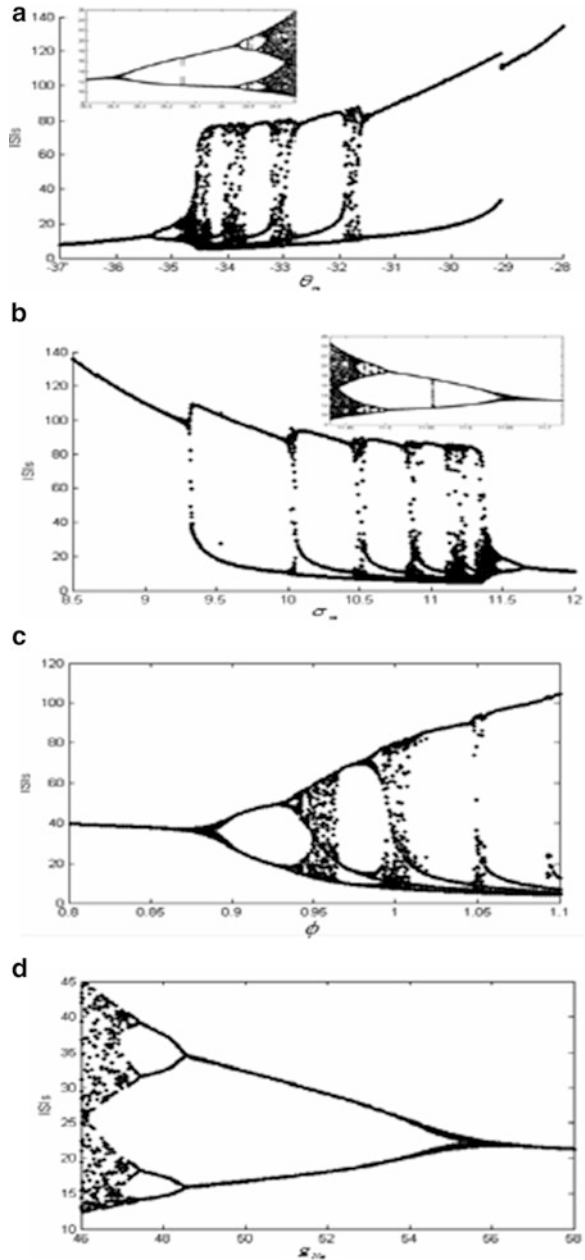
From the above figures we can get several bifurcation patterns in neuronal action potential ISIs. In diagram a~b, the sequences of action potential ISIs show a clear bifurcation phenomenon with the perturbation of ion channel variable m . Both diagram a and b contain a clear period doubling phenomenon, a clear period adding phenomenon and a clear inverse period doubling phenomenon. In diagram c, we can see the period doubling bifurcation and period adding bifurcation clearly. So we know only a little change of the perturbation variables m and h of the transient sodium current can change the firing modes of CA1 pyramidal neuron easily. And the ISIs sequences have good bifurcations. Diagram d shows the influence of the ion conductance of transient sodium current to neuron activity. With the decreasing of g_{Na} from 58 to 46, the ISIs sequence of this neuron model appears three period doubling bifurcations, and then turns into a complex region.

The numerical results above show that the perturbation variables and ion conductance of transient sodium current have great influence on neuronal activities (action potential). These rich bursting patterns and the switching between different patterns of firing tell us that transient sodium current is very important in the generation of the rich bursting.

4 Discussions

From the analysis of simulation results in this paper we can find that the firing modes in zero $[Ca^{2+}]_0$ model of CA1 pyramidal neuron are very rich. And it allowed us to use a single-compartment model to analyze the underlying mechanism of bursting. The model results above tell us that the CA1 pyramidal neuron can show a variety of firing patterns when the electrophysiology parameters vary in a certain region, not only periodic spiking but also various bursting patterns. The ISI bifurcation

Fig. 2 Bifurcation diagrams of neuronal action potential ISIs. **(a)** ISIs vs. θ_m . **(b)** ISIs vs. σ_m . **(c)** ISIs vs. ϕ ($\phi_h = \phi_n$). **(d)** ISIs vs. g_{Na}



phenomenon we drew can show more intuitive results of how these firing patterns change from one pattern to another, the period doubling phenomenon and the period adding phenomenon contained in the ISI bifurcation diagrams tell us the intrinsic properties of corresponding parameters on the spiking transition modes and firing

patterns in the CA1 pyramidal neuron. In fact many others parameters in this model can affect the fire patterns transition, such as the delayed rectifier potassium current, A-type potassium current and A-type potassium current et al and all these currents change demonstrate the basic rule of neuron codes.

Acknowledgments This work is supported by the National Nature Science Foundation of China under Grant Nos. 10872069.

References

1. Yue, C.Y., Remy, S., Su, H.L., Beck, H., Yaari, Y.: Proximal persistent Na⁺ channels drive spike after depolarizations and associated bursting in adult CA1 Pyramidal Cells. *J. Neurosci.* 25(42) (2005) 9704–9720
2. Su, H., Alroy, G., Kirson, E.D., Yaari, Y.: Extracellular calcium modulates persistent sodium current-dependent burst-firing in hippocampal pyramidal neurons. *J. Neurosci.* 21 (2001) 4173–4182
3. Durstewitz, D., Gabriel, T.: Dynamical basis of irregular spiking in NMDA-driven prefrontal cortex neurons. *Cerebral Cortex* 17 (2007) 894–908
4. Saraga, F., Wolansky, T., Dickson, C.T., Woodin, M.A.: Inhibitory synaptic plasticity regulates pyramidal neuron spiking in the rodent hippocampus. *Neuroscience* 155 (2008) 64–75
5. Royeck, M., Horstmann, M.T., Remy, S., Reitze, M., Yaari, Y., Beck, H.: Role of axonal NaV1.6 sodium channels in action potential initiation of CA1 pyramidal neurons. *J. Neurophysiol* 100 (4) (2008) 2361–2380
6. Rinzel, J., Lee, Y.S.: Dissection of a model for neuronal parabolic bursting. *J. Math. Biol.* 25 (1987) 653–675
7. Terman, D.: The transition from bursting to continuous spiking in excitable membrane models. *J. Nonlinear Sci* 2 (1992) 135–182
8. Izhikevich, E.M.: *Dynamical systems in neurosciences: the geometry of excitability and bursting*. Cambridge: The MIT Press, 2005
9. Golomb, D., Yue, C., Yaari, Y.: Contribution of persistent Na⁺ current and M-type K⁺ current to somatic bursting in CA1 pyramidal cells: combined experimental and modeling study. *J. Neurophysiol* 96 (2006) 1912–1926
10. Yue, C., Yaari, Y.: KCNQ/M channels control spike afterdepolarization and burst generation in hippocampal neurons. *J. Neurosci* 24 (2004) 4614–462
11. Yue, C., Yaari, Y.: Axo-somatic and apical dendritic Kv7/M channels differentially regulate the intrinsic excitability of adult rat CA1 pyramidal cells. *J. Neurophysiol* 95 (2006) 3480–3495

The Effects of Leakage Conductance on Firing Properties in a Compartment Neuron Model

Lei Wang and Shenquan Liu

Abstract Leakage current is a critical factor which can balance ions flow across channels in neuron. In this study, a simple case is considered about the influence of leakage conductance g_L on neuronal firing activities in a two compartment model, the detailed analysis includes two aspects: (1). the values of g_L in the two compartments are equal, (2). the values of g_L in the two compartments are not equal. With computer simulation, it is found that numerical results obtained from the variation of g_L in somatic compartment and dendritic compartment show much difference, simulation results obtained from variation of g_L in dendritic compartment have much similarity with results got in case (1) when g_L varies, while the variation of g_L in soma gives some difference with the case in (1). In the final the changing of membrane capacitance to the potential spike is also discussed here. All these results may give us a general rule of neuronal firing properties.

1 Introduction

As to neuronal intrinsic properties, such as their bio- chemistry, the distribution of ion channels, and cell morphology contribute to the electrical responses of neurons [1, 2]. The influence of ion channels on neuronal firing properties has been subject to intensive research due to their physiological significance and dynamical complexity [3, 4], while the leakage current which plays the central role of balancing ions flow across channels in neuron is well worth studied [5].

Literatures on the study of leakage conductance are rich. Schreiber et al. studied the effect of leakage conductance on spiking reliability of cortical neurons for

L. Wang • S. Liu (✉)

Department of Mathematics, South China University of Technology, Guangzhou 510640, China
e-mail: mashqliu@scut.edu.cn

suprathreshold rhythmic inputs [6]. Wang et al. analyzed the hopf bifurcation induced by leakage conductance in Hodgkin-Huxley model [7], and Yin et al. presented a bifurcation analysis with the change of parameter potassium leakage current in a thalamic relay neuron model [8]. In the present paper, we explore the influence of leakage conductance g_L on firing activities in a two-compartment pyramidal neuron, various firing patterns are obtained with the change of g_L , with the aid of InterSpike Intervals (ISI) bifurcation diagram, it is found that the transition between different firing patterns with parameter g_L shows an apparent periodic bifurcation phenomenon, by considering two cases about the value of g_L in somatic compartment (g_{Ls}) and dendritic compartment (g_{Ld}), similarity is found between g_L and g_{Ld} , while difference is observed between g_L and g_{Ls} . Simulation results presented here can not only illustrate the important role of g_L in the generating, conducting and switching of various neuronal action potential patterns, but also give the transition modes from which we can see how these firing patterns change from one to another.

2 Model and Method

The model we investigated in this paper is a two compartment model of pyramidal neuron [9], the schematic diagram of this neuron is shown in Fig. 1, in the diagram, the ionic currents in each compartment are given. The somatic compartment includes only the channels necessary for spike generation (Na^+ and K^+) while the dendritic compartment includes a slow potassium and a persistent sodium current.

The model description of this pyramidal neuron is the following equations.

$$C_m \frac{dV_s}{dt} = -I_{Na} - I_K - I_{Ls} - \frac{g_c}{p}(V_s - V_d) + I_{soma}$$

$$C_m \frac{dV_d}{dt} = -I_{NaP} - I_{KS} - I_{Ld} - \frac{g_c}{1-p}(V_d - V_s) + I_{dendrite}$$

where I_{soma} and $I_{dendrite}$ are current injections to the compartment. The voltage dependent conductances are described using standard Hodgkin-Huxley formalism, detailed expressions and parameters can be found in [9].

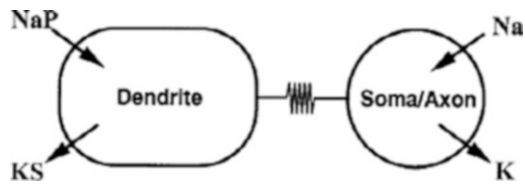


Fig. 1 Two-compartment model of cortical pyramidal neuron [9]

Simulations were performed using MATLAB software, and the fourth-order Runge–Kutta algorithm was employed to calculate the values of membrane potential with time step being 0.01 ms. We only inject direct current into the dendritic compartment, and investigated the somatic action potential in this study.

3 Simulation Results and Analysis

In the model description, we have noticed that the value of g_L can influence leakage current I_L so as to impact on neuronal firing activities. For the important role of g_L in neuronal action potential generation and propagation, next, we give detailed analysis about the influence of g_L on neuronal firing patterns under two aspects, which are presented in Sects. 3.1 and 3.2, with computer simulation, a variety of firing patterns are obtained when g_L varies in a certain region, and the transition of these patterns show a clear periodic bifurcation phenomenon with the change of g_L .

3.1 The Case $g_{Ls} = g_{Ld}$

In this section, we assume the values of g_L in the two compartments are equal, that is $g_{Ls} = g_{Ld} = g_L$, the detailed simulation results are demonstrated in Fig. 2.

From Fig. 2a1–a9 we can see that the cell has a clear period-adding firing phenomenon, with the decrease of g_L from 0.4 to 0, the cell period-adding bifurcates from period-1 spiking to period-2 bursting, and then period-adding bifurcates to period-3 bursting, this period-adding bifurcation phenomenon lasts until the period number reaches eight and then bifurcates back to period-1 bursting in this parameter region. Figure 2b can show an obvious period-adding bifurcation phenomenon between different firing patterns, while in Fig. 2c the transition rule of firing patterns shows much difference with Fig. 2b when $C_m = 0.5$, this may give us some new insights into the role of C_m which can be given attention in further studies. Simulation results shown in Fig. 2 can provide us an apparent variation rule on how g_L impacts on neuronal burst firing sequences.

3.2 The Case $g_{Ls} \neq g_{Ld}$

In this section, we consider the value of g_L in somatic and dendritic compartment are different which means $g_{Ls} \neq g_{Ld}$, detailed simulation results are demonstrated in Figs. 3 and 4.

(1) Variation of g_{Ld} when $g_{Ls} = 0.18$.

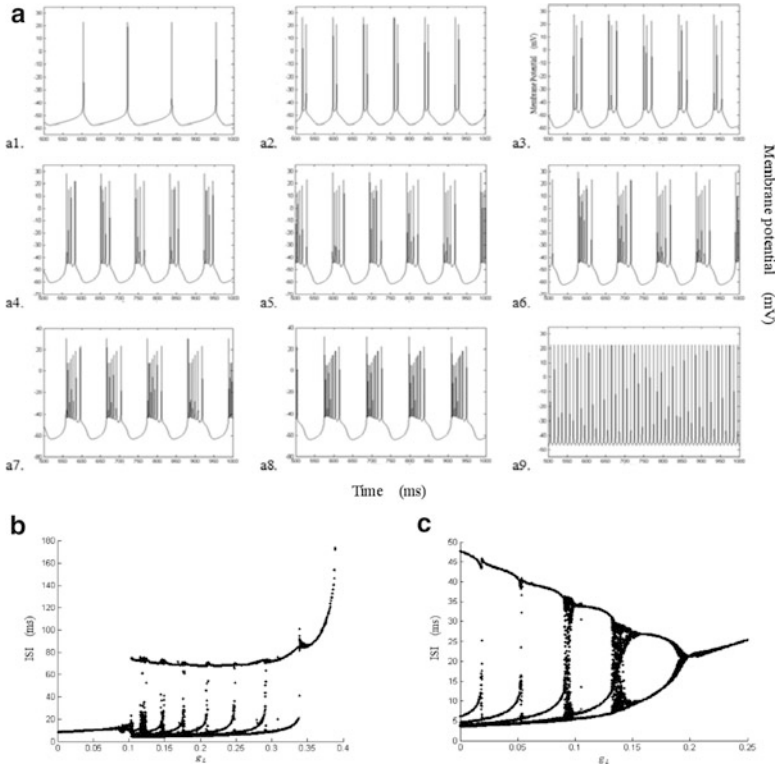


Fig. 2 Periodic firing sequences and ISI bifurcation diagrams in pyramidal neuron. (a1–a9) are periodic firing sequences with the decrease of g_L , the value of g_L is 0.38, 0.3, 0.28, 0.23, 0.2, 0.17, 0.14, 0.11 and 0.05, time scale:500–1,000(ms). (b) Bifurcation diagram of ISI with g_L . (c) Bifurcation diagram of ISI with g_L when $C_m = 0.5$

We can see from Fig. 3a1–a9 that the cell can also show a clear period-adding firing phenomenon, with the decrease of g_{Ld} from 0.4 to 0, the cell period adding bifurcates from period-1 spiking to period-2 bursting, and then period-adding bifurcates to period-3 bursting, this period adding bifurcation phenomenon lasts until the period number reaches eight and then bifurcates back to period-1 bursting in this parameter region, we can find it easily that this transition rule is much similar with the one demonstrated in Fig. 2.

(2) Variation of g_{Ls} when $g_{Ld} = 0.18$.

Figure 4a1–a6 gives us an apparent appearance on the period-adding phenomenon with the decrease of g_{Ls} from 1.5 to 0, but by observing Fig. 4b, c we can find that the bifurcation diagrams are very different with the ones demonstrated in Figs. 2b and 3b if g_{Ls} varies in the region similar as Figs. 2b and 3b, then the question is arisen that why the change of g_L in dendritic compartment can induce a bifurcation patterns similar with Fig. 2b, while the variation of g_L in

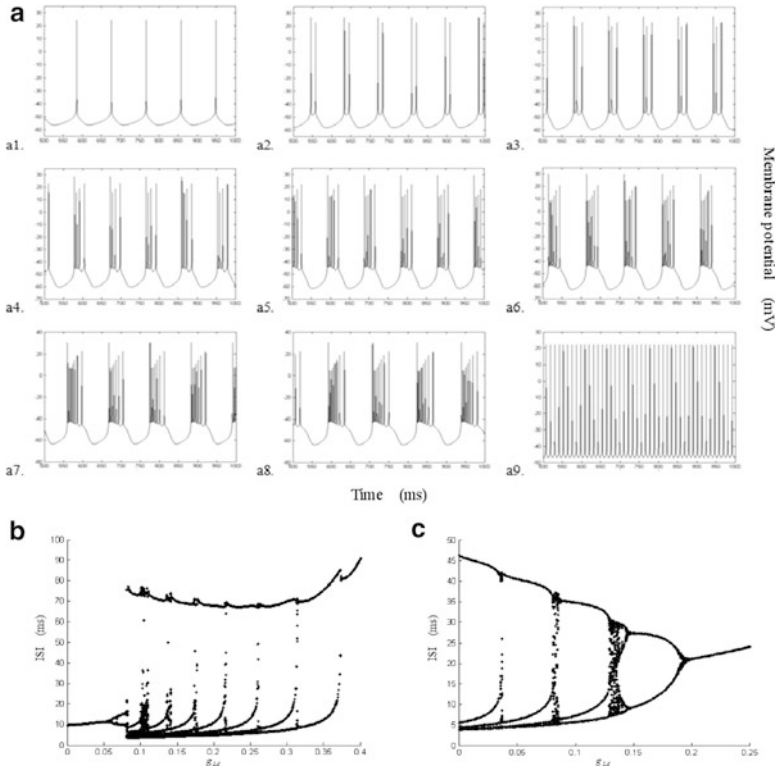


Fig. 3 Periodic firing sequences and ISI bifurcation diagrams in pyramidal neuron. (a1–a9) are periodic firing sequences with the decrease of g_{Ld} , the value of g_{Ld} is 0.4, 0.35, 0.3, 0.25, 0.2, 0.15, 0.13, 0.1 and 0.05, time scale:500–1,000(ms). (b) Bifurcation diagram of ISI with g_{Ld} . (c) Bifurcation diagram of ISI with g_{Ld} when $C_m = 0.5$

somatic compartment show so much difference with Fig. 2b. The reason may be that burst firing is usually induced in neuronal dendrites, intracellular recordings on hippocampal CA1 pyramidal cells shown that burst firing is more likely elicited in dendrites than soma [10]. In this model the crucial rule in bursting generation are the ionic currents located in dendritic compartment, so the change of g_{Ld} can have great impacts on burst firing patterns and the influence on their transitions is vital, while the change of g_{Ls} can not change the bursting shapes or firing patterns greatly, so the bifurcation diagram in Fig. 4c varies little when comparing with Figs. 2c and 3c.

In fact, many factors can influence the spike activity of neuron and their bifurcation diagram always appears from period-adding to chaotic phenomena. If we consider the changing of capacity of soma and dendrite, we can get the model results in the following Sect. 3.3.

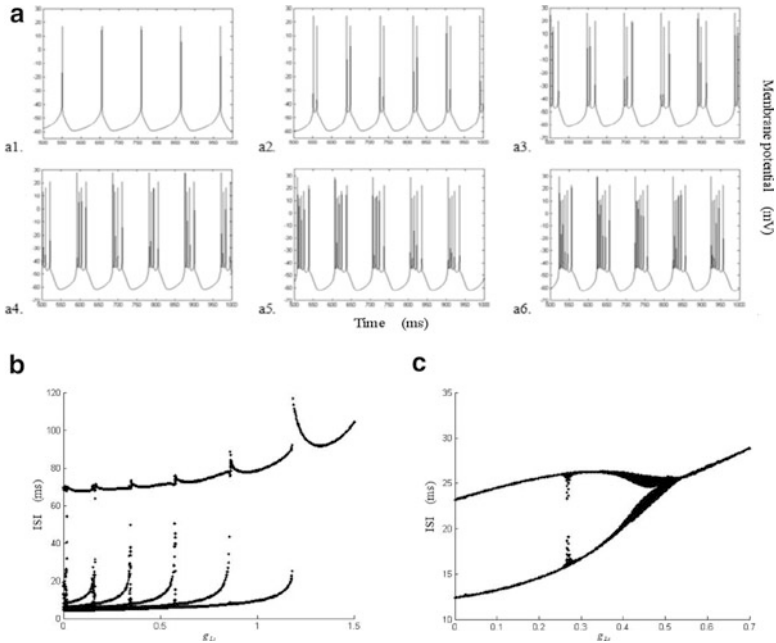


Fig. 4 Periodic firing sequences and ISI bifurcation diagrams in pyramidal neuron. (a1–a6) are periodic firing sequences with the decrease of g_{Ls} , the value of g_{Ls} is 1.5, 1.0, 0.8, 0.5, 0.3 and 0.1, time scale: 500–1,000(ms). (b) Bifurcation diagram of ISI with g_{Ls} . (c) Bifurcation diagram of ISI with g_{Ls} when $C_m = 0.5$

3.3 Variation of C_m

In this section, we assume the values of C_m in the two compartments are equal, the detailed simulation results are demonstrated in Fig. 5.

We can see from Fig. 5a1–a6 that the cell has a clear period-adding firing phenomenon, with the increase of C_m from 0.1 to 1.2, the cell period-adding bifurcates from period-1 spiking to period-2 bursting, and then period-adding bifurcates to period-3 bursting, this period-adding bifurcation phenomenon lasts until the period number reaches seven in this parameter region. Figure 5b can show an obvious period-adding bifurcation phenomenon between different firing patterns. These simulation results can give us an apparent variation rule on how C_m impacts on neuronal firing sequences in this neuron.

4 Discussions

By determining the exact mechanisms of neuronal leakage current impacts on firing properties of neuron, one can gain insights into the influence of leakage conductance on firing behavior and the nature of transition between them. These

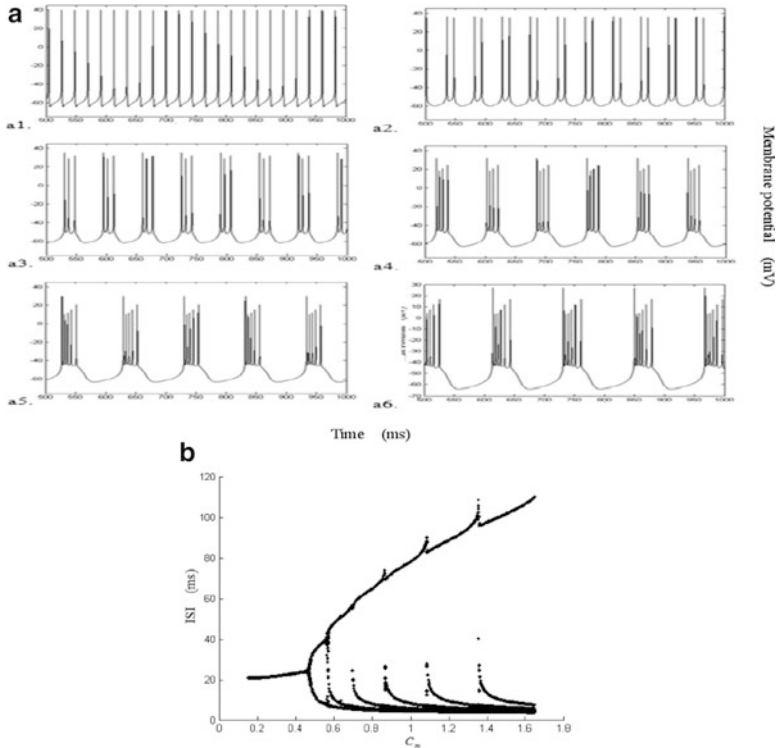


Fig. 5 Periodic firing sequences and ISI bifurcation diagram in pyramidal neuron. (a1–a6) are periodic firing sequences with the increase of C_m , the value of C_m is 0.3, 0.5, 0.6, 0.8, 1.0 and 1.2, time scale: 500–1,000(ms). (b) Bifurcation diagram of ISI with membrane capacitance C_m

understanding can facilitate the studying of leakage current in neuron models and neuron networks. In this paper, we give a detailed analysis of the impacts caused by leakage conductance in a two-compartment pyramidal neuron and obtain several theoretical results:

- (1) Various firing patterns can be obtained when g_L varies, and transition of these patterns can show a clear period-adding bifurcation phenomenon with the variation of g_L .
- (2) From the detailed analysis of g_L in two aspects,

we find that the change of g_L in dendritic compartment in the second aspect can give the similar results with the one in the first aspect, while the variation of g_L in somatic compartment in the second aspect have much difference with the one in the first aspect.

As in the present paper, we have mainly discussed the role of leakage conductance g_L on neuronal firing properties, for the parameter g_L we have discussed has electrophysiology significance, so the simulation results we get are meaningful and

instructive. Other parameters such as: membrane capacitance, external stimulus, and environmental temperature et al., which can be given full attention in the future studying of this neuron model.

Acknowledgments This work is supported by the National Nature Science Foundation of China under Grant Nos. 10872069.

References

1. Mainen, Z., Sejnowski, T.: Influence of dendrite structure on firing pattern in model neocortical neuron. *Nature* 382 (1996) 363–366
2. Schreiber, S., Fellous, J.M., Tiesinga, P., Sejnowski, T.J.: Influence of ionic conductances on spike timing reliability of cortical neurons for suprathreshold rhythmic inputs. *J Neurophysiol* 91 (2004) 194–205
3. Duan, L.X., Lu, Q.S., Wang, Q.Y.: Two- parameter bifurcation analysis of firing activities in the Chay neuronal model. *Neurocomputing* 72 (2008) 341–351
4. Xu, J., Clancy, C.E.: Ionic mechanisms of endogenous bursting in CA3 hippocampal pyramidal neurons: a model study. *PLoS ONE* 3(4) (2008) e2056(1–12)
5. Hodgkin, A.L., Huxley, A.F.: A quantitative description of membrane current and its application to conduction and excitation in nerve. *J Physiol* 117 (1952) 500–544
6. Schreiber, S., Fellous, F.M., Tiesinga, P., Sejnowski, T.J.: Influence of ionic conductances on spike timing reliability of cortical neurons for suprathreshold rhythmic inputs. *J Neurophysiol* 91 (2004) 194–205
7. Wang, J., Chen, L.Q., Fei, X.Y.: Analysis and control of the bifurcation of Hodgkin-Huxley model. *Chaos, Solitons & Fractals* 31 (2007) 247–256
8. Yin, H.B., Cox, C.L., Mehta, P.G., Shanbhag, U.V.: Bifurcation analysis of a thalamic relay neuron model. *American Control Conference* 10–12 (2009) 337–342
9. Kepecs, A., Wang, X.J.: Analysis of complex bursting in cortical pyramidal neuron models. *Neurocomputing* 32–33 (2000) 181–187
10. Wong, R.K., Stewart, M.: Different firing patterns generated in dendrites and somata of CA1 pyramidal neurones in guinea-pig hippocampus. *J Physiol* 457 (1992) 675–687

Numerical Analysis of Parkinson's Disease in a Basal Ganglia Network Model

Xiaofeng Xie, Shenquan Liu, Xuemiao Pan, and Lei Wang

Abstract The paper constructed a network of basal ganglia and considered the normal state, Parkinson Disease (PD) state and Deep Brain Stimulation (DBS) therapy in this basal ganglia (BG) model. The membrane potential of neurons in BG are obtained with the help of Winnerless Competition (WLC) model. The indexes of EI (Error Index) and phase plane are used in normal state, PD state and DBS therapy state respectively to show the validity of the DBS therapy. In the end, we add the receptor and effector to this network to discuss the neural network information processing of BG and explore what effect that different kinds of connectivity strength between the cortical neurons bring to the network information processing.

1 Introduction

Parkinson's disease is a common disease in basal ganglia, although a number of experiments are carried on the neuroprotective treatment of Parkinson's disease in these years, and some positive results are obtained in basic research [1]. While in neuroscience, only clinical tests are not enough to cure the disease efficiently, it needs some researches on theoretical side to supplement the shortage of clinical trial, mathematical model is one of the main theoretical analysis method. Studies

X. Xie

College of Automation Science and Engineering, South China University of Technology, Guangzhou 510640, People's Republic of China

S. Liu (✉) • L. Wang

Department of Mathematics, South China University of Technology, Guangzhou 510640, People's Republic of China

e-mail: mashqliu@scut.edu.cn

X. Pan

School of Electronic and Information Engineering, South China University of Technology, Guangzhou 510640, People's Republic of China

on neuronal network have last for long times, many neuron models have been analyzed, such as: Hodgkin-Huxley (HH) model, Chay model, and Hindmarsh-Rose (HR) model which are useful models. In recent years, Rabinovich has put forward a network model which can simulate the response of olfactory neural systems named as WLC model [2], and model study of PD can also use this method. Alejandro Pascual [3] proposed that HH model can be used to analyze the DBS therapy that is applied to PD patients. They all study the processing of DBS therapy with simulation in mathematical models, and give theoretical analysis from the mechanisms of Subthalamic nucleus (STN) high frequency simulation in PD patients. For the treatments method of DBS, selection of targets is usually very important, generally there are three kinds of targets: STN, the internal segment of the globus pallidus (GPi), and ventral intermediate (VIM), so in clinical trial, target is selected after doing some testes in PD patients. There are two pathways, direct pathway and indirect pathway. Through these two ways, BG can modulate people's action and balance the relationship between these two pathways precisely [4].

2 Method/Models

According to the study of Frank MJ [4] about decision-making model in neurological conditions, we have constructed a basal ganglia network model which contains thalamus, cerebral cortex, and basal ganglia. See the following network model we constructed for more details. There are four kinds of nerve nuclei are included by the basal ganglia: (1) striatum, it is main receiver which receives the information from thalamus, cerebral cortex and the brainstem and it includes two kinds of receptors, D1 receptor and D2 receptor; (2) substantia nigra, it includes substantia nigra pars compacta (SNc), substantia nigra pars reciculata. The Dopamine Neurons to make up the Substantia nigra pars compacta and products the dopamine to modulate the striatum; (3) Internal globus pallidus and external globus pallidus, as we know, they are connected to the substantia nigra pars reciculata in functions. And γ -aminobutyric acid (GABA) is neurotransmitter both in internal globus pallidus and substantia nigra pars reciculata (SNr); (4) STN, as we find, it is connection with substantia and globus pallidus from the anatomy. We constructed the frontal cortex and thalamus as external construction connected with the basal ganglia to build a network (Fig. 1).

There are three kinds of effect from Dopamine: excitatory, inhibitory and modulatory for the D1 and D2 receptors. As computational model, we consider Dopamine from the SNc excites synaptically driven direct pathways via D1 receptors and inhibits indirect pathways activity via D2 receptors [4].

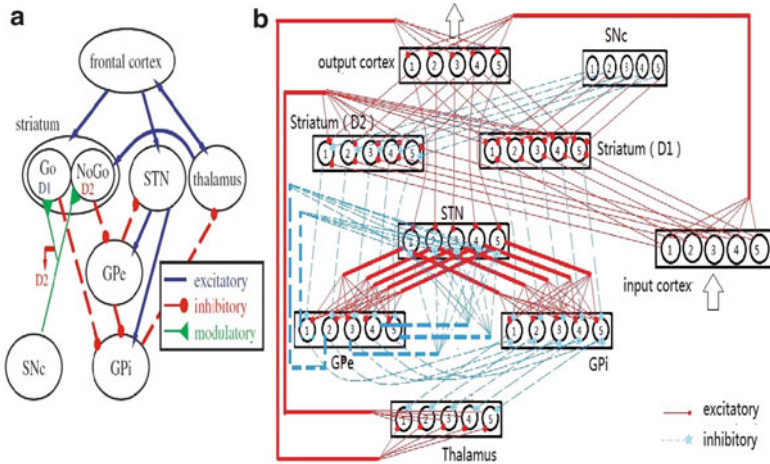


Fig. 1 (a) The basal ganglia network from the Frank MJ [4] research. (b) The basal ganglia network we constructed. One STN cell activates five GPi cells and five GPe cells. One GPe cell inhibits five STN cells. The else connection are one to one. Input cortex direct activate output cortex to ensure the network enough strong output signal

3 Numerical Analysis of Model Results

3.1 Analysis the Discharge of Parkinson’s disease

Physically, the PD definition is no dopamine or little dopamine from SNc lead to the basal ganglia out of order. In mathematical model, we give a definition for the PD that no or little stimulus on SNc. And the DBS therapy is giving high frequency stimulus on corresponding target spots without giving SNc additional stimulus. According to this definition, we can get the four discharge graph of normal people, PD patient, STN-DBS patient and GPi-DBS patient through mathematical model calculation.

In Fig. 2a, by giving the input cortex nerve nucleus group a $0.3\cos(0.15 t)$ sine-signal electrical stimulus, we can get normal people’s discharge graph of BG network. Figure 2b doesn’t give signal stimulus to SNc, simulating no dopamine from SNc. Obviously, there are many neurons present resting phenomenon, such as GPi, STN, striatum, while Thalamus and GPe present full discharge phenomenon. By giving high frequency square wave stimulus to STN and GPi, simulating the DBS therapy, like (c) and (d), the BG network will produce cluster discharge again, especially the Thalamus and Striatum.

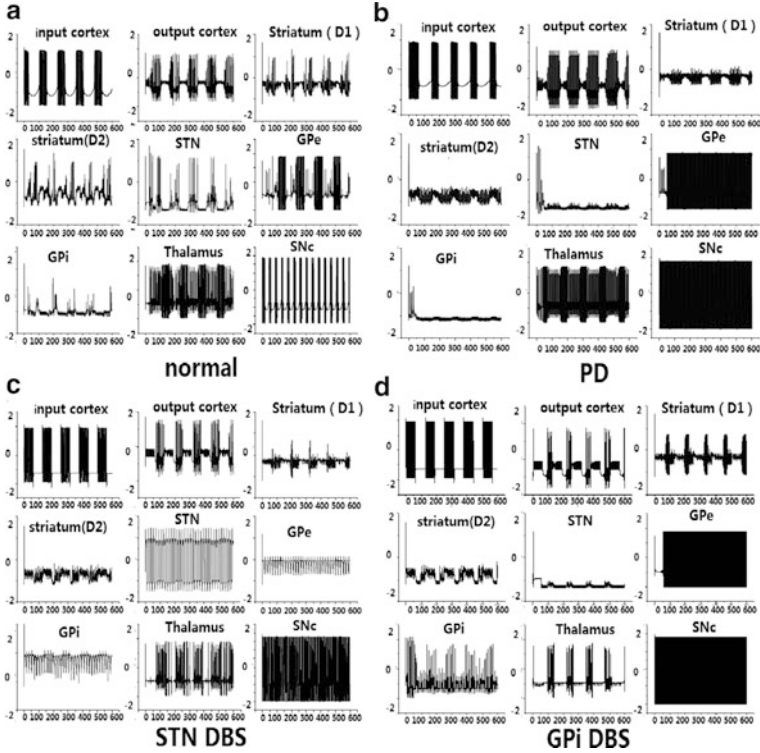


Fig. 2 Four types of discharge graph (normal PD STN-DBS and GPi-DBS state). (a) is the firing pattern of normal state in the BG network. The order is Input and Output cortex, D1 and D2, STN, GPe, GPi thalamus and SNc. The same with (b), (c), (d)

3.2 Analysis for the Index

3.2.1 Analysis of PD Using Index EI

According to the research [3], they proposed the Error Index from the research of signal degradation. The signal degradation can be show by the number of the peak in the discharge. There are three type of peak area: normal peak area, incomplete peak area and lost peak area. We define the 90–100% value of maximum peak amplitude as the normal peak area (M_{zc}); the 20–90% value of maximum peak amplitude as the incomplete peak area (M_{cq}); the rest as the lost peak area(M_{ss}). So we concluded the value of EI index:

$$EI = M_{cq}/M_{zc}$$

Calculation of the EI for normal person, PD patient and the DBS patient is shown in the following Fig. 3:

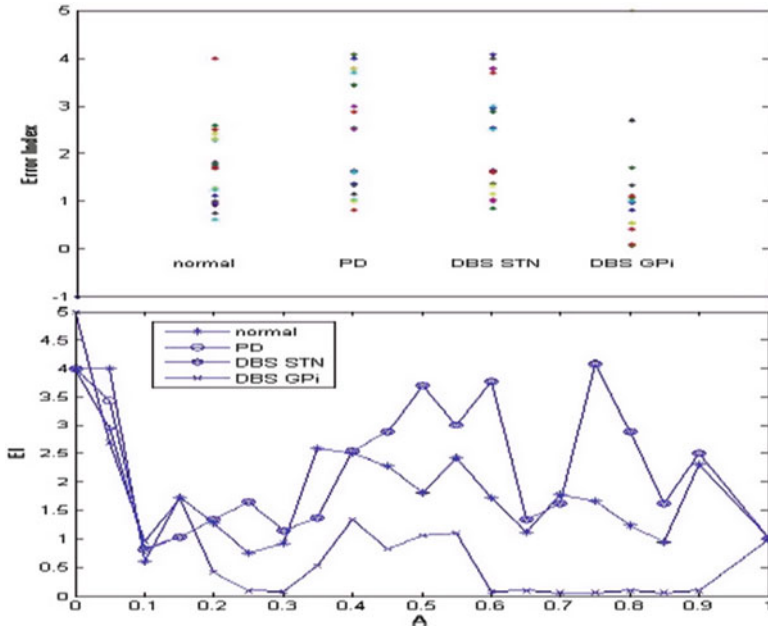


Fig. 3 Four types of EI index in the different input situation, the amplitude of input signal (A) changes from 0 to 1 and calculate the corresponding EI index

In Fig. 3, the PD patient EI index is above the normal person EI index. After the DBS treatment, give the high frequency stimulation to the STN or GPi for PD patient, the PD patient EI index decrease and close to the normal person EI index. The PD patient appears the state of hand and foot unsteady and fidget due to the signal from the basal ganglia to the output cortex neurons lost some information. In the discharge, it means that the number of incomplete peak increases and the number of normal peak decreases, the EI index becomes larger. The abnormal signal degradation lead to the PD patient cannot effectively control action by themselves.

3.2.2 Analysis of PD Using Phase Diagram Index

We propose the phase diagram index to explain the mechanism of signal degradation by choose the GPi-thalamus neuron channel. The GPi neuron is the efferent neuron of basal ganglia and the channel which signal had to pass. It also can describe to the condition of the transmission channel.

In Fig. 4, the normal phase diagram is bigger than the PD phase diagram in the x-coordinate's span. After the STN DBS treatment and GPi DBS treatment, the x-coordinate's span becomes large and close to the normal phase diagram.

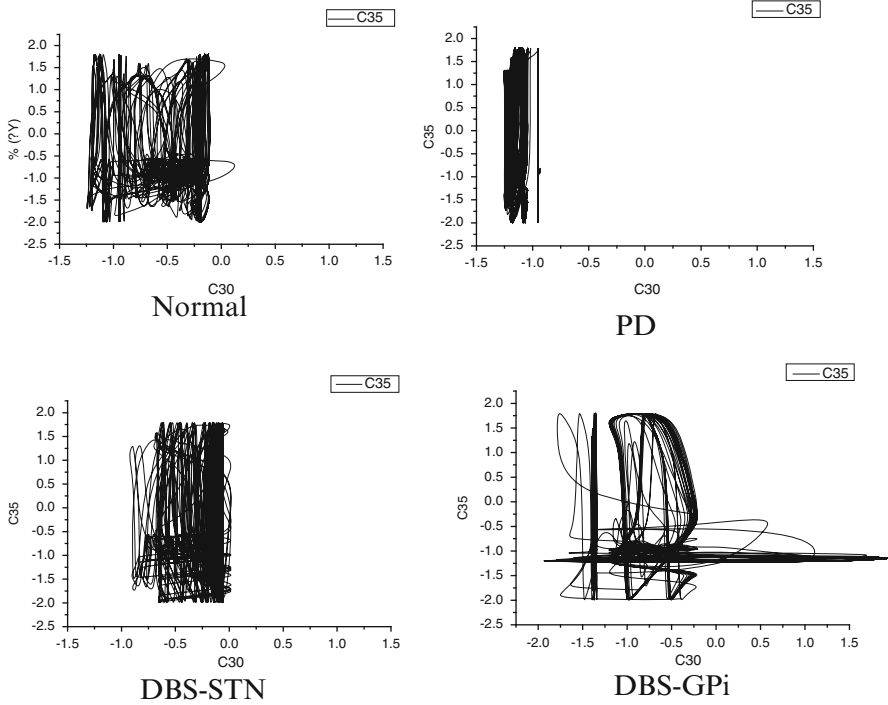


Fig. 4 Four type of phase diagram index in the GPI-thalamus channel. x-coordinate is potential of GPI neuron and y-coordinate is potential of thalamus neuron

The lack of the Dopamine from the SNc leads to the GPI-thalamus channel shows the problem about the functional barriers. The signal from basal ganglia lost in the channel.

4 Discussion

4.1 Network Expansion

As illustrated in Fig. 5, we expand the BG network, add the input cell and output cell to the cerebral cortex, which representing the receptor and effector. According to Jim Houk’s research about Motor cortex-Basal Ganglia-Cerebellum Circuit [5], the connection between input cell and input cortex is excitatory, so it is with Thalamus. And the connection between output cell and output cortex is excitatory, while it is inhibitory with Thalamus.

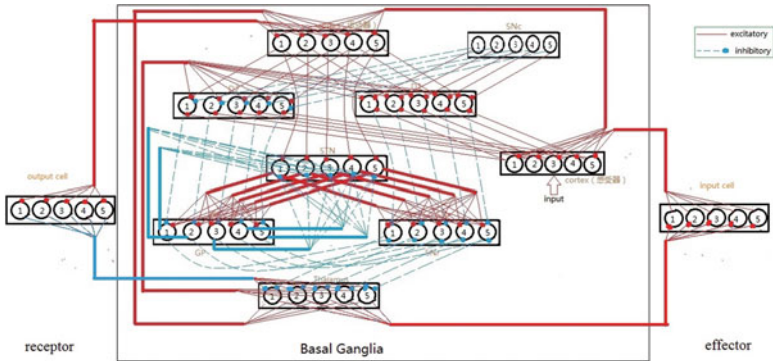


Fig. 5 The expanded network connection though adding the input cell and output cell to the cerebral cortex, which representing the receptor and effector

4.2 Discuss the Connectivity Strength

Inferring from the principle of signal superposition, after signal entering the input cortex, there are two routes to flow: one is directly from input cortex to output cortex; the other one is from input cortex to BG and then to output cortex. The linking strength directly from input cortex to output cortex is related to the BG adjustment effect. When the strength increases, the signal transmission is mainly from cortex, weakening the BG adjustment effect.

From the Fig. 6a, we can find that when there is no link between input cortex and output cortex, the output signal is hazy without clear cluster discharge. Under this situation, the output signal comes from BG without directly transmitted signal from input cortex. Increase the linking strength, clear cluster discharge appears in the output cortex and the output signal is superposition of two routes of signal. The output signal frequency is the same, but the amplitude of each peak changes, so as other neurons of BG.

5 Conclusions

By means of WLC model, we have constructed a network model of BG, through the comparison of three states: PD state, normal state and DBS therapy state, several PD patients’ features in BG are concluded:

- (1) Five-neuron system of BG network can respond to five different stimulus and simulate five neuron pathways, indicating connections among them.
- (2) Cortex and GPi are mainly neurons for information output. Cortes is the output nucleus group of BG network and GPi is the output nucleus group of BG. They often remain active and have rich information.

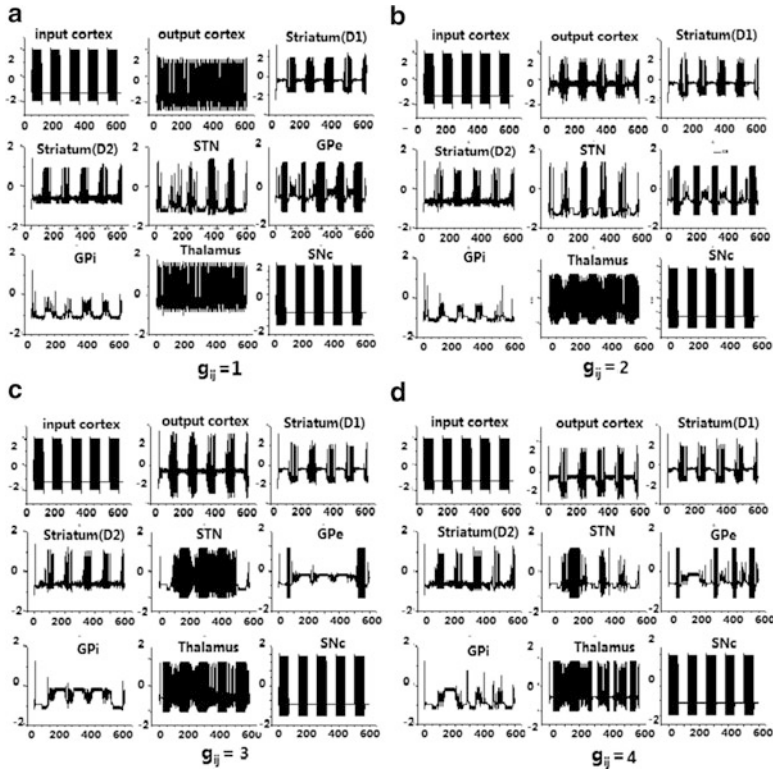


Fig. 6 The results of changing linking strength between the input cortex and output cortex. It is reflected by the Connection value in the WLC model

(3) With different input, the discharge of SNc remains the same. But if we give the SNc stimulus which can change from weakly to strong, then the obvious branches phenomenon will appears and there is only one branch point.

Finally, expanding the network is good for analysis of the BG information processing procedure. By adding the receptor and effector to the BG network, we can get the discharge of the receptor and effector and finally learn the whole procedure of BG network information processing. And to discuss the linking strength between the input and output cortex.

Acknowledgments This work is supported by the National Nature Science Foundation of China under Grant Nos. 10872069.

References

1. Olanow, C.W., Kieburtz, K., Schapira, A.H.: Why have we failed to achieve neuroprotection in Parkinson's disease? *Ann Neurol* 64 (2008) 101–110
2. Rabinovich, M., Volkovskii, A., Lecanda, P., Huerta, R., Abarbanel, H.D., Laurent, G.: Dynamical encoding by networks of competing neuron groups: winnerless competition. *Phys Rev Letter* 87 (2001) 068102
3. Pascual, A., Modolo, J., Beuter, A.: Is a computational model useful to understand the effect of deep brain stimulation in Parkinson's disease? *J Integr Neurosci* 5 (2006) 541–559
4. Frank, M.J., Scheres, A., Sherman, S.J.: Understanding decision-making deficits in neurological conditions: insights from models of natural action selection, *Phil Trans R Soc B* 362 (2007) 1641–1654
5. Houk, J.: Models of basal ganglia. *Scholarpedia*, 2 (2007) 1633.

ERRATUM

Advances in Cognitive Neurodynamics (III)

Yoko Yamaguchi

Y. Yamaguchi (ed.), *Advances in Cognitive Neurodynamics (III)*,
DOI 10.1007/978-94-007-4792-0,
© Springer Science+Business Media Dordrecht 2013

DOI 10.1007/978-94-007-4792-0_110

Unfortunately not all editors of the book have been named and we would like to clarify the correct order of editors:

Takashi Omori
Brain Science Institute
Tamagawa University
Tokyo, Japan

Yoko Yamaguchi
Laboratory for Dynamics of Emergent Intelligence
RIKEN Brain Science Institute
Wako City, Japan

Yutaka Sakaguchi
Information Systems
University of Electro-Communications
Tokyo, Japan

Naoyuki Sato
Future University Hakodate
Hokkaido, Japan

Ichiro Tsuda
Research Institute for Electronic Science
Hokkaido University
Hokkaido, Japan

Index

A

Abe, K., 443, 599
Abe, Y., 803
Aihara, K., 9, 97, 213, 331, 641
Aihara, T., 387, 765
Alan Fung, C.C., 131
Alexander, D.M., 303
Allison, E., 429
Alnajjar, F., 267
Amari, S., 31, 123, 169
Aonishi, T., 649
Aoto, F., 673
Arai, Y., 673
Arai, Z., 665
Arie, H., 615
Arita, T., 339
Asada, M., 251
Asai, Y., 113
Asano, T., 559
Avinash, M., 543
Ay, N., 147, 499

B

Babu, K.S., 543
Bányai, M., 787
Bett, D., 429

C

Chakravarthy, V.S., 53, 69, 543
Chander, B.S., 69
Chao, Z.C., 745
Cichocki, A., 175

D

Dauwels, J., 175
Delgado-García, J.M., 491
Detorakis, G.Is., 281
Devasahayam, S., 543
Diesmann, M., 91, 317
Diwadkar, V., 787
Dudchenko, P.A., 429

E

Elgendi, M., 175
Érdi, P., 787

F

Feng, J., 169
Fenton, A.A., 421
Firouzi, M., 59
Fujii, H., 97, 683
Fujii, N., 745
Fujii, T., 437, 781
Fujimoto, A., 575
Fujita, K., 221
Fukai, T., 161
Fukazawa, Y., 803
Fukuda, H., 191
Fukushima, Y., 387, 635
Furukawa, T., 567
Furusawa, Y., 691

G

Garcia-Ojalvo, J., 475
Gepshtein, S., 289

Gruart, A., 491
Gupta, A., 543

H

Hara, Y., 227
Harper, D.N., 401
Hartono, P., 355
Hasegawa, N., 745
Hashimoto, T., 453, 523
Hayasaka, N., 191
Hidaka, S., 347
Hilgetag, C.C., 77, 207
Hisatsune, T., 803
Honma, K., 185
Honma, S., 185
Hütt, M.-T., 77

I

Ide, Y., 765
Inagaki, K., 515
Inamura, T., 607
Ishihara, T., 469
Isomura, Y., 635, 773
Izawa, J., 559
Izuma, K., 623

J

Jurica, P., 303

K

Kaefer, K., 429
Kanamaru, T., 97
Kandaswamy, D., 543
Kaneko, K., 379, 509, 537
Karube, F., 45
Kashimori, Y., 227, 297
Katayama, M., 591
Katori, Y., 9
Kawaguchi, N., 691
Kawaguchi, Y., 45
Kawasaki, M., 717
Kay, L.M., 17
Kelemen, E., 421
Kelso, J.A.S., 259
Kim, J.W., 83
Kinoshita, J., 393
Kitajo, K., 155, 509, 717
Kitano, H., 113
Kleberg, F., 717
Kokubu, H., 665

Konno, T., 453
Kozma, R., 233
Kubota, Y., 45
Kumar, M., 543
Kuniyoshi, Y., 243, 727
Kurikawa, T., 537
Kurusu, T., 591
Kuroda, S., 635

L

Lauwereyns, J., 393, 765, 773
Lee, S.-Y., 3
Leleu, T., 641
Li, Y., 551
Liu, S., 817, 825, 833
Lu, W., 169

M

Ma, D., 817
Maithreye, R., 53
Mathiak, K., 303
Matsumoto, K., 623
Matsumoto, M., 623
Matsuoka, K., 531
Matsushita, S., 567
Minoya, K., 339
Miyazaki, A., 795
Miyota, R., 155
Montúfar, G., 147
Mori, H., 243
Mori, R., 673
Morita, J., 453
Morizono, M., 251
Murayama, K., 623
Mushiake, H., 9, 331, 691, 795
Muto, Y., 297
Myers, M.H., 233

N

Nagai, T., 443, 599
Nagasaka, Y., 745
Nagase, Y., 297
Nakada, K., 531
Nakagawa, Y., 155
Nakajima, T., 795
Nakamura, W., 199
Nakatani, C., 311
Nakatani, H., 325
Namikawa, J., 615
Nara, S., 673
Natsume, K., 759

Nikolaev, A.R., 289, 303
Nishida, H., 393
Nishida, S., 575
Nishikawa, J., 629
Nishimoto, R., 615
Nishimura, M., 759
Nishiura, Y., 371
Nomura, M., 45
Nomura, T., 113
Norihiro, S., 623
Notoya, T., 745

O

Obayashi, I., 665
Ogawa, T., 575
Ohkubo, T., 567
Ohsaki, H., 803
Oka, H., 113
Okada, M., 649
Okanoya, K., 629
Oku, M., 213
Okuda, J., 437, 781
Okumura, T., 657
Okuno, K., 607
Omori, T., 339, 443, 599, 649
Onaka, T., 753
Ono, D., 185
Osada, M., 657

P

Pan, X., 833
Pipa, G., 475
Pitti, A., 727
Pons, A.J., 475
Ponzi, A., 139
Postnova, S., 105
Potjans, T.C., 91

R

Rauh, J., 147
Rebsamen, B., 175
Robinson, P.A., 23, 83, 105
Rostami, M.G., 59
Rougier, N.P., 281
Russo, E., 483

S

Saito, N., 331, 691
Sakagami, M., 409
Sakaguchi, Y., 461, 559

Sakamoto, K., 9, 331, 691
Sakurai, Y., 773
Samejima, K., 623
Sánchez-Campusano, R., 491
Sancristóbal, B., 475
Sato, N., 809
Sato, Y.D., 123, 531
Sekino, M., 803
Shima, K., 9, 795
Shimaoka, D., 509
Shimono, M., 155
Shimotomai, T., 599
Shouraki, S.B., 59
Sugisaki, E., 387
Sumioka, H., 251
Suzuki, M., 437
Suzuki, Y., 347

T

Takahashi, M., 393, 765, 773
Takayanagi, Y., 753
Tani, J., 267, 275, 615
Tanji, J., 331, 691
Tateno, T., 699
Teramae, J., 161
Teramoto, T., 371
Tognoli, E., 259
Tokuda, I., 191
Torii, T., 523
Trappenberg, T., 355
Tregove, C., 317
Treves, A., 483
Tsubo, Y., 161
Tsuda, I., 97, 415, 551, 635, 683
Tsukada, H., 683
Tsukada, M., 37, 387, 635, 765, 773

U

Ueno, A., 781
Uno, Y., 155
Usui, S., 515

V

van Leeuwen, C., 289, 303, 311, 317
Vialatte, F., 175
Vicente, R., 475

W

Wagatsuma, H., 363
Wang, L., 817, 825, 833

Wang, S., 207
Wang, Y., 753
Waxman, D., 169
Wickens, J., 139
Wong, K.Y.M., 131
Wood, E.R., 429
Wu, S., 131

X

Xie, X., 833

Y

Yadome, M., 371
Yamaguchi, Y., 155, 325, 509, 717

Yamaguti, Y., 635, 683
Yamamoto, K., 331
Yamanaka, K., 155
Yamashita, Y., 267, 275
Yanagita, T., 583
Yawo, H., 803
Yokoyama, A., 443, 599
Yoshida, M., 711
Yoshikawa, Y., 251

Z

Zahedi, K., 499
Zhou, C., 77, 207
Zvyagintsev, M., 303